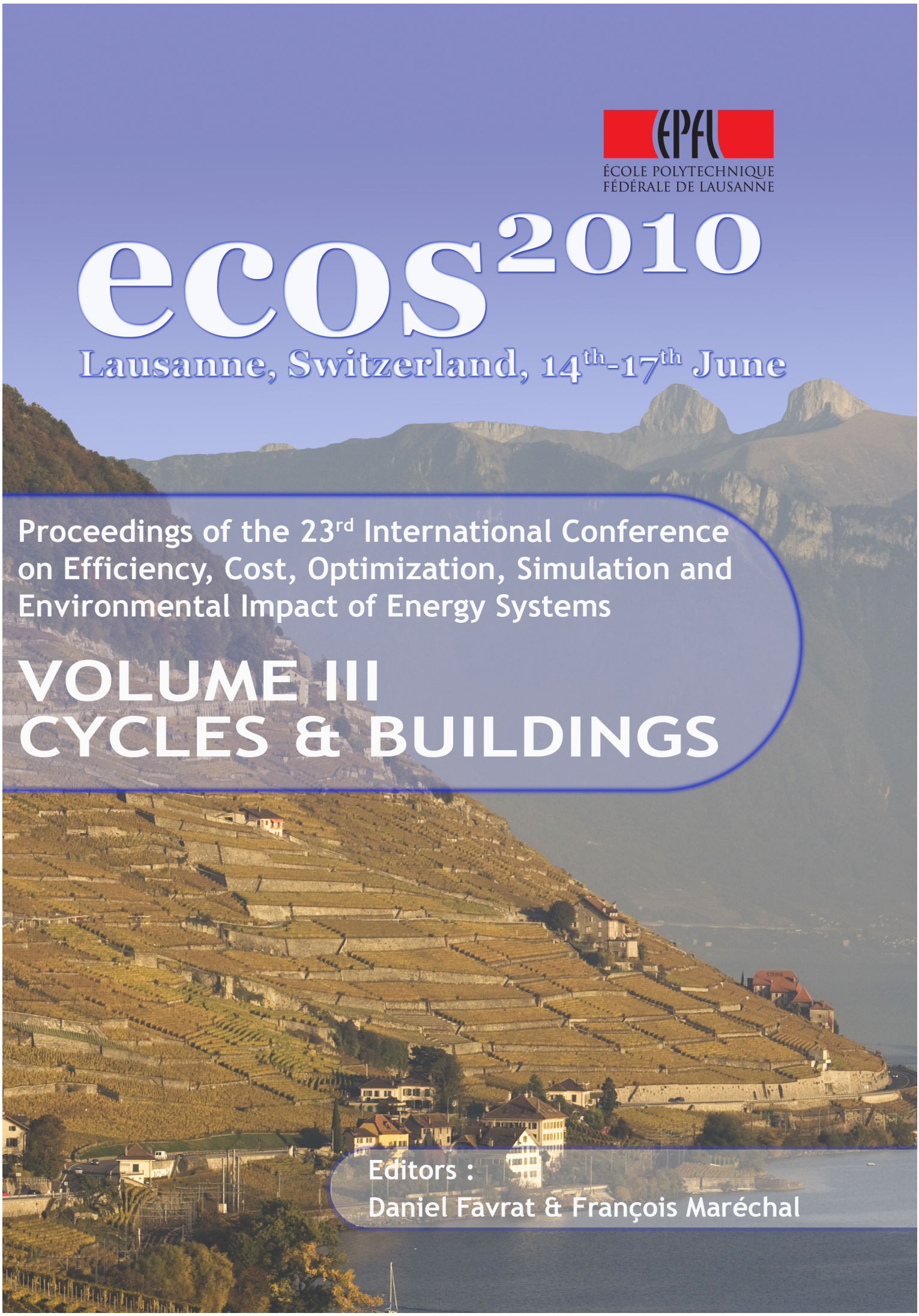
ÉCOLE POLYTECHNIQUE
FÉDÉRALE DE LAUSANNE
ecos2010
Lausanne, Switzerland, 14th-17th June
Proceedings of the 23rd International Conference on Efficiency, Cost, Optimization, Simulation and Environmental Impact of Energy Systems
VOLUME III
CYCLES & BUILDINGS
Editors :
Daniel Favrat & François Maréchal

ecos2010

Proceedings of the 23rd International Conference on
Efficiency, Cost, Optimization, Simulation,
and Environmental Impact of Energy Systems

Lausanne, Switzerland
June 14-17, 2010

Volume III
Cycles & Buildings

Editors
Daniel Favrat and François Maréchal

Organised by
Laboratoire d'Énergétique Industrielle (LENI)
École Polytechnique Fédérale de Lausanne (EPFL)

Official Website of the conference
www.ecos2010.ch

Corresponding e-mail
ecos2010@epfl.ch

Corresponding address
EPFL / LENI – ISE - STI
Bat. ME A2
Station 9
CH-1015 Lausanne
Switzerland

Book creation
Nicolas BORBOËN, Yannick BRAVO

PREFACE

Energy plays a major role in human societies. The supply of energy services is also a major contributor to the global and, too often, local environmental problems the World is facing. According to the International Energy Agency, actions to target future CO_2 concentrations in atmosphere below either 550ppm, or even below 450ppm, will have to be primarily focused on efficiency. A broader use of renewable, nuclear power and perhaps carbon sequestration will also contribute. To maintain a viable economic development these actions will have to be cost effective while globally reducing all emissions and caring about energy and material resources. A systemic approach is therefore essential to get a holistic vision, design better systems and optimize money and resources utilization.

The ECOS conferences have a long tradition in fostering the key aspects and the scientific knowledge that are essential for the engineers. The organizers of this 23rd edition are proud to acknowledge one of the largest participation ever with many original and high quality papers.

Our thanks go to the authors who accepted to travel from all continents and meet in Lausanne to present and share their scientific contributions. Many thanks also to all reviewers and members of the scientific committee who contributed to the quality of these proceedings. The conference chairmen are also grateful to the local organizing team including in particular, Nicolas Borboën, Stina Zufferey, Brigitte Gabioud, Yannick Bravo, Suzanne Zahnd and Irène Laroche. Many thanks also to the other members of the Industrial Energy Systems Laboratory of EPFL, the MEDIACOM EPFL team and the sponsors who greatly helped the organization of this fruitful event.

Daniel Favrat & François Maréchal

ORGANISING COMMITTEE

Prof. Daniel Favrat (chairman)
François Maréchal (chairman)

Nicolas Borboën, Yannick Bravo, Brigitte Gabioud,
Irène Laroche, Suzanne Zahnd, Stina Zufferey

INTERNATIONAL ADVISORY BOARD

Ozer Arnas, United States
Christos A. Frangopoulos, Greece
George Tsatsaronis, Germany

SCIENTIFIC COMMITTEE

Monika Axel, Sweden
Rangan Banerjee, India
Adrian Bejan, United States
Thore Berntsson, Sweden
Asfaw Beyene, United States
Paolo Bosshard, Italy
Denis Clodic, France
Stephen R. Connors, United States
R.L Cornelissen, Netherlands
Michel Feidt, France
Carl-Johan Fogelholm, Finland
Richard Gaggioli, United States
Yalçın A. Göğüş, Turkey
Gershon Grossman, Israel
Simon Harvey, Sweden
Abel Hernandez-Guerrero, Mexico
Gerard Hirs, Netherlands
Andrew Forbes Alexander Hoadley, Australia
Koichi Ito, Japan
Hervé Jeanmart, Belgium
Signe Kjelstrup, Norway
Jiri Klemes, Hungary
Zygmunt Kolenda, Poland
Andrea Lazzaretto, Italy
Noam Lior, United States
Sylvie Lorente, France
Giampaolo Manfrida, Italy
Philippe Mathieu, Belgium
Alberto Mirandola, Italy
Michael Moran, United States
Zhang Na, China
Silvia Azucena Nebra, Brazil
Eduardo de Oliveira Fernandes, Portugal
Silvio de Oliveira Júnior, Brazil
Ricardo Rivero, Mexico
Marc A. Rosen, Canada
Dominick A. Sama, United States
Peter Schossig, Germany
Enrico Sciubba, Italy
Luis M. Serra, Spain
Samuel Stucki, Switzerland
Pascal Terrien, France
Jules Thibault, Canada
Daniel Tondeur, France
Vittorio Verda, Italy
Laura Vanoli, Italy
Michael R. von Spakovsky, United States
Carl-Jochen Winter, Germany
Li Zheng, China
Andrzej Ziębik, Poland
Ron Zevenhoven, Finland

Thermodynamic analysis of a scroll-type Ericsson engine

Y. M. Kim[a], D. G. Shin[b], S. T. Lee[c] and Daniel Favrat[d]

[a,b] *Korea Institute of Machinery & Materials, Daejeon, Korea*
[c] *Wooshin Industrial Co. Ltd., Kyungsan-si, Korea*
[d] *Swiss Federal Institute of Technology of Lausanne (EPFL), Lausanne, Switzerland*

Abstract: Stirling and Ericsson engines each have great potential for many applications, including micro-cogeneration, solar power, and biomass. However, ideal cycles of both types of engines are difficult to achieve in practice because neither isothermal compression nor isothermal expansion is practical with reciprocating piston engines or with turbomachinery. On the other hand, scroll compressor and expander can be very suitable for effective cooling and heating because of the high area-to-volume ratio of scroll geometry or the application of two-phase flow. To achieve quasi-isothermal compression, either a large amount of liquid is injected into the inlet of the compressor or the compressor is externally cooled by liquid. Similarly, for quasi-isothermal expansion, either hot liquid, such as thermal oil, is injected into the inlet of the expander or the expander is externally heated by a heat source. In this current study, we have undertaken a theoretical investigation of thermodynamic analyses of several kinds of scroll-type engines, in particular with regard to associated compression and expansion processes, adiabatic or quasi-isothermal processes, and the highest cycle temperature. We selected power density, or thermal efficiency, as an objective function, and then deduced optimal design parameters for the scroll-type engine.

Keywords: Ericsson engine, scroll compressor/expander, CO_2 cycle

1. Introduction

Although external combustion engines, such as the Stirling engine and the Ericsson cycle engine, are very promising and have many potential applications (i.e., micro-cogeneration, solar power, and biomass), there are still some drawbacks to realize the potentiality of them. Until now, small-scale external combustion engines have been using reciprocating piston engines or turbomachines. However, the scroll compressor has been used extensively for refrigeration since the early 1980s because of its excellent efficiency, great reliability, smooth operation, low noise, and minimum vibration. Recent use of the scroll mechanism is expanding, albeit in a niche market.

Our research began with the aim of developing a new external combustion engine utilizing scroll machines. In this current study, we have undertaken a theoretical investigation of thermodynamic analyses of several kinds of scroll-type engines, in particular with regard to associated compression and expansion processes, adiabatic or quasi-isothermal processes, and the highest cycle temperature. We selected power density, or thermal efficiency, as an objective function, and then deduced optimal design parameters for the scroll-type engine.

2. System description

2.1. Scroll-type Ericsson engine

Although the theoretical Ericsson cycle is made up of two isothermal processes and two isobaric processes, the real Ericsson engine is a Joule (or Brayton) cycle reciprocating piston engine with external heat supply and recuperator. A scroll-type Ericsson engine consists of one paired scroll compressor and scroll expander, as shown in Fig. 1 [1].

The scroll-type Ericsson engine has several advantages compared to the reciprocating Ericsson engine. First, there is no need for a valve system to isolate the cylinders. Second, it is possible to approach two isothermal processes because the scroll compressor and expander can be very effective for cooling and heating owing to the high area-to-volume ratio of the scroll geometry or the application of two-phase flow. In the process of compression, heat generated in the compression space between the orbiting scroll and the fixed scroll of the scroll compressor is carried to the

Corresponding Author: Young-Min Kim, Email: ymkim@kimm.re.kr

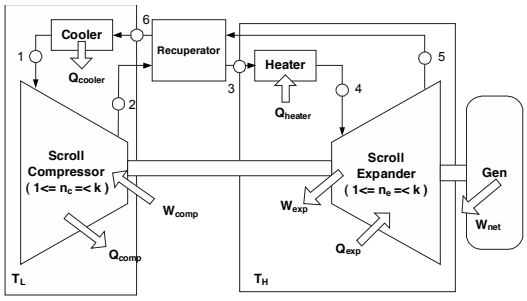

Fig. 1. Schematic of scroll-type Ericsson engine

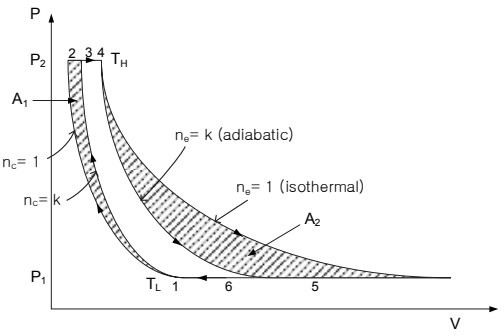

Fig. 2. Brayton and Ericsson cycle (P-V plot)

external dump (cooling fluid) through liquid injection or external cooling. Then the compressed working fluid enters the inlet port of the scroll expander. In the process of expansion, heat is added from an external heat source (heating fluid) to the working fluid in the expansion space through external heating or injection of hot liquid. Expanded hot and compressed cold working fluid streams enter the counter-flow heat exchanger from opposite ends, and heat transfer takes place between them.

However, even the scroll-type Ericsson cycle engine must have a remote heater and cooler, as shown in Fig. 1, because its processes of compression and expansion are not ideally isothermal. As the processes of compression and expansion approach isothermal, the smaller the heater and the cooler become. Fig. 2 shows a comparison of P-V diagrams between given limits of pressure and temperature for the Brayton and Ericsson cycle engines with a working fluid (specific heat ratio, k). In general, the gas compression or expansion process can be modeled as a polytropic ($Pv^n = const$) process, where the value of n varies between k and 1; as an isentropic ($n = k$) process (involves no heat transfer); as a polytropic ($1 < n < k$) process (involves some heat transfer); or as an isothermal ($n = 1$) process (involves considerable heat transfer). The shaded areas A_1 (decrease in compression work) and A_2 (increase in expansion work) represent the additional work made available by substituting isothermal processes for adiabatic processes.

2.2. Simple Ericsson cycle engine model

We developed an ideal Ericsson cycle engine model and used it to explore the behavior of the Ericsson cycle engine. Our model made use of the following simplifying assumptions: (A) ideal gas with a constant specific heat, (B) no pressure drops in all heat exchangers, and (C) ideal regenerator ($T_3 = T_5$, $T_2 = T_6$).

q_h is the heat transferred from the heat source to the heat engine in the heater, and q_e is the heat transferred from the heat source to the heat engine in the expander. The first law of thermodynamics can be expressed as follows:

$$\Delta q = \Delta h - \int v dp \tag{1}$$

$$q_h = c_p(T_4 - T_3) = c_p(T_4 - T_5) \tag{2}$$

$$q_e = c_p(T_5 - T_4) + w_e \tag{3}$$

The total heat from the heat source to the heat engine is as follows:

$$q_{in} = q_h + q_e = w_e \tag{4}$$

The gas compression or expansion process can be modeled as polytropic processes ($Pv^n = const$). For simplicity, we assume that the polytropic index for compression, n_c , is equal to that for expansion, n_e , and we designate both as n .

The ideal compression work for the polytropic process can be written as follows:

$$w_{c,i} = \frac{n_c}{n_c - 1} R(T_2 - T_1) = \frac{n}{n-1} RT_1 \left(\frac{T_2}{T_1} - 1 \right) = \frac{n}{n-1} RT_1 \left[\left(\frac{P_2}{P_1} \right)^{(n-1)/n} - 1 \right] \tag{5}$$

Likewise, the ideal expansion work for the polytropic process can be written as such:

$$w_{e,i} = \frac{n_e}{n_e - 1} R(T_4 - T_5) = \frac{n}{n-1} RT_4 \left(1 - \frac{T_5}{T_4} \right)$$

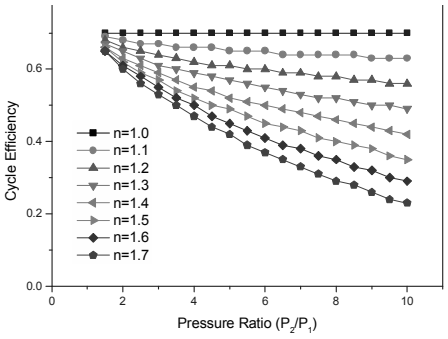

(*a*) $T_1 = 20°C,\ T_4 = 700°C,\ \eta_c = \eta_e = 1.0$

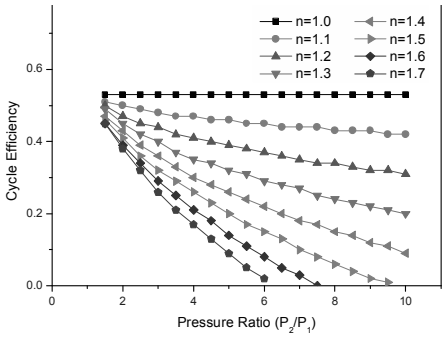

(*b*) $T_1 = 20°C,\ T_4 = 700°C,\ \eta_c = \eta_e = 0.8$

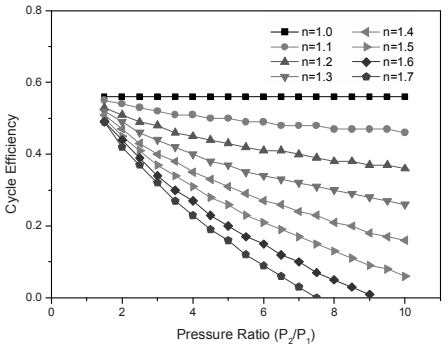

(*c*) $T_1 = 20°C,\ T_4 = 400°C,\ \eta_c = \eta_e = 1.0$

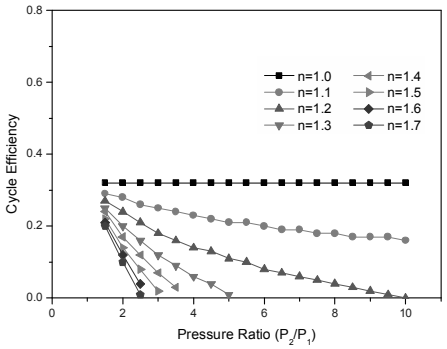

(*d*) $T_1 = 20°C,\ T_4 = 400°C,\ \eta_c = \eta_e = 0.8$

Fig. 3. Thermal efficiency with polytropic index and pressure ratio

$$= \frac{n}{n-1} RT_4 \left[1 - \left(\frac{P_5}{P_4} \right)^{(n-1)/n} \right]$$
$$= \frac{n}{n-1} RT_4 \left[1 - \left(\frac{P_1}{P_2} \right)^{(n-1)/n} \right] \quad (6)$$

The actual compression work for the gas is determined using the compression efficiency, which is defined as follows:

$$\eta_c = \frac{w_{c,i}}{w_c} \quad (7)$$

The actual expansion work for the gas is determined using the expansion efficiency, which is defined as follows:

$$\eta_e = \frac{w_e}{w_{e,i}} \quad (8)$$

Then, the thermal efficiency of the simple Ericsson cycle engine becomes the following:

$$\eta_{th} = \frac{w_{net}}{q_{in}} = 1 - \frac{w_c}{w_e} = 1 - \frac{1}{\eta_c \eta_e} \frac{T_1}{T_4} \left(\frac{P_2}{P_1} \right)^{(n-1)/n} \quad (9)$$

For several different sets of the highest cycle temperatures (T_4) and efficiencies of the compressor and expander (η_c , η_e), thermal efficiencies are plotted in Fig. 3 for various pressure ratios and polytropic indices. We can see that thermal efficiency decreases as the pressure ratio rises and as the polytropic index n rises from 1, which constitutes an ideal Ericsson cycle.

By comparing case (a) with case (b) and case (c) with case (d), we see that thermal efficiency of the simple Ericsson cycle is very sensitive to the efficiencies of the compressor and the expander. Especially for a low temperature difference engine with a low T_4, thermal efficiency is particularly sensitive to the efficiency of the compressor and expander and to the polytropic index of compression and expansion.

3. Closed Brayton cycle

In the first stage of development of the scroll-type Ericsson engine, it is not easy to realize the advantages of the isothermal compressor and expander. First of all, we considered a closed Brayton cycle with adiabatic compression and expansion. For a simple model of the Brayton cycle, we assumed that the polytropic index for compression and expansion (n_c, n_e) is equal to k, the specific heat ratio of the working fluid. From Eq. (9), thermal efficiency of the simple Brayton cycle engine becomes the following:

$$\eta_{th} = \frac{w_{net}}{q_{in}} = 1 - \frac{w_c}{w_e} = 1 - \frac{1}{\eta_c \eta_e} \frac{T_1}{T_4} \left(\frac{P_2}{P_1} \right)^{(k-1)/k} \quad (10)$$

By substituting k for n in the previous plots, we can see that thermal efficiency decreases as the pressure ratio rises and as the specific heat ratio, k, rises from 1, which constitutes an ideal Ericsson cycle.

3.1. Working fluid

From the previous results, we see that a lower specific heat ratio, k, permits higher thermal efficiency of the Brayton cycle. Specific heat ratio also varies with temperature, but this variation is very small. For monatomic gases (e.g., He, Ne, etc.), k is essentially constant at about 1.66. Many diatomic gases (e.g., H_2, O_2, air, etc.) have a specific heat ratio of about 1.4 at room temperature. Triatomic gases (e.g., H_2O, CO_2, etc.) have a specific heat ratio of about 1.3. Polyatomic gases with more atoms have specific heat ratios closer to 1 [2].

Nevertheless, lighter gases (e.g., He and H_2) have some advantages because of their lower friction. In the case of Stirling engines operating at high pressure and high speeds, hydrogen or helium must be used as the working fluid in order to achieve the necessary rates of heat and mass transfer with tolerable flow losses [3]. However, with lighter gases, sealing problems are very severe. Also, smaller molecular weight leads to larger masses for the machines because of decreased fluid momentum and the need for a larger heat exchanger because of smaller specific heat [4].

Nowadays, CO_2 is regarded as a promising working fluid in closed gas-turbine cycles for a high-temperature gas-cooled reactor (HTGR) [5]. A carbon dioxide (CO_2) gas-turbine reactor with a partial pre-cooling cycle attains a cycle efficiency of 45.8% at a medium temperature of 650°C and a pressure of 7 MPa, which is comparable to the 47.7% of a typical helium gas-turbine reactor GT-MHR at the higher temperature of 850°C. A peculiar drop in the compressibility factor around the critical point can be utilized to reduce compressor work in a CO_2 gas-turbine cycle.

We designated air as the basic working fluid in this study, because it is so freely available, and we identified CO_2 as a promising working fluid.

3.2. Brayton cycle model

For detailed analysis of the Brayton cycle, we obtained properties of the working fluid (air and CO_2) from the NIST database. We considered inefficiencies and irreversibilities of the components, including pressure drop and effectiveness of the heat exchangers. This model makes use of the following simplifying assumptions:

- Efficiencies of the compressor and expander are 0.8 ($\eta_c = \eta_e = 0.8$).
- Pressure drops in the heat exchangers on both the high-pressure side and the low-pressure side are defined by the following expressions:

$$\beta = \frac{P_{out}}{P_{in}} = 1 - \frac{\Delta P}{P} \quad (11)$$

$\beta_h = \frac{P_4}{P_2}$ and $\beta_l = \frac{P_1}{P_5}$, assuming

$$\beta_h = \beta_l = 0.95 \quad (12)$$

- Effectiveness of the recuperator, ε_R, is assumed to be 0.95.

Deviation of actual compressor and expander behavior from idealized isentropic behavior can be accounted for by isentropic efficiency of the compressor and expander, defined as follows:

$$\eta_c = \frac{w_{c,s}}{w_c} \cong \frac{h_{2s} - h_1}{h_2 - h_1} \quad (13)$$

$$\eta_e = \frac{w_c}{w_{c,s}} \cong \frac{h_4 - h_5}{h_4 - h_{5s}} \quad (14)$$

where states 2 and 5 are the actual exit states of the compressor and the expander, respectively, and 2s and 5s are the corresponding states for the isentropic case (see Fig. 4).

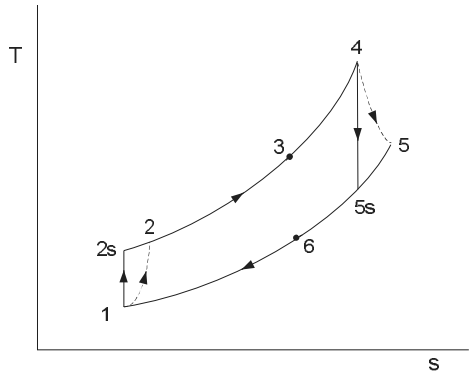

Fig. 4. T-s diagram of regenerative Brayton cycle

Effectiveness of the recuperator, ε_R , can be expressed as follows:

$$\varepsilon_R = \frac{T_5 - T_6}{T_5 - T_2} = \frac{T_3 - T_2}{T_5 - T_2} \quad (15)$$

Exit temperatures of the recuperator, T_6 and T_3 , can be obtained from Eq. (15).

Heat transferred from the heat source to the heat engine in the heater, q_h , is determined from the energy balance, as follows:

$$q_{in} = q_h = h_4 - h_3 \quad (16)$$

Thermal efficiency of the Brayton cycle is given by the following expression:

$$\eta_{th} = \frac{w_{net}}{q_{in}} = \frac{w_e - w_c}{q_{in}} \quad (17)$$

4. Results and discussion

Optimization of design on the basis of design parameters ($\dot{W}/P_{\max}V_T$) results in a machine configuration with the maximum possible power within limits of the maximum pressure and combined swept volume. Maximum pressure of the working fluid is an important design criterion, because this property affects the strength and, hence, the weight of the machine structure. Clearly then, the power parameter ($\dot{W}/P_{\max}V_T$) should be used for optimization purposes [3].

In this study, the power parameter ($\dot{W}/P_{\max}V_T$) can be expressed as a specific net work parameter ($w_{net}/P_{\max}v_T$) on a unit of mass of working fluid. Maximum pressure of the working fluid ($P_{\max}$) is P_2 , and combined swept volume, v_T , as a barometer of the sizes of the compressor and the expander, can be approximately the sum of the largest specific volumes of the working fluid in the scroll compressor (v_2) and the expander (v_5).

Fig. 5 shows the thermal efficiency (η_{th}) and specific net work parameter ($w_{net}/P_{\max}v_T$) at various pressure ratios. Although thermal efficiency is a function that is closely related to peak temperature, peak temperature is limited by material problems. In this study, we considered two cases of high temperature (700°C) and two cases of medium temperature (400°C) with the same low temperature (20°C). Maximum pressure of the working fluid ($P_{\max}$) was assumed to be 6.0MPa for the strength of the machine.

For the optimization of design of the cycle, we also considered temperature drop of the working fluid during expansion, as shown in Fig. 6 together with the thermal efficiency and specific net work, because continuous expansion of the gas causes a wide range of temperature distribution over the entire scroll wrap. This phenomenon leads to a difference in thermal expansion between the innermost and outermost zones of the scroll wrap and causes different clearances in the radial and axial directions [1]. Therefore, temperature drop during expansion must be minimized while we strive to achieve a cycle with high thermal efficiency and a high specific net work.

Optimum pressure ratios for four cases are summarized in Table 1. For the air cycle with high temperature (700°C), specific net work and thermal efficiency are lower by 38% and 17%, respectively, than for the CO_2 cycle. For the air cycle with medium temperature (400°C), specific net work and thermal efficiency are lower by even more—78% and 74%, respectively, than for the CO_2 cycle.

From our analyses of the cycles, it appears that CO_2 is a promising working fluid because of its higher thermal efficiency and specific power and lower temperature drop during expansion, compared to air. Higher efficiency of CO_2 is attributable to reduced compression work around the critical point of CO_2. The work of a real gas in isentropic expansion and compression processes is proportional to the compressibility factor (z). If we plot z against $P_R(=P/P_c)$ and $T_R(=T/T_c)$, we obtain a single curve for all gases, as shown in Fig. 7. At the critical temperature and pressure, the z

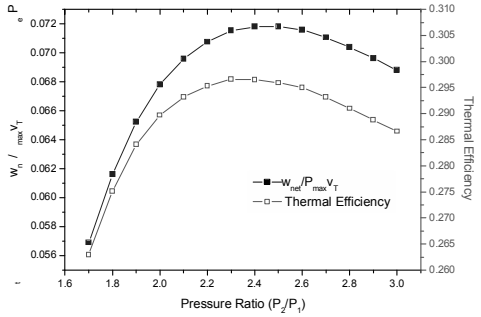

(a) Working fluid: Air, $T_1 = 20°C$, $T_4 = 700°C$

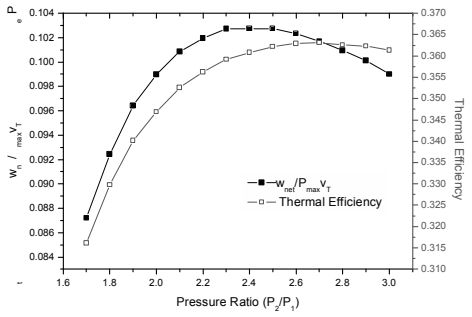

(b) Working fluid: CO_2, $T_1 = 20°C$, $T_4 = 700°C$

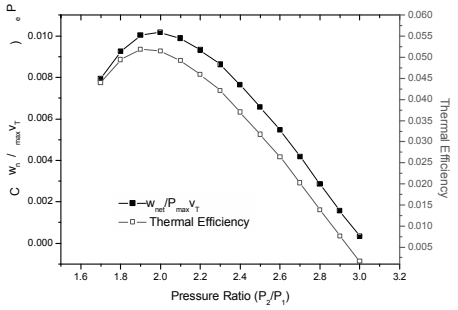

(c) Working fluid: Air, $T_1 = 20°C$, $T_4 = 400°C$

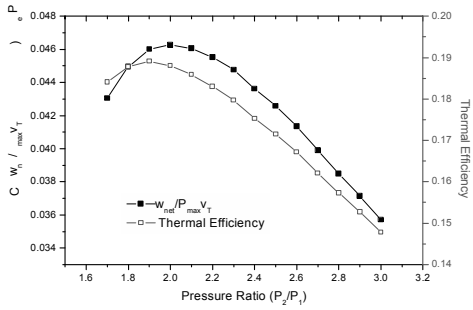

(d) Working fluid: CO_2, $T_1 = 20°C$, $T_4 = 400°C$

Fig. 5. Thermal efficiency and power parameter with pressure ratio

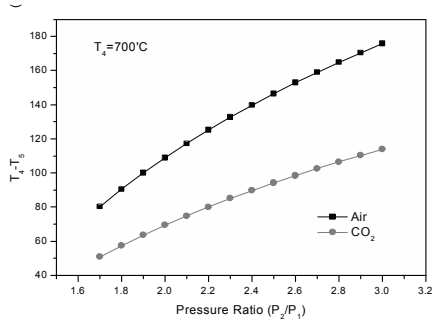

(a) $T_1 = 20°C$, $T_4 = 700°C$

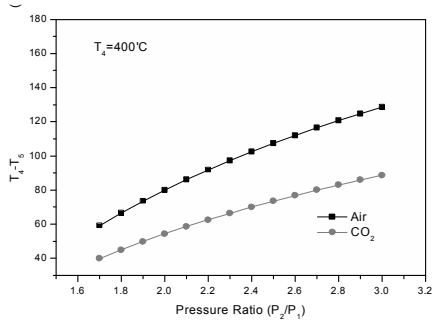

(b) $T_1 = 20°C$, $T_4 = 400°C$

Fig. 6. Temperature drop during expansion with two working fluids

value dips sharply below the ideal line of unity, where the low z value indicates that the gas is more compressible than the ideal gas. Because compressor inlet temperature is very close to the CO_2 critical temperature (31.0°C) and the pressure approaches the CO_2 critical pressure (7.38 MPa) during compression, we estimate that z values of CO_2 under compression are smaller than those of air (or He). However, z values for both CO_2 and air approach unity at high-temperature and high-pressure conditions in the expander. Table 2 shows the compression and expansion work and the ratios of compression work to expansion work for each optimal condition.

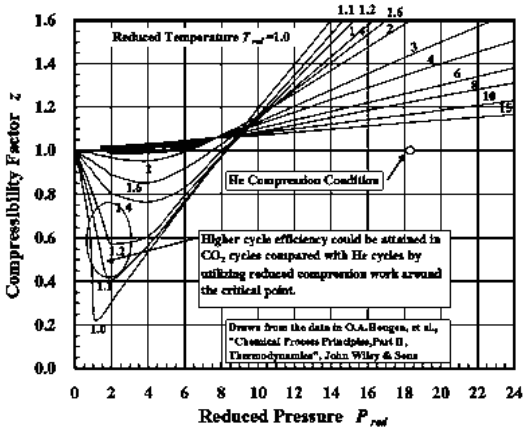

Fig. 7. Compressibility factor with P_R and T_R [5]

Table 1. Optimal pressure ratio in four cases

	$\frac{P_2}{P_1}$	$\frac{w_{net}}{p_{\max} v_T}$	η_{th} (%)	$T_4 - T_5$ (°C)
Air	2.3	7.154 E-2	29.66	132.64
T_4 = 700 °C	2.4	7.180 E-2	29.65	139.70
CO_2	2.4	10.275 E-2	36.08	89.70
T_4 = 700 °C	2.5	10.233 E-2	36.22	94.21
Air	1.9	1.003 E-2	5.19	73.33
T_4 = 400 °C	2.0	1.017 E-2	5.15	80.02
CO_2	1.9	4.600 E-2	18.91	49.78
T_4 = 400 °C	2.0	4.626 E-2	18.80	54.29

Table 2. Compression and expansion work ratio in four optimized conditions

	$\frac{P_2}{P_1}$	w_c (kJ/kg)	w_e (kJ/kg)	$\frac{w_c}{w_e}$
Air	2.3	99.24	151.07	0.657
T_4 = 700 °C	2.4	105.03	158.96	0.661
CO_2	2.4	56.85	107.76	0.528
T_4 = 700 °C	2.5	60.20	113.12	0.532
Air	1.9	74.18	78.92	0.940
T_4 = 400 °C	2.0	80.76	85.79	0.941
CO_2	1.9	38.45	52.08	0.738
T_4 = 400 °C	2.0	42.35	56.76	0.746

5. Conclusions

Stirling and Ericsson engines each have great potential for many applications, including micro-cogeneration, solar power, and biomass. However, ideal cycles of both types of engines are difficult to achieve in practice because neither isothermal compression nor isothermal expansion is practical with reciprocating piston engines or with turbomachinery. On the other hand, scroll compression and expansion can be very suitable for effective cooling and heating of these engines because of the high area-to-volume ratio of scroll geometry. In this current study, we have undertaken a theoretical investigation of thermodynamic analyses of several kinds of scroll-type engines, in particular with regard to associated compression and expansion processes, adiabatic or quasi-isothermal processes, and magnitude of cycle temperature.

In the first stage of development of the scroll-type Ericsson engine, it is not easy to realize the advantages of the isothermal compressor and expander. First of all, we considered a closed Brayton cycle with adiabatic compression and expansion. We selected power density, power within limits of maximum pressure and combined swept volume, and thermal efficiency as objective functions, and we then deduced optimal design parameters for the scroll-type engine. We designated air as the basic working fluid in this study, because it is so freely available. We identified CO_2 as a promising working fluid because of the reduced compression work around the critical point of CO_2. From our analyses of the cycles, it is apparent that CO_2 exhibits higher thermal efficiency and specific power and lower temperature drop during expansion than air, which is important for minimizing differential thermal expansion of scroll wraps.

Nomenclature

k specific heat ratio (c_p / c_v)

n polytropic exponent

q specific heat transfer (kJ/kg)

h specific enthalpy (kJ/kg)

w specific work (kJ/kg)

c specific heat (kJ/kgK)

T temperature (K)

P pressure (kPa)

R universal gas constant (kJ/k K)

Greek symbols

η efficiency (dimensionless)

β pressure-drop parameter

ε_R effectiveness of the recuperator

$\dot{W}$ cycle power-output (kW)

V_T combined swept volume (m^3)

z compressibility factor

P_R reduced pressure

P_c critical pressure

T_R reduced temperature

T_c critical temperature

Subscripts and superscripts

h heater

c compression

e expansion

i ideal case

net net

max maximum

References

[1] Y. M. Kim, D. K. Shin, J. H. Lee. *Heated scroll expander and its application for distributed power source*. In Proceedings of the International Conference on Conference on Compressors and their Systems 2005, p. 133-142.

[2] Cengel, Y.A., Boles, M.A., Thermodynamics : An engineering approach. McGraw-Hill, 1989. p. 115.

[3] Walker G. Stirling engine. Oxford: Clarendon Press; 1980. p. 160-161, see also p. 94-101.

[4] Sridhar, K.R., Nanjundan, A., Gottmann, M., Swanson, T.D. and Didion, J., *Evaluation of a reverse Brayton cycle heat pump for lunar base cooling*. In Proceedings of 24th International Conference on Environmental Systems 1994.

[5] Kato, Y., Nitawaki, T., Muto, Y., *Medium temperature carbon dioxide gas turbine reactor*. Nuclear Engineering and Design 230 (2004) 195-207.

[6] S. Bonnet, M. Alaphillippe, P. Stouffs, *Energy, exergy and cost analysis of a micro-cogeneration system based on an Ericsson engine*. International Journal of Thermal Sciences 44 (2005) 1161-1168.

[7] Erbay, L.B., Yavuz, H., *Analysis of an irreversible Ericsson engine with a realistic regenerator*. Applied Energy 62 (1999) 155-167.

Numerical Model and Performance Analysis of a Scroll Machine for ORC Applications

Stefano Clemente [a], Diego Micheli [a], Mauro Reini [a] and Rodolfo Taccani [a]

[a] *Dipartimento di Ingegneria Meccanica, University of Trieste, Italy*

Abstract: The paper presents the development of a numerical one-dimensional model of a scroll machine, used both as a compressor and as an expander. The aim of the work is the realization of an instrument capable to estimate the performance of an expander obtained, with few modifications, from a commercial scroll compressor. This code will be inserted in the general simulation of an Organic Rankine Cycle (ORC), usable to obtain electrical power from low temperature thermal sources. The main outputs of the program are represented by some working parameters of the machine, such as volumetric and global efficiencies, and by the values assumed by the thermodynamic properties of the fluid in each chamber at every orbiting angle. In order to validate the model, these outputs are compared with experimental data obtained by measurements on a commercial variable speed hermetic scroll compressor. To simplify the test bench, air is chosen as operating fluid to allow a simple open circuit to be used. Then the code is used for predicting the scroll performances when it is used as an expander. Few real working fluids conveniently usable in an ORC are modeled and results of series of simulations are worked out.

Keywords: Scroll Compressor, Scroll Expander, ORC.

1. Introduction

The scroll machine working principle is based on the interaction of two nested identical spirals, often called "scrolls", which move relatively and form some variable volume chambers, filled by the working fluid. The machine, used as a compressor, has become more and more popular, thanks to its main features, such as high efficiency, few moving parts, low level of noise and vibration and high reliability. Scroll expander, instead, has rarely been used up to now, because traditionally power generation was centralized in power plants equipped with multi-MW steam and gas turbines. Today there is a new sensibility toward environment and energy saving, so a great number of researches has been made on new ways to produce electric power from low-temperature thermal sources (less than 350-400 °C). Available heat can be converted in mechanical energy using an organic Rankine cycle (ORC). Moreover, available thermal sources are often small, so small-sized expanders are required (few kWe): in this range the use of a turbine involves a number of disadvantages, first of all a high cost [1-2]. A possible alternative is represented by a modified commercial scroll compressor used as an expander [3-14]. This opportunity is interesting because it has a high-series low-cost production and it is designed to work with refrigerants, which are very similar, in physical and thermodynamic properties, to organic fluids, but high expansion efficiency must also be obtained in order to avoid an unacceptable reduction of the already scarce effectiveness of low temperature ORC cycles. Such efficiency depends on the matching between some scroll characteristics (hermetic or open drive, oil-free or not, built in volume ratio) and operating fluid ones, that determine the values of volumetric efficiency, built in pressure ratio and heat transfer that contribute to the overall machine efficiency, not to mention the contribute of mechanical losses. In literature adiabatic efficiency values about 60-65% [3, 4, 7, 10] and up to about 68-70% [5, 7, 11, 14] are reported, but lower values can also be found. In [7] tests carried out on three different scroll expanders fed with air and water steam, also mixed with propylene glycol, and running at various operating conditions showed that efficiencies can vary in the range 0.3-0.7 depending mainly on fluid nature. In [9, 12] efficiencies in the range 0.3 - 0.4 were detected due to an excessive clearance between the scrolls and the improvable interaction with lubricating oil [12]. Aim of this paper is to describe a numerical model for predicting the performances of a scroll expander as well as of the scroll compressor from which it derives. This model can be used to know

Corresponding Author: Diego Micheli, Email: micheli@units.it

if a commercial scroll compressor can be effectively used, with few modifications, as expander in an ORC operating with another fluid. The simulation code has been calibrated and checked comparing its results with experimental measurements on a commercial hermetic scroll compressor, fed for simplicity with atmospheric air.

2. The scroll machine

The scroll is a positive displacement machine essentially formed by two identical spiral-shaped wraps fixed on back plates. One wrap has a hole in the back plate and is held fixed, while the other can orbit. The working principle for a compressor is illustrated in Fig.1: the working fluid enters the suction chambers through openings at external endings of wraps and exits from the central chamber through the fixed back-plate hole. If the machine is used as an expander, the working fluid moves from central chamber towards the external ones and the orbiting wrap changes its direction of rotation. The major difference between the ideal behavior of a scroll machine and the real one is leakage: a certain quantity of working fluid flows from high-pressure chambers to low-pressure ones through gaps between the scroll wraps. There are two different kinds of leakage: the radial one has the path formed by a gap between a back-plate and a scroll, while the tangential (or flank) leakage has the path formed by a gap between the flanks of the two scrolls. Leakage causes first of all a significant degradation of volumetric efficiency, defined as:

$$\eta_v = \frac{\dot{m}}{\rho V n} \qquad (1)$$

where the density of working fluid, ρ, is always referred to the inlet fluid conditions. Moreover leakage raises requested compression work or reduces available expansion work. Another important difference between an ideal and a real scroll machine is heat exchange involving the working fluid that often leads to sensibly not adiabatic processes.

3. Model description

There is a relatively abundant literature on scroll machine simulation models, which are classifiable in two main categories. Semi-empirical models, as the ones proposed by Lemort et al. [14] for expanders or by Winandy et al. [15] for compressors, are made up by a limited number of

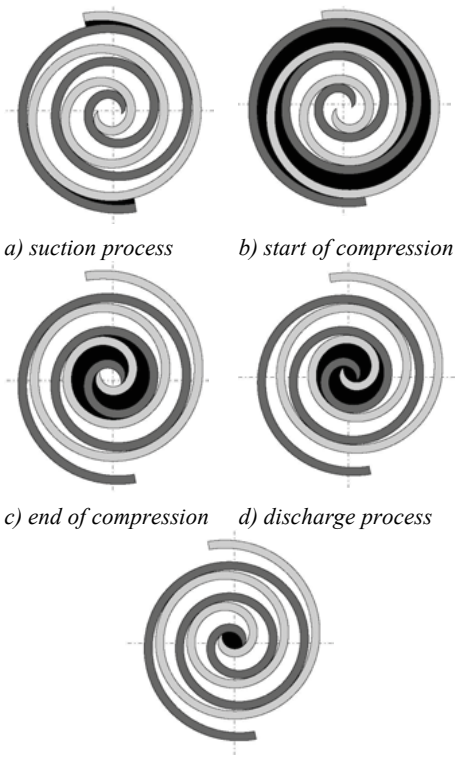

a) suction process *b) start of compression*

c) end of compression *d) discharge process*

e) end of discharge

Fig. 1. Working principle of a scroll compressor

equations whose parameters are identified by minimizing functions that take into account the errors between the model outputs and the results of laboratory measurements [16]. Deterministic models, instead, are constituted by a larger series of equations, in order to describe exactly the geometry of the machine and all the actual phenomena which take place into it. While the first type of models requires shorter simulation times but needs available experimental data, the second ones allow a more detailed knowledge of the machine functioning and can be used as design tools, so in this paper a deterministic model is presented. In Halm [17] and in Chen et al. [18, 19] there are detailed descriptions of a compressor model: starting from these works and referring also to Wang et al. [20], a new numerical code has been developed, applicable not only to compressors but also to expanders. For simplicity, this paragraph refers to the compressor case.

3.1. Chambers volume

The most diffused shape of the scrolls is an involute of a circle. Every wrap is defined by two

involutes which develop from the same basic circumference and are offset by a constant distance, the wrap thickness, as shown in Fig 2. The inner portion is usually defined by the cutter used to machine the scroll: here a circular arc connecting two involutes is assumed, as shown in Fig. 3. This accurate definition of geometry allows to calculate exactly the volume of all the machine chambers, at every orbiting angle, as the product of scroll height and area enclosed by the scrolls between two consecutive contact involute angle. Detailed equations for the calculation of the suction volume, compression chamber volume and discharge region volume as functions of the orbiting angle are reported in Appendix A. They are derived and fully described in [17] and [18].

3.2. Suction and discharge sections

The flow area through the openings at external endings of wraps can be simply expressed by:

$$A_s(\theta) = h\, r_o\, (1 - \cos\theta) \tag{2}$$

The discharge ports are represented by the openings between scrolls in the inner portion of the wraps: the flow area is

$$A_{d-dd}(\theta) = w_{d-dd}\, h \tag{3}$$

where $w_{d\text{-}dd}$ is defined by (A8).

The flow rates of all porting processes are calculated using the flow equation for isentropic flow of a compressible ideal gas.

3.3. Thermodynamic process

The core of the model is represented by energy conservation and mass balance equations, applied to each chamber, in the hypothesis of uniform thermodynamic properties in each volume:

$$\frac{dT}{d\theta} = \frac{1}{m\, c_v}\left\{\frac{\dot{Q}}{\omega} + \sum \frac{\dot{m}_{in}}{\omega}(h_{in} - h) - \right.$$

$$\left. - T\left(\frac{\partial p}{\partial T}\right)_v \left[\frac{dV}{d\theta} - \frac{v}{\omega}\left(\sum \dot{m}_{in} - \sum \dot{m}_{out}\right)\right]\right\} \tag{4}$$

$$\frac{dm}{d\theta} = \sum \frac{\dot{m}_{in}}{\omega} - \sum \frac{\dot{m}_{out}}{\omega} \tag{5}$$

Equations 4, 5 are derived in [17] and [18].

The model requires a third equation to correlate all the thermodynamic properties of the fluid: in the code air with ideal behavior is implemented by the perfect gas law, while the fundamental equations of state described by Lemmon and Span [21] are used to describe refrigerant R245fa, isopentane and toluene. Other than the equations of state, the model is equipped also by correlations to calculate the needed values for fluid thermo-physical properties such as specific heat capacities, thermal conductivity and dynamic viscosity.

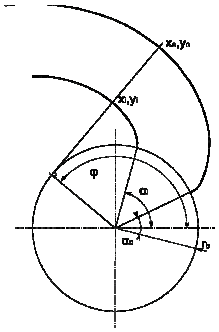

Fig. 2. General geometry

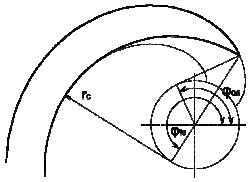

Fig. 3. Internal geometry

3.4. Internal leakage

A fixed value is assigned both to radial gap and to flank (or tangential) gap, so flow areas can be simply calculated considering wraps length and height. The flow model adopted for leakage is the isentropic one for a compressible ideal gas through a constant area.

3.5. Heat transfer

The main problem in calculating thermal fluxes in the machine is the choice of a suitable heat transfer coefficient, because no matching case in geometry and fluid motion can be found in literature. As suggested by Chen [18], a correlation based on Dittus-Boelter equation, derived for a spiral plate heat exchanger [22], has been used. In this formula a hydraulic diameter is used, so the area enclosing each chamber at every orbiting angle has to be calculated. Moreover, the temperature of two wraps is needed to determine heat fluxes involving working fluid in the scroll zone: it's assumed that the temperature along the scrolls grows linearly, from outer end to inner zone. The mean value of this distribution is determined by summing the intermediate temperature between suction and isentropic discharge conditions and a quantity increasing with the shaft speed, defined in accord with experimental data. Total thermal flux involving a fluid pocket in a chamber at a particular orbiting angle can finally be calculated according to the method described in [17]. Other than the heat transfers with the wraps, it's necessary to determine the fluid heating-up before

it enters the scroll zone (this may be caused, for example, by the fluid passage in the motor zone in the case of hermetic compressor) and the cooling-down in the discharge volume after the compression end. These thermal fluxes are calculated by a global energy balance of the compressor.

3.6. Discharge process

Although a scroll machine doesn't need valves, commercial compressors are often equipped with a check valve on the discharge duct, in order to prevent the fluid from going back after shut-off and therefore from causing backward rotations. This device has been modeled as a simply one-degree-of-freedom plate valve driven by a spring, so the flux area depends on the differential pressure between the central discharge chamber and the pipe. The isentropic flux theory is used to calculate also the mass flow rate through this valve.

4. Model validation

The performances of an hermetic commercial scroll compressor have been measured in order to calibrate and validate the numerical code.

The tested machine was designed to operate at variable speed, thanks an inverter driven motor, in a refrigerating closed cycle with R410a as working fluid. However in this case the compressor has been used with air in an open cycle, in order to simplify the test bench. A digital thermal mass flow meter has been inserted in the suction tube, while a manual valve has been installed at the end of the discharge pipe in order to control the discharge pressure. A thermocouple and a pressure transducer have been installed on both the suction and discharge pipe of the compressor. Finally, the parameters of the electrical feeding of the compressor, i.e. voltage, current, frequency and absorbed power, have been measured by the inverter internal instrumentation. Lubricating oil was changed in order to accomplish air instead of R410a as working fluid, taking also into account the higher temperatures reached using a lower heat capacity fluid. An oil separator was installed at the compressor exit. The main geometrical data of the tested scroll device are detailed in Table 1.

Since the compressor is a hermetic machine, no direct measurements of gaps between wraps were possible, so a preliminary set of numerical simulations has been conduced, in order to find

displacement V	34,31 mm^3
radius of basic circumference r_b	2,1 mm
wrap thickness t	3,7 mm
Scroll height h	30,4 mm
Outer involute starting position angle α_0	-80°
Inner involute starting position angle α_i	-63°
Final involute angle φ_e	1086°

Tab. 1. Compressor geometrical data

tangential and radial gaps values that allow to reach the best matching between calculated and experimental volumetric efficiency. It was assumed that tangential gap depends on compressor speed (see Fig. 4), since it is determined by the thickness of the oil film on the wraps, while radial gaps depend on both compressor speed and pressure imposed in the discharge pipe. In fact the machine is equipped with a gasket seal on the top of the scrolls, which is kept in position by the difference of pressure between two contiguous chambers: so the sealing is more efficient when the machine works with an higher discharge pressure. The radial gap law utilized by the model is:

$$\delta_r = \delta_r\left(p_{dis} / p_{suc}\right)\cdot\left(1+\gamma\right) \qquad (6)$$

where γ is a coefficient obtained by interpolating data in Table 2 and the dependence from pressure ratio $\delta_r\left(p_{dis} / p_{suc}\right)$ is shown in Fig. 5.

It can be seen that the flank gap size is approximately 10 times greater than the radial one, since the latter is widely decreased by the seals; so the main leakage path in the tested machine is the tangential one. The values calculated for this gap, variable from 20 to 60 μm, are comparable with those found in literature [9, 17].

A first comparison between the experimental and the numerical data has been made considering the discharge mean temperature and the machine volumetric efficiency, defined by (1). Trends of these parameters as function of discharge pressure at various shaft speed are shown in Fig. 6 and 7. It can be seen that these trends are well predicted by the model, in particular at medium and high discharge pressure, i.e. in the best working conditions for the machine, the maximum gaps between experimental and numerical data is, respectively, 5 K and 3 points per cent. It's important to note that only few working points showed in the Fig. 6 and 7 have been used to

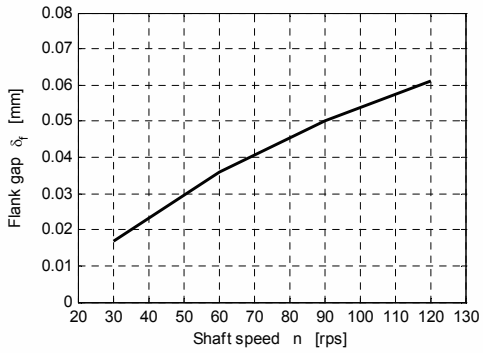

Fig. 4. Flank gap as a function of shaft speed

n [rps]	*γ [-]*
30	-0,460
60	0
90	0,675
120	2,000

Tab. 2. Corrective factor for radial gap size

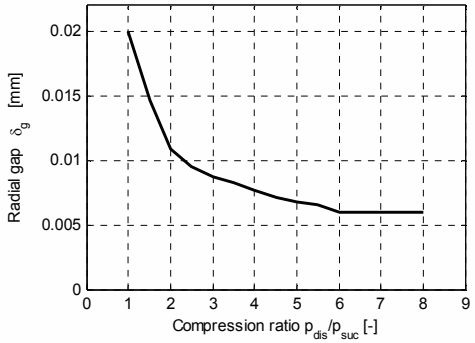

Fig. 5. Radial gap as a function of p_{dis}/p_{suc} at 60 rps

calibrate the model, so the diagrams reveal an effective good agreement between experimental and numerical data. The values measured and calculated for volumetric efficiency (always below 50%) are very poor if compared with the best data found in literature (in [16] values above 90% are reported at every operating conditions). This is due to the fact that the compressor has been tested with a working fluid (air instead of refrigerant) and with a lubricating oil different from those it was designed to operate with, in order to simplify the test bed.

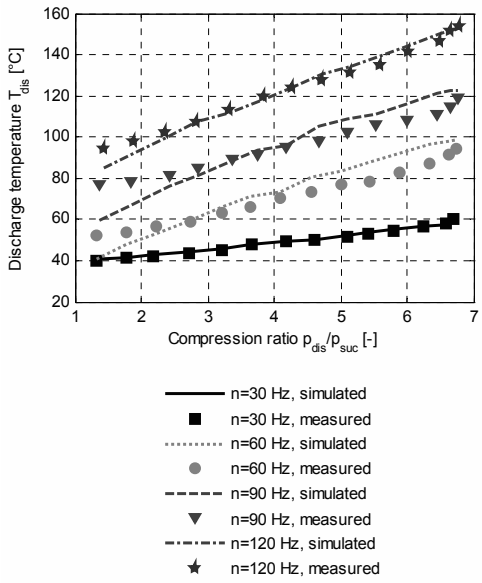

Fig. 6. Discharge mean temperature as a function of compression ratio

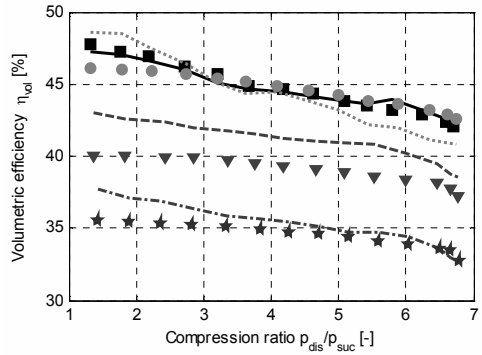

Fig. 7. Volumetric efficiency as a function of compression ratio (for legend see Fig. 6)

The overall isentropic efficiency is defined as the ratio between the power needed to pressurize the fluid with an isentropic process and the shaft power absorbed by the device. In the present code, the shaft power is calculated adding the net heat flow rate involving the fluid and adding a constant mechanical loss to the work rate of the fluid. The latter is the product of the actual mass flow rate by the sum of the fluid specific enthalpy variation in the scroll zone and the work made by the fluid during a quasi-isochoric expansion in the discharge chamber [15]:

$$\eta_{is} = \dot{m}\left(h_{dis,is} - h_{suc}\right) \Big/ \left(\dot{Q} + \dot{W}_{loss} + \dot{W}_f\right), \qquad (7)$$

$$\dot{W}_f = \dot{m}\left[h_{scr1} - h_{scr2} + v_{scr2}\left(p_{scr2} - p_{dis}\right)\right]. \quad (8)$$

Mechanical losses are assumed to be constant at varying discharge pressure and equal to 10% of the entire absorbed power at maximum compression ratio. This value has been fixed after a comparison between the results of a preliminary set of simulations and experimental data. Trends of numerical and experimental overall isentropic efficiencies as function of compression ratio at a shaft speed equal to 60 rps are shown in Fig. 8.

It can be seen that a maximum gap of 5 points per cent was found between experimental and numerical results. However it must be noted that in the parameters defined by (7) electric motor losses are neglected; these depend on the compression ratio requested to the device, so they can affect significantly the trends shown in Fig. 8. Moreover, it must be considered that the efficiency expressed by (7) could be affected by an error introduced measuring discharge temperatures in the discharge pipe instead directly in the discharge chamber, due to difficulties connected with opening an hermetic machine.

5. Expander simulation results

Once the compressor model has been calibrated and verified, it has been adapted to predict the performance of the scroll machine working as an expander. All internal parameters of the code were the same of compressor case.

A first series of simulations has been conducted considering R245fa as working fluid in order to obtain the expander performances in function of the expansion ratio imposed between inlet and discharge conditions. The overall isentropic efficiency is defined in this case as the ratio between the real power available at the shaft and the power obtained from an ideal isentropic expansion from supply to discharge pressure. In analogy to the compressor case it is defined by the following equations:

$$\eta_{is} = \left(\dot{Q} - \dot{W}_{loss} + \dot{W}_f\right) / \left[\dot{m}\left(h_{inl} - h_{dis,is}\right)\right], \quad (9)$$

$$\dot{W}_f = \dot{m}\left[h_{scr1} - h_{scr2} + v_{scr2}\left(p_{scr2} - p_{dis}\right)\right]. \quad (10)$$

The sub-models forming the code have been progressively de-activated in order to quantify the influence of the phenomena involving the fluid on the expander efficiency, obtaining a series of curves showed in Fig. 9.

The higher curve has been generated taking into account only of the losses connected with an un-adapted expansion ratio: it can be seen that an unitary efficiency can be reached only if the machine built-in pressure ratio is imposed between inlet and discharge; otherwise, for smaller ratios, the fluid is re-compressed at the discharge, while for higher ratios a part of the expansion is un-exploited. The evolutions of the pressure with respect of the volume filled by the fluid for an expansion ratio equal, lower or greater than the built-in one are showed in Fig. 10, 11 and 12 respectively. When heat transfers are considered (first only between fluid and wraps, then also with the inlet pipe, finally also from machine towards ambient), the isentropic efficiency decreases: it can be noted that the main of these effects is relative to ambient losses, so the scroll expander has to be thermally insulated in order to achieve better performances. Since mechanical losses are approximately independent from expansion ratio, they have a greater influence on the efficiency at smaller ratios, when a smaller work is done by the fluid. Finally also the leakage model is activated in the code: this phenomenon causes a great decreasing in the isentropic efficiency, as shown by the lowest curve in Fig. 9: the maximum value reached during these simulations is about 65%, a value comparable with the ones found in literature [3,7,14]. It's also interesting to note that the expansion ratio that ensure the best isentropic efficiency is quite greater than the one defined by the machine geometry (which lead the higher curve in Fig. 9 to 100%), as observed in [14].

Several fluids have been implemented in the code: to evaluate the model, a series of runs has been launched to compare the performance of a machine fed by R245fa, isopentane and air. In Fig. 13 a comparison in term of isentropic efficiency has been carried out: the trends shown for R245fa and isopentane are quite similar, with the maximum reached for a built-in pressure ratio and with the best performances achieved with the first fluid. Instead the behavior of the expander fed by air is very different, because of the different thermo-physical properties of this fluid.

The evaluation of the volumetric efficiency of the expander is made by the same index introduced by (1) for the compressor.

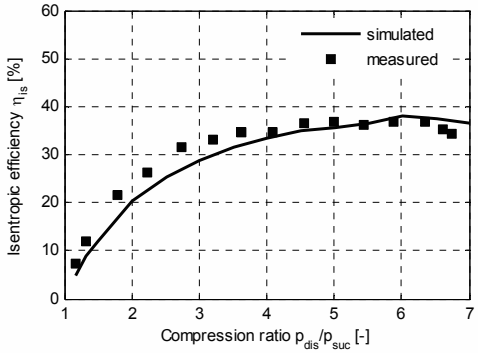

Fig. 8. Overall isentropic efficiency as a function of compression ratio at 60 rps

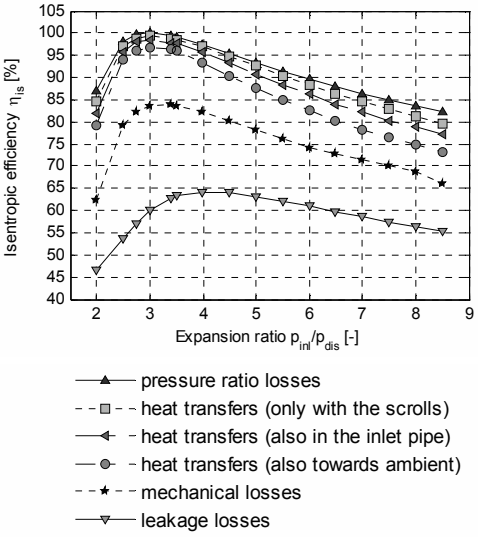

Fig. 9. Expander isentropic efficiency versus expansion ratio for R245fa.

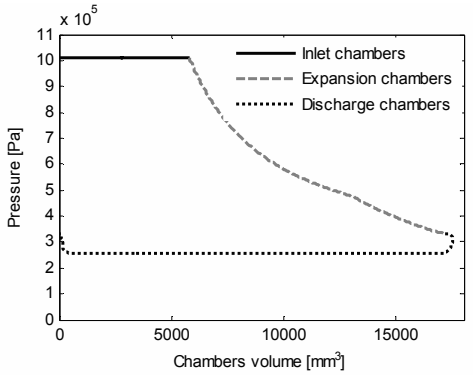

Fig. 10. Expansion on the (p,V) diagram, pressure ratio equal to the built-in one.

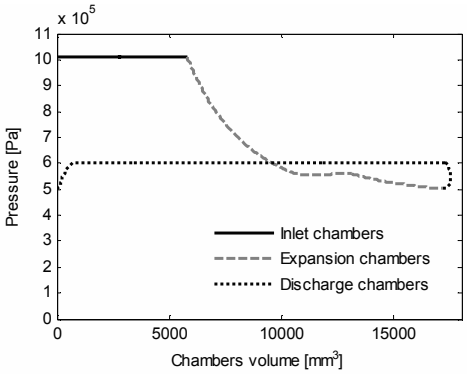

Fig. 11. Expansion on the (p,V) diagram, pressure ratio lower than the built-in one.

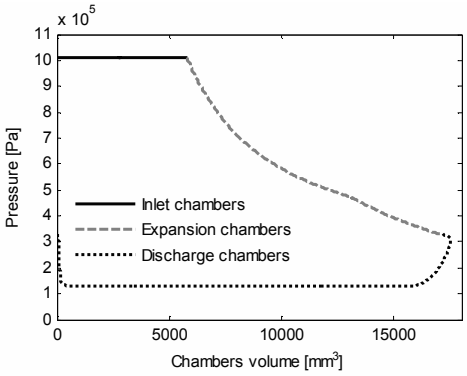

Fig. 12. Expansion on the (p,V) diagram, pressure ratio greater than the built-in one.

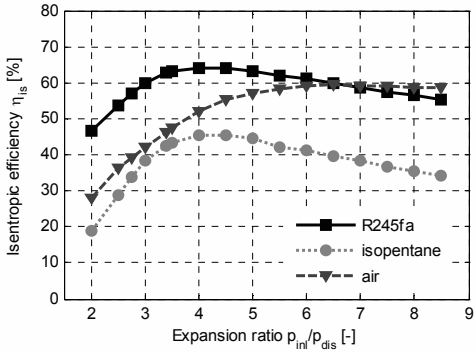

Fig. 13. Expander isentropic efficiency versus expansion ratio for three working fluids.

Since the main phenomenon affecting the volumetric performance of the machine is leakage, which consists in a flow through the gaps between scrolls from the inlet zone to the discharge chambers, for an expander the index defined by (1) always assumes values greater than 1 and

decreases for better performances. The trends of the volumetric efficiency for the three fluids above mentioned are shown in Fig. 14. It can be seen that the performances achieved by R245fa and isopentane are quite similar, while the same machine fed by air is affected by larger leakage losses, since a greater percentage of fluid flows through gaps.

One of the best opportunities offered by the use of a simulation code is the possibility of determine the instantaneous conditions of the fluid evolving in the machine without placing a large number of sensors inside it: some trends of thermodynamic properties with respect of orbiting angle have been obtained in order to test the effective prediction capacity of the model; for example, the temperature assumed by R245fa worked out by the scroll machine with a built-in pressure ratio imposed is reported in Fig. 15.

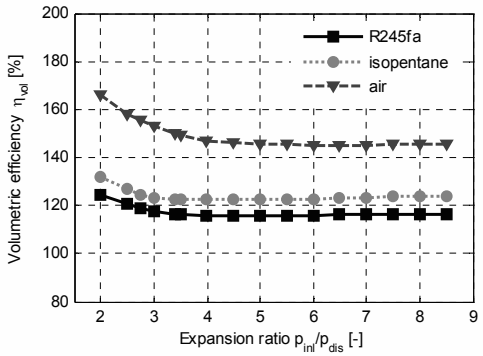

Fig. 14. Expander volumetric efficiency versus expansion ratio for three working fluids.

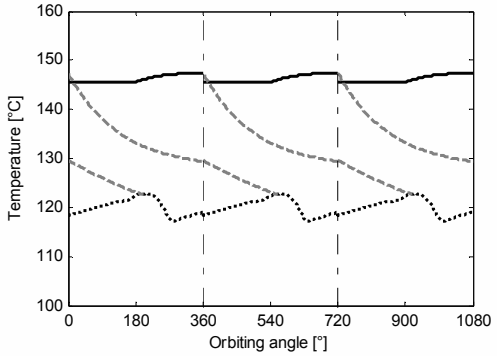

Fig. 15. Temperature assumed by R245fa during expansion process (for legend see Fig. 10)

6. Conclusions

The aim of this work was the realization of a scroll machine numerical model, capable of estimating the performances of the device, operating both as a compressor and as an expander. The code has been verified by confronting its outputs with a set of experimental data. This check revealed the program good skill to evaluate the main working parameters with the change of imposed boundary conditions, such as compression/expansion ratio and shaft speed. Finally, some working fluids have been implemented in the code, such as the real refrigerants used by scroll compressor and the organic fluids suitable for use in an ORC. The code is suitable to be inserted in a general model of the entire organic Rankine cycle.

Nomenclature

c	specific heat, J/(kg K)
h	specific enthalpy, J/kg
h	scroll height, m
k	level of the compr./exp. chamber
m	mass, kg
$\dot{m}$	mass flow rate, kg/s
n	shaft speed, rev./s
p	pressure, Pa
$\dot{Q}$	heat flow rate, W
r	radius, m
R	gas constant, J/(kg K)
T	temperature, K
v	specific volume, m^3/kg
V	volume, m^3
w	width of the opening between scrolls, m
$\dot{W}$	mechanical power, W

Greek symbols

α	involute starting position angle, rad
η	efficiency
θ	orbiting angle, rad
ρ	density, kg/ m^3
φ	involute angle, rad
ω	rotational speed, rad/s

Subscripts and superscripts

b	basic circle
c	circular arc forming the scroll inner position
c	compression chambers

cl	clearance
d	discharge chambers
d	discharge position
dis	discharge
d-dd	unique discharge zone
e	ending angle
e	expansion chambers
i	inner
i	lateral inlet chambers
ii	central inlet chamber
in	flow rate entering the control volume
inl	inlet
is	isentropic
i-ii	unique inlet zone
$\bar{k}$	innermost contact point between scrolls
loss	losses
o	orbiting circular path
o	outer
os	initial angle of outer spiral
out	flow rate exiting the control volume
s	suction
scr1	conditions at scroll zone inlet
scr2	conditions at scroll zone outlet
v	constant volume
vol	volumetric

References

[1] Smith, I., Stosic, N., Kovacevic, A., Langson, N., 2007, Cost effective small scale ORC systems for power recovery from low enthalpy geothermal resources, Geothermal Resources Council Transactions, 31.

[2] Micheli, D., Reini, M., 2007, On bottoming a micro turbine with a micro ORC section: Part a) preliminary design of the ORC expander, Ecos 2007, vol. 2, pp. 1025-1034.

[3] Zanelli, R., Favrat, D., 1994, Experimental Investigation of a Hermetic Scroll Expander-Generator, Proc. International Compressor Engineering Conference, Purdue, pp. 459-464.

[4] Yanagisawa, T., Fukuta, M., Ogo, Y., Hikichi, T., 2001, Performance of an Oil-Free Scroll-Type Air Expander, IMechE C591/027/2001, pp. 167-174.

[5] Kane, M., Larrain, D., Favrat, D., Allani, Y., 2003, Small hybrid solar power system, Energy, 28 (14), pp. 1427-1443.

[6] Xiaojun, G., Liansheng, L., Yuanyang, Z., Pengcheng, S., 2004, Research on a Scroll Expander Used for Recovering Work in a Fuel Cell, Int. J. of Thermodynamics, 7(1), pp. 1-8.

[7] Lemort, V., Teodorese, I.V., Lebrun J., 2006, Experimental Study of the Integration of a Scroll Expander into a Heat Recovery Rankine Cycle, International Compressor Engineering Conference, Purdue, pp. 1-8.

[8] Kane, M., Favrat, D., Gay, B., Andres, O., 2007, Scroll expander Organic Rankine Cycle (ORC) efficiency boost of biogas engines, Ecos 2007, vol. 2, pp. 1017-1024.

[9] Kim, H.J., Ahn, J.M., Park, I., Rha, P.C., 2007, Scroll Expander for Power Generation from a low-grade steam source, Proc. IMechE Vol. 221 Part A, pp. 705-711.

[10] Saitoh, T., Yamada, N., Wakashima, S.I., 2007, Solar Rankine cycle system using scroll expander, J. Environ. Eng., 2 (4), pp. 708-719.

[11] Hugenroth, J., Braun, J., Groll, E., King, G., 2008, Experimental Investigation of a Liquid-Flooded Ericsson cycle cooler, Int. J. Refrig., 31, pp. 1241-1252.

[12] Peterson, R.B., Wang, H., Herron, T., 2008, Performance of a Small-Scale Regenerative Rankine Power Cycle Employing a Scroll Expander, Proc. IMechE Vol. 222 Part A, pp. 271-282.

[13] Yang, L., Wang, J., Mangan, S., Derby, J.W., Lu, N., 2008, Mathematical Model and Energy Efficiency Analysis of a Scroll-type Air Motor, IAENG Int. J. Appl. Math., 38 (1).

[14] Lemort, V., Quoilin, S., Cuevas, C., Lebrun, J., 2009, Testing and Modeling of a Scroll Expander Integrated into an Organic Rankine Cycle, Appl. Therm. Eng., 29, pp. 3094-3102.

[15] Winandy, E., Saavedra, C., Lebrun, J., 2002, Experimental analysis and simplified modeling of a hermetic scroll refrigeration compressor, Appl. Therm. Eng., 22, pp. 107-120.

[16] Cuevas, C., Lebrun, J., Lemort, V., Winandy, E., 2009, Characterization of a scroll compressor under extended operating conditions, Appl. Therm. Eng., In Press.

[17] Halm, N., 1997, Mathematical modeling of scroll compressors, Master Thesis of Herrick Lab, School of Mechanical Engineering, Purdue University.

[18] Chen, Y., Halm, N., Groll, E., Braun, J., 2002, Mathematical modeling of scroll compressors – part I: compression process modeling, Int. J. Refrig., 25, pp. 731-750.

[19] Chen, Y., Halm, N., Braun, J., Groll, E., 2002, Mathematical modeling of scroll compressors – part II: overall scroll compressor modeling, Int. J. Refrig., 25, pp. 751-764.

[20] Wang, B., Li, X., Shi, W., 2005, A general geometrical model of scroll compressors based on discretional initial angles of involute, Int. J. Refrig., 28 (6), pp. 958-966.

[21] Lemmon, E., Span, R., 2006, Short fundamental equations of state for 20 industrial fluids, J. Chem. Eng. Data, 51, pp. 785-850.

[22] Kakac, S., Shah, R., Aung, W., 1987, *Handbook of Single-Phase Convective Heat Transfer*, Wiley & Sons.

Appendix A

Meaning of the symbols are given in Figs. 2, 3 and in Nomenclature. The suction volume is:

$$V_s(\theta)=\frac{1}{2}h\,r_b\,r_o\Big[2\varphi_e\,\theta-\theta^2-\\-\theta\left(\alpha_i+\alpha_o+\pi\right)+2\left(1-\cos\theta\right)-\\-2\left(\varphi_e-\pi\right)\sin\theta-\frac{\alpha_i+\alpha_0}{2}\sin\left(2\theta\right)\Big] \quad \text{(A1)}$$

Compression chambers are organized in k_{max} couples, where k_{max} depends on the wraps length. While the outer levels (until k_{max} *-1*) exist for the whole working cycle, the k_{max}*-th* one opens to discharge region at a defined orbiting angle θ_d. The volume of one *k-th* level chamber is:

$$V_{c,k}(\theta)=\pi\,h\,r_b\,r_o\{2\varphi_e-2\theta-\\-\left[\alpha_i+\alpha_o+\left(4k-1\right)\pi\right]\} \quad \text{(A2)}$$

The discharge region is formed by three different chambers: the lateral ones V_d, that were compression chambers before θ_d, and the inner zone V_{dd}, directly connected to the discharge hole. This volume reaches his minimum at θ_d and is called "clearance volume" V_{cl}. The discharge process begins at θ_d, when the two k_{max}*-th* level chambers open to discharge region. Initially, the gap between scrolls is too small to permit pressure equalization, so the three chambers must be treated separately. When pressure equalization is reached, a unique discharge zone $V_{d\text{-}dd}$ must be considered. The final expressions are:

$$V_{cl}=h\,r_c^2\left[\pi-\arcsin\left(2\,r_b/r_c\right)-2\,r_b/r_c\right] \quad \text{(A3)}$$

$$V_{d-dd}(\theta)=h\,r_b\,r_o\Big[\varphi_{\bar{k}}^2-\left(\varphi_{os}+\pi\right)^2-\\-\left(\pi+\alpha_i+\alpha_o\right)\left(\varphi_{\bar{k}}-\varphi_{os}-\pi\right)\Big]+V_{cl} \quad \text{(A4)}$$

where the involute angle of the innermost contact point between scrolls is:

$$\varphi_{\bar{k}}=\begin{cases}\varphi_e-2\,\pi\,k_{\max}-\theta, & \theta\le\theta_d\\ \varphi_e-2\,\pi\left(k_{\max}-1\right)-\theta, & \theta_d<\theta\le 2\,\pi\end{cases} \quad \text{(A5)}$$

$$V_{dd}(\theta)=h\,r_c\left[r_c\,\beta-\left(r_c-w_{d-dd}\right)\sin\beta\right] \quad \text{(A6)}$$

where:

$$\beta(\theta)=\pi-\arccos\left[\frac{r_c-r_o+r_o\cos\left(\theta-\theta_d\right)}{r_c-w_{d-dd}}\right]-\\-\arcsin\left(2\,r_b/r_c\right) \quad \text{(A7)}$$

and the width of the opening between the discharge regions is:

$$w_{d-dd}(\theta)=r_c-\\\sqrt{r_o^2+\left(r_c-r_o\right)^2+2\,r_o\left(r_c-r_o\right)\cos\left(\theta-\theta_d\right)} \quad \text{(A8)}$$

The volume of lateral discharge chambers is:

$$V_d(\theta)=\frac{1}{2}\left(V_{d-dd}-V_{dd}\right) \quad \text{(A9)}$$

HFC-245fa Working Fluid in Organic Rankine Cycle - A Safe and Economic Way to Generate Electricity from Waste Heat

Gary J. Zyhowski[a], *Andrew P. Brown*[b], *Abdennacer Achaichia*[b]

[a] *Honeywell, Buffalo, New York, USA*
[b] *Honeywell, Heverlee, Belgium, NV*

Abstract: Climate change, environmental legislation and binding targets for renewable energy, alongside an increased focus on the economic benefits of energy and fuel conservation, are driving the adoption of new technologies as sources of energy. With these dynamics, it is evident that waste heat recovery technologies can play a key role in reducing the dependency on fossil fuels and in meeting future energy needs. These technologies can be important in reducing the CO_2 footprint of existing fossil power generation and achievement of renewable energy targets. Since the recovered heat is effectively 'free of charge', there is a direct positive impact on the energy costs to the end user. There has been considerable focus on the recovery of high temperature waste heat but less attention has been paid to the extensive opportunities that exist to recover lower grade heat. This paper focuses on the Organic Rankine Cycle (ORC) as an effective technology for low to medium temperature heat recovery. Recovery of low to medium temperature waste heat from installations such as power plants, diesel & gas generators, and industrial plants using ORC technology can provide additional electrical output, thus boosting overall efficiency and reducing the ratio of emissions/kWe produced. When available process heat cannot be readily utilized to satisfy a thermal requirement, Organic Rankine Cycle offers flexibility since the additional electrical output can be used in many ways, eliminating the associated expense and engineering required to use this heat in methods that require site-specific design. The availability of a non-flammable working fluid with appropriate thermophysical properties is an important aspect affecting the efficiency of the Organic Rankine Cycle. This paper describes the properties of HFC-245fa and discusses its potential application in power generation systems. The commercially available Refrigeration Grade HFC-245fa meeting Air-Conditioning and Refrigeration Institute Standard 700 has provided a viable option for safe, flexible, and economically efficient conversion of waste heat to electric power using Organic Rankine Cycle technology.

Keywords: HFC-245fa, Organic Rankine cycle, geothermal energy, bottoming cycle.

1. Introduction

Predictions of the growth in energy consumption around the world offer a clear picture that fossil fuel energy resources alone will not be capable of meeting future energy requirements. Additionally, climate change, environmental legislation and binding targets for renewable energy, alongside an increased focus across the manufacturing sector on the economic benefits of energy and fuel conservation, are driving the adoption of alternative technologies as sources of both thermal and electrical energy. On the basis of these dynamics it is evident that heat recovery and waste heat recovery technologies can be important in reducing the dependency on fossil fuel power. To date, both the industrial world and the power generation sector have predominantly focused on the utilization and recovery of high temperature heat and waste heat, but less attention has been paid to the large number of opportunities that exist to recover and use lower temperature heat.

In terms of off-setting current fossil fuel power generation, it is clear that a mix of both renewable and cleaner energy technologies will be necessary to meet future demand. Geothermal power, for example, will be part of this energy mix. In Europe, 2030 targets are for the geothermal sector to contribute to 5% of the total electricity production,

and 3.5 % of the total heat generation [1]. In North America, geothermal sources hold huge theoretical potential for power generation. In the US alone it is assumed to be as high as ~350 GW. The targeted growth in geothermal electricity production will require the development of lower temperature geothermal heat sources utilizing binary ORC cycles. Quite a number of examples of this are already in existence, for example Raser Technologies power plant in Utah, and a number of other projects are under development, for example in Germany, New Mexico, Nevada and Mozambique.

While ORC has become recognized as an established technology to recovery lower temperature geothermal heat, its implementation to recovery low temperature waste heat from installations such as power plants, diesel & gas generators, and industrial plants is in its relative infancy. The opportunity is a substantial one. Energetic, Inc has estimated that there may be as much as 10 Quads of industrial waste heat energy available in the United States [2]. (This equates to 10^{16}BTUs or approximately $1.06x10^{13}$ megajoules). However, historically neither the economic or regulatory drivers have been in place to stimulate a significant focus on this opportunity. The lansdscape is changing however, and as energy prices increase, and environmental regulations tighten, e.g. anticipated developments come 2013 in CO_2 emissions legislation, commercial companies are increasingly being required to take additional steps to offset their power costs and reduce their environmental footprint. Low temperature waste heat recovery using Organic Rankine Cycle technology can provide the dual benefit of additional electrical output that reduces cost by offsetting existing power consumption, and the reduction of the CO_2 footprint. For example, recovery of waste heat streams from a coal fired power plant using Organic Rankine cycle Technology, provides the opportunity to achieve the same electrical power output, but with a lower fuel consumption, thus offering a net reduction in CO_2 emissions.

A critical element in the design of an Organic Rankine Cycle is the selection of the working fluid. Thermodynamic properties of a working fluid are not the only criteria to be taken into account during this selection. The impact of the working fluid on total system cost and safety in the end-user environment are also key criteria as they directly impact the economic fit, acceptability and ultimately market growth of Organic Rankine Cycle systems. This paper examines the suitability of one such fluid HFC-245fa or 1,1,1,3,3-pentafluoropropane, which is a non-flammable, single-component hydrofluorocarbon working fluid.

2. HFC-245fa organic Rankine cycle applications

2.1 Organic rankine cycle system characteristics

Figure 1 is a basic ORC system diagram. ORC systems convert thermal energy to mechanical shaft power. Typically, the mechanical shaft power is then used to drive an electric generator.

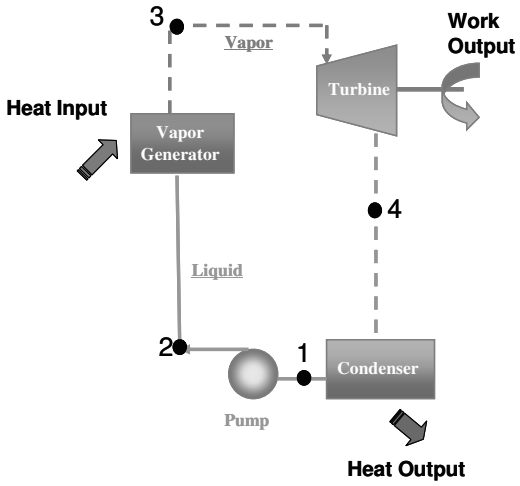

Fig. 1. Simple organic Rankine cycle system diagram.

ORC can be used for waste heat recovery from industrial plants, efficiency improvement in power stations, and utilization of geothermal and solar heat. The efficiency of an ORC is typically between 10 and 20%, depending on temperature levels and availability of a suitably matched fluid. ORC is an attractive option for heat recovery in the range of 90 ºC to 200ºC, particularly if no other use for the waste heat is available on site. At temperatures of 650-980 ºC, water is a very cost-effective working fluid, whereas; when source temperatures drop low enough that a steam cycle is no longer thermodynamically efficient, organic fluids are more suitable. One such fluid is HFC-

245fa or 1,1,1, 3, 3-pentafluoropropane. Cycle performance and heat exchanger limitations relating to the use of water, isopentane, and HFC-245fa as working fluids are discussed later in this paper. In the section that follows is a comparison of HFC-245fa and water as working fluids in a bottoming cycle application.

2.2 Bottoming cycle

Coal-fired thermal power plants consume vast amount of fossil fuel. Interest in efficiency improvement is currently high. With some systems, it is possible to utilize the low-grade heat that might otherwise be abandoned. Often, not quite 40% of the heat imparted to the steam is converted to mechanical work, with the rest being abandoned to a "cold reservoir". Consider a simple example where a steam boiler feeds a primary turbine (or 1st stage) and then effluent is reheated and routed to a secondary turbine operating at lower pressure (or 2nd stage). In Table 1 below is an example with conditions chosen such that condensation does not occur in the turbines. At the conditions given in Table 1, the theoretical cycle efficiency is 36.3%. Thermodynamic data used to develop the examples and illustrations in this paper were taken from NIST Refprop 7.0 [3].

In this example, if HFC-245fa is used in a bottoming cycle arrangement, the overall thermal energy efficiency can be improved 25%. Table 2 lists example conditions/quantities for the HFC-245fa cycle. The energy efficiency improvement attainable for a given plant will depend on the particular operating conditions.

Table 3 includes a cursory payback assessment which illustrates that for this example, the ORC system payback is less than 3 years.

2.3 Geothermal hot water

Geothermal power can address growing demand for power without consuming more fossil fuel. With Rankine cycle systems that obtain heat from a liquid source, it is important to consider the implications of latent heat of vaporization and heat capacity as they bear on boiling and sensible heating. Looking to the previous example where water was one of the working fluids, it brings this to light. Since water and HFC-245fa differ significantly with regard to latent heat of vaporization, it makes the example illustrative. A comparison of HFC-245fa and a second organic fluid, isopentane, are discussed in Section 3.2. Heat exchange limitations associated with water relate to the high ratio of latent heat of vaporization to heat capacity. In Figure 2, point A represents the condition for transfer of heat from flowing source fluid to the working fluid (10°C temperature difference in heat exchanger) in order to supply the heat required to vaporize the working fluid. This determines the maximum flow rate for the working fluid. At those flow rates, the heat required to raise the temperature of the liquid working fluid from the condensing condition to the evaporating condition can then be determined. In Figure 2, the sensible heat required is the thermal power difference between points A and B (water) or points A and B' (HFC-245fa). The temperature of the flowing source is lowered to a greater extent with HFC-245fa (point b') than with water (point b). Thus, more heat can be extracted from the source with HFC-245fa. Overall efficiency, defined as the cycle efficiency times the ratio of thermal power extracted to the total thermal power available, is influenced by heat exchange limitations. In the example of Figure 2, the higher cycle efficiency of water is offset by a heat exchange limitation and results in a lower overall efficiency versus HFC-245fa.

3.0 HFC-245fa as a Rankine cycle working fluid

3.1 Fluid properties and equipment configuration

ORC cycle fundamentals establish that the greater the temperature difference between the source and sink, the more work that is available. However, the properties of a particular working fluid will dictate the practical extraction points. When HFC-245fa is subjected to isentropic expansion, the exiting gas is more superheated than at the outset of expansion. The thermal energy associated with this exit superheat provides no benefit if it is only to be rejected at the condenser. A recuperator (heat exchanger) located between the turbine exhaust and the condenser can be employed to recover the superheat into the condensate return thus improving cycle efficiency.

Table 4 lists the enthalpy drop associated with expansion and the enthalpy difference between superheated and saturated conditions at the expander outlet. The data show that increasing expander inlet temperature reflects increasing

expander inlet superheat and that the enthalpy drop associated with the expansion (work extraction) step increases with increasing expander inlet superheat and with decreasing condensing temperature. Table 4 shows the enthalpy difference between the exit superheat and saturated condition can be of comparable magnitude to the expander enthalpy drop. Thus the benefit of a recuperator becomes clear.

3.2 Comparison of HFC-245fa and Isopentane

When selecting a working fluid for a particular application, it is important to match the working fluid to the source temperature. Typically, the boiler must operate at a temperature such that the corresponding thermodynamic state is sufficiently below the fluid critical point so that the latent heat of vaporization is not so small as to dictate an unrealistically high mass flow rate. As noted in Section 2.3, in the comparison of HFC-245fa and water, it is also important to

Table 1. Steam Conditions for Simple Turbine Arrangement.

Outlet Location	Temperature, ºC	Pressure, kPa	Enthalpy,liq.	Enthalpy,vap.	Entropy,vap.
			kJ/kg	kJ/kg	kJ/kg K
From Boiler	537.8	8274		3486.7	6.8229
From 1st turbine	152.0	500.0	640.0	2748.8	6.8299
From Reheater	482.2	413.7		3446.3	8.1256
From 2nd turbine	135.0	29.2	552.0	2676.3	8.1274
From condenser	55.0	19.3	223.9		
From Pump	58.0	8619	243.1		
Net Heat Output		1389.2 kJ/kg steam			
Heat Input		3822.1 kJ/kg steam			
Theoretical cycle efficiency		0.363			

Enthalpy, entropy values use ASHRAE thermodynamic reference state.

Table 2. HFC-245fa Rankine Cycle.

Outlet Location	Temperature,ºC	Pressure, kPa	Enthalpy, liq.	Enthalpy, vap.	Entropy, vap.
			kJ/kg	kJ/kg	kJ/kg K
From Boiler	125.0	2113		490.1	1.811
From turbine	51.9	213		447.5	1.811
From condenser	95	213	246.5		
From pump	97.7	2113	249.1		
Work done on 245fa - pump		2.53 kJ/kg			
Net mechanical energy/unit mass		39.95 kJ/kg			
Thermal input to 245fa/cycle		241.0 kJ/kg			
Mass ratio		9.07 kg 245fa per kg steam condensed			
Net ORC Work/unit mass steam		362.7 kJ/kg			
Combined cycle work output		1792.5 kJ/kg			
Combined cycle efficiency		0.456			
% Increase in efficiency		25.6 (compared to Table 1 case)			

(Enthalpy, entropy values use ASHRAE thermodynamic reference state.)

Table 3. High Level Payback Analysis.

Mechanical Power (W) = Power in load circuit (We)/commercial efficiency	1.39 x 10^9 W or 5.0 kJ/hr
Steam mass flow (kg/hr) = mechanical power (kJ/hr)/heat input with reheat (kJ/kg)	1.27 x 10^6 kg/hr steam
ORC work = Mass Flow Steam (kg/hr) x Net Work Out/Unit mass steam (kJ/kg)	4.6x10^8 kJ/hr or 128MW
Plant electric output increase, %	25
ORC System Cost ($1500 to $2000/KW)	$192M to $256M
Value of Power produced in ORC ($0.085/kWhr)	$95M
Payback (assumes operating cost is small)	2 to 3 years

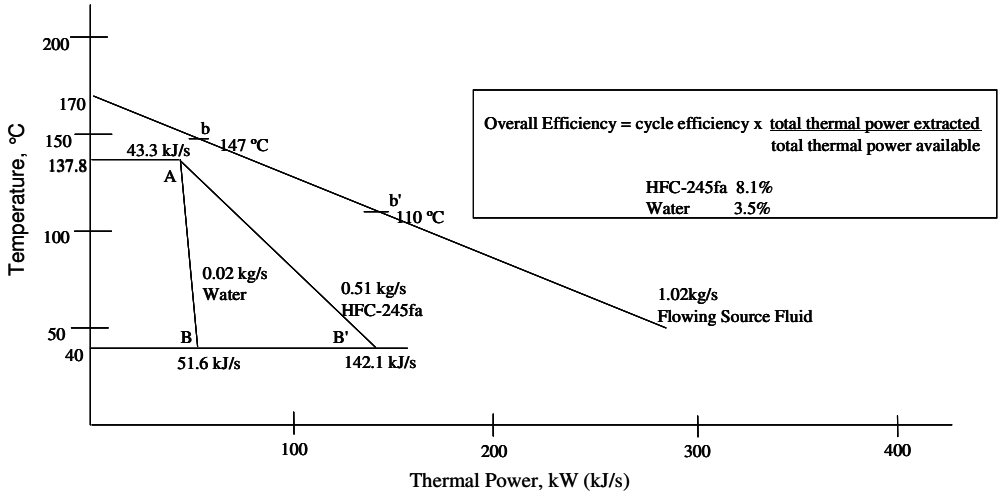

Fig. 2. Comparison of boiling and sensible heating contributions to overall efficiency.

Table 4. Enthalpy drop and superheat enthalpy of HFC-245fa (isentropic expansion).

Temperature Expander Inlet °C	Temperature Condensing °C	Enthalpy Drop Expansion kJ/kg	Superheat Enthalpy kJ/kg
148.9	21.1	56.0	29.3
162.8	21.1	61.1	48.1
176.7	21.1	64.9	65.1
148.9	15.4	60.1	29.8
162.8	15.4	65.5	48.4
176.7	15.4	69.9	64.7

understand the impact of the sensible heating component. One application where sensible heating is of particular interest is geothermal energy conversion. In geothermal ORC applications, it is desirable to maximize per pass heat removal from the source; that is, to lower the temperature of the source effectively as this impacts overall efficiency. Both HFC-245fa and isopentane may both be considered for use as ORC system working fluids for geothermal hot water sources. Examining a hypothetical case of a 245fa ORC system and an isopentane ORC system each sized so that 5000kJ/s goes to the boiler, the following data was derived for a 90ºC source and a 120ºC source. A specific diameter

of 4 was assumed (taken from a Balje diagram) [4]. To determine the diameter, the equation

$$D = d_s \, Q^{0.5} / H^{0.25} , \quad (1)$$

was used where

Q is the volumetric flow rate (m^3/s),
H is head ($m^2/s^{2)}$ and
d_s is specific diameter (dimensionless).

Head is determined from the equation

$$PR = [1+(\gamma-1) H / a^2]^{\gamma/\gamma-1} , \quad (2)$$

where

PR is the turbine pressure ratio (dimensionless),
γ is the isentropic exponent (dimensionless, for an ideal gas the term is the ratio of heat capacity at constant pressure to heat capacity at constant volume, Cp/Cv), and
a is the speed of sound in the particular working fluid (m/s).
The term H was introduced previously.

Table 5. Geothermal hot water: HFC-245fa and isopentane comparison.

90ºC source*	Mass flow, kg/s	Turbine Exit flow, m^3/s	Turbine Diameter, m	Theoretical electrical output, kWe
HFC-245fa	22.4	2.34	0.474	473.5
Isopentane	11.9	3.94	0.526	476
120C source**				
HFC-245fa	20.6	2.30	0.418	646.5
Isopentane	10.6	4.06	0.470	531

*30ºC condensing (fluid temperature)

** exit condition governed by 9:1 pressure ratio

Analysis of the data in Table 5 reveals that the isopentane turbine diameter would be approximately 11% larger than the 245fa turbine diameter for the case of a 90ºC and about 12% larger for the 120ºC source. This would, of course, result in an equipment cost increase. The electrical output, without de-rating for efficiency of the generator, is about 0.5% more for isopentane with the 90°C source and about 4.0 % more with the 120°C source. The turbine and generator efficiency are ignored in this comparison. It is reasonable to conclude that the achievable optimized turbine efficiency would be comparable for the two fluids. Bearing in mind that equipment is often built at a fixed size, it is more realistic to compare the output for a given turbine size using the two fluids, HFC-245fa and isopentane.

A comparison of electrical output for a 245fa system versus an isopentane system for the same size turbine is summarized in Table 6. One may think it as "dropping-in" isopentane in place of HFC-245fa; essentially replacing HFC-245fa with isopentane on a 1:1 volume basis. Equation (1) can be rearranged to determine the volumetric flow rate from the known turbine diameter. Equation (2) can be rearranged to determine head at the given conditions. From the volumetric flow rate and density at the given conditions, the mass flow rate is found. Knowing the mass flow rate and the latent heat of vaporization at the conditions of the cycle, the corresponding thermal input is derived. Finally, the product of the thermal input and the theoretical thermodynamic cycle efficiency provides an estimate of the electrical output. Theoretical thermodynamic efficiencies used were 0.0952 and 0.1344 for isopentane at 90°C and 120°C, respectively. Corresponding efficiencies for HFC-245fa were 0.0947 and 0.1293, respectively. For the conditions in Table 5, using isopentane instead of HFC-245fa would result in an estimated 19% reduction in electrical output for a 90°C source and nearly an 18% reduction for a 120°C source.

An analysis of piping sizing was also conducted; however, for the sake of brevity, a detailed discussion has been omitted. Looking at the 90°C source condition, if the piping diameters determined for HFC-245fa are used for isopentane at the corresponding isopentane mass flow, velocities for the expander outlet and

Table 6. "Drop-in" of isopentane in a turbine initially sized for HFC-245fa.

90°C Source	Turbine Diameter, m	Volumetric flow rate (turbine exit), m^3/s	Mass flow, kg/s	Electrical Output, kWe	% Change kWe vs. HFC-245fa
Isopentane	0.474	3.20	9.6	383	(19.0)
HFC-245fa	0.474	2.34	22.4	473.5	
120°C Source					
Isopentane	0.418	3.22	8.4	531	(17.9)
HFC-245fa	0.418	2.30	20.6	646.5	

liquid line are outside the acceptable range by about 1% and 15%, respectively. The isopentane expander inlet velocity was within acceptable parameters.

In Section 2.3, it was mentioned in broad terms that the temperature drop of a flowing source is an indicator of how effectively heat is being delivered to the organic Rankine cycle system. If follows that a greater temperature drop is more desirable since it has a positive impact on overall efficiency. An organic Rankine cycle system sized to deliver 5000kJ/s (from a 90°C source) to the boiler will have contributions from the latent heat of vaporization of HFC-245fa at 80°C and the sensible heating from 30°C to 80°C totalling about 224 kJ/kg. The product of the corresponding mass flow rate from Table 6 and the total heat delivered to the working fluid can be set equal to the heat given up by the flowing source water, which is, in this instance, 5000kJ/s. From the relationship

$$q = mC_p\Delta T, \quad (3)$$

where

q is the heat removed (kJ/s),

m is mass flow (kg/s),

Cp is heat capacity at constant pressure (kJ/kg K), and

ΔT is the temperature difference (°C),

the latter can be determined. Assuming a source flow rate of 100kg/s and using the heat capacity of water at 90°C, the estimated drop in the source temperature would be 12°C. As a check, the total latent and sensible heat delivered to isopentane, 419kJ/kg times the corresponding mass flow rate in Table 5 results in expectedly 5000kJ/s. Since both systems are sized to 5000kJ/s heat input, the temperature drop in the source water would be the same 12°C.

Finally, the most obvious difference between HFC-245fa and isopentane is that the former is non-flammable while the latter is flammable. The use of a flammable working fluid typically means that significant additional costs are incurred relating to the end-user site and the equipment. A 5MWe geothermal power plant utilizing an organic Rankine cycle system containing a flammable working fluid could require on the order of an additional $500,000 for flammability and site safety-related costs [5]. Additional factors such as site permitting, which is also more involved when a flammable fluid is used and impact on insurance premiums also should be taken into account when making a choice between flammable and non-flammable working fluids. Flammability risk would also be a concern with transportation, storage, handling, and during system operation.

4. Benefits to the environment

Increasing the use of solar, geothermal, biomass and waste heat energy to produce electricity curbs the use of fossil fuels and thereby helps reduce air emissions. The additional power output from ORC systems appended to power generation systems can help meet growing demand for power while offering a more attractive emissions profile since there is a gain in output without additional fuel consumption. Optionally, integrated ORC/distributed generation equipment can be downsized relative to unmodified distributed generation equipment, potentially using less fuel and producing fewer emissions while providing

the same power output. Equation (3) can be used to reasonably estimate the electric power that can be derived using organic Rankine cycle to convert thermal energy from a flowing fluid source [6]. A notable example of a flowing liquid source would be geothermal hot water.

$$NEP = [(0.18T - 10)\ ATP]/278\ , \quad (4)$$

In (4),

T is the inlet temperature of the flowing source fluid (ºC),

NEP is the net electric power (kW) and

ATP is the available thermal power (kW).

The available thermal power is the heat available from the flowing source fluid and is typically determined using a temperature 10ºC above the bottom cycle temperature. With liquid sources such as diesel genset engine coolant, organic Rankine cycle systems can produce on the order of 10% to 15% additional electric power from the waste heat. In addition to the increased electric power output without consumption of additional fuel, there is the concomitant benefit of no additional emissions.

5.0 CONCLUSIONS

HFC-245fa thermophysical properties make it a suitable working fluid for organic Rankine cycle applications. The high heat capacity of HFC-245fa results in improved theoretical cycle efficiency and heat exchanger performance that translates into improved overall efficiency. In a bottoming cycle, the advantages of HFC-245fa as compared to water include higher cycle efficiencies, lower latent heat-to-heat capacity ratio (heat exchange pinch point for water), and higher gas densities (lower volumes). Geothermal, solar, and industrial waste heat sources can be used to drive HFC-245fa as the working fluid in organic Rankine cycle systems in order to achieve useful thermal energy utilization via thermal energy conversion to electric power. When coupled with fossil fuel-driven distributed power generation systems, improved air emissions profiles and fuel consumption profiles can be realized.

References

[1] European Geothermal Energy Council Press Release, February 11, 2009.

[2] Vilayanur Viswanathan, et. al., 2005, Pacific Northwest National Laboratory, Opportunity Analysis for Recovering from Industrial Waste Heat and Emissions, DOE-ITP Industrial Materials of the Future Program Review, Chicago, IL, June 1, 2005.

[3] Refprop, Reference Fluid Thermodynamic and Transport Properties, NIST Standard Reference Database 23, Version 7.0, National Institutes of Standards and Technology, Boulder, CO 80305, USA.

[4] Brasz, Joost J., Design, Analysis and Applications of Centrifugal Compressors, Short Course, Purdue University, July 10-11, 2004.

[5] Honeywell estimate.

[6] Onbasioglu, S. U., October, 2000, Renewable Energy Systems, Lecture 2 (Geothermal Energy), *www.mkn.itu.edu.tr/~onbasiogl1/RES2.htm*, p. 13.

Investigation of the criteria for fluid selection in Rankine cycles for waste heat recovery

M. Aslam Siddiqi [a] *and Burak Atakan* [a]

[a] *Thermodynamics, IVG, Faculty of Engineering, University of Duisburg Essen, Lotharstr. 1, 47048 Duisburg, Germany*

Abstract: The organic Rankine cycle is a promising way for the conversion of low temperature heat to electricity. Different fluids can be used in Rankine cycles for the utilization of waste heat. The suitability of a certain fluid will depend on its thermodynamic properties as well as on the conditions at which the heat is available, thus it is often unclear if an organic fluid has any advantage compared to inorganic fluids like water. Various substances starting from the refrigerants to high boiling organic liquid have been investigated as possible working fluid for the different temperature ranges at which the waste heat is available. The present communication reports exemplary the results for three different classes of substances, a hydrocarbon (n-heptane), two refrigerants 1.1.1.3.3-pentafluoropropane (R245fa) and pentafluoro butane mixture (Solkatherm, SES36), and water in the intermediate temperature range (473 to 773 K) where the exhaust gases of combustion engines may be used as energy source for cogeneration. In this range it turns out that for many conditions, water and heptanes are a well suited working fluids for cogeneration systems. In the present investigation, the attention was not laid on the cycle efficiency alone, but also on the total exergy usage from an enthalpy stream (e.g. exhausts gas). This is used for defining the total efficiency for the process. The results for the thermodynamic parameter total heat recovery efficiency and the surface area of the heat exchanger have been discussed. $T-\dot{H}$ diagrams were also used for judging the suitability of a fluid. It turns out that water is well suited for many cases in the intermediate temperature regime.

Keywords: ORC, Rankine cycle, thermal efficiency, $T-\dot{H}$ -diagram, exergy loss, CHP

1. Introduction

In the last years, the utilization of low grade heat sources, such as exhaust gases of gas turbines, engines, geothermal resources, and the waste heat from industrial plants, is becoming more and more important [1-4]. Energy recovered from waste heat streams could supply a substantial part or all of the electric power required by a plant, at no additional cost [5]. Therefore, heat recovery offers a great opportunity to conserve by productively using the waste energy to reduce overall plant energy consumption and simultaneously decrease CO_2 emission.

The organic Rankine cycle is a promising way for the conversion of low and medium temperature heat to electricity [1-4]. There are a number of fluids which can be used as the working medium. So the question is which fluid is most suitable under the specified conditions. The suitability of the fluid will depend on its thermodynamic properties as well as on the conditions at which the heat is available [6]. We are working on a long term program to investigate various substances starting from the refrigerants to high boiling organic liquids to suggest suitable working fluid for the different temperature ranges at which the waste heat is available:

a) 373 K to 473 K e.g. geothermal resources
b) 473 K to 773 K e.g. waste heat from industries, exhaust from engines
c) above 773 K e.g. biomass combustion.

A large amount of waste heat energy is released into the environment from exhaust gases from turbines and engines as well as from industrial plants. The geothermal resources and solar energy also offer themselves as low grade heat sources.

The present study assumes a constant exhaust gas stream at 773 K as the exergy source which transfers heat to the cycle, which is a reasonable temperature for (Diesel generator) engine exhausts. In contrast to most previous publications the combined generation of heat and power (CHP) using organic Rankine cycles is studied in the present work, meaning that the heat rejection of the cycle shall be used for heating purposes. Such systems can e.g. be used as the energy supply for hospitals. Thus, to be useful for this purpose, a heating of the cooling water to 85°C was studied.

a xg 4Ec z- bf e z- pb- g f2f [g t e 4ddgEv z 1 gz- q4 Egf 4TgE zq [gzvq z] zEq 4d [4C cEzwg xgzq a xg Egf 4TgE2 4d [4C cEzwg Czvqg xgzq bv - 4q 4- [2 gf 4- 41 bf z[o5q z[v4 xg[] v q4 Egw5f g qxg zql 4v] xgEbf] 4[[5qb4- g1 bvvb4- 4d t n t o t z- w 4qxgE] 4[[5qz- qv q f z- og z]] [bgw q4 v1 z[[v2vqg1 v q44 l 41 g Egf g- q vcfwbgv 4- qxg 5vg 4d 4Ec z- bf e z- pb- g f2f [g d4E[4C cEzwg xgzq Egf 4TgE2 dE41 TzEb45v v45Ef gv f z- og d45- w b- u i 4CgTgE qxg ogvq fx4bf g 4d qxg d[5bw z- w qxg] zEz1 gqgEv d4E z cbTg- xgzq Egf 4TgE2] E4o[g1 Eg1 zb- v 5- Egv4[Tgw 2wE4f zEo4- v v5f x zv] g- qz- g q4 w4wgf z- g zE41 zqbf v z- w - 51 gE45v EgdEbc gEz- qv xzTg ogg- b- Tgvqbc zqgw u i b-] zEq z[v4 b- f 41] zEbv4- q4 CzqgEu i - qxbv] z] gEqxg Egv5[qv d4E Eg] Egvg- qzqbTg v5ovqz- f gv TbR xg] qz- g qC4 EgdEbc gEz- qv e dz z- w l l Cxbf x bv z- zRg4qE4] bf 1 bQcfEg 4d z- w z] gEd[54E4] 4[2gqxgE z- w CzqgE zEg] Egvg- qgw d4E qxg f zvg 4d Czvqg xgzq zTzb[zob[bq2 zq e gdEbc gEg- qv [bpg qxg [zqgE qC4 zEg 1 zEpgqgw d4E v] gf bz[z]] [bf zqb4- v g c zq [4C qg1] gEzcfEgv o5q 4dqg- bq bv 5- f [gzE Cxgqxg E qxg2 1 z2 z[v4 og 5vgd5[b- wbdgEg- q qg1] gEzcfEg Ez- cgv t dqg- v1 z[[f 41] z- bgv Cx4 1 zwg c44w gO] gEbg- f gv Cbqx z f gEqzb- d[5bw b-] EgTb45v z]] [bf zqb4- v] EgdgE q4 vqf p q4 qxbv d[5bw z[v4 b- wbdgEg- q qg1] gEzcfEg Ez- cg z]] [bf zqb4- v 1 5f x pb- w 4d . 5gvqb4- v 1 4qbTzqgw 5v q4 vg[gf q qxgvg qC4 d[54Eb- zqgw EgdEbc gEz- qv q4 qxg] Egvg- q b- Tgvqbc zqb4-

] zEq dE41 qxg q4qz[gddbf bg- f bgv qxg vbRg 4d qxg xgzq gOf xz- cgE zEgz bv E45c x[2 gvqbl zqgw d4E gzf x] E4f gvv vb- f g qxbv bv z- bl] 4Eqz- q dzf q4EEgc zEwb- c qxg b- Tgvql g- q f 4vqv a xg f2f [gv zEg vcfwbgv d4E wbdgEg- q gTz] 4Ezq4E] Egvv5Egv 4d 5] q4 ozE Cxbf x bv z Egzv4- zo[g Tz[5g d4E vb- c[g vqzcg qfEob- gv z- w z[v4 d4E vzdgq2 Egzv4- v b- v1 z[[wgTbf gv

2. Method

a xg C4Epb- c] Eb- f b] [g 4d z e z- pb- g f2f [g bv Cg[[p- 4C- z- w f z- og d45- w b- z- 2 vqz- wzEw qxgEl 4w2- z1 bf qgOq o44p s vb- c z- 4Ec z- bf d[5bw w4gv - 4q f xz- cg z- 2qxb- c b-] Eb- f b] [g t - [2 qxg vxz] g 4d qxg vzcfEzqb4- Egcbl g f xz- cgv wg] g- wb- c 4- qxg d[5bw 4CgTgE qxg 1 4wg[5vgw d4E qxg f z[f 5[zqb4- v z- w qxg - 51 ogEb- c 4d qxg wbdgEg- q vqzqgv bv vx4C- b- bc5Eg d4Ez Egzw2 EgdgEg- f g

a xg Eg[zqgw . 5z[bqzqbTg a v wbzcEz1 bv z[v4 wEzC- - g- qxz[] 2 vqEgz1 4d x4q zbE vbl 5[zqb- c z- gOxz5vq czv zq z wgdb- bqg qg1] gEzcfEg bv zTzb[zo[g dE41 z- b- w5vqEbz[ ] E4f gvv 4E z- g- cb- g - gEc2 Cb[[og qEz- vdgEgw zv xgzqq4 qxg C4Epb- c d[5bw 4d z e z- pb- g f2f [g a xg e z- pb- g f2f [g] E4w5f gv g[gf qEbf bq2 z- w Egmgf qv qxg xgzq zq z [4CgE qg1] gEzcfEg Cxbf x fz- og 5vgw d5Eqxg E d4E qxg xgzqb- c 4d f4[w CzqgE r a xg g. 5zqb4- v 5vgw d4E qxg 1 4wg[ ] E4f gvv fz[f 5[zqb4- v zEg v51 1 zEbRgw og[4C

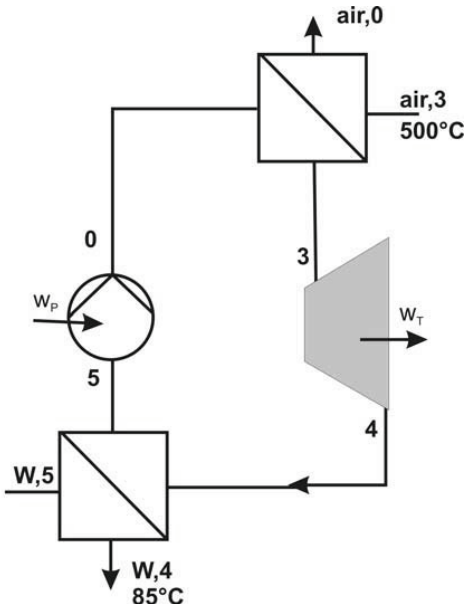

(a)

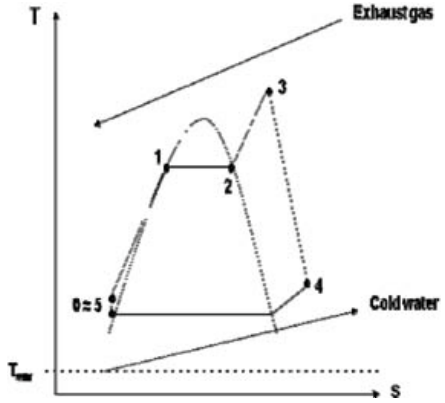

(b)

Fig. 1 The ORC system used in this study (a) and the related T-s diagram (b).

The working fluid which leaves the condenser as boiling liquid at a lower pressure (state 5, p = p_{cond}) is brought to a higher pressure (p = p_{boiler}, state 0) with the help of a pump.

The specific work of the pump is then

$$w_{50} = \frac{v(p_{boiler} - p_{cond})}{\eta_P} \quad (1)$$

where v is the specific volume of the pure boiling liquid in state 5. Thus

$$h_{F,0} = h_{F,5} + w_{50} \quad (2)$$

The subscript F refers to the fluid of the Rankine cycle and the numbers refer to different states.

The working fluid receives energy from the hot gas stream via a counter current heat exchanger and is vaporized in three stages:

a) Heating of the working fluid up to boiling (state 0 → state 1)

b) Complete vaporization of the working fluid (state 1 → state 2)

c) Superheating of the fluid (state 2 → state 3).

The energy balance across the heat exchanger gives:

$$\dot{m}_F \cdot (h_{F,3} - h_{F,0}) + \dot{m}_{air} \cdot (h_{air,0} - h_{air,3}) = 0 \quad (3)$$

The heat exchanger may be thought to be made up of three parts and in each part one of the above operations takes place. So the first part, i.e. the heat transfer needed for raising the temperature of the working fluid to the boiling temperature can be written as:

$$\dot{Q}_{add,01} = k_{01} \cdot A_{01} \cdot \Delta T_{LMTD,01} = \dot{m}_F \cdot (h_{F,1} - h_{F,0}) \quad (4)$$

The logarithmic mean temperature difference ΔT_{LMTD} is defined as:

$$\Delta T_{LMTD,01} = \frac{\Delta T_0 - \Delta T_1}{\ln(\frac{\Delta T_0}{\Delta T_1})} \quad (5)$$

The pinch point for the heat exchanger (states: 0-3) restricts the maximum mass flow rate in the cycle, while the pinch point in the heat rejection from the cycle limits the maximum cooling water flow rate.

The temperature of air in state 1 is written as

$$T_{air,1} = T_{air,0} + \frac{\dot{m}_F \cdot (h_{F,1} - h_{F,0})}{\dot{m}_{air} \cdot c_{p,air}} \quad (6)$$

Similar equations hold for the second and the third part of the heat transfer.

The superheated vapour is then expanded in a turbine (state 3→state 4) to the pressure of the condenser, p_{cond}:

$$w_{34} = \eta_T \cdot (h_{F,4s} - h_{F,3}) \quad (7)$$

The isobaric condensation of the vapour to the state of boiling liquid (state 4 → state 5). The heat will be transferred from the cycle to the cold water (Index: W) running in the condenser.

$$\dot{Q}_{rem} = \dot{m}_F \cdot (h_{F,5} - h_{F,4}) = \dot{m}_W \cdot (h_{W,4} - h_{W,5}) \quad (8)$$

Various parameters (e.g. the thermal efficiency of the cycle $\eta_{th,F}$, the total efficiency $\eta_{th,total}$, the net power of the process P_{net}, the exergy loss of the hot stream and the T- diagram for the process) are used to evaluate system performance. The thermal efficiency of a Rankine cycle is defined as

$$\eta_{th,ORC} = \frac{|w_{50} + w_{34}|}{q_{03}} = \frac{|w_{50} + w_{34}|}{(h_{F,3} - h_{F,0})} \quad (9)$$

This efficiency of the cycle does not take into account the residual enthalpy which is lost due to exhausting the cooled air at a temperature higher than the temperature of the surroundings. A more realistic approach will be, to consider this enthalpy loss and define the thermal efficiency of the complete process, viz., $\eta_{th,total}$

$$\eta_{th,total} = \frac{|\dot{m}_{ORC} \cdot (w_{50} + w_{34}) + \dot{m}_W \cdot w_{P,W}|}{\dot{m}_{air} \cdot c_{p,air} \cdot (T_{air,3} - T_{air,0})} \quad (10)$$

In order to make the comparisons easier, the mass flow rate of the air was chosen such, that the term in the denominator gives 1000 kW. Meaning the maximum possible heat transfer to the cycle would correspond to this value.

The net power delivered by the system is

$$P_{net} = |\dot{m}_F \cdot (w_{50} + w_{34}) + \dot{m}_W \cdot w_{P,W}| \quad (11)$$

$$w_{P,W} = v_{W,5} \cdot \Delta p_{P,W} / \eta_{P,W} \quad (12)$$

If the air is cooled only up to $T_{air,0}$ the exergy loss rate is

$$\dot{E}_v = \dot{m}_{air} \cdot [(h_{air,3} - h_{air,0}) - T_{surr} \cdot (s_{air,3} - s_{air,0})] + P_{el} \quad (13)$$

If the exhausted air is not used for other purposes but cooled to the surroundings temperature then the exergy loss rate is given by:

$$\dot{E}_{v,he} = \dot{m}_{air} \cdot [(h_{air,3} - h_{air,surr}) - T_{surr} \cdot (s_{air,3} - s_{air,surr})] + P_{el} \quad (14)$$

Besides this, the surface area of the heat exchanger required for the complete heat transfer is also very important from the point of view of its cost. This may be estiamted using equation (4) for the three parts of the heat exchanger using typical values for the overall heat transfer coefficient *k*.

Description of the model process. All properties were taken from References [7, 8]. The model process was described by the following parameters:

Surroundings: T_{surr} = 298.15 K, p_{surr} = 101.3 kPa

Gas Stream: Air, id. gas[c_p = 1.004 kJ/(kg K)] entering at 773 K. The mass flow rate was constant at 2.097 kg/s resulting in a maximum possible heat flow rate of 1000 kW. The exit temperature of the gas stream from the heat exchanger was calculated according to a pinch point analysis for the studied maximum temperature and pressure of the cycle fluid, leading to gas exhaust temperature T_{surr}.

Heat Exchangers: adiabatic towards the surrounding, isobaric heat transfer. Overall heat transfer coefficients, gas to liquid: $k_{l,g}$ = 40 W/(m^2 K) [also in 2-phase] and gas to gas: $k_{g,g}$ = 20 W/(m^2 K). ΔT_{pinch}=10 K were taken as temperature difference at the pinch point. Thus, the temperature of the hot exhaust gas at the exit of the heat exchanger is throughout higher than the ambient temperature.

Condenser: The conditions for the cooling water were $T_{W,5}$ = 298.15 K; $T_{W,4}$ = 358.15 K; $\eta_{P,W}$ = 0.7. The cycle pressure in the condenser was chosen such that the saturation temperature of the fluid was $T_{F,sat}$=363.15K, if not mentioned otherwise.

The isentropic efficiencies of the turbine and pump were taken as 0.85, respectively.

The boiler pressure was varied between 3 and 16 bar. The turbine entrance temperature $T_{F,3}$ was varied from the saturation temperature of the investigated fluid up to the maximum temperature calculated according to the pinch point analysis. At higher pressures the design of the turbine gets complex, due to the flow velocities at the turbine exit more than one stage is needed.

Table 1: Temperature $T_{F,3}$, mass flow rate of the working fluid m_F, total thermal efficiency $\eta_{th,total}$, rate of exergy loss E_v and the required surface area of the heat exchanger A at 16 bar and 523.15K boiler temperature.

Fluid $T_{F,3}$ (K)	$\dot{m}_F$ (kg/s)	$\eta_{th,total}$	$\dot{E}_v$ (kW)	A (m^2)
Water 523.15	0.282	0.130	220.0	219.0
Heptane 523.15	1.299	0.119	259.4	320.3
R245fa 523.15	2.512	0.031	349.7	300.3
SES36 493.15	3.300	0.058	321.1	322.1

3. Results and Discussions

The parameters defined by equations (9)-(11), (13) and the required surface areas for the heat exchanger were calculated. The needed thermodynamic parameters, viz. the enthalpies in different states were taken from [7] and [8]. Some representative results of the calculations are summarized in Table 1.

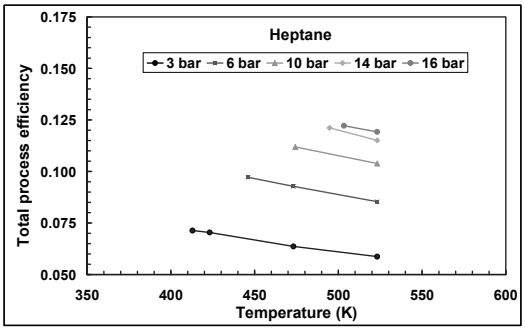

Fig. 2 The total thermal efficiency of the process for n-heptane as a function of upper pressure level and the turbine entrance temperature T_3.

In Fig. 2 the total efficiency results for heptane are shown as a function of pressure and turbine entrance temperature. It is recognized that the efficiency drops with maximum temperature. This is easily explained by the shape of the T-s-Diagram (not shown) which leads to superheated vapour at the turbine exit and thus, to an increased average temperature of heat rejection. This is not

balanced by the increased average temperature of heat addition to the cycle. Therefore, for a given pressure the state at the turbine entrance is best chosen as saturated vapour for such a simple Rankine cycle. Regarding the pressure, the highest possible is recommended, in the present case this is 16 bar. This leads to a maximum total thermal efficiency of 12.2%, while the thermal efficiency of the Rankine cycle is 14.8%. Most of the difference comes from the exhausting of relatively hot air, thus, not all of the 1000kW are transferred due to the pinch point.

The situation is similar for the other two organic fluids, but less favourable. This is shown in Fig. 3, where the results for the four fluids are compared for the maximum pressure of 16 bar, which leads throughout to the highest total efficiency. The lowest efficiencies are found for the refrigerant R245fa, while the efficiencies for SES36 is slightly better, but far from those of heptane and water. It is also noticed that with all the three organic liquids the efficiency decreases with increasing temperature level and is highest without superheating. Similar results were reported in [4]. Water as working fluid exhibits the highest ORC cycle efficiency as well as the total process efficiency. This increases with the increasing higher (boiler) pressure level and with superheating.

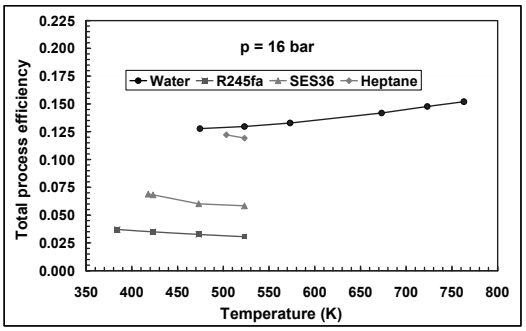

Fig. 3 A comparison of the total thermal efficiency of the process for various working fluids at 16 bar.

Examining the total process efficiency at lower pressures (not shown), it is also noticed that the results for heptane approach those for water. This is due to the fact that the hot air stream may leave the heat exchanger at a lower temperature for the organic liquids, because the pinch point for most of the organic liquids is found to be at state 0, at the outlet of the heat exchanger, whereas for water it is near to state 1 and thus the exhausted air is at a relatively high temperature, leading to a higher 'heat loss'. Depending on the case 15-25% of the incoming enthalpy remains unused and is exhausted, this is in part a consequence of the usage of the cycle for cogeneration, leading to relatively high condenser temperatures. This becomes clear if one compares the T-s diagrams of various working fluids. For water the highest total efficiency would be 15.2%, while the thermal efficiency of the cycle is 21.5%, the latter being misleading. Regarding the water heating, it is clear from the energy balance, that the remaining energy is split in the part which is used to heat the water to the desired 358 K. Between 60 and 80% of the initial enthalpy stream are used to heat the cooling water; for heptanes at 16 bar; without superheating the value is 71.7%. This means that for an enthalpy stream input of 1000kW, 717 kW heating power at 85°C would be available. This amount of heating power was regarded as sufficient, so the main concern was the electrical power output.

The process and its partial deficiencies are easiest rationalized in $T-\dot{H}$ -diagrams [9] where not only the Rankine cycle, but also the process lines for the air and the cooling water are included. So, the temperature differences along the heat transfer processes can easily be seen as direct measures of thermodynamic irreversibilities. One example is seen in Fig. 4 for heptanes with superheating to 523 K.

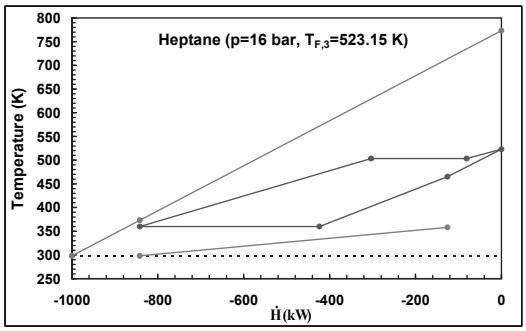

Fig. 4 T-$\dot{H}$ *diagram n-heptane for superheating to 523.15 K at 16 bar, the condenser pressure is 71.2 kPa (T_{sat}=363.15K).*

The exergy losses would be minimized, when the lines along the heat transfer from and to the cycle would fall on each other. However, the distance between the upper line which shows the temperature change of the heat source (hot air), from high to low temperature and for the upper

part of the blue curve showing the change of temperature of the cycle fluid heptane from a sub-cooled liquid to a superheated vapour. It is easily recognized that the mean temperatures of these two fluids differ considerably. This is also true for the heat transfer in the condenser. The low red line shows the temperature increase of the cooling water, while the distance to the blue curve is quite large. It is also recognized that the average temperature of heat rejection from the cycle is considerably above the saturation temperature, leading to reduced efficiencies.

The situation is worse the two other investigated fluids; the $T-\dot{H}$ -diagram for R245fa is exemplary shown in Fig. 5. The distance between the heat source line and the cycle gets extremely large leading to negligible thermal efficiencies and total efficiencies. It is also seen that the effect of superheating is negative, because the average temperature of heat rejection increases faster than the mean temperature of heat addition to the cycle. The question arises, why the situation is more favourable for water as the cycle fluid. Inspecting the according $T-\dot{H}$ -diagram (Fig. 6) it is found, that the main advantage, compared to heptane, is not the heat addition to the cycle, the average temperature in this part remains relatively low, as long as the pressure remains in the range around 16 bar. But the temperature of heat rejection is much lower, leading to slightly higher total efficiencies. Compared to RF245fa, both temperature levels are more favourable.

Further improvements of the organic Rankine cycles were investigated. The pressure level in the condenser can also be fixed after performing a pinch point analysis for the condenser. This was not done in the initial calculations, where the saturation pressure at a temperature of 90°C was selected. This reduction of the condenser pressure helps to reduce the average temperature of heat rejection and is exemplarily shown in Fig. 7. The total efficiency for this case is increased considerably from 11.9% to 15%. This efficiency is even superior to water, where similar improvements by changing the condenser conditions are not possible, since the pinch point is already regarded at the condenser entrance.

A second, well known approach was also investigated, the addition of an internal recuperator to use a part of the enthalpy of the fluid leaving the turbine, to preheat the fluid exiting the pump.

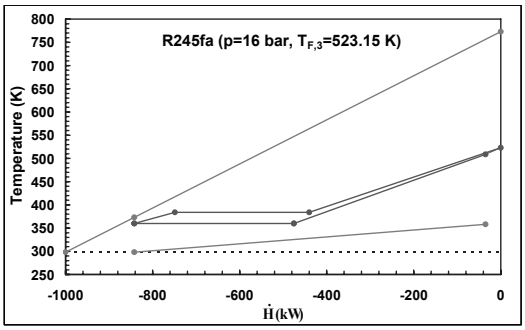

Fig. 5 T-$\dot{H}$ *diagram R245fa for a superheating at 523.15 K as a function of upper pressure level.*

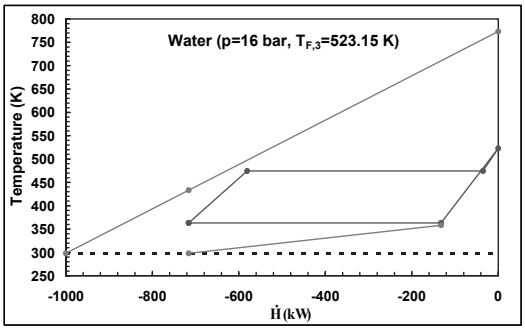

Fig. 6 T-$\dot{H}$ *diagram water for a superheating at 523.15 K as a function of upper pressure level.*

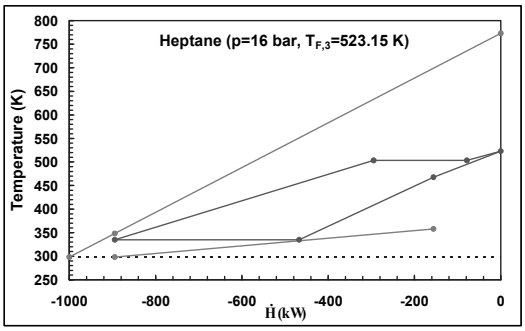

Fig. 7 T-$\dot{H}$ *diagram n-heptane for a superheating at 523.15 K at a reduced condenser pressure of 0.3007 bar at* p_{boiler} *= 16 bar.*

Regarding a cycle, with the parameters given in Table 1 and including such a heat exchanger, increases the total efficiency for heptane as the cycle fluid to 14.3%, the thermal efficiency of the cycle would even be increased to 21.4%.

As mentioned earlier, one important cost factor for these cycles is the heat exchanger. The estimated heat exchanger area may be regarded as one

important measure of the relative investment costs. The values from Table 1 give some insight: The heat exchanger area for water is throughout smaller by approximately 30% at 16 bar compared to the organic fluids. In part this difference comes from the different mass flow rates, originating from the different enthalpy levels. At lower evaporator pressures the difference is smaller, but these cases are less interesting. Including an internal heat exchanger increases the size by further 15-20%, while the reduction of the condenser pressure to the lowest possible value leads to an increase of 10%.

In total the question arises, if the quite small increase in thermal efficiency is worth choosing an organic fluid as working fluid. The advantages of water as a cheap, harmless, non-ignitable and well established fluid may be outweighing the small difference in total thermal efficiency. Also the total size of the process would be considerably smaller, as seen from the mass flow rates and heat exchanger areas.

If the needed amount of heating power is lower, another approach is worth consideration: The condenser pressure could be reduced to a reasonable minimum and the exhaust gas temperature $T_{air,0}$ could be increased. The exhausted air at a higher temperature could be used for heating, while the cooling water would no longer be useful for this purpose. However, the reduction of the condenser temperature may compensate this. To investigate this possibility, a series of calculations for an evaporator pressure of 16 bar, were performed. The condenser pressure was chosen at the saturation pressure of the given fluid at 323 K and the exhaust gas temperature $T_{air,0}$ was increased and fixed to 175°C (448.15 K). The latter temperature leads to a maximum heating power of 316 kW, compared to 600-800 kW in the initial approach. However, the total thermal efficiency for water as a working fluid is increased to values between 16.7% and 18.7%, depending on the exact temperature. This approach is less effective for heptanes, the total efficiencies change to a value of 13%.

In summary several combined heat and power generation processes to use exhaust gases from engines seem promising.

4. Conclusions

Rankine cycles working with four different fluids were investigated for their usage in combined heat and power generation systems, which utilize the waste enthalpy stream of typical combustion engines. For this investigation a fixed temperature level of 500°C was assumed. It turns out that the total efficiency of energy conversion has to be regarded and not only the efficiency of a given cycle, mainly because the largest exergy losses come from the heat transfer through relatively large temperature differences to and from the cycle. Also the energy source is not isothermal along heat transfer. If this is neglected, the fluid for the best cycle but not for the highest total energy conversion efficiency will be chosen.

It seems that there is not a single simple criterion for the selection of the best fluid. However the usage of $T - \dot{H}$ -diagrams [9] is perhaps the best and most intuitive way to judge the performance or the weakness of a certain combination of a fluid and the heat source and heat sink, as was also done in [1, 6] but is not often found in the recent publications about fluid selection for ORC's. As it was shown for the presented selection of fluids, water may be a good choice for these conditions, even if the steam generator pressure is not selected too high, so that a single turbine stage is sufficient and also the process safety is easier to be ensured. Under certain conditions the alkane heptane leads to a higher total efficiency with the drawback of larger heat exchanger areas and being more expensive than water and flammable. The two fluorinated hydrocarbons are not suited for the investigated temperature range, where e.g. the exhaust of Diesel generators may be used.

Other hydrocarbons or siloxanes may be even a better choice than water or heptane. They will be investigated in near future.

Acknowledgement: Some of the calculations were done by Florian Müller. This is gratefully acknowledged.

References

[1] Drescher U., Brüggemann D., 2007, Fluid selection for the Organic Rankine Cycle (ORC) in biomass power and heat plants, Applied Thermal Engineering. 27, pp. 223-28.

[2] Hung T. C., 2001, Waste heat recovery of organic Rankine cycle using dry fluids, Energy Conversion and Management. 42, pp. 539-53.

[3] Hung T. C., Shai T. Y., Wang S. K., 1997, A review of organic Rankine cycles (ORCs) for the recovery of low-grade waste heat, Energy. 22, pp. 661-67.

[4] Yamamoto T., Furuhata T., Arai N., Mori K., 2001, Design and testing of the Organic Rankine Cycle, Energy. 26, pp. 239-51.

[5] Mago P. J., Chamra L. M., 2008, Exergy analysis of a combined engine-organic Rankine cycle configuration, Proceedings of the Institution of Mechanical Engineers Part a-Journal of Power and Energy. 222, pp. 761-70.

[6] Saleh B., Koglbauer G., Wendland M., Fischer J., 2007, Working fluids for low-temperature organic Rankine cycles, Energy. 32, pp. 1210-21.

[7] Lemmon E. W., Huber M. L., Mclinden M. O. NIST Standard Reference Database 23: Reference Fluid Thermodynamic and Transport Properties-REFPROP, Version 8.0, National Institute of Standards and Technology, Standard Reference Data Program. Gaithersburg, 2007.

[8] Solvay. Solkane Refrigerant Software Version 6.0.1.6. Hannover.

[9] Bejan A., Tsatsaronis G., J.Moran M. Thermaldesign and optimization. New York Wiley, 1996.

Dynamic Model of an Organic Rankine Cycle System. Part I – Mathematical Description of Main Components

Iacopo Vaja and Agostino Gambarotta

University of Parma, Dept. of Industrial Engineering, Parma, Italy

Abstract: a set of flexible, fast and scalable models, specifically developed for the dynamic simulation of an ORC (Organic Rankine Cycle) system, is presented. A basic ORC features a pump, an evaporator, a turbine and a condenser. The paper provides an insight on the way these components have been mathematically modeled and the corresponding Simulink® models created. Each model features a dialog window where the type of fluid and geometrical dimensions can be set, allowing full scalability and generalization.
Evaporator and condenser are the most complex components to model and they are designed as counterflow pipe in pipe heat exchangers with phase change in the inner pipe. The exchangers have been split into n_x longitudinal volumes where the conservation equations are applied in differential form, according to a 2D *grey-box*, *state determined* approach. Four state parameters can be defined for each axial node leading to a $4 \times n_x$ system of partial differential equations, solved in time according to a finite difference approach through a discrete state *S-Function* written in Matlab®.
Turbine and pump have been modeled as *black-box*, *not state determined* components since it is assumed that energy mass and momentum storage is negligible for them. The modeling approach followed for these components is based upon characteristics. The applications of these components to create a dynamic ORC model in the Simulink® environment is presented in 'Part II' of this paper.

Keywords: Organic Rankine Cycle, Dynamic Models, Simulation

1. Introduction

In creating dynamic models of fluid system usually the modular approach is applied which leads to consider the whole system as the result of interconnecting several components. The mathematical model of the plant therefore can be carried out by identifying the relevant components and sub-systems and properly connecting them by means of signals that can be either a mechanical-energy coupling or a working fluid stream. The overall model therefore results modular in structure, leading to a "component based"-"object-oriented" modeling approach, where each main component of the system is mathematically modeled and integrated with the other to simulate the plant behaviour in steady and transient operating conditions.

In [1] a comprehensive set of models developed in the Simulink® environment and based on Matlab® scripts to be used for the simulation of energy conversion systems (mainly power generating systems) is presented. The models created fall in two libraries depending on whether or not state variables can be defined for the component; these libraries have then been embedded in the standard Simulink® library for ease of use.

The components of "state determined library" are characterized by the possibility to store energy mass or momentum, hence a set of differential equations (expressed in terms of time derivatives of the state variables) must be defined. The existence of time derivatives of the state variables allows to determine the value of the block outputs as a function of the input variables and the value of state variables at each time step of simulation.

If any storage of mass energy or momentum is assumed negligible for the component no state variables can be defined and a *not state determined* model is created. The output vector at time t only depends on the value of the input vector at the same time instant, according to purely algebraic correlations; the component will fall in the "not state determined library".

A basic Organic Rankine Cycle (ORC) is a power system based upon four main components: a pump, an evaporator (where the working fluid observes the phase change from liquid to vapour), a turbine (where useful power is delivered) and a condenser.

Corresponding Author: Iacopo Vaja, Email: vaja@ied.eng.unipr.it

The paper provides a detailed insight on the way these components have been mathematically modeled, and description is reported in Paragraphs 2 to 4. Evaporator and condenser belong to the "state determined library" while pump and turbine are assumed with no state and appear in the "not state determined library". In Part II of this paper the way to assemble the single blocks to create the full unit is then presented.

All the components here discussed present a Simulink® block with several inputs and outputs and a dialog window where the main geometrical and physical parameters, as well as the type of fluid employed in the system, can be easily set. This allows full scalability and generalization of the models. Fluid properties are implemented using the NIST-REFPROP® database, which allows considering any technical fluid to be employed as working fluid of the system.

2. The evaporator

The evaporator and condenser are assumed to be counterflow pipe in pipe heat exchanger with phase change in the inner pipe. The modeling approach chosen here is based on the finite difference method by applying the energy and mass conservation equations in differential form, and comes from an enhancement of a previously developed model of solar collector [2]. The model should be characterized by a sufficient flexibility to allow simple generalization of the design since it is a crucial component in determining the overall dynamics and behaviour of ORCs.

Given the general way in which the equations are implemented, the same component can be employed as evaporator or condenser.

2.1. The modeling approach

In the approach here adopted the exchanger has been approximated as a straight pipe in pipe system which has been split into n_x longitudinal lumped volumes, each of length Δx, that are the places where the conservation equations are applied and where energy and mass storages are considered. For each discrete volume three nodes can be defined in the radial direction: one referring to the state of the transfer fluid in the annulus, one to the state of the metal pipe and one referring to the organic fluid within the internal pipe, leading to a *white box*, *state determined*, 2-D model (Fig.1).

The assumptions introduced in the analysis of the evaporator are the following:

- thermodynamic properties of the pipe and fluids are function of space and time;
- thermal capacitance of the metal pipe and the fluids are considered;
- the axial conductive heat fluxes is neglected for the fluids [3] but have been considered for the pipe;
- the external pipe is assumed to be adiabatic;
- head losses are neglected for both fluids; this renders redundant the momentum conservation equation that is hence not applied [4];
- heat transfer due to conduction between fluids and pipe is neglected;
- turbulent, transitional or laminar flow are considered to model convective heat transfer;
- lumped thermal capacitance is assumed for both the metal pipe and the fluids;
- mass accumulation is considered for the evaporating/condensing fluid only due to the significant density variation;
- energy accumulation is considered in both the metal pipe and the two fluid volumes.

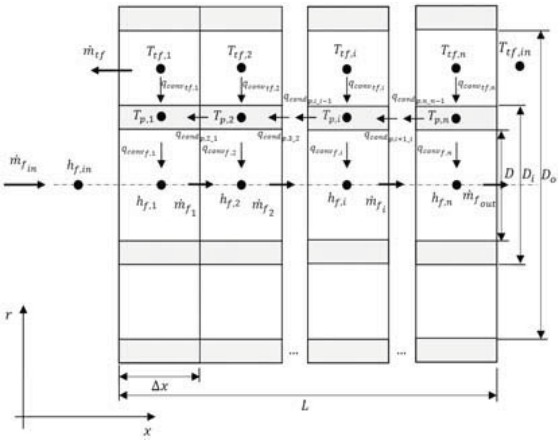

Fig. 1. The discretization scheme adopted for the evaporator.

Given these assumptions 4 state variables can be defined for each axial lump of the pipe (fluid temperature in the annulus, pipe wall temperature, organic fluid enthalpy and mass stored in the inner pipe, see Fig.1); their value in time can be determined applying a set of 4 cardinal equations:

- energy conservation equations applied at the three radial nodes (which allows determining the node temperatures);
- continuity equation applied to the volumes of the internal pipe.

The literature proposes similar approaches in representing dynamic behaviour of evaporators or condensers. In [5], for example, a discretized model for the evaporator of an ORC is described. The approach is quite similar to the one here adopted but one overall momentum balance has also been considered for the entire evaporating mass in order to determine the pressure existing in the pipe. A different approach has been considered here for determining the fluid pressure time evolution and an hot drum is introduced for the scope (see Part II of the paper).

Another interesting work on the topic is [6] where a detailed numerical simulation of the thermal and fluid dynamic behaviour of a double pipe heat exchanger to be used as either evaporator or condenser is proposed. The governing equations applied are again momentum, continuity and energy conservation inside the internal tube and the annulus, together with energy conservation for the pipe. The model proposed in [6], while substantially similar to the one here presented is however much more detailed since more radial nodes are considered. Such a degree of precision is not believed to be significant for the scope of this work and the sole 3 radial nodes of Fig. 1 will be considered.

The cardinal equations adopted in each control volume of the system are now briefly presented.

- **2.1.2. Anulus**

For each control volume of fluid in the external annular region an energy balance equation can be applied in order to determine the associated fluid temperature. The energy fluxes involved are the convective heat exchanged between the fluid and internal pipe along with the term related to transport. In this case, being the fluid assumed as incompressible, continuity equation implies that the fluid entering and leaving each control volume is the same but the temperature is different, hence a global net energy balance can be considered referring to the transport phenomena.

The overall energy balance equation at a given node *i* and time *t* is hence provided by:

$$\dot{m}_{tf}\,\bar{c}_{p_{tf\,i}}\left(T_{tf\,i+1}-T_{tf\,i}\right)-q_{conv_{tf\,i}}=\bar{\rho}_{tf}V_{tf}\,\bar{c}_{p_{tf\,i}}\,\frac{\partial T_{tf\,i}}{\partial t} \qquad (1)$$

- **Pipe wall**

Each anular control volume of the metal pipe is subject to a series of heat fluxes. Convective heat exchange takes places both in the external and internal side and axial conduction is also considered (each control volume receives or provides heat to the neighbouring metal annuli). The general overall energy balance equation, can be written as follows:

$$q_{conv_{tf\,i}}-q_{conv_{f\,i}}+q_{cond_{p\,i}}=\rho_{p,i}V_p\bar{c}_{p_{p\,i}}\,\frac{\partial T_{p\,i}}{\partial t} \qquad (2)$$

- **2.1.3. Internal pipe**

For each control volume defined within the internal pipe, where the organic fluid flows and exchanges heat with the metal pipe in order to change its phase, both energy conservation and continuity equations are applied, the latter being necessary to determine the actual fluid mass flow rate flowing in and out each control volume.

The continuity equation can be expressed in the following differential form at the i^{th} node of the pipe at time *t*:

$$\dot{m}_{f\,i-1}-\dot{m}_{f\,i}=V\,\frac{\partial\rho_i}{\partial t} \qquad (3)$$

Solving the continuity equation is first necessary since the organic fluid mass flow rate entering and leaving each cell of the pipe is required, for the energy balance that can be defined by the following equation, expressed in enthalpy form for convenience:

$$q_{conv_{tf\,i}}+\dot{m}_{f\,i-1}h_{f\,i-1}-\dot{m}_{f\,i}h_{f\,i}=V_f\,\frac{\partial\left(\rho_{f\,i}h_{f\,i}-p_f\right)}{\partial t} \qquad (4)$$

Equations (1) to (4) represent the state equations required to calculate the 4 state variables defined for each axial node. The overall state parameters, given the number of axial nodes, are therefore:

- n_x axial temperatures for the heat transfer fluid in the annulus, $T_{tf,i}$;
- n_x axial metal pipe wall temperatures, $T_{p,i}$;
- n_x axial enthalpies for the fluid experiencing phase change in the internal pipe, $h_{f,i}$;
- n_x organic fluid masses stored within each control volume in the internal pipe, $m_{f,i}$.

The mentioned state equations have been implemented in the *S-function* that constitutes the core of the model and solved together leading to a linear system of partial differential equations that is implemented in matrix form.

At each time of simulation the state of the system is known and the only unknowns are the time derivatives of the state variables, hence the system is numerically integrated according to a forward finite difference approach, thus providing a discrete state *S-Function*; values of the state

parameters at start of simulation are therefore required for system initialization.

To close the system of equations proper boundary conditions must also be introduced. These are: $T_{tf,in}{}^{t}$, $T_{p,in}{}^{t}$, $h_{f,in}{}^{t}$ and $\dot{m}_{f,in}{}^{t}$.

The dimensions of the solving system of equations depend on the number of axial nodes considered ($4\times n_x$ state variables). A specific procedure is therefore created in order to allow scalability of the system of equations.

The Simulink® block can be schematically represented as in Fig. 2, where the main inputs outputs and state variables are recognizable.

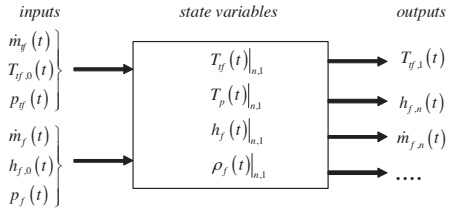

Fig.2. Scheme of the evaporator block.

2.2. Heat exchange correlations

Proper heat exchange correlations are introduced to calculate, at each step of simulation, the instantaneous heat fluxes observed in Equations (1) to (4).

▪ 2.2.1. Convection between fluid in the annulus and pipe

For the anular duct in case of laminar flow the Nusselt number depends upon the diameter ratio ($Nu=f(D_i/D_o)$) while in case of transitional and turbulent flow the Gnielinski correlation applies [7]:

$$Nu_{tf} = \frac{(f/8)(\mathrm{Re}-1000)\mathrm{Pr}_{tf}}{1+12.7\sqrt{f/8}\left(\mathrm{Pr}_{tf}^{2/3}-1\right)} \tag{5}$$

where f is the friction factor that, for a smooth pipe can be determined by the Petukhov correlation.

▪ Axial pipe wall conduction heat flux

Fourier law has been applied to each pipe control volume in order to take into account the axial heat flow:

$$q''_{cond} = -\lambda_p \left(\frac{\partial T}{\Delta x}\right)_p \tag{6}$$

▪ Convection between evaporating fluid and pipe

Under normal operating conditions the organic fluid enters the evaporator as subcooled liquid and leaves it as saturated or superheated vapour; different fluid phase regions may exist within the i^{th} cell of the internal pipe of the evaporator and different heat exchange correlations apply depending on whether the fluid is single phase ($h_i<h_l$ or $h_i>h_v$) or two phase ($h_l<h_i<h_v$).

In single phase the approach is similar to that adopted for the anular pipe and the Gnielinski correlation (5) is applied for turbulent flow.

In the two-phase fluid region the Chen correlation is instead adopted for determining the Nusselt number [8]:

$$Nu = Nu_{Dc} + Nu_{Db} \tag{7}$$

where Nu_{Dc} expresses the Nusselt number for vaporization in forced convection, written from the Dittus-Boelter correlation [7]:

$$Nu_{Dc} = 0.023\,\mathrm{Re}_l^{0.8}\,\mathrm{Pr}_l^{0.4}\,F \tag{8}$$

where F is a correction empirical factor.

Nu_{Db} represents instead the Nusselt number in case of nucleation boiling, and can be expressed according to the following:

$$Nu_{Db} = 0.00122\,S\,Ja^{0.24}\,\mathrm{Pr}_l^{0.21}\left(\frac{\rho_l}{\rho_v}\right)^{0.24}\left(\frac{d\Delta p}{\sigma}\right)^{0.5}\left(\frac{\rho_l d^2\Delta p}{\mu_l^{\,2}}\right)^{0.5} \tag{9}$$

where S is a factor smaller than 1 that takes into account of the decreasing importance of nucleation with increasing two phase Reynolds number.

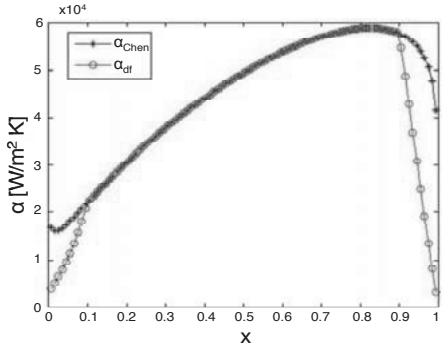

Fig.3 Heat transfer coefficient in the two phase zone as function of vapour fraction for water evaporating in a 20 mm diameter pipe.

Some issues related to discontinuities in the heat exchange coefficients must be taken into account. When the organic fluid is single phase it exchanges sensible heat with the pipe wall, while when phase change occurs the latent heat is involved, which is usually on order of magnitude higher than sensible heat [9]. This implies that, due to the discretized approach adopted, in

neighbouring control volumes the heat transfer coefficient may experience a step change. These discontinuities in the correlations adopted cause serious stability issues to the solution of the explicit set of equations. For this reason a "dumping" coefficient is introduced in order to "soften" the change in the heat transfer coefficient reducing stability concerns of the model and rising computational speed. Fig. 3 shows an example of the heat transfer coefficient as function of the vapour fraction x in the two phase region as from Chen correlation (α_{Chen}) and in the hypothesis of smoothing the step change for $x=0$ and $x=1$ (α_{df}).

Some of the assumptions previously introduced for the evaporator have also been verified for standard geometries of the component.

It was checked the Biot number to be $Bi<<0.1$ in order to accept the hypothesis of lumped thermal capacitances, that allowed assuming the temperature of any discretized volume to be constant and uniform.

The second strong hypothesis introduced is that of constant pressure within the pipe where the organic fluid flows. Besides the pressure losses due to friction between the flowing fluid and the pipe which, within some extent, can reasonably be neglected, another important phenomena occurs when a fluid that undergoes phase change flows within a straight pipe, that is here called "backpressure of inertia" [10].

When a fluid experiences phase change its density varies significantly and, by applying Bernulli's equation, a decrease in the fluid density corresponds to a decrease in the hydrostatic pressure being conversely increased the speed. For this reasons, also in the hypothesis of completely neglecting friction, a pressure drop along the pipe should still be considered.

It has however been verified that the backpressure of inertia, calculated according to:

$$\Delta p = p_{f,in} - p_{f,out} = \rho_{f,in} v_{f,in}^2 \left(\frac{\rho_{f,in}}{\rho_{f,out}} - 1 \right) \qquad (10)$$

is, for standard geometries of the evaporator, limited to at most 6% of the pressure at the inlet section and its effect have hence been neglected.

The Simulink® model of the evaporator and its block dialog window are displayed in Fig.4. The parameters to be set include geometrical data of the exchanger, type of evaporating fluid, type of heat transfer fluid, simulation parameters (geometrical discretization and time step of integration) as well as initial values of the state variables of the system.

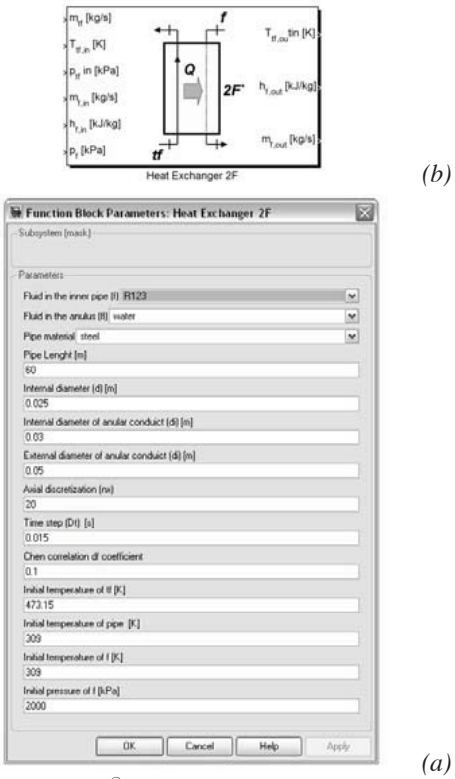

Fig.4. (a) Simulink® model of the evaporator and (b) dialog window.

The proposed model of evaporator was validated recurring to data found in [11] where steady state distribution of some peculiar variables along the pipe abscissa are provided for a pipe in pipe straight evaporator similar to the model here defined. The transfer fluid employed is water while R22 is the evaporating fluid.

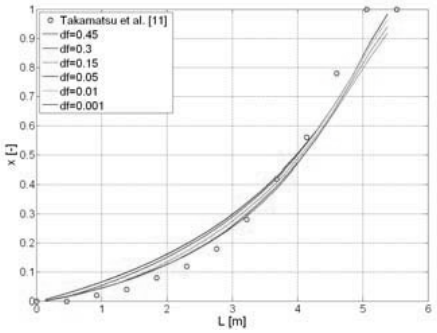

Fig. 5. Organic fluid vapor fraction measured at varying distance from pipe inlet by Takamatsu et. al. [11] (dots) and calculated from the model with different values of damping coefficient.

Fig.5 reports some of the results of validation and shows the organic fluid vapour fraction (calculated at different values of the Chen coefficient "dumping factor") as function of pipe length showing that very good accuracy is provided by the model and that the approximation in the Chen coefficient has limited effect on overall results.

3. Turbine

A general model of axial, dynamic, single stage turbine for ORC applications has been created according to a *black box*, *not state determined* approach.

The model is displayed in Fig. 5 (a) where overall block input and outputs are recognizable (no state parameters are defined in this case).

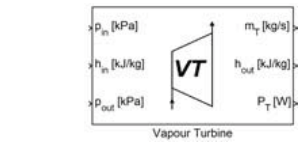

(a)

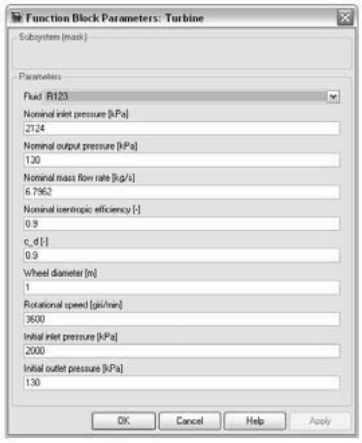

(b)

Fig.5. (a) Simulink® model of the Turbine and (b) dialog window.

The approach followed is similar to that employed in a previous work [12] for a gas turbine, and the resulting model is based on characteristics. With reference to ORC modeling, it is in fact quite uniquely accepted in literature to recur to representation based on performance maps for pump and turbine [13].

The general form of the turbine mass flow rate and efficiency characteristics can be expressed as from Eq. 11 and 12 respectively; they are assumed weak function of the shaft rotational speed hence the parameter ω_T is neglected:

$$f_1(\varepsilon, \dot{m}_T) = 0 \tag{11}$$

$$f_2(\eta_T, \dot{m}_T) = 0 \tag{12}$$

The explicit expression of the mass flow rate characteristic has been approximated recurring to the correlations valid for orifices according to the following semi empirical formulation of the Stodola equation, that can be applied when a vapour expansion is considered [13]:

$$\dot{m} = K\sqrt{\rho_{in} p_{in}\left[1-\left(\frac{1}{\varepsilon}\right)^2\right]} \tag{13}$$

where $K=c_d \cdot A$ is the product between the coefficient of discharge and the equivalent nozzle cross area at inlet.

To be noted that Eq. 13 has general validity and is capable to approximate also the condition of chocking, as displayed by the *3D* plot of Fig. 6 where Eq. 13 is represented.

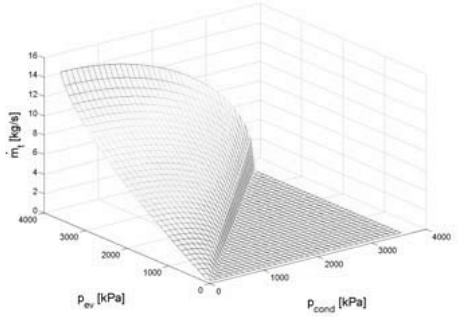

Fig.6. The Stodola equation providing the turbine mass flow rate given the turbine inlet/outlet pressure.

The turbine rotational speed is also neglected in the efficiency characteristic and the explicit representation of Eq. 12 is defined by a polynomial function of second grade that can be calculated given the operational point at maximum efficiency:

$$\eta_T(c_{us}) = \eta_{T,\max}\left[2\frac{c_{us}}{c_{us,\max}} - \left(\frac{c_{us}}{c_{us,\max}}\right)^2\right] \tag{14}$$

From the turbine efficiency the net power delivered can be written as:

$$P_T = \dot{m}_T \eta_T \left(h_{in} - h_{out}|_s\right) \tag{15}$$

4. The pump

The pump represents another flow control device and the model proposed has been created again according to a *black box*, *not state determined* approach based on characteristics. The physical pump modeled is of centrifugal type.

The Simulink® block with model inputs and outputs is shown in Fig. 7 along with the block dialog mask.

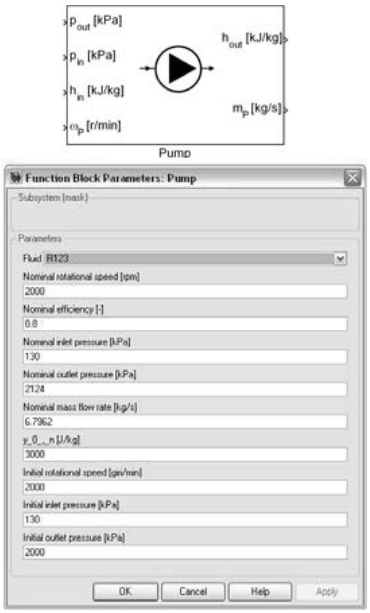

Fig.7. (a) Simulink® model of the Pump and (b) dialog window.

The general expressions of the volumetric flow rate and efficiency characteristic are the following:

$$f_1\left(y,\omega_p,\dot{V}\right)=0 \tag{16}$$

$$f_2\left(\eta_p,\omega_p,\dot{V}\right)=0 \tag{17}$$

For shake of generality the nominal flow rate characteristic curve can be created given the nominal flow rate and head at the nominal rotational speed (y_{0_n}), from the following:

$$y=\frac{y_n-y_{0_n}}{\dot{V}_n^{\,2}}\dot{V}^2+y_{0_n} \tag{18}$$

Starting from the nominal curve described by Eq. (18), the full set of curves at different rotational speed (ω_P') can be determined applying proper scaling rules:

$$\dot{V}=\dot{V}_n\left(\frac{\omega_{P,n}}{\omega_P}\right) \tag{19}$$

$$y=y_{0,n}\left(\frac{\omega_{P,n}}{\omega_P}\right)^2 \tag{20}$$

For pumps, in fact, the dependency from the rotational speed of the flow rate characteristic cannot be neglected and ω_P. appears as input to the model (Fig. 7a).

The pump isentropic efficiency has been instead approximated by a polynomial curve on the $\eta_p-\dot{V}$ plane, given the nominal values and according to the following:

$$\eta_p=-\frac{\eta_{p_n}}{\dot{V}_n^{\,2}}\dot{V}^2+2\frac{\eta_{p_n}}{\dot{V}_n}\dot{V} \tag{21}$$

Starting from pump efficiency, the required power can be easily computed, and the curves can be once again scaled recurring to scaling rules:

$$P=P_n\left(\frac{\omega_{P,n}}{\omega_P}\right)^3 \tag{22}$$

From the block dialog mask (Fig. 7b) it can be observed that, among the parameters, nominal operating values of the main variables must be provided. These values are employed within an initialization function that calculates the parameters that appear in the nominal characteristic curves of Eqs. 18 and 21. It can be easily appreciated the flexibility of the model proposed that can provide representation of any desired pump by simply tuning these parameters.

Conclusions

In the context of the modeling activity conducted by the authors in the field of energy systems and internal combustion engines, two complete libraries of components have been created and embedded in the Simulink® standard library. Among the many components created three models have been here described since they are the main constituent of a complete ORC system which will be presented in Part II of the paper.

The model of evaporator and condenser have been developed recurring to a finite difference approach applied in a parameterized way. This approach, if complex from a computational standpoint, allows great flexibility and different degree of detail in the spatial discretization can be achieved by simply defining the number of axial nodes (n_x). The solving system of differential equations (expressed in matrix form) will automatically scale itself upon that parameter, providing a number of states equal to $4\times n_x$, since 4 state variables have been defined for any axial node.

Turbine and pump have instead been designed as not state determined components since it has been assumed the mass, energy or momentum storage within these components to be negligible. Despite both the components have been modeled recurring to very simplified forms of the characteristic equations, for the scope of present work generality is a far more desired requirement than a too detailed description of the component. The approach followed therefore shows its strength in the great flexibility achievable, and by simply

tuning some parameters, displayed in the block dialog window of the models (Fig. 5 (b) and 7 (b)), different turbine or pump sizes can be modeled, allowing the design and study of different plant sizes and configurations.

Nomenclature

c	specific heat, J/(kg K)
$\dot{m}$	mass flow rate, kg/s
q	heat transfer rate, W
h	specific enthalpy, kJ/kg
t	time, s
v	velocity, m/s
x	vapour mass fraction
y	manometric head, m
T	temperature, K
V	volume, m^3

Greek symbols

α	convection heat transfer coefficient, W/m^2K
ε	turbine pressure ratio
η	efficiency
ω	angular speed, rad/s
ρ	density, kg/m^3

Subscripts and superscripts

cond	conduction, condenser
conv	convection
f	fluid
i	general axial node of discretization
in	inlet
l	liquid
out	outlet
p	pipe
s	isoentropic
tf	transfer fluid
v	vapour
P	pump
T	turbine

References

[1] Vaja I., 2009, Definition of an Object Oriented Library for the Dynamic Simulation of Advanced Energy Systems: Methodologies, Tools and Application to Combined ICE-ORC Power Plants, Ph.D. Dissertation, University of Parma, Parma, Italy.

[2] Gambarotta A. and Vaja I., 2007, Dynamic model of a thermal solar collector, *Proc. EUROSIM 2007 Int. Conference*, Ljubljana, Paper 364.

[3] Prabhankar P.R., 1975, Two dimensional configuration analysis of a flat plate solar collector, Ph.D. Dissertation, University of Oklahoma, USA.

[4] Bestrin R., Vermeulen A.G., 2003, Mathematical modeling and analysis of vapour compression system, Tech. Report, University of Technology, Eindhoven Netherlands.

[5] Wei D., et al., 2008, Dynamic modelling and simulation of an organic Rankine cycle (ORC) for waste heat recovery, Appl. Thermal Engineering, 28(10), pp. 1216-1224.

[6] García-Vallardes O., Pérez-Segarra C. D., Rigola J., 2004, Numerical simulation of double-pipe condensers and evaporators, Int. J. of Refrigeration, 27, pp. 656-670.

[7] Incroprera F.P., De Witt D.P., 2001, Fundamentals of Heat and Mass Transfer, John Wiley & Sons.

[8] X. Jia, et al., 1995, A distributed model for prediction of the transient response o fan evaporator, Int. J. of Refrigeration, 18, pp.336-342.

[9] García-Vallardes O., et al., 2004, Numerical simulation of double-pipe condensers and evaporators, Int. J. of Refr., 27, pp. 656-670.

[10] Acton O., Caputo C., 1979, *Collezione Macchine a Fluido, Vol. I: Introduzione allo studio delle macchine*, UTET (in Italian).

[11] Takamatsu H., et al., 1993, A correlation for forced convective boiling heat transfer of pure refrigerants in a horizontal smooth tube, Int. J. Heat and Mass Transfer, 36(13), pp. 3351-60.

[12] Gambarotta A., Vaja I.,2007, A Real Time Dynamic Model of a Micro-Gas Turbine CHP System with Regeneration, ASME POWER Int. Conference, San Antonio, TX.

[13] Colonna P., van Putten H., 2007, Dynamic modeling of steam power cycles. Part II – Simulation of a small simple Rankine cycle system, Appl. Th. Eng., 27, pp. 2566-2582.

Dynamic Model of an Organic Rankine Cycle System. Part II – The Full Model: Description and Simulation

Iacopo Vaja and Agostino Gambarotta

University of Parma, Dept. of Industrial Engineering, Parma, Italy

Abstract: In order to gather a deep understanding on the way Organic Rankine Cycle (ORC) systems behave, and to assess new system arrangements and geometries, a detailed dynamic model of the plant has been developed using the Simulink® models of each subcomponent described in 'Part I' of this paper. The different components have been assembled together according to the typical ORC lay-out. Two further state determined components (drums) are introduced in order to calculate the dynamic behaviour of the pressure in the evaporator and condenser and to define all the state variables required by the whole model. The cause-effect approach used to create the complete model leads to alternating *not state determined* and *state determined* elements, favouring the numerical stability of the solution, since algebraic loops are avoided. A set of simulation results is proposed assuming the ORC working fluid to be R123, diathermic oil used as heat transfer medium and water to cool the condenser.

Keywords: Organic Rankine Cycle, Dynamic Models, Simulation

1. Introduction

In order to gather a deep understanding on the way Organic Rankine Cycles (ORCs) operate and to design new energy conversion systems where ORCs can find their place for the recovery of low-medium temperature heat from waste heat sources, a proper detailed dynamic model of the ORC system has been developed and will be illustrated within this paper. The need for such a tool arises from the experimental activity the authors will soon start on ORCs; it is believed that a reliable model of the unit could constitute a precious support in pre-testing new solutions, designing control strategies or assessing off-design operation prior to their application on the real system.

Little examples of complete dynamic models of ORC system have been found in literature. The most complete is provided in [1] where two alternative approaches for creating a dynamic model of an ORC are used. The model, intended for the design of the control and diagnostics systems, has been developed in Modelica® language and simulated with Dymola®. The paper focus is on the model of the evaporator which is the key component to be represented. The two modeling approaches adopted for this component, based on moving boundary and discretization techniques, are compared in terms of accuracy, complexity and simulation speed.

With reference to experimental data, simulations evidenced that while both models have good accuracy, the moving boundary model is faster, therefore more suitable for control design applications. Since the aim of this work is mainly system design, the discretized approach here adopted is preferred as it allows a broader understanding and representation of the phenomena occurring within the evaporator for the transfer fluid and the organic fluid while it experiences phase change.

Another extensive work in the field of dynamic modelling of Rankine cycles is that described in [2,3]; despite the work does not refer to organic fluids but to ordinary steam Rankine cycles, it provides an interesting approach for the design of components of vapour power plants. The realized software, called SimECS and developed at the Delft University of Technology, is a modular, hierarchical and causal paradigm, which means that systems are formed by components that in turn are formed by modules with predefined causal interactions. SimECS therefore is based on elementary modules that can be appropriately combined to obtain main components. In the approach followed all main phenomena occurring within the components (as heat exchangers) are lumped within single logical blocks that describe the physical phenomena through implementation of proper physical relations and conservation laws in the lumped parameters form.

Corresponding Author: Iacopo Vaja, Email: vaja@ied.eng.unipr.it

The approach proposed in the present paper to create the ORC dynamic model is based on properly linking together the Simulink® models of each subcomponent, which physical and mathematical description is reported in 'Part I'. The sub-components have been assembled according to an "object-oriented" approach based on cause-effect correlations where *not state determined* and *state determined* elements are alternated favouring the numerical stability in the solution, since algebraic loops are avoided in most cases.

However, prior to create the full model (described in Par. 3), a special component must be developed to close the solution of the state variables of the whole plant. This component is the *drum*, described in the next section.

2. The drum

As seen in Part I of this paper the proposed models of heat exchangers, pump and turbine require, as input, the pressure of the organic fluid that can vary with time according to the overall system dynamics. For example the actual pressure existing within the evaporator can be calculated by balances applied to the hot drum, a component that has the double effect of providing the turbine with satured vapour (moisture is separated from the vapour) and determining the pressure existing within the evaporator, that is constant for its entire length given the assumption of negligible head losses and 'backpressure of inertia'. Within the drum hence saturation condition exist during ordinary operation.

The component can be developed as *0D*, *state determined*, *white-box* (the last meaning that no empirical equations are adopted), and presents the input, outputs and main state variables shown in Fig. 1.

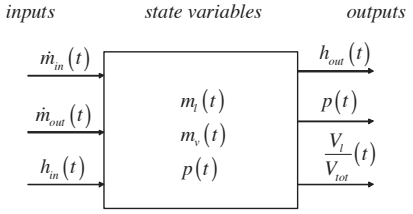

Fig.7. Schematic block of the drum.

Inputs to the model are the mass flow rate entering and leaving the system and the enthalpy of the fluid coming from the evaporator (or condenser). The calculated outputs are the enthalpy of the fluid leaving, the fluid pressure and the liquid fraction with respect to the overall drum volume.

2.1. The model

Given the existence of seven state variables (m_l, m_v, p, u_l, u_v, ρ_l and ρ_v) the following 7 equations are considered:

- **Mass balance**

The difference in the mass flow rates entering and leaving the drum at each instant t must result in a mass change in time. Expressing this principle with finite difference approach, the mass stored within the component can be calculated in the next step of simulation $t+\Delta t$:

$$m_l^{t+\Delta t} + m_v^{t+\Delta t} = m_l^{t} + m_v^{t} + \Delta t\left(\dot{m}_{in}^{t} - \dot{m}_{out}^{t}\right) \quad (1)$$

- **Energy balance**

The overall energy balance states that the energy flow entering the system with the organic fluid from the evaporator (or condenser), and the energy flow leaving the drum must result in a system energy change in time. Expressing the energy conservation equation according to the finite difference approach, the internal energy can be calculated through the following:

$$m_l^{t+\Delta t}u_l^{t+\Delta t} + m_v^{t+\Delta t}u_v^{t+\Delta t} = m_l^{t}u_l^{t} + m_v^{t}u_v^{t} + \Delta t\left(\dot{m}_{in}^{t}h_{in}^{t} - \dot{m}_{out}^{t}h_{out}^{t}\right) \quad (2)$$

- **Volume conservation**

Indeed another physical condition to be considered is that volume of the liquid phase and vapour phase must equal the overall drum internal volume, that is assumed constant in time:

$$\frac{m_v^{t+\Delta t}}{\rho_v^{t+\Delta t}} + \frac{m_l^{t+\Delta t}}{\rho_l^{t+\Delta t}} = V_{TOT} \quad (3)$$

- **State equations**

Since the component features 7 state variables, four equations are needed for system closure. These equations come from applying the fluid equation of state that is in fact used to determine internal energy and fluid density for satured liquid ($x=1$) and satured vapour ($x=0$):

$$\begin{cases}\left(u_v^{t+\Delta t}, \rho_v^{t+\Delta t}\right) = f\left(p^{t+\Delta t}, x=1\right)\\ \left(u_l^{t+\Delta t}, \rho_l^{t+\Delta t}\right) = f\left(p^{t+\Delta t}, x=0\right)\end{cases} \quad (4)$$

The Simulink® model of the hot drum component and its dialog window interface are shown in Fig.2. To be noted that behind geometrical parameters, required are also parameters for initializing the system state variables at simulation time $t=0$.

The main geometrical parameter to be provided to the model (drum volume) has significant effect in determining the time evolution of the main system outputs. Fig. 3 shows for example the effects played by drum volume in the dynamic response of the fluid pressure due to a step change in one of the system inputs (vapour enthalpy); R123 is considered as fluid. It can be noted that, as expected, the smallest the drum volume, the faster is the system response.

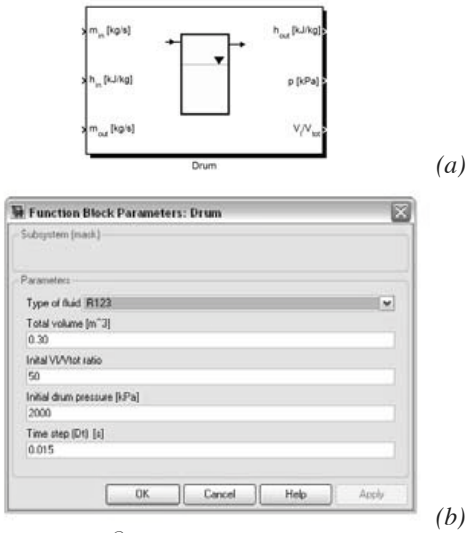

(a) (b)

Fig. 2. Simulink® model of the drum (a) and block dialog mask (b).

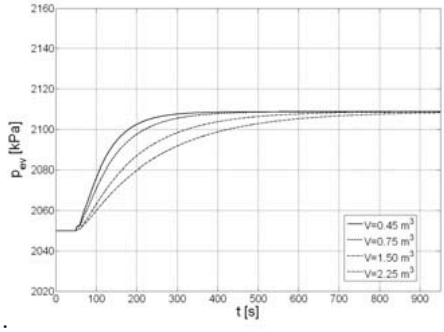

Fig. 3. Pressure response of the hot drum due to a step change in the enthalpy of the fluid entering at varying drum volumes.

2.2. The hot drum-evaporator system

The mutual interactions between hot drum and evaporator are strong and the dynamic behaviour of each component cannot be really separated from the other. In fact what happens within the evaporator has effect on the evaporator outputs which, in turn, affects the energy and mass conservation equations of the hot drum that would result in a new pressure within the component, that is fed backward to the evaporator and so on. To be noted that even if the drum does not correspond to any physical component of the ORC plant, the component can still be introduced in the full model as a 'virtual' volume required to calculate the pressure dynamics.

Evaporator and hot drum models have therefore been tested together and the following plots are proposed as example of their mutual interactions. The model of the evaporator linked to the model of the hot drum in the Simulink® environment is proposed in Fig. 4; the system, where R123 is employed as working fluid, has then been studied.

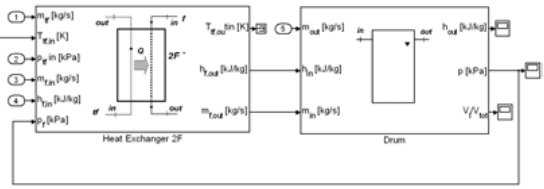

Fig. 4. Simulink® model of an evaporator-drum system.

The number of nodes adopted for the axial discretization of the evaporator is n_x=20, the value resulting from a convergence analysis. In Tab. 1 in fact the value of pressure existing within the evaporator-drum system at varying number of nodes is reported. The higher the number of axial nodes considered the higher is the pressure reached by the system. This is a consequence of the fact that the organic fluid specific enthalpy entering the drum is lower when a low number of nodes is considered since it is evaluated as average over a bigger control volume. It can also be noticed that increasing from 20 to 30 nodes the pressure change is negligible and usually, when smaller than 5%, it can be assumed that convergence is reached.

Table 1. Analysis of convergence on the number of nodes for the axial discretization of the evaporator.

n	***p_{vap}* [kPa] (steady state)**	**Relative variation [%]**
5	1586	-
10	1885	+18.85
20	2051	+8.81
30	2104	+2.58

After the evaporator-drum system has reached steady state operating conditions one of the main external inputs is changed with a step. In this

example the temperature of the heat transfer fluid (diathermic oil) is changed from 473 to 465 K at time *t*=50 s and this has effects on both the hot drum (Fig. 5) and the evaporator (Fig. 6).

The decreased energy flow that the evaporator provides through the organic fluid to the drum (observable by the decrease in fluid temperature) causes a decrease in the pressure (Fig. 5) which in turn causes a fraction of the liquid within the component to evaporate.

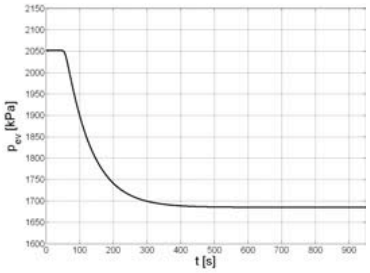

Fig. 5. Pressure in the hot drum.

At the end of transient all values stabilize on a new steady state; to be noted that the pressure and hence the saturation temperature within the evaporator are lower. From Fig. 6 (a) the full temperature distribution of the organic fluid inside the evaporator can be observed in a *3D* plot as function of simulation time and pipe equivalent abscissa. Such a representation is possible being known the 20 nodal fluid temperatures. It is possible to notice the heating region and the plateau at constant temperature where phase change occurs. The saturation temperature slightly falls at *t*>50 s as consequence to the pressure decrease.

Interesting is also Fig. 6 (b) that shows the nodal organic fluid mass flow leaving each discretized cell of the evaporator. To be remembered that the organic fluid mass flow rate entering the evaporator does not change with time. The sudden drop in the wall temperature makes the vapour within some cells to condensate thus reducing the actual mass flow rate through these cells, resulting in an overall decrease in the organic fluid mass flow rate in the two phase region. The subsequent fall in the evaporating pressure causes start of vaporization in some cells were, at the previous pressure level, liquid phase still existed. Part of the mass contained within these cells is then discharged, causing an increase in the leaving mass flow rate in all the following cells. To be noted that when steady state conditions are reached the mass flow rate flowing through each cell remains constant. Also it can be appreciated that no changes in the mass flow rate can be observed, even during transients, in the zone where only liquid exists (where density is roughly independent from existing pressure).

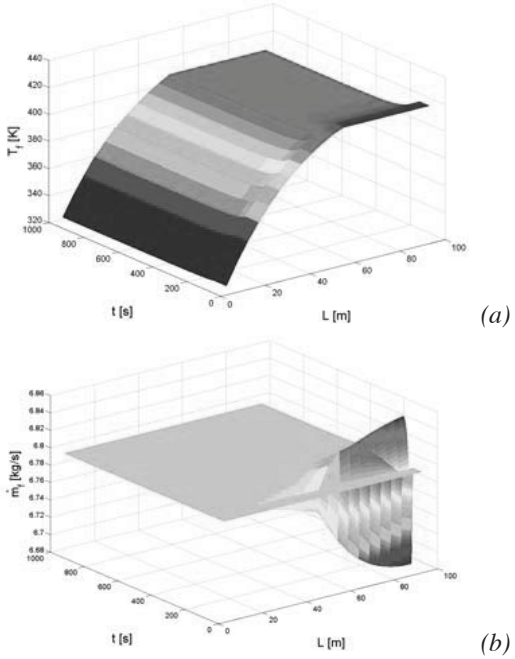

Fig. 6. Organic fluid temperature distribution (a) and nodal mass flow rate (b) within the evaporator.

3. The ORC model

3.1. The modeled system

ORCs are power cycles based on the Rankine vapour cycle typical of steam power plants. In the case of ORCs however a different fluid is employed in place of water that allows some benefits under certain circumstances. Particularly, the fluids employed (typically hydrocarbons or refrigerants) have low boiling points and high specific volume of the vapour at the typical evaporation pressures, that makes the stream at the expander inlet suitable for an efficient expansion, reducing the leakage losses that would occur if water were used instead. These cycles in fact are usually adopted when the thermal power of the heat source and its temperature are limited; under these circumstances the steam volumetric flow rate would be too low and the cycle efficiency would be compromised by the extremely low expansion efficiencies.

Besides the different fluid that can be adopted in ORCs, the overall cycle layout can be considered conceptually similar to that of a steam power cycle.

As displayed in Fig. 7, which refers to a simple Organic Rankine Cycle with no regeneration, reheating or superheating, the fluid is first heated and evaporated through the evaporator and then expanded in order to convert its pressure energy into useful mechanical work. A condenser is then necessary in order to desuperheat and condensate the fluid which then passes trough the feeding pump which provides the liquid with the required head.

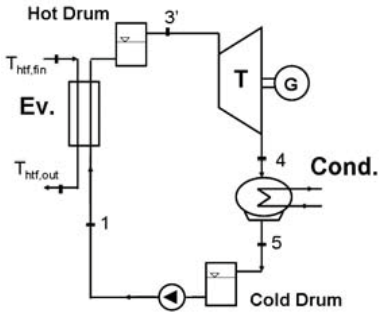

Fig. 7. Schematic layout of an ORC.

As anticipated moisture separators (drums) have also been considered in the scheme. The first separator is at the evaporator exit and used to avoid that the liquid droplets carried by the vapour stream are dragged into the expander. Analogously, another moisture separator is considered at the condenser outlet and its use is to separate the vapour fraction that might be mixed to the liquid, hence avoiding the presence of vapour at the pump suction. The presence of these elements is considered also in some cycle setups described in literature [1,4,5].

The dynamic model of the entire system therefore will be realized by assembling together the models of the different subcomponents that have been identified. Indeed more complex designs of the cycle could be considered: particularly thermal regeneration is a common practice when it comes to ORCs based on overhanging fluids. These fluids are not only favourable because they allow dry expansions without superheating, but also make convenient to regenerate the cycle by sub cooling the vapour at the end of expansion (the fluid is superheated at turbine exit) through a direct regeneration (no vapour extractions from turbine).

Other cycle designs may involve recurring to other heat exchangers, besides the evaporator or the regenerator, in order to recovery heat from other low temperature heat sources and providing a preheating of the organic fluid that allows overall efficiency enhancing.

More complex cycle designs have already been considered and modeled [6] and will be proposed in future works. The simple ORC system of Fig. 7 is modeled and presented in the next paragraph.

3.2. The Simulink® model

The different model blocks presented in Part I of this paper have been properly linked creating a complete ORC plant in the Simulink® platform.

Matlab®/Simulink® environment has been chosen as modeling-simulation software for its extreme capabilities. It features an its own language that allows great flexibility in typing customized codes where all the physical or empirical equations that describe the components can be properly defined. The immediateness of an icon based environment, that is the Simulink® package, is also appreciated, where the built in code sources can be embedded into block icons through proper functions called *S-functions*, and solved in the time domain.

The Simulink® model of the full ORC plant is presented in Annex I where the main components displayed in Fig. 7 are easily recognizable. Highlighted in red are the overall external inputs of the complete ORC module:

- hot heat transfer fluid temperature, pressure and mass flow rate;
- refrigerant temperature, pressure and mass flow rate.

The thermodynamic conditions of the two heat transfer fluids necessary to vaporize and condense the organic fluid are in fact the actual driving forces of the plant: a change in the mechanical power delivered by the ORC can be achieved if the thermal power input changes, for example by increasing the hot transfer fluid mass flow rate and/or temperature.

From the model of Annex I it can also be appreciated how the evaporator-hot drum and condenser-cold drum constitute the two main places of energy and mass storage of the plant (and therefore these components, as seen, are *state determined* and described by means of differential equations) while the two flow control devices (feed pump and turbine) are positioned in between them (these components are *not state determined* and described by purely algebraic correlations).

To guarantee stable operation of the system a proper PID controller of the pump speed had to be introduced. It should be noted in fact that an open loop operation of these plants would not be feasible [7], since if the mass flow rate from the pump were not controlled during transients and off design operation, the drums would experience rapid emptying or full filling which are not acceptable in ordinary operations.

The whole ORC of Annex I can be masked within a single block that constitutes the full ORC plant, displayed in Fig. 8. Actual mechanical power and cycle efficiency, along with the temperatures of the transfer fluids leaving the evaporator and condenser, have been chosen as system outputs even if any other desired state variable or parameter could have been selected instead.

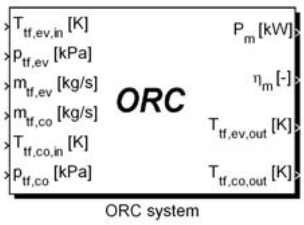

Fig. 8. Simulink® interface of the Organic Rankine Cycle unit. Upper level.

3.3 Simulation results

A simulation example of the ORC model is here proposed.

The organic fluid employed for the cycle is R123; diathermic oil is the heat transfer medium to the evaporator and water is used to cool the condenser. The same 20 nodes heat exchanger showed in the previous Paragraph is used as evaporator and condenser.

Simulations have been conducted imposing a step change in one of the main overall external inputs, namely the heat transfer fluid mass flow rate to the evaporator, that changes from 12.5 to 14 kg/s at simulation time *t*=50 s starting from a steady state operating condition. All other external inputs are maintained constant.

The sudden increase in the heat transfer fluid mass flow rate, not being changed its temperature, determines an increase in the energy flow input to the system.

Fig. 9 (a) and (b) demonstrate how the pressure existing within hot and cold drum, and hence in the evaporator and condenser, changes due to the increased heat transfer fluid mass flow rate that in fact, determines an increase in the organic fluid temperature leaving the evaporator (Fig. 12 (b)).

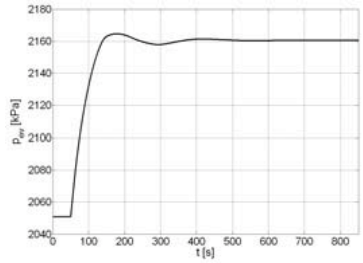

(a)

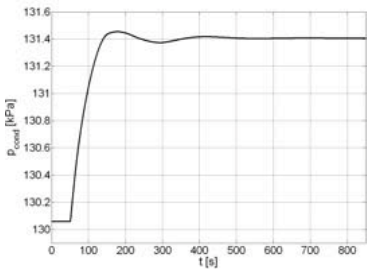

(b)

Fig. 9. Pressure in the hot (a) and cold drum (b).

The liquid volume fraction within the hot drum however remains nearly constant after the transient (Fig. 10 (b)) and this is due to the action of the controller on the pump speed (Fig. 10 (a)).

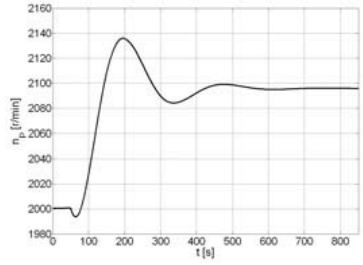

(a)

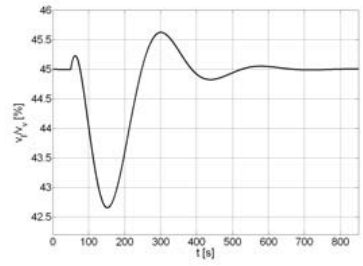

(b)

Fig. 10. Pump rotational speed (a) and liquid volume fraction in the hot drum (b).

Cycle net electrical power and thermodynamic efficiency are presented in Fig. 11, where the net power has been calculated from the turbine and pump power and taking into account of electrical efficiencies for generator and motor. It can be

noted that while the cycle efficiency remains substantially unchanged, a power increase can be observed at the end of transient as consequence to the increased thermal power to the system through the increased transfer fluid mass flow rate.

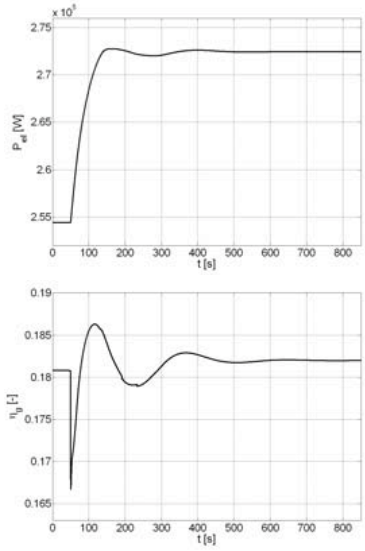

(a)

(b)

Fig. 11. Net system electrical power (a) and efficiency (b).

Fig. 12 displays the 3D plots where some of the state variables of the evaporator are plotted with respect to simulation time and heat exchanger equivalent abscissa. It can be observed how the organic fluid mass flow rate changes in time as consequence of the controller's action on the main pump (Fig. 12 (c)). Also the increasing transfer fluid temperature determines an increase in the pipe wall temperature (Fig. 12 (a)) which in turn determines an increase in the organic fluid specific enthalpy and temperature (Fig. 12 (b)). It can be observed that the pipe temperature is always higher than that of the organic fluid.

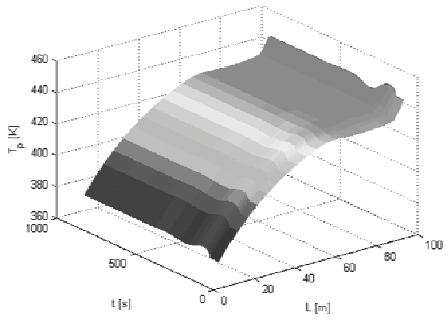

(a)

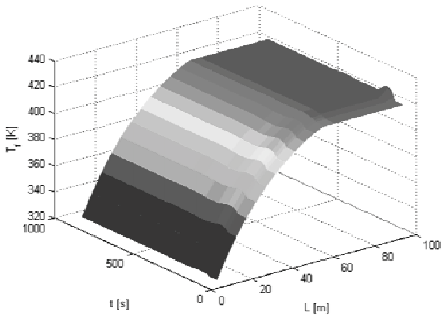

(b)

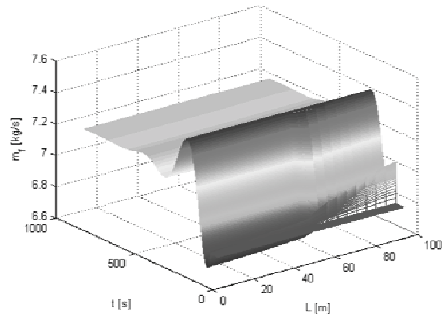

(c)

Fig. 12. Evaporator response: pipe wall temperature (a), organic fluid temperature (b) and organic fluid mass flow rate (c) as function of time and distance from evaporator inlet.

The pipe temperature rises at the end of the evaporator as consequence to the reduced heat transfer coefficient in the inner pipe where the fluid is almost entirely in vapour phase.

Conclusions

In the paper a full model for the simulation of ORC systems has been introduced and described. The model, based on custom components created in the Simulink® environment recurring to specifically written Matlab® codes, turned out to be sufficiently flexible, fast and robust for use as predictive tool for actual testing, pre-prototyping and design of real ORC plants.

As will be shown in future works, the ORC model here presented has been employed to design and study a combined ORC-ICE (Internal Combustion Engine) power unit helping to assess off design conditions, control strategies as well as different system setups [6]. For example a design with two heat exchangers (pre-heater and evaporator) helped to assess a setup where both the engine

exhaust gases and refrigerant are employed as heat transfer media.

A validation of the full model has not been possible so far but will be conducted as soon as the experimental activity on ORC that the authors are going to begin will provide sufficient results.

Nomenclature

m	mass, kg
$\dot{m}$	mass flow rate, kg/s
h	specific enthalpy, kJ/kg
p	pressure, Pa
t	time, s
u	specific internal energy, kJ/kg
x	vapour mass fraction
T	temperature, K
V	volume, m^3

Greek symbols

η	efficiency
ρ	density, kg/m^3

Subscripts and superscripts

ev	evaporator
f	fluid
i	General axial node of discretization
in	input
l	liquid
out	output
p	pipe
tf	transfer Fluid
v	vapour

References

[1] Wei D., et al., 2008, Dynamic modelling and simulation of an organic Rankine cycle (ORC) for waste heat recovery, Appl. Thermal Engineering, 28(10), pp. 1216-1224.

[2] Colonna P., van Putten H., 2007, Dynamic modeling of steam power cycles. Part I - Modeling paradigm and validation, Appl. Th. Eng. 27, pp. 467-480.

[3] Colonna P., van Putten H., 2007, Dynamic modeling of steam power cycles. Part II – Simulation of a small simple Rankine cycle system, Appl. Th. Eng., 27, pp. 2566-2582.

[4] Wei D., et al., 2007, Performance analysis and optimization of organic Rankine cycle (ORC) for waste heat recovery, Energy Conversion and Management, 48, pp. 1113-1119.

[5] Yamamoto T., et al., 2001, *Design and Testing of the Organic Rankine Cycle*, Energy, 26, pp.239-251.

[6] Vaja I., 2009, Definition of an Object Oriented Library for the Dynamic Simulation of Advanced Energy Systems: Methodologies, Tools and Application to Combined ICE-ORC Power Plants, Ph.D. Dissertation, University of Parma, Parma, Italy.

[7] Colonna P., van Putten H., 2007, Dynamic modeling of steam power cycles. Part II – Simulation of a small simple Rankine cycle system, Appl. Th. Eng., 27, pp. 2566-2582.

Annex I. Simulink® model of the ORC power plant.

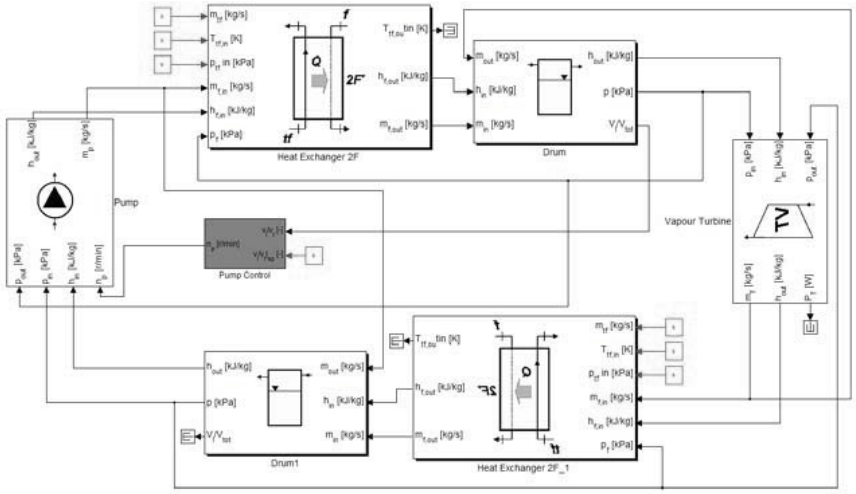

High efficient engine or heat pump based on thermal-hydraulic conversion

Sylvain MAURAN[ab], Driss STITOU[a] and Matthieu MARTINS[ab]

[a] *CNRS-Promes, Perpignan, France*
[b] *University of Perpignan, Perpignan, France*

Abstract: A new concept of heat engine or heat pump is presented. The cycle followed by the working fluid is nearly close to the Carnot cycle (reverse or engine). Heat exchanges with the environment occur during isothermal steps of the cycle with a liquid/vapor phase change of the working fluid. Work exchange involved during each step is realized by an alternating movement of an inert liquid LT which acts as a liquid piston. The work-transfer liquid LT flows either through a hydraulic motor (for the engine mode) or through a hydraulic pump (for the heat pump mode). This intermediary hydraulic fluid avoids the main irreversibility inherent to conventional engine or heat pump. Work generation, cooling and/or heating with work or heat input are possible with this thermal-hydraulic process. According to the available heat source and sink and to the aimed application, associations of basic thermal-hydraulic elements (engine or heat pump) are required, such as thermal cascade or mechanical coupling. The estimated performances, engine efficiency or heat pump COP, are very high: upper than 70% of the corresponding Carnot efficiencies.

Keywords: Carnot cycle, Cogeneration, Liquid piston, multipurpose process.

1. Introduction

Improving the efficiency of engines and / or heat pumps is a major issue for sustainable development [1] in order to minimize greenhouse gas emissions. To achieve this goal there are two complementary ways: increasing the temperature ratio between hot and cold heat sources and /or increasing the exergy efficiency of the cycle. The Ericsson or Stirling engines [2] combine the two approaches. The use of gas as working fluid allows a possible use of heat source at high temperature but on the other hand it induces low heat transfer coefficient with both heat external source and sink and also at the internal level of the regenerator, which ultimately leads to a significant decrease of exergy efficiency.

Inversely, the Organic Rankine Cycle engine [3, 4] or the classical mechanical heat pump, using both steam as working fluid, have excellent heat transfer coefficients with heat source and sink in the evaporator and condenser, but the adiabatic stages of compression and expansion require, for technical reasons, the working fluid to be at a single-phase state (sub-cooled liquid or super-heated steam) and this induces exergy losses [5].

The process engine or heat pump proposed in this paper shows the advantages of both ways: it approaches the ideal Carnot cycle with liquid/vapor changes with the heat source/sink. The technical difficulty to compress or expand a two-phase mixture is circumvented by using another inert liquid LT as a piston. The work is exchanged between the system (engine or heat pump) and the environment by pressurization or expansion of this liquid. It is therefore a thermal-hydraulic conversion process.

2. Principle of the thermal-hydraulic conversion

The working fluid (natural, HFC or HC) follows, in the ideal case, the Carnot cycle (engine or reverse). As the liquid piston allows a work exchange between different components of system, this process is called CAPILI (for CArnot with PIston LIquid). In fact, two main options are possible if one or two isentropic steps of the cycle occur with the liquid/vapor mixtures. The CAPILI (engine or heat pump) is said respectively of the "1st type" or the "2nd type" according to these two options. The 2nd type CAPILI corresponds exactly to the Carnot cycle while CAPILI 1st type deviates slightly.

The work-transfer liquid LT must have a very low saturation pressure (oil for example) for the operating temperatures of the process, and must be

Corresponding Author: Mauran Sylvain, Email: mauran@univ-perp.fr

immiscible with the working fluid and preferably more dense than it.

2.1. CAPILI engine

The components of the engine (1st or 2nd type) are presented in Fig. 1.

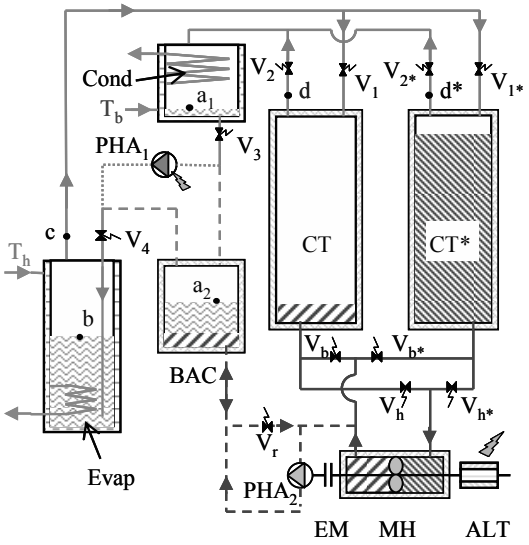

Fig. 1. Common (1st and 2nd types) and exclusive (1st or 2nd type) components of thermal-hydraulic CAPILI engine.

The common components for both types are:

- An evaporator (Evap in Fig. 1) connected to the heat source at high temperature T_h.
- A condenser (Cond) connected to the heat sink at low temperature T_b.
- Two insulated work-transfer cylinders (CT, CT*).
- A hydraulic motor (MH).
- An optional alternator (ALT).
- Some solenoid valves (V_1,V_{1*},… V_b, V_{b*},…) either on working fluid pipes or work-transfer liquid pipes.

The exclusive components of the 1st type CAPILI engine are an auxiliary hydraulic pump (PHA_1), that can be driven by the hydraulic motor (MH) with a clutch (EM). The exclusive components of the 2nd type consist in another auxiliary hydraulic pump (PHA_2), also possibly driven by MH, the valves V_r, V_3 and V_4 and a bottle for the adiabatic compression (BAC in Fig. 1) of the liquid/vapor mixture of the working fluid.

Some examples of CAPILI engine cycles are given in Fig. 2 with water as working fluid.

The 2nd type CAPILI cycle "abcd" consists of two successive steps (Figs 1 and 2):

- **Step αβγ (with opened valves V_{1*}, V_{h*} and V_4 after t_β):** The saturated steam at high pressure P_h (≈ 792 kPa for this example) flows between the evaporator and the work-transfer cylinder CT*. The work-transfer liquid LT is pushed down to an intermediate level, flows through the hydraulic motor MH and generates work by expanding until the low pressure P_b (≈ 70 kPa). A part of generated work is withdrawn by the hydraulic pump PHA_2. LT is pumped by PHA_2 and pressurized at high pressure P_h within the BAC vessel which contains liquid/vapor mixture of water. This mixture is isentropically compressed and when the pressure P_h is reached (at the time t_β) the saturated liquid is introduced in the evaporator. This step corresponds to the transformations a→b in BAC and b→c in Evap and CT*.
- **Step γδ (with opened valves V_2, V_3, V_b, V_{h*} and V_r):** The vapor contained in CT* follows an isentropic expansion between the pressures P_h and P_b. LT is pushed down to the lowest level in CT*, flows through the hydraulic motor MH and generate work again. The BAC vessel, in communication with the condenser, is now at low pressure and LT contained in its lower part flows by gravity to the cylinder CT which should be preferred below of BAC. The two flows of LT (coming from BAC and CT*) reduce the steam volume in CT that induces its condensation in the condenser at P_b. This step corresponds to the transformations c→d in CT* and d→a in CT and Cond.

After these two steps the working fluid has made a full cycle but the process has not reached the beginning state; two complementary steps are required where CT and CT* are switched:

- **Step δελ (with opened valves V_1, V_h and V_4 after t_ε):** transformations a→b in BAC and b→c in Evap and **CT**.
- **Step λα (with opened valves V_{2*}, V_3, V_{b*}, V_h and V_r):** transformations c→d in **CT** and d→a in **CT*** and Cond.

Note that LT flows throughout MH always in the same direction.

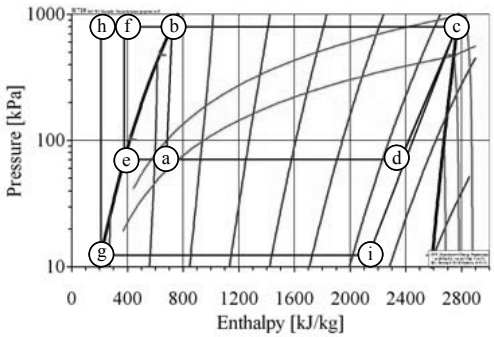

Fig. 2. Examples of CAPILI engine cycles of 1st type (efcd, ghci) or 2nd type (abcd) with water (R718) as working fluid.

The cycle "abcd" described above is a special case for which there is equality for two specific volumes of the working fluid: $v_a = v_c$ (see isochores in Fig. 2). In the general case, at the state "b" of the cycle, the work-transfer liquid LT at P_b fills a part of the CT cylinder connected to the condenser. There is an intermediate point "j" between the points "a" and "d" which verifies:

$$v_j - v_a = v_d - v_c \quad (1)$$

The half cycle has two supplementary steps (four steps in total instead of two). The general case is systematic at the start of the process when temperatures in the evaporator and condenser are still mixed up ($v_j = v_a$ in this extreme case). But gradually as the temperature of the evaporator and condenser diverge, the cycle tends to the particular case "abcd" above presented. This second extreme case (unsurpassable because v_c must remain upper than or equal to v_a) is the most favourable: from one hand because the operating cycle is simpler (two steps instead of four) and secondly it leads to the maximum permitted difference between the temperatures of the evaporator and condenser, so finally to the maximum efficiency of the engine.

The efficiency of the CAPILI engine is defined by:

$$\eta = \frac{|\Sigma w|}{q_h} = 1 - \frac{|q_b|}{q_h}, \quad (2)$$

where Σw is the net work delivered, q_b and q_h heats exchanged at the temperatures T_b and T_h of respectively the condenser and evaporator.

The 1st type CAPILI engine is simpler than the 2nd type. It includes almost the same components (Fig. 1). The cycles "efcd" and "ghci" in Fig. 2 are two examples of such 1st type cycles. As previously the half-cycle is composed of two steps. For example with the cycle "efcd":

- **Step αβ (with opened valves V_{1*}, V_2, V_{h*} and V_b):** The saturated steam at high pressure P_h (≈ 792 kPa) flows between the evaporator and the work-transfer cylinder CT*. The work-transfer liquid LT is pushed down to an intermediate level, flows through the hydraulic motor MH and generates work by expanding until the low pressure P_b (≈ 70 kPa). A part of expansion work is withdrawn by the hydraulic pump PHA_1. The liquid LT at low pressure P_b is introduced within CT until an intermediate level is reached; so a part of steam condenses in the condenser connected to CT cylinder. The saturated liquid at the bottom of the condenser is pressurized by PHA_1 and introduced in the evaporator at a sub-cooled state "f". This step corresponds to the transformations e→f through PHA_1, f→c in Evap and CT* and a partial condensation d→j in CT and Cond (with "j" an intermediate point, between points "d" and "e", which is not drawn in Fig. 2).
- **Step βγ (with opened valves V_2, V_{h*} and V_b):** The vapor contained in CT* follows an isentropic expansion between the pressures P_h and P_b. The liquid LT is pushed down until the lowest level in CT* is reached, flows through the hydraulic motor MH and generate work again. LT ends to fill CT and achieves the condensation of steam in the condenser at P_b. This step corresponds to the transformations c→d in CT* and j→e in CT and Cond.

As for the 2nd type cycle, there are two symmetrical steps "γδ" and "δα" where CT and CT* are switched to realize the other half-cycle.

Efficiencies of three cycles "abcd", "efcd" and "ghci" (Fig. 2) are shown in Table 1 and compared with the Carnot engine efficiency η_C between the same **internal** temperatures high and low.

Table 1. Energetic and exergetic efficiencies of some CAPILI engines with water (cycles of Fig. 2).

Cycle	CAPILI type	$T_h - \Delta T_e$ (°C)	$T_b + \Delta T_e$ (°C)	η (%)	η/η_C (%)
abcd	2nd	170	90	18.1	**100.0**
efcd	1st	170	90	16.9	**93.4**
ghci	1st	170	50	24.7	**91.2**

Even if the thermal pinch ΔT_e for the heat exchange in the evaporator or condenser is quite low (≈ 10°C), it is sufficient to allow the liquid/vapor phase change thanks to the high values of heat transfer coefficients.

The exchanged heats q_h and q_b in (2) are determined by the variations of the specific enthalpies input and output to the evaporator and condenser respectively. For example with cycle "efcd": $q_h = (h_c - h_f)$ and $|q_b| = (h_d - h_e)$.

The cycle "abcd" constitutes a perfect Carnot engine cycle. The exergetic efficiency, defined as the ratio η/η_C, is 100%! Obviously some simplifying assumptions are not fully realized in practice. Thus it is optimistic to assume that:

- The compressions of the liquid/vapor mixture (in case of 2nd type) or saturated liquid (1st type) are fully isentropic.
- The expansion of the saturated vapor (1st or 2nd type) is fully isentropic.
- There are no friction losses (on LT and working fluid) or heat losses (through the work-transfer cylinders CT, CT*).
- The performance of the transformation process of hydraulic work of the liquid LT to mechanical work transmitted to the alternator is supposed to be equal to 100%.

In fact the aim of this paper is to evaluate the intrinsic thermodynamical irreversibilities of the CAPILI cycle and not those which are dependent on inevitable technical imperfections of the components.

In a conventional Rankine cycle work must be recovered by a turbine with a dry expansion of the working fluid. With the CAPILI engine it is not a problem if the adiabatic expansion results in a liquid/vapor mixture as it is always the case with the use of water as working fluid. Indeed, at the end of expansion that liquid (immiscible with LT) can be returned to the condenser if it floats above LT. If its density is greater, then a flexible membrane must be inserted, with a very weak resistance to the movement of the liquid piston.

The cycle "abcd" has a best exergetic efficiency but its energetic efficiency η (more important for the user of the engine) is limited by the condition $v_a \leq v_c$. With a chosen high temperature of 170°C in the evaporator this condition ($v_a \leq v_c \approx 0.243$ m^3/kg and $s_a = s_b$) implies a minimal temperature of 90°C in the condenser (see isochors in Fig. 2).

The CAPILI 1st type is not limited because the specific volume of the liquid is always lower than those of saturated vapours (far from the critical point). For example with the cycle "efcd": $v_e = 1.036\ 10^{-3}$ $m^3/kg << v_c$.

However, as a sub-cooled liquid is introduced in the evaporator the efficiency of the 1st type cycle can not reach those of Carnot engine. The degradation is relatively low; so the efficiency of the cycle "efcd" reachs 16.9% instead of 18.1% for the cycle "abcd" with the same temperatures T_h and T_b (Table 1). In practice as the 1st type engine is less limited by the temperature drop (T_h-T_b) its efficiency η can be higher than those of a 2nd type engine. An example is given with the cycle "ghci" (Fig. 2, Table 1): with the same high temperature (170°C) and a lower temperature in the condenser (50°C), the efficiency η reachs 24.7%.

2.2. CAPILI heat pump

The components of the heat pump (1st or 2nd type) are presented in Fig. 3.

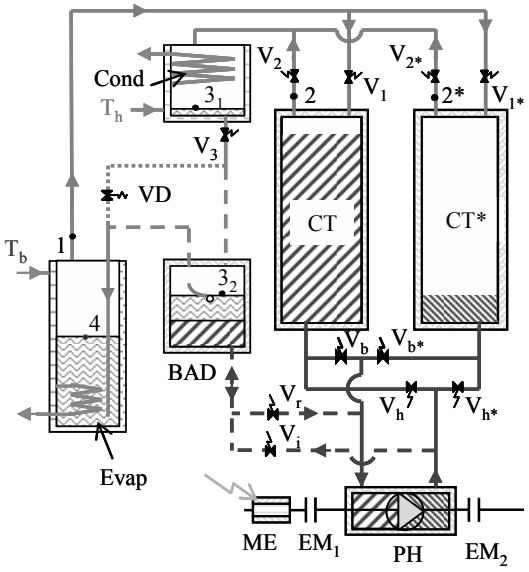

Fig. 3. Common (1st and 2nd types) and exclusive (1st or 2nd type) components of thermal-hydraulic CAPILI heat pump.

Lots of them are identical to those of the CAPILI engine. In fact the main differences are:

- A hydraulic pump (PH) takes the place of the hydraulic motor (MH). This PH can be driven

by an electric motor (ME) or by another engine through the clutch EM_2.

- For the 2nd type CAPILI heat pump, BAD is now a bottle for the adiabatic **expansion** of a liquid/vapor mixture of the working fluid. This implies that the entry of the pipe connected to the evaporator to BAD sucks up only the saturated liquid as shown in Fig. 3.
- For the 1st type CAPILI heat pump, a throttling valve (or a capillary tube) takes the place of the pump PHA_1.

Two examples of CAPILI heat pump cycles (named "1234" and "5678") are given in Fig. 4 with isobutane (R600a) as working fluid. In addition with this same working fluid three other CAPILI engine cycles ("abcd", "efcd" and "ghci") are drawn.

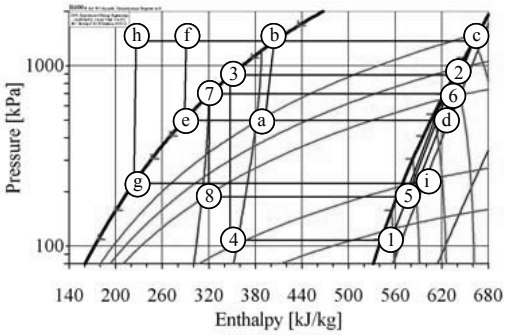

Fig. 4. Examples of CAPILI engine or heat pump cycles with isobutane (R600a) as working fluid. 1st type engine cycles (efcd, gfch) or 2nd type (abcd). 1st type heat pump cycles (1234, 5678).

The steps of the heat pump cycle are very similar to those of the engine cycle with of course a reverse flow of the working fluid. For example with the cycle "1234" (1st type CAPILI heat pump) the half-cycle is composed of two steps:

- **Step αβ (with opened valves V_1, V_3, V_b and V_{h^*}):** The vapour, which is slightly superheated at low pressure P_b (≈ 504 kPa), flows between the evaporator and the work-transfer cylinder CT. The work-transfer liquid LT is sucked toward the bottom to an intermediate level by the hydraulic pump PH. The liquid LT plays the role of a liquid piston which compress the working fluid within CT*. In this cylinder CT* the pressure increases until P_h (≈ 1344 kPa) and LT reached also an intermediate level. Also, the fluid R600a in a saturated liquid state at the bottom of the condenser is expanded (isenthalpically) through VD and introduced at low pressure and at a liquid/vapor mixture state in the evaporator. This step corresponds to the simultaneous transformations 3→4 through the throttle valve VD, 1→2 in CT* and a partial evaporation 4→0 in Evap and CT (the point "0" is an intermediate point between points "4" and "1", not drawn in Fig. 4).
- **Step βγ (with opened valves V_1, V_{2^*}, V_3, V_b and V_{h^*}):** The pressures in the condenser and the cylinder CT* are identical when the valve V_{2^*} is opened. The evaporation continues, the liquid transfer gradually reaches a low level in CT and a high level in CT*. The saturated vapors of R600a are condensed in the condenser. This step corresponds to the transformations 0→1 in Evap and CT, and 2→3 in CT* and Cond.

As for the other CAPILI cycles, there are two symmetrical steps "γδ" and "δα" where CT and CT* are switched to realize the other half-cycle.

Similarly with the engine cycle the specific volumes of the working fluid at the various states of the cycle "1234" must verify:

$$v_0 - v_3 = v_1 - v_2 \tag{3}$$

But in this case the limit to the temperature drop (T_h-T_b) is practically very low. As the specific volume at point "3" is still the lowest in the cycle, it is always possible, whatever T_h and T_b, to obtain a state "0" between the state "4" and "1" (i.e. $v_4 < v_0 < v_1$). Obviously the difference (T_h-T_b) is still limited to extreme case where states "4" and "1" are identical.

According to the aimed application, i.e. cooling or heating, the performance of the process is quantified respectively by the COP or COA coefficients, defined as:

$$COP = \frac{q_b}{\Sigma w} = \frac{q_b}{|q_h| - q_b}, \tag{4}$$

$$COA = \frac{|q_h|}{\Sigma w} = \frac{|q_h|}{|q_h| - q_b} = COP + 1, \tag{5}$$

where Σw is the net work consumed by PH, q_b and q_h heats exchanged at the temperatures T_b and T_h of the evaporator and condenser respectively. They are determined by the variations of the specific enthalpies input and output these two components.

For example with cycle "1234": $q_b = (h_1 - h_4)$ and $|q_h| = (h_2 - h_3)$.

COP of two CAPILI heat pump cycles "1234" and "5678" and efficiencies of three other CAPILI engine cycles "abcd", "efcd" and "ghci" (Fig. 4) are shown in Table 2 and compared with the Carnot heat pump COP_C or the Carnot engine efficiency η_C between the same respective high and low **internal** temperatures.

Table 2. Energetic and exergetic efficiencies of some CAPILI engines or heat pumps with isobutane (cycles of Fig. 4).

Engine cycle	CAPILI type	$T_h - \Delta T_e$ (°C)	$T_b + \Delta T_e$ (°C)	η (%)	η/η_C (%)
abcd	2nd	80	38	11.8	**99.5**
efcd	1st	80	38	10.2	**85.5**
ghci	1st	80	10	16.1	**81.3**
HP cycle	CAPILI type	$T_h + \Delta T_e$ (°C)	$T_b - \Delta T_e$ (°C)	COP	COP/COP_C (%)
1234	1st	60	-10	2.52	**67.1**
5678	1st	50	5	4.91	**79.4**

The comments for the engine cycles are quite the same for the two working fluids (water and isobutane): the cycle "ghci" of 1st type is simpler and finally leads to a better efficiency η, even if its exergetic efficiency is lower than the cycle "abcd".

The aimed application of heat pump cycle "1234" can be for example the heating of a house by pumping "free" outside heat. Taking into account the thermal pinch of exchangers, the heat is released at about 50°C (ie, 60 $-\Delta T_e$) and pumped outside at 0°C (ie, -10 $+\Delta T_e$). For this application the COA coefficient is more relevant. The obtained value of 3.52 (COP +1, Table 2) is excellent for this amplitude of temperature even if the exergetic efficiency (here the ratio COA/COA_C) of 74% is slightly lower than those of the CAPILI engines.

The aimed application of heat pump cycle "5678" is the air-conditioning of a house in summer. The cold produced at 15°C (= 5 $+\Delta T_e$) is compatible with the need of a refreshing floor while the heat can be released outside at a maximal ambiant temperature of 40°C (= 50 $-\Delta T_e$). Logically the COP and the ratio COP/COP_C are better because the temperature drop is reduced.

2.3. Cogeneration by association of CAPILI engine and heat pump

Two types of associations of CAPILI engine and/or heat pump are examined: the thermal cascade and the mechanical coupling (Fig. 5).

These associations permit to satisfy all the energetic needs of a domestic house: work converted in electricity, heating (including Hot Domestic Water) and cooling.

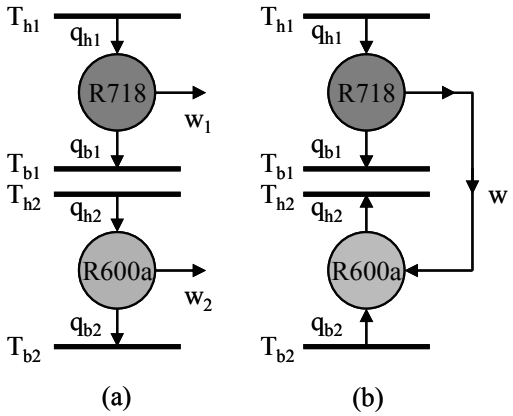

Fig. 5. Associations of CAPILI engines or heat pump: a) Thermal cascade, b) Mechanical coupling.

Most elements of CAPILI engine and heat pump are identical; it is quite possible to achieve a **multipurpose** process with the specific elements in by-pass. For example, for a multipurpose CAPILI process of 1st type, it is enough to put in parallel the throttle valve VD and the auxiliary pump PHA_1 and secondly the hydraulic pump PH and motor MH. It is also possible to have a single hydraulic-mechanical converter that can perform both functions.

Thus a user with a CAPILI engine and a multipurpose CAPILI process can satisfy all its energy needs that vary during the day and year, by associating on request these two processes and **by consuming only heat as primary energy**. The Table 3 shows three possible associations between CAPILI engine and a multipurpose CAPILI process using some cycles drawn in Figs 2 and 4 with water (R718) and isobutane (R600a) as working fluids respectively.

The energetic and exergetic efficiencies of the applications listed in Table 3 are defined by:

1. Power.

   The 1st type cycle "efcd" (R718) is associated with the 1st type cycle "efcd" (R600a) in thermal cascade according to Fig. 5a.

The energetic efficiency is:

$$\eta_{TC} = \frac{|w_1| + |w_2|}{q_{h1}} = \eta_1 + (1 - \eta_1) \cdot \eta_2 , \quad (6)$$

with η_1 and η_2 the efficiencies of the topping and bottoming cycles respectively.

The exergetic efficiency is:

$$\xi_{TC} = \eta_{TC} \Big/ \left(1 - \frac{T_{b2}}{T_{h1}}\right), \quad (7)$$

It includes the thermal pinches ΔT_e (= 10°C) required for all heat exchanges.

2. Heating.

The 1st type cycle "efcd" (R718) is associated with the 1st type cycle "1234" (R600a) in mechanical coupling according to Fig. 5b.

The COA coefficient is:

$$COA_{MC} = \frac{|q_{b1}| + |q_{h2}|}{q_{h1}} , \quad (8)$$
$$COA_{MC} = (1 - \eta_1) + \eta_1 \cdot (COP_2 + 1)$$

with η_1 and COP_2 the efficiency and COP of the topping and bottoming cycles respectively.

The heat is delivered at two different temperatures T_{b1} (= 80°C), which are compatible with the production of the Hot Domestic Water and T_{h2} (= 50°C), i.e. compatible with the house heating. Depending if the heat produced at T_{b1} is effectively used for HDW, we can define two exergetic efficiencies (Equations (9) below):

$$\xi_{MC,min} = COA_{MC} \Big/ \left[\left(\frac{T_{h2}}{T_{h1}}\right) \cdot \left(1 - \frac{T_{h1} - T_{h2}}{T_{h2} - T_{b2}}\right) \right]$$
$$\xi_{MC,max} = COA_{MC} \Big/ \left[\left(\frac{T_{b1}}{T_{h1}}\right) \cdot \left(1 - \frac{T_{h1} - T_{b1}}{T_{h2} - T_{b2}}\right) \right]$$

3. Cooling.

The 1st type cycle "ghci" (R718) is associated with the 1st type cycle "5678" (R600a) in mechanical coupling according to Fig. 5b. The heat is pumped at a temperature T_{b2} (= 15°C) compatible, after heat exchange, with the input and output (18 to 25°C) of a refreshing floor.

The COP coefficient is:

$$COP_{MC} = \frac{q_{b1}}{q_{h1}} = \eta_1 \cdot COP_2 \quad (10)$$

The exergetic efficiency is:

$$\xi_{MC} = COP_{MC} \Big/ \left[\frac{T_{b2}}{T_{h2} - T_{b2}} \cdot \left(1 - \frac{T_{b1}}{T_{h1}}\right) \right] \quad (11)$$

Excepted for the last application (refreshing floor) all the exergetic efficiencies ξ are quite high.

With the heat source at a moderate temperature ($T_{h1} \approx 180$°C), i.e. compatible with a wood burner or gas-fired boiler, such associations of CAPILI engine and heat pump can provide cogeneration (power and/or heating and/or refreshing) useful for domestic house with high energetic efficiencies (Table 3).

Table 3. Energetic and exergetic efficiencies of some associations of CAPILI engines or heat pump for cogeneration. Primary energy: heat at T_{h1} ≈180°C (ΔT_e included).

Application	Power $T_{b1} - T_{h2} = \Delta T_e$ T_{b2} = 28°C	Heating T_{b1} = 80°C T_{h2} = 50°C T_{b2} = 0°C	Refreshing $T_{b1} = T_{h2}$ = 40°C T_{b2} = 15°C
R718 cycle	efcd	efcd	ghci
R600a cycle	efcd	1234	5678
Efficiency, COA or COP	25.4 %	1.43	1.21
Exergetic efficiency	75.7 %	> 55.7 % < 64.8 %	34.0 %

3. Conclusion

A new concept of thermal hydraulic process has been presented. It leads to engines or heat pumps with high exergy efficiencies. Some simplifying assumptions are still too optimistic, especially the efficiency assumed equal to the unity of the processing chain hydraulic– mechanical–electrical. However the robust technology of hydraulic–mechanical converters which is well controlled for high pressure drop ΔP (= $P_h - P_b$) lets hope, with further developments, future good performances with lower ΔP as those of CAPILI processes.

Two main options (1st and 2nd types) of the process have been detailed. Engines or heat pumps of the 2nd type are more efficient but also more complex (and therefore expensive). For engine, the 1st type seems the best cost-effectiveness compromise.

By integrating some specific elements of the CAPILI engine or heat pump it is possible to realize a multipurpose process to ensure the application of one or the other functions. This

possibility increases for the user the interest of the associations (thermal cascade or mechanical coupling) between multipurpose and engine CAPILI. An example was given for the cogeneration (power/heating/refreshing) adapted to domestic house.

Nomenclature

COA coefficient of amplification

COP coefficient of performance

h specific enthalpy, J/kg

P pressure, kPa

q specific heat, J/kg

s specific entropy, J/(kg K)

T temperature, °C

t time, s

v specific volume, m^3/kg

w specific work, J/kg

Greek symbols

η energy efficiency

ξ exergy efficiency

Subscripts and superscripts

1, 2 relative to engine "1" or "2" or heat pump "2", if subscript of COA, COP, w or η

a, b, …, j and 0, 1, …, 8 relative to the state of the working fluid, if subscript of h, s or v

b low, if subscript of q, T or P

b1, b2 low and relative to engine "1" or "2" or heat pump "2", if subscript of q or T

C Carnot

e heat exchange, if subscript of T

h high, if subscript of q, T or P

h1, h2 high and relative to engine "1" or "2" or heat pump "2", if subscript of q or T

MC mechanical coupling

TC thermal cascade

References

[1] Hepbasli, A., 2008, A key review on exergetic analysis and assessment of renewable energy resources for sustainable future, Renewable & Sustainable Energy Reviews, 12(2008), pp. 593-661.

[2] Kuhn, V., et al., 2008, MicroCHP: Overview of selected technologies, products and field test results, Applied Thermal Engineering, 28(2008), pp. 2039-2048.

[3] Mago, P. J., et al., 2008, An examination of regenerative organic Rankine cycles using dry fluids, Applied Thermal Engineering, 28(2008), pp. 998-1007.

[4] Kane M., et al., 2003, Small hybrid solar power system, Energy, 28(2003), pp. 1427-1443.

[5] Wei, D., et al., 2007, Performance analysis and optimization of organic Rankine cycle (ORC) for waste heat recovery, Energy Conversion & Management, 48(2007), pp. 1113-1119.

Acknowledgments: This work is included in the research project TrigéBât, supported by the French research program 'ENERGIE' funded by C.N.R.S.

Evaluation of fuel saving and economics for an Organic Rankine Cycle as bottoming cycle in utility vehicles

Richard Aumann, Andreas Grill, Andreas Schuster and Hartmut Spliethoff

Institute for Energy Systems, Technische Universität München, Germany

Abstract: Waste heat recovery for power production by means of ORC is on the threshold to market and can be considered to be state of the art in the power range above 50 kW_{el}. However the utilization of waste heat from internal combustion engines in vehicles is being discussed very recently. In this paper the fuel and respectively the cost saving potential for the national economies with such systems is evaluated and discussed. Measurement results of waste heat potential in real driving cycle are presented and compared to test bench data. An approach for the design point identification for highway driving of heavy utility vehicles is shown. Based on a simulation of real part load behavior of components like heat exchangers and expansion machines the system efficiency of an experimental ORC system is calculated. Finally fuel saving potential for an experimental prototype set up is determined. The potential of this technology for national economies is calculated in an elementary way and compared to other technologies.

Keywords: dynamic heat source, Organic Rankine Cycle (ORC), utility vehicles, waste heat recovery.

1. Introduction

Organic Rankine Cycle (ORC) systems in the power range of 50 kW_{el} up to several megawatts can be considered to be state of the art or at least are on the threshold of being introduced into the market. They are applied for electricity generation from low grade waste heat, geothermal energy or biomass [1,2].

The cost effectiveness of such applications from the plant operator point of view is linked very closely to the availability of waste heat, which is free of cost but mostly is dependent on granted feed in tariffs for example for geothermal electricity or biomass. For waste heat from non regenerative sources such as industrial processes normally no feed in tariff is established although the additional power production can be considered as CO_2 free. When considering a conversion system for waste heat into electricity at an industrial site, the power produced by the ORC replaces power consumption from the grid and therefore has to compete with very low prices for industrial electricity supply and is regularly discarded because of that reasons.

Considering utility vehicles like buses and heavy duty trucks the situation is different. Internal combustion engines (ICE) show typically efficiencies above 40 % at nominal load [3]. However the cost for mechanical energy onboard can reach up to 0.40 € per kWh_{mech} depending on the fuel price and efficiency loss when operating in part load. If an ORC system could be built in a suitable power range and for an acceptable price to be applied for production of additional power from the waste heat of the ICE this additional power would replace a part of the energy coming from the ICE. It would increase the total efficiency of propulsion and decrease fuel consumption. The market for ORC applications in utility vehicles is immense and therefore the impact of the ORC technology on reducing primary energy consumption and CO_2 emissions is considerable.

Two main challenges have to be solved when designing an ORC as a waste heat recovery unit for vehicles. First there has to be mentioned the small system power of the ORC below 10 kW results in new types of components for the ORC system. Especially one stage radial inflow turbines which are quite common in state of the art ORC applications above 50 kW_{el} run into problems of very high rotational speed [4]. Other expander technologies such as volumetric expanders have shown that they are more eligible for the power range below 50 kW_{el}. [5-7]

The second challenge lies in the dynamic behavior of the waste heat source in contrary to stationary operation of normal power production cycles. ORC plant control has to ensure that the ORC reacts very fast on heat load variations so that the cycle is operated in stable behavior. This important question will not be discussed in this paper, because it is part of another work.

Corresponding Author: Richard Aumann, Email: aumann@es.mw.tum.de

The dynamic behavior of the ICE has also a big influence on finding the optimum nominal power capacity for the ORC system. Taking into account only averaged heat load over a complete driving cycle would be misleading.

For the correct dimensioning of ORC systems for utility vehicles there have to be considered realistic driving cycles and a good simulation of the cycle behavior in each load point. In the following paper the dimensioning question is discussed on the example of an experimental mobile ORC which will be attached to a utility vehicle for the purpose of proof of concept. It will be attached to an existing vehicle with a very low degree of integration. The here calculated and later on the measured fuel saving potential will give a bottom line for improvement of vehicle propulsion by means of ORC. In a future second step the efficiency of the ORC could be improved by deeper integration of the cycle into the vehicle.

2. Driving cycles for utility vehicles

In a utility vehicle with a diesel ICE there are three potential sources of waste heat. The intercooler i.e. inlet air cooling with useable temperatures from 30 to 40 °C. Heat from engine coolant with temperatures of 75 to 90 °C and exhaust gas with temperatures between 300 and 500 °C. Approximately one-third of the total diesel energy leaves the engine via the exhaust gas [8]. This high heat load and the high exergetic level of the exhaust gas make it favorable for utilization in processes of energy conversion i.e. Organic Rankine Cycle (ORC). Furthermore the low impact on the internal engine management by extracting energy via a heat exchanger offers the possibility to demonstrate the technology in mobile applications with reasonable efforts.

In a first step driving cycle data is analyzed in order to obtain boundary conditions for the design of an ORC system. Measurements from engine test bench experiments [9] are evaluated and afterwards validated by on-the-road measurement on a traveling coach. Finally the design methods are presented and fuel saving potential for highway driving is calculated via a multi point steady state simulation.

2.1. Test bench data

For the analysis of the exhaust gas heat load test bench data for a typical utility vehicle diesel engine is used:

Table 1. Diesel engine data [9]

Type	Euro2, R6
Displacement (l)	12.1
Nominal power (kW)	279

The data comprises exhaust gas parameters for stationary tests as well as transient tests with real driving cycles[9]. Those were used in order to compare different cycle parameters. Raw data for mechanical power, fuel consumption, exhaust gas mass flow and temperature (after turbo charger) are given for a specific power of 12.5 kW/t.

The specific power is a parameter that characterizes the level of motorization of utility vehicles. The considered value of 12.5 kW/t is typical for low loaded trucks or heavy loaded intercity coaches.

In the test scenario three different typical driving cycles were measured:

- *City*
- *Interurban*
- *Highway*

The main parameter for the comparison of the different cycles is the heat load of the exhaust gas. It is calculated from measurements of the exhaust gas mass flow and the temperature and is defined for a maximal cooling down to 0 °C.

$$\dot{Q}_{EG} = \dot{m}_{EG}\left(h_{EG}(T_{EG}, c_p) - h_{EG}(0\,°C, c_p)\right) \quad (1)$$

For the calculation of the specific heat capacity constant gas composition and constant pressure is assumed.

In a first step the mean heat load for the three different cycles are compared

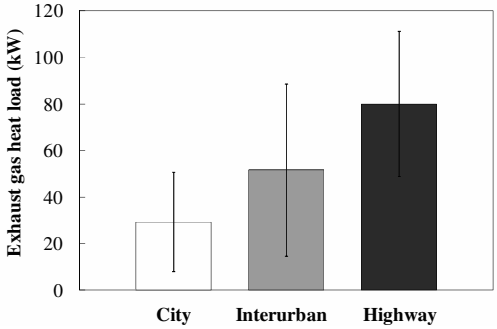

Fig. 1. Exhaust heat load and standard deviation of different driving cycles

As a measure for the energetic variation of heat that can be expected in each cycle the standard deviation is shown in Fig. 1.

The average heat load in the city cycle is at approximately 30 kW with high relative variance. The interurban cycles show higher performance at similar standard deviation. The lowest relative variation and the highest mean heat load can be found for highway driving.

2.2. On-the-road measurements

In order to validate absolute values as well as the realistic definition of the transient characteristics of the heat load for highway driving an on-the-road measurement was performed. The measurement was done on a 280 kW travel coach (Euro2, 12 l). The set up was placed at the end of the exhaust piping and was comprised of:

- Mass flow calculation from measurement of dynamic pressure via Prandtl probe
- Temperature of exhaust gas (Thermocouple)

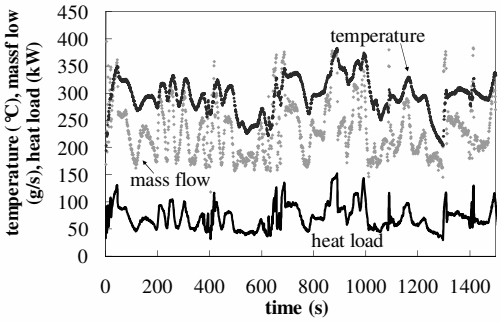

Fig. 2. Measurement of temperature and mass flow for real highway driving of a 280 kW coach

In Fig. 2 the highly transient behavior of exhaust gas parameters during a representative highway driving is shown. The heat load is changing according to mass flow and temperature changes. Due to the large inertia of the exhaust piping material the temperature respond is rather slow. Therefore the heat load is highly correlating with changes in mass flow. This could also be observed in the maximal gradients of the measured parameters. The maximal gradients that were measured are 130 g/s² for the mass flow, whereas temperature changes are in a range of a few K/s. As a result the heat load changes with gradients up to 44 kW/s. Needless to say that the dynamic of the heat source causes widespread challenges for the ORC system, which can only be overcome by smart design and control strategies. As mentioned before it shall not further be considered in this paper since it is part of additional work.

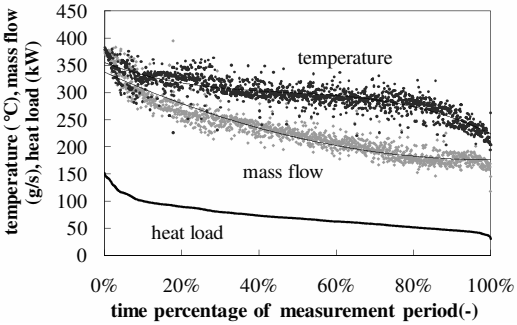

Fig. 3. Duration curve of exhaust gas parameters for the highway on-road-measurement

In the duration curve (Fig. 3) of the highway measurement the heat load is sorted from highest (approx. 150 kW) to lowest (approx. 30 kW) with correlated temperature and mass flow. For each heat load a corresponding, cycle specific, mass flow and temperature curve can be defined which finally are used as input values for the ORC simulation.

The following table shows major parameters of the measurement in comparison to the test bench data.

Table 2. Mean exhaust gas parameters for test bench and real highway driving measurements (incl. standard deviation)

	Test bench	On-the-road
temperature (°C)	336 ± 13%	295 ± 11%
mass flow (g/s)	235 ± 30%	227 ± 22%
heat load (kW)	80.0 ± 39%	70.6 ± 31%

The temperatures of the on-the-road measurement are slightly lower than from the test bench. Besides the fact that the compared engines are not identical, the highway characteristics and the measurement of the temperature at the end of the not insulated exhaust piping, could explain these small differences. Nevertheless the characteristic distribution of mass flow and temperature are almost identical. Hence the test bench data could be seen as highly realistic.

3. Design point optimization for mobile ORC

In order to find the optimum design for an ORC system with a highly dynamic heat source, the distribution over time is analyzed.

In Fig. 4 heat load distributions of different cycles are shown. Maximal values for city as well as for interurban driving are found for low heat loads of around 10 kW. For highway driving heat loads are predominately in between 60 to 100 kW with a second high power peak around 130 kW.

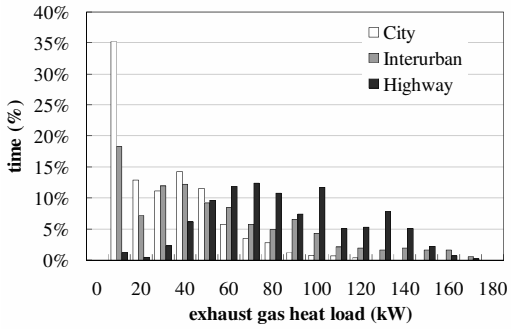

Fig. 4. Time based distribution of power for different driving cycles

Since the energy content rather than the power is decisive for the reachable fuel saving there is a shift of importance towards higher heat loads.

Therefore the energy content, i.e. the power distribution multiplied by the time, gives information about which range of heat load is important to be considered for the design of ORC systems in terms of adaption to different cycles.

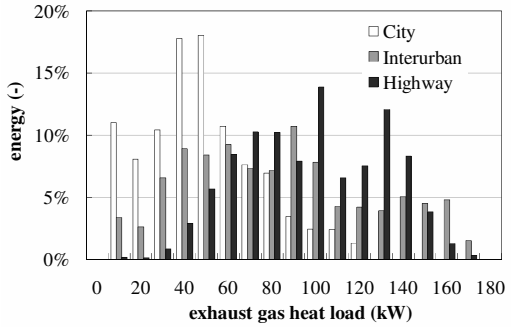

Fig. 5. Energy based distribution of energy for different cycles

Since utility vehicles in the transport section show highest full load hours per year and predominant highway driving can be expected, the design of an exhaust gas utilization system is done in consideration of the heat load distribution of highway driving as illustrated in Fig. 4.

In comparison to the time based distribution a shift of importance towards higher heat loads can be seen in Fig. 5.

For an optimized design of the ORC system all components must be dimensioned in such a way that a rather wide range of heat loads, approximately 50 to 140 kW, can effectively be transformed into mechanical work.

In order to ensure high effectiveness within the whole range of operation some general rules of design should be taken into account:

- *Expansion machine with good part load and overload characteristics*
- *Exhaust gas heat exchanger with sufficient heat exchange area and low back pressure*
- *Sufficient condenser performance to avoid high losses for peak load operation*
- *Smart control for optimization of power output and save operation of transient conditions*

4. Fuel saving potential for highway driving

In a next step the characteristic distribution of heat load, i.e. temperature and mass flow of the exhaust gas, together with a component-fixed model of an ORC cycle was used to obtain a realistic fuel saving potential for highway driving.

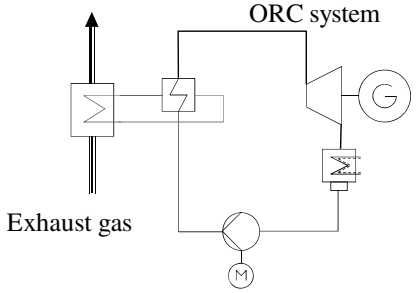

Fig. 6. Scheme of an ORC system for exhaust gas utilization

The cycle-specific heat loads in terms of variation in temperature and mass flow are used as input variables for the exhaust gas heat exchanger of the ORC System.

Main characteristics of the model are:

- *Physical behavior of volumetric expander*
- *Simulation of heat transfer fluid loop*
- *Fixed heat exchanger areas for realistic part load calculations*
- *Fixed Isentropic efficiencies:*
  - *Pump: 70%*
  - *Expansion machine: 70%*

In order to determine the performance of the ORC system an overall, comparable system efficiency is calculated. It is defined as the product of thermal efficiency and exhaust gas heat exchanger efficiency [10]. In all calculations real fluid properties were used [11].

$$\eta_{system,ORC} = \eta_{th,ORC} \quad \eta_{HEX} = \frac{P_{mech,ORC}}{\dot{Q}_{EG}} \tag{2}$$

with

$$\eta_{HEX} = \frac{\dot{Q}_{ORC}}{\dot{Q}_{EG}} \tag{3}$$

and

$$\eta_{th,ORC} = \frac{P_{mech}}{\dot{Q}_{ORC}} \tag{4}$$

Based on the typical curves for temperature and mass flow in the highway driving cycle (see Fig. 3) a characteristic efficiency curve for the ORC system is evaluated (Fig. 7).

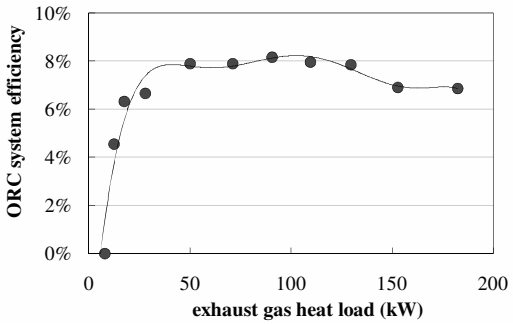

Fig. 7. ORC system efficiency with variation of heat load for highway driving

The highest efficiency of more than 8 % is reached at a heat load of 90 kW. Due to limitations in the heat exchanger area and the condenser power the efficiency declines for high heat loads to values of about 7 %. For heat loads lower than 40 kW_{th}, a lower temperature of the exhaust gas and part load operation of the ORC system lead to a sharp drop of efficiency. Moreover a useful operation for heat loads lower than 15 kW_{th} is not possible.

The mechanical power of the ORC expander is determined according the efficiency curve for each load point as evaluated for highway driving in chapter 3.

$$P_{mech,ORC} = \eta_{system,ORC}(T_{EG}; \dot{m}_{EG}) \cdot \dot{Q}_{EG}(t) \tag{5}$$

The integrated ratio of ORC power and ICE efficiency gives the energy-saving-potential:

$$E_{FS} = \int \frac{P_{ORC}}{\eta_{ICE}} dt \tag{6}$$

The saved energy in terms of fuel divided by the total energy of fuel that was consumed during a fixed period of driving:

$$E_{FS}(\%) = \frac{E_{FS}}{E_{Fuel}} \tag{7}$$

For a measured efficiency of the internal combustion engine of 40.4 % during highway driving the potential of fuel saving via an ORC system was determined to be 5.6 %.

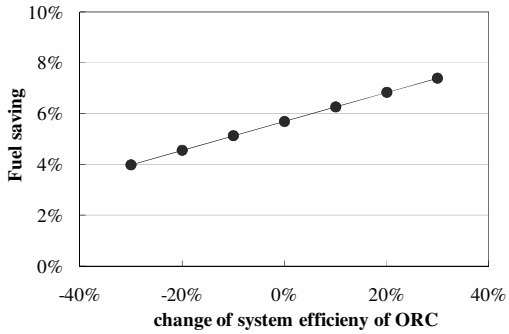

Fig. 8. Sensitivity of fuel saving on ORC system efficiency

A sensitivity analysis (Fig. 8) shows an increase to 7.4 % of fuel save for 30 % increase in ORC efficiency and an improvement of 3.0 percentage points in ICE efficiency.

Finally it has to be pointed out that the ORC modeling was done based on realistic assumptions for a first step experimental set up with further potential of optimization, e.g.:

- *Staged ORC system in order to minimize exergy destruction (e.g. use of engine coolant as second heat source)*
- *Direct vaporization*
- *Supercritical cycles*
- *Better insulation of exhaust gas piping*
- *Better integration in ICE*

Although the current design of the presented bottoming cycle for exhaust gas show results that are worth being tested, further improvements in efficiency and therefore fuel saving for heavy utility vehicle applications are desirable and realistic to be implemented in near future.

5. Economic analysis

After having discussed design methods for mobile ORC systems it should be determined whether it is favorable for the individual market actors e.g. a freight transportation company as end user.

As well the price of CO_2 reduction for the economy as a whole can be calculated in order to get to a conclusion whether such measurements are favorable from the point of view of policy makers. The price for the specific reduction for 1 ton of CO_2 allows good comparison of costs with completely different measurements for CO_2 reduction e.g. renewable energy or carbon dioxide capture (CCS) and storage.

All the following economic calculations are elaborated with the fuel saving potential taken from the proposed experimental system design which was calculated in chapter 4. It has to be emphasized that this potential was calculated for a experimental demonstration and not for a future product.

It is obvious that any predictions concerning product price or manufacturing costs for vehicle ORC applications are highly uncertain. Because of that it was decided to calculate the acceptable investment cost for a given value of annual benefit or for a given CO_2 reduction price. This gives the target price at which ORC systems in vehicles start to be cost effective.

5.1. Cost effectiveness for single market actor

For a future scenario it can be assumed that a transport company has the choice of operating vehicles with built in waste heat recovery ORC or without. The additional ORC might result in a difference of investment cost but decreased fuel consumption. This is compared to a conventional vehicle.

The assumptions for all calculations (single market actor and macroeconomic) are shown in Table 3. For an economic analysis a single market actor would take into account for his decision:

- *Surplus prize for a vehicle with ORC*
- *Personal rate of interest for capital*
- *Fixed cost due to maintenance*
- *Price for saved fuel without VAT but including petroleum tax*
- *Driving distance/year and rate of fuel saving*

The typical lifetime of 9 years for utility vehicles is shorter than lifetime of industrial applications. However the expected lifetime does not correspond to the typical time span that a freight transportation company considers for its business decisions. A typical time span for this business is only 3 years.

Table 3. Assumptions mobile cost calculation

specific investment cost (€/kW_{mech})	?
rate of interest for capital (%) [12]	4.76
average rate of inflation (%)	2.50
annual cost for operation and maintenance (€/kW_{el} / year)	50
kilometers per year	167,500
(full load hours per year)	(2791)
net price for replaced diesel fuel consumption (€/liter) without VAT [13]	0.97
cost for production of 1 liter diesel (€/liter) [13]	0.45
average consumption of truck without ORC for waste heat recovery (liter/100 km) [14]	34
average consumption of truck with ORC for waste heat recovery according to calculations of this paper (liter/100 km)	32.1
time span under consideration for macroeconomic analysis (years)	9
time span under consideration for single market actor analysis (years)	3

The economic analysis following [15] is done for fixed annual revenue. The corresponding calculated investment cost for the additional ORC system is shown in Table 4.

Table 4. Acceptable product price and revenue

aimed revenue of ORC System (€/a)	acceptable investment cost (€)
0	7,214
500	5.864
1,000	4,478
1,500	3,310
2,000	1,743

It can be seen that the given ORC system starts to be cost efficient for the end user at investment costs below 7,214 € for a single unit and for a considered time span of only 3 years. The target cost is apparently realistic due to cost reduction potential for mass production.

5.2. Macroeconomic analysis

The macroeconomic analysis considers not only the cost effectiveness for a single market actor but the sum of costs for all market actors. The global optimum is reached when the sum of costs for all actors reaches the minimum. Macroeconomic analysis will give the conclusion whether waste heat recovery with ORC systems in vehicles shows positive or negative influence on economic growth. Policy makers can use the calculated macroeconomic costs for decisions whether mobile ORC systems are more favourable for CO_2 reduction than other measurements, or not.

For the macroeconomic analysis prices for which individual market actors buy and sell goods are not of interest because they include cost for production, revenues and taxes. Here only real costs for the production of goods must be considered [16]. Fuel price without taxes [13] still includes revenues of refineries and petroleum companies. In order to reduce the problem it was assumed, that 10 % of this price forms the revenue and the rest represents the real costs of production. The authors accept that it could be discussed controversial whether this is realistic or not.

The rate of interest for capital in this analysis is not equal to the rate that a single market actor has to pay for his capital because this rate includes also the revenues of banks. For the whole economy the realistic cost of capital is equal to the average rate of inflation which represents the discounting of the total capital of a national economy.

The considered time period should correspond with the expected lifetime of the vehicle with waste heat recovery unit, because this is the average time in which it will create benefit for the economy and save CO_2 emissions.

According to driving distance and decreased fuel consumption, the given mobile ORC unit will save 8.5 metric tons of CO_2 per year.

Table 5. CO_2 reduction cost for mobile ORC units

aimed cost for CO_2 reduction (€/t)	acceptable production cost for mobile ORC unit (€)
40	11,154
13	9,317
0	8,432
-10	7,751
-20	7,071

Facing again the problem of lacking data for production cost for mobile ORC units, the corresponding equilibrium production cost for ORC units was calculated for fixed prices for CO_2 reduction.

Results in Table 5 show, that for production cost below 8,432 € per ORC unit, the fuel reduction does not only decrease CO_2 emissions but also shows negative costs, which is favourable economic growth. The mark of 13 €/t represents the current average price of CO_2 EU emission allowances. [16] showed, that worldwide all measures that can reduce CO_2 emissions for costs below 40 €/t should be taken in order to reach the 450 ppm goal for CO_2 concentration in the atmosphere. The calculated costs can be compared very easily with other measures shown in Fig. 9.

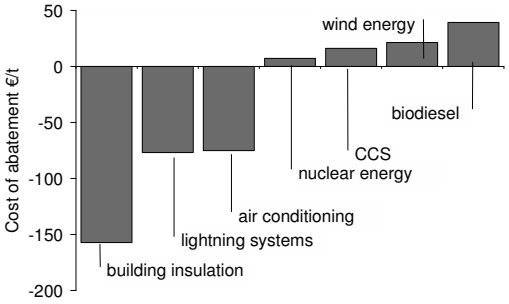

Fig. 9. Cost of CO_2 reduction overview [17]

6. Conclusion

This paper showed design calculations in order to find the suitable power range for ORC units for heat sources with dynamic behavior e.g. the ICE of utility vehicles. It could be shown that even with a very simple arrangement of extracting the heat on the end of the exhaust pipe as planned for a demonstration experimental setup a fuel saving of 5.6 % can be achieved. Even with this rather moderate improvement of efficiency the technology can be attractive for end users and offers high cost effectiveness for CO_2 reduction compared to other technologies. Further improvements can be achieved by integrating the ORC module better into the vehicle and engine system.

References

[1] Erhart, T., 2009, MWe Bbiomass ORC-CHP Power Plant-Setup and Evaluation Scharnhauser Park, , *Proc.*

Restwarmterecuperatie via een Organische Rankine Cyclus, Kortrijk, Belgium.

[2] Schuster A., Karellas S., and Karl J., 2006, Innovative applications of Organic Rankine Cycle. *Proc. ECOS*, Aghia Pelagia, Crete, Greece.

[3] Regner, G., et. al., 2006, A Quantum Leap for Heavy-Duty Truck Engine Efficiency, *Proc. 12th Diesel Engine Efficiency and Emissions Research Conference*, Detroit, Michigan, USA

[4] Invernizzi, C., et al., 2007, Bottoming Micro-Rankine Cycles for Mirco-Gas turbines, Applied Thermal Engineering, 27(1), pp. 100-110.

[5] Kane, M., et al., 2007, Scroll Expander Organic Rankine Cycle Efficiency Boost for Biogas Engines, *Proc. 20th Ecos,* Padova, Italy.

[6] Quoilin, S., Lemort, V., et al., 2010, Experimental Study and Modeling of an Organic Rankine Cycle Using Scroll Expander, Applied Energy, 87(4), pp. 1260-1268.

[7] Berger, J., 2009, Umsetzung und Erprobung eines thermischen Rekuperationssystems mittels Rankine Cycles in einem Schienenfahrzeug, *Proc. 1. Fachtagung Thermische Rekuperation im Kraftfahrzeug*, München, Germany

[8] Mollenhauer, K., Tschöke, H., 2007, Handbuch Dieselmotoren, 3rd ed., Springer-Verlag, Berlin Heidelberg.

[9] Hausberger, S., and Rexeis, M., 2009, Test Bench Measurement of Exhaust Gas Parameters for Heavy Duty Vehicle Diesel engines - Transient and Stationary Data for Different Driving Cycles, TU Graz, Institut für Verbrennungskraftmaschinen und Thermodynamik.

[10] Schuster, A., et al., 2010, Efficiency Optimization Potential in Supercritical Organic Rankine Cycles, Energy, 35(2), pp. 1033-1039.

[11] Refprop, Reference Fluid Thermodynamic and Transport Properties, 2007, Software Database 23, Version 8.0, NIST National Institute for Standards and Technology, Gaitherssburg, Maryland, USA.

[12] Deutsche Bundesbank, 2010, Interest Rate Statistics February 2010, http://www.bundesbank.de/download/statistik/S11BATSUHDE.PDF

[13] Aral, 2010, Net fuel prices, date of access 26.02.2010 http://www.aral.de/toolserver/retaileurope/netSellingPrice.do?categoryId=9013422&contentId=7026382

[14] Institut für Energie- und Umweltforschung, 2002, Vergleichende Analyse von Energieverbrauch und CO -Emissionen im Straßengüterverkehr und Kombinierten Verkehr Straße/Schiene, Heidelberg

[15] VDI, 2000, VDI Richtlinie 2067, Economic Efficiency of Building Installations – Fundamentals and Economic Calculation, Beuth Verlag, Berlin.

[16] Stern, N., 2009, Der Global Deal, C.H. Beck, Munich.

[17] Enkvist, P. A., et al., 2007, A Cost Curve for Greenhouse Gas Reduction, The McKinsey Quarterly.

Acknowledgments: This work and the corresponding project ORCAN for setup of a mobile ORC demonstration unit was funded by the Federal Ministry of Economics and Technology of Germany in order to enhance transfer of scientific results into spin off companies.

Nomenclature

$\dot{Q}$	heat load, kW
P	power, kW
E	energy, kJ
T	temperature, °C
$\dot{m}$	mass flow, g/s

Subscripts

mech	mechanical
HEX	heat exchanger
ORC	Organic Rankine Cycle
th	thermal
EG	exhaust gas
ICE	internal combustion engine
FS	fuel saving
ppm	parts per million

Greek letters

η	efficiency

Exergy Cost Analysis of a Multifunctional Heat Pump System Based on the Structural Theory of Thermoeconomics

Jean-Pierre Bédécarrats[a], Tarik Kousksou[a], Jean Castaing-Lasvignottes[a], Stéphane Gibout[a], Michèle Mondot[b]

[a] *Laboratoire de Thermique, Énergétique et Procédés, Université de Pau et des Pays de l'Adour, Rue Jules Ferry, BP 7511, 64075 Pau Cedex, France.*
[b] *Centre Technique des Industries Aérauliques et Thermiques (CETIAT), BP 52042, 69603 Villeurbanne Cedex, France*

Abstract: In this paper, an exergy cost analysis method based on the structural theory of thermoeconomics is applied to a multifunctional heat pump system, which offers the basic functions of domestic hot water DHW and hydronic heating, together with ventilation. The thermoeconomic model for the system based on the fuel–product concept is defined to quantify the productive interaction between various components. The distribution of the resources and costs of all flows in the productive structure are calculated by solving a set of equations according to an energetic model validated by experimental data. By adopting the exergy cost analysis method, the production performance of components at operating conditions of combined heating and ventilation are evaluated in detail.

Keywords: Multifunctional heat pump, Structural theory of thermoeconomics, Exergy cost, heating, ventilation.

1. Introduction

The successive energy crises have stimulated the study of more efficient ways for the comprehensive utilization of the available energy in buildings. So, low-energy solutions for house heating and domestic hot water (DHW) generation are more and more investigated. New compact devices offering the following functions: ventilation, domestic hot water production and hydronic heating are growing up [1].

These systems, so-called multifunctional heat pumps, are specially designed and suited for energy-efficient houses. The ventilation device, including a heat recovery heat exchanger and a heat pump, draws energy from the extract air and feeds it back into the heating circuit. The recovered thermal energy is then also used to heat hot water. Moreover the system can be combined with solar energy for DHW production.

The performance analysis of these systems is extremely important to adjust the energy structure and to improve the energy utilization efficiency. Research has been made on these systems [2]. Most investigations are based on energy analysis. However, this method, although useful, has been proved not to be sufficient. For example, what is the exact cost of the quality of the different energy outputs and how is energy degraded in these systems? Which parts of the degradation are most important, and how can design and operation be improved to reduce resource consumption? Thermoeconomics or exergoeconomics, which combine the second law of thermodynamics with economics by applying the concept of cost to exergy, can provide answers to achieve a better production management with a more cost-effective operation.

Exergy is the most adequate thermodynamic property to associate with cost since it accounts for energy quality. Among the main and more general thermoeconomic methodologies, we can cite the specific exergy costing method [3], the thermoeconomic functional method [4] and the structural theory [5].

This latter provides a general mathematical formulation using a linear model, includes all the thermoeconomic methodologies developed up to now, and is considered as standard formalism of thermoeconomics [6, 7].

The structural theory of thermoeconomics uses the productive structure, which attributes well-defined functional relationship for each exergy flow

Corresponding Author: Jean-Pierre Bédécarrats, Email : jean-pierre.bedecarrats@univ-pau.fr

entering or leaving the subsystems in terms of fuel and product.

Several authors have applied the structural theory of thermoeconomics to performance analysis of complex energy systems: combined cycle power plants [6], conventional coal fired power plants [8], multi-stage flash desalination plants [9] and microcogeneration [10].

In order to evaluate the performance of a multifunctional heat pump which is mainly composed of a heat pump using air (ventilation) and water (heating), the exergy cost analysis method based on the structural theory of thermoeconomics is presented in this paper. The thermoeconomic models of the units of the system are defined properly; the interactive relationships among components of the system and the causality chains processes of product formation have been quantified. After solving the characteristic equations, the unit exergy costs of all components are obtained. The production performance of each component at a specific condition is analyzed in detail.

2. The multifunctional heat pump system

The system has balanced mechanical ventilation with heat recovery unit and exhaust air heat pump. The heat pump works alternately on a floor heating emission system and a DHW storage. The schematic diagram of the studied installation is represented in Fig. 1. During winter, the heating of the dwelling is ensured by a heating floor supplied with a hot water loop drawing its heat from the condenser of the heat pump. The new air introduced into the dwelling is heated thanks on the one hand to the subcooler exchanger (also called preheater) of the heat pump and on the other hand to a cross-counter flow heat exchanger laid out on the return air. The return air is then mixed with the surrounding air to supply the evaporator of the heat pump.

Moreover, an electrical back-up heater is installed to cover peak loads. The return of the heating floor has an additional exchanger for a possible contribution of solar origin.

The refrigerant used in the heat pump is R407C. Only operation in winter is considered in this study.

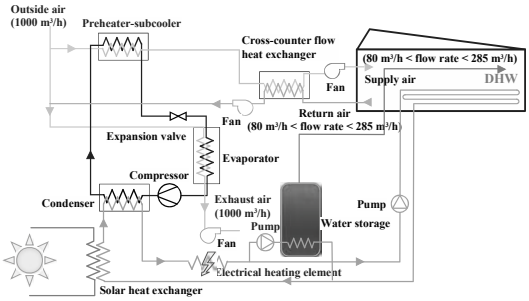

Fig. 1. Schematic diagram of the studied multifunctional heat pump system. (winter operation).

A previous work consisting in making a physical model considering energetic balance was made. This model was validated by experimental data [11].

In order to perform the thermoeconomic analysis of the system, the exergy *Ex* of the flows must be calculated. The determination of *Ex* requires the specific enthalpy *h* and the specific entropy *s* to be known:

$$Ex = \dot{m}\left(h - T_0 s\right) \quad (1)$$

with T_0 the reference temperature and $\dot{m}$ the mass flow rate.

h and *s* can be evaluated thanks to the results obtained by the energetic model.

The determination of *Ex* is based on the following assumptions:

- For simplicity, only steady-state process is considered.
- The pressure and temperature of the reference environment are P_0 = 0.1013 MPa and T_0 = the ambient temperature corresponding to the outdoor temperature.
- The gain and loss of heat, pressure and exergy in the pipe connections have been neglected.
- Only the thermal component of exergy is considered.

3. Thermoeconomic modelling based on the structural theory

When applying a thermoeconomic analysis, it is necessary to define a thermoeconomic model for the studied system, which is the mathematical representation of the productive structure. The general analysis procedure based on the structural theory of thermoeconomics formalism is: (1) building a physical structure of the system, (2)

selecting the fuel–product definition for each subsystem, (3) transforming the physical structure into a productive structure, and finally (4) constructing the thermoeconomic model.

3.1. Physical structure

The physical structure is obtained by aggregating several units into one subsystem or disaggregating one unit into several individual components. The finally chosen adequate aggregation level should take into account that the thermoeconomic analysis will start from real measured or simulated data, such as temperatures, pressures, mass flow rates and compositions of all mass flows together with the heat and power rates of the energy flows in the real system.

In our case, these data are obtained from the physical energy model.

The solar heat exchanger (in option) is not taken into account. Auxiliary electrical heating element and production of DHW are not considered for the thermoeconomic study. Fig. 2 shows the physical structure of the studied system.

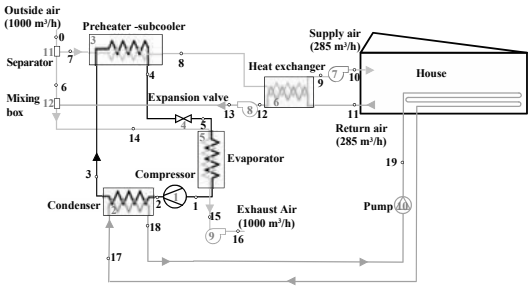

Fig. 2. Physical structure of the studied system.

3.2. Fuel–product definition

A productive purpose can be defined for each component in an overall production process [10]. The productive purpose of a component measured in terms of exergy is called product. To create this product, another exergy flow(s) is consumed, and it is called fuel(s) of that component. The fuel–product definitions for each component of the multifunctionals heat pump system depicted in Fig. 2 are shown in Table 1.

Table 1. Fuels and products for the multifunctional heat pump.

N°	Component	Function	Fuel (W)	Product (W)
1	Compressor	Compress the refrigerant	Mechanical power of the compressor $F_1 = \dot{W}_{cp}$	Exergy variation supplied to the refrigerant $P_1 = Ex_2 - Ex_1$
2	Condenser	Heat the water loop	Exergy variation supplied at the refrigerant $F_2 = Ex_2 - Ex_3$	Exergy variation supplied to the water $P_2 = Ex_{18} - Ex_{17}$
3	Preheater	Avoid air icing	Exergy variation supplied to the refrigerant $F_3 = Ex_3 - Ex_4$	Exergy variation supplied to the air $P_3 = Ex_8 - Ex_7$
4	Expansion valve	Expand the refrigerant	Inlet Exergy flux $F_4 = Ex_4$	Outlet exergy flux $P_4 = Ex_5$
5	Evaporator	Vaporize the refrigerant	Air Exergy variation + Inlet refrigerant exergy. $F_5 = Ex_{14} - Ex_{15} + Ex_5$	Outlet refrigerant exergy flux $P_5 = Ex_1$
6	Heat exchanger	Heat supply air	Return air exergy variation $F_6 = Ex_{11} - Ex_{12}$	Return air exergy variation $P_6 = Ex_9 - Ex_8$
7	Supply air fan	Air ventilation	Electric power $F_7 = \dot{W}_7$	Air exergy variation $P_7 = Ex_{10} - Ex_9$
8	Return air fan	Air ventilation	Electric power $F_8 = \dot{W}_8$	Air exergy variation $P_8 = Ex_{13} - Ex_{12}$
9	Exhaust air fan	Air ventilation	Electric power $F_9 = \dot{W}_9$	Air exergy variation $P_9 = Ex_{16} - Ex_{15}$
10	Pump	Water circulation for heating floor	Electric power $F_{10} = \dot{W}_{10}$	Water exergy variation $P_{10} = Ex_{19} - Ex_{18}$
11	Separator		$F_{11} = Ex_0$	$P_{11} = Ex_6 + Ex_7$
12	Mixing box		$F_{12} = Ex_6 + Ex_{13}$	$P_{12} = Ex_{14}$
Total			$\mathbf{Ex_0 + \dot{W}_{cp} + \dot{W}_7 + \dot{W}_8 + \dot{W}_9 + \dot{W}_{10}}$	$\mathbf{Ex_{10} - Ex_{11} + Ex_{19} - Ex_{17} + Ex_{16}}$

3.3. Productive structure

Using the fuel–product definition presented above to describe the analyzed system, the physical structure of the system is converted into a productive structure, as presented in Fig. 3. The productive structure is a graphical representation of resource distribution throughout the system. Various productive structures can be defined depending on the fuel and product definitions as well as decisions on how the resources are distributed among the components. The inlet arrows going into squares are the fuels of the corresponding components, and the outlet arrows represent the products. Each component has one output product and one or more input fuels. The capital cost of the units is also considered as an external resource and is presented as inlet flows

coming directly from the environment. Two types of fictitious devices appear in the productive structure: junctions (represented by rhombs), where the products of two or more components are joined to form the fuel of another component, and branching points (represented by circles), where an exergy flow is distributed between two or more components. In all of the junctions and branching points, there is no irreversibility, and the exergy resources of the inlet and outlet flows are subject to conservation.

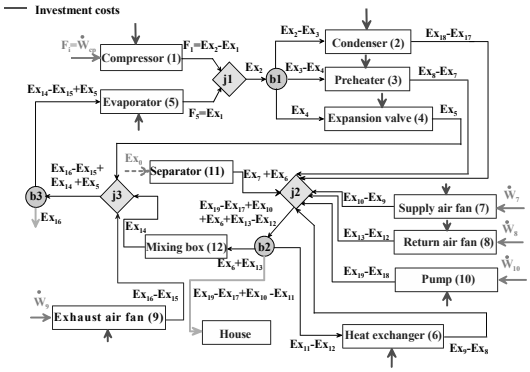

Fig. 3. Productive structure of the installation.

The fuels and products of junctions and branching points are presented in Table 2.

Table 2. Fuels and products for the multifunctional heat pump.

N°	Component	Fuel (W)	Product (W)
j1	Junction 1	$F_{j1} = P_1 + P_5$ With $P_1 = Ex_2 - Ex_1$ $P_5 = Ex_1$	$P_{j1} = Ex_2$
b1	Branching point 1	$F_{b1} = P_{j1} = Ex_2$	$P_{b1} = F_2 + F_3 + F_4$ with $F_2 = Ex_2 - Ex_3$ $F_3 = Ex_3 - Ex_4$ $F_4 = Ex_4$
j2	Junction 2	$F_{j2} = P_2 + P_3 + P_6 + P_{11} + P_{10} + P_8 + P_7$ with $P_2 = Ex_{18} - Ex_{17}$ $P_3 = Ex_8 - Ex_7$ $P_6 = Ex_9 - Ex_8$ $P_{11} = Ex_7 + Ex_6$ $P_{10} = Ex_{19} - Ex_{18}$ $P_8 = Ex_{13} - Ex_{12}$ $P_7 = Ex_{10} - Ex_9$	$P_{j2} = Ex_{19} - Ex_{17} + Ex_{10} + Ex_6 + Ex_{13} - Ex_{12}$
b2	Branching point 2	$F_{b2} = P_{j2} = Ex_{19} - Ex_{17} + Ex_{10} + Ex_6 + Ex_{13} - Ex_{12}$	$P_{b2} = F_{House} + F_6 + F_{12}$ with $\mathbf{F_{House} = Ex_{19} - Ex_{17} + Ex_{10} - Ex_{11}}$ $F_6 = Ex_{11} - Ex_{12}$ $F_{12} = Ex_6 + Ex_{13}$
j3	Junction 3	$F_{j3} = P_{12} + P_9 + P_4$ $P_{12} = Ex_{14}$ $P_9 = Ex_{16} - Ex_{15}$ $P_4 = Ex_5$	$P_{j3} = Ex_{16} - Ex_{15} + Ex_{14} + Ex_5$
b3	Branching point 3	$F_{b3} = P_{j3} = Ex_{16} - Ex_{15} + Ex_{14} + Ex_5$	$P_{b3} = F_5 + F_{residue}$ $F_5 = Ex_{14} - Ex_{15} + Ex_5$ $F_{residue} = Ex_{16}$

Note that the productive structure provides the resources distribution, among the different components when converting them into final products.

The exergetic product F_{House}, which corresponds to the exergetic fuel of the dwelling, is the total product. It is the cost of this final product which must be analysed.

3.4. Characteristic equations

The characteristic equations for the productive structure (Fig. 3) are presented in Tables 3 and 4. These equations express each inlet flow as a function of the outlet flows and a set of internal parameters. There are three types of characteristic equations in thermoeconomics:

- those connecting each fuel of physical component to its product ($F_i = k_i P_i$) with k_i the unit exergetic consumption or technical production coefficient. k_i is a measure of the thermodynamic efficiency of the process and equals one for reversible processes and is greater than one for all real processes because of the destroyed exergy due to irreversibility.
- Structural equations which describe the productive model of junctions and branches. The former adopts exergy ratio (r_i) to describe the portion of the ith flow of fuel in the product of the jth junction ($F_i = r_i P_j$). The latter one shows how the fuel of a branch is distributed through the other components ($F_i = \Sigma P_i$).
- Costing equations which relate the investment cost of the component with thermodynamics variables and its product.

After solving the characteristic equations in Tables 3 and 4, the unit exergy consumption *k* and the junction exergy ratio *r* can be calculated.

Table 3. Characteristic equations of the different components i of the installation.

N°	Component	Unit exergy consumption	Characteristic equations	k* = unit exergetic cost
i		$k_i = F_i / P_i$	$F_i = k_i P_i$	$k^*_{P_i} = k_i k^*_{R_i} + \frac{\dot{Z}_i}{P_i}$

Table 4. Equations characteristic of the junctions and the branching points of the installation.

N°	Component	Coefficients	Charactéristic equations	k* = unit exergetic cost
j1	Junction 1	$r_1 = P_1/P_{j1}$ $r_5 = P_5/P_{j1}$	$P_1 = r_1 P_{j1} = r_1 (F_2 + F_3 + F_4)$ $P_5 = r_5 P_{j1} = r_5 (F_2 + F_3 + F_4)$	$k^*_{j1} = r_1 k^*_{P_1} + r_5 k^*_{P_5}$
b1	Branching point 1		$P_{j1} = F_2 + F_3 + F_4$	$k^*_{R_2} = k^*_{R_3} = k^*_{R_4}$
j2	junction 2	$r_2 = P_2/P_{j2}$ $r_3 = P_3/P_{j2}$ $r_6 = P_6/P_{j2}$ $r_{11} = P_{11}/P_{j2}$ $r_{10} = P_{10}/P_{j2}$ $r_8 = P_8/P_{j2}$ $r_7 = P_7/P_{j2}$	$P_2 = r_2 P_{j2} = r_2 (F_{House} + F_6 + F_{12})$ $P_3 = r_3 P_{j2} = r_3 (F_{House} + F_6 + F_{12})$ $P_6 = r_6 P_{j2} = r_6 (F_{House} + F_6 + F_{12})$ $P_{11} = r_{11} P_{j2} = r_{11} (F_{House} + F_6 + F_{12})$ $P_{10} = r_{10} P_{j2} = r_{10} (F_{House} + F_6 + F_{12})$ $P_8 = r_8 P_{j2} = r_8 (F_{House} + F_6 + F_{12})$ $P_7 = r_7 P_{j2} = r_7 (F_{House} + F_6 + F_{12})$	$k^*_{j2} = r_2 k^*_{P_2} + r_3 k^*_{P_3} + r_6 k^*_{P_6} + r_{11} k^*_{P_{11}} + r_{10} k^*_{P_{10}} + r_8 k^*_{P_8} + r_7 k^*_{P_7}$
b2	Branching point 2		$P_{j2} = F_{House} + F_6 + F_{12}$	$k^*_{R_{local}} = k^*_{R_6} = k^*_{R_{12}}$
j3	Junction 3	$r_{12} = P_{12}/P_{j3}$ $r_9 = P_9/P_{j3}$ $r_4 = P_4/P_{j3}$	$P_{12} = r_{12} P_{j3} = r_{12} (F_5 + F_{residue})$ $P_9 = r_9 P_{j3} = r_9 (F_5 + F_{residue})$ $P_4 = r_4 P_{j3} = r_4 (F_5 + F_{residue})$	$k^*_{j3} = r_{12} k^*_{P_{12}} + r_9 k^*_{P_9} + r_4 k^*_{P_4}$
b3	Branching point 3		$P_{j3} = F_5 + F_{residue}$	$k^*_{R_5} = k^*_{R_{résidu}}$

4.Exergy cost analysis

The unit exergy cost k^* indicates the additional resources exergy required to obtain one unit of product exergy [12, 13]. It is defined for the component i as:

$$k^*_{P_i} = k_i k^*_{F_i} + \frac{\dot{Z}_i}{P_i} \qquad (2)$$

$\dot{Z}$ is the capital cost which relates the investment of the component in monetary units per second.

Once the thermoeconomic model has been defined and the characteristic equations corresponding to the productive structure of the system are solved, the costs of all flows in the productive structure can be calculated.

These unit exergy cost k^* do not only represent the operation costs. They include the investment cost of each component.

For the junctions, the cost is proportional to the cost of the fuels via the coefficient r_i. For the branching points, the cost of each product is the same one and is equal to the cost of the fuel. All these equations are deferred in Table 4.

The cost of the exergetic fuel corresponding to an electric work (or power) is directly the cost of electricity.

The capital cost $\dot{Z}$ represents the monetary units per second. The capital cost of each component is expressed as a function of operating parameters and constants derived by regression analysis of market. The cost Z (€) of each component is established by considering the following relations:

- For the compressor:
  $Z_1 = \frac{A_1 \dot{m}_r}{B_1 - \eta_{isentropic}} \left(\frac{HP}{LP}\right) ln\left(\frac{HP}{LP}\right)$ where HP is the high pressure, LP the low pressure, $\eta_{isentropic}$ the isentropic efficiency and $\dot{m}_r$ the refrigerant mass flow rate in kg s^{-1}. $A_1 = 1760$ and $B_1 = 0.9$.
- For the air fans: $Z_{fan} = \left[A_V + B_V \left(Power\right)^{0.5}\right]^2$ with A_v = 10.7822 and B_v = 10.0777 where $Power$ is the fan power input in kW
- For the pump: $Z_{pump} = A_p + B_p \left(\dot{m}_{water}\right)^{0.5}$ with A_p = 16.9049 and B_p = 566.444 where $\dot{m}_{water}$ is the water mass flow rate in kg s^{-1}.
- For the heat exchangers:
  $Z_{exchanger} = A_e \left(Power\right)^{B_e}$ where $Power$ is the amount of heat exchanged in kW and A_e = 356.78, B_e = 0.4557.

The cost of the expansion valve is considered constant with a price of about 150 €. The cost of the preheater is constant and equal to 160 €.

To have the capital cost $\dot{Z}$ (€/s):

$$\dot{Z} = \tau\, Z \qquad \text{with} \qquad \tau = \frac{i(1+i)^N}{(1+i)^N - 1}\left(\frac{1}{t_{op}}\right) \qquad (3)$$

τ is the amortization factor which takes into account the economic life period of the installation. i is the interest rate per year taken equal to 8%, N is the number of annuities received taken for each component equal to 10 years and t_{op} is the time per year of operation expressed in seconds taken equal to 2800 hours per year (corresponding to the duration of the heating season).

5. Results and discussion

The knowledge of the cost of the fuels coming from outside is sufficient to obtain the results.

The external resources correspond to the electric power of the different components. Calculations are made with a cost of electricity equal to 0.1106 Euros/kWh corresponding to the on-peak hours tariff in France.

The cost of the air at the inlet of the installation is free because it is at ambient temperature (exergy reference).

The results are only presented for one standard operation (drawn from the specifications):

- Winter operation when the outdoor air is at a dry bulb temperature T_d = - 7 °C and a wet bulb temperature T_w = - 8 °C.
- The temperature of the house is equal to 20 °C for a load of 3375 W.
- The parameters of operation are as follows: effectiveness of the preheater = 30%, effectiveness of the heat exchanger = 80%, efficiency of the air fans = 80%, efficiency of the pump = 15%, swept volume of the compressor = 7.5 $m^3 h^{-1}$.

The pressure and temperature of the reference environment are P_0 = 0.1013 MPa and T_0 = -7 °C the outdoor air temperature.

The capital cost is calculated with the obtained values of the energetic model (Table 6).

Table 6: Data for the standard winter operation (values of the energetic model)

R407C
Mass flow rate: 0.0235 kg s^{-1}
Evaporation pressure: 3.1 bar
Condensation pressure: 13.3 bar
Compressor inlet or evaporator outlet temperature: T_1 = -12.2 °C
Compressor outlet or condenser inlet temperature: T_2 = -34.6 °C
Condenser outlet or preheater inlet temperature: T_3 = 30.0 °C
Preheater outlet or expansion valve inlet temperature: T_4 = 16.3 °C
Expansion valve outlet or evaporator inlet temperature: T_5 -17.2 °C

Air
Pressure: 1 bar
Outside air flow rate: 1000 $m^3 h^{-1}$
Outside air dry bulb temperature: $T_{d0} = T_0$ = - 7 °C
Outside air wet bulb temperature: T_{w0} = - 8 °C
Supply and return air flow rate: 285 $m^3 h^{-1}$
Preheater inlet temperature: T_7 = -7 °C
Preheater outlet or heat exchanger inlet air temperature: T_8 = 4.1 °C
Heat exchanger outlet or supply air fan inlet temperature: T_9 = 16.8 °C
Supply air fan outlet temperature: T_{10} = 19.4 °C
Return air or heat exchanger inlet temperature: T_{11} = 20 °C
Heat exchanger outlet or return air fan inlet temperature: T_{12} = 4.7°C
Return air fan outlet temperature: T_{13} = 7.3 °C
Evaporator inlet temperature: T_{14} =-5.2 °C
Evaporator outlet air temperature: T_{15} =-13.4 °C
Exhaut air temperature: T_{16} = -12.7 °C

Water
Mass flow rate: 0.26 kg s^{-1}.
Condenser inlet temperature: T_{17} = 21.8 °C
Condenser outlet temperature: T_{18} = 25.0 °C
Inlet temperature of the flow heating emission system: T_{19} = 25 °C

Under these conditions, the exchanged powers for the heat pump are as follows:

Table 5: Operation parameters of the heat pump for an operation winter.(T_d = - 7 °C and T_w = - 8 °C)

Components	Power (W)
Compressor	1038
Condenser	3528
Preheater/subcooler	505.7
Evaporator	2996

The heat pump COP is equal to 3.4.

Table 7 gives the percentage of destroyed exergy as well as the coefficient of production for each component:

Table 7: Percentage of destroyed exergy and coefficient of production for each component

Component	Destroyed exergy (%)	Production coefficient k_i
Compressor	25.64	1.48
Condenser	6.27	1.23
Preheater/subcooler	2.62	4.36
Expansion valve	5.38	1.09
Evaporator	8.74	1.17
Heat exchanger	0.88	1.32
Supply air fan	10.48	14.50
Return air fan	10.84	26.90
Exhaust air fan	23.25	53.73
Pump	4.79	62.03
Mixing box (unit 12)	1.12	7.91

Considering the percentage of destruction of exergy represented in the form of sectors on Fig. 4, one realises that the components which create the most irreversibilities are initially the compressor (25.64%), followed closely by the exhaust air fan (23.25%). Then the return air fan and the supply air fan with a destruction of about a 10% come. One finds then the evaporator, the condenser, the expansion valve, the pump, the heater, the mixing box and finally the heat exchanger. The last two elements have a very small percentage of destroyed exergy.

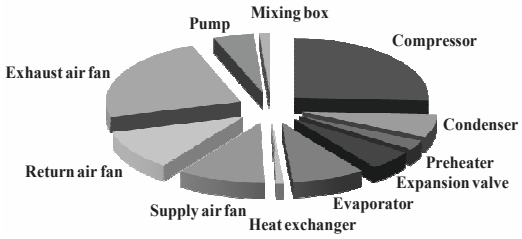

Fig. 4 Distribution of the destruction of exergy (values in Table 7)

It is important to notice that the closer the coefficient *k* is to 1, the more the product is close to the fuel and the component more efficient from an exergetic point of view.

Considering the coefficient of production *k*, one sees that in fact primarily the air fans and the pump produce little from the exergetic point of view compared to the fuel (high value of *k*).

It is possible to improve operation of the installation by minimising the irreversibilities what will result in an improvement of the coefficient *k*.

For each component, the fuel and the product costs are deferred in Table 8. The costs of the product without and with investment were separated in order to see the influence of the latter on the cost.

Flow streams further down the productive process are more costly. All processes in the system are irreversible and the total exergy destruction continuously increases throughout the productive process, and thus, the final products have the highest exergy cost.

Table 8: Monetary exergetic costs for each component

Component	Fuel cost (€/kWh)	Product cost (€/kWh)	Product cost (with investment) (€/kWh)
Compressor	0.1106	0.1638	0.2281
Condenser	0.4954	0.6083	0.7016
Preheater	0.4954	2.16	3.518
Expansion valve	0.4954	0.5381	0.5479
Evaporator	0.6204	0.7255	0.7717
Heat exchanger	**1.000**	1.325	1.564
Supply air fan	0.1106	1.604	2.725
Return air fan	0.1106	2.975	5.054
Exhaust air fan	0.1106	5.943	8.476
Pump	0.1106	6.861	22.63
Mixing box	**1.000**	7.917	7.917
ce=0.1106 {Euros/kWh on-peak hours}			

The final product of interests corresponds to the heating of the room, its cost is also equal to that of the fuel of the heat exchanger and to that of the mixing box (see diagram of productive structure fig. 3). Its value is here **1.00 €/kWh.**

The costs of the different components were compared by plotting them on Fig. 5.

The cost of the product of the compressor is smallest although it functions in a very irreversible way (25.64% of the total exergy destruction). This is due to a good coefficient of production. The cost of the product of the pump is primarily highest because of a very bad coefficient of production but also of a high cost of this component compared to the produced flow of exergy. If the whole of the costs is looked at, it is seen that the passage of flow in a component naturally increases the cost proportionally with the coefficient k. By adding the investment, this cost can increase considerably especially if product exergetic flow is weak. It is the case for example of the air fans.

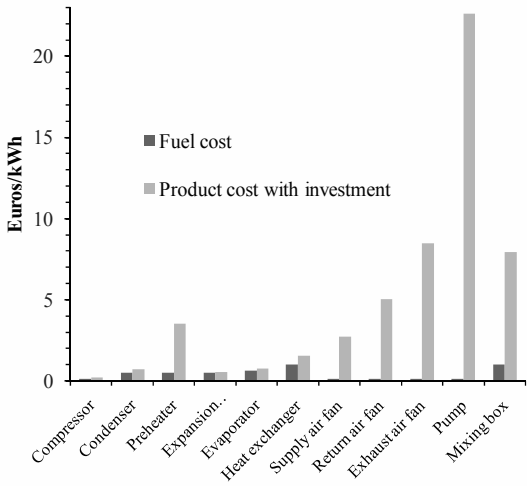

Fig. 5 Costs of the fuel and the product for each component (standard operation)- Values in Table 8.

It is rather difficult to find why the cost of the exergetic product of a component is high or not because of the various links between each component. Several parameters are influent like the cost of the fuel, the coefficient of production or the capital cost compared to the product. These results show that the model is essential to optimize the system. This is the perspective of this study.

6. Conclusions

The presented study analyses the performance of a multifunctional heat pump system using a complete modelling based on thermodynamics (energy and exergetic balances) coupled with economic considerations. Because of the complexity of the architecture of the chosen system, there is a strong interdependence of the various components whose weight is given during calculations.

The sources of destruction of exergy in the process are mainly the compressor and the exhaust air fan. But the determination of the coefficient of production *k* shows that primarily the air fans and

the pump produce little from the exergetic point of view compared to the fuel.

The cost of the products of the installation was calculated providing the tools necessary for the total analysis of this complex system.

The influence of the various parameters (effectiveness of the exchangers, outputs of the pump and the air fans, isentropic output of the compressor…) on the total result (cost of the final product) will be studied in a next paper.

Nomenclature

COP	Coefficient of Performance
LP	Low Pressure
Ex	Exergy flow rate, W
i	interest rate
k	unit exergy consumption
k^*	unit exergy cost, €/kJ
h	specific enthalpy, J/kg
HP	High Pressure
$\dot{m}$	mass flow rate, kg/s
N	duration of refunding in year
P	Product exergy, W, or Pressure, Pa
F	Fuel exergy, W
r	Exergy rate
s	specific entropy, J $kg^{-1}K^{-1}$
t_{op}	time of operation per year, s
T	Temperature, K
$\dot{W}$	Mechanical or electrical power, W
Z	Capital cost, €
$\dot{Z}$	Capital cost, €/s

Greek symbols

τ	amortization factor, s^{-1}

References

[1] Wemhoener, C., Afjei, T., Dott, R., 2008, IEA HPP Annex 28 – standardised testing and seasonal performance calculation for multifunctional heat pump systems, Applied Thermal Engineering, 28, pp. 2062-2069

[2] Hepbasli, A., Kalinci, Y., 2009, A review of heat pump water heating systems, Renewable and Sustainable Energy Reviews, 13, pp. 1211-1229.

[3] Tsatsaronis, G., Pisa, J., 1994, Exergoeconomic evaluation and optimization of energy systems, Application to the CGAM problem, Energy, 19(3), pp. 287-321.

[4] Frangopoulos, CA., 1987, Thermoeconomic functional analysis and optimization, Energy, 12(7), pp. 563-571.

[5] Lozano, M.A. et Valero, A., 1993, Thermoeconomic analysis of gas turbine cogeneration systems, *Proc. Thermodynamics and the Design, Analysis and Improvement of Energy Systems*, ASME, N. York, 311-320.

[6] Erlach, B., Serra, L. et Valero, A., 1999, Structural theory as standard for thermoeconomics, Energy Conversion & Management, 40, pp. 1627-1649.

[7] Valero A, Serra L, Uche J., 2006, Fundamentals of exergy cost accounting and thermoeconomics, Part I: theory. J Energy Resour Technol, 128, pp. 1-8.

[8] Zhang, C, Wang, Y, Zheng, C.G, Lou, X.S., 2006, Exergy cost analysis of a coal fired powerplant based on structural theory of thermoeconomics, Energy Convers Manage., 47(7–8), pp. 817-843.

[9] Uche J., Thermoeconomic analysis and simulation of a combined power and desalination plant, PhD. thesis, Department of Mechanical Engineering, University of Zaragoza, 2000.

[10] Deng, J., Wang, R., Wu, J., Han, G., Wu, D. et Li, S., 2008, Exergy cost analysis of a micro-trigeneration system based on the structural theory of thermoeconomics, Energy, 33, pp. 1417-1426.

[11] Castaing-Lasvignottes et al., 2008, Analyse thermoéconomique d'un appareil multifonctions, Technical Report, CETIAT.

[12] Torres, C., Valero, A., Serra, L. et Royo, J., 2002, Structural theory and thermoeconomic diagnosis - Part I: On malfunction and dysfunction analysis, Energy Conversion and Management, 43, pp. 1503-1518.

[13] Valero, A., Lerch, F., Serra, L. et Royo, J., 2002, Structural theory and thermoeconomic diagnosis - Part II: Application to an actual power plant, Energy Conversion and Management, 43, pp.1519-1535.

Acknowledgments: The authors wish to thank CETIAT for their financial aid and interest in this work.

Implementation of a scroll booster compressor into a single-stage air-water heat pump for peak winter day

Michele Zehnder [a], *Jürg Schiffmann* [b], *Jean-Baptiste Carré* [c], *and Daniel Favrat* [c]

[a], *CTA AG Klima Kälte Wärme, Hunzikenstrasse 2, CH-3110 Münsingen, Switzerland*
[b], *Fischer Engineering Solutions AG, Birkenweg 3, CH-3360 Herzogenbuchsee, Switzerland*
[c], *École Polytechnique Federale de Lausanne, EPFL STI IGM LENI, Station 9, CH-1015 Lausanne, Switzerland*

Abstract: This paper shows an implementation of a scroll booster compressor mounted at the suction line of a single-stage air-water heat pump. The compressor selected to be used as booster is a belt-driven scroll compressor initially dedicated to automotive refrigeration. For the tests reported here, it is driven by an electrical motor and has been modified to obtain a lower built-in volume ratio. The computations for those modifications have been made with our own software called GeoScroll. Tests of the heat pump at A-11/W65 show a large improvement of the heat output, which is doubled (raising from 7.39 kW, in the normal single-stage configuration, up to 15.7 kW) while the COP decreases by less than 10% (from 2.08 to 1.89). This performance degradation is not due to bad performances of the booster compressor, that are at the level expected, but to a decrease of the evaporation pressure (1 bar, which is equivalent to 11 K), as the evaporator has not been designed for such heating powers. Even with working conditions outside its design range, the heat pump behavior with the booster has been proved to be very stable (the experiments were performed over few weeks). Furthermore, no oil accumulation has been noticed in the booster compressor, which is favorable to an integration of the device into existing heat pumps, currently in service. Indeed, it can be easily included into existing single-stage heat pumps with few adaptations. The concept is attractive in comparison to backup with heating devices, used in case of low temperatures, with a far better exergy efficiency and with contribution to the reduction of the electric demand peak.

Keywords: booster, scroll compressor, single-stage, two-stage, heat pump, Air/Water heat pump

1. Introduction

Heat pump application and market exhibited a considerable increase over the last two decades, especially in Switzerland, in Austria, and in the Scandinavians countries. In the time period 2005–2008 the volume of the heat pump units has particularly developed in Europe from 250 000 to 580 000 units [1]. This increase corresponds to an average growth of over 30% a year. A further increase can be expected due to European Union commitments of a CO_2 reduction until 2020. The major part of this development is linked to the new house market with low heating temperatures (floor heating or large size radiators), where the economic benefits are comparatively the highest. Already during the 90s emerged new ideas to boost the heat pump technologies towards higher temperature lifts in order to substitute fossil fuel fired boilers in existing houses and satisfy the domestic hot water as well. This development coincided also with a tendency to get away from the direct electrical (Joule) heating boosters, meeting the whole demand with the electrical heat pump alone. Variable speed compressors started also to be considered. An example of this development is a two-stage heat pump prototype tested in [2]. The latter included a variable speed first stage compressor. However oil migration problems as well as the low cost of the fossil fuels during the 90s slowed down these developments. A cheaper alternative ("the two-stage cycle of the poorer") proposed to use of a single-stage scroll compressor with vapor injection port [2, 3, 4] showing a slight increase of coefficient of performance and a substantial increase of heat power. Recently full two stage units with two separate hermetic units of scroll compressors lubricated with oil have been introduced on the market [5]. In parallel and for air-water heat pumps, enhanced evaporator tubes have been proposed primarily with internal microfins. In most of the quality range however oil tends to degrade the local heat transfer coefficients

Corresponding author: Michele Zehnder, Email: michele.zehnder@cta.ch

so that new oil-free single or two-stage compressor concepts are appearing [6, 7, 8]. The latter are based on high speed direct electrically driven miniature turbo-compressors on refrigerant vapor bearings. The present paper presents the results of an intermediate two stage concepts potentially applicable to the retrofit of air-water heat pumps. It consists in adding a booster compressor to a prototype air-water heat pump to increase the heating power during the very cold days while keeping an acceptable exergy efficiency. The prototype heat pump described in [2] includes a scroll compressor with two vapor injection holes and an intermediate economizer heat exchanger (The original circuit of the commercial Air/Water domestic heat pump used as reference, the intermediate injection circuit, and the booster module, are represented Fig. 1).

2. Design of the booster module

2.1. Booster module

For the tests, the vapor injection lines of the main scroll compressor are shutoff and the vapor is deviated to the discharge line of the booster and the suction line of the main compressor. The booster compressor module is represented with blue dashes and red dots on Fig. 1. The red dotted part represents the booster compressor setup with its bypass and the junction between the two compression stages. The booster compressor is to produce a pre-compression (*pt. 1* to *pt. 2*). The blue dashed part shows the economizer circuit which is added after the condenser outlet. It is constituted by an economizer heat exchanger and an expansion device (capillary tube or thermostatic or digital expansion valve). Some subcooled liquid is removed from the main line (*pt. 8*), expanded to intermediate pressure (*pt. 6*), and heated by the main subcooled liquid line (*pt. 6* to *pt. 7*). The wet vapor resulting from those operations is then injected between the two compression stages (*pt. 3*).

The booster module results in two simple and compact elements (blue dashed and red dotted parts) which can be added to existing single-stage heat pumps requiring only few modifications of the piping system.

2.2. Selection and adaptation of the booster compressor

A booster compressor, when the study has been performed, did not exist with the needed characteristics. Consequently, a compressor had to be selected and modified. The requested compressor had (a) to require only few modifications to match the characteristics (high suction volume rate, notably), (b) to be variable-speed-compliant, (c) to offer only little space for oil retention, (d) to be adapted to refrigeration applications (i.e. be compliant with the refrigerants used in domestic heat pumps circuits), (e) to be immediately and easily available. An automotive scroll compressor used for vehicle air-conditioning purpose has been selected with the characteristics detailed in Tab. 1. Since it is an automotive compressor, it is a belt-driven compressor connected with an electromagnetic coupling to an electrical motor. Originally designed for R134a applications, it has been used with R407C in this project. Material compatibility has been assumed, but the performance is being negatively affected due to higher density of the used refrigerant blend. To be used in this installation, the motor which drives the booster compressor has to provide 1 kW of electrical power and 3 kW during the starting phases. Thus, a 4 kW motor has been selected and is used with an inverter. Its characteristics are summarized in Tab. 1. To ensure the needed maximum rotational speed of 4260 rpm, a factor 3 pulley has been mounted on the motor.

Booster compressor	
Built-in volumetric flow rate	85.7 cm^3/rotation
Displacement volume	15.3 m^3/h @ 50 Hz
Refrigerant	R134a
Contained oil	150 cm^3
Weight	3.8 kg
Electric supply[2]	12 V DC
Diameter of the pulley	100 mm
Electrical motor	
Electrical power	4 kW
Nominal voltage	380 V
Nominal current	8.9 A
Maximum rotational speed	1420 rpm
cos ϕ	0.83

Table 1: Initial characteristics of the booster compressor and the electrical motor selected for this study.

The volume ratio required by our application ranged between 1.5 and 3. Thus, the built-in volume ratio

[2]Electric supply is needed to power the electromagnetic coupling pulley.

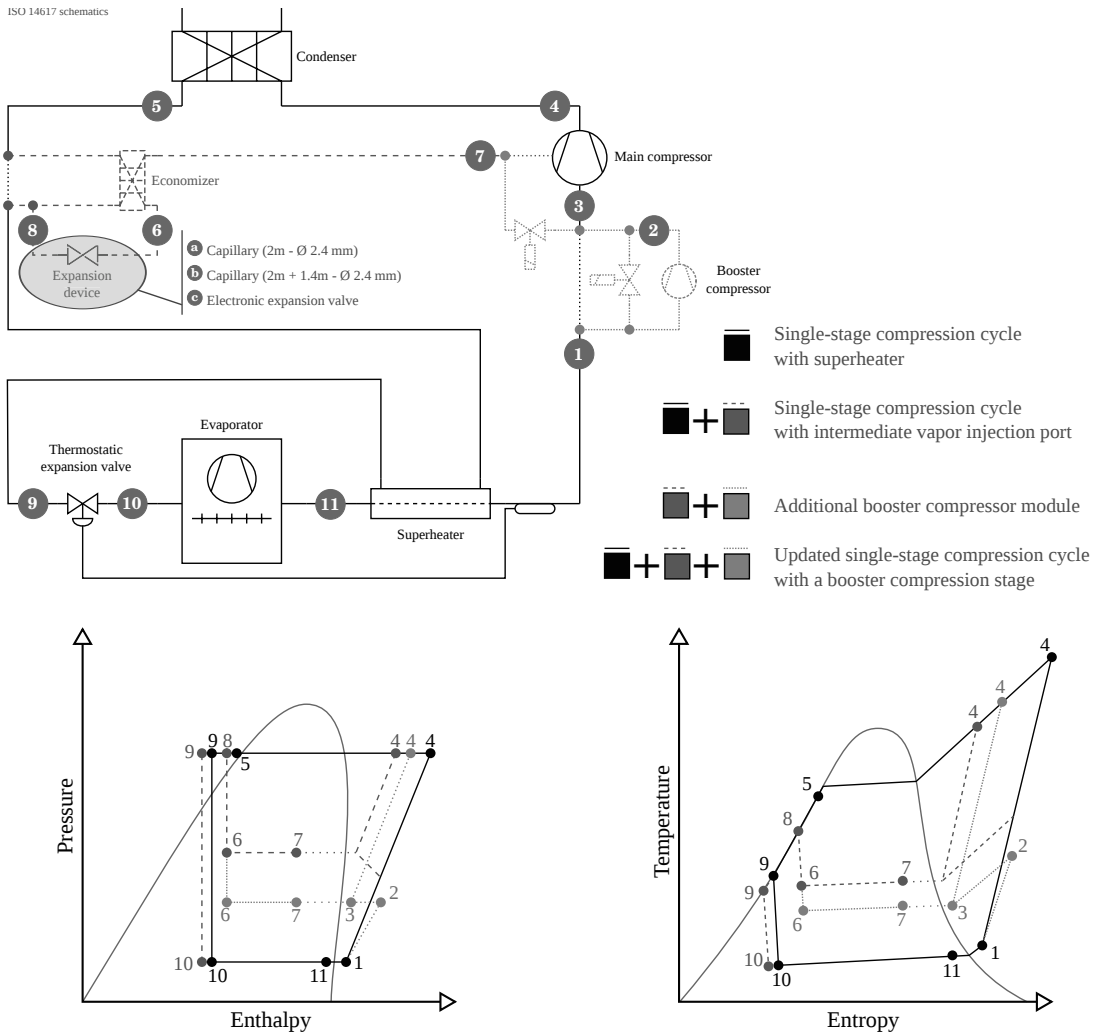

Figure 1: Principle of the updates performed on the single-stage heat-pump.

had to be modified mechanically. This was achieved by drilling holes in the fixed scroll in order to allow an earlier communication with the exhaust port and therefore reducing the effective internal volume ratio. By using a dedicated inhouse software[2], the scroll system has been modeled, based on measurements performed on the booster compressor and presented in Tab. 2. This modeling has been used to determine where to drill the two porting holes necessary to adapt the volume ratio. Those holes can be seen on Fig. 4. As the first positions computed with GeoScroll was located above the compressor discharge line check valve and was consequently not able to achieve they function, two new holes positions have had to be calculated and drilled.

Generation radius	3 mm
Thickness of the volute	4.6 mm
Height of the volute	30.5 mm
Excentricity[4]	4.82 mm

Table 2: Measured characteristics of the booster scroll system.

[2]GeoScroll is a software developed in the Industrial Energy Systems Laboratory. It is dedicated to the simulation and design of scroll compression devices.

[4]The excentricity has been computed with GeoScroll.

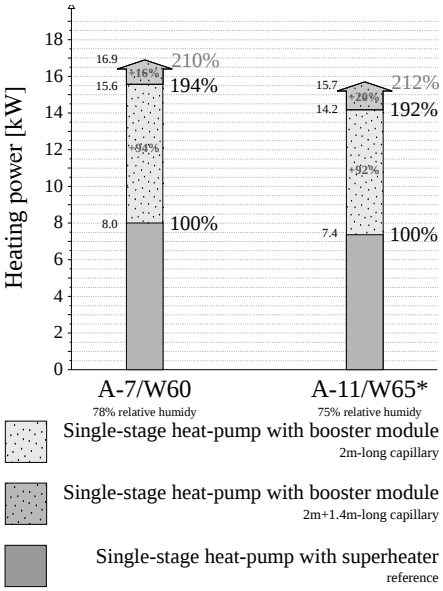

Figure 2: Increase of the heat transfer rate obtained by the addition of the booster module to the single-stage heat pump.

3. Performances indicators and measurements

The coefficient of performance is defined in Rel. (1) as the heat power transferred to the water in the condenser $\dot{Q}^-_{cd}$ over the electrical power consumed by the motor(s) of the compressor(s) and the fans and pumps $\dot{E}^+_{cons}$.

$$\eta_{I,real} = COP = \frac{\dot{Q}^-_{cd}}{\dot{E}^+_{cons}} \tag{1}$$

$$\text{with } \dot{Q}^-_{cd} = \dot{M}_{cd_w} c_{p_{cd_w}} \left(T_{cd_w,out} - T_{cd_w,in}\right) \tag{2}$$

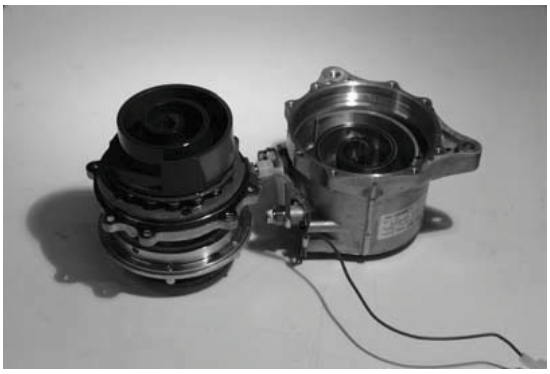

Figure 3: Global view of the domestic heat-pump booster compressor (opened).

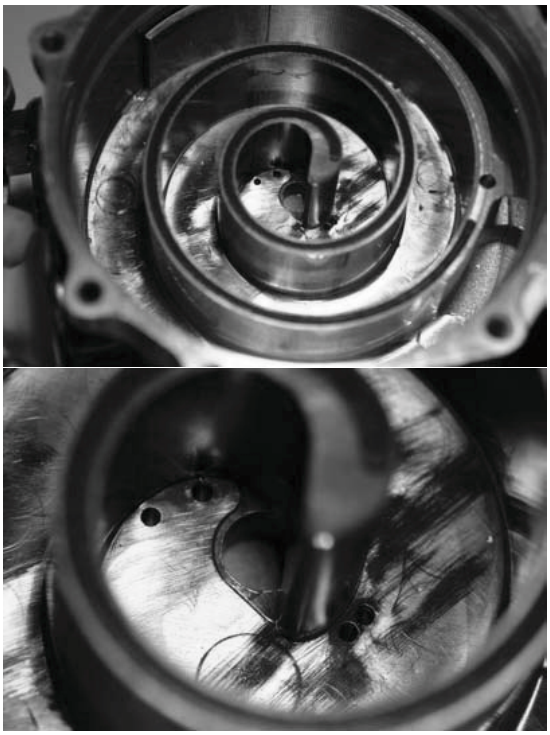

Figure 4: Views of the modified booster compressor fixed scroll.

The exergy efficiency (Rel. (3)) is calculated with a simplified relation using the ratio between the real COP and the Lorenz's COP, more convenient to use with experimental data than the usual and more rigorous definition given in [9].

$$\eta_{II,Lorenz} = \frac{\eta_{I,real}}{\eta_{I,Lorenz}} = \left(1 - \frac{T_{ev,in} + T_{ev,out}}{T_{cd,in} + T_{cd,out}}\right) \cdot \eta_{I,real} \tag{3}$$

$$\text{with } \eta_{I,Lorenz} = \frac{\dot{Q}^-_{cd}}{\dot{Q}^-_{cd} - \dot{Q}^+_{ev}} = \left(1 - \frac{\dot{Q}^-_{ev}}{\dot{Q}^+_{cd}}\right)^{-1}$$

Thermodynamic properties of refrigerant are determined through pressure and temperature measurements and computed with a homemade MatLab computation code, called Flint, which is based on Refprop [10], a real gas computational code. The pressure is measured with piezo-resistive sensors ranging between 1 and 30 bar with an uncertainty of ± 0.05 bar (1%). The temperature in the refrigerant system is measured with thermocouples type K. They range between -20°C and 150°C with an uncertainty of ± 0.1°C. Relative humidity is measured with an hygrometer which ranges between 35% to

100% of relative humidity. Its uncertainty is ± 1%. The water flow rate is measured with a Coriolis-type flow meter in liquid phase ranging from 0 to 250 l/min with an uncertainty of ± 0.2 l/min. The 3-phase electric power is measured with a power analyser ranging from 0 to 5 kW with an uncertainty of ± 0.1% and the auxiliaries electric power is measured with a power analyser ranging from 0 to 2 kW with an uncertainty of ± 0.5%. The uncertainty on the heat power is of ± 2%, and the uncertainty on the COP is of ± 2.1% (details below with Rel. (4) and Rel. (5)).

The uncertainties on the calculated heat power (calculated with water-side data) and the COP are estimated through the following expressions:

$$(2) \Rightarrow \dot{Q}^{-}_{cd} = \dot{V}_{cd_w}\rho_{cd_w}c_{p_{cd_w}}(T_{cd_w,out} - T_{cd_w,in})$$

$$\begin{aligned}\frac{\Delta\dot{Q}^{-}_{cd}}{\dot{Q}^{-}_{cd}} &= \left|\frac{\Delta\dot{V}_{cd_w}}{\dot{V}_{cd_w}}\right| + \left|\frac{\Delta\rho_{cd_w}}{\rho_{cd_w}}\right| + \overbrace{\left|\frac{\Delta c_{p_{cd_w}}}{c_{p_{cd_w}}}\right|}^{\leq 0.1\%} \\ &\quad + \left|2^{\dagger}\cdot\frac{1}{3}^{\ddagger}\cdot\frac{\Delta(T_{cd_w,out} - T_{cd_w,in})}{T_{cd_w,out} - T_{cd_w,in}}\right| \\ &= \pm(0.5\% + 0.2\% + 0 + 1.33\%) \\ &= \pm 2.0\% \end{aligned} \quad (4)$$

† 2 times the single-sided uncertainty as to be considered.

‡ There are 3 thermocouples at each measurement points on the water-side.

$\leq 0.1\%$ Uncertainties below 0.1 % are neglected.

$$(1) \rightarrow \eta_I = COP = \frac{\dot{Q}^{-}_{cd}}{\dot{E}_{cons}}$$

$$\begin{aligned}\frac{\Delta\eta_I}{\eta_I} &= \left|\frac{\Delta\dot{Q}^{-}_{cd}}{\dot{Q}^{-}_{cd}}\right| + \left|\frac{\Delta\dot{E}_{cons}}{\dot{E}_{cons}}\right| \\ &= \pm(2.0\% + 0.1\%) = \pm 2.1\% \end{aligned} \quad (5)$$

$\frac{\Delta\dot{E}_{cons}}{\dot{E}_{cons}}$ This uncertainty is equal to 0.1% as the electric power uncertainty is of 0.1 %.

4. Booster module performances

Data presented in Tab. 3 and 4 bring the following observations. By simply adding the booster module to the existing single-stage heat pump, the heat pump power is more than doubled for the more restrictive operation points (Fig. 2) while COP is decreased by about 10% (Fig. 5). As illustrated by

		Reference without inj.	Ref. with booster module cap. 2m	cap. 2+1.4m
T air ev inlet	[°C]	−7.3	−7.0	−6.9
T water cd outlet	[°C]	59.9	59.8	59.7
Rel. humidity	[%]	77.2	75.1	74.7
P ev	[bar]	3.3	2.2	2.3
T in booster	[°C]	–	−5.7	−4.4
T out booster	[°C]	–	56.2	50.4
P out booster	[bar]	–	7.6	6.7
PR booster	[-]	–	3.5	2.9
Elpow. boost. mot.	[kW]	–	3.31	3.08
Boost. isentropic eff.	[-]	–	70.2	68.3
Boost. elmeca. eff.	[-]	–	76.4	76.7
Injected mass flow	[g/s]	–	25.6	11.8
T main cp outlet	[°C]	122.7	115.9	125.1
P main cp outlet	[bar]	24.4	25.4	25.3
Elec. power cp	[kW]	3.35	4.66	4.39
Tot. PR	[-]	7.4	11.6	11.1
Heat power	[kW]	8.03	16.89	15.57
Tot. h.p. elec. pow.	[kW]	3.67	8.29	7.79
COP_{Ext}	[-]	2.19	2.04	2.00
COP_{Carnot}	[-]	4.95	4.98	5.00
Exergy eff.	[%]	44.2	41.0	40.0

Table 3: Data for the operation point A-7/W60.

		Reference without inj.	Ref. with booster module cap. 2m	cap. 2+1.4m
T air ev inlet	[°C]	−11.1	−11.4	−11.1
T water cd outlet	[°C]	59.0	64.6	64.7
Rel. humidity	[%]	74.6	78.1	77.5
P ev	[bar]	3.0	1.9	1.9
T in booster	[°C]	–	−7.5	−6.9
T out booster	[°C]	–	57.8	50.8
P out booster	[bar]	–	7.3	6.2
PR booster	[-]	–	3.9	3.2
Elpow. boost. mot.	[kW]	–	3.18	2.89
Boost. isentropic eff.	[-]	–	72.4	69.7
Boost. elmeca. eff.	[-]	–	74.8	75.6
Injected mass flow	[g/s]	–	28.0	12.8
T main cp outlet	[°C]	119.7	120.6	133.4
P main cp outlet	[bar]	24.2	27.9	27.8
Elec. power cp	[kW]	3.24	4.82	4.55
Tot. PR	[-]	8.1	14.7	14.6
Heat power	[kW]	7.39	15.7	14.18
Tot. h.p. elec. pow.	[kW]	3.56	8.32	7.76
COP_{Ext}	[-]	2.08	1.89	1.83
COP_{Carnot}	[-]	4.74	4.44	4.46
Exergy eff.	[%]	43.9	42.6	41.0

Table 4: Data for the operation point A-11/W65∗.

∗ : The operation point A-11/W65 has not been reached for the reference configuration (the regular single-stage heat pump, without modification) due to a too high compressor outlet temperature for the compressed vapors. Consequently, for the reference configuration, the A-11/W65 operation point is in fact a A-11/W60 operation point.

Fig. 6, the efficiencies of the booster compressor are at reasonable levels. Indeed, the electromechanical efficiencies are common values for open-type scroll compressors and the isentropic efficiencies, considering the modifications made on the compressor, are at the level expected. The decrease of the COP is in fact mainly due to the significant decrease of the evaporation pressure. This decrease can reach 1 bar, which is equivalent to a 11K-decrease of the evaporation temperature, and is due to the undersized evaporator, which has not been designed to transfer such a heat power. The phenomena taking place in the evaporator in those conditions are (a) the increase of the temperature pinch, (b) the increase of the pressure drop. Moreover, since the fan speed was not modified, the air temperature drop increase from 3°C to 6°C.

We consider the case of a house requiring 15.7 kW of heat power when the outside temperature is -11°C, which is the heat power delivered by the single-stage heat pump chosen as a reference in this study, with the additional booster module (operation point A-11/W65). If this house was to be heated with the single-stage heat pump and with backup electrical (Joule effect) devices, the COP and the exergy efficiency of the whole system would only reach 1.32 and 19.36 % respectively. However if heated with the single-stage heat pump with the booster module proposed here, the COP and the exergy efficiency of the whole system reach 1.83 and 43.9 %. Moreover, the total electric consumption of the first solution would reach 11.97 instead of 8.29 for the second solution (booster). Thus, the addition of the booster module represents a decrease of the electric consumption of 30% for this example taken at a given operation point. This reduction suggests that using booster modules in addition to heat pumps instead of backup electrical devices could help to reduce electric demand peaks which occur in winter. It also suggests that this booster module could be used to downsize heat pumps to the heat capacity needed during most of heating period, the extra heat needed being provided by the booster module when the heat pump capacity is exceeded.

5. Conclusion

This paper presents a booster concept taking the form of a module that can be added to an existing single-stage domestic heat pump. The experiments revealed a doubled heat pump capacity for

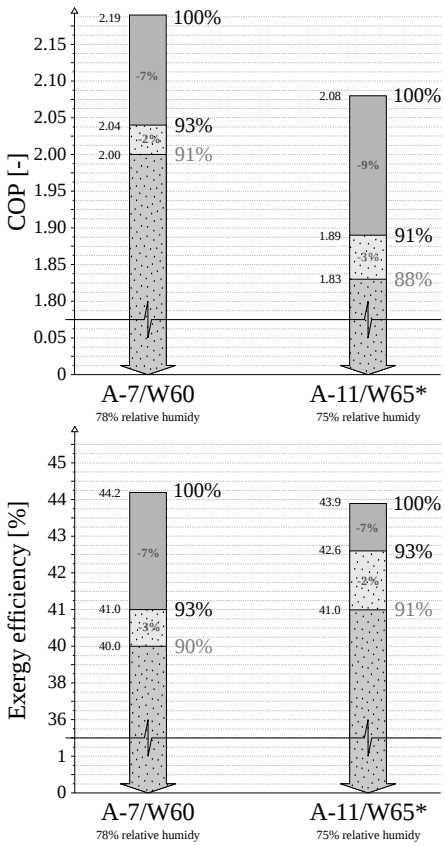

Figure 5: Decrease of the coefficient of performance and the exergy efficiency with the addition of the booster module. Same legend than Fig. 2.

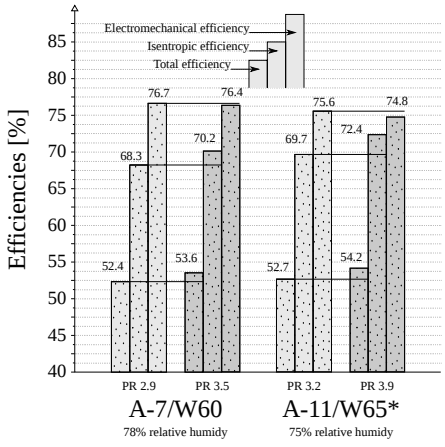

Figure 6: Evolution of the booster compressor efficiencies between the two studied operation points. Same legend than Fig. 2.

a decrease of the COP up to 10%, for extreme operating conditions (up to A-11/W65). The booster concept is very interesting for high temperature lift heat pump applications, as it allows a wider operation range, a high heat output at the extreme operating conditions, and enables an adapted functionality at the more frequent temperature range, of the mid-winter season or for the hot water preparation. It can also be imagined as an optional feature to a standard or an intermediate injection heat pump. During several weeks of testing, no significant oil hold up in the booster could be detected. The concept as presented is viable, and different points can be further optimized to increase the system efficiency: hermetic booster compressor and two level speed fan for the evaporator.

Acknowledgments: The authors gratefully acknowledge funding provided by the Swiss Federal Office of Energy (OFEN).

Nomenclature

Roman and Greek Letters

- COP Coefficient of Performance
- c_p specific heat at constant pressure, $\left[\frac{J}{kg \cdot K}\right]$
- $\dot{E}$ power, $[W]$
- h specific enthalpy, defined as $u + vP$, $\left[\frac{J}{kg}\right]$
- $\dot{M}$ mass flow rate, $[kg/s]$
- P pressure, $[Pa]$
- $\dot{Q}$ heat power, $[W]$
- T temperature, $[K]$
- $\dot{V}$ volume flow rate, $[L/min]$
- Δ difference
- η efficiency, $[-]$
- ρ density, $\left[\frac{kg}{m^3}\right]$

Subscripts and superscripts

- $^{+}$ which enters the frontier of the system
- $^{-}$ which leaves the frontier of the system
- $\dot{}$ rate, $\left[s^{-1}\right]$
- $_{cd}$ condenser
- $_{cons}$ consumed
- $_{cp}$ compressor
- $_{ev}$ evaporator
- $_{I}$ relative to the First Law
- $_{II}$ relative to the Second Law
- $_{w}$ water

For more details about the nomenclature, please refer to [9].

References

[1] European Heat Pump Association (EHPA), "European Heat Pump Statistics - Summary - Outlook 2009," tech. rep., European Heat Pump Association (EHPA), 2009.

[2] D. Favrat, E. Nidegger, D. Reymond, and G. Courtin, "Comparison Between a Single Stage and a Two Stage Air to Water Domestic Heat Pump with one Variable Speed Compressor," in *IIR Conference on Heat Pump Systems, Energy Efficiency, and Global Warming, Linz, Austria.*, Oct. 1997.

[3] B. Wang, W. Shi, L. Han, and X. Li, "Optimization of refrigeration system with gas-injected scroll compressor," *International Journal of Refrigeration*, vol. 32, no. 7, pp. 1544–1554, 2009.

[4] X. Wang, Y. Hwang, and R. Radermacher, "Two-stage heat pump system with vapor-injected scroll compressor using R410A as a refrigerants," *International Journal of Refrigeration*, vol. 32, pp. 1442–1451, Sep 2009.

[5] J.-B. Ritz and B. Horber, "Patent n°EP2088388 (A1) - Heat pump system," 2009. European Patent Application, Publication date: 2009-08-12, Applicant: STIEBEL ELTRON GmbH & Co. KG.

[6] J. Schiffmann and D. Favrat, "Experimental investigation of a direct driven radial compressor for domestic heat pumps," *International Journal of Refrigeration*, vol. 32, no. 8, pp. 1918–1928, 2009.

[7] J. Schiffmann and D. Favrat, "Design, experimental investigation and multi-objective optimization of a small-scale radial compressor for heat pump applications," *Energy*, vol. 35, no. 1, pp. 436–450, 2010.

[8] J. Schiffmann and D. Favrat, "The effect of real gas on the properties of herringbone grooved journal bearings," *Tribology International*, vol. In press, pp. –, 2010. doi:10.1016/j.triboint.2010.03.006.

[9] L. Borel and D. Favrat, *Thermodynamics and energy systems analyses*. EPFL Press, 2010.

[10] E. Lemmon, M. Huber, and M. McLinden, "NIST Standard Reference Database 23: Reference Fluid Thermodynamic and Transport Properties-REFPROP, Version 8.0, National Institute of Standards and Technology, Standard Reference Data Program, Gaithersburg," 2007.

Development and application of an energy and environmental certification method for residential buildings

Umberto Desideri[a],Daniela Leonardi[a], Livia Arcioni[a] , Maria Chiara Barzotti[a], Nicola Sorbi[a]
[a] *Perugia University, Industrial Engineering Dept., Perugia, Italy*

Abstract: The energy and environmental certification of buildings is a strategic tool to evaluate the sustainability of a building from the beginning of construction to the final demolition and disposal, taking into account not only the energy consumption, but also many other aspects like quality of design and living. In this paper, some of the most used energetic and environmental certification procedures in Italy have been studied and applied to a residential building. Among them the following protocols were compared: ITACA in its reduced form, LEED Italy, VEA, BIOVER, SB100 and SBC. Particular attention was dedicated to the SBC protocol developed by IISBE (International Initiative for a sustainable Built Enviroment), developed for commercial, office, high rise and school buildings, which takes account of 5 thematic areas: selection of the site, energy and resources consumption, environmental impact, indoor ambient quality and quality of the services. Starting from this protocol and comparing it with the other ones, a novel proposal of a protocol for the energetic and environmental certification of residential buildings was developed. This novel protocol was created by joining the essential issues and eliminating those that are not applicable or not interesting for residential buildings. To this aim, a new calibration of the weights of the five thematic areas was also considered. The novel protocol was applied to a residential building located in Città di Castello (Umbria, Italy).

Keywords: Sustainability, Environmental Certification, Life Cycle Assessment, Building.

1. Introduction

ENEA has recently published the results of a calculation of the energy consumption of buildings in Italy, based on data provided by the Italian Ministry of Economic Development, from which it is clear that the primary energy consumption of this sector accounts for 23% of the overall Italian energy consumption but it has also increased from 42 to 45 MTOE from 2005 to 2008. This shows that energy consumption in buildings has continued to increase notwithstanding the slow economic development which has affected other economic and industrial sectors in the same period [2]. Therefore, it is of prime importance to enforce all kind of policies aimed at increasing the energy efficiency of buildings, which allow to reduce energy consumption and mitigate greenhouse gases emissions. This is nowadays possible by means of new technologies, materials and building design criteria [3]. Within this framework, the environmental certification of buildings becomes a strategic tool to evaluate the energetic and environmental performance of buildings. These kind of certification allows to determine the environmental sustainability of the building and its impact from the design process, through the construction, utilization and demolition until its final disposal [4]. In the last decade, the research activities in this field have developed different international protocols for the evaluation of energy and environmental certification of buildings: the BREEAM, the LEED and the Green Building Challenge (GBC). In Italy, due to the absence of national guidelines for the environmental certification of buildings, a number of different methods and procedures have been proposed by some organizations and research centers, which have often defined in quite different ways, criteria and points to be used in the protocols.

From the general methodology developed by the Green Building Challenge the SBC protocol was proposed. This protocol is based on the evaluation procedure SBMethod developed IISbe (International Initiative for a Sustainable Built Enviroment) for use in commercial, office, high rise and school buildings. This protocol is quite complete and takes into account a large number of parameters and criteria, but it cannot be directly applied to residential buildings.

However, the SBC protocol was considered the most complete and suitable one to be the starting point for the proposal of a new protocol, which could be integrated with other parameters taken from the most widely used protocols in Italy. Therefore, the SBC protocol was modified with the addition of a few criteria taken from other protocols and adapted to be applied to residential buildings. To this aim, a new set of weights in the calculation of the final mark was also proposed.

Corresponding Author: Livia Arcioni, Email: liviaarcioni@unipg.it

Among the most widely used protocols in Italy for the certification of sustainability of building the following were considered: LEED Italy NC v. 0.9 (Leadership in Energy and Environmental Design) [10], ITACA (Institute for Transparency, Updating and Certification of Contracts, reduced form TN1) [11], VEA (Evaluation of the Energetic and Environmental Quality) [12], Umbria Regional protocol for the sustainability of buildings [13], ITACA (complete) [14]. In order to evaluate the validity of the proposed new protocol, it was applied to a group of residential buildings, newly built in Città di Castello in central Italy, that had already been studied with the BIOVER [15] (System of Energy and environmental evaluation for buildings) and SB100 [16] (Sustainable Building in 100 actions) protocols in a previous paper [17].

2. A novel energetic and environmental protocol for residential buildings

The SBC Protocol was considered the basis of the proposed new protocol which is aimed at residential buildings. The SBC protocol allows to evaluate the energetic and environmental performance of a building for the tertiary sector during its life cycle: design, construction, utilization, demolition and final disposal. Five thematic areas are considered in the evaluation of the environmental sustainability of a building according to the SBC protocol: selection of the site including project and urban planning, energy and consumption of natural resources, environmental impact, indoor quality, quality of the service. Within each area, the criteria are further grouped into sub-categories. The evaluation criteria are relevant from the environmental point of view, may be quantified with measurable parameters, have been validated scientifically, and are based on international and national legislation. Each criterion may be assessed by using a form, where the method and the verification procedure are described and a performance index may be calculated. The performance index may be a measurable or a qualitative parameter which allows to identify the performance level in comparison with the best and worse practice. To each evaluation criterion a mark ranging from [-1] to [+5] may be assigned. The [0] is generally assigned when the case under study may be considered equal or very close to the benchmark, which may be assumed as the construction practice which follows the current standards and legislation. From a weighted average of all the marks it is possible to define the degree of energetic and environmental sustainability of the building. Each evaluation criterion in each thematic area has a different weight as a function of its importance (Table 1). It is worth noticing that the Energy and Natural Resources Consumption area has the largest weight, whereas the quality of the services the smallest.

Table 1. Thematic areas and weights in the SBC Protocol.

SBC Protocol	
Thematic area	*Weight(%)*
Selection of site, project and urban planning	7.42%
Energy and natural resources consumption	49.29%
Environmental impact	19.55%
Indoor quality	21.02%
Quality of the service	2.73%

In order to apply the SBC protocol to residential buildings it was necessary to make changes to the performance indexes, by adding new fields and parameters in the thematic areas and evaluation criteria. Those new fields were generally taken by other protocols and adapted to the insertion in the SBC protocol. The general structure of the SBC protocol and its division in five thematic areas was left unchanged.

2.1. Selection of the site, project and urban planning

The first thematic area, concerning the selection of the site and project and urban planning, was greatly enlarged to allow a more accurate evaluation of it. The SBC protocol is not very exhaustive in this area, and some criteria are missing. At the same time, the LEED Italy protocol presents a very detailed and precise analysis of the site and a few criteria extracted from the "Sustainability of the site" have been transposed to the proposed new protocol. Table 2 shows the structure of the first thematic area in the new protocol. Newly added criteria are shown in red and marked with a star (*), whereas the old ones already included in the SBC protocol are shown in black.

In particular, it was considered quite important to add the criterion of the LEED protocol concerning the pollution prevention during construction, which has been included in the first thematic area. In order to prevent pollution of the soil in the construction phase, the "Planning for control of the erosion and sedimentation", to be included in the "Planning for the environmental management of the construction site", was added. In the same category two additional criteria were also included for the site selection. The first is to encourage planning of new buildings in already developed areas, to avoid damage to still undeveloped areas. The second is to build on areas which are subject

to redevelopment and soil remediation. In addition it was considered of prime importance to plan the development of new housing towards urban areas where services and infrastructures are already in place. This was evaluated by adding a performance index based on inhabitants density and vicinity to services.

Table 2. Thematic Area 1.

Thematic Area #1: Selection of the site, Project Planning and Urban Planning		
Selection of the site	A.1.1	*Pollution prevention during construction
	A.1.2	Ecological value of the site
	A.1.3	*Avoiding edification in inappropriate areas to mitigate the environmental impact due to the site localisation
	A.1.4	Contamination level of the site
	A.1.5	*Recovery and redevelopment of contaminated sites
	A.1.6	*Inhabitants density and vicinity to services
	A.1.7	Distance from public transportation
Project planning	A.2.1	Collection and recycling of wastes
Urban planning	A.3.1	*Habitat protection and remediation
	A.3.2	*Maximising green spaces
	A.3.3	Support to the use of bicycles and access* to bicycle* lanes*
	A.3.4	Use of local vegetation
	A.3.5	*Alternative transportation: low or zero emission vehicles
	A.3.6	*Alternative transportation: capacity of parking spaces

2.2 Energy and natural resources consumption

No modification was proposed in the category of "Project planning", whereas the third and last category "Urban planning" was completed by adding few criteria implemented from the LEED Italy protocol. Those added criteria were chosen to privilege the attention to the conservation of natural areas and existing agricultural landscape, by promoting the development of green areas such as gardens and public green spaces. The added criteria were also selected and implemented to consider an increased utilization of alternative means of transportation such as bicycles, low or zero emission vehicles, car sharing and car pooling.

The second thematic area is dedicated to energy and natural resources consumption. The area was originally divided into five categories grouped in two sub-areas. The proposed new protocol includes a sixth category which was inserted in the first sub-area. The first category of the second thematic area "Energy and natural resources consumption", dedicated to the "Non renewable energy requested during the life cycle", was left unchanged, because all the current and existing laws and regulations are followed. Similarly, no change was considered necessary for the second category concerning the peak demand of electric energy during building utilization. Instead, it was considered very important to add a new category called "Energy saving", containing six criteria which allow to evaluate the technologies to save energy in the building. Some criteria were taken from other protocols and some were newly created. They include: thermo-hygrometric properties of the building components and shell, the type of heat generation and distribution, the presence of active or passive solar systems, the presence of technologies to favor natural lighting of indoor spaces, the behavior of the building in summer without air conditioning. In table 3, the criteria included in the first sub-area of the second thematic area are listed. The new criteria are listed in red.

The second sub-area of thematic area #2 includes the categories of renewable energy, materials and water saving. The "Renewable energy" category was left unchanged because it was considered complete in all its criteria.

Table 3. Thematic Area 2: First sub-area.

Thematic Area #2: Energy and Natural Resources Consumption		
Non-renewable energy during the life cycle	B.1.1	Yearly primary energy demand for winter heating
	B.1.2	Yearly primary energy demand for summer cooling
Electric energy: peak demand during utilization	B.2.1	Electric energy: peak demand during utilization
***Energy saving**	B.3.1	*Thermo-hygrometric properties of the building components and shell
	B.3.2	*Heat generation
	B.3.3	*Heat distribution
	B.3.4.1	*Natural lighting
	B.3.4.2	*Indoor solar radiation and lighting
	B.3.5	*Passive solar systems
	B.3.6	Passive cooling
	B.3.6.1	Indoor temperature without cooling systems
	B.3.6.2	Control of solar radiation
	B.3.6.3	Phase displacement and attenuation of thermal wave

In the "Materials" category two new criteria from the LEED and VEA protocols were added. The main goal was to give more importance to the type of materials which are used in the building, with particular attention to materials provided with environmental certifications and coming from local or regional manufacturers and producers. An additional criterion is the "Management of disposal of building materials" to keep track and possibly reduce the disposal of wastes in landfill during the construction phase. The last category of the second thematic area concerns "Water utilization". It was assumed important to expand this concept to all types of water for indoor and outdoor utilization, without limiting it to potable water. For this reason, the title of the category was changed to "Water saving". Since the SBC protocol only takes into account potable water for indoor and outdoor utilization, the criterion of the VEA protocol, which considers control and pollution of water, was included. Table 4 shows the changes in the structure of the second sub-area of thematic area #2. The thematic area dedicated to the environmental impact of the building is titled "Environmental impact" and the criteria are listed in table 5. The criteria included in this area are sufficient to thoroughly evaluate the environmental impact of the building. The only changes are in a different weighing of the criteria which will be described later.

Table 4. Thematic area 2: Second sub-area.

Thematic area #2: Energy and Natural Resources Consumption		
Renewable Energy	B.4.1	Renewable energy not produced on-site
	B.4.2	Renewable energy produced on-site (thermal energy)
	B.4.3	Renewable energy produced on-site (electric energy)
Materials	B.5.1	Recycling of existing structures
	B.5.2	Use of recycled materials
	B.5.3	Use of materials produced with renewable energy
	B.5.4	Use of cement substitutes in concrete
	B.5.5	Use of recuperated/unmounted materials
	B.5.6	*Reduction of landfill disposal of construction materials
	B.5.7	*Use of local materials
	B.5.8	*Use of materials with environmental certifications
Water saving	B.6.1	Use of potable water for irrigation
	B.6.2	Indoor use of potable water
	B.6.3	*Pollution control of water
	B.6.4	Soil permeability

The fourth thematic area "Indoor quality" concerns the quality level and comfort inside the building, by means of controlling the ambient conditions in terms of temperature and humidity and the presence of different types of pollutants and noise. Since SBC is mainly focused on buildings for the tertiary sector, the evaluation of indoor quality is done by using criteria and parameters which are either not always influential for residential buildings or disregard some important parameters. Due to these reasons, new criteria have been added and some were eliminated and new weights have been defined. In addition, since some of the newly added criteria concern outdoor quality, the thematic area was renamed as "Indoor and outdoor quality", similarly to the VEA protocol (Table 6).

Table 5. Thematic Area 3.

Thematic Area #3: Environmental impact		
Greenhouse gas emissions	C.1.1	Greenhouse gas emissions during utilization
Other emissions	C.2.1	Yearly emissions of acidifying pollutants
	C.2.2	Yearly emissions of photo-oxidants
Solid wastes	C.3.1	Solid wastes during utilization
Sewage waters	C.4.1	Sewage waters
Impact on the local environment	C.5.1	Thermal effect of solid outdoor floors
	C.5.2	Thermal effecf of roofs

In the "Ventilation" category the SBC protocol only addresses forced ventilation systems which are commoner in the tertiary sector buildings. Since these technologies are not commonly used in residential buildings, a new criterion was added, which is included in the ITACA protocol and takes account of natural ventilation in indoor spaces. The “Indoor air quality" was extended to outdoor pollutants, such as it is done in the VEA and ITACA protocols. This allows to consider, not only the radon emissions, but also those of mineral fibres, VOC, and outdoor pollutants as commonly measured in urban areas. In the same category, the criteria considering the migration of pollutants among spaces. which may be common in tertiary sector buildings, but not in residential ones. This category is mainly dedicated to buildings where industrial activity are close to offices and there might be a migration of pollutants from the former to the latter. The "Air temperature and humidity" category was modified to make it more suitable for residential buildings. The SBC protocol criteria, focused on monitoring of temperature and humidity inside the

buildings, which can be easily done with air conditioning systems, was replaced by the one in the ITACA protocol, which is more focused on the evaluation of indoor comfort. The criterion "Natural and artificial lighting" was replaced by the LEED "Control and management of lighting plants". To this aim the LEED criterion was modified to make it more suitable for residential buildings. One specific feature that has been included is the automatic control and switching of artificial lighting depending on natural lighting. In the same category, the "Level of lighting and quality of artificial lights" criterion aimed at buildings of historical and artistic value as well as the "Natural lighting in main spaces" criterion were eliminated, being the first of limited interest for residential buildings and the second being transferred to the energy saving category of thematic area #2. The criterion titled "Dazzling", which is typical of working places, was replaced by "Artificial lighting" described in the ITACA protocol and aimed at guaranteeing the users a good artificial lighting level in indoor spaces, in terms of both quality and quantity. In the category "Electromagnetic pollution" the single criterion included in the SBC protocol was replaced by two divided as a function of the frequency of the electromagnetic fields: 50 Hz and high frequency (100 kHz to 3 GHz). A new category was eventually inserted to provide a significant relevance to the acoustic comfort of living spaces. This category is completely disregarded in the SC protocol, but is becoming more and more relevant to define the indoor quality of spaces and it is more and more important in residential buildings. The inserted criterion is based on the "Acoustic insulation" criterion in the VEA protocol. The aim of this criterion is to evaluate all the measures to reduce the transmission of outdoor, adjacent buildings' and technical plants' noise indoor. In the fifth and last thematic area "Quality of service", the three original categories of the SBC protocol were left unchanged. However in the category titled "Keeping the performance level" a new criterion was added from the ITACA protocol, where the importance of informing the users on the utilization of the building and the technical plants is stressed. The criterion "Flexibility and adaptability" was changed to include the flexibility of indoor spaces and technical plants. Table 7 shows the structure of the thematic area "Quality of the service".

After the definition of the new criteria to include in the SBC protocol, to make it applicable to residential buildings, new evaluation forms were created for each criterion.

Table 6. Thematic Area 4.

Thematic Area #4: Indoor and outdoor quality		
Quality of indoor and outdoor air	D.1.1	*Pollution from mineral fibres
	D.1.2	*Pollution from VOC
	D.1.3	Monitoring of air quality
	D.1.4	Control of air pollution (Radon)
	D.1.5	*Atmospheric pollution
Ventilation	D.2.1	*Natural ventilation
	D.2.2	Quality of air and ventilation in spaces with forced ventilation
	D.2.3	Speed of air in spaces with forced ventilation
	D.2.4	Ventilation efficiency in spaces with forced ventilation
Air temperature and humidity	D.3.1	*Winter Air temperature
	D.3.2	Vertical distribution of temperature
Natural and artificial lighting	D.4.1	*Artificial lighting
	D.4.2	*Artificial lighting control and management
Electromagnetic pollution	D.5.1	*Electromagnetic pollution/industrial frequency (50Hz)
	D.5.2	*Electromagnetic pollution/high frequency (100KHz – 3GHz)
***Acoustic pollution**	D.6.1	*Acoustic insulation

Thirty new forms were created on the basis of SBC forms, and each of them needed the definition of a new performance scale and performance index to be weighed to provide the final result. When the new criterion was transferred from other protocols, it was enough to scale the performance index of the other protocols to that of the SBC. When the criterion was created for this purpose, it was necessary to define the benchmark and the two extreme values of the index.

Table 7. Thematic Area 5.

Thematic Area #5: Quality of the service		
Controllability	E.1.1	BACS and TBM
Keeping the performance level	E.2.1	Keeping the performance level of the building shell
	E.2.2	Maintenance plan
	E.2.3	Conservation of technical documents "as built"
	E.2.4	Performance monitoring
	E.2.5	Records of the history of the building
	E.2.6	*User's manuals
Flexibility and adaptability	E.3.1	Possibility of changes of the building

After the definition of new categories, new criteria and new performance indexes it was necessary to create new weights for criteria and thematic areas. Starting from the weights used in the SBC protocol, the new ones were defined as follows: the "Energy and natural resources consumption" thematic area was considered the most important one for two reasons: it has a very significant impact on the environment and the utilization of the building and all performance indexes it can be quantified precisely and accurately. Due to this reason the new weight was fixed at 50%. The remaining 50% was distributed among the four other areas as described in Table 8. Similarly, new weights were assigned to each category and criterion. The largest weights were given to those criteria that are most important in the environmental and energetic impact. In most cases the weights assigned in the SBC protocol were left unchanged. The proposed new protocol for the energetic and environmental certification of residential buildings based on the framework of the SBC protocol consists of: 5 Thematic areas, 23 Categories, 72 Criteria. An application of the proposed protocol was studied to validate the new criteria and weights on a residential building complex. This complex had already been studied with two other certification protocols: SB100 and BIOVER.

Table 8. Thematic areas e and new weights.

New weights	
Thematic areas	weight %
Selection of the site, project and urban planning	10%
Energy and natural resources consumption	50%
Environmental impact	18.6%
Indoor and outdoor quality	18.6%
Quality of the service	2.8%

3. The case study

The residential building complex that was studied consists of three buildings arranged on line, designed and built by Coop Umbria Casa in Città di Castello (in central Italy) following the criteria to have a high energy efficiency and low environmental impact. The object of the study is the third building block with 12 apartments.

The following features were considered in the design to improve the quality of living and comfort of inhabitants and to reduce the energy consumption:

- Ten vacuum tubes solar panels facing South-East which allow to reduce by 60% the energy consumption for warm sanitary water and to avoid 5134 kg/year of CO_2 emissions;
- Fiftyfive Aleo S18 multicrystal silicon PV panels with a peak power output of 220 Wp facing South-East, with an overall peak power output of 1 kWp per apartment and avoiding 7656 kg/year of CO_2 emissions;
- Centralized heat generation with a geothermal heat pump with a nominal thermal power of 44 kW with an overall thermal energy production of 146.9 MWh/year;
- Heat distribution with a radiant low temperature floor with expected saving of 5%-10% in comparison with traditional systems;
- Walls and windows with a very low thermal conductivity (lower than 0.4 W/m2K). The very large thickness of insulation (larger than 7.5 cm) also ensures an improved thermal inertia;
- Very good acoustic insulation of walls;
- Silencers in ventilation bores to avoid noise passing through air openings;
- Passive solar systems such as six sunspaces in six apartments facing South-West;
- Active solar systems such as aluminum shields on the South-West side;
- Rainwater collection system for irrigation of public green spaces which allow savings of water of more than 50% for this purpose;
- Network switches to mitigate electromagnetic pollution.

4. Results of the application of the new protocol

The compilation of the 72 forms to calculate the performance indexes of each criterion allowed to calculate the parameters of each thematic area and to calculate the level of energetic and environmental sustainability of the building. The final mark is +2.4 out of a maximum of +5. This means that the case study is in the interval between +2 and +3 which corresponds to a level between an "improvement" and a "significant improvement" in comparison with the current regulations and current practice.

In Fig. 1, the five thematic areas are shown with the marks obtained in each area. It is possible to note that the building has marks higher than +2 in each area. This shows that the design criteria and the technical solutions are better than average in several aspects.

In order to show the contribution of each thematic area to the overall mark, the weighted marks of each area are plotted in the pie chart in Fig. 2.

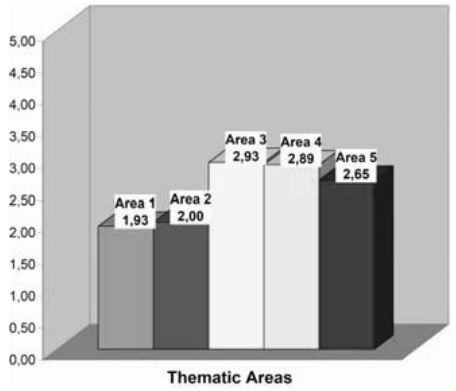

Fig. 1. Results for the thematic areas

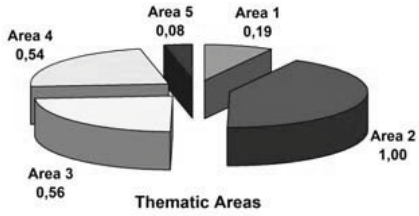

Fig. 2: Weighted marks of each thematic area.

Figure 2 provides a more general view of the areas and categories that contribute more to the sustainability of the building. The largest contribution is due to the "Energy and natural resources consumption" which accounts for 1 point. The most relevant contribution to this area is due to the primary energy for winter heating (40.4 kWh/m2year) and for summer cooling (10.7 kW/m2year). The smallest contribution is given by the thematic area "Quality of the service" with 0.08 points. The areas of "Environmental impact" and "Indoor and outdoor quality" have a quite similar influence on the overall results with 0.56 and 0.54 points respectively. In the former area the final mark was mainly determined by the low emission values of CO_2, SO_2 and ethylene equivalent. In the latter, the criteria with the greatest influence are the internal temperature distribution the very good acoustic insulation of the building shell and technical plants. In the thematic area "Selection of the site, project and urban planning" the final mark is 0.19 where the categories which have the largest influence are the vicinity to services and availability of public transportation.

5. Validation of the new protocol

The application of the new protocol is simple and quick, allowing a correct evaluation of all the characteristics of the building which are fundamental to evaluate its sustainability. In most criteria, the calculation of the performance indexes was possible with a simple visual examination of the building, whereas in other criteria calculations with simple spreadsheets is necessary.

The new protocol was validated by comparing the results with those obtained by two different protocols for the energetic and environmental certification of buildings: the SB100 and the BIOVER which were also applied to the same building complex. In all three protocols the final results reached an intermediate mark corresponding to a level between an "improvement" and a "significant improvement" in comparison with current legislation and practice (Table 9).

Table 9. Final marks obtained with the three protocols.

Building final marks		
New protocol	BIOVER	SB100
2.4 [scale: -1 / 5]	**2.71** [scale: -1 / 5]	**63** CLASS D [scale: 0 / 100]

In all three protocols, the thematic areas which have contributed most to the final marks are the consumption of energy and natural resources, the indoor comfort and environmental impact. It can be noted that the new protocol provides a more detailed analysis including more criteria that define the sustainability of a building. The first thematic area allows a more complete definition of the site and the urban planning. Such aspects are completely disregarded in the BIOVER protocol, where only the mobility and distance from the services is considered. Similar comments can be done of the SB100 protocol. A second important characteristic of the new protocol is the possibility to evaluate the technologies for energy saving, for which a specific category titled "Energy saving" was included in the protocol. This new category consists of 6 criteria which consider different aspects of energy saving. This category is absent in the BIOVER protocol and is partially included in the "passive behaviour of the building" criterion in the SB100 protocol. If we compare the new protocol for residential buildings with the BIOVER protocol it is possible to state that in all the five thematic areas the former allows a more detailed and comprehensive definition of the characteristics of the building. As an example, in the "Indoor and outdoor quality" area the new protocol keps track of many more pollution sources than the BIOVER and it is also possible to evaluate either the natural and the forced draft ventilation. The new protocol is

therefore, valid, accurate and does not require more complicated calculations than other protocols, but it considers many more characteristics of the building and more parameters that are important in the definition of a sustainable building. The comparison among the proposed new protocol and two other ones has allowed to validate the changes that have been proposed and the consistency of the new categories and criteria in the general framework for the evaluation of residential buildings.

6. Conclusions

The new protocol proposed in this paper allows to improve the SBC protocol for the energetic and environmental certification of buildings expanding it to the evaluation of residential buildings. The new protocol is based on the SBC protocol with the addition of new categories and criteria to the five thematic areas in which it is divided. The new categories have been in part transferred from other protocols and in part created from scratch. The 72 criteria are quite easy to be calculated and do not require specific tools but only the use of simple expressions which have been implemented in spreadsheets and the required input data are normally available from the technical documentation which is available and required to build a building. The new protocol was also compared to other protocols which are commonly used in Italy for these kind of evaluations and the results are comparable with them. The structure of the protocol and its division in thematic areas, categories and criteria is the same used in similar cases and the final index which represents the sustainability is given by means of a mark which identifies within a scale which is the energetic and environmental quality of the building in comparison with the current practice and legislation.

References

[1] Stanghellini S., 1997, What is the sense of the term sustainable cities?, *Conference on "Sustainable development and the city", on Disc [CD-ROM]*, Venezia, Italy.

[2] Meadows, D.H., Meadows, D. L. Randers, J., Behrens, W.W., 1972, The limits to growth, New York Universe, III, USA.

[3] Brown L., Lrsen J., Fischlowitz B, 2004, Budget Earth. Environmental effects of localized economy, Ed. Ambiente, Italy.

[4-5] Bruntland G., 1987, Our common future Technical Report, The World Commission on Environment and Development.

[6] Herman E. Daly, “Over the growth. The economy of the sustainable development”, Ed. Comunita, 2001.

[7] Intergovernmental Panel on Climate Change, 2007, Climate Change 2007: Synthesis Report. Contribution of Working Groups I, II and III to the Fourth Assessment Report of the Intergovernmental Panel on Climate Change.

[8]Arcioni L., Leonardi D. 2008, Descriptive technical relationship, inherent to the building complex of City of Castle, place Riosecco, Perugia, Italy.

[9] AA.VV., SBC Protocol, Sustinable Building Council – Italia, Technical Report, Italy.

[10] AA.VV., Green Building Council Italia, LEED Italia NC v.0.9, Technical Report, Italy.

[11] AA.VV, Synthetic Protocol ITACA TN1 for assessing energy and environmental quality of a building, Technical Report, Autonomous Province of Trento, Italy.

[12] AA.VV, VEA regional protocol for the Assessment of energy and environmental quality of buildings, Technical Report, Autonomous Region of Friuli Venezia Giulia, Italy.

[13] Umbria Region, 2008, Regional Law n.17 of 18.11.2008, the Technical Regulations, “Certification of Environmental Sustainability for buildings", Umbria, Italy.

[14] A.A.V.V., ITACA, Green Building Work Group, 2004, ITACA Protocol 2003 for energy and environmental evaluation of a building – Reports and documents. 15 Jan. 2004, Italy, URL: http://www.itaca.org.

[15] A.A.V.V, 2008, SB100 – Sustainable building - 100 actions, Italy, URL:http://www.sb100.it.

[16] A.A.V.V., 2008, System of Energy and environmental evaluation for buildings, Biover, iiSBE Italia, ITC-CNR and Metadistretto Veneto della Bioedilizia, Italy.

[17] Desideri U.et al., 2009, Analysis of different methodologies for energy and enviromental certification applied to a residential building in central Italy, ECOS *Meeting Papers on Disc* [CD-ROM], Foz do Iguaçu, Paraná, Brazil.

[18] Janssen, R., 2004, Towards Energy Efficient Buildings in Europe, Technical Report, URL: http://www.euroace.org.

Prototype of a thermally driven heat pump based on integrated organic Rankine cycles (ORC)

Demierre, J., Henchoz, S. and Favrat, D.

Ecole Polytechnique Fédérale de Lausanne, LENI-IGM-STI, Station 9, 1015 Lausanne, Switzerland

Abstract: The concept studied in this work is a low power ORC-ORC system (about 20 kW heat at the condenser) which is composed of an ORC engine cycle driving a reversed ORC heat pump cycle, both using the same fluid. The radial compressor and turbine are directly coupled on the same shaft rotating on refrigerant gas bearings. This gives the system the advantage of being oil-free, fully hermetic and with low maintenance costs. The paper presents the development of an ORC-ORC prototype, with HFC-134a as working fluid. The main critical parts of the system are the compressor-turbine unit, the supercritical evaporator and the pump. The selected type of heat exchanger for the supercritical evaporation is the double tube coil (DTC). A first experimental setup has been built to test the pump and the supercritical evaporator. A comparison has been done between the results obtained with an in-house supercritical evaporator simulation tool and the measurements made on the DTC. The design steps of the compressor-turbine are briefly presented. The compressor-turbine unit has been balanced and tested, with air, at speeds up to 140'000 rpm.

Keywords: thermally driven heat pump, ORC, supercritical evaporator, gas bearings, residential heating, oil-free, high speed

1. Introduction

Single combustion in boilers is a very inefficient way of heating. The higher cost of fuels and pollution concerns are likely to put more and more political pressure to prevent the use of boilers for most heating purposes. Alternatives are all linked to heat pumps allowing to value the renewable heat from the environment. Thermally driven heat pumps from a variety of fuels including wood pellets or natural gas are usually realized using an absorption heat pump or by a combination of heat engine cycle with a compression heat pump cycle or a combination of both. One concept of the second category has been proposed by Strong [1] and is based on the use of an ORC engine cycle driving a reversed ORC heat pump cycle, both using the same fluid. Such a concept can be made using a scroll expander and a scroll compressor usually lubricated with oil or by an oil-free high speed dynamic compressor-expander assembly rotating on refrigerant vapor bearings. Unfortunately earlier attempts of the latter failed because of lack of appropriate materials and of the problematic of the CFC refrigerants, which were, at the time, among the best candidates for high temperature cycles. Progress in materials and in finding new fluids, to substitute the CFCs with a reasonably high temperature chemical stability and/or acceptance, allow the reconsideration of this approach with HFC-134a or R600 as key working fluid candidates. The recent demonstration of one concept of miniature high speed centrifugal compressor directly driven by a high speed electric motor rotating on refrigerant gas bearings [2, 3] opens the way to such devices with or without electric motor.

2. ORC-ORC High Speed Concept

An ORC-ORC system is composed of an ORC engine cycle and a reversed Rankine heat pump cycle (see Fig. 1). The condenser (and the subcooler if introduced) is common to both cycles. The power from the ORC turbine is used to drive the compressor of the heat pump cycle. This system works between three main temperature levels and is therefore similar to an absorption heat pump. Heat is provided at high temperature (by a boiler for example) at the supercritical evaporator of the topping ORC and at low (geothermal probe) temperature at the evaporator of the heat pump ORC. Heat is supplied to the house heating system by the unit condenser at medium temperature.

The studied concept is a low power system (about

Corresponding author: Jonathan Demierre, Email: jonathan.demierre@epfl.ch

20 kW heat at the condenser in the case treated here) with one-stage radial compressor and turbine. The compressor and turbine are directly coupled on the same shaft rotating on refrigerant gas bearings. This gives the system the advantage of being oil-free, fully hermetic and with low maintenance costs in spite of the more complex circuitry. Because of the characteristics of dynamic compressors and turbines a low density fluid is preferred and refrigerant HFC-134a has been selected at this stage. It is chemically stable at relatively high temperatures (at least up to 180°C).

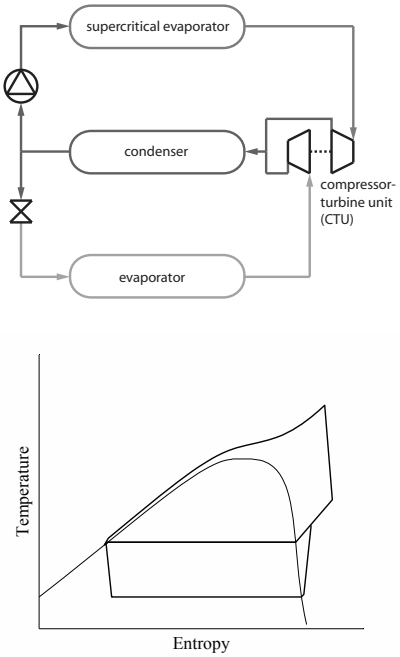

Figure 1: Schematic flowsheet and T-s diagram of a simple ORC-ORC heat pump unit

3. Preliminary Design

A preliminary design was made based on the results of previous studies [4, 5]. An ORC-ORC system design and optimization tool had been developed. The tool consists of a model developed on a commercial flowsheeting software, *Belsim-Vali* [6] that is linked to an in-house energy integration tool [7] and an in-house multiobjective optimization tool [8]. The three pieces of software are linked using an interface, *OSMOSE*, developed at our laboratory.

The ORC-ORC system design and optimization tool enables to calculate the optimal pressure and temperature levels, the optimal refrigerant mass flow rates, as well as the optimal compressor and turbine preliminary design (rotational speed and diameter of the wheels). A polynomial approximation of the correlation of Rohlik (1968) [9] is used to model the turbine isentropic efficiency η_t. This relation gives the maximum efficiency that can be achieved for a fixed turbine specific speed n_{st}. The compressor isentropic efficiency η_c is modeled following a similar method. A correlation (adapted from Balje 1981 [9, 10]) that relates the maximum efficiency to the compressor specific speed n_{sc} is approximated. Pressure drops in the heat exchangers and pipes, and heat losses are neglected. The expansion in the valve is considered to be isenthalpic. The pump isentropic efficiency is considered to be constant and equal to 0.5. The losses related to the compressor-turbine shaft are calculated using the model given in [2, 3]. (eventually, details on how the wheel diameter is estimated)

The ORC-ORC heat pump studied in this work is a system for residential heating purpose. The system has to be designed to produce hot water at 60°C (water initial temperature is 10°C) and to heat up water for floor heating from 30°C to 35°C. The total heating power (hot water production + floor heating) is about 20 kW. The hot heat source is the combustion gases resulting from a stoichiometric combustion of methane that cools down to a temperature as low as possible (for example to 4°C in winter time of our calculations). The cold heat source is the glycol water from a geothermal probe (that cools down from 4°C to 0°C in our calculations).

A bi-objective optimization was done, with the conditions given above, with the system COP (coefficient of performance) as first objective and the compressor-turbine unit (CTU) rotational speed as second objective. The CTU rotational speed is chosen as second objective, because for such low power compressor and turbine the optimal rotational speed becomes critically high. The COP of the system is defined as follows:

$$COP = \frac{\dot{Q}^-_W}{\dot{Q}^+_{fumes} + \left(\dot{E}^+_{pump}/0.56\right)} \qquad (1)$$

$\dot{Q}^-_W$ is the heat given to the water (hot water and heating), $\dot{Q}^+_{fumes}$ is the heat given by the fumes resulting from the methane combustion and $\dot{E}^+_{pump}$ is the electrical power consumed by the ORC-ORC pump (which is the only electrical power consumed

by the ORC-ORC). $\dot{E}^{+}_{pump}$ is divided by 0.56 to take into account for the efficiency of a modern combined cycle power plant that produces this electrical power, in order to define a COP which is strictly based on the conversion of the fuel (here, methane) into heat. At first approximation, in our calculations, $\dot{Q}^{+}_{fumes}$ is evaluated as follows [11]:

$$\dot{Q}^{+}_{fumes} \cong \dot{m}_F \cdot \Delta h^0_i \quad (2)$$

$\dot{m}_F$ is the mass flow of the fuel (methane, in our calculations) and Δh^0_i is the lower heating value of the fuel (here, for the standard state, P^0 = 1.01325 bar and T^0 = 25°C).

The Pareto curve resulting from the optimization with the system COP and the rotational speed of the CTU as objectives is shown at Fig. 2. Each point corresponds to a particular design solution. It appears that the COP increases with the CTU rotational speed to reach a maximum value of about 1.7 at a speed of about 250'000 rpm. In theory, the optimal compressor and turbine rotational speed is even higher than 250'000 rpm, but the losses linked to the shaft (gas bearings losses and windage losses) increase with the increase in rotational speed. This result shows the importance to use a bearing technology that enables to reach high speeds and so, justifies the use of gas bearings.

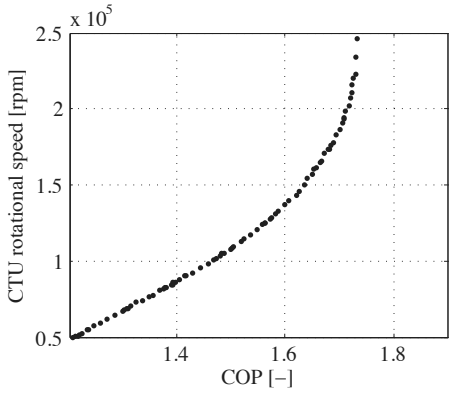

Figure 2: Pareto curve of the optimization with the COP and the CTU rotational speed as objectives

The optimal values of some main design parameters as a function of the COP are plotted in Fig. 3. It appears that the optimal temperature, of almost all solutions, is about 180°C, that corresponds to the upper limit that was set in our calculations and which is assumed to be the temperature limit of the HFC-134a (chemical stability). Following those results, the values of the preliminary design parameters for the ORC-ORC prototype were chosen and are given in the Tab. 1.

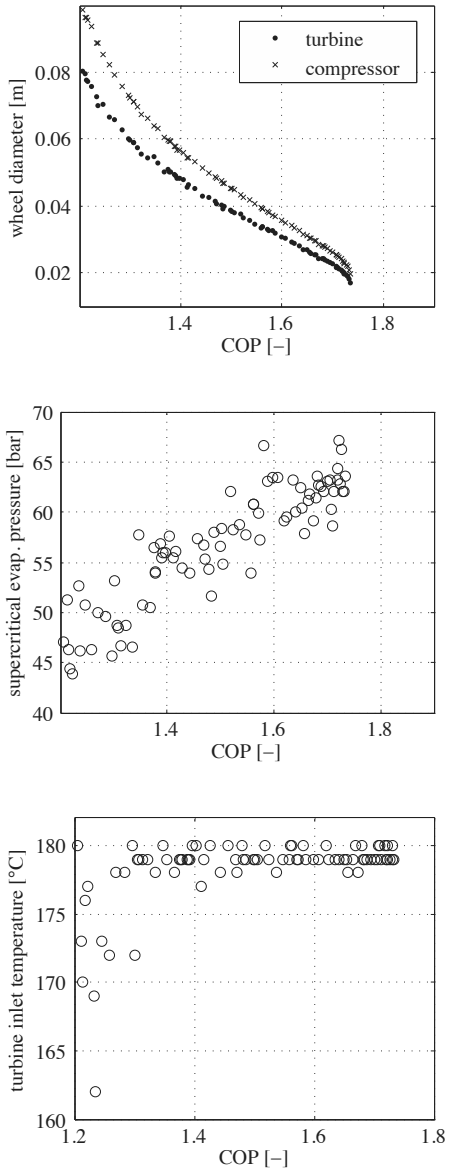

Figure 3: Design parameters regarding the COP

Table 1: Values of the preliminary design parameters

supercritical evaporation pressure	: 65 bar
turbine inlet temperature	: 180°C
condensation temperature	: 40°C
heat pump evaporation temperature	: -5°C
turbine wheel diameter	: 18 mm
compressor wheel diameter	: 20 mm

4. Prototype layout

The layout of the prototype is shown at Fig. 4. In this first prototype, instead of having a unique condenser for both cycles, there is a condenser for each cycle in order to control easily the system. This gives also the possibility to test the turbine and the compressor "more" independently, since, with this layout, the turbine outlet pressure and the compressor outlet pressure can be different. Two on/off valves enable to connect both condensers together in order to simulate a unique condenser. The CTU housing is connected to the low pressure of the heat pump cycle and a valve enables to regulate the pressure in the gas bearings. The turbine bypass and the valves at the turbine inlet and outlet allow to start and heat up the cycle without the working fluid passes through the turbine, in order to start the turbine only when it is guaranteed that the refrigerant at the inlet is entirely in vapor form. In fact, at high speed, any droplet would damage the CTU rotor. A vertical tube with a large section (about 150 mm diameter) after the heat pump cycle evaporator serves as separator to ensure that there is no droplet at the compressor inlet.

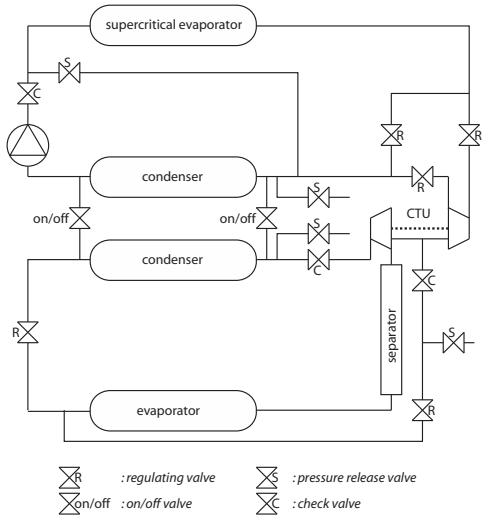

Figure 4: ORC-ORC prototype layout

5. Selected equipment

Supercritical evaporator

The supercritical evaporator has to work under relatively severe conditions. In fact, the supercritical evaporator has to allow to reach refrigerant pressure up to 70 bar, to heat up the refrigerant, in the worst case, from 15°C to 180°C and to work with a temperature of thermal oil (Syltherm 800) up to about 200°C. Several types of heat exchanger have been reviewed (details are given in [12]). The selected type is "the double tube coil" (DTC) (see Fig. 5). A DTC heat exchanger is composed of a tube inside an other that are coiled together. This design allows to work with high temperature differences and high pressures.

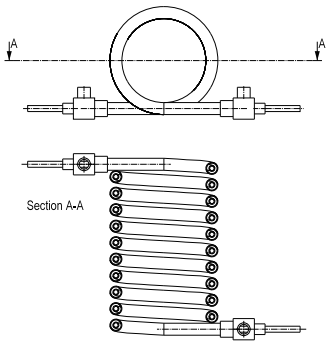

Figure 5: Double tube coil (DTC) heat exchanger

Engine cycle pump

The pump has to work with a pressure difference up to 55 bar. Another constraint is that there must be no contact between the refrigerant and the pump lubricating oil. Consequently, a diaphragm pump has been selected.

6. First test rig

A first test rig was built to test the critical tests equipment (the supercritical evaporator and the diaphragm pump) before the construction of the complete prototype. Several tests were performed to characterize the diaphragm pump and the DTC heat exchanger under supercritical conditions.

6.1. layout

The test rig corresponds, more or less, to the engine cycle without the turbine (see Fig. 6). The turbine is replaced by a manual regulating valve (noted *V* in Fig. 6). The R134a is evaporated in the DTC with the thermal oil (Syltherm) coming from a regulated electric boiler. The refrigerant condenses in the plate heat exchanger (*PHX*) with water at about 9°C at inlet as cold fluid. The diaphragm pump (*P*) is connected directly at the outlet of the condenser (the plate heat exchanger) and is followed by a check valve (*c*). The mass flow of the refrigerant is measured with a coriolis flow meter (*M*). The R134a temperature is measured at inlet and outlet

of each heat exchanger with thermocouples (T_1, T_2, T_3 and T_4). The refrigerant pressure is measured at three points with piezoresistive pressure sensors (P_1, P_2 and P_3). The water temperature is measured with thermocouples (T_{C1} and T_{C2}) at inlet and outlet of the condenser and the thermal oil temperature is also measured with thermocouples (T_{H1} and T_{H2}) at each side of the DTC. A pressure relief valve (s_1) is connected from the high pressure side to the low pressure side of the cycle. It opens when the high pressure exceeds 70 bar. Another pressure relief valve (s_2) opens when the low pressure exceeds 17 bar. The pressure limits of 70 bar and 17 bar correspond to the maximum allowable operating pressures, respectively, at the outlet and inlet of the diaphragm pump. A pressure gauge (P_{Vin}) is placed after the DTC to check directly the level of the high pressure when the manual regulating valve (V) is actuated.

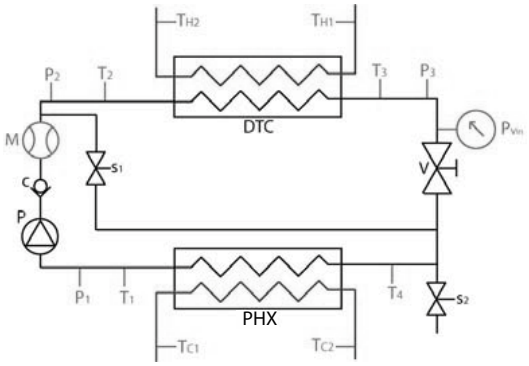

Figure 6: First test rig

6.2. Test results

Supercritical evaporator

The tested DTC has the following specifications:

- Heat transfer area: 0.23 m^2
- inner tube outer diameter: 1/2 inch
- inner tube wall thickness: 0.049 inch
- outer tube outer diameter: 1 inch
- outer tube wall thickness: 0.083 inch
- material: stainless steel
- estimated tube roughness k: 50 μm
- tube thermal conductivity λ: 15.2 W/m K

Tests were performed with different values of R134a mass flow $\dot{m}_R$, thermal oil temperature at the DTC inlet T_{H1} and R134a pressure at the DTC inlet P_2. The tested values are approximately:

- $\dot{m}_R$ (kg/s): 0.05, 0.08, 0.1, 0.13
- T_{H1} (°C): 50, 120, 180, 220
- P_2 (bar): 45, 55, 65

The volume flow rate of thermal oil is approximately the same for all tests and is about 4 m^3/h. The R134a temperature at the DTC inlet T_2 is more or less different for all tests and between 15°C and 50°C. By combining the different values given to $\dot{m}_R$, T_{H1} and P_2, measurements were done for 41 operating points.

The measured heat load is between 0.5 kW and 30 kW. The overall heat transfer coefficient U calculated with the measurements is between 360 W/(m^{2}K) and 1020 W/(m^{2}K). The overall heat transfer coefficient is evaluated as follows:

$$U = \frac{\dot{Q}_R}{A \cdot \Delta T_{lm}} \tag{3}$$

where $\dot{Q}_R$ is the heat power given to the refrigerant, A is the heat transfer area of the DTC and ΔT_{lm} is the log-mean temperature difference. The log-mean temperature difference is calculated as follows:

$$\Delta T_{lm} = \frac{\Delta T_2 - \Delta T_1}{\ln(\Delta T_2 / \Delta T_1)} \tag{4}$$

where

$$\Delta T_1 = T_{H1} - T_3 \quad \text{and} \quad \Delta T_2 = T_{H2} - T_2 \tag{5}$$

The experimental results have been used to validate an in-house DTC supercritical evaporator simulation tool [12]. Several correlations for the evaluation of the Nusselt number Nu and the friction factor f are implemented in the tool (see Tab. 2 for Nu and Tab. 3 for f). Five heat transfer correlations have been considered:

- Gnielinski with Darcy-Wiesbach friction factor (G D-W)
- Gnielinski with Gnielinski friction factor (G G)
- Gnielinski with Filonenko friction factor (G F)
- Petukhov-Kirillov-Popov with Filonenko friction factor (P-K-P F)
- Dittus-Boelter (D-B)

The 41 operating points, that were tested, were simulated. For each operating point, the simulations were done for all possible combinations of heat transfer correlations (25 combinations). The error

Table 2: Heat transfer correlations implemented in the DTC model (f is given in the Tab. 3)

correlation	range of application
Gnielinski:	
$\mathrm{Nu} = \frac{\frac{f}{8}(\mathrm{Re}_\phi - 1000)\,\mathrm{Pr}}{1+12.7\sqrt{\frac{f}{8}}(\mathrm{Pr}^{2/3}-1)}$	$2300 < \mathrm{Re}_\phi < 5\cdot 10^6$ $0.5 < \mathrm{Pr} < 2000$
Petukhov-Kirillov-Popov:	
$\mathrm{Nu} = \frac{\frac{f}{8}\mathrm{Re}_\phi\,\mathrm{Pr}}{1.07+12.7\sqrt{\frac{f}{8}}(\mathrm{Pr}^{2/3}-1)}$	$10^4 < \mathrm{Re}_\phi < 5\cdot 10^6$ $0.5 < \mathrm{Pr} < 2000$
Dittus-Boelter:	
$\mathrm{Nu} = 0.023\mathrm{Re}_\phi^{4/5}\mathrm{Pr}^n$ with $n = 0.4$ for heating and $n = 0.3$ for cooling	$\mathrm{Re}_\phi > 10^4$ $0.7 \le \mathrm{Pr} \le 160$ $\frac{L}{\phi} > 10$

Table 3: Friction factor correlations implemented in the DTC model

correlation	application
Gnielinski:	
$f = (0.79\ln\mathrm{Re}_\phi - 1.64)^{-2}$	smooth pipe
Filonenko:	
$f = (1.82\log_{10}\mathrm{Re}_\phi - 1.64)^{-2}$	smooth pipe
Darcy-Wiesbach:	
(Churchill empirical formula)	
$f = 8\left[\left(\frac{8}{\mathrm{Re}_\phi}\right)^{12} + \frac{1}{(A+B)^{3/2}}\right]^{1/12}$	
where	
$A = \left[2.457\cdot\ln\frac{1}{\left(\frac{7}{\mathrm{Re}_\phi}\right)^{0.9}+0.27\cdot\frac{k}{\phi}}\right]^{16}$	rough pipe
$B = \left[\frac{37'530}{\mathrm{Re}_\phi}\right]^{16}$	

on the overall heat transfer coefficient ϵ_U is calculated as follows:

$$\epsilon_U = \frac{U_s - U_m}{U_m} \tag{6}$$

where U_s and U_m are the overall heat transfer coefficients calculated with, respectively, the results of the simulation and the measurements. The overall heat transfer coefficient error ϵ_U averaged on the 41 tested operating points is given at Tab. 4 for each combination of heat transfer correlations. The average value of ϵ_U is also shown in Fig. 7, as well as the minimum and maximum. The results show that the best prediction is obtained when the correlation of Dittus-Boelter is used for both the R134a and the Syltherm. The average of the error ϵ_U is less than 2%, which means that the DTC model with the Dittus-Boelter correlation is accurate enough to well size a supercritical evaporator for such an application. Following the results, it was decided to use three DTC heat exchangers (in parallel), with a heat transfer area of 0.23 m^2 each, for the supercritical evaporation of the ORC-ORC prototype.

Table 4: Tested correlation combinations and corresponding average errors on the overall heat transfer coefficient ϵ_U

model nb.	Syltherm corr.	R134a corr.	ϵ_U aver. (%)
1	G D-W	G D-W	5.37
2	G G	G D-W	4.69
3	G F	G D-W	4.65
4	P-K-P F	G D-W	6.26
5	D-B	G D-W	3.12
6	G D-W	G G	4.30
7	G G	G G	3.69
8	G F	G G	3.68
9	P-K-P F	G G	4.83
10	D-B	G G	2.18
11	G D-W	G F	4.29
12	G G	G F	3.70
13	G F	G F	3.64
14	P-K-P F	G F	4.83
15	D-B	G F	2.16
16	G D-W	P-K-P F	4.20
17	G G	P-K-P F	3.57
18	G F	P-K-P F	3.58
19	P-K-P F	P-K-P F	4.76
20	D-B	P-K-P F	2.11
21	G D-W	D-B	3.88
22	G G	D-B	3.25
23	G F	D-B	3.21
24	P-K-P F	D-B	4.16
25	D-B	D-B	1.78

Engine cycle pump

The required rise in pressure (about 55 bar) has been reached with the diaphragm pump. Nevertheless, the pump nominal mass flow is a little bit too high regarding the required mass flow of R134a for our application. As it is a volumetric pump, the delivered mass flow is more or less proportional to the rotational speed. So in our case, the rotational speed of the pump is too low regarding its nominal speed that induces high torque peaks. Therefore, after a few minutes of operation, the temperature of the electric motor becomes too high. A way to solve the problem is to add a bypass between the outlet and inlet of the pump, in order to increase the mass flow of the latter without changing the mass flow

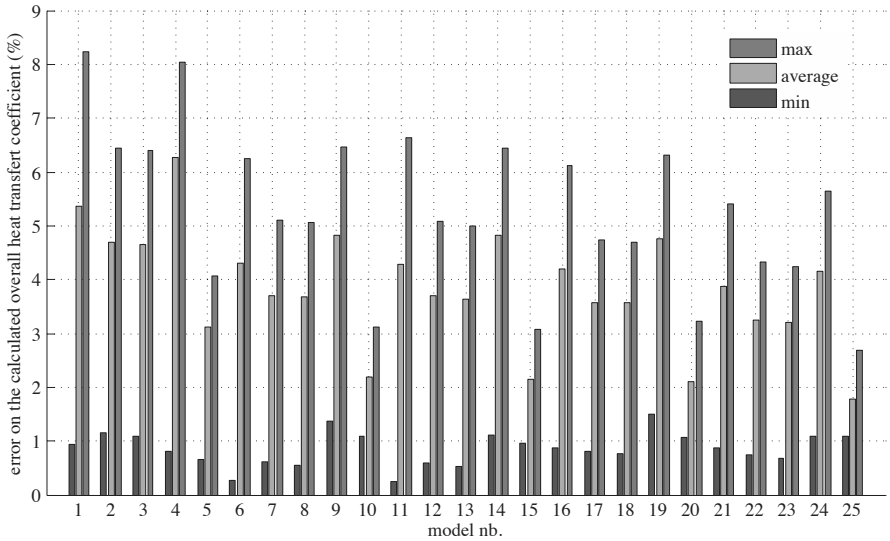

Figure 7: Average, minimal and maximal error on the overall heat transfer coefficient ϵ_U for the 25 tested correlation combinations (for "model nb." refer to Tab. 4)

in the rest of the system. This is a solution for the first experiments, but in the future a new diaphragm pump which is more adapted to the required mass flow should be acquired.

7. Compressor-turbine unit (CTU) design

The compressor-turbine unit (see Fig. 8) was designed on the basis of an electrically driven oil-free compressor (about 3 kW) described in [2, 3]. The electric motor was replaced by a turbine.

The turbine shape was designed in two steps using the *Concepts NREC* [13] software. At first, a preliminary design was made using the 1-D simulation tool. This step consists of determining the optimal geometry of the inlet and outlet of each element (volute, nozzle, interspace, rotor and diffuser). The second step is the 3-D design of the different elements. To evaluate the performances and check the flow, CFD calculations have been performed.

The different elements of the turbine side were designed with the main constraint that the clearances between the rotor and the static parts have to be as small as possible. On this prototype the clearances between the compressor and turbine wheels and the static parts is about 0.1 mm. Finite element analysis were done to check the thermal and mechanical stresses and the displacements due to the high rotational speed (up to 240'000 rpm), the high pressure (up to 70 bar) and the high temperature differences (about 0°C on the compressor side and 180°C on the turbine side). The CTU has been balanced and tested with air at rotational speeds up to 140'000 rpm.

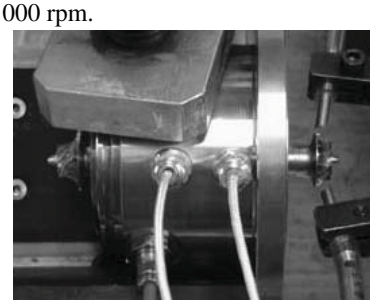

Figure 8: Compressor-turbine unit without the compressor and turbine stator parts during the balancing (compressor on the left and turbine on the right.)

8. Conclusion

The preliminary design of a prototype of an ORC-ORC thermally driven heat pump for residential application (about 20 kW heating power) was done. The chosen diameter of the compressor and turbine wheels are respectively 20 mm and 18 mm and their nominal speed of rotation is about 200'000 rpm. The selected heat exchanger type for the supercritical evaporation is the double tube coil, because of its robust design. The layout for the ORC-ORC prototype has been defined. A first test rig has

been built to test the supercritical evaporator and the diaphragm pump of the engine cycle. The results obtained with an in-house supercritical evaporator model has been compared to the measurements done on the DTC heat exchanger. The error between the predicted overall heat transfer coefficient and the one calculated with the measurements is less than 3%. The tests have shown that the diaphragm pump is able to provide the required pressure rise (about 55 bar). Finally, the compressor-turbine unit has been tested with air and shows a good behavior at rotational speeds at least up to 140'000 rpm.

Nomenclature

$\dot{m}$ mass flow rate, kg/s

P pressure, Pa

T temperature, °C

h heat transfer coefficient, W/(m^2 K)

U overall heat transfer coefficient, W/(m^2 K)

Nu $= \frac{h\phi}{\lambda}$, Nusselt number

Re_ϕ $= \frac{C\phi}{\mu/\rho}$, Reynolds number (based on ϕ)

Pr $= \frac{c_p\mu}{\lambda}$, Prandtl number

C flow velocity, m/s

μ dynamic viscosity, Pa s

ρ density, kg/m^3

ϕ $= \frac{4\times \textit{cross sectional area}}{\textit{perimeter}}$, hydraulic diameter, m

L tube length, m

f $= -\frac{\frac{dP}{dL}\phi}{\frac{1}{2}\rho C^2}$, friction factor

λ thermal conductivity, W/(m K)

c_p isobaric specific heat, J/(kg K)

References

[1] D.T.G. Strong. *Development of a directly fired domestic heat pump*. Ph.D. Thesis, University of Oxford, UK, 1980.

[2] J. Schiffmann and D. Favrat. Design, experimental investigation and multi-objective optimisation of a small-scale radial compressor for heat pump applications. *Energy*, (35(1)):436–450, 2010.

[3] J. Schiffmann and D. Favrat. Experimental investigation of a direct driven radial compressor for domestic heat pumps. *Int. J. of Refrigeration*, (32(8)):1918–1928, 2009.

[4] J. Demierre and D. Favrat. Low power ORC-ORC systems for heat pump applications. In *9th International IEA Heat Pump Conference*, pages s5–p29, Zürich, Switzerland, 2008.

[5] J. Demierre and D. Favrat. Thermally driven residential heat pumps based on integrated organic Rankine cycles (ORC). In *Smart Energy Strategies*, Zürich, Switzerland, 2008.

[6] Belsim. Vali IV. `http://www.belsim.com`, 2006.

[7] F. Maréchal and B. Kalitventzeff. Process integration: Selection of the optimal utility system. *Computers and chemical engineering*, (22):S149–S156, 1998.

[8] A. Molyneaux, G. Leyland and D. Favrat. Environomic multi-objective optimisation of a district heating network considering centralized and decentralized heat pumps. *Energy*, (35(2)):751–758, 2010.

[9] A. Whitfield and N.C. Baines. *Design of Radial Turbomachines*. Longman Scientific & Technical, Harlow, UK, 1990.

[10] O.E. Balje. *Turbomachines : A Guide to Design, Selection and Theory*. John Wiley & Sons, New York, USA, 1981.

[11] L. Borel and D. Favrat. *Thermodynamics and energy systems analysis*. EPFL Press, Lausanne, Switzerland, 2010.

[12] S. Henchoz. Study of a Supercritical Evaporator for an ORC-ORC Thermally Driven Heat Pump (student semester project). Technical report, Laboratory for Industrial Energy Systems (LENI), Ecole polytechnique fédérale de Lausanne, Switzerland, 2008.

[13] Concepts NREC. AGILE Engineering Design System. `http://www.conceptsnrec.com`, 2007.

Acknowledgments: The authors would like to thank the *Swiss Federal Office of Energy (OFEN)* for its financial support and *Fischer Engineering Solutions AG* in Herzogenbuchsee (BE, Switzerland) to have supplied the gas bearings and to have assembled and balanced the compressor-turbine unit.

Finite Time Thermodynamic Analysis of Phase Change Packed Bed Storage Systems

Nóbrega, C.E.L.[a] *, Braga, S.L.B.*[b]

[a] *Centro Federal de Educação Tecnológica CEFET-Rio , Rio de Janeiro, Brazil*
[b] *Pontifícia Universidade Católica do Rio de Janeiro, Rio de Janeiro, Brazil.*

Abstract: The role of thermal energy storage in the HVAC industry has been continuously increasing over the last years, powered by the adoption of "peak" and "off-peak" power consumption periods (and rates) by electrical utilities. As a result, many works have been devoted to modeling and predicting the transient response of both sensible and latent heat storage units, over a variety of geometry. Phase change units have some advantages over sensible heat units, due to its higher storage capacity (per unit volume) and lower average chiller operation, which impacts the system performance as a whole. Accordingly, the present work is dedicated to the development and solution of a simple mathematical model for the heat transfer phenomena within a latent heat storage unit, consisting of a tank containing phase change material (PCM) enclosed within spherical capsules. Several assumptions are made with a view to maintain the model as simple as possible, without disregarding a careful reflection about its accuracy and impact on the reliability of the solution. In particular, a simulation is carried out for small values of the Stefan number (Ste), which allows the solidification to be predicted by a quasi-stationary model. The model results in a system consisting of a partial differential parabolic equation, which describes the temperature field along the channel, and an integral equation, which is to represent the phase change evolution within a spherical capsule. The model is solved using a fully implicit finite-volume discretization technique. To obtain more general results, all the physical variables are arranged in non-dimensional groups, the influence of which on the response of the storage unit is evaluated.

Keywords: Phase Change, Packed Beds, Thermal Storage.

1. Introduction

Thermal energy storage's role on the struggle for a more rational use of energy resources has increased over the last decades. This could be explained by the wide variety of applications in which it can be found, such as in solar energy, air-conditioning and power generation, to name a few. Thermal energy can be stored as both sensible and latent heat. The latter allows a higher storage capacity per unit volume, as well as a storage constant temperature. The use of sensible heat, however, allows constant heat transfer rates, which cannot be accomplished using PCMs due to the variation of the thermal resistance imposed by the solidified or melted layer. There are a number of techniques of latent heat storage, but they can be generally divided into two main categories [1-2]:

- "Bulk storage", where the total amount of PCM is fully contained within a single volume.
- "Encapsulation", where the total amount of PCM is divided over a number of capsules.

The objective of this work is to investigate why encapsulation has become more popular than bulk storage over the last years, that is, why should one use several (smaller) capsules rather than just one to contain a certain amount of PCM. The present study uses more familiar non-dimensional parameters, when compared to previous efforts. Accordingly, the transient response of a latent heat storage unit, as described in Figure 1 will be studied. The PCM is contained in spherical capsules, randomly disposed within the storage tank.

2. Mathematical Model

A model for thermal energy storage using rectangular containers has been developed [3], which takes into account the unavoidable sensible heat which accompanies latent heat storage. A numerical code [4, 5] to predict the charge and the discharge of latent heat storage within spherical capsules was developed, however the analysis was restricted to physical parameters, instead of non-dimension parameters.

Corresponding Author: Carlos Eduardo Nóbrega, e-mail: nobrega@pobox.com

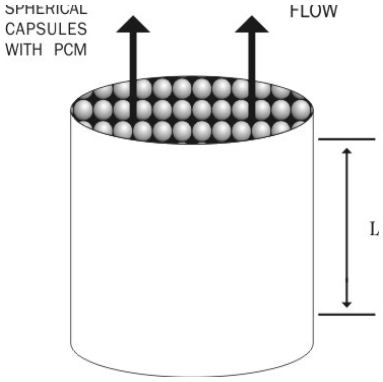

Figure 1: Storage Tank

Reference [6] considers the use of several PCMs in a system consisting of multiple shell-and-tube thermal storage units. Reference [7] presents a model which takes under consideration both PCM sensible heat and temperature distribution during phase change, and suggested the use of several PCMs with different melting temperatures, in order to achieve more uniform heat transfer rates throughout the tank. Although several works have been recently devoted to the study of encapsulated PCMs ([8], [9]), a simple comparison between bulk and fragmented volumes seems to have been disregarded by previous efforts. The mathematical model is based on some simplifying assumptions:

1) The tank is represented by a control volume with one inlet and one outlet.
2) The tank is initially "hot", filled with both PCM and transport fluid at phase change temperature T_m.
3) All walls are perfectly insulated.
4) All vertical walls are impermeable.
5) The thermal capacitance and resistance of the tubes walls are negligible.
6) The sensible heat stored within the PCM is small when compared to the latent heat.
7) The spherical capsules bed is represented by a porous media, through which the transport fluid flows. The heat transfer is represented by a heat generation rate per unit volume, which is distributed along the flow direction

All the assumptions are realistic within the scope of the present study. The first four assumptions, for instance, are common to all model and experimental devices. The fifth is as good as smaller are the thickness and thermal conductivity of the capsules, which is also a common feature of actual devices. The sixth is reasonable for small values of the Stefan number, which is frequently the case in latent heat units. This assumption allows the use of a simple and yet effective phase-change model. The seventh assumption enables us to represent this two-dimensional domain by two separate domains, which are coupled through the heat generation rate.

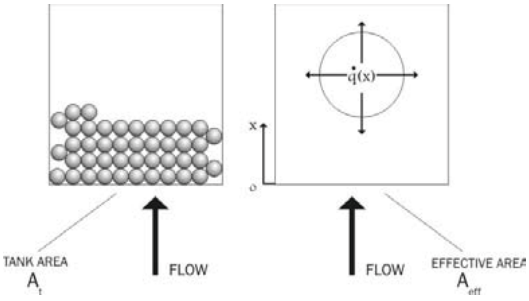

Figure 2: A comparison between physical and numerical domains

As depicted in Figure 2, the flow cross-section in the real tank is wider than in the model. This happens because when one assumes a uniform flow field throughout the tank, a representative area can be found only on a volume rate basis:

$$\overline{A}_{eff} = \frac{\left(V_T - NS\frac{4\pi}{3}R_0^2\right)}{L} \tag{1}$$

$$u = \frac{\dot{V}}{\overline{A}_{eff}} \tag{2}$$

This enables us to write the one-dimensional transport equation, from which the transport fluid temperature field will be obtained:

$$\rho\ Cp\left(\frac{\partial T}{\partial t} + u\frac{\partial T}{\partial x}\right) = K\frac{\partial^2 T}{\partial x^2} + \dot{q} \tag{3}$$

where $\dot{q}$ is a heat generation rate (per unit volume) which is locally distributed according to

$$\dot{q} = N_s \frac{(T_m - T(x))}{W_{th}(x)} \frac{1}{HA_{eff}} \quad (4)$$

which represents the heat transferred from the PCM to the transport fluid. The overall thermal resistance W_{th} combines in series the thermal resistances offered by convection through the capsules surface and conduction through the progressively increasing layer, as represent by Figure 3.

$$W_{th}(x) = \frac{1}{4\pi K_{pcm}} \left[\frac{1}{R_m(x)} - \frac{1}{R_0} \right] + \ldots \quad (5)$$

$$\ldots + \frac{1}{4\pi h R_0}$$

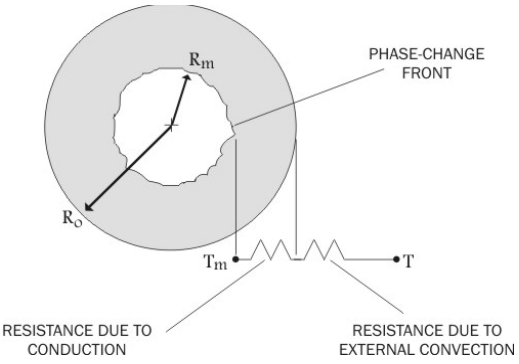

Figure 3: Schematic of the heat transfer process within a capsule

The position of the solidification front R_m will be found by using a quasi-stationary model of change of phase [10]. Accordingly,

$$\frac{k_{pcm}}{R^2} \frac{\partial}{\partial R} \left(R^2 \frac{\partial T_{pcm}}{\partial R} \right) = 0 \quad (6)$$

$$R_0 > R > R_m \quad , \quad t > 0$$

Subjected to the following boundary conditions:

$$T_{pcm}(R_m, t) = T_m \quad (7a)$$

$$K_{pcm} \left. \frac{\partial T_{pcm}}{\partial R} \right|_{R_0} = h \left[T(t) - T_{pcm}(R_o, t) \right] \quad (7b)$$

$$t > 0$$

to obtain

$$T_{pcm}(R,t) = T_m + \left[(T - T_m) \frac{1 - R_m / R_0}{1 - \left(1 - \frac{k_m}{hR_0} \right) \frac{R_m}{R_0}} \right] \quad (8)$$

$$R_0 \le R \le R_m \quad t > 0$$

Knowing the temperature profile, it is possible to apply a differential balance on the solidification front

$$\rho_{pcm} \gamma \frac{\partial R_m}{\partial t} = -K_{pcm} \left. \frac{\partial T_{pcm}}{\partial R} \right|_{R_m} \quad t > 0 \quad (9)$$

(5)

in which γ is the latent heat of the phase change material. Applying the initial condition to Eq. (9)

$$R_m \ (0) = R_0 \quad (10)$$

And integrating from 0 to an unspecified time t results in

$$2\left(1 - \frac{2K_m}{hR_o}\right)\left(\frac{R_m}{R_0}\right)^3 - 3\left(\frac{R_m}{R_0}\right)^2 + \cdots$$
$$\ldots 1 + \frac{2K_m}{hR_0} = \frac{6K_m}{\rho_{pcm} \gamma R_0^2} \int_0^t (T - T_m)\, dt \quad (11)$$

Since one cannot obtain an explicit form for R_{fs}/R_0, it is necessary to solve (11) simultaneously with (3). In order to conduct a more concise analysis, it is advisable to rewrite (11) and (3) in non-dimensional forms. Defining the following non-dimensional parameters,

$$\theta = \frac{(T - T_m)}{(T_{in} - T_m)} \quad (12)$$

$$\tau = \frac{tu}{L} \quad (13)$$

$$x^* = \frac{x}{L} \quad (14)$$

$$R^* = R_m(x) / R_0 \quad (15)$$

$$k^* = k_{pcm} / k \quad (16)$$

$$Pe = Lu / \alpha \quad (17)$$

$$Bi = hR_0 / k_{pcm} \quad (18)$$

and replacing them in (3)

$$\frac{\partial\theta}{\partial\tau} + \frac{\partial\theta}{\partial x^*} = \frac{1}{Pe} \frac{\partial^2\theta}{\partial x^{*2}} - \cdots$$
$$\cdots \; 4\pi \frac{k^*}{Pe} N_s \frac{\left(L/R_0\right)}{\left(D_T/2R_0\right)^2} \frac{\theta}{\left(\frac{1}{Bi} + \frac{1}{R^*} - 1\right)} \quad (19)$$

$$\theta(x^*, 0) = 0 \quad (19a)$$

boundary conditions

$$\theta(0, \tau) = 1.0 \quad \tau > 0 \quad (19b)$$

$$at\ x^* = 1, \quad \frac{\partial\theta}{\partial x^*} = 0 \quad (19c)$$

Also, defining the modified Stefan number

$$Ste_{mo} = \frac{\rho\, C_p (T_m - T_{in})}{\rho_{pcm}\gamma} \quad (20)$$

and introducing the non-dimensional variables into (11) one would obtain

$$2\left(1 - \frac{1}{Bi}\right) R^{*3} - 3R^{*2} + 1 + \frac{2}{Bi} = \cdots$$
$$\cdots 6 \frac{k^*}{\rho^*} \frac{Ste_{mo}}{\mathrm{P}e} \left(\frac{L}{R_0}\right)^2 \int_0^\tau \theta d\tau \quad (21)$$

The solution is then obtained by solving simultaneously (19) and (21). The domain relative to (19) is divided into a finite number of volumes by using the upwind scheme to represent advection and the fully implicit scheme for the transient term, [11-12]. The resulting tri-diagonal matrix is then solved for each time step, and after the temperature field ($\theta(x^*)$) is obtained, the radii ratio field $R^*(x^*)$ is calculated from (21). Since the value of the integral in (21) is available from simple numeric integration, this equation turns into a simple algebraic cubic equation for R^*, which is solved by Newton's method. Accordingly, a discretization scheme is only required by (19). It is convenient to introduce a geometric aspect ratio for a capsule, as well as the effectiveness and number of thermal units:

$$CR = D_t / 2R_0 \quad (22)$$

$$NTU = 12\pi \frac{k^*}{Pe} \frac{CR^2}{\sqrt{3}} \frac{1}{\left(\frac{1}{Bi} + \frac{1}{R^*} - 1\right)} \quad (23)$$

$$\varepsilon = 1 - \theta_{out} \quad (24)$$

In order to asses the effectiveness regarding the second law of thermodynamics, it is convenient to redefine the non-dimensional temperature as

$$\theta^* = (T - T_m) / T_m \quad (25)$$

Consider the charge process, in which the PCM material is melted by the surrounding fluid at a higher temperature. Since the present analysis disregards fluid friction, the only mechanism of entropy generation is the heat transfer under a finite temperature difference. Accordingly, the local and total entropy generation rates are given by

$$\dot{\sigma}(x) = \left[\frac{\dot{Q}}{T_m} - \frac{\dot{Q}}{T(x)}\right] \quad (26)$$

(20)

$$\dot{\sigma} = \sum_{i=1}^{N} \left[\frac{\dot{Q}}{T_m} - \frac{\dot{Q}}{T(x)}\right] \frac{\Delta x}{L} \quad (27)$$

This can be rearranged as

$$\frac{\dot{\sigma} T_m}{\dot{Q}} = \sum_{i=1}^{N} \left[1 - \frac{T_m}{T(x)} \right] \Delta x^* \tag{28}$$

Recalling that $\theta^* + 1 = T / T_m$ (29)

$$\frac{\dot{\sigma} T_m}{\dot{Q}} = \sum_{i=1}^{N} \left[1 - \frac{1}{\theta^* + 1} \right] \Delta x^* \tag{30}$$

Equation (30) shows that the entropy generation tends to a minimum as $\theta^* \to 0$, but according to Equation (25) $T \to T_m$ and the charge process would then require an infinity time. Conversely, as $\theta^* \to \infty$, the charge process tends to be completely irreversible as the entropy generation tends to a maximum. Its possible to define a second law efficiency as

$$\eta = 1 - \frac{\dot{\sigma} T_m}{\dot{Q}} \tag{31}$$

3. Results

Since the mathematical model adopted disregards the sensible heat capacity of the PCM, the storage unit is considered to be initially at the phase change temperature. Accordingly, the phase-change front shields the capsule core (which remains at T_m throughout the process) and all the heat flux is dedicated to the phase change progress. A typical evolution of the phase-change position field with time is illustrated by Figure (4). At the onset of the discharge process, the radial position of the phase change equals the capsule radius, i.e., $R^* = 1.0$. It can be seen that the phase change quickly develops nearby the tank inlet, $x^* = 0$, where temperatures are always higher. By the end of the discharge process, R^* tends to zero throughout the unit. Figure (5) shows the evolution of the effectiveness along the discharge processes. It is observed that lower values for Pe allow a much more effective energy recovery than higher values. Although all the energy stored is always fully recovered, a high effectiveness implies a high difference between the inlet and outlet temperatures, consequently reducing the required time to discharge the unit.

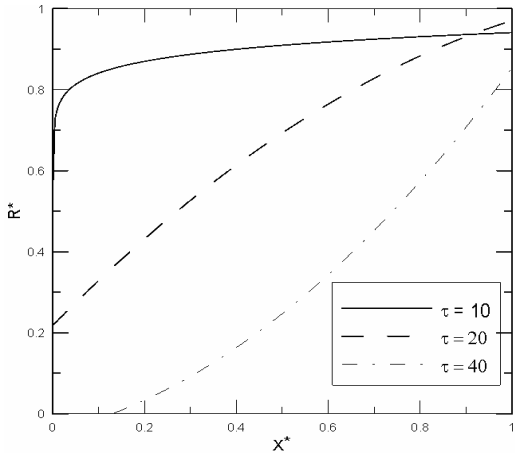

Figure 4: Evolution of the phase-change position field with dimensionless time, Bi = 0.1, Pe =100, CR = 25.

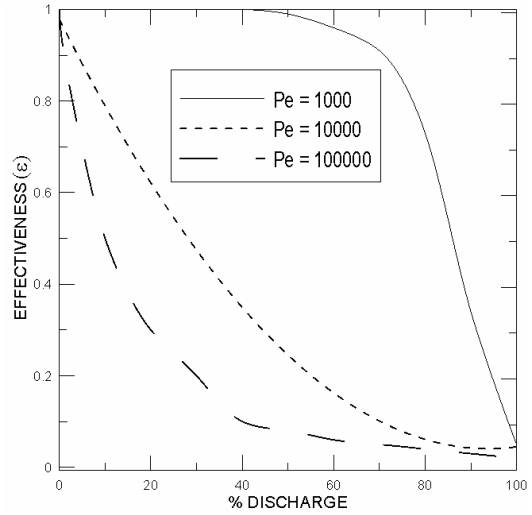

Figure 5: Influence of Pe over the discharge effectiveness, Bi = 0.1, CR = 25.

Figure (6) shows that, for a given volume of PCM, an increase in the number of capsules, i.e., an increase in the capsule aspect ratio CR causes a continuous increase in the effectiveness. The decrease in the value of Bi is associated to the decrease in diameter, as a consequence of the increased number of capsules. Accordingly, the increasing in the number of capsules represents a trade-off between the increase of the total heat transfer area and the increase of the thermal resistance offered by an individual capsule. It can be concluded that the increased heat transfer surface offsets the decreased Bi values, providing

better heat transfer rates. The area enclosed by each curve is the same, since it represents the energy stored within the fixed volume of PCM.

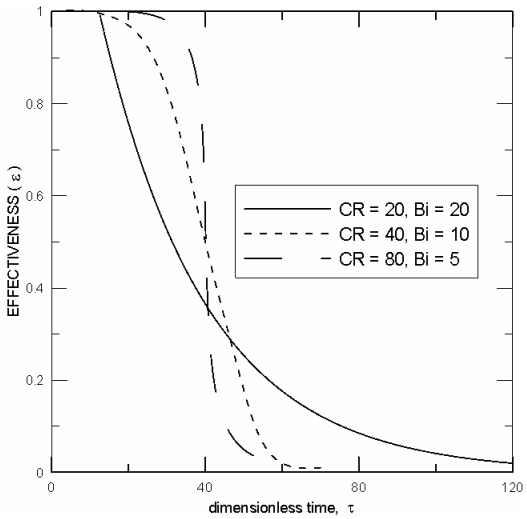

Figure 6: Influence of the number of capsules over the effectiveness, Pe =10^4 , K^*=1.

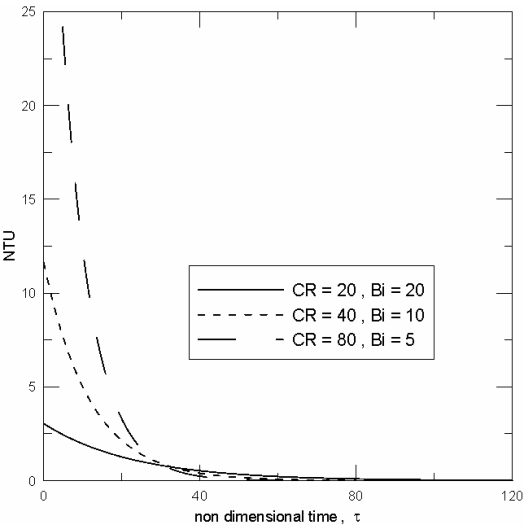

Figure 7: Influence of the number of capsules over the NTU evolution, Pe =10^4, K^*=1.

Figure (7) shows that an increase in the number of capsules causes a significant increase in the initial value of NTU, which explains the increased effectiveness observed in the previous figure. The continuous decrease in NTU with time is a consequence of the phase change progress. Equation (23) shows that the NTU will range from an initial value to null, as R^* progresses from one (at the onset of the process) to zero (as the phase change is completed).

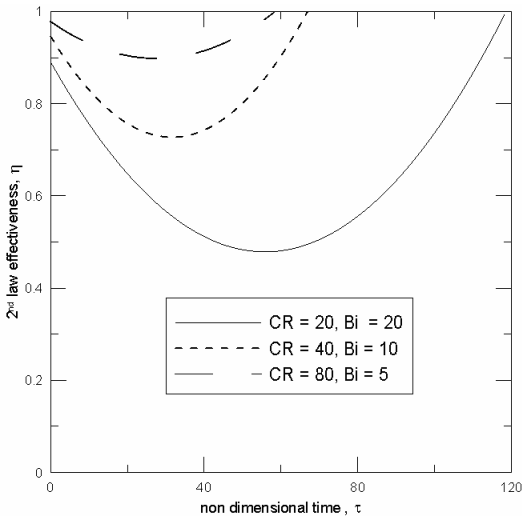

Figure 8: Influence of the number of capsules over the 2nd law effectiveness, Pe =10^4, K^*=1..

Figure (8) illustrates the influence of CR over the 2nd law efficiency of the thermal storage process. It is interesting that the thermal storage unit is in thermal equilibrium with the surrounding fluid at the onset and at the end of the charge process, which implies $\eta = 1$ at both instances. Accordingly, the value of η necessarily reaches a minimum during the process. It can be seen that the number of capsules has a major impact in the entropy generation associated to the heat transfer. Figure (9) shows the impact of increasing the PCM thermal conductivity, for a small number of capsules (CR =20). It is shown that the effectiveness of the energy recovered can be significantly increased for an increased value of K^*. Figures (10) and (11) also confirm that increasing the value of K^* has an equivalent effect of increasing the number of capsules CR. Accordingly, this allows the design of thermal storage units with lesser number of capsules, which have a significant contribution to the initial cost of such systems. A lesser number of capsules filling a given volume will also imply in greater void fractions, demanding smaller pumping power to drive the flow across the packed bed, thus allowing a reduction on the operation cost.

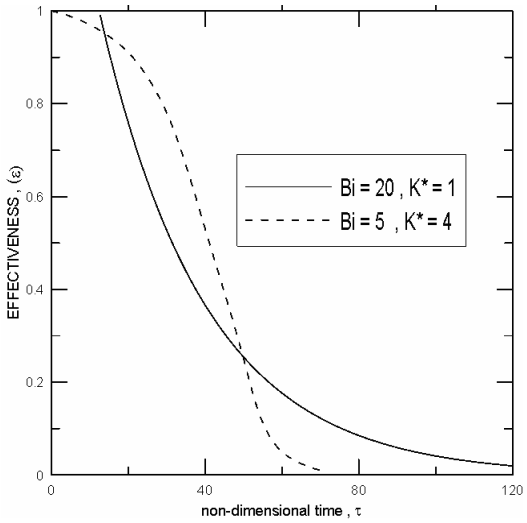

Figure 9: Influence of the non-dimensional conductivity over the effectiveness, Pe =10^4, CR=20.

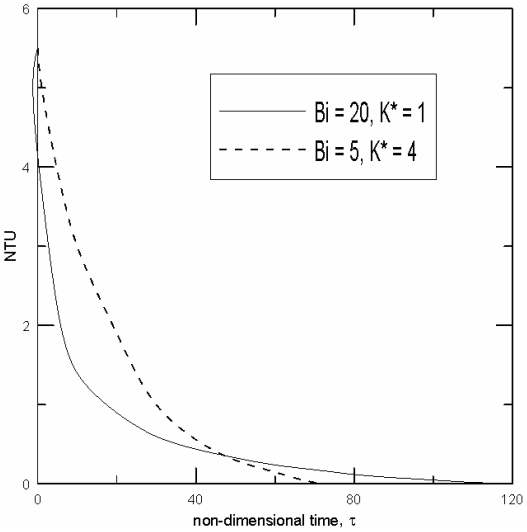

Figure 10: Influence of the non-dimensional conductivity over NTU, Pe =10^4, CR=20.

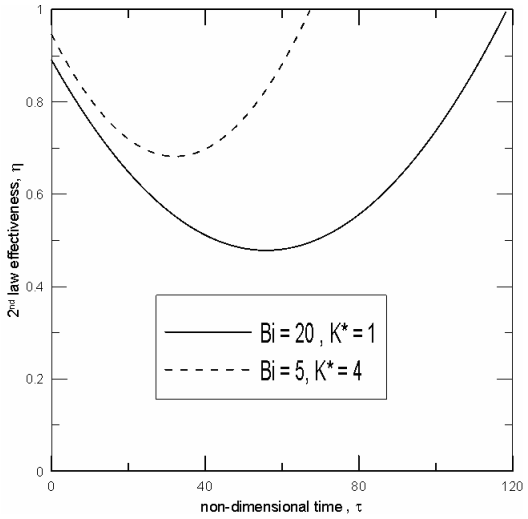

Figure 11: Influence of the non-dimensional conductivity over 2nd law effectiveness, Pe =10^4, CR=20.

4. Conclusions

A simple mathematical model for the thermal storage within phase change packed beds has been developed and solved using a discretization technique. The results show that the current trend in the design of such systems in fact allows a continuous reduction on the time required by the storage process. The use of encapsulated media simultaneously offers both higher heat transfer areas and average thermal resistances, one effect tending to offset the other. The effectiveness however, always increases with the number of capsules CR, regarding both first and second laws of thermodynamics. It was also shown that the number of thermal units (NTU) is inversely proportional to the thermal capacitance of the flow, represented by Pe. Accordingly, an excessively high value for Pe might result in an extremely ineffective energy and exergy recovery. The results of increased values for CR can be alternatively reached by increasing the values of K^*, even for a smaller number of capsules. This might represent a significant contribution to the economical feasibility of thermal storage units.

Nomenclature

A_{eff}	effective flow area
Bi	Biot Number
c_p	specific heat, J/(kg K)
CR	aspect ratio
D_t	tank diameter, m
h	heat transfer coefficient, W/(m^2 K)
k	conductivity, W/(mK)
k^*	conductivity ratio
L	tank height, m
$\dot{m}$	mass flow rate, kg/s
N_s	number of capsules
PCM	phase change material
Pe	Peclet number
R	radial coordinate, m
R_m	phase change position, m
R_0	capsule outer radius, m
R^*	dimensionless phase change position
Ste_{mo}	modified Stefan number
T	temperature, °C
T_m	melting temperature, °C
u	uniform flow velocity, *m/s*
V_t	tank volume, m^3
$\dot{V}$	volume flow rate, m^3/s
x	longitudinal coordinate
x^*	dimensionless longitudinal coordinate
W_{th}	local thermal resistance, m/(WK)

Greek symbols

ε	effectiveness
γ	latent heat, kJ/kg.K
θ	dimensionless temperature
τ	dimensionless time
ρ	density, kg/m^3
ρ^*	dimensionless density

Subscripts and superscripts

in	inlet conditions
pcm	phase change material

References

[1] Dorgan, C.E; Elleson, J.S., 1993, "Design Guide for Cool Thermal Storage", ASHRAE, Atlanta, GA

[2] Mehling, H; Cabeza, L., 2010, "Heat and Cold Storage with PCM", Springer Verlag, Berlin.

[3] Prusa, G.M. Maxwell, K.J. Timmer, ASHRAE Report, Project Number 481-RP (1989).

[4] Arnold, D., 1990, "Dynamic simulation of encapsulated ice stores, part I – the model", ASHRAE Transactions, 96(1), pp.1103-1110.

[5] Arnold, D**.,** 1991, "Laboratory Performance of encapsulated ice store", ASHRAE Transactions, 97(2), 1170-1178.

[6] Farid, M. and Kanzawa, A, 1989, "Thermal performance of a heat storage module using PCM´s with different melting temperatures: Mathematical Modelling", Journal of Solar Energy Engineering, 111, pp.152-157

[7] Gong, Z.X. and Mujundar, A., 1997, "Thermodynamic optimization of the thermal process in energy storage using multiple phase change materials", Applied Thermal Engineering, vol.17, (11), pp. 1067-1083.

[8] Hendra R., Hamdani H, Mahia T.M., Majuski H., 2005, " Thermal and melting heat transfer characteristics in a latent heat storage system using mikro", Applied Thermal Engineering 25(11),pp: 1503-1515.

[9] Vyshak NR, Jilan G., 2007, "Numerical analysis of latent heat thermal energy storage system", Energy Conversion and Management, (48), pp. 2161-2168.

[10] Alexiades, V., Solomon, A.D**.**, 1993. "Mathematical Modelling of Melting and Freezing Processes", Hemisphere Publishing Corporation, Washington

[11] Patankar, S.V, 1980, "Numerical Heat Transfer and Fluid Flow", Hemisphere Publishing Corporation, Washington.

[12] Jaluria, Y, 2003, "Computational Heat Transfer," Taylor & Francis, New York.

Energy and Exergy Analyses of a Closed Thermochemical Energy Storage System: Methodology and Illustrative Application

Marc A. Rosen, Ali Haji Abedin

University of Ontario Institute of Technology, Oshawa, Ontario, Canada

Abstract: Thermal energy storage (TES) is an advanced technology for storing thermal energy that can mitigate environmental impacts and facilitate more efficient and clean energy systems. Among various types of TES systems, thermochemical TES is a promising method with the potential for higher energy storage densities and greater compactness. The assessment of such systems is enhanced greatly when exergy analysis is used to complement energy analysis. Here, a general closed thermochemical TES is investigated using energy and exergy analyses. An example using experimental data is presented to illustrate the analyses. Efficiencies are determined for the overall TES cycle and its charging, storing and discharging processes. The overall energy and exergy efficiencies for system considered in the example are determined to be 50% and 9%, respectively. This result indicates that the efficiency of the thermochemical TES based on exergy is much lower than that based on energy, and that there is a significant margin for loss reduction and efficiency improvement.

Keywords: Thermal energy storage, Thermochemical energy storage, Energy analysis, Exergy.

1. Introduction

Thermal energy storage is the temporary holding of thermal energy in the form of hot or cold substances for later use. TES is a significant technology in systems involving renewable energies as well as other energy resources as it can make their operation more efficient. Also, TES is helpful for balancing between the supply and demand of energy [1].

There are three main types of TES: Sensible, latent and chemical. Sensible TES systems store energy by changing the temperature of the storage medium, which can be water, brine, rock, soil, etc. Latent TES systems store energy through phase change, e.g., cold storage via water/ice and heat storage by melting paraffin waxes. In thermochemical energy storage, energy is stored after a dissociation reaction and then recovered in a chemically reversed reaction. Thermochemical energy storage has a higher storage density than the other types of TES, allowing large quantities of energy to be stored using small amounts of storage substances. The selection of a TES system for an application is a complex process, which is dependent on such factors as storage duration, economics, supply and utilization temperature requirements, storage capacity, thermodynamic losses and available space.

Various aspects of thermal energy storage have been studied by many researchers for several types of thermal storage systems, including general TES [1, 2], sensible TES [3] and latent TES [4]. A comprehensive review of thermochemical energy storage in 1989 by Wettermark [5] describes the main concepts, criteria for choosing appropriate storage media and candidate reaction pairs. Several investigations of thermochemical TES have been reported [6-12].

Exergy methods are used in this article. Exergy provides a useful complement to energy since energy analysis is based on the first law of thermodynamics and exergy analysis is based mainly on the second law. Numerous examples have been reported of energy and exergy analyses of TES-related systems relevant to this article. These include exergy assessments of TES systems [13], ammonia-based solar thermochemical power systems [14, 15], aquifer TES systems [16] and latent TES systems [17].

In this article, energy and exergy analyses are carried out of thermochemical TES. An illustrative example is included based experimental data. The objective is to improve understanding and thereby support development and ultimate implementation of the technology.

2. Thermochemical energy storage

In general, a thermochemical TES cycle includes three main processes, which are illustrated in Fig. 1 for a closed thermochemical TES:

Corresponding Author: Marc A. Rosen, Email: marc.rosen@uoit.ca

- Thermal energy is absorbed from an energy resource in this endothermic process and used for dissociation of the thermochemical material. The required energy is equivalent to the heat of reaction or enthalpy of formation.
- Storing: After the charging process, two materials (A and B) with different properties are formed that can be stored.
- Discharging: Materials A and B are combined in this exothermic process and the energy released from this reaction permits the stored energy to be recovered.

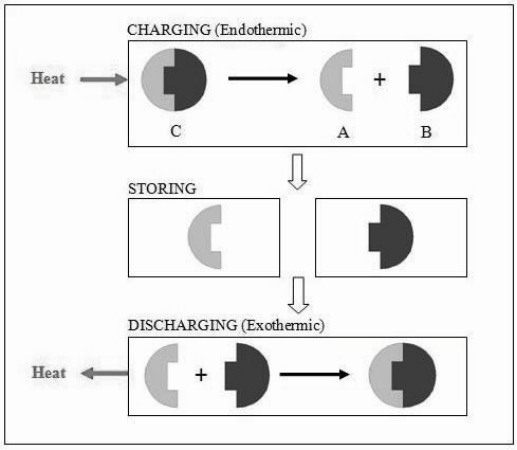

Fig. 1. Processes in a closed thermochemical TES cycle: charging, storing and discharging.

3. Energy and exergy analyses of closed thermochemical TES

A general closed thermochemical TES is considered and energy and exergy analyses are performed. This system considered consists of a working fluid and a thermochemical material. Thermal energy from an energy resource is transferred to a working fluid. This thermal energy provides the necessary energy for dissociation of the thermochemical material. After a storing period, a charging period occurs during which energy released from synthesis of thermochemical material is absorbed by the working fluid for heating purposes. The analysis is limited to closed TES systems where internal substances are separate from the heat transport fluid.

The following assumptions are made here:

- Chemical reactions within the reactor occur at constant pressure.
- Work interactions into and out of the control volume are neglected, as are kinetic and potential energy. Thus pump, compressor and fan work are neglected.
- During charging, the initial temperature of the thermochemical material is assumed to be that of the reference environment T_0. There are no energy losses during the storing period and thermochemical materials are stored at the reference-environment temperature.
- The physical exergy change of components is neglected relative to chemical exergy changes.

3.1. Charging process

A general charging process for a thermochemical TES is illustrated in Fig. 2. The required temperature for dissociation of the thermochemical material is denoted T_s and the initial temperature of thermochemical material is that of the reference environment T_0. A heat transport fluid passes through the reactor, entering at temperature T_1 and exiting at T_2 is the outlet temperature of the charging reactor. The thermochemical TES medium changes during charging from material C at the start of the process to materials A and B after the dissociation reaction occurs.

3.1.1. Energy balance for charging

An energy balance for the charging process, accounting for the net heat input and the accumulation of energy in the storage material, as well as the heat loss, Q_{loss}, can be written as

$$Net\ energy\ input - Heat\ loss = Energy\ accumulation\ in\ TES$$

or

$$m_c C_p (T_1 - T_2) - Q_{\text{loss}} = \Delta H_{\text{reaction}} \quad (1)$$

where m_c and C_p are the mass and specific heat at constant pressure of the working fluid, T_2 and T_1 are the final and initial temperatures of the working fluid and $\Delta H_{\text{reaction}}$ is the enthalpy change of the reaction. The term Q_{loss} denotes the total heat loss, which can be expressed as follows:

$$Q_{\text{loss}} = Q'_{\text{loss}} + \left(Q_{\text{cooling}} - Q_{\text{preheat}}\right) \quad (2)$$

where Q'_{loss} denotes the total heat loss for the charging process expressed in terms of the heat transfer between the reactants and the reactor surface and $(Q_{\text{cooling}} - Q_{\text{preheat}})$ corresponds to the net cooling loss before and after the dissociation reaction. The energy (or first-law) efficiency of the charging process can consequently be expressed as follows:

$$\eta_c = \frac{\Delta H_{reaction}}{m_c C_p (T_1 - T_2)} \quad (3)$$

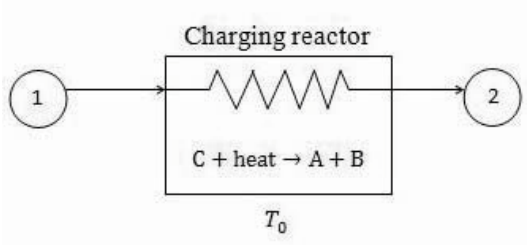

Fig. 2. Charging process in thermochemical TES.

3.1.2. Exergy balance for charging

A general exergy balance for this system is

$Exergy\ input - \epsilon_D - \epsilon_{loss} = Exergy\ accumulation$

Here,

$$Exergy\ input = m_c[h_1 - h_2 - T_0(s_1 - s_2)] \quad (4)$$

where h_1 and h_2 denote the specific enthalpy of the charging fluid at the input and output conditions, s_1 and s_2 denote the specific entropy of the charging fluid at the input and output conditions. Also, ϵ_D denotes the exergy destruction and T_0 the reference temperature. Here,

$$\epsilon_{loss} = \epsilon'_{loss} + (\epsilon_{cooling} - \epsilon_{preheat})$$

$$Exergy\ accumulation = \Delta\epsilon_{reaction}$$

where $\Delta\epsilon_{reaction}$ denotes the exergy accumulation in the charging process. The evaluation of the exergy accumulation during reaction $\Delta\epsilon_{reaction}$ is now considered. The exergy of the control volume before the reaction is the sum of the exergies of the reactants before the reaction. This exergy includes physical, potential, kinetic and chemical exergy components of the reactants. As pointed out earlier, potential and kinetic energy are neglected. Consequently, we focus on the physical and chemical exergies of the reactants. The chemical exergy of compounds is determined following the treatment in [18]. The standard chemical exergy of a chemical compound ϵ_{chn} can be calculated by means of the exergy balance for a reversible reaction:

$$\epsilon_{chn} = \Delta G_f + \sum_e n_e \epsilon_{chne} \quad (5)$$

Here, ΔG_f denotes the Gibbs energy of formation, n_e denotes the amount of element e (in kmol), and ϵ_{chne} denotes the standard chemical exergy of the element. The physical exergy of a compound is evaluated as follows [19]:

$$\epsilon_{ph} = m[(h - h_0) - T_0(s - s_0)] \quad (6)$$

The exergy change (exergy accumulation) associated with the reaction can be evaluated as

$$\Delta\epsilon_{reaction} = \epsilon_{tot,products} - \epsilon_{tot,reactants} \quad (7)$$

We can evaluate the exergy (second-law) efficiency of the charging process ψ_c as follows:

$$\psi_c = \frac{\epsilon_{tot,products} - \epsilon_{tot,reactants}}{m_c[h_1 - h_2 - T_0(s_1 - s_2)]} \quad (8)$$

3.3. Discharging process

A general discharging process for a closed thermochemical TES is illustrated in Fig. 3. In this process, components A and B are combined, allowing the reaction to occur. The energy released by this exothermic reaction is recovered by a working fluid in a closed TES. The working fluid enters the reactor at T_3 and exits at T_4.

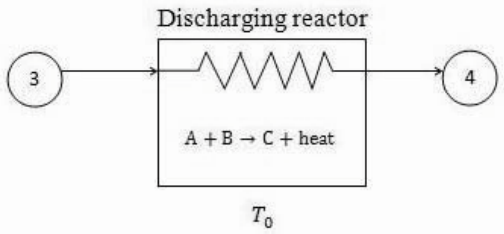

Fig. 3. Discharging process in thermochemical TES.

3.3.1. Energy balance for discharging

The net input energy is the energy released by the reaction (enthalpy of formation). We can write an energy balance for this process as follows [1]:

$-(Energy\ recovered + Heat\ Loss) = Energy\ accumulation$

We can evaluate discharging energy efficiency as

$$\eta_d = \frac{m_d C_p (T_4 - T_3)}{\Delta H_{reaction}} \quad (9)$$

3.3.2. Exergy balance for discharging

We can write an energy balance for discharging as

$Exergy\ recovered - Exergy\ destruction - \epsilon_{loss} = \Delta\epsilon_{reaction}$

and the discharging exergy efficiency as

$$\psi_d = \frac{m_d[h_4 - h_3 - T_0(s_4 - s_3)]}{\epsilon_{tot,products} - \epsilon_{tot,reactants}} \quad (10)$$

3.4. Overall TES process

3.4.1. Overall energy balance and efficiency

An energy balance for the overall storage process can be written as

$$m_c C_p (T_1 - T_2) - m_d C_p (T_4 - T_3) - Q_{loss,tot} = \Delta E \quad (11)$$

where ΔE denotes the energy accumulation, given as the difference between the initial and final

energy contents of the storage, and $Q_{\text{loss,tot}}$ is the total heat loss during the process (charging, storing and discharging). For the case of a complete cycle with identical initial and final states, $\Delta E = 0$ and the overall energy balance simplifies.

The energy efficiency for the overall storage process can be written as follows:

$$\eta_{\text{o}} = \frac{m_{\text{d}} C_p (T_4 - T_3)}{m_{\text{c}} C_p (T_1 - T_2)} \quad (12)$$

3.4.2. Overall exergy balance and efficiency

Similarly, an exergy balance for the overall storage process can be written as

$$Exergy\ input - (Exergy\ recovered + \in_{\text{loss,tot}}) - \in_{\text{D,tot}} = \Delta\in$$

Here, $\in_{\text{loss,tot}}$ and $\in_{\text{D,tot}}$ denote the total exergy loss and the total exergy destruction during the overall TES process, accounting for charging, storing and discharging. Exergy losses are related to heat losses during each process. The exergy accumulation $\Delta\in$ is the difference between the initial and the final exergy contents of the storage. For the case of a complete cycle with identical initial and final states, $\Delta\in = 0$ and the overall energy balance simplifies.

The exergy efficiency for the overall storage process can be expressed as follows:

$$\psi_{\text{o}} = \frac{m_{\text{d}}[h_4 - h_3 - T_0(s_4 - s_3)]}{m_{\text{c}}[h_1 - h_2 - T_0(s_1 - s_2)]} \quad (13)$$

4. Illustrative example

To illustrate the analysis and efficiencies of a thermochemical TES system, we consider an existing system for which experimental data have been reported [8].

4.1. System description

This illustrative example is based on the integration of a flat plate solar collector and a chemical (solid/gas sorption) process using bromide strontium as the reactant and water as the working fluid in a closed TES system. This TES enables a high energy density relative to other types of TES systems as well as the possibility of energy storage without large losses. The system is intended to provide heating and cooling storage functions to facilitate direct floor heating and cooling. The storage reaction can be expressed as

$$\text{SrBr}_2 \cdot \text{H}_2\text{O} + 5\text{H}_2\text{O} \leftrightarrow \text{SrBr}_2 \cdot 6\text{H}_2\text{O} + 5\Delta H$$

where $\Delta H = 3732\ \text{kJ/kg}\ \text{H}_2\text{O}$.

In this reaction, $\text{SrBr}_2 \cdot \text{H}_2\text{O}$ and $\text{SrBr}_2 \cdot 6\text{H}_2\text{O}$ are in solid phase and H_2O is a vapor. We have selected data for the heating operation (floor heating) during the mid seasons of fall and spring.

The system is comprised of two heat transfer loops. The first is between a plate-type heat exchanger and solar panels, and the second is between the heat exchanger and the building floor. The mass of $\text{SrBr}_2 \cdot \text{H}_2\text{O}$ is 171.3 kg and the mass of exchanged water in the reactor is 57.9 kg. The water (working fluid) flows at a rate of 6 l/min. The thermodynamic constraints for the reactive pair and for mid-season conditions follow:

- Maximum output temperature of the flat-plate solar collector = 80 ℃
- Temperature of the external environment = 7 ℃
- Inlet temperature for floor heating = 35 ℃
- Solid/gas equilibrium temperature for the dehydration phase = 43 ℃
- Solid/gas equilibrium temperature for the hydration phase= 43 ℃

The total volume of the prototype reactor is 1 m^3 and the system is able to store 60 kWh in heating.

4.2. Energy analysis of TES processes

The energy efficiencies are determined for charging and discharging for the considered thermochemical TES, as well as for the overall process. Note that the energy efficiency for the storing period is not discussed, as it is 100%.

4.2.1 Charging

The charging energy efficiency is calculated using (3). The solid/gas reaction is

$$\text{SrBr}_2 \cdot 6\text{H}_2\text{O} + \text{heat} \rightarrow \text{SrBr}_2 \cdot \text{H}_2\text{O} + 5\text{H}_2\text{O}$$

According to [8], the dehydration cycle occurs over 42 hours. The energy efficiency of charging (i.e., dehydration) can be evaluated with the following data, which are obtained using EES (Engineering Equation Solver) software:

- Water input temperature, $T_1 = 70$ ℃
- Water output temperature, $T_2 = 50$ ℃
- $\rho = 983.2\ \text{kg/m}^3$ (at the mean temperature of the inlet and outlet conditions of the working fluid, $T_{\text{mean}} = (T_1 + T_2)/2 = 60$ ℃)
- $C_p = 4.183\ \text{kJ/kg K}$ (at $T_{\text{mean}} = 60$ ℃)
- Nominal flow of pouring water (working fluid) $= 6\ \text{l/min}$
- $m_{\text{c}} = \rho V = (983.2\ \text{kg/m}^3 \times 10^{-3}\ \text{l/m}^3) \times (6\ \text{l/min} \times 60\ \text{min/hour} \times 42\ \text{hour}) = 14{,}866\ \text{kg}$
- Mass of water as product= 57.9 kg

- Dehydration duration = 42 hours

To calculate the energy efficiency of the dehydration process, (3) is used. For this example, the value of $\Delta H_{\text{reaction}}$ is the enthalpy of separation reaction which is equal to 3732 kJ/ kg H_2O. But there is 57.9 kg water in this closed loop system, so the enthalpy of the charging reaction regarding the number of moles of water (5 moles) can be evaluated as the numerator of the (3). The net energy input to the system during the charging process can be determined by calculating the mass of the working fluid (m_c) during the charging process which has been calculated earlier as 14866 kg. The temperature difference and C_p are known, so the energy efficiency of the dehydration process becomes

$$\eta_c = \frac{(5\times 3732 \text{ kJ/kg } H_2O \times 57.9 \text{ kg } H_2O)}{14866 \text{ kg} \times 4.183 \text{ kJ/kg K} \times (70-50)\text{K}} = 0.86$$

4.2.2 Discharging

The energy efficiency of the discharging process (i.e., hydration) can be calculated using $\Delta H_{\text{reaction}}$ of the reaction and the expression for energy efficiency given by (9). The solid/gas reaction is:

$$SrBr_2 \cdot H_2O + 5H_2O \rightarrow SrBr_2 \cdot 6H_2O + \text{heat}$$

Other data for discharging follow:

- Water input temperature, $T_3 = 25$ ℃
- Water output temperature, $T_4 = 35$ ℃
- $\rho = 995.7$ kg/m^3 (at the mean temperature of the inlet and outlet conditions of the working fluid, $T_{\text{mean}} = (T_3 + T_4)/2 = 30$ ℃)
- $C_p = 4.183$ kJ/kg K (at $T_{\text{mean}} = 30$ ℃)
- Nominal flow of pouring water =6 l/min
- $m_d = \rho V = (995.7 \text{ kg/m}^3 \times 10^{-3}\text{l/m}^3) \times (6 \text{ l/min} \times 60 \text{ min/hour} \times 42 \text{ hour}) = 15{,}055$ kg
- Mass of water as reactant= 57.9 kg
- Hydration duration= 42 hours

The energy efficiency of the hydration process can therefore be evaluated as follows:

$$\eta_d = \frac{15055 \text{ kg} \times 4.183 \text{ kJ/kg K} \times (35-25)\text{K}}{(5\times 3732 \text{ kJ/kg } H_2O \times 57.9 \text{ kg } H_2O)} = 0.58$$

4.3. Exergy analysis of TES processes

4.3.1. Charging

The exergy efficiency of the charging process can be evaluated by using (8). According to the inlet and outlet conditions of the working fluid (water), the relevant properties are as follows:

$h_1 = 293.1$ kJ/kg ($T_1 = 70$ ℃, $P_1 = 100$ kPa)

$s_1 = 0.9549$ kJ/kg K ($T_1 = 70$ ℃, $P_1 = 100$ kPa)

$h_2 = 209.4$ kJ/kg ($T_2 = 50$ ℃, $P_2 = 100$ kPa)

$s_2 = 0.7037$ kJ/kg K ($T_2 = 50$ ℃, $P_2 = 100$ kPa)

As mentioned earlier, in calculating the exergy values for the products and reactants, the physical exergy change of the components can often be neglected relative to their chemical exergy changes. This assumption is applied in this analysis. The standard chemical exergy of components can be evaluated using (5). A methodology of calculating the standard chemical exergy of components is described in [18] for normal reference-environment conditions ($T_0 = 298.15$ K; $P_0 = 0.101325$ MPa. The compounds considered are $SrBr_2$ and H_2O, and the standard chemical exergy values are as in Table 1.

Table 1. Standard chemical exergy of selected components. All units are in kJ/mol.

Compound	ΔG_f^*	ϵ_{chne}		ϵ_{chn}
$SrBr_2$	-696.64	749.8 Sr	101.2 Br_2	154.36
H_2O (gas)	-228.59	236.09 H_2	3.97 O_2	9.49
H_2O (liquid)	-237.18	236.09 H_2	3.97 O_2	0.9

* Taken from [20].

In this example there are 171.3 kg of $SrBr_2 \cdot H_2O$ and, according to a mass balance for the system, 229.2 kg of $SrBr_2 \cdot 6H_2O$. With the molecular weights of the components we can calculate the number of moles for each component (see Table 2). In calculating the standard chemical exergy of reactants and products, we can evaluate ΔG_f for $SrBr_2 \cdot 6H_2O$ and $SrBr_2 \cdot H_2O$ as the sum of ΔG_f for $SrBr_2$ and six times and one time that of liquid water, respectively, and follow the same methodology. For $SrBr_2 \cdot 6H_2O$, for instance,

$\epsilon_{\text{chn}} = [-696.64 + (-237.18 \times 6)] + [(749.8 + 101.2) + 6 \times (236.09 + 3.97/2)] = 159.76$ kJ/mol

Table 2. Standard chemical exergy of selected components.

Component	Molecular weight (g)	Mass (kg)	Moles	Standard chemical exergy (kJ/mol)
$SrBr_2 \cdot H_2O$	265.44	171.3	645	155.25
H_2O (gas)	18.01	57.9	3198	9.49
$SrBr_2.6H_2O$	355.49	229.2	645	159.76

In order to calculate the charging exergy efficiency, the numerator of (8) denotes the difference between the standard chemical exergy of products and reactants. In the charging reaction, $SrBr_2 \cdot H_2O$ and H_2O are products of the reaction and $SrBr_2.6H_2O$ is the reactant. The standard chemical exergy of each of the components and their corresponding number of moles are evaluated and shown in Table 2. For the denominator of the fraction, the total mass of the working fluid has been evaluated before and other required properties of the working fluid are known as well. Therefore, the charging exergy efficiency is

$\psi_c = \{[(645\ \text{mol} \times 155.25\ \text{kJ/mol}) + (3198\ \text{mol} \times 9.49\ \text{kJ/mol})] - (645\ \text{mol} \times 159.76\ \text{kJ/mol})\}/[(14866\ \text{kg} \times (293.1\text{kJ/kg} - 209.4\ \text{kJ/kg} - 298\ \text{K} \times (0.9549\ \text{kJ/kg K} - 0.7037\ \text{kJ/kg K})] = 0.21$

4.3.2. Discharging

The discharging exergy efficiency can be evaluated using (10). For the inlet and outlet conditions of the working fluid (water), the relevant properties are as follows:

$h_3 = 104.8\ \text{kJ/kg}$ ($T_3 = 25$ °C, $P_3 = 100$ kPa)

$s_3 = 0.3669\ \text{kJ/kg K}$ ($T_3 = 25$ °C, $P_3 = 100$ kPa)

$h_4 = 146.7\ \text{kJ/kg}$ ($T_4 = 35$ °C, $P_4 = 100$ kPa)

$s_4 = 0.5049\ \text{kJ/kg K}$ ($T_4 = 35$ °C, $P_4 = 100$ kPa)

During discharging, $SrBr_2 \cdot H_2O$ and H_2O are reactants and $SrBr_2 \cdot 6H_2O$ is the product. Consequently, the discharging exergy efficiency is

$\psi_d = [15055\text{kg} \times (104.8\ \text{kJ/kg} - 146.7\ \text{kJ/kg} - 298\ \text{K} \times (0.3669\ \text{kJ/kg K} - 0.5049\text{kJ/kg K})]/\{(645\ \text{mol} \times 159.76\ \text{kJ/mol}) - [(645\ \text{mol} \times 155.25\ \text{kJ/mol}) + (3198\ \text{mol} \times 9.49\ \text{kJ/mol})]\} = 0.42$

4.4. Energy and exergy analyses of overall TES process

The energy efficiency of the overall TES process can be written as the ratio of the energy recovered from the TES during discharging to the energy input during charging, as expressed in (12). Thus,

$\eta_o = \frac{15055\ \text{kg} \times 4.183\ \text{kJ/kg K} \times (35-25)\text{K}}{14866\ \text{kg} \times 4.183\text{kJ/kg K} \times (70-50)\text{K}} = 0.50$

Analogously, the exergy efficiency of the overall TES process can be written using (13). Thus,

$\psi_o = [(15055\ \text{kg} \times (104.8\ \text{kJ/kg} - 146.7\ \text{kJ/kg} - 298\ \text{K} \times (0.3669\ \text{kJ/kg K} - 0.5049\ \text{kJ/kg K})]/[(14866\ \text{kg} \times (293.1\ \text{kJ/kg} - 209.4\ \text{kJ/kg} - 298\ \text{K} \times (0.9549\ \text{kJ/kg K} - 0.7037\ \text{kJ/kg K})] = 0.09$

5. Discussion

The methodology applied in this analysis, based on energy and exergy, is similar to that employed for analyses of other types of TES systems. General efficiency expressions are determined for the charging, storing and discharging processes, as well as the overall TES process. These efficiencies are calculated for an illustrative example based on an actual system. Exergy analysis is seen to be useful, when applied with or in place of energy analysis, for assessing efficiencies of the various processes occurring in TES systems as well as other aspects of their thermodynamic performances. Exergy analysis is more useful than energy analysis for identifying the locations and reasons of thermodynamic losses in a TES system and can assist efforts to improve or optimize designs. Such efforts contribute to society's efforts to achieve more advanced, clean and efficient energy systems.

Efficiencies of the storing process have been taken to be 100%, based on the assumption that there is no energy loss during storing period. This assumption is likely reasonable, in that the materials stored are at ambient conditions so no heat losses are expected. Nonetheless, the storing-period efficiencies could be lower than 100%, depending on the characteristics of the thermochemical material, the working fluid, the storing temperature, the storing duration, etc.

In this study, a single cycle of TES system operation is considered. Therefore, degradation of the thermochemical materials over time, as they undergo repeated cycles, is not considered. However, the effects of degradation are potentially significant, especially if it is found that repeated thermochemical cycles affect performance and the properties of the thermochemical material degrade notably over time.

A TES system for heating capacity only is investigated here. The system considered in the illustrative example supplies heat to the floor of a building during winter or mid-season periods. With an analogous approach, it is possible that cold TES systems could be assessed in terms of efficiency, cost, thermochemical materials and other factors.

For the illustrative example, the energy and exergy efficiencies respectively are determined to be 86% and 21% for the charging process and 58% and 42% for the discharging process. The results demonstrate that the energy efficiency of the

charging process is higher than the corresponding efficiency for the discharging process and that the exergy efficiency of the discharging process is higher than the corresponding efficiency for the charging process. The overall energy and exergy efficiencies are found to be 50% and 9%, respectively. The results demonstrate that the energy efficiencies of the charging and overall processes are higher than the corresponding exergy efficiencies. Exergy analysis takes into account the loss of availability of energy in a thermochemical TES system and indicates the thermodynamic and economic value of the system. The differences between energy and exergy efficiencies for the thermochemical TES and its processes are dependent on various factors, including the characteristics of the working fluid and thermochemical material, the nature of the synthesis or dissociation reaction, the desired heating temperature, the maximum output temperature of the heat source (a flat solar collector in the case study), and the level of insulation on the TES and associated piping. The TES energy or exergy losses likely vary with all of these factors and others.

The factors discussed above suggest that the performance attained with other types of TES (sensible and latent) may be attained with thermochemical TES, but with more compact storage systems.

6. Conclusions

The thermodynamic analysis presented here of a closed thermochemical TES allows energy and exergy efficiencies for the overall TES and its processes, as well as other performance measures, to be determined and better understood. Exergy analysis is particularly useful for specifying the locations and reasons of thermodynamic losses in TES systems. Energy and exergy analyses help understand and contrast efficiencies for the various processes occurring in TES systems and thereby assist efficiency improvement efforts. The results presented here suggest that further research is needed to improve understanding of thermochemical TES. The results suggest that thermochemical TES may be as efficient other types of TES but more compact. For decision making regarding the selection of thermochemical TES for a particular application, other factors beyond the thermodynamic ones considered here need to be assessed, including the environmental effects of the TES system, economics, the degradation of the thermochemical material over time as well as its cycling behaviour, the reliability of the overall system and required maintenance. Feasibility studies that consider these factors for specific applications appear to be merited.

Nomenclature

C_p	specific heat at constant pressure, kJ/kg K
E	energy, kJ
h	specific enthalpy, kJ/kg
m	mass of working fluid, kg
n	number of moles, -
P	pressure, kPa
Q	heat, kJ
s	specific entropy, kJ/kg K
T	temperature, °C or K
V	volume, m^3

Greek symbols

ΔG_f	Gibbs energy of formation, kJ/mol
ΔH	enthalpy change of reaction, kJ
ΔE	energy accumulation, kJ
$\Delta \in$	exergy accumulation, kJ
$\in$	exergy, kJ
ϵ_{chn}	standard chemical exergy of a compound, kJ/mol
ϵ_{chne}	standard chemical exergy of an element, kJ/mol
η	energy efficiency, -
ρ	density, kg/m^3
ψ	exergy efficiency, -

Subscripts

0	reference environment
c	charging
ch	chemical
d	discharging
D	destruction
e	element
o	overall
ph	physical
s	storing
tot	total

References

[1] Dincer, I., and Rosen, M. A., 2002, *Thermal Energy Storage: Systems and Applications*, Wiley.

[2] International Energy Agency (IEA), 2008, Compact Thermal Energy Storage: Material Development and System Integration, Technical Report (draft), Task 42, Annex 28, Solar Heating and Cooling Programme.

[3] Shilei, L., et al., 2007, Experimental Study and Evaluation of Latent Heat Storage in Phase Change Materials Wallboards, Energy and Buildings, 39(10), pp. 1088-1091.

[4] Dincer, I., Dost, S., and Li, X., 1997, Performance Analyses of Sensible Heat Storage Systems for Thermal Applications, International Journal of Energy Research, 21(12), pp. 1157-1171.

[5] Wettermark, G., 1989, Thermochemical Energy Storage, *Proc. NATO Advanced Study Institute on Energy Storage Systems*, 167, pp. 673-681.

[6] Weber, R., and Dorer, V., 2008, Long-term Heat Storage with NaOH, Vacuum, 82(7), pp. 708-716.

[7] Lahmidi, H., Mauran, S., and Goetz, V., 2006, Definition, Test and Simulation of a Thermochemical Storage Process Adapted to Solar Thermal Systems, Solar Energy, 80(7), pp. 883-893.

[8] Mauran, S., Lahmidi, H., and Goetz, V., 2008, Solar Heating and Cooling by a Thermochemical Process: First Experiments of a Prototype Storing 60 kWh by a Solid/gas Reaction, Solar Energy, 82(7), pp. 623-636.

[9] Van Essen, V. M., et al., 2009, Characterization of $MgSO_4$ Hydrate for Thermochemical Seasonal Heat Storage, Journal of Solar Energy Engineering, 131(4), p 041014 (7 pp.).

[10] Azpiazu, M. N., Morquillas, J. M., and Vazquez, A., 2003, Heat Recovery from a Thermal Energy Storage based on the $Ca(OH)_2/CaO$ Cycle, Applied Thermal Engineering, 23(6), pp. 733-741.

[11] Lovergrove, K., Luzzi, A., and Kreetz, H., 1999, A Solar-driven Ammonia-based Thermochemical Energy Storage System, Solar Energy, 67(4), pp. 309-316.

[12] Kreetz, H., and Lovergrove, K., 1999, Theoretical Analysis and Experimental Results of a 1 kW_{chem} Ammonia Synthesis Reactor for a Solar Thermochemical Energy Storage System, Solar Energy, 67(4), pp. 287-296.

[13] Rosen, M. A., and Dincer, I., 2003, Exergy Methods for Assessing and Comparing Thermal Storage Systems, International Journal of Energy Research, 27(4), pp. 415-430.

[14] Lovergrove, K., et al., 1999, Exergy Analysis of Ammonia-based Solar Thermochemical Power Systems, Solar Energy, 66(2), pp. 103-115.

[15] Kreetz, H., and Lovergrove, K., 2002, Exergy Analysis of an Ammonia Synthesis Reactor in a Solar Thermochemical Power System, Solar Energy, 73(3), pp. 187-194.

[16] Rosen, M. A., 1999, Second-law Analysis of Aquifer Thermal Energy Storage Systems, Energy, 24(2), pp. 167-182.

[17] Koca, A., et al., 2008, Energy and Exergy Analysis of a Latent Heat Storage System with Phase Change Material for a Solar Collector, Renewable Energy, 33(4), pp. 567-574.

[18] Szargut, J., 1980, International Progress in Second Law Analysis, Energy, 5(8-9), pp. 709-718.

[19] Bejan, A., 2006, *Advanced Engineering Thermodynamics*, 3rd Edition, Wiley.

[20] Woods, T. L., and Garrels, R. M., 1987, *Thermodynamic Values at Low Temperatures for Natural Inorganic Materials: An Uncritical Summary*, Oxford University Press, New York, pp. 242.

Acknowledgments: The authors acknowledge the financial support of the Natural Sciences and Engineering Research Council of Canada.

A MAGNETIC COOLING MACHINE FOR DOMESTIC APPLICATION

O. Sari[a], M. Balli[a], C. Mahmed[a], Ch. Besson[b], Ph. Bonhote[c], J. Forchelet[c]

[a] University of Applied Sciences of Western Switzerland, Institute IGT Yverdon-les-Bains, Switzerland

[b] University of Applied Sciences of Western Switzerland, Institute IESE, Yverdon-les-Bains, Switzerland

[c] University of Applied Sciences of Western Switzerland, Institute COMATEC, Yverdon-les-Bains, Switzerland

Abstract: *In this paper, a new type of reciprocating magnetic refrigerator working with high remanence permanent magnets as the source of the magnetic field is presented. The simulated and measured magnetic field at the machine air gap is about 1.45 Tesla. Initially, gadolinium metal (Gd) was used as the magnetocaloric refrigerant. Its magnetocaloric performances and its quality were checked experimentally in a developed test bench and confirmed by theoretical calculations based on the mean field theory (MFT). To attain high values of temperature difference between the hot and the cold sources (temperature span), a new kind of the Active Magnetic Refrigeration (AMR) cycle was implemented. However, in order to reduce the energy consumption and then increase the thermodynamic performances of the magnetic system, a special configuration of the magnetocaloric materials is developed. The numerical results of the applied magnetic forces on the new configuration are given and analyzed in details. The developed machine is designed to produce a cooling power between 80 and 100 Watt with a temperature span larger than 20 °C. The obtained results demonstrate that magnetic cooling is a promising alternative to replace traditional systems*.

Keywords: Magnetic refrigeration, Magnetocaloric effect, Magnetic refrigerating system, Optimization of system, Active magnetic refrigeration.

1. Introduction

The impact of synthetic refrigerants on the environment as well as the legal safety obligations drive the refrigeration industry to seek for new ways for completely phasing out greenhouse gases or for decreasing their charge in numerous installations. In order to be free from synthetic refrigerants, industries are continuously searching for environmentally friendly and suitable new technologies that will enable high energy savings, therefore reducing indirect CO_2 emissions. During the last fifteen years, both, namely the load reduction of the refrigerants in the installations and the use of natural, non-flammable, environmentally friendly refrigerants have been the preferred options by many end-users. Research on future refrigeration technologies orients itself on the indirect cooling technology as e.g. Phase Change Slurry (PCS), CO_2 vapor compressor technology, thermo-electric refrigeration, thermo-acoustic refrigeration and magnetic refrigeration (MR).

Since the discovery of the high polarization permanent magnet in Nd-Fe-B, the giant magnetocaloric effect in $Gd_5Ge_2Si_2$ and the development of the higher performance magnetic cooling systems close to room temperature, intensive studies were motivated on the magnetocaloric materials and magnetic cooling devices. Magnetic refrigeration is based on the magnetocaloric effect (MCE). This intrinsic property of some magnetic materials was discovered by Warburg in 1881 [1]. It is defined as the response of some magnetic materials to a changing magnetic field which manifests as the isothermal entropy change ΔS and adiabatic temperature change ΔT_{ad} (see Fig.1). When a magnetic field is applied to magnetic material close to the phase transition region, the magnetic moments change their ordering state and as consequence the magnetic entropy. Under adiabatic condition, this change in magnetic entropy is compensated by a modification in the lattice (atoms vibration) part of the full entropy which increases or decreases the material

Corresponding Author: Sari Osmann, Email: osmann.sari@heig-vd.ch

temperature depending on the sign of the applied field and the nature of magnetic order in the refrigerant.

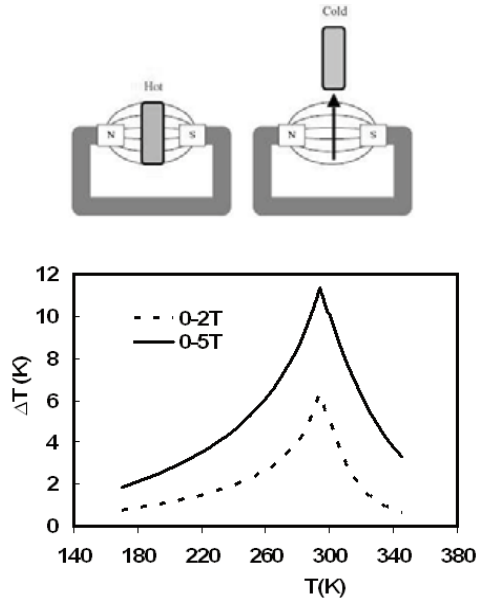

Fig. 1: Adiabatic temperature change with magnetization for pure Gadolinium

The origin of the MCE was explained independently by Debye and Giauque [2, 3] and pointed out that low temperatures could be reached by using a paramagnetic salt. In 1933 [4], Giauque and MacDougall have achieved successfully temperatures below 1 Kelvin by the use of the demagnetization cooling. Brown was the first to demonstrate the feasibility of MR close to room temperature [5]. In 1976, he obtained a temperature difference of 46 K between the hot and cold end of a simple refrigerator using 158 g of gadolinium metal and an applied field of 7 Tesla. The carrier fluid consisting of a mixture of 80 % water and 20 % ethyl alcohol solution was used as a heat transfer fluid. Compared to the classical refrigeration, magnetic cooling is an environment-safe technique (absence of CFC and HCFC) with many advantages, such as high efficiency, low noise, low pressure and compact configuration.

The modern magnetic cooling technology was born when Zimm et al developed successful operating machines showing that this technology is a feasible and competitive for large scale domestic and industrial applications. The first proof (reciprocating) operated with a magnetic field of 5 Tesla using a superconducting magnet [6]. With 10 K temperature span (between 281 and 291 K), it achieved a cooling power of 600 W, a coefficient of performance (COP) of 10 and maximum of 60 % of Carnot efficiency. The COP represents a ratio between the cooling energy (Q_{cool}) and the total energy input (W). It is worth noting that the COP of the traditional refrigerator is about 30 to 40% of Carnot efficiency [7, 8 and 9].

The second developed prototype by Zimm et al [10] was a rotating machine working with some rare earth based compound as magnetocaloric refrigerant magnetized and demagnetized through a magnetic field of 1.5 Tesla produced by a magnetic source based on Nd-Fe-B permanent magnets (PM). The obtained cooling power was 50 W at 0 K temperature span and 25 K as the maximum temperature difference between hot and cold source. Later, several demonstrators were reported in the literature. For more details, see Gschneidner et al [11].

The magnetocaloric material is an important key for the development of the magnetic refrigeration technology. However, up to today the principal material used in magnetic cooling prototypes is gadolinium (Gd) metal and its alloys. This is attributed essentially to its good magnetocaloric performances at room temperature, good mechanical properties, low hysteresis, availability in the market and its ability to answer the several engineering requirements. However, the high cost and the chemical instability limit the use of Gd as refrigerant on a large scale application. Aiming to replace Gd, a giant MCE was discovered in the first order transition materials $Gd_5(Ge_{1-x}Si_x)_4$ [12]. A few years later, several other families of MC materials were reported and found to exhibit high level of MCEs on large temperature range: from ambient to low temperatures. These include series such as $MnAs_{1-x}Sb_x$ [13] $MnFeP_{1-x}As_x$ [14], $LaFe_{13-x}Si_x$ [15, 16] and their derivatives. From a practical point of view, $LaFe_{13-x}Si_x$ materials seem to be the most promising in magnetic cooling systems due to their high MCE, low cost and low hysteresis. In our Laboratory, many efforts are focused on the development, improvement and the implementation of this family in collaboration with industrial and academic partners. In this paper, we present the initial results of a preindustrial magnetic cooling system. This

machine was designed and developed taking into account the design, market and thermodynamic performance requirements.

2. Magnetic field source

In addition to the magnetic refrigerants, the optimization of permanent magnets to generate high magnetic field is an important key for the development of magnetic cooling technologies. In magnetic refrigeration systems, the magnetic field source is equivalent to the compressor in the conventional compression cycle systems. In magnetic systems, the higher the generated magnetic field is, the higher the temperature and entropy change of working substance and as consequence the more powerful system may be. Considering the magnetocaloric performance of the available materials, an applied magnetic field higher than 1 Tesla is required.

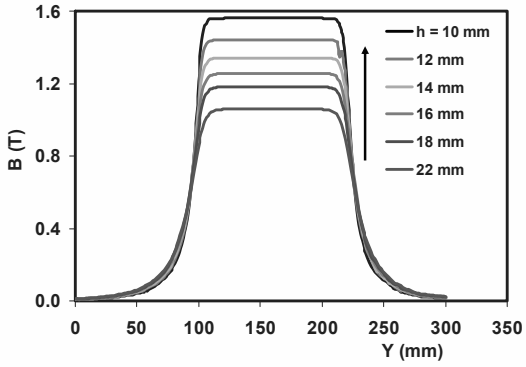

Fig. 2: Magnetic field distribution along the axis of the magnetic source given for different air gap height values.

For industrial applications, i.e. supermarket chillers, building air-conditioning, gas liquefaction, etc, superconducting magnets can be used to achieve induction level up to 8-10 Tesla with the restriction to utilize liquid helium or a cryocooler to maintain the superconducting coil near 4 K. However, as pointed out by Gschneidner et al [11] for domestic applications and small cooling systems, the superconducting magnet is out of question and the design of low-cost permanent magnet arrays with high induction is an important aspect of the commercialisation of MRs in the consumer market. With PM machines, the thermal energy is induced without electricity consumption, only an actuator is required to magnetize and demagnetize the magnetocaloric materials. In the literature, several types of magnetic flux sources were reported [17, 18]. For the one developed by Lee et al [17], the magnetic field for a side-opening PM can attend 3 T with an air gap 5.8 mm.

For the machine presented here, an innovative magnetic source is developed and designed. The latter is based on a modified Halbach rotation theorem and can be used for both: reciprocating and rotating magnetic systems. In the first step of the process, we started the optimized design of the new source's geometry by studying theoretically this structure as a function of the air gap, magnets, remanence flux density, etc.

Due to the complexity of the geometrical structure and the presence of different soft magnetic materials, the analytical formulations are out of question. For this purpose, numerical simulations of the generated magnetic field were carried out.

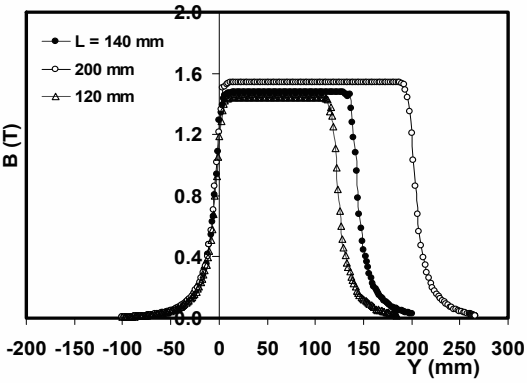

Fig. 3: Magnetic field distribution along the axis of the magnetic source as a function of magnet length

In this present work, the finite-element Flux3D program was used to simulate the magnetic field in the PM circuit. Flux3D is based on a Fortran code running in both operating systems Unix and Windows. It uses Maxwell's equations as the basis to determine the magnetic potential in static conditions based on this equation:

$$\mathrm{div}\left[\mu \cdot \mathrm{grad}(V_m) + \mu_0 \cdot M_r\right] = 0$$

Where μ is the relative magnetic permeability and M_r is the remanence.

The obtained magnetic potential allows the calculations of all the magnetic quantities at any point of space.

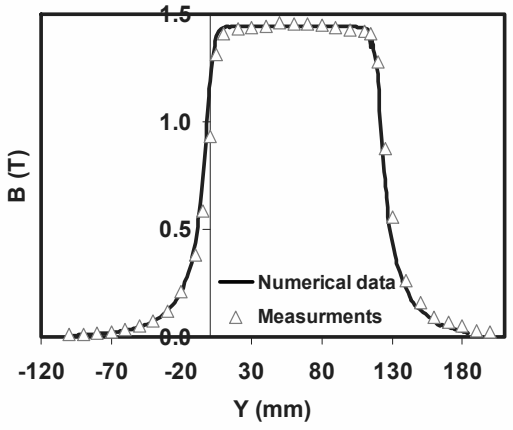

Fig. 4: Calculated and measured magnetic field along the axis of the magnetic source as a function of magnetic length (L = 120 mm, h = 12 mm)

In this study, the magnetic field was calculated as a function of the length and the height of the air gap of the magnetic source. The magnet structure is designed on the basis of Nd-Fe-B. The permanent magnets have a highest remanence of about 1.45 Tesla. In order to study and to optimize the structural parameters, the height h of the air gap was varied from 10 mm to 22 mm for a fixed length L = 120 mm and the latter was changed from 120 mm to 200 mm for h = 12 mm. The strength of magnetic induction along y-orientation in the centre of air gap is given in Fig.s 2 and 3. As shown in Fig.s, the geometric structure of permanent magnets can be adapted easily depending on the required application. The induced magnetic field is very sensitive to the air gap height and increases almost linearly when decreasing h. While, the length of the magnetic source influences slightly the magnetic field in the air gap. For the developed here prototype, the adopted field source air gap has a cross of 12 mm x 50 mm and a length of 120 mm. The calculated induction in the centre of the magnet by Flux 3D is about 1.44 Tesla. To check the validity of the magnetic field obtained by 3 D simulations, we have measured the generated magnetic flux density using Hall probe. The measurements results compared with the numerical data are shown in Fig. 4. The comparison indicates very good agreement of results confirming the ability of Flux 3D evaluating the magnetic field in such systems.

3. Magnetocaloric refrigerant : Gadolinium

The choice of the magnetocaloric refrigerant is of great importance as it influences strongly the thermodynamic performances of the cooling machine. Pure gadolinium is the only material used in most magnetic refrigeration prototypes. This is attributed essentially to its important MCE, its ability to answer the several engineering requirements and the availability in the market.

Firstly, we have used Gd flat plates refrigerants in our machine. The thermomagnetic properties of Gd such magnetization, entropy, adiabatic temperature change and specific heat were widely studied and reported in the literature [19]. However, before placing the material in the machine, we have measured the magnetocaloric performances in practical running conditions using a set-up developed in our Laboratory. This system allows the measurement of temperature change close to room temperature in a magnetic induction of about 2 Tesla.

The measurement results are given in Fig. 5 (Gd: 2 mm). The obtained normalized ΔT with respect to the magnetic field is about 2 K/ T which is comparable with that reported in the literature [19].

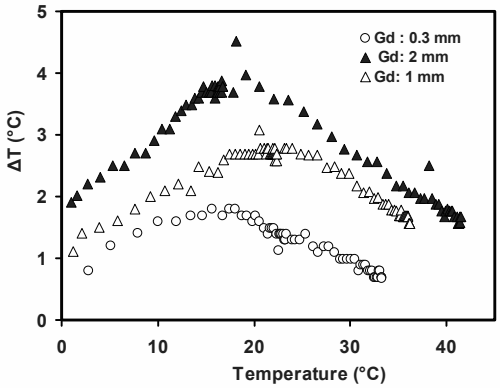

Fig. 5: Effect of the demagnetization field on the Gd magnetocaloric properties (under 2 Tesla)

In order to study the demagnetization effect on the magnetocaloric properties of Gd, several ΔT measurements were performed on gadolinium sheets with different thickness and the magnetic field was applied perpendicularly to the surface of plates. The temperature change for three plates

with a thickness of 0.3 mm, 1 mm and 2 mm are compared in Fig. 5. We can observe that the MCE of Gd decreases drastically when decreasing the sheet thickness from 2 to 0.3 mm.

This difference is attributed to the demagnetization effect due to the shape of the sample. The application of a perpendicular field to the material surface induces an internal field in the inverse direction called the demagnetization field. The latter cancels out a part of the applied field which reduces the total internal field of the magnetocaloric material and decreasing as a consequence the magnetocaloric performances. To avoid the demagnetization effect in our machine, the plates were placed parallel to the applied field.

4. Magnetic refrigerator description and preliminary results

A general view of the designed magnetic cooling machine is presented in Fig. 6. The experimental apparatus is composed of two permanent magnetic sources producing about 1.45 Tesla, two regenerators with Gd plates, four heat exchangers.

The regenerator is divided into two parts; each part contains Gd flat plates with 1 mm thickness and 100 mm length, corresponding to about 400 grams of Gadolinium.

Fig.6: A view of the developed magnetic cooling machine

The magnetic work constitutes a large part of the fully absorbed energy by the magnetic cooling system. Furthermore, the reduction of the magnetic forces is of great importance for the development of machines with high efficiency. For this purpose and aiming to compensate magnetic forces, the regenerator was divided into two parts separated by a distance of about 30 mm. Fig. 7 demonstrates the difference between magnetic forces calculated numerically for 1 and 2 blocs of Gd.

As shown in Fig. 7, the magnetic force can be decreased drastically when using a bed constituted of 2 blocs of Gd. The numerical calculations developed in Fig. 7 were confirmed experimentally by the measurements performed in the here reported machine. A detailed study of the magnetic forces in magnetic cooling systems will be published in a forthcoming communications.

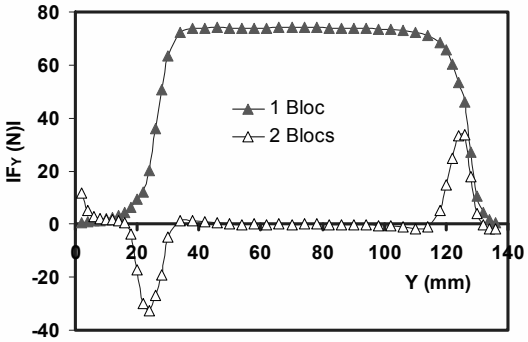

Fig.7: The calculated magnetic forces for 1 and 2 blocs in the regenerator

The temperature span between hot and cold ends was amplified using special thermodynamic cycles called active magnetic refrigeration regeneration (AMR) [19]. Such cycles break up into four steps:

- magnetization of the magnetic materials inducing heating,
- flow of a fluid from the cold source to hot source to evacuate heat: the temperature of the fluid increases and the heat generated by MC material is removed and evacuated in direction of the hot end,
- demagnetization of the material when it is removed from magnetic field, thus leading to potential increase of magnetic entropy, decreasing the refrigerant temperature,
- flow of the heat transfer fluid from hot to cold source in order to evacuate cooling energy.

The operating process of the AMR can be controlled by adjusting the movement of the

actuator and the valve. The operation frequency of the cycle was 0.5 Hz.

Fig. 8 shows an example of an experimental data results. At each heat source, the temperature changes progressively to a limit value at steady state. After several AMR cycles, the maximum temperature span achieved between cold and hot ends is about 12 °C.

The relatively low temperature span is attributed essentially to the bad thermal properties of the heat carrying fluid. The Basylon was used especially to protect Gd bed from corrosion and oxidation.

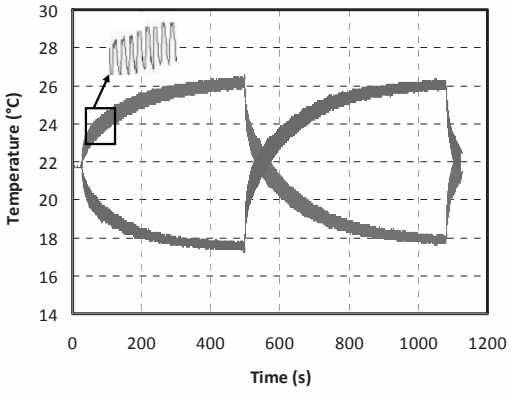

Fig.8: Temperature span: experimental results for f = 0.5 Hz and Basylon as heat transfer fluid.

However, the preliminary results show that by using water or Zitrec as heat transfer fluids, a temperature difference of about 22 °C can be reached. More details about machine with optimized parameters will be communicated in the future.

5. Conclusion and future work

A linear reciprocating permanent magnet cooling system has been designed and built. Gadolinium was used as the first magnetocaloric test material, but other materials are considered for test in particular $NaZn_{13}$ based compounds. However, much effort was dedicated in order to make the developed machine more compact, to obtain sufficient magnetic induction in the air gap (1.45 Tesla) and to reduce the magnetic forces acting on the magnetocaloric refrigerant during the magnetization-demagnetization process.

Preliminary tests of the machine were made and encouraging results were obtained. To investigate the device, more experimental runs will be carried out and a detailed report about the machine with optimized parameters will be communicated in the future.

Nomenclature

B magnetic induction, Tesla

COP coefficient of performance

F_Y magnetic force along y axis, N

h height of the magnetic source, m

L length of the magnetic source, m

Mr remanence , A/m

Q_{cool} cooling energy, J

ΔS entropy change, J/(kg K)

ΔT_{ad} adiabatic temperature change, K

V_m magnetic potential,(T m^2)/H

Greek symbols

μ magnetic permeability, H/m

μ_0 magnetic permeability of vacuum, $4\pi 10^{-7}$ H/m

References

[1] E. Warburg, Ann. Phys. (Leipzig), 13 (1881)141

[2] P. Debye, Ann. Phys. 81 (1926)1154

[3] W. F. Giauque, J. Am. Chem. *Soc.* **49 (**1927)1864

[4] W F Giauque and D P MacDougall, Phys. *Rev.* **43 (**1933) 768

[5] G. V. Brown, JAP, 47 (1976) 3673

[6] C. Zimm, A. Jastrab, A. Sternberg, V. K. Pecharsky, K. Gschneidner Jr, M . Osborne and I. Anderson *Adv.Cryog. Eng.* **43 (**1998)1759

[7] A. Rowe, Performance Metrics for Active Magnetic Refrigerators, Third IIF-IIR International Conference on Magnetic Refrigeration at Room Temperature, Des Moines, Iowa, USA, May 11-15, 2009.

[8] A. Kitanosvski, C. Gonin, D. Vuarnoz, O. Sari, P. W. Egolf, A Standardization of the coefficient of performance for magnetic refrigerators, heat pumps and energy conversation machines, Third IIF-IIR International Conference on Magnetic Refrigeration at Room Temperature, Des Moines, Iowa, USA, May 11-15, 2009.

[9] C. Zimm, S. Russek, Near Room temperature magnetic refrigeration : The Path to Applications, Third IIF-IIR International Conference on Magnetic Refrigeration at Room Temperature, Des Moines, Iowa, USA, May 11-15, 2009.

[10] C. Zimm, A. Boeder, J. Chell, A. Sternberg, A. Fujita, S. Fujieda, K. Fukamichi, Int. J. Refrig, 29(2006)1302.

[11] K.A. Gschneidner, Jr., V.K. Pecharsky, Int. J. Refrig., 31 (2008) 945.

[12] V.K. Pecharsky, and K.A. Gschneidner., Jr. Phys. Rev. Lett. 78 (1997) 4494.

[13] H. Wada and Y. Tanabe, Appl. Phys. Lett. 79 (2001) 3302.

[14] O. Tegus, E. Brück, K.H.J. Buschow and F.R. de Boer, Nature. 415 (2002) 150.

[15] A. Fujita, S. Fujieda, Y. Hasegawa and K. Fukamichi, Phys. Rev. B. 67 (2003) 104416.

[16] M. Balli, D. Fruchart and D. Gignoux, J. Phys.: Condens. Matter. 19 (2007) 236230.

[17] S. J. Lee, J.M. Kenkel, and D.C. Jiles, IEEE. Trans. Magn, 38 (2002) 2991.

[18] C. Vasile and C. Muller, Inter. Jr. Ref, 29 (2006)1318–1326.

[19] A.M. Tishin and Yu.I. Spichkin, *The Magnetocaloric Effect and Its Applications*, IOP Publ., Bristol, U.K. (2003).

Acknowledgements

We further are grateful to Direction Générale de l'Enseignement Supérieur du canton de Vaud-Switzerland, the Office fédéral de l'Energie (OFEN) – Switzerland, INTERREG IVa and the Haute Ecole de Suisse Occidentale (HES-SO).

We acknowledge their financial support.

Optimum Thermo-economic Performance Characteristic of a Class of Irreversible Ferromagnetic Stirling Refrigerators

Houcheng Zhang, Guoxing Lin

Department of Physics and Institute of Theoretical Physics and Astrophysics, Xiamen University, Xiamen 361005, P. R. of China

Abstract: The performance analysis and parametric study of a class of irreversible ferromagnetic Stirling refrigerators using thermo-economic approach are carried out, in which multi-irreversibilities including finite-rate heat transfer, internal irreversibility, heat leak as well as regeneration loss are taken into account. Based on the statistical mechanics and thermodynamics analysis method, the analytical expression of thermo-economic function is derived and the influences of the multi-irreversibilities on the thermo-economic function are analyzed and evaluated in detail. Furthermore, the other performance characteristics and the related operating parameters of the ferromagnetic Stirling refrigerator at the optimum thermo-economic function are determined and several important performance bounds are also discussed. The results obtained here may provide some parametric design message for the performance improvement of magnetic refrigerators.

Keywords: Ferromagnetic material, Stirling refrigeration cycle, Thermo-economic function, Optimum performance.

1. Introduction

With the increasing concerns for energy requirement and ozone depletion substance, many researchers have been searching for more environment friendly refrigerants and high efficiency designs of refrigeration cycles. A magnetic refrigerator, which has more advantages in refrigeration efficiency, reliability, low noise and environmental friendliness than a gas refrigerator, is becoming a promising technology to replace the conventional gas-compression/ expansion technique in use today [1-10]. Some scholars have studied the performance characteristics of magnetic Stirling refrigerators [11-15]. These investigations all based on the thermodynamic performance analysis and the optimal control theory methods. To understand more deeply the performance characteristics of the magnetic refrigeration systems, it is a necessary and significant new investigation to use the thermo-economic performance analysis approach to magnetic refrigeration systems [16-19]. In fact, it is also one of the interesting extended subjects in the optimum theory of thermodynamics.

In the present paper, a thermo-economic function of an irreversible ferromagnetic Stirling refrigerator cycle is presented. On the basis of the statistical mechanics theory, the analytical expression of thermo-economic function for the irreversible ferromagnetic Stirling refrigerator is derived. By using the optimal control theory and numerical calculation technology, the effects of multi-irreversibilities, including finite-rate heat transfer, the internal irreversibility inside the working substance, the heat leak between the high and low temperature reservoirs as well as the regenerator efficiency, and the economic parameters on the thermo-economic function are analyzed and evaluated. Furthermore, the other performance characteristics at maximum thermo-economic function and the optimum operating regions and design parameters of the ferromagnetic Stirling refrigerator are discussed.

2. The thermodynamic properties of a class of homogeneous ferromagnetic material

According to the phenomenological theory of molecular field, when the volume change is negligible, the state equation, fundamental thermodynamic equation and entropy equation of a homogeneous ferromagnetic material are, respectively, given by [14, 15]

$$M = ng\mu_B JB_J(X) \tag{1}$$

$$du = Tds + \mu_0(H + \lambda M)dM \quad (2)$$

$$s = s_0(T) - \frac{\mu_0 M(H+\lambda M)}{T} + \mu_0 nk\left[\ln\sinh(\frac{2J+1}{2J}X) - \ln\sinh(\frac{1}{2J}X)\right] \quad (3)$$

where

$$B_J(X) = \frac{2J+1}{2J}\coth(\frac{2J+1}{2J}X) - \frac{1}{2J}\coth(\frac{1}{2J}X)$$

is the Brillouin function and $X = g\mu_B\mu_0 J(H+\lambda M)/kT$, n the number of magnetic moments per unit volume, g the landé factor, μ_B the Bohr magneton, J the quantum number of angular momentum, M the magnetization, H the magnetic field, $\lambda = 3kT_c/[ng^2\mu_B^2 J(J+1)]$ the molecular-field constant, T_c the curie temperature, T the absolute temperature, k the Boltzmann constant, u and s are the internal energy and the entropy of ferromagnetic system, μ_0 is the permeability of vacuum, $s_0(T)$ is the entropy of ferromagnetic system when $M = 0$.

3. An irreversible regenerative ferromagnetic Stirling refrigeration cycle

A magnetic Stirling refrigeration cycle consisting of two isothermal processes and two iso-magnetization processes can be represented by a magnetization-temperature diagram, as shown in Fig. 1, where Q_1 and Q_2 are, respectively, heats released to the environmental reservoir at the temperature T_H and absorbed from the cooled

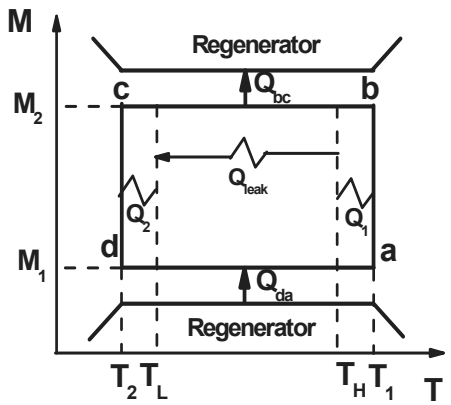

Fig. 1. The M-T diagram of an irreversible ferromagnectic Stirling refrigeration cycle

space at the temperature T_L , Q_{da} and Q_{bc} are the heat-exchange amounts between the working substance and the regenerator during the iso-magnetization processes M_1 and M_2, respectively.

Using Eq. (3) and Fig. 1, one has

$$Q_2 = T_2(s_d - s_c) = T_2\Delta s_{cd} \quad (4)$$

where $\Delta s_{cd} = \mu_0(G + nkY)$, $G = M_2G_2 - M_1G_1$, $G_1 = (H_d + \lambda M_1)/T_2$, $G_2 = (H_c + \lambda M_2)/T_2$, $Y = \ln\{sh(\frac{2J+1}{2J}X_d)sh(\frac{X_c}{2J}) / sh(\frac{X_d}{2J})sh(\frac{2J+1}{2J}X_c)\}$, $X_c = g\mu_B JG_2/k$, $X_d = g\mu_B JG_1/k$.

For iso-magnetization processes, one has [14]

$$(H + \lambda M)/T = const \quad (5)$$

Based on Eq. (5) and Fig. 1, one can prove that $\Delta s_{cd} = \Delta s_{ab} = \Delta s$ and Δs is a consta+9+8nt independent of H and T.

When heat transfer obeys the Newton's law, Q_1 and Q_2 can be written as

$$Q_1 = \alpha(T_1 - T_H)t_1 \quad (6)$$

$$Q_2 = \beta(T_L - T_2)t_2 \quad (7)$$

where α and β are the thermal conductances between the working substance and the reservoirs at temperatures T_H and T_L, respectively; t_1 and t_2 are the corresponding heat exchange times.

On the other hand, the internal dissipation resulting from eddy currents and other irreversible effects inside the cyclic working substance is inevitable, such that the ferromagnetic Stirling refrigerator cycle is an irreversible one. And the dissipated heat resulting from the internal irreversibility has to be released to the cooled space that the actual cooling quantity Q_2' of the ferromagnetic Stirling refrigerator is smaller than that of the ferromagnetic Stirling refrigerator without the internal dissipation. In order to define the internal irreversibility inside the working substance, one may introduce an internal irreversibility parameter

$$I = Q_2 / Q_2' \geq 1 \quad (8)$$

Generally, I is larger than 1, only when the internal dissipation may be neglected, $Q_2' = Q_2$ and $I = 1$.

A magnetic Stirling refrigerator cycle may possess the condition of perfect regeneration, that is, $Q_{bc} = Q_{da} = Q_R$ and

$$Q_R = \int_{T_2}^{T_1} C_M dT = C_{MA}(T_1 - T_2) \quad (9)$$

where C_M and C_{MA} are, respectively, the heat capacity and average heat capacity of the working substance at the iso-magnetization processes. However, for an actual regenerator perfect regeneration cannot be realized entirely that efficiency of regenerator $\eta < 1$. And, the regeneration loss may be assumed to be proportional to the temperature difference, i.e.,

$$\Delta Q_R = (1-\eta) C_{MA}(T_1 - T_2) \tag{10}$$

Furthermore, it is assumed that the time of regenerative processes is proportional to the temperature difference, that is,

$$t_R = D(T_1 - T_2) \tag{11}$$

where D is a proportion constant independent of temperature. Thus, the period of the cycle

$$\tau = t_1 + t_2 + 2t_R \tag{12}$$

For a refrigerator, heat leak per cycle is inevitable and generally it may be assumed to be proportional to the temperature difference of the two heat reservoirs, that is,

$$Q_{Leak} = K_L(T_H - T_L)\tau \tag{13}$$

where K_L is the heat leak coefficient.

According to Fig. 1 and the above analysis, one obtains the net heat amounts released to the environment and absorbed from the cooled space per cycle are, respectively, given by

$$Q_H = Q_1 - \Delta Q_R - Q_{Leak} \tag{14}$$

$$Q_L = Q_2^{'} - \Delta Q_R - Q_{Leak} \tag{15}$$

It is well known that for a refrigerator, the cooling rate, coefficient of performance (COP) and power input are the three important performance parameters. By using the equations above, one has

$$R = \frac{I^{-1} - E(1-\eta)(x-1)}{x[\alpha(xy - T_H)]^{-1} + [\beta(T_L - y)]^{-1} + A(x-1)} - N \tag{16}$$

$$\varepsilon = \frac{-N\left\{x[\alpha(xy - T_H)]^{-1} + [\beta(T_L - y)]^{-1} + A(x-1)\right\}}{x - I^{-1}} + \frac{I^{-1} - E(1-\eta)(x-1)}{x - I^{-1}} \tag{17}$$

$$P = \frac{x - I^{-1}}{x[\alpha(xy - T_H)]^{-1} + [\beta(T_L - y)]^{-1} + A(x-1)} \tag{18}$$

where $A=2D/[\mu_0(G+nkY)]$, $E=C_{MA}//[\mu_0(G+nkY)]$ and $N=K_L(T_H-T_L)$, $x=T_1/T_2$, $y=T_2$.

The thermo-economic function F is defined as the cooling rate divided by the total cost including annual investment, energy consumption and maintenance costs, i.e.,

$$F = \frac{\dot{Q}_L}{C_i + C_e + C_m} \tag{19}$$

where C_i, C_e and C_m refer to the annual investment, energy consumption and maintenance costs and they may be further written as

$$C_i = a(\dot{Q}_H + \dot{Q}_L + \dot{Q}_R) + a_P P \tag{20}$$

$$C_e = a_e P \tag{21}$$

$$C_m = a_m \dot{Q}_L \tag{22}$$

where proportionality constant a is the annual cost per unit heat transfer rate, a_P is the annual cost per unit power input**,** a_e and a_m are the annual cost per unit power input and cooling rate, respectively. All the dimension of proportionality constant are ncu/(year-kw) and the unit ncu stands for the " National Currency Unit ".

Now substituting Eqs. (20)-(22) into Eq. (19), it yields

$$F = \frac{Q_L}{a(Q_H + Q_L + Q_R) + b(Q_H - Q_L) + a_m Q_L} \tag{23}$$

where $b = a_P + a_e$. Combining Eqs. (9), (14) and (15) with Eq. (23), we obtains

$$bF = \frac{b[1 - EI(1-\eta)(x-1) - INz]}{a_1 Ix + a_2 - a_3 I(x-1) - a_4 INz} \tag{24}$$

where bF is called as the dimensionless thermo-economic function and $a_1 = a + b$, $a_2 = a + a_m - b$, $a_3 = [2a + a_m - a(1-\eta)^{-1}]E(1-\eta)$, $a_4 = 2a + a_m$, $z = \left\{x[\alpha(xy - T_H)]^{-1} + [\beta(T_L - y)]^{-1} + A(x-1)\right\}$. Equation (24) is an important equation of thermo-economic function with respect to x and y. Now Substituting Eq. (24) into extreme condition $\partial(bF)/\partial y = 0$, one has

$$y = \frac{T_L x + \sqrt{\alpha/\beta}\,T_H}{(\sqrt{\alpha/\beta} + 1)x} \tag{25}$$

Furthermore, substituting Eq.(25) into Eqs.(24), (16), (17) and (18), we obtain

$$(bF)_x = \frac{[b - bIE(1-\eta)(x-1)]\gamma x - bINU}{[a_1 Ix + a_2 - a_3 I(x-1)]\gamma x - a_4 INU} \quad (26)$$

$$R_x = \frac{[1 - EI(1-\eta)(x-1)]\gamma x}{UI} - N \quad (27)$$

$$\varepsilon_x = \frac{[1 - EI(1-\eta)(x-1)]\gamma x - INU}{(Ix-1)\gamma x} \quad (28)$$

$$P_x = \frac{(Ix-1)\gamma x}{IU} \quad (29)$$

where $U = \frac{[\alpha^{-1} + (\alpha\beta)^{-0.5}]}{(T_L x - T_H)} + A[(\alpha/\beta)^{0.5} + 1](x^2 - x)$

and $\gamma = \sqrt{\alpha/\beta + 1}$.

4. Results and discussion

From Eq. (26), one can generate the variation curves of the dimensionless thermo-economic function with respect to the temperature ratio *x,* as shown in Fig. 2. In Fig.2, the related parameters are given by T_H = 300 K, T_L = 260 K, $\alpha = \beta$ = 1 J/(K s), K_L= 0.1α, A= 0.01, E = 1, a = 0.2 ncu/(year-kw), I = 1.1, a_P = 1 ncu/(year-kw), a_e = 0.1 ncu/(year-kw), a_m = 0.05 ncu/(year-kw), η = 0.8. One can see from Fig.2 that if the heat leak can not be neglected, the thermo-economic function first increases then decreases as the temperature ratio *x* increases such that there exists an optimum temperature ratio at which the thermo-economic function attains its maximum. However, if the heat leak may be neglected, the thermo-economic function is a monotonous decreasing function of the temperature ratio *x.* In fact, the effects of the heat leak and internal irreversibility on the thermo-economic function are also shown in Fig. 2 and it shows the thermo-economic function decreases with increasing heat leak coefficient K_L and increasing internal irreversibility parameter *I*.

Figure 3 shows that the dimensionless thermo-economic function *bF*, COP ε, dimensionless cooling rate R^* ($=R/\alpha T_L$) and dimensionless power input P^*($=P/\alpha T_L$) versus the temperature ratio *x* curves. From Fig.3 one can see that *bF*, ε and *R** first increase and then decrease while P^* monotonously increases as *x* increases. We can also find from Fig. 3 that when the temperature ratio tends to x_{min}= T_H/T_L=1.17, the values of above performance parameters all tend to be zero. Note that $x \to x_{min}$ means $T_1 \to T_H$ and $T_2 \to T_L$. In such a case, the heat-transfer

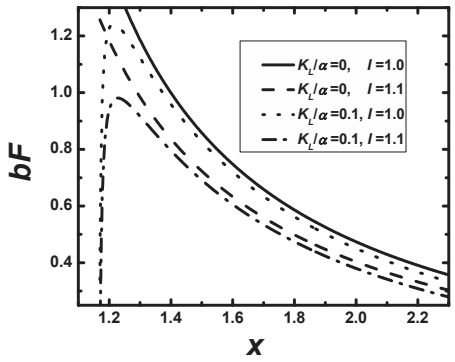

Fig. 2. Effects of heat leak and internal irreversibility on the objective function.

irreversibilities at the hot and cold side would disappear and the heat transfer area or the heat transfer time tends to be infinite and hence, the cost of the ferromagnetic Stirling refrigerator is wondrously expensive. At the same time, there is not any cooling rate for this kind of refrigerator. It is clear that no engineer wants to construct an expensive refrigerator without any cooling rate.

It can be also seen from the Fig.3 that the value of *x* at maximum thermo-economic function and that at maximum COP are almost the same, but they are all smaller than that at maximum cooling rate. As an example, when dimensionless thermo-economic function attains its maximum 0.981, x = 1.228, and when COP attains its maximum 2.149, x = 1.230, while when cooling rate attain its maximum 0.252, x = 1.641.

Figure 4 shows the variations of dimensionless thermo-economic function *bF*, cooling rate *R** and *COP* with respect to the dimensionless power input *P**. One finds from Fig.4 that the dimensionless power input P^*_{bF} at maximum thermo-economic function is smaller than the dimensionless power input P^*_R at maximum cooling rate, and a little smaller than the dimensionless power input P^*_ε at maximum *COP*. For example, when *bF*, *R** and *COP* attain their maximums, the corresponding dimensionless power input are P^*_{bF} =0.027, P^*_R=0.250 and P^*_ε=0.028, respectively. Therefore, we should felicitously design the related parameters of the ferromagnetic Stirling refrigerator according to different optimal criterions. If one emphasizes

particularly on investment benefit, we should set the dimensionless power input close to P^*_{bF}; and if one emphasizes on cooling rate, we should set the dimensionless power input close to P^*_R.

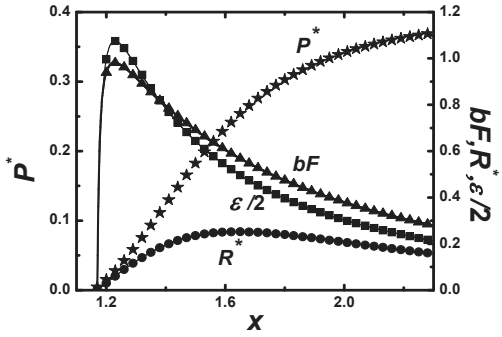

Fig. 3. The optimum dimensionless thermo-economic function, COP, dimensionless cooling rate and power input versus the temperature ratio x curves.

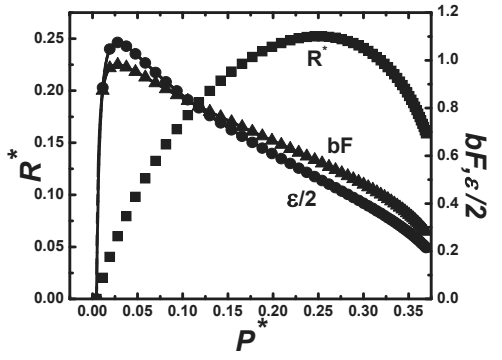

Fig. 4. The dimensionless thermo-economic function, cooling rate and COP vs dimensionless power input curves

Note that both bF_{max} and R^*_{max} are all important performance bounds of the irreversible ferromagnetic Stirling refrigerator and they are upper bounds of the dimensionless thermo-economic function and cooling rate. And, bF_m is the dimensionless thermo-economic function at the maximum cooling rate, and R^*_m is the dimensionless cooling rate at maximum thermo-economic function and they are the lower bounds of the dimensionless thermo-economic function and cooling rate, respectively. Thus, the optimal operating region of the irreversible ferromagnetic Stirling refrigerator should be located in $R^*_m \le R \le R^*_{max}$ and $bF_m \le bF \le bF_{max}$. In other words, the optimal operating region should be located in the negative slope parts in Fig. 5. Moreover, the influence of the internal irreversibility parameter I on the $bF \sim R^*$ characteristic curves is shown in Fig. 5. One can find from Fig. 5 that both the maximum value and the optimal operating regions

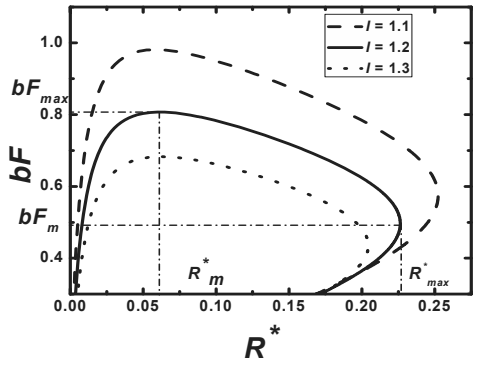

Fig. 5. The dimensionless thermo-economic function vs the dimensionless cooling rate curves

of the thermo-economic function and cooling rate are all decreased as the internal irreversibility parameter I increases. As an example, when I = 1.1, bF_{max} =0.981, R^*_{max}= 0.252, bF_{max} -bF_m=0.406, R^*_{max} - R^*_m =0.194; when I = 1.2, bF_{max} = 0.807, R^*_{max} =0.226, bF_{max} - bF_m = 0.311, R^*_{max} -R^*_m =0.165; when I = 1.3, bF_{max} =0.683, R^*_{max} =0.204, bF_{max} - bF_m =0.247, R^*_{max} - R^*_m = 0.142.

The effects of the internal irreversibility parameter I, heat leak coefficient K_L and efficiency of regenerator η on the maximum dimensionless thermo-economic function are shown in Fig.6. From Fig.6 one can find that bF_{max} decreases as I and K_L increase, while increases with increasing efficiency of regenerator η.

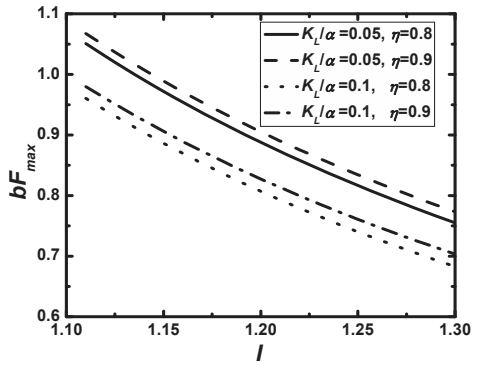

Fig. 6. The effects of K_L and η on $bF_{max} \sim I$ curve

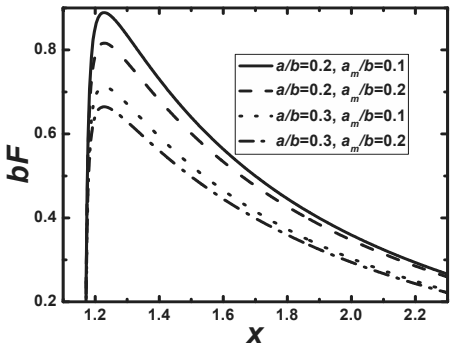

Fig. 7. The effects of the economic parameters on the dimensionless thermo-economic function vs the temperature ratio x curve

The influences of the economic parameters on the dimensionless thermo-economic function versus the temperature ratio x curve are shown in Fig. 7. It can be seen from Fig.7 that the dimensionless thermo-economic function decreases as the economic parameter a or a_m increases, where a/b is the relative investment cost of heat transfer rate to the cost to investment of power input and a_m/b is the relative investment cost of maintenance to the cost to investment of power input. Since the economic parameters are dependent of the economical conditions of a country and thus, generally, the system manufactured in developing countries has a better thermo-economic performance advantage than developed countries.

It should be pointed out that the working substance in the ferromagnetic Stirling refrigeration cycle established in the present paper may include those magnetic materials like some rare earth based compounds and so on. Moreover, owing to using the magnetic material as the working substance, there is less mechanical friction such that it will have a better thermo-economic performance than conventional compression / expansion gas refrigerators.

5. Conclusions

The detailed parametric analysis of an irreversible ferromagnetic Stirling refrigerator cycle is presented in this paper, in which multi-irrversibilities including finite-rate heat transfer, internal irreversibility, efficiency of regenerator and heat leak are taken into account. Based on the thermo-economic objective function approach, the analytical expressions of the thermo-economic function with respect to the temperature ratio x and other performance parameters, as well as the corresponding cooling load, *COP* and power input are derived and the effects of the multi-irreversibilities on the thermo-economic function are revealed. Integrated thermo-economic optimization criterion with cooling load optimization one, the optimal operating region of the irreversible ferromagnetic Stirling refrigerator is determined. Moreover, the optimum temperature ratio and the optimum power input with different performance criterions are analyzed and discussed. The results obtained in the present paper would be helpful to deeply understand the thermo-economic performance characteristic of a class of ferromagnetic Stirling refrigeration cycles.

Acknowledgement

This work was supported by the National Natural Science Foundation (No.50776074), People's Republic of China.

Nomenclature

C heat capacity/Cost, (J/K)/ (ncu/year)
F thermoeconomic function
H magnetic field , A/m
M magnetization, A/m
Q heat, J
P power input J/s
R cooling rate J/s
T temperature, K
k Boltzmann constant
s entropy, J/K
a annual cost per unit heat transfer rate, ncu/(year-kw)

Greek symbols

α, β thermal conductances, J/(K s)
ε coefficient of performance
η efficiency of regenerator
τ cyclic period, s

Subscripts

H high temperature side
L low temperature side
R regeneration
e energy consumption
i annual investment

m maintenance

Leak heat leak

References

[1] Huang, J., et al., 2006, Development of permanent magnetic refrigerator at room temperature, Rare metals, 25(6), pp.641-644.

[2] Okamura, T., et al., 2006, Performance of a room-temperature rotary magnetic refrigerator, Int. J Refri., 29(8), pp.1327-1331.

[3] Yao, G., et al., 2006, Exerimental study on the performance of a room temperature magnetic refrigerator using permanent magnets. Int.J Refri., 29(8), pp.1267-1273.

[4] Zheng, Z., et al., 2009, Design and performance study of the active magnetic refrigerator for room-temperature application. Int. J Refri., 32(1), pp.78-86.

[5] Li, P., et al., 2006, A practical model analysis of active magnetic regenerative refrigerators for room temperature applications. Int. J Refri., 29(8), pp.1259-1266.

[6] Kawanami, T., et al., 2006, Optimization of a magnetic refrigerator at room temperature for air cooling systems. Int J Refri., 29(8), pp.1294-1301.

[7] Brück, E., et al., 2003, Magnetic refrigeration-towards room-temperature applications. Physica B, 327(2-4), pp.431-437.

[8] Gschneidner, K. A. and Pecharsky, J. V. K., 2006, Rare earths and magnetic refrigeration. Journal of Rare Earths, 24(6), pp.641-647.

[9] Othmani, S., et al., 2009, New complex magnetic materials for an application in Ericsson refrigerator. Solid State Communication, 149(25-26), pp.969-972.

[10] Tušek, J., et al., 2009, Development of a rotary magnetic refrigerator. Int. J Refri., 33(2), pp.294-300.

[11] Steyert, W. A. 1978, Stirling-cycle rotating magnetic refrigerators and heat engines for use near room temperature. J Applied Physics, 49(3), pp.1216-1226.

[12] He, J., Chen, J., Wu, C. 2003, The influence of heat-transfer laws on the performance characteristics of a magnetic Stirling refrigerator cycle. Int. J Ambient Energy, 24(2), pp.75-82.

[13] Wu, F., et al., 2001, Optimization of irreversible magnetic Stirling cryocoolers. Int. J. Engineering Science, 39(4), pp.361-368.

[14] Lin, G., et al., 2004, General performance characteristics of an irreversible ferromagnetic Stirling refrigeration cycle. Physica B, 344(1-4), pp.147-156.

[15] Ye, X., et al., 2006, Performance optimization of an irreversible ferromagnetic Stirling refrigerator with finite thermal sources. Proc.ECOS 2006, pp.1303-1310.

[16] Tyagi, S., et al., 2004, Thermoeconomic optimization of an irreversible Stirling cryogenic refrigerator cycle. Int. J. Refri., 27(8), pp.924-931.

[17] Kodal, A., et al., 2003, Thermoeconomic optimization for irreversible absorption refrigerator and heat pumps. Energy Conversion and Management, 44(1), pp.109-123.

[18] Sahin, B., et al., 2006, Thermoeconomic analysis of a solar driven heat engine. Renewable Energy, 31(7), pp.1033-1042.

[19] Tyagi, S., et al., 2004, Thermoeconomic optimization and parametric study of an irreversible Stirling heat pump cycle. Int. J Thermal Science, 43(1), pp.105-112.

Experimental Investigation of a Solid/Gas Thermochemical Storage Process for Solar Air-Conditioning

Driss STITOU, Nathalie MAZET, Sylvain MAURAN

Laboratory PROMES-CNRS (PROcédés, Matériaux et Energie Solaire), Rambla de la Thermodynamique, Tecnosud, 66100 Perpignan, France

Abstract: This paper focuses on studying the experimental performances of a solar air-conditioning pilot plant for housing, which is running in PROMES laboratory (Perpignan-Odeillo, France) since 2006. This pilot of daily cooling capacity of 20 kWh, consist of a solid/gas thermochemical sorption process powered at 60-70°C by 20 m² of flat plate solar collectors. The thermochemical sorption process is based on the coupling of a liquid/gas phase change of a refrigerant (NH3) and a reversible chemical reaction between a reactive solid (BaCl2) and this refrigerant. Its functioning mode is intrinsically discontinuous and cyclic. It is well adapted to the storage/transformation of solar energy. An analysis of experimental results leads to an averaged efficiency of 50% for the solar collectors and a process COP ranging from 30 to 40%, leading thus to a daily cooling productivity for the thermochemical process of about 0.8 to 1.2 kWh of cold produced at 4°C per m² of solar collector.

Keywords: Solar Air-Conditioning, Solid/Gas Sorption, Thermochemical Reactor, Solar Collector

1. Introduction

Nowadays, peaks in electricity demand occur more frequently during the summer period in most developed countries, because of the increasing use of air-conditioning. The reasons for this lie in higher thermal comfort expectations, in lower initial costs for air-conditioning equipments and in the heat island effect in urban areas, which leads to microclimatic changes. Moreover, final energy consumption in buildings in the European Union represents about 40% of the total energy consumption. This energy consumption means that the building sector is responsible for about 20% of the total CO_2 emissions.

Moreover, solar assisted refrigeration appears to be a promising alternative to the conventional electrical driven air-conditioning units from an environmental point of view, since it results in decreased CO_2 emissions and in the elimination of CFCs and HCFCs. Considering the problem of peak load increase during summer months caused by electrically driven air-conditioning systems, and the close coincidence of the maximum solar irradiation with both the cooling loads and the peak electricity, solar assisted refrigeration may be an interesting option to handle successfully the issue of reducing peak electricity demand due to air-conditioning.

Solar sorption refrigeration technologies such as thermochemical reaction, adsorption, absorption and desiccant cooling processes, are the prevailing option for the utilisation of solar energy in air-conditioning. Solar coolers and refrigerators have been developed for more than 40 years using solid adsorption [1-3], liquid absorption [4,5] or thermochemical reaction processes [6,7].

These solar heat driven cooling processes seem to have an excellent potential in the space air-conditioning business, albeit that so far they are not really a competitive alternative to the conventional vapour compression chillers. There is still a development demand to optimise these systems and to carry out experimental investigations on such processes.

The present study focuses on experimental investigations carried out on a solar powered solid/gas thermochemical pilot plant whose size is representative for air conditioning in housing.

Corresponding Author: Driss STITOU, Email: stitou@univ-perp.fr

2. Principle of solid-gas thermochemical sorption process

Thermochemical processes are usually based on a monovariant reversible reaction between a solid reactant and a gas:

$$S_1 + \nu.G \leftrightarrows S_2 + \nu.\Delta H_R$$

By coupling such a solid-gas reaction with a liquid/gas phase change of the same working gas, a sorption cooling production process can be designed:

$$L + \Delta H_V \leftrightarrows G$$

Following the right direction, the solid S_1 (gas G-free) reacts with the gas G produced by evaporation, to form the solid S_2. This synthesis reaction is exothermic and produces the heat of reaction ΔH_R. In the reverse direction, the decomposition reaction is endothermic: S_2 is decomposed into the initial salt S_1 and releases the gas G which is condensed. This endothermic reaction requires the heat quantity ΔH_R to proceed.

The two processes are monovariant and their equilibrium conditions follow the Clausius–Clapeyron relation (1). The thermodynamic equilibrium conditions of the reactor are determined by only one parameter (P or T):

$$\ln\left(\frac{P}{P_{ref}}\right) = -\frac{\Delta H_i}{RT} + \frac{\Delta S_i}{R} \qquad (1)$$

Then, the simplest sorption machine consists of a solid/gas reactor coupled with an evaporator/ condenser. A solar sorption process operates according to two different phases that correspond to the diurnal period during which the system is regenerated and nocturnal period during which the cooling effect is produced by the system:

- During de daytime, the reactor is heated by solar energy and desorbs the gas that condenses in the condenser at ambient temperature. The system is thus regenerated at a high pressure due to the condensation temperature of reactive gas.
- During the nightime, as the reactor is cooled down, it reabsorbs the gas and induces a pressure decrease in the system. This enables the boiling of the liquid in the evaporator that produces the cooling effect below the ambient temperature.

The reactive salt chosen for the pilot plant is the barium chloride, $BaCl_2$, that reacts with 8 moles of ammonia to form $BaCl_2.8NH_3$.

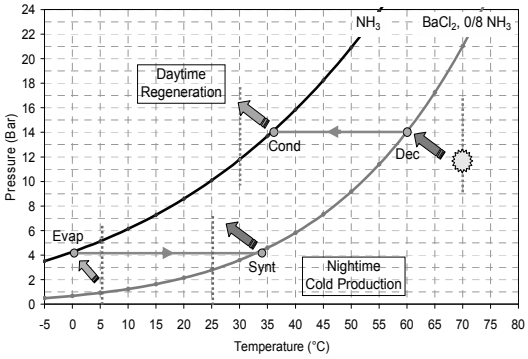

Fig. 1 : Operating thermodynamic conditions of the solar solid/gas sorption process

This salt has already been used for refrigeration and air-conditioning processes [8-10]. Its main advantages lie in the low decomposition temperature of the salt which is ranging from 50–70 °C for the high-pressure phase depending on the condensing pressure (Fig. 1). This allows simple heating systems such as flat plate solar collectors. Moreover, it presents a high stoechiometry ν, which minimizes the size of the reactor.

For these thermochemical processes, the solid reactant is mixed with natural expanded graphite (GNE), and recompressed together in order to form in consolidated blocs. Expanded graphite has been widely used as a porous additive in composite reactive medium due to its high thermal conductivity and gas permeability. This implementation was first developed in PROMES laboratory in 1983 to enhance heat and mass transfer in the reactors [11].

3. Pilot Plant Description

The pilot plant was designed to provide a cooling capacity of 20 kWh of cold per day. This corresponds to the air-conditioning needs of a conference room of 120m² during 4-5 hours.

3.1 Components of the pilot plant

Figures 2 and 3 display some views of the pilot plant and a schematic diagram of the installation.

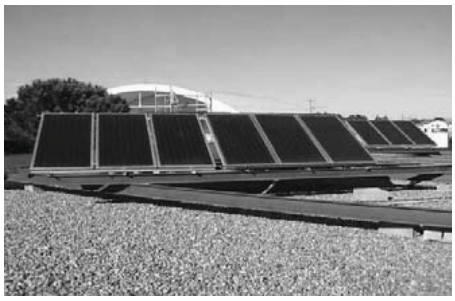

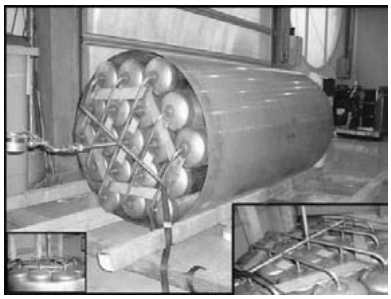

Fig. 2: Flate plate solar collectors and the thermochemical reactor design

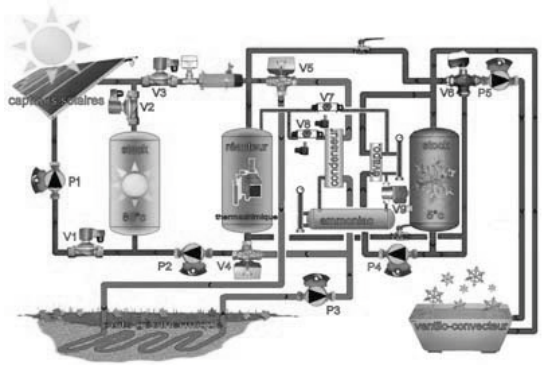

Fig 3 : View of the solar sorption pilot plant and schematic description of the solar air-conditioning thermochemical unit.

The pilot plant consists of four subsystems:

- a solar heating loop,
- a thermochemical sorption unit,
- a water cooling loop,
- a cold water loop.

The solar heating loop, which consists of 21.6 m² of flat plate collectors connected to the reactor and a thermal storage filled with 360 kg of a phase change material (wax) that melts at 78°C. The PCM heat storage enables:

- the storage of the surplus of the available solar heat when the reactor decomposition is accomplished during the afternoon,
- the partial storage of the sensible heat released by the reactor when it begins to cool down at the end of the decomposition phase,
- the heating of the reactor at the beginning of the day, when the solar heat is not sufficient.

The thermochemical sorption unit consists of one reactor, which is composed of a set of 19 tubes filled with a composite reactive porous medium, consisting of a recompressed mixture of 140 kg of $BaCl_2$ and 35 kg of expanded natural graphite to enhance heat and mass transfer in the reactive composite. The reactor is either connected to a condenser during the day and the evaporator during the night through the valves V7 and V8. The condensed ammonia is stored in a reservoir in order to be used during the night.

The water cooling loop enables alternatively the cooling of the condenser during the day and the cooling of the reactor during the night thanks to a set of two 3-way valves (V4 and V5). This cooling loop is composed of a horizontal in-ground plate heat exchanger of 16m², which is buried at two meters depth.

The cold water loop is connected to the evaporator. The cold water is produced at 2°C during the night phase. The cooling capacity is stored into a second cold storage, which is filled with 340kg of a PCM (wax) that solidify at 5°C. During the day, fresh water at 13°C is distributed from the PCM storage via a mixing valve (V6) to the fan-coil units placed in the conference room.

3.2. Control of the solar process

The pilot plant is instrumented and controlled under Labview software :

- The solar heating loop is controlled by a pyranometer and temperature measurements at the outlet of solar collectors, and inside the reactor and hot PCM storage.
- The connection of the reactor with either the condenser or the evaporator is controlled by pressure sensors (reactor, evaporator and condenser) and a level gauge placed in the reservoir of the condensed ammonia. When the high level is reached then the decomposition phase stops, and the reactor is cooled down by the cooling loop. The synthesis phase is stopped when a low level in the liquid reservoir is reached due to the absorption of the ammoniac by the reactor.
- The cooling of the condenser is started when the reactor is connected to the condenser during the decomposition reaction, while the cooling of the reactor is started when the pyranometer indicates a low irradiation value at the end of the afternoon or when a high level of liquid ammonia in the reservoir is obtained. The cooling loop feeds separately either the reactor or the condenser.
- The cold water loop is started when the reactor is connected the evaporator and if the evaporating temperature is lower than the cold PCM storage temperature.
- The distribution of the fresh water from the cold PCM storage to the fan-coil units is activated on user's demand during the day.

Some security procedures are foreseen to prevent an overpressure that may occur during hot summer days in the reactor. In this case, the solar heating loop is stopped and/or the connection between the reactor and the condenser is strained.

4. Experimental Results

A typical thermal cycling of the pilot plant is shown in Fig. 4. During the day, the solar collectors deliver hot water at a maximum temperature of 75-80°C and enable the heating of the reactor, which reaches a maximum temperature of 68-73°C. The connection of the reactor with the condenser begins when the reactor attains a temperature of around 60°C or more precisely when its pressure becomes greater than the condenser pressure. During the night, as the reactor is cooled down below 40°C, cold is produced at the evaporator at a temperature of about 0°C (Fig. 1). Chilled water is then produced at a temperature below 3°C, which is enough to solidify the PCM contained in the cold storage. During the day, fresh water is delivered at 13°C by a mixing valve to fan-coil units placed in the conference room.

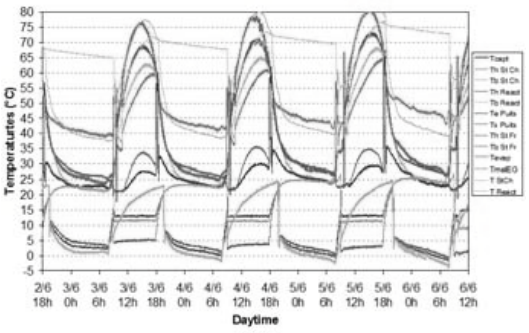

Figure 4: Temperature evolutions for the main components of pilot plant

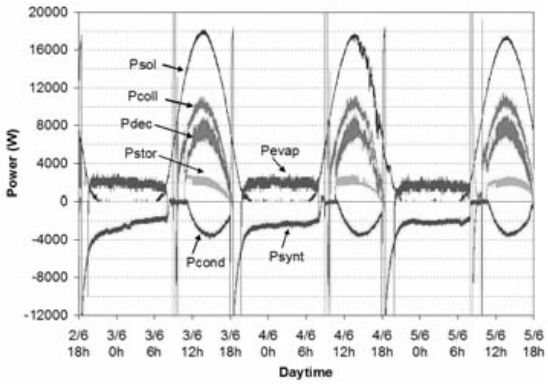

Fig. 5. Evolution of the thermal powers (W) involved in the thermochemical process

Fig. 5 represents the thermal powers obtained in the process. The solar collectors supply a maximum power of 10 kW. The reactor absorbs approximately 70% of the supplied power for the decomposition reaction and the rest is stored in the hot PCM. The efficiency of the solar collector is in the order of 55% for these sunny days.

During the night, the evaporator enables a cooling power of about 2 kW during 10 hours. The heat of synthesis reaction is released into the ground with a power of about 3 kW.

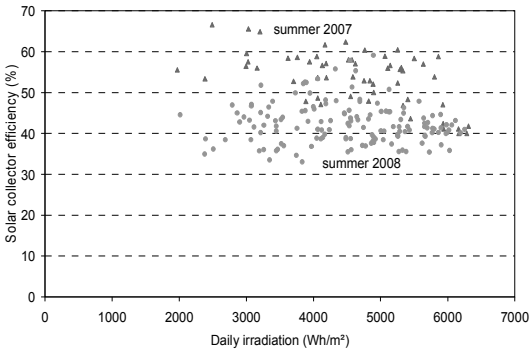

Fig. 6. Evolution of the solar collector efficiency over the summer periods of 2007 and 2008

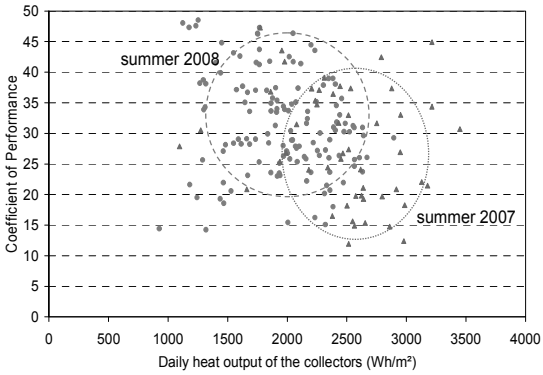

Fig. 7. Evolution of the daily process COP over two summer periods

The pilot plant is running since 2006. Figures 6 and 7 present the performance of the thermochemical process over the two summer periods 2007 and 2008. Each point in the graphs represents a daily performance. A decrease of the efficiency of the solar collector is observed in Fig. 6. In summer 2007 the collector efficiency was about 50 to 60% while in summer 2008 the solar collector efficiency was reduced to a value ranging from 40 to 50% due to a bad aging of the solar collectors.

This decrease in the solar collector efficiency has been counter-balanced by a better control and management of the solar heating loop that has been improved during the summer 2008. As a result, the solar collectors heat output is efficiently used by the reactor, enabling thus a greater cooling production. Figure 7 shows the evolution of the coefficient of performance of the thermochemical process, which is defined as the ratio of the cold production to the heat supplied to the reactor. Even if the heat supplied by the collectors during summer 2007 is greater, due to a better solar collector's efficiency, the daily COPs were globally lower than those obtained during summer 2008. Thus the daily COPs are ranging from 25 to 45 % with an improved management of the different components of the sorption pilot plant.

The daily cooling productivity of such thermochemical process is ranging from about 800 to 1200 Wh of cold produced at 4°C per m² of solar collector.

5. Conclusions

Solar cooling can become a promising solution for the clean and sustainable air-conditioning of urban buildings. As the demand for air-conditioning is increasing in the urban environment and, considering the fact that soft technologies like passive cooling are very difficult to apply in existing buildings, the sorption cooling technology discussed in this paper may provide a competitive alternative to conventional air-conditioning systems. Solar refrigeration is a technology that has a great variety of methods of producing low temperatures; however, very few have demonstrated a technical and economical viability.

The experimental study presented in this paper shows that is possible to develop thermochemical solid-gas sorption process for air-conditioning using only simple flat plate solar collectors operating at 70°C. Our results shows that an optimal management and control of the different components of the sorption pilot plant, e.g. the coupling of the solar collector loop with the hot PCM storage and the reactor or the connection of the reactor with the condenser and evaporator, can result in a substantial increase in the daily cooling production. The yearly solar COP of such process is around 18%, which is not far from those obtained (around 22 %) by other more efficient solar sorption process, e.g. liquid/gas absorption machines.

References

[1] K. Sumathy, K.H. Yeung, L. Yong, Technology development in the solar adsorption refrigeration systems, *Progress in Energy and Combustion Science,* 29 (2003) 301-327.

[2] A. Boubakri, J.J. Guilleminot, F. Meunier, Adsorptive solar powered ice maker: experiments and model, *Solar Energy* 69 (2000) 249-263.

[3] M. Li, R.Z. Wang, Y.X. Xu, J.Y. Wu, A.O. Dieng, Experimental study on dynamic performance analysis of a flat-plate solar solid-adsorption refrigeration for ice maker, *Renewable Energy*, 27 (2002) 211-221.

[4] A. Erhard, E. Hahne, Test and simulation of a solar-powered absorption cooling machine, *Solar Energy* 59 (4-6) (1997) 155-162.

[5] A. De Francisco, R. Illanes, J.L.Torres,M. Castillo, M. De Blas, E. Prieto, A. Garcia, Development and testing of a prototype of low-power water/ammonia absorption equipment for solar energy applications, *Renewable Energy,* 25 (2002) 537-544.

[6] B. Spinner, Ammonia-based thermochemical transformers, *Heat Recovery Systems and CHP,* 13 (4) (1993) 301-307.

[7] [7] M. Balat, G. Crozat, Conception and study of a prototype of a solar refrigerator based on a solid/gas reaction, *International Journal of Refrigeration,* 11 (1988) 308-314.

[8] L.W. Wang, R.Z. Wang and R.G. Oliveira, A review on adsorption working pairs for refrigeration, *Renewable and Sustainable Energy Reviews*, Vol 13 (3), (2009), 518-534.

[9] [9] C. Rivera, I. Pilatowsky, E. Méndez, W. Rivera, Experimental study of a thermo-chemical refrigerator using the barium chloride–ammonia reaction, *International Journal of Hydrogen Energy*, *Vol 32 (15)*, 2007, 3154-3158

[10] C. Dueñas, I. Pilatowsky, R. J. Romero, A. Oskam and A. Finck, Dynamic study of the thermal behaviour of solar thermochemical refrigerator: barium chloride-ammonia for ice production, *Solar Energy Materials and Solar Cells*, Vol 70 (3), 2001, 401-413

[11] Coste C, Crozat G, Mauran S. Procédé de mise en oeuvre et réaction solide-gaz. Patent FR 8,309,885, US patent 4,595,774 (1983).

Acknowledgments: The authors wish to acknowledge the French Agency ADEME and the research program ANR-PREBAT "ORASOL" for their financial support in this project.

Carbon Dioxide as Hydrogen Vector: Storage and Delivery

Gábor Laurenczy

École Polytechnique Fédérale de Lausanne (EPFL), Institut des sciences et ingénierie chimiques (ISIC), Laboratoire de chimie organométallique et médicinale (LCOM), Lausanne, CH-1015, Switzerland

Abstract: Safe and convenient hydrogen storage and delivery is the central question for the further development of the hydrogen economy. Formic acid is among the potential candidates, among the small organic molecules, suitable for H_2 storage. It has been shown that the selective homogeneous catalytic decomposition of formic acid in aqueous solution can be carried out using hydrophilic ruthenium-based catalysts, generated from the highly water soluble ligand meta-trisulfonated triphenylphosphine (TPPTS) and $RuCl_3$. The formic acid splitting reaction takes place under mild experimental conditions, in a wide range of temperature, and at a controllable rate, generating hydrogen in a very vide pressure range, so HCOOH is considered as a viable hydrogen storage material. Several catalysts and processes are developed for the homogeneous catalytic hydrogenation of carbon dioxide, bicarbonate and carbonate in water. Aqueous systems are well suited for this process. On the basis of these results one can envisage the practical application of carbon dioxide as hydrogen vector for storage and delivery.

Keywords: hydrogen storage, high pressure H_2 generation, hydrogenation, CO_2 reduction, catalysis in water, formic acid.

1. Introduction

Hydrogen is one of the promising candidates to replace traditional fossil fuels both for environmental and economic reasons. Hydrogen has the advantage of being non-toxic and to form only water when it burned, combined with fuel cell technology, very efficient energy conversion can be achieved. However, its storage remains a challenge: Conventional hydrogen storage like high pressure gas containers and cryogenic liquid containers have weight and safety issues. Therefore a variety of new materials have been developed, such as metal hydrides, metal-organic frameworks, carbon nanostructures, small inorganic and organic "hydrides". These strategies having their own technical and cost problems, solutions to overcome them are currently an active area of research.

Formic acid is among the potential candidates, among the small organic molecules, for H_2 storage (*Table 1.*). HCOOH contains 4.4 weight % of hydrogen, having a flash point of + 69 °C, much higher than that of the gasoline (-40 °C) or methanol (+12 °C). It also has the advantage that only gaseous products (H_2/CO_2) are formed during the dehydrogenation process, the accumulation of any by-products is avoided (eq. 1). The 85% aqueous formic acid solution is not any more inflammable and dilute formic acid is approved as a food additive (US Code of Federal Regulations: 21 CFR 186.1316, 21 CFR 172.515). However, until now potential applications of this process have been limited by the reaction conditions and catalyst efficiency.

Table 1. Volumetric hydrogen storage capacities for the conventional H_2 storage methods and for HCOOH.

Storage	Pressure	Temperature	H "density"
hydrogen gas	200 bar	25 °C	**16 g / l**
hydrogen gas	350 bar	25 °C	**28 g / l**
liquid H_2	1 bar (700 bar)	- 253 °C	**70 g / l***
formic acid	1 bar (1200 bar)	25 °C	**53 g / l**

$$HCOOH \rightarrow H_2 + CO_2 \quad (eq.\ 1)$$

On the other hand, carbon dioxide is present with increasing concentration in the atmosphere as

Corresponding Author: Laurenczy Gábor, Email: Gabor.Laurenczy@epfl.ch

"greenhouse gas", calcium and magnesium carbonates are widely available on the Earth. (Scheme 1).

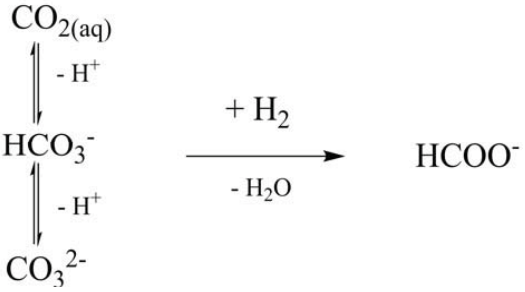

Scheme 1. Hydrogenation of carbon dioxide, bicarbonate and carbonate into formic acid.

Their conversion into useful organic C_1 building blocks (e.g. into formic acid) is a great challenge for chemistry. Since carbon dioxide is a thermodynamically stable, highly oxidized compound, its synthetic utilization requires some kind of a reduction – e.g. reaction with molecular hydrogen. The first product of the stepwise reduction of CO_2 with H_2 is the formic acid, the most common product of the aqueous organometallic catalytic reduction. In aqueous solution this reaction becomes slightly exergonic with $\Delta G_{298} = -4$ kJ mol^{-1}.

2. Results and discussion

The selective homogeneous catalytic decomposition of formic acid in aqueous solution can be carried out using hydrophilic ruthenium-based catalysts, generated from the highly water soluble ligand meta-trisulfonated triphenylphosphine (TPPTS, Scheme 2) and $RuCl_3$.

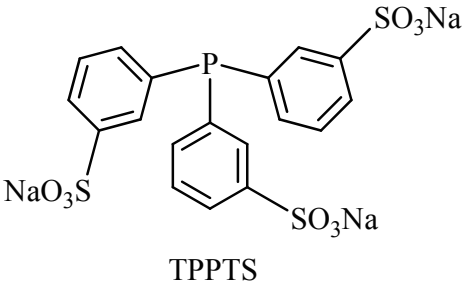

TPPTS

Scheme 2. The highly water soluble (1100 g/L) phosphine ligand, the meta-trisulfonated triphenylphosphine.

The formic acid splitting reaction takes place under mild experimental conditions, in a wide range of temperature (*Fig. 1.*), and at a controllable rate. On the basis of this catalytic system, HCOOH can be used as a viable hydrogen storage material.

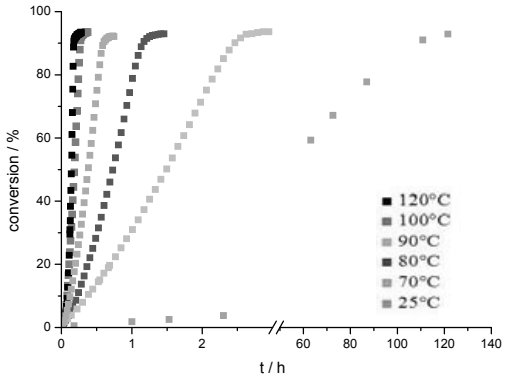

Fig. 1. Effect of temperature on the decomposition of formic acid (22 mM $RuCl_3$, 2 eqv. phosphine, 4 M HCOOH/HCOONa (9:1), 2.5 ml H_2O/D_2O (1:1), 90°C, addition of 0.38 ml HCOOH for recycling, kinetic curves displayed after the activation period).

A continuous high pressure hydrogen generator has been built, in this setup, the catalyst remained active after a large number of times stopping and re-starting the process, having a total turnover number for the reaction TON = 86400. The catalytically active species are formed in situ from $[Ru(H_2O)_6]^{2+}$, $[Ru(H_2O)_6]^{3+}$ or $RuCl_3 \bullet xH_2O$, with the water soluble phosphine TPPTS, as co-catalyst. The decomposition of formic acid is slow, unless sodium formate is present as an initiator. An induction period, which can be reduced by pre-treatment with H_2, is required to generate the active catalyst. The robustness of the formed catalyst allows a very large number of recycles to be carried out without loss of activity, and hence, the system can also operate in continuous mode. Kinetic observations, spectroscopic studies and comparisons with stabilised ruthenium nanoparticles, active for hydrogenation reactions, led to the conclusion that the catalyst is homogeneous. Multinuclear NMR spectroscopy allowed several intermediates to be identified, which led to a reaction mechanism consisting of two competitive catalytic cycles involving a

T F" F, ° .):. -)%4, -":%T vFT 2q-9 a % s nns i e l uOu vFT T F" :"4-)T -. :u4-

q4, F%v, 4, :O)-uv4-F")-O%q4O :" F"q° 46 F wuO 2)F. %v4O , -4-)Fw-"-F%O vu4uq°Q4O vF%q b-u. +u"4uw-F%O xF))-v°vq"w -O2-v:uqq° xF) . :q%4-xF)T :v uv:. OFq%4F"O F) xF) T Fb:q- 2F)4ubq-u22qvu4F"O i -+-)uqu22)Fuv, -O, u+- b--" 4):-. 4F :T T Fb:q0- OFq. :x° 4, - , FT Fw-"-F%O)%4, -":%T R s nns i vu4uq°Q4 buO-. F" :F" -9v, u"w-vFF). :"u4F" u". 2, °Ovuqu. OF)24F" s , - uv4+:4° Fx 4, - +u):F%O , -4-)Fw-"-F%O vu4uq°Q4O xF) 4, -. -vFT 2FO4F" Fx xF)T :v uv:. , uO b--" . -4-)T :"-. s , - , -4-)Fw-":0-. vu4uq°Q4O 6 F%q Fxx-) 4, - u. +u"4uw- Fx -uO° vu4uq°Q4 O-2u)u4F")-v°vq"w :" . :q%4- xF)T :v uv:. F) xF) T Fb:q- 2F)4ubq-u22qvu4F"O

s F)-v°vq- vu)bF" . :F9:. - 4)u"OxF)T :"w 4, - e e , °.)Fw-"-")w° O4F)uw- O°O4-T 4F e "-%4)uq 2)Fv-. %)- u" -xx:v:-"4 e)-. %v4F" T -4, F. "-v-O0u)° e %) 2)-+:F%O)-O%q4OO, F6 4, u4 4, - vu)bF" . :F9:. - u". vu)bF"u4-O vu" b-, °.)Fw-"u4-. vu4uq°4:vuqq° :" 6u4-) :" :F":v q(%. Ou". uO6-qquO:" b:2, uOv O°O4-T O :w

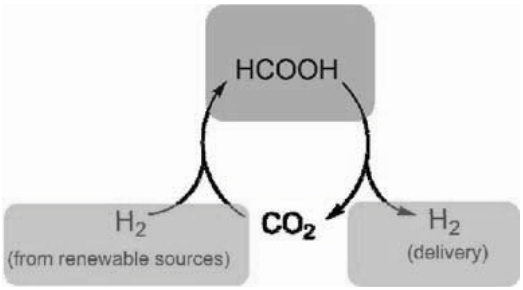

Eq oun 0qEnma5 t PEyLa hELSFhn l iLEr If PtIh t Cl dh

i -+-)uq %HH u". , H vFT 2q-9-O , u+- b--" xF%". vu4uq°4:vuqq° uv4+- xF) 4, :O)-. %v4F" a % q ns a lu"-i l uqOF vu4uq°0-O 4, -, °.)Fw-"u4F" Fx e b:vu)bF"u4- u". vu)bF"u4-:F"O4F xF)T :v uv:. xF)T u4-:F" :" u(%F%OOFq%4F" %". -) T :q vF". :4F"O h , :q- 4, - vu4uq°4:v uv4+:4° :OqF6 4, - xF)T u4-F" Fx u" :"4-)T -. :u4- :"+Fq+:"w vFF). :"u4F" Fx bF4, °.):. - u". b:vu)bF"u4- 4F 4, -)%4, -":%T v-"4)- , uO b--" %"uT b:w%F%0q° -O4ubqO, -. b° n u". g o O2-v4)FOvF2° i %v, u" :"4-)T -. :u4- , uO 2)-+:F%0q° b--" xF)-O-" s , - a % e ns a lu"-i l , °.):. F b:vu)bF "u4- vFT 2q-9 :w , uO b--" . -4-v4-. :" O4% b° T %q4"%vq-u) g o O2-v4)FOvF2° s , -)-. %v4F" Fx e 4uk-O2quv-+:u b:vu)bF"u4- O2-v:-Ou". 4, -)u4- . -4-)T :":"wO4-2

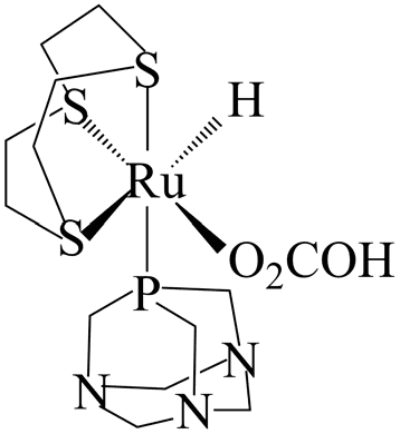

Eq c,Et ,I En Li uChEFhL yIf PEyLaP,n t Lr s dhS yP)nh La É P))Eqar na,)

u22-u)O4F b- 4, - :"4)uT Fq-v%qu) , °.):. - 4)u"Ox-) x)FT 4, - T -4uq4F 4, - vFT 2q-9-. b:vu)bF"u4- e g F F4, -) :"4-)T -. :u4-OF) %xF)T u4- vFT 2q-9-O 6 -)- . -4-v4-. . %):"w 4, - vu4uq°4:v)%"O OF :4 T u° b- uO0%T -. 4, u4 4, -)-. %v4F" Fx e b:vu)bF"u4-4uk-O2quv-+:u 4, - , °.):. F b:vu)bF"u4- O2-v:-O O 4, :O vFT 2q-9 :O 2)-O-"4 :" T -uO%)ubq-vF"v-"4)u4F"O :" 4, -)-uv4F" T :94%)- :4 :O)-uOF"ubq- 4F O%22FO- 4, u4 4, -)u4- . -4-)T :":"wO4-2 :O 4, - 4)u"OxF)T u4F" Fx 4, :O , °.):. F b:vu)bF"u4- O2-v:-O : - :"4)uT Fq-v%qu) , °.):. - 4)u"Ox-) x)FT 4, - T -4uq 4F 4, - vFT 2q-9-. b:vu)bF"u4- 6, :v, OF%q b- 4)u"OxF)T -. 4F u e vFT 2q-9 b-xF)- F) 4, - -(%+uq-"4 O4-2 4, - b:vu)bF"u4- TF)- 2)-v:O-q° 4, - e :"O-)4F" :"4F 4, - %HH bF". :w

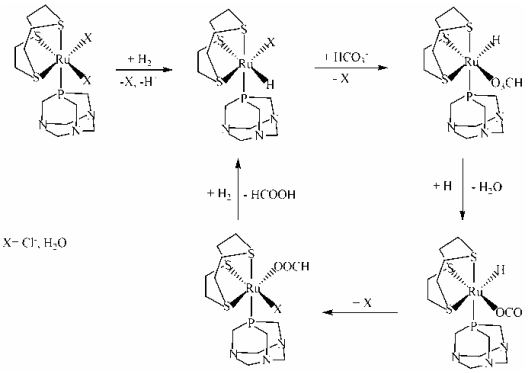

Eq ELsL)nh r nt uPaHyr Li ,un t P,PdC,If uChELqn aP,HLa Li t PEyLa hELSFhn ,L iLEr If PtIh

We have tested the $[RuCl_2PR_3(\eta^6\text{-arene})]Cl$, ($PR_3$ = PPh_3, PCy_3) as catalysts in the hydrogenation of aqueous $CO_2/HCO_3^-/CO_3^{2-}$ system. Kinetic data was obtained using the sum of the integrals stemming from the $[HCOO]^-$ resonances relative to the integral of the $[HCO_3]^-$ resonance (Fig. 5). No induction period was observed and the initial reaction rates were determined from the slope of the curves at time zero, expressed as catalyst turnover frequencies (TOF). At T = 333 K and $p(H_2)$ = 100 bar, the TOFs of 9.4 $mol \cdot mol^{-1} \cdot h^{-1}$ were determined. The conversion at the end of the reaction varied between 61 and 84%, depending on the reaction conditions. While the activity of these compounds in aqueous CO_2 reduction is not very high, a carbonate-hydride complex has been identified as intermediate by high-pressure NMR measurements.

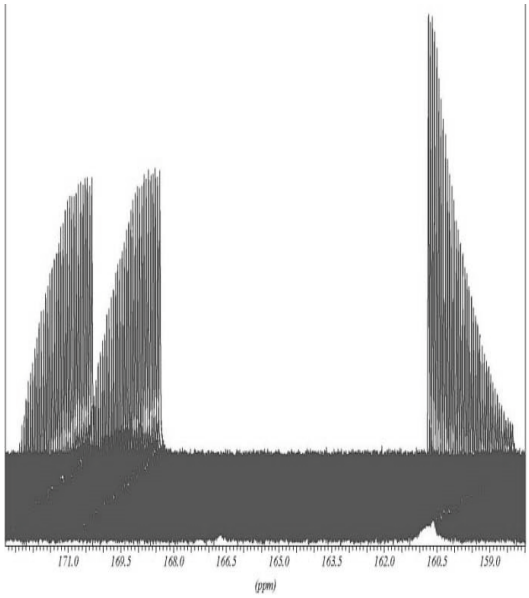

Fig. 5. Evolution of the ^{13}C NMR signals of the formate $[H^{13}COO]^-$ (δ = 171.7 ppm, $^1J_{CH}$ = 194 Hz), and the decrease of the bicarbonate (δ = 160.8 ppm) with time, followed in situ at T= 333 K. The time delay between each spectrum is 1 hour, initial conditions: $[NaH^{13}CO_3]$ = 0.10 M, $p(CO_2)$ = 0 bar, $p(H_2)$ = 100 bar.

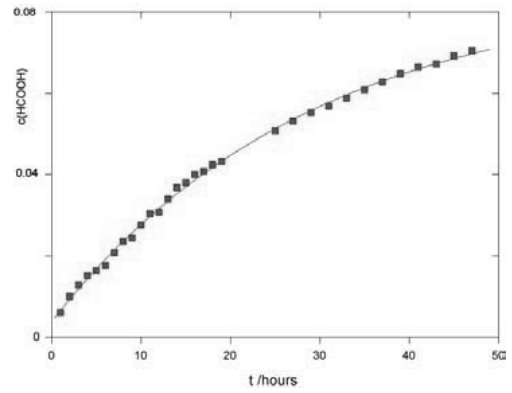

Fig. 6. Typical concentration - time profile for formate formation from bicarbonate, followed in situ by ^{13}C NMR spectroscopy at T= 333 K. Initial conditions: $[NaH^{13}CO_3]$ = 0.10 M, $p(CO_2)$ = 0 bar, $p(H_2)$ = 100 bar.

To make this reduction efficient and applicable in the formic acid – carbon dioxide hydrogen/energy storage/delivery cycle, in stand alone and off the grid units, the reaction conditions have to be optimised and new, more active catalysts need to be developed.

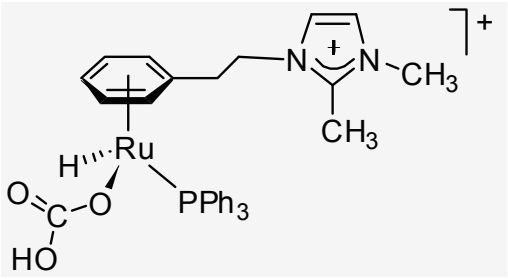

Fig. 7. Structure of hydrido-bicarbonate complex, based on NMR assignments.

Experimental

Hydrogen generation. Kinetic experiments were performed in 10 mm medium-pressure sapphire NMR tubes.[43] In a typical experiment, the ruthenium pre-catalyst (22.5 mM, unless otherwise stated) was dissolved in a formic acid/sodium formate (9:1, 4 M) aqueous solution (2.5 ml, 1:1 D_2O/H_2O) containing TPPTS (63.9 mg, 45 mM, unless otherwise stated). For the Ru(II) complexes the formic acid/formate solution was degassed

prior to the addition of the complex and the tube was sealed under a flow of nitrogen. The tube was then thermostated at 90°C, unless otherwise stated, with an electric heating jacket or directly in the spectrometer, the temperature of which was determined before and after measurement using an external temperature probe. The reaction was followed by monitoring the pressure as a function of time with a pressure transducer connected to the tube via a high pressure capillary, either manually or with a home-made LabView 8.2 program with a NI USB 6008 interface, and/or by ^{1}H NMR spectroscopy. Conversions were determined using ^{1}H NMR spectroscopy by integration of the formic acid/formate peak relative to that of water. Recycling of the catalyst was performed without any protection against oxygen/air, by cooling the sapphire tube to room temperature, depressurisation and addition of formic acid (10 mmol, 0.38 ml).

Carbon dioxide reduction. D_2O (99.9 %) and $NaH^{13}CO_3$ (99 % enriched in ^{13}C) were purchased from Cambridge Isotope Laboratories. Na_2CO_3 and $NaHCO_3$ were obtained from Fluka. H_2 was acquired from Carbagas-CH. All materials were used as received. The reactions were carried out in high pressure sapphire NMR tubes (pressure <120 bar) and were followed by NMR spectroscopy. ^{1}H, ^{13}C and ^{31P} NMR spectra were recorded on Bruker DRX 400 NMR spectrometer. TSPSA and phosphoric acid were used as reference for the ^{1}H, ^{13}C and ^{31}P NMR measurements, respectively. The spectra were fitted with WINNMR and NMRICMA/MATLAB programs (non-linear least square fit to determine the spectral parameters). In a typical reaction $[RuCl_2(PTA)([9]aneS_3]$ (1.5 mg, $3.0 \cdot 10^{-6}$ mol) $NaH^{13}CO_3$ (32 mg, $3.75 \cdot 10^{-4}$ mol), H_2O (1.8 mL) and D_2O (0.7 mL) were introduced under nitrogen atmosphere into a 10 mm high pressure sapphire NMR tube. After the dissolution of all solids, the system was pressurised with H_2. The tube was thermostated to 303.0 (±0.1) K and the reactions were followed by NMR spectroscopy. The concentrations of HCO_2^-, CO_3^{2-} /HCO_3^- and CO_2 were determined from integration of the corresponding ^{13}C and ^{1}H NMR signals. The initial rates and turnover frequencies (TOF = mol formate/mol catalyst/h^{-1}) were calculated by non-linear least squares fits of the experimental data from the initial part of the reactions.

3. Conclusions

The homogeneous catalytic decomposition of formic acid in aqueous solution presented here provides an efficient in situ method for hydrogen production that operates over a wide range of pressures, under mild conditions, and at a controllable rate. Previous limitations to the application of formic acid as hydrogen storage material, notably catalyst deactivation and the formation of side products, have been overcome.

An efficient catalytic system for the generation of hydrogen from the decomposition of formic acid has been realized. The robustness of the formed catalyst allows a very large number of recycles to be carried out without loss of activity, and hence, the system can also operate in continuous mode.

Several catalysts and processes are developed for the homogeneous catalytic hydrogenation of carbon dioxide, bicarbonate and carbonate in water. Aqueous systems are well suited for this process. No further additive (e.g. amine) is needed for an efficient reduction, the pH can be regulated through the CO_2/HCO_3^- buffer by varying the CO_2 pressure. Slightly acidic/neutral conditions are beneficial for the reaction rate as a compromise between increased concentration of the catalytically active Ru hydride and the highest available concentration of $[HCO_3^-]$. It seems that the main role of amines used in earlier studies is in the shift of pH in favor of the formation of bicarbonate.

On the basis of these results one can envisage the practical application of carbon dioxide as hydrogen vector: storage and delivery (*Figs. 8 - 9*).

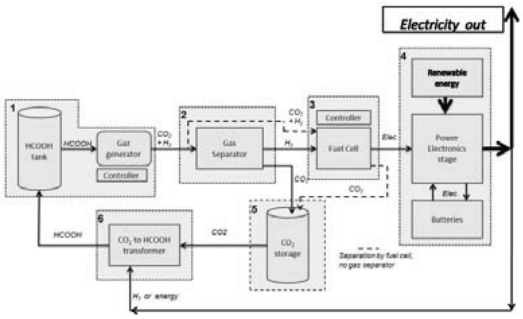

Fig. 8. Schematic diagram for the hydrogen/energy storage - recovery in the formic acid/carbon dioxide system.

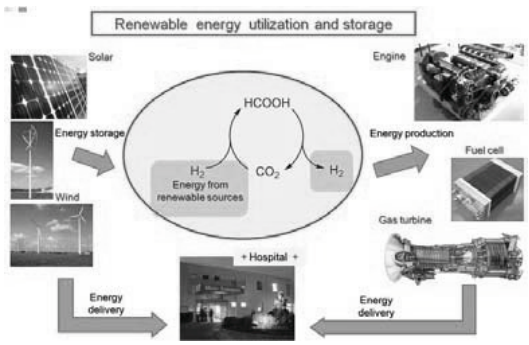

Fig. 9. Renewable energy storage and utilization.

References

[1] Zuttel, A., Borgschulte, A., Schlapbach, L., 2008, *Hydrogen as a Future Energy Carrier*, Wiley VCH, Weinheim.

[2] Fellay, C., Dyson, P. J., Laurenczy G., 2008, A Viable Hydrogen-Storage System Based On Selective Formic Acid Decomposition with a Ruthenium Catalyst, Angew. Chem. Int. Ed., 47, p. 3966.

[3] Fellay, C., Dyson, P. J., Laurenczy G., 2006, *Hydrogen production from formic acid*, Patent Application: EP 1918247, WO 2008047312 20071017

[4] Céline Fellay, Ning Yan, Paul J. Dyson, Gábor Laurenczy, 2009, Selective formic acid decomposition for high pressure hydrogen generation: a mechanistic study, Chem. Eur. J., 15, p. 3752.

[5] S. Enthaler, 2008, Carbon Dioxide - The Hydrogen-Storage Material of the Future? ChemSusChem, 1, p. 801.

[6] F. Joo, 2008, Breakthroughs in Hydrogen Storage - Formic Acid as a Sustainable Storage Material for Hydrogen, ChemSusChem, 1, p. 805.

[7] F. Joó, G. Laurenczy, L. Nádasdi, J. Elek, 1999, Homogeneous hydrogenation of aqueous hydrogen carbonate to formate under exceedingly mild conditions - a novel possibility of carbon dioxide activation., Chem. Comm., p. 971.

[8] G. Laurenczy, F. Joó, L. Nádasdi, 2000, Formation and Characterization of Water Soluble Hydrido-Ruthenium(II) 1,3,5-Triaza-7-phosphaadamantane Complexes and their Catalytic Activity in Hydrogenation of CO_2 and HCO_3^- in Aqueous Solutions under Mild Conditions. Inorg. Chem., 39, p. 5083.

[9] H. Horváth, G. Laurenczy and Á. Kathó, 2004, Water-soluble (η6-arene)ruthenium(II)-phosphine complexes and their catalytic activity in the hydrogenation of bicarbonate in aqueous solution, J. Organomet. Chem., 689, p. 1036.

[10] Urakawa, F. Jutz, G. Laurenczy, A. Baiker, 2007, Carbon Dioxide Hydrogenation Catalyzed by a Ruthenium Dihydride: A DFT and High-Pressure Spectroscopic Investigation, Chem. Eur. J., 13, p. 3886.

[11] T. Geldbach, G. Laurenczy, R. Scopelliti, P. Dyson, 2006, Synthesis of Imidazolium-Tethered Ruthenium(II)-Arene Complexes and Their Application in Biphasic Catalysis Organometallics, 25, p. 733.

[12] G. Papp, J. Kovács, A. Bényei, L. Nádasdi, G. Laurenczy, F. Joó, 2001, Diphenyl-phosphanyl-benzene-para-sulfonic acid and its ruthenium(II) complexes. An old water soluble phosphane ligand in a new perspective, Can. J. Chem., 79, p. 635.

[13] G. Laurenczy, F. Joó, L. Nádasdi, 2000, Towards an easy carbon dioxide reduction in aqueous solution, High Pressure Research, 18, p. 251.

[14] F. Joó, G. Laurenczy, P. Karády, J. Elek, L. Nádasdi, R. Roulet, 2000, Homogeneous hydrogenation of aqueous hydrogen carbonate to formate under mild conditions with water soluble rhodium(I)- and ruthenium(II)-phosphine catalysts, Appl. Organomet. Chem., 14, p. 857.

[15] J. Elek, L. Nádasdi, G. Papp, G. Laurenczy, F. Joó, 2003, Homogeneous hydrogenation of carbon dioxide and bicarbonate in aqueous solution catalyzed by water-soluble ruthenium(II)-phosphine complexes, Appl. Catal. A: General, 255, p. 59.

[16] Á. Kathó, Zs. Opre, G. Laurenczy and F. Joó, 2003, Water-soluble analogs of $[RuCl_3(NO)(PPh_3)_2]$ and their catalytic activity in the hydrogenation of carbon

dioxide and bicarbonate in aqueous solution, J. Mol. Catal. A: Chemical, 204-205, p. 143.

[17] A. Ohlin, G. Laurenczy, 2003, Carbon dioxide reduction in biphasic aqueous – ionic liquid systems by pressurized hydrogen, High Pressure Research, 23, p. 239.

[18] Sylvain S. Bosquain, Antoine Dorcier, Paul J. Dyson, Mikael Erlandsson, Luca Gonsalvi, Gábor Laurenczy, Maurizio Peruzzini, 2007, Aqueous phase carbon dioxide and bicarbonate hydrogenation catalyzed by cyclopentadienyl ruthenium complexes, 21, p. 947.

[19] G. Laurenczy, S. Jedner, E. Alessio, P. J. Dyson, 2007, In situ NMR characterization of an intermediate in the catalytic hydrogenation of CO_2 and HCO_3^- in aqueous solution Inorg. Chem. Commun., 10, p. 558.

[20] W. Gan, Paul J. Dyson, Gábor Laurenczy, 2009, Hydrogen storage and delivery: immobilization of a highly active homogeneous catalyst for the decomposition of formic acid to hydrogen and carbon dioxide, React. Kinet. Catal. Lett., 98, p. 205.

Acknowledgments: Granit Green Networks (Lausanne), Swiss National Science Foundation (FNS), Swiss Innovation Promotion Agency (CTI) and EPFL are thanked for financial support.

Numerical Simulation and Entropy Generation Maps of an Ultra-Micro-Turbogas Compressor Rotor

Giovanni Pierandrei, Enrico Sciubba

University "La Sapienza"-Department of Mechanics and Aeronautics, Rome, Italy

Abstract: The study is aimed at a more thorough understanding of the thermal-fluid-dynamic fields in an ultra-small compressor stage consisting of a radial rotor with an outlet diameter of 0.038 m endowed with a vaneless diffuser. The design stage pressure ratio is β=1.8 at 175 000 rpm. The processed mass flow rate is m = 0.020 kg/s, with inlet and outlet temperatures of 298 K and 380 K respectively. The device is derived from an automotive supercharger, and is part of a single shaft ultra-micro-turbogas generator delivering a design electrical output of 300 watts. A complete analysis has been performed on the geometrical features of the machine and a numerical simulation has been run with a commercial code (FLUENT®) under realistic conditions (turbulent compressible flow). The resulting temperature- and velocity fields have been used for a Second-Law analysis, to use the entropy generation maps to obtain a better insight of the effects of local irreversibilities on the overall stage efficiency.

Keywords: Centrifugal compressor, CFD, Entropic maps, Entropy generation, UMTG,.

1. Introduction

The main goal of this study is an improved understanding of the temperature- and fluid-dynamic fields of an ultra-micro compressor, part of an ultra-micro-turbogas. An existing automotive turbo-charger has been adapted [2] to an innovative electrical power production system for portable use, such as drones, pilotless small planes, and similar self-moving devices. The choice of such an internal combustion engine is suggested by the much higher power output density it displays *vis-à-vis* fuel cells or Li-Ion batteries [4]. Recently, studies aimed at the development of ultra-small scale power generators have received new impulse thanks to the progress obtained in extending thermo-fluiddynamic numerical simulations towards this extremely small scales, and also on the basis of a substantial experience in reverse engineering in the automotive field. In this perspective, the essence of this work is the derivation of detailed entropic maps that will show the entropy generation rate inside the rotor channel, in order to obtain a reliable quantitative assessment of the actual performance, identify possible design improvements and measure their effects. The main challenge of this "portable" power generator is to ensure an acceptable efficiency and stable operation, and the small scales make the turbomachinery part by far the most important in this regard.

2. The hardware

The 0.0038 m compressor wheel has 6 full blades and 6 splitter blades, with a purely axial inlet, 35° back lean at the outlet and a rotational speed of 175,000 rpm; its degree of reaction is R_ρ = 0.59. The rotor is constructed by an Ergal investment casting and it has been simulated here as shrouded. The casing coinsists of a vaneless diffuser and a spiral volute machined from a steel block. The overall radial dimension is 80 mm, and the diameter of the outlet manifold that directs the fluid to the combustion chamber is 35 mm.

2.1. The thermodynamics conditions of compressor rotor

The air mass flow rate processed by the compressor is m = 0.020 kg/s, its inlet temperature has been set to T_{inlet} = 298 K at atmospheric pressure (p_{inlet} = 101 325 Pa). An accurate estimate of the compression process has been performed with CAMEL-PRO™ [1], a process simulator proprietary of the University of Roma 1. The calculated value of the rotor compression ratio is β_{rotor} = 1.55 and the recovery in the diffuser leads to an additional $\beta_{diffuser}$ = 1.16. The overall efficiency of the compressor has been evaluated to be $\eta_{overall}$ = 0.67. The temperature of the air in the outlet manifold is T_{outlet} = 383 K and its pressure is p_{outlet} = 182 385 Pa, so that the overall compression ratio is β = 1.8.

Corresponding Author: Giovanni Pierandrei, Email: g.pierandrei@aesinet.it

3. The grid generation and its features

The geometry has been modelled with a CAD software (Solid Edge® v.18) whose output was formatted in IGES standards and fed to the grid generator programme. The mesh creator used in this study work is Gambit (ver. 2.2.30), the standard feature of the Fluent-Ansys®. The grid is an almost perfectly structured hexahedral mesh, composed of 981,932 cells, 28 along the spanwise length and 120 along the meridional coordinate. An estimate of the boundary layer thickness has been preliminary performed via the equation (1)

$$\delta = \frac{D}{\sqrt{\mathrm{Re}}}, \qquad (1)$$

that results in a thickness $\delta = 1.0765 \times 10^{-5}$ m=10.765 μm.

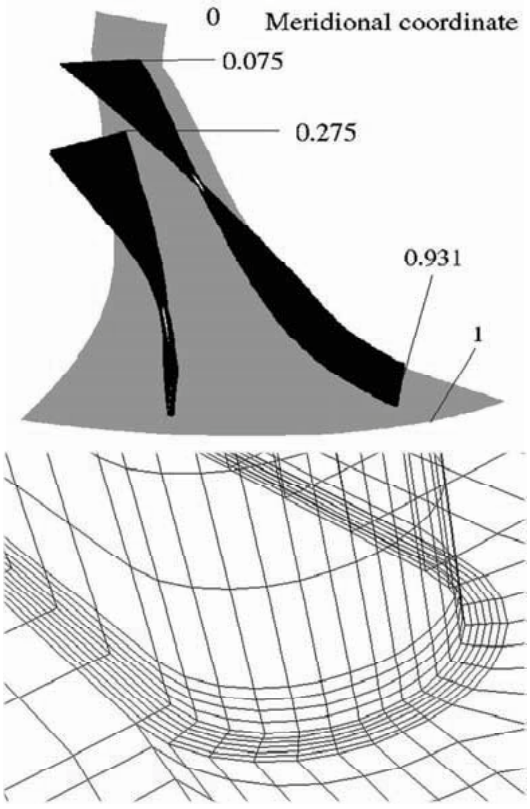

Fig. 1-The simulated geometry (top) and a detail of the mesh in the boundary region at the trailing edge of the full blade.

Along the blades a 6-rows cell layer was implemented, with the first cell thickness of 0.2 μm, and a growth ratio between two consecutive cells of 1.01, obtaining a total length of 1.624 μm. This choice guarantees that the viscous layer will be completely resolved, see Fig. 1. Similar considerations led to the creation of two boundary layer structures on the hub and shroud surfaces, each with 4 rows of cells and the same growth ratio, but with a first cell thickness of 0.4 μm.

4. The numerical simulation

The commercial software used for this research is Fluent (ver. 6.2.16), one of the most popular numerical solver for computational fluid dynamics.

4.1. The boundary conditions

The boundary conditions set for the numerical simulations are:

1. Mass flow inlet: m = 3.333 10^{-3} kg/s, Total temperature: $T_{\text{Inlet tot}}$ = 300 K, Pressure inlet p = 101.325 kPa, Hydraulic diameter D_{H} = 0.00479 m;
2. Pressure outlet: $T_{\text{Outlet,tot}}$ = 355 K, Pressure outlet p = 157.054 kPa, Hydraulic diameter D_{H} = 0.00996 m;
3. Periodic surfaces: there are two boundary faces located at mid-pitch that are defined as periodic, allowing for a "complete" simulation of the compressor rotor.

A clarification is required about the latter boundary condition. Setting a periodic condition at the pitchwise borders means that every flow instability "running across" the rotor channels is neglected and the same applies to inlet and outlet perturbations due to the spinning blades. Thus the real object of the numerical simulations is an almost ideal wheel. Removing the periodic B.C. in the pitch direction would require a much larger mesh and presumably a substantially higher number of iterations to achieve a self-similar unsteady solution .

4.2. The solver settings

The simulations performed for this study have been carried out with the following settings:

i) Coupled explicit solver, slower than its implicit counterpart, but necessary for the use of the multigrid approach;

ii) Multigrid levels extended to 8 coarser sub-grids, the most powerful way to reduce the "global error" (low-frequency) for a large number of cells;

iii) Standard k-ε turbulent model: the main goal of this research is the understanding of large- and medium scale dissipative phenomena, and a more advanced turbulent model was deemed unnecessary in this phase;

iv) Molecular viscosity and specific heat have been defined via 4th order polynomial expressions;

v) Definition of "custom field functions" for the calculation of the local entropy generation rates and of the Bejan number (*Be*) [5].

The custom field functions defined are:

1 The viscous entropy generation rate:

$$\dot{s}_V = \frac{\left(\mu + \mu_{Turb}\right)}{\rho}\frac{\Phi}{T}, \qquad (2)$$

where μ_{Turb} represents the turbulent viscosity, and Φ is the dissipation function, defined as

$$\Phi = \left(\frac{\partial u_i}{\partial x_j}\right)^2;$$

2 The thermal entropy generation rate:

$$\dot{s}_T = \frac{\left(k + k_{Turb}\right)}{\rho}\frac{\left(\nabla T\right)^2}{T^2}, \qquad (3)$$

where k_{Turb} represents the turbulent thermal conductivity

3 The total entropy generation rate:

$$\dot{s}_{Tot} = \dot{s}_T + \dot{s}_V, \qquad (4)$$

4 The Bejan number

$$Be = \frac{\dot{s}_T}{\dot{s}_T + \dot{s}_V}. \qquad (5)$$

Because of the large number of cells, the heavy twisted geometry and the adverse pressure gradient, the simulations have been carried out with a quite small Courant number and under-relaxation factors in order to minimize numerical instabilities and error diffusion. These conditions, on the other hand, have substantially increased the needed computational time.

4.3. Grid sensitivity analysis

The grid sensitivity is a fundamental analysis for all numerical investigations. It allows for a rational evaluation of the mesh capability to capture the phenomena evolving in the control volume. A refinement of the grid normally leads to a better evaluation of dissipative processes, at the expense of computer resources. A grid refinement has been performed within the Fluent environment via the grid adaption tool, which allows for a coarsening-refinement procedure based on the gradient of a selected field variable: in this study this iterative procedure has been based upon the viscous entropy generation rate. The number of cells has been increased of 1 % at every iteration step. After every mesh refinement the numerical simulation has been restarted until a new converged solution has been obtained. Although this method does not allow to select the sub-region involved in the refinement, the grid tuning is performed on the areas where some imbalance for the viscous entropy generation rate exists because of the great magnitude of its gradient. Therefore the gradient-based adaption function automatically identifies, refines and adapts the most critical cells for the objective-field-function. In the case under study the refinement involves regions of higher entropy generation rate that are somewhat predictable *a priori*: the blades' boundary layers and the areas strongly affected by secondary flows, such as stagnation points and wakes.

4.4. Computational resources and required computational time

The numerical simulations have been almost entirely performed on a Double-Pentium® 4 at 3.60 GHz with 2 GB of RAM desktop PC. The required time for every iteration performed on the basic mesh was 90 s. The latter was obviously increased for refined meshes and by the implementation of polynomial expressions for the fluid properties like molecular viscosity and specific heat. An average CPU time for the achievement of the first convergence was in the order of 2.3×10^6 s.

5.The results

The first results one must analyse are of course those related to overall energy performance of the compressor. The fluid is initially accelerated until it reaches the leading edge of the full blade. From this meridional coordinate the flow behaviour changes strongly along the pitchwise direction because of the interaction with the blades pair. A large-scale turbulent structure is generated by an extensive flow detachment occurring at the suction side of the full blade leading edge, travels downstream along the rotor channel and is split in two by the splitter blade. From the meridional coordinate corresponding to the leading edge of the splitter blade, the pressure sides of the blades

begin a more effective compression action, and thus the static pressure rises along the rotor channel. The values obtained from the numerical simulation are remarkably different for the full- and splitter blade, therefore implicitly demonstrating the correctness of the overall results. Figure 2 shows the pressure field on four surfaces plotted along constant pitchwise coordinates, respectively before and after the full- and splitter blades

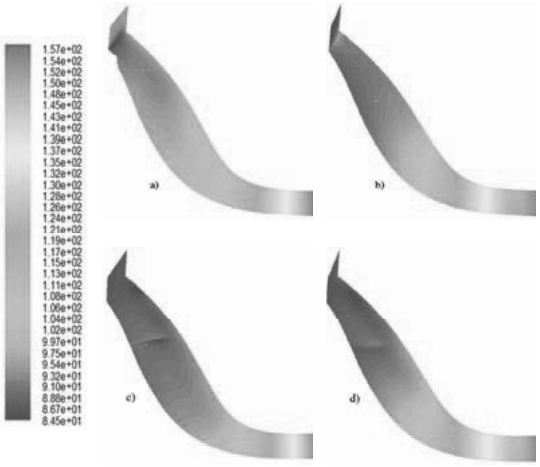

Fig. 2-Plots of the static pressure displayed on pitch-wise surfaces: a)suction side; b)pressure side of the complete blade; c)suction side; d)pressure side of the splitter blade[kPa].

One of the peculiar characteristics of this study is the analysis of the entropy generation rate in the fluid, in order to suggest improvements that may lead to an overall higher efficiency. The entropy generation rates are defined per unit mass, the total

Table 1.-Total-mass integration results for the entropy generation rates [W/K].

	Cells number	Δ%	Basic	1st Refin.	2nd Refin.
$\dot{S}_T$	981,932	N.A.	2.524×10^{-3}	2.795×10^{-3}	2.796×10^{-3}
$\dot{S}_V$	991,956	1.02	1.071×10^{-1}	1.134×10^{-1}	1.137×10^{-1}
$\dot{S}_{Tot}$	1,004,640	1.29	1.096×10^{-1}	1.162×10^{-1}	1.165×10^{-1}

generation rate affecting the fluid as it travels downstream through the compressor wheel an integration over the mass of the finite volumes is necessary. The result of this integration provides the total amount of generated entropy. Table 1 displays the results of the thermal, viscous and total entropy generation rates for the basic mesh and for two grid refinements. As expected, the total entropy generated, as well as both of its components, grows with the refinement. Indeed, smaller volumes allow for the solver to catch a larger number of dissipative turbulent scales, the core of the turbulent dissipative mechanism. Most of the refinement involves the already rather small cells that lay in the boundary layer regions. The size reduction allows for a more finely tuned simulation of the phenomena therein, and lead to the capture of the energy contained in the smaller scales of turbulent energy cascade (though still in the inertial zone). The results reported in Table 1 show an interesting trend: the first mesh improvement performs a strong enhancement of the entropy generation rate capture. The second step further improves this trend and the solver ability to catch the dissipative structures but this capability is far smaller. Extending the refinements would deliver always decreasing improvements on the grid sensitivity and a strongly decaying sharpness of the capture procedure. Once the numerical solution has converged, a smooth thermal-fluid-dynamics field has been evaluated; refining the most critical regions and their cells performs the improvement, sharpening the simulator ability in the most relevant areas for the entropy generation rates. A standard parameter for the evaluation of grid quality is the dimensionless distance:

$$y^+ = \frac{\rho u_\tau y_P}{\mu}, \tag{6}$$

where

$$u_\tau = \sqrt{\tau_w / \rho_w}, \tag{7}$$

is the friction velocity. Further steps in the same direction would either involve less critical fluid regions or reduce the cells volume without further benefit. Table 2 shows the variation of the y^+ from its original value on the basic mesh after two successive mesh refinements. The largest values can be found at the trailing and leading edge of the blades, and the improvement obtainable via additional refinements would be inefficient with regard to the computational time. In order to gain a more sensitive capture of small-scale phenomena other paths ought to be followed, like selective refinement in specific areas or the adoption of

Table 2.-Variation of the y^+ value for the basic mesh and after two refinement steps.

	Basic mesh	2nd Ref mesh
Cells	981,932	1,004,640
$y^+ < 2$	944,615 (99.1996%)	966,512 (96.2050%)
$y^+ > 5$	1264 (0.1287%)	1208 (0.1202%)
$y^+ > 6$	65 (0.0066%)	55 (0.0055%)

refined turbulence models, but neither procedure has been adopted here. Figure 3 displays the

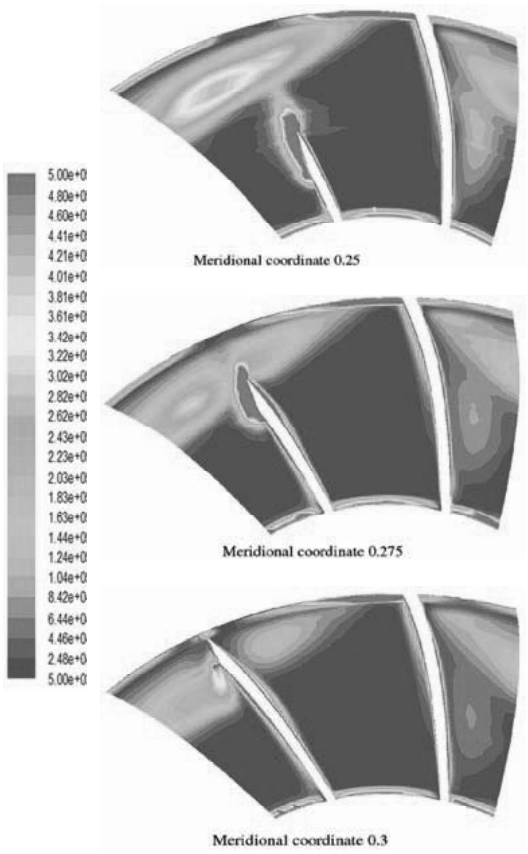

Fig. 3-Development of the viscous entropy generation rate at the splitter blade leading edge [W/(kg K].

viscous entropy generation rate development at the splitter blade leading edge. The large yellow area that develops across the channel from the suction side of the full blade to the leading edge of the splitter blade is the previously mentioned turbulent structure caused by the rather inefficient coupling between the flow and the inlet of the full blade. A similar viscous dissipation, generating another turbulent structure, develops on the suction side of the splitter blades: these two structures merge downstream. These phenomena result in a double "viscous core", the first developing at the tip directly from the turbulent structure sweeping the rotor channel, the second being generated by a poor interaction between the fluid and the splitter blade. Both structures migrate toward the centre of the blade-bounded channel. Figure 4 displays the evolution of the Bejan number. This dimensionless quantity is defined as the ratio of the thermal- to the total entropy rate. Recalling that the last stage

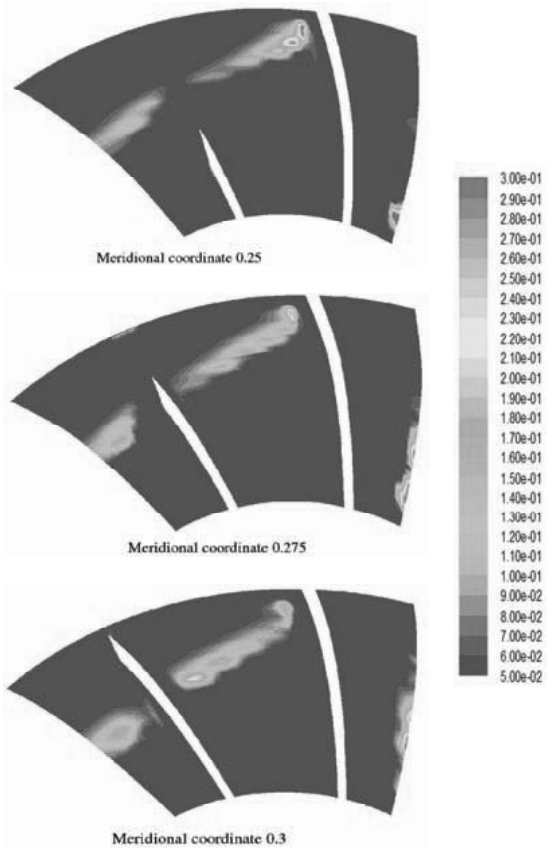

Fig. 4-Development of the Bejan Number at the splitter blade leading edge.

of the turbulent kinetic energy degradation is a micro-scale dissipative heating, it can be easily seen that *Be* is positive definite, since some degree of thermal entropy generation always exists. On the other hand the Bejan number can be equal to- but not exceed-1, in areas where there is no viscous entropy generation. On Figure 4 it can be noticed that the thermal field , characterised by a meaning quite small *Be*, is almost uniform, the physical being that there is a pretty small

temperature difference within the fluid. Therefore the first part of the compression is not affected by any relevant compression heating, due to the acceleration imposed to the fluid. The only regions showing a relevant thermal contribution to the entropy generation rate are the "buffer" areas between the regions with a high viscous generation rate and those with a low one. This interface region promotes the turbulent kinetic energy dissipation in the small scales. Within the high viscous generation rate area, the turbulent energy cascade has not completely developed and the so called Kolmogorov's micro-scales [6,7,9] have presumably not been yet attained, therefore the viscous heating can not be captured by the simulation. On the other hand the region marked by a small Bejan number is scarcely dissipative in both thermal and viscous terms revealing a small influence on the total entropy generation rate. As stated by Denton [3] the flow within the impeller is always highly three dimensional: the blade loading induces secondary flows convecting the hub and casing boundary layers toward the suction surface. The net result is that a large concentration of high-entropy fluid collects in the vicinity of the casing-suction surface corner. This phenomenon has been captured by the numerical simulations performed in this work, as confirmed by the entropy maps along the rotor channel between the meridional coordinate 0.5 and 0.6. Figure 6 shows the relative tangential velocity and Figure 5 the thermal entropy generation rate on the mentioned meridional sections. The blade on the right is the full one, that on the left the splitter, and the pressure side of the full blade is looking toward the splitter. Running through the meridional coordinate one can notice a strong migration of fluid at the casing from the full blade pressure side toward the splitter blade. There is a stretched bubble of fluid endowed with a strong relative tangential velocity driving the entropy generation. The plots on the same meridional coordinate reveal the agreement between the present results and Denton's statement about the entropy generation. Another interesting region is the leading edge of both blades. Figures 7 and 8

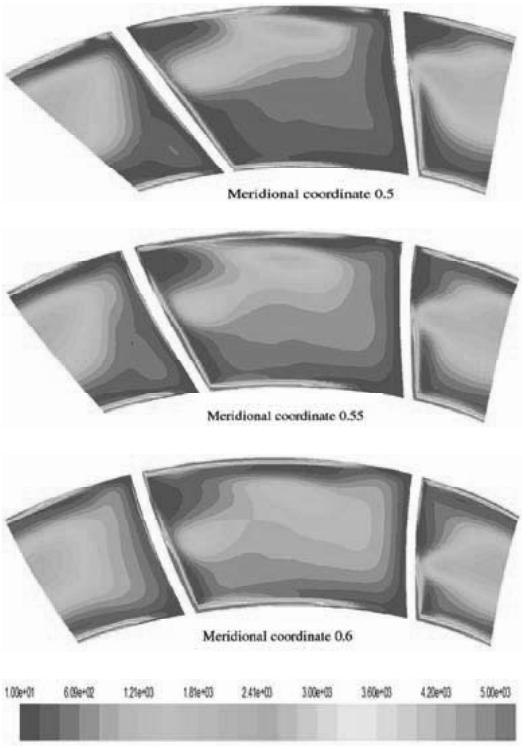

Fig. 5-Plots of the thermal entropy generation rate [W/(kg K)]

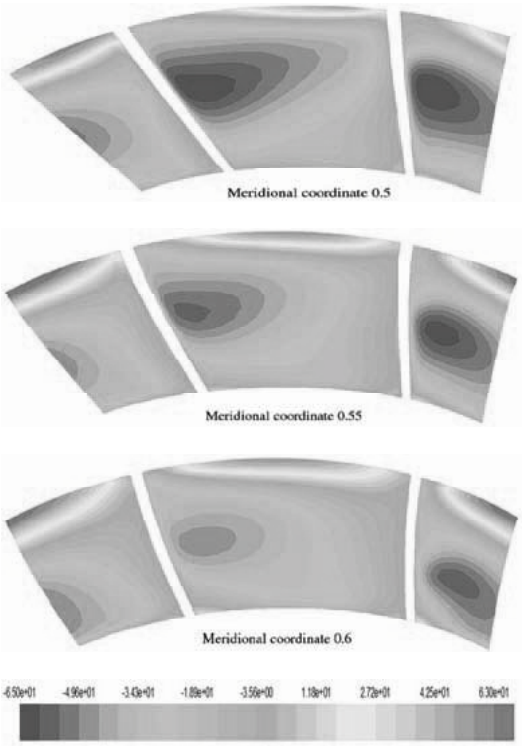

Fig. 6-The development of the relative tangential velocity in the fluid migration from the P.S. to the S.S.

display the area included between the full blade pressure side, on the right, and the splitter blade suction side, on the left. The three plots in Figure 7 represent the viscous entropy generation rate on different meridional sections, while those on Figure 8 represent the corresponding vorticity magnitude. Since the vorticity is a measure of the rotation of a fluid element as it moves in the flow field and is defined as the curl of velocity:

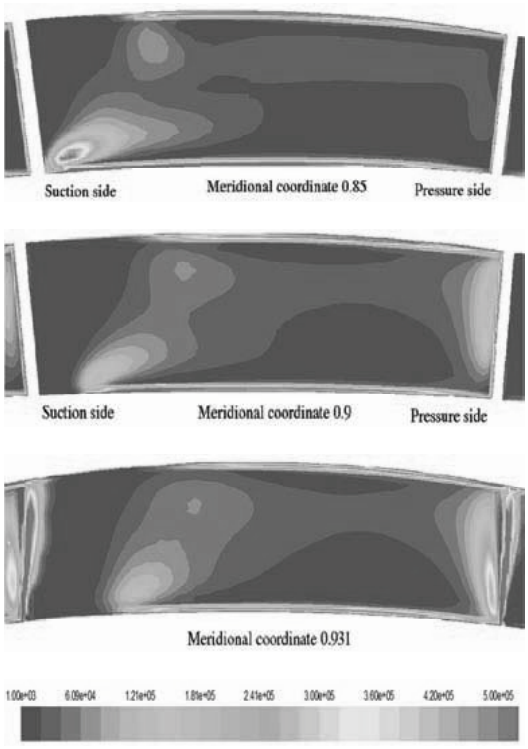

Fig. 7-Viscous entropy generation rate evolution at the trailing edge of both blades [W/(kg K)].

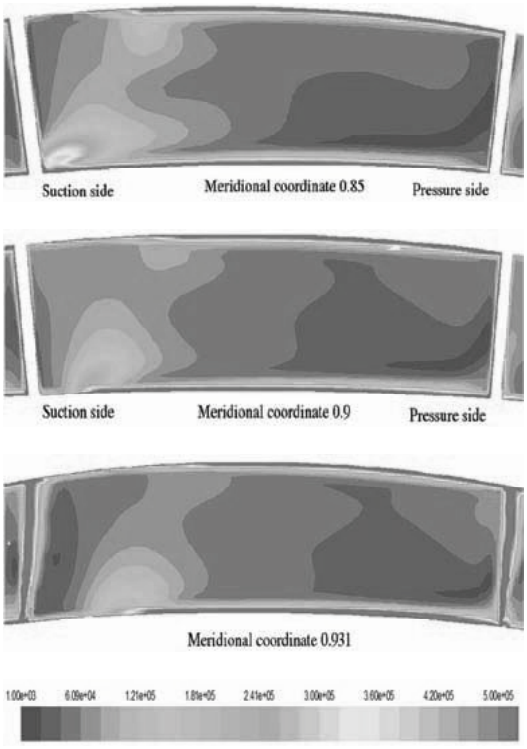

Fig. 8-Vorticity magnitude evolution at the trailing edge of both blades [1/s].

$$\vec{\Omega} = \vec{\nabla} \times \vec{v}\,, \tag{8}$$

It is quite clear that -see the definition of the viscous entropy generation rate (2)- there must be a strong correlation between $\dot{s}_V$ and Ω. The only substantially difference is that the viscous entropy generation rate is composed by squared velocity derivatives and thus is positive definite. This is clearly displayed by the plots. On the meridional section at 0.85 two strong dissipative structures are clearly visible: the first, located almost on the shroud of the rotor channel, is the result of an upstream flow detachment and is fading away. The second larger turbulent core generates on the suction side endwall of the splitter blade, upstream of which the boundary layer becomes unstable because of the excessive radial leaning of the blade profile and a nucleus just downstream of the separation point stretching towards the rotor channel can be identified. This fluid behaviour is mirrored on both figures. Recall that the vorticity represents just the rotation of the fluid element, generally large in highly three dimensional flow, but the large-scale vertical structures identified here must develop much further to reach the smaller scales of the turbulent cascade. The viscous entropy generation rate instead is a measure of the strength of the last stage of this mechanism, and captures some "hot spots" where there is turbulent kinetic energy dissipation. The plots on the meridional coordinate 0.9 show a decay of the intensity of the viscous entropy generation rate, that adapts to the decreasing turbulent kinetic energy as this structure moves away from its source. The same happens for the vorticity that offers though a smoother appearance. On the last couple of plots, on the meridional coordinate 0.931 (the trailing edge location of both blades Fig. 1), the weakening of previous dis-

sipative cores is exposed by the contours of the viscous entropy generation rate. At the corner of both figures two vertically stretched red regions are clearly visible: these are the wakes, obviously some of the most influent areas for the entropy generation. From the colour maps it is apparent in the wakes both the viscous entropy generation rate and the vorticity show the respective highest values for the entire region. In these areas the dissipative viscous mechanism is fully developed, therefore there is almost no difference in the sketches between vorticity and entropy generation rate. Further downstream meridional sections [8] confirm that both the turbulent kinetic energy dissipation and the viscous entropy generation rate show a marked decrease as they separate from the blades trailing edge. At the computational exit of the control volume there is a small fingerprint of the entropy generation rate on the wake region, surrounded by a smooth vorticity field.

6. Conclusions

As expected, the most interesting regions for the entropy generation rates are located at the leading and trailing edges of the blades, including the strongly turbulent wake areas. A highly three dimensional behaviour of the fluid is confirmed, clarifying the intense interference between each pair of full & splitter blades. Based upon our numerical results, the suggested improvements should involve the design of the leading edge of both blades, to cure the rather inefficient coupling caused in part by a somewhat ill-drafted geometry and in part by a excessively small mass flow rate. Another possibility of improvement might include a higher exit angle and a smoother bend for last part of both blades, in order to achieve a well guided flow with smaller fluid detachments. The performance of the wheel compressor is, by the way, excellent, the numerical estimate for the isentropic efficiency being equal to 89.96 %, on the higher end for a small-scale machine like the one analysed here.

Nomenclature

Be Bejan Number = $\dot{s}_T / \left(\dot{s}_T + \dot{s}_V \right)$
m Mass flow rate, kg/s
$\dot{s}_T$ Thermal entropy generation rate, W/(kg K)
$\dot{s}_V$ Viscous entropy generation rate, W/(kg K)
$\dot{s}_{Tot}$ Total entropy generation rate, W/(kg K)
y^+ Dimensionless boundary layer distance

Greek symbols

β Compression ratio
δ Boundary layer thickness, m
μ Molecular viscosity, kg/(m s)
Ω Vorticity, 1/s

References

[1] CAMEL-PRO™, 2008, *User's guide*, http://www.turbomachinery.it.

[2] Capata, R., Sciubba, E., 2006, *Preliminary Consideration on Thermodynamics Feasibility and Possible Design of Ultra-, Micro-, and Nano-Gas-Turbines*, Int. J. Thermodynamics, 9 (2), pp. 81-91.

[3] Denton, J. D., 1993, *Loss Mechanisms in Turbomachines*, J. Turbomachinery, 1993 IGTI Scholar Lecture, 115, pp. 621-656.

[4] Epstein, A. H., 2004, *Millimeter-Scales, MEMS Gas-Turbine Engines*, J. Engineering for Gas-Turbines and Power, 126, pp.205-226.

[5] Iandoli, C. L., Sciubba, E., Zeoli, N., 2008, *The Computation of the Entropy Generation Rate for Turbomachinery Design Applications: Some Theoretical Remarks and Practical Examples*, Int. J. Energy Techn. & Policy, 6(1), pp. 64-95.

[6] Mathieu, J., Scott, J., 2000, *An Introduction to Turbulent Flow*, Cambridge University Press, Cambridge, Massachusets.

[7] Monin, A. S., Yaglom, A. M., 2007, *Statistical Fluid Mechanics*, Dover, Massachusetts.

[8] Pierandrei, G., 2010, *CFD Simulation and Entropic Maps of an UMTG*, M. E. Thesis, Uniroma1- La Sapienza, Roma.

[9] Tennekes, J., Lumley, J. L., 1972, *A First Course in Turbulence*, The MIT Press, Cambridge, Massachusetts.

Acknowledgements: This study work has been co-funded within the frame of National Research Project n° 714, co-sponsored by the Italian Ministry of Defence. The Authors would like to express their thanks to Air force Colonel Romolo Grasso, Head of the Technical Unit, and to Major Gianluca Blasi, Technical Responsible for the Project. The Authors have profited of several discussions with Dr. Luciano Bernardini, R&D engineer at Honeywell Turbo Technologies (Garrett® Division), whose advice on the off-design behaviour of small turbochargers are gratefully acknowledged.

Model of a steam Wankel Expander

Manfrida Giampaolo [a], Padula Stefano[a]

[a] *Università degli Studi di Firenze, Dipartimento di Energetica "Sergio Stecco"*
Via C. Lombroso 6/17 – 50135 Firenze - Italy

Abstract: A complete kinematic and thermodynamic model of a Wankel expander engine has been realized. The applications are small-size, distributed CHP systems, with a special attention to off-grid applications using low-temperature thermal energy (geothermal, solar,...). The model allows to calculate and analyse the performance of the system, including its dependence on the main design parameters, and to evaluate possible operating modes for meeting variable power demand.

Keywords: Expanders, Combined Heat and Power, Off-Grid, Solar thermal Energy Conversion, Organic Rankine Cycles.

1. Introduction

The Wankel engine concept was developed about 50 years ago for internal combustion engines. Over the years it has proved to be potentially competitive with reciprocating IC engines [1, 2, 3, 4, 5], gaining satisfactory reliability but with a tendency to higher fuel consumption, which has fostered application to sports car (such as the Mazda RX-8).

In search of small and compact expanders, able to work with limited flow rates and with an eye to distributed CHP applications, the volumetric rotative Wankel engine makes some sense, also in comparison with other volumetric devices which are currently being developed [6, 7, 8]. In this case, operation with steam is usually considered. The potential applications range from recovery of heat at discharge of IC engines, developing small combined cycles [9], to the low-temperature field typical of some renewable energy sources (geothermal, solar).

The documented research on the Wankel engine as a steam expander has addressed both modelling and technological problems [9, 10, 11]; experimentation has been done on a modified Mazda engine [12]. Certainly problems connected with materials and lubrication are crucial in the development of this engine: however, as significant progress has been done in the challenging field of internal combustion engines [5], these problems can be re-visited with present-day technology. Preliminary experimental work, aimed at demonstrating a good potential coupling to biomass conversion systems, has been also performed [14, 15]. It makes thus sense then to develop a user-friendly model of the Wankel engine used as an expander in a Rankine cycle, using a modern modelling environment [16] which allows easy change of working fluid characteristics and parameters in order to adapt the performance to the temperature level and size of the low-temperature source. The sensitivity of the performance to the basic design parameters can also be parametrically studied.

2. Mode of operation

The Wankel engine is built around the idea of a triangular-shaped rotor rotating off-centered inside a suitable two-lobed stator. The possible location of admission (blue) and discharge (green) valves - necessary when considering the device in a steam circuit actuating a Rankine cycle - is indicated in Figure 1. The Wankel expander is placed between the steam vessel (where saturated conditions ensure availability of steam when the admission valves are opened) and the condenser (which is cooled and maintained at low pressure and represents the exhaust for the discharge flow). The External Heater 1 can be a combination of geothermal and solar low-temperature heat providers; the recirculation loop ensures a low

quality of the two-phase flow inside the heater circuit, which is recommendable for good heat transfer performance; the steam vessel provides gravity separation between steam (upper) and the liquid phase (lower). A second external heater (2) provides direct superheating for the flow rate routed to the expander.

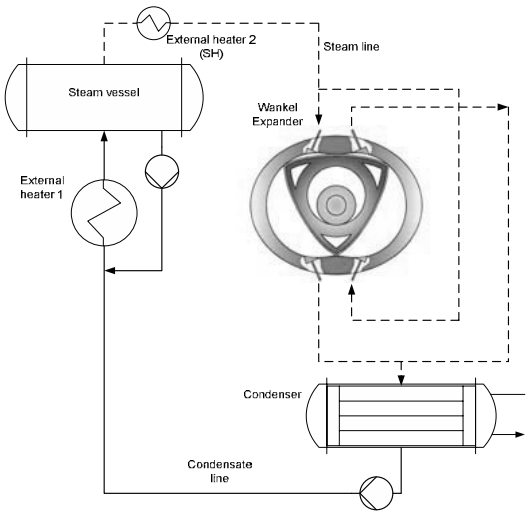

Fig. 1. Wankel engine and steam circuit

The thermodynamic cycle is sketched in Figure 2. The transformations and points of the cycle are named according to Table 1 and 2. The cycle begins at the dead end at point 1', where the admission valve is opened. Pressure rises rapidly (constant-volume) reaching the pressure vessel conditions (Point 1); admission continues at constant pressure until the admission valve is kept open (Point 2). The expansion phase 2-3 is modeled as adiabatic (isentropic). At point 3 the discharge valve is opened, and a rapid (constant-volume) discharge of the fluid inside the control volume towards the condenser at low pressure takes place (3-3'). When the condenser pressure is reached (Point 3'), discharge proceeds at constant pressure until the discharge valve is closed (Point 4). Limits in valve dimensions (discharge/ admission) do not allow to reach the minimum volume V_1. The limited amount of steam remaining in the dead volume is thus re-compressed adiabatically until reaching the pressure conditions at point 1'.The cycle described is a limit cycle: this means that no effects of friction and heat transfer are considered.

The admission/discharge transformations are treated either as constant-volume (rapid adjustment to pressure vessel/condenser conditions) or constant-pressure (displacement of fluids with variable volume, valve open).

The expansion/compression transformations are considered adiabatic.

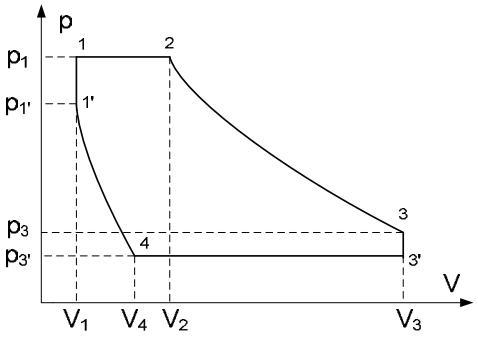

Fig. 2. Wankel steam cycle

Table 1 – Wankel steam cycle transformations

Transformation	Name
1'-1	Constant-volume admission
1-2	Constant-pressure admission
2-3	Expansion (adiabatic)
3-3'	Constant-volume discharge
3'-4	Constant-pressure discharge
4-1'	Compression of dead volume steam (adiabatic)

Table 2 – Wankel steam cycle reference points

Point	Name
1'	Admission valve opens
1	End of constant-volume admission
2	Admission valve closes
3	Discharge valve opens
3'	End of constant-volume discharge
4	Discharge valve closes

The working fluid is steam, with properties calculated from the pressure/volume conditions[1].

[1] The model can be developed into a real-cycle one providing pressure loss/flow rate correlations in function of poppet position, and with an adequate heat

It is well known [1] that the Wankel engine works with three chambers of variable volume, and that the gear ratio between the rotor and the main shaft is 1:3. Using steam with external admission, 6 complete cycles are performed for 2 complete turns of the crank shaft (which is twice the value of the internal combustion case).

3. Influence of rotor-stator geometry

The rotor-stator geometry, and the size and location of the admission/discharge valves, determine the cycle points in terms of absolute volume. The following parameters are used to describe the rotor geometry:

Admission grade:

$$\sigma = \frac{V_2 - V_1}{V_D} \tag{1}$$

With $V_D = V_3 - V_1$. V_2 is determined by closing of the admission valve. V_1 and V_3 are determined by the choice of the rotor/stator geometry [1]:

$$V_1 = Le^2\left(\frac{\pi}{3} + 2K\cos\varphi_{\max} + \left(\frac{2}{9}K^2 + 4\right)\varphi_{\max} - \frac{3\sqrt{3}}{2}K\right) \tag{2}$$

$$V_3 = Le^2\left(\frac{\pi}{3} + 2K\cos\varphi_{\max} + \left(\frac{2}{9}K^2 + 4\right)\varphi_{\max} + \frac{3\sqrt{3}}{2}K\right) \tag{3}$$

and

$$\sin\varphi_{\max} = \frac{3}{K} \tag{4}$$

Expansion ratio:

$$\varepsilon = \frac{V_3}{V_2} \tag{5}$$

Introducing the dead volume ratio:

$$\mu = \frac{V_1}{V_D} \tag{6}$$

One obtains:

$$\varepsilon = \frac{1+\mu}{\sigma+\mu} \tag{7}$$

Considering existing Wankel units, typically $0{,}05 < \mu < 0{,}07$; Figure 3 shows the relation between ε and σ for these limit values of μ.

transfer model (fluid to wall), as is common practice by IC engines.

Finally, the compression grade – depending on the location and timing of the discharge valve closing – must be defined:

$$\gamma = \frac{V_4 - V_1}{V_D} \tag{8}$$

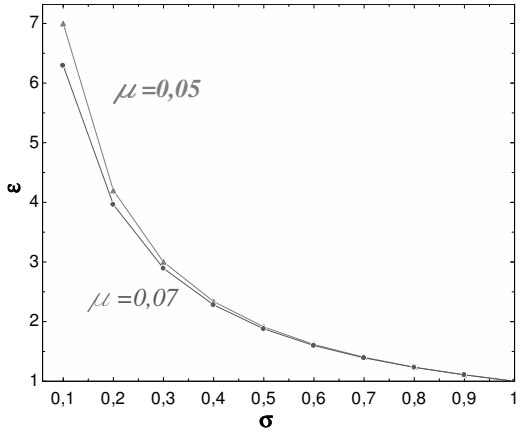

Fig. 3. Expansion ratio ε vs. admission grade σ for limit values of the dead volume ratio μ.

4. Performance evaluation

The work performed during one cycle in each chamber is generally given by a sequence of integral calculations:

$$W_{ab} = \int_a^b p dV \tag{9}$$

For transformations 1-2 and 3'4, which take place at constant pressure, the calculation is direct:

$$W_{12} = p_1(V_2 - V_1) = p_1 \sigma V_D \tag{10}$$

$$W_{3'4} = p_{3'}(V_4 - V_{3'}) = -p_{3'}V_D(1-\gamma) \tag{11}$$

For transformations 2-3 and 4-1', rather than using a perfect-gas isentropic law, it is possible to calculate for each crank angle position the local conditions of internal energy, which are multiplied by the mass present inside the control volume to give the work (Q = 0, adiabatic):

$$W_{ab} = m\int_{\theta_a}^{\theta_b} u d\theta \tag{12}$$

This way of calculating work in adiabatic (or polytropic) conditions is a considerable advantage of the model (which makes full use of a modern property calculator [11]) with respect to considering a perfect-gas assumption [7]. The indicated work is given by:

$$W_l = W_{12} + W_{23} + W_{3'4} + W_{41'} \quad (13)$$

Following IC engine practice, it is possible to calculate an indicated average pressure from the cycle diagram:

$$W_l = p_{mi} V_D \quad (14)$$

And considering the number of cycles performed for each crank shaft rotation:

$$P = \frac{2 p_{mi} V_D n}{60} \quad (15)$$

The model calculates the mass of residual steam at the end of compression, m_{RS}, considering the effective volume and the specific volume conditions. Consequently, it is possible to calculate the amount of fresh steam $m_{FS} = m_{FSV} + m_{FSP}$ charged inside the engine when the admission valve is opened (transformations 1'1 – constant volume - and 1-2 – constant pressure). The equivalent high-temperature heat input is calculated as:

$$Q_H = \frac{2n}{60}\left[m_{FS} \cdot (h_1 - h_0) \right] \quad (16)$$

The cycle efficiency η_c is calculated as the ratio of W_l to Q_H.

5. Reference conditions and results

The reference application is a small CHP system, possibly applied to an off-grid building, which uses a combination of geothermal and solar as the external heat source, and rejects heat at a temperature which is still adequate either for thermal utilization or possibly for refrigeration using an absorption system.

Accordingly, the highest temperature (steam vessel) was set in the range T_H = 130-300°C, while the condenser temperature at T_C = 70°C. The pressure conditions considered were in the range p_H = 120 – 500 kPa at the steam vessel, 31 kPa at condenser. An adaptation of an existing IC engine was considered (Mazda 745; R =0,118 m; VD = 0,000746 m^3). The engine speed was fixed at a safe value of 3500 rpm.

As a first step, values of σ = 0,32 and γ = 0,1 were considered, which produced a cycle with complete expansion and compression: the resulting cycle (p-V diagram) is shown in Figure 4 for the case p_H = 120 kPa. The valve setting angles corresponding to the desired conditions (complete expansion and compression) are also indicated (α_{AVC} = Admission Valve Closure; α_{EVC} = Exhaust Valve Closure[2]),

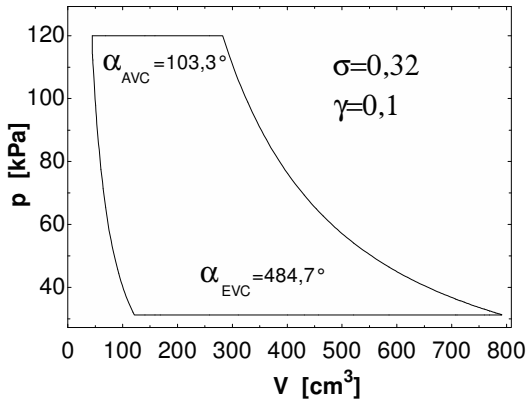

Fig. 4. p-V diagram; p_H = 120 kPa; complete expansion and compression.

Figure 5 shows the power output of the engine as a function of expansion ratio (condenser pressure fixed at 31 kPa) and steam temperature (200, 250 and 300 °C). Figure 5 shows that optimum conditions exist – at fixed values of σ and γ – for the power output, which is limited because of the low value of p_H. This result corresponds to the typical maximization of the work in a steam cycle, with limited conditions for maximum superheated steam temperature. Figure 6 shows the calculated efficiency for the same conditions as for Figure 6. The cycle efficiency continues to rise with steam pressure after the maximum power conditions. It should be considered that the reference Carnot cycle efficiencies range between 0,27 and 0,4 (T_H = 200 – 300°C).

[2] The Exhaust valve opens always at 270° crank angle (limit cycle)

The performance can be improved considerably (both for power and efficiency) with a different timing of the admission and discharge valves. This produces a cycle of the type sketched in Figure 2.

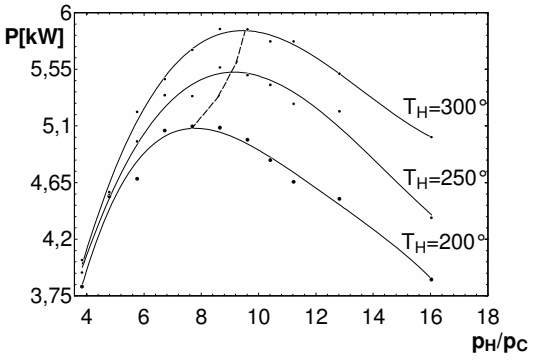

Fig. 5. Power output; complete expansion and compression. Variable steam pressure and temperature.

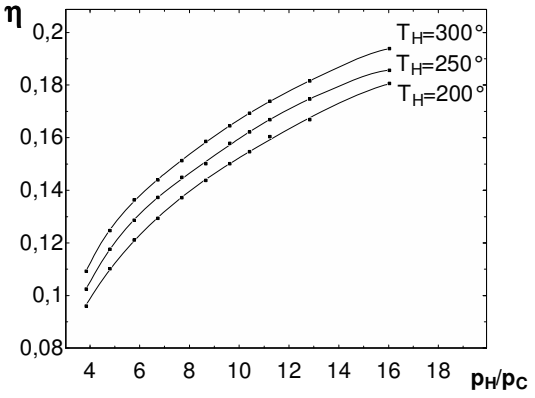

Fig. 6. Efficiency; complete expansion and compression. Variable steam pressure and temperature.

The results of a parametric analysis with variable σ and γ are shown in Figures 7 and 8, where the admission conditions were set at p_H = 500 kPa and T_H = 151 °C (Saturated steam conditions)[3].

Figures 7 and 8 show that a trade-off exists between power output and efficiency:

- High power outputs can be obtained increasing the admission grade (σ > 0,5); accordingly, low values of the compression grade γ should be adopted (Figure 7)

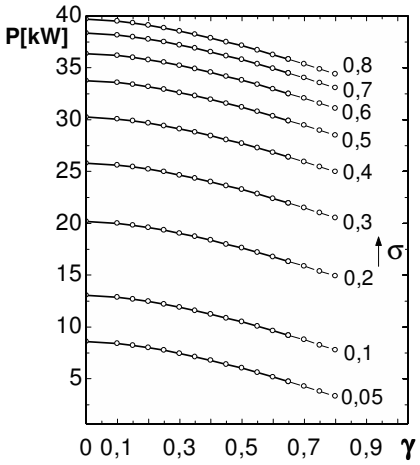

Fig. 7. Power Output at variable σ and γ; p_H = 500 kPa and T_H = 151 °C (Saturated steam conditions)

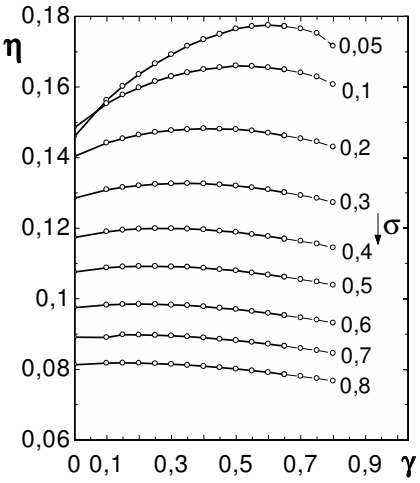

Fig. 8. Cycle efficiency at variable σ and γ; p_H = 500 kPa and T_H = 151 °C (Saturated steam conditions)

- From the point of view of efficiency (Figure 8), small values of the admission grade (σ < 0,3) should be recommended; an optimum value of γ exists (0,3<γ<0,7 depending on σ)

The reasons for the existence of a maximum of efficiency with variable γ (recompression parameter) are well documented in the specific

[3] This eliminates the necessity of the External heater 2) Super-Heater, Figure 1, which is a considerable point in favour of the solution, with special reference to solar collectors)

literature [3]: for optimum η (limit cycle), the steam conditions at point 1'(end of recompression) get very close to point 1 (admission), so that irreversibilities in mixing of the fluid remaining in the dead volume with the live steam are substantially avoided.

The effect of increasing the steam pressure was also considered. Figures 9 and 10 compare the performance with p_H = 800 kPa (saturated steam at T_H = 170,4 °C) to the case p_H = 500 kPa.

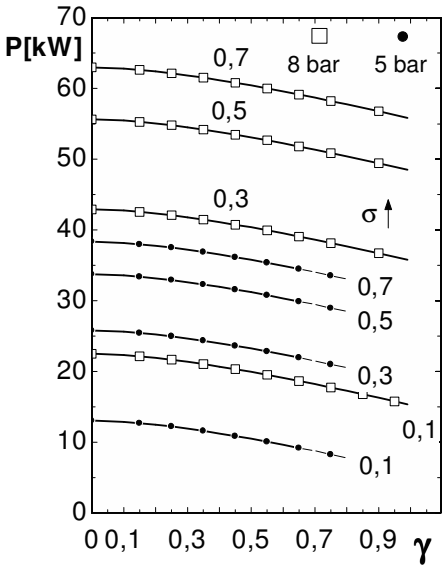

Fig. 9. Power Output at variable σ and γ; p_H = 800/500 kPa (Saturated steam conditions)

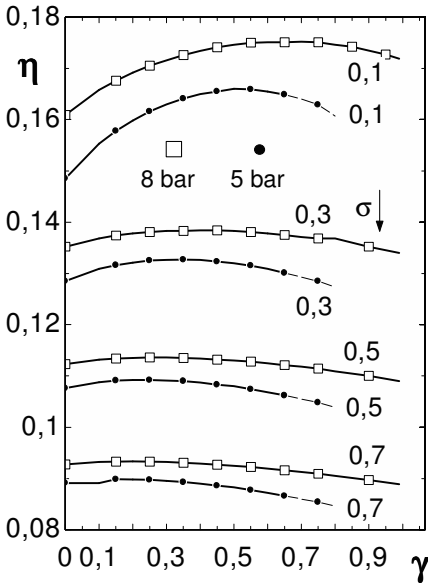

Fig. 10. Efficiency at variable σ and γ; p_H = 800/500 kPa (Saturated steam conditions)

Examining Figures 9 and 10 it is clear that the power output is strongly improved by an increase in p_H; the effects on efficiency are less relevant.

The reference case considers an existing engine (Mazda 745), but at least the rotor should be remanufactured; it was then considered profitable to increase the volumetric compression ratio ρ from 17,7 to 21,8. The performance was evaluated again with the modified rotor, for the case p_H = 500 kPa and T_H = 151 °C. The results are shown in Figures 11 and 12. The modified engine offers marginal advantages over the original design rotor, with special reference to low values of the admission grade (σ<0,3)

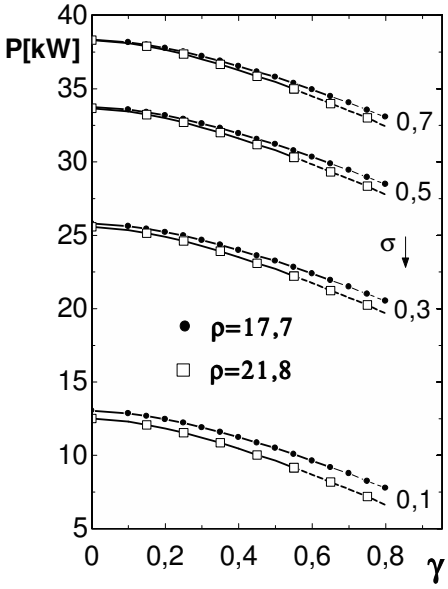

Fig. 11. Power Output at variable σ and γ; p_H = 500 kPa and T_H = 151 °C (Saturated steam conditions). Modified rotor (increased compression ratio)

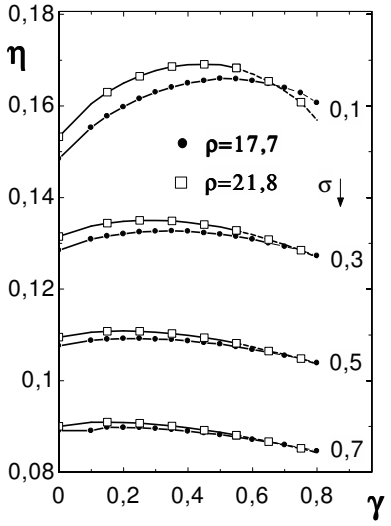

Fig. 12. Power Output at variable σ and γ; p_H = 500 kPa and T_H = 151 °C (Saturated steam conditions). Modified rotor (increased compression ratio)

6. Control issues (adaptability to variable heat input)

The power and efficiency curves shown in Figures 7 and 8 suggest the possibility of adapting the working conditions (power and efficiency) to the availability of heat (with special reference to solar thermal systems), if a variable valve timing can be developed. In practice, when solar heat is plenty available, it can be advantageous to operate the engine with an increased admission grade (and an adjusted compression grade), obtaining a larger power output at a lower efficiency.

Considering the data collected in Figures 9 and 10, it is also worth considering the possibility of operating the engine with other variable parameters depending on the amount and quality of heat available:

- Variable pressure p_H
- Variable temperature T_H.
- Variable-speed (with DC current generation and AC inverter)

Conclusions

A model for evaluating the performance of the Wankel Engine as a steam expander, in the frame of small CHP systems using local geothermal/solar energy resources, has been developed and tested.

The model makes reference to limit conditions (real fluid, steam properties; ideal machine with no heat transfer and friction effects). An admission/discharge valve system was considered, with full flexibility of timing; the effects of variable admission and exhaust valve tuning were studied. The sensitivity to steam production parameters, and the possible improvement of performance with limited adjustments (rotor geometry) have been analyzed.

The system performance appears of potential interest, as levels of efficiency in the range of 0,10 to 0,12 seem to be achievable, still with condenser conditions (T_C = 70°C) which are compatible with a CHP system and possibly also with tri-generation using an absorption cooling system. Also from the point of view of control and adaptability to variable conditions (e.g. solar radiation), considering the number of adjustable variables with modern technology, the steam Wankel expander appears to be a flexible candidate for small CHP system.

List of symbols

e	Eccentricity (rotor/stator)
K	Fundamental ratio, K = R/e
L	Rotor axial length, m
m	Mass of working fluid, kg
n	Crank shaft rotational speed, rpm
p	Pressure, kPa
P	Power, kW
Q	Heat rate, kW
R	Rotor radius, m
T	Temperature, °C
V	Volume, m^3
V_D	Displacement $V_D = (V_3 - V_1)$, m^3
W	Work, J (per transformation)
W_I	Indicated work (limit), J/cycle
α	Crank angle for valve opening or closing, °
γ	Compression grade, $\gamma = (V_4 - V_1)/V_D$
η	Efficiency
μ	Dead volume ratio, $\mu = V_1/V_D$
φ_{max}	Maximum Obliquity angle, °
ρ	Volumetric compression ratio, $\rho = V_3/V_1$
σ	Admission grade $\sigma = (V_2 - V_1)/V_D$

Subscripts:

AVC	Admission Valve Closure timing
a, b	Initial, final conditions (transformation)
c	cycle
C	Condenser
EVC	Exhaust Valve Closure timing
FS	Fresh steam
FSP	Fresh steam, constant pressure (1-2)
FSV	Fresh steam, constant volume (1'-1)
H	Higher value (cycle)
RS	Residual steam
SV	Steam vessel (admission)

References

[1] Yamamoto, K., 1981, *Rotary Engine*, Sankaido Co. Lt, Tokyo, 11-17.

[2] Quaggiotti, V., 1972, *Il Motore Wankel*, Patron.

[3] Acton, O., Caputo, C., 1992, *Compressori ed espansori Volumetrici*, UTET.

[4] SAE, Rotary Engine Design: Analysis and Developments", ISBN 0-89883-695-6, SAE/SP-89/768

[5] Ohkubo, M., Tashima, S., Shimizu, S., Fuse, S., Ebino, H., 2004, Developed Technologies of the New Rotary Engine (RENESIS), *SAE Paper 2004-01-1970*

[6] Badami, M., Mura, M., 2008, Design and performance evaluation of an innovative small scale combined cycle cogeneration system, Energy 33, 1264– 1276

[7] Badami, M., Mura, M., 2009, Preliminary design and controlling strategies of a small-scale wood waste Rankine Cycle (RC) with a reciprocating steam engine (SE), Energy 34, 1315–1324

[8] Manfrida, G., Marraccini, L., 2010, Model of a Steam/Organic Vapour Volumetric Reciprocating Expander, *ECOS* 2010, Lausanne.

[9] Stobart, R., Weerasinghe, R., 2006, Heat Recovery and Bottoming Cycles for SI and CI Engines – A Perspective, *SAE Paper 2006-01-0662*.

[10] Badr, O., Naik, S., O'Callaghan, P.W., Probert, S.D., 1991, Rotary Wankel Engines as Expansion Devices in Steam Rankine-cycle engine, Applied Energy, 39, 59-76.

[11] Badr, O., Naik, S., O'Callaghan, P.W., Probert, S.D., 1991, Expansion Machine for a Low Power-Output Steam Rankine-cycle engine, Applied Energy, 39, 93-116.

[12] Badr, O., Naik, S., O'Callaghan, P.W., Probert, S.D., 1991, Wankel Engines as Steam Expanders: Design Consideration, Applied Energy, 40, 157-170.

[13] Antonelli, M., Lensi,R., Martorano,L., Nuti, L., Provenzale, M., 2006, Prospettive di sviluppo di un espansore volumetrico rotativo per microgenerazione di energia, *61° Congresso Nazionale ATI*, Perugia.

[14] Antonelli, M., Lensi,R., Martorano,L., 2007, Development and validation of a numerical model of a rotary steam engine for electric power micro generation using biomass, *Proceedings ECOS 2007*, 719-728, Padova.

[15] Antonelli, M., Lensi,R., Martorano,L., 2007, Development and Testing of a rotative steam engine for Biomass based Distributed Electric Power Micro Generation, *15th European Biomass Conference & Exhibition*, 2460-2463, Berlin.

[16] http://www.fchart.com/ees/ees.shtml

Model of a Steam/Organic Vapour Volumetric Reciprocating Expander

Manfrida Giampaolo[a], *Marraccini Leonardo*[a]

[a] *Università degli Studi di Firenze, Dipartimento di Energetica "Sergio Stecco"*
Via C. Lombroso 6/17 – 50135 Firenze - Italy

Abstract: A small expander for steam or organic vapour has the versatility of coupling easily to different low-grade heat resources, such as geothermal, solar, and recovery of waste heat (e.g. from fuel cells systems). The product to be developed should be able to work with small flow rates and low upper temperature (100- 150°C), while rejecting heat at a level still interesting for heating or cooling (with an absorption machine), that is, 50 to 80°C. The efficiency is necessarily low, but electricity can be seen within this views as a by-product with respect to heat, which already is exploited using these energy resources (e.g. solar thermal, geothermal heat pumps). The device should be compact, simple and capable of easy control in order to match electric production and loads, which is a key point in off-grid applications. The paper presents a thermodynamic model of the reciprocating engine using real-fluid assumptions. It allows to calculate and analyse the performance of the system, including its dependance on the main design parameters, and to study the operating mode with respect to meeting variable power demand.
Keywords: Expanders, Combined Heat and Power, Off-Grid, Solar thermal Energy Conversion, Organic Rankine Cycles.

1. Introduction

Expanders of steam or organic vapours will probably be devices needed on the market of small CHP and distributed electricity production [1, 2, 3, 4]. There is presently a growing attention to off-grid concepts, allowing small houses and/or activities to be independent from services (energy, sewage, information flows) requiring expensive networks of wires and pipings.

Expanders considered for organic vapours are usually of the scroll or screw type [5, 6, 7, 8]; these expanders have been developed or adapted from compressors used in refrigerating units, and typically cover a range from 10 to 25 kW.

Reciprocating engines represent a very developed technology, as they are the standard for IC engines. Their use as steam expanders can be traced back to 19th-century tradition; however the technology can be revisited considering advances in materials and in engine control systems, derived from the IC engine sector. Nowadays valve opening/shutoff can be largely controlled by electronic/hydraulic systems, and for small sizes direct DC electricity production, possible at variable speed, can be proposed. The possibility of using organic vapours as a substitute for steam paves the way to matching with low-temperature heat sources and allows to develop engines of reasonable sizes, or even to consider transformation of existing IC engines.

2. Mode of operation

The reciprocating engine operates with the traditional rod mechanism. The engine is placed between two reservoirs (Figure 1): the high-pressure reservoir (HPR) works as a steam accumulator, connected to the external heat source. A recirculation loop ensures favorable conditions for heat transfer (a low quality of steam). The dry steam is taken from the upper part of the reservoir, and routed to an external super-heater working directly on the engine flow rate. The low-pressure reservoir (LPR) acts as a condenser: typically it is kept at a temperature of 60 to 70 °C, mainly providing building heating load. During summer it is possible to consider operation at higher temperature and coupling to an

absorption cooling loop. A small pump makes up for the pressure difference between the reservoirs.

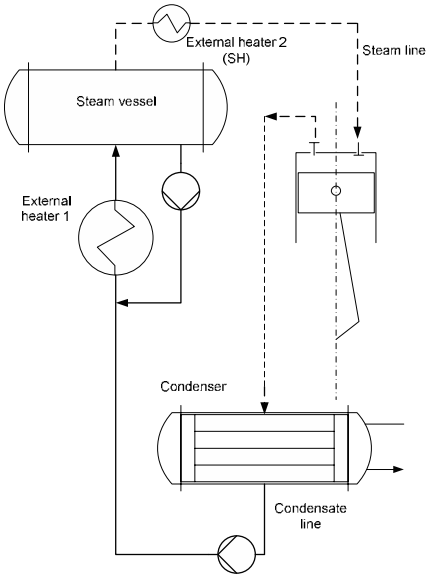

Fig. 1. Schematic of reciprocating steam engine circuit

In practice the engine would be a multi-cylinder unit, of a type similar to what has been developed for heat recovery in IC engines [1] or for biomass applications [2]. With respect to a traditional cycle of IC engine, the valve timing is completely different. A full cycle is realized in one single turn. The following description applies to limit cycle (ideal engine, real fluid conditions). With reference to Figure 2, the Discharge Valve is maintained open to the upper dead end (UDE), so that the compression phase is absent..

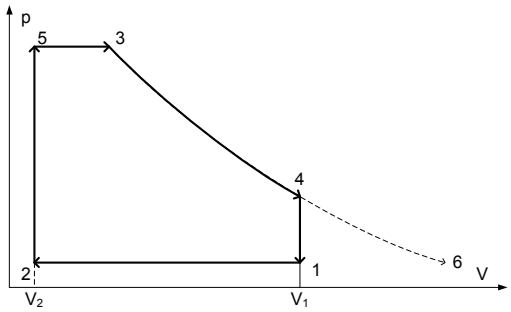

Fig. 2. RE steam cycle

At the UDE the Discharge Valve is closed and the Admission Valve is opened. Steam flows under high pressure difference, rapidly filling the dead space volume (constant-volume admission, 2-5). When the HPR pressure is reached, steam flows inside the cylinder at constant pressure, with increasing volume, until the Admission Valve closes (Constant-pressure admission, 5-3). The expansion phase 3-4 is treated as adiabatic and isentropic (limit cycle). At the Bottom Dead End, the Discharge valve is opened, and steam exits the cylinder under relevant pressure difference, at constant volume (4-1); when the condenser pressure is reached, discharge of steam continues at constant pressure until reaching the upper dead end (1-2).

3. Model of the RE steam cycle

The model was developed in EES [9] environment, using real fluid properties (steam or different working fluids, such as organic vapours). In order to have a parametric description of the cycle, the following parameters were introduced:

Volumetric compression ratio:

$$\rho = \frac{V_1}{V_2} \tag{1}$$

Cut-off ratio:

$$\sigma = \frac{V_1 - V_3}{V_D} \tag{2}$$

Where V_D is the engine displacement volume, $V_D = V_1 - V_2$. A critical point for cycle closure is determining the mass of fluid present in the different volumes: in fact, the mass of steam admitted per cycle, m_{in}, is dependent on the mass which is left in the dead space in the preceding cycle, m_2. Conventionally, it is assumed that m_2 is known, using an initial guess value; The steam parameters at point 5 and 3 are determined from the HPR conditions, $\rho_5 = f(p_5, T_5)$, so that

$$m_5 = \frac{V_5}{\rho_5} \tag{3}$$

And the mass of steam admitted at constant volume is:

$$m_V = m_5 - m_2 \tag{4}$$

The mass at point 3 is determined accordingly:

$$m_3 = \frac{V_3}{\rho_3} \tag{5}$$

With V_3 from Equation (2); the mass of steam admitted at constant pressure is:

$$m_p = m_3 - m_5 \quad (6)$$

So that the overall mass of steam expanding is:

$$m_{in} = m_V + m_p = m_3 = m_4 \quad (7)$$

At point 1 (piston at the LDE), the condenser pressure is reached, the DV is open and the fluid occupying volume V_1 is supposed to be saturated steam; its mass is consequently:

$$m_1 = \frac{V_1}{\rho_1} \quad (8)$$

The fluid remaining in the Dead Space continues its adiabatic expansion ($s_6 = s_4 = s_3$) until point 6 (condenser pressure); physically it is confined within volume V_2, so that its mass is:

$$m_6 = \frac{V_2}{\rho_6} \quad (9)$$

Defining the error

$$\delta m = \frac{|m_6 - m_2|}{m_2} \quad (9)$$

The minimum condition for δm is searched using the standard Golden Search algorithm [5]. This effectively closes the mass balance. m_2 is highly dependent on the cutoff, as is shown for a reference case in Figure 3.

4. Performance evaluation

The equivalent heat supplied per cycle can be calculated as:

$$Q_1 = Q_{1V} + Q_{1p} = (u_5 - u_2) + (h_3 - h_5) \quad (10)$$

Heat is rejected during the two discharge transformations, (4-1; constant-volume) and (1-2; constant pressure):

$$Q_2 = (u_4 - u_1) + (h_1 - h_2) \quad (11)$$

The work extracted per cycle is the sum of work done at constant pressure (admission/discharge) and of work done during the adiabatic expansion:

$$W = p_5(V_3 - V_5) + (u_3 - u_4) - p_1(V_1 - V_2) \quad (12)$$

The cycle efficiency is given by:

$$\eta = \frac{W}{Q_1} = 1 - \frac{Q_2}{Q_1} \quad (12)$$

As usual for volumetric engines, the indicated pressure can be calculated as:

$$p_{mi} = \frac{W}{V_D} \quad (13)$$

The power output is given by:

$$P = \frac{p_{mi} V_D n}{60} \quad (14)$$

Finally the Specific Speed is calculated:

$$N_s = \frac{n \dot{V}^{0,5}}{\Delta h^{0,75}} \quad (15)$$

with

$$\Delta h = \frac{(h_3 - h_4)}{m_3} \quad (16)$$

$$\dot{V} = \frac{\dot{m}}{\rho_3} = \frac{m_{in}\, n}{60\, \rho_3} \quad (17)$$

The specific diameter is given by:

$$D_s = \frac{D\, \Delta h^{0,25}}{\dot{V}^{0,5}} \quad (18)$$

5. Reference conditions and results

As a reference case to check the performance of the model, the data from [1] were assumed. This means p_3 = 100 bar and T_3 = 450°C; the engine considered is a single-cylinder unit with V_D = 300 cc and N = 2300 rpm. Figure 3 shows the calculated relative mass in the dead space as a function of σ, for two reference values of the volumetric compression ratio, ρ = 10 and ρ = 30. The high ρ is clearly favored, with lower values of m_{res}.

Figure 4 and 5 show the calculated efficiency and power output as a function of σ (ρ = 10 and ρ =

30). As commonly encountered, a tradeoff exists between efficiency and power: efficiency is large at low admission grade values, and decreasing rapidly with increasing σ; the opposite happens for power. Considering that values of (limit-cycle) efficiency lower than 0,16 are little attractive, and that ideal power in the range of 60 to 80 kW is satisfactory, the admission grade range considered would be $0,2<\sigma<0,4$.

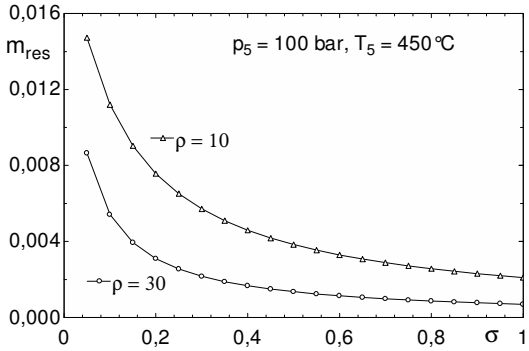

Fig. 3. Residual mass ratio (Dead Space) vs. cutoff.

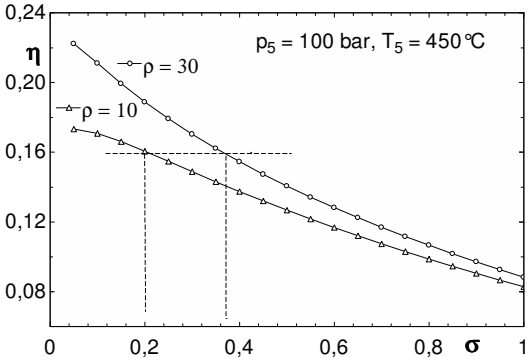

Fig. 4. Calculated Efficiency vs. cutoff.

Always considering this reference application, it is interesting to examine the trend of the non-dimensional variables N_s and D_s (Figure 6). It is evident that the single-cylinder unit is a "slow" engine, with $N_s < 0,002$ (for $\sigma < 0,4$) and $16<D_s<24$. The power level is notably large for a small engine (V_d = 300 cc), and as the rotational speed is moderate the torque values are considerable.

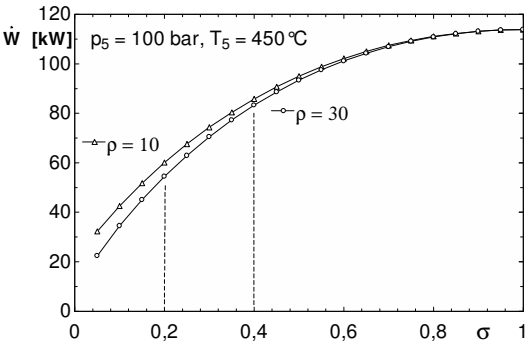

Fig. 5. Calculated Power vs. cutoff.

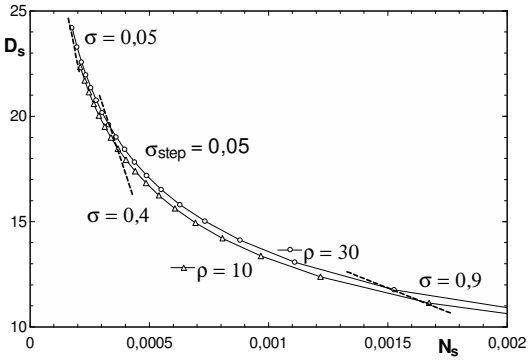

Fig. 6. Non-dimensional parameters N_s and D_s with variable cutoff.

As a final comment on the results collected in Figures 3 to 6, it is important to state that they are substantially in line with those published in Refs. [1] and [2], which compare a simplified analytical model (using perfect gas transformation assumptions) with experimental results. However, this reference application is considering high-quality steam conditions, as can be encountered in applications developed for heat recovery at IC engine exhaust, or biomass external firing of the steam engine. After validating the results with this reference case, in the following attention is rather focused on applications for renewable energy using low-temperature resources (solar, geothermal).

6. Operation at reduced temperature (renewable energy)

As discussed in the introduction, the idea of a small reciprocating engine is appealing for applications of small geothermal and/or solar units

including co-generation of heat (or cold) and power. Considering steam, the operating parameters were reduced at 7 bar together with saturated steam inlet (that is, T_5 = 165°C). The condenser was maintained at 1 bar, 100 °C for a simplified coupling to the CHP or absorption cycle cooling system. The performance is resumed in Figure 7, showing the efficiency and power output as a function of the admission grade. In this case – which differs substantially from the reference case examined at section 5 - efficiency is optimized (at much lower values, $\eta max < 0{,}115$) in the range $0{,}16 < \sigma < 0{,}32$, and the power output under these conditions is between 3 and 5 kW. These results are considered interesting considering the low temperature range; the power output can be augmented with a multi-cylinder arrangement.

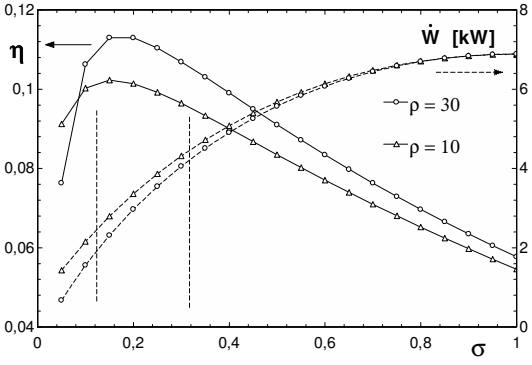

Fig. 7. Calculated efficiency and power vs. cutoff. Operation at reduced steam parameters.

7. Reduced temperature - Organic fluid

For low-temperature applications, it is logical to consider working fluids different from water/steam for operating a Rankine Cycle [10]. The reciprocating volumetric expander, with a careful selection of the working fluid, can be a good candidate for such applications. In the present case, considering that the condenser should be kept at least at 70°C in order to maintain the possibility of generating heat for residential heating, a nearly-supercritical cycle with R245fa was chosen (p_5 = 30 bar, T_5= 164 °C; ρ = 30 or 10). The results are resumed in Figure 8.

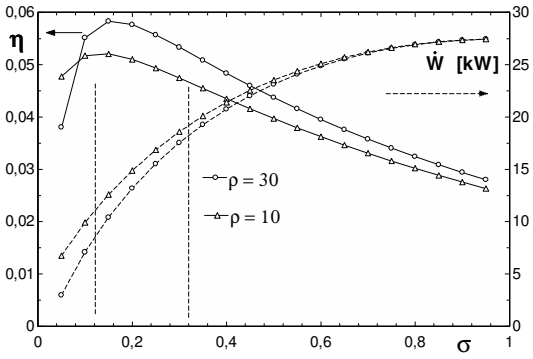

Fig. 8. Calculated efficiency and power vs. cutoff. Operation with R245fa.

The use of R245fa determines a reduced cycle efficiency but a considerably larger power output for the same displacement and rotational speed. Also in this case, values of $0{,}16 < \sigma < 0{,}32$ can be recommended.

8. Conclusions

A model for evaluating the performance of a volumetric steam/organic vapour expander has been developed and presented; the reference application is for small CHP systems using local geothermal/solar energy resources.

The model applies limit conditions (real fluid properties; ideal machine with no heat transfer and friction effects). It has been first applied to a reference case [2], considering biomass feeding with high steam pressure and temperature. The performance has then be scaled down to conditions interesting for low-temperature geothermal and/or solar driven applications (7 bar, 165°C saturated steam). Finally, substitution of steam with a suitable organic fluid (R245fa), recommendable for the same temperature conditions, has been implemented and analyzed.

The results show that low-pressure steam generation would be an interesting option for very small CHP systems (size 1-10 kW) driven by geothermal and/or solar energy resources.

List of symbols

D Cylinder diameter (bore), m
D_s Specific diameter,
DT Temperature difference, °C
h Enthalpy, J
m Mass of working fluid, kg
m_{res} Residual mass ratio (Dead Space)
n Crank shaft rotational speed, rpm
p Pressure, kPa
p_{mi} Average Indicated Pressure, kPa
P Power, kW
Q Heat rate, kW
T Temperature, °C
u Internal energy, J
V Volume, m^3
V_d Displacement $V_d = (V_1 – V_2)$, m^3
$\dot{V}$ Volume flow rate, engine exhaust, m_3/s
W Work, J/cycle
Δh Enthalpy difference (isentropic), J/kg
η Efficiency
ρ Volumetric compression ratio, $\rho = V_2/V_1$
ρ_i Density at point i, kg/m^3
σ Cut-off ratio $\sigma = (V_2 – V_1)/V_D$

Acronyms:

AV Admission Valve
DV Discharge Valve
HPR High Pressure Reservoir
LDE Lower Dead End
LPR Low Pressure Reservoir (condenser)
UDE Upper Dead End

Subscripts:

AVC Admission Valve Closure timing
a, b Initial, final conditions (transformation)
c cycle
C Condenser
EVC Exhaust Valve Closure timing
FS Fresh steam
FSP Fresh steam, constant pressure (1-2)
FSV Fresh steam, constant volume (1'-1)
H Higher value (cycle)
RS Residual steam
SH Superheating
SV Steam vessel (admission)

References

[1] Badami, M., Mura, M., 2008, Design and performance evaluation of an innovative small scale combined cycle cogeneration system, Energy 33, 1264– 1276
[2] Badami, M., Mura, M., 2009, Preliminary design and controlling strategies of a small-scale wood waste Rankine Cycle (RC) with a reciprocating steam engine (SE) Energy 34, 1315–1324
[3] Acton, O., Caputo, C., 1992, *Compressori ed espansori Volumetrici*, UTET.
[4] Badr, O., Naik, S., O'Callaghan, P.W., Probert, S.D., 1991, Expansion Machine for a Low Power-Output Steam Rankine-cycle engine, Applied Energy, 39, 93-116.
[5] Quoilin, S., Lemort, V., Lebrun, J., 2010, Experimental study and modeling of an Organic Rankine Cycle using scroll expander, Applied Energy, 87, 1260–1268
[6] Kane, M., Larrain, D., Favrat, D., Allani, Y., 2003, Small hybrid solar power system, Energy 28, 1427–1443
[7] Kim, H.J., Ahn, J. M., Park, I., Rha, P. C., 2007, Scroll expander for power generation from a low-grade steam source, Proceedings of the Institution of Mechanical Engineers, Part A: Journal of Power and Energy, 221, 5, 705-712
[8] Smith, I. K. Stosic, N and Aldis, C. A., 1996, Development of the trilateral flash cycle system Part 3: The design of high efficiency two-phase screw expanders. Proc Instn Mech Engrs, Part A, 210 (A2), 75-93
[9] http://www.fchart.com/ees/ees.shtml
[10] Schuster, A., Karellas, S., Kakaras, E., Spliethoff, H., 2009, Energetic and economic investigation of Organic Rankine Cycle applications, Applied Thermal Engineering 29, 8-9, 1809-1817

The Implications of CHP Planning Restrictions on the Efficiency of Urban Energy Systems

James Keirstead [a], *Nouri Samsatli* [a], *Nilay Shah* [a], *Céline Weber* [a] *and David Fisk* [a]

[a] *Imperial College London, United Kingdom*

Abstract: Cities account for approximately two-thirds of global primary energy consumption and have large heat and power demands. Combined heat and power (CHP) systems offer significant efficiency gains and emissions reductions, but they can have high upfront investment costs and create nuisance pollution within the urban environment. Urban planners therefore need to understand the tradeoffs between limitations on CHP plant-size and the performance of the energy system. This paper uses a mixed-integer linear programming model to evaluate energy system designs under a range of scenarios. The results suggest that cost penalties of up to 10% and energy-efficiency penalties of up to 60% may be implied by restrictions on maximum CHP plant size.

Keywords: Optimization, Urban energy systems, Combined heat and power.

1. Introduction

Recent research has shown that cities are responsible for approximately two-thirds of global primary energy consumption and nearly 75% of energy-related greenhouse emissions [19]. As a result, there is a growing interest in improving the energy efficiency of cities so that environmental impacts are reduced while maintaining economic opportunity and quality of life.

One of the most significant areas for improvement is the integration of energy services such as heat and power. Exergy analyses of cities such as Vienna and London indicate that only about 10 to 20% of a fuel's available work is recovered, with significant amounts of exergy lost in the conversion of fossil fuels to electricity or low-temperature heat [15, 12]. Cogeneration technologies offer the potential to reduce these losses by converting more of the input exergy into useful service. Furthermore, by embedding such systems within the urban fabric, transmission and distribution losses can be significantly reduced.

However the operation of combined heat and power (CHP) technologies within an urban area can be constrained by several factors. Planning restrictions on noise or air quality, for example, might require that such facilities are located on the outskirts of an urban area or restrict the size of feasible technologies [26]. Similarly, space limitations may exclude the use of large systems within dense urban neighbourhoods. Yet these large CHP plants are able to operate at higher temperatures than smaller plants and can attain higher thermodynamic efficiencies, as well as achieving economies of scale in capital costs. Limits on the size of urban CHP plants can therefore restrict the overall efficiency of the urban energy system, potentially making it difficult to reach desired energy-efficiency and carbon-reduction targets.

The goal of this paper is to understand how such restrictions might quantitatively affect the performance of urban energy systems for the provision of heat and power. To perform this analysis, we first present an optimization model for the conceptual design of integrated urban energy systems. Then, using an idealised grid city, we determine the optimal energy supply systems for a range of demand patterns and technology mixes. The paper concludes with a summary of the main findings and a discussion of how the work might be extended.

2. The resource-technology network (RTN) model

This section describes the optimization model used in this paper. Given a pattern of resource demands varying in time and space, the model seeks to identify the combination of conversion technologies and distribution networks that best meets the demand requirements. It is therefore called the resource-technology network (RTN) model.

Corresponding author: James Keirstead, Email: j.keirstead@imperial.ac.uk

2.1. Previous work

Researchers have been developing models of energy systems for at least three decades. However advances in computing power since the mid 1990's have encouraged led to a plethora of models and tools. As space is limited, a few models similar to the RTN are described now. The interested reader is referred to [9] for a more comprehensive review.

- MARKAL (Market Allocation), and its related models, has been used extensively in a wide variety of countries. Its purpose is to consider the evolution of a specific energy system, which may be at a variety of scales from distict to national, over a period of up to 50 years. It is frequently used for national energy policy planning [e.g. 1].
- Decco is a tool for optimising energy supply systems [5, 6]. Based on a previous modelling framework called NEMESS [14], it uses optimisation to determine the relative utilisation of the (prespecified) available energy technologies at each time interval that minimises some criterion (e.g. primary energy consumption, cost, emissions). The temporal resolution of the model is very high, by default considering one year using intervals of one hour, but this is achieved by optimising (using linear programming) the supply of energy for each interval independently of the others.
- MODEST is also an optimisation model that aims to minimise investment and operating costs while satisfying energy demands [17, 18]. It can be used for a wide variety of settings, from local to national level, for a variety of sectors and at various temporal resolutions. The linear-programming formulation used by MODEST ensures that large problems can be handled with relative ease but it also introduces some limitiations, such as modelling the capital investment costs as a linear function of installed capacity. There is also no spatial dependence.

2.2. Model design

The RTN model seeks to expand on this previous work by considering multiple time periods and discrete spatial locations within a single optimization problem that determines the choice of technologies as well as their operation. It is based on the premise that any urban energy system can be represented as a set of resources and a set of technologies that interconvert those resources. The concept of resources is generalised, in that they can represent energy carriers (such as gas and electricity), non-energy resources (such as potable water) and any other material or energy stream involved in the provision of urban energy services (such as waste heat, carbon dioxide, and so on). "Technologies" represent any process that can convert a set of input resources to a set of output resources. For example, a *CHP unit* might convert a certain amount of natural gas into electricity, high-quality heat, waste heat, carbon dioxide and other atmospheric pollutants. The high-quality heat may then be converted to space and water heat in buildings by using a *heat exchanger* connected to a district heating network.

The city is divided into a number of zones (of any shape and size), each of which has time-varying resource demands specified exogeneously. The RTN model will determine how best to satisfy these demands through the provision of technologies in various zones and networks to transport resources between zones. Depending on the problem, this might result in distributed provision of resources, with small-scale technologies in each zone; or a large-scale technology in a single zone with a network to transport the resource to the rest of the city; or some combination of these two strategies. The operation of transport processes may also involve other resources, e.g. transporting a liquid fuel by road would require a certain amount of diesel and result in the generation of waste heat, carbon dioxide and other pollutants.

Finally, unless the city is entirely self-sufficient, it will need to import some resources from other cities and surrounding hinterlands. The model can choose to import any resource into any zone, subject to a number of constraints such as bounds on the rate of import in each zone and import may be restricted to a certain subset of the zones. Similarly any excess production of resources may be exported, subject to there being demand for them.

The main constraint in the RTN model is the resource balance, which is shown in simplified form below.

$$P_{rit} + Q_{rit} + I_{rit} + -E_{rit} - D_{rit} = 0, \quad \forall rit, \quad (1)$$

where P_{rit} is the net production rate of resource r in zone i at time t, Q_{rit} is the net inflow of resource from all of the other zones (transportation), I_{rit} is the rate of import, E_{rit} the rate of export and D_{rit} is the

demand of resource r in zone i at time t. Whereas I_{rit} and E_{rit} are degrees of freedom, and D_{rit} is a parameter (given as input), the other terms are variables that depend on which technologies are selected and their rates of utilization. P_{rit} may be positive or negative, representing production or consumption of the resource. Similarly, negative Q_{rit} represents a net outflow of resource to other zones and Q_{rit} depends on the rates of all transport technologies connected to zone i. The relationships are defined by technology-specific parameters such as maximum and minimum operating rates, coefficients of performance and so on.

Since the resource balance allows demands to be met in a variety of ways (e.g. import, local production, or internal transfers), the RTN framework can model complex resource chains, facilitating simultaneous comparisons of diverse energy provision strategies operating at multiple scales. As binary variables represent the locations of technologies and network links, continuous variables represent the rates of processes and all of the constraints are linear, the RTN is a mixed-integer linear programming model. The objective function is to minimize the total annualized cost (capital, operating, fuel imports etc.) of satisfying the resource demands.

3. Experimental design

Previous studies of urban energy systems have often focused on individual cities due to the availability of data or a desire to provide specific policy recommendations [e.g. 13, 23]. This is a sensible strategy for most studies but it can limit the applicability of the findings to other contexts, since adjusting the model and collecting data for a new city can be time-consuming and difficult. Since our goal here is to identify the broad trends associated with limitations on CHP plant size, we adopt a generalized model of the city to represent a range of situations.

Each modelled city has an idealised grid layout with individual cells measuring 400m×400m (16 ha.); connections between cells are allowed in the Moore neighbourhood (eight neighbours). We assume that the housing density within the city varies linearly with the distance from the centre (with some random variation added). Using London as a template, the maximum density was taken as 65 dwellings per hectare and the minimum as 10; the average household size was 2.3 people. 2007 energy consumption data for each London borough was then used to calculate the annual average power demands per capita for natural gas and electricity (1.1 and 0.60 kW per capita respectively) [11]. As the model requires heat demand as the input, it was assumed that the natural gas was used to provide hot water and space heating in 70% efficient boilers, the 1996 UK stock average [4]. Using this information, heat and power resource demands were generated for grid cities ranging from 16 to 256 cells (4×4, 6×6, ..., 16×16), representing populations from 10000 to 200000 residents (see Figure 1 for an example).

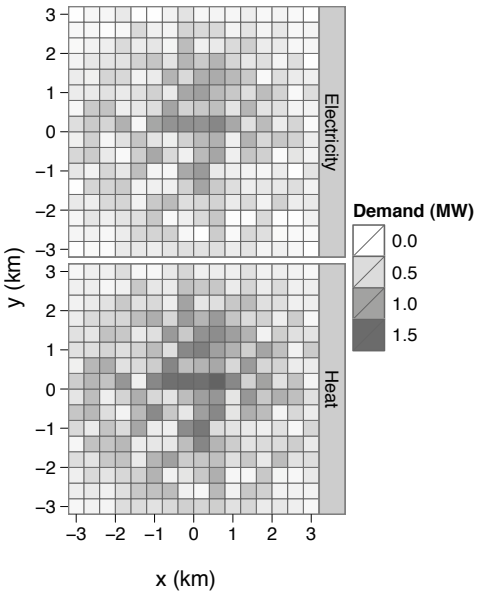

Figure 1: An indicative pattern of resource demands for a 16×16 grid city.

For each city configuration, the RTN model was run to determine the optimal (lowest cost) mix of supply technologies and distribution networks that satisfy the demand requirements. Table 1 summarizes the technologies available to the model. The size of the three CHP technologies were selected to span the typical CHP applications described by the UK Combined Heat and Power Association; micro-CHP units (less than 50 kW) were omitted as we are interested in technologies that can be used as part of a district heating system.

The model needs additional data to determine the full cost of the energy system. The parameters given in Table 2 describe the costs of building the distribution systems, as well as the resource import costs.

Table 1: Technology data. Data from [25, 8, 24, 7] and author estimates.

Parameter	Value
1. Boiler	
Capital cost	£850
O&M cost	£50/y
Max capacity	26 kW
Efficiency	90%
2. Heat exchanger	
Capital cost	£500
O&M cost	£50/y
Max capacity	32 kW
Efficiency	99%
3. Gas CHP (small)	
Capital cost	£1 million
O&M cost	£35 000/y
Max capacity	1 MW_e
Efficiency (total)	70%
Efficiency (elec)	30%
4. Gas CHP (medium)	
Capital cost	£12 million
O&M cost	£390 000/y
Max capacity	10 MW_e
Efficiency (total)	80%
Efficiency (elec)	40%
5. Gas CHP (large)	
Capital cost	£200 million
O&M cost	£5.8 million/y
Max capacity	100 MW_e
Efficiency (total)	88%
Efficiency (elec)	45%

Table 2: Other model data. Data from [21, 22, 20, 10, 3] and author estimates.

Parameter	Value
Electricity network	
Losses	0.033% per km
Capital cost	£80 000 per km
O&M cost	£900 per km
Gas network	
Losses	neglible
Capital cost	£150 000 per km
O&M cost	£2500 per km
District heat network	
Losses	0.018% per km
Capital cost	£350 000 per km
O&M cost	£11 000 per km
Resource costs	
Electricity	£0.0910/kWh
Gas	£0.0269/kWh

For each modelled city, the same pattern of demand was used but with five different technology suites: boilers (technology 1 only), small CHP (1–3), medium CHP (1,2,4), large CHP (1,2,5), and all technologies (1–5). The model was constrained so that surplus electricity production from the CHP units was not allowed to be exported from the city. For this reason, gas boilers had to be included with each of the CHP scenarios in order to make the problems feasible.

4. Results

The 35 scenarios were run (7 grid sizes × 5 technology suites) and a preliminary analysis performed. Two of the scenarios were genuinely infeasible: both the 4×4 and 6×6 cities had demands too small for the inclusion of a single 100 MW CHP unit. All of the other scenarios were feasible, although the quality of the model solution varied depending on the optimality gap and problem scaling; in most cases the gap was less than 5%.

4.1. Indicative results

Each model solution determines an energy supply strategy including distribution networks and the location and number of conversion technologies. To give a brief overview of the model's output, this section considers the results of the 8×8 case study.

Table 3 summarises the technology combinations used in this case. As noted above, all of the CHP scenarios incorporate a number of gas boilers to ensure feasibility. With the exception of the large CHP scenario, where demand is just above the minimum capacity of the large CHP unit, the chosen technologies run very close to their maximum capacities. This is an artefact of the model's design, which aggregates both supply and demand, thereby effectively "sharing" the output of household-scale technologies, such as boilers and heat exchangers, between multiple dwellings.

Figure 2 illustrates the resource networks for the large CHP scenario. It shows that the inclusion of a large CHP unit facilitates a simplified gas network,

Table 3: Summary of technology combinations for the 8 × 8 city scenarios. CF = capacity factor, i.e. average operating rate as % of maximum operating capacity.

Scenario	Technology	Number	CF
Boilers	Gas boiler	1571	98
Small CHP	CHP units	30	98
	Heat exchanger	1220	98
	Gas boiler	64	97
Med CHP	CHP units	3	100
	Heat exchanger	979	94
	Gas boiler	407	99
Large CHP	CHP units	1	31
	Heat exchanger	953	98
	Gas boiler	396	97
All techs	Small CHP	6	67
	Med CHP	3	89
	Large CHP	-	-
	Heat exchanger	987	98
	Gas boiler	350	97

which feeds a small number of gas boilers along the top and bottom of the city, but delivers most of its supply to the centrally-located CHP plant. (Note that we have assumed there is no additional gas demand, e.g. for cooking.) The high costs of the district heat network results in a distinct radial pattern for its respective network. The electricity network, costing approximately one-fifth of the district heat network, has a more convoluted structure. Neither network structure is designed for robustness or other performance characteristics.

4.2. System costs

Moving beyond this single case, Figure 3 shows overall trends in the total annual cost of the energy system when normalised by total final energy demand, which consists of the cost of imported fuels, as well as the annualised capital and operating costs for the conversion technologies and distribution networks. In almost all scenarios, the most cost-efficient energy system requires a combination of technology scales. However while one might expect increased returns to scale, the costs per delivered kilojoule increase slightly as the city gets larger *but only once the technology has reached the limit of its operating capacity*. This can clearly be seen in

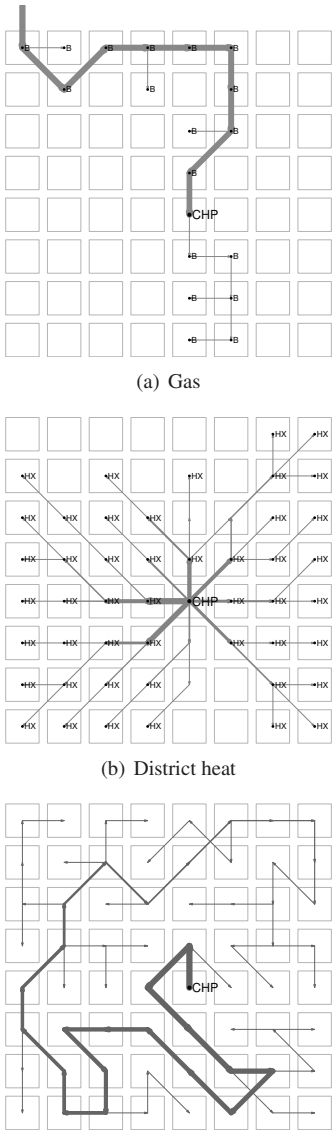

(a) Gas

(b) District heat

(c) Electricity

Figure 2: Resource distribution networks and technology locations for the large CHP 8 × 8 city scenario. B = boiler, HX = heat exchanger, CHP = 100 MW CHP.

the initial decreasing slopes for the large CHP and medium CHP scenarios. This is a consequence of the shared output of household-scale technologies, mentioned above, and it reflects a distinction between the marginal cost of a single kilojoule and the average marginal cost, i.e. because the technologies are running at their full capacity, a marginal unit of

demand typically requires an additional generating plant [see 16].

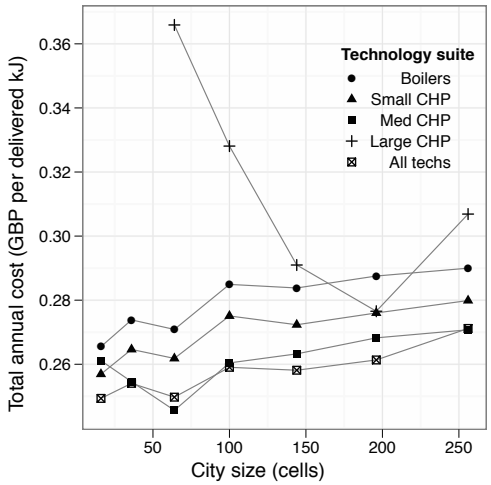

Figure 3: Cost efficiency of energy system scenarios. Costs represent annualised capital costs, maintenance costs, and fuel costs.

This figure also shows that a cost penalty is incurred if planning restrictions prevent the use of the CHP units. Relative to the boiler only scenario, the small CHP solutions are typically 3–5% cheaper and the medium CHP solutions 10% cheaper per delivered kilojoule.

The total costs were then broken down into their constituent parts: equipment (i.e. capital and operating costs) and fuel costs. The boiler scenarios are the least capital intensive with equipment costs representing 50% of the total cost. However in the large CHP scenarios, equipment costs represented on average 76% of the total costs. The most cost-efficient "all technology" scenarios balance these end-points with equipment costs representing approximately two-thirds of the total cost.

4.3. System efficiency

An alternative way of comparing the solutions is to examine their energy efficiency: namely, how much primary energy is required to service the final demands for heat and electricity? For these calculations, we have assumed that imported electricity is produced at 38.7% efficiency [2].

Figure 4 shows that, for each given technology, the primary energy efficiency is nearly constant. This can be explained by the demand generation algorithm and the maximum operating rates of the selected technologies. As the city gets larger, there is a corresponding increase in demand, linearly related to the number of cells in the city. As shown above, for each city size the model chooses technologies operating at their maximum capacity and a larger city will therefore require additional plant units. If the analysis investigated the effect of increased demand within a city of a given size, one might see economies of scale. Instead, these results show a clear rank order to the technologies and the "all technologies" scenario falls between the medium and small CHP systems.

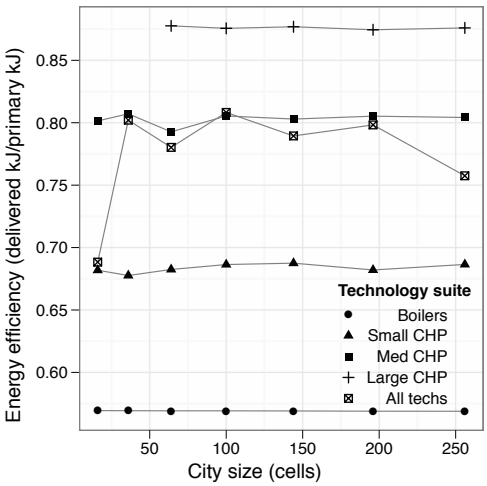

Figure 4: Energy efficiency of each scenario, as measured by delivered energy consumption per unit of primary energy.

The consequences of planning restrictions can also be seen from this graph. Relative to the boiler-only scenario, the CHP scenarios are typically 20% (small), 43% (medium), and 57% (large) more efficient.

Cost and energy-efficiency are considered together in Figure 5. Although this assessment could potentially be handled with a full multi-objective optimisation, this basic analysis suggests that the "all technologies" solution represents a good compromise in most cases. Large CHP systems offer better energy performance but at a significant cost penalty, and boiler-only systems are both less energy-efficient and, as the city grows, less cost-efficient as well. The medium CHP scenario also performs very well, although this is unique to the size of the cities studied here (which have total power demands ranging from 3 to 57 MW, compared with the medium

CHP's 10 MW_e rated capacity). In much larger cities, one would expect the large CHP system to move nearer to the optimal point.

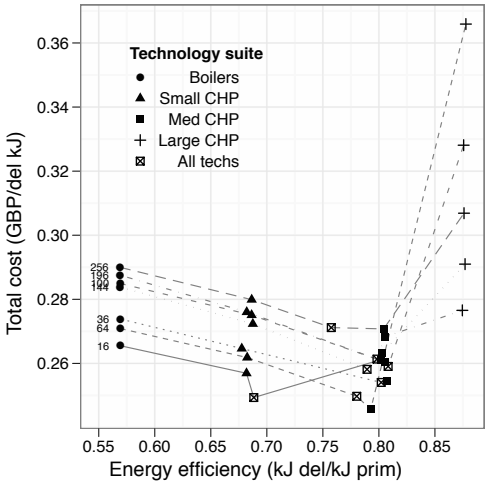

Figure 5: Summary of cost and energy-efficiency performance. Line types and numbers represent city size (cells).

5. Discussion and conclusions

The goal of this paper was to assess the potential impact of planning restrictions on the size of urban combined heat and power systems. Using a mixed-integer linear programming model, we simulated grid cities of 10000 to 200000 people under five technology scenarios. The results indicate that the most efficient urban energy systems, from both a cost and primary energy-efficiency perspective, require a mix of technologies in order to satisfy demand at an appropriate scale. As the demands were not extremely large in this case, these compromise solutions therefore included a mix of both small and medium-sized CHP systems, as well as gas boilers to serve areas of lower demand density.

The actual penalty cost of forbidding a particular technology size will of course depend on the specific city at hand. However the results here suggest that, by restricting a completely free choice of CHP technologies, the energy system may face cost penalties of approximately 10% and energy-efficiency penalties (i.e. increased primary energy demand) of up to 60%. These results are relatively constant with city scale.

The analysis has highlighted several issues that need to be considered when seeking to improve and generalise the results. First, the cost analysis showed that the structure of a local energy utility, i.e. who pays the upfront costs of equipment versus the running fuel costs, is likely to have a significant impact on which technology mix might be selected. Secondly, cross-scale analyses (i.e. looking at cities of many different sizes) appear to hide many of the economies of scale that one might expect to see from a "larger" city (i.e. more demand in the similar sized city). This suggests that for a given city size, energy systems are guided by unit marginal costs. However across cities, one must consider the significant plant requirements needed to satisify a large increase in demand (i.e. the average marginal cost).

The paper also alluded to local air pollution as a driver of such plant size restrictions. This has not been explicitly considered here, but clearly offers a profitable area for further research, for example, by adding a monetary penalty to the objective function based on health impacts. Similarly the optimisation model could be enhanced to consider network robustness and more realistic plant load limitations. Specifically, constraints should be added to differentiate household scale technologies which cannot share their output versus larger common technologies. Finally a multi-objective optimisation framework would be useful for a formal analysis of the cost and energy-efficiency trade-offs evaluated here.

References

[1] BERR. *The UK MARKAL Energy Model in the 2007 Energy White Paper*. Dept. of Business, Enterprise and Regulatory Reform, 2007.

[2] BERR. *Digest of UK Energy Statistics*. Dept. of Business, Enterprise and Regulatory Reform, London, 2008.

[3] BERR. *Quarterly Energy Prices*. Dept. of Business Enterprise and Regulatory Reform, London, 2009.

[4] B Boardman, S Darby, G Killip, M Hinnells, C Jardine, J Palmer, and G Sinden. *40% House*. Environmental Change Institute, Oxford, 2005.

[5] T Bruckner, H.M. Groscurth, and R Kümmel. Competition and synergy between energy technologies in municipal energy systems. *Energy*, 22(10):1005–1014, October 1997.

[6] T Bruckner, R Morrison, C Handley, and M Patterson. High-Resolution Modeling of Energy-Services Supply Systems Using decco: Overview and Application to Policy Development. *Annals of Operations Research*, 121:151–180, 2003.

[7] CHPA. Fact Sheet: CHP Scales and Startup. http://www.chpa.co.uk/about_chp/fact_sheets/FactSheet-CHPScales\&Startup.pdf, 2007.

[8] Cogen3. Available Cogeneration Technologies in Europe: Part II Technologies and Products, 2003.

[9] D. Connolly, H. Lund, B.V. Mathiesen, and M. Leahy. A review of computer tools for analysing the integration of renewable energy into various energy systems. *Applied Energy*, 87(4):1059–1082, 2010.

[10] CTR. The Main District Heating Network in Copenhagen, 2004.

[11] DECC. *Total final energy consumption at sub-national level*. Dept Of Energy And Climate Change, 2008.

[12] F DeMartial. *Rapport de stage scientifique: Urban energy systems*. École des Ponts ParisTech, 2009.

[13] L Girardin, F Marechal, M Dubuis, N Calame-Darbellay, and D Favrat. EnerGis: A geographical information based system for the evaluation of integrated energy conversion systems in urban areas. *Energy*, 35:830–840, 2010.

[14] H.M. Groscurth, T. Bruckner, and R Kümmel. Modeling of energy-services supply systems. *Energy*, 20(9):941–958, 1995.

[15] A Grubler. The Urban Sustainability Challenge. In Global Carbon Project - Urban and Regional Carbon Management, editor, *International Symposium Realizing Low Carbon Cities: Bridging Science and Policy*, Nagoya, 2009. GCP-URCM.

[16] T Hartford. A marginal victory for the well-meaning environmentalist. *The Financial Times*, 2010.

[17] D Henning. MODEST: An energy-system optimisation model applicable to local utilities and countries. *Energy*, 22(12):1135–1150, 1997.

[18] D Henning, S Amiri, and K Holmgren. Modelling and optimisation of electricity, steam and district heating production for a local Swedish utility. *European Journal of Operational Research*, 175(2):1224–1247, 2006.

[19] IEA. *World Energy Outlook*. International Energy Agency, Paris, 2008.

[20] National Grid. Seasonal and Annual Data, 2009.

[21] Ofgem. Electricity Distribution Cost Review 2005-2006, 2007.

[22] Ofgem. Gas Distribution Price Control Review: Final Proposals, 2008.

[23] L Parshall, K Gurney, S.A. Hammer, D Mendoza, Y Zhou, and S Geethakumar. Modeling energy consumption and CO2 emissions at the urban scale: Methodological challenges and insights from the United States. *Energy Policy*, 2009.

[24] PowerTechnology.com. Avedore Multi-Fuel Power Plant, Denmark. http://www.power-technology.com/projects/avedore/, 2010.

[25] Vokèra. Vokèra Linea HE combi boiler. http://www.vokera.co.uk/home-owners/condensing-boiler/combi-boiler/linea-he, 2010.

[26] X Yuan, J Kellett, and C Ma. Conflicts between state planning, market development and environmental sustainability: A case study of the electric power industry in Shandong Province. *International Journal of Sustainable Development and World Ecology*, 15(5):430–439, 2008.

Acknowledgments: The authors would like to acknowledge the support of BP through the BP Urban Energy Systems project at Imperial College London.

Trade-offs between Layout of Cities and Design of District Energy Systems

Céline Weber [a], *James Keirstead* [a], *Nouri Samsatli* [a], *Nilay Shah* [a] *and David Fisk* [a]

[a] *Imperial College, Centre for Process and Systems Engineering, Energy Futures Laboratory, Room 410C, Roderic Hill Building, South Kensington Campus, London, SW7 2AZ, United Kingdom*

Abstract: The reduction of CO_2 emissions linked with transport and energy services (heating, domestic hot water, cooling and electricity), together with the increased use of renewable energies, remains a high priority on various political agendas. In this paper, the trade-offs between the optimal layout of a city in terms of transport and the resulting district energy system are analysed. The starting point of the study is a greenfield site in England, on which a small eco-town, with a pre-defined number of inhabitants, shall be built. Conventional assumptions are made about the number and types of buildings according to the number of inhabitants. A layout model is then used to define the optimal layout of the city to reduce transport requirements. Finally, the optimal mix of technologies that will satisfy the energy services, taking into account spatial and other constraints, is computed using advanced process optimization techniques. The results show how increasing the density of cities to reduce transport energy requirements influences the opportunities offered by certain renewable energy technologies for heat and power services.

Keywords: District energy system, City layout, Network.

1. Introduction

The reduction of CO_2 emissions is a challenge for the coming decade and a priority on many political agendas. Various examples of policies to decrease CO_2 emissions and/or promote the use of renewable energy sources exist [19, 9, 10]. Transportation and space heating are responsible for a large share of the total greenhouse gas emissions. In the United Kingdom, transport is responsible for 21% of the total CO_2 emissions (excluding aviation) and space heating for 25% [1]. These two sectors are therefore priority candidates when targeting CO_2 reductions.

In 1989, Kaya built on work started by Holdren et al. [14] and proposed a formulation linking the CO_2 emissions with the population of a country. The equation became famous as the *Kaya identity*. It emphasizes the multiplicative effect of the different factors influencing environmental deterioration:

$$CO_2 = Pop \cdot \frac{GDP}{Pop} \cdot \frac{En}{GDP} \cdot \frac{CO_2}{En} \qquad [\text{ton-}CO_2] \quad (1)$$

with: Pop the population, GDP the gross domestic product, En the energy consumption, $\frac{GDP}{Pop}$ the living standard [£/capita], $\frac{En}{GDP}$ the energy intensity [J/£] and $\frac{CO_2}{En}$ the carbon intensity [ton-CO_2/J]. Looking at the Kaya identity, there are two reasonable ways to decrease CO_2-emissions: reduce the energy intensity, or reduce the carbon intensity. The reduction of energy intensity can be achieved by implementing more efficient processes. For transport this means for instance: decreasing the petrol consumption per kilometre driven for a car by using hybrid engines, reducing the need for transport, promoting public transport; for heating examples include: increasing the insulation thickness in buildings or implementing heat recovery systems. The reduction of the carbon intensity on the other hand can be achieved by the use of renewable energy sources for both transport and heating [22].

While in cities the high population density is a main cause of negative environmental externalities, the high density of energy services required creates opportunities to reduce per-capita energy consumption [6]. In this paper, the influence of the layout of a city on the CO_2 emissions related to energy services is analysed using an eco-town including 6 500 inhabitants and located in central England. The question addressed is: can an appropriate layout for a city decrease the energy intensity and/or the carbon intensity simultaneously on both the transport and the energy services.

Corresponding author: Céline Weber, Email: c.weber@imperial.ac.uk

Models to simulate and/or optimise energy systems have been extensively developed by researchers. As space is limited, only HOMER [4] and EnergyPLAN [3] shall be mentioned here, as they feature some similarities with the tool developed in this paper. While HOMER considers the design and optimisation of energy systems as is done here, it focuses more on a building level than on a city level, and does not include transport. EnergyPLAN on the other hand does include transport, but optimises operating costs only (and not capital costs). The interested reader is referred to the recent paper of Connolly et al. [8] for a more comprehensive review.

2. Methodology

The starting point of the study is a greenfield site in England, on which a small eco-town shall be built. The eco-town has a pre-defined number of inhabitants. The following steps are included in the methodology: using the *layout-model* of the *SynCity* tool developed by Keirstead et al. [15], conventional assumptions are made according to the number of inhabitants about the number and types of building (for instance dwellings, schools, shops) and the layout of the city is computed by minimising yearly transportation costs, energy consumption or CO_2 emissions; for each type of building, consumption profiles are then derived; finally, the optimal mix of technologies that will satisfy the needs in terms of energy services is computed using the DESDOP tool [22, 24] and advanced process optimisation techniques.

This paper focuses on the last part of the methodology, namely the definition of the optimal mix of technologies. The objective function, defining the optimal mix of technologies, can be expressed in terms of costs or emissions (primarily CO_2 emissions, but any other greenhouse gas could be chosen). The question that is addressed is: Given the small city (with its layout defined as described above), its available renewable energies, its buildings and their related consumption profiles, which combination of energy conversion technologies (and therefore energy sources) will be best suited to meet the energy services, how will these technologies be combined, where in the district should these technologies be located (centralised or distributed), and how should the layout of the energy distribution network be arranged (provided a network is required).

The choice of technologies includes centralised and distributed technologies, and renewable and non-renewable energy powered technologies. The list of technologies considered in this paper is given in Table 1, based on what were considered to be sensible technologies for the eco-town. Different technologies can easily be added to or removed from the tool, according to the problem to be solved. This allows restricting the search space, rather than considering *all* existing technologies.

Table 1: Available technologies

Centralised	Distributed
Wind turbine	PV cells
Large scale heat-pump (HP)	Solar thermal collectors
Free cooling	Individual heat pump
Combined heat and power (CHP)	Individual Chiller
	Boiler

The optimisation of the mix of technologies is complex for the following reasons [23]:

- District energy systems combine spatial and temporal (consumption profiles) aspects.
- There is a high number of combinations including centralised and distributed, renewable and non-renewable energy powered technologies.
- The consumption profiles of the different energy services vary during the day, and from one day to the other, in a stochastic manner. Hence the problem becomes a multi-period problem.
- The temperature level at which a building requires heating or cooling needs to be considered.
- If a district network is the optimal solution, there are usually a lot of different ways to link the buildings together.
- The availability of renewable energy sources follows stochastic distributions (wind profile for instance); this requires robust solutions.
- The specificities of the technologies vary significantly between technologies: while a CHP can be turned on by an operator at any point, the same is not true for a wind turbine.
- Some technologies have part load restrictions (involving binary variables) while other do not.

The tool is implemented in GAMS using the Cplex Mixed Integer Linear Programming optimiser. The main decision variables refer to the type and size of

the technologies, the location of the technologies in the district, the operating strategy of the technologies, and the layout of the distribution network (if required).

3. Technologies

The main equations and assumptions for each of the technologies are given in the following subsections [24].

3.1. Heat pump

Heat pumps (HP) are modelled by the general two equations:

$$COP = \frac{\dot{Q}}{\dot{E}} \tag{2}$$

$$COP = \eta \cdot \frac{T_{cond}}{T_{cond} - T_{evap}} \tag{3}$$

with $\dot{Q}$ the heat delivered in kW, $\dot{E}$ the electricity consumed in kW, η the exergy efficiency, T_{cond} and T_{evap} the temperatures in the condenser and evaporator. The following assumptions prevail for the test case analysed in this paper:

1. Both the centralised and the distributed heat pumps are closed loop ground source heat pumps, connected to boreholes via a heat exchanger.
2. The temperature of the ground (the cold source) is constant at 10°C.
3. The temperature in the condenser has been set to 70°C for the centralised heat pump (to meet the supply temperature of the heating network as defined in Section 4.), and to the required temperatures for heating and hot water for the distributed heat pumps (see Section 4.).
4. The exergy efficiency is 0.55 for the centralised heat pump and 0.43 for distributed heat pumps, based on Girardin et al. [13].
5. The minimum part load is set to 20% for the centralised heat pump (and 0% for the distributed heat pumps).
6. The specific investment costs for the heat-pump are 1 600 £/kW$_{th}$. This includes the investment for the heat pump, the boreholes and the installation. The same investment costs were considered for both centralised and distributed heat pumps[1].

[1] According to several manufacturers the specific investment costs of centralised ground source heat pumps are not necessarily lower than the specific investment costs of distributed heat pumps, as centralised heat pumps imply larger costs for the boreholes and are generally tailor-made.

3.2. Combined heat and power

The combined heat and power (CHP) technologies used for this test case are reciprocating engines. In the optimisation, the efficiency of a CHP plant is given by a piecewise linearisation of the following correlation which approximates the values given by various manufacturers [24]:

$$\epsilon_{\text{el}} = 0.0272 \cdot \ln S_{CHP} + 0.2084 \tag{4}$$

with S_{CHP} the design size of a CHP plant.

As far as the operation of the CHP plant is concerned, the following assumptions have been made:

1. The temperature of the engine exhaust gas is about 350°C and it may be cooled down to an average value of 40°C for heat recovery. The inlet and outlet temperatures of the cooling circuit of the engine are 90°C and 100°C (outlet temperature). These are averages based on data from manufacturers.
2. The minimum part load is set to 70% of the design load (based on Dupleac et al. [11] and discussions with several manufacturers).
3. The sum of the electrical and thermal efficiencies equal 90% regardless of the part load factor.
4. The CHP plant cannot be turned on for less than 4 hours per day, and can only be switched on and off once a day. This is to take into account the facts that CHPs need some time to warm up and reach the indicated efficiencies [7].

The costs used are shown in Table 2. They include the costs of investment, installation, foundations and mains connection. These costs are averages based on information from manufacturers as well as Streckiene et al. [20].

Table 2: Investment costs for CHPs (based on information from manufacturers as well as [20])

Range [kW]	Costs [£/kW]
500 - 1000	750
1000 - 2000	650
2000 - 5000	620

3.3. Wind turbines

The rated output of wind turbines given in data sheets from manufacturers often corresponds to wind speeds of 15-16 m/s. Therefore the design size of the turbine (and hence its investment costs) cannot be taken as the maximum over all periods of the

average periodic output (the average wind speed at the location of the eco-town is 5-6 m/s). The *capacity factor*, which is defined as the actual electricity produced over the maximum rated output, needs to be taken into account. In order to maintain the model linearity, a piecewise linearisation has been defined to compute the actual output of the turbine as a function of its size, including the capacity factor corresponding to the wind speed at the location of the eco-town as a parameter. The costs used, shown in Table 3, include the costs of investment, installation, foundations and mains connection.

Table 3: Investment costs for wind turbines (based on information provided by manufacturers as well as published costs [18, 17])

Range [kW]	Costs [£/kW]
20 - 100	2 000
100 - 500	1 500
500 - 3000	1 200

3.4. PV cells

The electricity generated by PV cells is given by:

$$\dot{E}_t = A_{pv} \cdot \epsilon_{pv} \cdot I_t \tag{5}$$

where A_{pv} is the design size of the PV cells in m^2, ϵ_{pv} the efficiency of the PV system and I_t the irradiation in kW/m^2 during period t. The correlation between the design area of the cells and the design output[2] in kWp is given by:

$$S_{pv} = A_{pv} \cdot S_{pv_0} \tag{6}$$

with S_{pv} the design size in kWp of the installation and S_{pv_0} the output in kWp of a panel taken as reference and for which the area is known. The following assumptions have been made:

1. The cell efficiency at standard conditions is 14% (the Sharp NU 185 was taken as a reference) and the losses due to the inverter, dust and temperature are 25% [21].
2. The PV panels are fixed planes, south orientated, with a 35° inclination.
3. The investment costs are 7 500 £/kWp (based on information provided by manufacturers).

[2]The output of a PV cell is given in kWp, which corresponds to the output of the cell under standard test conditions: 25°C and an irradiation of 1000 W/m^2.

3.5. Solar thermal collectors

The following assumptions have been made for solar thermal collectors:

1. The collectors are of the evacuated tube type.
2. The system efficiency is 39% based on the gross area[3] [16].
3. The average electricity required to pump the fluid around the system (between the collectors and the storage tank) is 8.5% of the generated heat [16].
4. The investment costs are 950 £/m^2, including installation [16].

3.6. Boilers

The following assumptions were made for boilers:

1. The efficiency of the boilers is 90%.
2. Distributed gas boilers generate heat directly as and when it is needed.
3. The investment costs are 100 £/kW_{th} (including flue evacuation and installation).

4. Description of the layouts and assumptions

Three different layouts have been considered for the eco-town. Each layout comprises the same gross internal area of dwellings, schools and mixed-use spaces[4]. As can be seen in Table 4, the eco-town includes an overwhelming majority of dwellings. The first layout, *As planned*, corresponds to the layout that was initially defined by the developers who launched the project (see Figure 1(a)). The second layout, *Unconstrained*, has been computed using the layout model (see Figure 1(b)) without setting any major constraints apart from an upper boundary on the density of dwellings (65 dwellings per hectare). This results in a concentration of high-density housing in the North-East part of the city. For the third layout, *Constrained*, a constraint was added on the maximum number of high-density dwellings to allow more room for people between the buildings (Figure 1(c)). The resulting annual costs and CO_2 emissions are given in Table 5. The unconstrained layout clearly has the lowest costs and emissions for transport, as the majority of dwellings and mixed use spaces are concentrated in the same area of the town.

[3]The gross area is the overall area of the collector, including the frame.

[4]A mixed-use space is a combination of retailers, restaurants and offices.

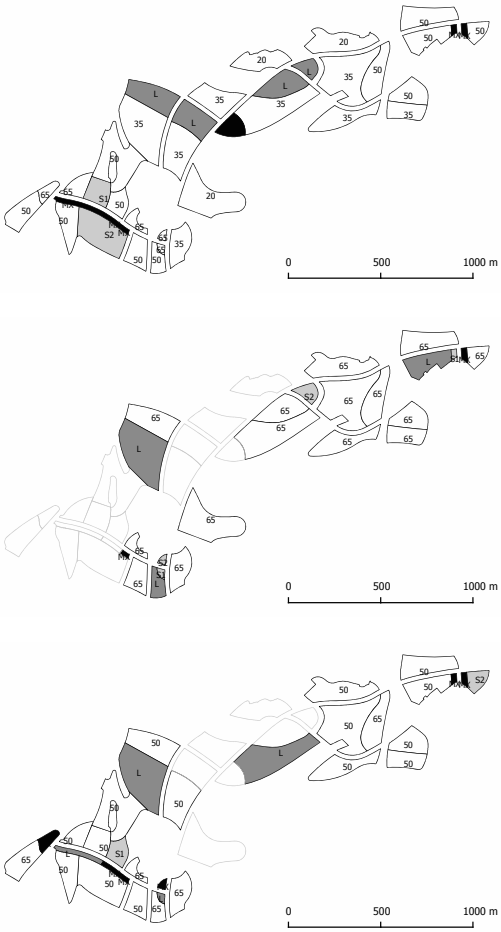

Figure 1: Layouts considered: 1(a) As planned; 1(b) Unconstrained; 1(c) Constrained. Legend — white shapes with pale grey border, empty cells; white shapes with numbers and black border, dwellings at specified density (dwellings/ha); light grey shapes, schools; darker grey shapes, open space/park; black shapes, mixed use.

Table 4: Total gross internal area for each type of building in the layout

Type of building	Total gross internal area in the city
Residential building	421 000 m^2
School	6 000 m^2
Mixed use	8 100 m^2

Table 5: Costs and CO_2 emissions for each layout for transport and energy services (when designing the energy system minimising CO_2 emissions)

	As planned	Uncons-trained	Cons-trained
CO_2 emissions [kg/year/capita]			
Transport	316	196	307
Energy services	385	522	467
Cost [£/year/capita]			
Transport	711	332	743
Energy services	1183	828	945

The following assumptions have been made to run the district energy system design and optimisation tool [24]:

1. The consumption profiles have been defined using 18 different periods in total: 6 periods per day (see Table 6), for 3 representative days per year (one summer day, one mid-season day, one winter day). To compute the annual energy requirements, the year has been assumed to include 92 summer days, 153 mid-season days and 120 winter days.

Table 6: Periods

Period	Hours in the day
1	7.00am-9.00am
2	9.00am-12.00am
3	12.00am-1.00pm
4	1.00pm-6.00pm
5	6.00pm-10.00pm
6	10.00pm-7.00am

2. All the buildings are built to PassivHaus standards [5] according to information provided by the developers. The resulting consumptions are given in Table 7. Cooling has been neglected[5].

Table 7: Consumptions

	Peak [kW]	Total [MWh/year]
Heat	3 217	8 433
Hot water	11 099	15 672
Electricity	3 958	14 646

[5]The cooling of the mixed use buildings has been converted into electricity requirements, assuming a seasonal efficiency ratio of 3.5. This is acceptable considering that they are the only buildings requiring cooling and therefore there would be no district cooling system in the eco-town.

3. If centralised technologies form a part of the optimal solution, the choice of the potential locations of the plant room is dictated by the following factors:
   - The plant room can not be located on a node locating an existing building to avoid nuisance.
   - The proximity to renewable energy sources (easy access to the soil, lake, waste incineration plant) shall be considered.
4. Space heating and domestic hot water can be provided directly or via distributed storage tanks (except for gas boilers that generate the heat directly as and when it is needed).
5. Thermal storage losses are 10% of the stored energy [20].
6. The average heat losses in the heating distribution network are 5% of the distributed heat.
7. The design supply temperature for the heating network is 70°C and the return temperature is 40°C. These temperatures allow for the network to meet domestic hot water requirements[6].
8. The required supply temperature for space heating in the dwellings is 35°C (which is sufficient for underfloor heating) and 60°C for domestic hot water.
9. The total available area for solar thermal collectors and PV cells is the total roof area of the buildings at the node.
10. For wind turbines, a maximum total rated output of 10 MW for the eco-town has been set, with a maximum of 500 kW per turbine.
11. The price of grid electricity averages 0.13 £/kWh during the day and 0.06 £/kWh during the night.
12. The price of electricity sold back to the grid (for instance whenever PV cells or wind turbine generate more electricity than currently required in the eco-town) has been set to 0.01 £/kWh. This reflects the situation as it stands currently for small- and medium-scale technologies in the UK.
13. The price of natural gas is 0.04 £/kWh throughout the day.
14. The grid and the gas network (also used for cooking) are already existing.
15. The CO_2 emissions linked to natural gas are 0.194 kg-CO_2/kWh, and the CO_2 emissions linked to grid electricity to 0.422 kg-CO_2/kWh [19].
16. The interest rate is 7% [12].

[6]Calculations based on data from [2] show that the supply temperature decreases by 0.2°C/1000m in DN100 pipes and by 0.65°C/100m in DN20 pipes assuming polyurethane insulation.

5. Results

The resulting district energy systems for each layout, when minimising yearly investment and operating costs, are shown in Figures 2 and 3. Because the requirements for energy services do not change between layouts, and the heating density is large enough even for the layout with the lowest dwelling density to feature district heating, there is no major difference between the layouts. They all include a centralised plant including a 2 290 kW_{el} CHP unit and a 1 546 kW_{th} HP connected to a district heating scheme. Electricity is taken partly from the CHP unit and partly from the grid (6.7 GWh/year). No wind turbines, PV cells or thermal solar collectors are implemented. The CO_2 emissions are 1 420 kg-CO_2/year/capita and the costs 385 £/year.

To assess how the layout of the city influences the CO_2 emissions of the energy services, a constraint was added to the district energy system design and optimisation model to limit as much as possible the CO_2 emissions[7]. The results (Table 5 and Figure 3) show that as the dwelling density of the city decreases and more space is available on roofs for solar technologies (layout *As planned*), the CO_2 reduction potential increases (layout *As planned* features the lowest CO_2 emissions for energy services in Table 5 with 385 kg/year/capita). On the other hand, lower density cities typically result in greater CO_2 emissions due to transport, unlike high density cities (layout *Unconstrained*). Therefore the two effects need to be balanced. Although these two conclusions, considered independently, are intuitive, a tradeoff between the two effects cannot be made without the use of a model. Moreover, these results provide the necessary confidence that will allow to consider more complex cases, including the opportunity offered by undeveloped land to assess ground-based solar or biomass renewable energy.

[7]The reduction of CO_2 is limited because of: the limits imposed on the renewable energy powered technologies (Assumptions 9 and 10 in Section 4.); the availability of renewable energy sources following stochastic distributions; the lack of electricity storage.

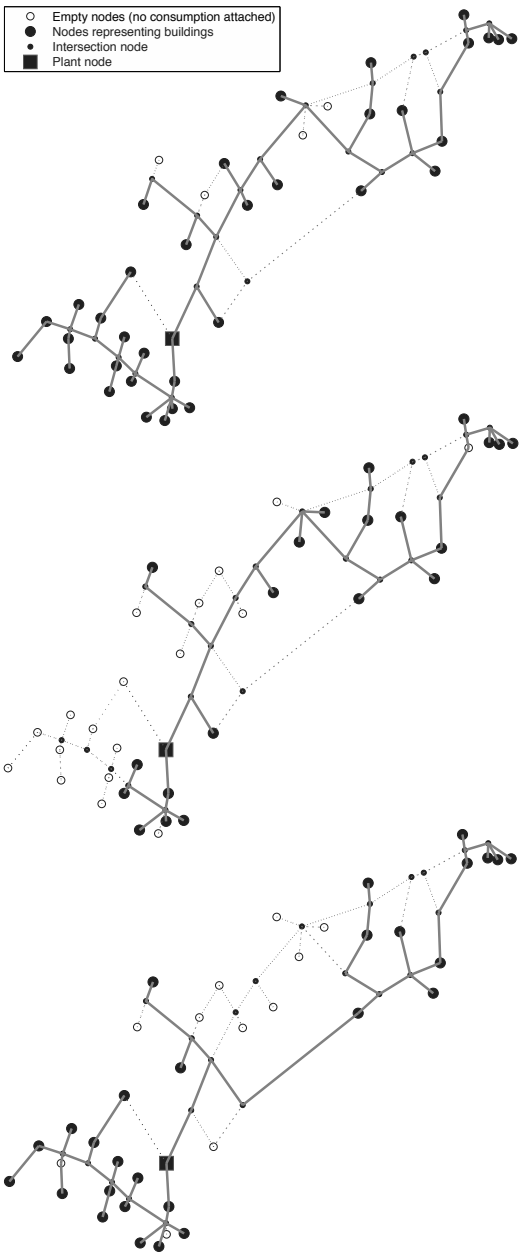

Figure 2: District heating schemes for the different layouts (the shapes from Figure 1 have been replaced by nodes, the dotted lines represent allowed connections, the thick black line the effective network): 2(a) As planned by the developers, 2(b) Without concentration constraint, 2(b) With concentration constraint.

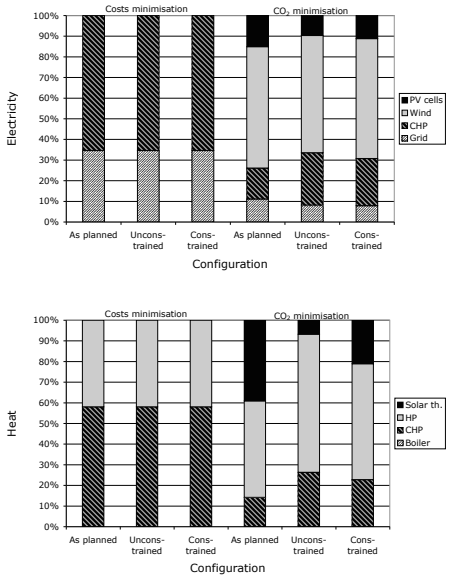

Figure 3: Generation of electricity and heat (for space heating and domestic hot water) for each layout, when costs, and CO_2 emissions are minimised.

The next question therefore to address in future work is: how should a city be designed in order to be dense enough to allow district heating (and cooling) as well as low transport requirements, without jeopardising the low carbon intensity of renewable energies? Or, to go back to the *Kaya identity*: can both the *energy intensity* and the *carbon intensity* be simultaneously minimised, and if yes, how?

References

[1] Act On CO2. http://www.actonco2.com, last accessed February 5th 2010.

[2] Cost benefits and long term behaviour of a new plastic piping system. International Energy Agency.

[3] Energyplan. http://energy.plan.aau.dk/, last accessed February 5th 2010.

[4] Homer. http://www.homerenergy.com, last accessed February 5th 2010.

[5] PassivHaus. http://www.passivhaus.co.uk, last accessed January 8th 2010.

[6] M. Burer, K. Tanaka, D. Favrat, and K. Yamada. Multi-criteria optimization of a district cogeneration plant integrating a solid oxide fuel cell-gas turbine combined cycle, heat

pumps and chillers. *Energy*, 28(6):497–518, 2003.

[7] Cogenco. Personal communication, 2009.

[8] D. Connolly, H. Lund, B.V. Mathiesen, and M. Leathy. A review of computer tools for analysing the intergration of renewable energy into various energy systems. *Applied Energy*, 87(4):1059–1082, 2010.

[9] UK Department for Energy and Climate Change. The renewable energy strategy, 2009.

[10] Deutsches Bundesministerium für Umwelt, Naturschutz und Reaktorsicherheit . Erneuerbare Energie Gesetz, 2009.

[11] R. Dupleac, M. Tazerout, V. Mahieu, S. Rousseau, and B. Leduc. Experimental database for a cogeneration gas engine efficiency prediction. *Proceedings of the Institution of Mechanical Engineers Part A*, 215(1):55–62, 2001.

[12] I. Ellingham. *New generation whole-life costing : property and construction decision-making under uncertainty*. Taylor and Francis, 2006.

[13] L. Girardin, M. Dubuis, N. Darbellay, F. Marechal, and D. Favrat. Energis: A geographical information based system for the evaluation of integrated energy conversion systems in urban areas. *Energy (in press)*, doi:10.1016/j.energy.2009.08.018, 2009.

[14] J.P. Holdren and P.R. Ehrlich. Human population and the global environment. *American Scientist*, 62:282–292, 1974.

[15] J. Keirstead, N. Samsatli, and N. Shah. Syncity: an integrated tool kit for urban energy systems modelling. In *Proceedings of the 5th Urban Research Symposium, Marseilles (France)*, 2009.

[16] C. Martin and M. Watson. Side by side testing of eight solar water heating systems. ETSU S/P3/00275/REP/2 DTI/Pub URN 01/1292, ETSU UK, 2001.

[17] M.R. Patel. *Wind and solar power systems*. CRC Press, Taylor& Francis Group, 2006.

[18] V. Quashning. *Understanding renewable energy systems*. Earthscan, 2005.

[19] UK Building Regulations. Approved Document L2A: Conservation of fuel and power (New buildings other than dwellings), 2006.

[20] G. Streckiene, V. Martinaitis, N.A. Andersen, and J. Katz. Feasibility of CHP-plants with thermal stores in the German spot market. *Applied Energy*, 86(11):2308–2316, 2009.

[21] M. Suri, T.A. Huld, E.D. Dunlop, and H.A. Ossenbrink. Potential of solar electricity generation in the european union member states and candidate countries. *Solar Energy*, 81(10):1295–1305, 2007.

[22] C. Weber. *Multi-objective design and optimization of district energy systems including polygeneration energy conversion technologies*. PhD thesis, Swiss Federal Institute of Technology Lausanne, 2008.

[23] C. Weber, F. Maréchal, and D. Favrat. Design and optimization of district energy systems. In *PRES06*. PRES06 Conference, Prag, August, 2006.

[24] C. Weber and N. Shah. Optimisation based design of a district energy system for an eco-town in the united kingdom. *Energy (submitted)*.

Acknowledgments: The financial support of BP via the Urban Energy Systems project at Imperial College London is gratefully acknowledged. The numerous manufacturers are also deeply thanked for all the information provided.

Comparative assessment of processes for the transportation of thermal energy over long distances

Nathalie MAZET[a], Pierre NEVEU[a,b], Driss STITOU[a]

[a] PROMES-CNRS Laboratory - Rambla de la Thermodynamique, Tecnosud – F-66100 Perpignan
[b] University of Perpignan UPVD, 52 avenue Paul Alduy, F-66860 Perpignan

Abstract: This papers deals with the heat transportation over long distances that could allow the recovery of waste industrial heat. Processes involving thermochemical transformations can be relevant for such purpose as they involve the transportation of a reactive fluid at ambient temperature, and thus allow large distances between source and users. This paper proposes to evaluate the performances of all the systems allowing the transportation of energy, including classical processes (involving electricity, coolant, slurry). A general method has been developed to assess the performances of all the paths of energy transportation. The aim is to analyze the relevance of each process on the same basis. Thus, the exergy destruction in each part of these systems are analyzed and the exergy yields are compared.

Keywords: thermochemical process, heat transportation over long distance, exergy.

1. Introduction

Industrial waste heats represent a huge amount of thermal energy, which is usually located several tens kilometers away from potentiel users. The most obvious application is the recovery of low temperature waste heat from industrial sites for distant heat and/or cold needs (district heating, food-processing industry…). Therefore, the transportation of heat over long distances (over 10 km) represents a real scientific and technological challenge for a better and sustainable management of the energy resources.

Since the 70', several research projects [1] focus on this research area. The basic idea is to implement a thermochemical process between the source and user sites, in order to replace the transportation of thermal energy by the transportation of an active fluid (a reactive gas for example) at ambient temperature. As a result, the thermal losses due to the transportation are low, and transportation over long distances can be considered.

2. Thermochemical processes for transportation of thermal energy

Processes involving thermochemical transformations can be relevant for such purposes. The transformations can be ab- or ad-sorption, chemical reaction, phase change… For example, such a thermal energy transportation process based on solid-gas reactions involves two solid gas reactors, one on the source site and the other on the user site, coupled by the transportation of the reactive gas between them (figure 1). On the source site, an endothermal decomposition takes place, releasing the reactive gas, which then flows to the user site where it is involved in an exothermal reaction. Such solid gas reactions are reversible, and reversing both reactions (using a free low temperature source on the user site) allows the gas to flow back to the source site. As the gas is transported at ambient temperature, the source-to-user distance less affects the energy transportation efficiency.

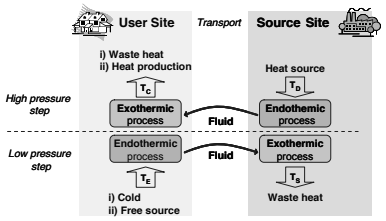

Fig. 1. Principle of the thermal energy transportation over long distance by a single-effect thermochemical process, using a remote source at T_D, to provide heat at T_C (ii) or cold at T_E (i) to the user.

Moreover, such thermochemical systems allow producing several functionalities on the user site: cold production or heat production or heat

upgrading. This multifonctionnality is a really innovative characteristic of this concept.

Such systems based on solid-gas thermochemical processes are investigated at CNRS-PROMES since a few years [2,3,11]. We have thoroughly studied several concepts of cycles (single effect or cascade) fulfilling the requirements of the transport of thermal energy, and the potentialities of these concepts according to the reactive pairs.

Now, the performances of these systems have to be evaluated, according to operating temperatures, power, source-to-user distances... In order to strengthen this analysis, classical processes of energy transportation (i.e. electricity network coupled with heat pump, transport by coolant (sensible heat) or slurries (latent heat)) are included in this evaluation. The final objective of this work is to rank these various systems and to define the scope of relevance of each process according to the temperatures of the source and the users, the distance for transportation.

3. Comparative assessment

This assessment will compare the innovative thermochemical processes and the classical systems. All of them operate through three means:

- an electrical network : this most classical exergy system transportation (i.e. electricity coupled with a mechanical heat pump on user site) involves a conversion step from waste heat to electricity. The low temperature of the waste heat can disadvantage this system.

- a coolant network, that widely exists as district heating or cooling system, but the length of the network is usually limited beyond 10 km.

- a slurry network (ice slurry), that also exists as cooling systems,

- gas or liquid chemical reagent network, coupled with thermochemical converters on the user and source sites. This last means takes advantage of a fundamental difference with the other systems: when transporting chemical reagents, the pressure drop has usually a weak effect on the chemical potential, so that the exergy output on the user site has nearly the same value than the exergy input at the source site, whatever the distance is.

For this assessment, all the systems are driven by heat released from the source site at a given temperature and all of them produce the same utility on the user site. In this paper, we focus on cold production for air conditioning applications.

3.1. Principle

A general method has to be developed to assess the performances of all these paths of energy transportation on the same basis, whatever the form of the transported energy is (chemical, 1 .9 . E Thermodynamics offers such a tool, especially exergy analysis.

All these processes can be divided in three sub-systems (figure 2): two 'exergy converters', coupled to the exergy transportation network. Each sub system is characterized by exergy efficiency or exergy destruction :

the converter on the source site converts the waste heat in a flow n of an extensity (electrons, gas, liquid, solid), characterized by a specific generalised chemical potential μ or exergy. This conversion process is characterized by its exergy efficiency:

$$\eta_s = n \cdot (\mu_1 - \mu_2) \Big/ q_s \cdot \left(1 - \frac{T_0}{T_s}\right) \qquad (1)$$

the transportation network, which transports this extensity through one or several pipes to and from the user site, involving some exergy losses, characterized by its exergy destruction:

$$ex_d = n \cdot (\mu_1 - \mu_1') + (\mu_2' - \mu_2) \qquad (2)$$

the converter on the user site which produces the useful heat or cold. Its exergy efficiency is:

$$\eta_u = q_u \cdot \left(1 - \frac{T_0}{T_u}\right) \Big/ n \cdot (\mu_1' - \mu_2') \qquad (3)$$

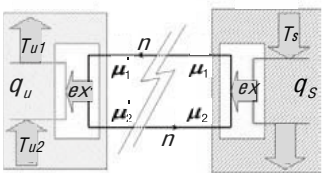

Fig. 2. Generic scheme for thermodynamics analysis of energy transportation.

Then, the overall exergy efficiency η and the overall energy efficiency ε can be easily deduced:

$$\varepsilon = q_u / q_s = \eta_{ex} \left(1 - \frac{T_0}{T_s}\right) \Big/ \left(1 - \frac{T_0}{T_u}\right) \qquad (4)$$

The main advantage of using exergy efficiencies rather than energy efficiencies to characterize the converters is that the former always lies between 0.3 and 0.5, depending on the complexity and the development of a technology, when the latter deeply depends on both technologies and operating temperatures.

3.2. Assumptions for systems under study

The systems under study are described in figure 3.

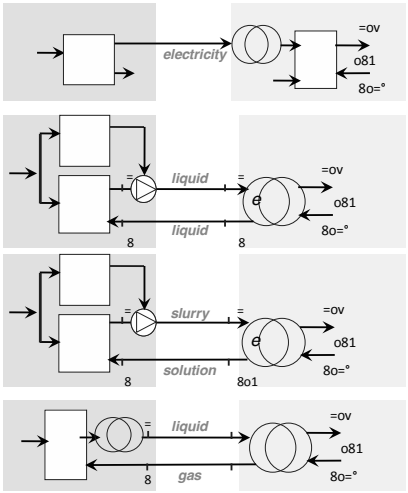

Fig. 3. Energy transportation systems under study. Transport of : a) electricity, b)coolant, c)slurry, d)reactive fluid.

They are all fired only by a heat source at T_S. If mechanical energy is required (for pump for example), it is produced by a converter using the same input thermal source. Two cases are investigated: T_s=100°C or 400°C .

All these systems provide the same cold utility on the user site. Thus, the user site operating conditions are fixed as: T_{u1}=8°C, T_{u2}=12°C, q_u=20 MW .

The following assumptions are required depending on the process:

- according to industrial standards [4], we assume that all the thermodynamic converters (motor, heat pump or thermochemical reactor converting heat to electricity, electricity to heat or cold, or heat to cold) have the same exergy yield : $\eta_{el} = \eta_{ch} = 0.4$

- the heat exchangers effectiveness is e=0.8 [5], and their energy yield is ε=1 (no thermal losses);

- the reference temperature for the exergy analysis is $T_o = T_{ext}$= 35°C in summer.

- the energy efficiency of the transport of electricity by extra-high voltage transmission lines is η_{hv}=0.97 [6], and the efficiency of the conversion from extra-high to low voltage is $\eta_{hv/lv}$=0.9. In this case, the energy and exergy efficiencies are equal.

3.3. Methodology

It consists in evaluating the system from the user site, to the source site.

On the user site, the cold power and the operating temperature are known, thus the output exergy is:

$$ex_u = q_u \cdot \left(1 - \frac{T_o}{\tilde{T}_u}\right) = q_u \cdot |\tilde{\theta}_u| \qquad \tilde{T}_u = \frac{T_{u1} - T_{u2}}{Ln(T_{u1}/T_{u2})} \qquad (5)$$

According to the process, the exergy destruction due to the transport and the exergy yield on the source site are evaluated as follows:

Electricity network :

The electric power required at the source site outlet is:

$$W_{hv} = ex_u / (\eta_{hv} \eta_{hv/lv} \eta_{ch}) = ex_s \eta_{el} \qquad (6)$$

thus the inlet thermal power is :

$$q_s = q_u \cdot (|\tilde{\theta}_u| / \theta_s) (\eta_{el} \eta_{hv} \eta_{hv/lv} \eta_{ch}) \qquad (7)$$

and the overall exergy and energy yields are:

$$\eta = \eta_{el} \eta_{hv} \eta_{hv/lv} \eta_{ch} \qquad (8a)$$

$$\varepsilon = \eta \cdot (\theta_s / |\tilde{\theta}_u|) \qquad (8b)$$

Coolant network :

The temperatures of the coolant at the boundaries of the transport lines are calculated thanks to the expressions of :

-the effectiveness of user heat exchanger e=0.8,

- the thermal power supplied to the user q_u,

- the steady state heat balances of each line :

$$0 = q_i + m.(h_i - h_i') \qquad (9)$$

with the heat losses q_i on each line :

$$q_i = hS_i.(T_i - T_i') / Ln((T_i - T_O)/(T_i' - T_O)) \qquad (10)$$

and the enthalpy variations (assuming an incompressible liquid):

$$h_i - h_i' = c.(T_i - T_i') + v(p_i - p_i') \qquad (11)$$

For the transport lines, typical values of roughness (r=0.1mm) and liquid velocity (u=3m/s) are used to estimate the pressure drop during the transport (using Colebrook correlation). The pipe diameter is deduced from u and q_u, which gives the coolant flowrate. We fixed h= 5W/(m^2.K).

Thus, we can calculate the cold and mechanical powers provided by the source site:

$$q = m.c.(T_1 - T_2)$$
$$w = m.v.(p_1 - p_1' + p_2' - p_2) \qquad (12)$$

Two conversions are required on the source site: a heat/cold conversion by means of a sorption chiller

(to cool the coolant) and a heat/electricity conversion (to produce the power for the pumps). Both are supposed to have the same exergy yield: $\eta_{ch} = \eta_{el} = 0.4$

Thus, the input exergy is :

$$ex_S = \left| q \left(1 - \frac{T_0}{\tilde{T}} \right) + W \right| / \eta \qquad \tilde{T} = \frac{T_1 - T_2}{Ln(T_1/T_2)} \qquad (13)$$

and the overall exergy and energy yields are:

$$\eta = q_u \cdot |\tilde{\theta}_u| / ex_S \qquad (14a)$$

$$\varepsilon = \eta \cdot \theta_s / |\tilde{\theta}_u| \qquad (14b)$$

Slurry network :

On the source and user sites, the system is similar to the previous one. It only differs in the thermodynamic data of the transported fluid (a slurry). Among the very few slurries described in the literature, we have selected an ice/ethanol slurry which has been studied for cold production applications by several authors [7-10]. The alcohol mass ratio is w_a=10% that leads to a freezing temperature at -4°C. Due to technical limits with pumps and valvles, the ice mass ratio must be lower than w_i=40% [10]. Thus, for w_a=10% and w_i=0 to 40% , the temperature of the water-ice-ethanol slurry varies from -4 to -8°C [9]. The variations of the density, viscosity and enthalpy of the two-phase solution according to the ice mass ratio and temperature are calculated thanks to published data [7,9]. Then, an equivalent specific heat of the slurry is deduced from a linear regression of the enthalpy variation vs. T. Moreover, we assume that the slurry is fully melted at the outlet of the user site i.e. $x'_2 = 0$. Thus, the fluid that flows back to the source is a one-phase water/ethanol solution. For sake of simplicity, we also fixed the ice ratio at the inlet of the user site : $x'_2 = 0.2$.

With these data, we are able to calculate the thermal energy provided by the source and the mechanical power required for the transportation:

$$q = m \cdot \left[c_{solution} \cdot (T_2 - T_{freezing}) + c_{slurry} \cdot (T_{freezing} - T_1) \right]$$

$$W = m \cdot \left[\frac{1}{\rho_{slurry}} (p_1 - p'_1) + \frac{1}{\rho_{solution}} (p'_2 - p_2) \right] \qquad (15)$$

and the exergy and energy yields as previously.

Thermochemical process :

The solid/gas reactor and the condenser are located on the source site, and the evaporator on the user site to produce cold. Thus, the reactive fluid flows in liquid phase from the source to the user site, and then flows back in gas phase.

One advantage of this system lies in the possibility of using the pressure difference between the condenser and the evaporator to drive the liquid flow to the user site [11]. Therefore, we fixed the pressure drop $\Delta p = p_1 - p'_1$, which maximal value is the available pressure drop $\Delta p_{max} = p_{cond} - p_{evap}$. Then, the liquid velocity and pipe diameter can be deduced from Δp and q_u. The values of p_{cond} and p_{evap} are the saturated pressures at respectively T_{air}=35°C (summer ambient air, used as heat sink by the condenser) and T_{evap}=6.8°C (the required evaporator temperature, assuming the effectiveness of the evaporator e = $(T_{u2}-T_{u1})/(T_{u2}-T_{evap})$ = 0.8 as in previous section).

For the back flow gas line, the pressure is bounded by $p_{sat}(T_{evap})$ on the user site, and by the pressure of the synthesis reaction that occurs in the reactor on the source site : $p_{synthesis}=p_{eq}(T_{air})+ Dp_{eq}$. Dp_{eq} is the equilibrium drop required for the reaction (corresponding to the temperature drop DT_{eq}=10° usually used). So, for this line, we get $\Delta p_{max} = p_{evap} - p_{synthesis}$.

Heat losses are neglected as the fluid is supposed at the constant temperature of the soil (20°C) all along both pipes.

For sake of simplicity in this assessment, we consider the $BaCl_2/NH_3$ reactive pair, whose thermodynamic data are well known [12-14].

4. Results

Figure 4 compares the exergy yields vs. the transportation distance for these four energy transportation processes described in figure 3.

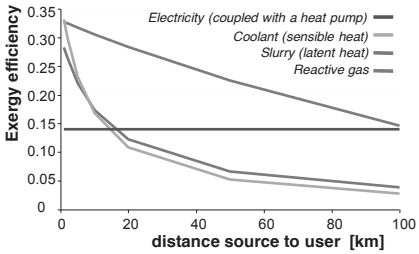

Fig. 4. Exergy yields for the four processes investigated for the transportation of energy

Thus, compared to electricity network, the transport of sensible or latent heat is relevant only for distances lower than about 10 km. On the other

hand, a thermochemical process is relevant for the wider range of distance. As the transportation of the reactive fluid is driven by the existing pressure difference between the condenser and the evaporator, this system can work without any additional exergy destruction due to the transport.

Complementary information is given by the analysis of the exergy destructions in each part of the energy transportation system. They are defined as follows :

- source site : $ex_S^d = q_S.\Theta_S - ex$ (16)
- transportation: $ex_{tr}^d = ex - ex'$ (17)
- user site : $ex_U^d = ex' - ex_U$ (18)

Then, the number of exergy destruction N is defined as the ratio of the destroyed exergy to the inlet exergy ex_S. As the exergy efficiency of the converters on the source site is fixed (η=0.4), this part of the exergy destruction is the same for the three systems : N_S = 0.6. The number of exergy destruction resulting from the transport and the conversion on the user site are plotted figure 5.

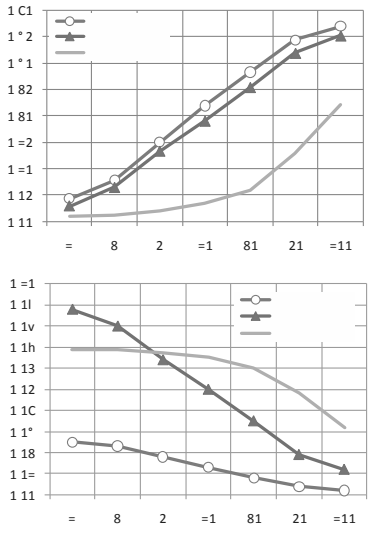

Fig. 5. Number of exergy destruction due to the transport and the conversion on the user site, for the 3 systems involving the transportation of a fluid.

It shows that the user site has a moderate effect, as it involves less than 10% of the exergy destruction for all the systems. The transportation has a more important effect, and it exhibits a significant difference between systems based on a coolant or slurry and on a reactive fluid.

For example, for 20 km, the part of exergy destruction related to the transport is 5.9% for thermochemical systems, and more than 25% for the two others systems. Moreover, as the inlet exergy ex_S is also lower for thermochemical systems (as highlighted by the higher exergy yield, figure 4), the resulting exergy destruction due to the transportation ex_{tr}^d is much more lower for thermochemical systems.

The last comparison deals with the flowing conditions for the 3 processes involving liquid or gas flows, which are summarized as follows:

	flow to user	flow to source
coolant	u_{liq}=3m/s, d=0.61m	
slurry	u_{liq}=3m/s, d=0.35m	
reactive fluid	u_{liq}=0.5m/s d=0.27m	u_{gas}=2.5m/s d=0.12m

Thus, the thermochemical process presents a significant advantage regarding the civil engineering required for the network.

Moreover, for such systems, the velocities of the reactive fluid and the pipe diameters are calculated by fixing the pressure drop at its maximal available value Δp_{max} (see § 3.3) in the case of 100 km between the user and source. Then, the same values (u, d) are used for all the distances to compare them on the same basis. Thus, for lower distances, these flowing conditions are overestimated and the diameters could be smaller by applying $p_1 - p_1' = \Delta p_{max}$ at each distance.

Concerning the influence of the source temperature, 11 1 . . , as the exergy yield on the source site is fixed in all the cases ($\eta_{HP} = \eta_{el} = 0.4$), the overall exergy yield does not depend on the source temperature, while the energy yield does, according to equation 14b. Figure 5 is an example of these energy yields at different T_S , for the electricity network and for the coolant transportation system.

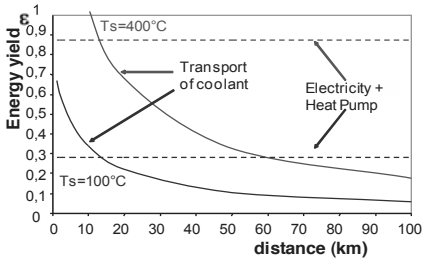

Fig. 6. Energy yields for processes based on electricity grid and coolant network, and two source temperature T_S.

Nomenclature

c specific heat, J/(kg K)

$\tilde{c}$ equivalent specific heat of the slurry, J/(kg K)

d pipe diameter, (m)

e heat exchangers effectiveness

ex exergy, W

v specific volume, m^2/kg

h heat transfer coefficient, $W/(m^2 K)$

h_i specific enthalpy

p pressure, Pa

q thermal power, W

m mass flow rate, kg/s

$N=ex^d/ex_S$ number of destruction of exergy

T temperature, °C

$\tilde{T}$ equivalent temperature $\tilde{T} = \frac{T_1 - T_2}{Ln(T_1/T_2)}$

x ice mass ratio in the slurry

w mechanical power, W

Greek symbols

exergy efficiency

ε energy efficiency

ρ density, kg/m^3

$\tilde{\theta}, \tilde{\theta}_u$ Carnot factor

Subscripts and superscripts

1 source to user line

2 user to source line

ch chiller

d destruction

el electrical

ev electrical

eq equilibrium

hv, lv extra -high voltage, low voltage lines

s source site

tr transport

$, u$ user site

References

[1] Liu, Q., et al., 2002, A review of study on thermal energy transport system, JSME Int.J. B, 45(3),pp.473-480.

[2] Spinner, B., et al., N., 2002, New sorption cycles for heat and/or cold production adapted for long distance heat transmission, *Mece'02 ASME Int. Mechanical engineering congress, New Orleans, november 17-22.*

[3] Spinner, B., et al., 2005, New cascades for thermo-chemical refrigeration, Int. journal of thermal sciences, 44(12), pp1110-1114.

[4] Favrat, D., 2008, The challenge of introducing an exergy indicator in a local law on energy., Energy,33, pp.130F136.

[5] Incropera, F.P.,et al., 2007, *Fundamentals of heat and mass transfer,* 6th ed.,Wiley, Chap.11.

[6] Website of the french company of electricity distribution : *www.erdfdistribution.fr*

[7] 1 . 1 .9 1 9 fluide frigoporteur diphasique 1 : Caractéristiques thermophysiques intrinsèques 9 1 . 1 9 1 9. 9.) 9. Refrigeration , 22, pp.164-174.

[8] Ionescu, C., Lallemand, A., 2007, Local and global heat transfer coefficients of a stabilised ice slurry in laminar and transitional flows, Int. J. of Refrigeration, 30 (6), pp. 970-977.

[9] Kousksou, T., et al., 2007, Equilibrium liquidus temperatures of binary mixtures from differential scanning calorimetry, Chemical Engineering Science, 62, pp.6516-6523.

[10] Marvillet C., Fluides frigoporteurs : , 1 9 1 1 9 9 1 F Traité Génie énergétique BE 9 572.

[11] Mazet, N., et al., 2009, Feasibility of long-distance transport of thermal energy using solid sorption processes, International Journal of Energy Research, DOI 10.1002/er.1578.

[12] Coolpack, *www.et.web.mek.dtu.dk*

[13] Fenghor, A., et al., 1995, The viscosity of Ammonia, Journal of Physical and Chemical Reference Data, 24, pp.1650-1667.

[14] Touzain, P., 1999, Thermodynamic values of ammonia salts reactions for chemical sorption heat pumps. *International Sorption Heat Pump Conference, Munich, Germany.*

Acknowledgments: This work is supported by the French research program 'ENERGIE' (project Valotherm) funded by the CNRS (Centre National de la Recherche Scientifique).

Integration of Heat pump in district heating and cooling systems

Maatouk Chantal[a], *Assaad Zoughaib*[a], *Denis Clodic*[a]

[a] *Mines ParisTech, Center for energy and Processes, Paris, France*

Abstract: Buildings of North-West of Paris are connected to a district heating and cooling network. Energy circulated by this network is 370 GWh for heating and 190 GWh for cooling. CO2 emissions associated to this network are estimated to 115,000 tons per year. Detailed analyses of heating and cooling capacities show that, even in winter 18MW cooling capacity is delivered and 10MW heating capacity in summer season. Heat is produced via fuel-fired boilers at temperature going up to 160°C. Cooling capacity at 4°C is generated by chillers.

Several schemes of heat pumps integration are studied. The Pinch analysis is used to determine the optimum point for the HP integration. Additional scenarios integrating economical and technical constraints are also studied:

- The first scenario consists in installing heat pumps as a second stage of chillers and is used to preheat water before entering boilers
- The second scenario consists in installing heat pumps directly in customers' buildings. The heat pumps produce simultaneously required heating and cooling capacities with different connection options to the network.

A technical and economical analysis is performed, and CO2 emission abatement is evaluated depending on those scenarios in the context of the French energy-mix.

Keywords: District heating, thermal integration, Heat Pump, techno-economical analysis.

1. Introduction

The growing threat of climate change has led to global agreements to reduce emissions of greenhouse gases (Kyoto Protocol). The increase of oil prices remains a persistent worry and today's energy challenges are truly critical. In this context, heat pumps appear to be an interesting solution to reduce energy consumption and gas emissions.

Offices buildings of north-west of Paris are characterized of having a simultaneous need for heating and cooling: apart from seasonal changes in consumption, a detailed analysis of heating and cooling capacity show that in winter part of the buildings are in need of refreshment, while in summer a minimum heat load is needed primarily for domestic hot water. Buildings are connected to a district heating and cooling (DHC) network.

Many examples of heat pump integration in district heating and cooling plants have been investigated in the literature, aiming to optimise the energy consumption of the heating system. A multi-criteria optimisation of district cogeneration plant integrating heat pumps has been performed [1]. The study shows high efficiency of heat pump for heating in the French mix context, and combined with cogeneration engine, gas turbine cogeneration systems. In Montpellier, five sites for production of heating and cooling where equipped with heat pumps, allowing the production of heating and cooling simultaneously [2]. This introduction has permitted an increase of the energy performance of the plant. In Japan, a study has been performed comparing the energy saving effects between centralised production of heating and cooling, and individual systems for each buildings [3]. The simulation results showed a 5% energy saving for heating in individual systems.

In this paper, several schemes of heat pumps integration are studied. The case of gas turbine cogeneration is presented as well in addition to the HP integration. Additional scenarios integrating technical constraints are also studied. A techno-economical analysis is performed, and CO2 emission abatement is evaluated depending on

those scenarios in the context of the French energy-mix.

2.Description of current status

The production of hot and chilled water vary widely depending on seasonal variations, with day and night cycles and with building occupancy, leading to very high fluctuations of heating and cooling needs. Figure 1 shows the hourly heating and cooling load over a one year period. The GHG emissions generated are also presented. The GHG emissions take into account direct emissions due to oil combustion and direct refrigerant leak, and indirect emissions due to electricity consumption.

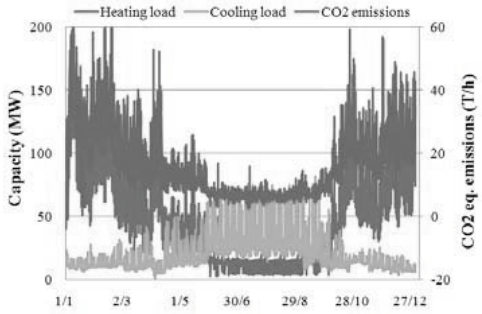

Fig.1: Heating, cooling load and GHG emissions of the district network

Heat energy is produced via fuel oil-fired boilers. A total installed heat capacity of 195 MW can be provided. The network heating load is controlled with the water outlet temperature. It varies between 90 and 180°C, depending on the heat demand. Return water temperature varies between 70 and 75°C. The cooling capacity is 108 MW, and is produced in chillers at 4°C. The chilled water returns at 10°C. Chillers condensers are cooled via forced draft cooling tower that releases the heat into the atmosphere.

The temperature at the condenser discharge is typically around 30 to 35 ° C, while the outlet temperature of the water heating network varies between 90 and 180 ° C. Exergy of the heat released at the chillers' condensers is not directly recoverable since the temperature level is not the same. The introduction of a heat pump (HP) is a mean to recover this heat. The heat rejected at the condensers of the chillers is then recovered at the evaporator of the HP permitting to produce the hot water. The remaining heat capacity will be offset by the boilers.

Based on this analysis it can be concluded that a potential of heat recovery exists. Indeed, the operation of cooling towers in winter seems paradoxical, since it corresponds to the waste heat of refrigeration units that must operate even when the outside temperature is 0 ° C. It seems of common sense to reuse that heat.

Considering the needs of simultaneous heating and cooling load, the installation of a heat pump appears as a key solution to recover the waste heat released at the chillers condensers. Three technical options are studied:

- Installation of cogeneration plant together with heat pumps, chillers and fuel oil boilers
- Installation of heat pumps as a second stage of chillers and used to preheat water before entering boilers. This scenario does not require additional investment cost, other than the price of the HPs and pipe connections to the network.
- Installation of heat pumps directly in customers' buildings. The heat pumps produce simultaneously required heating and cooling capacities with different connection options to the network.

Thus, the study of technical options permitting to reduce GHG emissions from the network must be based on an hourly analysis, in order to take into consideration these fluctuations.

3. Simulation model

3.1 Technical data of the heat cooling source system

Technical characteristics of the existing equipment of the DHC plant are taken as they are in the model.

Technical characteristics of an existing electrical driven heat pump type installed in a district heating plant, which achieves a high COP among the district heating plant in Gothenburg has been selected for the case study [4]. The COP is defined as the total amount of supplied heat,

divided by the total electricity consumption. An existing gas turbine installed in a district heating plant in Paris has been selected for the calculations of the cogeneration plant.

3.2 Model of the heat source system

The plant was modeled in the case of the DHC. The heat source system configuration and capacity of the existing boilers and chillers are set to the same values as those of the plant. The heat capacity of the GT is considered at the minimum heat demand of the network ie at 12 MW. The heat capacity of the HP is considered equal to the maximum amount of the heat that can be produced by recovering the waste heat from the chillers. The simulations parameters are derived from the measured data of the existing heat source system.

4. Cases studied

The system consists of a pipeline network for distributing the heat and the chilled water from the heating and cooling plant to the consumer. The essential element of such a system is the pipeline, which enables the transport of energy. Another important part of the system is the heat stations, where the heat is transferred from a high to a low temperature medium, resulting in decreased heat quality. The chilled water passes through a cooling station, where the temperature difference between the primary and secondary circuit remains low and exergy losses are negligible compared to those in the heat station.

The aim of these simulations is to present a thermo-economic study of different designs and operating conditions of district heating and cooling plant. The amount of the CO2 emissions rates, achievable with the different scenarios as well as the operating cost reduction is calculated, based on hourly analysis.

Table 1: Cost and GHG of energy used

	Electricity	Gas	Fuel oil
Price (€/MWh)	48	26	23
CO2 emissions (kg CO_2/MWh)	0.18	0.3	0.26

4.1 Scenario 1: Installation of cogeneration plant combined with heat pumps, chillers and fuel oil boilers

This scenario consists on installing a gas turbine cycle, a heat pump with heat recovery of the waste heat of the chillers in addition to the existing fuel oil boilers. In the actual plant, a significant source of exergy losses is associated with the current way of supplying heat, ie from direct fossil fuel combustion in boilers, which is characterized by a large temperature difference. In this scenario, the water temperature is decreased down to 65°C for the production of the domestic hot water and 40°C to supply the heat for space heating using air convector. 30% of heating energy is used for domestic hot water; the rest is used for space heating. We will consider two distinct water networks for the heat distribution, one for the domestic hot water distribution and the other for the water of the space heating.

In the simulations, the priority is to produce the heating and cooling load. The waste heat released from the chillers is then recovered in the heat pump, installed in the buildings, in order to produce the heat needed for space heating in priority. If heat provided by the chillers waste heat exceeds the demand for heating, then it is used for the domestic hot water. Part of the energy demand remaining is produced by the gas turbine with a limited capacity. In the latter, the heat is recovered from the exhaust gases for heating purposes and produces electricity. Finally, the rest of the heat demand is produced by the fossil fuel boilers. Figure 2 shows the layout of the heating and cooling plant.

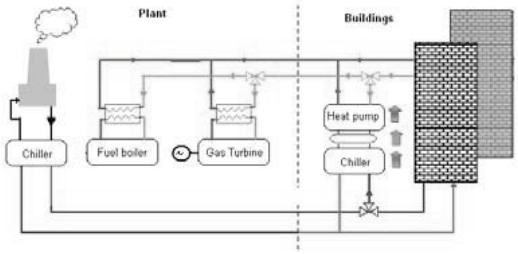

Fig. 2: Structure considered for the scenario 1

In the calculation, it will be taken into consideration the electrical energy consumed in

the accessories of the boiler, the gas turbine, the heat pumps and the chillers. The direct and indirect greenhouse gases emissions, caused by the combustion of fossil fuels, electricity consumption and refrigerant leakage are accounted for. The operating cost of the plant is calculated, based on the energy prices presented in table 1. In the case of electricity generation in the gas turbine, the CO2 avoided is deducted from the total CO2 emissions of the plant. The electricity produced is sent to the electrical network, with a purchased rate twice the selling price.

The realization of this scenario implies lots of modification of the DHC plant and of the network itself ie installation of supplementary pipelines in order to distribute the heat at low temperature levels. In addition, a gas turbine should be installed in the plant. All these modifications imply a lot of investment cost and time. At the moment, quick solutions with low investment costs are of great interest for the plant managers. In this context, other scenarios of HP integration only are studied, in order to take into consideration the technical constraints of the network and the plant.

4.2 Scenario 2: Installation of HP to preheat water before entering the boiler

In this scenario, the same DHC plant is considered. Only heat pumps are installed in the plant, in order to recover the waste heat from the chillers. The heat pumps are installed in series with the fuel oil boilers, where the return water is preheated up to 90°C. Then preheated water enters the boiler, where it is heated at the necessary temperature level. It should be highlighted, that in this case, heat demand is controlled by the temperature level of the supplied water, where the water flow rate circulating in the network is constant. Figure 3 show the plan of the DHC of scenario 2.

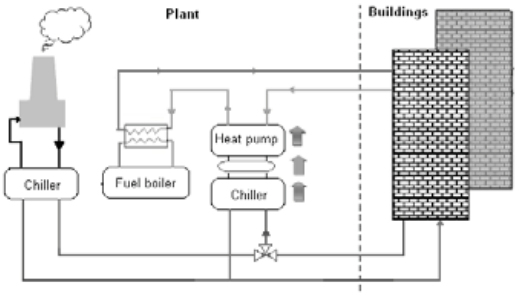

Fig. 4: Structure considered for the scenario 3

For the calculations, the inputs of the model are the heat and cooling demand. Then, the heat that can be provided by the heat pump is calculated. Two parameters are fixed in this case, the water flow rate of the hot water network, and the maximum hot water that can be produce by the HP. The rest of the heat demand is covered by the boiler. In this case study, the GHG emissions and the operating cost is also calculated.

4.3 Scenario 3: Installation of HP in the consumers' buildings at lower temperature levels

A heat station is present in every building, where a heat pump and a chiller can be installed. In this scenario, the chillers and heat pumps will be installed in the consumers' buildings. Heat pumps produce all the heat that can be provided by recovering the waste heat from the chillers. The heat produced in the heat pump is only limited by the heat demand of the buildings. The hot water is produced at 80°C and feed directly the building network.. The chilled water produced is injected in the cooling network (see Fig. 4)

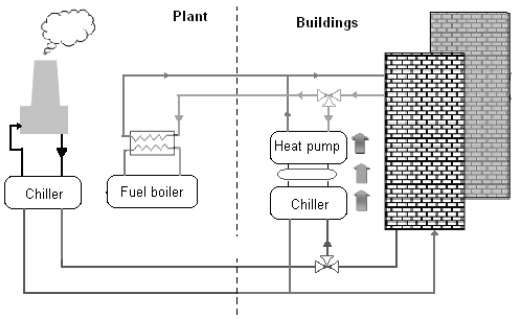

Fig. 4: Structure considered for the scenario 3

For the calculations, the inputs of the model are the heat and cooling demand. Then, the heat that can be provided by the heat pump is calculated. If the heat produced in the HP are greater than the heat demand, only part of the waste heat is recovered. The rest is discharged in the atmosphere via cooling towers. As for the scenario 2, if the heat capacity produced by the HP is not sufficient to cover all the needs, the rest is produced by the boiler.

5. Simulation results

A comparison between the simulation results and the measured data of the existing plant is performed. A comparison of the electrical power consumption, the GHG emissions and the operating cost of the plant presented in scenario 1 is compared with the data measured on the existing plant.

5.1 Source of heat producing systems

The repartitions of the heat source system used in the scenarios are presented in figures 4, 5 and 6.

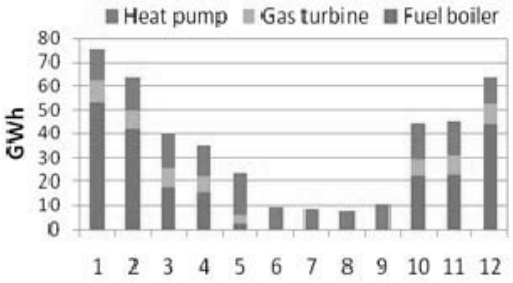

Fig. 4: Scenario 1

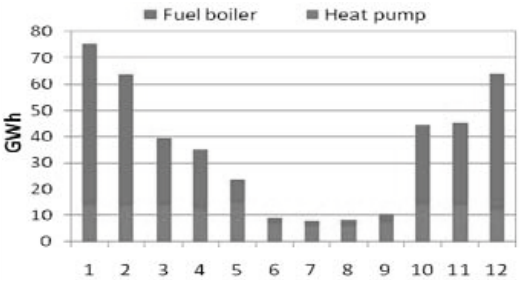

Fig. 5: Scenario 2

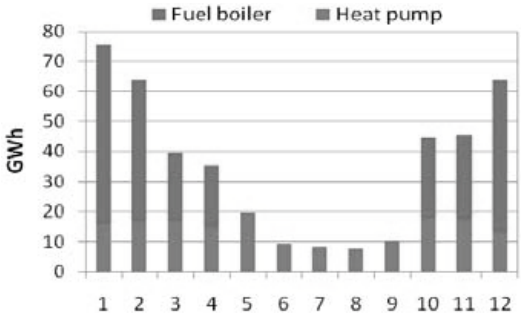

Fig. 6: Scenario 3

Scenario 1: The GT is employed as a base load for producing the heat demand and it generates at the same time electrical power that will be sold. As it can be seen, only 3 months a year, the boiler is needed. In summer period, the GT is sufficient to cover the needs.

Scenario 2: The heat pump provides the base heating capacity, and the rest is produced in the boilers. As it can be seen, even in summer period part of the heat load demand is produced in the boilers. Indeed, this is due to the limitation of the water temperature supplied by the HP and the limited water flow rate. Indeed, in summer where the waste heat available is very large, and where the potential of heat recovery is interesting, part of the heat is evacuated in the atmosphere.

Scenario 3: It can be seen that in summer season, there is no need for the boilers, to cover the heat load demand. Indeed, only part of the recovered waste heat from the chillers is sufficient to produce all the heat demand of the network.

5.2 GHG emissions

The sources of GHG emissions are of two types;

- direct emissions caused by the combustion of fossil fuels and refrigerant leakage from heat pumps and chillers;
- indirect emissions due to electricity consumption.

In the three scenarios studied, the emissions of CO2 and CO2 eq. are calculated. For the electricity generation in the gas turbine in scenario 1, the CO2 avoided by kWh of electricity produced is considered equal to the CO2 content of a kWh of electricity consumed. Figure 7 shows

the annual evolution of the CO2 emissions calculated for the three scenarios and compared with the existing case study. Table 2 shows that a reduction of 50% of CO_2 emissions is obtained in sc1, where the reduction is of 21% for sc2 and 40% for sc3. It can be noticed that the scenario 1 has the smallest impact on the environment, compared to the existing state.

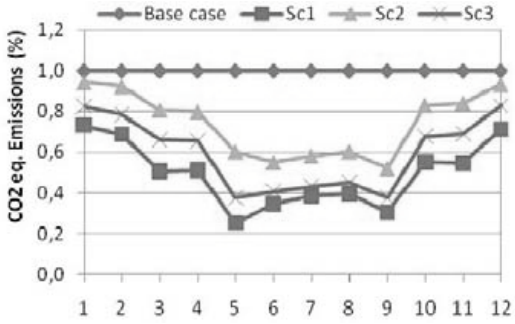

Fig. 7: Evolution of the CO2 emissions in the studied cases

Table 2: Comparison of the studied cases

	Base case	Sc1	Sc2	Sc3
CO_2 emissions ($kg\ CO_2/\ MWh_{th}$)	358	179	286	215
Operating cost (€/ MWh_{th})	36	22	30	27
Exergy Efficiency	0,13	0,41	0,27	0,33

5.3 Operating cost

Table 2 shows the operating cost reduction, compared to the existing case. It can be seen that the scenario 1 is the best. This is related to the price of the purchased electricity. The investment cost of the studied scenario is not taken into consideration. But it should be noticed that the investment cost associated to the scenario 1 will represent the highest cost, compared to the two other cases studied. However, the scenarios 2 and 3 respond to the EU directive that aims to reach 3x20%[1] in the industrial installations. Figure 8 shows the evolution of the operating cost reduction, compared to the existing case.

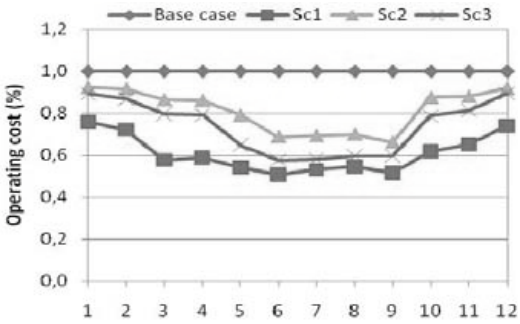

Fig. 8: Trend of the operating cost reduction.

5.4 Exergy losses

The exergy consumed and produced in the heat source systems is calculated separately. The exergy efficiency (see table 2) of each scenario is defined as the sum of the produced exergy divided by the sum of the consumed exergy [5]. In scenario 1, and due to the generation of electricity in the GT, and because of the diminution of the temperature levels in the HP, the efficiency of the system remains high compared to the other scenarios. However, if we compare scenario 2 and 3, we can see that it is more interesting to install HPs in the consumers' side. Indeed, the water temperature level is lower which induces less exergy losses in the heat exchangers.

Conclusion

Three scenarios of improvement of a heating and cooling plant supplying the north west of Paris buildings have been performed. In all scenarios, the integration of the heat pump was the main target, aiming to recover the waste heat of the chillers. In scenario 1, additional integration of a cogeneration GT system has been studied. The results obtained showed that the combination of HP and cogeneration in GT presents the optimal solution that reduces fuel consumption and divide the GHG emissions by 2. This solution must be coupled with radical changes of the network and operating temperature levels. The investment cost induced by these changes requires a motivation of the network managers and owners of buildings,

[1] EU directive that aims to introduce 20% of renewable energy, to reduce the GHG emissions by 20% and to reduce the operating cost of the installation of 20%

which is not always easy to achieve. However, the scenarios 2 and 3 show a GHG emissions and operating cost reduction as well. When high fuel oil and natural gas prices encountered, in the French energy mix context, the integration of HPs represent a promising option in the future, both economically and environmentally.

Nomenclature

HP Heat pump
GT Gas turbine
DHC District heating and cooling
COP Coefficient of performance
GHG Greenhouse gas

References

[1] Burer, M. et al., 2003. Multi-criteria optimisation of a district cogeneration plant integrating a solid oxide fuel cell-gas turbine combined cycle, heat pumps and chillers. *Energy,* 28, pp. 497-518.

[2] La Centrale Thermofrigorifique de l'Hôtel de Ville, Montpellier. www.serm-montpellier.fr.

[3] Nagota, N., et al., 2007. Verification of the energy-saving effect of the district heating and cooling system_ Simulation of an electric-driven heat pump system. *Energy and Buildings*, 40, pp 732-741.

[4] Karin E., 2009. Göteborg Energi's district energy system. *Application for Global District Energy Climate Awards. Copenhagen energy summit.*

[5] Lallemand, A., 2007. Energie, exergie, économie thermo-économie. *Journées internationales de Thermique, Albi*, 28-30 août.

Energy management for the "Perpignan Méditerranée" agglomeration community

Van Giang Tran[a], Stéphane Grieu[a], Monique Polit[a] and Quoc Tuan Tran[b]

[a]*ELIAUS Laboratory, University of Perpignan Via Domitia, Perpignan, France*

[b]*IDEA, Grenoble Electrical Engineering Laboratory, Grenoble Institute of Technology, Grenoble, France*

Abstract: This paper presents a tool for managing a system of multi-sources with a reduced cost and a low CO_2 emission and to facilitate to integrate renewable energy. Two scenarios for the hybrid PV-wind system in "Perpignan Méditerranée" with four strategies of back-up electricity power are studied. The objective is dial to a technical – economical and environmental analysis with satisfying the electricity demand.

Keywords: Energy management, renewable energy, back-up power, virtual power plant.

1. Introduction

Nowadays in France, the nuclear energy includes the 78.3% of electricity generation, far above the EU-27 average (31%). In 2004, the 59 installed nuclear power plants produced more than 115 Mtoe of nuclear energy, about 43% higher than in 1990. The share of renewable sources, mainly hydro generation, in electricity slightly is around 10%. Electricity generation in France increased by 36% over the 1990-2004 period [1]. In the energy policy, two major objectives are promoting both energy savings and renewable energy. Mankind's traditional uses of wind, water, and solar energy are widespread in some countries, but the mass production of electricity using renewable energy sources, allowing reducing gas emissions, has become more commonplace recently, reflecting the major threats of climate change and fossil fuels exhaustion.

The present work takes place in a global development of robust and reliable tools for managing energy sources, reducing energy consumption and promoting renewable energy.

This paper starts by showing the forecasting data of hourly electric load, solar irradiance and wind speed for one day ahead. The electricity price on the PowerNext market [2] is used for two days from June 27th-28th, 2006. Let us note that June 28, 2006 was a typical day about energy consumption, that is why the present paper focuses on managing energy sources for the "Perpignan Méditerranée" agglomeration community on this day. The mathematical model of the components, followed by the description of the objective functions, the basic concepts and the collection of data for the model parameters. Finally, the results of four strategies to satisfy the electricity demand are shown.

The proposed tool is dedicated to the management of the existing and future energy production systems of the "Perpignan Méditerranée" agglomeration community. The city of Perpignan is located in southern France, near the border with Spain, and enjoys a typical Mediterranean climate. The agglomeration community is about 250000 inhabitants.

2. Database

Perpignan's hourly average wind speed, solar irradiance and electric load during years 1997 to 2006 allowed developing forecasting tools, based on artificial neural networks and wavelet-based multi-resolution analysis [3,4,5]. Data used for the present study were provided by the just-mentioned tools. Electricity price given by PowerNext for June 27 and June 28, 2006 were used. Both electricity price and forecasted data are shown in tables A1 and A2 (Apendix), respectively.

3. Scenarios & strategies

We propose two scenarios: an actual scenario and a future scenario (Table 1). The only difference between the two scenarios deals with the sizing of the considered energy production systems. The nominal powers of wind turbines are 7.4 MW and 127 MW respectively. 5400 m^2 and 120ha of PV solar panels are installed, respectively. The "Grenelle 2015" [6] plans the construction of about 120 MW of wind turbines and more than

100ha of PV solar panels for the "Perpignan Méditerranée" agglomeration community.

Table 1. Scenarios about wind/PV installations.

Scenario	*Actual*		*Future*	
	Wind turbine	*PV*	*Wind turbine*	*PV*
P_{ins} (S_{ins})	7.4×10^3 *kW*	5.4×10^3 m^2	1.27×10^5 *kW*	1.2×10^5 m^2
η_g	*21%*	*14.1%*	*21%*	*14.1%*
η_c	*95%*	*95%*	*95%*	*95%*

where P_{ins} is the total power (kW) for wind turbines, S_{ins} is the total area of PV solar panels, η_g is the efficiency of the generator and η_c the efficiency of the inverter. Let us note that 80% and 40% of the daily energy consumed is provided by nuclear plants for the actual and future scenarios respectively. Four strategies are proposed:

- *Strategy 1:* buying energy tomorrow, to meet tomorrow's back-up requirements, according to the hourly price given by PowerNext Spot Auction,
- *Strategy 2:* using diesel generators tomorrow to meet tomorrow's back-up requirements,
- *Strategy 3:* buying energy today at the lowest price, according to the hourly price given by PowerNext Spot Auction, to meet tomorrow's back-up requirements and stocking energy in battery tanks,
- *Strategy 4:* buying energy today at the lowest price, according to the hourly price given by PowerNext Spot Auction, to meet tomorrow's back-up requirements, electrolyzing and stocking H_2, using H_2 fuel cells.

4. Mathematical models

4.1 Wind turbines

The energy production of a wind generator is expressed in terms of wind speed. These are many mathematical models used in wind power studies. The average power produced by a wind generator given in [7], as:

$$Pw = \int_{V_{in}}^{V_{out}} P(v) f(v) dv \quad (1)$$

with: V_{in} the wind speed when the electricity production starts [m/s], V_{out} the wind speed when the electricity production ends [m/s], P(v) the wind generator's power curve (given by the manufacturer) and f(v) the weibull probability density function.

In this paper, a Nordex wind generator is used. Many wind generators of this type are installed at the city of Rivesaltes, about 10 km from Perpignan. The characteristics of those generators (power production according to wind speed) are supplied by the manufacturer, considering wind generator of type N60/1300 (Nordex) [8]. So, the average power [W] produced by a wind generator is:

$$P_w = \begin{cases} (A) 0.0538v^4 - 3.5973v^3 + 73.4533v^2 \\ -443.4775v + 853.5148, if\ 4 \le v \le 17 \\ (B) 0, if\ v < 4 \\ (C) 0.2031v^4 - 17.4593v^3 + 560.2264v^2 \\ -7956.5v + 43533, if\ 17 < v \le 25 \\ (D) 0, if\ v > 25 \end{cases} \quad (2)$$

where v is the average wind speed [m/s].

4.2 PV generators

The PV modules which are composed of many solar cells are integrated to form solar array. The hourly energy generated (E_{pv}, kWh) from the PV system is calculated using the equation [9]:

$$E_{pv} = S \eta_m P_f \eta_{pc} I \quad (3)$$

with: S is the array area in m^2, η_m is the module conversion efficiency ($\eta_m = 0.141$), Pf is the packing factor ($Pf = 0.9$), η_{pc} is the power conditioning efficiency ($\eta_{pc} = 0.95$) and I is the hourly irradiance (kWh/m^2). The PV modules NU185E1 (Sharp) are used for this calculation. The details related to this module parameters are provided in [10].

4.3. Hydrogen production & storage

Depending mainly on the production capability of the plant and of the country where the alkaline electrolysis is implemented, the estimation of the cost of the hydrogen produced will vary between 1.6 €/kgH_2 and 5 €/kgH_2 [11]. A study carried out by the French CEA (Commissariat à l'Energie Atomique) deals with the cost of producing hydrogen by alkaline electrolysis in four countries (Iceland, France, Norway and USA). So, the production cost of 1 kg of hydrogen (including compression and storage) is [11]:

$$C_{H2} = 0.3H^{-0.23} + 0.37H^{-0.025} + 52.2C_P \quad (4)$$

where C_{H2} is the average hydrogen generation cost [€/kg.H_2], H is the production capacity of the plant [kg/s] and C_P is the electricity price [€/kWh]. The first part of the equation is maintenance cost, second part is capital cost and the last is electricity cost. The equation is valid for a production rate between 0.1 kgH_2/s and 1.2kgH_2/s. For the present

study, we use equation (4) for the actual scenario. The cost of hydrogen production will be reduced in the future, so the cost for producing 1kg of hydrogen for the future scenario is $0.4xC_{H2}$. Let us note that one way to produce hydrogen without CO_2 emissions is to electrolyze water. Indeed, if the electricity source used to power the electrolyzer does not generate CO_2, then the entire cycle of energy production and consumption can be free of greenhouse gas generation.

4.4. Hydrogen fuel cells

Acquisition, Operation and Maintenance (O&M) costs of fuel cells depend on the technology used, the manufacturer, and functioning conditions. According to [12], for the different technological types of stationary fuel cell, acquisition costs vary between 1300 and 1500 $/kW, and fixed O&M costs can be from 8 to 30 $/kW/year, while variable O&M costs are between 1.4 and 2.5 $/MWh. Taking into account about 1000 h/year of working at full capacity, O&M costs for each electrical power kWh would be between 0.0094 and 0.0325 $/kWh. Useful lifetime for stationary units is about 40.000 h.

For this study, the capital cost of fuel cell is so 1300€/kW for the actual scenario and 350€/kW for the future scenario [12]. The O&M cost is 0.012 €/kWh, lifetime station units is about 40.000 h while the maximum efficiency rate is 0.45 for both scenarios. The hydrogen consumed by fuel cells, F_{H2} (kg/h), is modeled as dependent on the output power [13]:

$$if\ P/P_{N\_FC} \le P_{max\_ef}: \quad F_{H_2} = B_{FC} \cdot P_{N\_FC} + A_{FC} \cdot P_{FC} \tag{5}$$

$$if\ P/P_{N\_FC} > P_{max\_ef}: \quad F_{H_2} = B_{FC} \cdot P_{N\_FC} + A_{FC} \cdot P_{FC} \cdot \left(1 + F_{ef}\left(\frac{P}{P_{N\_FC}} - P_{\max\_ef}\right)\right) \tag{6}$$

where P_{FC} is the output power of the fuel cell (kW), P_{N_FC} (kW) is the nominal output power of the fuel cell, A_{FC} and B_{FC} are the coefficients of the consumption curve (kg/kWh), P_{max_ef} (% of P_{N_FC}) is the fuel cell output power that has the maximum efficiency and F_{ef} is the fuel cell consumption factor to consider the high consumption above P_{max_ef}. The efficiency of the Low Heating Value of hydrogen LHV_{H2} is calculated using equation 7:

$$\eta_{FC\%} = \frac{100P}{F_{H2}LHV_{H2}} \tag{7}$$

where LHV_{H2} = 33.3 kWh/kg, A_{FC} = 0.05 kg/kWh, B_{FC} = 0.004 kg/kWh, P_{max_ef} = 0.2 and F_{ef} = 1.

4.5. Diesel generators

The use of diesel generator is common in many hybrid combinations to ensure supply continuity. For an interval, the rate of fuel (F), consumed by the diesel generator delivering a power (P), is expressed as follows [14]:

$$F = a.P^2 + b.P + c \tag{8}$$

where a, b, c are the coefficients of the diesel generator, obtained from the manufacturers' data. The considered values are: a = 12.202×10^{-6} l/kWh, b = 0.223 l/kWh, c = 40.706 l/kWh.

The heavy fuel oil price is 0.11€/l (150$US/ton [15]) for the actual scenario and 0.20€/l for the future scenario. CO_2 emissions are 3.09 $kgCO_2$/l. The capital cost of a diesel generator is 300€/kW while O&M cost is 0.0025 €/kWh. The running hour is about 7000 hours per years and lifecycles are 20 years for both scenarios.

4.6. Battery bank

The simple battery model used for the hybrid model is expressed by [16]. In this model, the hourly state, at hour t, of a battery unit is depicted as a function of its precedent state, at hour (t-1), of the charge and of the renewable energy produced at hour (t). In case of batteries charge, the state can be calculated as follows:

$$E_{bat}(t) = E_{bat}(t-1) + \left(E_G(t) - \frac{E_L(t)}{\eta_r}\right)\eta_{bat,ch} \tag{9}$$

In case of batteries discharge, the state can be calculated as follows:

$$E_{bat}(t) = E_{bat}(t-1) + \left(\frac{E_L(t)}{\eta_r} - E_G(t)\right)\eta_{bat,dch} \tag{10}$$

where η_r is efficiency of rectifier (0.90), $\eta_{bat,ch}$ is the charge efficiency of batteries (0.80), $\eta_{bat,dch}$ is the discharge efficiency of batteries (0.85), $E_L(t)$ is the demand energy of charge (consumption) at an hour t, $E_{bat}(t)$ and $E_{bat}(t-1)$ are the energy storage in the bank of batteries at an hour t and at an hour t-1, respectively, $E_G(t)$ is the total energy supply at hour t. The self-discharge factor of battery is equal 0. In case of dimension, the capacitor of battery bank is equal to $1.2xE_{max\_bat}$, where E_{max_bat} is the maximum of E_{bat}.

A lead-acid battery power plant has currently the lowest battery cost at around $150/kWh because it has been the longest and most fully developed battery technology. The battery cost is projected to

reduce to $100/kWh in the future [17]. In this study, the capital cost of battery is 100€/kWh for the actual scenario and 60€/kWh for the future scenario. The O&M cost is 0.0012 €/kWh. Lifecycle of a battery is about 20 years or 8000 cycles of charge/discharge for both scenarios.

4.7 Inverters & Rectifiers

The inverter cost is 250€/kW nominal power (commercial data). The lifespan is 10 years; the efficiency depends on the output power. O&M cost is included in each system.

There is no inverter added for both strategies 1 and 2 but there is one for strategies 3 and 4. The efficiency depends on the output power:

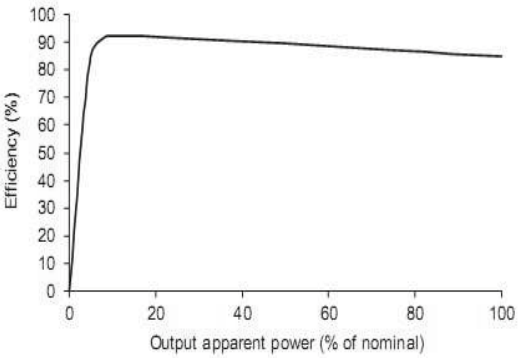

Fig. 1. Inverter efficiency curve.

The rectifier is selected for strategies 3 and 4. For strategies 1 and 2, there is no rectifier added. The cost of the rectifiers is 120€/kW, the lifetime is 10 years, and the efficiency is 0.9. O&M cost is included in the system. For the actual scenario, the price of inverter and rectifier are as just-mentioned. For the future scenario, prices are half.

5. Results and discussion

5.1. Actual scenario

Fig. 2 shows the hourly electric load and supply during the next day (24h). Power is supplied by three energy sources: nuclear energy (80% of the daily load), wind energy and PV solar energy. In this scenario, the supplied power does not satisfy the load. Fig. 3 shows both hourly excess and unmet powers during June 28, 2006. Excess power will be sold on the PowerNext market.

Table 2 shows, considering the four previously-defined strategies, the total cost for back-up power and CO_2 emissions for June 28, 2006. Considering the actual scenario, applying the first strategy leads to the lowest energy cost and there are no CO_2 emissions (let us note that CO_2 emissions are only related to both the backup and production systems of the "Perpignan Méditerranée" agglomeration community; when electricity is bought, no emissions are considered). In the other hand, applying the second strategy leads to very high CO_2 emissions while applying the third strategy leads to the biggest energy cost.

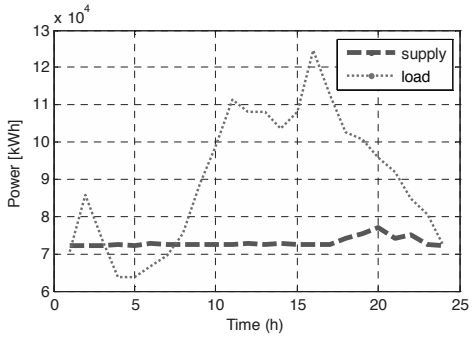

Fig. 2. Hourly electric load and supply in the next day.

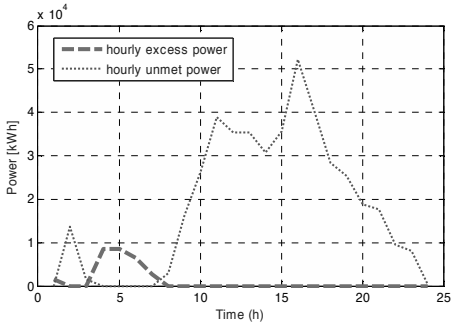

Fig. 3. Hourly overall and unmet power in the next day.

Table. 2. Costs & CO_2 emissions (actual scenario).

Strategy	*Cost (€)*	*CO_2 (kg)*
Strategy 1	*23302.86*	*0*
Strategy 2	*31616.44*	*1.35×10^6*
Strategy 3	*64026.79*	*0*
Strategy 4	*37525.95*	*0*

5.2. Future scenario

Fig. 4. shows the hourly electric load and supply during the next day (24h). Considering this scenario, the supplied power is higher than it was for the actual scenario, due to a higher both number of wind turbines and PV area, even if the nuclear power is decreased (only 40% of the daily energy consumed is provided by nuclear plants for this scenario).

Fig. 5 shows both hourly excess and unmet powers during June 28, 2006. Excess power will be sold on the PowerNext market. Table 3 shows,

considering the four previously-defined strategies, the total cost for back-up power and CO_2 emissions for the just-mentioned day.

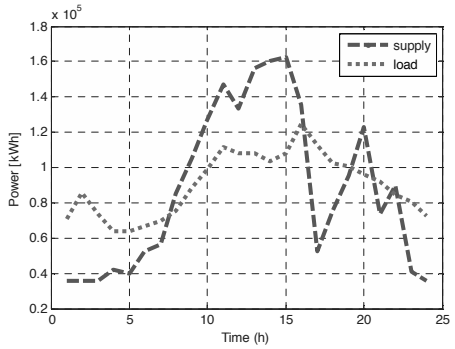

Fig. 4. Hourly electric load and supply in the next day.

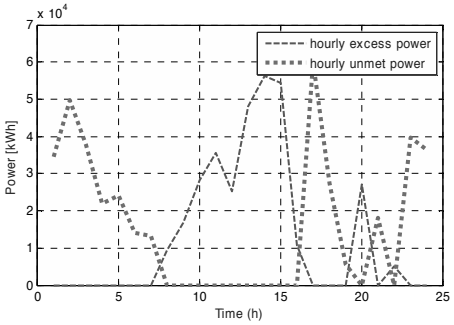

Fig. 5. Hourly overall and unmet power in the next day.

Table. 3. Costs & CO_2 emissions (future scenario).

Strategy	*Cost (€)*	*CO_2 (kg)*
Strategy 1	*13097.86*	*0*
Strategy 2	*53362.18*	*1.18×10^6*
Strategy 3	*32571.43*	*0*
Strategy 4	*11413.04*	*0*

Considering the future scenario, applying the fourth strategy leads to the lowest energy cost, because of a reduction of the capital cost of fuel cells and of hydrogen production, and there are no CO_2 emissions. In the other hand, applying the second strategy leads to both the biggest energy cost and very high CO_2 emissions because of fossil energy cost will increase in the future. Considering both actual future scenarios, the total electricity sold is about 449 €and 18.0 M€respectively.

6. Conclusion

The present paper deals with several strategies to manage energy resources as well as production and backup systems in a Mediterranean area (the "Perpignan Méditerranée" agglomeration community, south of France). These strategies mainly focus on energy cost and CO_2 emissions. The main conclusion of the work is that, thanks to a good energy strategy, one can implement and manage efficiently renewable energy production and backup systems. As a consequence, one can meet energy demand and limit CO_2 emissions while producing a not too expensive energy. Complementary work deals with the combination of the proposed strategies and the sizing of both the production and backup systems, with the aim of optimizing the energy management. That is why a virtual power plant, including forecast modules about meteorological parameters and electric load, is currently under development.

References

[1] France – Energy Mix Fact Sheet. http://ec.europa.eu/energy/energy_policy/facts_en.htm

[2] Powernext. http://www.powernext.com.

[3] Tran, V.G., et al., 2009, Forecasting of wind speed using Wavelets analysis and Cascade-correlation neural networks. The European Wind Energy Conference and Exhibition (EWEC2009), Marseille, France.

[4] Tran, V.G., et al., 2008, Wavelet decomposition and BJ methodology or neural networks for short-term electric consumption forecast, International Conference on Renewable Energy and Eco-Design in Electrical Engineering (iREED2008), Montpellier, France.

[5] Grieu, S., Tran, V.G., Polit, M., Tran, Q.T., 2009, Transformée en ondelettes discrète et réseaux de neurones artificiels pour la prédiction d'irradiation solaire à court terme. Energies renouvelables et éco-conception en génie électrique, Revue de l'Electricité et de l'Electronique (REE), France.

[6] http://www.grenelle2015.fr/

[7] Saheb-Koussa, D., Haddadi, M., Belhamel, M., 2009, Economic and technical study of a hybrid system (wind–photovoltaic–diesel) for rural electrification in Algeria. Applied Energy 86, pp. 1024-1030.

[8] Nordex. http://www.nordex-online.com/fileadmin/MEDIA/Produktinfos/EN/Nordex_N60_F.pdf.

[9] Elhadidy, M.A., Shaahid, S.M., 2003, Promoting applications of hybrid (wind -

photovoltaic- diesel -battery) power systems in hot regions. Dhahran 31261, Saudi Arabia. Renewable Energy 29, pp.517–528.

[10] Sharp France. http://www.sharp.fr/produits/modules_photovoltaiques/nu180e1.html.

[11] Sigurvinsson, J., Werkoff, F., 2005, On the cost of the hydrogen produced by alkaline electrolysis, Proceedings of the international Hydrogen Energy Congres and Exhibition IHEC, Istanbul, Turkey.

[12] Brown, D.R., Jones, R., 1999. An Overview of Stationary Fuel Cell Technology. Pacific Northwest National Laboratory, Richland (WA), USA.

Dufo-Lopez R., Bernal-Agustın J. L., 2008, Multi-objective design of PV-wind-diesel-hydrogen-battery systems. Renewable Energy 33, pp.2559– 2572.

[13] Ashok, S, 2007, Optimised model for community-based hybrid energy system, India. Renewable Energy 32, pp.1155–1164.

[14] Wärtsilä 20 Powerskid, www.wartsila.com/wartsila20

[15] Kaabeche, A., et al., 2006, Optimisation d'un système hybride (éolien – photovoltaïque) totalement autonome. Revue des Energies Renouvelables Vol. 9 N°3, pp.199 – 209.

[16] Sedighizadeh, M., Rezazadeh, A., 2007, Comparison between Batteries and Fuel Cells for Photovoltaic System Backup. Word Academy of Science, Engineering and Technology 36.

Appendix

Table. A1. Hourly electricity price for June 27 and 28, 2006 on PowerNext EpexSpot auction [€/MWh] (France)

Date	Hour1	Hour2	Hour3	Hour4	Hour5	Hour6	Hour7	Hour8	Hour9	Hour10	Hour11	Hour12
28/06/2006	34,00	31,00	27,00	22,00	9,00	29,00	31,00	48,99	51,00	67,91	71,00	79,19
27/06/2006	32,00	27,99	22,01	10,00	10,00	23,10	31,31	42,00	49,74	53,01	60,99	66,58

Date	Hour13	Hour14	Hour15	Hour16	Hour17	Hour18	Hour19	Hour20	Hour21	Hour22	Hour23	Hour24
28/06/2006	74,00	74,00	73,00	70,00	61,00	55,00	54,00	49,00	48,99	46,99	50,01	41,18
27/06/2006	58,00	61,00	59,99	53,78	53,00	48,00	47,99	41,07	41,65	40,39	44,01	36,21

Table. A2. Hourly meteorological parameters and electric load forecasting for June 28, 2006 (Perpignan)

hour	Electric load (MWh)			Solar irradiance (J/cm^2)			Wind speed (m/s)		
	actual	forecast	ab.error	actual	forecast	ab.error	actual	forecast	ab.error
1	71,00	70,60	0,40	0,00	0,00	0,00	2,00	1,95	0,05
2	85,00	85,68	0,68	0,00	0,00	0,00	2,00	1,82	0,18
3	73,00	73,62	0,62	0,00	0,00	0,00	3,00	2,99	0,01
4	64,00	63,85	0,15	0,00	0,00	0,00	5,00	5,05	0,05
5	63,00	63,70	0,70	0,00	0,00	0,00	4,00	4,04	0,04
6	66,00	66,55	0,55	5,00	5,20	0,20	6,00	6,18	0,18
7	69,00	69,62	0,62	41,00	41,19	0,19	4,00	4,02	0,02
8	76,00	75,50	0,50	107,00	106,04	0,96	5,00	5,16	0,16
9	87,00	88,52	1,52	171,00	172,28	1,28	4,00	3,84	0,16
10	97,00	98,80	1,80	230,00	226,66	3,34	3,00	3,12	0,12
11	103,00	111,48	8,48	277,00	276,11	0,89	2,00	2,02	0,02
12	107,00	108,04	1,04	232,00	232,60	0,60	4,00	4,12	0,12
13	109,00	108,04	0,96	299,00	299,03	0,03	4,00	3,89	0,11
14	107,00	103,70	3,30	297,00	294,54	2,46	5,00	5,03	0,03
15	107,00	108,15	1,15	313,00	315,02	2,02	3,00	3,11	0,11
16	123,00	124,77	1,77	250,00	247,75	2,25	3,00	3,03	0,03
17	112,00	112,57	0,57	30,00	31,92	1,92	4,00	4,04	0,04
18	103,00	102,50	0,50	7,00	5,95	1,05	8,00	7,93	0,07
19	100,00	100,60	0,60	5,00	5,01	0,01	9,00	9,26	0,26
20	96,00	95,80	0,20	3,00	2,57	0,43	11,00	11,10	0,10
21	89,00	91,81	2,81	1,00	1,02	0,02	8,00	7,98	0,02
22	84,00	84,70	0,70	0,00	0,00	0,00	9,00	9,04	0,04
23	81,00	80,44	0,56	0,00	0,00	0,00	5,00	4,80	0,20
24	72,00	72,30	0,30	0,00	0,00	0,00	2,00	2,04	0,04

Nota: "ab.error" is the absolute error.

Energy Analysis of a Coupled ORC-Compression Refrigeration Cycle

Maneesh Dubey[a], Archana Nema[a], R.D. Misra[b] and PK Nag[c]

[a] *Department of Mechanical Engineering, MANIT, Bhopal-462051, India.*
[b] *Department of Mechanical Engineering, NIT Silchar-788010, India.s*
[c] *Ex Professor, Department of Mechanical Engineering, IIT Kharagpur, India.*

Abstract: This paper presents the energy analysis of a coupled power-refrigeration cycle which eliminates the requirement of electrical power for driving the compressor of the vapour compression refrigeration cycle. The coupled cycle which uses pentafluropropane R-245ca as the working fluid in topping power loop and bottoming refrigeration loop have been assessed with different combinations such as cycle with recuperator, reheater and economizer with a view to augment its performance. At the condenser temperature range of 30-42°C and recuperator effectiveness range of 0.7-0.9, the overall COP of the coupled cycle with the introduction of the recuperator, increased by 19.5-50.7% and in the cycle with recuperator, reheater and economizer, it increased by 41.6-59.3%. Overall COP at a constant turbine inlet temperature remains almost invariant with boiler pressure in the condenser temperature range of 30-42 °C for a coupled power-refrigeration base cycle and cycle with recuperator, reheater and economizer. Significant decrease in overall COP is observed for boiler pressure greater than 5 MPa at constant turbine inlet temperature and recuperator effectiveness for the coupled cycle with recuperator.

Keywords: Coupled Power-Refrigeration Cycle, Organic Rankine Cycle, Overall COP, R-245ca.

1. Introduction

In a tropical country like India, cooling the living environment is much more desirable and a great need for multifarious activities such as food preservation and cold chain for life saving medicines as against heating which is very common in colder nations. It is more difficult to produce and maintain a temperature in the system lower than that of the surroundings than maintaining it at higher temperatures by simply heating. The environmental issues of ozone depletion and global warming have forced the refrigeration based industries to direct the research trend in search of alternative refrigerants and alternative technologies [1]. Absorption systems are in principle a good option for the direct conversion of low grade heat into cold with COP in the range of 0.6-1.0. However, absorption systems are recommended for larger capacity systems as against smaller ones due to poorer performance.

Refrigeration and air conditioning today represent about 10% of the total energy demand and hence a small change will have a sizeable global impact [1]. The enactment of Montreal and Kyoto Protocols emphasized the need of using renewable energies like solar, wind, biomass and geothermal heat as well as recovery of industrial waste heat to generate electricity [2-4]. The organic Rankine cycle (ORC) is a promising process for conversion of low and medium temperature heat to electricity. The ORC is a Clausius-Rankine Cycle in which an organic fluid is used instead of water-steam [5-11]. Due to the great advantage of the ORC to use renewable energies, many innovative concepts coupling the ORC processes are being developed [11]. One such system is a coupled organic Rankine and compression refrigeration cycle which completely eliminates the requirement of electrical power for driving the compressor. The coupled cycle uses the same working medium in topping power loop and bottoming refrigeration loop. The ratio of the fluid flows through the two loops allows the turbine to produce just enough power to drive the compressor and boiler feed pump. The two exiting streams mix and enter the condenser. Using such a coupled cycle is energy effective system as the vapour turbine could be

Corresponding Author: Maneesh Dubey, Email: d.maneesh@gmail.com

made to drive the compressor of the refrigeration cycle and the boiler feed pump [12-15].

Several fluids have been studied for ORC applications. The selection of working fluid plays a significant role for the use of ORC and is determined by the application and the waste heat level. Generally, a good working fluid should exhibit low toxicity, good material compatibility and fluid stability limits, and low flammability, corrosion, and fouling characteristics. Refrigerants are good candidates for ORC applications because of their low-toxicity characteristics [4, 10-11, 16-22]. Chlorofluorocarbon (CFC) compounds, especially R-11 (trichlorofluoromethane) and R-12 (dichlorodifluoromethane) that boil and condense at convenient combinations of pressure and saturation temperature were commonly used as the working medium in the past. The CFCs however decompose in the stratosphere and the chlorine released can destroy the ozone layer that shields the surface of the earth from ultraviolet radiation. CFCs and HCFCs are being phased out under the Montreal Protocol. [2]. Also, environmental emissions and their negative impacts can in part be overcome through increased efficiency. Better resource utilization and less pollution are normally associated with higher efficiency processes. Therefore, if the cycle efficiency alone is considered, the most important parameter is the critical temperature of the working fluid. If the critical temperature is too low, the heating process at a constant pressure stays longer at a low temperature and thus the mean temperature during the boiling process is low, which is directly related to the overall cycle efficiency [12]. Studies reveal that halogenated ethane R-123 (1, 1, dichloro-2, 2, 2-trifluoroethane), R-134a (1, 1, 1, 2-tetrafluoroethane) and R-245ca (1, 1, 2, 2, 3-pentafluoropropane) are substances suitable for obtaining a high thermal efficiency. The chlorine in R-123 has only 2% of the ozone depletion potential of traditional CFCs. R-123 is supposed to be phased out by 2030 in industrialized countries and by 2040 in developing countries. Though R-134a does not contain the chlorine responsible for ozone depletion and though being commonly used in chillers presently, it has been included in the Kyoto agreement as a candidate for phase-out due to its global warming potential [10, 16-23]. Therefore, considering the cycle efficiency and environmental issues, R-245ca has been opted as a working medium in the proposed coupled power-refrigeration cycle.

The objective of this paper is to make an energy analysis of a coupled power-refrigeration cycle along with performance augmentation modifications to provide an efficient, alternative cooling technology using renewable energy sources for its operation. Thermodynamic state at all salient points of the coupled cycle are located and governing equations for energy analysis are developed. Refrigerant properties are computed by NIST Database REFPROP Version 8.0 [24] Simulation is carried to investigate the effect of operating parameters for performance evaluation.

2. Coupled Power-Refrigeration Cycle (CPR Cycle)

To simplify the analysis, following assumptions are made:

- The control volume is at steady state.
- The effects of motion and gravity are ignored.
- No pressure drop is considered in evaporator, condenser, recuperator, reheater and economizer.
- The isentropic efficiencies of compressor, turbine and pump are assumed constant within realistic limits.
- Condenser has given outlet sub cooling of $5^{o}C$ to avoid cavitation in the boiler feed pump.
- The refrigerant vapours are dry-saturated at the suction of the compressor.
- Heat exchange between the system and surroundings, other than that prescribed by heat transfer at the evaporator, condenser, boiler and reheater does not occur.

2.1 Coupled Power-Refrigeration Base Cycle (CPR Base Cycle)

The schematic and T-s diagrams of a coupled power-refrigeration base cycle are shown in figure 1 and 2 respectively. Rankine cycle and the refrigeration cycle share a common condenser. The turbine of the Rankine cycle is connected to the compressor of the refrigeration cycle by a shaft. Refer to the T-s diagram of the base cycle as shown in figure 2. Thermodynamic states at all salient points of the coupled cycle are located considering the input data given in Table 1 and refrigerant properties are computed by NIST Database REFPROP Version 8.0.

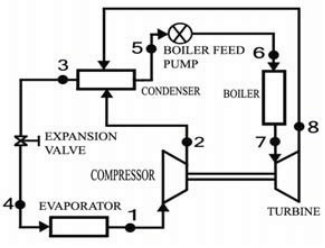

Fig. 1. Schematic diagram of CPR cycle

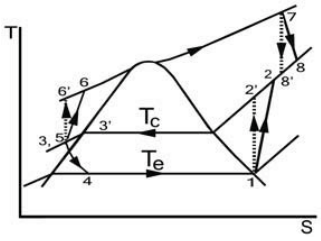

Fig. 2. T-s diagram of CPR cycle

Table 1. Input data for CPR base cycle

Saturation temperature of evaporator	T_e	6°C
Isentropic efficiency of compressor	η_c	0.73
Saturation temperature of condenser	T_C	30-42°C
Subcooling at the condenser	T_{sub}	5°C
Isentropic efficiency of boiler feed pump	η_p	0.7
Boiler pressure	p_b	4-8 MPa
Boiler exit temperature	T_b	220-300°C
Isentropic efficiency of turbine	η_t	0.8

Assuming that pump shaft is connected to the turbine, the ratio of the fluid flows through the power and refrigeration loop allows the turbine to produce just enough power to drive the compressor and boiler feed pump. Therefore,

$$\frac{m_t}{m_r} = \frac{(h_2 - h_1)}{[(h_7 - h_8) - (h_6 - h_5)]} \quad (1)$$

COP of the refrigeration cycle is the ratio of the cooling produced to the input energy required to operate the system. Input energy required in the coupled power-refrigeration cycle is the heat supplied in the boiler. Overall COP for the whole installation then becomes:

$$COP_{overall} = \frac{(h_1 - h_4)}{[m_t(h_7 - h_6)]} \quad (2)$$

The values of the input data for the analysis of base cycle are summarized in Table 1.

2.2 Coupled Power-Refrigeration Cycle with Recuperator (CPRR Cycle)

To recover the energy at the exit of the turbine, a recuperator is installed between the boiler feed pump and boiler. The installation of recuperator maximizes the temperature difference of two heat exchanging fluids. The working fluid at the outlet of the boiler feed pump is heated by the turbine exhaust, increasing the mean temperature of heat addition and reducing the heat to be supplied in the boiler, thus improving the performance. Thermodynamic model for the coupled cycle with recuperator is not presented as this cycle is basically the same as base cycle except for the addition of the recuperator as shown in figure 3.

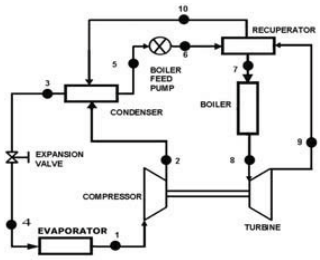

Fig. 3. Schematic diagram of CPRR cycle

2.3 Coupled Power-Refrigeration Cycle with Recuperator, Reheater and Economizer (CPRRRE Cycle)

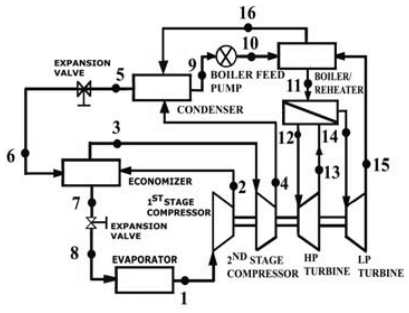

Fig.4. Schematic diagram of CPRRRE cycle

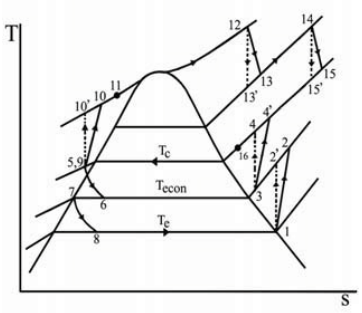

Fig.5. T-s diagram of CPRRRE cycle

The schematic and T-s diagrams for coupled cycle with recuperator, reheater and economizer are shown in figure 4 and 5 respectively. Refer to the corresponding T-s diagram as shown in figure 5. Thermodynamic states at all salient points are located considering the input data shown in Table 2.

Table 2. Input data for CPRRRE Cycle

Saturation temperature of evaporator	T_e	6°C
Isentropic efficiency of I stage compressor	η_{c1}	0.73
Saturation temperature of economizer	T_{econ}	25°C
Isentropic efficiency of II stage compressor	η_{c2}	0.77
Saturation temperature of condenser	T_C	30-42°C
Sub cooling of the condenser	T_{sub}	5°C
Isentropic efficiency of boiler feed pump	η_p	0.7
Effectiveness of recuperator	ε	0.7-0.9
Boiler exit temperature	T_b	220-300°C
Boiler pressure	p_b	4-8 MPa
Isentropic efficiency of HP turbine	η_{t1}	0.8
Isentropic efficiency of LP turbine	η_{t2}	0.8

The cycle is analyzed in the ranges of boiler exit pressure and temperature values with the constraint of the same boiler and reheater exit temperatures. The discharge pressure of the high pressure turbine is one of the critical parameters to augment performance of the coupled cycle with recuperator, reheater and economizer. The optimum value of the high pressure turbine exit pressure is calculated for each given boiler exit pressure and temperature using the following relation: [25-26],

$$p_{rh} = 0.25 p_b \tag{3}$$

The characteristics of the recuperator are simply analyzed by the effectiveness ε of the heat exchanger, which is defined as follows [27],

$$\varepsilon = (t_{hi} - t_{ho}) / (t_{hi} - t_{ci}) \tag{4}$$

where t_{hi} and t_{ho} are the inlet and outlet temperatures of the refrigerant flowing from the turbine into the recuperator respectively and t_{ci} is the inlet temperature of the refrigerant from the boiler feed pump into the boiler. For unit mass flow rate in the evaporator, the mass flow rate in the second stage compressor is obtained from,

$$m_3 = 1/(1 - x_6) \tag{5}$$

Since turbine work is directly supplied to the compressor and boiler feed pump, mass flow required for turbines per kg of refrigerant passed through the evaporator is,

$$m_9 = \frac{[(h_2 - h_1) + m_3(h_4 - h_3)]}{[(h_{12} - h_{13}) + (h_{14} - h_{15}) - (h_{10} - h_9)]} \tag{6}$$

Overall COP of the whole installation is,

$$COP_{overall} = \frac{(h_1 - h_8)}{m_9[(h_{12} - h_{11}) + (h_{14} - h_{13})]} \tag{7}$$

3. Results and Discussion

The performance of the coupled power-refrigeration cycle has been investigated at different boiler pressures, turbine inlet temperatures, condenser temperatures and recuperator effectiveness's. The temperatures at the exit of the turbine for coupled power-refrigeration cycles are shown in Fig. 6. It is quite obvious that temperature at the exit of the turbine decreases with increase in boiler pressure at a particular boiler exit and turbine inlet temperature. However, higher temperatures at the exit of the turbine are achieved with increase in turbine inlet temperatures at a constant boiler pressure. The temperatures at turbine exit are high in the coupled power-refrigeration base cycle ranging from 81.82-223.62 °C. The exergy in exit stream of the turbine will be wasted to the coolant in the condenser. Hence the base cycle has a low COP.

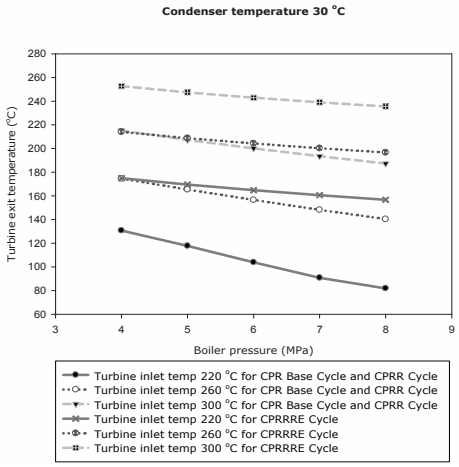

Fig. 6. Comparison of turbine exit temperatures for CPR cycles

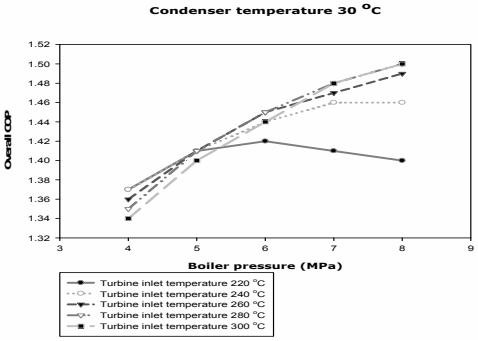

Fig. 7. Variation of overall COP with boiler pressure for a CPR base cycle

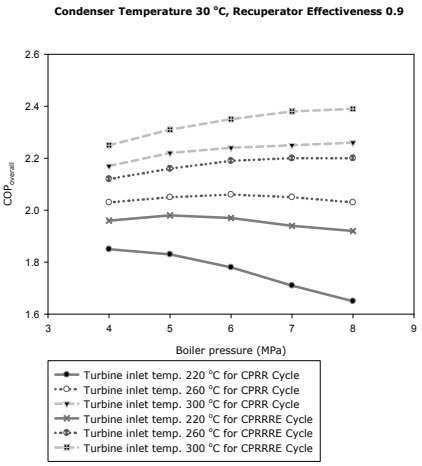

Fig. 8. Overall COP vs. boiler pressure for CPRR and CPRRRE cycles

Temperatures at the exit of turbine in coupled power-refrigeration cycle with recuperator are same as that of the base cycle. The exergy in the exit stream of turbine is utilized in raising mean temperature of heat addition in the boiler in CPRR cycle which results in enhanced overall COP compared to base cycle. It is seen that as compared to the base cycle and cycle with recuperator, higher turbine exit temperatures ranging between 156.73-261.58 ^{o}C are achieved in the CPRRRE cycle due to reheating. Utilization of the increased exergy at exit of turbine in CPRRRE cycle for pre-heating the working fluid before entering the boiler results in higher mean temperature of heat addition in the boiler. Consequently, better performance is obtained in CPRRRE cycle as compared to CPR base cycle and CPRR cycle. Overall COP for the base cycle depends mainly on boiler pressure. Boiler exit temperature does not have the significant effect on the overall COP as observed from Fig. 7 implying that increased energy supply for raising the turbine inlet temperature is not fully utilized in the base cycle. The temperature of the refrigerant at the turbine exit is much higher than its saturation temperature at the condenser. In particular, temperature of the refrigerant increases at the turbine exit almost at the same rate as its temperature at turbine inlet for a given boiler pressure. Hence there is no improvement in overall COP. This problem may be solved by installing a recuperator before the boiler to maximize the temperature difference of two heat exchanging fluids. It is found that for the coupled power-refrigeration cycle with recuperator having recuperator effectiveness of 0.7-0.9, an improvement in overall COP from range of 0.77-1.50 to 0.92-2.26 is observed, whereas in the coupled power-refrigeration cycle with recuperator, reheater and economizer, an improvement in overall COP in the range of 1.09-2.39 is obtained.

Hence, at the condenser temperature range of 30-42°C and recuperator effectiveness range of 0.7-0.9, the overall COP of the coupled cycle with the introduction of the recuperator, increased by 19.5-50.7% and in the cycle with recuperator, reheater and economizer, it increased by 41.6-59.3% indicating that the available energy at the exit of turbine is utilized in increasing the mean temperature of heat addition in the boiler. The coupled cycle with recuperator, reheater and

economizer gives the added advantages of reheating, multistage compression and multistage expansion. Significant increases in overall COP have been observed with increase in turbine inlet temperature for CPRR and CPRRRE cycles as shown in Fig. 8. The overall COP first increases and then decreases with boiler pressure at all turbine inlet temperatures in coupled power-refrigeration cycle with recuperator. Thus, an optimum boiler pressure exists where the overall COP becomes maximum for a given turbine inlet temperature in coupled cycle with recuperator. However, in coupled cycle with recuperator, reheater and economizer, at turbine inlet temperatures lower than 270 ^{o}C, an optimum boiler pressure exists. Overall COP increases with increase in boiler pressure for turbine inlet temperatures greater than 270 ^{o}C. Hence, no optimum pressure exists for turbine inlet temperatures greater than 270 ^{o}C in the coupled power-refrigeration cycle with recuperator, reheater and economizer.

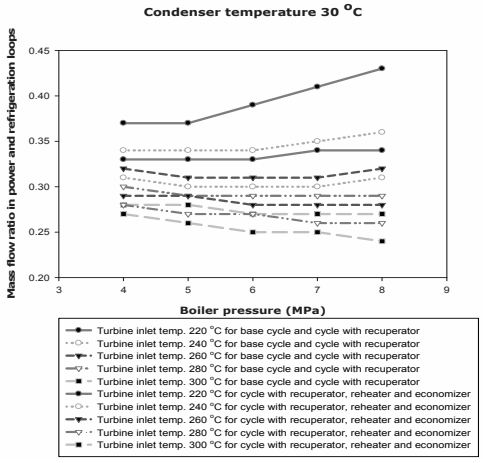

Fig. 9. Comparison of mass flow ratio in power and refrigeration loops of CPR cycles

As can be seen from figure 9 that mass flow ratio of topping power and bottoming refrigeration loop in CPR base cycle and CPRR cycle decreases with increase in turbine inlet temperature at a constant boiler pressure. The mass flow ratio increases with increase in boiler pressure up to 240^{o}C and remains approximately constant in the range of 250-300^{o}C in CPR base cycle and CPRR cycle. At a particular turbine inlet temperature in CPRRRE cycle, it is seen that the mass flow ratio is independent of variation in boiler pressure. CPR base cycle and CPRR cycle has mass flow ratio in the range of 0.27-0.71; however CPRRRE cycle has a decreased mass flow ratio in the range of 0.24-0.58. Hence, the mass flow in power loop of the CPRRRE cycle has 11.1-18.3% decrease as compared with the CPR base cycle and CPRR cycle. This reduction in mass flow of power loop is the result of the increased specific work output of the turbine due to reheating and decreased compressor work input due to multistage compression with intercooling.

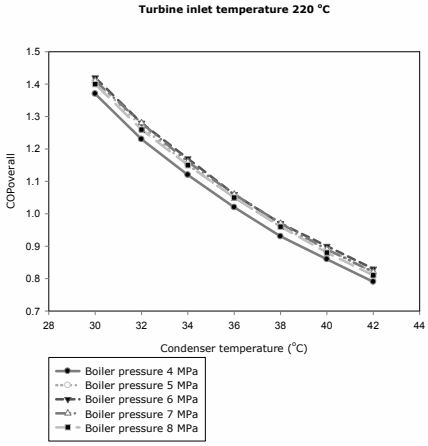

Fig.10. Overall COP vs condenser temperature for CPR base cycle

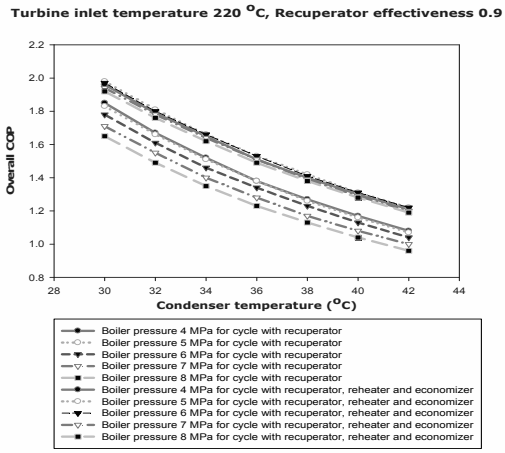

Fig. 11. Overall COP vs condenser temperature for CPRR and CPRRRE cycles

The condenser temperature significantly affects the performance of the system. With increase in

condenser temperature, the overall COP of the system decreases due to high work input of the compressor which may be compensated by increasing the boiler temperature or pressure. It can be observed from Figs. 10 and 11 that overall

COP at a constant turbine inlet temperature remains almost invariant with boiler pressure in the condenser temperature range of 30-42 ^{o}C for CPR base cycle and CPRRRE cycle. However, for the CPRR cycle, significant decrease in overall COP is observed for boiler pressure greater than 5 MPa at constant turbine inlet temperature and recuperator effectiveness as shown in Fig. 11. The reason for such significant decrease is the ineffectiveness in the use of higher amount of energy supplied in the boiler to produce necessary cooling effect.

4. Conclusions

The effect of various operating parameters on the performance of the system was investigated. The key conclusions are as follows:

1. The overall COP for the base cycle varied from 0.77 to 1.50 in the condenser temperature range of 30- 42 °C. In the same condenser temperature range for the coupled power-refrigeration cycle with recuperator having effectiveness 0.7-0.9, overall COP varied from 0.92 to 2.26 which is 19.5-50.7% higher than that for the base cycle. The overall COP range for coupled cycle with recuperator, reheater and economizer varied from 1.09 to 2.39 which are 41.6-59.3% higher than that of base cycle.
2. For the base cycle, overall COP depends mainly on boiler pressure. The gain in overall COP due to increase in the temperature at the turbine inlet is insignificant. However, significant increases in overall COP have been observed with increase in turbine inlet temperature for CPRR and CPRRRE cycles. Overall COP increases with increase in boiler pressure for turbine inlet temperatures greater than 270 ^{o}C. However, at temperatures lower than 270 ^{o}C, the overall COP first increases and then decreases with boiler pressure.
3. The mass flow ratio increases with increase in boiler pressure up to 240^{o}C and remains approximately constant in the range of 250-300^{o}C for a coupled power-refrigeration base cycle and cycle with recuperator. It is seen that the mass flow ratio is independent of variation in boiler pressure at a particular turbine inlet temperature in a coupled power-refrigeration cycle with recuperator, reheater and economizer.
4. Coupled power-refrigeration cycle with recuperator, reheater and economizer has a decrease in mass flow ratio in the range of 0.27-0.71 to 0.24-0.58. Hence, mass flow rate in the power loop of the coupled cycle with recuperator, reheater and economizer has a reduction of 11.1-22.4% as compared to the base cycle and cycle with recuperator.
5. Overall COP at a constant turbine inlet temperature remains almost invariant with boiler pressure in the condenser temperature range of 30-42 ^{o}C for a coupled power-refrigeration base cycle and cycle with recuperator, reheater and economizer.
6. Significant decrease in overall COP is observed for boiler pressure greater than 5 MPa at constant turbine inlet temperature and recuperator effectiveness for the coupled cycle with recuperator.

Nomenclature

$h; s$	enthalpy, kJ/kg; entropy, kJ/kg-K
p	pressure, Mpa
T	temperature, K
m	mass flow rate, kg/s
q, Q	specific and total heat transfer, kJ/kg & kJ

Greek symbols

η	efficiency
ε	effectiveness

Subscripts and superscripts

c, t, p	condenser, turbine, pump
b	boiler, boiler exit (or turbine inlet)

References

1. McMullan, T., 2002, Refrigeration and The Environment-Issues and Strategies for the Future, Int. J. of Refrig., 25, pp.89-99.
2. UNEP 1999, Synthesis of the Scientific, Environmental Effects and Technology, and

Economic Assessment Panels of the Montreal Protocol, United Nations Environment Programme, Ozone Secretariat.

3. Kyoto Protocol, 1997, United Nations Framework Convention on Climate Change, Kyoto.
4. Hung, T. C., et al., 1997, A Review of Organic Rankine Cycles for the Recovery of Low-Grade waste heat, Energy, 22(7), pp. 661-667.
5. Lee, W. Y., et al., 1990, Thermodynamic Optimization of an Organic Rankine Power cycle, Solar Energy, 10(3), pp. 35-45.
6. Shin, S. H., et al., 1999, A study of Ocean Thermal Energy Conversion Systems using Kalina Cycle and Regenerative Rankine Cycle, Solar Energy, 19(3), pp. 101-113.
7. Gurgenci, H., 1986, Performance of Power Plants with Organic Rankine Cycles under Part-Load and Off-Design Conditions, Solar Energy, 36(1), pp. 45-51.
8. Lee, K. M., et al., 1988, Parameter Analysis on Organic Rankine Cycle Energy Recovery System, Energy Convers. and Mgmt., 28(2), pp. 129-136.
9. Donghong, et al., 2007, Performance Analysis and Optimization of Organic Rankine Cycle for Waste Heat Recovery, Energy Convers. and Mgmt., 48, pp. 1113-1119.
10. Mago, P. J., et al., 2007, Performance Analysis of Different Working Fluids for Use in Organic Rankine Cycles, Journal of Power and Energy, Proc. IMechE, 221, Part A, pp. 255-263.
11. Schuster, A., et al., 2009, Energetic and Economic Investigation of Organic Rankine Cycle Applications, Applied Thermal Engineering, 29, pp. 1809-1817.
12. Bejan, A., 2006, *Advanced Engineering Thermodynamics,* Third Edition, John Wiley and Sons Inc, New Jersey.
13. Sonntag, R. E., et al., 2006, *Fundamentals of Thermodynamics,* 6th edition, John Wiley and Sons (Asia) Pvt. Ltd., Singapore.
14. Burmeister, L. C., 1998, *Elements of Thermal-Fluid System Design,* Prentice Hall, New Jersey.
15. Christensen, R. N., and Santoso, M., 1990, An Evaluation of a Rankine Cycle driven Heat Pump, Heat Recovery Systems and CHP, 10(2), pp. 161-175.
16. Gozdur, A. B., and Wladyslaw, N., 2007, Comparative Analysis of Natural and Synthetic Refrigerants in Application to Low Temperature Clausius-Rankine cycle, Energy, 32, pp. 344-352.
17. Hung, T. C., 2001, Waste Heat Recovery of Organic Rankine Cycle using Dry Fluids, Energy Convers. and Mgmt, 42, pp. 539-553.
18. Maizza, V., and Maizza, A., 2001, Unconventional Working Fluids in Organic Rankine Cycles for Waste Energy Recovery Systems, Applied Thermal Engineering, 21, pp. 381-390.
19. Angelino, G., and Paliano, P. C., 1998, Multi-Component Working Fluids for Organic Rankine Cycles, Energy, 23(6), pp. 449-463.
20. Maizza, V., and Maizza, A., 1996, Working Fluids in Non-Steady Flows for Waste Energy Recovery Systems, Applied Thermal Engineering, 16(7), pp. 579-590.
21. Cavallini, A., 1996, Working Fluids for Mechanical Refrigeration, International Journal of Refrigeration, 19, pp. 485-496.
22. Saleh, B., and Wendland, M., 2006, Screening of Pure Fluids as Alternative Refrigerants, International Journal of Refrigeration, 29, pp. 260-269.
23. Saleh, B., et al., 2007, Working Fluids for Low-Temperature Organic Rankine Cycles, Energy, 32, pp. 1210-1221.
24. Dubey, M., and Rajput, S. P. S., 2009, Performance Analysis of Rankine Powered Refrigeration System using R-134a for Cold Storage like Applications, *Proceedings of National Conference on Refrigeration and Air Conditioning, NCRAC 2009,* Paper no. P-45, IIT Madras, Chennai, India.
25. ASHRAE, 1999, ASHRAE Transactions, Vol. 95, Part 2; American Society of Heating, Refrigerating and Air-Conditioning Engineers, Inc., Atlanta, USA.
26. Nag, P. K., 2006, *Engineering Thermodynamics,* 3rd Edition, Tata Mc Graw Hill Publishing Company Limited, New Delhi.
27. ASHRAE, 2005, *ASHRAE handbook – fundamentals,* American Society of Heating, Refrigerating and Air-Conditioning Engineers, Inc., Atlanta, USA.

Design and thermoeconomic optimization of hybrid solar heating and cooling systems for an Italian university building

F. Calise[a,1] *, M. Dentice d'Accadia*[a]*, A. Palombo*[a]

[a] *DETEC – University of Naples Federico II, P.le Tecchio 80, 80126 Naples, Italy*

Abstract:

The paper investigates the performance of a solar-assisted heating and cooling system (SHC) for an Italian university building. The SHC system under investigation is based on the coupling of evacuated solar collectors with a single-stage LiBr-H_2O absorption chiller; auxiliary heating and cooling are supplied by an electric-driven heat pump. The cooling capacity of the absorption chiller and the solar collector area are designed on a fixed fraction of the maximum cooling load. Besides providing thermal energy for cooling and heating, in summer and winter, respectively, the SHC system produces Domestic Hot Water (DHW), all year long. The analysis was carried out by means of a zero-dimensional transient simulation model, developed with the TRNSYS software; the simulation of the dynamic behavior of the building in which the SHC systems were supposed to be installed was included. An economic analysis was also performed, in order to assess the operating and capital costs of the systems under evaluation. Furthermore, a parametric analysis and a subsequent mixed heuristic-deterministic optimization algorithm was implemented, in order to determine the set of the synthesis/design variables that maximize the overall profitability of the system. The results are encouraging, with regard to the potential of energy saving. As for economic aspects, the analysis showed that the SHC economic profitability can be achieved only in case of public incentives (e.g. feed-in tariffs), as always happens for the great majority of renewable energy systems.

Keywords: solar energy, evacuated collectors, absorption chiller, dynamic simulation

1. Introduction

Solar heating and cooling (SHC) is considered a very promising technology, based on the use of solar radiation not only for space heating but also for cooling, by means of an heat-driven chiller. SHC may significantly contribute to goals of energy savings, emissions reductions and increase in the use of renewable energy sources, stated by EU in the Directive 2009/28/EC. In fact, the energy consumption of buildings significantly contributes to the overall EU energy demand. Presently, this consumption is mainly due to the heating demand (about 93%), so it is expected to grow significantly in the next years as a consequence of the dramatic increase of the air conditioning market [1]. Therefore, several Mediterranean States of EU are promoting appropriate actions in order to limit the expected growth in building primary energy demand; for example, in Italy a State Law (Decree n. 311/06) enforces severe limits for the primary energy consumption due both to space heating and cooling and for the global efficiency of the HVAC system. Such Law also enforces the installation of solar systems, which must produce at least 50% of the overall Domestic Hot Water (DHW) yearly demand. In this framework, SHC systems show a big market potential in Italy. In fact, such systems could be designed and installed as a simple extension of the mandatory DHW solar systems. In addition, the high values of solar irradiation and the corresponding high cooling energy demand, typical of most Italian climates, make the application of SHC systems very promising. However, SHC technology is still scarcely used in Europe, mainly due to economic barriers; the number of SHC systems operating in EU is

[1] Corresponding author: email: frcalise@unina.it, tel. +390817682301, fax. +390812390364

estimated in about 100 [2]. Therefore, a significant effort is required in terms of research, demonstration projects and incentive policies. Many institutions are presently involved in R&D activities in this field, and many demonstration projects have been developed [3]. In the last few years, a lot of experimental and theoretical research work has been done. For example, Florides et al. developed a very interesting simulation model in TRNSYS for a Cypriot building [4-5]. The same analysis and optimization was performed by Gaddhar et al. for a solar cooling prototype located in Beirut [6]. Atamaca and Yigit performed the study for the city of Antalya (Turkey) [7]. An interesting study for the EU climates was recently presented by Mateus et al. [2]. Most of the studies cited above analyze the operation and design of SHC systems only in the cooling mode. In addition, such works are mainly focused on the energy analysis, whereas the economic point of view is scarcely investigated, except for the paper by Mateus et al. [2]. A preliminary study on this topic was also performed by the authors, including the dynamic simulation of a specific SHC system, operating only during the summer [8]. In ref. [9] the authors investigated three different SHC configurations from an energetic point of view, using the Design of Experiments technique. In the present paper, a complete dynamic model of a solar-assisted heating and cooling system is presented and used to develop a case study, including a detailed energy and economic analysis and optimization for an Italian building, namely a university hall. A few important innovations were introduced with respect to the existing literature: i) a different system layout was considered, including an auxiliary electric-driven heat pump operating as a water-to-water chiller during the summer and as an air-to-water heat pump during the winter; ii) detailed models of the buildings were implemented, based on the TRNBuild software, included in TRNSYS package; iii) the winter operation and the production of DHW are included in the analysis; iv) an algorithm for thermoeconomic optimization was introduced.

2. Building

The building considered in the case-study was a small university hall, consisting of 7 classrooms (A1, A2, A3, C1, C2 and C3) and a common area (B1). The building net volume is 2250 m^3. The net height of the zones is 4.5 m. This building is compliant with the requirements of Italian Laws in terms of walls and windows transmittances, system efficiency and primary energy consumption and is located in Naples, South Italy. The building was simulated in TRNSYS environment, using the TRNBUILD application included in TRNSYS package. Four different walls were considered, whose values of transmittance and front and back solar absorbance are shown in Table 1.

Table 1 - Walls properties

Wall	*s(m)*	*U(W/m²K)*	*U_{lim}(W/m²K)*	*α_{front}*	*α_{back}*
ground	0.425	0.313	0.420	0.80	0.40
intwall	0.074	0.652	//	0.60	0.60
outwall	0.355	0.339	0.400	0.75	0.30
roof	0.400	0.233	0.380	0.35	0.75

Table 2 - Building parameters

Parameter	*Value*	*Unit*
Occupancy	0.60	person/m^2
Mech. Air Change (SHC ON)	3.80	Vol/h
Natural Air Change (SHC OFF)	0.30	Vol/h
Sensible radiative load, summ.	92	W/person
Sensible convective load, summ.	138	W/person
Sensible latent load , summ.	0.080	kg/h person
Sensible radiative load, wint.	133	W/person
Sensible convective load , wint.	200	W/person
Sensible latent load, wint.	0.035	kg/h person
Equipment radiative load	0.80	W/m^2
Equipment convective load	4.2	W/m^2
Light radiative load	6.67	W/m^2
Light convective load	3.34	W/m^2
External Radiation -Light on	120	W/m^2
External Radiation -Light off	200	W/m^2
External Radiation –Shad. on	140	W/m^2
External Radiation -Shad. off	120	W/m^2

The values of wall transmittances (U, W/m^2K) are largely compliant with the limits of the Italian Law (U_{lim}, W/m^2K). Similarly, the data of windows transmittance (1.574 W/m^2K) is lower than the corresponding limit. All the windows are also provided with shadings. The occupancy and the mechanical air change of the building is suggested by the Italian Standard (UNI 10339) and shown in Table 2. The values of the radiative and convective people load (latent and sensible), summarized in Table 2, are established by the same Standard. The same table also shows the light and the equipment load. Furthermore, in order to achieve a realistic simulation of the use of the light and shadings, threshold values for both lighting and shading were fixed. Based on the values of the external total radiation on horizontal and on the

corresponding fixed thresholds, the lights and shadings are activated or de-activated. Finally, the university hall was also assumed to be located close to the university fitness centre, so that the DHW produced by the SHC can be also used there, all year long. The winter set point temperature is established by the Italian Law at 20 °C, whereas the summer set-point temperature is not ruled by Law and was arbitrarily set at 26 °C. The controllers of the zone air temperature operate with dead-bands of ± 1.0 °C. According to Italian Laws, the heating system operates from November 15th to March 31st. As for the summer, the operating period is not fixed by Law, and the interval from May 1st to October 21st was assumed, on empirical basis. The building was supposed to be occupied all over the year, from Monday to Saturday, from 8.00 am to 6.00 pm.

3. SHC System

Several studies showed that the most promising configuration for SHC systems is based on the coupling of evacuated tube solar collectors with single-stage LiBr-H_2O absorption chillers [2]. In order to achieve an efficient and cost-effective configuration, it is also very important the selection of auxiliary devices, with special reference to the auxiliary heater. In the SHC configuration proposed in the paper, the use of a traditional auxiliary gas-fired heater was discarded. In fact: i) the combination of gas-fired hears and single stage absorption chiller has a very low efficiency; ii) the SHC system under investigation was designed to provide only a small fraction of the total heating and cooling demand of the building, requiring a lot of integrations. Therefore, an electric-driven chiller/heat pump was selected as the auxiliary system, operating as an air-to-water heat pump in the winter and as a water-to-water chiller during the summer operation, also requiring the use of an adequate cooling tower. Previous studies showed that SHC systems designed to cover the entire heating and cooling demand are not profitable, since the yearly utilization factor of the installed capacity is too low [8]. Therefore, in the present study, the solar collectors area and the nominal capacity of the absorption chiller were selected in order to satisfy only a part (20%) of the maximum cooling load of the building. Five different loops are present: solar collector water (SCW), hot water (HW), cooling water (CW), domestic hot water (DHW) and chilled/hot water (CHW). Basically, the SHC system consists of the following main components: a 200 m^2 solar field with evacuated-tube collectors (SC); a 10.8 m^3 hot water inertial storage tank (TK1); a 50 kW LiBr-H_2O single stage absorption chiller (ACH), activated by the thermal energy provided by the solar field; a 250 kW water/air cooled electrical heat pump (EHP), providing auxiliary energy for both cooling and heating needs; a closed circuit cooling tower (CT), providing cooled water to the condensers of both EHP and ACH; a fixed-volume pump (P1) for the HW loop, pumping water from TK1 to ACH (summer) or to the EHP (winter); a variable speed pump (P2) for the SCW loop; a fixed-volume pump (P3) for the CW loop; a fixed-volume pump (P4) for the CHW loop; an inertial chilled/hot water storage tank (TK2); a hydraulic separator (HS), balancing fluid flows between the primary and secondary hydraulic circuits; a plate-fin heat exchanger to produce Domestic Hot Water (HE); pipes connecting the HS with the fan-coils of the zones of the building.

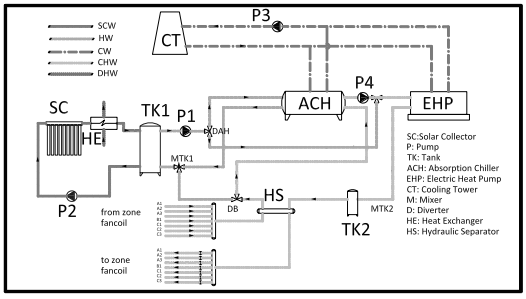

Figure 1 –SHC Layout

The TRNSYS scheme used to simulate the system also includes additional components, not displayed in Figure 1, such as: controllers, schedulers, weather database, etc. The basic operating principle of the SHC system is quite simple: the solar irradiation incident on the Solar Collector field (SC) increases the outlet temperature of the corresponding circuit up to the fixed set-point, determining the temperature rise of the water in the storage tank TK1. In case of scarce request of cooling/heating energy by the building, the energy provided by SC is used by the HE to produce DHW to be used for the showers installed in the building. In summer operation, the hot fluid drawn by P1, from the top of TK1, reaches the ACH, which produces the chilled water (CHW) required for cooling the building. The cooling tower CT provides the cold water required to cool the

absorption chiller, ACH. However, as above mentioned, the ACH nominal capacity is lower than the maximum building load. Therefore, the CHW exiting the ACH enters the EHP, which provides the additional cooling energy required to cool the chilled water down to the fixed set-point. Thus, ACH and EHP often operate simultaneously. However, in order to prevent significant decrease of TK1 temperature, when the TK1 outlet temperature falls down a fixed set-point (T_{offACH}), the ACH is shut-down and the EHP provides all the required cooling energy. During the operation of the sole EHP, the water temperature in TK1 can be increased again by the SC. The ACH is re-activated when the TK1 temperature overcomes a given temperature ($T_{offACH}+\Delta T_{TK1}$). During the heating season, the water exiting the TK1 directly flows toward the HS passing through the auxiliary EHP, which is activated when the TK1 outlet temperature falls down a fixed set point. The volumes of TK1 and TK2 are sufficiently high to prevent an excessive number of EHP and ACH shut-off and start-up.

4. Simulation Model

The components of the solar-assisted refrigeration system were simulated using the TRNSYS built-in library [10], as well as user-developed models. The built-in simulation models of solar collectors, pumps, cooling towers, absorption chiller and storage tanks are described in references [9-10]. Details regarding the simulation of pipes and building are given in [10]. The user-developed simulation models added in the present work are briefly described in the following, paying special attention to the variables used as the synthesis/design parameters in the optimization.

Electric Heat Pump (EHP). The EHP considered was a reversible model, operating as a traditional water-to-water chiller during the summer, when the condensing coil of the EHP is cooled by the cold water coming from the cooling tower; during the winter, the system operates as a simple air-to-water heat pump. The simulation model for such EHP was developed with a catalogue lookup method, based on manufacturers' data (used in the air-to-water chiller, included in TRNSYS), in which the chiller capacity ratio, R_Q, and the COP ratio, R_{COP}, are function of the chilled water set-point temperature and the inlet cooling water temperature [9-10].

Heat Exchanger. The DHW is produced by a plate-fin compact Heat Exchanger, HE, equipped with a control which enables DHW production only when the SC outlet temperature overcomes the fixed set point. The HE is equipped with a diverter placed upstream the DHW inlet, a by-pass duct and a mixer downstream the DHW outlet. The diverter and the mixer are managed by the HE control system. The model of such device was developed using a modified version modified of the well-known ε-NTU method [11]. When the outlet SC temperature is lower or equal than the fixed set-point, the HE heat flow and the DHW flow are zero. In the other cases, the HE actual heat flow is given by:

$$\dot{Q}_{HE} = \dot{m}_{SCW}\left(t_{out,SC} - t_{set,out,SC}\right) \quad (1)$$

On the basis of the thermal flow given in (1), the model calculates the DHW water flow and the DHW bypass factor in order to achieve both the desired temperatures of the DHW and SCW exiting the HE, respectively $t_{set,out,DHW}$ (set at 45 °C) and $t_{set,out,SC}$. The DHW temperature entering the HE was set at 15 °C. The calculation of the DHW flow rate and the HE bypass factor is performed by the HE controller which is based on the following algorithm. On the basis of the guess value for the DHW flow circulating in the HE ($f_{DHW}\cdot\dot{m}_{DHW}$), the minimum and maximum thermal capacity flow rates and the HE efficiency are calculated as follows.

$$\dot{C}_{\min} = \min\left(\dot{m}_{SCW}\cdot c_{SCW},\ f_{DHW}\cdot\dot{m}_{DHW}\cdot c_{DHW}\right) \quad (2)$$

$$\dot{C}_{\max} = \max\left(\dot{m}_{SCW}\cdot c_{SCW},\ f_{DHW}\cdot\dot{m}_{DHW}\cdot c_{DHW}\right) \quad (3)$$

$$\varepsilon = \varepsilon\left(\frac{UA}{\dot{C}_{\min}}, \frac{\dot{C}_{\min}}{\dot{C}_{\max}}\right) \quad (4)$$

Then, the guess value is iteratively varied until convergence is reached on the HE energy balance equation:

$$\dot{Q}_{HE} = \dot{m}_{SCW}\left(t_{out,SC} - t_{set,out,SC}\right) = \varepsilon\,\dot{C}_{\min}\left(t_{out,SC} - t_{in,DHW}\right) \quad (5)$$

Convergence is guaranteed by the appropriate selection of the HE exchange, area so that the HE is capable the cool down the SCW to the fixed set point for any DHW flow rate. Finally, the DHW flow rate to the user can be calculated by a simple energy balance:

$$\dot{m}_{DWH} = \frac{\dot{Q}_{HE}}{\left(t_{set,out,DHW} - t_{in,DHW}\right)} \quad (6)$$

Hydraulic Separator. This device is required in order to balance the flow rates between the primary (*pr*) and secondary (*se*) loops of the system. For such device, a new TRNSYS model was introduced, using the following criterion, based on simple energy and mass balances. In case the primary mass flow rate is higher than the secondary one, the primary and secondary outlet temperatures are calculated as follows:

$$t_{pr,out} = \frac{\dot{m}_{se} t_{se,in} + \left(\dot{m}_{pr} - \dot{m}_{se}\right) t_{pr,in}}{\dot{m}_{pr}} \quad (7)$$

$$t_{se,out} = t_{pr,in} \quad (8)$$

When the primary mass flow rate is lower than the secondary one, the primary and secondary outlet temperatures are:

$$t_{pr,out} = t_{se,in} \quad (9)$$

$$t_{se,out} = \frac{\dot{m}_{pr} t_{pr,in} + \left(\dot{m}_{se} - \dot{m}_{pr}\right) t_{se,in}}{\dot{m}_{se}} \quad (10)$$

Fan-coils (winter and summer operation). Each thermal zone of the building is equipped with a 2-pipes loop, supplying hot/chilled water to the respective fan-coils. Therefore, the same fan-coils operate in cooling mode during the summer and in heating mode in the winter. Fan-coils were simulated with a new TRNSYS type, based on a data lookup approach. In fact, TRNSYS library lacks in a fan-coil model able to operate in both cooling and heating modes. The data file includes four correction factor, depending on actual fluid mass flow rate, inlet fluid temperature, air dry and wet bulb temperature and air flow rate.

Primary energy consumption. The primary energy required by the SHC system, in terms of non-renewable sources was calculated by dividing the electric energy consumption (EHP, pumps and auxiliary equipment) by the mean efficiency of the Italian power grid:

$$PE_{SHC} = \frac{E_{el}}{\eta_{el}} \quad (11)$$

In order to estimate the energy saving potential of the SHC system, a reference, conventional system was also introduced, based on two devices; an air-to-water electric-driven heat pump (EHP_{RS}) for space cooling and heating, and a natural gas-fired boiler for DHW production, characterized by a mean efficiency η_c. The primary energy required by the reference system RS was then calculated as:

$$PE_{RS} = \frac{E_{el,RS}}{\eta_{el}} + \frac{Q_{DWH}}{\eta_c} \quad (12)$$

Economic analysis. A detailed cost model was also implemented in the simulation tool, relating the cost of each component to the main design parameters. In addition, the operating costs due to natural gas and electrical energy consumption were evaluated, whereas maintenance costs were neglected. The capital costs were reported on a yearly base by means of the annuity factor AF, depending on the expected life of the system and on the discount rate. So, the total cost of owning and operating the SHC plant was expressed as:

$$C_{tot} = \frac{\sum_i J_i}{AF} + C_{op,SHC} = \frac{\sum_i J_i}{AF} + \frac{\sum_i E_{el,i} c_{EE}}{3600} \quad (13)$$

Capital costs were estimated by introducing a cost function for each component, obtained by regression of manufacturers' data [9]. As for the reference system, the capital cost was calculated using the same approach, and the operating costs were calculated as:

$$C_{op,RS} = \frac{c_{EE}}{3600}\left(E_{el,RS}\right) + \frac{c_{NG} Q_{DHW}}{\eta_c LHV_{NG}} \quad (14)$$

In the economic analysis, the time horizon and the discount rate were set to 20 years and 5%, respectively, corresponding to an AF value of 12.5 years. The unit costs of electric energy (c_{EE}) was assumed equal to 0.13 €/kWh. The economic performance of the SHC system was estimated in terms of Simple Pay-Back period, SPB. A public incentive was also considered for the SHC system: otherwise, no economic profitability would be possible, as happens for most technologies based on renewable energy sources. So, in the base-case the economic analysis was performed assuming a feed-in tariff of 0,50 Euro per 1 kWh of electric energy saved with respect to the reference system. As a possible alternative, an investment subsidy equal to 60% of the capital cost was considered, limited to "non-conventional" devices: ACH, CT, TK1 and SC.

5. Results and discussion

A complete energy and economic analysis was performed for the SHC and the building described

above. Some results obtained for a typical summer day are shown in Figure 2.

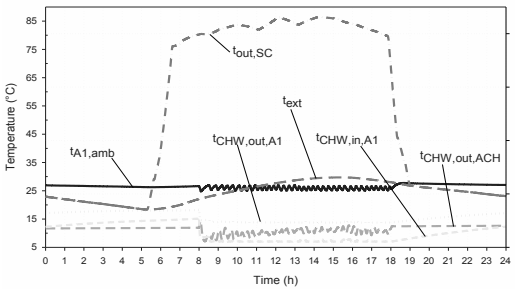

Figure 2- Summer Day

The SC starts producing hot water in the early morning, achieving a temperature ($t_{out,SC}$) of around 80 °C at the HVAC activation (8.00 am). Then, between 8.00 and 10 am, the cooling energy is provided only by the EHP. In fact, at this time, SC outlet temperature is still below 82°C, which is the fixed set-point for ACH activation. After 10.00 am, the ACH operates at full load until 6.00 pm (HVAC deactivation). During this period, the remaining cooling energy is provided by the EHP. In Figure 2 it is also displayed the ambient temperature of zone A1 which continuously varies between 25 °C and 26 °C as a consequence of the operation of the ON/OFF controller. Similarly, temperatures of the water entering ($t_{CHW,in,A1}$) and exiting ($t_{CHW,out,A1}$) the fan-coils of zone A1, stably fluctuating respectively around 7 °C and 13 °C. Conversely, the trend of the temperature of water exiting ACH ($t_{CHW,out,ACH}$) is much more irregular, as a consequence of the variations of the cooling load and of the availability of solar energy (the ACH capacity is 20% of that of the EHP). During the day under evaluation, the SC outlet temperature is always lower than the fixed set point (90 °C). Consequently, no DHW is produced. Figure 3 shows the monthly heating, cooling, primary, radiative and electrical energy flows. Here, for all winter months, the useful thermal energy produced by the SC (Q_{SC}) is largely higher than the building heating load ($Q_{h,FC}$). This is mainly due to the winter internal useful gains, which determines a building heating load ($Q_{h,FC}$) significantly lower than the cooling load ($Q_{c,FC}$). Note also that summer DHW production (Q_{HE}) is significantly lower than in the winter, since the SC thermal energy is almost entirely used for the ACH.

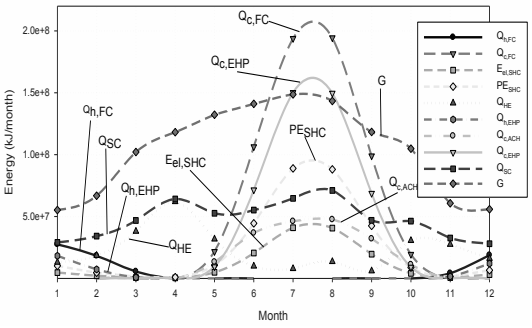

Figure 3 - Monthly Results

In addition, Figure 3 shows that the electrical energy and Primary Energy consumption (PESHC) consumption are mainly due to the summer operation. Most of the comments above discussed also apply to the yearly analysis, whose results are summarized in Table 3. The building energy demand for heating (7.41 107 kJ/h) is an order of magnitude lower than for cooling (6.35 108 kJ/h). As a consequence, the solar fraction in the winter (46.2 %) is significantly higher than in the summer (27.7%). It is also noteworthy the that annual average SC efficiency is considerably high (45.8%) as a consequence of the above discussed control strategy based on a variable speed pump and seasonal set point temperatures. Table 3 also shows that the SHC system, although sized only on 20% of the total load, achieved a PES value of 59%. This is due both to the solar energy contribution and to the high efficiency of the EHP, which produces auxiliary cooling and heating energy with seasonal winter and summer COP of 4.98 and 4.77, respectively. The savings in terms of primary energy also determine a significant annual cost saving (23600 €/year) mainly due to the incomes from the feed-in tariff (14189 €/year, i.e. 60%). On the other hand, it must be observed that the actual capital cost of the SHC is very high (365 k€, i.e. 285 k€ higher than the capital cost of the Reference System); such investment can be recovered approximately in 12 years (SPB), that is an acceptable result for a system using a renewable energy source, with an operating life estimated in 20 years. Such results are encouraging, but still scarcely attractive for market penetration, since the DPB period is not much lower than the estimated operating life.

Table 3 - Yearly results

Q_h	kJ/y	7.41E+7	$COP_{w,EHP}$	-	4.98E+0
Q_c	kJ/y	6.35E+8	COP_{AHP}	-	8.72E-1
E_{el}	kJ/y	1.42E+8	$COP_{s,EHP}$	-	4.77E+0
PE	kJ/y	3.09E+8	$F_{sol,s}$	-	2.77E-1
Q_{HE}	kJ/y	2.75E+8	$F_{sol,w}$	-	4.62E-1
$Q_{h,EHP}$	kJ/y	3.99E+7	PES	-	6.47E-1
$Q_{c,ACH}$	kJ/y	1.87E+8	J_{tot}	€	3.65E+5
$Q_{c,EHP}$	kJ/y	4.59E+8	$C_{op,SHC}$	€/y	5.14E+3
Q_{SC}	kJ/y	5.72E+8	C_{DHW}	€/y	5.73E+3
G/A_{SC}	kJ/m^2y	6.24E+6	DC	€/y	2.36E+4
A_{SC}	m^2	2.00E+2	SPB	y	1.21E+1
m_{P4}	kg/h	4.30E+4	DPB	y	1.90E+1
η_{SC}	-	4.58E-1	SPB1	y	1.16E+1

A sensitivity analysis was also performed, in order to investigate the variation of the results when varying some of the most significant design parameters, such as: SC and ACH capacity, set point temperatures, tank volumes, pump flows, etc. For brevity, the sensitivity analysis is only discussed for the SC/ACH capacity and for the TK1 volume, which showed the highest influence on the thermoeconomic results. In Figure 4, the SHC energy and economic performance is analyzed as a function of the ACH capacity and the SC area. The best economic performance is achieved at the lowest SC area and ACH capacity (expressed in terms of f_{ACH}, that is the ratio of the ACH capacity to the maximum building cooling load). Therefore, the EHP is much more profitable than the SC/ACH, and the possible feed-in tariff would promote only the EHP, scarcely encouraging SCH technology. Hence, a possible, alternative incentive was considered, based on an investment subsidy equal to 60% of the capital costs of the SHC devices (SC, SCH, CT and TK1). In this case, the trend of SPB (SPB1 in Figure) decreases for higher SC and ACH capacity. The SC efficiency is negligibly affected by the variation of SC and ACH capacity. Finally, it is also noteworthy that PES and F_{sol} values increase less than proportionally with ACH and SC capacity. The sensitivity analysis to v_{TK1} is shown in Figure 5. Here it is clearly displayed that the best economic profitability (according both SPB and SPB1 criteria) and energy efficiency could be achieved at the lowest value of 25 L/m^2. On the other hand, larger TK1 volumes would determine a slight increase of the summer and winter solar fractions, due to the higher TK1 heat storage capacity.

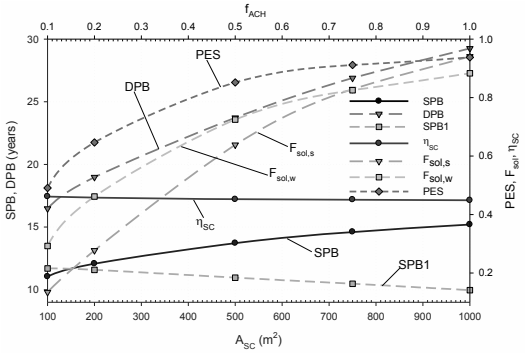

Figure 4 - Sensitivity analysis, SC and ACH capacity

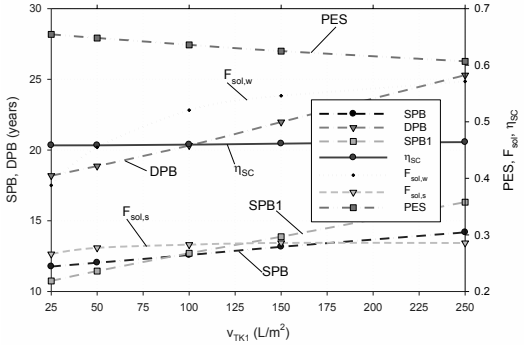

Figure 5 - Sensitivity analysis, TK1 Volume

Scuh increase is much more evident in case of winter solar fraction, due to the above discussed phase shift between solar irradiation and building space heating demand. Finally, a rigorous optimization was carried out using the TRNOPT [10], linking to the optimization algorithm called GENOPT [12]. The optimization operated on 6 variables: ASC, fACH, φP2, TSC,w,set , TSC,s,set and vTK1. Except for TSC,s,set the thermoeconomic optimization returned the optimal values corresponding to the considered lower bounds: ASC=200 m^2; fACH=0.20; φP2=25 kg/hm^2; TSC,w,set=50 °C; TSC,s,set=100 °C; vTK1=25 l/m^2, corresponding to a minimum value of SPB equal to 11.6 years. So, just a slight improvement in the optimum value of SPB was obtained, with respect to the initial value shown in Table 3, in fact, the initial configuration was very close to the optimum one, mainly due to the fact that SC area and ACH capacity were set at their lower bounds. Also, using SPB1 as objective function, the improvement found by the optimization are marginal. In this case, the optimal calculated variables are: ASC=1000 m^2; fACH=1.00; φP2=25 kg/hm^2; TSC,w,set=50 °C; TSC,s,set=100 °C; vTK1=25 l/m^2.

6. Conclusions

In the paper, a complete dynamic model of an innovative layout of a solar heating and cooling system was presented and used to develop a case-study, also including a parametric study and a detailed thermoeconomic optimization. The system, designed to provide just 20% of the maximum cooling load through the solar source, was capable to achieve a significant Primary Energy Saving (64.7%), with winter and summer solar fractions of 46.2% and 27.7%, respectively. Among the possible funding policies, it was found that capital investment subsidies could be more effective and rational than a feed-in-tariff. Future developments of this work include the investigation of high temperature SHC systems, as well as the use of a biomass-fired auxiliary heater.

Nomenclature

U Transmittance (W/m2K)
$\dot{Q}$ Heat flow (kW)
t temperature (°C)
$\dot{m}$ mass flow (kg/s)
c specific heat (kJ/kg K)
A Area (m^2)
ε Heat exchanger efficiency
PE Primary energy (kJ)
E_{el} Electrical energy (kJ)
η_{el} mean thermoelectric efficiency
Q Thermal energy (kJ)
C_{tot} Total cost (€/y)
C_{op} Operating cost (€/y)
J_i Capital cost (€)
c_{EE} Electricity cost (€/kWh)
c_{NG} Natural gas cost (€/Sm^3)
LHV Lower Heating Value (kWh/Sm^3)
COP Coefficient of Performance
η_c Boiler efficiency
G Solar radiation (kWh)
PES Primary energy saving
SPB Simple Pay Back (years)
DPB Simple Pay Back (years)
Fsol Solar Fraction
η_{SC} Solar Collector efficiency

subscripts

h heating
c cooling
in inlet
out outlet
w winter
s summer

References

[1] Agency, E.E., *Energy and environment report 2008*. 2008.
[2] Mateus, T., Oliveira, A.C., Applied Energy, 2009. 86: p. 949-957.
[3] IEA. *Solar heating and cooling. Ongoing tesearch relevant for solar assisted air conditioning systems. Technical Report Task 25: Solar Assisted Air Conditioning of Building.* October 2002; Available from: http://www.iea-shc.org/.
[4] Folrides, G.A., Kalogirou, S.A., Tassou, S.A., Wrobel, L.C., Solar Energy, 2001. 72(1): p. 43-51.
[5] Folrides, G.A., Kalogirou, S.A., Tassou, S.A., Wrobel, L.C, Applied Thermal Engineering, 2002. 22: p. 1313-1325.
[6] Ghaddar, N.K., Shihab, M., Bdeir, F., Renewable Energy, 1996. 10(4): p. 539-558.
[7] Atamaca, I., Abdulvahap, Y., Renewable Energy, 2003. 28: p. 1277-1293.
[8] Calise F., D.d.A.M., Palombo A., Vanoli L. *Simulation model and analysis of a small solar-assisted refrigeration system: dynamic simulation and optimization*. in *Proceedings of the ASME International Mechanical Engineering Congress & Exposition 2008 IMECE08*. 2008. Boston, USA.
[9] Calise, F., Palombo, A., Vanoli, L., *Maximization of primary energy savings of solar heating and cooling systems by transient simulations and computer design of experiments.* Applied Energy, 2009. In press.
[10] Solar Energy Laboratory, *TRNSYS. A transient system simulation program*: University of Wisconsin, Madison.
[11] Kakac, S., Liu, H., *Heat Exchanger Selection, Rating, And Thermal Design.*, ed. CRC Press. 1998.
[12] Wetter, M., *Design optimization with GenOpt*. Sept./Oct. 2000, Lawrence Berkeley National Laboratory.

Particle Swarm Optimization for the Optimal Sizing of a Solar Thermal Building Installation

R. Bornatico [a], *M. Pfeiffer* [a,b] *A. Witzig* [b] *and L. Guzzella* [a]

[a] *Institute for Dynamic Systems and Control ETH Zürich, CH-8092 Zürich, Switzerland*
[b] *Vela Solaris AG, CH-8400 Winterthur, Switzerland*

Abstract: In recent years the domestic energy management has become a non-trivial task as the number of available energy sources and system components involved have increased and all components have to operate coordinately in order to maximize global efficiency measures.
In this paper a methodology is presented for finding the optimal size of the main components for a solar thermal system where particular attention is given to the optimization framework. The use of the Particle Swarm Optimization (PSO) algorithm is proposed and the results obtained are compared with a Genetic Algorithm (GA) solution. Further, the relative influence of certain system parameters on the optimal configuration is investigated by means of a sensitivity analysis where the size of the collector is shown to have the greatest influence on all main output quantities while the size of the auxiliary power unit presents a relatively negligible influence on the solution.
Finally, it is demonstrated that the accurate sizing of the energy components is necessary to minimize the energy consumption and cost of installation, while maximizing the solar fraction. The proposed methodology is shown to successfully solve the problem.

Keywords: Particle Swarm Optimization, Polysun, Solar Combisystem.

1. Introduction

Solar energy for space heating and the production of Domestic Hot Water (DHW) has become an important factor in reducing the global CO_2 emissions. Within the previous and the last United Nations climate change conferences it has been analyzed what needs to be done to limit the long-term concentration of greenhouse gases in the atmosphere to 450 ppm of CO_2 equivalent, in line with a 2°C increase in global temperature by 2100. Solar energy is considered as one of the most promising candidates to tackle our dependency on and use of fossil fuels, and thus for reducing the related emissions. The International Energy Agency (IEA) with its Task 26 on Solar Combisystem emphasizes that if the direct use of solar energy for heating purposes is to make a significant contribution to the energy supply, it is necessary that solar-heating technologies be developed and widely applied over and beyond the field of DHW preparation only [1, 2]. Accordingly, the focus of this research has been set on a solar combisystem installation that simultaneously fulfills DHW and space heating needs. Previous publications on solar combisystems have presented analyses of geographic influences [3] and DHW load profiles [4] specifically on solar fraction and energy consumption. This paper considers a mid-sized single-family house located in Zurich, Switzerland, and presents a methodology for finding the optimal component sizes for a solar combisystem. All simulations are carried out with Vela Solaris Polysun®, which is a well-established software tool in the field of planning and optimization of building energy systems. The simulation kernel is based on a plug-flow simulation of the thermal system [5], and it uses statistical meteorological data as an input [6, 7].
This paper is structured as follows: In the following section the modeling assumptions and the simulation set up are presented. Section 3 describes the optimization framework and all parameters necessary for the optimization routine to succeed. Section 4 describes the main features of the PSO algorithm used and introduces the subsequent results section.

2. Modeling and Simulation

The simulation software Polysun offers a broad range of functionalities required for the analysis and design of domestic energy systems. In the Polysun catalogues, a variety of components is available with all characteristic data and efficiency maps nec-

Corresponding author: Raffaele Bornatico, Email: rbornati@ethz.ch

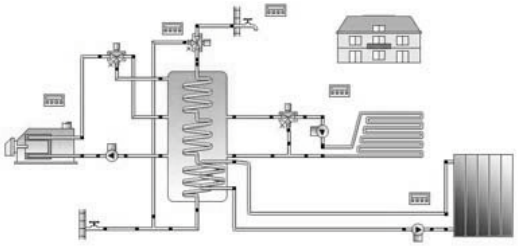

Figure 1: A model of a solar combisystem using Polysun

essary for the hydronic and thermal analysis of such systems. Also possible are analysis and design of photovoltaic systems, solar cooling, and combinations of solar thermal and heat pump systems.

Polysun calculates all relevant system parameters related to the production of heat and electricity. It also comprises the calculations for system amortization and the data required for subsidy applications. The variable step solver adapts the simulation step size down to a minimum of 4 minutes. Clearly, a sufficiently good precision of the system's simulated characteristics and in particular of its dominant transients can be assumed. The user friendly interface of Polysun allows for the easy parameterization of the system, while the software itself is capable to output and store practically any relevant physical quantity in convenient data formats. Furthermore a mean simulation time of 1 minute for a one-year simulation makes the software Polysun an ideal platform to perform the mentioned analyses [7].

The setup of the solar combisystem used in this research is depicted in Fig. 1. Leftmost is the Auxiliary Power Unit (APU) and rightmost is the solar collector. Both components are connected to the storage tank in the center of the picture. The loads are characterized by a DHW and a space heating demand. The DHW profile used divides 200 l/d of water at 45°C into the periodic daily demand depicted in Fig. 2. The effects of using a realistic profile as opposed to a conventional profile are discussed in detail in [4], where it is shown that the heat demand difference between the two profiles is 0.1% and the fractional energy saving difference is just around 1.5% when using a flow regulation device. The greatest influence is shown to be caused by the reduced demand during the summer holidays in the realistic profile. Considering that with Polysun absences can be included in the simulations, it is reasonable to assume that the profile used hereafter approximates sufficiently well a real DHW load.

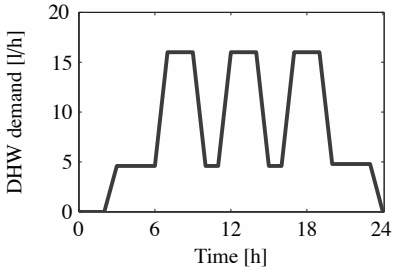

Figure 2: Daily domestic hot water heat demand

Energy for space heating is less straightforward to determine since it depends on current ambient temperature and house insulation parameters for ensuring a heating set-point temperature of 20 and 18 °C during day and night, respectively. The resulting simulated heating requirements are shown in Fig. 3 and introduce the importance of the availability of comprehensive meteorological data.

2.1. Statistical Meteorological Data

To a large extent, the accuracy of solar system simulations for a given location depends on the availability of realistic data for solar irradiation, humidity, etc. In Polysun, meteorological data are provided by the Meteonorm database [8] containing data based on measurements from 8,055 weather stations worldwide. For any given location, the data of the closest weather stations are interpolated. The generation of yearly series of weather data utilizes stochastic models, where stored monthly mean values and Markov Transition Matrices are used to generate hourly weather data [9, 10]. The resulting hourly data have the same statistical properties as the measured data (i.e. average value, variance, autocorrelation), and thus represent an accurate approximation. In Fig. 4, the outdoor temperature and global irradiance time series are shown over a one-year period.

3. Optimization Framework

The main components of the system as presented in the previous section are the collector, the tank, and the APU. In order for these components to be optimally dimensioned, the corresponding sizes have to populate the input parameter set that is fed to the simulation kernel. In Table 1 the input set is listed together with the corresponding minimal and maximal values used throughout this work. The extreme values for the output set shown in Table 2 do not represent a given constraint.

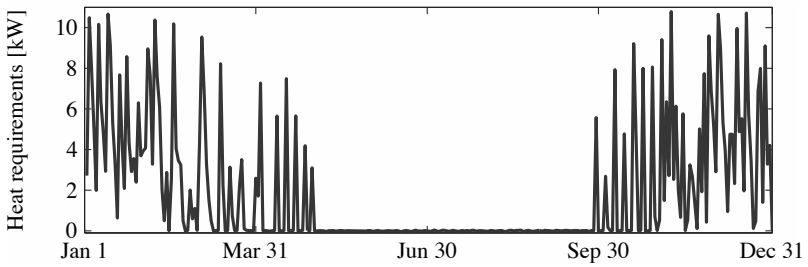

Figure 3: Yearly heat requirements for space heating in a mid-sized single-family house

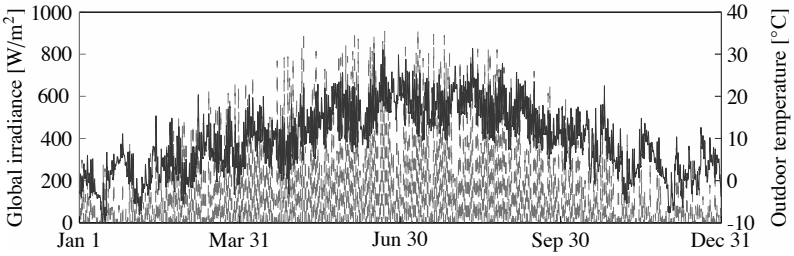

Figure 4: Meteorological data for Zurich, Switzerland. Solid line: outdoor temperature, dashed line: global irradiance

Table 1: Input parameter set

Item	Symbol	Min / Max	Unit
Collector area	ϑ_1	1 / 50	m^2
Tank volume	ϑ_2	100 / 5000	l
APU size	ϑ_3	5 / 250	kW

Table 2: Output parameter set

Item	Symbol	Min / Max	Unit
Solar fraction	f_1	2.8% / 42.7%	-
Energy	f_2	12'988 / 45'407	kWh
Cost	f_3	12'988 / 46'226	€

Rather, these values have been obtained from simulations throughout this work. They are to show that the investigated range for these values is significant. The goal of the optimization routine consists of finding the parameters ϑ^{opt} that minimize a general function $f : \mathbb{R}^n \rightarrow \mathbb{R}$ that is formulated in the canonical form as follows:

$$\begin{aligned} \min_{\vartheta} \quad & f(\vartheta) \\ \textit{subject to} \quad & g(\vartheta) \quad < 0,\ h(\vartheta) = 0. \end{aligned} \tag{1}$$

The functions g and h include all constraints to the problem defining the set Θ of the acceptable $\vartheta \in \Theta$. These constraints include the boundary values of ϑ and two physical constraints on the system. First, for a given ϑ to be acceptable, the heat requirements for DHW and space heating must be satisfied. Secondly, the temperature of the fluid flowing in the collector must not exceed the 100 °C threshold for longer than 1% of the simulation time. This last condition limits the stagnation time to reasonable values, thereby ensuring the safe operation and a long life of the collector.

In the presented problem a numeric optimization is necessary because an algebraic solution to the problem does not exist. Furthermore it is clear that the topographical properties of the function f play a crucial role in how the optimization algorithm converges from starting values ϑ^0 towards ϑ^{opt}, and also that the choice of the right cost function is determinant for the successful convergence of the algorithm to the point of interest. Accordingly, all relevant quantities should appear in the cost function. In the case of the optimization of the combisystem, the objectives of the authors are to maximize the solar fraction, to minimize the total energy use, and to minimize the additional cost of the installation.

$$f(\vartheta) := \left\{ y \mid y = \sum_j w_j \cdot \frac{f_j(\vartheta)}{f_{jmax}} \right\} \tag{2}$$

Therefore, the rather intuitive linear form (2) is chosen where the solar fraction term $f_1(\vartheta) = SFn(\vartheta)$, the total energy use of the system $f_2(\vartheta) = Etot(\vartheta)$ and the cost of the installation $f_3(\vartheta) = Cost(\vartheta)$ depend on the sizes of the components ϑ. Since a scalar value of f is required by the minimization algorithm, the weighted sum, with weights w_i of the normalized f_i, yields a dimensionless, normalized cost function $f(\vartheta)$. Note that in order to maximize the solar fraction by a minimization of f a negative weighting value for w_1 must be used. An important result from a user's point of view is the pricing of the components. This term is based on a linear pricing assumption for each component and on current oil prices. This choice is shown in [11] to produce meaningful results. The relevant values used for the installation pricing are listed in Table 3.

Table 3: Relevant factors for component pricing

Item	Value	Unit
Collector	100	€
Collector	360	€/m^2
Storage tank	4.22	€/l
APU	50	€/kWh
Heating oil	10.5	kWh/l
Heating oil	0.85	€/l
Maintenance	100	€/year

4. Particle Swarm Optimization

The analogy of a swarm of bees having the common goal of finding the region with the best flowers is useful to picture how the algorithm converges towards an optimal solution. The communication between particles and the memory of the particles are assumed to be ideal in the sense that each particle i remembers where its personal best (P_i) had been found and where the global best of the entire swarm up to iteration k (G) is. Starting with random initial velocities v_i^0 and random initial positions p_i^0 inside a closed set, the basic PSO algorithm computes the velocity and position of the i-th particle, $i = 1, 2, ..., n$ for every iteration $k = 0, 1, 2, ...k_{max}$.

$$v_i^{k+1} = v_i^k + \gamma_{1i}\left(P_i - p_i^k\right) + \gamma_{2i}\left(G - p_i^k\right) \quad (3)$$

$$p_i^{k+1} = p_i^k + v_i^{k+1} \quad (4)$$

The random numbers $\gamma_{1,2} \in [0, 1]$ influence the magnitude of the two vectors $\left(P_i - p_i^k\right)$ and $\left(G - p_i^k\right)$, thus influencing indirectly the magnitude and direction of v_i^{k+1}. Figure 5 depicts how the update from k to $k + 1$ is performed for a simplified two dimensional problem with no randomness $\gamma_{1,2} = 1$. Note that every dimension represents a system parameter to be optimized.

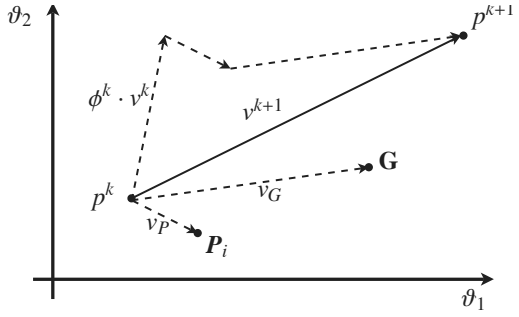

Figure 5: Simplified PSO iteration in two dimensions

The common PSO algorithm includes three more parameters, namely an inertia function ϕ^k and two acceleration constants $\alpha_{1,2}$. The inertia function is usually linearly decreasing with respect to iterations, thus reducing the influence of past velocities, thereby enabling the algorithm to adapt also to small regions as the optimization converges. This adaptation capability is a key advantage over more sophisticated algorithms such as Genetic Algorithms (GA) since it makes the use of hybrid methods unnecessary, for instance in combination with gradient search algorithms. The resulting velocity equation, together with the position update, represents the core of the PSO algorithm [12, 13].

$$v_i^{k+1} = \phi^k v_i^k + \alpha_1\left[\gamma_{1i}\left(P_i - p_i^k\right)\right] + \alpha_2\left[\gamma_{2i}\left(G - p_i^k\right)\right] \quad (5)$$

$$p_i^{k+1} = p_i^k + v_i^{k+1} \quad (6)$$

Further extensions of the algorithm can include natural selection considerations such as a varying population size where bad particles are killed and new particles are generated in the vicinity of the global best. Note that in this case the comparative advantage with respect to GAs in terms of the number of parameters of the algorithm is reduced. The work of Clerk and Kennedy [14] clearly describes the importance of constraints on the velocity vector. Their work shows that if no constraints are set the algo-

rithm can become unstable. In the problem presented here a linearly decreasing inertia function already accounts for stability, since the introduction of velocity limits can be shown to be a loose constraint. In this work a fixed population of 20 particles has been deemed to be sufficiently effective.

5. Optimization Results

The results reported in this section have been based on simulation results of the software Polysun when simulating the model presented in Section 2. The converged results of the minimization of (2) by means of the PSO algorithm are presented in 5.1, while results obtained using a genetic algorithm follow in Section 5.2. A detailed analysis of the results is presented in the form of a sensitivity analysis, which concludes this section.

5.1. Particle Swarm Optimization

The minimization of the cost function by means of the PSO algorithm is shown in Fig. 6. The cost function is plotted against particle generations where each generation consists of 20 particles. Note that points which do not satisfy the optimization constraints have been omitted. By means of an averaged value for each generation and by considering the variance around this value, it is possible to visually judge the convergence of the algorithm. The average line is shown in red in all Figs 6 to 9. The PSO algorithm converges towards a minimal cost function value of $f^{opt,PSO}(\vartheta) = 1.798$ and the interpretation of this value, with respect to its physical terms, is presented in Table 4. The initial population was randomly selected inside the boundary values of Θ. It follows that the results before the optimization as reported in Table 4, are averaged values of the feasible points of the initial population. Figure 7 illustrates the convergence of all particles, for all parameters considered in this study. It can be seen that after 25 generations the algorithm has already converged to the vicinity of the optimal values which settle after 55 generations to the optimal values $\vartheta^{opt,PSO} = \{13.7m^2, 1010l, 9.7kW\}$.

Table 4: PSO optimization of cost function terms

Term	Before / after optimization	Improvement
f	2.152 / 1.798	−16%
SFn	16.8% / 22.7%	+35.1%
$Etot$	17'865 / 16'533 kWh	−7.5%
$Cost$	24'807 / 10'896€	−56.1%

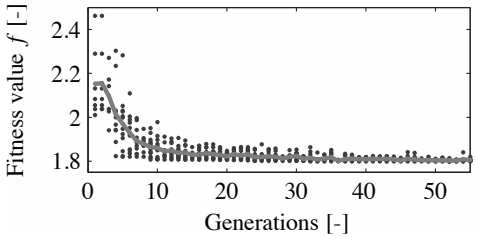

Figure 6: Cost function minimization with PSO

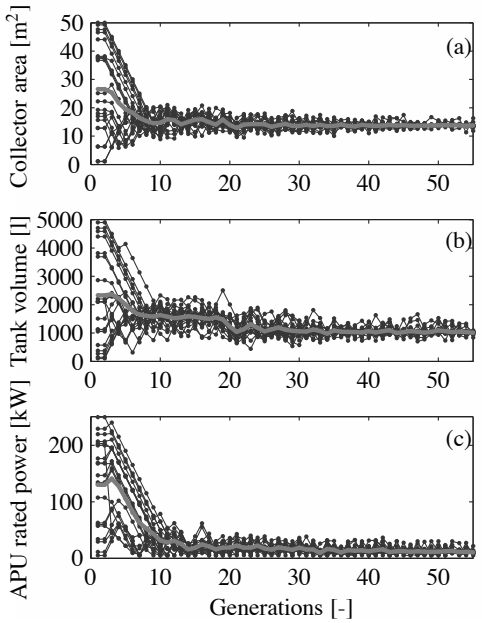

Figure 7: PSO convergence of system parameters towards 13.7 m^2 (a), towards 1010 l (b), and towards 9.5 kW (c).

5.2. Genetic Algorithm Optimization

On the same problem a standard GA has been applied where, if applicable, the same optimization parameters as in the PSO were used, specifically, a population of 20 particles and the same parameter set boundaries. In this case also, the fitness function decreases towards a minimal value of $f^{opt,GA}(\vartheta) = 1.799$, a value that is consistent with the result of the PSO optimization. The comparison of all other optimal cost function terms between PSO and GA shows that the two solutions differ by a minimal amount only.

Also shown in Figs 8 and 9 is the value averaged over the generations averaged value represented by the thickest line. Figure 9 shows that the evolution of all parameters is comparable to those obtained with the PSO optimization as the algorithm

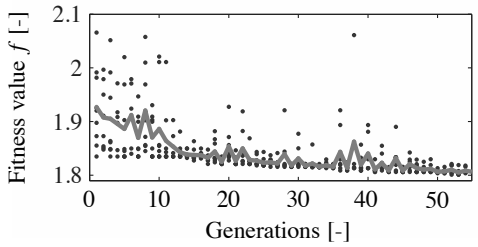

Figure 8: Cost function minimization with GA

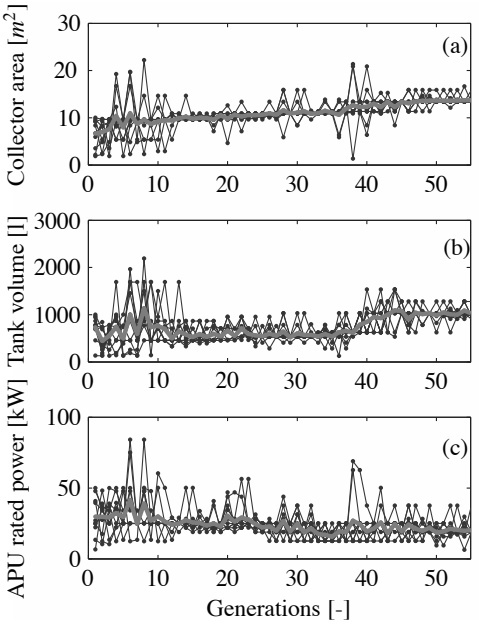

Figure 9: GA convergence of system parameters towards 13.4 m^2 (a), towards 905 l (b), and towards 17.2 kW (c)

converges toward an optimal value of $\vartheta^{opt,GA} = \{13.4m^2, 905l, 17.2kW\}$.

A slight difference in the optimal parameters obtained for the tank volume and the size of the APU can be noticed. However, this does not influence significantly the cost function values, thus proving that both algorithms converge to a similar solution. Nevertheless more than 45 generations are needed for a stable solution highlighting, in this case, a twice slower convergence than the results obtained by using the PSO algorithm.

5.3. Sensitivity Analysis

A sensitivity analysis has been performed in order to investigate the relative influence of each parameter on the optimal solution. The variation of each output f_j is measured after a 10% increase in each parameter ϑ_i. The optimal PSO values $\vartheta_i^{opt,PSO}$ and $f_j^{opt,PSO}$ have been used for this analysis

$$S_{ij} = \frac{\Delta f_j / f_j^{opt,PSO}}{\Delta \vartheta_i / \vartheta_i^{opt,PSO}} \quad (7)$$

The sensitivity results are shown in Fig. 10 for each output. The sensitivity of the solar fraction S_{i1} is depicted in Fig. 10 (a) where it can be seen that an increase in collector size as well as an increase in tank volume have a positive effect on the solar fraction. However, an increase in APU size in the vicinity of the optimal solution does not affect the solar fraction. As Fig. 10 (b) shows, the size of the collector and the tank volume influence in a similar way the total energy consumption as a consequence of a greater amount of solar energy exploitation capability, whereas with an increased APU size, the value

Table 5: GA optimization of cost function terms

Term	Before / after optimization	Improvement
f	1.927 / 1.798	-7%
SFn	13.3% / 22.3%	+67%
$Etot$	18'168 / 16'573kWh	-8.8%
$Price$	8'361 / 10'732€	+28%

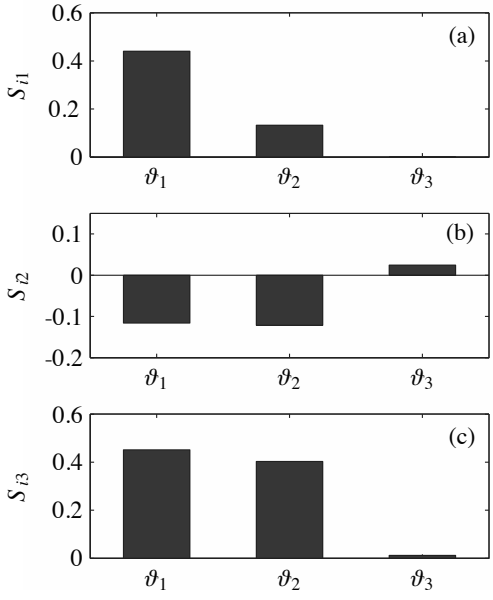

Figure 10: Sensitivity of the optimal solar fraction (a), total energy consumption (b) and price of installation (c) related to a 10% increase of collector size ϑ_1, tank volume ϑ_2, and APU rated power ϑ_3

of *Etot* increases as a result of a larger consumption of heating oil. Figure 10 (c) shows that the increase in collector size has the greatest relative influence on the cost of the installation. The tank volume has a slightly smaller influence, while the influence of the APU size in all measures is relatively low.

6. Conclusions and Outlook

In this paper a method for the optimization of a solar thermal system has been presented. The system investigated is a solar combisystem for a mid-sized single-family house in Zurich, Switzerland. While the optimization framework is in principle independent of the type of optimization algorithm used, a detailed analysis has been carried out on the performance of the Particle Swarm Optimization algorithm when it is applied for solving this problem. The results are comparable to those obtained with the more common Genetic Algorithm. When the implementation efforts and the computational power demand are considered as well, the PSO is a better algorithm for solving the problem presented, especially since the PSO converges to the optimal solution twice as fast as the GA. A collector size of 13.7 m^2 together with a tank volume of 1'010 l and an APU of 9.7 kW, are the optimal sizes for the main system's components, which lead to a solar fraction of 22.3 %, a total energy use of 16'573 kWh and a cost of the installation of 10'732 €. The sensitivity analysis of this solution confirmed that the size of the collector has the greatest influence on the solar fraction and the installation cost, while for energy use and installation cost the influence of the tank volume is significant as well. The size of the APU has a relatively negligible effect on the solution.

While the work presented takes into account the main system components only, its continuation will include all system parameter influences, targeting the creation of parametric models capable of describing arbitrary systems. The final model is then to be optimized with respect to the concurrent goals of high simulation speed and maximum accuracy of the results.

Nomenclature

p Particle position

v Particle velocity

w Cost function weighting factor

SFn Solar fraction

$Etot$ Total energy consumption

Greek Letters

α Acceleration factor

ϕ Inertia

γ Random factor

ϑ System parameter

Θ System parameter space

Subscripts and superscripts

i Particle index

j Cost function term index

k Iteration step

0 Initial

opt Optimal

References

[1] E. Sawin et al. Final Copenhagen Accord. *Sustainability Institute Press Release*, 2009.

[2] J.M. Suter et al. IEA SHC task 26, solar combisystems. *Buro N+1, Bern, Switzerland*, 2000.

[3] P.D. Lund. Sizing and applicability considerations of solar combisystems. *Solar Energy*, 78:59–71, 2005.

[4] U. Jordan and K. Vajen. Influence of DHW load profile on the fractional energy savings: a case study of a solar combi-system with TRNSYS simulations. *Solar Energy*, 69(1-6):197–208, 2000.

[5] S.A. Klein et al. TRNSYS, a Transient System Simulation Program. User's Manual (ver 14.2). *Solar Energy Laboratory, University of Wisconsin-Madison*, 1997.

[6] J.A. Duffie and W.A. Beckman. *Solar Engineering of Thermal Processes, 2nd ed*. Wiley Interscience, New York, NY, 1991.

[7] A. Witzig et al. Simulation tools for architects: Optimization of active and passive solar use. In *Proc. of CISBAT 2009*, 2009.

[8] Meteonorm Database. *Provided by Meteotest, Bern, Switzerland*.

[9] Meteonorm Handbook, part 2: Theory. *Meteotest, Bern, Switzerland*, 2000.

[10] R. Aguiar and M. Collares-Pereira. A simple procedure for generating sequences of daily radiation values using a library of Markov transition matrices. *Solar Energy*, 40(3):269–279, 1988.

[11] G. Fraisse et al. Comparative study of various optimization criteria for SDHWS and a suggestion for a new global evaluation. *Solar Energy*, 83:232–245, 2009.

[12] B. Birge. PSOt - a Particle Swarm Optimization toolbox for use with Matlab. pages 182–186, 2003.

[13] D. Bratton and J. Kennedy. Defining a standard for particle swarm optimization. pages 120–127, 2007.

[14] M. Clerk and J. Kennedy. The particle swarm explosion, stability, and convergence in a multidimensional complex space. *IEEE Transactions on Evolutionary Computation*, 6(1):58–73, 2002.

Acknowledgments: This work has been funded by the Swiss Innovation Promotion Agency CTI, whose support is gratefully acknowledged. The authors would like to thank all the members of the Vela Solaris team and IDSC staff for their help in this research.

Experimental comparison of two domestic heating systems: floor heater and radiators

Daniele Fiaschi [a]

[a] *Università degli Studi di Firenze, Dipartimento di Energetica "Sergio Stecco"*
Via C. Lombroso 6/17 – 50135 Firenze – Italy – email: daniele.fiaschi@unifi.it

Abstract: Floor heaters are increasing their attractiveness in space heating, due to their low operating temperature, that makes them suitable for joining low temperature heat sources. For this reason, often manufacturers tend to address their use to a large field of applications with rather aggressive promotional campaigns, that often miss technical data that reliably address their performance under several possible conditions and required daily and seasonal room temperature profiles.

So, a test rig consisting of two equal 16 m^2 footstep and 3 m height rooms, one equipped with floor heater and the other one with two low temperature radiators and the related measurement and data acquisition chain was set up and a four months test campaign was carried out. In these tests, several different daily room temperature profiles were set up and the heat consumption of the two heating systems under representative time intervals through different seasonal environmental conditions was determined. The water flowing through radiators and floor heater was heated by two equal heat pumps and the inlet/outlet temperature was monitored, as well as their electrical consumption. By the use of these data and heat pumps performance datasheet, the heat input to radiators and floor heater in the two rooms was determined, under the different temperature profiles of the two rooms. Thus, the overall daily consumption of the two heating systems in the selected seasonal representative days was determined.
The results of measurements evidenced reduced heat consumption for radiators, ranging from 4 to 40%. The floor heaters consumption is reduced when relatively constant room temperature profiles are adopted (i.e. continuous operation), while the gap with radiators increases with variable profiles (i.e. discontinuous operation). These remarkable differences were partially attributable to the different external heat loss of the two rooms. In fact, despite of their equal walls material, geometry and size, the floor heated room showed consistently higher heat losses through the floor (about 30-40% of total), due to the higher downstairs wall temperature. It suggests that under continuous operation floor heating is less energy demanding, provided that it is not placed above a non heated room or enough insulation is adopted.

Keywords: Floor heating, Domestic heater, Radiant panels, Radiators, Heat pump, Building heat loss

1. Introduction

Use of low grade heat for building heating is a topic of last ten years' research programs, also in the view of joining and integration of renewable heat sources like solar thermal, geothermal heat pumps and so on [1]. In the traditional building heating systems, based on radiators, water is typically supplied in the 80 – 90 °C range and returned in the 50 – 60 °C range. In this way, the ΔT between the heat source and the air into living rooms is about 50 °C, which is a source of primary exergy degradation and discomfort in some cases [1]. The increased insulation levels of modern buildings also gave a noticeable contribution to savings in primary energy supplied to building heaters, which allowed further reduction in average room temperature. It gave a remarkable contribution to the use of low grade heat, with subsequent reduction of heating surfaces temperature [1, 2]. On the basis of supply/return (S/R) water temperature range, the building heat emitters may be classified as [1, 3]:

- High temperature (HT, S/R=90/70 °C);
- Medium temperature (MT, S/R=55/35-40 °C);
- Low temperature (LT, S/R=45/25-35 °C);
- Very Low temperature (VLT, S/R=35/25 °C).

Generally, the ways to reduce the temperature of heaters emitting surface are to increase the surface itself or blowing air on it, in order to sum the effects of forced convection [4]. Exploiting the contribution of radiant heat transfer between emitting and room surfaces is the most interesting feature of floor heating systems, that are largely diffused as LT and VLT, especially in northern Europe countries [2, 3]. They can also provide occupants with a comfortable, clean and healthy environment. They are, however, slow in temperature adjustment required in frequent daily variable temperature profiles and require rather large investment cost, often prohibitive in existing buildings

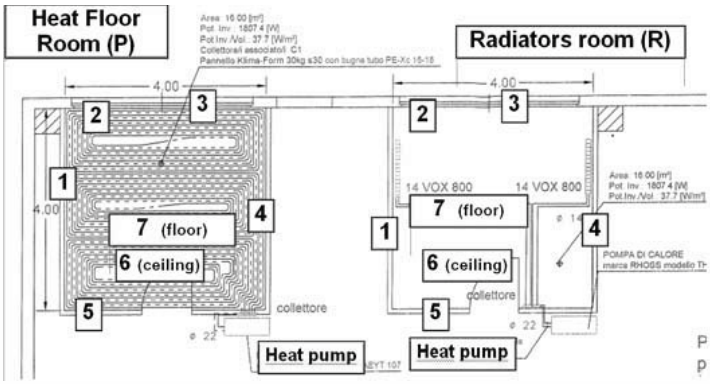

Figure 1 – schematic of the two experimental rooms

under partial restoring. Manufacturers of these systems often claim their higher efficiency over traditional ones with radiators, without providing clear operating conditions to support this outcome [5, 6]. On the other hand, only a little scientific literature is available about low temperature radiators and their performance (both in terms of comfort and energy consumption) compared with traditional HT ones, floor heating and hybrid systems [2, 3, 4]. Myhren and Holmberg [3], in a study about flow patterns and thermal comfort, compared four heating systems, two of which with HT and LT radiators, one with LT floor heating and one with LT wall heating into an office room. They concluded that all investigated system gave acceptable indoor climate, even though large heat transferring surfaces at low temperature have weaker counteraction of cold downflow from air suppliers.

Hasan et al. [2] analyzed a combined low temperature system consisting of radiators (LT and HT) and floor heating into an apartment building in Finland and found that drifts and ramps in operative temperature were all within the limits of ASHRAE Standard 55-2004. Anyway, the floor heating system produced higher fluctuations of the indoor air temperature compared to radiators, whereas the vertical temperature profile revealed only very small difference, that would not produce any significant discomfort.

The main goal of this paper was to give a contribution to the lacks of literature, specially focused to energy consumption aspects, by the experimental comparison of the behavior of two identical test rooms, one of which equipped with floor heating and the other one with MT and LT radiators. These came from standard current production ones, with radiant surface increased by 10 – 30 % with respect to HT versions. The tests were carried out for a 3 months long time, under some different climatic and operating conditions. These tests were performed by comparing two commercial systems, at current production and technological level, in order to assess their critical aspects in energy consumption and to address some good practice of floor heating, often neglected in their installation and utilization.

2. Experimental setup

The experimental apparatus was made of two identical rooms of 4 x 4 m footstep by 3 m height, the first one heated with floor heaters (i.e. radiant Panels P) and the second one with two radiators (R). Not people nor other heat source was present into the rooms during tests (doors were locked). The water flowing into these systems was heated by two identical heat pumps (RHOSS THAEYT 107 model), in order to represent a possible realistic MT/LT building heating system. At the same time, instantaneous electric power input can be easily monitored. The two test rooms were placed at the first floor, within a big unheated store, where the temperature was monitored. The schematic of the two rooms and the related heating systems are shown on figure 1.

The following parameters were measured during the day, with 5 minutes time intervals:

- Supply/return water temperatures from the two heating systems;
- Rooms temperature;
- Local temperature outside rooms (i.e. in different points of the store in the near of test rooms);
- Power and electrical consumption of the two heat pumps.

Hot water temperatures at heating systems supply and return was measured by diving probes equipped with thermal resistance (certified PT100 ±0.5 °C precision). The same kind of sensors were adopted for measurement of rooms temperature.

The measurements consisted of continuously monitoring and recording the above listed parameters.

The tests were carried out along a 3.5 months time period, where five different ways of conduction of the heating systems were setup. The daily ON/OFF timetable, summarized on table 1, corresponds to common practice of several domestic heating plants. The rooms switch on temperature was fixed at 20 °C.

Table 1 – timetable and modes of test campaign

Mode and time	Hour 1 2 3 4 5 6 7 8 9 10 11 12 13 14 15 16 17 18 19 20 21 22 23 24 (ON / OFF; $T_{setpoint\,rooms}$ = 20°C)
1 (19 Feb – 20 Feb)	Continuous operation (ON/OFF regulation of radiators circulation pump)
2 (24 Feb – 03 Mar)	ON/OFF regulation of radiators circulation pump
3 (04 Mar – 18 Mar)	Radiators control by 3 way valve and circulation pump always ON
4 (19 Mar – 08 Apr)	Radiators control by 3 way valve and circulation pump always ON
5 (09 Apr – 05 May)	ON/OFF regulation of radiators circulation pump; T_{mR}=45°C, T_{mP}=35°C

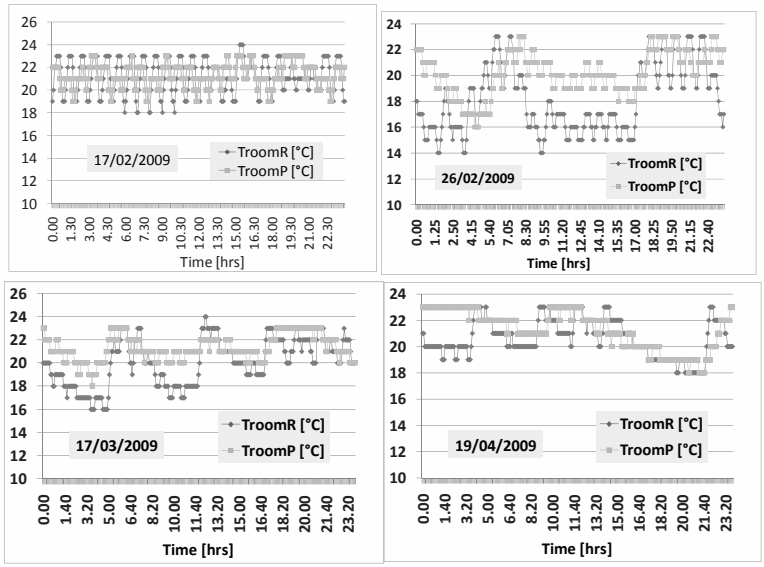

Figure 2 – rooms temperature profiles along 4 sample days

The comparison of the two heating systems was based on the evaluation of the heat consumption of each one along five days, selected in order to be representative of the five conduction modes. These days were identified by a particular data selection criterion, which allowed the cutoff of bias affected or unreliable measurements daily series.

3. Data selection criteria

The measurements performed with the experimental setup and guidelines described in the previous chapter allowed the collection of almost 230000 data in the test campaign time period (February – May, 2009). All of these data were average values referred to time steps of five minutes, collected along 24 hours a day. The choice of an effective criteria for the selection of a consistently reduced number of data that were sufficiently representative of the five different conduction modes of heating systems, was necessary to allow a concise, significant and effective analysis. As the main objective of measurements was the comparison of primary heat consumption of the two heating systems, the selected sample days had to satisfy two basic requirements:

1) To be reliable and bias free;
2) To be representative of different measurement times;
3) To have comparable temperature profiles of the two different rooms, in order to ensure the same useful effect of the heating systems, at least from the energy consumption point of view.

The chosen criteria of data treatment lead to the selection of five sample working days, representative of the five different working modes and times: 17th and 26th February, 17th March, 1st and 19th April. The temperature profiles of rooms in four of these days along the 24 hours are shown on figure 2. The temperature profiles of water supply and supply – return temperature difference for the two heating systems, as well as hosting store temperature (T_{store}, outside the rooms) in four of the selected sample days are shown on figure 3.

4. Results: comparison of heat consumptions of the two heating systems

In order to have an accurate evaluation and comparison of the energy consumption of the two heating systems, it was necessary to calculate the actual heat input from heat pumps. From the measurements, their electric power demand within all time intervals was known. Thus, as I/O temperatures of hot water was measured as well, it was possible to calculate the heat input to the

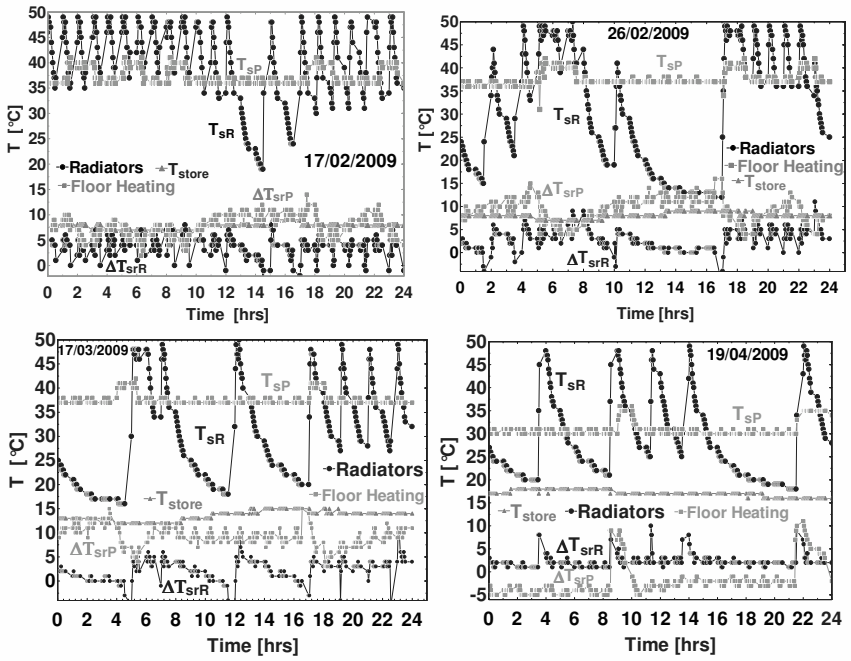

Figure 3 – water supply temperatures, radiators and panels ΔT supply-return and T_{store} in 4 sample days

heating plants by the use of heat pumps working chart [7], which provides COP and electrical consumption as functions of external room temperature (evaporator, T_{store}) and condenser outlet water temperature (i.e. supply temperature to heaters). It was done by a dedicated code, which is able to solve the heat pump thermodynamic cycle with R410A as working fluid under design and off design conditions, once I/O water temperatures, design conditions and working chart are provided. As the scroll compressor equipping the heat pump has variable performance with working conditions (i.e. pressure ratio determined by the room external and hot water temperatures and flowrate), it was taken into account providing isentropic efficiency of compression by a function accounting for pressure ratio and flowrate, built from a set of experimental data from literature [8].

The developed calculation model was also able to provide the uncertainty analysis on the calculated parameters (mainly heat consumption of the two heating systems), starting from the uncertainties on the basic measurements like water flows temperatures, internal and external rooms temperatures. The evaluation of uncertainty was necessary to ensure that the differences found in heat consumption of the two investigated systems did not fall within the uncertainty range, with subsequent unreliability of results.

The electric power actually converted into the heat delivered to the rooms' heating systems is only that due to the compressor, not including auxiliaries (substantially the water circulating pumps). Thus, their power consumption (180 W [7]) was subtracted from the measured heat pumps electric absorption, which was inclusive of auxiliaries.

The behaviors of thermal power input to the heating systems of the two rooms (Q_R and Q_P for radiators and floor heaters respectively) and the uncertainty bars along the 24 hours of two of the selected sample days are shown on figure 4 (working modes 1 and 3 of table 1). In mode 1 (continuous, figure 4a), it is evident that radiators turn on more frequently than floor heaters, but at reduced power input. Moreover, floor heaters show an almost permanent base load of 0.5 – 1.5 kW, also when radiators are turned off. In mode 3 (discontinuous, figure 4b), in the first time period of room heat demand (5 – 8 hrs), radiators turn on twice at the maximum power input (8 – 9 kW) and twice at intermediate values (3 – 5 kW). In the same time, floor heaters turn on 3 times at maximum power (at the beginning of the interval) and some other times at lower power (0.5 – 1.5 kW). In the middle day hours (8 – 17) radiators turn on once only at top power (8 – 9 kW), whereas floor heaters turn on roughly once per hour at minimum power (0.5 – 1.5 kW). Finally, in the last 17 – 23 hrs time period, radiators turn on four times at maximum power, whereas floor heaters, after the initial activation at 9 – 10 kW, turn on every two hours at 1 – 2 kW. This operating mode is quite characteristic of floor heaters that, after having satisfied the required room temperature with the initial activation at high power, are subsequently turned on at very reduced power, as a result of their higher thermal inertia [2].

The relative uncertainties on Q_R and Q_P generated by the uncertainties on measurements of radiators and floor

heaters supply/return temperatures, range between 4 and 4.5 %, with higher values at higher heat input. The magnitude is at the same level for floor heaters and radiators. Generally, it is substantially lower than the differences found for the two investigated heating systems, which confirmed the reliability of comparison.

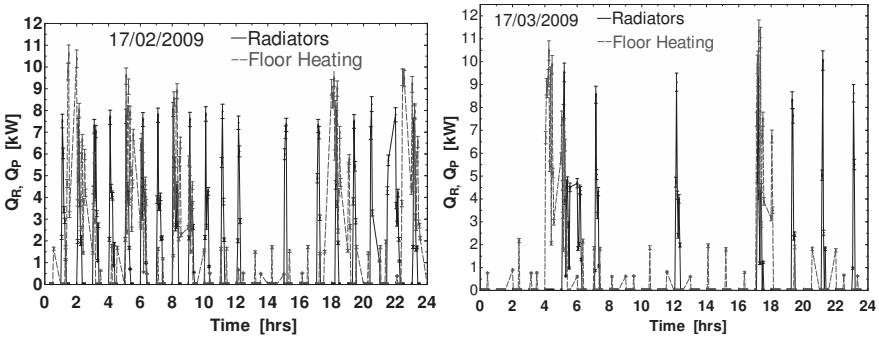

a) continuous operation, mode 1 *b) discontinuous operation, mode 3*

Figure 4 – heat power input from heat pumps along two sample days of measurements

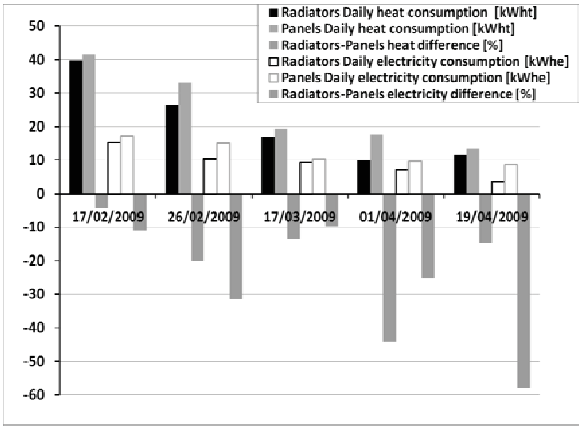

Figure 5 – radiators and panels daily heat and electricity consumption

The same results were achieved on the other investigated operating modes 2, 4, 5, here not shown for the sake of brevity.

The heat transferred by the heat pumps to the heating systems through the 24 hours of the five selected representative days, is their actual daily consumption and the basis for the comparison of the two investigated heating systems. It is summarized on figure 5. Higher daily heat consumptions were found for floor heaters, varying from 4 to 44%, depending on the considered working mode. The lowest differences were found in mode 1 (continuous operation) whereas the gap consistently increases moving toward discontinuous conduction. It confirmed the attitude of floor heating to steady working conditions [2].

The difference in energy consumption between the two systems were reduced when outside rooms temperature increased, due to the reduced heat demand. It happened in warmer days of early spring like 17/03/2009 and 19/04/2009. It is mainly attributable to two effects:

1) Lower COP of radiators heat pump (range 3÷3.5 vs. 3.5 – 4 of floor heaters), due to the higher working temperature, which leads to a reduced heat input to radiators. From the overall system point of view (i.e. heat generator + heating system), it could be regarded as a confirmation that radiant panels match better heat pumps.
2) Lower electricity consumption of the circulating pumps in the radiators plant, which was subtracted in the calculation of heat input from heat pumps. Their overall incidence on electric energy consumption amounts to 5 – 10% for panels and 2 – 5% for radiators, due to different head losses in the hydronics.

5. Heat losses of the two rooms

In order to verify that the comparison of the investigated heating systems was done in the same conditions (at least approximately), the evaluation of heat losses of the two test rooms was carried out. They are practically identical and made of the same building materials, but their slightly different placement within the store could potentially lead to some cases with not negligible differences in heat losses.

For these reasons, a heat transfer model of the two rooms was built. It was based on natural convection through the three lateral vertical walls inside the store, not exposed to wind forced convection (1, 4, 5 figure 1). The window (3, 2.88 m^2 surface) and the wall (2) shared with the store (figure 1), were modeled as vertical walls exposed to the action of forced convection, due to local average wind velocity. The resulting overall heat transfer coefficient was quite higher on the last ones. The heat transfer through the two horizontal walls (ceiling 6 and floor 7 of figure 1) was evaluated with natural convection models on horizontal walls, with hot side on the top for floor and on the bottom for ceiling. In the determination of the overall walls heat transfer coefficient, the radiant

contribution of those directly exposed to surfaces with appreciably different temperatures, like the (2) vs. sky, the (1) of panels room vs. external store wall and the roofs (6) vs. store roof.

Table 2 – resistance and heat transfer coefficients of rooms' walls

Wall number	R [K m^2/W]	U_P [W/K m^2]	U_R [W/K m^2]
1	1.88	0.37	0.31
2	3.09	0.25	0.24
3	0.305	2.16	2.16
4	1.88	0.32	0.37
5	1.88	0.32	0.31
6	1.88	0.28	0.28
7	1.18	0.78	0.39
Average rooms		0.47	0.39

The environmental temperature outside the store was assumed on the basis of local data from a near meteorological station. It was daily variable in the range -1 ÷ 12 °C on 17/02 and 26/02 and in the range 7 ÷ 18 °C on 17/03, 01/04 and 19/04.

The thermal resistance of lateral walls, window, floor and ceiling were provided by the manufacturers of the two boxes and are shown on table 2. The overall heat transfer coefficients of each wall (U_P for floor heating room and U_R for radiators room) and the resulting average overall values of the two rooms are substantially at the same level of those related to modern high end green buildings [9], but rather higher than current northern Europe values [2]. They are very close for the two rooms, except the floor value (wall nr. 7) of panels room, which is responsible for its larger overall average value and the related higher heat losses.

A controlled external air supply of 0.5 volumes/hour was setup in the two rooms and the related heat losses were taken into account. Finally, no internal or external heat gains were considered (rooms were empty during tests and equally exposed to sun).

The circulating water at the average supply/return temperature into the floor heating system, is the heat source responsible for consistently higher downside floor temperature profile ($T_{dfP} - T_{dfR} = 4 \div 7$ °C), resulting into higher (four to five times) heat losses downstairs compared to radiators room. The daily behavior of heat losses in modes 1 and 3 of table 1 is shown on figure 6 a) and b). On the other sample days, substantially analogous results were found, thus they are not shown here for brevity.

From these results, it would seem that the comparison was unreliable, as the floor of radiant panels room showed larger heat losses. But actually, the main objective of this analysis was the comparison of primary energy consumption of the two commercial heating systems, at their current state of the art. From this point of view, the adopted bottom side floor insulation, mainly consisting of 0.03 m thick polystyrene layer, is completely within floor heaters manufacturers' recommended range [5, 6]. It leads to an overall bottom side thermal resistance of about 1.49 K m^2/W, which is in full agreement with manufacturers' proposed values for an overall floor thickness of 0.28 m, like the one here considered [5]. Obviously, if largely higher layer insulation thickness was adopted, consistently reduced down floor heat losses were achieved. In the current case, in order to reach the same level of radiators' room down floor heat losses, an unpractical excessively large insulation thickness of about 0.22 m should be adopted, while manufacturers suggest 3 to 5 cm [5, 6]. Moreover, the ratio between downside heat loss and useful upside heat delivered to the floor heated room is between 4 and 8%, which is plausible and in agreement with the lowest levels of some kinds of underfloor heaters [10]. The overall daily heat losses of the two rooms and the related differences, in the five considered sample days, are shown on figure 7. It also shows the overall daily heat losses of the two rooms calculated with standard technical UNI EN ISO 13790 method [11] to have a comparison of results. The lower heat losses of floor heated room coming out from this method is evident and is attributable to the fact that it does not consider the presence of the internal floor heat source, which is actually the main responsible of floor heat losses. The values found for radiators room were in total agreement.

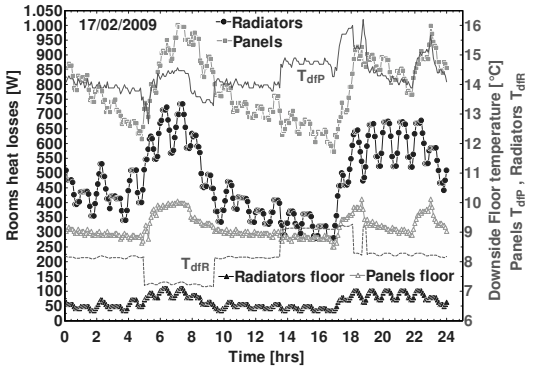

a) Experimental Mode 1

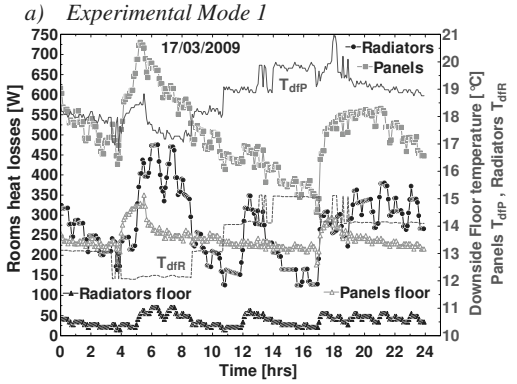

b) Experimental Mode 3

Figure 6 – daily heat losses and downside floor temperatures of the test rooms

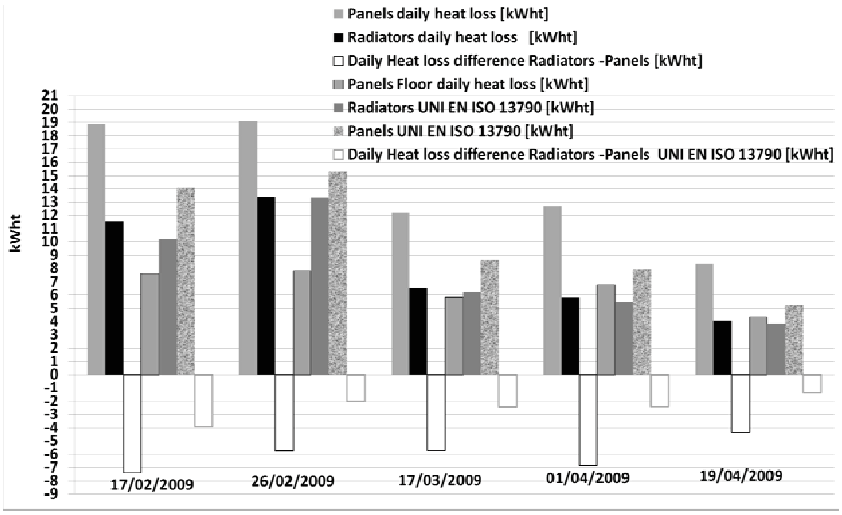

Figure 7 – overall daily heat loss of the two test rooms

These results are also in agreement with [2], where in an apartment with hybrid radiators/floor heating system, bathrooms floor heating energy demand was 33 to 43% of the total, while their surface was 16% only.

The larger heat consumption of floor heating system due to downside heat flow, partially offsets the better score of radiators described in section 4. It could suggest that the whole carried out analysis was altered, as rooms have different levels of heat losses. But the main objective of this work was not only the comparison of energy demand of the two different heating systems, but also the addressing of some critical aspects related to their installation and placement.

Thus, coupling the analysis of rooms heat losses and the energy consumption reported on section 4, it can be concluded that:

- The consistently higher heat consumption of floor heating system is partially attributable to the higher down floor heat losses;
- the above results suggest that placing floor heaters on a floor adjacent to cold rooms (i.e. garages, stores etc. generally unheated) is to be avoided as far as possible, or, either, the insulation must be consistently increased with respect to current practice;
- the heat losses coming from the remaining walls (i.e. 1 … 6 of figure 1) are at the same level for the two rooms, thus the higher loss through the bottom side of floor heaters can be considered a peculiar feature of this heating system;
- when downstairs rooms are a fraction of the same house, downside heat losses can contribute to their thermal comfort;
- when downstairs rooms are not a fraction of the same house, the amount of downfloor heat loss is strongly dependent on the difference in thermal management of the downstairs neighborhood: also in this case, higher layer insulation thickness should be adopted.

The above results and the conclusions drawn in section 4, meet up partially with previous simulation results presented in [12]. Here, the Author stressed that the increased energy consumption of the floor heating system (in comparison to the radiators system) was mainly due to the tested building characteristics, which was not designed for floor heating solutions (standard building design). In the same way, we could conclude here that generally, the installation of floor heaters requires higher insulation than current practice if the average temperature difference with downstairs room is rather large.

Conclusions

The comparison between two different heating systems (i.e. MT radiators and floor heaters) was carried out by a four months experimental test campaign within two equal and rather well caulked 16 m^2 rooms, one equipped with radiators and the other one with floor heaters.

Five different modes of conduction were applied and the comparison between the two systems was based on the analysis of primary heat consumption needed to achieve the same useful effect into the rooms, which was a similar temperature profile (thermostatically controlled) along the 24 hours of the selected sample days. The results showed a generally higher heat consumption of floor heating system (4 to 40%), increasing with the discontinuity of heat demand.

The analysis of rooms heat losses showed consistently higher values of the one equipped with floor heating, mainly attributable to the larger heat flow through the floor from the hot water inside vs. the cold downstairs environment. It partially offsets the better score measured for MT radiators. Anyway, as bottom insulation and thermal resistance of floor heated room are in agreement with floor heating systems manufacturers' data, they should address customers to install these systems with adapted floor insulation and localization of the heated rooms: for example, their placement above unheated rooms should be avoided as

far as possible or, either, the insulation consistently increased. In other words, floor heating should be adopted in buildings designed to integrate them efficiently and with continuous operation. In fact, given the large difference in floor heat losses and the small difference of heat consumption, the results found in continuous operation mode makes the floor heating solution advantageous.

In discontinuous operation mode, the higher heat consumption is partially due to the higher heat losses and mainly to the larger thermal inertia of the floor heating system. Moreover, in this working mode, the average room temperature is higher for the room equipped with floor heating, which leads to higher heat loss. Thus, in this case, radiators should be suggested, unless very special boundary conditions were verified in the building.

Acknowledgments

The Author acknowledges Global Company for the support given to the research, the setup and hosting of the experimental setup and Ing. Francesco Paoletti from Delta Engineering srl for tests management.
Ing. Paolo Pecorario is gratefully acknowledged for data selection and sampling during his graduating thesis.

List of symbols

ΔT	Temperature difference,°C
m	Mass flow rate, kg/s
Max	Maximum value
Q	Heat power provided to the rooms, kW
RMS	Root Mean Square value
Σ	Sum
T	Temperature, °C
U	Overall heat transfer coefficient, W/(m^2°C)

Subscripts:

average	Average value
average ON	Average value with heating system ON
dfP	Panels downside floor value
dfR	Radiators downside floor value
P	Floor heaters (Panels)
r	Return value
R	Radiators
roomP	Floor heaters (Panels) room
roomR	Radiators room
s	Supply value
srP	Floor heaters Supply-Return difference
srR	Radiators Supply-Return difference
store	Store temperature outside the rooms

Acronyms:

COP	Coefficient of Performance
HT	High temperature
I/O	Input/Output
LT	Low temperature
MT	Medium temperature
P	Floor heaters (Panels) room
R	Radiators room
VLT	Very Low temperature

References

[1] M.A. Juusela (Ed.), Heating and Cooling with Focus on Increased Energy Efficiency and Improved Comfort, Guidebook to IEA ECBCS Annex 37, Low Energy Systems for Heating and Cooling of Buildings, VTT Building and Transport, Espoo, ISBN 951-38-6489-8, 2003.

[2] Ala Hasan, Jarek Kurnitski, Kai Jokiranta, "*A combined low temperature water heating system consisting of radiators and floor heating*", Energy and Buildings, Volume 41, Issue 5, May 2009, Pages 470-479

[3] Jonn Are Myhren, Sture Holmberg, "*Flow patterns and thermal comfort in a room with panel, floor and wall heating*", Energy and Buildings, Volume 40, Issue 4, 2008, Pages 524-536

[4] Jonn Are Myhren, Sture Holmberg, "*Design considerations with ventilation-radiators: Comparisons to traditional two-panel radiators*", Energy and Buildings, Volume 41, Issue 1, January 2009, Pages 92-100

[5] Doninelli, M., "*GLI IMPIANTI A PANNELLI RADIANTI*", Quaderni Caleffi, in Italian

[6] *Sistemi a pannelli radianti Geberit*, Geberit Marketing e Distribuzione, www.geberit.it , in Italian.

[7] TCAEY-THAEY 105÷111 Mini-Y range, K11011-GB ed. 3, RHOSS Technical Catalogue Data.

[8] Cristian Cuevas, Jean Lebrun, "*Testing and modelling of a variable speed scroll compressor*", Applied Thermal Engineering 29 (2009) 469–478.

[9] L. Pagliano, S. Carlucci, T. Toppi, P. Zangheri, *"Combining High-End Architecture and Low Energy: Energy Analysis to Support the Design of a Large Office Building"*, Within the Greenbuildingplus Project, available online at http://re.jrc.ec.europa.eu/energyefficiency/pdf/IEECB08/IEECB08%20proceedings/101_Pagliano_final.pdf

[10] P. Weitzmann et al., "*Modelling floor heating systems using a validated two-dimensional ground-coupled numerical model*", Building and Environment 40 (2005) 153–163

[11] UNI EN ISO 13790:2005 – "*Thermal performance of buildings – Calculation of energy use for space heating"* – CTI, 04/2005.

[12] Qingyan Chen (1990), Comfort and energy consumption analysis in buildings with radiant panels. Energy and Buildings. Vol. 14(4), p. 287-297. doi:10.1016/0378-7788(90)90091-V

Methodology for designating thermal and cooling building requirements based on the European standard ISO 13790:2008

Kalliakoudi K.P [a], Koronaki I.P [b]

[a] Msc Mechanical engineer , Athens, Greece
[b] Professor in department of mechanical engineering NTUA, Athens, Greece

Abstract: In the present study, we make a short presentation of the European standard ISO 13790:2008 pointing out the basic parameters for calculating thermal losses as well as thermal gains. Based on this methodology, in order to calculate the thermal and cooling requirements of buildings, we developed a software, which is based on the matlab programming language.Matlab software is being applied in real conditions. It is being used to simulate the energy behavior of an existing building in Athens. An energy inspection is being effected and the characteristics of the building shell and the central heating are being recorded. The energy demand and the energy consumption of the building is being calculated. A comparison of the energy consumption between matlab and the energy audit results shows that the deviation between them is not significant. A saving energy scenarios is being proposed . The new energy requirements are being calculated using matlab. The two energy situations of the building (before the interventions of saving energy and after) are being compared . The results are presented through the use of visual diagrams.

Keywords: Building energy requirements, Building energy consumption, thermal gains, utilization factor

1. Introduction

The contemporary trend in the European Union seems to be the energy saving in buildings. In Greece there is a lack of a legislated procedure which indicates how to calculate the energy requirements of a building. It is therefore strongly required to have procedures for estimating the heating and cooling requirements in buildings. This need and practice is being served by this study in which a software is created in order to have a tool to simulate the energy behavior of buildings. The software is based on the European standard ISO 13790:2008.

2. Calculation of energy requirements

A presentation of the basic steps of the method ISO 13790:2008 follows. The calculation step which is used is the month.

2.1. Energy need for heating and cooling

For each building zone and each calculation step (month) the building's energy need for heating, Q_{Hnd}, [1] is given by the following equation:

$$Q_{H,nd} = Q_{H,ht} - \eta_{H,gn} Q_{H,gn} \quad (1)$$

$Q_{H,ht}$ represents the heat transfer for the heating mode expressed in MJ/month

$Q_{H,gn}$ represents the total heat for the heating mode expressed in MJ/month

$\eta_{H,gn}$ is the dimensionless utilization factor

For each building zone and each calculation step (month) the building's energy need for cooling, Q_{Cnd}, [1] is given by the following equation:

$$Q_{C,nd} = Q_{C,gn} - \eta_{C,ls} Q_{C,ht} \quad (2)$$

$Q_{C,ht}$ represents the total heat transfer for the cooling mode expressed in MJ/month

$Q_{C,gn}$ represents the total heat gains for the cooling mode during expressed in MJ/month

$\eta_{C,ls}$ is the dimensionless utilization factor

2.2. Heat transfer by transmission and ventilation

For each building zone and calculation step (month) the total heat transfer Q_{ht} [1] is given by the equation:

$$Q_{ht} = Q_{tr} + Q_{ve} \quad (3)$$

Q_{ht} is the total heat transfer by transmission in MJ/month

Q_{ve} is the total heat transfer by ventilation in MJ/month

Total heat transfer by transmission and ventilation are calculated for the heating and cooling mode as given by the equations:

For heating mode:

$$Q_{H,tr} = H_{tr,adj}\left(\theta_{\text{int},set,H} - \theta_e\right)t \quad (4)$$

$$Q_{H,ve} = H_{H,ve,adj}\left(\theta_{\text{int},set,H} - \theta_e\right)t \quad (5)$$

For cooling mode:

$$Q_{C,tr} = H_{tr,adj}\left(\theta_{\text{int},set,C} - \theta_e\right)t \quad (6)$$

$$Q_{C,ve} = H_{H,ve,adj}\left(\theta_{\text{int},set,C} - \theta_e\right)t \quad (7)$$

$H_{tr,adj}$ represents the overall heat transfer coefficient by transmission of the zone, adjusted for the indoor – outdoor temperature difference, expressed in W/K

$H_{ve›adj}$ represents the overall heat transfer coefficient by ventilation of the zone, adjusted for the indoor – outdoor temperature difference, expressed in W/K

$\theta_{\text{int},set,H}$ is the set point temperature of the building zone for heating in ^{o}C

$\theta_{\text{int},set,C}$ is the set point temperature of the building zone for cooling in ^{o}C

θ_e is the temperature of external environment in ^{o}C

t is the duration step expressed in Ms

2.3 Thermal gains

The total heat gains, Q_{gn}, of the building zone for a given calculation step are calculated [1] by the given equation:

$$Q_{gn} = Q_{\text{int}} + Q_{sol} \quad (8)$$

Where,

Q_{gn} is the sum of internal heat gains over the given period in MJ/month

Q_{sol} is the sum of solar heat gains over the given period in MJ/month

The sum of internal heat gains is calculated for the heating and cooling mode as given by the equations:

$$Q_{gn} = \left(\sum_k \Phi_{H,\text{int},k}\right)t + \left(\sum_l \left(1 - b_{tr,l}\right)\Phi_{H,\text{int},u,l}\right)t \quad (9)$$

$b_{tr,l}$ is the reduction factor for the adjacent unconditioned space with internal heat source l

$\Phi_{H,\text{int},k}$ is the time average heat flow rate from internal heat source k expressed in W

$\Phi_{H,\text{int},u,l}$ is the time average heat flow rate from external heat source l in the adjacent unconditioned space expressed in W

t is the duration step expressed in Ms

The sum of solar heat gains is calculated for the heating and cooling mode as given by the equations:

$$Q_{sol} = \left(\sum_k \Phi_{H,sol,k}\right)t + \left[\sum_l \left(1 - b_{tr,l}\right)\Phi_{H,sol,u,l}\right]t \quad (10)$$

$b_{tr,l}$ is the reduction factor for the adjacent unconditioned space with internal heat source l

$\Phi_{H,sol,k}$ is the time average heat flow rate from solar heat source k expressed in W

$\Phi_{H,sol,u,l}$ is the time average heat flow rate from external heat source l in the adjacent unconditioned space expressed in W

t is the duration step expressed in Ms

2.4 Thermal gains

The dimensionless gain utilization factor for heating, $\eta_{H,gn}$, is a function of the heat-balance ratio, γ_H , and a numerical parameter, a_H, that depends on the building inertia [1], as given by Equations:

$$\text{If } \gamma_H > 0 \text{ and } \gamma_H \neq 1 \qquad \eta_{H,gn} = \frac{1-\gamma_H^{a_H}}{1-\gamma_H^{a_H+1}}$$

$$\text{If } \gamma_H = 1 \qquad \eta_{H,gn} = \frac{a_H}{a_H+1} \qquad (11)$$

$$\text{If } \gamma_H < 0 \qquad \eta_{H,gn} = \frac{1}{\gamma_H}$$

where (for each month or per season and for each building zone)

γ_H is the dimensionless heat-balance ratio for the heating mode $\gamma_H = \frac{Q_{H,gn}}{Q_{H,ht}}$

$Q_{H,ht}$ is the total heat transfer for the heating mode expressed in MJ/month

$Q_{H,gn}$ represents the total heat gains for the heating mode expressed in MJ/month

a_H is a dimensionless numerical parameter depending on the time constant, τ_H , defined by

$$a_H = a_{H,0} + \frac{\tau}{\tau_H} \qquad (12)$$

τ is the time constant of the building zone, determined expressed in hours. It depends on the internal heating capacity of the building [1].

τ_H is a reference time constant expressed in hours.

$\alpha_{H,0}$ is a dimensionless numerical parameter [1].

The dimensionless loss utilization factor for cooling, $\eta_{C,ls}$, needed for the monthly or seasonal cooling method, is a function of the heat-balance ratio for cooling, γ_C, and a numerical parameter, α_C, that depends on the building thermal inertia, as given by the following Equations

$$\text{If } \gamma_C > 0 \text{ and } \gamma_C \neq 1 \qquad \eta_{C,ls} = \frac{1-\gamma_C^{-a_C}}{1-\gamma_C^{-(a_C+1)}}$$

$$\text{If } \gamma_C = 1 \qquad \eta_{C,ls} = \frac{a_C}{a_C+1} \qquad (13)$$

$$\text{If } \gamma_C < 0 \qquad \eta_{C,ls} = 1$$

γ_C is the dimensionless heat-balance ratio for the heating mode $\gamma_H = \frac{Q_{C,gn}}{Q_{C,ht}}$

$Q_{C,ht}$ is the total heat transfer for the heating mode expressed in MJ/month

$Q_{C,gn}$ represents the total heat gains for the heating mode expressed in MJ/month

a_C is a dimensionless numerical parameter depending on the time constant, τ_H , defined by

$$a_C = a_{C,0} + \frac{\tau}{\tau_C} \qquad (12)$$

τ is the time constant of the building zone, determined expressed in hours. It depends on the internal heating capacity of the building [1].

τ_C is a reference time constant expressed in hours.

$\alpha_{C,0}$ is a dimensionless numerical parameter [1]

3.1. Simulation procedure for estimating the energy need of heating and cooling of an building in Athens

According to the methodology described above, is created a software using matlab. This software from now on will be reported for reasons of brevity as matlab software. This software is used in real conditions in order to calculate the energy demand and the energy consumption of a school located in Athens [2] .

3.1.1. Building's shell characteristics

The school consists of 3 floors and its surface is 790 m^2. The walls consist of double bricks without insulation of overall heat transfer coefficient U=1.81 W m^{-2} K^{-1}. The 23% of all external wall area is composed by windows of double panes and of overall heat transfer coefficient 3.2 W m^{-2} K^{-1} The wall's heat transfer coefficient is so high because the building was constructed in 1968 before in Greece insulation was obligatory [4] .

Table 1. The building shell 's characteristics

Total external wall surface	*766.2 m^2*
Type of wall construction	Double brick wall without isolation U=1.81 W/ m^2 *K*
Thickness of external wall	28 cm
Roof	U= 1.41 W/m^2 *K*
Total glazing area	186 *m^2*
Type of glazing	Double glazing, *U=3,2* W/m^2 *K*
Schedule per day	Mon –Fri,8.00-14.00
Persons per day	165 (140 students+20 teachers)

3.1.2. Central heating system

The central heating system of the building contains an oiled fired boiler with thermal power 140 000 kcal/h. Measurements are being made using a combustion analyser in order to check the oil burner of the heating system [2] .

Table 2. Oil's burner characteristics

CO_2	10.3%
O_2	5.4%
Smoke temperature	260 ^oC
efficiency of the combustion	87%

The efficiency factor of the combustion is what interest most in order to calculate the building's energy consumption for heating.
Furthermore we need to estimate the losses in the hot water distribution system. The hot water distribution system consists of a pipeline which connects the oil burner with the radiators. By observing the pipeline we realize that they have no insulation. Beside that, the bigger part of the pipes " run" outside of the building. This indicates that distribution losses can't be negligible. In order to be more specific we use an infrared thermometer and measure the temperature on the surface of the tubes. It is a way to draw conclusion on the heating – water temperature.

Table 3. Temperatures on the surface of the pipeline

Position on the pipeline	^oC
Supply pipe	75
Return pipe	45
Before the radiators	55

Because the temperature deviation between supply and return pipe is bigger than 20 ^oC, it is a logical approach to estimate the distribution losses around 25%.

During the inspection of the heating system we observe that there doesn't exist any thermostatic control of the heating system. The control of the heating system is manual. There is also a lack of energy efficient control at the heating system.

3.1.3. Input data

The admissions being made for the ventilation, the thermal gains and the internal average temperature of the building are given in the table below [2] .

Table 4. Admissions for ventilation, thermal gains

Natural ventilation requirements	17m^3/h per person
Parasitic ventilation	0.6 ACH
Thermal gains from equipment	4 W/m^2
Thermal gains from people	14 .6W/m^2
Internal temperature of the building during winter	17 ^oC
Internal temperature of the building during summer	26 ^oC

The numbers given in the table above are some of the input data of matlab.

3.2. Energy demand of the building

Considering the methodology described, as well as the monthly average external temperatures [10], the energy demand for heating and cooling is given in the following table per month.

Table 5. Energy demand for heating per month

Month	Energy demand for heating in kWh/m^2
JAN	12.57
FEB	9.62
MAR	4.77
APR	0
OCT	0
NOV	0
DEC	8.21
TOTAL	35.18

In the following diagram the variation is presented per month of total heat gains, total heat transfer and energy demand for the winter period [2] .

Diagram 1. Variation of total heat gains and total transfer during the heating period

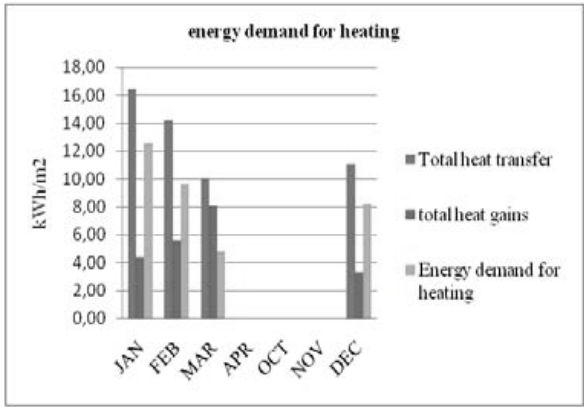

Table 6. Energy demand for cooling per month

Month	Energy demand for cooling in kWh/m^2
MAY	4.48
JUN	14.87
JUL	22.50
AUG	19.40
SEP	5.53
TOTAL	66.85

In the following diagram the variation per month is presented of total heat gains, total heat transfer and energy demand for the summer period [2] .

Diagram 2. Variation of total heat gains and total transfer during the cooling period

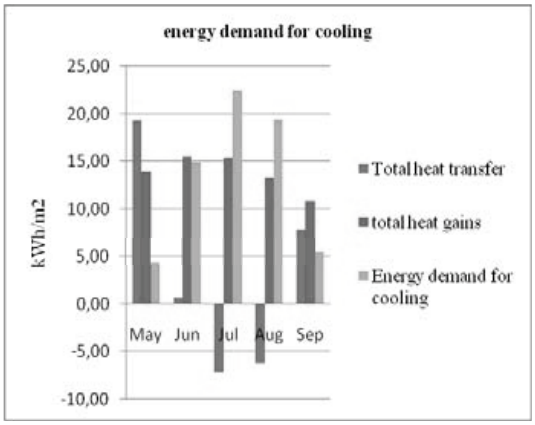

As we can observe from diagram 2, during July and August the total heat transfer is negative. This is because in July and August the external temperature is higher than the internal temperature [10] .

3.3. Energy consumption of the building

Considering the energy demand for heating and 2 2 A 00 A 0 2 energy consumption for heating is calculated and given in the following table .

In the following table the consumption of heating per month is given.

Table 7. Energy consumption for heating per month

Month	Energy consumption for heating in kWh/m^2
JAN	22.09
FEB	18.11
MAR	10.19
DEC	13.68
TOTAL	64.07

According to the methodology the CO_2 emissions due to heating consumption are calculated and presented in the following diagram. The total the

CO_2 emissions of the building per year are 13.33 tn.

Diagram 3. CO_2 emissions due to heating consumption

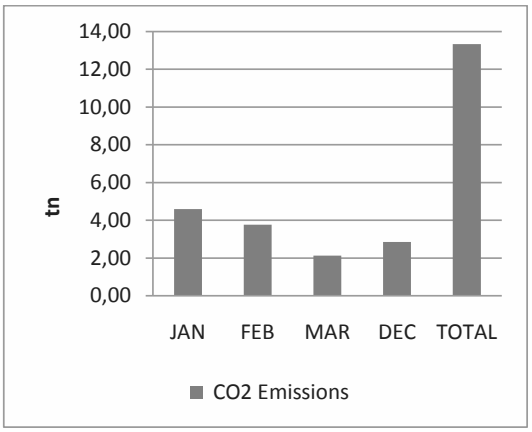

In the following table the results of the energy audit (the real consumption like it is recorded in the files of the building) are given in order to compare the simulation with the real conditions.

Table 8. Comparison liters of oil being consumed in real conditions and in methodology

Month	Real condition	Methodology
JAN	1850	1720
FEB	1520	1410
MAR	980	790
OCT	440	0
NOV	560	0
DEC	1200	1070
TOTAL	6550	4990

From the table above, it is concluded that the difference result are 1560 liters, thus 23,8%. This deviation could be due to the fact that in the methodology is a lack of data concerning peoples reactions. For example when the external temperature as in October is not so low, the persons of the building still use the heating system [4]. Another explanation for this deviation could be this: The model (methodology) uses monthly average external temperatures. Due to this, it is possible that the model underestimates the energy demand. This fact can be observed from the table above during October and November, where the model calculates zero energy demand. Another reason for the deviation of 23,8% could be that the estimation for distribution losses we have made is not precise. The audits could also include an error.

3.4. Interventions for saving energy

In order to improve the levels of energy consumption of the building some interventions of saving energy are being proposed. The methodology described above is used to estimate the new energy requirements of the building.

Important percentage of thermal losses of building is owed in the absence of heat insulation in the roof, as well as in the absence of insulation in the wall. Therefore is proposed the placement of exterior insulation in the building. Due to this intervention the thermal heat transfer of the building will be decreased from 1.81 W/m^2K in 0.55W/m^2K for the walls and from 1,41 $W/m^{2o}C$ in 0,46 W/m^2K for the roof.

As it is mentioned above, the problems that are related with the central heating are the increased losses of distribution, the increased combustion efficiency factor and the increased heating consumption because of the management of the heating system from the users of the building. For the restriction of losses of distribution is proposed the insulation (insulation with thickness 13mm) of the supply main piping, while for the restriction of consumption of heating energy beyond the needs of the building, is proposed the placement of thermostatic valves in each one of the baseboards. It is also proposed the replacement of the oil burner with the natural gas burner, because the natural gas is a more "friendly" fuel for the environment.

Due to these interventions the efficiency factor of combustion (as we can conclude from the technical data of the new oil burner) will be increased in 0.95.Overmore due to the pipes insulation we estimate that the distribution losses will be decreased in 8% .

3.5. Comparison

As it shown in the following diagram after the interventions the building will have a new energy consumptions level. The annual energy consumption for heating will be reduced 73,7% and the CO_2 emissions 79.7% The new scenario of

the building is less energy consuming and more environmental friendly.

Diagram 4. Comparison between the two conditions of the building, before and after the interventions

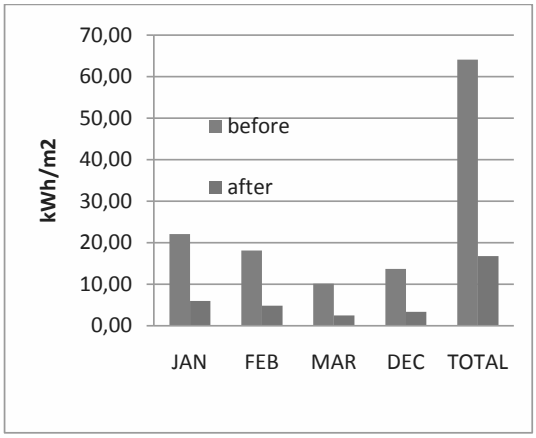

Diagram 5. Comparison CO_2 emissions between the two conditions of the building, before and after the interventions

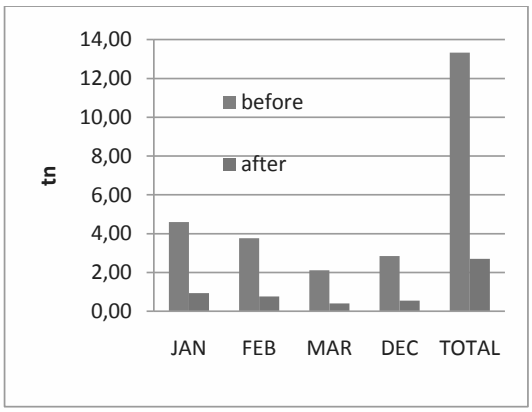

3.6. Conclusions

The described calculation procedure based on the European Standard ISO 13790:2008 is an approximate method as it has been shown that the values of the cooling and heating load requirements estimated by the model equation are not the same as the values given by the energy audits. In fact the methodology underestimates the heating consumption .

The methodology is an useful tool in order to calculate the energy saving potential in a building after applying interventions of saving energy. Using the methodology described above is possible to compare different saving energy scenarios in buildings concerning CO_2 emissions and energy consumption.

References

[1] International standard ISO 13790:2008

[2] Kalliakoudi K., 2009, Methodology of designating thermal and cooling requirements of buildings based on European standards, Masterthesis NTUA

[3] "Thermal performance of the exterior envelopes of buildings II", Proceedings of the ASHRAE/DOE Conference, Dec.6-9, 1982, Las Vegas, Nevada.

[4] Koronaki I., Lazari E., Lytras K., Polychroni E., "Noval approach of cooling requirements calculations in Non-Residential Buildings according to the Greek Building Energy Codes", PLEA 2002, Design with the Environment, Proceedings of the 19th International Conference, pp.891-900, Toulouse – France, July 2002.

[5] Netherlands Building Energy Codes, Energy Performance of non-residential buildings, NEN 2916, 1998.

[6] S. Mirasgedis, E. Georgopoulou, Y. Sarafidis, C. Balaras, A. Gaglia and D. P. Lalas," CO_2 emission reduction policies in the greek residential sector: a methodological framework for their economic evaluation ", Energy Conversion and Management Volume 45, Issue 4, March 2004, Pages 537-557

[7] Athina G. Gaglia Constantinos A. Balaras, Sevastianos Mirasgedis, Elena Georgopoulou, Yiannis Sarafidis and Dimitris P. Lalas," Empirical assessment of the Hellenic non-residential building stock, energy consumption, emissions and potential energy savings ", Energy Conversion and Management, Volume 48, Issue 4, April 2007, Pages 1160-1175 .

[8] Elena G. Dascalaki, Kaliopi Droutsa, Athina G. Gaglia, Simon Kontoyiannidis and Constantinos A. Balaras, "Data collection and analysis of the building stock and its energy performance—An example for Hellenic buildings ", In press, Available online 24 February 2010

- Computer Software:

[9] EPA-NR, EBM-consult, National Observatory of Athens

- Websites

[10] http://www.cres.gr/kape/datainfo/clima/asterosk.htm

Low Exergy Building Systems Review

Forrest Meggers [a], *Volker Ritter* [a] *and Hansjürg Leibundgut* [a]

[a] *ETH Zurich, Switzerland*

Abstract: Low exergy building systems create more flexibility and generate new possibilities for the design of high performance buildings. Instead of maximizing the barrier between the building and the environment using thick walls containing large amounts of insulation, low exergy systems maximize the connection to the freely available dispersed energy in the environment. These connections to what we call "anergy sources" reduce exergy use and thus primary energy demand. This is achieved through the potential of new low temperature-lift ultra-high COP heat pumps. They achieve their low temperature-lift and subsequent high COP by providing low temperature heating with low exergy supply systems combined with a connection to a variety of technologies for capturing freely available renewable anergy sources. We present a review of these low exergy technologies being developed at the Chair of Building Systems at the ETH Zurich. These systems provide many methods for conditioning buildings using moderate supply temperatures and heat pumps that exploit more valuable anergy sources. This combination of low exergy systems maintains very low temperature-lifts, which can drastically increase heat pump performance from the typical COP range of 3-6 to values ranging from 8-15.

Keywords: Buildings, Exergy, High Performance, Energy Efficiency, LowEx, Heat Pump, Active

1. Introduction

The concept of exergy was developed in the middle of the twentieth century as a tool to optimize the performance of thermodynamic machinery. Originally, the concept primarily applied to thermal plant analysis for minimization heat flows that do not generate utilizable work, thereby producing valuable output. This was made possible by the creation of the term exergy, which is a combination of the energy balance of the first law of thermodynamics, and the entropy balance of the second law of thermodynamics. This combination helps define directly the potential of a system to produce a useful output while interacting with its surrounding environment. The limits defined by Carnot to which all thermodynamic cycles are constrained, are inherently considered in exergy analyses. Exergy quantifies the net potential of a system as influenced by both the quantity of energy available, as well as the temperature, or quality, available. This is relative to the system's surroundings, with which it will interact [3, 8].

When a system is at the same thermodynamic state as its surrounding environment, it does not have potential to do work. Thus it has zero exergy. As a thermodynamic system moves toward equilibrium with its surroundings, a part of that movement in state can be extracted and part of the energy is dispersed. This flux of energy to a dispersed state generates entropy, or in terms of exergy analysis, it is the destruction of exergy and the generation of anergy. Carnot and Clausius proved that a certain amount of energy must flow to a cold sink for work to be extracted from a thermodynamic cycle. The maximal amount of work that can be extracted is then directly linked to this temperature gradient. In this way exergy provides us with a tool to better evaluate the value inherent in heat fluxes occurring across different temperature gradients.

More recently, this concept of exergy has been extended into the field of building design [11, 12, 13, 15]. At the Chair of Building Systems at the ETH Zurich we have extended the definition of exergy and anergy for the analysis and development of building systems [6]. Figure 1 demonstrates the difference between the heat engine, for which exergy was originally developed, and a heat pump, which is the core of our low exergy systems. In order to maximize the work output of a heat engine, the exergy output is maximized while the anergy is minimized. This is limited by the Carnot efficiency of a heat engine operating between a heat source and anergy sink, $\eta_{Carnot} = W_{max}/Q_{in} = (T_{hot} - T_{cold})/T_{hot}$.

Corresponding author: Forrest Meggers, Email: meggers@arch.ethz.ch

In order for the heat engine to operate, some heat must flow to the cold source, and thus there is a limit to the possible efficiency, which can be increased by increasing the temperature difference between hot and cold.

Now when we consider the heat pump, which is just a heat engine operating in reverse, the limit is in how much heat can be provided with a certain amount of work, or exergy input. When a heat pump is set up for heating it moves heat from what we define as an anergy source to a heat sink (i.e. the building). The maximum amount of heat per unit work input is also limited by a Carnot value of the COP, as in $COP_{Carnot} = Q_{max}/W_{in} = T_{hot}/(T_{hot} - T_{cold})$. Here instead of maximizing exergy output, we want to minimize exergy input while maximizing heat output, and the COP is increased in this case by decreasing the temperature difference, or temperature-lift, that the heat pump must provide. As shown in Fig. 1, the heat output is just a combination of exergy and anergy inputs, $Q = Ex_{in} + An_{in}$. As stated, the heat output is controlled by the COP, $Q = COP * Ex_{in}$. Therefore the fundamental goal of providing heat with a minimal amount of exergy input can be achieved by maximizing the heat pump COP by minimizing the temperature-lift.

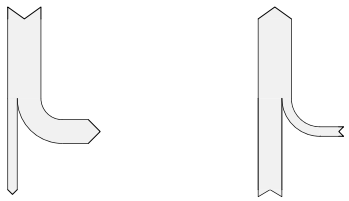

Figure 1: The heat engine represents the origin of exergy analysis and the heat pump represents a principle component for exergy analysis of building systems. For both, the performance is dependent on the temperature difference between hot and cold.

We achieve this goal by developing systems that maximize the anergy source temperature while minimizing the heat supply temperature. There are many potential sources of heat around a building that have more potential than just the ambient air. These potentials may be due to variations in the location of heat sources. For example, the heat below the ground or in a local body of water may be greater. Also, seasonal changes in temperature provide higher value sources that can be exploited with appropriate technology. This is complemented by systems that utilize lower temperatures in the building to supply heat, which is made possible by increased heating surface area, for example from activated thermal mass. These systems can be further optimized by an exergy analysis of the supply chain. Software tools have been developed and implemented that evaluate exergy destruction in building heating supply chains [9, 10]. This reduces the amount of energy that must be supplied as well as the temperature at which it is supplied. Combining supply system exergy analysis and anergy source evaluation results in a system with low temperature-lift and a very high COP. Thus it has the potential to provide a large amount of heating with little exergy input, which translates to a very small primary energy input.

We have illustrated the potential COP for a heat pump in Fig. 2. Real machines cannot operate at the ideal Carnot COP, but instead operate at some fraction of this ideal usually ranging from 0.4 to 0.6. The Carnot factor or "g-value" is a better indicator of the actual machine performance than the COP. Even with typical g-values, it is clear that a much higher COP is possible as shown in Fig. 2.

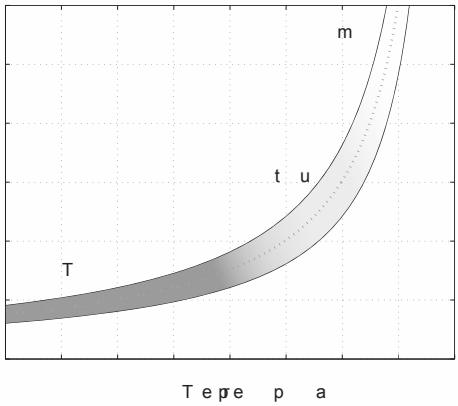

Figure 2: Variation of COP with decreasing temperature-lift. Below temperature-lifts of 20 K the COP increases rapidly. A typical range from g=0.4 to 0.6 for Carnot factors for existing machines are illustrated.

As a result of increased COP, the fraction of heat coming from anergy sources increases, and thus

the demand for systems to provide heat increases. Therefore we must find sources of high enough quality, as well as with large enough quantity. This is facilitated by accounting for both freely available environmental anergy sources, as well as sources of waste heat from the building that would otherwise be lost out of the building and dispersed as anergy into the environment. This is analogous to a heat engine capturing heat from exhaust, which would otherwise flow into the environment as anergy. In this case the heat is captured and can be used to increase heat pump COP.

Finally, it is important to note that heat pumps can of course be operated to cool buildings. The performance is again limited by the temperature-lift, but this time operating with a different goal. In this case, the desired output is the removal of heat, or in other words the supply of cool exergy, as described by Shukuya and Hammache [14]. Cool exergy is provided as the heat is removed into an anergy source. It is often the case for cooling that anergy sources with adequate temperatures for direct cooling can be found. These include the ground or night cooling, but one major obstacle is finding methods to supply adequate dehumidification if needed. Cooler temperatures can be supplied with a heat pump or desiccant systems can be used, but our research has focused on the development of low exergy heating systems.

We present a review of a variety of low exergy systems that have been developed through our methods of supply system exergy analysis and anergy source evaluation. These systems are in various stages of design, but the majority are being piloted in the B35 building project currently under construction in Zurich, Switzerland, www.viagialla.ch.

2. Technology Summary

As described, the heart of the system is a low temperature-lift heat pump system. Currently, the ultra-high COP heat pumps that we have shown to be possible with integrated low exergy systems [7] are not commercially available. This is therefore the focal point of ongoing research between ETH Zurich and HSLU Luzern. Operation with a COP higher than 14 has already been demonstrated while maintaining Carnot factors greater than 0.5 at temperature-lifts below 20 K [16]. Based on the potential of the heat pump as our core component, we have developed a new integrated concept to minimize the required system temperature-lift for all aspects of building operation. These systems minimize primary energy demand, which is achieved without excessive building shell insulation and fenestration requirements, making the architectural design more flexible while maintaining very high performance. These technologies create an active approach to building operation efficiency as opposed to a passive one.

The technology that provides the base heat source is a new dual-zone borehole. This system uses one warmer deep borehole of approximately 300 m and a cooler shallow one of approximately 50-100 m so that the summer and winter operation can extract and deposit heat at appropriate temperatures. This optimizes seasonal storage temperatures using the geological thermal gradient. The heat pump is fed this improved primary anergy source to supply or remove heat from the building. This is accomplished with activated thermal mass that maximizes heating or cooling surface area and minimizes temperature demand, and thus temperature-lift.

Higher temperatures for hot water production are achieved using hybrid Photovoltaic-thermal (PVT) panels. Unlike PV-only or solar thermal installations that try to produce warm enough temperatures for direct hot water production, we combine the two and collect electricity along with lower temperature heat. Even at a lower temperature this heat is still valuable at around 35 °C, which maintains a high COP for hot water production. In case of a lack of sun, the warm wastewater is captured in an insulated tank and acts as a secondary higher temperature source for hot water production. Not only that, but we don't produce the unnecessarily high-temperature hot water. We use the average utilization temperature of around 40 °C and employ a small electric booster system for the small demands at higher temperatures and for sterilization. We have also developed new façade and floor systems for capturing and distributing radiant and geothermal energy better throughout the building structure to minimize temperature gradients and maximize performance. The reduction in price and size of technologies has produced new decentralized air supply techniques as well as small decentralized pumps that maximize flexibility of operation. Finally the resulting structure is highly steerable and does not need as much material for construction, while the benefits from the integrated low exergy systems

make primary energy demand very low. This demand is easily met by renewable sources such as the PVT panels. We illustrate the combination of these systems, which strive for the performance and flexibility demonstrated by the concept of low exergy buildings.

3. Building Integration

Figure 3 shows how these technologies can be integrated into a building design. In this case we use the schematic from the B35 project. This is where most of these systems will be piloted and the potential integration is illustrated here.

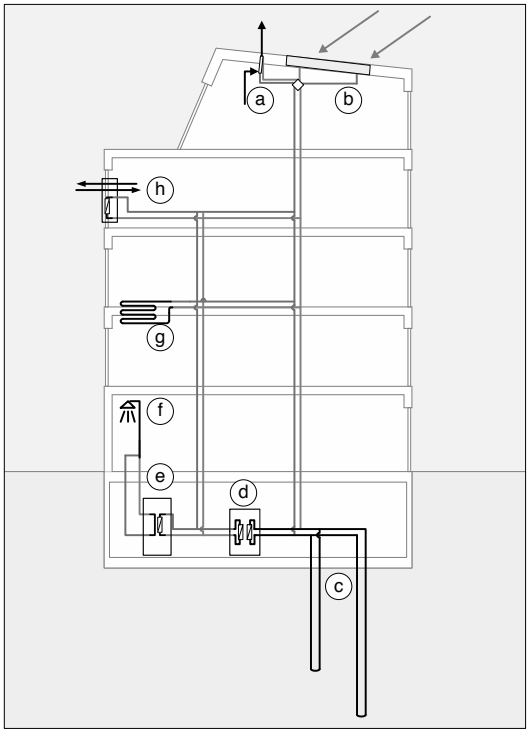

Figure 3: Schematic of a low exergy system integrated into a building. The various components are illustrated: (a) Exhaust heat recovery, (b) PVT hybrid panels, (c) dual zone boreholes, (d) high COP heat pump, (e) low temp hot water storage, (f) warm wastewater heat recovery

Heating and cooling are supplied to the structure from the heat pump, Fig. 3(d), connected to the dual-zone borehole Fig. 3(c). The boreholes are dug to two different depths for optimal heat recovery. In the B35 project, one is dug to 100 m and the other to 380 m. The system is connected over a series of switching valves that allow heat to be supplied to the heat pump, or to be potentially supplied to the heating or cooling system directly.

Ceiling panels can be attached to activate the thermal mass or the concrete structure can incorporate a hydronic system as in Fig. 3(g). The use of ceiling panels allows for the centralized collection of exhaust air for heat recovery, and it has been demonstrated that the ports can be controlled by CO2 sensors to optimize air supply and contaminant removal [2]. This exhaust is centralized and assisted by natural convection to exit through the roof, Fig. 3(a). Here the heat can be removed to a lower temperature by traveling through a heat exchanger to recover the heat back into the heat pump system.

The decentralized air supply system, Fig. 3(h) utilizes the concrete structure to supply air through ducts integrated into the form, and eliminates large spatial losses due to typical plenum installations. The decentralized air supply units also utilize the same hydronic loop to condition the incoming air. As described, the hot water is stored at a lower temperature in a tank in the basement, Fig. 3(e) and heat from warm water usage is captured for heat pump operation, Fig. 3(f).

The PVT panels are mounted on the roof and connected to the hydronic loop, Fig. 3(b). Switching-valves allow the system to operate in various modes. The system can be connected to the heat pump to supply heat for hot water production, it can be connected directly to the heat system, or it can be connected to the deep warm borehole to regenerate its higher temperature. These valves along with the other systems are controlled by a digital building controller that optimizes the temperature of supplies and sources to maximize heat pump COP for the operation of the heating and coolings systems along with any hot water production.

4. Building Operation

The control and subsequent operation of the building are what give it the potential for very high performance. The standard heating operation is illustrated in Fig. 4.

In the heating mode, the heat pump is supplied by the deep borehole, Fig. 4(C). For our pilot in Zurich we expect temperatures around 15 °C. These temperatures will easily maintain a temperature-lift of less than 20 K. This will in turn guarantee a minimum COP of 8. In the heating mode, the decentralized air systems Fig. 4(H), with their small size,

only condition the air to a minimal comfortable temperature, thus reducing the exergy losses associated with using air as a heat transport medium.

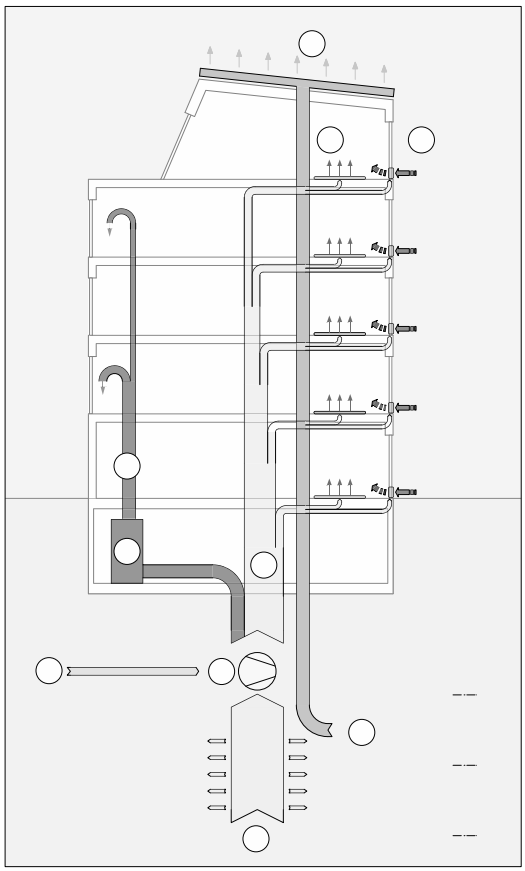

Figure 4: Operation of the system during the heating season. Capital labels correlate to lower-case labels in Fig 3 where applicable. The deep borehole (C) provides higher temperature base load heat to the heat pump (D), which can be supplied with a small amount of renewable energy (K) to produce low temperature heating (L) provided to the thermal mass (G) and decentralized air supply (H). The low temperature hot water storage (E) provides hot water which can be recovered for the heat pump (F). The shallow borehole (M) can be regenerated by cool temperatures captured by the PVT panesl (J).

During the heating season the hot water production becomes the critical limiter to the heat pump performance Fig. 4(E). There are a variety of means of operation that we have included to maintain a very low temperature-lift during hot water preparation. First of all, the hot water is prepared at only 40 °C because this is the average usage temperature. It is a direct loss of exergy to store it at higher temperatures only for it to be mixed with cold water at the usage point. Higher temperatures that are infrequently needed are achieved with electric boosters as found in common dishwashers. This would also be used to meet the brief temperature requirements for elimination of Legionella. Higher temperature anergy sources for hot water production are used first, such as warm wastewater. Initially by simply capturing and briefly storing the warm wastewater with its temperatures usually greater than 30 °C a higher temperature is supplied to the heat pump. This stochastic storage and capture has been modeled and optimized using exergy analysis [5]. Also, when considering the heating season, sunny periods should still achieve warm temperatures from the PVT in the range of 30 °C, which can be used as another supplement for hot water production. Finally, exhaust air has been shown to be a useful potential source for hot water production [1]. It should provide temperatures greater than 20 °C, which would provide a final backup to insure a temperature lift of less than 20 K.

During the heating season cold outside temperatures are encountered with cool nights and longer overcast periods. Under these circumstances the PVT panels can be used to regenerate the shallow borehole by dissipating any excess heat that may have increased the temperatureFig. 4(J,M). This may be possible as well during warmer periods in the cooling season when clear night sky temperatures provide a radiation sink that can be used to dissipate heat directly following a warmer day. These potentials are currently under investigation. The different depths of the dual zone borehole not only provide optimal temperatures, but they also provide independent operation so that supply and regeneration do not have to be as carefully balanced as with many seasonal storage methods. This system facilitates the optimal extraction, storage, and utilization of the anergy sources.

During the cooling season, the system uses the building thermal mass to provide high-temperature cooling. Thus cooling is provided by removing heat from the building, which is sent into the shallow borehole, and is illustrated in Fig. 5.

For the cooling mode, the shallow borehole will provide the average seasonal temperature of the region. For Zurich this is usually in the range of 8 °C, and for the 100 m deep borehole of the B35 project

the temperature should be around 10 °C, Fig. 5(M). At this temperature, direct cooling of the structure should be possible, Fig. 5(G). With the activated thermal mass, a surface temperature of 18 °C provides high temperature cooling to the space, while the 10 °C temperature can be used to achieve some dehumidification if necessary. Again, the decentralized air supply does not participate in actively cooling the space, but rather on providing adequately comfortable temperature air upon entry to the space, Fig. 5(H).

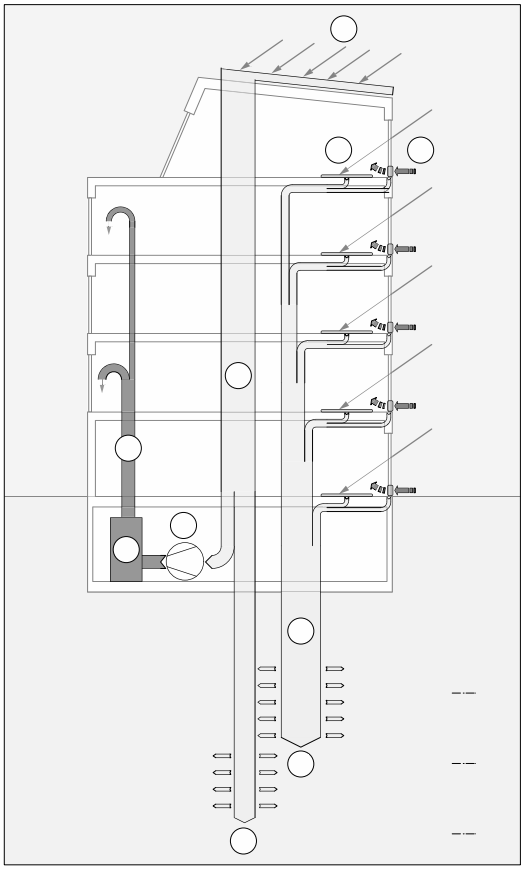

Figure 5: Operation of the system during the cooling season. Labels again correlate to Fig. 3 and 4 where applicable. The shallow borehole (M) absorbs heat to provide direct cooling at around 10 °C (P) to the thermal mass (G) and decentralized air supply (H). The deep borehole (C) is regenerated by excess heat around 35 °C (O) absorbed by the PVT panels (B), which can also be used by the heat pump (D) to generate average temperature hot water (E) with heat recovery (F).

Most important to consider during the warmer weather of the cooling season is the regeneration of the deep borehole. This is because the heating demand in winter is generally greater than the cooling demand in summer for Zurich as well as most continental climates. The PVT panels will easily provide warm enough temperatures to generate hot water during summer, and the excess heat production will be sent into the deep borehole to increase the temperature for the heating season as demonstrated by Fig. 5(B,O,D,C). Not only that, but the heat extracted from the thermal mass can be used to regenerate the warmer deep borehole as well. Even overheating from radiation can be seen as an anergy source. That excess radiation striking the floor behind a window, shown by Fig. 5(G), can be captured with an appropriately designed hydronic system, thereby eliminating the potential of overheating and turning a potential source of exergy destruction in the building cooling system into an anergy store for the building heating system.

Finally, we must also consider that this operation will require a robust control system. New control systems such as digitalstrom are being developed at the ETH (www.digitalstrom.org). This allows for a very simple installation and advanced and robust control via readily available modern computing power.

5. Expected Performance

The pilot project is expected to achieve a minimal COP of around 8 as described. Nevertheless, it is clear that much higher performance would be possible when higher anergy source temperatures are achieved. We have already demonstrated that the performance of these integrated systems outperform generic passive house standards [7]. In this case the pilot project will not have a heat demand less than 15 kWh/m^{2}yr as required by the most high performance passive standards, which look only at heat demand. Instead, a heat demand of 36 kWh/m^{2}yr is achieved, but even if the estimated minimum COP of 8 is achieved, this results in an exergy demand of only 8 kWh/m^{2}yr.

The great reduction in the required input facilitates the use of renewable supply, which could be provided by the PVT panels. This system is still under development in collaboration with various PV manufacturers, and performance data of the actual system has not been precisely measured yet. Cur-

rently, development is toward newly developed cells with efficiency in the range of 10-12%. This would mean that with around 800 kWh/m^{2}yr of solar irradiation for Zurich (about a third of the potential found in sunny regions), 80 kWh per m^2 of panel can be generated. Thus the floor space can be up to 10 times greater than the PVT installation space. In other words, for a flat-roof PVT installation, up to about 10 stories worth of heating could be supplied with heating from renewable electricity combined with a high-COP heat pump.

The potential multiplication of the electricity output from the PV cells using a heat pump increases the performance far beyond what is possible with solar thermal units alone. With a COP of 8 and a PV efficiency of 10%, 80% of the irradiation is transformed into heat supply, and if a COP greater than 10 is achieved, as has been already been shown experimentally [16], then more than 100% is transferred to heating. With our system operation for example, a temperature lift of 10 K for PVT supply to hot water production as shown in Fig. 5 should accomplish a COP of about 15 according to Fig. 2.

For the hot water production itself, there is a large savings potential from the simple change in the storage temperature. At about 50 Liters of 60 °C hot water per person per day for example in Switzerland [4], about 17 kWh per person per year are needed to heat that water. If this can be supplied at a lower average temperature, the temperature lift can be reduced down to a range between 10 and 20 K. This could improve the COP of the heat pump from around 3-4 to around 8-15, bringing the exergy input needed down by an order of magnitude compared to natural gas or electric resistance heaters. Instead of 17 kWh, less than 2 kWh are needed for each person's annual hot water needs.

In general, the low exergy system design creates a way to separate the various heating and cooling demands from the actual input needed to create them. By optimizing the anergy source temperature and using exergy analysis on the supply system, a new method arises to limit the primary energy demand without needing excess limits on transmission heat losses. We can achieve very high performance with walls that are not extremely thick. The B35 project has rather good thermal performance at 36 kWh/m^{2}yr for heating, which meets the Minergie Standard, but it does not make sense to try to reach the passive house or Miniergie P standard. Instead, with walls that are less than 35 cm thick, a primary energy demand is achieved that can easily be met with renewable energy supply. This is provided by the high performance low exergy system, which creates more flexibility in the design of the structure and reduces the material demand and usable space reductions caused by excess insulation.

6. Conclusion

We have presented a review of low exergy systems. The concept of exergy and anergy have been extended to instigate a better method of building design. Examples of results of these design practices have been presented in the form of various technologies. These are being implemented in an integrated system that minimizes the temperature-lift of a high COP heat pump. The concept is being piloted in the B35 project in Zurich, www.viagialla.ch.

We have shown how the performance of such an integrated system is expected to be very high. It outperforms passive house constructions by eliminating the direct restriction placed on design by building heat demand. Heat demand can potentially be supplied by the heat pump system with very high COP, thus making the heat demand itself easily supplied by a small amount of exergy input in the form of renewable electricity. This active system performance creates a wider range of design possibilities.

We have presented a broad review of both developed, and potential low exergy building systems. The principle component is the heat pump. The lack of a market for very low temperature-lift heat pumps in the building sector is a major obstacle. Nevertheless, there is no reason why these machines would not be thermodynamically feasible. The collaboration between the ETH Zurich and HSLU Horw will hopefully lead to a more rapid development in this field with a first prototype heat pump due in 2010. The B35 project will also be completed by 2011. Testing and results from some preliminary pilots of these technologies that are not on the market yet will be very valuable when completed.

Development of low exergy building systems will increase the palette of tools available to building architects and engineers to create buildings that have low energy and exergy demand. These new systems and methods will lead to building construction and operation that generates a minimal amount of CO_2 emissions, and will move us down the path toward zero emissions for the building sector.

Nomenclature

COP Coefficient of Performance

T temperature of hot source or sink (K)

Q heat (W)

W work = exergy (W)

Ex exergy = work (W)

An anergy (W)

Greek Letters

η efficiency

Subscripts and superscripts

Carnot Ideal irreversible performance

hot hot source or sink

cold cold source or sink

References

[1] Domestic hot water heat pumps for residential and commercial buildings: a survey and analysis of the state-of-the-art of the equipment, applications and markets. Technical report, Caneta Research Inc., Sittard, 1993.

[2] L. Baldini and HJ. Leibundgut. Increasing the effectiveness of building ventilation systems through use of local waste air extraction. In *CLIMA 2005*, Lausanne, Switzerland, May 2005. REHVA.

[3] A. Bejan. *Advanced engineering thermodynamics*. Wiley, Hoboken, NJ, 3rd ed edition, 2006.

[4] M. Blatter, M. Borel, H. Hediger, and P. Simmler. Warmwasserbedarfszahlen and verbrauchscharakteristik. Technical Report 724.397.23.58 D, Bundesamtfür Konjunkturfragen and RAVEL, 1993.

[5] F. Meggers, L Baldini, and HJ. Leibundgut. Exergy recovery from warm waste water for an integrated low exergy building system. In *Proceedings of PLEA 2008*, Dublin, Ireland, October 2008.

[6] F. Meggers and HJ. Leibundgut. The reference environment: Redefining exergy and anergy for buidlings. *International Journal of Exergy*, In Press, 2010.

[7] F. Meggers, M. Mast, and HJ. Leibundgut. The missing link for low exergy buildings: low temperature-lift, ultra-high cop heat pumps. In *CLIMA 2010*. REHVA, May 2010.

[8] M. J. Moran and H. N. Shapiro. *Fundamentals of engineering thermodynamics*. Wiley, New York, NY, 4th edition, 2000.

[9] A. Schlueter and F. Thesseling. Building information model based energy/exergy performance assessment in early design stages. *Automation in Construction*, 18(2):153 – 163, 2009.

[10] D. Schmidt. Design of low exergy buildings method and a pre-design tool. *International Journal of Low Energy and Sustainable Buildings*, 3:1–47, December 2004.

[11] M. Shukuya. Thermodynamics for sustainable architecture. In *PLEA 96 Buildings and Urban Renewal*, Louvain-la-Neuve, July 1996. Passive and Low Energy Architecture.

[12] M. Shukuya. Exergetic view and thinking - for the development of environment-conscious technologies. *Ieej Transactions On Electrical and Electronic Engineering*, 2(1):8–11, JAN 2007.

[13] M. Shukuya. Exergy concept and its application to the built environment, JUL 2009. Building and Environment.

[14] M. Shukuya and A. Hammache. Introduction to the concept of exergy. Technical report, IEA ECBCS Annex 37, Musashi Institute of Technology, April 2002.

[15] H. Torio, A. Angelotti, and D. Schmidt. Exergy analysis of renewable energy-based climatisation systems for buildings: A critical view. *Energy and Buildings*, 41(3):248–271, MAR 2009.

[16] I. Wyssen, L. Gasser, B. Wellig, and M. Meier. Chiller with small temperature lift for efficient buildings. In *CLIMA 2010*. REHVA, May 2010.

Acknowledgments: IEA ECBCS Annex 49, Swiss Federal Office of Energy

Exergy Analysis of a Coupled Power-Refrigeration Cycle

Maneesh Dubey[a], SPS Rajput[a], R.D. Misra[b] and PK Nag[c]

[a] *Department of Mechanical Engineering, MANIT, Bhopal-462051, India.*
[b] *Department of Mechanical Engineering, NIT Silchar-788010, India.*
[c] *Ex Professor, Department of Mechanical Engineering, IIT Kharagpur, India.*

Abstract: This paper presents exergy analysis of a coupled power-refrigeration cycle, which eliminates the requirement of electrical power for driving the compressor of the compression refrigeration cycle. The coupled cycle which uses R-245ca as the working fluid in topping power loop and bottoming refrigeration loop have been assessed with different combinations with recuperator, reheater and economizer. Energy analysis shows that for condenser temperature of 30-42°C and recuperator effectiveness of 0.7-0.9, the overall COP of the coupled cycle with recuperator increases by 19.5-50.7% and by 41.6-59.3% in the cycle with recuperator, reheater and economizer as compared to the simple cycle. Overall exergy destruction for coupled power-refrigeration cycle varies in the range 11.14 to 20.75 kJ per kg of refrigerant through evaporator. For the same condenser temperature and recuperator effectiveness, overall exergy destruction for the cycle with recuperator varies from 14.03 to 26.00 kJ per kg of refrigerant through evaporator (~26% higher) and for the cycle with recuperator, reheater and economizer varies from 14.70 to 27.48 kJ per kg of refrigerant through evaporator (~32% higher). The overall second law efficiency for coupled power-refrigeration cycle is found to be in the range of 16.81-38.03%, whereas for the cycle with recuperator and the cycle with recuperator, reheater and economizer, it varies in the ranges of 20.42- 40.28% and 20.77-39.58% respectively. Hence, the coupled power-refrigeration cycle with recuperator is recommended for commercial adoption since the incorporation of reheater and economizer brings performance improvement of the installation marginally that does not justify the increase in capital cost and design complexity.

Keywords: Energy, Exergy, Second Law Efficiency, Exergy Destruction, Overall Cycle.

1. Introduction

The environmental issues of ozone depletion and global warming have forced the refrigeration based industries to direct the research trend in search of alternative refrigerants and alternative technologies [1]. Refrigeration and air conditioning today represent about 10% of the total energy demand and hence a small change will have a sizeable global impact [1]. The enactment of Montreal and Kyoto Protocols emphasized the need of using renewable energies like solar, wind, biomass and geothermal heat as well as recovery of industrial waste heat to generate electricity [2-4]. The Organic Rankine cycle (ORC) is a promising process for conversion of low and medium temperature heat to electricity. The ORC is a Clausius-Rankine Cycle in which an organic fluid is used instead of water-steam [5-11]. Due to the great advantage of the ORC to use renewable energies, many innovative concepts coupling the ORC processes are being developed [11]. One such system is a coupled organic Rankine and compression refrigeration cycle which completely eliminates the requirement of electrical power for driving the compressor. The coupled cycle uses the same working medium in topping power loop and bottoming refrigeration loop. Such a coupled cycle is energy effective system as the vapour turbine could be made to drive the compressor of the refrigeration cycle and the boiler feed pump [12-15].

Several fluids have been studied for ORC applications. The selection of working fluid plays a significant role for the use of ORC and is determined by the application and the waste heat level. Refrigerants are good candidates for ORC applications because of their low-toxicity characteristics [4, 10-11, 16-22]. CFCs and HCFCs are being phased out under the Montreal Protocol. Studies reveal that halogenated ethane R-123, R-134a, and pentafluropropane R-245ca are substances suitable for obtaining high thermal efficiency. The chlorine in R-123 has only 2% of the ozone depletion potential of traditional CFCs. R-123 is supposed to be phased out by 2030 in industrialized countries and by 2040 in developing countries. Though R-134a does not contain the

Corresponding Author: Maneesh Dubey, Email: d.maneesh@gmail.com

chlorine, responsible for ozone depletion, it has been included in the Kyoto agreement as a candidate for phase-out due to its global warming potential [10, 16-23]. Therefore, considering the cycle efficiency and environmental issues, R-245ca has been opted as a working medium in the coupled power-refrigeration cycle.

Dubey et al. [24] have analyzed the coupled ORC and compression refrigeration cycle along with performance augmentation by well known technologies of recuperation and reheating based on the principles of conservation of energy. Many researchers have suggested that the impact of energy use on the environment and the achievement of increased resource utilization efficiency and the economics of energy systems are best addressed by considering exergy [25-31]. Consequently, many methodologies based on exergy have been developed, e.g., exergy analysis for improving the efficiency of energy systems and exergoeconomics for improving the economics of energy systems. Exergy analysis helps in locating system non-idealities that are not identified or misevaluated by energy analysis. In essence, exergy analysis consists of using the first and second laws together for the purpose of analyzing the performance in the reversible limit and for estimating the departure from this limit [12,25-31].

The objective of this paper is to make component wise and overall cycle exergy analysis of a coupled power-refrigeration cycle along with modifications to provide an efficient, alternative cooling technology which uses renewable energy sources for its operation. Thermodynamic states at all salient points of the coupled cycle are evaluated using the refrigerant properties from NIST Database REFPROP Version 8.0 [32]. Simulation is carried out to investigate the effect of operating parameters for performance evaluation.

2. Basics of Exergy Analysis

Exergy is defined as the maximum amount of work which can be produced by a system or a flow of matter or energy as it comes to equilibrium with a reference environment [25-30]. Unlike energy, exergy is destroyed, due to non-idealities or irreversibilities in any real process. The exergy destruction during a process is proportional to the entropy created due to irreversibilities associated with the process. In absence of magnetic, electrical, nuclear, surface tension effects, and considering the system is at rest relative to the environment, the total exergy of a system can be written as

$$e_f = e^{PH} + e^{CH} = (h - h_o) - T_o(s - s_o) + e^{CH} \qquad (1)$$

If there is single inlet and exit, steady state form of exergy rate balance becomes

$$\sum_j \left(1 - \frac{T_O}{T_j}\right)\dot{Q}_j - \dot{W}_{CV} + \dot{m}\left(e_{f,i} - e_{f,o}\right) - \dot{E}_D = 0 \qquad (2)$$

The exergetic efficiency (η_{II}) of a component is defined as the ratio between exergetic values of product and fuel, i.e.

$$\eta_{II\,k} = \dot{E}_{P,k} \Big/ \dot{E}_{F,k} = 1 - \left[\left(\dot{E}_{D,k} + \dot{E}_{L,k}\right) \Big/ \dot{E}_{F,k}\right] \qquad (3)$$

Examples of η_{II} for several different types of plant components can be found in [25, 26, 29, 35]. The exergy destruction rate within the k^{th} system component is obtained from the exergy balance as:

$$\dot{E}_{D,k} = \dot{E}_{F,k} - \dot{E}_{P,k} - \dot{E}_{L,k} \qquad (4)$$

Exergy destruction is caused by effects such as chemical reaction, heat transfer through a finite temperature difference, mixing of matter at different compositions or states, unrestrained expansion, and friction.

The exergy destruction ratio $(y_{D,k})$ compares the exergy destruction in the k^{th} component with the fuel exergy supplied to the overall system $(\dot{E}_{F,tot})$ [26-27, 29-31, 33-36], i.e.,

$$y_{D,k} = \dot{E}_{d,k} \Big/ \dot{E}_{F,tot} \qquad (5)$$

3. Exergy Analysis of the Cycles

3.1. Assumptions

Following assumptions are made to develop the simplified thermodynamic model for energy and exergy analyses of the considered cycles.

- Steady state control volume.
- No pressure drop across the heat exchangers.
- Environment is regarded as a simple compressible system, large in extent, uniform at $T_o = 25^{o}$C and $p_o = 1$atm.
- The $\eta_t, \eta_c, \& \eta_p$ are assumed constant within realistic limits.
- Condenser subcooling of 5^{o}C.

- The refrigerant vapours are dry-saturated at the suction of the compressor.
- Heat addition in the boiler is externally reversible.

3.2. Coupled Power-Refrigeration Cycle (CPR Cycle)

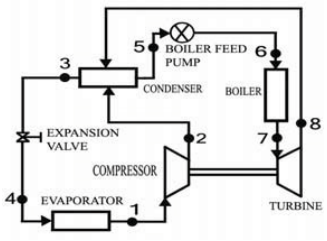

Fig. 1. Schematic diagram of CPR cycle

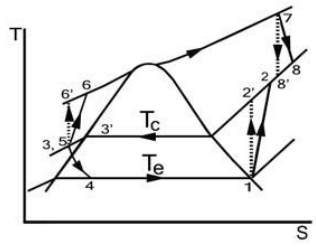

Fig. 2. T-s diagram of CPR cycle

The schematic and T-s diagram of the coupled power-refrigeration (CPR) cycle are shown in Figs. 1 and 2 respectively. In the refrigeration cycle, dry-saturated refrigerant vapours from the evaporator flows into the compressor, and then is discharged into the condenser. The subcooled liquid refrigerant from the condenser returns to the evaporator through the expansion valve to complete the cycle. In the power cycle, the subcooled refrigerant from the condenser is pressurized by the boiler feed pump, and is heated at constant boiler pressure. It then returns to the condenser after flowing through the turbine to complete the cycle. The work required for the compressor of the bottoming refrigeration loop and boiler feed pump of topping power loop are supplied from the work produced at the turbine.

3.2.1. Energetic Modeling

Thermodynamic states at all salient points are evaluated considering the input data as: $T_{e,sat}$ = 6°C, η_c = 0.73, $T_{c,sat}$ = 30-42°C, $T_{c,sub}$ = 5°C, η_p = 0.7, p_b = 4-8 MPa, T_b = 220-300°C,and η_t = 0.8. Assuming that pump shaft is connected to the turbine, the ratio of the fluid flows through the power and refrigeration loop allows the turbine to produce just enough power to drive the compressor and boiler feed pump. Therefore,

$$\frac{m_t}{m_r} = \frac{(h_2 - h_1)}{[(h_7 - h_8) - (h_6 - h_5)]} \tag{6}$$

COP of the refrigeration cycle is the ratio of the cooling produced to the input energy required to operate the system, i.e., the heat supplied in the boiler. Overall COP of the cycle then becomes,

$$COP_{overall} = \frac{(h_1 - h_4)}{[m_t(h_7 - h_6)]} \tag{7}$$

Mean temperature of heat addition,

$$T_{bm} = \frac{q_b}{(s_7 - s_6)} \tag{8}$$

3.2.2. Exergetic Modeling

The Fuel, Product, and Loss for the each component as well as for overall cycle required are summarized in Table 1. Special considerations are applied to devices such as the throttle valve, the condenser, and the evaporator. In case of the throttling valve, its product is not readily defined if it is considered in isolation [12, 29]. Therefore, evaporator assembly is considered consisting of condenser, expansion valve and evaporator as the control volume. Product of the overall cycle is the exergy associated with the cooling effect per kg of refrigerant through evaporator. Exergy associated with the heat supplied in the boiler per kg of refrigerant through evaporator is considered as fuel.

Table 1. Product, Fuel and Loss for CPR Cycle

Control Volume	Product	Fuel	Loss
Compressor	$(e_{f2} - e_{f1})$	$w_c = (h_2 - h_1)$	-
Evaporator Assembly	$\left(1 - \frac{T_0}{T_e}\right)(h_4 - h_1)$	$(e_{f2} - e_{f1}) + m_t(e_{f8} - e_{f5})$	$\left(1 - \frac{T_0}{T_{cm}}\right)q_c$
Boiler Feed Pump	$m_t(e_{f6} - e_{f5})$	$m_t(h_6 - h_5)$	-
Boiler	$m_t(e_{f7} - e_{f6})$	$\left(1 - \frac{T_0}{T_{bm}}\right)q_b$	-
Turbine	$m_t(h_7 - h_8)$	$m_t(e_{f7} - e_{f8})$	-
Overall Cycle	$\left(1 - \frac{T_0}{T_e}\right)(h_4 - h_1)$	$\left(1 - \frac{T_0}{T_{bm}}\right)q_b$	$\left(1 - \frac{T_0}{T_{cm}}\right)q_c$

3.3. Coupled Power-Refrigeration Cycle with Recuperator (CPRR Cycle)

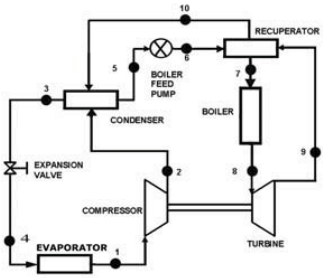

Fig. 3. Schematic diagram of CPRR cycle

The schematic diagram of the CPRR cycle is shown in Fig. 3. The recuperator between the boiler feed pump and boiler maximizes the temperature difference of two heat exchanging fluid streams. The working fluid at the outlet of the boiler feed pump is heated by the turbine exhaust, increasing the mean temperature of heat addition and reducing the heat to be supplied in the boiler, thus improving the performance based on the first law of thermodynamics. The thermodynamic analysis of this cycle is not presented since they are the same as that of the CPR cycle except for the recuperator.

3.4. Coupled Power-Refrigeration Cycle with Recuperator, Reheater and Economizer (CPRRRE Cycle)

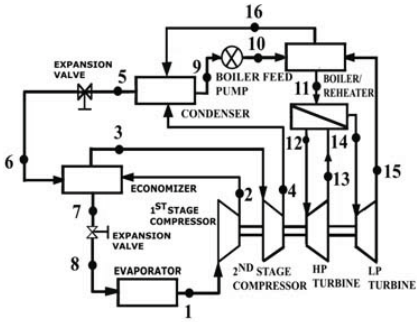

Fig.4. Schematic diagram of CPRRRE cycle

Refer to schematic and T-s diagram of a coupled power-refrigeration cycle with recuperator, reheater and economizer (CPRRRE) in Figs 4 and 5 respectively. Thermodynamic states at all salient points are evaluated considering the input data as: $T_{e,sat}$ = 6°C, η_{c1} = 0.73, T_{econ} = 25°C, η_{c2} = 0.77, $T_{c,sat}$ = 30-42°C, $T_{c,sub}$ = 5°C, η_p = 0.7, ε = 0.7-0.9, p_b = 4-8 MPa, T_b = 220-300°C, η_{t1} = 0.8, and η_{t2} = 0.8.

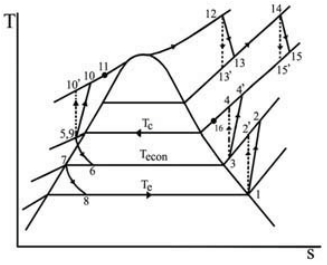

Fig.5. T-s diagram of CPRRRE cycle

3.4.1. Energetic Modeling

The cycle is analyzed in the ranges of boiler exit pressure and temperature values with the same boiler and reheater exit temperatures. The discharge pressure of the high pressure turbine is one of the critical parameters to augment performance of the CPRRRE cycle, the optimum value of which is calculated using [37, 38]:

$$p_{rh} = 0.25 p_b \tag{9}$$

The recuperator effectiveness is defined as [39],

$$\varepsilon = (t_{hi} - t_{ho}) / (t_{hi} - t_{ci}) \tag{10}$$

For unit mass flow in the evaporator, the mass flow in the 2nd stage compressor is obtained from,

$$m_3 = 1/(1 - x_6) \tag{11}$$

Since turbine work is directly supplied to the compressor and boiler feed pump, mass flow required for turbines per kg of refrigerant through the evaporator can be written as,

$$m_9 = \frac{\left[(h_2 - h_1) + m_3(h_4 - h_3)\right]}{\left[(h_{12} - h_{13}) + (h_{14} - h_{15}) - (h_{10} - h_9)\right]} \tag{12}$$

Overall COP of the whole cycle is,

$$COP_{overall} = \frac{(h_1 - h_8)}{m_9\left[(h_{12} - h_{11}) + (h_{14} - h_{13})\right]} \tag{13}$$

3.4.2 Exergetic Modeling

Product, Fuel and Loss for each component as well as for the overall cycle are summarized in Table 2. Boiler assembly consists of boiler and reheater. The exergy destruction of the whole cycle is the sum of the exergy destruction of individual components of the cycle.

Table 2 Product, Fuel and Loss for CPRRRE Cycle

Control Volume	Product	Fuel	Loss
1st Stage Compressor	$(e_{f2}-e_{f1})$	$w_{c1}=(h_2-h_1)$	-
Evaporator Assembly	$\left(1-\frac{T_0}{T_e}\right)(h_8-h_1)$	$(e_{f2}-e_{f1})+m_3(e_{f4}-e_{f3})+m_9(e_{f16}-e_{f9})$	$\left(1-\frac{T_0}{T_{cm}}\right)q_c$
2nd Stage Compressor	$m_3(e_{f4}-e_{f3})$	$w_{c2}=m_3(h_4-h_3)$	-
Boiler Feed Pump	$m_9(e_{f10}-e_{f9})$	$m_9(h_{10}-h_9)$	-
Recuperator	$m_9(e_{f11}-e_{f10})$	$m_9(e_{f15}-e_{f16})$	-
Boiler Assembly	$m_9(e_{f12}-e_{f11})+m_9(e_{f14}-e_{f13})$	$\left(1-\frac{T_0}{T_{bm}}\right)q_b+\left(1-\frac{T_0}{T_{rhm}}\right)q_{rh}$	-
1st Stage Turbine	$m_9(h_{12}-h_{13})$	$m_9(e_{f12}-e_{f13})$	-
2nd Stage Turbine	$m_9(h_{14}-h_{15})$	$m_9(e_{f14}-e_{f15})$	-
Overall Cycle	$\left(1-\frac{T_0}{T_e}\right)(h_8-h_1)$	$\left(1-\frac{T_0}{T_{bm}}\right)q_b+\left(1-\frac{T_0}{T_{rhm}}\right)q_{rh}$	$\left(1-\frac{T_0}{T_{cm}}\right)q_c$

4. Results and Discussion

The performance of the CPR cycle has been investigated at different boiler pressures, turbine inlet temperatures, condenser temperatures and recuperator effectiveness. Energy analysis shows that overall COP for the CPR cycle varies in the range of 0.77-1.50. Figure 6 presents the variation of overall COP with boiler pressure for different turbine inlet temperatures at $T_{c,sat}=30^{o}$C. In CPRR cycle with recuperator effectiveness of 0.7-0.9, an improvement in overall COP from 0.77-1.50 to 0.92-2.26 is observed, whereas in the CPRRRE cycle, an improvement in overall COP in the range of 1.09-2.39 is obtained. Hence, for the considered parametric range, the overall COP is increased by 19.5-50.7% and by 41.6-59.3% in the CPRR cycle and the CRPRRE cycle respectively, indicates effective utilization of the available energy at the exit of turbine in increasing the mean temperature of heat addition in the boiler. The CPRRRE cycle gives the added advantages of reheating, multistage compression and multistage expansion. Here, comparison of overall COP for CPRR and CPRRRE cycles at $T_{c,sat}=30^{o}$C, $\varepsilon=0.9$ is shown in Fig. 7.

Component wise exergy analysis of CPR cycles show that exergy destruction for compressor and evaporator assembly increases with increase in condenser temperature and is constant with increase in boiler pressure and turbine inlet temperature at a particular condenser temperature.

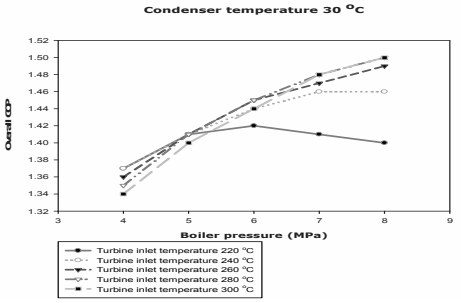

Fig. 6. Overall COP vs boiler pressure for CPR cycle

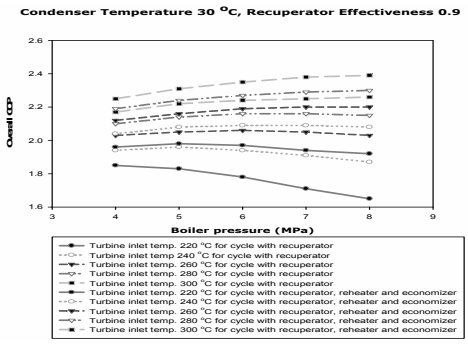

Fig.7. Overall COP vs. boiler pressure for CPRR and CPRRRE cycles

The exergetic efficiency for compressor remains constant with increase in p_b and T_b at the same $T_{c,sat}$ and it rises with increase in $T_{c,sat}$. For evaporator it decreases with increase in T_b at

constant $T_{c,sat}$ and p_b whereas it increases with increase in p_b at constant $T_{c,sat}$ and T_b . Lower values of the exergetic efficiencies are found at higher $T_{c,sat}$ for evaporator assembly. For turbine, the exergetic efficiency decreases with increase in T_b at a particular $T_{c,sat}$ and p_b and it increases with increase in p_b at a constant $T_{c,sat}$ and T_b . The exergy destruction for boiler feed pump and turbine decreases with increase in T_b at constant $T_{c,sat}$ and p_b , however more exergy destruction is observed at higher p_b at particular $T_{c,sat}$ and T_b . For boiler feed pump, it remains constant for all the T_b at a particular $T_{c,sat}$ and p_b . It increases with increase in $T_{c,sat}$ at constant p_b and T_b . Comparison of overall exergy destructions and the overall cycle exergetic efficiencies for CPR cycles are shown in Figs. 8 and 9 respectively. The data sets $\left(p_b : T_b : T_{c,sat}\right)$ in (*MPa:^{o}C: ^{o}C*) for these plots are: 1st – (8:220:30), 2nd – (8:220:42), 3rd – (8:300:30), 4th – (8:300:42), 5th – (4:220:30), 6th – (4:220:42), 7th – (4:300:30), and 8th – (4:300:42).

Overall exergy destruction reduces with increase in T_b at a constant p_b and $T_{c,sat}$ and increases with increase in p_b at a constant $T_{c,sat}$ and T_b . As seen in Fig. 8, the overall exergy destruction for CPRR cycle and CPRRRE cycle are higher than that of CPR cycle as the recuperator contributes additional exergy destruction. However, insignificant difference in overall exergy destruction is found between the CPRR cycle and CPRRRE cycle. Overall exergy destruction for CPR cycle varies in the range 11.14-20.75 kJ per kg of refrigerant through evaporator for $T_{c,sat} = 30$-42^{o}C. In the same parametric condition, overall exergy destruction, in kJ per kg of refrigerant through evaporator, varies from 14.03 to 26.00 for the CPRR cycle and from 14.70 to 27.48 for CPRRRE cycle, which are @26% and @32% higher than that for the CPR cycle respectively.

The overall cycle exergetic efficiency decreases with rise in T_b at a particular p_b and $T_{c,sat}$ and increases with increase in p_b at constant $T_{c,sat}$ and T_b . It decreases with increase in $T_{c,sat}$ at a constant p_b and T_b . Its value is found to be in the range of 16.81-38.03%, 20.42- 40.28%, and 20.77-39.58% for CPR cycle, CPRR cycle, and CPRRRE cycle respectively. Higher overall second law efficiency for CPRR and CPRRRE cycles as compared to CPR base cycle at the same parametric conditions is due to the reduction in exergy corresponding to the heat supplied. However, as shown in Fig. 9, this difference between the CPRR cycle and CPRRRE cycle is insignificant. Fluctuations in overall exergy destruction and overall second law efficiency as shown in Figs. 8 and 9 are due to the variation in one of the operating parameters in the considered data sets. Considering the design complexity and cost, CPRR cycle is recommended over the CPRRRE cycle for commercial adoption as there is insignificant difference in the exergetic efficiencies and overall exergy destructions between them.

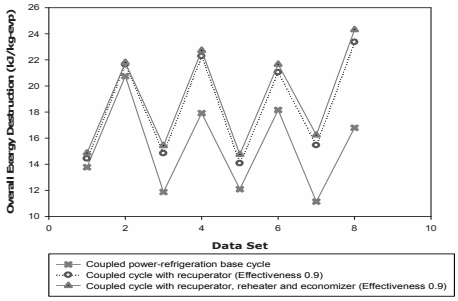

Fig. 8. Comparison of overall exergy destruction for CPR cycles

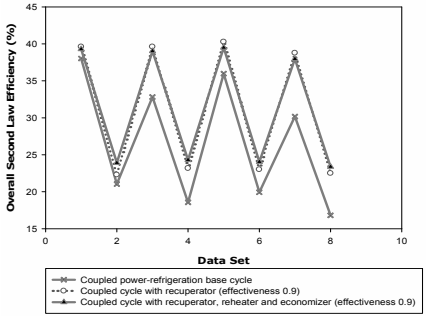

Fig. 9. Comparison of overall second law efficiencies for CPR cycles

5. Conclusions

The exergy analyses of a coupled power-refrigeration cycle with its two modified configurations have been carried out and

presented. Based on the results obtained from the analyses, the following key conclusions are drawn:

- Within the considered parametric range, the overall COP increases from its base cycle (i.e. CPR) by @ 50% in CPRR cycle and by @ 60% in CPRRRE cycle.
- Overall cycle exergy destruction and exergetic efficiency decrease with increase in turbine inlet temperature at a constant boiler pressure and condenser temperature and increases with increase in boiler pressure at a constant condenser and turbine inlet temperature. However, these differences between the CPRR cycle and CPRRRE cycle are insignificant.

Hence, the coupled power-refrigeration cycle with recuperator (CPRR) can be recommended for commercial adoption since the incorporation of reheater and economizer brings marginal performance improvement and does not justify the increase in capital cost and design complexity.

Nomenclature

$h;s$	enthalpy, kJ/kg; entropy, kJ/kg-K
e	specific exergy, kJ/kg
p	pressure, Mpa
T	temperature, K
m	mass flow rate, kg/s
q,Q	specific and total heat transfer, kJ/kg & kJ
W	work transfer

Greek symbols

η	efficiency
ε	effectiveness

Subscripts and superscripts

PH, CH	physical, chemical
$sat; sub$	saturated; subcooled
c, t, p	compressor, turbine, pump
b	boiler, boiler exit (or turbine inlet)
C	condenser
D	destruction (exergy)
f	flow
o	environment
P	product
F	fuel
L	loss
rh	reheater

References

[1] McMullan, T., 2002, Refrigeration and the Environment-Issues and Strategies for the Future, Int. J. of Refrig., 25, pp.89-99.

[2] UNEP 1999, Synthesis of the Scientific, Environmental Effects and Technology, and Economic Assessment Panels of the Montreal Protocol, United Nations Environment Programme, Ozone Secretariat.

[3] Kyoto Protocol, 1997, United Nations Framework Convention on Climate Change, Kyoto.

[4] Hung, T. C., et al., 1997, A Review of Organic Rankine Cycles for the Recovery of Low-Grade waste heat, Energy, 22(7), pp. 661-667.

[5] Lee, W. Y., et al., 1990, Thermodynamic Optimization of an Organic Rankine Power cycle, Solar Energy, 10(3), pp. 35-45.

[6] Shin, S. H., et al., 1999, A Study of Ocean Thermal Energy Conversion Systems using Kalina Cycle and Regenerative Rankine Cycle, Solar Energy, 19(3), pp. 101-113.

[7] Gurgenci, H., 1986, Performance of Power Plants with Organic Rankine Cycles under Part-Load and Off-Design Conditions, Solar Energy, 36(1), pp. 45-51.

[8] Lee, K. M., et al., 1988, Parameter Analysis on Organic Rankine Cycle Energy Recovery System, Energy Convers. and Mgmt., 28(2), pp. 129-136.

[9] Donghong, et al., 2007, Performance Analysis and Optimization of Organic Rankine Cycle for Waste Heat Recovery, Energy Convers. and Mgmt., 48, pp. 1113-1119.

[10] Mago, P. J., et al., 2007, Performance Analysis of Different Working Fluids for Use in Organic Rankine Cycles, Journal of Power and Energy, Proc. IMechE, 221, Part A, pp. 255-263.

[11] Schuster, A., et al., 2009, Energetic and Economic Investigation of Organic Rankine Cycle Applications, Applied Thermal Engineering, 29, pp. 1809-1817.

[12] Bejan, A., 2006, *Advanced Engineering Thermodynamics,* Third Edition, John Wiley and Sons Inc, New Jersey.

[13] Sonntag, R. E., et al., 2006, *Fundamentals of Thermodynamics,* 6th edition, John Wiley and Sons (Asia) Pvt. Ltd., Singapore.

[14] Burmeister, L. C., 1998, *Elements of Thermal-Fluid System Design,* Prentice Hall, New Jersey.

[15] Christensen, R. N., and Santoso, M., 1990, An Evaluation of a Rankine Cycle Driven Heat Pump, Heat Recovery Systems and CHP, 10(2), pp. 161-175.

[16] Gozdur, A. B., and Wladyslaw, N., 2007, Comparative Analysis of Natural and Synthetic Refrigerants in Application to Low Temperature Clausius-Rankine Cycle, Energy, 32, pp. 344-352.

[17] Hung, T. C., 2001, Waste Heat Recovery of Organic Rankine Cycle using Dry Fluids, Energy Convers. and Mgmt, 42, pp. 539-553.

[18] Maizza, V., and Maizza, A., 2001, Unconventional Working Fluids in Organic Rankine Cycles for Waste Energy Recovery Systems, Applied Thermal Engineering, 21, pp. 381-390.

[19] Angelino, G., and Paliano, P. C., 1998, Multi-Component Working Fluids for Organic Rankine Cycles, Energy, 23(6), pp. 449-463.

[20] Maizza, V., and Maizza, A., 1996, Working Fluids in Non-Steady Flows for Waste Energy Recovery Systems, Applied Thermal Engineering, 16(7), pp. 579-590.

[21] Cavallini, A., 1996, Working Fluids for Mechanical Refrigeration, Int. J. of Refrig., 19, pp. 485-496.

[22] Saleh, B., and Wendland, M., 2006, Screening of Pure Fluids as Alternative Refrigerants, Int. J. of Refrig., 29, pp. 260-269.

[23] Saleh, B., et al., 2007, Working Fluids for Low-Temperature Organic Rankine Cycles, Energy, 32, pp. 1210-1221.

[24] Dubey, M., and Rajput, S. P. S., 2009, Performance Analysis of Rankine Powered Refrigeration System using R-134a for Cold Storage like Applications, *Proceedings of National Conference on Refrigeration and Air Conditioning, NCRAC 2009,* Paper no. P-45, IIT Madras, Chennai, India.

[25] Moran, M. J., and Sciubba, E., 1994, Exergy Analysis: Principles and Practice, Journal of Engineering for Gas Turbines and Power, 116 (4), pp. 285-290.

[26] Moran, M. J., and Shiparo, H. N., 2006, *Fundamentals of Engineering Thermodynamics,* 5th Ed., John Wiley and Sons Inc, New York.

[27] Kotas, T.J., 1985, *The Exergy Method of Thermal Plant Analysis,* Butterworths.

[28] Bejan, A., 1982, *Entropy Generation through Heat and Fluid Flow,* Wiley, New York.

[29] Bejan, A., Tsatsaronis, G., and Moran, M.J., 1996, *Thermal Design and Optimization,* John Wiley and Sons Inc., New York.

[30] Moran, M. J., 1989, *Availability Analysis, A Guide to Efficient Energy Use,* Second Edition, ASME Press, New York.

[31] Rosen, A., et al., 2008, Role of Exergy in Increasing Efficiency and Sustainability and Reducing Environmental Impact, Energy Policy, 36, pp. 128-137.

[32] NIST, Standard Reference Database 23, Reference Fluid Thermodynamic and Transport Properties- REFPROP, 2009, Version 8.0, National Institute of Standards and Technology (NIST), Gaithersburg, Department of Commerce, Government of USA.

[33] Tsatsaronis, G., and Cziesla, F., 2004, Basic Exergy Concepts, Exergy Balance and Exergetic Efficiency, Exergy Analysis of Simple Processes, Energetic and Exergetic Analysis of Complex Systems, Strength and Limitations of Exergy Analysis, in: Encyclopedia of Life Support Systems (EOLSS), Topic Energy, Developed under the Auspices of the UNESCO, Eolss Publishers, Oxford, UK, Available online at: http://www.eolss.net.

[34] Bejan, A., 1987, Second Law Analysis of Thermal Systems, ASME, 1.

[35] Moran, M.J., 1998, Fundamentals of Exergy Analysis and Exergy-Aided Thermal Systems Design, *Proceedings of the NATO Advanced Study Institute on Thermodynamics and the Optimization of Complex Energy Systems,* pp. 73-92, Neptun, Romania.

[36] Szargut,, J., 1998, Exergy in Thermal Systems Analysis, *Proceedings of the NATO Advanced Study Institute on Thermodynamics and the Optimization of Complex Energy Systems,* pp. 137-150, Neptun, Romania.

[37] ASHRAE, 1999, ASHRAE Transactions, Vol. 95, Part 2; American Society of Heating,

Refrigerating and Air-Conditioning Engineers, Inc., Atlanta, USA.

[38] Nag, P. K., 2006, *Engineering Thermodynamics,* 3rd Edition, Tata Mc Graw Hill Publishing Company Limited, New Delhi.

[39] ASHRAE, 2005, *ASHRAE Handbook–Fundamentals,* American Society of Heating, Refrigerating and Air-Conditioning Engineers, Inc., Atlanta, USA.

Energy savings with advanced control of reciprocating liquid chillers

H. Fallahsohi [a], C. Changenet [b], S.Placé [a] , G. Duhot [a], C. Ligeret [c] and X.Lin-shi [d]

[a] *EDF R &D, Moret-sur-Loing, France*
[b] *Université de Lyon, ECAM, Laboratoire d'Energétique, Lyon, France*
[c] *Schneider-Electric, Grenoble, France*
[d] *Université de Lyon, INSA-Lyon, Ampère, CNRS UMR5005, Villeurbanne, France*

Abstract: A Predictive Functional Control (PFC) method is proposed to control the evaporator superheat, the condensing pressure and the cooling capacity on a variable-speed refrigeration system. This method is based on the physical modelling of the machine in order to determine parameters needed for the use of PFC (gain, time constant…). Some experiments were performed on a refrigeration unit by changing cooling loads. It is shown that PFC controller succeed in maintaining a precise chilled liquid temperature. As this controller appears to be a lot more robust from disturbances point of view than a conventional Proportional-Integral-Derivative controller, the superheat may be reduced in a significant ratio and PFC controller leads to increase the coefficient of performance.

Keywords: refrigerating system, variable-speed compressor, predictive control, energy saving.

1. Introduction

The control of flows is essential in any refrigerating system. Several physical parameters may be regulated such as temperature, pressure or liquid flow rate. On the one hand, the advanced control of evaporator superheat may be performed via an expansion valve which modulates the refrigerant flow, and the control of condensing pressure is carried out via the flow rate of the condenser cooling fluid. On the other hand, the methods of refrigerating capacity control include the following: (i) on-off cycling of compressors (ii) loading or unloading of cylinders for reciprocating compressors (iii) compressor speed control. Several studies [1-4] have demonstrated the potential savings associated with the use of optimal control. When a refrigerating plant has a number of actuators, it is possible to provide the cooling power for a desired temperature by various combinations of operating conditions. The purpose of these papers is to obtain an optimal control by considering the plant in its global nature. Another way consists to increase the Coefficient Of Performance (COP) by optimizing control on a single component of a refrigerating machine. As an example, some authors [5,6] have pointed that an accurate control of compressor speed can lead to energy savings on variable-speed refrigeration systems. According to Chen et al. [7] the use of variable speed compressors can also generate an unstable behaviour of the superheat. It has to be noticed that this parameter is of primary importance on a refrigerating machine. On the one hand, the refrigerant at the evaporator outlet should be superheated to prevent any unevaporated liquid from reaching the compressor. On the other hand, a high value of superheat has also an adverse effect on COP. Several control methods are available for controlling the evaporator superheat via an Electrically driven Expansion Valve (EEV). Some are based on Proportional-Integral-Derivative (PID) control [8,9] others combine PID laws with fuzzy parameters [10] or use dynamic neural network [11]. More recently Changenet et al. [12] have developed a method based on the physical modelling of the evaporator in order to use a Predictive Functional Controller (PFC). This proposed methodology has been extended by the authors [13] to regulate the condensing pressure in order to reduce disturbances in EEV inlet. As a conclusion, it appears that it is possible to minimize the superheat setting value.

In addition to the above-mentioned study, this paper presents how the control system created is now implemented for regulating the cooling capacity. The previous physical model is completed to calculate the required refrigerant flow, which means the compressor swept volume and its rotational speed, to adjust the freezing

Corresponding Author: Christophe Changenet, Email: christophe.changenet@ecam.fr

potential. Some experiments are conducted on a test bench with the three above-mentioned regulation loops. Then investigations are performed on the chilled liquid temperature and the superheat behaviour. In the end, some energy savings are quantified.

2. Refrigerating machine under consideration

The refrigerating machine used in this study is located in Les Renardières, one of EDF research centres. This machine runs with the refrigerant mixture R410A and it is composed of two shell and tube heat exchangers and a reciprocating compressor. The 4-cylinder single stage motor-compressor has an actual displacement of 97m^3/h at 1500rpm. It is possible to reduce the compressor displacement by modifying the compressor rotational speed or by a cylinder-unloading scheme: the compressor can operate with one, two, three or four cylinders. The evaporator is used with a flow of water and antifreeze mixture as the secondary fluid, whereas the condenser is water cooled. A 160kW electric heater is used to simulate a refrigerating charge on the mixed-water flow. The cooling capacity of this refrigerating machine may vary from 20kW to 160kW. The evaporator and condenser are both counter-flow heat exchangers. The refrigerant mixture is vaporized inside tubes, whereas its condensation occurs outside the tube bundle.

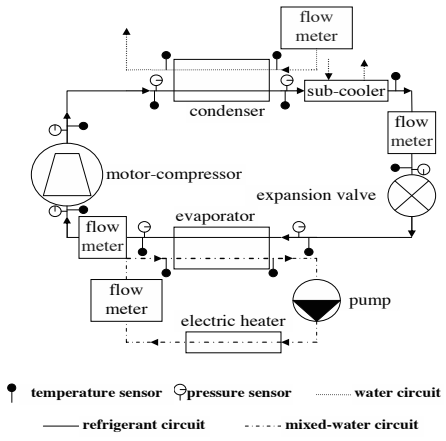

Fig. 1. Schematic representation of EDF refrigerating machine

In order to define the operating thermodynamic cycle, several sensors are used for measuring refrigerant temperatures and pressures at different points of the machine, as presented in Fig.1. Different flow meters are used for measuring the refrigerant mass flow rate and the secondary fluids. The electrical power provided by the motor-compressor is measured with a wattmeter.

3. PFC for evaporator superheat control

3.1. Physical model

Some papers [14,15] have shown that the response of superheating to variation of refrigerant flow can be represented using a first-order plus time delay model:

$$G(p) = \frac{\text{process output}}{\text{process input}} = \frac{K\, e^{-Td\, p}}{1+\tau\, p} \qquad (1)$$

The model parameters are generally obtained from an evaporator open-loop response to a step excitation [14,16]. In Changenet et al. [12], the same simplified model is used to control evaporator superheat with a PFC, but the model parameters are determined by a physical model in order to improve the model accuracy. To this end, the evaporator has been divided into two control volumes: the first one corresponds to the refrigerant vaporization and once R410A is completely vaporized a single-phase flow occurs, which is the second volume of control. The refrigerant pressure at the expansion valve inlet (*HP*) is considered as input data and the aim of the model is to calculate the value of the required vaporization pressure (*BP*) to obtain the desired superheat. Calculations are initialized with a given value of *BP*; then it is possible to determine the refrigerant mass flow rate:

$$\dot{m}_f = \rho_{su}(Cyl * N)\eta_v \qquad (2)$$

where the volumetric efficiency (η_v) is estimated as a function of pressure ratio.

The energy balance is then written for each control volume which enables to determine the temperature profile in the evaporator. The log mean temperature difference method [17] is applied on the first control volume to calculate the surface area needed for a complete vaporization of refrigerant mixture. The surface area available for superheating the vapour is then deduced from this previous value and the effectiveness-NTU method

[17] is used on the second control volume (single-phase flow). The refrigerant outlet temperature can be calculated and compared to the required one. The initial value of *BP* is modified until the convergence is reached.

As stated earlier, the control of evaporator superheat is performed by the expansion valve. To quantify the valve position, a parameter (O_p) is introduced which corresponds to the opening degree of this one: (i) for wide open position O_p = 100 per cent; (ii) for totally closed position O_p = 0 per cent. According to Park et al. [18], the R410A mass flow rate through EEVs can be determined by using a single-phase orifice equation:

$$O_p = \frac{\dot{m}_f}{\beta\sqrt{\rho_{li}(HP - BP)}} \tag{3}$$

By using equation (3) it is possible to link the vaporization pressure (*BP*) to the valve position. This calculation is then performed for two different values of superheat: T^0_{sup} and T^∞_{sup}. Then the evaporator gain may be estimated by:

$$K_e = \frac{(T^0_{sup} - T^\infty_{sup})}{O^0_p - O^\infty_p} \tag{4}$$

As far as the time constant is concerned, the global approach proposed by Azilinon et al. [19] for single-phase flow heat exchangers has been extended to liquid chillers. To this end a counter-flow heat exchanger is considered as control volume (Fig.2).

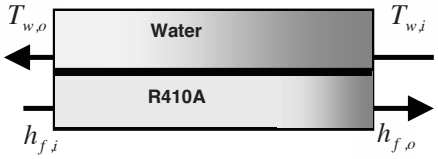

Fig. 2. Control volume for time constant estimation

The energy balance on this control volume can be written as:

$$\frac{dU}{dt} = \dot{Q}_{\text{lost via hot fluid}} - \dot{Q}_{\text{récovered via cold fluid}} \tag{5}$$

As in the process phase change occurs, enthalpy is used to express heat fluxes:

$$\frac{dU}{dt} = \dot{m}_w\left[h_{w,i} - h_{w,o}\right] + \dot{m}_f\left[h_{f,i} - h_{f,o}\right] \tag{6}$$

Where *U* is the internal energy of heat exchanger.

By considering a first-order model, Fig.3 represents the internal energy evolution versus time.

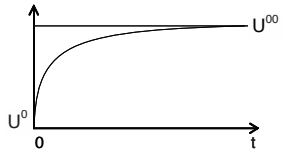

Fig. 3. Transient evolution of internal energy

Then *U* can be expressed as time function:

$$\frac{U(t) - U^\infty}{U^0 - U^\infty} = e^{-\frac{t}{\tau}} \tag{7}$$

In a similar manner, the enthalpies of mixed-water and refrigerant mixture at outlet are given by:

$$\frac{h_{w,o}(t) - h^\infty_{w,o}}{h^0_{w,o} - h^\infty_{w,o}} = e^{-\frac{t}{\tau}} \tag{8-a}$$

$$\frac{h_{f,o}(t) - h^\infty_{f,o}}{h^0_{f,o} - h^\infty_{f,o}} = e^{-\frac{t}{\tau}} \tag{8-b}$$

Thanks to these expressions equation (6) becomes:

$$\frac{dU}{dt} = \dot{m}_w\left[h_{wi} - h^\infty_{wo} - \alpha_w\left(U(t) - U^\infty\right)\right] + \dot{m}_f\left[h_{fi} - h^\infty_{fo} - \alpha_f\left(U(t) - U^\infty\right)\right] \tag{9}$$

where: $\alpha_w = \frac{h^0_{wo} - h^\infty_{wo}}{U^0 - U^\infty}$ and $\alpha_f = \frac{h^0_{fo} - h^\infty_{fo}}{U^0 - U^\infty}$

For steady state operating condition, equation (6) leads also to the following relationship:

$$\dot{m}_w\left(h_{wi} - h^\infty_{wo}\right) = \dot{m}_f\left(h^\infty_{fo} - h_{fi}\right) \tag{10}$$

Finally formula (11) is obtained:

$$\frac{dU}{dt} + \lambda U(t) = \lambda U^\infty \tag{11}$$

where $\lambda = \dot{m}_w\alpha_w + \dot{m}_f\alpha_f$

From (7), it can be deduced that *U* is also solution of the following differential equation:

$$\tau \frac{dU}{dt} + U(t) = U^{\infty} \tag{12}$$

Then the time constant is given by:

$$\tau = \frac{1}{\dot{m}_w \left[\frac{h_{w,o}^0 - h_{w,o}^{\infty}}{U^0 - U^{\infty}} \right] + \dot{m}_f \left[\frac{h_{f,o}^0 - h_{f,o}^{\infty}}{U^0 - U^{\infty}} \right]} \tag{13}$$

As far as the time delay is concerned, tests carried out on the evaporator have shown that it is very small, so a constant value of three seconds has been taken into account.

3.2 Predictive control

The theory of PFC is based on an open-loop control linked to a perfect understanding of the relevant process [20]. Indeed, if the process can be modelled with precision, it is possible to define the action to be taken directly without considering the output measurement. In reality a model is more or less inaccurate, so the predictive controller has to establish a trade-off between the understanding of the process structure and the data provided by the sensors. To this end, a closed loop control is used. The prediction of future changes at the process output is based on an internal model which is incorporated into the calculator. Here formula (1) is used as internal model whereas gain or time constant are calculated according to the above mentioned formulae. The ultimate objective of the control system is to determine a future action (*uc*) that will allow the prediction to reach the set point (*C*) at the end of a time period referred to as the coincidence horizon.

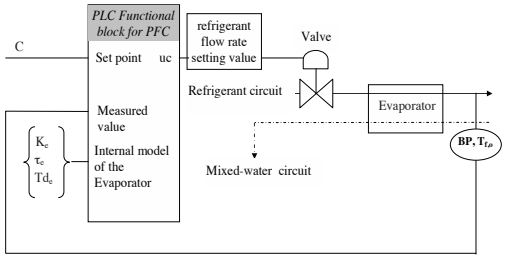

Fig. 4. Schematic representation of superheat control for PFC

The PFC has been implemented by programming a functional block in an industrial Programmable Logic Controller (PLC), made by Schneider-Electric. It has been incorporated in EEV instead of the original PID controller package, as described in Fig.4. It can be shown that the measurement of the evaporator outlet pressure (*BP*) is used to determine the refrigerant saturation temperature (T_{sat}). This value is then subtracted from the refrigerant outlet temperature ($T_{f,o}$) in order to calculate the superheat.

4. PFC to regulate the condensing pressure

4.1. Physical model

A similar approach to the one described in section 3.1 has been used by the authors [13]. Since a specific heat exchanger is used to generate subcooling (Fig.1), it has been assumed that a negligible subcooling occurs in condenser. Then it has been divided into two control volumes. The properties of the refrigerant at the compressor inlet (*BP* and $T_{f,su}$) are considered as input data and the aim of the model is to calculate the value of water mass flow rate ($\dot{m}_w$) that is required to obtain the desired value of *HP*. Enthalpy at condenser inlet is determined by using the internal isentropic efficiency of the reciprocating compressor. The refrigerant mass flow rate is estimated by using equation (2) and calculations are initialized with a given value of $\dot{m}_w$. The energy balance is written for each control volume, then the water temperature profile is determined. The log mean temperature difference method is applied on each control volume to calculate heat exchange surface areas. The surface area required for condensation is then compared to the physical one and the initial value of $\dot{m}_w$ is modified until the convergence is reached.

The calculation of water flow rate is performed for two different values of condensing pressure: HP^0 and HP^{∞}, and the condenser gain may be estimated by:

$$K_c = \frac{HP^0 - HP^{\infty}}{\dot{m}_w^0 - \dot{m}_w^{\infty}} \tag{14}$$

The time constant τ_c is determined according to equation (13) and a constant value of one second is used to take into account the time delay Td_c.

4.2. Predictive control

The parameters described in section 4.1 are calculated and transmitted to an industrial PLC

where PFC has been implemented. This PLC controls the valve which modulates the quantity of water passing through the condenser as described in Fig. 5.

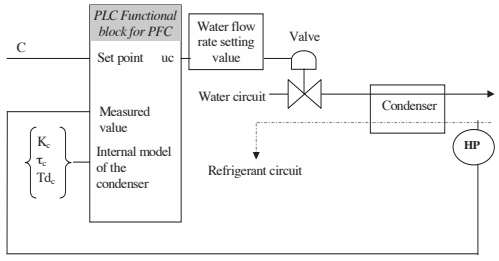

Fig. 5. Schematic representation of condensing pressure control for PFC

5. PFC for cooling capacity control

5.1. Physical model

To adjust the freezing potential, the characteristics of water and antifreeze mixture flow ($\dot{m}_w$, $T_{w,i}$, $T_{w,o}$) are considered as input data and the aim of the model is to calculate the value of the refrigerant mass flow rate ($\dot{m}_f$) to obtain this cooling capacity and maintain a required superheat. Calculations are initialized with a given value of *BP* in order to estimate the refrigerant enthalpies at evaporator inlet and outlet (Fig. 2). Then the energy balance is written:

$$\dot{m}_f = \frac{\dot{m}_w Cp_w \left(T_{w,i} - T_{w,o}\right)}{\left(h_{f,o} - h_{f,i}\right)} \qquad (15)$$

It is necessary to check that the calculated mass flow rate belongs to the compressor displacement range:

$$\dot{m}_f \in \left[1Cyl.N_{min},\ 4Cyl.N_{max}\right] \qquad (16)$$

Where N_{min} and N_{max} correspond respectively to the minimum and maximum rotational speed. If the calculated flow rate is outside this range the initial value of *BP* has to be changed.

The same model than the one described in section 3.1 is then used to calculate heat-transfer in the evaporator, and the value of *BP* is modified until the convergence is reached. From the calculated value of the refrigerant mass flow rate a logical number of operating cylinders (n) is deduced. Then the compressor rotational speed (N) is determined according to equation (2).

As mass flow rate and inlet temperature of water and antifreeze mixture are considered as constant, the calculation of n and N is performed for two different values of outlet temperature: $T^0_{w,o}$ and $T^\infty_{w,o}$, and the gain is estimated by:

$$K_{cc} = \frac{\left(T^0_{w,o} - \Delta T^\infty_{w,o}\right)}{n^0 Cyl\, N^0 - n^\infty Cyl\, N^\infty} \qquad (17)$$

where *Cyl* represents the size of one cylinder.

Time constant and time delay are determined as explained in section 3.1.

5.2. Predictive control

As previously mentioned, the above parameters are calculated and transmitted to an industrial PLC where PFC has been implemented. This PLC has been incorporated in the reciprocating compressor in order to select the number of cylinder and the rotational speed which provide the required refrigerant flow rate.

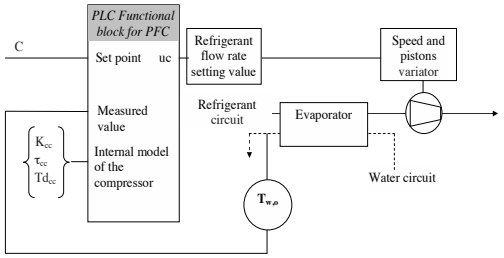

Fig. 6. Schematic representation of cooling capacity control for PFC

6. Energy savings with advanced control

One of the aims of this study is to compare the energy efficiency of the refrigerating machine by using: (i) an advanced control (PFC) and (ii) a standard commercial regulation (SCR).

Some experiments were conducted by changing the cooling capacity of the refrigerating machine described in section 2. These investigations were carried out in order to investigate the control performance in maintaining the superheat and the mixed-water outlet temperature at a setting value for different cooling power. The same testing protocol was used to compare PFC and SCR.

During these tests, the liquid chiller cooled the mixed-water which was heated with an electrical heater from 100 to 25 kW. The outlet temperature condition on mixed-water was set at 6°C. As far as the superheat control is concerned, the authors have shown in a previous paper [13] that PFC is a lot more robust from disturbances point of view than a standard controller. As a consequence, it is possible to reduce the setting value in accordance with cooling power. While, for SCR tests, the superheat was set at 8°C.

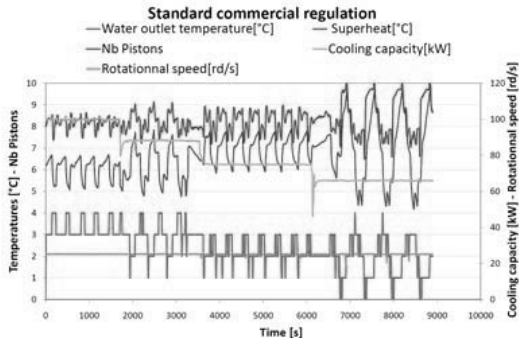

Fig. 7. Refrigerating machine controlled with SCR

Figure 7 shows the behaviour of the refrigerating machine when SCR control is used. This figure focuses on a cooling power variation from 100 to 50 kW. It can be noticed that the mixed-water outlet temperature and the superheat are different from set points: the discrepancy reaches 10% for nominal load and 25% for partial load.

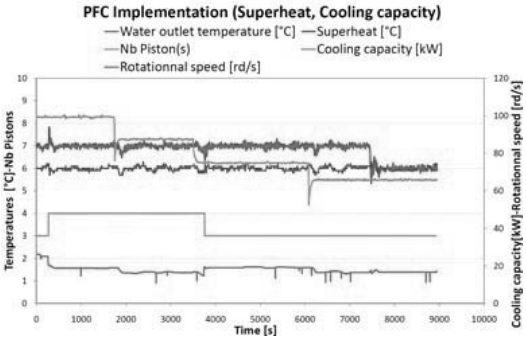

Fig. 8. Refrigerating machine controlled with PFC

On the contrary, Fig.8 indicates that both mixed-water temperature and superheat are rather the same than setting values when PFC is used. Thanks to this behaviour, the superheat set point can be automatically adapted according to machine load. In order to maintain an optimum filling up of the evaporator, the set point can be reduced for partial load [13]. As an example, the superheat set point is fixed to 6°C at 50 kW.

During these experiments COP has also been measured at any time. Figure 9 shows that, from nominal load up to a partial load equal to 50%, energy performances are better with PFC than with SCR control.

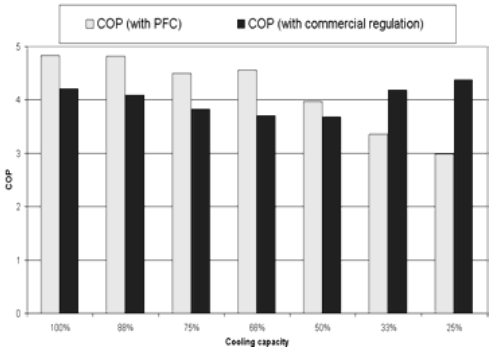

Fig. 9. COP measurements with PFC and SCR control

For small cooling capacity (33 and 25%) Fig.9 indicates that COP may be lower when PFC is used. In fact, during SCR tests, it was observed that the machine was often turned off for small partial load. On the one hand, this behaviour leads to no energy consumption. On the other hand, the mixed-water outlet temperature becomes very different from the set point. In order to quantify this discrepancy, Fig.10 presents the time percentage when the difference between measured temperature of mixed-water and setting value is smaller than 10% of set point.

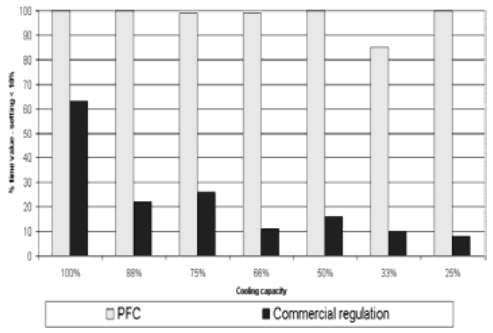

Fig. 10. Discrepancy between mixed-water temperature and set point

For the considered partial load (33 and 25%) it appears that the set point is reached less than 10% of total time when SCR control is used, whereas this percentage reaches at least 85% with PFC. For higher values of load this percentage is almost equal to 100%. In order to quantify a COP average value for an industrial context, the following part load weighting factors are used by EDF:

$$COP_{industrial\ site} = 0.08COP_{100\%} + 0.3COP_{88\%} + 0.2COP_{75\%} + 0.2COP_{66\%} + 0.15COP_{50\%} + 0.05COP_{33\%} + 0.02COP_{25\%} \quad (18)$$

By applying this formula on results presented in Fig.9, COP increases of 12% when the liquid chiller operates with PFC.

7. Conclusion

A PFC method is proposed to control the evaporator superheat, the condensing pressure and the cooling capacity on a variable-speed refrigeration system. Physical models of evaporator, condenser and compressor are used to determine parameters required by PFC, such as gain and time constant. Thanks to these models a machine operator just needs to define geometrical data and the fluids used in a given refrigerating machine. The control parameters are automatically calculated and can be set in an industrial PLC. As a conclusion, the operator does not have to know the mathematical model of the controller and this method is an easy way for using PFC.

In order to quantify the COP variation when PFC is used instead of a standard commercial controller, some experiments have been performed on a refrigerating machine composed of two shell and tube heat exchangers and a reciprocating compressor. These tests have been carried out by changing the cooling capacity. The analysis of COP average values indicates that it is possible to increase the COP by 12% with PFC.

As PFC controller leads to an improvement in disturbance rejection and accurate control in cooling conditions, it prevents any unevaporated refrigerant from reaching the compressor. Therefore a method using PFC for controlling a liquid chiller can increase the reliability of a refrigerating machine.

The physical model developed here enables to calculate easily the system parameters for different operating conditions. This is very important for refrigerating systems which are highly nonlinear. Then PFC can be easily implemented for positive and negative cooling process. Moreover this method will be extended to another refrigerating machine which is composed of a plate evaporator, a finned-tube condenser and a screw compressor. Some investigations will be conducted to control the condensing pressure as a function of the outdoor temperature in order to minimize the energy consumption.

Nomenclature

BP	pressure at compressor suction line (bar)
C	setting value
COP	coefficient of performance
Cp	specific heat (J/kg K)
Cyl	cylinder size (m^3)
G	transfer function
h	enthalpy (J/kg)
HP	pressure at compressor discharge line (bar)
K	gain
$\dot{m}$	mass flow rate (kg/s)
n	number of operating cylinders
N	compressor's rotational speed (tr/s)
O_p	opening degree of the valve
$\dot{Q}$	heat flow (W)
t	time (s)
T	temperature (K)
Td	time delay (s)
U	internal energy (J)
uc	control

Greek symbols

β	coefficient of the orifice equation
η_v	volumetric efficiency
ρ	density (kg/m^3)
τ	time constant (s)

subscripts

c	condenser
cc	cooling capacity
e	evaporator
f	refrigerant flow
i	inlet
li	liquid phase

o outlet

su compressor's suction

sup superheat

w flow of water or mixed-water

superscripts

∞ final operating condition

0 initial operating condition

References

[1] Braun, J.E., et al., 1989, Methodologies for optimal control of chilled water systems without storage. ASHRAE Trans. 90, pp. 652-662.

[2] Jakobsen, A., and Rasmussen, B., 1998, Energy-optimal speed control of fans and compressors in a refrigeration system. *Proc. Eurotherm Seminar*, Nancy, France, pp. 317-323.

[3] Yao, Y., et al., 2004, Optimal operation of a large cooling system based on an empirical model. Appl. Therm. Eng. 24, pp. 2303-2321.

[4] Leducq, D., Guilpart, J. and Trystram, G., 2006, Non-linear predictive control of a vapour compression cycle. Int. J. Refrigeration 29, pp. 761-772.

[5] Hua, L., Jeong, S.K., and You, S.S., 2009, Feedforward control of capacity and superheat for a variable speed refrigeration system. Appl. Thermal Eng. 29, pp. 1067-1074.

[6] Aprea, C., Mastrullo, R., and Renno, C., 2004, Fuzzy control of the compressor speed in a refrigeration plant. Int. J. Refrigeration 27, pp. 639-648.

[7] Chen, Y., et al., 2008, A study on the operational stability of a refrigeration system having a variable speed compressor. Int. J. Refrigeration 31, pp. 1368-1374.

[8] Outtagarts, A., Haberschill, P., and Lallemand, M., 1995, Etude des lois de commande adaptatives utilisables pour des détendeurs électroniques de machines frigorifiques. *Proc. 19th International Congress on Refrigeration*, B2, La Haye, Netherlands, pp. 421-428.

[9] Lin, J.L., and Yeh, T.J., 2007, Modeling, identification and control of air-conditioning systems. Int. J. Refrigeration 30, pp. 209-220.

[10] Zhu, R.Q., Zheng, X.Q., and Wu, Y.Z., 2000, Fuzzy-PID methods for controlling evaporator superheat. *Proc. 8th Int. Refrigeration Conference,* Purdue University, West Lafayette, Indiana, pp. 337-344.

[11] Nanayakkara, V.K., Ikegami, Y., and Uehara, H., 2002, Evolutionary design of dynamic neural networks for evaporator control. Int. J. Refrigeration 25, pp. 813-826.

[12] Changenet, C., et al., 2008, Study on predictive functional control of an expansion valve for controlling the evaporator superheat. Proc. IMechE, Part I: Systems and Control Engineering 222 (I6), pp. 571-582.

[13] Fallahsohi, H., et al., 2010, Predictive functional control of an expansion valve for minimizing the superheat of an evaporator. Int. J. Refrigeration 33, pp. 409-418.

[14] Outtagarts, A., Haberschill, P., Lallemand, M., 1995, Comportement dynamique d'un évaporateur de machine frigorifique soumis à des variations de débit. *Proc. 19th International Congress on Refrigeration,* B2, La Haye, Netherlands, pp. 413-420.

[15] Finn, D.P., and Doyle, C.J., 1999, A BEMS-integrated electronic expansion valve for real-time optimisation of refrigerant evaporation. *Proc. 20th International Congress on Refrigeration,* IIR/IIF, Sydney, Australia, vol. III, 8 p.

[16] Zhou, X., et al., 1999, Study on fuzzy control of the electronic valve in the air-conditioner with inverter. *Proc. 20th International Congress on Refrigeration, IIR/IIF,* Sydney, Australia, vol. III, 6 p.

[17] Holman, J.P., 1989, *Heat Transfer*. 7th edition, Mac Graw – Hill book company, New York, 676 p.

[18] Park, C., et al., 2007, Mass flow characteristics and empirical modelling of R22 and R410A flowing through electronic expansion valves. Int. J. Refrigeration 30, pp. 1401-1407.

[19] Azilinon, D., Pierson, P., and Padet, J., 1990, Constante de temps des échangeurs thermique. Rev. Gén. Therm. 338, pp. 64-78.

[20] Richalet, J., 1993, *Pratique de la commande predictive*. Hermès Editions, Paris, 352 p.

Pressure drop considerations in optimum design of multi- stream plate- fin heat exchanger

M.H. Panjeshahi[a], N. Tahouni[a] and S. Iman shayan[a]

[a] *Department of Chemical Engineering, University of Tehran, Tehran, Iran*

Abstract: This study presents a new approach based on considering the optimum pressure drop values, when designing the multi-stream heat exchangers (MSHE). A hybrid method of Simulated Annealing algorithm (SA) and Pinch Thermodynamic concepts is presented to design and optimization of MSHE. The main objective is minimizing the total annual cost (TAC), taking into account the optimum stream pressure drops, which has been achieved by a trade-off between operating and capital costs. The new procedure is applied to an example discussed previously in literature. The results proved that the algorithm not only significantly explores the solution with lower TAC, but also it allows a more optimum utilization of stream pressure drops through the heat recovery network.

Keywords: Multi-Stream Heat Exchangers, Optimization, Plate-and-Fin Heat Exchangers, Pressure Drop, Simulated Annealing.

1. Introduction

Plate-and-fin heat exchangers (PFHE) are one of the most important subtypes of compact heat exchangers and are designed to create the capacity for significant heat transfer in a small volume. Figure 1 depicts a typical scheme of a PFHE.

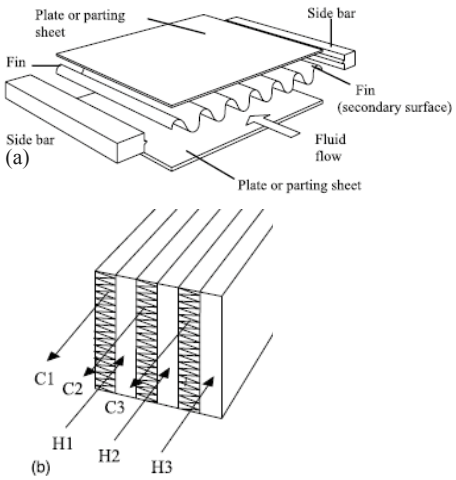

Figure1. (a) Typical scheme of a PFHE (b) MSHE [1]

One of the most recent methods of designing multi-flow plate-and-fin heat exchangers was presented by Picon-Nunez, based on the maximization of stream pressure drops [1]. The main shortcoming of this method is that no function was introduced to control the trade-off between pressure drops and heat-transfer surfaces. To summarize, in an optimal heat-exchanger network, the total cost, including the cost of required external energy for heating and cooling of the process streams, as well as the cost of installation, operation and maintenance of the heat exchangers must be optimized. However, in current design methods, one cannot avoid the introduction of the hydraulic and thermodynamic equations of all the fluids involved in the process. To achieve the stated objectives in MSHE optimization, the basic concepts of pinch technology were combined with an optimization approach, implemented in an SA algorithm, for determining the optimal states of the thermodynamic and hydraulic equations.

2. Design objective

A typical optimization problem usually consists of three main parts: objective function, variables, and constraints. The aim of optimization is to find the best division of surface and power-consumption costs. In making a trade-off between these two parameters, many of the specifications of the exchanger will be determined. Therefore, the total annual cost would have the role of a controlling function, as summarized below:

Total annual cost (TAC) = operating and maintenance cost (OMC) + capital cost(IC) (1)

The total annual cost of a MSHE is made up of smaller blocks of exchangers specified in the enthalpy intervals of T-H composite curves according to Figure2.

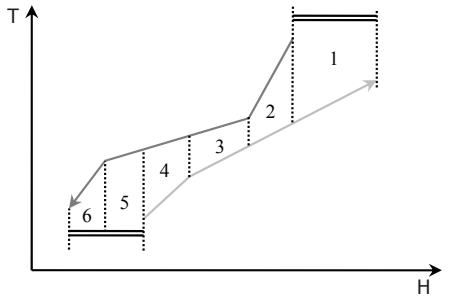

Figure2. Composite curves for the streams of an MSHE

Therefore, the TAC_{block} may be assumed as an objective function with multiple variables. The geometric parameters of these blocks are determined when the summation of TAC_{block}s is minimized.

The TAC per length of an exchanger is found by Eq. (2) [2]. The first and second parts of this equation show the IC and OMC costs, which are capital costs and operating costs of an MSHE, respectively [3].

$$TAC_L = \left[fc + uc \times \sum_{j=1}^{n} \alpha_j \frac{V_t}{L} \right] \times C_1 + \left[\sum_{k=1}^{n_c} \frac{\Delta P_{L,k} \dot{m}_k}{\rho_k \eta_p} + \sum_{l=1}^{n_h} \frac{\Delta P_{L,l} \dot{m}_l}{\rho_l \eta_p} \right] \times AH \times fe \quad (2)$$

Eq. (2) is the objective function to be minimized by the SA optimizer [4, 5]. In this equation, fc presents the fixed cost of the PFHE, uc is the exchanger cost per unit area, and C_1 is the annual capital-cost factor, which can be calculated from the operating period (tp) and the annual interest rate (i):

$$C_1 = \frac{(1+i)^{tp}}{tp} \quad (3)$$

AH is the annual operating period, f_e is the electric-cost factor.

The objective variables of this function to be optimized by the algorithm are fin height, fin pitch and number of flow passages.

In a compact heat exchanger, the pressure drop is related to fin parameters and physical and hydraulic specifications of the fluid by Eq. (4): [6, 7]

$$\Delta P = \frac{2Lf\dot{m}^2}{\rho D_h A_c^2} \quad (4)$$

where f indicates the friction factor for fluid between the layers and is correlated over a wide range of Reynolds numbers as given by Eq. (5): [8]

$$f = x . \mathrm{Re}^{-y} \quad (5)$$

Moreover, the volume equation of MSHE is defined as: [2]

$$\frac{V_t}{L} = \left[1 + \sum_{i=1}^{n} N_i \right] \varepsilon + \sum_{i=1}^{n} \left[N_i (d_i + \tau_i) \times \left(\frac{1}{s_i} + \tau_i \right) s_i \right] \quad (6)$$

In a plate-and-fin exchanger, the heat-transfer surface of each flow is expressed in terms of a coefficient of the total volume. This coefficient can be directly calculated through the specifications of the secondary surfaces (Eqs. (7-10)):

$$A_i = \alpha_i V_t \quad (7)$$

$$\alpha_i = \frac{d_i}{d_i + d_{i+1} + 2\tau_w} \beta_i \quad (8)$$

$$\beta_i = \frac{4A_{Ci}}{V_t D_{hi}} \quad (9)$$

$$A_{Ci} = W N_i d_i \quad (10)$$

By substituting the pressure drop and volume equations into Equation (2), the parts of the TAC equation will be determined.

Also, the length of a plate-and-fin heat exchanger is a function of the pressure drops and heat duties of the passing streams. This length is usually less than 8.5 m and can be found by dividing the volume of a specified section of a heat exchanger by the corresponding height:

$$L = \frac{V_{section}}{W . HT_{section}} \quad (11)$$

In a section of a plate-and-fin heat exchanger including n streams, the height can be calculated using the following summation: [1]

$$HT = \sum_{i=1}^{n} (Nd)_i + \left[1 + \sum_{i=1}^{n} N_i \right] \times \varepsilon \quad (12)$$

3. Design and optimization procedure

The design methodology developed in this paper involves the following seven major steps:

(1) Construction of composite curves at optimum ΔT_{min} to determine enthalpy intervals and heat load of streams in each interval [9]

(2) Calculation of maximum velocity for streams according to allowable stream pressure drops

(3) Calculation of maximum allowable stream pressure drops per length of unit (ΔP_L)

(4) Implementation of SA optimizer to minimize the objective function (Eq. 2), which is total annual cost of heat exchanger. SA is a powerful stochastic optimizer with two loops. The outer loop determines by annealing temperature parameter and the inner sets by Marcov chain Length (MC_L) [5]

The SA algorithm uses a control parameter to guide the optimization, which by analogy with the original annealing process, which is called annealing temperature, Ta_0. At the beginning of the algorithm, the annealing temperature is initialized to an appropriated high value. The process starts with an initial trial solution.

A trial solution is then generated by a random change or move, in the current solution. The objective function of this new prospective solution is calculated and compared with the objective function of the current trial solution. If the new value is lower than the previous one, the new trial solution is accepted immediately. Otherwise, it is accepted with a probability given by any defined suitable acceptance criterion. At each annealing temperature, this process is repeated a number of times, before the annealing temperature is reduced, and the whole cycle is repeated. The algorithm stops when a pre-established termination condition is met.

In the SA algorithm, the sequence of moves carried out at each temperature corresponds to a Markov Chain and the number of these moves is known as the Markov Chain Length [5].

The output results are optimum fin specifications and number of passages per stream, ΔP_L, heat transfer areas and minimum TAC per length of unit (TAC_L)

(5) Determination of the greatest heat duty of the stream process through each interval, which is met by two streams, Calculation of volume, length and height of the blocks based on these two streams.

(6) Calculation of stream pressure drops, heat transfer areas and minimum TAC for unit

(7) Reconciliation of block dimensions by ΔP relaxation

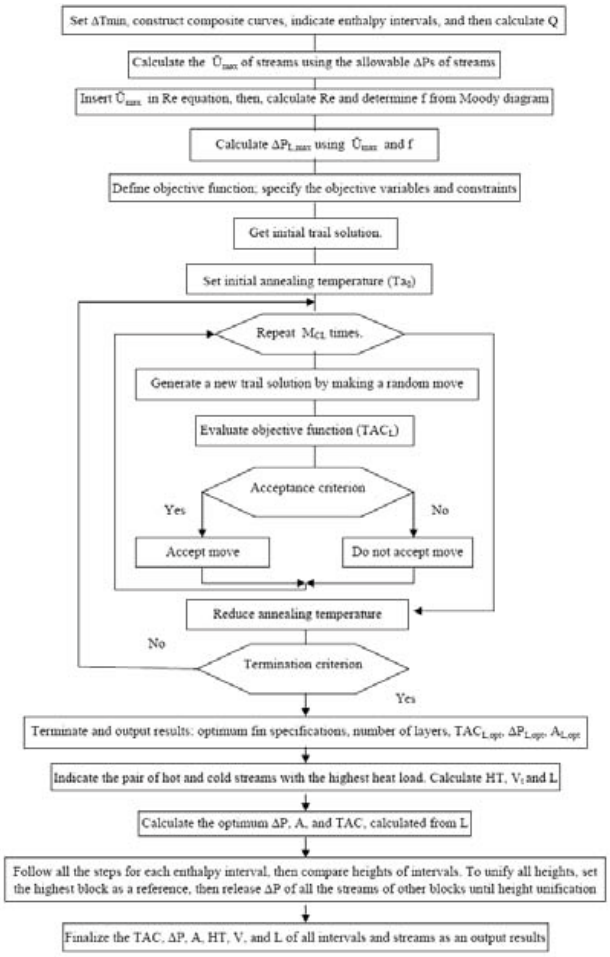

Figure3. Design and optimization procedure

4. Case study

The problem is designing an MSHE for a nine-stream problem [10] using the new presented method. Table 1 shows the stream process data

and physical properties. All the streams are in liquid form. The targeting stage indicates the ten enthalpy intervals for a minimum temperature approach at 15 °C. Detailed range targeting results for the problem has not been reported here. At ΔT_{min} = 15 °C, there are ten enthalpy intervals for process to process heat recovery.

Table 2 presents the inlet and outlet stream temperatures of each enthalpy interval of composite curves. Also, cost data are summarized in Table 3.

Table 1. Process data for case study.

	Ts (°C)	Tt (°C)	Mass flow rate (kg/sec)	ΔP (kPa)	ρ (kg/m^3)	CP (J/kg°C)	μ (cP)
H1	220	60	26.6	62	730	2250	0.3
H2	327	40	47.6	86	700	2120	0.4
H3	160	60	160	50	800	2500	0.3
H4	220	160	74.4	45	920	2150	0.3
C1	85	138	125	35	830	2800	0.2
C2	140	300	133	65	850	1500	0.5
C3	35	164	25	55	810	2800	0.3
C4	60	170	35	55	780	1715	0.5
C5	100	300	47.6	97	800	2100	0.4

Table 2. Inlet and outlet temperatures of intervals.

Interval	$T_{H, in}$ (°C)	$T_{H, out}$ (°C)	$T_{C, in}$ (°C)	$T_{C, out}$ (°C)	ΔT_{LM} (°C)
1	327	220	199.6	235.2	47.44
2	220	192.3	170	199.6	21.34
3	192.3	185.6	164	170	21.94
4	185.6	160	145	164	18.1
5	160	156.2	140	145	15.6
6	156.2	155.3	138	140	16.74
7	155.3	116	100	138	16.64
8	116	103.2	85	100	17.08
9	103.2	97.3	60	85	26.61
10	97.3	94.3	35	60	47.45

Table 3. Cost data.

uc ($/m^2)	f_C ($)	AH (hr/year)	fe ($/kWh)	i (%)	tp (years)
1900	30000	8000	0.065	15	10

Following the optimization procedure shown in Figure 3, the final design results were obtained, reported in Tables 4 to 13, for each of the intervals.

Table 4. Final detailed design of block 1.

	No. of passages	Fin height (mm)	Fin pitch (L/m)	Total area (m^2)	h (W/m^2 °C)	ΔP (Pa)
H_2	98.43	0.004	285	159	760	397
C_2	74.62	0.01	243	259	282	475
C_5	23.83	0.0043	221.45	144	1817	4279

Table 5. Final detailed design of block 2.

	No. of passages	Fin height (mm)	Fin pitch (L/m)	Total area (m^2)	h (W/m^2°C)	ΔP (Pa)
H_1	17.56	0.0043	443	116.6	1004	4467
H_2	52.22	0.0072	638	204.5	327	722
H_4	49.12	0.0047	349	103.5	1635	2646
C_2	90.06	0.0046	356.84	102.7	1218	2808
C_5	28.76	0.0045	490	122.8	784	5418

Table 6. Final detailed design of block 3.

	No. of passages	Fin height (mm)	Fin pitch (L/m)	Total area (m^2)	h (W/m^2°C)	ΔP (Pa)
H_1	13.28	0.0044	443.28	20.73	1219	839
H_2	56.97	0.005	871.17	31.69	1136	181
H_4	37.16	0.0047	349	15.93	1966	522
C_2	68.13	0.0046	357	15.28	1465	659
C_4	17.44	0.0045	407.58	18.27	900	717
C_5	21.73	0.015	930	86.99	1299	148

Table 7. Final detailed design of block 4.

	No. of passages	Fin height (mm)	Fin pitch (L/m)	Total area (m^2)	h (W/m^2°C)	ΔP (Pa)
H_1	9.44	0.0045	392.21	52.28	1468	6157
H_2	18.69	0.0091	318.62	81.43	474	1300
H_4	50.03	0.0048	316.39	73.37	839	1476
C_2	46.09	0.0098	332.8	86.90	409	600
C_3	8.10	0.012	397.18	140.37	1405	1171
C_4	11.79	0.011	379.81	131.86	1010	1323
C_5	12.21	0.0079	267.65	59.02	808	2304

Table 8. Final detailed design of block 5.

	No. of passages	Fin height (mm)	Fin pitch (L/m)	Total area (m^2)	h (W/m^2°C)	ΔP (Pa)
H_1	9.1	0.0045	392	16.87	2432	2338
H_2	24.05	0.006	348	14.95	525	426
H_3	59.63	0.0048	320.7	15.01	2409	1565
C_2	44.77	0.0098	332.7	24.11	417	316
C_3	7.87	0.013	397.18	32.48	1501	430
C_4	11.45	0.01	379.8	30.51	1088	490
C_5	28.74	0.0033	516.3	14.52	1170	1614

Table 9. Final detailed design of block 6.

	No. of passages	Fin height (mm)	Fin pitch (L/m)	Total area (m^2)	h ($W/m^2°C$)	ΔP (Pa)
H_1	12.74	0.0043	443.28	7.92	880	692
H_2	20.76	0.018	365.54	51.43	293	43
H_3	32.17	0.0075	198.89	10.28	913	617
C_3	16.54	0.0048	311.87	10.48	920	204
C_4	24.31	0.0049	301.28	9.21	1200	349
C_5	25.02	0.015	394.5	32.47	386	38

Table 10. Final detailed design of block 7.

	No. of passages	Fin height (mm)	Fin pitch (L/m)	Total area (m^2)	h ($W/m^2°C$)	ΔP (Pa)
H_1	10.01	0.0075	281	125	2282	18281
H_2	26.23	0.006	248	110	495	1775
H_3	65.09	0.0048	320.7	152	2273	10876
C_1	53.06	0.0074	280.9	236	712	1821
C_3	8.59	0.013	397.18	240	1417	1992
C_4	11.97	0.012	379.81	226	1057	2498
C_5	26.03	0.0045	543.7	144	993	5582

Table 11. Final detailed design of block 8.

	No. of passages	Fin height (mm)	Fin pitch (L/m)	Total area (m^2)	h ($W/m^2°C$)	ΔP (Pa)
H_1	11.31	0.0044	443.28	568	1185	4239
H_2	2.67	0.076	152.6	111	470	272
H_3	77.30	0.0048	320.75	28	2029	2643
C_1	63.02	0.0049	297.58	28	670	1506
C_3	13.36	0.0042	541.06	35	1119	3973
C_4	14.85	0.015	169.2	36	299	169

Table 12. Final detailed design of block 9.

	No. of passages	Fin height (mm)	Fin pitch (L/m)	Total area (m^2)	h ($W/m^2°C$)	ΔP (Pa)
H_1	3.92	0.0043	443.28	49	4928	5110
H_2	53.33	0.0014	2741.64	47	235	71
H_3	24.6	0.0048	320.75	12	4325	3220
C_3	33.61	0.0039	1257.7	25	1923	359
C_4	48.25	0.0039	1182.87	25	1373	479

Table 13. Final detailed design of block 10.

	No. of passages	Fin height (mm)	Fin pitch (L/m)	Total area (m^2)	h ($W/m^2°C$)	ΔP (Pa)
H_1	14.9	0.0044	443.28	16.27	950	260
H_2	26.31	0.0043	476.88	15.71	853	312
H_3	100.82	0.0048	320.75	13.88	1702	149
C_3	142.04	0.0039	2749	49.13	211	37

Table 14 presents the total geometric and economic results for the exchanger. As can be seen in Table 14, the ten sections have achieved uniform heights, which is for after re-designing the sections. The results of stream pressure drops have been reported in Table 15.

Table 14. Final block dimensions and TAC.

Interval	Length (m)	Width (m)	Height (m)	Volume (m3)	TAC ($/yr)
1	0.61	1	1.3	0.73	445331
2	0.48	1	1.3	0.56	512674
3	0.11	1	1.3	0.13	157908
4	0.57	1	1.3	0.68	403264
5	0.14	1	1.3	0.17	177571
6	0.12	1	1.3	0.10	105814
7	1.1	1	1.3	1.2	964047
8	0.56	1	1.3	0.64	633081
9	0.08	1	1.3	0.081	135353
10	0.05	1	1.3	0.05	1074

Table 15. The results of TAC, volume and stream pressure drops.

Results	New method
TAC ($/Yr)	3627017
Total volume (m^3)	4.34
ΔP H_1 (Pa)	42383
ΔP H_2 (Pa)	5499
ΔP H_3 (Pa)	19070
ΔP H_4 (Pa)	4644
ΔP C_1 (Pa)	3327
ΔP C_2 (Pa)	4858
ΔP C_3 (Pa)	8166
ΔP C_4 (Pa)	6025
ΔP C_5 (Pa)	19383

5. Conclusion

The method proposed here presents some improvements over previous methods presented in the literature [1, 10]. (1) The new method can be reliably used for all flow conditions of counter-, cross-, and co- current flows, whereas the prior method is applicable only for countercurrent

flows. (2) The current method is not flexible in the determination of the optimum number of flow layers and selection of fins per streams, as these parameters are calculated at the end of procedure based on the calculated geometric specifications. In new method, however, the number of passages (channels) of each stream and fins are optimized as design variables. (3) In current method, two streams i.e. the critical and reference stream, determine the dimensions of the blocks, whereas in the present method, all streams are involved in the determination of geometric specifications of the exchanger. (4) The presented method avoided the assumption of linear ΔP distributions, which was the main consideration of current method.

The new procedure was applied to an example discussed previously in literature [10]. The results proved that the algorithm not only significantly explores the solution with lower TAC, but also it allows to better utilization of ΔPs through the heat recovery network.

Nomenclature

A superficial heat transfer area, (m^2)
A_C free-flow area, (m^2)
CP heat capacity, (J/kg °C)
d plate spacing, (m)
D_h hydraulic diameter, (m)
E pumping power, (W)
f friction factor
fc fixed cost, ($)
fe electric cost, ($/kW h)
HT exchanger height, (m)
h heat transfer coefficient, (W/m^2 °C)
i annual interest rate
IC capital cost, ($)
k fluid thermal conductivity, (W/m°C)
L exchanger length, (m)
$\dot{m}$ mass flow rate, (kg/s)
M_{CL} Markov chain length
N number of passages per stream
OMC operation and maintenance cost, ($)
ΔP pressure drop, (Pa)
Re Reynolds number
s fin pitch
T temperature (°C)
TAC total annual cost ($)
TAC_L total annual cost per length of exchanger($)
Ta_0, annealing temperature
tp operating period (yr)
uc unit cost of MSPFHE per area ($/$m^2$)
$\bar{U}_{max}$ maximum velocity
V volume (m^3)
W exchanger width (m)
x coefficient in friction factor vs. Re correlation
y exponent in friction factor vs. Re correlation

Greek symbols

η_P pump efficiency
α total heat-transfer area of one side of exchanger to total exchanger volume (m^2/m^3)
β total heat-transfer area of one side of exchanger to volume between plates in that side (m^2/m^3)
ε plate thickness (mm)
κ thermal conductivity (W/m °C)
μ viscosity (kg/ms)
ρ density (kg/m^3)
τ fin thickness (mm)

Subscripts and superscripts

c cold side of exchanger
h hot side of exchanger
i inlet
L per length
LM logarithmic mean temperature difference
o outlet
opt optimum
s Supply
t target
t total
w wall condition

References

[1] Picon- Nunez, M., Polley, G. T., and Medina-Flores, M., 2002, Thermal design of multi-stream heat exchangers, Applied Thermal Engineering, 22(14), pp. 1643- 1660.

[2] Peng, H., and Ling, X., 2008, Optimal Design Approach for the Plate-Fin Heat Exchangers using Neural Networks Cooperated with Genetic Algorithms, Applied Thermal Engineering, 28(5-6), pp. 642- 650.

[3] Hoffman, T.W., 1974, *Optimal design of heat exchanger network and evaluation of current procedures in Heat exchangers, Design and Theory Sourcebook*, McGraw Hill Book Co., New York, pp. 121- 153.

[4] Pedamallu, C.S., and Ozdamar, L., 2008, Investigating a hybrid simulated annealing and local search algorithm for constrained optimization, European Journal of Operational Research, 185(3), pp. 1230-1245.

[5] Clemente A. Rodriguez, 2005, Fouling Mitigation Strategies for Heat Exchanger Networks, Ph.D. thesis, University of Manchester, England.

[6] Polley, G. T., Panjeshahi, M. H., and Picon Nunez, M., 1991, Rapid design algorithms for shell- and- tube and compact heat exchangers, Trans IChemE, 69(A), pp. 435- 444.

[7] Picon- Nunez, et al., 1999, Surface selection and design of plate- fin heat exchangers, Applied Thermal Engineering, 19(9), pp. 917-931.

[8] Kays, W. M., and London, A. L., 1984, *Compact Heat Exchangers*, 3rd ed., McGraw Hill, New York, Chaps. 9,10.

[9] Smith, R., 2005, *Chemical Process Design and Integration*, John Wiley and sons Ltd, New York, Chap. 16.

[10] Khorrammanesh, M., Amidpour, M., and Nasr, M.R.J., 2007, Application of Process Decomposition in Multi-Stream Plate Fin Heat Exchangers Design to Use in Heat Recovery Networks, Chemical Engineering and Processing: Process Intensification, 46(10), pp. 941–954.

CFD Analysis of the Heat Dissipation of Plates with Novel Flow Fields for the Cooling of Electronic Devices

Ramos-Alvarado Bladimir, Peiwen Li**,*
Hernandez-Guerrero Abel, Elizalde-Blancas Francisco
** Aerospace and Mechanical Engineering, University of Arizona, Tucson, Arizona, USA, on leave from University of Guanajuato, Mexico*
***Aerospace and Mechanical Engineering, University of Arizona, Tucson, Arizona, USA*
Department of Mechanical Engineering, University of Guanajuato, Salamanca Gto, Mexico

Abstract: The continuous advances in electronic devices require new and efficient heat dissipation techniques to achieve an acceptable performance of these equipments. Conventional airflow heat sinks are not sufficient when high heat fluxes are present. Therefore, using liquid cooling becomes a suitable alternative due to the high convection heat transfer coefficients that can be achieved by these means. This work presents the numerical study of a non-conventional flow pattern employed for the heat dissipation of plates with moderate heat fluxes. The numerical model consist of the flow channels and a solid aluminum structure. The energy and flow equations are solved including a model of non-constant properties. These new flow fields present very low pressure drops as well as an excellent uniformity of flow distribution, such aspects, make plausible to increase the operating flow rates and therefore, to improve the performance of the heat dissipation process.

Keywords: Heat sinks, CFD, flow distribution.

1. Introduction

The continuous demand of smaller and faster computers and other electronic devices has led to increase in the need of heat dissipation. The high operating frequencies of current central processing units and the small designs are the main cause of having such heating issues. Currently, air heat exchangers or heat sinks continue to be the most viable thermal solution for the electronics industry, primarily, because of low cost and high reliability [1]. Using heat sinks for electronics cooling is the simplest way to maintain a CPU working in appropriate conditions, however, this method is no longer adequate for the recent developed computer chips [2]. Many works have been published reporting improvements in heat sinks design using CFD techniques [3,4] as well as experimental methodologies [5,6].

One of the main parameters in every heat transfer device is the available area exposed to the cooling fluid. A new way to improve the performance of conventional heat sinks is using porous media as base material. Most metal foams are highly porous and therefore have a high permeability. The porosity of sintered metal beads is around 0.4 and the typical magnitude of permeability is 10^{-10} m^2. Hence, a comparison with sintered porous materials at a given pumping power shows that these metal foams permit more coolant to pass through, carrying more heat away [7]. Hetsroni et al. [8] reported important experimental results about heat transfer and pressure drop when using different sintered porous inserts in a rectangular channel removing an important amount of heat. An impressive performance, in terms of heat transfer, was reported in [8] at the same time that high pressure drops were related with the best design for heat transfer due to the flow through porous media.

The greatest heat transfer coefficients are achieved when phase change is present and this phenomenon has not been avoided by researchers interested in the heat dissipation of electronics. Phase change materials store heat to be dissipated over time; this gained energy is then released by convection, radiation or both mechanisms. The objective of the phase change materials heat sinks is to maintain the operating temperature below a critical value [8]. In general, the heat sink optimization analysis with phase change materials is similar to those of common conductive materials. Nayak et al. [9] presented a numerical model of a heat sink with phase change materials.

These authors reported important results about improvements by means of implementing heat transfer enhancers such as fins and porous materials. A parametric analysis of a composite heat sink is reported by Akhilesh et al. [10] with the objective of maximizing the energy storage and the time of operation until all of the latent heat storage is exhausted.

Micro-channel heat exchangers are devices which enable liquid flow through parallel channels having a hydraulic diameter of 10 1000 m. These devices are ideally suited for high heat flux dissipation from small surface areas in a broad range of high performance electronics [11]. A lot discussion has been reported in the last twenty years about the validity of the classical governing equations and correlations for heat transfer when applied to micro systems. About this discussion, Kroeker et al. [12], presents an extended report. Numerical analysis have been reported [12,13] presenting the classical models of momentum and heat transfer as well as models for temperature dependant fluid properties obtaining good matches between the numerical models and experimental results reported so far.

Fluid flow devices often employ multiple parallel channels to enhance heat transfer in heat exchangers, to enhance mass transfer in absorbers, or to improve fluid transport and distribution in fuel cell gas channels. The smaller channels provide increased surface area, while the inlet and exit manifolds facilitate the necessary distribution and provide connections to external inlet and outlet conduits [14]. Flow maldistribution will lower the process efficiency by bringing backmixing or creating local temperature or concentration differences. Several studies have reported analyses and improvements in the flow characteristics of many flow devices in recent years [15-18], which are mainly focused in heat dissipation devices. Recently, Peiwen et al. [19] reported a numerical and experimental investigation of the flow characteristics of a new type of symmetric flow distributor for PEM fuel cells, as well as experimental results [20] showing good performance of their flow distributors as a bipolar plate in comparison with previous designs [21]. The analogies and similarities between heat transfer and mass transfer phenomena, as well as the uniformity of flow distribution achieved by [illegible] performance of these designs as flow patterns in mini-channeled heat sinks for electronics. This paper reports a numerical analysis of performance of a heat sink using three novel flow geometries designs and one conventional pattern. All the new configurations are compared in terms of thermal resistance and pressure drop under a wide range of operating conditions. It could be thought that the proposed geometries are not novel because somehow they are similar to some of the dendritic geometries proposed by Lorente and Bejan [22], however those geometries follow a pattern predicted by the minimum entropy generation and the proposed geometry of this paper uses a symmetric bifurcation of flow, aiming to obtain a uniform flow.

2. FLOW FIELDS CONFIGURATION

Peiwen et al. [21] presented two new serpentine flow configurations to be applied as gas distributors for PEMFC (see Fig. 1). The design called serpentine 2D is basically a conventional serpentine with continuous channels and continuous land areas. The serpentine 3D consists of a similar geometry except for the addition of a discontinuous land structure over the machined plate, producing interconnections between every turn of the serpentine.

Fig. 2 shows two novel symmetric flow distributors reported in [20]. These new flow configurations present a bifurcated structure in the inlet and in the outlet zones given by 2^n, where n is the bifurcation level; between the bifurcated channels there is a region with a manifold and twenty parallel channels instead of sixteen as it was reported in [19]. The objective of the inlet bifurcated structure is to provide a uniform flow distribution to the parallel channels and the outlet bifurcated zone has the function of carrying out the fluid to a simple exit. The symmetric flow distributors showed a better performance when applied as gas distributors in the anode side of a proton exchange membrane fuel cell than that of the serpentine designs [20]. The best design was the flow distributor 3D followed by the flow distributor 2D. The reported results can be

explained due to the uniformity of flow distribution achieved by the symmetric designs. The better performance of the flow distributor 3D is related to the area provided by the discontinuous structure present in this design. After the previous documented investigation, similar results are expected in the heat transfer analysis.

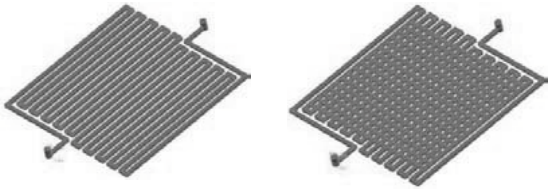

(a) Serpentine 2D. *(b) Serpentine 3D.*

Fig 1. Serpentine configurations reported in [21].

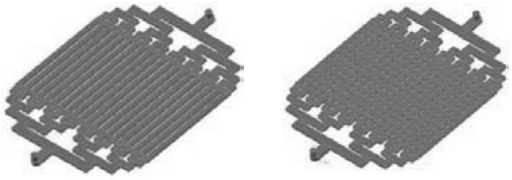

(a) Flow distributor 2D. *(b) Flow distributor 3D.*

Fig 2. Symmetric flow distributor configurations reported in [20 The physical model of the heat sink was developed and fabricated in Energy and Fuel Cell Laboratory at the University of Arizona.

The dimensions employed in the fuel cell plates of previous works [20,21] will be used in the present analysis. Table 1 shows dimensions of the serpentine designs while Table 2 shows dimensions of the flow distributor designs.

Table 1. Serpentine designs dimensions.

Parameter	Serpentine 2D	Serpentine 3D
Inlet diameter	1.9 mm	1.9 mm
Channels width	0.9 mm	0.9 mm
Land width	1.4 mm	1.4 mm
Channels height	1.2 mm	1.2 mm
Turns	10	10
Fin dimensions	---	1.4 mm × 1.6 mm

Table 2. Flow distributor dimensions.

Bifurcation level	Length [mm]	Width [mm]
Main channel	5.73	2.84
1st level	3.47	2.55
2nd level	3.11	2.06
3rd level	2.69	1.77
4th level	2.3	1.49
Parallel channels	29.23	1.2

The channels height of the flow distributors is 1.2 mm, the interspacing width is 1.2 mm and fin dimensions in the flow distributor 3D are 1.2 mm × 1.4 mm.

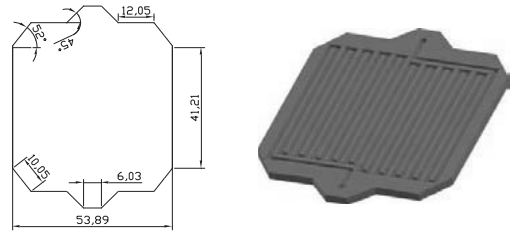

(a) Dimensions of the base aluminum plate. *(b) Computational model of the channels machined on the aluminum plate.*

Fig 3. Base plate over which the flow channels are going to be machined.

The heat sink is going to be modeled as an aluminum plate with the channels machined on it (see Fig. 3). The thickness of the plate illustrated in Fig. 3(b) is 2.2 mm; another plate without channels and having the dimensions shown in Fig. 3(a), where the chips are going to be placed, will be the cover of the channels to enclose the fluid and therefore to construct the complete channels. The thickness of the second plate is 1 mm.

3. NUMERICAL AND COMPUTATIONAL PROCEDURES

3.1. Governing equations

The phenomena studied in this paper are completely described by the momentum, continuity and heat transfer equations in the fluid domain. In the solid phase the energy equation

describe the complete model. The assumptions employed are listed below:

1) Steady state for the fluid flow and heat transfer.
2) Incompressible fluid.
3) Laminar flow.
4) No radiation effects.

Based on these considerations, the governing equations become:

For the fluid:

Continuity equation

$$+ \vec{V} \quad \vec{0} \tag{1}$$

Momentum equation

$$_{f} \vec{V} + \vec{V} \quad + P \quad _{f} + {}^{2}\vec{V} \tag{2}$$

Energy equation

$$_{f} C_{p,f} \vec{V} + T \quad k_{f} + {}^{2}T \tag{3}$$

For the solid

Energy equation

$$k_{s} + {}^{2}T \quad 0 \tag{4}$$

The cooling fluid employed in the present simulations is water and the solid conductive phase was selected to be aluminum. Water viscosity is the property most affected by temperature changes. A temperature dependent model reported by Tho et al. [13] was employed in the present simulation:

$$2.414) \; 10^{5} \quad 10^{247.8/(T \quad 140} \tag{5}$$

3.2. Boundary conditions

The fluid inlet boundary condition will be defined using the Reynolds number as follows:

$$\mathrm{Re}_{in} \quad \frac{_{f} V_{in} D_{h}}{_{f}} \tag{6}$$

The thermal condition of the fluid at the inlet is set at 293.15 K. The outlet condition is defined in such way that the continuity equation holds (Eq. 8) and also a thermal condition of symmetry is set (Eq. 9).

$$\dot{m}_{in} \quad \dot{m}_{out} \tag{7}$$

$$\frac{T}{} \quad 0 \tag{8}$$

where is any x, y, z coordinate. Using the outlet boundary conditions described is possible to ensure that all values of the nodes downstream will be correctly calculated. The wall boundary conditions are illustrated in Fig. 4. The side and top walls boundary conditions were defined as adiabatic walls and a constant heat flux was defined in the bottom wall.

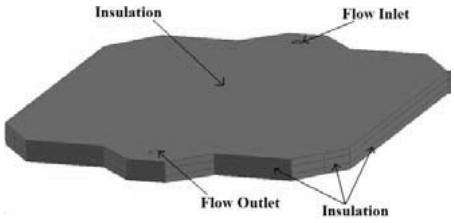

Fig 4. Wall boundary conditions of the heat sink model.

3.3. Numerical squemes

A commercial CFD code was employed to simulate the thermal and flow phenomena. The numerical procedure followed to solve the governing equations with the boundary conditions described so far is showed in Fig. 5. The convergence criteria established for the flow equations is 1) 10^{-5}, and 1) 10^{-12} for the energy equation. Together with a precise calculation of the governing equations, two tracking monitors were selected to describe the evolution of the pressure and temperature at the flow outlet. The overall convergence criteria was considered achieved when no variation in the tracked variables was observed over twenty consecutive iterations at the same time that the governing equations achieved enough precision.

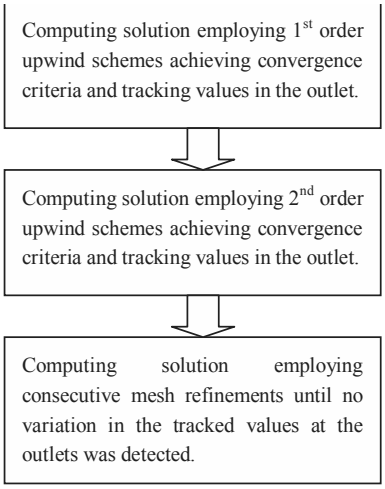

Fig 5. Computational procedure followed.

The average mesh size in all the four different heat sinks was 300,000 elements including the fluid and solid phases.

4. RESULTS AND DISCUSSION

4.1. Validation of the numerical results with energy balance

The The results of implementing the numerical procedures described in Fig. 5 were compared with theoretical analytical values of temperature change in the fluid. The analytical model employed is given by:

$$Q \quad q'' A \quad \dot{m}_f C_{p,f} \square T_f \tag{9}$$

Fig. 6 shows the comparison of the analytical and numerical results obtained for different flow configurations. Because all the heat transfer surfaces are the same in each heat sink, the total amount of heat supplied (Q) to the water is the same, likewise, operating at the same inlet conditions (Re_{in}) and with the given outlet boundary condition, the temperature rise will be similar in all designs and at the same time similar to the analytical solution. This behavior is observed, and therefore it can be concluded that the numerical model and procedures are correctly applied when solving the heat transfer problem described.

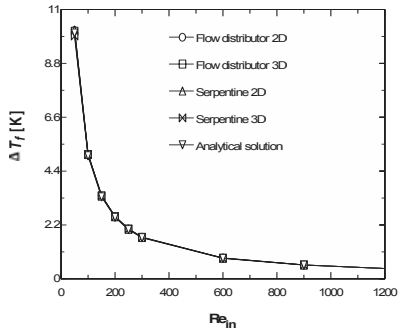

Fig 6. Energy balance check between analytical and numerical results for a heat flux condition of 1000 W/m^2.

4.2. Flow uniformity in flow distributors

The importance of a good flow distribution has been already discussed lines above. In every multi-channeled flow distributor this parameter can be determined using the relations reported by Fan et al. [23]. The standard deviation of flow rate (Eq. 11) and the maximum ratio of flow rate (Eq. 12) are dimensionless parameters that describe the uniformity of flow distribution in the sub-streams generated by a flow distributor.

$$D_g \quad \sqrt{\frac{1}{N \quad 1} \frac{N}{i \quad 1} \quad \frac{(_i}{(_{ave}} \quad 1 \quad ^2} \tag{10}$$

$$\frac{(_{min}}{(_{max}} \tag{11}$$

Fig. 7 reports the uniformity of flow distribution achieved by the symmetric flow distributors 2D and 3D. The tendencies obtained numerically agree qualitatively with experimental data published by Fan [23]; although Fan did not investigate the same flow configuration, it is observed that the two dimensionless parameters tend to increase as the velocity inlet increases. Likewise, Fan results show similarity between the curves of the standard deviation and the maximum flow rate ratio in every flow configuration.

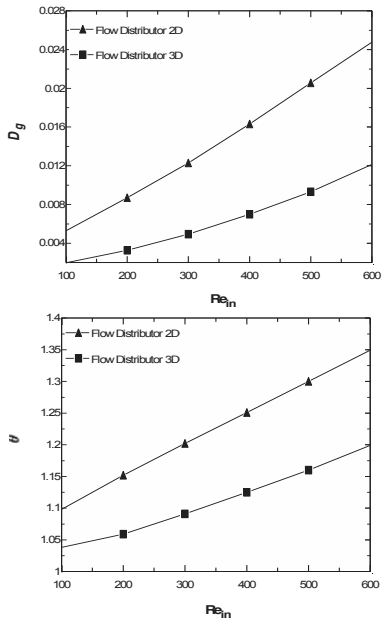

Fig. 7. Uniformity of flow distribution analysis of the symmetric flow distributors.

It can be observed that the presence of a discontinuous structure on the plate configuration of the flow distributor 3D helps to enhance the flow distribution through the main channels. This phenomenon is understandable due to the existing communication of the main parallel channels through the small connecting channels formed by the 3D structure. The average velocity at the twenty sub-streams was calculated with the objective of showing a schematic distribution of the flow. Fig. 8 shows this schematic flow distribution for different inlet conditions, showing in the left side the flow distributor 2D configuration and on the right side the flow distributor 3D configuration. It is observed that most of the fluid flows through lateral channels; this is due to the flow inertia between two consecutive bifurcations. When the flow passes through the first bifurcation, it is divided in two sub-streams and each sub-stream acquires a new inertia when it moves parallel to the manifold; however, at the inlet of the next level the flow finds less resistance to keep moving in the same direction taken in the previous bifurcation than the resistance found by the fluid in changing its direction by almost ninety degrees. Using the previous explanation, it is possible to qualitatively predict the flow distribution in each sub-stream. Another important result is that the flow patterns observed in Fig. 8 demonstrate that the flow distributor produces a symmetric profile, just as it was sought.

4.3. Pressure drop for the different flow field configurations

A very important parameter in all flow devices is the pressure drop. This parameter is directly related with the power necessary to move the fluid across the channels and therefore there is an economical implication related with this phenomenon. The pressure drop obtained for a wide range of inlet conditions is showed in Fig. 9 for all the four flow patterns.

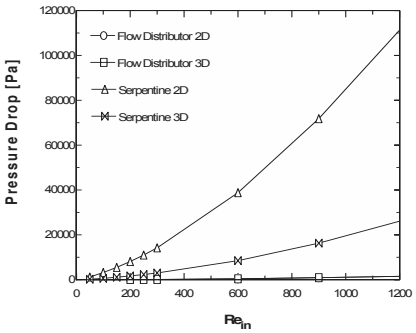

Fig. 9. Pressure drop for the different flow configurations.

Just as it was expected, the serpentine 2D configuration exhibits the higher pressure drop in comparison with the other designs. The consecutive turns of a single channel introduce a lot of pressure loss due to the consecutive changes in direction. The implementation of the discontinuous structure present in the serpentine 3D helps to reduce the effects of the sharp turns because the fluid has the possibility of being distributed through the connecting channels formed by the fins. On the other hand, the pressure drop developed by the symmetric flow distributors is considerably lower than that of the serpentines. This extremely low pressure drop is reasonable because of the absence of sharp turns in the flow pattern.

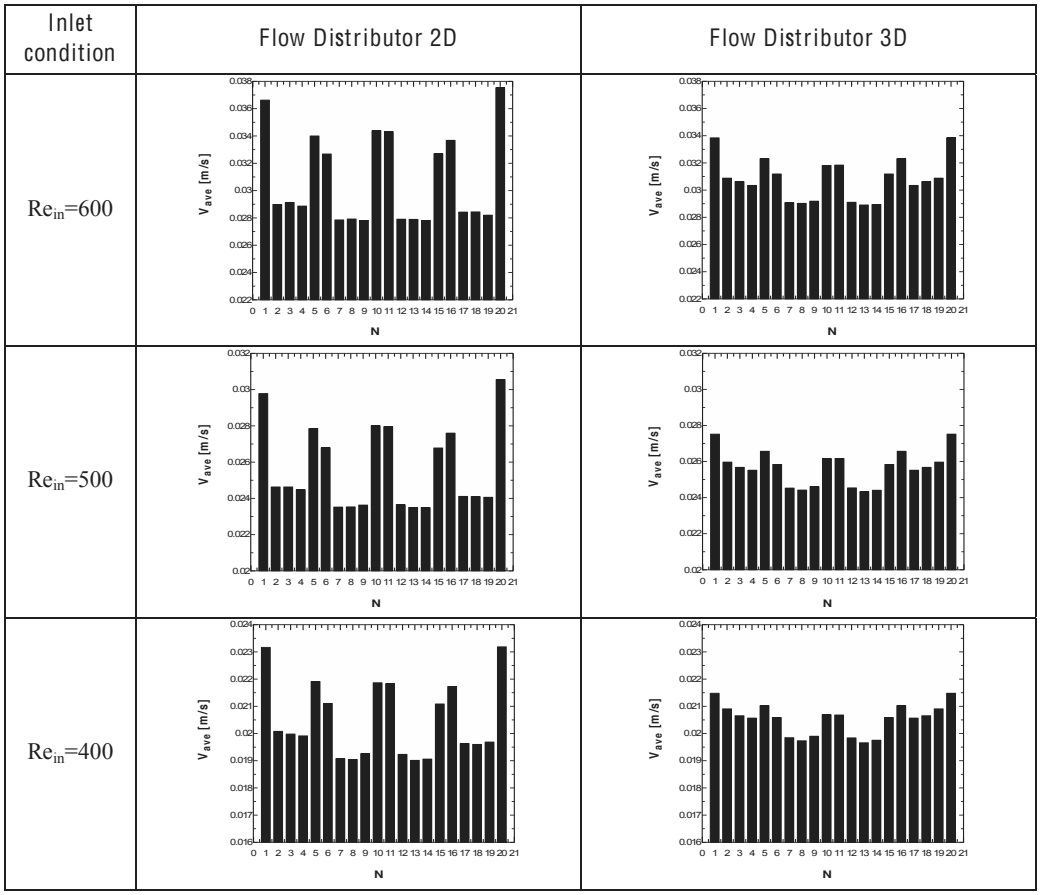

Fig 8. Flow distribution profiles in terms of the average velocity at the twenty sub-streams for different inlet conditions

4.4. Heat transfer and temperature distribution on the heating surface

The main interest of this work is to determine the temperature distribution over the surface on which a heat flux is imposed; this surface is where the chips or electronics devices are going to be placed for cooling. The temperature contours over the surface of interest for a heat flux of 6000 W/m^2 are shown in Fig. 10.

Serpentine configurations show higher temperature zones for Reynolds inlet conditions below 300 but more uniform temperature distribution over the heat flux surface than symmetric flow distributors for all the inlet conditions. The reason of the high temperatures and the uniformity of this variable over the heat surface for low Reynolds for the serpentine 2D is explained looking at this flow configuration. The channels take the fluid up and down many times and some of those channels and turns near the inlet channel will be cooled in some way. The channels and turns near the outlet channel will be warmed. This explanation aims to explain also the temperature contours for Reynolds of 600 and 900. For those two high inlet conditions the inlet channel may take more heat from the channels in the central zone and the outlet channel may warm the same channels at a higher rate; this is why the temperature over the heat flux surface is that uniform for the serpentine 2D design at high Reynolds. The serpentine 3D does not show the same properties of the other serpentine due to its structure that allow the fluid to be mixed between the main channels and turns.

Fig 10. Temperature contours on the heat flux surface for the different flow patterns and under different inlet conditions and a het flux of 6000 W/m^2

The symmetric flow distributors produce higher temperature difference on the heat flux surface. The reason of this behavior is because these designs develop a main flow direction that is followed downstream except in the manifolds of each bifurcation zone; therefore, temperature gradients are expected in the flow direction having the colder zones in the flow inlet region and the warmer regions near the flow outlet. The good flow uniformity achieved by the symmetric designs helps to produce almost a uniform temperature distribution in a perpendicular direction respect to the main flow; this behavior is affected by high inlet conditions which lead to have less uniformity in the uniformity of flow distribution.

Thermal resistance in the solid phase will be defined as:

$$R = \frac{T_{max} - T_{min}}{q''} \tag{12}$$

Fig. 11 shows the thermal resistance for all the four flow patterns studied when a hear flux of 6000 W/m^2 is applied. The different curves confirm the results shown in Figure 10. Serpentines achieve the lowest thermal resistance due to the uniformity of temperature on the heat flux surface and the symmetric flow distributors present higher thermal resistance due to the high temperature gradients produced by these flow configurations.

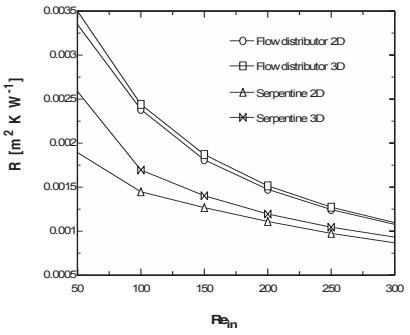

Figure 11. Thermal resistance of the different flow distributors under a heat flux of 6000 W/m^2.

Although results shown in Fig. 11 aim to choose the serpentine designs as the best flow patterns to be used as flow distributors in a heat sinks, is necessary to take a look again at Fig. 9, and remember that the serpentine designs present considerably high pressure drops under the same operating conditions than the flow distributors.

5. CONCLUSIONS

A CFD analysis of new flow patterns for channeled heat sinks using a cooling fluid was conducted. The present numerical model was successfully compared with analytical results after using different discretization schemes and mesh refinement processes in order to obtain highly precise results.

To obtain a general conclusion on the performance of the flow patterns studied here is necessary to take a look at both results, thermal and flow. On one hand, serpentine designs achieve low thermal resistance in comparison with symmetric distributors, but flow distributors show a better temperature distribution on the heat flux surface. On the other hand, working at the same flow inlet conditions, flow distributors show a remarkable performance obtaining very low pressure drop in comparison with the extremely high pressure losses on the serpentine designs. Therefore, it is possible to realize that symmetric flow distributors can achieve a better performance increasing the flow rate without having significant energy losses.

At this point, it is important to realize that is necessary a new parameter to relate the results obtained here, thermal and flow. One solution could be an entropy generation analysis in order to quantify irreversibilities, one due to friction flow and one due to the heat transfer process.

Acknowledgments

This work was mostly accomplished in Energy and Fuel Cell Laboratory at the University of Arizona. The first author is grateful to the University of Arizona and University of Guanajuato Summer Research Program and Dr. Peiwen Li's host in his laboratory.

Nomenclature

A	Area
C_p	Specific heat [J kg^{-1} K^{-1}]
D_h	Hydraulic diameter [m]
D_g	Standard deviation of flow rate
k	Thermal conductivity [W m^{-1} K^{-1}]
$\dot{m}$	Mass flow rate [kg s^{-1}]
n	Level of bifurcation
N	Number of sub-streams
P	Pressure [Pa]
Q	Heat rate [W]
	Heat flux [W m^{-2}]
R	Thermal resistance [m^2 K W^{-1}]
Re	Reynolds number
T	Temperature [K]
v	Velocity magnitude [m s^{-1}]
$\vec{V}$	Velocity vector [m s^{-1}]

Greek letters

	Maximum ratio of flow rate
	Kinematic viscosity [kg m^{-1} s^{-1}]
	Density [kg m^{-3}]
(	Flow rate [m^3 s^{-1}]

Subscripts

in	Inlet condition
ave	Average
f	Fluid
max	Maximum
min	Minimum
out	Outlet condition
s	Solid

References

[1] M. Baris Dogruoz, Mario Urdaneta, Alfonso XKE TI M IRXV ERH SHIPRK SJ XLI hydraulic resistance and heat transfer of in-line square pin fin heat sinks with top by-TEWJPS[a International Journal of Heat and Mass Transfer 48 (2005) 5058 5071.

CD. EHVSXL 37YHE[E SSPRK SJE multichip electronic module by means of confined X[SHM IRVSREPNXVSJHMEHGXMGEMYMa 4SYREP of Heat Transfer, Transactions of ASME 112 (1990) 891 897.

[3] Yue-Tzu Yang, Huan- IR IRK 8Y IMEP study of pin-fin heat sink with un-uniform fin LIMXLXHIVWRa 3RX REXSREP 4SYREP SJ 2IEXERH Mass Transfer 51 (2008) 4788 4796.

[4] Paisarn Naphon, Setha Klangchart, Somchai SRK[NMW 8Y IMEP investigation on the heat transfer and flow in the mini-fin heat sink for a 3RX REXSREP S YRMEXSRWNA 2IEXERH Mass Transfer, Article in Press.

C(D HEPVL SREER 1MIW 6S[TSJMHJER and heat sink thermal management solution for portable ETTPMEXSRVa 3RX REXSREP 4SYREP SJ Thermal Sciences 46 (2007) 1182 1190.

C)D HEPVL SREER 1MIW 6S[TSJMHJER and heat sink thermal management solution for TSXEFPH ETTPMEXSRVa 3RX REXSREP 4SYREP SJ Thermal Sciences 46 (2007) 1182 1190.

[7] Sheng- LYRK IRK TEXSMP XLIEP regulation of aluminum foam heat sink using a VWRXIHTSYWGSRHYGXSV TMMa 3RX REXSREP Journal of Heat and Mass Transfer 50 (2007) 117 126.

[8] G. Hetsroni, M. Gurevich, R. Rozenblit, NRX IHTSYW IHMm heat sink for cooling of high-power mini-HIZMa 3RX REXSREP4SYREPSJ Heat and Fluid Flow 27 (2006) 259 266.

[9] K.C. Nayak, S.K. Saha, K. Srinivasan, P. . YXE , RY IMEP SHIPJS LIEXVWMOW[MXL phase change materials and thermal conductivity IRLERGIVa 3RX REXSREP 4SYREP SJ 2IEXERH Mass Transfer 49 (2006) 1833 1844.

[10] R. Akhilesh, Arunn Narasimhan, C. Balaji, 7IXLSHXS MTSZI KIS IX] JS LIEXXERWMI IRLERGI IRX NR 7GS TSWRX LIEXVWMOWa International Journal of Heat and Mass Transfer 48 (2005) 2759 2770.

C D. 5HMR 12IXWSRM, 7SWJEO 2IEX transfer characteristics of water and APG surfactant solution in a micro-GLERRIPLIEXVWMOa International Journal of Multiphase Flow 31 (2005) 393 415.

[12] C.J. Kroeker, H.M. Soliman, S.J. Ormiston, "Three-dimensional thermal analysis of heat sinks with circular cooling micro-channels", International Journal of Heat and Mass Transfer 47 (2004) 4733–4744.

[13] K.C. Toh, X.Y. Chen, J.C. Chai, "Numerical computation of fluid flow and heat transfer in microchannels", International Journal of Heat and Mass Transfer 45 (2002) 5133–5141.

[14] S.G. Kandlikar, Z. Lua, W.E. Domigana, A.D. Whitea, M.W. Benedicta, 2008, "Measurement of flow maldistribution in parallel channels and its application to ex-situ and in-situ experiments in PEMFC water management studies", International Journal of Heat and Mass Transfer, Volume 52, Issues 7-8, March 2009, Pages 1741-1752.

[15] Lalot S., P. Florent, S.K. Lang, A.E. Bergles, "Flow maldistribution in heat exchangers", Applied Thermal Engineering 19 (8) (1999) pp. 847–863.

[16] Wang Junye, "Pressure drop and flow distribution in parallel-channel configurations of fuel cells: U-type arrangement", International Journal of Hydrogen Energy 33 (2008) 6339–6350.

[17] Wen J., Y.Z. Li, "Study of flow distribution and its improvement on the header of plate-fin heat exchanger", Cryogenics 44 (11) (2004) 823–831.

[18] Wen J., Y.Z. Li, A.M. Zhou, K. Zhang, "An experimental and numerical investigation of flow patterns in the entrance of plate-fin heat exchanger", International Journal of Heat and Mass Transfers 49 (9–10) (2006) 1667–1678.

[19] Peiwen Li, Devasubramaniam Coopamah, Nikesh Dhar, "Analysis and optimization of flow distribution channels for uniform flow in fuel cells", Proceedings of FEDSM2008 2008 ASME Fluids Engineering Conference August 10-14, 2008 Jacksonville, Florida USA.

[20] Peiwen Li, Devasubramaniam C., Jeong-Pill Ki, "Uniform distribution of species in fuel cells using a multiple flow bifurcation design", Proceedings of FUELCELL2008 Sixth International Conference on Fuel Cell Science, Engineering and Technology June 16-18, Denver Colorado.

[21] P.W. Li, S.P. Chen, M.K. Chyu, "Novel gas distributors and optimization for high power density in fuel cells", Journal of Power Sources 140 (2005) 311–318.

[22] S.Lorente, A. Bejan. "Heterogeneous porous media as multiscale structures for maximum flow access", Journal of Applied Physics, 100 (2006).

[23] Zhiwei Fan, Xinggui Zhou, Lingai Luo, Weikang Yuan, "Experimental investigation of the flow distribution of a 2-dimensional constructal distributor", Experimental Thermal and Fluid Science, vol. 33. pp. 77-83, 2008.

Influence of Supercritical ORC parameters on Heat Exchanger Design

Sotirios Karellas[a], Andreas Schuster[b], Aris Leontaritis[a], Rolf Chritensen[c], Claes Stenhede[c]*

[a] *Laboratory of Steam Boilers and Thermal Plants, National Technical University of Athens, Athens, Greece*
[b] *Institute of Energy Systems, Technische Universität München, Munich, Germany*
[c] *Alfa Laval, Lund AB, Lund, Sweden*

Abstract: The applications of Organic Rankine Cycle (ORC) seem to become more and more present in the field of waste heat utilisation. This thermodynamic cycle can be successfully used in the field of biomass combustion, geothermal systems or solar desalination systems, providing efficient systems. In the last years, a very intense investigation on the utilization of low temperature waste heat for generating ORC systems has brought new research potential in the area of thermodynamic optimization of this cycle. More specifically, the use of supercritical fluid parameters in the ORC processes seems to become more and more attractive leading to lower exergy destruction systems together with higher heat utilisation systems. However, the investigation of the heat exchanger design and the heat exchange coefficients is of high importance for these applications as the effective heat transfer reflects to the overall process energetic and exergetic efficiency. It is important to study the basically unknown heat transfer mechanisms around the critical point to improve both the heat exchanger surface and the design algorithms. The aim of this paper is to investigate the influence of the ORC parameters in the heat exchanger design. More specifically the basic parameters of the design of the heat exchangers will be defined in the cases of supercritical fluid parameters and the convective coefficients as well as resulting heat transfer areas will be calculated for various fluid parameters.
.

Keywords: ORC, supercritical, heat exchange coefficients

1. Introduction

The difference between the Organic Rankine cycle (ORC) and the classical Clausius Rankine cycle is the use of organic working fluid instead of water-steam. ORC has a lot of advantages in applications in which low temperature heat source is used (e.g. geothermal energy, solar desalination and waste heat recovery) [1]. One of the main challenges of ORC process is the choice of the appropriate working fluid and of the particular cycle design with which maximum thermal efficiency as well as effective heat source utilization can be achieved.

Apart from the subcritical Organic Rankine, many investigations can be found in the literature in order to apply this cycle in supercritical parameters [2]. These parameters result to lower exergy destruction providing important advantages which lead to more effective heat utilization, especially in the cases of low temperature level waste heat.

Therefore, the main challenge is the dimensioning of the heat exchanger, which prerequisites the appropriate determination of the design parameters after having investigated the heat transfer mechanisms in the supercritical conditions.

2. Thermodynamic approach of supercritical ORC

Fig.1 shows the process of a sub- and supercritical ORC in a T-s-Diagram for a constant superheated vapour temperature.

* Corresponding author: Sotirios Karellas, email: sotokar@mail.ntua.gr

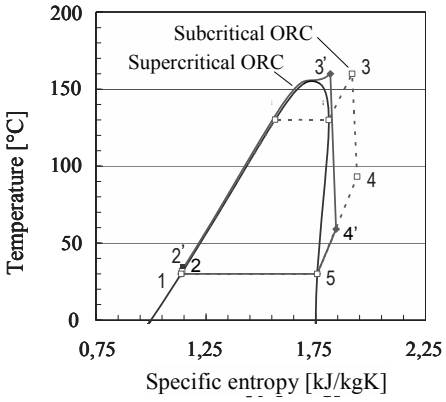

Fig. 1. Sub- and supercritical ORC. Example of R245fa

Even for constant temperature of the superheated vapour, the heat input occurs at a higher average temperature level in the case of supercritical vapour parameters, compared to subcritical. In reality such big superheating of the subcritical vapour as shown in the diagram would not be realized due to the tremendous heat exchange area needed due to the low heat-exchange coefficient of the gaseous phase [3].

The thermal efficiency of the cycle is defined as follows:

$$\eta_{th} = \frac{P_{mech}}{\dot{Q}_{Organic\ fluid}} \qquad (1)$$

P_{mech} is the net mechanical power produced with the ORC process (which will be assumed as equal the net electrical power). This power output of the subcritical process is analogue to the enthalpy fall in the turbine minus the enthalpy rise in the pump:

$$P_{mech} = \dot{m}_{ORC} \cdot \left[(h_3 - h_4) - (h_2 - h_1) \right] \qquad (2)$$

The heat input to the ORC process is done usually with the help of the thermal oil and is equal to:

$$\dot{Q}_{Organic\ fluid} = \dot{m}_{ORC} \cdot (h_3 - h_2) \qquad (3)$$

h_1, h_2, h_3 and h_4 are the specific enthalpies according to fig. 1.

In the case of supercritical process, the enthalpy fall ($h_{3'}$-$h_{4'}$) is much higher than in the subcritical one, when on the other hand, the feed pump's additional specific work to reach supercritical pressure, which corresponds to the enthalpy rise ($h_{2'}$-h_2), is very low.

Therefore, according to equation (1), the efficiency of the process is higher in the case of supercritical ORC parameters and this fact provides new frontiers in the investigation of ORC applications.

The efficiency of the heat exchange system which transfers the heat from the heat source to the organic fluid is defined by the following equation:

$$\eta_{HEx} = \frac{\dot{Q}_{Organic\ fluid}}{\dot{Q}_{HS}} \qquad (4)$$

Finally, the efficiency of the whole system is defined as follows:

$$\eta_{System} = \frac{P_{mech}}{\dot{Q}_{HS}} = \eta_{HEx} \cdot \eta_{th} \qquad (5)$$

As the system efficiency is directly linked with the efficiency of the heat exchange system, it is obvious that the aim is to maximise the transferred heat. The exploitation of the heat source in a supercritical ORC can be also seen in the diagram shown in Fig. 2. This diagram shows the enthalpy flow of the heat source to the ORC medium.

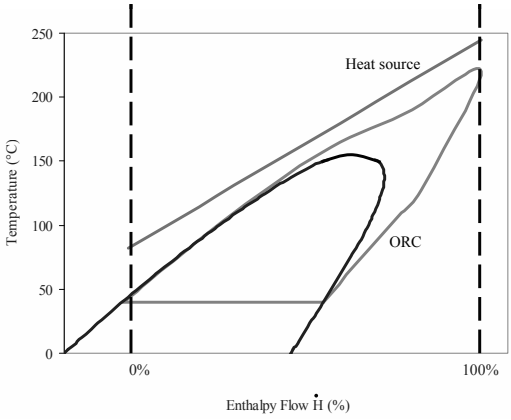

Fig. 2. T-$\dot{H}$ diagram of R245fa Live vapour parameters: 60bar, 220°C

3. Plate heat exchangers

Correctly installed and operated, the Plate Heat Exchangers (PHE) have excellent properties both as evaporator and condenser. One limitation of the PHE is the relatively small port areas.

In order to utilize the heat source as effectively as possible, the heat exchanger has to operate in a pure counter current flow as possible. In certain cases, e.g. in order to provide a high starting pressure difference in an evaporator, co-current flow could be better. All flow disturbances such as cross current, back flock, by-passes, unequal channel flow, unequal channel heat transfer, etc. tend to destroy the Mean Temperature Difference (MTD) and thus lower the efficiency, as defined in equation (4).

In order to economically utilize a PHE, the frame has to be filled with as many plates as possible as the frame is a very large part of the total cost. Unfortunately, that can mean very high velocities in the ports (the header holes in the plate). This is important especially for the exit port of an evaporator. A high velocity means a high port pressure drop, which corresponds to a difference in the channel pressure drop between the first and the last channels and a decrease of the MTD.

There are mainly two solutions to this. First of all, the use of a PHE with the correct port size can eliminate the problem of the decrease of the MTD. However, this leads to the construction of a heat exchanger with few plates in the frame. The necessary port size for a given cycle depends mainly on the exit vapour temperature and therefore, low temperature means low mass flow amount of low density vapour (high volume flow).

Secondly, a distributor in the inlet port could be also a solution, leading to a pressure drop restriction before each channel inlet. A good distribution is obtained if the pressure drop ratio between the channels and headers is high. It is also important to mention that a pressure drop before the channel entrance has no influence on the thermal performance.

Fig. 3 shows the layout of an ORC using plate heat exchangers. The organic working fluid is compressed with a pump, which forces the fluid through a preheater which raises the temperature of the liquid working fluid by desuperheating the expanded vapour. The preheated working fluid is then evaporated, superheated and expanded in a turbine. The desuperheated vapour is condensed in a plate heat exchanger condenser.

As the figure shows, the plant is equipped with a separator. This is not necessary in a supercritical cycle, but can serve as a security in case of disturbances in the system, which can lead to unevaporated liquid leaving the evaporator. In a subcritical system, the liquid droplets are separated in the separator and returned to the evaporator inlet. In this way the evaporator can operate with a fairly large liquid content at the exit, which improves the heat transfer.

A subcritical evaporator is controlled either by the superheat or by the liquid level in the separator. This is not possible in a supercritical cycle where no phase change takes place. For an efficient cycle operation, an acceptable method is to control the pressure by changing the speed of the feed pump. The temperature could be set free, while its upper limit is in any case set by the heating fluid.

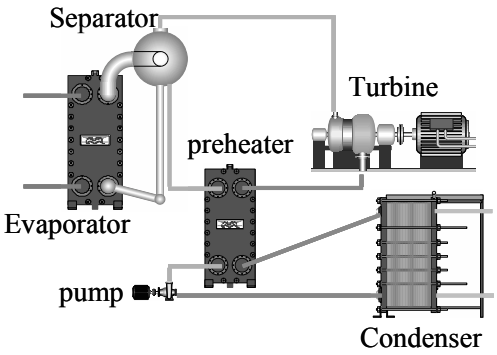

Fig. 3. Heat exchangers used in an ORC.

If in the cycle presented in Fig. 3, the fluid 236fa, in the subcritical range is used, it is concluded that the output is low because of the pinch point. The thermal properties are not very good but the low volume ratio, compared to a normal refrigeration evaporator, makes it easier to find a suitable PHE (Table 1).

In Fig. 4, 5 and Table 1 the properties of a R227ea cycle for two pressures are presented. The pressures are just above the critical pressure of 29,3 bar and the end final temperature 115°C is super-critical.

Table 1. Comparison of the cycle for R236fa and R227ea.

Refrigerant:	236fa	227ea	227ea
Water flow (kg/s)	100	100	100
Inlet temperature (°C)	120	120	120
Exit	100	85	50
Cycle state	Sub-critical	Super-critical	Super-critical
Exit temperature/ pressur (°C/bar)	115/20	115/30	115/45
Condensing (°C/bar)	30/3,2	30/5,3	30/5,3
Volume Exit/Inlet:	9,2	4,83	1,68
Power output (kW):	248	447	774
Turbine efficiency:	80%	80%	80%

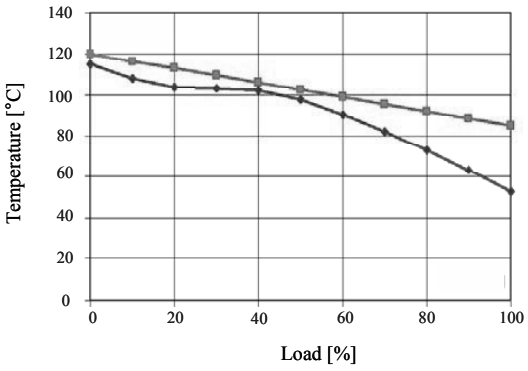

Fig. 4. R227ea Evaporator. Water temperature 120°C, Evaporator temperature 101,8°C and evaporator pressure 30 bar

In the supercritical cycles, there is no evaporation range, the state changes from liquid to vapour when the critical temperature is reached. The 30 bar cycle (Fig. 4), has a pinch point, even though small. There is no constant evaporation but as the specific heat is very high around the critical point, the temperature increase is very small, the temperature curve looks almost like an evaporation curve.

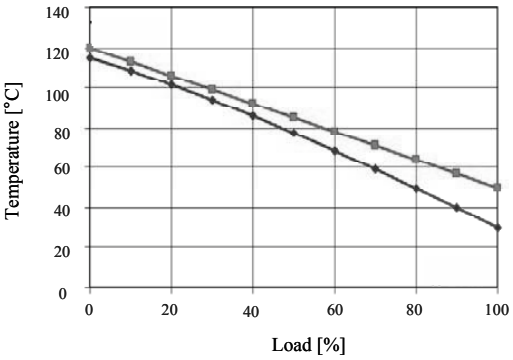

Fig. 5. R227ea Evaporator. Water temperature 120°C, Evaporator temperature 101,8°C (Critical) and evaporator pressure 45 bar

The 45 bar cycle (Fig. 5) has no pinch point it is only slightly curved upside. The result is that the water exit temperature can be very low and thus a very large power output can be achieved. Both cycles, but especially the 45 bar cycle, has very small ratio exit/inlet fluid volume.

It is very important though to investigate the heat transfer around the critical point which is quite unknown. As there is little difference between the vapour and liquid densities, there will be little phase separation in the flow. Furthermore, the heat transfer coefficients are probably somewhat smaller, but because of the higher velocities in a multi-pass unit, the difference is low.

There is a high challenge in the understanding of the plate heat exchangers in order to use them in supercritical ORC. In order to analyse the heat transfer mechanisms in these heat exchangers, the relevant heat transfer coefficients will be investigated.

4. CALCULATION OF THE MEAN OVERALL HEAT TRANSFER COEFFICIENT

The most challenging issue in the design of a heat exchanger for supercritical fluid parameters is the calculation of the mean overall heat transfer coefficient U as well as the necessary area of the heat exchanger. The aim of this paper is to investigate the influence of the main ORC parameters, such as vapour pressure and

superheating temperature, on the heat exchanger design.

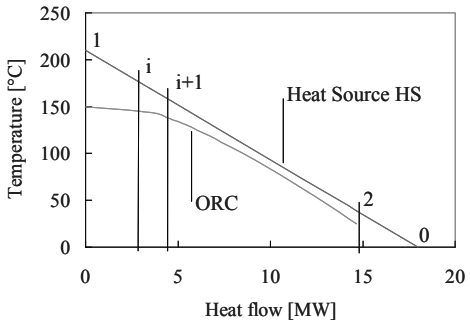

Fig. 6. $\dot{Q}$-T diagram of the heat exchanger

In fig. 6, the heat transfer between the hot medium and the organic medium is presented. Due to the variable inclination of the curve of the organic medium, a global logarithmic temperature difference between the input and the output of the organic fluid is not an acceptable assumption.

As already discussed, the thermal properties of the fluid in supercritical state are strongly dependant on temperature, especially in the pseudo-critical temperature range, the definition of which will be discussed later in this paper. The U value of the heat exchanger also depends on those properties and therefore cannot be considered constant through the heat transfer procedure.

For those reasons a numerical approach to the problem is needed.

The heat exchanger is divided into n elementary areas assuming equal enthalpy difference. Equation (6) can be used, where the logarithmic temperature difference is provided from the input and output of each elementary area of the heat exchanger (ΔT_i and ΔT_{i+1} respectively).

$$\dot{Q} = U \cdot A \cdot \Delta T_{\log} = U \cdot A \cdot \frac{\Delta T_i - \Delta T_{i+1}}{\ln\left(\frac{\Delta T_i}{\Delta T_{i+1}}\right)} \qquad (6)$$

In the heat transfer process, the heat flow between two points i and i+1 is considered:

$$\dot{Q}_{i;i+1} = \dot{m}_{ORC} \cdot \left(h_i(t_i; p_{sc}) - h_{i+1}(t_{i+1}; p_{sc})\right) \quad (7)$$

In this approach, the heat transfer is considered without pressure losses and therefore the supercritical pressure p_{sc} is also considered to be constant.

As the transfered heat from the heat source to the organic fluid is known, the temperature of the heat source medium (HS) can also be defined as follows:

The heat that is transferred from the heat source to the ORC medium is:

$$\dot{Q}_{ORC} = \dot{Q}_{HS} \qquad (8)$$

Therefore the heat provided from the heat source from point 1 to the point i is equal to:

$$\dot{Q}_{ORC,1-i} = \dot{Q}_{HS,1-i} = \dot{m}_{HS} \cdot c_p \cdot (t_{HS1} - t_{HSi}) \Rightarrow$$

$$t_{HS,i} = t_{HS,1} - \frac{\dot{Q}_{HS,1-i}}{\dot{m}_{HS} \cdot c_p} \qquad (9)$$

The heat flow of the Heat Source is supposed to be linear. A dependence of the specific heat capacity with the temperature is not considered.

Using equations (7),(8) and (9), the corresponding temperatures of points i and i+1 can be calculated.

With all the points of the procedure defined, all the necessary fluid properties for the calculation of the U value are known. In each elementary area of the heat exchanger the factor UA is:

$$\left(U \cdot A\right)_{i,i+1} = \frac{\dot{Q}_{i,i+1}}{\Delta T_{\log}} = \frac{\dot{Q}_{i,i+1}}{\frac{\Delta T_i - \Delta T_{i+1}}{\ln\left(\frac{\Delta T_i}{\Delta T_{i+1}}\right)}} \qquad (10)$$

The special feature of fluid at supercritical pressures is that their thermodynamic properties vary rapidly with temperature and pressure. Fig. 7 shows the specific heat capacity and Prandtl number variation according to the temperature, for R227ea and R245fa at critical and supercritical pressure. The specific heat capacity as well as the Prandtl number of both fluids change significantly near the critical temperature at critical pressure. For supercritical pressures there is a temperature where the c_p and the Prandl number rise to a peak and then fall steeply. This temperature is the so-called pseudo-critical temperature. Thermo-physical properties undergo significant changes near the pseudo-critical point in a similar way to

the critical point but with relatively smaller variation.

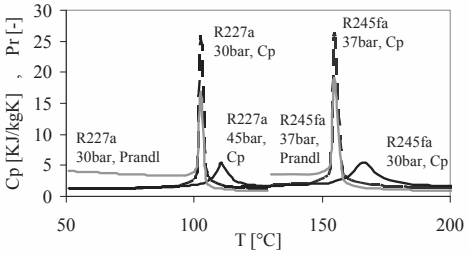

Fig. 7. Variation of the cp and Pr with the temperature

In Fig. 7, the variation of the Prandtl number before and after the critical temperature should be commented. In subcritical temperatures it has a value around 4, so the medium can be described as liquid. After the rise of the temperature almost instantly passing into the supercritical area it drops to 1 and the medium can be described as gas. Conclusively the phase change takes place almost instantly in the critical or pseudo-critical point, according to the applied pressure.

For those reasons, the classical heat transfer correlations, as the Dittus Boelter correlation (see eq. 16) for the calculation of the Nusselt number cannot be used. Therefore, the Nusselt number is calculated using the Jackson correlations for supercritical fluid parameters [4], [5] which include a correction factor which neutralises the effect of the variation of the thermo-physical properties around the pseudo-critical point:

$$Nu_b = 0{,}0183 \cdot \mathrm{Re}_b^{\,0{,}82} \cdot \mathrm{Pr}^{0{,}5} \cdot \left(\frac{\rho_w}{\rho_b}\right)^{0{,}3} \cdot \left(\frac{\overline{c}_p}{c_{p_b}}\right)^{n} \quad (11)$$

where b refers to bulk fluid temperature and w to wall temperature

In this last equation, the average specific heat capacity of the medium is considered:

$$\overline{c}_p = \frac{h_w - h_b}{T_w - T_b} \quad (12)$$

And if T_{pc} is the pseudocritical temperature, then the exponent of equation (11) is defined as follows [6]:

$$\begin{aligned} &n = 0{,}4 \ \textit{for}\ T_b < T_w < T_{pc} \ \textit{and}\ 1{,}2 \cdot T_{pc} < T_b < T_w \\ &n = 0{,}4 + 0{,}2 \cdot \left(\frac{T_w}{T_{pc}} - 1\right) \ \textit{for}\ T_b < T_{pc} < T_w \\ &n = 0{,}4 + 0{,}2 \cdot \left(\frac{T_w}{T_{pc}} - 1\right) \cdot \left(1 - 5 \cdot \left(\frac{T_b}{T_{pc}} - 1\right)\right) \\ &\textit{for}\ T_{pc} < T_b < 1{,}2 \cdot T_{pc} \end{aligned} \quad (13)$$

The convective heat transfer coefficient is:

$$Nu = \frac{\alpha \cdot d}{\lambda} \Rightarrow \alpha = \frac{Nu \cdot \lambda}{d} \quad (14)$$

The mean overall heat transfer coefficient U is defined as:

$$\frac{1}{U} = \frac{1}{\alpha} + \frac{1}{\alpha_{hot}} + \frac{\delta}{\lambda} + R_f \quad (15)$$

α_{hot} is calculated using the Dittus Boelter correlation [7]:

$$Nu = 0{,}023 \cdot \mathrm{Pr}^n \cdot \mathrm{Re}^{0{,}8} \quad (16)$$

where n=0,4 for heating processes and 0,3 for cooling processes.

As the factor $U \cdot A$ and the mean overall heat transfer coefficient U are known for each step, the necessary elementary area A_i can also be calculated. The total heat exchanger area A_{tot} is:

$$A_{tot} = \sum_{i=1}^{i=m} A_i \quad (17)$$

The minimum temperature difference between the heat source medium and the supercritical fluid is defined as the Pinch Point temperature difference ΔT_{pinch}, which is kept constant at 10 K for the calculations. The ΔT_{pinch} is controlled by the organic fluid and hot source medium mass flows.

As for the geometry and the fluid velocity in the heat exchanger, a rectangular cross-section is used and the respective hydraulic diameter is calculated. The geometrical characteristics are presented in Table 2.

Table 2. Geometrical characteristics of the Heat Exchanger

Width	100 mm
b (distance between plates)	2 mm
δ (plate thickness)	0,45 mm

In all numerical calculations presented in this work, real fluid properties according to the Refprop Database by NIST were used [8].

5. Results

Setting the pinch point temperature difference at 10 K, the mean overall heat transfer coefficient U of the heat exchanger was calculated for various fluids, live vapour temperatures and pressures. Table 3 presents the three fluids that were considered and their critical points.

Table 3. Fluids considered

Fluid	P_{crit} [MPa]	T_{crit}(°C)
R134a	4,06	101,06
R227ea	2,92	101,75
R245fa	3,65	154,01

Fig. 8 shows the influence of pressure and temperature on the U value.

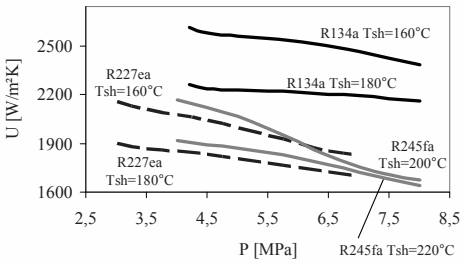

Fig. 8. Mean overall heat transfer coefficient vs. pressure for 3 fluids and superheating temperatures

There is an almost linear relation in which the rise of the pressure leads to lower mean overall thermal coefficient. An interesting observation is the influence of the live vapour temperature to the shape of those lines. For lower temperatures the absolute gradient of the U-P lines rises and therefore the impact of pressure upon the U value is even stronger. As seen in the above figure, under constant pressure, the live vapour temperature affects significantly the mean overall thermal coefficient. For example, when the working fluid is R134a at 65 bar, U drops from 2500 W/m^{2}K at 160°C to 2200 W/m^{2}K at 180°C.

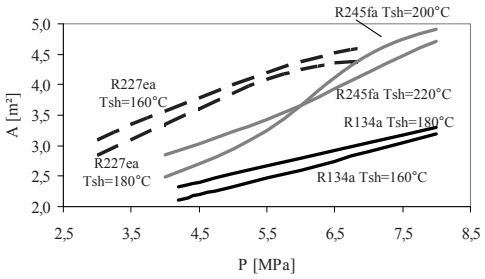

Fig. 9. Dependence of the needed heat exchanger area from the pressure for three organic fluids and superheating temperatures

Regarding the needed heat exchanger area as a function of pressure (fig. 9), it should be noted that there are two factors which contribute to those results. Obviously, the first one is the drop of the U value and the second has to do with the T-H or T-Q diagram (Fig. 2, 4,5 and 6). In order to keep the pinch point fixed at 10 K when the pressure rises, a higher heat exchanger efficiency needs to be achieved. Therefore the surface of the heat exchanger needs to be also larger.

Fig. 10 shows the heat exchanger efficiency as a function of pressure. It should be noted that it is not possible to use the NTU method for the calculation of the heat exchanger efficiency, as neither the temperature nor the specific heat capacity are constant at every point of the heat transfer procedure. Normally, in a subcritical heat exchanger one of the two values is constant. In the sensible heat transfer procedures, c_p is considered constant, where in latent heat transfer procedures (vaporisation) the temperature remains constant. Therefore, the following definition was used for the efficiency of the heat exchanger:

$$\varepsilon = \frac{\dot{Q}}{\dot{Q}_{\max}} \qquad (18)$$

Q is the heat transferred to the organic fluid and Q_{max} is the maximum transferable heat, defined as

$$Q_{\max} = C_{\min} \cdot \left(T_{hot,in} - T_{cold,in}\right) \qquad (19)$$

$$C_{\min} = \min\left\{\left(\dot{m} \cdot \bar{c}_p\right)_{Hot\ Source}, \left(\dot{m} \cdot \bar{c}_p\right)_{ORC}\right\} \qquad (20)$$

The heat exchanger efficiency was calculated for a fixed heat exchanger area of 3,5 m^2. Generally, rising pressure leads to higher efficiency rates. A significant observation is that there is a pressure range in all fluids (from critical pressure up to 10-15 bar above the supercritical pressure), where rising pressure leads to a constant of slightly dropping heat exchanger efficiency.

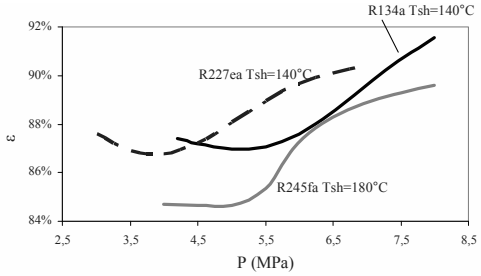

Fig. 10. Heat exchanger efficiency

Finally, the impact of the heat exchanger area on the heat exchanger efficiency is qualitatively the same as in a sub-critical heat exchanger.

6. Conclusions

The application of ORC for waste heat utilization, especially in the cases of supercritical parameters, seems to be very attractive and should become more and more applicable in many cases.

In this paper, the heat transfer properties of a plate heat exchanger when working in supercritical ORC applications was investigated.

From the analysis presented, the heat transfer coefficients applied to these heat exchangers have been determined making their dimensioning more and more accurate to the needs of the supercritical fluid parameters.

Nomenclature

A	Surface (m²)
b	distance between plates (mm)
c_p	specific heat capacity (kJ/kgK)
d	hydraulic diameter (m)
$\dot{H}$	Enthalpy flow (kW)
h	Specific enthalpy (kJ/kg)
$\dot{m}$	Mass flow (kg/s)
n	exponent
Nu	Nusselt Number
P	Power (kW)
p	Pressure (MPa)
PHE	Plate Heat Exchanger
$\dot{Q}$	Heat flow (kW)
Re	Reynolds number
R_f	Fouling factor (m²K/W)
s	specific Entropy (kJ/kgK)
T, t	Temperature (°C)
U	Mean overall heat transfer coefficient (W/m²K)

Subscripts/superscripts

b	bulk fluid
cr	critical
HEx	Heat Exchanger
HS	Heat Source
max	maximum
mech	mechanical
ORC	Organic Rankine Cycle
th	thermal
tot	total
pc	pseudocritical
sh	superheated

Greek symbols

α	Heat transfer coefficient (W/m²K)
δ	plate thickness (mm)
ε	Heat exchanger efficiency
η	Efficiency
λ	Thermal conductivity (W/mK)

References

[1] Schuster A., Karellas S., Kakaras E., Spliethoff H., 2009, Energetic and economic investigation of Organic Rankine Cycle, Applied Thermal Engineering, 29, pp. 1809-1817.

[2] Schuster A., Karellas S., Aumann R., 2010, Efficiency optimization potential in supercritical Organic Rankine Cycles, Energy, 35, pp. 1033-1039.

[3] Karellas S., Schuster A., 2008, Supercritical fluid parameters in Organic Rankine Cycle applications, International Journal of Thermodynamics, Vol.11 (No.3), pp.101-108.
[4] Jackson J.D., Hall W.B., 1979, Forced convection heat transfer, in: S. Kakac, D.B. Spalding (Eds.), Turbulent Forced Convection in Channels and Bundles, vol. 2, p. 563.
[5] Jackson J.D., Hall W.B., 1979, Influences of buoyancy on heat transfer to fluids flowing in vertical tubes under turbulent conditions, in: S. Kakac¸, D.B. Spalding (Eds.), Turbulent Forced Convection in Channels and Bundles, vol. 2, p. 640.
[6] Kang K-H., Chang S-H., 2009, Experimental study on the heat transfer characteristics during the pressure transients under supercritical pressures. International Journal of Heat and Mass Transfer Vol. 52, Issues 21-22, pp. 4946 - 4955.
[7] Sharabi M., Ambrosini W., He S., Jackson J.D., 2008Prediction of turbulent convective heat transfer to a fluid at supercritical pressure in square and triangular channels. Annals of Nuclear Energy 35, pp. 993–1005.
[8] Lemmon, E., McLinden, M., Huber, M., 2002, NIST Reference Fluid Thermodynamic and Transport Properties – REFPROP. U.S. Department of Commerce, National Institute for Standards and Technology, Gaitherssburg, Maryland, USA.

ECOS: Thermo-ecological optimisation of a heat exchanger based on CFD modelling

Ireneusz Szczygieł, Wojciech Stanek and Marek Rojczyk

Institute of Thermal Technology
Silesian University of Technology
44-100 Gliwice, ul. Konarskiego 22, POLAND
tel. (+48 32)237 1448, fax. (+48 32) 237 2872
e-mail: ireneusz.szczygiel@polsl.pl

Abstract: In this paper, an example of thermo-ecological optimisation using CFD techniques is presented. The annual thermo-ecological cost of the heat exchanger operation is used as the objective function. The operational parameters in each step of the iterative procedure are evaluated using a CFD heat exchanger model. The heat exchanger's entire life cycle is investigated. Finally, the results of the multi-variant analysis are presented.

Keywords: exergy, thermo-ecological cost, CFD, optimisation, heat exchanger

1. Introduction

One important ecological application of exergy is the determination and reduction of the depletion of non-renewable natural resources. The quality of different natural resources may be evaluated by means of exergy [3,5,11,12,13]. Szargut [5] defined "thermo-ecological cost" as the cumulative consumption of non-renewable exergy connected with producing a particular useful product. In general, the thermo-ecological cost analysis can be applied for the solution of the following problems:

- the influence of the operational parameters of energy and technological systems on the depletion of non-renewable natural resources,
- the selection of technology that ensures minimal consumption of non-renewable natural resources,
- the optimisation of structural and operational parameters to ensure minimum depletion of natural resources,
- the evaluation of harmful impacts from waste products,
- the investigation of the influence of interregional exchange on the depletion of domestic natural resources,
- the evaluation of the ecological harmfulness of particular useful goods over their entire lifetimes (thermo-ecological lifecycle analysis).

In this paper, the authors use thermo-ecology for the minimisation of thermo-ecological cost. The example presented in the paper concerns the optimisation of operational parameters for a heat exchanger. The example calculations for minimising thermo-ecological cost are based on the objective function formulated by Szargut [5]. This function fulfils the rules of lifecycle analysis because it contains both the investment expenditures (measured by the cumulative exergy consumption of non-renewable natural resources) and the final effects of decommissioning the installation. Each optimisation requires a mathematical model of the investigated system. The model can be expressed either by simplified empirical characteristics or by an exact model based on physical laws. The second method is relatively more complicated and time-consuming. However, contemporary computer techniques let us build such advanced models with satisfactory accuracy. In this paper, the authors apply the CFD techniques for modelling heat exchangers. The presented computational example is the first attempt to connect thermo-ecology and CFD modelling techniques.

2. Minimisation of thermo-ecological cost

The index of operational thermo-ecological cost can be determined by solving the thermo-ecological cost balance presented in Fig. 1.

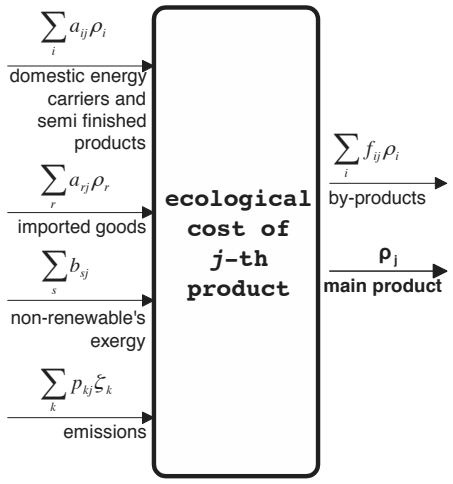

Fig. 1. Balance of thermo-ecological cost.

The equation for the balance of thermo-ecological cost takes the following form:

$$\rho_j + \sum_i \left(f_{ij} - a_{ij}\right)\rho_i - \sum_r a_{rj}\rho_r = \sum_s b_{sj} + \sum_l z_{lj}\sigma_l + \sum_k p_{kj}\xi_k \quad (1)$$

This set should comprise all branches of domestic economy. However, it would be difficult to solve such a problem. For this reason, practical calculation only takes into account strongly connected production [4]. Exergy as a resource depletion indicator is also applied [3,11-13]. The method for determining the factors is discussed in the following sections. The results of calculations for thermo-ecological cost have been presented [4,8]. To express the total natural resource expenditures, the thermo-ecological cost method should include the total life of installation [2]. A Thermo-Ecological Life Cycle Assessment (TELCA) consists of three main parts:

1. The construction phase encompasses project, extraction of raw materials, semi-finished product fabrication, and transport expenditures in the construction phase. All of these expenses influence the thermo-ecological cost burdening the final useful consumptive product. This phase can have a significant contribution to thermo-ecological cost in the case of processes based on renewable energy. For instance, the thermo-ecological cost of a wind power plant results mainly from expenses in the construction phase.

2. The operation phase is defined as the period of time between the end of the construction phase and the beginning of the decommissioning phase. In processes utilising non-renewable resources, this phase is the predominant consumer of natural resources, mainly energy carriers.

3. The decommissioning phase concerns the period at the end of installation. Thermo-ecological cost in this phase results from expenditures for developing the remains of the system and for reclamation of terrain.

The general form of the objective function for thermo-ecological cost minimisation, taking into account the lifetime of the product, has been formulated by Szargut [5,6] and applied for example investigation in the work of Szargut and Stanek [8]. This function has the following form:

$$K_{TH} = \tau_n\left(\sum_j \dot{G}_j\rho_j + \sum_k \dot{P}_k\xi_k - \sum_u \dot{G}_u\rho_i s_{iu}\right) + \frac{1}{\tau}\left(\sum_m G_m\rho_m\left(1-u_m\right) + \sum_r G_r\rho_r\right) \quad (2)$$

The presented formula expresses the yearly thermo-ecological cost of a given product, including consideration of its complete lifetime. Equation (2) can also be used for optimisation of the construction and operational parameters of different resource intensive systems. In this case, the function should be minimised:

$$K_{TH} \rightarrow \min . \quad (3)$$

Optimisation based on Equation (3) requires a mathematical model of the process or device. The model can be developed from the simplified empirical characteristics or from an exact model based on physical laws. The physical model can be developed by means of numerical simulation. In this paper, the Computational Fluid Dynamics (CFD) model was applied.

3. Description of the CFD model.

To present the optimisation procedure, the example of a tube-shell heat exchanger is considered. A diagram of the exchanger and a typical distribution of fluid temperature are shown in Figs. 2 and 3, respectively. It was assumed that there is certain amount of waste heat to be utilised. The amount of heat, the stream and the heated water temperatures were all fixed. The geometrical parameters of the number of tubes and the tube diameter were chosen as decision variables. Only the tube side was investigated. The whole heat exchanger with both shell and tube side will be considered in future investigations.

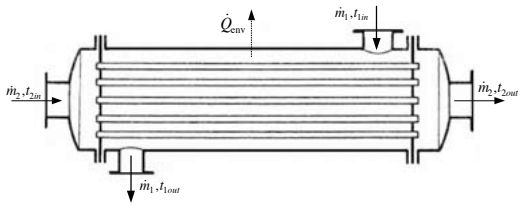

Fig. 2. Diagram of the considered heat exchanger.

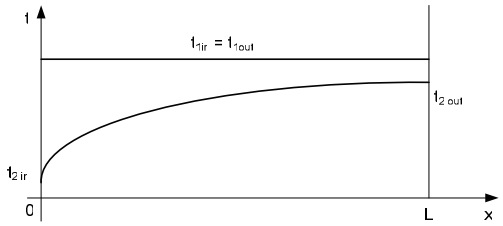

Fig. 3. Typical distribution of fluid temperature.

For this example, the following data have been assumed:

- heat load of the exchanger: $\dot{Q}$ =600 kW
- mass flow rate of the tube fluid: $\dot{m}$ =5 kg/s
- steam temperature: t_v =150 °C

The source of heat was assumed as a saturated vapour, and therefore, the shell-side fluid temperature was constant. The convective heat transfer coefficient in the shell side was estimated based on similarity theory analysis.

The variability in the number of tubes influences the mass flow rate in the single tube. The diameter of the single tube determines the fluid velocity in the tube, which determines the heat transfer coefficient and the exchanger length. All of the mentioned parameters are strongly connected to the pressure drop in the tubes. The pressure drop, tube diameter and tube length all influence the thermo-ecological cost, and therefore, their values in the optimisation are essential. These quantities can be evaluated using similarity theory formulas [7,8] or by performing full numerical analysis of the fluid flow inside the tubes. Advances in numerical techniques allow the possibility to solve not only the fluid flow field but also to perform multi-variant analysis, which is necessary in the presented procedure.

The mathematical description of the flow within the tubes consists of the following equations [1]:

- the momentum equations (Navier-Stokes)
- the mass balance equation (continuity equation)
- the energy balance equation (Fourier-Kirchhoff)
- the turbulence model equations

These equations are partial differential equations, which in most cases cannot be solved analytically. This makes numerical analysis necessary, which can be very difficult, especially for complicated geometries. This set of equations should be supplemented by the appropriate initial conditions and boundary conditions [10].

The computations of flow phenomena within the tubes were performed with the commercial CFD package Fluent/Ansys. The scheme of the computations is presented in Fig. 4.

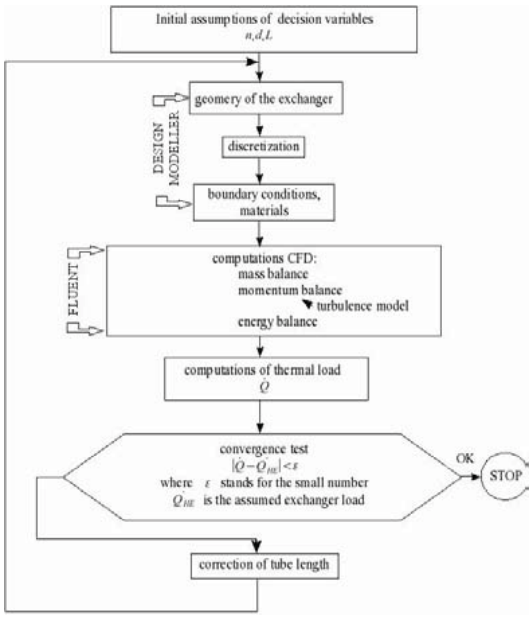

Fig. 4. Block scheme of CFD procedure.

The following boundary conditions were assumed:

- mass flow rate at the tube inflow
- outflow at the tube outlet
- temperature at the tube inlet
- Robin BC at the external tube side

The resulting discretisation of the tube and distributions of temperature, fluid velocity and pressure are presented in Figs. 5-8.

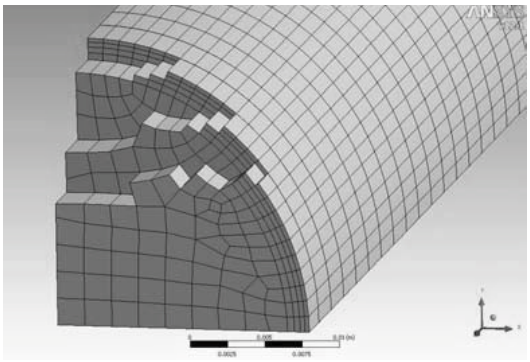

Fig. 5. Discretisation of the example tube.

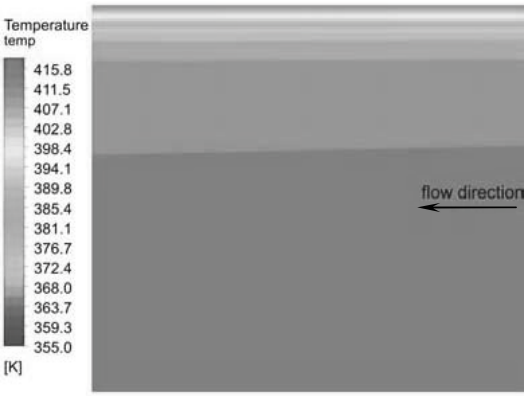

Fig. 6. Temperature distribution in the end of the tube.

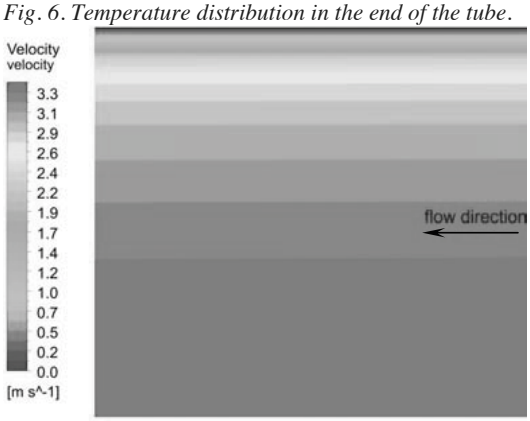

Fig. 7. Velocity distribution in the end of the tube.

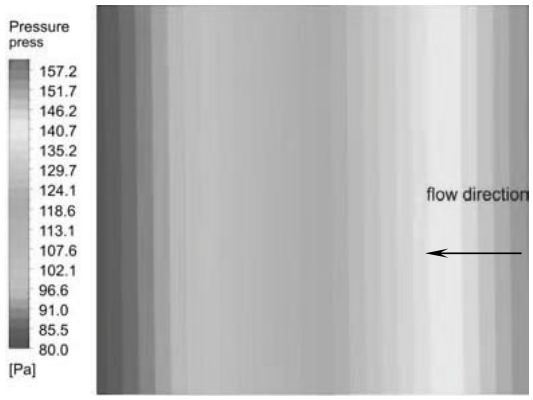

Fig. 8. Pressure in the end of the tube.

4. Description of the optimisation procedure.

The yearly thermo-ecological cost of the heat-exchanger operation can be expressed as follows:

$$K_{TE} = \frac{\rho_{\mathrm{el}}}{\eta_{\mathrm{P}}} \int_0^{\tau_P} \dot{V}\,\delta\,p\,\mathrm{d}\tau + \frac{\rho_s(1-u_s)}{\tau_Z}\cdot\left(G_p + G_s'\right) \quad (4)$$
$$+ E_{el}\rho_{el} \rightarrow \min$$

The amount of steel necessary for the tube in the heat-exchanger is determined from the following equation:

$$\mathrm{G_p} = \left(\frac{\pi}{4}(\mathrm{D}+2\mathrm{t})^2 - \frac{\pi \mathrm{D}^2}{4}\right)\mathrm{L}\gamma_s \quad (5)$$

It can be assumed [7] that the diameter of the heat exchanger jacket is proportional to the diameter of the tubes and to the square root of the number of tubes:

$$\mathrm{G_s'} = \sigma \mathrm{D}\sqrt{\mathrm{n}}\left(1+\kappa \mathrm{L}\right), \quad (6)$$

Consumption of electricity for the construction of the heat exchanger should be a function of decisive variables. It can be expressed as follows [7]:

$$\mathrm{E_{el}} = \mu \mathrm{Dn} + \nu \mathrm{D}\sqrt{\mathrm{n}}\ , \quad (7)$$

The following data have been assumed:

ρ_{el} =3.5 MJ/MJ

ρ_s =59 MJ/kg

σ =700 kg/m

κ =0.15 1/m

μ =0.08 kJ/m

ν =0.3 kJ/m

Equation (4) contains two main components:

1. the investment component containing the thermo-ecological cost of the materials used for the construction of the exchanger,
2. the operational components expressing the consumption of electricity in the pump.

The investment component takes into account the life time τ_Z of the installation and the possibility to reuse steel after the completion of the lifecycle of the installation. The operational components take into account the yearly operation time τ_P of the pump. The whole optimisation procedure is shown in Fig. 9.

The main difference from previous works [8] is the replacement of the device characteristic by the numerical model based on the CFD model.

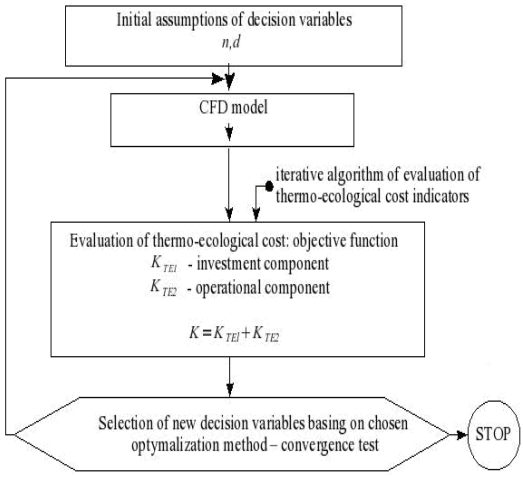

Fig. 9. The scheme of the optimisation procedure.

Such an attempt makes the procedure more exact, but it also results in a much longer computational time.

The results of the example optimisation are shown in Figs. 10 and 11.

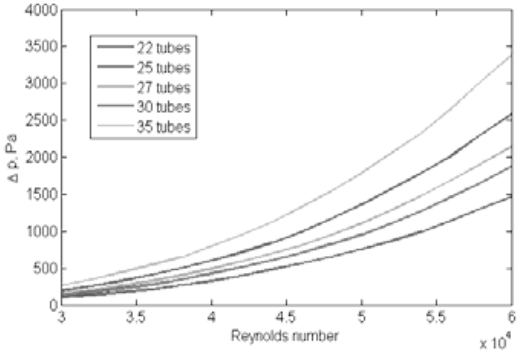

Fig. 10. Total pressure increase as a function of Reynolds number.

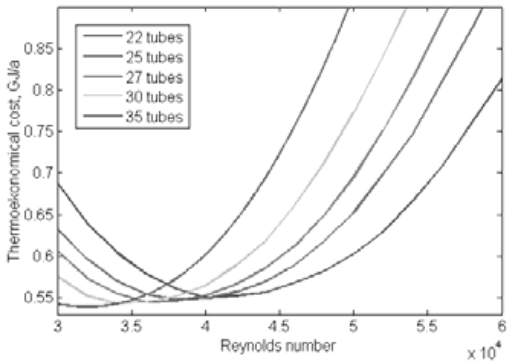

Fig. 11. Thermo-ecological cost as a function of Reynolds number dependence.

5. Summary and conclusions.

1. Due to the small influence of the number of the tubes on the objective function, the decision regarding the number of tubes should be performed by the constructor. The optimisation procedure resulted in optimal values as follows: number of tubes = 35 tubes; Re=32000; L=1660 mm; d=20,3 mm; Δp=345,9 Pa.
2. The formulated objective function and the determined duration curves can also be used in an economic optimisation by using purchase prices instead of the values of thermo-ecological cost.
3. The presented coupled analysis combining exergy analysis and CFD modelling can be applied to other optimisation problems after reconstruction of the device numerical model.

Nomenclature

a_{ij} coefficient of the consumption of the i-th product per unit of the j-th major product

a_{rj} coefficient of the consumption of the r-th imported product per unit of the j-th major product

b_{sj} exergy of the s-th non-renewable natural resource immediately consumed in the process under consideration per unit of the jth product

d inside dimension

D internal diameter of tubes

E_{el} electricity consumption during exchanger construction

f_{ij} coefficient of by-production of the i-th product per unit of the j-th major product

G_j nominal flow rate of the j-th major product

G_u nominal flow rate of the useful u-th by-product

G_m consumption of m-th material or energy carrier used for construction of installation

G_p, G_s' mass of steel tubes and exchanger jacket

L length of the tube

n number of tubes

Δp difference of inlet and outlet total pressure

p_{kj} amount of the k-th aggressive component of waste products rejected to the environment per unit of the j-th product

P_k nominal flow rate of the k-th deleterious waste product rejected to the environment

Re Reynolds number

s_{iu} replacement ratio in units of the i-th replaced product per unit of the u-th by-product

t thickness of tube wall

u_m expected recovery factor of the m-th material

z_{lj} amount of the l-th aggressive component of waste products entering the cleaning installation

Greek symbols

γ_s density of steel

σ, κ coefficients resulting from construction concept of exchanger

σ_l cumulative exergy consumption of non-renewable resources due to the removing of k-th aggressive product from wastes

ζ_k cumulative exergy consumption of non-renewable resources due to the emission of unit of the kth waste product

η_p electric efficiency of pump and electric engine

μ, ν proportionality coefficients (as determined by producer of exchanger, for example)

ρ_{el} unit thermo-ecological cost of electricity

ρ_s thermo-ecological cost of steel

ρ_i thermo-ecological cost of the i-th product

ρ_m thermo-ecological cost of m-th material or energy carrier used for construction of installation

ρ_r specific thermo-ecological cost of the r-th imported good

τ lifetime of installation,

τ_n annual operation time with nominal capacity

τ_z nominal lifetime of installation

τ_n annual time of use at nominal capacity

References

[1] Cengel Y.A., Heat Transfer, McGraw Hill, New York, 2003.

[2] Cornellisen RL, Marquart EN, Hirs GG. The value of exergetic life cycle assessment besides LCA. In: M. Ishida, G. Tsatsaronis, MJ. Moran, H. Kataoka (eds), Proc. ECOS'99, Tokyo 1999, p. 282-203.

[3] Sciubba, E. Beyond thermoeconomics? The concept of Extended Exergy Accounting and its application to the analysis and design of thermal systems. Exergy Int. J., Vol.1., 2001.

[4] Stanek W. Iterative evaluating method of the ecological cost of imported goods. Proc. of ECOS'01, Istanbul 2001, 575-80.

[5] Szargut J. Exergy method, technical and ecological applications. Southampton, Boston: WIT Press, 2005.

[6] Szargut J. Minimization of the depletion of non-renewable resources by means of the optimization of design parameters. Energy 2004;29(12-15):2161-2169.

[7] Szargut J., Stanek W. Comparison of economic and thermo-ecologic optimization of thermal processes. Report from research

project 8T10B05518, Gliwice 2005 (in Polish).

[8] Szargut J., Stanek W.: Thermo-ecological optimization of a solar collector. Energy 32 (2007) 584–590.

[9] Szargut J., Ziębik A., Stanek W.: Depletion of the Unrestorable Natural Exergy Resources as a Measure of the Ecological Cost, Energy, Conversion and Management 42, 2002.

[10] Szczygieł I.: Temperature-Velocity Coupling of the Convective Heat Transfer-Sensitivity Analysis; Numerical Heat Transfer, An International Journal, Part B, 48: pp. 165-190, 2005.

[11] Valero A., Botero E. An exergetic assessment of natural mineral capital (1): Reference environment, a thermodynamic model for s degradated, Proc. Conf. ECOS 2002, Berlin.

[12] Valero A., Botero E., An assessment of the Earth's clean fossil exergy capital based on Exergy Abatement Cost. Proc. Conf. ECOS'2002, Berlin

[13] Wall, G., Gong M. On exergy and sustainable development, Exergy Int. J., Vol.1., 2001.

Acknowledgements

The paper has been prepared within the RECENT project (**RE**search **C**enter for **E**nergy and **N**ew **T**echnologies) supported by 7th Framework Programme, Theme 4, Capacities.

New Novel Green Computer Two-Phase Cooling Cycle: A Model for Its Steady-State Simulation

Jackson Braz Marcinichen, John Richard Thome

Laboratory of Heat and Mass Transfer (LTCM), Faculty of Engineering (STI)
École Polytechnique Fédérale de Lausanne (EPFL)
Station 9, CH-1015, Lausanne, Switzerland

Abstract: The performance of a two-phase cooling cycle with micro-evaporator elements (multi-microchannel evaporators) for direct cooling of the chips and memories on blade server boards is simulated. The two-phase cooling cycle is driven by a liquid pump, has a micro-evaporator for cooling of the chip and its memories, and a microfin tube-in-tube condenser for heat recovery. The simulation code was used to perform a case study on two-phase cooling of a blade server's electronics, comparing the thermal performance of HFC134a to the new more environmentally friendly refrigerant HFO1234ze, both of which are dielectric fluids. An evaluation was also made with respect to the pumping power consumption to drive such a cooling cycle compared to a water-cooled cycle. The results so far demonstrate that the pumping power consumption of a water-cooled cycle is on the order of 10-30 times that of one with a two-phase refrigerant. The new HFO1234ze refrigerant is found to have similar cooling characteristics as HFC134a, but with a slight (20%) pumping power penalty (much less than a single-phase liquid system's pumping power penalty).

Keywords: microprocessor, micro-evaporator, single and two-phase, cooling cycle, simulation code.

1. Introduction

Currently, the most widely used cooling technology is refrigerated air cooling of the data centers' numerous servers. According to recent articles published at ASHRAE Winter Annual Meeting at Dallas (January, 2007) typically 40% or more of the refrigerated air flow by-passes the server racks in datacenters. This poor energetic performance in one of the leading industrial technological sectors is quite startling and motivates the search for a green thermal solution for future generations of higher performance servers. The objective is to consume much less energy to operate and cool while they also recovering the large quantity of waste heat rejected by the data center. This is the topic of research addressed here.

The cost of energy to operate a server for 4 years is now on the same order as the first cost to purchase the server itself, meaning that the choice of future servers should be evaluated on their total 4 year cost, not just their first cost. Based on the above issues, thermal designers of data centers and server manufacturers now seem to agree that there is an immediate need to improve the server cooling process by implementing liquid or two-phase cooling directly in the server on the chip level itself, eliminating the poorly performing air as a coolant all together. Therefore, there is a clear need for a detailed design and evaluation of these new cooling strategies in order to arrive at an improved solution. The new cooling technology should provide more efficient heat transfer from the chips, memories, etc. using water-cooled or boiling-cooled elements, eliminating air as a means of heat transfer, while also reducing electrical energy consumption for driving the cooling system by a significant amount. Current data centers apparently consume on the order of 40-45% for cooling purposes. Since data centers often dissipate on the order of 5 to 15MW of heat, this makes heat recovery an important energetic and environmental issue to consider. Heat recovery will greatly reduce the CO_2 footprint of the system.

Recent publications show the development of primarily four competing technologies for cooling chips: microchannel single phase (water) flow, porous media flow, jet impingement cooling and microchannel two phase flow [2]. The first three technologies are characterized negatively for the relatively high pumping power to keep the temperature gradient in the fluid from inlet to outlet within acceptable limits, i.e. to minimize the axial temperature gradient along the chip and its differential expansion with the TIM. Two-phase

flow in microchannels, i.e., evaporation of dielectric refrigerants, is a promising medium to long term solution, despite the higher complexity involved. This solution consumes a low pumping power (only 1/10 as much as water cooling [3]), has good temperature uniformity [4], very high heat transfer coefficients when using high aspect ratio microchannels (as high as 270'000W/(m^2K) [5]), and provides high heat flux dissipation. Possible problems with flow instabilities have been resolved using micro-orifices at the channel inlets [2] while the prediction methods of local heat transfer coefficients [6], the critical heat flux [7], and pressure loss [8] in the two phase region are still improving.

In this context, the objective of the present study is to propose and analyze potential two-phase cooling cycles able to maintain the temperature of the chip below its upper operating limit (about 85°C) and to recover energy from the cycle's condenser for reuse, such as for heating a building, residence, hospital, district heating, etc. To do this an integrated simulation code was developed which is able to design the components and determine the performance of liquid pump cooling cycles under steady state conditions and for different working fluids. The code is also able to evaluate the performance of the cooling cycles for single-phase and two-phase flow in the micro-evaporators.

The new refrigerant HFO1234ze of Honeywell Inc. is considered here as a potential substitute of HFC134a. This fluid has a "Global Warning Potential" of only 6 against 1410 of the HFC134a, i.e. it is considered as a immediate/future replacement for HFC134a. Both HFC134a and HFO1234ze are dielectric fluids and thus compatible with electronics. HFC134a is currently the most widely used refrigerant for refrigeration and air-conditioning systems.

2. Literature review

The focus of previous studies [3,7,9-13] has been the development of multi-microchannels evaporators able to remove "in loco" the heat load generated by the microprocessors and also the development of two-phase cooling systems able to: i) control the operating conditions in the micro-evaporator, ii) maintain the microprocessor temperature at acceptable levels, iii) recover the heat for a secondary process and iv) operate at a much lower pump energy consumption compared with a single-phase liquid water cooling system. Apparently, no detailed study in the literature has so far considered an integrated simulation code able to the design and evaluate the performance of all components of the two-phase cooling cycle, what is considered fundamental for a preliminary investigation of new novel cooling cycles. Such a code was developed and used in the present study.

3. Single-phase and two-phase micro-evaporator cooling cycles

The micro-evaporator cooling cycle to be simulated here has a liquid pump as the driver of the working fluid. Figure 1 depict the cycle where the goal is to control the chip temperature to a pre-established level by controlling the inlet conditions of the micro-evaporator (pressure, subcooling and mass flow rate). It is imperative to keep the micro-evaporator (ME) outlet vapor quality below that of the critical vapor quality, that latter which is associated with the critical heat flux. The critical heat flux and outlet vapor quality are predicted using methods developed by [14], which are a function of micro-evaporator inlet conditions and microchannel dimensions.

The components considered and their main functions are:

a) *Variable speed liquid pump*: controls the mass flow rate circulating in the system.

b) *Stepper motor valve*: controls the liquid flow rate to control the outlet vapor quality in each micro-evaporator (0% to 100%).

c) *Pre-heater (PH)*: transfers the heat generated by the electronic components before the ME and guarantee a low subcooling at the ME inlet.

d) *Micro-evaporator (ME)*: transfers the heat generated by the microprocessor to the refrigerant.

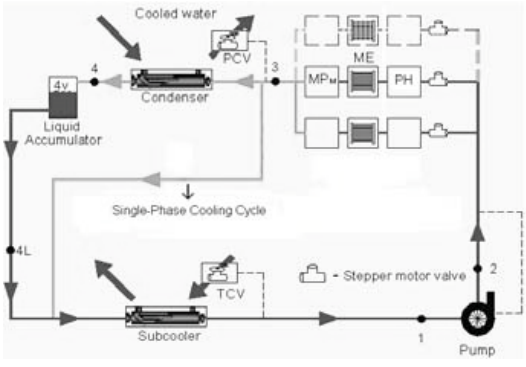

Fig. 1. Two-phase cooling cycle with liquid pump.

e) *Microchannel cold plate for memories (MPM)*: additional component used to cool the memories and improve the COP of the cycle (use the latent heat available).

f) *Pressure control valve (PCV)*: controls the condensing pressure, only for two-phase cooling cycle.

g) *Condenser*: counter-flow tube-in-tube heat exchanger, only for two-phase cooling cycle.

h) *Liquid accumulator*: guarantees that there is only saturated liquid at the subcooler inlet, independent of changes in thermal load, only for two-phase cooling cycle.

i) *Subcooler*: counter-flow tube-in-tube heat exchanger.

j) *Temperature control valve (TCV)*: controls the subcooling at the inlet of liquid pump.

It is worth mentioning that the applicability of the cooling cycle is not restrict to only one microprocessor but can be applied to blade servers and clusters, which may have up to 64 blades or more per rack cabinet. Each blade can have two (or more) microprocessors with a heat generation higher than 150W. If the auxiliary electronics (memories, etc.) on the blade are considered, the total heat generation per blade can be 300W or higher. Thus, the pre-heater and the microchannel cold plate described in the cooling cycle have the function to cool the auxiliary electronics that can represent about 60% of the total heat load on the blade, but have a larger surface area compared to the CPU and thus a lower heat flux.

Finally, when considering an entire rack, a very sizable heat load is generated, which represents a good opportunity to recover the heat rejected, generate an "income" from the energy saved, and greatly reduce the CO_2 "footprint" of the system. For example, if we consider a data center with 50 vertical rack cabinets, where each rack cabinet has 64 blades and each blade dissipates 300W, the total potential amount of heat to be recovered will be 0.96MW. Such a heat recovery system requires a secondary heat transfer fluid to pass through all the condensers (either water or a refrigerant) and then transport the heat to its destination.

4. Integrated Simulation Code

A *green two-phase cooling cycle simulation code* was developed to design and evaluate the performance of the liquid pump cooling cycle under steady state conditions. The simulation code is able to design the condenser, to evaluate the performance of the ME and various component coolers for a given heat load, and to calculate the pumping power consumption to drive the cooling cycle. The pressure drop of each component and piping are also calculated. Table 1 shows the principal methods implemented in the code.

Table 1. Methods in the code.

Component	Type	Method
ME	Multi Microchannel	Critical heat flux, outlet vapor quality and pressure drop [14]
Condenser (tube-in-tube)	inner tube: Herringbone μ-fin (two-phase flow)	Heat transfer coefficient [15]
		Pressure drop [15]
	annulus: Smooth (single-phase flow)	Hydraulic diameter [16]
		Heat transfer coefficient [17]
		Pressure drop [18]
Subcooler (tube-in-tube)	inner tube: Ribbed (single-phase flow)	Heat transfer coefficient [19]
		Pressure drop [19]
	annulus: Smooth (single-phase flow)	Hydraulic diameter [16]
		Heat transfer coefficient [17]
		Pressure drop [18]
Straight horizontal pipes	adiabatic (single-phase flow)	Pressure drop [18]
	adiabatic (two-phase flow)	Pressure drop [20]

Figure 2 presents a flowchart with the main steps followed by the simulation code. Basically the input data are: (i) the geometrical parameters of ME's and heat exchangers, (ii) the heat load on the ME's and spreaders (PH and MPM), (iii) the evaporation temperature and subcooling at the ME inlet, the water temperature at the condenser inlet and outlet (secondary fluid flowing in the annulus), and (iv) the length of the pipes joining the components. Presently only straight horizontal pipes were considered, i.e. the effects of bends and static height difference between components and pipes were so far ignored. The component MPM was also not considered for the present study.

The analysis of results were developed taking into account the thermal performance, the pumping power consumption and the total pressure drop of the cooling cycle. A comparison of 5 simulated cases considering different working fluids and internal diameter of the pipes was accomplished. In summary the following comparisons were made: i) single-phase water (SP_W) versus two-phase (TP) HFC134a for an internal diameter of the pipes of 3mm, ii) TP_HFO1234ze versus TP_HFC134a for an internal diameter of the pipes

of 2.4mm, and iii) SP_W versus TP_HFC134a for an internal diameter of the pipes of 6.5mm and 2.4mm, respectively.

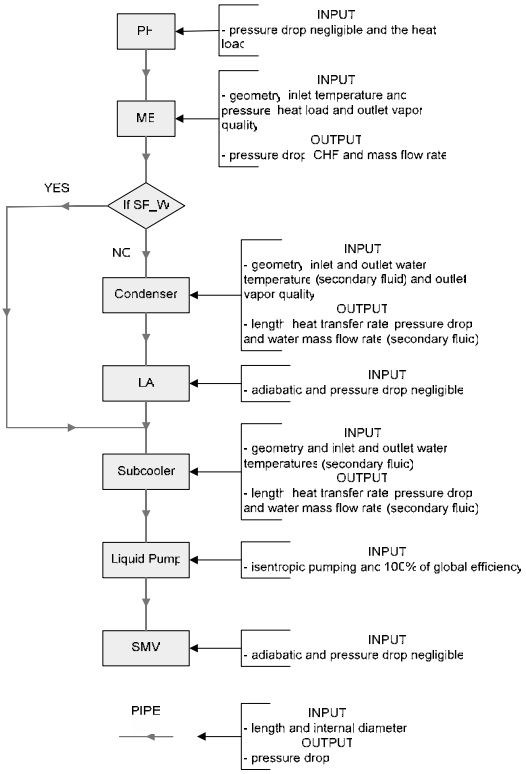

Fig. 2. Steps of the simulation code.

Table 2 shows the input data considered for each working fluid evaluated. The other thermodynamic parameters required to determine the total energy balance of the cycle come from the linkage to the methods shown earlier in Table 1.

Equation (1) shows the total energy balance of the cooling cycle. The last term of the right side of (1) represents losses associated with pipes and components from the outlet of the condenser to the inlet of the subcooler. At this moment these losses were neglected.

$$\underbrace{Q_{ME} + Q_{PH}}_{\text{Heat load}} + W_{LP} = Q_{cond} + Q_{sub} + \text{losses} \qquad (1)$$

It is worth pointing out that the condenser is a double-pipe, tube-in-tube heat exchanger with herringbone microfins on the internal surface of inner tube and a smooth external surface. For the tube-in-tube subcooler, the internal surface of the inner tube is "ribbed" and smooth on the external surface. For both heat exchangers the internal diameter of the outer tube was considered 1.5 times of the fin root diameter of the inner tube and the design of them was based to find its length, while the other geometrical parameters were considered to be fixed. In the annulus, water was considered as the secondary fluid.

Table 2 Input data.

Component	Working fluid	Input data
PH	All of them	Q_{PH} = 18W per PH
ME	HFC134a HFO1234ze	T_{i_evap} = 60°C
		ΔT_i = 5°C
		x_o = 30%
		Q_{ME} = 162.5W per ME
	Water	T_i = 60°C
		T_o = 60.74°C
		Q_{ME} = 162.5W per ME
Condenser (tube-in-tube)	HFC134a HFO1234ze	x_o = 1%
	Secondary fluid: water	T_{i_w} = 15°C
		$T_{o\_w} = T_{i\_cond}$ - 10K
Subcooler (tube-in-tube)	HFC134a HFO1234ze	x_i = 0%
	Secondary fluid: water	T_{i_w} = 15°C
		$T_{o\_w} = T_{i\_sub}$ - 10K

Tables 3 and 4 show the geometrical parameters considered for the condenser, subcooler, pipes and ME. For the ME the same geometrical parameters were considered in all cases evaluated, the only exception was in the cases of SP_W cooling cycles where the orifice distribution plate, normally used at the inlet of ME's to avoid problems of mal-distribution in the channels in two-phase flow [2], was not considered. It is important to mention that to have a comparable basis, all cases were simulated for a value of 0.74K as the maximum axial rise in the chip's temperature from inlet to outlet of the ME. The actual temperature rise could be more (especially for a water cooled unit where this represents also the rise in the water temperature from inlet to outlet), depending on the computer manufacturer's design specifications. *Increasing this temperature difference will decrease the water flow rate for its simulation, and hence also reduce its pressure drop and pumping power accordingly, but will increase the local temperature of the microprocessor at the exit.* On the other hand, unless the water is charged into the server's cooling system on site, then glycol must be added to the water circuit before shipment to

prevent freezing, which will increase the pressure drop by about 50%.

Table 3 Geometrical parameters / condenser and subcooler.

	Condenser	Subcooler
Inner tube	Herringbone μ-fin	Ribbed
Fin tip diameter [mm]	6.01	9.224
Fin height [m]	0.22	0.203
Thickness of the tube [mm]	0.25	0.356
Helix angle [°]	16	18
Apex angle [°]	18	---
Number of fins [-]	60	60
Equivalent diameter [mm]	6.39	---
Outer tube	Smooth	Smooth
Internal diameter [mm]	9.68	13.227

Table 4 Geometrical parameters / pipes and ME.

Micro-evaporator	
Fin Height [μm]	1700
Fin width [μm]	170
Channel width [μm]	170
Base thickness [mm]	1
Length [mm]	13.5
Width [mm]	18.5
Area [cm^2]	2.5
Material	Copper
Split flow	1 inlet and 2 outlets
Pipes (joining the components)	
Length [m]	0.3
Internal diameter [mm]	2.4, 3.0 and 6.5
Type	Straight horizontal
Flow	Adiabatic

Table 5 shows the results of thermal performance for the ME designed considering the different working fluids. A much higher mass flow rate of water is required for the SP_W cooling cycle than for the TP cooling cycles, which is justified by the low maximum junction temperature rise defined as an input parameter (and because the latent heat of the refrigerants is many times larger than the liquid specific heat of the water). The pressure drop is low for all the fluids, in part as a consequence of the split flow design.

Table 5 ME performance.

Cooling Cycle	TP		SP_W
Working Fluid	**HFC134a**	**HFO1234ze**	**Water**
T_{i_evap} [°C]	60	60	-----
T_{o_evap} [°C]	59.9	59.9	-----
m_{wf} per ME [kg/h]	**11.8**	**12.1**	**189.0**
x_o [%]	30	30	-----
T_i [°C]	55	55	60
T_o [°C]	-----	-----	60.74
Δp_{wf} [bar]	0.01	0.01	0.05
q [W/cm^2]	65	65	65
CHF [W/cm^2]	208.5	231.2	-----

For the outlet vapor quality considered, the predicted CHF was higher than 3 times the actual maximum heat flux of the 65W/cm^2. This safety factor is more than sufficient since the accuracy in predicting CHF is about ±20%.

Tables 6 and 7 show the simulation results for the five cases mentioned beforehand. The pressure drop in each component and pipe, pumping power consumption, total pressure drop, heat transfer rate in the heat exchangers and their calculated length, water mass flow rate and pressure drop (secondary fluid in the heat exchangers) are shown. It is important to remember that the SP_W cooling cycle does not consider the condenser and liquid accumulator that are not required in that cycle.

Table 6 Pressure drop and pumping power.

CASES	**1**	**2**	**3**	**4**	**5**
Working Fluid	**HFC134a**		**HFO1234ze**	**Water**	
Di_p [mm]	**3.0**	**2.4**	**2.4**	**3.0**	**6.5**
W_{LP} [W]	**0.48**	**1.22**	**1.52**	**597.80**	**20.13**
	ΔP_{wf}, bar (%)				
Pre-heater	0 (0)	0 (0)	0 (0)	0 (0)	0 (0)
Pipe (PH → ME)	0.003 (0.8)	0.009 (0.9)	0.010 (0.8)	0.60 (2.1)	0.015 (1.6)
ME	0.040 (9.8)	0.040 (3.9)	0.031 (2.5)	0.05 (0.2)	0.05 (5.3)
Pipe (ME → Condenser or Subcooler)	**0.150 (36.8)**	**0.432 (42.1)**	**0.566 (46.8)**	6.77 (24.2)	0.172 (18.2)
Condenser	0.037 (9.1)	0.037 (3.6)	0.046 (3.8)	-----	-----
Pipe (Condenser → LA)	0.036 (8.8)	0.103 (3.6)	0.113 (9.3)	-----	-----
LA	0 (0)	0 (0)	0 (0)	-----	-----
Pipe (LA → Subcooler)	0.035 (8.7)	0.102 (9.9)	0.111 (9.2)	-----	-----
Subcooler	0.001 (0.2)	0.001 (0.1)	0.001 (0.1)	0.22 (0.8)	0.189 (20.0)
Pipe (Subcooler → LP)	0.035 (8.6)	0.101 (9.8)	0.111 (9.1)	6.80 (24.3)	0.172 (18.3)
Liquid Pump	**0.406 (100)**	**1.025 (100)**	**1.209 (100)**	**28.01 (100)**	**0.944 (100)**
Pipe (LP → SMV)	0.035 (8.6)	0.101 (9.8)	0.111 (9.1)	6.79 (24.2)	0.172 (18.3)
SMV	0 (0)	0 (0)	0 (0)	0 (0)	0 (0)
Pipe (SMV → PH)	0.035 (8.6)	0.101 (9.8)	0.111 (9.1)	6.79 (24.2)	0.172 (18.3)
	ΔP_{wf}, %				
PIPES	**80.9**	**85.9**	**93.4**	**99**	**74.7**
COMPONENTS	**19.1**	**14.1**	**6.6**	**1**	**25.3**

Comparing the cases 1 and 4, those with the same internal diameter of the pipes (3mm), is worth noting the large difference regarding the total pressure drop and pumping power consumption. Case 4 with the SP_W cooling cycle presented the highest values, respectively, 28.01bar and

597.80W, which were a consequence of the highest mass flow rate of water (see Table 5). It can also be observed that the pressure drop in the pipes represents more than 80% of the total pressure drop for both cases. The highest pressure drop on the TP_HFC134a cooling cycle, case 1, was observed in the pipe between the outlet of the ME and inlet of the condenser, where the flow is two-phase. Table 7 shows that the water mass flow rate (secondary fluid) in the condenser and subcooler is higher for the SP_W cooling cycle, which will result in a higher pumping power consumption.

Table 7 Heat exchangers simulations.

CASES	1	2	3	4	5
Condenser					
Length [m]	1.91	1.90	1.95	-----	-----
Q [W]	549.74	553.52	577.53	-----	-----
m_w [kg/h]	13.73	14.12	15.08	-----	-----
ΔP_w [bar]	0.87	0.92	1.05	-----	-----
Subcooler					
Length [m]	1.27	1.18	1.12	1.39	1.21
Q [W]	162.90	141.07	117.46	1319.45	742.14
m_w [kg/h]	4.10	3.67	3.15	31.79	17.89
ΔP_w [bar]	0.017	0.013	0.010	0.66	0.21

For the cases 2 and 3, the internal diameter of the pipes was considered to be 2.4mm. This internal diameter was chosen so that the total pressure drop in the TP_HFC134a cooling cycle (case 2) was about 1bar. The comparison of the results shows an increase in the pumping power consumption and total pressure drop of about 24.7% and 18% when using HFO1234ze in place of HFC134a, but its values are still much lower than that obtained for the SP_W (case 4) presented beforehand.

Finally, case 5 shows the simulation results of the SP_W cooling cycle for an internal diameter of the pipes so that the total pressure drop is about 1bar. A value of 6.5mm was found. The increase in the internal diameter from 3mm (case 4) to 6.5mm was followed by a reduction of the pumping power consumption from 29.7 times but still is 16.5 times higher than that for TP_HFC134a cooling cycle (case 2, Di_p = 2.4mm). If one allowed the water inlet to outlet temperature rise to be 3.0K as opposed to 0.74K (decreasing the water flow rate) and an internal diameter of 3mm is used for the water and for the refrigerants, the pumping power for the water cooled cycle is still 26.5 times that of the HFC134a cycle and 21.6 times that of the HFO1234ze cycle (for the refrigerants the maximum junction temperature rise was maintained, i.e. 0.74K).

5. Conclusions

A two-phase cooling cycle has been proposed and simulated to cool microprocessors and auxiliary electronics of blade server boards with two-phase evaporating flow in the micro-evaporator cooling elements. A simulation code was developed and 5 cases were simulated considering 3 different working fluids; HFC134a, HFO1234ze and water (in an analogous single-phase cooling cycle), and different internal diameter of the pipes joining the components. The results showed that for a design of the cooling cycle so that the total pressure drop is about 1bar, the liquid water cooling cycle has a pumping power consumption 16.5 times that obtained for the two-phase HFC134a cooling cycle. When comparing with the HFO1234ze cooling cycle, which showed a total pressure drop of 1.209bar, the difference drops to 13.2 times. It is important to mention that the simulations presented here can be considered as a benchmark and that the actual energetic comparison should be applied to an actual server's specifications.

Nomenclature

CHF critical heat flux, W/cm^2
Di internal diameter, mm
m mass flow rate, kg/h
q heat flux, W/cm^2
Q heat transfer rate, W
T temperature, °C
W power consumption, W
x vapor quality, %

Greek symbols

ΔP pressure drop, bar or %
ΔT subcooling, °C
μ micro

Subscripts and superscripts

cond condenser
i inlet of a component
i_evap inlet evaporation
LP liquid pump
ME micro-evaporator
o outlet of a component
o_evap outlet evaporation

o_w outlet water (secondary fluid)

p pipe

sub subcooler

w water as a secondary fluid

wf working fluid

References

[1] Koomey, J. G., 2007, Estimating Total Power Consumption by Servers in the U.S. and the World, *Analytics Press*, Oakland, CA, URL: http://enterprise.amd.com/us-en/AMD-Business/Technology-Home/Power-Management.aspx.

[2] Agostini, B., et al., 2007, State of the Art of High Heat Flux Cooling Technologies, Heat Transfer Engineering, Vol. 28, pp. 258-281.

[3] Hannemann, R., Marsala, J., and Pitasi, M., 2004, Pumped Liquid Multiphase Cooling, *IMECE*, CA, USA, paper 60669.

[4] Agostini, B., et al., 2008, High Heat Flux Two-Phase Cooling in Silicon Multi-microchannels, IEEE Trans. Compon. Packag. Technol., Vol. 31, N° 3.

[5] Madhour, Y., et al., 2010, Flow Boiling of R134a in a Multi-Microchannel Heat Sink Hotspot Heaters for Energy-Efficient Micro-electronic CPU Cooling Applications, IEEE Trans. Compon. Packag. Technol., In press.

[6] Consolini, L., and Thome, J. R., 2010, A Heat Transfer Model for Evaporation of Coalescing Bubbles in Micro-Channel Flow, Int. J. Heat Fluid Flow, Vol.31, pp.115-125.

[7] Mauro, A. W., et al., 2009, Saturated Critical Heat Flux in a Multi-Microchannel Heat Sink Fed by a Split Flow System, Experimental Thermal and Fluid Science.

[8] Cioncolini, A., Thome, J. R., and Lombardi, C., 2009, Unified Macro-to-Microscale Method to Predict Two-Phase Frictional Pressure Drops of Annular Flows, Int. J. of Multiphase Flow, Vol.35, pp. 1138-1148.

[9] Mongia, R., et al., 2006. Small Scale Refrigeration System for Electronics Cooling within a Notebook Computer, *ITHERM*.

[10] Trutassanawin, S., et al., 2006, Experimental Investigation of a Miniature-Scale Refrigeration System for Electronics Cooling, IEEE Trans. Compon. Packag. Tech., Vol. 29, N°3.

[11] Thome, J. R., et al., 2007, Recent Advances in Thermal Modeling of Micro-Evaporators for Cooling of Microprocessors, *IMECE*, Seattle.

[12] Thome, J. R., and Bruch, A., 2008, Refrigerated Cooling of Microprocessors with Micro-Evaporation Heat Sinks: New Development and Energy Conservation Prospects for Green Datacenters. IOR.

[13] Park, J.E., and Thome, J. R., 2009, Critical Heat Flux in Multi-Microchannel Copper Elements with Low Pressure Refrigerants, Int. J. Heat Mass Transfer.

[14] Revellin, R., and Thome, J. R., 2007, A Theoretical Model for the Prediction of the Critical Heat Flux in Heated Microchannels, Int. J. Heat and Mass Transfer.

[15] Olivier, J. A., et al., 2007, Heat Transfer, Pressure Drop, and Flow Pattern Recognition during Condensation inside Smooth, Helical Micro-Fin, and Herringbone Tubes, Int. J. of Refrigeration, 30, pp. 609-623.

[16] Kakaç, S., Shah, R. K., and Aung, W., 1987, *Handbook of Single-Phase Convective Heat Transfer*, John Wiley & Sons.

[17] Dittus, F. W., and Boelter, L. M. K., 1930, Publications on Engineering, 2, University of California, Berkeley, pp. 443.

[18] Blasius, H., 1913, Das Ähnlichkeitsgesetz bei, Reibungsvorgängencin Flus-sigkeiten, Fors-chg. Arb. Ing. -Wes., 131 Berlin.

[19] Ravigururajan T. S., and Bergles A. E. 1985, General correlations for pressure drop and heat transfer for single-phase turbulent flow in internally ribbed tubes, Augmentation of Heat transfer in Energy Systems 52, pp. 9-20.

[20] Muller-Steinhagen, H., and Heck, K., 1986, A Simple Pressure Drop Correlation for Two-Phase Flow in Pipes, Chem. Eng. Process., 20, pp. 297–308.

Acknowledgments: The Commission for Technology and Innovation (CTI) contract number 6862.2 DCS-NM entitled "Micro-Evaporation Cooling System for High Performance Micro-Processors: Development of Prototype Units and Performance Testing" directed by the LTCM laboratory sponsored this work along with the project's industrial partners: IBM Zürich Research Laboratory (Switzerland) and Embraco (Brazil). J.B. Marcinichen wishes to thank CAPES ("Coordenação de Aperfeiçoamento de Pessoal de

Nível Superior") for a one year fellowship to work at the LTCM laboratory. The authors also wish to thank Honeywell Inc. for providing the thermophysical properties of HFO1234ze for the calculations.

Study of a R134a Supercritical Evaporator in a modified condensing gas boiler

Johannes WEGELE [a], *Jonathan DEMIERRE* [a] *and Daniel FAVRAT* [a]

[a] *Industrial Energy Systems Laboratory, Ecole Polytechnique Fédérale de Lausanne, Switzerland*

Abstract: Improving the efficiency of natural gas heating by using thermally driven heat pumps will be of growing importance among the future measures to reduce greenhouse gas emissions. Apart from absorption heat pumps, ORC-ORC heat pump technology is a serious candidate for this application. In the concept described in this paper a radial inflow turbine directly drives the radial compressor of a reverse Rankine Cycle. This paper deals with the supercritical evaporator and covers in detail the adaption of a gas-fired condensing heater to meet this purpose.

Keywords: Supercritical evaporator, R134a, natural gas combustion, condensing heater, heat exchanger ORC, heat pump, radial compressor, radial turbine.

1. Introduction

As shown in [2] fossil fuel boilers have among the lowest exergy efficiency of all the heating modes. Their modification in a trithermal heat pump cycle could be one way to improve substantially their performance. One first attempt was made by Strong [7] on the basis of CFC refrigerants. Unfortunately the mutation to chlorine-free refrigerants, the materials and the accuracy of machining were not advanced enough for a success. Time has changed, new chlorine-free refrigerants are available and thus similar techniques can now be applied.

The main elements of the presented heat pump system are shown in Fig. 1 and derived from [1, 7]

- The heat pump cycle is common to many other compression heat pumps working with R134a. In this case, however, a radial compressor compresses the refrigerant flow of the reverse Rankine cycle. The temperature levels and the heat exchanger surface determine the pressure ratio.
- The Organic Rankine Cycle (ORC) is pressurized by the feed pump with a pressure difference of up to 60 *bar*. In the envisaged prototype the supercritical evaporator heats the refrigerant to 180 $°C$ for a high cycle efficiency. Note that higher stable temperatures have been quoted as possible for R134a and possibly for its successor R1234yf.

For this particular project, the gas burning domestic heat pump, the objective is to test a prototype using a modified domestic condensing gas burner of Cipag-Remeha with a maximum of 18 kW_{th} capacity. For the actual system design [1] the micro turbine needs a mass flow of about 150 g/s of fully evaporated R134a at 180 $°C$ and 70 *bar* for efficient operation. The required pressure and the massflow is provided by the feed pump which for the prototype will be a piston diaphragm type. The object of this paper is the design of a supercritical evaporator for residential duty, based on natural gas combustion.

The high pressure in the ORC is a major technical and financial constraint. In order to minimize development costs the adaption of an existing burner technology was desired. So as to find the best solution, several gas combustors and gas-fired heater have been examined and various configurations have been investigated. The final decision was taken for a standard condensing water heater running on natural gas.

Common domestic gas boilers are conceived for a working pressure of about 3 *bar* and are tested to maximum 10 *bar*. Thus the structure has to be modified to resist an absolute pressure of 70 *bar*. For this reason the coil-shaped flattened tubular heat exchanger has been completely replaced by a newly designed coil of steel tubes. In order to measure the impact of this new construction a model has been developed with respect to the flue gas and refrigerant properties.

Corresponding author: Johannes Wegele, Email: johannes.wegele@epfl.ch

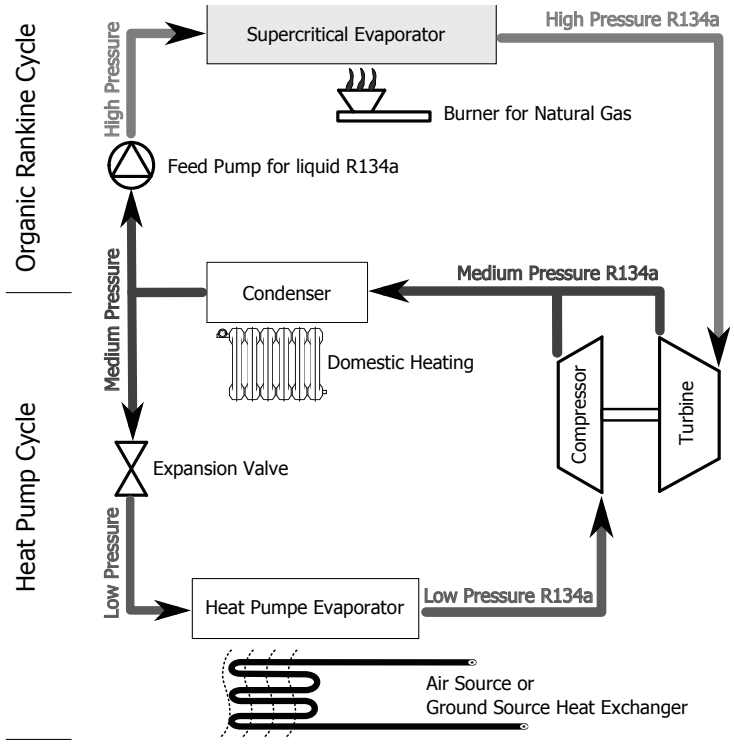

Figure 1: Flowsheet and parts of an ORC-ORC heat pump system fired by natural gas. (Above, the high pressure turbine cycle (ORC); Below, the heat pump cycle; The yellow underlaid box symbolizes the supercritical heat exchanger)

No formal optimization of the design has been applied so far. By progressively adjusting the input values the simulation results indicated further design modifications.

Physical tests should follow in the months to come.

2. The Supercritical Evaporator and its Role in the Present Setup

The envisaged thermal heat pump system reaches a theoretical coefficient of performance (COP) of 1.7 [1] when used for domestic heating with a ground source heat exchanger. Its driving energy comes from the natural gas combustion, which is therefore one of the major part of the integral system.

With the previously mentioned objective in mind the following development aims have been set:

1. Refrigerant heating from 30 $°C$ to 180 $°C$
2. Refrigerant pressure drop within 0.5 *bar*
3. Fuel efficiency > 93 $\%\Delta h_i^0$
4. Secure operation in domestic environment
5. Functional and low cost design

For laboratory cycle tests these tasks are presently accomplished by three parallel coiled heat exchangers with an inner and outer tube configuration. This setup allows a counter current flow of thermal oil used as the heat source.

3. Design Guidelines and Constraints

With the decision for a standard water heater several design presettings have to be considered. The most important constraint is the combustor shape, see Fig. 2. The combustor will be reused as is, whereas the heat exchanger has to be modified. The entity is designed to efficiently rise the temperature of the returning heating water from 25 $°C$ to 35 $°C$ or of the

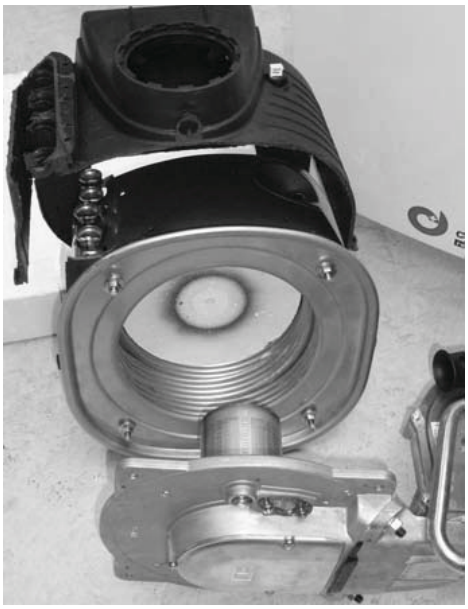

Figure 2: The disassembled heating unit with its combustor in the foreground. One can see the perforated sheet metal cylinder.

domestic hot water from 10 $°C$ to 50 $°C$. According to these low temperatures some parts, like the exhaust gas housing, could be made of plastics.

- The combustor is conceived for a premix surface bound combustion. It is made of a cylinder shaped perforated sheet metal and has a radially distributed exhaust, see Fig. 2. The combustion is flameless at about 700 $°C$ to 800 $°C$.

- The heat exchanger consists of about 15 windings of flattened tubes of 0.7 *mm* stainless steel. The 0.8 *mm* spacings between the windings allow the exhaust gas to pass through in a laminar flow.

- The device components, like the premix fan, the gas valve, the spark igniter, the feed pump and several sensors are controlled by a circuit board. First priority thereby is the secure operation - ignition check and prevention from overheating.

For this new development the combustion part can directly be transfered and the control can be adapted easily. Hence, the main attention of the following is attributed to the heat exchanger.

4. Four Different Heat Transfer Modes

In order to describe the model of the new heat exchanger, its interaction with the heat source and heat sink can be classified as follows:

4.1. Radiative Heat Emission from the Combustor

The radiative heat depends mainly on the combustion process. The premix gas goes through a perforated sheet metal cylinder and is burned at nearly atmospheric pressure on the surface of this grid. This type of flameless combustion has a temperature range from 700 - 800$°C$. At low power regimes a blue shine coming from the grid can be observed which changes into a reddish glow of the heated grid at high power regime. For the calculation only the one dimensional radiation from combustor to tube coil is taken into account (surface to surface radiation)[4]. Considering that all heat will sooner or later be absorbed by the heat exchanger this approximation is valid. The more radiative heat will be absorbed by the heat exchanger the lower the exhaust gas temperature.

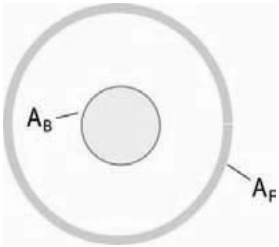

Figure 3: The Radiative Heat Exchange between two Concentric Cylinders [5]

The Radiative heat transfer between the burner surface, A_B, and the heat exchanger surface, A_F, see figure 3, is best approximated with the following formula [3]:

$$C_{BF} = \frac{\sigma_{rad}}{\frac{1}{\epsilon_b} + \frac{A_B}{A_F}\left(\frac{1}{\epsilon_F} - 1\right)} \tag{1}$$

$$\dot{Q}_{absorb} = C_{BF}\, A_B\, (T_B^4 - T_{ext}^4) \tag{2}$$

Where T_{ext} is the external heat exchanger temperature and T_B the emissive surface temperature, here the burner surface.

4.2. Flue Gas Convection around the Tubes

The convective heat transfer from the combustion gas to the tube wall of the heat exchanger represents the highest heat resistance. It is therefore the bottle neck of the overall efficiency. It was calculated with common formulas for crossflow of hot gas over single tubes [3]. In order to minimize the tube length, L, for low material costs and less weldseams let us take a closer look to the related equations.

$$\dot{Q} = \alpha \cdot A \cdot (T_{fluegas} - T_{tube}) \tag{3}$$

with

$$A = L \cdot D \cdot \pi$$

$$\alpha = \frac{\lambda \cdot Nu}{L_{charact}}$$

$$L_{charact} = D \cdot \pi$$

hence,

$$L = \frac{\dot{Q} \cdot \pi \cdot D}{D \cdot 2 \cdot \pi \cdot \Delta T \cdot \lambda \cdot Nu} \tag{4}$$

that simplifies to:

$$L = \frac{\dot{Q}}{2 \cdot \Delta T \cdot \lambda \cdot Nu} \tag{5}$$

Equation 5 shows that in a single tube heat exchanger the length L is not dependent on the diameter D. Yet, small tubes have a favourable impact, as they occupy less space, have an increased resistance to pressure and make a more compact heat exchanger possible.

4.3. Conduction through the Tube Wall

The conduction from the outer tube wall surface to its inner surface has the lowest heat resistance of the four modes of heat transfer. It was calculated based on the thermal conductivity, the wall thickness and a form factor for round tubes [5]. The conduction along the tube is insignificantly small and thus is neglected.

Having high temperatures and high pressures as constraints, only few possible alterations of the tube geometry are feasible. However the tube diameter can be changed.

The thermal conduction in the tube wall with its length, L_i, is considered as follows:

$$\dot{Q}_{COND} = L_i \; s \; \lambda \; (T_{ext} - T_{int}) \tag{6}$$

where T_{ext} and T_{int} are the external and internal temperatures, L_i is the length of the tube during one model iteration and s is the form factor due to the tubular shape:

$$s = 2\pi / \ln \frac{D}{d} \tag{7}$$

4.4. Refrigerant Convection in the Tube

The convective heat transfer towards the refrigerant happens mainly depending on the tube diameter, on parallel or serial arrangements and on the massflow.

It was calculated with the formulas of forced convection hot gas in round tubes according to the VDI-Wärmeatlas [3]. The single phase character is due to the supercritical regime of R134a. The refrigerants volume is drastically expanding with temperature. As a result it will develop a more turbulent flow the higher its temperature and its velocity is.

$$\dot{Q} = \alpha \cdot A \cdot (T_{tube} - T_{R134a})$$

with α for turbulent flow:

$$\alpha = Nu \cdot \frac{\lambda}{d}$$

and finally Gnielinski equation

$$Nu = \frac{(f/8) \cdot (Re - 1000) \cdot \; Pr}{1 + [12.7 \cdot (\sqrt{f/8}) \cdot (Pr^{2/3} - 1)]} \tag{8}$$

f is the friction factor and is calculated in this case by the Colebrook relation.

For low Reynolds numbers with laminar flow the following simplification was used:

$$\alpha = 3.657 \cdot \frac{\lambda}{d} \tag{9}$$

5. Calculating Method

The stepwise computation of the temperature and pressure starts at a point where the fluid properties are known: at the refrigerant outlet. At this point the desired temperature of R134a, the counter-current flue gas temperature, the desired pressure and the estimated radiative heat are fixed. Then the temperature is calculated along the heat exchanger tube.

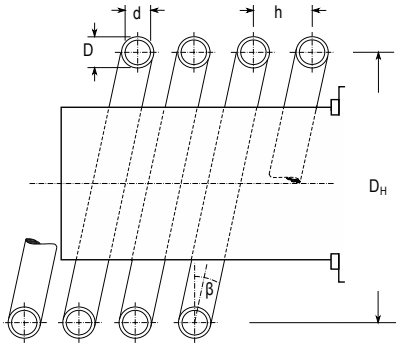

Figure 4: Section of the combustor in the centre and the first coil layer of the surrounding heat exchanger. Different parameter settings for the number of windings and the outer diameter D have been applied for the simulations.

The first coil faces the combustor and thus absorbs the radiative heat. For the second to sixth coil layers radiation is neglected. The fluegas temperature is averaged for each coil and the physical properties are taken from combustion gas tables [6].

6. Finding the Optimal Tube Configurations

Considering the evaluation ahead, different tube configurations have been determined. The tube diameter and the number coil layers have been fixed. Whether to have just one single tube or up to a maximum of three tubes in parallel has also been decided for each application point.

The outer tube diameter, corresponding to D in Fig. 4, was varied between 8 and 20 *mm*. Its wall thickness was adapted according to the material's mechanical resistance and constraints in purchasing. If not a single tube, up to three parallel tubes where placed in a way that covers the complete combustion chamber. The parameter D_H and h had been fixed according to the space available in the original device.

The best heat transfer was predicted for a single 8 *mm* tube and 15 windings per coil. This heat exchanger is conceived with six coils. It has a predicted energy efficiency of 95 % of the lower heating value, Δh_i^0. The flue gas output is slightly over the dew-point. So the latent heat of condensation is not recovered. However, the minimal efficiency of 93 %, which is set by the federal legislation and corresponds to European law, is respected.

A flow distribution in three parallel 8 *mm* tubes is close to the latter results. Slightly worse results were calculated for a single and two parallel 12 *mm* tubes at about 94 % fuel efficiency.

7. Conclusion

The adaption of a conventional condensing gas boiler is feasible way towards the integrated ORC heat pump system. The cylindric combustor enables a large heat exchange surface and a compact design of the supercritical evaporator. This new concept implies important redevelopments such as the heat exchanger and the exhaust gas housing.

Compared to the burner's original purpose the new design demands higher temperatures. As a result the combustion exhaust has a higher temperature and thus a lower efficiency. Still, the preliminary modeling and simulations resulted in a promising outcome of a 95 % efficiency based on the lower heating value. Physical testing has yet to confirm the results.

The overall efficiency of the ORC-ORC system is largely depending on the fuel efficiency of the boiler and thus further optimization has to follow. Further more, in order to exploit the latent heat of the exhaust gas, an additional heat exchanger could be introduced later.

References

[1] Demierre, J., Henchoz S. and Favrat D. Prototype of a thermally driven heat pump based on integrated organic Rankine cycle ORC. *ECOS2010, Lausanne*, 2010.

[2] D. Favrat and F. Marechal. *The challenge of introducing an exergy indicator in a local law on energy*. Energy, The International Journal, Elsevier, 2008.

[3] Dr.-Ing. V. Gnielinski. *VDI-Wärmeatlas*. Springer Verlag, Karlsruhe, 1984.

[4] F. P. Incropera. *Fundamentals of Heat and Mass Transfer, sixth edition*. John Wiley & Sons, New York City, 2006.

[5] J. H. Lienhard. *A Heat Transfer Textbook*. Phlogiston Press, Cambridge, Massachusetts, 2008.

[6] J. Oman et al. *Air, Fuels and Flue Gases: Physical properties and combustion constants*. Edizioni Libreria Progetto, Padova, Italy, 2006.

[7] D. T. G. Strong. *Development of a Directly Fired Domestic Heat Pump*. Ph.D. Dissertation, Oxford University, 1980.

Nomenclature

A Heat transfer surface, m^2

α Heat transfer coefficient, W/(m^2 K)

D Tube diameter, m

D_H Coil diameter, m

ϵ Emissivity of Radiation, a material property

f Friction Factor, dimensionless

h Helix displacement, m

Δh_i^0 Lower Heating Value

L Tube length, m

λ Conductivity, W/(m K)

$\dot{m}$ Mass flow rate, kg/s

Nu Nusselt Number, dimensionless

Pr Prandtl Number, dimensionless

$\dot{Q}$ Heat Transfer, Power, kW

Re Reynolds Number, dimensionless

σ_{rad} Stefan-Boltzmann Constant

T Temperature, °C or K

Acknowledgments: We want to thank Cipag and Mr. Steiner for their assistance.

Integrated Modeling Framework for Energy Systems Planning

Carlos Silva [a b], *André Pina* [b], *Gonçalo Pereira* [a] *and Alexandra Moutinho* [a]

[a] *IDMEC/Instituto Superior Técnico, TULisbon*
[b] *MIT-Portugal Program, Sustainable Energy Systems, Instituto Superior Técnico, TULisbon*
Av. Rovisco Pais, 1049-001 Lisboa, Portugal

Abstract: This paper proposes an integrated modeling framework for energy systems planning, where a TIMES model is used in combination with a half-an-hour resolution model for the system operation developed in MATLAB. The technical and economical feasibility of the long-term scenarios considering the installation of renewable resources plants are tested and validated at the operational level on the detailed operational model that considers half-an-hour dynamics. These results are then feed back into the TIMES model as parameters for resource availability and plant efficiency in order to calibrate scenario design. The proposed methodology is tested in the design of the electric system of the island of S. Miguel in Azores - Portugal, in particular to determine the wind-farms capacity installation. The results show that only when the short-term model is used to evaluate the energy balance between supply and demand, it is possible to determine the real cost-effectiveness of the capacity investment in the medium-term model and obtain feasible solutions.

Keywords: TIMES, Energy Planning, Energy Modeling

1. Introduction

TIMES [5] is a planning tool used to compile long term scenarios for in-depth national, multi-country and global energy and environmental analysis. Assuming partial equilibrium, TIMES is able to determine the optimal supply solution for the energy system in future time periods by maximizing the total energy surplus. The model requires: detailed and explicit information about available energy technologies (e.g. production capacity, efficiency and operation costs); the description of end-use consumption for different sectors and types of energy; and estimates of future energy demand needs and supply investments. Usually, this is done considering yearly resolution datasets. However, energy systems are changing towards the integration of large penetration of renewable resources, the implementation of aggressive end-use energy efficiency measures and the modernization of the networks [11]. Thus, an effective planning of such type of system requires high resolution models, e.g. hourly, in order to take into account the intermittent availability of renewable resources or the implementation of demand side management strategies.

A recent overview on existing energy planning tools [2] shows that there are many different energy planning tools covering different planning issues, from operation and simulation using hourly time steps like EnergyPLAN [15], to scenario analysis using year steps like TIMES [9], but none is able to integrate all the necessary dimensions for the design of the emerging energy systems. Apparently, there is a gap between long term modeling tools like TIMES and short term modeling tools like EnergyPLAN that is necessary to fill.

Several different approaches have been used to bridge this modeling gap. For example, in [10], EnergyPLAN is used to simulate specific future energy scenarios for the Denmark energy system in the years 2030 and 2050 using information regarding oil or CO_2 future prices. In [13], TIMES was used to simulate the hourly dynamics for 12 days of the year (weekdays, Saturdays and Sundays for the different four seasons in a total of 288 periods for each year) in order to evaluate the economic feasibility of a storage system in a scenario of large renewable penetration. In [7], TIMES has been used to simulate 5 periods per week for all 52 weeks of one year (in a total of 260 periods per year). These results were used in the energy market model for Norway in order to simulate the market prices, which were then fed back to TIMES to evaluate the energy demand considering these new prices. Nevertheless, none of these approaches is

Corresponding author: André Pina, Email: andre.pina@gmail.com

able to fully simulate the detailed operation of an energy systems for multiple years.

This paper proposes an integrated modeling framework for energy systems planning, where a TIMES model is used in combination with a half-an-hour resolution model for the system operation developed in MATLAB [12]. The technical and economical feasibility of the long-term scenarios considering the installation of renewable resources plants are tested and validated at the operational level on the detailed operational model that considers half-an-hour dynamics. These results are then feed back into the TIMES model as parameters for resource availability and plant efficiency in order to calibrate scenario design. The proposed methodology is tested in the design of the electric system of the island of S. Miguel in Azores - Portugal, in particular to determine the wind-farms capacity installation.

The paper proceeds as follows. In Section 2. we describe the energy planning problem of the island of S. Miguel. The mathematical framework of the planning problem is described in detail in Section 3., both for long-term economical conditions and short-term operational conditions. Section 4. describes the proposed methodology and in Section 5. the implementation results for the case study are presented and discussed. Section 6. concludes the paper and presents some guidelines for future research.

2. S. Miguel, Azores case study

Azores is a Portuguese archipelago in the Atlantic Ocean, located 1500km west from Portugal and 3900km east from the USA, with 240 thousand inhabitants living mainly from tourism, cattle raising, fishing and agriculture. Due to its remote location, the fossil fuels import costs have always been a burden for the local economy that has become heavier with the latest oil price increasing trends.

The Azores government, following the European Community energy policy guidelines [8] and the mainland national energy plan objectives [3], is deeply committed to implement a sustainable energy system in the region to achieve electricity generation independence based on aggressive end-use efficiency, renewable resources penetration and the network modernization. This effort will start in the island of São Miguel (54% of total Azores population) under the framework of the Green Islands Project, from the MIT Portugal Program [14].

In 2007, S. Miguel has achieved a penetration of 47% of renewable resources in the electricity generation [4], which is already a remarkable feature in Europe [6] and worldwide [1]. Its volcanic nature and its isolation from the mainland made the electricity generation in Azores always closely related to natural renewable resources, in particular Geothermal (27MW in 2007) and Hydro (5MW in 2007).

The plan of investments on renewable power plants for the next 10 years in the island of S. Miguel includes [4]:

1. a 9MW Wind farm to be built in 2011 that can be extended in the following years;
2. expanding Geothermal production to 40MW by 2013 (3MW in 2010 and 10MW in 2013), with the possibility of building another 10MW power plant in the following years.

Table 1 shows the size, the efficiency of the thermal engines, the maximum capacity factor for the renewable plants and the estimated costs (investment, fixed and variable) [16] of existing, planned and possible future plants in the island.

As it can be seen from Fig. 1, the present minimum base load is less than 40MW. Considering only the planned investments that will lead to a 40MW production capacity only in Geothermal - plus a deployment of 9MW of Wind and successful implementation of end-use efficiency plan and other renewable sources electricity production projects, such as micro-generation or biomass - it may happen that by 2013 S. Miguel produces more electricity in the evenings than required, unless the excessive electricity produced during the evening is stored to be used later in the day, with a pumped water system or electric vehicles.

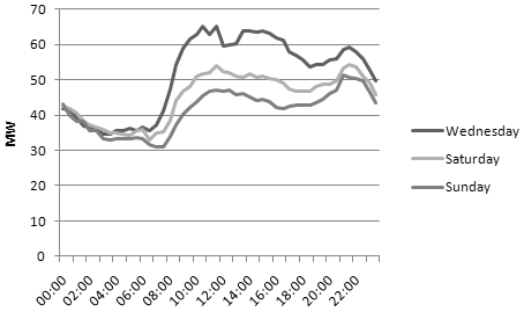

Figure 1: Electricity demand in S. Miguel in 2008

However, in S. Miguel, there are no large natural reservoirs except for lagoons and its use for pump-

Status	Type of plant	Capacity [MW]	Efficiency / Capacity factor	Investment costs [€/KW]	Fixed costs [€/KW]	Variable costs [€/MWh]
Existing	Fuel/Diesel	98	42%	-	9	1.15
	Geothermal	27	75%	-	50	0.36
	Hydro	5	50%	-	19	0.54
Planned	Geothermal	13	75%	2900	50	0.36
	Wind	9	26%	1600	19	0.72
Possible	Geothermal	10	75%	3000	50	0.36
	Wind	-	26%	1600	19	0.72

Table 1: Characteristics of existing, planned and possible future plants

ing would pose many environmental problems. Further, using electric vehicles as storage is still far from deployment. Therefore, the use of electricity storage is, in this case, unlikely to happen and the planning scenarios should consider this. In this context, the economic feasibility of Wind power plants installation becomes a critical issue for the system planning.

3. General mathematical formulation

The goal of the proposed methodology is to optimize the investment in new generation capacity and the operation of existing and new electricity plants, using an optimization model composed of medium- and short-term optimization sub-models. The medium-term sub-model optimizes the system until the year 2035, with the relevant time period for analysis being from 2011 till 2020. The optimization beyond 2020 is done in order for the model to be able to choose between investments close to 2020 and investments beyond that year. The short-term sub-model optimizes the daily operation of the system using half-an-hour time steps for the period of one year.

The general model is built upon the following assumptions:

- There are no startup or down-times for each power plant;
- Grid losses are a fixed percentage of the electricity demand;
- For each type of power plant, all electricity supply units are technologically equal.

Defining x_{O_i} as the electricity produced in MW by source i and x_{C_i} as the total (installed plus new) generation capacity in MW of source i, with $i = 1$ (Fuel), 2 (Wind), 3 (Geothermal), 4 (Hydro), a linear programming model is derived as follows:

Minimize

$$Z = \text{Var Costs} + \text{Fix Costs} + \text{Inv Costs} \quad (1)$$

with

$$\text{Var Costs} = \sum_i c_{O_i} x_{O_i} \quad (2)$$

$$\text{Fix Costs} = \sum_i c_{F_i} x_{C_i} \quad (3)$$

$$\text{Inv Costs} = \sum_i c_{I_i} x_{C_i} \quad (4)$$

subject to

$$\sum_i x_{O_i} \geq \text{Demand} + \text{Losses} \quad (5)$$

$$\frac{x_{O_1}}{\sum_i x_{O_i}} \geq 0.2 \quad (6)$$

$$x_{O_i} \leq \text{Potential} \quad (7)$$

$$x_{C_i} \leq \text{Maximum Capacity} \quad (8)$$

and

$$x_{O_i}, x_{C_i} \geq 0 \quad (9)$$

where c_{O_i} are the operating costs of source i, i.e. costs, such as Fuel costs, that depend only on the amount of electricity produced; c_{F_i} are fixed costs regarding the installed capacity of source i and include regular maintenance and salaries; and c_{I_i} are investment costs for the new generation capacity of source i and include equipment, construction and grid connection costs.

The model is subject to four functional constraints: (5) refers to the need for the electricity supply to be greater or equal to the demand plus the grid losses. Using historical data, an average value of 10% was estimated and assumed for all time periods; (6) requires that the electricity production by Fuel ($i = 1$)

represents at least 20% of the total electricity production, in order to allow immediate responses to demand fluctuations without affecting the grid quality; (7) indicates that the production from the resources is limited by the resource availability - for each type of renewable resource, a stochastic resource generator was considered based on the historical data, and for Fuel, the potential is limited only by the installed capacity; finally, (8) indicates the available installation capacity for each resource.

3.1. Medium-term model mathematical formulation

The medium-term model aims at optimizing the installation of new generation capacity by looking at an extended time horizon. The following assumptions are considered in the model:

- The model is deterministic and has perfect foresight;
- Electricity demand grows at the same rate for each time period for each sector.

The medium-term model optimizes over 25 years, with each year divided in 4 seasons, 3 days per season (weekday, Saturday and Sunday) and 24h per day, in a total of 7200 time steps, in order to include some seasonal, daily and hourly dynamics. Each hour for each type of day ($4 \times 3 = 12$ types of days) has a different demand, which is the average demand of those hours for that type of day. The potential (7) of each energy source in each time period is evaluated using:

$$\text{Potential}_i = \text{Capacity}_i \times \text{Availability factor}_i \quad (10)$$

where Capacity_i is the total installed capacity of source i and $\text{Availability factor}_i$ is the maximum fraction of the capacity that can be used in that time period.

While for Fuel, Geothermal and Hydro the availability factors are fixed between iterations, the availability factors of Wind are affected by the output of the short-term model. Since the model does not consider any storage system and the off-peak supply capacity without Wind is able to match the demand, it may happen that Wind turbines with the same efficiency have different capacity factors. These factors must be determined by the short-term model, which evaluates which fraction of the capacity factor considered is absorbed by the grid, for each group of Wind turbines (groups of 3×900kW turbines). These values can then be used by the medium-term model as a multiplier factor for the capacity factor considered for each time period.

3.2. Short-term model mathematical formulation

The short-term model optimizes the operation of the electric system minimizing the operation costs. This model considers the following assumptions:

- The installed capacities are provided by the medium-term simulation and are constant throughout the short-term simulation;
- The demand is provided by the medium-term model, but a stochastic term is introduced for each day;
- There is no continuity on the demand from the end of one day (23 hours and 30 minutes) to the beginning of the following day (0 hours).

The proposed scheduling model is based on half-an-hour steps (48 periods) over one year (365 days) in a total of 17520 time steps. The selection of this time length involves a trade-off between accurate operation and computational effort.

Since the short-term model only focuses on the operational point of view, the investments costs are optimized by the medium-term simulation. Therefore, all the restrictions associated with the generation capacity of source i, x_{C_i}, are not used. The short-term formulation simplifies the objective function of the general formulation using:

$$\text{Inv Costs} = 0 \quad (11)$$

As some of the operating costs are fixed, the objective function of the short-term model optimization only uses the Var Costs to maintain the proportionality property of the linear programming model. The final cost is calculated afterwards by adding the Fix Costs.

The Demand (5) in this model is based on the data provided by the medium-term model but it considers a stochastic term, based on historic data for several years in order to distinguish between the different days of the year.

The Potential in (7) is given by $N(\mu_i, \sigma_i)$ for $i = 3, 4$ representing a normal probability function that describes the maximum electricity production available for these sources at a given time period. The

values for the average power output μ_i and the resource variability σ_i are calculated for each source using historic production data from previous years. For Wind ($i = 2$), the potential is evaluated using a Weibull distribution. For Fuel ($i = 1$), the potential is limited by the installed capacity.

4. Integrated modeling framework

The method proposed in this paper consists of the use of both models in an iterative cycle, in which the medium-term model is used to optimize the investment in new generation capacity and the short-term model is used to calculate the energy balances over one year with higher time resolution (hourly or less) by optimizing the operational costs. The medium-term model provides to the short-term model the installed capacities of each energy source that it has to consider for the simulation of each year; the short-term model updates the medium-term model constraints parameters regarding the operation of the electricity generation facilities, such as the impossibility to start the operation on a certain year or the limitation on the amount of electricity that can be absorbed by the grid (effectively lowering the availability factor in that year).

Generally, the framework works as shown in Fig. 2. At the beginning of each iteration, a run of the medium-term model provides the inputs for the short-term model. Then, the short-term model runs for the first year being considered. After this run, the outputs are analyzed and three things may happen: (i) if the outputs show that some criteria are not met, then there are restrictions that need to be introduced in the medium-term model for that year; (ii) if the outputs show that the necessary criteria are met and the end year has not been reached, then the short-term model is run for the following year; (iii) if the outputs show that the necessary criteria are met and the year being considered is the end year of the optimization, then the process comes to an end.

4.1. Case study application

In this work, TIMES was used to build the medium-term model and MATLAB to build the short-term model. Following the described framework, TIMES provides as output the installed capacity for different energy sources in each year, which are then used to run the MATLAB model. If some criteria are not met, the medium-term model is updated with a new constraint regarding the operation of the new generation capacities. For the case study, the proposed

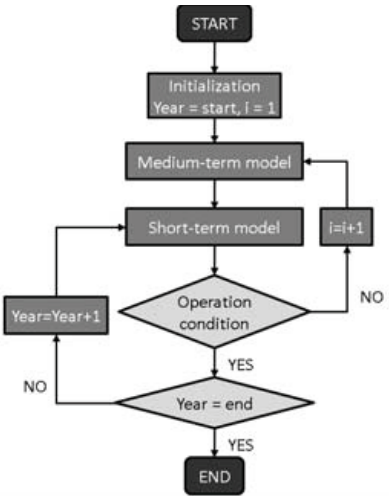

Figure 2: Proposed integrated modeling framework

methodology was used sequentially in two different situations: installation of a second 10MW Geothermal facility (in addition to the assumed installation of 3MW in 2010 and 10MW in 2013) and installation of Wind turbines.

First, the methodology was used to test the feasibility of introducing a second 10MW Geothermal facility, increasing the installed capacity from 40MW to 50MW. Here, the defined criterion was if the new plant would be used at a minimum level of 90% of the capacity factor, more than 95% of the time. If the criterion was not verified, the possible start year of this technology in the medium-term model was increased by one. With this approach, the model calculated what was the first possible year that allows the Geothermal to be built without having to be shut down during some period of time or producing a lot of excess electricity. This corresponds to the Geothermal iterative process.

Second, the methodology was used to analyze the electricity production from the Wind turbines that were installed by TIMES. Here, the defined criterion required that all Wind turbines produced more than 90% of the estimated electricity production potential. If the criterion was not verified, the availability factors of each group of turbines in TIMES were changed to be equal to the capacity factors calculated by MATLAB. This corresponds to the Wind iterative process.

It should be noted that it is possible to implement this sequential inquiry since Geothermal costs are considered to be lower than Wind energy costs. This

ensures that electricity produced from Geothermal is always favored over electricity produced from Wind turbines.

5. Results

Table 2 shows the total Wind power generation capacity installed for each year in each iteration, where the following nomenclature is adopted:

- TIMES initialization: first run done with TIMES, before either of the iterative cycles. It has no conditions;
- Iteration 1: last iteration from the Geothermal iterative process and first iteration of the Wind iterative process. It includes the condition that the second 10MW Geothermal unit can only be installed in 2019 or later;
- Iteration 2,...,10: successive iterations of the Wind iterative process.

The installed capacity of Wind power in the TIMES initialization is very low since the model considers that the second 10MW Geothermal unit comes into operation in the year 2013 together with the already planned 10MW plant, as shown in Fig. 3. Here, the very low cost of producing electricity from Geothermal energy would make it economically viable even if generation had to be stopped during the night periods.

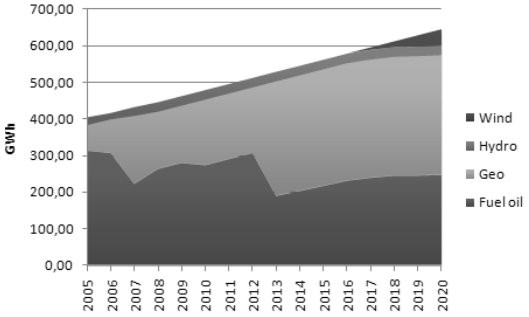

Figure 3: Electricity production by source from TIMES initialization

However, in iteration 1, after we implement the proposed methodology and consider the electricity demand growth rates, the second 10MW Geothermal plant is found to be technically feasible only in the year 2019, as shown in Fig. 4. To compensate this, the model then chooses to install a large amount of Wind power generation capacity early on, as shown in Table 2, iteration 1. It should be noted that in this iteration, the model does not have any information on the capacity factors of the Wind turbines and assumes that all have the same capacity factors.

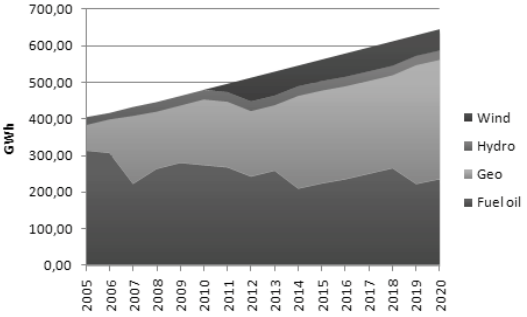

Figure 4: Results from iteration 1

In each iteration of the Wind iterative process, a new constraint is added regarding the capacity factors of the different groups of Wind turbines, and the model starts to decrease the investment on this technology. Every time the model finishes one iteration, new constraints are included in one of the remaining years of the TIMES model. The last iteration (iteration 10) shows that only 9.9MW of Wind power are economically feasible even without the second 10MW Geothermal power plant, with the evolution of the electricity system being shown in Fig. 5.

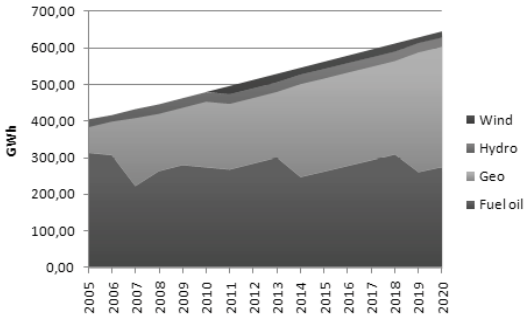

Figure 5: Results from iteration 10

The final solution contrasts heavily with the first run of all (TIMES initialization), where the early introduction of the Geothermal plant postpones the installation of Wind power. Further, even if a previous study had been done which determined that the second Geothermal unit would only come into operation in 2019, the medium-term model would still give a solution in which big investments should be made on Wind power. Only when the short-term model is used to evaluate the energy balance between supply and demand, it is possible to determine the real cost-effectiveness of those turbines and, in this way, produce a more feasible solution.

Iteration	2011	2012	2013	2014	2015	2016	2017	2018	2019	2020
TIMES initialization	0.0	0.0	0.0	0.0	0.0	0.0	3.5	8.3	16.3	23.3
1	9.7	28.7	28.7	28.7	28.7	30.5	30.5	30.5	30.5	30.5
2	9.7	12.2	26.3	26.3	27.3	29.9	29.9	29.9	29.9	29.9
3	9.7	12.2	15.4	16.9	27.3	29.9	29.9	29.9	29.9	29.9
4	9.7	9.9	9.9	9.9	27.3	29.9	29.9	29.9	29.9	29.9
5	9.7	9.9	9.9	9.9	9.9	29.9	29.9	29.9	29.9	29.9
6	9.7	9.9	9.9	9.9	9.9	9.9	28.7	28.7	28.7	28.7
7	9.7	9.9	9.9	9.9	9.9	9.9	13.5	27.0	27.0	27.0
8	9.7	9.9	9.9	9.9	9.9	9.9	13.5	14.8	14.8	22.3
9	9.7	9.9	9.9	9.9	9.9	9.9	9.9	9.9	9.9	22.3
10	9.7	9.9	9.9	9.9	9.9	9.9	9.9	9.9	9.9	9.9

Table 2: Installed capacity of Wind (MW) in each iteration

6. Conclusion

This paper proposes an integrated modeling framework for energy systems planning, where a TIMES model for medium-term planning is used in combination with a half-an-hour resolution model for the system short-term operation management developed in MATLAB. The methodology is tested in planning the electric system of the island of S. Miguel in Azores, in particular to determine the required capacity and year of installation of renewable resources power plants. The results show that only when the short-term model is used to evaluate the energy balance between supply and demand, it is possible to determine the real cost-effectiveness of the capacity investment in the medium-term model and obtain feasible solutions.

Future work is already being developed in order to include storage systems in both medium- and short-term models. Further, the methodology is being extended in order to allow the simultaneous evaluation of different types of investment.

References

[1] International Energy Agency. Renewables and waste in world in 2007. http://www.iea.org/stats/renewdata.asp?COUNTRY_CODE=29.

[2] D. Connolly, H. Lund, B. V. Mathiesen, and M. Leahy. A review of computer tools for analysing the integration of renewable energy into various energy systems. *Applied Energy*, 87:1059–1082, 2010.

[3] Minitério da Economia e Inovação. Plano nacional para a eficiência energética. Governo da República Portuguesa, 2007.

[4] Electricidade dos Açores. O presente e o futuro das energias renováveis pela EDA. *EDA Informa*, 120-121, 2008.

[5] ETSAP. TIMES. http://www.etsap.org/Tools/TIMES.htm, 2007.

[6] EuroStat. Electricity generated from renewable sources - % of gross electricity consumption. http://epp.eurostat.ec.europa.eu, 2008.

[7] A. Fidje et al. Regional TIMES model for Norway with high time resolution. http://www.iccgov.org/iew2009/speakersdocs/Fidje-et-al_RegionalTIMESModel.pdf, 2009. International Energy Workshop.

[8] Directorate-General for Energy and Transport. An energy policy for Europe: Commission steps up to the energy challenges of the 21st century. European Commission - MEMO/07/7, 2007.

[9] Richard Loulou and Maryse Labriet. ETSAP-TIAM: the TIMES integrated assessment model Part I: Model structure. *Computational Management Science*, 5(1-2):7–40, 2008.

[10] H. Lund and B. V. Mathiesen. Energy system analysis of 100% renewable energy systems: the case of Denmark in years 2030 and 2050. *Energy*, 34:524–531, 2009.

[11] Henrik Lund. *Renewable Energy Systems*. Academic Press, 2009.

[12] The Mathworks. MATLAB - the language of technical computing. http://www.mathworks.com/products/matlab/, 2010.

[13] A. Pina, C. Ioakimidis, and P. Ferrão. Economic modeling of a seawater pumped-storage system in the context of São Miguel. http://ieeexplore.ieee.org/stamp/stamp.jsp?tp=&arnumber=4747098, 2008. International Conference on Sustainable Energy Technologies.

[14] MIT Portugal Program. Green Islands Project. http://www.mitportugal.org, 2008.

[15] Aalborg University. EnergyPLAN: advanced energy system analysis computer. http://energy.plan.aau.dk/, 2010.

[16] K. Vaillancourt, M. Labriet, R. Loulou, and J.P. Waaub. The role of nuclear energy in long-term climate scenarios: An analysis with the World-TIMES model. *Energy Policy*, 36-7:2296–2307, 2008.

Acknowledgments: This work has partially been supported by Programa de Financiamento Plurianual de Unidades de I&D from the Portuguese Science and Technology Foundation (FCT) to the research activities of the associated laboratory LAETA, by the FCT scholarship SFRH/BD/35334/2007 within the MIT-Portugal Program and by the FCT project FLEXNET (Projecto SEN-ENR.101802.2008).

Energy and Exergy Analysis for the Electricity Sector of Turkey

Bora Şekip Güray[a],Derek Baker[b]

[a] *Mechanical Engineering Department, Middle East Technical University, Ankara, Turkey*
General Directorate for Energy, Ministry of Energy and Natural Resources, Ankara, Turkey
[b] *Mechanical Engineering Department, Middle East Technical University, Ankara, Turkey*

Abstract: The world energy system is expected to undergo a substantial transformation from the current patterns of supply and demand to address the challenges of energy security and climate security. Technology is anticipated to be the main driver of this transformation. The electricity sector is subject to the most significant transformation due to the penetration of new technologies. In this study, the electricity sector of Turkey is modelled as a complex energy system of electricity generation, transmission, distribution and consumption. Model input data were compiled according to the International Energy Agency's (IEA) statistics framework for its member countries and is a disaggregated representation of the electricity network in terms of resources, operational modes and technologies of conversion systems, and consumption sectors. The relevant energy and exergy indicators are presented, analyses are performed, and results are discussed. The level of aggregation provided by these data and model makes the analysis novel and allows for tracking the transformative effect of energy policies, strategies and technologies in an electricity system by use of thermodynamic indicators. Since this sector level thermodynamic analysis is based on the standard IEA statistics framework, it can be replicated for all 28 member countries of the IEA.

Keywords: Complex energy system, Electricity sector, Energy analysis, Exergy analysis.

1. Introduction

Energy is an essential element of a functioning economy. Since the Industrial Revolution, energy has been a key driver for economic vitality and social progress. Due to the unsustainable nature of present energy supply and demand patterns, the energy sector is expected to undergo a transformation by mobilising new policies, strategies and technologies to address energy security and climate security related challenges in a coherent manner [1].

This transformation, building on the vision of reducing the carbon intensity of the energy sector by new technology penetration, stands for a technology driven development model which will replace the rapid economic development model by mass production largely followed in the 20th Century [2].

The electricity sector stands as the most prominent area where a significant transformation is anticipated and undergoes the most remarkable change in the alternative scenarios by IEA where low-carbon and carbon-free energy technologies increase their share worldwide [1]. Therefore, dissecting the electricity sector from production to final use is important for tracking and evaluating any transformative effect of energy policies, strategies and technologies.

The electricity sector is a large and complex energy system comprised of a variety of coexisting transformations from primary energy supply to final consumption. Hence, thermodynamics based modelling and analysis of the electricity sector as a complex energy system requires identifying the functional characteristics of and interactions along different steps encountered from production to final use.

At a macroscopic level energy and exergy analyses has been a developing research field since 1975 [3-5]. The studies in the literature demonstrate that such analyses at a macroscopic level were primarily motivated by attempts to quantify issues related to resource utilization for responding to concerns over high energy prices [3].

Corresponding Author: Bora Şekip Güray, Email: bguray@enerji.gov.tr

Energy and exergy analyses at a macroscopic level have also been utilized recently to assess the economic valuation and environmental impacts of energy use [3,5,6]. In a wider perspective, energy policy advice, energy planning and sustainable development are amongst the areas for which thermodynamic analysis has been proposed as an instrument to assess performance at a macroscopic level [7-9].

The main methodologies for energy and exergy analyses at a macroscopic level can be categorized in three approaches. Being the pioneer of energy and exergy analyses at a macroscopic level, Reistad's approach is the most widely implemented model. Acar applied the approach of Reistad to Turkey [4]. Another recent application following this approach is for the residential and commercial sectors of Japan [10].

The approach proposed by Wall considers material flows as exergy carriers to extend Reistad's approach and quantifies metals, minerals as well as the waste and emissions in terms of their exergy content. Studies employing the approach of Wall include those for Japanese [11], Norwegian [12], Chinese [13] and UK [5] societies. Wall's approach is based on a cumulative exergy concept as it deals with the exergy conversion from the resource base to final use. Therefore, this approach can also be considered in the context of life cycle analyses.

The most recent approach of energy and exergy analyses at a macroscopic level has been proposed by Sciubba. Sciubba's approach of Extended Exergy Accounting (EEA) extends Wall's approach by including capital and labour as productive factors and aims at modelling capital and labour related flows in terms of their exergetic equivalent. EEA represents non-energetic flows as resources [14]. This is done by a multidimensional indicator as a linear combination of cumulative exergy content and of the equivalent exergy contents of capital, labour and environmental remediation. Studies built on this approach include applications for the UK and Norwegian societies, the energy sector of the Netherlands, and the province of Siena, respectively [5,15-17].

EEA is shown to be sensitive to capital and labour related conversion factors which are country specific and cross-sectoral [16].

It is observed that the modelling of the interactions and the definition of system boundaries constitute the essential elements of macroscopic level thermodynamics analyses where the level of aggregation or disaggregation is of significant importance [6,18]. The existing models in the literature for energy and exergy analyses at macroscopic level are largely built on aggregated representations for the energy supply-demand chain. These aggregated models do not follow a standard methodology pertaining to the use of data.

This study aims at providing a detailed representation developed upon a standard methodology for thermodynamics based modelling and analyses of the electricity sector. Detailed representation is considered important to enable integration of the thermodynamic based indicators into conventional forms of energy related indicators to contribute to the current energy debates related to energy security and climate security.

2. Modeling

The electricity sector includes a variety of stages from primary supply of energy to its final use. In this section, the modeling for developing energy and exergy indicators over a detailed representation is presented.

2.1. IEA Statistics Framework

IEA uses a standard statistics framework to provide a methodology for gathering and presenting energy data by its member countries. This standard framework, explained in a manual format, is employed for analyses by IEA and enables comparisons among different structures and practises in its 28 member countries [19].

The electricity module of the IEA energy statistics framework is one of the five modules constituting the energy supply-demand chain of any country or region. The electricity module is interrelated to each of the remaining four modules of natural gas, petroleum, solid fuels, and renewables and wastes.

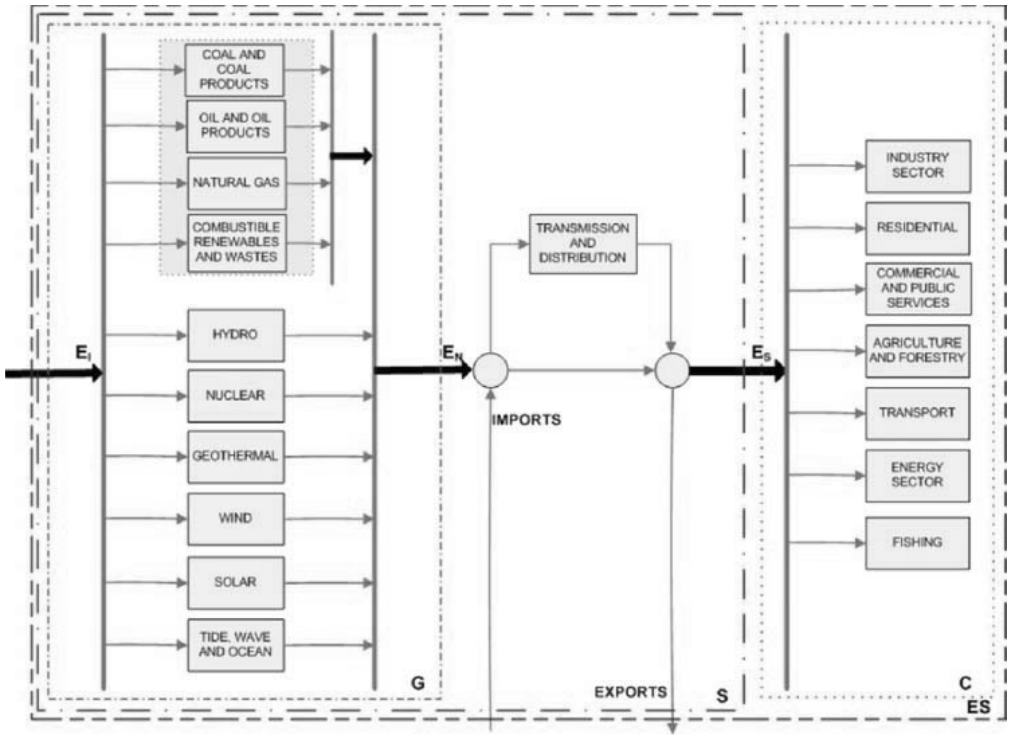

Fig. 1. The electricity sector model illustrating the input and output relationships and the system boundaries.

Figure 1 illustrates the generic model developed for the electricity sector by the use of the statistics framework. Detailed representations of both generation and final consumption structures linked by a transmission-distribution segment together with imports and exports are included.

Generation is represented by ten main types of technologies and the final consumption is represented by seven sectors. Further details are provided by disaggregating the combustible fuels into four different forms. This is particularly important for accuracy of the energy and exergy analyses.

The modeling also provides detail in terms of type of electricity producers, differing between the "main-activity producers", which supply electricity to the main transmission and distribution grid, and the "autoproducers", which generate electricity autonomously for their own use. This distinction is important for accurate energy and exergy analyses of the electricity sector.

Use of the IEA statistics framework in this study presents novelty for three main reasons. First, it relies on official statistics gathered and presented within a standard framework, ensuring a certain degree of accuracy and reliability in data. Second, building a model on this methodology facilitates its replication for each of the 28 member countries of IEA. Third, it includes a detailed representation of the electricity supply and demand structures by disaggregating the generation by sources and the final consumption by sectors. Hence, developing a model for energy and exergy analyses based on this standard framework is an improvement over the present studies in the field of energy and exergy analyses at a macroscopic level.

2.2. Modeling for the Electricity Sector of Turkey

The electricity sector model for Turkey is developed by use of the IEA Statistics Framework.

Data required by this standard framework are gathered into excel sheets in accordance with the Energy Statistics Manual [19], for the year 2008.

The major characteristics of the Turkish electricity sector are identified over an aggregated representation for accurate development of energy and exergy indicators.

Table1. An Aggregated Energy Balance for the Electricity Sector in 2008 (unit: TWh)

Gross Generation by Main Activity Producers	A	182.695
Internal Use by Main Activity Producers	B	7.923
Supply by Main Activity Producers	C = A - B	174.772
Imports	D	789
Exports	E	1.122
Transmission and Distribution Losses	F	25.904
Supply for Final Consumption by the Grid	G = C + D - E - F	146.957
Gross Generation by Autoproducers	H	15.723
Internal Use by Autoproducers	I	732
Supply for Final Consumption by Autoproducers	J = H - I	14.991
Total Final Consumption	K = G +J	161.948

Energy balance over the electricity sector, tabulated in Table 1, yields the following characteristics :

- 90.7 % of the total final consumption is provided by the electricity grid while 9.3 % is supplied by autonomous production.
- 14.8 % of the electricity supplied to the grid is lost in transmission and distribution networks.
- 4.3 % and 4.7 % of gross electricity generation is consumed internally for main activity producers and autoproducers, respectively.
- Turkey is a net exporter of electricity in 2008, net exports corresponding to 0.2 % of total final consumption.

Investigation of the energy sources used in the generation stage yield the following characteristics :

- Combustible fuels provide 82 % of gross generation in main activity producers. Natural gas and coal provide approximately 50 % and 30 % of gross generation by combustible fuels in main activity producers.
- Combustible fuels provide 95 % of gross generation in autoproducers, with natural gas providing approximately two thirds of this.
- Among non-combustible fuels, hydro is the main energy source generating less than 17 % of gross electricity in 2008. Electricity generation by wind contributes to less than 1 % in both types of producers, whereas geothermal, combustible renewables and wastes together also correspond to 0.14 % and 0.73 % of gross generation by main activity producers and autoproducers, respectively.

2.3. Formulation of Energy and Exergy Indicators

The modelling framework is based on input and output relationships for each element of the electricity sector. The indicators are developed for four system boundaries described in Section 2.1, taking into account the characteristics identified in Section 2.2.

Based on the model illustrated in Figure 1, five energy indicators and five exergy indicators in terms of first law and second law efficiencies e_1 and e_2 are developed.

These indicators are

- $e_{1,Gn,m}$ and $e_{2,Gn,m}$ for the generation stage,
- $e_{1,TD}$ and $e_{2,TD}$ for the transmission-distribution stage,
- $e_{1,S}$ and $e_{2,S}$ for the supply stage composed of generation and transmission-distribution stages,
- $e_{1,C,m}$ and $e_{2,C,m}$ for the consumption stage,
- $e_{1,ES}$ and $e_{2,ES}$ for the overall electricity sector.

These five indicators enable tracking of the performance in each stage of the electricity sector. Table 2 outlines the formulation of the indicators.

3. Analyses

Energy and exergy analyses for the Turkish electricity sector are performed using 2008 data and the developed model. Energy and exergy indicators along the sector are presented and discussed.

The average ambient temperature T_o of Turkey was 13.54 ^{o}C in 2008, according to the statistics of the State Meteorological Institute [20].

Table 2.Formulation of energy and exergy indicators.

$$e_{1,G_n,m} = \frac{E_N}{E_I} \cdot e_{1,G_g,m} \quad (1)$$

$$e_{2,G_n,m} = \frac{E_N}{E_I} \cdot e_{2,G_g,m} \quad (2)$$

$$e_{1,G_g,m} = \sum_{i=1}^{K} w_i \cdot e_{1,G_g,i} \quad (3)$$

$$e_{2,G_g,m} = \sum_{i=1}^{K} w_i \cdot e_{2,G_g,i} \quad (4)$$

for combustible energy sources :

$$e_{1,G_g,i} = \sum_{j=1}^{M} w_j . e_{1,G_g,j} \quad (5)$$

$$e_{2,G_g,i} = e_{1,G_g,i} / \varphi_i \quad (6)$$

$$\varphi = \varepsilon / (NCV) \quad (7)$$

for non-combustible energy sources :

$$e_{2,G_g,i} = e_{1,G_g,i} = \text{constant} \quad (8)$$

$$e_{1,TD} = E_S / E_N \quad (9)$$

$$e_{2,TD} = E_S / E_N \quad (10)$$

$$e_{1,S} = e_{1,G_n,m} \cdot e_{1,TD} \quad (11)$$

$$e_{2,S} = e_{2,G_n,m} \cdot e_{2,TD} \quad (12)$$

$$e_{1,C,m} = \sum_{k=1}^{O} w_k \cdot e_{1,C,k} \quad (13)$$

$$e_{2,C,m} = f(e_{1,C,m}) \quad (14)$$

$$e_{1,C,k} = \sum_{l=1}^{P} w_l \cdot e_{1,C,l} \quad (15)$$

$$e_{2,C,k} = f(e_{1,C,k}) \quad (16)$$

$$e_{1,ES} = e_{1,S} \cdot e_{1,C,m} \quad (17)$$

$$e_{2,ES} = e_{2,S} \cdot e_{2,C,m} \quad (18)$$

In this formulation, *g* denotes gross generation, *n* denotes net generation after the internal use by the generation plants, *m* denotes mean values, *w* denotes the weights and represents respective shares, K denotes the number of generation types, M denotes the number of fuels for each of the four combustible fuel categories represented in Figure 1, ε denotes the chemical exergy, *(NCV)* denotes the net calorific value, *O* denotes number of consumption sectors, *P* denotes number of processes or appliances in each consumption sector, and *f* denotes the functions representing second law efficiencies in terms of first law efficiencies for the consumption stage.

3.1. Generation and Supply

Energy efficiency for each combustible fuel category is calculated by dividing the gross electricity generation by the energy input expressed as (NCV). The analyses include five different types of coal and coal products, three different types of oil products, and four different types of combustible renewables and wastes. For each combustible fuel, mean efficiency values are calculated according to (5), (6) and (7), using φ values from [21]. For non-combustible generation types, efficiency values are taken from a previous study done for Turkey [4]. CHP plants correspond to 5.1 % of gross electricity generation by combustible fuels. Based on their small share, performing mean efficiency calculations for the electricity-only plants is considered as a valid simplification.

Table 3 presents the energy and exergy efficiencies $e_{1,Gg}$ and $e_{2,Gg}$ for seven generation types present in the electricity sector of Turkey together with their shares *w*. According to (3) and (4) $e_{1,Gg,m}$ and $e_{2,Gg,m}$ are calculated as 53.61 % and 51.94 % respectively.

Table 3. Analyses for Gross Electricity Generation

Generation Type	*w* (%)	$e_{1,Gg}$ (%)	$e_{2,Gg}$ (%)
Hydro	16.77	88.5	88.5
Geothermal	0.08	4.6	4.6
Wind	0.43	35	35
Coal	29.09	34.85	32.87
Oil	3.79	38.16	36.69
Natural Gas	49.74	54.29	52.2
Combustible Renewables and Wastes	0.1	34.85	30.3

Based on Table 1, (1), (9) and (11), $e_{1,Gn,m}$, $e_{1,TD}$ and $e_{1,S}$ are found as 51.28 %, 85.34 % and 43.76 %, respectively. Similarly, using Table 1, (2), (10) and (12), $e_{2,Gn,m}$, $e_{2,TD}$ and $e_{2,S}$ are found as 49.68 %, 85.34 % and 42.39 %, respectively.

3.2. Consumption

For the industry sector, 82 % of energy consumption is for process heating [4]. According to the Energy Balance for Turkey in 2008, electricity has around 20 % share in total energy use of industry [22]. Based on these two figures, the share of process heating in industrial electricity consumption is calculated as 10 %.

Motors represent 65 % of electricity consumption in industry. The remaining 25 % is for other uses, which are considered solely as lighting [4].

Calculations for process heating in industry are based on temperature classifications. Energy efficiency values e_1 for different mean temperature ranges of T_{pm} are 100 % for T_{pm} < 121 ^{0}C, 90 % for 121 ^{0}C < T_{pm} < 399 ^{0}C, and 70 % for T_{pm} > 399 ^{0}C [10]. Since the disaggregation provided by the modeling framework is different than the disaggregation used in studies present in the literature [4,33], approximations are made in order to use the data presented in these studies. The data and analyses for the process heating in industry are outlined in Table 4. The exergy relation $e_2=f(e_1)$ for process heating in industry is given in (19) where T_{pm} denotes the mean temperature for process.

$$e_2 = e_1 \cdot \left(1 - \frac{T_0}{T_{pm}}\right) \tag{19}$$

Table 4. Energy and Exergy Analyses for Process Heating in Industry

Classification in Modeling	Classification in [4,23]	T_{pm} (K)	w (%)	Breakdown for each T_{pm} (%)	e_1 (%)	e_2 (%)
Iron-Steel	Iron-Steel	318 1256	22.14	4.2 95.8	71.26	51.18
Non-metallic	Cement	315 859	12.46	91.7 8.3	97.51	12.57
Food-beverages	Sugar	356	6.68	100	100	19.51
Chemical-Petrochemical	Chemical-Petrochemical	315 414	5.1	62.5 37.5	96.25	16.04
Non-ferrous metals	Non-ferrous metals	334 405 674	3.42	10 9.4 80.6	74.88	36.33
Others	Others	330 405 673	50.2	10.6 89.3 0.1	91.04	24.94

Using (15), energy and exergy efficiencies for process heating in industry are calculated as 8,8 % and 2,9 % respectively from Table 4. Using energy and exergy efficiencies for motors as 90 %, and for industrial lighting as 18.5 % and 17.1 % respectively [4], energy and exergy efficiencies for the industry are found as 71.9 % and 65.67 %.

The exergy relations $e_2=f(e_1)$ for different process encountered in the residential and services sectors are given in (20), (21) and (22) for space and water heating, cooking, and refrigeration and air conditioning respectively. Temperature values T of 50 ^{0}C for space heating, 60 ^{0}C for water heating, 120 ^{0}C for cooking, -8 ^{0}C for refrigeration, and 35 ^{0}C for air conditioning are assumed for calculations of the residential and services sectors.

$$e_2 = e_1 \cdot \left[1 - \left(\frac{T_0}{T - T_0}\right) \cdot \ln\left(\frac{T}{T_0}\right)\right] \tag{20}$$

$$e_2 = e_1 \cdot \left(1 - \frac{T_0}{T}\right) \tag{21}$$

$$e_2 = e_1 \cdot \left(\frac{T_0}{T} - 1\right) \tag{22}$$

For the residential sector, official statistics published in 1998 are used similar to the approach followed in previous studies for Turkey [4,24]. Energy and exergy efficiency values for other appliances are taken from [4]. The data and the results for energy and exergy analyses for the residential and services sectors

using (15), (16), (20), (21), (22) are presented in Table 5. Due to lack of published data, in this analysis the services sector is assumed to exhibit the same breakdown of appliances as the residential sector. This approach, previously followed by a number of studies [4,24], is noted as a weakness in the energy and exergy analyses of the consumption stage.

Table 5. Analyses for the Residential and Services Sectors.

	w (%)	e_1 (%)	$e_{1,C}$ (%)	e_2 (%)	$e_{2,C}$ (%)
Lighting	35	9,5	3.33	8.7	3.05
Refrigeration	40	100	40	8.13	3.25
Water heating	4	90	3.6	6.59	0.26
Cooking	3	80	2.4	21.67	0.65
Space heating	2	98	1.96	5.75	0.12
Washing machine	2	80	1.6	80	1.6
Vacuum cleaner	1	70	0.7	70	0.7
Air conditioning	2	200	4	14.98	0.3
Television	6	80	4.8	80	4.8
Iron	1	98	0.98	30	0.3
Miscellaneous	4	70	2.8	65	2.6

Using (15), energy and exergy efficiency values for residential and services sectors together are found as 66.17 % and 17.62 %, respectively.

The agriculture and forestry sector is considered to utilize electricity in motors having 90 % energy efficiency [4].

Shares of the seven consumption sectors according to the disaggregated representation provided in Figure 1 are as follows : 44.66 % industry, 25.16 % commercial and public services, 24.44 % residential, 3.49 % agriculture and forestry, 1.56 % energy, 0.59 % transport and 0.10 % fishing. Industry, residential, commercial and public services, and agriculture and forestry represent 97.75 % of total electricity consumption. Energy and exergy efficiency values $e_{1,C,m}$ and $e_{2,C,m}$ based on these four sectors are calculated by (13) and (14) as 69.64 % and 42.16 %.

3.3. Results and Conclusion

In this study, a detailed model is developed for energy and exergy analyses of the electricity sector by using the standard statistics framework of the IEA.

Energy and exergy indicators are developed for different stages of the electricity sector and analyses are performed by applying this general model to the electricity sector of Turkey.

Energy and exergy indicators calculated for different stages of the electricity sector of Turkey are presented in Table 6. Energy and exergy efficiencies for the electricity sector are 30.47 % and 17.87 %, respectively. The difference between these two figures largely stems from the consumption sector. For a number of electricity driven processes and appliances employed in the consumption sector, exergy efficiencies deviate from the energy efficiencies significantly. This is attributed to the use of high quality energy for applications at relatively low temperatures.

Table 6. Results for energy and exergy indicators

	e_1 (%)	e_2 (%)
Generation	51.28	49.68
Transmission-Distribution	85.34	85.34
Supply	43.76	42.39
Consumption	69.64	42.16
Electricity Sector	30.47	17.87

These analyses illustrate the effectiveness of the developed model for tracking and evaluating performance in different stages of the electricity sector. The model, providing a certain level of disaggregation, is convenient for tracking the transformative effect of energy policies, strategies and technologies in an electricity system by use of thermodynamic indicators. Since the analyses provided by this study are based on the standard IEA statistics framework, they can be replicated for all 28 member countries of the IEA.

Apart from these major contributions, three areas are identified for furthering the effectiveness of the developed model :

- Different from the generation and supply stages, the energy and exergy analyses for the consumption stage do not rely on properly defined input and output relationships. Modification of the presented model is considered important to overcome this nonuniformity in the overall methodology.
- The standard statistics framework does not provide detailed representation of consumption sectors other than two sectors.

This imperfection can be overcome by the availability of detailed and country specific data and statistics at different levels of consumption stage.

- Performing EEA by use of the presented model can also be an important improvement over the present study, again subject to the availability of country specific data.

References

[1] International Energy Agency, 2009, *World Energy Outlook 2008*, OECD/IEA, Paris, France.

[2] Tester, J.W., 2005, *Sustainable Energy: Choosing Among Options*, The MIT Press, Cambridge, MA.

[3] Sciubba, E., and Wall, G., 2007, A Brief Commented History of Exergy From the Beginnings to 2004, International Journal of Thermodynamics, 10(1), pp. 1-26.

[4] Acar, B., 2008, An Analysis on the Utilization of Energy and Exergy in Turkey, MSc. Thesis, Middle East Technical University, Ankara.

[5] Gasparatos, A., et al., 2009, Assessing the Sustainability of the UK Society Using Thermodynamic Concepts: Part 2, Renewable and Sustainable Energy Reviews, 13(5), pp. 956-970.

[6] Milia, D., and Sciubba, E., 2006, Exergy-based Lumped Simulation of Complex Systems: An Interactive Analysis Tool, Energy, 31(1), pp. 100-111

[7] Dincer, I., and Rosen, M.A., 2007, *Exergy: Energy, Environment and Sustainable Development*, Elsevier, Oxford, UK.

[8] Rosen, A., et al., 2008, Role of Exergy in Increasing Efficiency and Sustainability and Reducing Environmental Impact, Energy Policy, 36(1), pp. 128-137.

[9] Chamchine, A.V., et al., 2006, Thermodynamic Indicators for Integrated Assessment of Sustainable Energy Technologies, International Journal of Low Carbon Technologies, 1(1), pp. 69-78.

[10] Kondo, K., 2009, Energy and Exergy Utilization Efficiencies in the Japanese Residential/Commercial Sectors, Energy Policy, 37(9), pp. 3475-3483.

[11] Wall, G., 1990, Exergy Conversion in the Japanese Society, Energy, 15(5), pp. 435-444.

[12] Ertesvag, I.S., and Mielnik, M., 2000, Exergy Analyses of the Norwegian Society, Energy, 25(10), pp. 957-973.

[13] Chen, G.Q, and Qui, Z.H., 2007, Systems Account of Societal Exergy Utilization: China 2003, Ecological Modeling, 208(2-4), pp. 102-118.

[14] Sciubba, E., 2004, From Engineering Economics to Extended Exergy Accounting : A Possible Path from Monetary to Resource Based Costing, Journal of Industrial Ecology, 8(4), pp.19-40.

[15] Ertesvag, I.S., 2005, Energy, Exergy, and Extended Exergy Analysis of the Norwegian Society 2000, Energy, 30(5), pp. 649-675.

[16] Ptasinski, K.J., et al., 2006, Performance of the Dutch Energy Sector Based on Energy, Exergy and Extended Exergy Accounting, Energy, 31(15), pp. 3135-3144.

[17] Sciubba, E., et al., 2008, Exergy and Extended Exergy Accounting of Very Large Complex Systems with an Application to the Province of Siena, Journal of Environmental Management, 86(2), pp. 372-382.

[18] Valero, A., 2006, Exergy Accounting: Capabilities and Drawbacks, Energy, 31(1), pp.164-180.

[19] International Energy Agency, 2005, *Energy Statistics Manual*, OECD/IEA, Paris, France.

[20] Turkish State Meteorological Service, web site, www.meteor.gov.tr

[21] Kotas, T.J., 1985, *The Exergy Method of Thermal Plant Analyses,* Anchor Brendan Ltd, Essex, UK.

[22] Ministry of Energy and Natural Resources of Turkey, web site, www.enerji.gov.tr

[23] Utlu, Z., and Hepbasli, A., 2007, A Review and Assessment of the Energy Utilization Efficiency in the Turkish Industrial Sector Using Energy and Exergy Analysis Method, Renewable and Sustainable Energy Reviews, 11(7), pp.1438-1459.

[24] Utlu, Z., and Hepbasli, A., 2005, Analysis of Energy and Exergy use of the Turkish Residential–Commercial Sector, Building and Environment, 40(5), pp.641-655.

Sustainability assessment of microgrids in the Northwestern European electricity market

Chiara Lo Prete[a], Benjamin F. Hobbs[a], Catherine S. Norman[a], Sergio Cano-Andrade[b], Alejandro Fuentes[b], Michael R. von Spakovsky[b] and Lamine Mili[c]

[a]*Johns Hopkins University, Department of Geography and Environmental Engineering*
[b]*Virginia Polytechnic Institute and State University, Department of Mechanical Engineering*
[c]*Virginia Polytechnic Institute and State University, Department of Electrical and Computer Engineering*

Abstract: The goal of this paper is to assess and quantify the sustainability of interdependent electric power infrastructures, focusing on the interaction of microgrids with a regional transmission/distribution grid. The Northwestern European electricity market (Belgium, France, Germany and the Netherlands) is used as a case study for our purposes. We present simulations of power market outcomes under various policies and levels of microgrid penetration, and evaluate the hypothetical microgrids using three types of sustainability indices (economic, environmental and thermodynamic).

Keywords: Sustainability, microgrids, Northwestern European electricity market, exergy, pollution, economics.

1. Introduction

A microgrid (MG) is a localized grouping of loads, generation and storage that can operate in parallel with the electricity grid or in island mode and can be supplied by renewable and/or fossil distributed generation. The goal of this paper is to assess the sustainability of MGs in the context of a regional power market, accounting for tradeoffs with operations and investment in central station generation. Sustainability is quantified in terms of multiple indices for the regional grid (thermodynamic, environmental and economic). The setting is the Northwestern European electricity market (Belgium, France, Germany and the Netherlands).

Sustainable development is often defined as "development that meets the needs of the present without compromising the ability of future generations to meet their own needs" [1]. However, translating this definition into quantifiable criteria that can be used to compare alternative power systems has proven difficult. For this reason several authors have adopted a multi-criteria (or multiple objective) approach. The function of multi-criteria analysis is to communicate tradeoffs among conflicting criteria and to help users quantify and apply value judgments in order to recommend a course of action [2]. In this manner, a range of dimensions of sustainability can be considered, while allowing stakeholder groups to have different priorities among the criteria. This method has been used, for example, to assess the tradeoffs in power infrastructure planning [3] and to evaluate the sustainability of power production [4].

We consider four alternative scenarios for satisfying the electric power and thermal needs of a regional power market, and we characterize their sustainability using three sets of indicators. The first set is based on CO_2 and conventional air pollutant emissions, while the second one emphasizes economic sustainability in terms of total generation costs.

We also include a third set of indices based on thermodynamic energy and exergy based efficiencies. An analysis relying on first law efficiency alone does not consider to what degree the outputs of a power plant are useful. For example, electricity is more valuable than low pressure and temperature steam, one of the typical by-products of power production, because the latter is characterized on a per unit energy basis by a lower value of exergy than the electricity. Therefore, not all outputs should be valued in the same way: outputs having a higher quality or exergy per unit energy (like electricity) should have a higher unit price than those having a lower quality or exergy per unit energy (like low-pressure and temperature steam) because the former possess a greater ability to do work. In contrast, when

the second law of thermodynamics is disregarded, the difference in quality of the various energy outputs is not considered and cannot be effectively compared for different energy conversion processes.

Thus, the use of exergy-based indicators can help decision makers to improve the effectiveness of energy resource utilization within a given power system. Such indicators have been widely adopted in the sustainability literature. Among others, [5] evaluates different alternative means to meet the energy needs of an industrial unit. The performance of each one is judged taking into account several aspects of sustainability. Ref.[6] develops three exergy-based indices to assess the sustainability of power generation in Norway.

The main contribution of our work is quantifying the sustainability of different power production paths in a regional system with the diverse set of metrics considered by [5]. However, unlike [5], we explicitly simulate the impacts of a generation investment decision upon operations and investment elsewhere in the grid, as evaluation of the net sustainability impacts of a decision should consider how a given investment choice propagates through the system. We include exergy-based sustainability indices because we believe that they may provide useful information on regional grid efficiency that complements the economic and environmental indicators. We emphasize economic and environmental sustainability in this analysis, both for lack of suitable data on social sustainability impacts and because we do not have strong reasons to believe that social sustainability will vary significantly across the choices modeled.

2. Methodology and assumptions

This section describes our modeling approach and assumptions concerning alternative power systems (with and without MGs) and CO_2 policies.

2.1. Optimization model

For the purposes of this paper, we represent the Northwestern European electricity market using COMPETES (Comprehensive Market Power in Electricity Transmission and Energy Simulator) [7]. Our version of COMPETES is a quadratically constrained model that is solved in ILOG OPL 6.3, using the optimizer Cplex12 [8].

The generation supply cost and network data is based upon [9], modified to allow for transmission resistance losses, exergy and emissions. The electricity network is represented by fifteen nodes: the Netherlands with three (Krim, Maas, Zwol), Belgium with two (Merc and Gram), and France and Germany with one each. A DC power flow model is being used to represent a system in which four intermediate nodes are distinguished in both France (Avel, Lonn, Moul, Muhl) and Germany (Diel, Romm, Ucht, Eich). At these nodes, no generation or demand occurs (except for 2000 MW of power exports to the UK at Avel). A sixteenth node representing a group of residential MGs is added to the model in the scenarios including MGs. The nodes of the network are connected by twenty-eight high voltage transmission corridors (or arcs), each one with a maximum MW transmission capacity. The group of MGs is connected to the transmission system by a radial link at Krim.

Overall, twelve power producers are modeled in the four countries: eight of them are the biggest ones in the region (Electrabel, Edf, Eon, ENBW, RWE, Vattenfall, Essent Nuon-Reliant), while the remaining four represent the competitive fringe in each country. Electricity demand is assumed to be fixed.

Our application of COMPETES calculates a competitive equilibrium among power producers, which under perfectly inelastic demand is equivalent to minimization of total generation costs. This is done for four representative hours (one peak hour in the summer, one peak hour in the winter, one off-peak hour in the summer, one off-peak hour in the winter) in order to characterize the distribution of operating costs. Computational convenience suggests starting the analysis with a competitive benchmark. In the future, we will assess the robustness of our conclusions to different assumptions on market power in our regional market using the oligopoly version of COMPETES.

We include resistance losses on high voltage transmission flows to make the model more

realistic because, on average, losses can contribute as much to spatial price variations as congestion does. Losses vary as a quadratic function of flow, using the linearized DC formulation in [10]. In the absence of other data, resistance loss coefficients, defined for the twenty-eight corridors of the network, are assumed to be proportional to reactance. Therefore, we set them equal to the reactance in [9] on each corridor times a constant α. The value of α (0.000005) is chosen so that high voltage transmission losses are approximately equal to 2% of generation during the peak periods.

2.1.1. Model formulation

COMPETES is a short-run optimization model: its objective function includes short-run marginal costs (i.e., fuel and other variable O&M costs) and disregards long-run retirement and entry decisions. For each MG scenario (with or without MG) and each CO_2 policy scenario (with and without a CO_2 price), we solve this model for each of the four different periods of the year representing a variety of load and generation capacity conditions. The four periods are appropriately weighted by the number of hours in each period to estimate annual cost. The problem statement is as follows:

$$Min. \quad \sum_i \sum_{j \in J_i} (MC_{ij} + CO_2 * E_{ij}) * gen_{ij} \qquad (1)$$

subject to:

$$\sum_{j \in J_i} gen_{ij} + \sum_{k \in A_i} [f_{ki} * (1 - Loss_{ki} * f_{ki}) - f_{ik}] \geq L_i \qquad \forall i \in I \qquad (2)$$

$$\sum_{ik \in M_m} R_{ik} * S_{ikm} * (f_{ik} - f_{ki}) = 0 \qquad \forall m \in M \qquad (3)$$

$$gen_{ij} \leq Cap_{ij} * (1 - FOR_{ij}) \qquad \forall i \in I, \forall j \in J_i \qquad (4)$$

$$f_{ik} \leq T_{ik} \qquad \forall i,k \in I \qquad (5)$$

$$f_{ik} \geq 0 \qquad \forall i,k \in I \qquad (6)$$

$$gen_{ij} \geq 0 \qquad \forall i \in I, \forall j \in J_i \qquad (7)$$

The goal is to minimize the objective function expressed as the total generation costs given by (1), where a linear short-run cost of production is assumed. The decision variables are gen_{ij} (the generation from aggregated power plant j located at node i) and f_{ik} (the MW transmission flow from node i to a nearby node k that is directly connected to i by a transmission corridor).

Constraint (2) represents Kirchhoff's Current Law (KCL) constraint defined for each node of the network. f_{ik} is the export flow from node i to node k, while $f_{ki}*(1-Loss_{ki}*f_{ki})$ represent the import flow (net losses) into node i from node k.

Equation (3) represents Kirchhoff's Voltage Law (KVL) constraint, defined for each of the fourteen meshes (or loops) connecting the nodes. Constraint (4) ensures that power generated at each node and each step is less than the available capacity at that location, while (5) constrains the transmission flow on a given arc. Constraints (6) and (7) are nonnegativity restrictions.

When microgrids are included, their generation costs are added to equation (1). Since the group of MGs is an additional node with an autonomous load, one KCL constraint is added in the model. Since MGs are assumed to be radially connected to the grid, no additional KVL is included. The power generated at the MG node must satisfy the capacity constraint (4) and the non-negativity constraint (7), and its flow to/from the grid must satisfy its bounds (5) and (6).

2.1.2. Data

Simulations of power market outcomes are based on a modified version of the Energy Research Centre of the Netherlands (ECN) simplified COMPETES database of transmission, demand, and generation [9]. This provides a multi-step supply function (one step per aggregate power plant) for each node where power generation occurs. In the scenarios including MGs, four additional aggregate power plants are added to the existing network representing the MG technologies operating at that node. Information on total capacity, dominant fuel type, energy efficiency, exergy calculations, marginal cost function, average CO_2, NO_x and SO_x emission rates is available from the authors.

Our four COMPETES simulations consider typical loads for the winter and summer seasons in each of two time periods (peak and off-peak), as well as data on maximum transmission capacity and reactance on the twenty-eight corridors of the network.

It is important to note that in the scenarios without MGs we only consider non-combined heat and power (non-CHP) bulk power

facilities: since CHP generators are dispatched earlier than all other plants due to their high efficiencies and thermal demands, their production is simply netted from the electricity demand of the network in the ECN database. On the other hand, CHP capacity is installed at the MG node, and we explicitly consider its contribution to system efficiency, economics and pollution. This is because this CHP capacity is incremental to the system if the MG is installed and is highly relevant to those indices.

2.2 Description of scenarios

We consider four alternative scenarios to satisfy the electric power and thermal needs of the Northwestern European electricity market. For each scenario we simulate four representative hours. Annual results are obtained by averaging the hourly results by the total number of hours in a year, assuming each case (peak summer, off-peak summer, peak winter, off-peak winter) is equally likely.

The scenarios can be described as follows:

- *Scenario1 (S1):* no MG, no CO_2 price

This scenario assumes that no MG operates in the Northwestern European power market and there is no price on CO_2 emissions. The characteristics of the network are summarized in Table 1. The only thermal load we consider is the incremental one that might be met by MG systems in the other scenarios; this is a thermal load of 41 TWh/yr, met by natural gas fueled boilers in this scenario.

Table 1. Characteristics of the network

Annual electric power load (TWh/yr)		1,165
Thermal load (MWht /yr)		41,066,880
Exergy content of the thermal load (MWh/yr)		13,376,739
Efficiency of the boiler		0.86
Capacity of the boiler (MW)		160
Generating capacity (MW)		215,149
of which:	Nuclear	47.4%
	Coal	29.1%
	Natural gas	14.5%
	Oil	6.3%
	Hydroelectric	2.2%
	Waste	0.5%

- *Scenario2 (S2):* MG, no CO_2 price

This scenario assumes that fifty residential MGs operate at a node connected to Krim in the Netherlands. Each residential MG has a 20 MW generating capacity, and there is no price on CO_2 emissions. The characteristics of the MG node are summarized in Table 2.

The annual electric power and thermal load of the network at the consumer voltage level are the same as in Scenario 1, in line with our zero elasticity assumption. However, the load at the bulk power level will be lower because MGs generate power closer to the consumers, lowering the transmission losses of the network.

Table 2. Characteristics of the MG node

Annual electric power load (MWh/yr)		4,364,385
Thermal load (MWht/yr)		41,066,880
Exergy content of the thermal load (MWh/yr)		13,376,739
Wind capacity factor		30%
Generating capacity (MW)		1,000
of which:	Wind	18%
	Solid Oxide Fuel Cell (SOFC)	50%
	Natural gas microturbines (MT)	12%
	Diesel reciprocating engines (RE)	20%

In our simulations the hourly load at the bulk level is reduced by 938 MW in the peak period. This amount is equal to the maximum hourly load of the MG node at the consumer voltage level (800 MW, occurring during winter peak hours), plus 2% of avoided transmission losses on that load and a 15% reserve margin. We assume that 816 MW less of central system combined cycle plant is built if MGs operate in the system, so this amount is subtracted from the cleanest type of generating capacity operating at node Krim (natural gas combined cycles – CC) in the MG scenarios. In addition, a peaking (combustion turbine - CT) capacity equal to 15% of that amount (122 MW) is assumed to no longer be needed as a reserve margin. The 41 TWh/yr thermal load is supplied by CHP to the MG residential district as saturated steam at p=20 bar [5].

- *Scenario3 (S3):* no MG, CO_2=25 €/ton

This scenario is the same as Scenario1 in terms of loads, generating capacity and efficiencies, but it also includes a price on CO_2 emissions of 25 €/ton. This results in additional dispatch of cleaner but more expensive capacity at the expense of cheaper but dirtier generation.

- *Scenario4 (S4):* MG, CO_2=25 €/ton

This scenario is the same as Scenario2 in terms of loads, generating capacity and efficiencies, but it also includes a price on CO_2 emissions of 25 €/ton.

2.3. Choice of indicators

We chose our indicators to assess different aspects of sustainability. The indicators are computed for each scenario described in the previous section and can be divided into three groups, following the classification in [5]:

- *Environmental indicators*:
  1. Annual emissions of CO_2 (Mton/yr)
  2. Annual emissions of NO_x (kton/yr)
  3. Annual emissions of SO_x (kton/yr)

In scenarios 1 and 3, CO_2 and NO_x emissions are produced by the power plants operating in the network as well as by the natural gas fueled boiler. In scenarios 2 and 4 the only pollutant emissions considered are due to the power plants operating in the network. The average emission rates for the network, MG and the boiler in S1 and S3 are given in Tables 3 to 5.

Table 3. Emission rates of the stand-alone boiler in S1 and S3 (ton/MWh)

	CO_2	NO_x	SO_x
Boiler	0.234	0.00038	-

Table 4. Average emission rates in the network by fuel (ton/MWh)

Fuel	CO_2	NO_x	SO_x
Natural gas	0.57	0.0004	-
Coal	0.99	0.0016	0.0021
Waste	0.63	0.0015	0.0020
Oil	0.73	0.0018	0.0016

Table 5. Emission rates in the MG by technology (ton/MWh)

Technology	CO_2	NO_x	SO_x
SOFC	0.402	0.000007	-
Gas MT	0.778	0.000238	-
Diesel RE	0.826	0.00095	0.00163

- *Economic indicators:*
  4. Annualized capital costs and variable costs (€/yr)

In scenarios 1 and 3, the capital cost impact is given by the annualized costs of the natural gas combined cycle and combustion turbine generation that would not be necessary in the MG scenario, plus the cost of the boiler capacity. We compute the annualized capital costs by multiplying the current value of capital by an annualization factor $[r(1+r)^n]/[(1+r)^n-1]$, where r is the discount rate and n is the useful life of the item. The assumptions used are given in Table 6.

The economic impact also includes the variable costs of operation of each scenario. The costs of the CO_2 allowances are not included in the economic indices; they simply represent a money transfer from the power generators to the government.

Table 6. Economic data for S1 and S3

Capital cost of CC capacity ($/kW)	1,200
Capital cost of CT capacity ($/kW)	1,000
Total unbuilt CC capacity (MW)	816
Total unbuilt CT capacity (MW)	122
Useful life of gas capacity (years)	20
Capital cost of the boiler ($/kW)	240
Useful life of boiler (years)	20
Cost of natural gas (€/MBtu)	3.7
Discount rate	0.05
Exchange rate (€ per US$)	0.724

In scenarios 2 and 4 we consider the annualized capital costs and operating variable costs of the new MG capacity. The characteristics of the MG technologies are given in Table 7.

Table 7. Characteristics of the MG technologies

MG technology	Capital cost ($/kW)	Useful life (years)	Unitary size (kW)	Energetic efficiency
Wind turbines	1,467	20	1,800	18%
SOFC	4,700	10	1,000	50%
Microturbine	2,500	20	60	26%
Diesel RE	350	20	180	34%

  5. Annualized capital costs and variable costs, including environmental externalities (€/yr)

We include an additional term, the external environmental costs of the pollutants, among the variable operating costs of each scenario. This allows us to assess the real cost of the pollutant emissions to the society, which cannot be done simply by introducing CO_2 allowances. The environmental costs of the pollutants used in our analysis are derived from [5] and shown in Table 8.

Table 8. Environmental costs of pollutants

Pollutant	Environmental cost (€/kg)
CO_2	0.019
NO_x	3.4384
SO_x	1

- *Technical indicators:*

6. Annual energetic *electric* efficiency of the network

This indicator is obtained by dividing the annual power production by the annual fuel use for power production in each scenario.

7. Annual energetic *total* efficiency of the network

This is given by

$$\eta_{tot} = \frac{\dot{W} + \dot{Q}}{\dot{W}/\eta_e + \dot{Q}/\eta_b} \quad (8)$$

The heat requirement $\dot{Q}$ is the same in all scenarios. However, the MG produces both heat and electricity through cogeneration, while in S1 and S3 the thermal load has to be met with a separate boiler. Therefore, the second term in the denominator of equation (8) is excluded in the scenarios with MGs, because all the fuel necessary to produce both heat and power is already included in the first term.

8. Annual exergetic *electric* efficiency of the network

In each scenario, this is given by

$$\varsigma_e = \frac{\eta_e}{\phi_e} \quad (9)$$

ϕ_e is obtained as the ratio of the total exergy of the annual fuel use for power production and the total energy of the annual fuel use.

9. Annual exergetic *total* efficiency of the network

This is given by

$$\varsigma_{tot} = \frac{\dot{W} + \dot{E}_s^Q}{\dot{W}/\varsigma_e + \dot{E}_{NG}} \quad (10)$$

where $\dot{E}_{NG} = \dot{M}_{NG} H_{NG} \phi_{NG}$ (11)

For the reasons explained for indicator 7, the last term in the denominator is excluded in the scenarios including the group of MGs. ϕ_{NG} = 1.042 and H_{NG} = 38.1 MJ/kg.

3. Results

The values of our indicators are in Table 9.

To analyze the trend of the emissions from power generation alone, we disregard the CO_2 and NO_x emissions of the boiler, which are included in S1 and S3 (Table 10).

Table 9. Values of the indicators in the scenarios

Indicator	S1	S2	S3	S4
1 (Mton/yr)	409.95	396.45	393.94	380.50
2 (kton/yr)	315.82	299.45	305.53	289.58
3 (kton/yr)	260.35	260.79	245.84	246.73
4 (M€/yr)	10,773	10,943	10,938	11,106
5 (M€/yr)	19,838	19,776	19,649	19,578
6	0.4486	0.4487	0.4508	0.4508
7	0.4561	0.4645	0.4582	0.4667
8	0.4111	0.4111	0.4132	0.4132
9	0.4453	0.4538	0.4474	0.4560

In the scenarios without MGs, CO_2 and NO_x emissions are higher than in the ones including MGs, while SO_x emissions are lower.

Table 10. Emissions from power generation in the four scenarios

Pollutant	S1	S2	S3	S4
CO_2 (Mton/yr)	396.65	396.45	380.63	380.50
NO_x (kton/yr)	300.21	299.45	289.92	289.58
SO_x (kton/yr)	260.35	260.79	245.84	246.73

This is because in the MG scenarios most of the unbuilt CC capacity is replaced by clean technologies like SOFCs (with very low CO_2 and NO_x emission rates). Furthermore, the share of generation from renewable sources increases. However, two high SO_x power plants fueled by coal and oil also increase their output to meet the load of the network, replacing the output of the central CC plant that exists in the nonMG scenarios but not in the MG scenarios. The costs of the scenarios with MGs are higher because, while more efficient technologies decrease the annual fuel consumption in the network, the annualized capital costs of the technologies are significant. The capital cost of the fuel cells is particularly large and accounts for most of the cost difference. The efficiencies of the MG scenarios (in particular total efficiencies) are higher than those of the other scenarios because of the increased amount of cogeneration.

It is difficult to assess the overall performance of the scenarios if each sustainability indicator is expressed in different units. In line with [5], we normalize the values in Table 9 after specifying a lower and upper threshold for each indicator. For the first five indicators the lower threshold is set equal to the lowest value among scenarios of the indicator, while the upper threshold is set equal to the highest

value of the indicator. For the remaining indicators, a lower threshold of zero is chosen. Following [5], the upper threshold of η_e is set equal to 80% (the efficiency of a Carnot cycle operating between the environmental temperature of 298.15°K and an assumed temperature of 1486.7°K at the exit of the combustion chamber of the cogeneration system in the MG). Other efficiencies have an upper threshold of 1.

In Table 11 we then calculate a sub-index for each group, obtained as the average of the indicators in the group. Each indicator is equally weighted. We finally aggregate our results in a composite sustainability index to gauge the overall performance of each scenario. In each scenario the composite index is an average of the three sub-indices. This implicit equal weighting may, of course, not be appropriate, depending on societal willingness-to-pay for emission reductions, cost reductions and efficiency improvements. However, the results provide one comprehensive perspective on overall attractiveness of the MG system.

Table 11. Normalized values of the indicators, sub-indices and composite sustainability index in the four scenarios

Indicator	S1	S2	S3	S4
1	0	0.46	0.54	1
2	0	0.62	0.39	1
3	0.03	0	1	0.94
Environmental sub-index	*0.01*	*0.36*	*0.65*	*0.98*
4	1	0.49	0.51	0
5	0	0.28	0.73	1
Economic sub-index	*0.50*	*0.38*	*0.62*	*0.50*
6	0.5608	0.5608	0.5635	0.5635
7	0.4561	0.4645	0.4582	0.4667
8	0.4111	0.4111	0.4132	0.4132
9	0.4453	0.4538	0.4474	0.4560
Technical sub-index	*0.4683*	*0.4726*	*0.4706*	*0.4749*
Composite sustainability index	***0.3260***	***0.4052***	***0.5776***	***0.6517***

From an environmental point of view, the scenarios including MGs are *more* sustainable because they yield a reduction in both CO_2 and NO_x emissions. However, SO_x emissions may increase. This result indicates that the specific environmental impacts of a microgrid can depend on its complex interactions with investment and operations of the regional power market. The difference in environmental performance is particularly evident comparing the first two scenarios and becomes smaller when a CO_2 price of 25 €/ton is introduced. From an economic point of view, MG scenarios are *less* sustainable due to the high capital costs of the MG technologies, especially fuel cells. Finally, MG scenarios are more energetically and exergetically efficient because the same electric power and thermal load is satisfied using less energy and exergy. Thus, CHP in the MG produces both heat and power, while in the network electricity is provided by power plants and thermal energy by separate boilers.

4. Conclusions

Using the methodology presented in [5], this paper assesses the economic and environmental sustainability of microgrids in the Northwestern European electricity market. Our analysis suggests that a power network in which MGs and a price on CO_2 emissions are included has a composite sustainability index that doubles the one of a scenario excluding both. The introduction of MGs leads to an improvement in the energetic and exergetic efficiency of the system. However, MGs could also potentially lead to environmental problems if they displace the latest clean technologies (like natural gas combined cycle plants) rather than accelerate the retirement of old technologies (like oil and coal steam turbines), as we observed with the increase in SO_x emissions in our simulations. Future analyses will assess the robustness of our conclusions to different assumptions on market power in the Northwestern European electricity market and on microgrid generation technologies. Since reducing energy consumption is one of the main goals of the EU energy policy and an important tool for reducing carbon emissions, we will also evaluate scenarios involving additional energy conservation efforts.

Nomenclature

Indices of the optimization model

i node in the network

i-k arc linking node i to node k

j company

m voltage loop

Sets of the optimization model

I set of all nodes

J set of aggregate plants, differing in location, ownership, fuel type and cost

J_i set of aggregate plants at node i

M set of Kirchhoff's voltage loops

A_i set of nodes adjacent to node i

M_m ordered set of links i-k in voltage loop m

Parameters of the optimization model

CO_2 CO_2 price, €/ton

L_i power demand at node i, MW

R_{ik} reactance on arc i-k

S_{ikm} ± 1 depending on the orientation of arc i-k in voltage loop m

$Loss_{ik}$ resistance loss coefficient on arc i-k, 1/MW

T_{ik} maximum transmission capacity on arc i-k, MW

MC_{ij} marginal cost for generation at node i and aggregate plant j, €/MWh

E_{ij} CO_2 emission rate at node i and aggregate plant j, ton/MWh

Cap_{ij} maximum generation capacity at node i and aggregate plant j, MW

FOR_{ij} forced outage rate for aggregate plant j

Decision variables of the optimization model

f_{ik} export flow from node i to node k, MW

gen_{ij} generation at node i by aggregate plant j, MW

Technical variables

$\dot{W}$ annual electric power load of the network, MWh

$\dot{Q}$ annual heat load of the network, MWh

η_b efficiency of the boiler

η_e annual energetic electric efficiency of the network

η_{tot} annual energetic total efficiency of the network

ς_e annual exergetic electric efficiency of the network

ς_{tot} annual exergetic total efficiency of the network

ϕ_e exergy to energy ratio of fuels used for electricity generation by the network

$\dot{E}_s^Q$ exergy content of the heat load, MWh

$\dot{E}_{NG}$ exergy flow rate of natural gas, MJ/s

$\dot{M}_{NG}$ mass flow rate of natural gas, kg/s

H_{NG} Lower Heating Value of natural gas, MJ/kg

ϕ_{NG} exergy to energy ratio of natural gas

References

[1] WCED, 1987, Our common future, Report of the UN World Commission on Environment and Development, Oxford University Press, Oxford.

[2] Hobbs, B.F., and Meier, P., 2000, *Energy Decisions & The Environment: A Guide to the Use of Multicriteria Methods*, Kluwer Academic Publishers, Boston.

[3] Lebre LaRovere, E., et al., 2010, Sustainable expansion of electricity sector: Sustainability indicators as an instrument to support decision making, Renewable and Sustainable Energy Reviews, 14, pp. 422–429.

[4] Giannantoni, C., et al., 2005, Multicriteria approach for the improvement of energy systems design, Energy, 30(10), pp. 1989-2016.

[5] Frangopoulos, C.A, and Keramioti, D.E., 2010, Multi-criteria evaluation of energy systems with sustainability considerations, Entropy, in press.

[6] Zvolinschi et al., 2007, Exergy sustainability indicators as a tool in industrial ecology, Journal of Industrial Ecology, 11(4), pp.85-98.

[7] Hobbs, B.F., and Rijkers, F.A.M., 2004, Modeling Strategic Generator Behavior with Conjectured Transmission Price Responses in a Mixed Transmission Pricing System I: Formulation, IEEE Trans. Power Systems, 19(2), pp. 707-717.

[8] http://www-01.ibm.com/software/integration/optimization/opl-cplex/analyst-studio/

[9] http://www.ecn.nl/fileadmin/ecn/units/bs/COMPETES/cost-functions.xls

[10] Hobbs, B.F., et al., 2008, "Improved Transmission Representations in Oligopolistic Market Models: Quadratic Losses, Phase Shifters, and DC Lines," IEEE Trans. Power Systems, 23(3), pp. 1018-1029.

Assessment of Acceptable Swiss Post-2012 Climate Policies with a CGE-Energy Coupled Model

André Sceia[a], Juan-Carlos Altamirano-Cabrera[a], Marc Vielle[a,b], and Nicolas Weidmann[c]

[a] *Economics and Environmental Management Laboratory - Swiss Federal Institute of Technology at Lausanne (EPFL), Lausanne, Switzerland*
[b] *Toulouse School of Economics (LERNA), Toulouse, France*
[c] *Energy Economics Group - Paul Scherrer Institute (PSI), Villigen, Switzerland*

Abstract: In the framework of the revision of the Swiss CO_2-Law and in view of the international negotiations that will take place at the next Conference of the Parties to the United Nations Framework Convention on Climate Change, the Federal Office for the Environment (FOEN) has proposed a set of instruments and two levels of abatement to define the Swiss climate policy for the post-2012 period. The proposed policies are the results of a consultation procedure that took place at the beginning of 2009 and allowed major stakeholders and lobbies to defend their views. Using a hybrid model, we evaluate two proposed scenarios at the 2030 horizon. We find important disparities in the prices of carbon faced by the different economic sectors and higher welfare costs than those that would be triggered by a uniform carbon tax.

Keywords: Climate policy, Environmental taxation, Hybrid modeling, Transport, Residential, Welfare economics.

1. Introduction

Switzerland represents a small share of global greenhouse gas (GHG) emissions but is strongly engaged in meeting its abatement objectives and has proved to be at the forefront of international climate negotiations. With 7.6 million inhabitants, GHG emissions amounted 51.3 million ton of CO_2 equivalent ($MtCO_2eq$) in 2007, slightly less than the 1990 level (52.7 $MtCO_2eq$). Since electricity is largely produced from hydro (56%) and nuclear (39%), transportation and housing are responsible for the major part of GHG emissions.

In the framework of the revision of the Swiss CO_2 Law for the post-2012 period and in view of the 15th Conference of the Parties to the United Nations Framework Convention on Climate Change, the Federal Office for the Environment has proposed a set of instruments and two levels of abatement to define the Swiss climate policy for the post-2012 period. As it is the case in the European Union, a first scenario is envisaged for the case where the climate negotiations would reach a moderate global abatement and a second more stringent scenario could be used in the case where the rest of the world would commit to strong emissions reductions. A detailed description of the envisaged targets and instruments is presented in section 4.

In order to adequately evaluate the post-2012 Swiss climate policies, to model all the envisaged instruments and to consider the influence of the choices that will be made in the rest of the world, we have coupled the GEMINI-E3 model, a worldwide computable general equilibrium (CGE) model, with MARKAL-CHRES and MARKAL-CHTRA, two energy models describing respectively the Swiss residential and transportation sectors. This paper builds on the work undertaken in [1] and uses a new coupling approach to assess the climate policies currently under discussion.

This paper is organized as follows: section 2 briefly presents the methodology; section 3 describes the baseline scenario. The policy scenarios and their respective results are presented respectively in sections 4 and 5, whereas section 6 concludes.

2. Methodology

We use an aggregated version of GEMINI-E3, a dynamic-recursive CGE model with a highly detailed representation of indirect taxation, that represents the world economy in 6 regions and 18 sectors based on the year 2001. We define the regions as follows: Switzerland (CHE), European Union (EUR), other European and Euro-asian

Corresponding Author: Vielle Marc, Email: marc.vielle@epfl.ch

countries (OEU), Japan (JAP), USA, Canada, Australia and New Zealand (OEC) and other countries, mainly developing countries (DCS). To complement the top-down model GEMINI-E3, we use the bottom-up models MARKAL-CHRES and MARKAL-CHTRA, which are energy models describing the Swiss residential energy system and the Swiss transportation energy system. They are sub-modules of a larger Swiss MARKAL model developed at the Paul Scherrer Institute. The models contain respectively 173 and 184 technologies using different energy sources (coal, oil, diesel, gasoline, gas, electricity, wood, pellets and district heat). Both MARKAL models use a 3.5% discount rate. For a more detailed description of the models, see Schulz [2].

We have used a soft-link method to couple the two models: we keep GEMINI-E3 and both MARKAL models in their complete form and dynamically couple them. Compared to previous studies [1,3], our coupling procedure has been amended to allow GEMINI-E3 to calculate taxes according to given sectoral emission profiles. The models are run alternatively while the coupling variables are exchanged between the models, until a defined threshold on the variation of the taxes is reached. The coupling procedure also takes into account a building improvement program.

3. Baseline Scenario

The GEMINI-E3 model with the disaggregated transportation sectors, once linked to the MARKAL-CHRES and MARKAL-CHTRA models and calibrated to Swiss GDP and population figures, calculates a baseline scenario until 2030. The baseline oil prices are also a key assumption for the model. We use a smoothed series of historical prices and keep the oil prices at 50 USD2008/bbl until 2020. The price of oil is then assumed to grow linearly to 100 USD2008/bbl in 2050, thus reaching 66 USD2008/bbl in 2030. In our baseline scenario, the world GHG emissions reach a little more than 55 $GtCO_2eq$ by 2030, which is in line with OECD [4]. On average, the Swiss baseline GHG emissions will decrease annually by 0.6%. The calibration of the baseline emissions is based on Swiss Federal Office of Energy [5]. Scenario I.A, which assumes the continuation of present climate policies and the construction of new nuclear power plants to replace those that will be phased out over the coming decades.

4. Policy Scenario

4.1. Swiss scenarios

Two scenarios are under consideration, a first one where international agreements target rather limited abatement, and a second one where stronger abatement is agreed upon by all world nations. Since no specific threshold allowing to differentiate the two cases has yet been defined, we define two sets of international abatement targets (see section 4.2) using expert judgment and the scenarios of the Energy Modeling Forum [6].

The envisaged Swiss post-Kyoto policies, is described in detail in table 1, the policies divide the economy in four parts, which will face different carbon prices.

Table 1: Swiss emissions targets (% of 1990 emissions)

	Scenario 1		Scenario 2	
	2020	2030	2020	2030
ETS[a] Certificates purchase cap[b]	-1.75 % p.a. 40%		-2.9 % p.a. 50%	
Transport[c] Technical regulations on cars[d]	-25% target on average emissions of new cars	-42%	-40%	-60%
Combustible fuels[c] Building improvement program[e] (2010-2020)	-25% 200 Mio. CHF p.a. [f]	-33%	-35%	-50%
Certificates purchase cap[c] (% of 1990 GHG)	9%	14%	14%	21%

[a] Starts in 2013 on the basis of the average emissions in the period 2008-2012 - [b] The cap on the purchase of certificates in the ETS sectors increase linearly over the periods 2010-2020 and remains unchanged from 2020-2030 - [c] The values of the objectives increase linearly over the periods 2010-2020 and 2020-2030 - [d] Modeled as a ban on standard cars as of 2015 [e] Modeled as a discount on refurbishment costs (energy saving technologies) - [f] 130 Mio. USD_{2008}

4.1.1. Taxes, levies and CO_2 markets

The energy intensive (ETS) sectors will participate as of 2013 in an ETS similar to the European Union (EU) ETS and they will be allowed to purchase a part of the required abatement through the purchase of certified emissions reductions (CER) purchased abroad. The transport sectors are potentially affected by two instruments. Firstly, as of 2010, the importers of transportation fuels will be required to offset a part of the transport emissions through the purchase of CERs. Assuming that the additional costs due to the purchase of the certificates will be passed on to the consumers through an increase in the price of transport fuels, we have modeled this through the

implementation of a levy (tax), whose revenues are sufficient to purchase the required amount of foreign certificates. Secondly, in order to ensure a minimum domestic abatement, the sum of the purchases from the ETS and transport sectors is limited. Therefore, if the cap on the purchase of CERs is reached and taking into account that the ETS sectors have the priority in the purchase mechanism, a CO_2 tax will be introduced on transportation fuels to ensure achieving the abatement target of the transportation sectors. As for the current CO_2-Law, combustible fuels will continue to be subject to a tax. Nevertheless an exemption will be introduced for those sectors taking part in the ETS. Finally, air transport is not subject to any constraint. In addition two specific programs will also contribute to the overall Swiss abatement effort: an average emission target for the CO_2 emissions of new passenger cars and a building improvement program. In order to evaluate the relative efficiency of the envisaged scenarios, we have also simulated the implementation of a uniform CO_2 tax, applied to the whole economy except from air transport, aimed at achieving equal domestic and total reductions.

4.1.2. Car regulations

Both policies under consideration envisage an average emission target value for the CO_2 emissions of new passenger cars, with the same requirements as those that will be imposed in the EU. The average emissions of new cars will be limited to 130 gCO_2/km as of 2012 and to 95 gCO_2/km in 2020.

Despite the technological richness of the MARKAL-CHTRA model, the descriptions of the available and future vehicles does not go into sufficient details to model precisely this aspect of the policy. Instead, as of 2015, we have implemented a technical restriction on the purchase of the less efficient diesel and gasoline personal cars (5.4 l/100km and 6.1 l/100km). This leaves the following choices to the consumers: gas internal combustion engines (ICE) cars (8.2 l/100km), efficient diesel and gasoline ICE cars (5.1, 5.8 l/100km), as well as hybrid cars using gas, diesel and gasoline (6.2, 4.2, 4.9 l/100km). As MARKAL models are perfect foresight models, due to anticipations, the restrictions have an effect before their implementation and, already in 2013, one half million tons of CO_2 are avoided. The abatement achieved by this measure exceeds 1.1 $MtCO_2$ in 2020, which represents respectively 26% and 18% of the required transport sector abatement efforts in scenarios 1 and 2.

4.1.3. Building improvement program

In the period 2010-2020, the revenue of the tax on combustible fuels will be affected up to one third of its values or maximum 200 Mio. CHF to a building improvement program, and the rest will be redistributed to households and economic sectors through social security. The building improvement program consists of financial help from the government to undertake refurbishments of houses and buildings with the scope of improving their energy efficiency. The use of a hybrid model with a bottom-up residential sector allows for modeling endogenously this building improvement program. We have implemented a procedure which determines a reduction in the investment prices of energy saving technologies (e.g. insulation) as well as efficient technologies such as heat pumps or solar. This affects relative prices in MARKAL-CHRES and ensures that households increase their investments in these technologies. The price rebate is calculated so that the difference between the real costs of the investments and the actual costs borne by the households after the rebate is equal to the 200 Mio. CHF available for the program. In GEMINI-E3, we have considered that the government spends this amount in constructions (services sector). When analyzed independently from all other instruments, we find that the building improvement program would save annually up to 680'000 tCO_2 by 2020, representing 23% and 15% of the abatement required in the residential sector in scenarios 1 and 2 respectively, at a shadow price of 191 USD2008/tCO_2eq.

4.2. International scenarios

In this paper, we consider two cases, where two different international agreements are agreed upon and enforced. The proposed target for the "low" and "high" scenarios for 2020 and 2030 are presented in Table 2. The "low" scenario is used to analyze the first Swiss scenario, where a weak international agreement is reached, whereas the "high" scenario is used for the second Swiss scenario, where all countries more actively participate in the global effort. For the sake of simplicity, we assume that all regions, except Switzerland, fully participate in a global emissions

cap and trade system providing a single world price for carbon. When no binding target is defined for a region, we cap its emissions to the baseline emissions in order to avoid that the overall effect of the policies is jeopardized by carbon leakage.

Table 2: International emissions targets (% of 2001 level)

Target year	2020		2030	
Scenario	Low	High	Low	High
CHE	-22	-32	-30	-46
EUR	-20	-30	-30	-45
OEC-JAP	-20	-30	-30	-47
OEU	-[a]	-10	-10	-23
DCS	-[a]	-[a]	0[b]	-13[b]

[a] baseline emissions [b] % of 2020 emissions

5. Results

5.1. Scenario 1

5.1.1. Carbon prices and emissions reductions

Tables 3 and 4 present respectively the taxes that allow to achieve the objectives and the detailed emission abatements in the various parts of the Swiss economy. As expected, the levy collected on transport fuels to offset the emissions of the transport sector is small in view of the low price of foreign CO_2 certificates. The additional combustible fuel tax is significant as it would have to reach approximately 89 USD2008/tCO2eq by 2020 to obtain 25% abatement, despite the technical possibilities offered by MARKAL-CHRES and the building improvement program. The price of the allowances in the ETS market remains rather low in view of the fact that the baseline abatement in those sectors is quite pronounced already, leaving small additional abatement to meet the target. As a consequence, the ETS carbon price equals the international price of CERs.

Table 3: Swiss environmental taxes and prices of certificates/allowances in scenario 1

In USD2008/tCO$_2$eq	2013	2015	2020	2030
Transport fuels levy	0.04	0.1	1	3
Combustible fuels tax	30	42	89	24
ETS certificate price	1	1	2	8
World certificate price	1	1	2	8
Uniform tax	*7*	*7*	*7*	*8*

The uniform tax presented in the last line of Table 3 allows for an equivalent total CO_2 abatement as the combination of the tax, levy and ETS markets. It is determined with a cap on the purchase of CERs set at the level of one reached with the combination of the instruments and maintaining both the building improvement program and the technical regulations on cars.

Table 4: Variation of the Swiss GHG emissions (% of 1990)

		Scenario 1		Scenario 2	
Emissions in 1990		2020	2030	2020	2030
Transport	*12.3*	2	-3	2	-3
incl. CER		-25	-42	-40	-60
-Households	*8.4*	5	5	5	6
-Transport sectors	*3.9*	-5	-19	-6	-21
Residential	*11.3*	-39	-47	-53	-75
ETS Sectors	*5.4*	-18	-26	-20	-32
incl. CER		-23	-35	-30	-48
Other sectors	*15.5*	-10	-19	-15	-23
-Air transport	*4.3*	-5	-17	-5	-16
-Other	*11.2*	-13	-20	-19	-26
Domestic CO_2	*44.6*	-15	-23	-21	-32
Domestic CO_2 (wo Air trans.)	*40.2*	-16	-23	-22	-33
-Combustible fuels	*22.5*	-26	-34	-36	-51
Other GHG	*8.2*	-10	-10	-11	-11
Domestic GHG emissions	*52.8*	-14	-21	-19	-28
Net GHG emissions	*52.8*	-21	-31	-30	-43

[a] in MtCO2eq

The figures relative to abatement of the emissions due to combustible fuels and those from the residential sector in Table 4 suggest that modeling the use of combustible fuels in commercial buildings with an energy-systems model, as it is the case in the residential sector, would lower the estimation of the combustible fuels tax. Indeed, it seems reasonable to assume that technologies available for residential buildings also be used for commercial buildings and that the tax should trigger a similar magnitude of abatement. Even if a part of the difference can be explained by the implementation of the building improvement program which triggers an abatement in the residential sector of 0.6 $MtCO_2$ and the fact that some industrial processes are still part of the other sectors, the effect of the tax on the other sectors (-20%) seems rather limited when compared to the reductions in the residential sector (-47%).

Both the transport and the ETS sectors can purchase CERs within predefined limits. Table 5

shows that in the first scenario the ETS sectors purchase a very limited amount of CERs to reach their target. In the transport sectors the small amount levied on fuel imports allows for the purchase of sufficient certificates to meet the 25% abatement target, but it is mainly the introduction of the regulations on cars that triggers the domestic abatement. The purchase cap on CERs is not reached, indicating that the policies ensure sufficient domestic abatement without having to impose an additional tax on transport fuels.

Table 5: Swiss purchase of certificates ($MtCO_2eq$)

	Scenario 1		Scenario 2	
	2020	2030	2020	2030
Transport	3.3	4.8	5.1	7.0
ETS	0.3	0.5	0.5	0.9
Total	3.5	5.3	5.6	7.8
Purchase cap	4.8	7.6	7.4	11.3
%1990 GHG emissions	9%	14%	14%	21%

5.1.2. Economic and welfare impacts

Table 6 presents the impacts of scenario 1 on welfare (households' surplus) as well as its decomposition into the gains and losses of the terms of trade (GTT), the trade of emissions permits and the deadweight loss of taxation (DWL). Furthermore, it presents the impacts of the uniform CO_2 tax that would allow for equivalent CO_2 reductions, while respecting a minimal share of domestic abatement equal to the one achieved in scenario 1. The welfare components are presented as a percentage of total households' consumption (HC). In the first scenario, the impact of the climate policies on welfare is above a third of a percentage point. The DWL is the main element influencing the welfare as both the GTT and the capital transfers due to the purchases of permits remain limited.

The numbers in the table 6 also show that if a uniform CO_2 tax is used instead of the combination of instruments, the resulting welfare effects are smaller. The difference between the two welfare effects can be seen as the loss of efficiency caused by the differentiation of the carbon price among sectors.

As expected, the overall impact of climate policies is negative for both production and consumption. Nevertheless, some sectors are more affected than others and some even benefit from the policies. The most affected sector is the refined petroleum sector, whose demand from households drops by 29% in 2030. Such structural changes are obviously the aim of climate policies. In this scenario, the gas sector turns out to be the economically viable alternative to petroleum products. The households' consumption of gas increase (66%) is obviously supported by a strong increase of imports (39%). The electricity sector also strongly benefits from the policies and sees its production increase by almost 4% in 2030. In view of the small transport fuels levy, as expected, most transport sectors are only slightly negatively affected. The rail and road passenger transport sectors do nevertheless slightly benefit from a slight reduction in personal car usage. Furthermore, pipeline transport production increases by up to 5.8% as it benefits from the increase in gas consumption.

Table 6: Economic impacts in Switzerland (% of HC)

	Scenario 1		Scenario 2	
	2020	2030	2020	2030
Surplus	-0.33%	-0.34%	-0.49%	-0.47%
GTT	0.06%	-0.03%	0.14%	0.09%
Sales of permits	0.00%	-0.01%	-0.01%	-0.08%
Deadweight Loss	-0.39%	-0.29%	-0.62%	-0.47%
in case of uniform tax				
Surplus	*-0.26%*	*-0.34%*	*-0.39%*	*-0.43%*
GTT	*-0.04%*	*-0.08%*	*0.09%*	*0.06%*
Sales of permits	*0.00%*	*-0.02%*	*-0.01%*	*-0.08%*
Deadweight Loss	*-0.21%*	*-0.24%*	*-0.47%*	*-0.41%*

It is worthy to say a word about international results despite the fact that they are not directly comparable with those of Switzerland. The first scenario assumes that OEU and DCS are not subject to emissions caps (other than their baseline emission) before 2020. As a consequence, both of these regions are in a position to sell CERs and have therefore positive welfare effect. The effects in other regions are smaller than in Switzerland, as the price of carbon is equal across sectors, no minimal share of domestic abatement is imposed and all GHGs are included in policies. In view of the small price of world certificates, the Swiss welfare losses are mainly due to the combustible fuels tax which is a purely national measure and is therefore not connected to the international emissions certificates market (see Fig. 4).

5.1.3. The residential and transport sectors

The coupled MARKAL-CHRES and MARKAL-CHTRA models allow us to analyze the technical implications of the scenarios more in detail.

Fig. 1 shows that in the residential sector the combination of the combustible fuel tax and the building improvement program reduce both the heating oil and gas usage by respectively 14% and 66% compared to the baseline in 2030. Except in existing multi-family houses where the use of heating oil remains predominant, electric heat pumps become the predominant technology for space heating, which triggers the major part of the increase of electricity use (21% compare to the baseline). The instruments also trigger an increase of 9% in the use of insulation and other energy saving technologies.

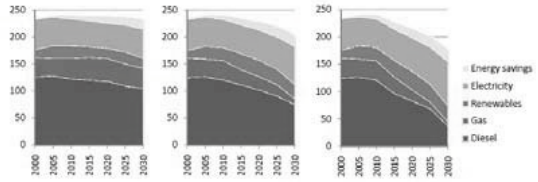

Fig. 1: Baseline/Scenario 1/Scenario 2 Fuel mixes in the residential sector (PJ)

Fig. 2 presents the passenger cars usage by car types in billion vehicle kilometers per year (bvkm/a) and shows that the car regulations have a significant impact on the composition of the vehicle fleet. The increase of gas powered vehicle is responsible for the increase of gas consumption by households as it largely compensates the decrease observed in the residential sector. The regulations also trigger an increased penetration of all types of hybrid car.

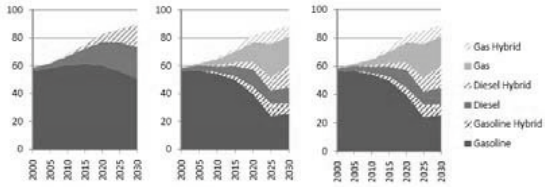

Fig. 2: Baseline / Scenario 1 / Scenario 2 Use of personal cars by types (bvkm/a)

5.2. Scenario 2

The second scenario targets a total reduction of GHG emissions by 30% in 2020 and 44% in 2030 using the instruments presented in Table 1.

5.2.1. Carbon prices and emissions reductions

Tables 7 and 4 present respectively the taxes that allow to achieve the objectives of scenario 2 and the detailed emissions abatements in the various parts of the Swiss economy. The levy collected on transport fuels, despite being up to five time higher than in the first scenario, remains at very reasonable levels as the price of foreign emission certificates remains low. Such a levy would trigger an increase in the price of gasoline of approximately 1.2 cents per liter. The combustible fuels tax is expected to increase strongly if an abatement of 35% by 2020 is desired.

Table 7: Swiss environmental taxes and prices of certificates/allowances in scenario 2

In USD2008/tCO$_2$eq	2013	2015	2020	2030
Transport fuels levy	0.2	1	2	18
Combustible fuels tax	49	74	190	134
ETS certificate price	2	3	6	30
World certificate price	2	3	6	30
Uniform tax	*31*	*47*	*103*	*82*

Indeed, achieving such a strong domestic abatement over a single decade would require significant incentives and despite the building improvement program a tax reaching 190 USD2008/tCO$_2$ would be necessary. As in the first scenario, the price of allowances in the ETS market remains rather low, in view of the moderate abatement compared to the baseline and because of the possibility to undertake 50% of this abatement abroad through the purchase of cheap emission certificates, in particular until 2020. By 2030 the certificates would reach 30 USD2008/tCO$_2$. Fig. 3 presents the domestic emissions for the various sectors and confirms that the share of emissions caused by motor fuels increases significantly from 23% in 1990 to 29% in 2030. Combustible fuels, ETS sectors excluded, see their share shrink from 43% to 36%.

The tax on combustible fuels seems particularly high when compared to the uniform tax that would allow for an equal domestic and total reduction of emissions and might trigger questions on the social equity aspects of the envisaged policies. Fig 4 shows clearly that the transport sector contributes greatly to achieving the overall objective in both scenarios, but to a very large extent through the purchase of CERs. The tax on combustibles fuels achieves 65% of the domestic abatement in 2030 and when adding the contribution of the building improvement program this share rises to 75%. When considering the total emissions reductions, 77% is achieved by the combustible fuels tax and the purchases of CER by the transport sector.

Regarding the purchase of emission certificates by the transport and the ETS sectors, table 6 shows

that, similarly to the first scenario, the overall emission cap is not reached and as a consequence no additional tax on transport fuels is required. The purchase of foreign emission certificates by the transport fuel importers financed by the levy reaches 7.8 tCO_2eq in 2030, which represents approximately 15% of 1990 emissions. As in the previous scenario the domestic abatement in the transport sector is attributable to the regulations on passenger cars rather than to the small increase of transportation fuels' prices.

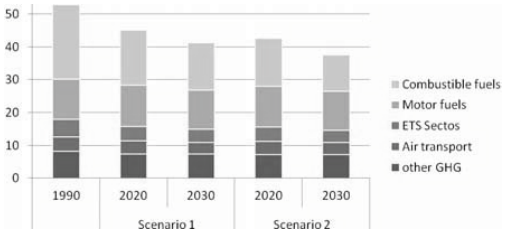

Fig. 3: Domestic Swiss GHG emissions (MtCO2eq)

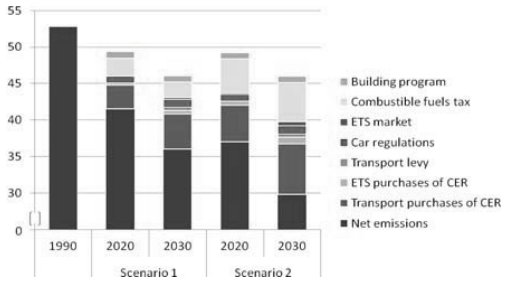

Fig. 4: Net Swiss GHG emissions, CER Purchases and abatements by responsible instrument (MtCO2eq)

5.2.2. Economic and welfare impacts

Table 6 presents the impacts of scenario 2 on welfare. As expected, the impact on welfare is more substantial than in the first scenario. The DWL reaches 0.6% of households' consumption in 2020 and the gains of the terms of trade are not sufficient to offset it. Again, the comparison with the uniform tax case confirms that setting up instruments which lead to differentiated marginal costs of abatement is suboptimal in terms of welfare. In view of the low prices of foreign emission certificates, the influence of their purchase on welfare remains low.

As expected, the overall impact of climate policies on both production and consumption is negative and stronger than in the previous scenario. The strongest effect is on the petroleum products sector, which is significantly affected (-18% of production in 2030), mainly because of a strong decrease in final consumption (-46%). When comparing with the previous scenario, with higher taxes gas turns out to be less of a viable substitute to petroleum products and therefore the substitution toward electricity is stronger. Gas consumption nevertheless increases by more than 50% and electricity consumption jumps by 40%. The electricity sector is the major beneficiary in this scenario as it increases its production by 6.7% in 2030. Again, the air transport sector is very slightly affected as it does not face any carbon price.

From the international perspective, the second scenario assumes stronger abatements and international agreements that would involve in the long run all regions with specific emissions reductions. By 2020, nevertheless, it is expected that DCS would only be restricted to their baseline emissions and, as a consequence, it is the only region selling large amounts of CER and therefore enjoying welfare gains. Switzerland is more affected than other regions before 2020, with the exception of OEU which is extremely sensitive to climate policies in view of its energy and energy intensive goods exports. In 2030, EUR and OEC face stronger welfare effects, due in particular to the greater baseline GDP growth that is expected in those regions.

5.2.3. The residential and transports sectors

Fig. 1 shows that the high tax on combustible fuels combined to the building improvement program reduces the use of gas and diesel in the residential sector by respectively 90% and 57% in 2030 compared to the baseline. The use of electric heat pumps, which have an energy efficiency three to four time superior to conventional diesel boilers, allows to compensate a large share of the final energy demand and increases the residential use of electricity by 50%. The rest of the final energy is compensated by an increase of 44% in the use of renewables and an additional installation of energy saving technologies (19%).

Fig. 2 show that only the car regulation influences the passenger cars fleet composition. Indeed, the limited amount of transport levy does not have further influences. The use of the uniform tax does not further affect the passenger cars fleet and has a very limited impact of other parts of the transport

sector, which is very inelastic over the time horizon until 2030.

6. Conclusions

This study underlines the benefits of the use of coupled model in the framework of the economic assessment of climate policies. Our coupled model simulates all the different policy instruments that are envisaged in Switzerland for the post-Kyoto period endogenously and therefore allows to analyze both envisaged scenarios in different international frameworks. Our simulations show that the policies have moderate economic impacts on the Swiss economy. In the first scenario, the various instruments would trigger a loss of welfare of about a third of a percent in 2020. In the second scenario, the maximum welfare loss would reach half percent in the same period. Furthermore, the welfare costs do not account for the avoided damages due to climate change, the potential adaptation costs or the ancillary benefits such as the avoided local air pollution. Nevertheless, we show that welfare costs of mitigation could be further reduced by introducing a uniform tax.

Two major factors affect the efficiency of climate policies. On the one hand, within a given country, the necessity to differentiate the carbon prices faced by different sectors is generally defended by arguments related to international competitiveness and carbon leakage. In our framework, we show that while ensuring the global emissions abatement levels, thus avoiding leakage, the competitiveness argument does not hold in Switzerland. Indeed, Swiss welfare suffers from the advantage given to transport and ETS industries by the introduction of the diversified instruments and overgenerous caps on CERs purchases. On the other hand, national restrictions on the purchase of CERs are a major factor affecting the efficiency of climate policies but they are necessary from the perspective of international equity. In the Swiss case, all sectors facing the combustible tax are deprived from using any sort of flexibility mechanism, thus increasing the cost of emissions abatement.

Both scenarios trigger an important switch away from petroleum products. In the first scenario, this turns out to be very beneficial for the gas sector that profits from the increased number of gas ICE and hybrid passenger cars. In the second scenario, a doubling of the tax on combustible fuels pushes further toward the use of electricity in the residential sector. Both policies generate gains from the terms of trade but they do not offset the deadweight loss of taxation.

Interestingly, in both scenarios the caps on the purchase of foreign emission certificates are not reached. The implications are twofold. On the one hand, the envisaged tax on transport fuels is not necessary to ensure the minimum domestic abatement and, on the other hand, additional purchases of certificates, particularly in the residential sector, would be possible without jeopardizing the domestic emissions targets.

From the technology perspective, we show that the transport sector is very inelastic to prices and that the car regulations are the only instrument affecting the passenger cars fleet composition. The car regulations are responsible for a strong penetration of gasoline and diesel hybrid cars as well as gas hybrid and conventional cars. As expected, the high taxes in the residential sector trigger a switch away from diesel and gas in favor of renewables and electricity, mainly thanks to the installation of efficient heat pumps.

In conclusion, both scenarios seem realistic and do not have dramatic impacts on the Swiss economy. This is due partly to the fact that in both scenarios the price of foreign emission certificates remains relatively low, allowing for cheap offsetting of Swiss emissions in transport and ETS industries.

References

[1] Sceia, A., et al., 2009, Sustainability, neutrality and beyond in the framework of Swiss post-2012 climate policy. NCCR-Climate Working Papers.

[2] Schulz, T. F., 2007, Intermediate steps toward the 2000 watt society in Switzerland : an energy-economic scenario analysis. PhD thesis, ETH Zürich.

[3] Sceia, A. et al., 2008, Integrated assessment of Swiss GHG mitigation policies after 2012 - focus on the residential sector. NCCR-Climate Working Papers.

[4] OECD, 2008, Environmental Outlook to 2030.

[5] Swiss Federal Office of Energy, 2007, Perspectives énergétiques pour 2035 (tome 1) synthèse. Technical report.

[6] Clarke, L., et al., 2009 International climate policy architectures: Overview of the EMF 22 international scenarios. Energy Economics,

Assessment of Energy Chains for Distributed Generation: Agricultural and Thermoeconomic Analyses within Emilia-Romagna Region

Roberto Bettocchi[a], Claudio Caprara[b], Roberta Martelli[b], Francesca Minarelli[b], Mirko Morini[a], Michele Pinelli[a] and Mauro Venturini[a]

[a] *Engineering Department, University of Ferrara, Italy*
[b] *Agricultural Economics and Engineering Department, University of Bologna, Italy*

Abstract: The process which includes production, collection, carriage and transformation of biomass into renewable fuels and then into energy (both electrical and thermal) involves a large number of decisions to select the most efficient chain. In this paper, the contribution margin of four different energy chains is evaluated both in terms of profits and energy gain per unit of cultivated surface. Four widely cultivated crops in Europe (corn, rapeseed, soybean and sunflower) are considered as feedstock. Four technologies are taken into consideration as conversion plants: (i) anaerobic digestion with internal combustion engines, (ii) direct combustion with Organic Rankine Cycle, (iii) gasification with internal combustion engines, and (iv) straight vegetable oil combustion within internal combustion engines.

Keywords: anaerobic digestion, biomass, combustion, distributed generation, energy crops, gasification, geographical information systems (GIS).

1. Introduction

Recent energy policies tend to encourage increased energy production from renewable sources for environmental, socio-economic and strategic reasons. Among the renewable sources, biomasses play a key role, since they are predictable energy sources. The characteristic of being predictable is an advantage in distributed grid-connected generation where unpredictable renewable energy sources, like solar photo-voltaic and wind, have proved to be critical for network voltage and frequency stability.

Moreover, the increasing interest in using biomass for energy production from agricultural materials depends on various economic, political and environmental factors: the need to diversify and improve energy supply security, reduce greenhouse gas emissions, encourage support income and employment in rural areas and promote the development of local agricultural chains by using raw materials. The policies of European governments focus on the promotion of bioenergy from agricultural sources encouraging the alternative use of lands under set-aside and of lands available after sugar sector restructuration (185,000 ha in Italy).

This paper aims to evaluate the potential of energy conversion of these areas, by considering the Emilia-Romagna region (IT), where the EU sugar reform has made approximately 50,000 ha of land available. Nevertheless, the methodology presented is general and can be extended to other situations.

The analysis is performed by considering some of the main sources of biomass energy from conventional crops (sunflower, rapeseed, soybean and corn) and agricultural residues (corn stalks). The crops under analysis offer high performance in terms of energy production. Moreover, the cultivation of these crops is diffused and well-established in the territories under study.

The potential production and the energy inputs are managed locally in a Geographic Information System (GIS). Then, thermoeconomic analysis is carried out to evaluate the profitability and energy output of four plants fed by the obtained biofuels. Plants are based on conversion technologies (anaerobic digestion, direct combustion, thermochemical gasification, straight vegetable oil combustion) consolidated for biomass-fed cogeneration. Finally, sensitivity analysis is performed by representing the profitability as a

Corresponding Author: Mirko Morini, Email: mirko.morini@unife.it

function of the electrical energy price and biomass cost.

2. Methodology

2.1. Agricultural analysis

Integration among all the information map layers is achieved in a GIS environment. In particular, the software MapInfo™ 8.0 was used for this territorial analysis. Vector cartography, supplied by the Cartography Service of the Emilia-Romagna Region, was based on Geodetic Coordinates on WGS 84. The administrative boundaries map (1:5,000), land use map (1:25,000) and soil type map were the considered territorial basis. The intersection of these maps defines homogeneous areas A_k used as a basis for all elaborations. Only homogeneous areas where land use attribute is "arable land" will be considered.

Alphanumerical information refers to data on energy crops calculated as an average of a ten-year yield, and on crop distribution in each Municipality [1,2].

2.1.1. Input calculation

Calculation of all energy inputs [3-8] necessary for crop production in a generic k-th area results from Eq. (1):

$$Ei_k = Eic_k + Eit_k + Eip_k, \quad (1)$$

where:

$$Eic_k = A_k \cdot (E_{rm} + E_{ao}), \quad (2)$$

Eic_k represents the energy input corresponding to agricultural activities. A_k area is the smallest area where all the elaborations are made. The first contribution (E_{rm}) represents the energy cost for raw materials (e.g. chemicals, fertilizer, etc.). The second contribution (E_{ao}) represents the energy cost for agricultural operations and fuel.

The term Eit_k is the energy input for transport of feedstock from the field to the transformation plant. This parameter is not calculated since this study focuses on the energy consumption of agricultural activities and conversion systems.

The term Eip_k represents the energy input for energy crop transformation. This term is taken into consideration only for oil extraction, while, for the other chains, it is embodied in the energy production plant analysis as a conversion efficiency.

The assessment of economic input is computed by estimating direct and indirect costs. The computation of such costs follows a set methodology known as cost of crop production given by the sum of all costs involved in crop cultivation.

2.2. Thermoeconomic analysis

2.2.1. Energy balance

The analysis of biomass transformation processes and of energy systems is performed by adopting a systemic approach.

$$P_{bf} = \eta_c \cdot Y \cdot m_b, \quad (3)$$

$$P_{el} = \eta_{el} \cdot P_{bf}, \quad (4)$$

$$P_{th} = \eta_{th} \cdot P_{bf}, \quad (5)$$

Equation (3) represents the biomass to biofuel transformation process (or biomass to heat in case of combustion).

The parameter Y can be considered as the energy potential of the biomass: i.e. the biomass lower heating value (LHV) in the case of thermochemical conversion or biogas LHV multiplied by biogas yield in the case of anaerobic digestion. The term η_c represents the efficiency of the conversion process with respect to the available biomass energy.

The values of the two efficiencies η_{el} and η_{th} in Eqs. (4) and (5), which represent the net electrical and thermal efficiency respectively, depend on the energy system under consideration and are considered at nominal conditions. So, they do not depend on ambient conditions and do not take into account load variation. It should be noted that they take both non-recoverable power losses and self-consumed power into account (e.g., plant auxiliaries).

2.2.2. Economics

The economic analysis is based on the Net Present Value (NPV) defined in Eq. (6)

$$\mathrm{NPV} = -I + \sum_{i=1}^{N} \frac{F_i}{(1+r)^i}, \quad (6)$$

where I is the investment cost, i.e. the total cost of the plant, F_i is the cash flow of the i-th year, N is the number of years and r is the discount rate in direct calculations and the Internal Rate of Return (IRR) in indirect calculations.

For the calculation of cash flow only electrical and thermal energy sales are taken into account as revenues. Biomass purchasing, plant operation and maintenance, and plant personnel are considered as a source of cost.

Interest and income tax are also taken into consideration. To calculate the income, a fixed amortization rate is used.

3. Assumptions

3.1. Agricultural analysis

In this paper economic input is calculated by referring to a medium size farm of 30-40 ha of which 20 ha are dedicated to energy crop production. In this analysis, labor and mechanical operations have been considered as outsourced factors, in order to obtain a more accurate assessment of effective costs.

Corn, rapeseed, sunflower and soybean crops are chosen for the analyses presented in this paper since they offer good performances in terms of energy production. Moreover the cultivation of these crops is diffused and well-established in the Emilia-Romagna Region.

The assessments are based on estimated average energy-crop yields of historic values extracted from ISTAT survey [2] and referring to the Emilia-Romagna Region [1]. Two alternative agricultural system approaches are reported in Tab. 1 for each crop production: high input (HI) and low input (LI). High input is the conventional type of agriculture, while low input is a methodology aimed at reducing machinery consumption and fertilizer use.

Table 1. Crop yields.

	Seed yield [t/ha]		Oil/seed [%]
	LI	HI	
Sunflower	2.7	2.9	48
Rapeseed	3.2	3.5	40
Soybean	3.0	3.2	17
	Yield [t/ha]		
Ensiled Corn	45	55	
Corn Stalk	4.5		

3.2. Thermoeconomic analysis

Four different technologies are taken into consideration for power generation: anaerobic digestion (AD) with internal combustion engine (ICE), direct combustion (DC) coupled with an organic Rankine cycle (ORC) turbogenerator, thermochemical gasification (TCG) with ICE and straight vegetable oil combustion (SVOC) in ICE.

Plant size is chosen to be representative of the most diffused plants for biomass-fed distributed combined heat and power generation for each technology.

For all the analyzed cases it is assumed that

- the price of electrical energy is equal to 280 €/MWh, which corresponds to the feed-in tariff granted by Italian law as an incentive to green energy production from biomass in a plant characterized by an electrical power lower than 1 MW;
- the price of thermal energy is equal to 25 €/MWh. This value corresponds to the cost of producing thermal energy alone, by using natural gas (current market price) for industrial purposes;
- the number of years N in Eq. (6) is equal to 15, since this is the period for which, at present, Italian law grants incentives;
- the value of discount rate r in Eq. (6) is 7 %;
- investment is considered to be paid by means of a loan (interest rate and payment time equal to 5 % and 5 years, respectively);
- personnel costs are equal to 40 k€/yr (i.e., a dedicated worker);
- the yearly amortization rate is equal to 9 %.

3.2.1. Anaerobic digestion

Biological conversion of biomass to biogas (a mixture of methane and carbon dioxide) and then to electrical and thermal energy has received increasing attention over the last two decades [9,10]. This technology is now widely diffused, in particular in farm-size plants where biomass from dedicated crops (e.g., ensiled corn as in this paper) is co-digested with cattle manure. This practice improves the methane production of anaerobic digestion by adjusting the C/N ratio [11].

Table 2 reports the assumptions for this plant. It can be noted that tax rate is assumed equal to 0 % since, also for farm-related activities, only the landlord income tax is due. In this case the efficiency η_c is assumed equal to 1 since it can be considered embodied in the biogas yield (which is a weighted average value of the yields of ensiled corn, up to 200 Ndm^3/kg, and cattle manure, up to 50 Ndm^3/kg).

Table 2. Assumptions for AD with ICE.

Economics			
Investment I	0.94	M€	[12]
Maintenance cost	35	€/MWh	[12]
Tax rate	0	%	
Energy			
Net electrical power P_{el}	0.2	MW	
Electrical efficiency η_{el}	21.4	%	
Annual working hours	7500	hr/yr	[12]
Biomass			
Ensiled corn/cattle manure	15.4	%	
Biogas yield	53.4	Ndm^3/kg	
Biogas LHV	23	MJ/Nm^3	

3.2.2. Direct combustion

Distributed cogeneration based on biomass direct combustion could be performed by (i) steam power plants or (ii) ORC turbogenerators. The latter option is chosen since the absence of high pressure steam in this type of plant does not require a skilled boiler worker. The assumptions for this case are resumed in Tab. 3. Thermochemical conversion processes (i.e. combustion, gasification and pyrolysis) need dry feedstock (humidity lower than 30 %). For this reason, corn stalks are chosen.

Table 3. Assumptions for DC with ORC.

Economics			
Investment I	4.8	M€	[13]
Maintenance cost	7	€/MWh	
Ash disposal cost	75	€/t	
Tax rate	37.5	%	
Energy			
Net electrical power P_{el}	0.95	MW	
Net thermal power P_{th}	4.1	MW	
Electrical efficiency η_{el}	18.5	%	
Thermal efficiency η_{th}	79.8	%	
Boiler efficiency η_c	88	%	
Annual working hours	7500	hr/yr	[13]
Biomass			
Corn stalk LHV Y	18.17	MJ/kg	[14]
Ash/biomass	2.3	% w/w	[14]

3.2.3. Termochemical gasification

Thermochemical gasification consists of a partial oxidation of the biomass. The product is a gaseous fuel, i.e. a mixture of carbon monoxide and hydrogen. The use of downdraft gasifier for wood chip is well-established. Nevertheless, some studies deal with the use of this technology for residues such as corn stalks [14,15] or sunflower and soybean residues [16]. The assumptions are resumed in Tab. 4 for the case of a gasification plant coupled with a fleet of ICEs.

Table 4. Assumptions for TCG with ICE.

Economics			
Investment I	5.5	M€	[17]
Maintenance cost	50	€/MWh	[17]
Char disposal cost	75	€/t	
Tax rate	37.5	%	
Energy			
Net electrical power P_{el}	0.9	MW	
Net thermal power P_{th}	1.1	MW	
Electrical efficiency η_{el}	25	%	
Thermal efficiency η_{th}	31	%	
Gasifier efficiency η_c	75	%	
Annual working hours	6500	hr/yr	[17]
Biomass			
Corn stalk LHV Y	18.17	MJ/kg	[14]
Char/biomass	15	% w/w	

3.2.4. Straight vegetable oil combustion

Straight vegetable oils have been used as fuel in the diesel engine since its invention. This type of plant is very similar to the fossil fueled one: it only differs in the fact that vegetable oil has to be heated before ignition in order to reduce its high viscosity [18]. The assumptions for this case are resumed in Tab. 5. It should to be underlined that since no transformation process is included in the plant, η_c can be considered equal to 1 (seed pressing is assumed to be outsourced and it is considered as an extra energy and economic cost). Moreover, although the different oils (rapeseed, soybean and sunflower) have different LHV in the range 37-39 MJ/kg [18], a mean reference value of 38 MJ/kg is assumed.

Table 5. Assumptions for SVOC in ICE.

Economics			
Investment I	0.54	M€	[17]
Maintenance cost	26	€/MWh	[17]
Tax rate	37.5	%	
Energy			
Net electrical power P_{el}	0.42	MW	
Net thermal power P_{th}	0.40	MW	
Electrical efficiency η_{el}	40	%	
Thermal efficiency η_{th}	38	%	
Annual working hours	8000	hr/yr	[18]
Biomass			
Seed pressing cost	31	€/t	[19]
Seed pressing energy	350	MJ/t	[19]
Vegetable Oil LHV Y	38	MJ/kg	

4. Results

4.1. Agricultural analysis

The energy analysis is carried out by considering the arable land in the plains of Emilia-Romagna. Soil characteristics, varying at each location, influence energy inputs, in particular mechanical power consumptions and fertilizations. As an example, Fig. 1 shows machinery energy inputs required by sunflower cultivation. Table 6 shows results in terms of the average economic and energy input values reported per hectare.

Machinery, fertilizers, chemicals, seeds and irrigation are considered inputs in the cultivation of energy crops (ensiled corn, rapeseed, soybean and sunflower).

Corn residual input analysis takes into account all costs related to stokes harvesting (e.g., shredders, rake, packer) and truck loading only. The grain, which represents the main output in corn cultivation, is intended for human or livestock nutrition and not for energy purposes. Therefore, all costs and benefits connected to this product are not considered.

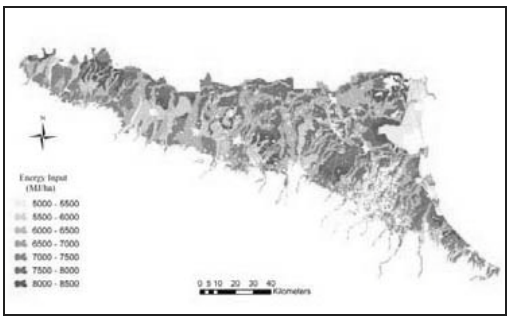

Fig. 1. Machinery energy input of sunflower cultivation in the plains of Emilia-Romagna.

4.2. Thermoeconomic analysis

An economic analysis is performed starting from the production cost calculated in section 4.1. The results are reported in Tab. 7 in terms of NPV, IRR and payback period (PBP). Moreover, the specific electrical energy (ElP) and thermal energy (ThP) productions are shown. It has to be underlined that for AD the high value of ElP is due to the fact that the energy is also produced from cattle manure.

Table 8 reports two parameters for the evaluation of the energy profitability of the chains: the Energy Returned Over Energy Invested (EROEI) ratio and the Net Energy Gain (NEG) balance. In order to consider the different value of electrical and thermal energy in terms of quality, they are normalized by means of the calculation of an equivalent primary energy by dividing by the reference electrical (equal to 43.5 %) and thermal (equal to 89.0 %) efficiency which account for separate generation.

Figures 2-5 show the parametric analysis performed by imposing different IRR values (from 5 % to 30 %). The value of the calculated biomass production cost is highlighted for each conversion technology.

Table 6. Agricultural energy and economic inputs.

	Energy Input [GJ/ha]		Economic Input [k€/ha]	
	HI	LI	HI	LI
Sunflower	21	14	0.58	0.40
Rapeseed	16	12	0.77	0.61
Soybean	20	11	0.79	0.52
Ensiled corn	33	26	1.1	0.78
Corn stalks	1.9		0.13	

Table 7. Thermoeconomic analysis results.

		AD		DC	TCG	SVOC	
		LI	HI			LI	HI
NPV @15th year	[M€]	1.5	1.4	10	3.1	3.0[a] 2.2[b] <0[c]	2.5[a] 1.9[b] <0[c]
IRR	[%]	28	27	35	16	74[a] 57[b] -[c]	63[a] 50[b] -[c]
PBP	[yr]	5	5	4	8	2[a] 2[b] -[c]	2[a] 3[b] -[c]
ElP	[MWh/ha]	21	26	3.7	4.3	5.4[a] 5.4[b] 2.0[c]	5.9[a] 5.9[b] 2.2[c]
ThP	[MWh/ha]	-	-	16	5.2	5.2[a] 5.1[b] 2.0[c]	5.6[a] 5.6[b] 2.2[c]

[a] sunflower [b] rapeseed [c] soybean

Table 8. Energy indices of the chains.

		EROEI [-]		NEG [GJ/ha]	
		LI	HI	LI	HI
Ensiled corn	AD	6.7	6.5	147	182
Corn stalks	DC	52		93	
Corn Stalks	TCG	31		55	
Sunflower oil	SVOC	4.5	3.2	51	49
Rapeseed oil		5.1	4.1	54	53
Soybean oil		2.1	1.3	13	6.1

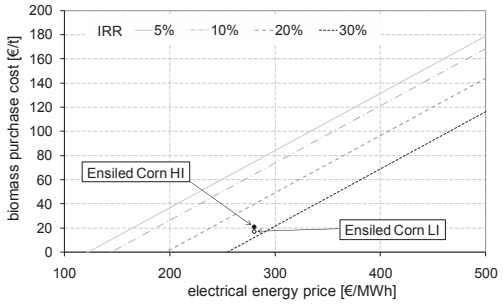

Fig. 2. Look-up chart for AD.

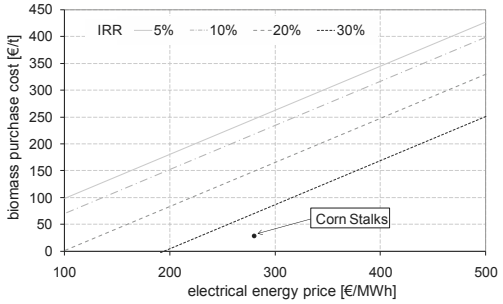

Fig. 3. Look-up chart for DC.

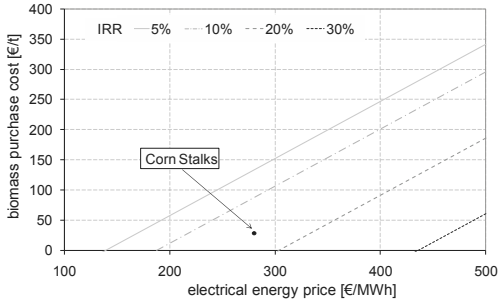

Fig. 4. Look-up chart for TCG.

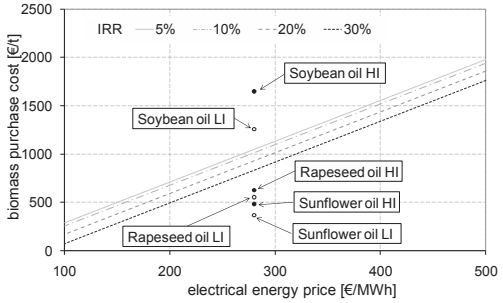

Fig. 5. Look-up chart for SVOC.

5. Discussion

As expected, the energy and economic input values of the LI agriculture systems are lower than those of the HI agriculture system (Table 6). The possibility of a less intensive agricultural approach strictly depends on soil characteristics. Nevertheless, such approach is strongly suggested in the case of energy crops. This is justified by the fact that the aim of energy crops is to maximize energy efficiency and not to produce quality food supply crops. Therefore, it is not necessary to obtain high and competitive yields.

Ensiled corn is characterized by the highest values in energy and economic inputs since it requires intensive irrigation and massive machinery employment during harvesting.

As regards sunflower, it can be noted that energy inputs are the highest among oil crops (i.e. rapeseed, soybean and sunflower), while the economic cost compared with the other two crops (soybean and rapeseed) is lower because these two latter crops need more expensive fertilizers. Moreover, soybean also requires irrigation. Finally, it is more difficult to grow rapeseed in Emilia-Romagna and in Italy in general, compared to North European region: this implies heavier mechanization.

Regarding corn stalks, it has to be underlined that the low value of the energy input does not consider the energy related to additional fertilization in order to replace some of the nutrients removed from the soil.

An important result of the economic analysis regards soybean oil: the high value of cultivation cost and low value of oil yield lead to a high oil cost (up to 1,600 €/t), making the energy chain based on soybean not profitable. It has to be highlighted that this analysis does not consider the profit obtainable from the sale of byproducts and coproducts (e.g., cake meal) when estimating the price of oil. This could have a strong influence particularly in the case of soybean, since it is also currently cultivated for its protein-rich soymeal used for animal and human foodstuffs.

For the other crops, the economic analysis shows that all plants have a PBP lower than 5 years, but the TCG plant is characterized by a PBP of 8 years. The performance of the plant is also confirmed in terms of IRR: DC and AD have an IRR of about 30 %, while the higher value is reached for SVOC (74 % for sunflower oil LI) and

the lower for TCG (16 %). Finally, Figs. 2-5 show that a different electrical energy price (and then a different feed-in tariff) should be defined as a function of biomass and technology in order to avoid over-incentivizing some chains (e.g. sunflower oil combustion in ICE).

In terms of energy profitability, it has to be underlined that for ensiled corn in AD the EROEI and the NEG do not give univocal results: EROEI is the highest in the case of LI while NEG is the lowest. This means that LI is the most efficient in terms of resources employment, while HI has the highest energy contribution margin.

The good performance of corn stalks both in DC and TCG is mainly due to the low energy input of the feedstock (see Tab. 6): the difference between the technologies is justified by the fact the thermal production of the DC is about 3 times that of TCG.

Regarding SVOC, rapeseed is the most efficient in terms of energy, while soybean is characterized by an EROEI about half that of the other two oil crops. This is mainly due to its low oil-seed ratio.

6. Final remarks

Italian Law grants incentives for plant owners producing electrical energy from biomass and derived biofuels. The incentive for plant electrical power up to 1 MW consists of a feed-in tariff of 280 €/MWh. Similar policies have also been adopted by other EU countries [20]. The bioenergy option is boosted for greenhouse effect mitigation (though this mitigation effect has not yet been definitively established) and for primary energy provision diversification. In particular, biomasses are an indigenous energy source and their use can (i) generate employment, (ii) restore degraded lands, (iii) be an alternative to set-aside agricultural policies, (iv) represent a profitable way for agricultural residues exploitation and (v) increase biodiversity. If biomass-based energy policies are chosen for these reasons, the lawmaker should drive this change in order to (i) avoid distortion of the foodstuff market (e.g. cereals, oils, etc.) and (ii) promote short energy chains, e.g. incentives may be provided to local crops only. Moreover, incentives should be tailored on specific conversion technology in order to promote the most efficient chains.

This paper presented a general methodology which can support these decisions, since it allows the calculation of per-hectare energy indices and the estimation of the proper incentive in order to grant decent economic profitability.

The analysis carried out does not take into account feedstock material transportation from the field to the energy conversion plant. This aspect has a relevant influence on the overall assessment and critically affects the convenience of the biomass transformation process. The logistics management between feedstock source and transformation sinks is a critical point that should be implemented across the country. Structuring an efficient transportation network can promote a biomass energy chain and prompt the interest of farmers to produce energy crops. Anyway, transportation costs (both in terms of economics and energy) define a maximum distance from the field to the energy conversion plants which makes the profitability or the net energy gain null.

This work could be further developed by implementing economic inputs in the GIS environment as function of soil type and by analyzing the transportation process.

Nomenclature

A	area, ha
E	energy, MJ/ha
Ei	energy input, MJ
Eic	agricultural activity energy input, MJ
Eip	transformation process energy input, MJ
Eit	transportation energy input, MJ
F	cash flow, €/yr
I	investment, €
i	index
k	index
m_b	annual biomass, kg/yr
P	power, MW
r	discount rate
Y	biomass energy potential, MJ/kg

Greek symbols

η	efficiency

Subscripts and superscripts

ao	agricultural operation
bf	biofuel supplied to energy system
c	conversion process
el	electrical
k	index

rm raw material
th thermal

References

[1] Emilia-Romagna Region, 2008, Statistiche Emilia-Romagna, URL: http://www.regione.emilia-romagna.it/statistica/.

[2] Italian Institute of Statistics, 2002, Censimento Generale Agricoltura, URL: http://www.istat.it/.

[3] Graboski, M. S., 2002, *Fossil Energy Use in the Manufacture of Corn Ethanol*, National Corn Growers Association, St. Louis, MO.

[4] Caprara, C., Gabellini, G., Martelli, R., 2008, A Territorial Model for the Energy Analysis of Oil Seed Crops Used as Biofuel Feedstocks, *Proc. AgEng2008 International Conference on Agricultural Engineering & Industry Exhibition* [CD-ROM], Crete, Greece.

[5] Caprara, C., Gabellini, G., Martelli, R., GIS-Based Modelling System for the Assessment of Agricultural Residues Production, *Proc. 15th European Biomass Conference and Exibition*, Berlin, Germany, pp. 261-265.

[6] Nagy, C. G., 1999, Energy Coefficients for Agriculture Inputs in Western Canada, Canadian Agriculture Energy End-Use Data Analysis Centre (CAEEDAC), URL: http://www.csale.usask.ca/PDFDocuments/energyCoefficientsAg.pdf.

[7] Patzek, T. W., 2004, Thermodynamics of the Corn-Ethanol Biofuel Cycle, Crit. Rev. Plant Sci., 23, pp. 519-567.

[8] Pimentel, D., Patzek, T.W., 2005. Ethanol Production Using Corn, Switchgrass, and Wood; Biodiesel Production Using Soybean and Sunflower, Nat. Resour. Res., 14, pp. 65–76.

[9] Gunaseelan, V. N., 1997, Anaerobic Digestion of Biomass for Methane Production: a Review, Biomass Bioenergy, 13, pp. 84-114.

[10] Bettocchi, R., et al., 2009, Energy and Economic Analyses of Integrated Biogas-Fed Energy Systems, J. Eng. Gas Turbines Power, 131, 061401.

[11] Ward, A. J., et al., 2008, Optimization of the Anaerobic Digestion of Agricultural Resources, Bioresour. Technol., 99, pp. 7928-7940.

[12] Fabbri, C., 2009, La Sostenibilità Economica: Soli Liquami e Integrazione con Biomasse, *Proc. Foragri Expo,* URL: http://www.foragriexpo.it/index.php?option=com_docman&task=doc_download&gid=26&Itemid=43.

[13] Dovia, A., et al., 2009, Explotation of Residual Agricultural Biomass in Small Size Plants for Power Generation with ORC Technology in Mediterranean Europe, *Proc. 17th European Biomass Conference and Exibition* [CD-ROM], Hamburg, Germany.

[14] Ioannidou, O., et al., 2009, Investigating the Potential for Energy, Fuel, Materials and Chemicals Production from Corn Residues (Cobs and Stalks) by Non-Catalytic and Catalytic Pyrolysis in Two Reactor Configurations, Renewable Sustainable Energy Rev., 13, pp. 750-762.

[15] Kumar, A., et al., 2008, Thermogravimetric Characterization of Corn Stover as Gasification and Pyrolysis Feedstock, Biomass Bioenergy, 32, pp. 460-467.

[16] Zabaniotou, A., et al., 2010, Bioenergy Production for CO_2-mitigation and Rural Development via Valorization of Low Value Crop Residues and their Upgrade into Energy Carriers: a Challenge for Sunflower and Soya Residues, Bioresour. Technol., 101, pp. 619-623.

[17] distributor personal communication.

[18] Bettocchi, R., et al., 2009, Assessment of the Performance and of the Profitability of CHP Energy Systems Fed by Vegetable Oils, *Proc. of ASME TurboExpo* [CD-ROM], Orlando, Florida.

[19] Riva, G., et al., 2006, Agroenergie: Filiere Locali per la Produzione di Energia Elettrica da Girasole, Technical Report, Marche Region.

[20] Faaij, A. P. C., 2006, Bio-Energy in Europe: Changing Technology Choices, Energy Policy, 34, pp. 322-342.

Acknowledgments: This paper was carried out within the framework of a research project conducted for LISEA (Laboratorio per l'Innovazione industriale e la Sostenibilità Energetico-Ambientale).

The Impact of Demand Side Management Strategies in the Penetration of Renewable Electricity

André Pina [a], *Carlos Silva* [b] *Paulo Ferrão* [a]

[a] *MIT-Portugal Program, Sustainable Energy Systems, Instituto Superior Técnico, TULisbon*
[b] *IDMEC/Instituto Superior Técnico, TULisbon*
Av. Rovisco Pais, 1049-001 Lisboa, Portugal

Abstract: High fuel costs, increasing energy security and lower greenhouse gas emissions have pushed governments to invest in renewable energies. However, the intermittence of most renewable energies can create problems to the local electricity grids. To deal with this issue, energy storage systems are often used, but they are usually an expensive solution, and might not be implementable.

One of the solutions being discussed to face the issue of renewable intermittence is the use of demand side management strategies, which can have the double effect of reducing electricity consumption and allowing greater flexibility in electricity production by doing load shifting.

This work analyzes the impact of using demand side management strategies in the evolution of the electricity mix in Flores. Flores is a small island in the Azores which is known for its high penetration of renewable energy. The potential for renewable energies and the small scale of the system make it an interesting case study for testing innovative solutions.

TIMES is used here to model the electricity system and optimize the installation and use of wind and hydro plants up until 2020 based on different scenarios for electricity consumption growth, deployment of demand response technologies in the domestic sector and promotion of energy efficiency plans to eliminate standby power.

Keywords: Demand Side Management, Dynamic Demand Response,Energy Planning, TIMES modeling

1. Introduction

Demand side management strategies are of great interest to utility companies throughout the World, as they can help ease the operation of the electricity system [11], and many governments are currently studying policies to promote their application [12]. One of the most recent strategies being developed is dynamic demand response.

Dynamic demand response is the ability to control devices (appliances) in order to reschedule their operation. With this ability, the utilities could decide to operate some of the appliances in periods where there is a large amount of renewable energy available, and not operate them when demand levels increase drastically. It is important to notice that these operations don't actually decrease the amount of electricity consumed, but merely shift it to when it is more convenient from the grid operation point of view [18].

While dynamic demand response is more oriented towards load shifting, energy efficiency plans have the primary goal of decreasing overall energy consumption in the medium/long-term. This can be achieved by educating people on how they can save energy by switching off unnecessary uses (eliminating standby power consumption or turning off lights that are not needed), promoting the change to more efficient devices (refrigerators, lights, washing machines, and others) and pushing for a more sustainable construction and renovation of buildings so that they require less artificial lighting and heating/cooling (good insulation, better performing windows, others).

This type of strategies might allow the increase in the penetration of renewable energies by creating the possibility of establishing a better match between electricity demand and the variations of renewable energy sources, enabling peak shaving and reducing the need for spinning-reserve supplied in

Corresponding author: André Pina, Email: andrepina@gmail.com

general by power plants that use fossil fuels. Particularly in systems with high penetration of renewable energies, these options might compete with the more traditional use of energy storage systems (such as flywheels, batteries and others) that are often expensive and not very efficient. This paper analyzes the impact of energy efficiency plans and the introduction of dynamic demand response in the island of Flores, Azores.

The archipelago of the Azores is located in the middle of the North Atlantic Ocean and is composed of 9 islands of different sizes and population.The location of the Azores, as well as the large potential for renewable energies has led the Government of the Azores and Electricidade dos Açores (EDA), the local utility, to invest in renewable energies for the production of electricity and, in 2009, renewable energies produced 26.0% of all electricity in the region and 54% in Flores [7]. Nevertheless, the Government of Azores wants to increase further the use of renewable energies and thus it is promoting the Green Island Project [17].

The Green Islands Project, being developed in collaboration with the MIT Portugal Program [15], has the purpose of developing sustainable pathways for the energy systems of the Azores islands. In Flores, the penetration of renewable energy in electricity production is very high due to the use of a flywheel system that already allows the electric system to run exclusively on renewable energy during several hours on some days of the year [7]. The main problem is that the flywheel energy storage system installed in the island is very expensive, has a low efficiency, and requires a lot of maintenance which makes it an unattractive investment for the local electricity company. With this in mind, Flores becomes a very interesting case study to install and test load management strategies.

To analyze the energy system of Flores, a TIMES model was developed. TIMES - The Integrated Markal-Efom System - is a tool developed within the Energy Technology Systems Analysis Programme (ETSAP) of the International Energy Agency [16]. It is an optimization partial equilibrium bottom-up model generator that finds the minimal cost solution for an energy system over a certain time period [13]. The model is based on detailed and explicit information about available energy technologies (e.g. production capacity, efficiency and operation costs) and the description of end-use consumption for different sectors and types of energy. In this way, the model allows the testing of different policy options from the implementation of energy efficiency on specific end-uses to demand side management policies, in case the model uses an hourly resolution [14].

2. Flores case study

Flores is a small island that belongs to the Western Group of the archipelago of the Azores, Portugal, and is one of the most isolated islands of the Region. Its area is around 141 km^2 and 2008 estimates say that it has around 4117 inhabitants [8]. It is the most renewable island in the archipelago, in what concerns electricity, as around 54% of all electricity produced in 2009 came from either hydro or wind power. In fact, renewable energies have provided a large part of the electricity needs of the island for many years now, as shown in Fig. 1.

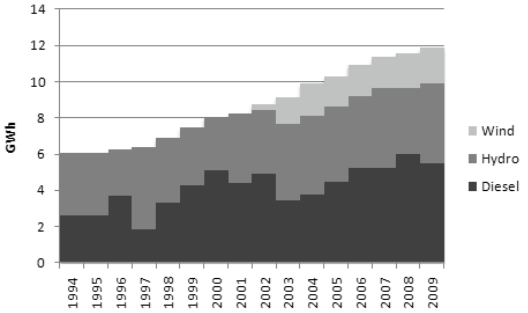

Figure 1: Electricity production in Flores by source

Due to its remote location and the small number of inhabitants, it is very expensive to transport the necessary fossil fuels to the island. Investing in local resources, not only for electricity production but also water and space heating, is a priority of the Government. Furthermore, the transition of a 4000 people community to an almost completely renewable society could promote tourism, which is already one of the main activity sectors in the region.

2.1. Electricity production system

Currently, the electricity system in Flores is a combination of wind turbines, hydropower and diesel engines, aided by a flywheel energy storage system. The system is composed of 4 hydropower generators, 2 wind turbines and 4 diesel engines. Table 1 shows the year of installation and the capacity of each generator [6].

In order to be able to use the total installed power of wind and hydro, a flywheel energy storage sys-

Table 1: Installed generation capacity in Flores

Plant	Group	Year	Capacity (KW)
Além-Fazenda (Hydro)	I	1966	296
	II	1966	296
	III	1966	296
	IV	1983	512
Além-Fazenda (Diesel)	VII	1991	500
	VIII	1995	500
	IX	2001	500
	XX	2005	810
Boca da Vereda (Wind)	I	2002	300
	II	2002	300

tem was installed in the island [10]. This system helps maintain frequency and voltage stability, which were the main problem for the wind-hydro-diesel system. Furthermore, this introduction of flywheels enabled the island to have 100% of the electricity coming from renewable energies, if the conditions are favorable. More recently, this occurred in 12 days of the year 2009, in which the electricity demands of the island were met exclusively by the combination of wind and hydro for several hours of the day.

Recently, EDA has announced plans to invest in the installation of 2 new hydro power generators. The first one, with a planned starting year of 2011, would be a refurbishment of an existing generator that will increase the already existing capacity by 1600 KW. The second investment, expected to start operations in 2012, will be a new plant of 1040 KW [9].

2.2. Electricity consumption

Being a small, services driven economy, the main electricity consumption sectors in Flores are Domestic and Commerce and services. Together they are responsible for more than 75% of all electricity consumed in the island, with the Domestic sector representing around 40%. However, the relative weight of each sector has been changing throughout the years, as electricity consumption has been growing at a higher rate in the Commerce and services sector than in the Domestic sector. Fig. 2 shows the evolution of electricity consumption in Flores, divided in 5 different sectors: Domestic, Commerce and services (private), Public services, Industries and Public lighting.

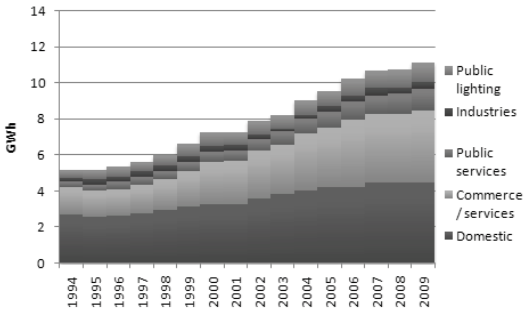

Figure 2: Electricity consumption in Flores by sector

Using more detailed information, electricity consumption was divided in 11 sectors (Agriculture, Industry, Food processing, Water distribution, Building and construction, Commerce, Public services, Private services, Tourism related activities, Domestic, Public lighting), with the Domestic sector being further divided in 9 subsectors (Dish washing machines, Washing machines, Drying machines, Refrigerators and freezers, Entertainment equipment, Personal computers, Heating and cooling, Lighting, Others). To be able to include some of the demand dynamics, each sector and subsector were assigned different load curves, which were designed based on available studies from Portugal and other European countries [4, 5, 3, 1]. Fig. 3 shows the load curve that was assumed for a Spring weekday in 2010.

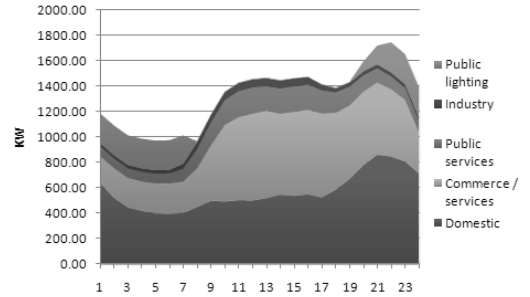

Figure 3: Hourly electricity consumption curve for a Spring weekday in 2010

For each sector (but not subsector), a linear regression method was used to estimate the evolution of electricity consumption. With this approach, the shapes of the load curves change throughout the years due to the different growths of each sector. Furthermore, it allows studying the impact of load management solutions that have an effect on specific hours of the day, such as the elimination of stand-by

power and responsive demand, which is one of the goals of this work.

3. Methodology

This work analyzes different demand-side management options and their impact in the energy system of Flores. A TIMES model of the island was built in order to find the optimal solution for the energy system, given different demand evolution. To do this, a scenario based approach is used, in which different scenarios for the future are tested independently.

3.1. The TIMES model

The Flores TIMES model optimizes the installation of new electricity generation capacity, as well as the operation of all existing plants, given a certain demand. For each scenario, the model was run until the year 2030 with the goal of comparing the installed capacities and use of the different electricity generation technologies up to the year 2020. The difference between the end year of optimization and the year chosen to present the results is to eliminate possible biases for or against technologies that would start operation close to 2020. By running the model until the year 2030, more operating years for the new plants in which the demand for electricity is growing are considered.

To make the model closer to reality and be able to include demand and supply dynamics (such as loads shifting and wind variation), each year is divided in 4 seasons, 3 days per season and 24h per day, which enables the model to have 12 different load profiles for each day.

The TIMES model built for this work uses a Mixed Integer Programming approach for the capacities to be installed, which is necessary due to the small scale of the system. The model must then choose if and when capacity increases should be done, using total cost minimization as the deciding factor. Regarding hydro power, the model can choose between a 1600 kW generator, a 1040 kW generator, or it could install both. Regarding wind energy, the model can install a maximum of 600 kW, which corresponds to two 300 kW wind turbines.

One of the main assumptions of this work is that the typical grid stability problems due to the increase of renewable energy penetration are solved either by the existing flywheels, or by new ones if necessary. Furthermore, it should be noted that the only costs that are being consider are investment, fixed and variable costs for the electricity production technologies, and fuel import costs. No costs related to CO_2 emissions or indirect benefits that result from using more renewable energy are accounted.

3.2. Scenarios

To create possible scenarios for the evolution of electricity consumption, some options were considered regarding:

- General efficiency
- No standby power
- Dynamic demand

”General efficiency” is the option to invest in energy efficiency programs across all sectors, starting in 2011, which have the effect of reducing demand growth per year to only 50% of the one estimated with the linear regressions for each sector.

”No standby power” is the option to gradually eliminate the standby power consumption of the Domestic sector by educating the population or the introduction of new technologies that do not have this. Standby power is estimated as being responsible for around 5% of the electricity consumed by the sector in Portugal [2]. If this option is chosen, the model gradually eliminates standby power, starting in 2011 and disappearing completely in 2015.

Finally, ”Dynamic demand” is the option to gradually enable the washing, dryer and dish washing machines to be operated remotely by the grid operator when it is more convenient. If chosen, the automation of these machines begins in 2013, with all of them having this capability in 2018.

Based on whether these options were considered or not, 8 different scenarios were designed. Fig. 4 shows what options each of the scenarios considers.

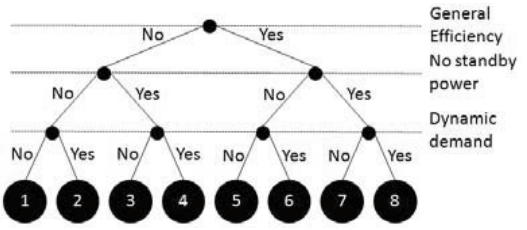

Figure 4: Scenarios description according to the available options for demand-side management

4. Results

The analysis of the results is divided in three parts: installation of new generation capacity, production of electricity by source and how the automation of the Domestic machines is used.

4.1. Installation of new generation capacity

Table 2 shows the total installed new capacity for hydro power for each scenario. In the table, only the years in which the installation of new generation capacity (of either hydro or wind) occurs are shown. From the table it is possible to see that the installation of the 1600 kW generator is done in the 2011 for all scenarios, which is in agreement with the plan EDA has until 2013. This is easily understood as the costs for the installation of this generator are quite low since it is a refurbishment of an existing facility.

However, according to the model, the installation of the second hydro power facility is only necessary in the year 2015 or even later depending on the energy efficiency measures that are used. From Table 2 it is possible to see that, in the scenarios in which there is a strong investment in energy efficiency (Scenarios 5 - 8), the 1040 kW hydro power generator is not installed in the time horizon that is considered in this work (up to 2020). This contrasts with the plan made by EDA, in which they estimated building this unit in 2012.

Table 2: Total installed capacity of new hydro power [kW]

Scenario	2011	2015	2016	2017	2019
1	1600	2640	2640	2640	2640
2	1600	1600	2640	2640	2640
3	1600	1600	2640	2640	2640
4	1600	1600	2640	2640	2640
5	1600	1600	1600	1600	1600
6	1600	1600	1600	1600	1600
7	1600	1600	1600	1600	1600
8	1600	1600	1600	1600	1600

Regarding wind energy, Table 3 shows the total installation of new generation capacity from wind energy for each scenario over the years. Once again, only the relevant years are shown in the table. The results show that the model ends up choosing to install the maximum amount of wind energy that it can in all scenarios. However, the year of installation is postponed depending on the energy options that are considered by the model. In the scenarios in which overall energy efficiency is not considered, the model chooses to install the wind turbines earlier than the other models.

Table 3: Total installed capacity of new wind power [kW]

Scenario	2011	2015	2016	2017	2019
1	0	600	600	600	600
2	0	0	600	600	600
3	0	0	600	600	600
4	0	0	600	600	600
5	0	0	0	600	600
6	0	0	0	600	600
7	0	0	0	600	600
8	0	0	0	0	600

The delay in the decision to install new generation capacity is mostly connected to the electricity demand growth considered. Low demand growth, especially during the night periods when demand is already low, reduces the amount of electricity that can be absorbed by the system. This means that if more investment on renewable energy was made, these new generators would have to be shut down during those periods, which reduces their cost effectiveness to the point where they are no longer economically viable. Alternatively, more energy storage systems could be installed, if it would benefit the system.

Comparing scenarios 7 and 8, in which the only difference is that scenario 8 considers the automation of domestic machines, it is possible to see that the model only chooses to install the wind turbines in 2019 for scenario 8, whereas for scenario 7 it happens in 2017. This is because, in scenario 8, the possibility of load shifting increases the amount of hydro power renewable electricity that is absorbed by the system during low demand periods and reduces the amount of diesel generated electricity that can be offset by the wind turbines, thus removing their economic feasibility in that year.

Finally, it should be noted that scenarios 1 to 4 install the maximum capacity of renewable generation considered in the model. This means that if electricity demand should continue to grow at a high rate, this electricity would have to be produced using non-renewable energy sources.

4.2. Electricity production

The installation of new generation capacity will have an impact on the penetration of renewable energies, as more electricity will be produced from

wind or hydro power. Fig. 5 shows the percentage of electricity that is produced from both of these sources, for the years 2011-2020, for each scenario. Comparing the results with the goal proposed by the Government of the Azores of having 75% of all electricity coming from renewable energies by 2018, one can see that all scenarios enable higher values since 2011. It is interesting to notice that the scenarios in which the "General Efficiency" option was not considered present higher shares of renewable electricity, which is a direct consequence of installing more new generation capacity of wind and hydro power.

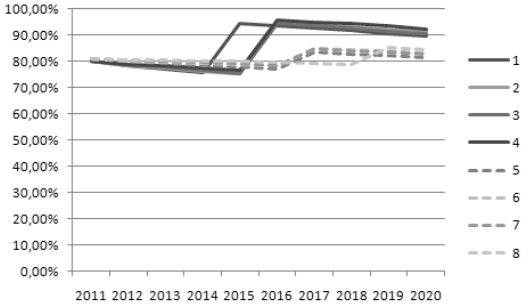

Figure 5: Percentage of electricity produced from renewable sources

One other aspect that is important to focus on is how much electricity is actually coming from the diesel generators. Given the lower demand levels presented in scenarios 5 to 8, due to the Efficiency option, it could happen that, despite the lower shares of renewable electricity, the amount of diesel used for electricity production would be smaller. However, Fig. 6 shows that in these scenarios the system ends up producing more electricity from diesel.

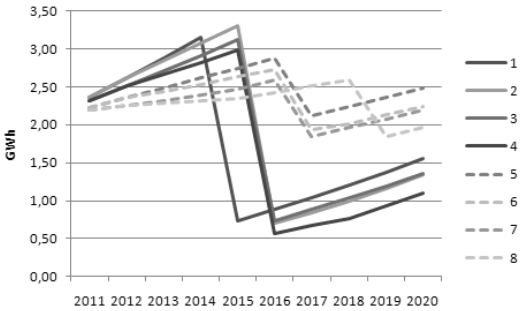

Figure 6: Electricity production from diesel

It must also be mentioned that if the high demand growth rates considered in the first four scenarios continue in to the future, the amount of electricity produced using diesel will increase as no new generation capacity using renewable energies could be installed by the system (with the assumed maximum capacities). This means that, while in the near future these scenarios present better results, they do not take into account long-term sustainability. On the other hand, scenarios 5 to 8 can still install a 1040 kW hydro power facility to meet their electricity demand growth. Furthermore, the fact that scenarios 5 to 8 already have a lower growth rate puts them closer to the stabilization of electricity consumption, which is crucial if the island is to be energetically independent in what concerns electricity.

4.3. Dynamic demand

The introduction of dynamic demand will have an impact on people's life. Therefore, in a study such as this one, it becomes relevant to identify how much of the domestic machines loads is shifted in order to help absorb the electricity produced from renewable energies. It should be noted that the model just takes into account what is best for the system, changing the load pattern of domestic machines if it allows the absorption of more renewable electricity. Fig. 7 shows the fraction of loads that are shifted in each of the scenarios that have this option enabled, as well as the maximum fraction of load that can be shifted according to the assumed technology deployment (starting in 2013 and growing gradually until all machines have this possibility in 2018).

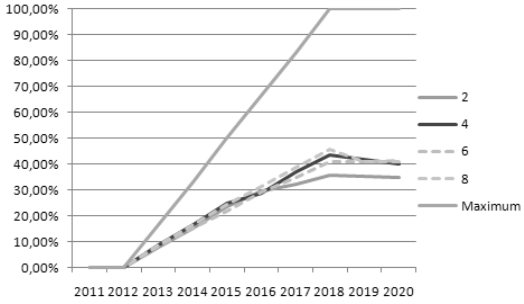

Figure 7: Fraction of shiftable loads that is shifted

The results show that all scenarios have a similar behavior, in which there is first an increase of the fraction of loads that are shifted, followed by a stabilization of this value. Despite the limit imposed by the deployment of the technology (100%), it is interesting to see that this does not create a problem as the use of this technology does not come close the its full potential. The use of this technology seems

to stabilize at around 40% for scenarios 4, 6 and 8, and at around 35% for scenario 2.

This difference in the stabilization between scenario 2 and the others is due to the fact that scenario 2 considers a higher electricity demand growth than scenarios 6 and 8, and also does not include the option of eliminating stand-by power as scenarios 4 and 8. This results in higher electricity demand during the night periods (periods where the load is lower and there is a higher chance of having a mismatch between supply and demand) which would be able to absorb more renewable electricity by itself, without the need of shifting loads.

One should be careful to say that this means that only that amount of machines should be equipped with dynamic demand technology as that would implicate the use of those machines would always be controlled by the system, effectively removing the chance of running the machines if people really needed it. The best way to interpret this is by saying that if all machines have this technology, the load of each machine will be shifted around 40% of the time and that if the penetration of this technology is lower, the machines that do have it will have their loads shifted a larger fraction of the time.

5. Conclusion

The introduction of load management strategies, be it technological energy efficiency, consumer behavior changes or introduction of dynamic demand-side management technologies is crucial for the long-term sustainability of any region. These options will play a large role in the transition to sustainable energy systems by keeping demand at levels in which renewable energies can be used effectively to meet that demand.

In the case of Flores, the scenarios in which a higher demand growth was considered installed more renewable generation capacity and achieved a higher penetration of renewable energy in electricity production. However, the fact that electricity growth was high can create serious problems for the future of the region as the continuous increase cannot be met in the future with more new renewable generation capacity since the model already installed the maximum it could. The scenarios with a lower electricity demand growth, on the other hand, can accommodate more years of increasing electricity demand as they did not install the 1040 kW hydro power generator in the time horizon that was analyzed.

Rather than helping introduce more generation capacity, the load shifting strategies was used to help increase the effective capacity factor of the existing and newer generators and further postpone the installation of more generators.

References

[1] Costumer segmentation, Sweden, Denmark, Finland and Norway. www.efflocom.com, 2004.

[2] ECOCASA. www.ecocasa.org, 2004.

[3] Eficiência energética em equipamentos e sistemas eléctricos no sector residencial. Technical report, Direcção-Geral de Energia e Geologia, 2004.

[4] Plano para a utilização racional de energia nos edifícios. Technical report, Consultores Saudáveis, 2004.

[5] Relatório Auditoria Energética - Iluminação Pública - Ponta Delgada - S. Miguel. Technical report, Agência Regional de Energia e Ambiente da Região Autónoma dos Açores, 2006.

[6] Caracterização das redes de transporte e distribuição de energia eléctrica na Região Autónoma dos Açores 2008. Technical report, Electricidade dos Açores, 2009.

[7] Informação Estatística - Dezembro. Technical report, Electricidade dos Açores, 2009.

[8] Statistical Yearbook of the Azores Region 2008. Technical report, Serviço Regional de Estatística dos Açores, 2009.

[9] Electricidade dos Açores. O presente e o futuro das energias renováveis pela eda. *EDA Informa*, 120-121, 2008.

[10] N. Hamsic et al. Increasing Renewable Energy Penetration in Isolated Grids Using a Flywheel Energy Storage System. http://ieeexplore.ieee.org/stamp/stamp.jsp?tp=&arnumber=4380112&userType=&tag=1, 2007. POWERENG, April 12-14, Setúbal, Portugal.

[11] D.G. Infield et al. Potential for Domestic Dynamic Demand-Side Management in the UK. http://ieeexplore.ieee.org/stamp/stamp.jsp?arnumber=04275305, 2007. IEEE.

[12] T. Jacopo et al. Demand response experience in Europe: Policies, programmes and implementation. *Energy*, 2009. In press.

[13] R. Loulou et al. Documentation for the times model - part i. Technical report, Energy Technology Systems Analysis Programme, 2005.

[14] A. Pina, C. Ioakimidis, and P. Ferrão. Economic modeling of a seawater pumped-storage system in the context of São Miguel. http://ieeexplore.ieee.org/stamp/stamp.jsp?tp=&arnumber=4747098, 2008. International Conference on Sustainable Energy Technologies.

[15] MIT Portugal Program. Green Islands Project. http://www.mitportugal.org, 2010.

[16] Energy Technology Systems Analysis Programme. TIMES - The Integrated MARKAL-EFOM system. http://www.etsap.org/index.asp, 2007.

[17] C. Silva et al. A Systems Modeling Approach to Project Management: The Green Islands Project example. http://esd.mit.edu/staging/symp09/submitted-papers/silva-carlos-paper.pdf, 2009. Second International Symposium on Engineering Systems.

[18] G. Strbac. Demand side management: Benefits and challenges. *Energy Policy*, 36:4419–4426, 2008.

Acknowledgments: This work has partially been supported by Programa de Financiamento Plurianual de Unidades de I&D from the Portuguese Science and Technology Foundation (FCT) to the research activities of the associated laboratory LAETA and by the FCT scholarship SFRH/BD/35334/2007 within the MIT-Portugal Program.

The Contribution of Heat Storage to the Profitable Operation of Combined Heat and Power Plants in Liberalized Electricity Markets

Andreas Christidis[a], Christoph Koch[b], Lothar Pottel[b] and George Tsatsaronis[a]

a Institute for Energy Engineering, Technische Universität Berlin, Berlin, Germany
b Vattenfall Europe Wärme AG, Berlin, Germany

Abstract: Combined heat and power (CHP) plants are characterized by high fuel efficiency and are therefore usually the thermal power producing units of choice within a district heating network. The operation of CHP units is typically controlled by the current heat demand and thus delimits the range of electricity production. Heat storage devices are a promising alternative to uncouple the heat load of the district heating network from the commitment of the units and to allow for electricity-price orientated power production.
In this paper we present numerical results for the combined optimization of the operation of nineteen existing power plant units and the design of six proposed heat accumulators which supply the district heating network of Berlin. A mixed-integer programming problem (MIP) is formulated in GAMS and solved with CPLEX, as described in [1]. This paper focuses on the potential for increasing profitability through the addition of heat accumulators in the energy system described above, on the optimal storage capacities for different price scenarios (variation of fuel costs and electricity price time series) as well as on the adjustment of the operation of the power plants due to this implementation.

Keywords: combined heat and power plants, district heating, heat storage, design optimization, unit commitment, mixed-integer program.

1. Introduction

The cogeneration of heat and electricity leads to a decrease in total fuel consumption when compared to the separate production of these two commodities. However, this higher fuel efficiency is offset by a lower flexibility because the heat and electricity production cannot be adjusted independently. Base-load cogeneration power stations are typically operated to satisfy the current heat demand. Nowadays with liberalized energy markets, with wide variations in the hourly price of electricity, it should be beneficial to decouple electricity production from heat demand. Heat accumulators, which store hot water, enable heat production and supply within the district heating network to be temporarily decoupled. This degree of freedom which arises from the storage of heat near power stations allows for price-orientated electricity production. To determine the size and placement of heat accumulators within the power plant park, one has to consider the operation of the entire heat and electricity generation system including the nature of the district heating network. Therefore, the design optimization of the heat storage systems is combined with the unit commitment problem and both must be solved as one. This problem lends itself to a mixed-integer linear formulation which we implemented in GAMS [2] and solved with CPLEX [3]. Throughout this paper the term “heat” is used, as it is common in practice, instead of the thermodynamically correct term “thermal energy”.

1.1. Model description

The case studies presented in this paper have been conducted using a prognosis of the power plant park of Berlin, Germany for the decade 2020 - 2030. The district heating network of Berlin is one of the world’s largest with over 1300 km of piping supplying more than half a million of households. Ten sites with 13 combined heat and power (CHP) units and 6 peak-load boilers (PLB) are assumed to supply the region of Berlin with heat. Some of these units already exist and some are to be built. Due to the historical development of Berlin, the western and eastern parts of the district heating network are only lightly connected through a bottleneck of a negligible capacity. Hence, the first decomposition of the optimization problem was made by splitting the model into a western part

(supply area 1) with 11 units and an eastern part (supply area 2) with 8 units. Figures 1 and 2 show simplified network diagrams for these two parts of Berlin's district heating network with the respective power plants.

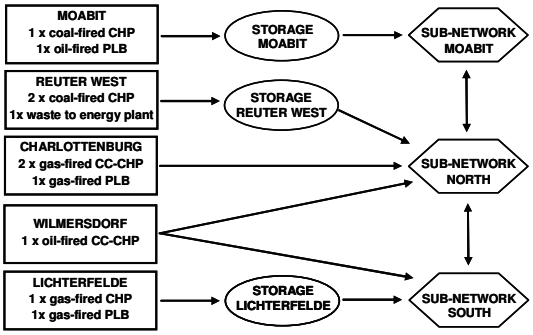

Fig. 1. Simplified network diagram of the western part of Vattenfall's district heating network (supply area 1).

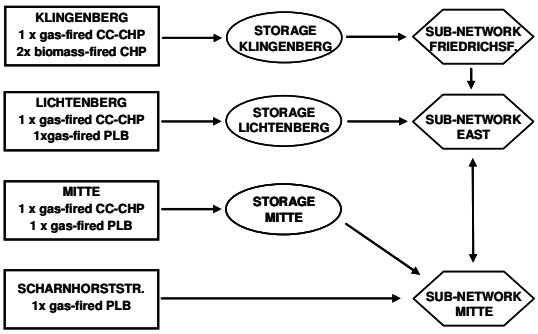

Fig. 2. Simplified network diagram of the eastern part of Vattenfall's district heating network (supply area 2).

We originally considered a time horizon of one year with an hourly temporal resolution, as described in [1], but not all calculations converged with an acceptable guarantee of optimality using that time discretization. A second decomposition had to be performed by splitting the time horizon into two half-years (first six months and second six months of the year) and implementing a time interval of four hours (see also sections 3.3). The resulting size of the models is given in Table 1.

Table 1. Number of variables and constraints for the two models.

Model	variables	constraints	binary variables
Supply area 1	480,668	828,630	10,458
Supply area 2	363,530	597,719	6,570

2.2. Relevant literature

The design optimization of the heat storage facilities is closely linked with the unit commitment problem, which has been well investigated for short-term planning (usually one to three days). In several publications [4-8] storage devices are included in the energy system, but as the energy content of the accumulator has to be set for the beginning and end of the planning period, charging and discharging cycles of one day are often obtained. The principal advantages in using mixed integer programming for short planning periods are reasonable computational cost and the guarantee of optimality. In order to identify the benefit of heat storage in [4-6] representative days have been used. In [5, 6], case studies with different sizes of storage facilities lead to the optimal design.

We believe the approach presented in this paper is unique due to the combination of the following aspects:

- Consideration of a half-year period and time intervals of four hours (1095 time intervals).
- Not using pre-specified accumulator sizes and thus implementing the investment costs of the storage devices into the objective function.
- Application on a real large scale system with unique unit and network characteristics.

2. Problem formulation

The basic idea is to calculate the economic potential of heat accumulators in the system under investigation by comparing one optimization for the case without heat storage devices (only power plant operation is optimized → unit commitment) and one with the addition of heat storage. The difference in the resulting objective value (1) quantifies the profitability which results from heat storage. Furthermore the optimal size of each storage tank is a fundamental result of the design optimization analysis, as it indicates the contribution of every single heat accumulator located next to a power plant to the profitable operation of the overall system. Therefore, the same specific investment costs (€/m³) are used for every accumulator.

The model can be divided into four components:

- Financial cost objective function
- Combined heat and power units and peak-load boilers (units)
- Heat accumulators
- District heating network (comprising pipes, pumps splitters and mixers)

The most important mathematical model formulations are given below. Further information about the model is provided after the description of the equations

Objective function:

$$\max O(V,\dot{P}^{sc},\dot{Q}^{sc}_{\mathrm{CT}},\dot{Q}^{sc}_{\mathrm{VT}},y)=\sum_{u=1}^{\nu}\sum_{t=1}^{\tau}C_{\mathrm{P}}(t)\cdot\dot{P}^{sc}(u,t)\cdot\Delta t - \sum_{u=1}^{\nu}\sum_{t=1}^{\tau}\left(C_{\mathrm{F}}(u)+C_{\mathrm{C}}\cdot ef(u)\right)\cdot\dot{F}(u,t)\cdot\Delta t - \sum_{s=1}^{\sigma}C_{\mathrm{V}}(s)V(s)\cdot\frac{\tau\cdot\Delta t}{8760}\cdot CRF \quad (1)$$

Where:

$$\dot{F}(u,t)=c_1(u,t)\cdot y(u,t)+c_2(u,t)\cdot\dot{P}^{sc}(u,t)+c_3(u,t)\cdot\dot{Q}^{sc}_{\mathrm{CT}}(u,t)+c_4(u,t)\cdot\dot{Q}^{sc}_{\mathrm{VT}}(u,t) \quad (2)$$

Selected constraints:

$$\Delta\tau_{\mathrm{d}}(u,t+1)=\left(\Delta\tau_{\mathrm{d}}(u,t)+1\right)\cdot\left(1-y(u,t+1)\right) \quad (3)$$

$$\left(y(u,t+1)-y(u,t)\right)\cdot\left(\Delta\tau_{\mathrm{d}}(u,t)-\Delta\tau_{\mathrm{d}}^{\min}(u)\right)\geq 0 \quad (4)$$

$$\Delta\tau_{\mathrm{o}}(u,t+1)=\left(\Delta\tau_{\mathrm{o}}(u,t)+1\right)\cdot y(u,t+1) \quad (5)$$

$$\left(y(u,t+1)-y(u,t)\right)\cdot\left(\Delta\tau_{\mathrm{o}}(u,t)-\Delta\tau_{\mathrm{o}}^{\min}(u)\right)\leq 0 \quad (6)$$

2.1. Objective function

Fuel costs and CO_2 certificate costs make up operational expenditures in the objective function (1), while the sales revenues from electricity represent the earnings. Revenues from selling heat are not accounted for because these are identical in both cases (with and without the possibility of heat storage) because the same given heat demand has to be satisfied. The investment costs of the heat storages are taken into account by linear depreciation. Therefore the investment costs of the heat storages (where applicable) are multiplied with the planning horizon $\tau\cdot\Delta t$ / 8760 and the capital recovery factor *CRF*.

2.2. Combined heat and power plants

Equation (2) is used for the calculation of the fuel requirement of the CHP plants (peak-load boilers are modeled by neglecting the first and second terms of (2)). The variables $\dot{P}^{sc}$, $\dot{Q}^{sc}_{\mathrm{CT}}$ and $\dot{Q}^{sc}_{\mathrm{VT}}$ are semi-continuous and are set to zero when the unit is shut down, or may vary between a lower and an upper bound (e.g. 40% - 100% partial load) when the unit is in operation. Semi-continuous variables can be obtained by multiplying a binary operating variable y with the respective continuous variable $\dot{P}^{c}$, $\dot{Q}^{c}_{\mathrm{CT}}$ or $\dot{Q}^{c}_{\mathrm{VT}}$. The binary variable y indicates whether the unit is in operation ($y = 1$) or shut down ($y = 0$) and the continuous variable is bounded by minimum and maximum load-values (see also Fig. 4). This bilinear term, the product of two variables, must be linearized in order to be implemented in a MIP problem. The linear formulation of a product of a binary and a continuous variable can be achieved by the use of Big-M-constraints which leads to four inequalities for every semi-continuous variable [1]. The coefficients c_1 to c_4 in (2) are originally dependent on the feed flow

temperature, as a higher temperature requires extraction steam from the steam turbine at a higher pressure. The feed flow temperature, on the other hand, is adjusted according to the ambient temperature, as shown in Fig. 3.

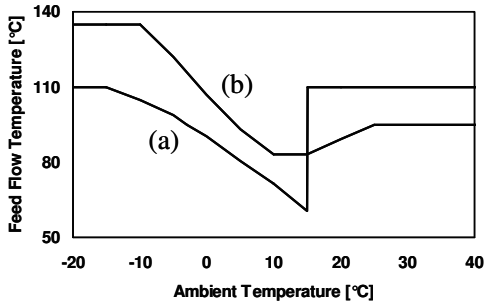

Fig. 3. Plot of variable feed flow temperature against ambient temperature: a) west Berlin (supply area 1) , b) east Berlin (supply area 2).

Since a representative column vector for the ambient temperature over time is implemented into the model as a boundary condition for the planning horizon, the resulting coefficients c_1 to c_4 are dependent on time as shown in (2).

Equation (3) defines the downtime interval $\Delta\tau_{\mathrm{d}}$ of unit u in the time interval t+1 and (4) assures that the minimum downtime interval $\Delta\tau_{\mathrm{d}}^{\min}$ is respected. The operating interval of a unit $\Delta\tau_{\mathrm{o}}$ is calculated in (5) and constrained in (6), respectively. Equations (3) to (6) contain products of binary and continuous variables which cannot be directly implemented in mixed-integer programs. Hence, these bilinear constraints have to be linearized. We used the Glover's linearization, as presented in detail in [1]. Equations (3) and (5) are replaced by four inequalities and constraints (4) and (6) are reformulated by the use of nine inequalities. For combined heat and power plants using backpressure steam turbines in the absence of cooling towers (the district heating network is the heat sink), the boundaries of the continuous variables $\dot{P}^c$, $\dot{Q}^c_{\mathrm{CT}}$ and $\dot{Q}^c_{\mathrm{VT}}$ are given by a linear, feed flow temperature dependent equation. Thus, as shown in Fig. 4 (a), electric power production and overall heat production $\dot{Q}^c_{\mathrm{CT}} + \dot{Q}^c_{\mathrm{VT}}$ are not independent. Cogeneration units equipped with extraction condensing steam turbines and cooling towers are characterized by a higher flexibility and therefore the boundaries of $\dot{P}^c$, $\dot{Q}^c_{\mathrm{CT}}$ and $\dot{Q}^c_{\mathrm{VT}}$ are given by a set of linear inequalities. In Fig. 4 the grey area (b), delimited by inequalities, represents the operating range of such a power plant.

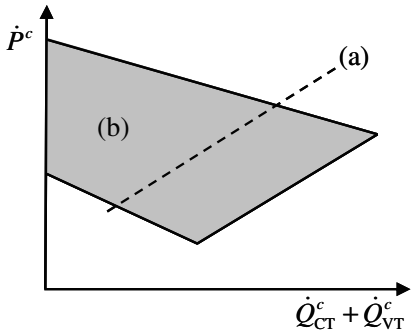

Fig. 4. $\dot{P},\dot{Q}$ -diagram as a graphical representation of the constrained operating range for two types of combined heat and power plants: a) backpressure turbine without cooling tower, b) extraction condensing steam turbine.

2.3. Thermal storage and district heating

Thermal storage facilities and nodes (splitters and mixers which together with pipes and pumps are used to model the district heating network) are modeled by means of energy and mass balances. The water temperature inside the storage devices is set to 110 °C in order to avoid the need for pressure vessels. For east Berlin, the heat accumulators are equipped with auxiliary boilers so that the use of stored hot water is possible in periods where the feed flow temperature needs to be above 110 °C. Due to the dependency shown in Fig. 3 and the implementation of a complete forecast for the ambient temperature, the temperature in the district heating network for every time interval is calculated during pre-processing for the whole planning period and thus is a parameter. Constant temperatures in the energy balances of the network and the heat storage systems result in linear expressions, dependent only on mass flow rates. The electricity needed for the pumps in the district heating network is calculated with respect to the feed flow. Hydraulic restrictions are implemented as an upper bound on the mass

flow rates within the pipes in order to account for the maximum load condition of the pumps.

2.4. Price scenarios

As the case studies were conducted for a commercially operated energy system, it is understandable that neither the price prognoses for electricity, fuel and CO_2 certificates nor the real investment costs for heat storages and detailed performance information concerning the power plants or network can be publicly presented.

Investigations were performed for a "low-price" and a "high-price" scenario, whereby prices for electricity, as well as fuel costs and the expenditures for CO_2 emissions have been varied.

3. Results

This section presents the economic potential of heat accumulators within the power plant park of Berlin. Furthermore, the change in operation of the units due to the possibility of heat storage is discussed.

3.1. Why heat storage is beneficial

Figure 5 shows the optimal size of each heat accumulator for every scenario. The values have been normalized through division by the greatest value.

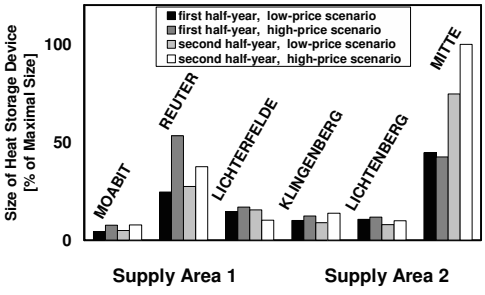

Fig. 5. Normalized resulting optimal sizes of the storage devices (V/V_{max}).

Since the resulting size of the heat storage device at a specified location is an indicator of its contribution to the profitable operation of the whole energy system, two locations are of direct interest: Mitte and Reuter.

The combined cycle CHP plant Mitte was originally constructed without a cooling tower (see Fig. 4 a) as it is located in the city and the district heating network was available as a heat sink. A dry cooling tower with a capacity of about one fourth the maximum thermal output was subsequently added in order to partly decouple the electricity production from the thermal load. Hence, it is not surprising that heat storage increases the full load hours of the power plant and, as shown in Fig. 5, the optimal capacity of the heat accumulators is considerably higher in the second half-year period, where the heat load of the district heating network is lower than the first.

With a total thermal output of about 800 MW, the coal and waste –fired units of Reuter are the main heat producers in west Berlin. Heat storage in this case offers the option to operate these units when the price for electricity is high and run at minimum load or shut down when the generation is not lucrative while still meeting heat demand obligations. This effect is enforced when fuel costs as well as electricity prices are set high (high-price scenario) as one shown in Fig. 5. Figure 6 presents the electric power production for the two coal-fired CHP units at Reuter for the scenario with and without the possibility of heat storage and Fig. 7 the heat production, respectively. The electricity production can be divided into weekdays (1 to 5) and the weekend (6 to 7) of the demonstrated week in January. The two units are shut down for eight hours on Tuesday, Friday and Saturday nights when the heat accumulators are introduced. The heat demand is covered by discharging storage devices earlier charged during profitable daytime operation with a small penalty on electric output, as shown in Fig. 6 (see also Fig. 4 b).

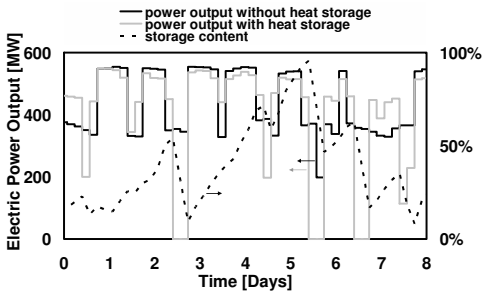

Fig. 6. Electric power output of the two coal-fired CHP units of Reuter for the scenario with and without heat storage (first half-year, high-price scenario).

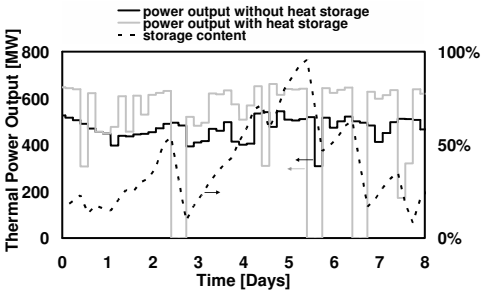

Fig. 7. Thermal power output of the two coal-fired CHP units of Reuter for the scenario with and without heat storage (first half-year, high-price scenario).

For a better understanding of the contribution provided by heat storage devices, the overall electricity production of the supply areas, as well as the heat production from the peak-load boilers for all scenarios is listed in Table 2 together with the percentage of heat delivered from buffered thermal power. The implementation of heat accumulators reduces the need of peak-load boiler operation and allows for an increase in the more lucrative and less carbon-intensive cogeneration. Indeed about 100 GWh/a of heat can be produced by cogeneration power plants instead of peak-load boilers in the whole power plant park of both parts of Berlin.

Table 2. Total electricity production, heat production of the peak-load boilers and percentage of heat buffered by accumulators for all presented scenarios.

			Electricity production (P) [GWh / half-year]			Heat production (Q) by PLB[1)] [GWh / half-year]			Stored Heat contribution [% of total supply]
			Without storage	With storage	ΔP	Without storage	With storage	ΔQ	
Supply Area 1	First half-year	Low prices	3576	3257	**-319**	19.0	7.0	**-12.0**	**28.5**
		High prices	3171	2934	**-237**	49.3	21.7	**-27.6**	**29.6**
	Second half-year	Low prices	3191	2962	**-229**	27.3	3.9	**-23.4**	**28.7**
		High prices	3265	3123	**-142**	51.7	25.9	**-25.8**	**34.5**
Supply Area 2	First half-year	Low prices	3224	3388	**+164**	113.8	82.5	**-31.3**	**33.4**
		High prices	2885	2956	**+71**	176.6	156.9	**-19.7**	**29.8**
	Second half-year	Low prices	2850	2994	**+144**	86.4	52.4	**-34.0**	**43.0**
		High prices	2778	3093	**+315**	126.6	82.7	**-43.9**	**42.1**

[1)] peak-load boilers

In west Berlin, the total electricity production decreases when heat storage devices are introduced. By partly uncoupling the heat production from demand, situations where a less profitable operation is necessary to satisfy the heat demand can be avoided, and as a consequence the mean return on electrical power increases by 2.5 to 4.5% (see also Figs. 6 and 7). The higher capacity utilization of Mitte leads to an increase of total electricity production for east Berlin and to a minor increase in return on electricity. The amount of heat which is not produced on demand, but rather buffered in the heat accumulators adds up to 29 to 43 % of the total heat supply.

3.2. Economic potential and numerical uncertainties

Considering MIP solvers, every optimization result (solution found) is accompanied by an upper bound (best possible). The smaller the difference between these two values, the better the guarantee of optimality since the real global maximum of the model has to be equal to or greater than the solution found and simultaneously equal to or smaller than the upper bound. For every scenario, three values for the static pay back period of the storage devices are given in Table 3: best case, worst case and solution found. Taking into account the two optimization results we get the value specified as “solutions found”. The value named “best case” is calculated by subtracting the upper bound value of the scenario with heat storage

from the value found in the solution of the base case scenario without accumulators. Comparing the upper bound of the objective function in the base case with the solution found when storages are implemented we get the value labeled "worst case". As shown in Table 3, optimally sized heat storage facilities have short static pay back periods, even taking into account the numerical uncertainties related to the guarantee of optimality. Considering the "solution found" values, a mean value of 0.8 years calculated for the pay back period reflects the profitability of heat storage.

The formulated objective function (1) specifies that the cumulative revenues for the scenario horizon are maximized. A marginal change of the resulting optimal size of the accumulators implies the same increase in total revenues as in levelized investment costs. Maximizing the return on investment instead would result in a smaller optimal capacity of the heat accumulators as the change of revenues per investment costs would determine the optimal capacity. Thus, capacities marginally smaller than those presented, lead simultaneously to a reduction of the pay back period and to a decrease of the cumulative earnings.

Table 3. Static pay back periods of the heat storage devices for the various scenarios.

Pay back period [a]			Best case	Solutions found	Worst case
Supply Area 1	First half-year	Low prices	0.5	**1.0**	1.9
		High prices	0.5	**1.6**	3.4
	Second half-year	Low prices	0.5	**1.0**	1.4
		High prices	0.5	**0.8**	1.1
Supply Area 2	First half-year	Low prices	0.6	**1.0**	1.2
		High prices	0.6	**0.7**	0.8
	Second half-year	Low prices	0.6	**0.7**	1.1
		High prices	0.4	**0.6**	2.0

3.3. Numerical experience

The main limitation on numerical convergence is given by the constraints on operating and downtime intervals (3) to (6) due to the coupling of the binary variables in time. On the other hand, these are necessary in order to obtain a realistic unit commitment schedule where power plants are not shut down and restarted on an hourly basis. A reasonable trade-off from our point of view was to use time intervals of four hours and splitting the period of one year into two half-years. By that, the number of coupled time periods is reduced, as well as the overall size of the problem and the acceptable numerical uncertainties presented in Table 3 were achieved.

4 Conclusions

In this paper, we present a method to optimize the operation of a power plant park supplying a large scale district heating network by introducing heat storage devices. Unlike other research works, an entire year of operation has been considered, in order to determine the economic potential and the optimal capacity of the heat accumulators located next to predefined power plants. The method was successfully applied to the power plant park and the district heating network of Berlin and the potential profit, as well as a change in unit operation was demonstrated. Partially decoupling the production of heat from the demand, and thus allowing for electricity-price-orientated operation, leads to pay back periods for the storage devices of approximately one year.

5 Outlook

Future investigations will focus on the following aspects:

- Assessment of the benefit of only one storage location per supply area
- Consideration of site-specific investment costs and maximum capacities for the heat storage devices
- Inclusion of start up costs of the units using the following conditions:

$$S = \sum_{u=1}^{\nu} \sum_{t=1}^{\tau} C_S(u) \cdot z(u,t) \quad (7)$$

$$y(u,t) - y(u,t+1) + z(u,t+1) \geq 0, \; z \in [0,1] \quad (8)$$

During start-up, the variable $z(u,t)$ has to equal 1, as the binary variable y of a unit u is 0 in t (unit is not in operation) and 1 in t+1 (unit is committed) in order to fulfill (8). If the operating

state does not change, or the unit is shut down from t to t+1, $z(u,t)$ may range between 0 and 1 without violating (8), but will eventually be forced to become 0 through the optimization as $\partial S / \partial z$ is positive and S is minimized.

Nomenclature

C	specific costs
c	coefficients of (2)
CRF	capital recovery factor
ef	CO_2 emission factor, t_{CO2}/MWh
$\dot{F}$	fuel flow rate, MW
O	objective function, €/horizon
$\dot{P}$	electrical power generation, MW
P	electrical energy produced, GWh
$\dot{Q}$	thermal power ("heat rate") output, MW
Q	thermal energy ("heat") produced, GWh
S	start up costs, €
s	storage device index, $s \in \{1,...,\sigma\}$
Δt	number of hours per time interval, h
t	time interval index, $t \in \{1,...,\tau\}$
u	unit index, $u \in \{1,...,\nu\}$
V	volume of a heat accumulator, m³
y	operating binary variable, $y \in \{0,1\}$
z	start up variable

Greek symbols

$\Delta\tau$	operating or downtime interval
ν	number of units
σ	number of storage facilities
τ	number of time intervals

Subscripts

C	expenditures related to CO_2 emission
CT	constant temperature of feed flow
d	downtime (interval)
F	fuel
o	operating (interval)
P	power generation
S	storage facility
V	storage tank volume
VT	variable temperature of feed flow

Superscripts

C	continuous (variable)
min	minimal (operating or downtime interval)
SC	semi-continuous (variable)

References

[1] Jüdes, M., et al., 2009, Combined Optimization of the Operation of Existing Power Plants with the Design and Operation of Heat Storage Systems for a Large District Heating Network, *Proc. 22nd International Conference on Efficiency, Cost, Optimization Simulation and Environmental Impact of Energy Systems*, S.A. Nebra, S. de Oliveira Jr., E. Bazzo eds., Foz do Iguaçu, Brazil, pp. 291–300.

[2] GAMS, General Algebraic Modeling System, 2010, Software Package, Ver. 23.3.2, GAMS Development Corporation, Washington, USA.

[3] CPLEX, 2010, Software Package, Ver. 12.1, IBM ILOG, New York, USA.

[4] Pfeiffer R. and Verstege J., 1996, Committing and Dispatching Units and Storage Devices in Cogeneration Systems with Renewable Energy Sources, *Proc. Power System Control and Management*, 421, pp. 21–25.

[5] Bogdan, Z., 2002, Optimization of District Heating Storage Capacity, *Proc. The 13th International DAAAM Symposium "Intelligent manufacturing & Automation: Learning from Nature"*, Katalinić, Branko eds., Vienna, Austria, pp. 47-48.

[6] Ito, K. et al., 1992, Optimal Operation of a Diesel Engine Cogeneration Plant Including a Heat Storage Tank, *Journal of Engineering for Gas Turbines and Power*, 114, pp. 687-694.

[7] Rolfsman, R., 2004, Combined Heat-and-Power Plants and District heating in a Deregulated Electricity Market, Applied Energy, 78, pp. 37-52.

[8] Murai, M. et al., 1999, An Optimizing Control for District Heating and Cooling Plant, Proc. International Conference on Control Applications, Hawai'i, USA, pp. 600-604.

Acknowledgments: The authors wish to thank Vattenfall Europe for supporting this work.

Economic Optimization of Small Scale Organic Rankine Cycles

Bertrand F. Tchanche[a], S. Quoilin[b], S. Declaye[b], G. Papadakis[a] and V. Lemort[b]

[a] *Agricultural University of Athens, Athens, Greece*
[b] *University of Liege, Liege, Belgium*

Abstract: The present paper focuses on the economic optimization of a small scale ORC in waste heat recovery application with specific investment cost as objective function. First, a pre-design model of the ORC was built and simulations run with different working fluids to evaluate their technical performance. In a second step, components and system cost models were built and simulations carried out to evaluate the cost effectiveness of systems associated with different fluids. The working fluids considered are R245fa, R123, R113, n-Pentane and n-Butane. Results indicate that for the same fluid, the point of high performance and that of cost-effectiveness do not match. The operating point for maximum power doesn't correspond to that of the minimum specific investment cost. For n-Pentane, the maximum net power of 1.98 kW is obtained for an evaporator pressure of 5.14 bar and the specific investment cost is 5450 €/kW. For this same fluid, a minimum specific investment cost of 4440 €/kW is obtained for an evaporator pressure of 8.5 bar and the corresponding power output is 1.745 kW. The mismatch aforementioned is due to the thermodynamic properties such as liquid/vapour densities, which significantly influence system performance and components sizes. Seeking for profitable environmental solutions, economic optimization as a necessary step in the optimization of any thermodynamic system is highly advised.

Keywords: Economic Optimization, Organic Rankine Cycle, Waste Heat Recovery, Working Fluid.

1. Introduction

Modern societies depend critically on energy and continued economic growth requires further increases in energy consumption and energy demand. According to official reports on future global primary energy production and use, the high energy growth rates of the 20th century will continue unabated until 2050 and even beyond. Presently, the global primary energy use is roughly 500 EJ and shall double by 2050 [1]. The world economy heavily depends on fossil fuels (oil, coal and natural gas) which represent an 81% share of total primary energy use. Renewable energy and nuclear energy share the remainder, 13% and 6% respectively. Nevertheless, the fossil fuel-based economy raises a certain number of issues. The dramatic destruction of the environment attributed to the excessive use of fossil fuels has reached a critical level with unpleasant consequences [2]. Moreover, the fossil fuel resources are finite. Their future depletion results in a considerable increase in the energy price with undesirable shocks on the global economy. The growing concern for the supply and safe transportation of fossil fuels as well as the increase in the energy demand reinforce the scaling-up of fossil fuel prices and fuel international tensions. Therefore, it is time to seek for alternate energy sources and to consider ways of saving the fast depleting fossil resources. Verbruggen [3] analyzed potential contenders for the future electricity supply from economic and sustainability viewpoints and proposed the twin efficiency/renewable power.

The Organic Rankine Cycles (ORC) as energy converter fall well in both sides of the twin. Their suitability in medium-scale power plants of few hundreds kW to MW power output has already been demonstrated in solar, geothermal, waste heat recovery and biomass power plants [4]. At the moment, there is a growing concern of recovering the heat wasted in industries during thermal processes as well as in thermal power plants and other thermal devices such as internal combustion devices. The potential for recovery is huge. For illustration, the analysis of manufacturing processes within the eight largest manufacturing sectors accounting for approximately 2/3 of the total energy used by the industrial sector in Canada showed that 70% (~1700 PJ) of the input energy was released to the environment [5].

Although investigated since the 1970s at the period of the oil crisis, the implementation of the recycling of

Corresponding Author: Bertrand F. Tchanche, Email: tfb@aua.gr, tfb_tchanchef@yahoo.fr

the wasted energy for electricity generation has been too slow or simply overlooked after the oil shocks as a result of the cheap fossil fuels prices. However, with growing concern on the environment and the fast depleting fossil fuels reserves, the interest on waste heat recovery for electricity is to know a new era. If the technology for medium and large scale ORCs is already mature, there is still room for research in small scale ORCs. In this perspective, a prototype of small scale ORC of few kWe was built and successfully tested at the University of Liège [6-8]. It uses R-245fa and R-123 as working fluids, and an oil-free scroll compressor adapted to run in expander mode. A thermodynamic model of the system was derived and validated for performance prediction. The validated thermodynamic model can be used to optimize the operation of the small ORC in waste heat recovery application. More recently, the economic evaluation of such small size systems was carried out to determine their cost effectiveness [9].

Most studies on ORCs as can be proven by the abundant relevant literature mainly focus on the optimization of the cycle efficiency and/or output power with respect to the cycle configuration and to the available working fluids [10-13]. Nevertheless, for the implementation of any new technology, the most important and determinant parameter is usually its affordability and not its performance. Thus, the present paper aims at performing the economic optimization instead of usual technical optimization. First, a pre-design model of the ORC is proposed and simulations are run with different working fluids candidates to evaluate their technical suitability. In a second step, components and system cost models are built and simulations run to evaluate the cost effectiveness of systems associated with different fluids.The working fluids used for the present study are: R245fa, R123, R113, n-Butane (R600) and n-Pentane (R601).

2. ORC in heat recovery application

The simple ORC system integrates four basic components: an evaporator, a turbine/alternator group, a condenser and a working fluid pump. Although many studies conclude that the introduction of regenerating processes (recuperator, feedliquid heater) increase the efficiency of the Rankine Cycle, the authors showed in a previous work that this is not justified in waste heat to power application for which the power output should be maximized instead of cycle efficiency [4]. The basic configuration is therefore selected in the present work. A heat source is needed to drive an ORC. Two ways exist to capture the wasted heat: (1) waste heat source and working fluid exchange in the same heat exchanger and (2) a thermal oil loop is integrated to transfer the heat from the waste heat site to the evaporator. The configuration illustrated in Fig. 1 will be considered in the present study. Depending upon the condensing pressure, the hot water at the condenser outlet can be used for space heating or as domestic hot water. In some cases, dry cooling can be applied at the condenser to save the water resources. The electricity produced can be used on-site or sent to the grid as in case of renewable energy systems (solar PV, wind turbine, biomass or geothermal power plants).

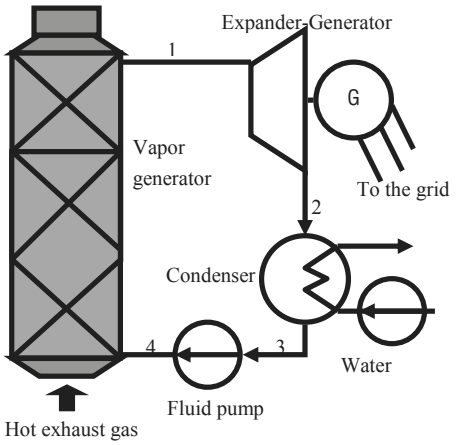

Fig.1. ORC in waste heat recovery application

3. Proposed fluid candidates

Selection of the most suitable working fluid is a critical step when designing an ORC. From numerous studies related to the selection of fluids for ORC-WHR, a certain number of criteria that should fulfil suitable fluids can be outlined. Fluids with high critical temperature or high boiling point such as toluene and silicone oils are adapted for high temperature heat sources. Hydrocarbons such as Pentanes, benzene, butanes and cryogens such as R227ea, R123, R245fa, and HFE7000 are good candidates for moderate and low temperatures. Zeotropic mixtures were suggested for best matching with exhaust stream which leads to better operation of the heat exchangers and resource recovery. Fluids with a high vapour density are advisable as they allow reduction of vapour turbine size and heat exchangers areas. Presently, only a few working fluids are available on the market and some are being progressively phased out because of their harmful effects on the environment (high ODP) reducing the

range of choice. In absence of specially designed ORC fluids, any fluid used in other thermal processes as engineering fluids is welcome. Hence, there is a need to start designing specific fluids for ORCs as ORC will become an important technology for harnessing low grade heat in the next future. Nevertheless, some of fluids present on the market are giving satisfactory results. A quick screening of several potential fluids was done and those listed in Table 1 emerged as suitable and will be considered in the present study.

Table 1. List of considered working fluids

	$\rho_{liq,wf}$ (kg/m^3)	2 Θ	Tc Θ	Pc (bar)
R-245fa	1352	15.3	154.1	36.4
R-123	1476.6	27.8	183.7	36.68
R-113	1574.9	47.6	214.1	34.39
R-600	625.7	-0.5	152	37.96
R-601	578.6	36.1	196.5	33.64
	UP_{wf} =	ASHRAE 34	GWP	ODP
R-245fa	32	B1	820	0
R-123	15	B1	77	0.02
R-113	25	A1	6130	1
R-600	1.7	A3	0	0
R-601	1.7	A3	0	0

4. Modelling of a small scale ORC

The ORC model is built by interconnecting several models related to the components.

4.1. The scroll expander model

Volumetric expanders, such as scroll, screw or reciprocating technologies present an internal built-in volume ratio corresponding to the ratio between the inlet pocket volume and the outlet pocket volume.

Under-expansion occurs when the internal pressure ratio imposed by the expander is lower than the system pressure ratio. In that case, the pressure in the expansion chambers at the end of the expansion process (P_{in}) is higher than the pressure in the discharge line. *Over-expansion* occurs when the internal pressure ratio imposed by the expander is higher than the system pressure ratio. Under and over expansion losses can be modeled by splitting the expansion into two consecutive steps [14]:

Isentropic expansion:

$$= \quad (1)$$

h_{in} being the isentropic enthalpy at pressure P_{in}.

Constant volume expansion:

$$p \quad - \quad m \quad (2)$$

w_2 is positive in case of under-expansion, and negative in case of over-expansion (Fig. 2).

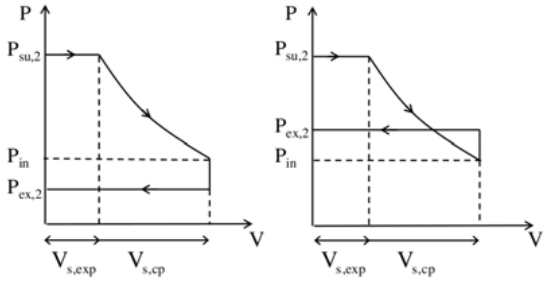

Fig. 2. Under and over-expansion losses

The total expansion work is then obtained by summing w_1 and w_2. Other losses such as internal leakage, supply pressure drop, heat transfers and friction are lumped into one single mechanical efficiency W_{mech}. Thus, the actual expander work is expressed as:

$$\quad (3)$$

For given rotational speed and fluid flow rate, the expander imposes the evaporating pressure. This is computed by:

$$M = \frac{FF \quad su \quad V_s \quad N_{rot}}{60} \quad (4)$$

4.2. The heat exchanger model

The condenser and the evaporator are modelled using U-NTU method for counter-flow heat exchangers. The heat exchanger is divided into three zones (Fig. 3)[7]: a liquid zone, a two-phase zone and a vapour zone. Each zone is characterized by the heat transfer area A and a heat transfer coefficient U. The heat transfer coefficient U is given by $1/U=1/h_r+1/h_{sf}$.

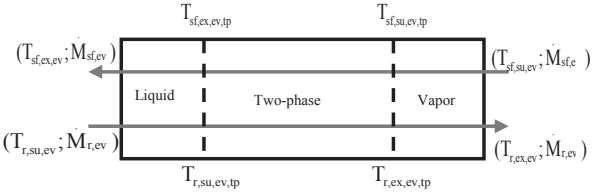

Fig.3. Three-zone model of the heat exchangers

4.3. The pump model

The pump is characterized by its swept volume and its global isentropic efficiency. Its electrical consumption is calculated using the relation

$$\dot{W}_{el,p} = \dot{V}_{s,p}\,(P_{r,ex,p} - P_{r,su,p})/\eta_p \quad (5)$$

In the latter model (Fig. 4), the mass flow rate displaced by the pump depends on the pump capacity and swept volume.

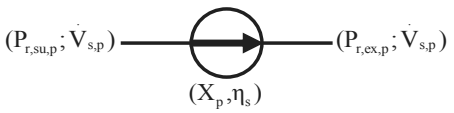

Fig. 4. Pump model

4.4. The global model

The global model of the ORC is built by interconnecting the models of different components above described to predict the system power output and cycle efficiency.

5. Thermodynamic optimization

5.1. Scope and method

The performance of a small scale ORC is predicted using the global model described in the previous section. Using that global model, the performance of the small scale ORC can be predicted. In the present case of an ORC in waste heat recovery application, the thermodynamic optimization aims at maximizing the net power output. However, other thermodynamic parameters can be used to characterize the thermodynamic behaviour of the system and are described in the following lines.

The cycle thermal efficiency is an indicative parameter of the quantity of heat converted into power and is given by:

$$\eta_{ORC} = (\dot{W}_{sh} - \dot{W}_p)/\dot{Q}_{ev} \quad (6)$$

The recuperation efficiency is the ratio of the heat recovered to the maximum heat recoverable. It can thus be written as

$$\varepsilon_R = \frac{\dot{Q}_{ev}}{\dot{Q}_{ev,max}} = \frac{\dot{M}_a\, c_{p,a}\,(T_{su,a} - T_{ex,a})}{\dot{M}_a\, c_{p,a}\,(T_{su,a} - T_{amb})} = \frac{T_{su,a} - T_{ex,a}}{T_{su,a} - T_{amb}} \quad (7)$$

The global energy conversion efficiency is the product of the cycle thermal efficiency and the recuperation efficiency.

$$\eta_{global} = \varepsilon_R\, \eta_{ORC} \quad (8)$$

For the present study, many assumptions are made:

- The heat source is exhaust gas at 180 ºC, assimilated to hot air with a mass flow rate of 0.21 kg/s.
- The condenser is cooled with cold water at 10 ºC.
- The pinch point at the evaporator is 15 K.
- The pinch point at the condenser is 10 K.
- The superheating at the expander inlet, 5 K.
- The subcooling after the condenser, 5 K.
- The volumetric ratio of the scroll expander, 3.4.
- Expander mechanical efficiency, 70%.
- The isentropic efficiency of the pump, 60%.

The ORC global model was implemented in EES (Engineering Equation Solver) and the behavior of the system simulated under various conditions to find the optimal operation point. Fig. 5 shows the T-s diagram of the ORC with R123 as working fluid.

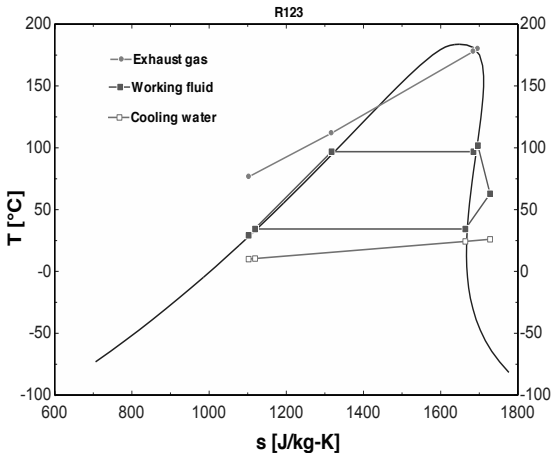

Fig.5. Temperature-entropy diagram with superposed heat source and heat sink profiles

Figs 6, 7 and 8 show the evolution of different parameters related to the system under different evaporator pressure at which heat is transferred to the power cycle. From Fig. 6, it can be seen that an increase in evaporator pressure reduces the amount of heat transferred to the cycle and the amount of heat rejected at the condenser. The reduction of the amount of heat captured in the evaporator affects the temperature of the exhaust effluent/gas rejected to the environment; its temperature increases.

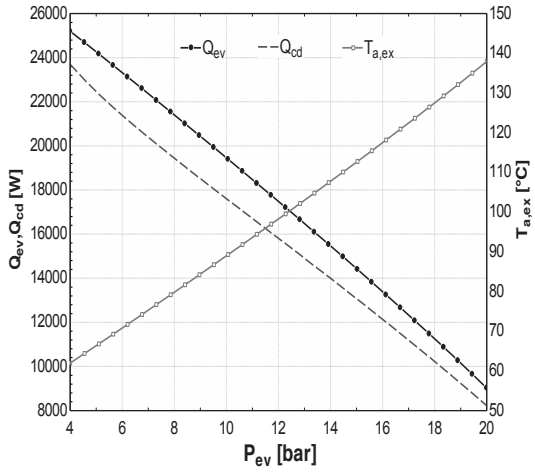

Fig. 6. Heat input, Heat rejected and temperature of the rejected exhaust

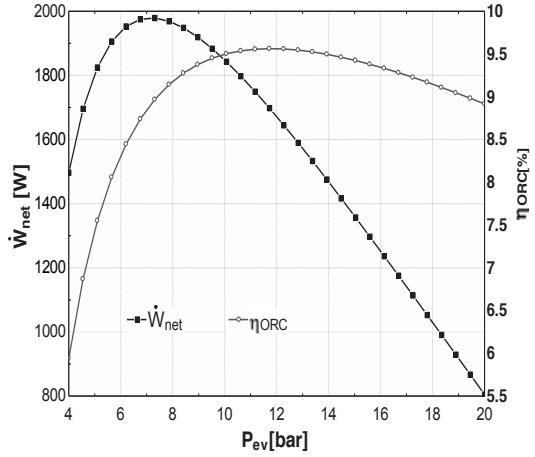

Fig. 7. Net power output and cycle efficiency

Fig. 7 shows the evolution of the net power output and cycle thermal efficiency. An optimum is obtained for both parameters but at different pressure values. The maximum net power of 1.80 kW is obtained for 7.31 bar while the maximum cycle efficiency (9.63%) is observed when the pressure reaches 11.72 bar. The maximum cycle efficiency is explained by under-expansion losses in the expander that increase when the pressure ratio is increased. In the case of heat recovery, since the heat source is free, the output power and not the cycle efficiency should be maximized.

Fig. 8 shows the evolution of the recuperation efficiency, cycle thermal efficiency and global efficiency. The recuperation efficiency decreases linearly as the evaporator pressure increases. The global efficiency has a maximum (5.45%) at about 7.31 bar and the same trend as the net power output. The cycle efficiency increases progressively and reach a maximum at about 11.72 bar and decrease slightly afterwards.

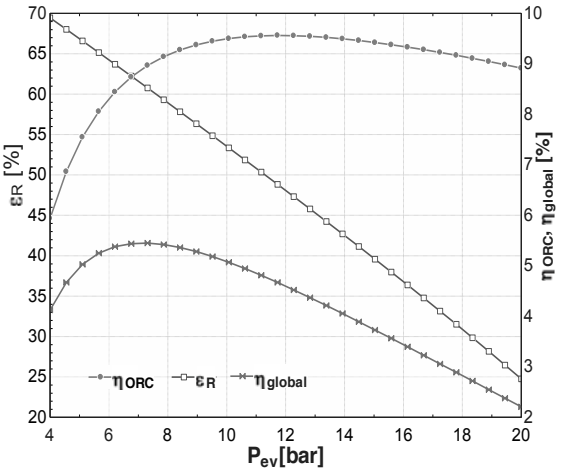

Fig. 8. Cycle, recuperation and global efficiency

5.2. Fluid comparison

Most criteria that should fulfil suitable working fluids in ORCs are well established [15]. These are: adequate critical parameters, high liquid and vapour densities, good thermal stability and compatibility with materials, appreciable safety characteristics, market availability and low cost, good thermodynamic performance and low environmental impact. The fluids in Table 1 will be considered further. The critical parameters for all fluids are suitable for subcritical cycles with the temperature of the heat source used. The thermal stability is not questionable for the considered fluids since the evaporating temperature does not exceed 200 °C. From compatibility point of view, only R123 is questionable as its corrosiveness has been reported. This can be solved by good selection of materials. All fluids proposed are available on the market with different prices as displayed in Table 1. Hydrocarbons are abundant at very cheap prices. Among the fluids proposed, R113 has a high ODP (1) and a high GWP (6130) and is phased-out in developed countries. N-Pentane and n-Butane raise the issue of flammability. Nevertheless, they can be considered as low risks substances as they are becoming familiar in domestic appliances. R245fa and R123 are toxic substances requiring special attention from the operator during manipulation. Performance parameters of ORCs associated with different fluids after power output

optimization are displayed in Table 2. The evaporating pressures recorded are well below the maximum acceptable limit of 25 bar. Both R245fa and n-Butane yield higher output and require high evaporating pressure. R245fa despite its toxicity has the highest vapour density at the expander inlet which would mean small expander. On the other hand, n-Butane is flammable but a very low cost fluid with the highest maximum power output. At this step, only a deep economic analysis could determine which one is to be selected.

Table 2. Thermodynamic parameters at maximum net power output

Fluids	P_{ev} (bar)	W_{net} (W)	$\rho_{p,su}$ (kg/m^3)	$\rho_{exp,su}$ (kg/m^3)
R245fa	11.79	2004	1324	64.98
R123	7.31	1979	1453	42.59
R113	3.93	1942	1554	26.42
n-Pentane	5.14	1979	616.6	13.78
n-Butane	15.31	2078	567.3	38.04

6. Economic optimization

6.1. Cost modelling

6.1.1. Expander cost model

For recall, the present expander is a scroll compressor adapted to run in reverse mode. The size of the compressor is linked to the thermodynamic characteristics of the fluid (density, volume flow rate) at the compressor outlet which corresponds to the expander inlet. From a catalogue of scroll hermetic compressors, and taking into account the cost of transformation, the expander cost is a linear function of the expander inlet volume flow rate:

$$C_{exp} = 450 + 340\,\dot{V}_s \quad (11)$$

6.1.2. Heat exchanger cost model

Heat exchangers are characterized by the heat exchange surface area which is one of parameters that determine the quantity of heat recuperated or rejected. For the present study, the cost model for heat exchangers deducted from a catalogue of flat plate heat exchangers is a linear function of the heat exchanger area:

$$C_{hx} = 388 + 480 A_{hx} \quad (12)$$

6.1.3. Pump cost model

Suitable pumps for small scale ORCs are small reciprocating pumps which can suck the liquid fluid at a pressure around 2-5 bar and deliver pressurized liquid fluid at about 10-20 bar while consuming small power input. However, it should be mentioned that there is no pump designed for liquid refrigerants. The cost model used in the present study is based on the relation between the power consumption and the cost as proposed by Bejan et al. [16]:

$$C_p = C_{p,ref} \left(\dot{W}_p / \dot{W}_{p,ref} \right)^m \quad (13)$$

m=0.25 for small reciprocating pumps (<300 W), and m=0.45 when the input power exceeds 300 W. From the offers obtained from suppliers in Liege, Belgium, the reference pump considered has a power input of 300 W and costs 900 €.

6.1.4. Pipes cost model

Given the same length and the same material characteristics, pipes are characterized by their diameter. In the present study, liquid and vapour pipes are distinguished and have different diameters. Depending upon the fluid, for the same state of fluid the diameter may differ. From offers of suppliers in Liege, Belgium, for cupper-type tubes which can stand pressure up to 30 bar, the cost model obtained is a linear function of the diameter:

$$C_{pp} = -6.90 + 6.75 D_{pp} \quad (14)$$

6.1.5. Fluid cost model

After examination of different prices of working fluids available on the market, it was difficult to build a correlation between the cost and thermodynamic characteristics. However, knowing the fluid charge, the cost of the working fluid for a particular system can be evaluated using the following relation:

$$C_{wf} = V_{liq,wf} . UP_{wf} . \rho_{liq,wf} \quad (15)$$

Where $V_{liq,wf}$ is the fluid charge; UP_{wf}, the unit price of the fluid and $\rho_{liq,wf}$, the density of liquid fluid.

The working fluid charge can be calculated based on the assumption that only the liquid part of the circuit is considered [17]; this is justified by the difference in density between vapor and liquid phases. The density of the fluid in liquid phase is much greater than the density in vapor state. Accordingly, the volume of the expander and the volume of vapor pipes as well as parts of heat exchangers are not taken into account. Thus, the liquid volume consists of ¾(1/2) of the evaporator volume, ¼(1/2) of the condenser volume, swept volume of the pump, liquid pipes volume and liquid reservoir volume.

$$V_{liq,wf} = (3/8) V_{ev} + (1/8) V_{cd} + V_{s,p} + V_{liq,pp} + V_{lr} \quad (16)$$

6.2. Influence of the working conditions

The cost models in the previous section (6.1) show that the costs of components are linked to the geometry/size of the components which in fact depends on the thermodynamic characteristics of the working fluid used. To appreciate the influence of the thermodynamic characteristics R123 will be used.

Fig. 9 shows the variation of the costs of the heat exchangers and the working fluid with the evaporating pressure. The cost of the condenser decreases linearly as the evaporating pressure increases. Fluid and evaporator costs present the same trend as power output. They increase, reach a maximum at about 7.31 bar and decrease as the pressure increases. The decrease with the above items is due to the reduction of the heat exchanger area which reduces as the evaporating pressure is increased.

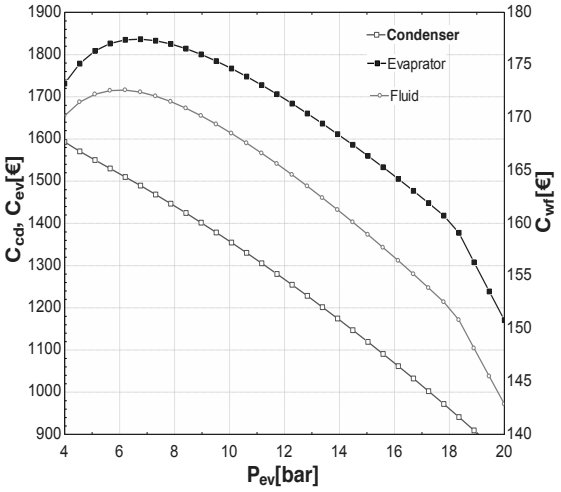

Fig. 9. Variation of the heat exchangers and working fluid costs with the evaporator pressure

In Fig. 10 can be appreciated the cost evolution of active components with evaporating pressure. With neglected pressure drop in the evaporator, evaporating pressure is the discharge pressure for the pump and the inlet pressure for the expander. The pump cost increases progressively, reaches a maximum at about 14 bar while the expander cost decreases gradually. The variations observed for both components are due to the density of the fluid at different states. For the same pressure, one discharges pressurized liquid while the other sucks superheated vapour.

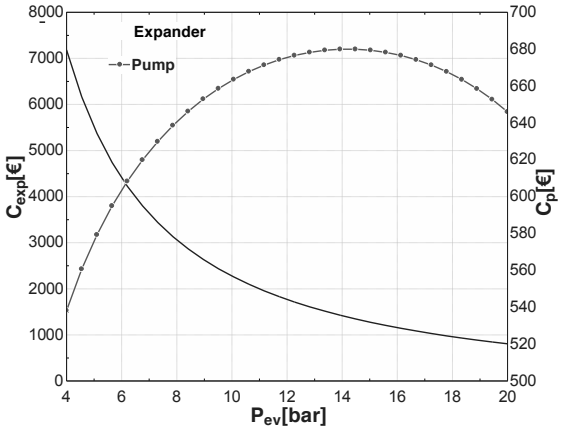

Fig. 10. Variation of the pump and expander costs with the evaporator pressure

6.3. Cycle cost model

In the previous section (6.2) it was seen that different components have different cost variations depending upon the working condition. This section aims at summing all components costs to build the total investment cost (TIC) and the specific investment cost (SIC). The TIC is the sum of various costs [9]:

- Scroll expander,
- Evaporator,
- Condenser,
- Fluid pump,
- Pipes,
- Working fluid charge,
- Other equipments: water cooling pump (300 €), liquid reservoir (200 €), control system (500 €) and miscellaneous hardware (300 €) for which the costs are neither dependant of fluids nor its thermodynamic state.
- The labour cost (10% of the total equipment cost).

$$TIC=\sum_{i=1}^{n} C_i \quad (17)$$

The specific system investment cost can be deducted:

$$SIC=TIC/\dot{W}_{net} \quad (18)$$

On Fig. 11, the evolution and weight of different components on the TIC are shown for R123. As can be seen, the most expensive components are the expander and the heat exchangers. The share of the expander compared to the total cost is particularly important at pressures below 11 bar, then decreases while the share of heat exchangers increases. This is due to the decrease of heat exchangers cost in narrow

ranges. The influence of the working fluids and pipes are almost negligible. However, the overall cost of the ORC decreases with an increase in evaporating pressure.

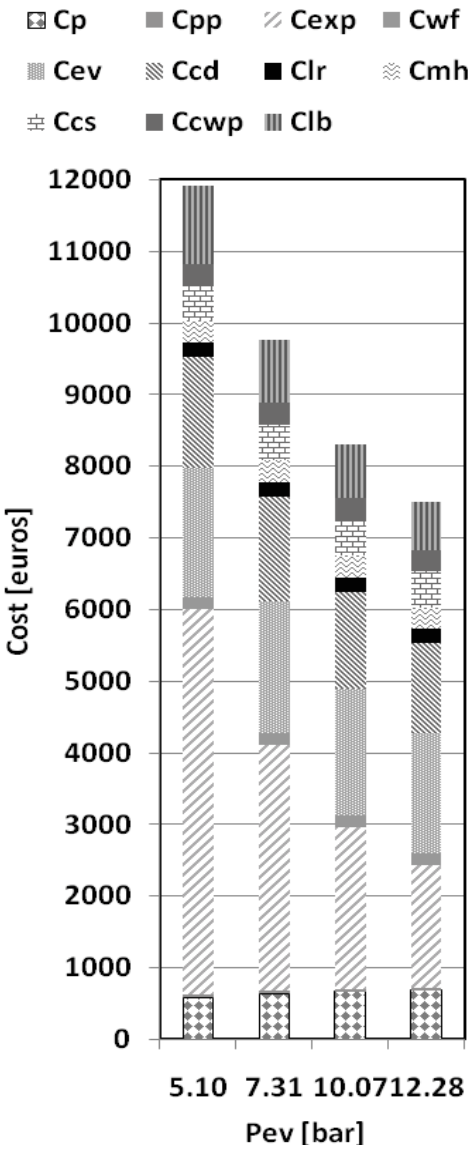

Fig. 11. Contribution of individual cost components on the TIC with R123 as working fluid

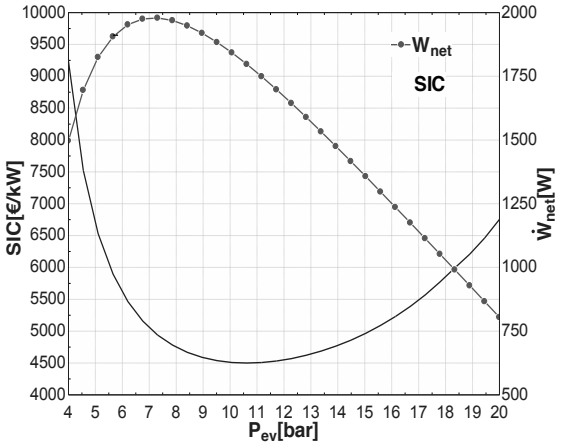

Fig. 12. Minimum SIC and Maximum net power

The specific investment/installed cost for any electricity generating system is a good indicator its cost effectiveness as it associates the investment with the capacity/performance. On Fig. 12, the evolution of the SIC with the evaporating pressure is depicted. A minimum value for the SIC is observed. For the case of R123 used here, this minimum occurs at an evaporating pressure of 10.62 bar. However, this minimum does not coincide with maximum power of 1979 W obtained at 7.31 bar. This observation can be extended to other fluids used in this investigation.

6.4. Cost optimization

The selected objective function for this optimization is the specific investment cost (SIC) expressed in €/kWe. Since WHR sources are cost-free by definition, optimizing this parameter is equivalent to optimizing the profitability of the system if maintenance and insurance annual costs are neglected. For a given working fluid, several different working conditions can be optimized. The evaporating pressure shows an optimum in terms of overall efficiency and also in terms of profitability. The pinch point on the heat exchangers also shows an optimum value: the lower this value, the higher the cycle efficiency but the higher the heat exchange area and the higher the cost. The choice of the pinch point value therefore results of a thermo-economic optimization of the system. Three parameters (P_{ev}, $\Delta T_{pp,cd}$, $\Delta T_{pp,ev}$) are therefore to be optimized with the objective of minimizing the SIC. This is done using the simplex algorithm [18]. The results of the optimization for each fluid are presented in Table 3. Table 4 shows results for maximum power for comparison.

Table 3. Three-parameters optimization of the SIC

Fluids	$\Delta T_{pp,cd}$ (K)	$\Delta T_{pp,ev}$ (K)	P_{ev} (bar)	W_{net} (W)	SIC (€/kW)
R245fa	15.66	18.58	15.50	1720	4413
R123	15.46	12.54	11.31	1750	4361
R113	17.92	10.7	7.39	1586	5128
n-Pentane	15.17	12.66	8.5	1745	4440
n-Butane	14.51	17.3	19.7	1816	3869

Table 4. One-parameter optimization of the net power output for $\Delta T_{pp,cd}$=10 K *and* $\Delta T_{pp,ev}$=15 K

Fluids	P_{ev} (bar)	W_{net} (W)	TIC (€)	SIC (€/kW)
R245fa	11.79	2004	9533	4757
R123	7.31	1979	9775	4939
R113	3.93	1942	12485	6430
n-Pentane	5.14	1979	10784	5450
n-Butane	15.31	2078	8475	4078

From Tables 3 and 4, it is seen that there is no fluid for which the minimum SIC and maximum net power coincide. For all fluids, increasing the evaporating pressure by about 3.5 bar from the point of maximum power, results in a loss in power and gain in specific cost reduction. The extent in the SIC reduction depends on the fluid. The economic optimization offers different results for different fluids. The SIC reduction is about 5.12% for n-Butane, 7.23% for R245fa, 11.70% for R123, 18.53% for n-Pentane and 20.25% for R113. Globally power loss of 200-400 W generates cost reduction from 1500 up to 4500 €. Transforming the reduction in SIC into net power and TIC reduction; 18.33% reduction in power leads to 34.85% of gain in TIC for R113. Table 3 shows that the optimum pinch point values for both the evaporator and the condenser are comprised between 10 and 20K, which could therefore be considered as reference values regarding the economical optimum for this kind of application.

7. Conclusion

The increase of the share of renewable energy in the global primary energy mix is slowed by the cheap fossil fuels although they have been recognized as a major treat to our environment. In the transition to the renewable energy era, efficiency through waste heat recovery has a role to play. ORC in waste heat recovery application better needs to be cost-effective than efficient. In the study performed, a pre-design model of the ORC was built and simulations run with different working fluids to evaluate their technical performance. Components and system cost models were built and simulations carried out to evaluate the cost effectiveness of systems associated with different fluids. Results indicate that efficient and cost-effective systems do not match. The mismatch is due to very different thermodynamic properties such as liquid/gas densities, which significantly influence system performance and components sizes. In the case of R113, a loss of 356 W on power output leads to a saving of 4352 € on total investment cost. The role of the pinch points on heat exchangers was also underlined. Good values are taken between 10-20 K. Seeking for profitable environmental solutions; economic optimization instead of thermodynamic optimization is advisable.

Nomenclature

A	Area (m^2)
C	Cost (€)
D	Diameter (cm)
FF	Filling factor (-)
h	Heat transfer coefficient (W/m^2K)
M	Mass flow rate (kg/s)
N	Rotational speed (tr/min)
P	Pressure (bar)
Q	Thermal heat (W)
T	Temperature (ºC, K)
U	Global heat transfer coefficient (W/m^2K)
V	Volume flow rate (m^3/s)
W	Power output (W)
X	Capacity (-)
	Greek symbols
ε	Recuperation efficiency (%)
η	Thermal or global efficiency (%)
ρ	Density (kg/m^3)
	subscripts
a	air/exhaust gas
am	ambient
b	
c	critical
cd	condenser
cs	control system
cw	cooling water pump
p	
ev	evaporator
ex	exit
hx	Heat exchanger
lb	labour

lea k	leakage
liq	liquid
los s	losses
lr	Liquid reservoir
m	maximum
me ch	mechanical
m h	Miscellaneous hardware
r	working fluid
p	pump
pp	pipe
s	isentropic
sh	shaft
su	supply
sf	secondary fluid
T R	trilateral or triangular
w	water
wf	working fluid

References

[1] Moriarty, P., Honnery, D., 2009, What energy levels can the Earth sustain?, Energy Policy (37), pp. 2469-2474.

[2] Sims, R.E.H., 2004, Renewable energy: a response to climate change, Solar Energy (76), pp. 9-17.

[3] Verbruggen, A., 2008, Renewable and nuclear power: A common future?, Energy Policy (36), pp. 4036-4047.

[4] Quoilin, S., and Lemort, V., 2009, Technological and Economical Survey of Organic Rankine Cycle Systems, In Proceedings of the 5th European Conference on Economics and Management of Energy in Industry, April 2009.

[5] Galanis, N., Cayer E., Roy, P., Denis E.S, Desilets M., 2009, Electricity Generation from Low temperature sources, Journal of Applied Fluid Mechanics (2), pp. 55-67.

[6] Declaye S, 2009. Design, optimization and modeling of an organic Rankine cycle for waste heat recovery, MSc Thesis, University of Liege.

[7] Quoilin, S., Lemort, V., Lebrun, J., 2010, Experimental study and modeling of an Organic Rankine Cycle using scroll expander. Applied Energy (87), pp. 1260-1268.

[8] Lemort V., Quoilin, S., Cuevas, C., Lebrun, J., 2009, Testing and modelling a scroll expander integrated into an Organic Rankine Cycle, Applied Thermal Engineering (29), pp. 3094-3102.

[9] Tchanche, B.F., Quoilin, S., Declay,e S., Papadakis, G., Lemort, V., 2010, Economic feasibility study of a small scale organic Rankine cycle system in waste heat recovery application, in Proceedings of ESDA 2010, July 12-14, Istanbul, Turkey.

[10] Tchanche, B.F., Papadakis, G., Lambrinos, Gr., Frangoudakis, A., 2008, Effects of regeneration on low temperature solar organic Rankine cycles, in Proc. of Eurosun 2008, 7-10 October, Lisbon, Portugal.

[11] Badr, O., Probert, S.D., O'Callaghan, P.W., 1985, Selecting a working fluid for a Rankine-Cycle Engine, Applied Energy (21), pp.1-42.

[12] Tchanche, B.F., Papadakis, G., Lambrinos, G., A. Frangoudakis, 2009, Fluid selection for a low-temperature solar organic Rankine cycle, Applied Thermal Engineering (29), pp. 2468-2476.

[13] Dai, Y., Wang, J., Gao, L., 2009, Parametric optimization and comparative study of organic rankine cycle (ORC) for low grade waste heat recovery, Energy Conversion and Management (50), pp.576-582.

[14] Zanelli, R., Favrat, D., 1994, Experimental Investigation of a Hermetic Scroll Expander-Generator, Proceedings of the 12th International Compressor Engineering Conference at Purdue, pp. 459-464.

[15] Tchanche, B.F., Papadakis, G., Lambrinos, Gr., Frangoudakis, A., 2008, Criteria for working fluids selection in low temperature solar organic Rankine cycles, in Proc. of Eurosun 2008, 7-10 October, Lisbon, Portugal.

[16] Bejan, A., Tsatsaronis, G., Moran, M., 1996, Thermal Design and Optimization, John Wiley & Sons.

[17] Quoilin, S., 2007, Experimental Study and Modeling of a Low Temperature Rankine Cycle for Small Scale Cogeneration, MSc Thesis, University of Liege.

[18] Nelder J. A., Mead, R., 1965, A simplex method for function minimization", Computer Journal, Vol. 7, pp. 308–313

Thermoeconomic Costs Analysis with Multi-period Operation of a Polygeneration Plant

Carlos Rubio-Maya[a], Javier Uche-Marcuello[b], César Torres-Cuadra[b] and J. Jesús Pacheco-Ibarra[a]

[a] *Faculty of Mechanical Engineering, UMSNH, Morelia, Mich., México*
[b] *CIRCE Foundation, University of Zaragoza, Spain*

Abstract: Simultaneous production of electricity, heat and cooling is a feasible option to provide them efficiently in hospitals, office buildings, airports and hotels. Moreover, fresh water production through desalination techniques can be integrated in the system yielding one additional product, i.e., fresh water. The synthesis, design and operation of this enhanced type of polygeneration plants is a complex task, and successive works to achieve a proper methodology for this purpose was proposed by the authors and presented in previous ECOS Conferences and other related events. Investigations still continue and the challenge of determining the physical cost of the various products in the system arose. Thus, in this work the thermoeconomic approach was applied to a polygeneration plant of a hypothetical tourist resort, with the purpose of knowing the instantaneous costs of the four products (electricity, cold, heat and water) under a multi-period operation. Thermoeconomic analysis was carried out applying the basic propositions of the Theory of the Exergetic Cost, obtaining the exergy costs of each product. Results show that lowest exergy costs were obtained when the plant was producing simultaneously the four products (mainly in summer period) but they increase considerably when one of the products is not produced, e.g., cold in the winter season. When the investment costs of the devices are also analyzed (including thermoeconomic costs), there is clear evidence that simultaneous production of water and energy (power, heat and cold) is desirable from the thermoeconomic point of view.

Keywords: Energy, Exergy cost theory, Polygeneration, Thermoeconomics, Water.

1. Introduction

Polygeneration systems [1,2] are a kind of energy systems that make use of diverse equipments to totally or partially meet variable demands and operate with the purpose of achieving the best operation mode. In order to ensure the lowest production costs, it is necessary to allocate the fuel cost in a rational form between the different products being generated, facing therefore a difficult challenge. Such a problem is not new, and several methodologies have been proposed in order to obtain the cost of both products in energy systems leading to a new discipline, the so-called Thermoeconomics.

A problem that could be classified as classical when allocating the production cost is the CGAM problem [3] defined to analyze a cogeneration plant with the aim of minimizing the production costs through the minimization of the product cost, i.e. electricity and heat. Four methodologies have been successfully applied to accomplish the challenge: Thermoeconomic Functional Approach, Exergoeconomics, the Theory of the Exergetic Cost and the Disaggregating Method. Although every methodology has its own criteria for cost allocation, their results are quite close. Those methodologies have been also applied to different energy systems but in all cases the system operation was at fixed load or matching constant demands [4,5]; however there is a possibility to analyze energy systems working at part load through the definition of periods of operation [6] enhancing in this way the application of thermoeconomics to energy systems with highly variable demands, such as in the case of polygeneration plants.

Therefore, in this work the thermoeconomic approach is applied to a polygeneration plant of a hypothetical tourist resort, with the purpose of knowing the instantaneous costs of the products (energy in several forms and desalted water) under a multi-period operation. Starting from an optimized configuration, the multi-period operation is defined through the characterization of day-types (typical days) representing operation in winter and summer seasons. Afterwards,

Corresponding Author: Rubio-Maya, Carlos Email: rmaya@umich.mx

thermoeconomic analysis is carried out applying the basic propositions of the Theory of the Exergetic Cost (TEC henceforward), so obtaining the exergy costs of each product.

To sum up, the knowledge of physical costs of a multi-purpose scheme answering to part loads is essential to get the adequate plant management, taking into account that additional auxiliary systems (peak boiler, power delivered to grid, heat, cold and water storage) could help to follow at any time period the demands of energy and water in the resort.

2. The polygeneration plant

This section shows the methodology proposed for the synthesis, design and operation of the polygeneration plant that will be analyzed in order to obtain the cost of each product at the system.

2.1. The methodology proposed

In earlier works it was proposed a two-level procedure of design, synthesis and operation of a system that meets simultaneously energy (electricity, heat, cold) and fresh water demands [7,8]. First level is a preliminary design and synthesis stage, second level is a detailed design and plant operation stage. Both levels used mathematical programming techniques. Next paragraphs give a brief description of that methodology, further details can be found in [9].

For the first level it was created a "superstructure" containing the suitable sets of conventional and renewable technologies candidates to integrate the final polygeneration system. Through the use of binary variables, the existence or inexistence of equipments was modeled. A monthly-basis profile was introduced here for the four demands, in order to reduce the computational effort. Finally, the preliminary configuration is the result of three criteria: energy savings, greenhouse gases emission reduction and economical feasibility, the latter evaluated through the maximization of the Net Present Value (NPV). The whole model was considered and solved as a mixed integer non-linear programming problem (MINLP).

Once non-feasible technologies were discarded and preliminary sizes of the feasible configuration were obtained, first-level solution is directly oriented as the starting point of the second level of the procedure, in which hourly demand analysis is performed in order to refine the size of equipments and evaluate thermal storage for both flattening the heating and cooling loads and for reducing peak demands. Thus, a continuous operation is maintained and plant over sizing is avoided. At this level, a detailed modeling of devices is required, and a multi-period optimization problem is originated, which was classified as a non-linear programming problem (NLP) one. The final result is a polygeneration plant with the size (capacity) of devices, interconnections between devices, the best operation mode (in the sense of which one of the four demands was the one followed) and other related (energy efficiency) parameters.

2.2. The case under study

The proposed procedure was applied to a typical tourist resort of the Mediterranean coast. Local demands were known from resort owners. On the other hand, several legal restrictions related to legislation (energy efficiency minimums) were considered through equality and inequality constraints. Afterwards, the model was solved using an optimization package with the following results: of course a positive NPV value and payback period of less than 8 years, primary energy savings (compared with conventional systems and their better efficiencies) of 16% and GHG emission reduction of 600 tonnes of equivalent CO_2 per year. The optimum configuration was composed by an internal combustion engine (ICE), single effect Lithium-Bromide absorption chiller (LBSE) and Low-Temperature Multi-effect desalination plant (MEDP). Their capacities were respectively 895 kWe for the ICE, 322 kW for LBSE and 7.5 m^3/h for MEDP. Cold and heat storage capacity as well as heat transfer area of heat exchangers were also obtained. A simplified version of the resulting polygeneration plant is depicted in Fig. 1.

At this point, the challenge of determining the physical and economic cost of each product arose. Thermoeconomic analysis has proven to be effective accomplishing this kind of problems, thus it will be used in order to find out in each operating period the cost of the four services that supplies the polygeneration plant.

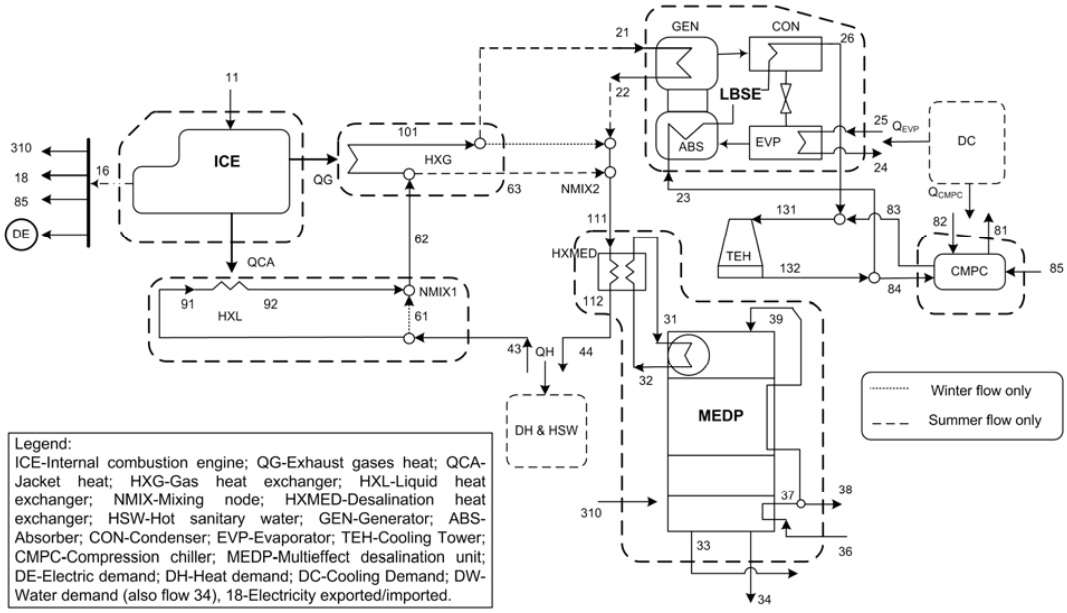

Fig. 1. Polygeneration plant and subsystem definition for the thermoeconomic analysis.

3. Thermoeconomic model

For the purpose of establishing a thermoeconomic cost analysis (TEC), first it is necessary to develop a thermodynamic model (TM) and subsequently determine the exergy of the most relevant system flows. In this case, the thermodynamic values were obtained from the optimization model, i.e. using only the equations dealing with the equality constraints in the second level of the methodology (detailed in section 2). To complete the thermoeconomic model, following assumptions were considered:

- Steady-state periods for the analysis, in which kinetic and potential energy effects are neglected.
- Air, natural gas and exhaust gases are considered perfect gases, with constant specific heat capacity.
- Reference conditions were P_0=101.3 kPa for the pressure, in the case of temperature two cases are considered: winter operation with a temperature of T_{0w}=283.15K and summer operation, in this case T_{0s}=303.15K.
- Heat and pressure losses of piping between devices are neglected.
- The exergy of the fuel is considered approximately equal to the value of its gross heating value (GHV) content.

Exergy content of a heat flow was calculated with:

$$B_Q = \int \left(1 - \frac{T_0}{T}\right) \cdot \delta Q \qquad (1)$$

When heat transfer process is carried out with increase or decrease in temperature the mean thermodynamic temperature [10] will be used in (1). In the present analysis, the majority of heat recovery processes used liquid water, therefore specific exergy is calculated as follows:

$$b = cp\left(T - T_0\left(1 + \ln\frac{T}{T_0}\right)\right) \qquad (2)$$

where Cp stands for specific heat of water. For seawater flows related to desalination, the expression is more complex, since chemical exergy contribution must be added in (2) [11].

3.1. Fuel-Product Definition

The TEC is based on the definition of products (P) and resources (called Fuels, F) of each subsystem in the plant, thus it is required the so-called F-P definition of the system under study. From the general scheme (Fig. 1) of the polygeneration

plant, it is possible to define the productive structure and formulate the F-P (Fuel-Product) definitions. For the ICE, inlet and outlet cooling flows in thermodynamic model were replaced with an equivalent heat flow recovered from jackets and oil circuit, QCA. In the same manner, gas outlet flow was replaced with an equivalent heat flow of exhaust gases, QG. That simplification leads to two fictitious devices, EFQCA and EFQG, resulting in a generalized model to obtain only the most relevant information. Thus, LBSE and MEDP equipments are considered only as black box subsystems because only the information about the cost of the products in the polygeneration plant is pursued. Fig. 1 shows the polygeneration plant and the subsystems for the TEC analysis.

F-P definition is a relative straightforward task, keeping in mind that each subsystem has a particular purpose. For instance, the purpose of the chiller is to produce a cooling effect using as a resource (fuel from the point of view of TEC) a thermal source in the case of absorption effect or electricity in the case of compression chiller. For the fictitious devices (EFQCA and EFQG) their purpose is to change the thermodynamic condition of a flow through any heat transfer process. MEDP plant is also trouble-free for defining the purpose, i.e. desalt seawater using thermal energy as a resource. The problem comes up with the ICE since its main purpose is not clear because two products are obtained: electricity and useful thermal energy. Therefore two alternatives are considered, the first alternative proposed by [12] consider both electricity and thermal energy as the main products in the ICE because the products are obtained from the same device. The second alternative, proposed by [13] considers that the main purpose of the ICE is the production of electricity and the useful heat is a product obtained from a subsystem operating in a series of reversible processes. In other words, it is considered that the irreversibilities are charged to the main purpose of the ICE (power generation). On the basis of these considerations two F-P definitions are investigated: Fig. 2 shows the F-P definition for the alternative one and Table 1 the equations for each subsystem; and Fig. 3 shows F-P definition for the alternative two and Table 2 the corresponding equations.

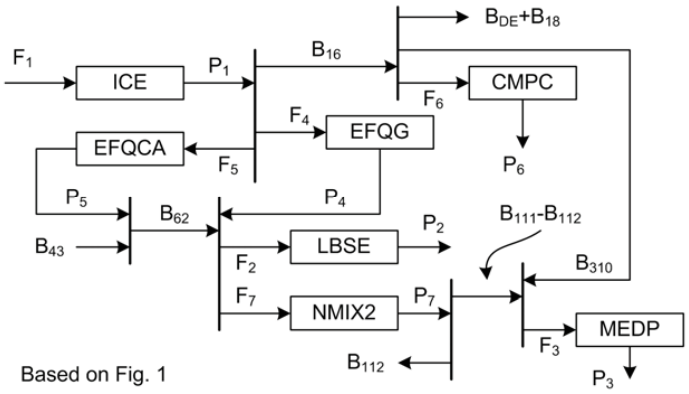

Fig. 2. F-P blocks of the polygeneration plant, alternative one.

Table 1. Fuel and product definition of each subsystem, alternative one.

Subsystem	Summer		Winter	
	FUEL	PRODUCT	FUEL	PRODUCT
ICE	B_{11}	$B_{16}+B_{QCA}+B_{QG}$	B_{11}	$B_{16}+B_{QCA}+B_{QG}$
LBSE	$B_{21}-B_{22}$	B_{QEVP}	---	---
LT-MED	$B_{111}-B_{112}+B_{310}$	B_{34}	$B_{111}-B_{112}+B_{310}$	B_{34}
EFQG	B_{QG}	$B_{63}+B_{21}-B_{62}$	B_{QG}	$B_{101}-B_{62}$
EFQCA	B_{QCA}	$B_{62}-B_{43}$	B_{QCA}	$B_{62}-B_{43}$
CMPC	B_{85}	B_{QCMPC}	---	---
NMIX2	$B_{22}+B_{63}$	B_{111}	B_{101}	B_{111}

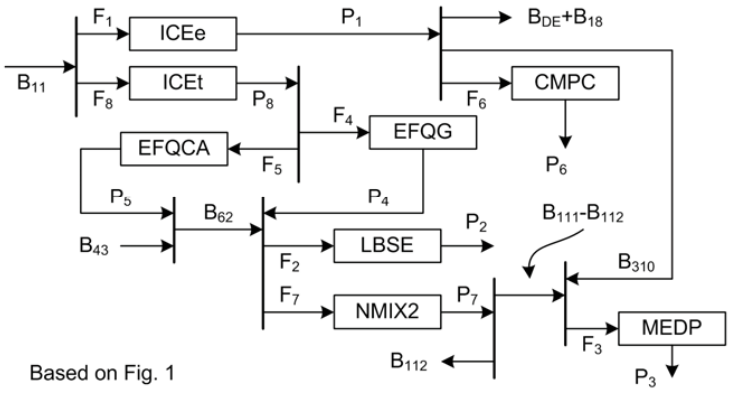

Fig. 3. F-P blocks of the polygeneration plant, alternative two.

Table 2. Fuel and product definition of each subsystem, alternative two.

Subsystem	Summer		Winter	
	FUEL	PRODUCT	FUEL	PRODUCT
ICEe	B_{11}-B_{QCA}-B_{QG}	B_{16}	B_{11}-B_{QCA}-B_{QG}	B_{16}
ICEt	B_{QCA}+B_{QG}	B_{QCA}+B_{QG}	B_{QCA}+B_{QG}	B_{QCA}+B_{QG}
LBSE	B_{21}-B_{22}	B_{QEVP}	---	---
LT-MED	B_{111}-B_{112}+B_{310}	B_{34}	B_{111}-B_{112}+B_{310}	B_{34}
EFQG	B_{QG}	B_{63}+B_{21}-B_{62}	B_{QG}	B_{101}-B_{62}
EFQCA	B_{QCA}	B_{62}-B_{43}	B_{QCA}	B_{62}-B_{43}
CMPC	B_{85}	B_{QCMPC}	---	---
NMIX2	B_{22}+B_{63}	B_{111}	B_{101}	B_{111}

Table 3. Investment cost and operation and maintenance costs.

Parameter	Symbol	Unit	Equipment, k			
			ICE	LBSE	LT-MED	CMPRY
Initial Investment cost	C_{fix}	€	393,980	98,405	190,164	265,860
O&M, equipment	OM	€/year	63,911	5,365.2	5,788.8	0
Total investment	C_{fixk}	€	482,600	187,025	278,784	0
Operation time	N_{op}	h	8,322	4,380	8,322	8,322
Investment	Z_k^I	€/h	5.59	4.11	3.23	0
O&M cost	Z_k^{OM}	€/h	7.68	1.22	0.696	0
Capital cost rate	Z_k	€/h	13.27	5.33	3.93	0

3.2. Physical and economic cost equations

Equations of physical costs are established through the use of the TEC and some complementary propositions resulting in a set of equation that can be solved using a simple approach as in [14], by means of applying (3) to each subsystem defined in Table 1 and Table 2:

$$\sum k_{in}^{*} B_{in} = \sum k_{out}^{*} B_{out} \quad (3)$$

Each set of equations were solved for each operating period, resulting in a set of equations representing a multi-period session. The economical costs were obtained in a similar way but additionally including the investment costs for each of the major equipment and the cost of the fuel required for operating the whole plant. Here, next equation was applied (4) to each subsystem and solved for the set of operational periods that were analyzed:

$$C_{Pk} = C_{Fk} + Z_k \quad (4)$$

In (4), Z represents the capital cost and O&M cost and it is calculated as:

$$Z_k = Z_k^I + Z_k^{OM} \quad (5)$$

Capital costs are calculated with (6), assuming the interest rate, useful life, hours of operation and capital cost of each subsystem:

$$Z_k^I = \left[\frac{r(1+r)^n}{(1+r)^n - 1}\right]\frac{C_{fixk}}{N_{op}} \quad (6)$$

Finally, O&M costs are determined with the following equation:

$$Z_k^{OM} = \frac{OM_k}{N_{op}} \quad (7)$$

In each equation written suffix *k* described the main equipments included in the analysis. It is worth noting again that the model must be solved in each period of operation, i.e. through typical days with 24 hour-periods. Table 3 shows the information required to perform the thermoeconomic analysis, in the table the CMPRY column groups the information of complementary devices required for the plant, such as: heat exchangers, cold storage, heat storage, pipes and so on.

4. Results

The thermoeconomic model was implemented in specific software suitable to manage the set of equations defined for each period considered. The results are shown in Fig. 4 (alternative one) and Fig. 5 (alternative two) grouping four plots that belong to the cost of each product generated in the polygeneration plant: electricity from the ICE, thermal energy recovered from the ICE, cooling from the absorption machine (LBSE) and desalted water from the desalination unit.

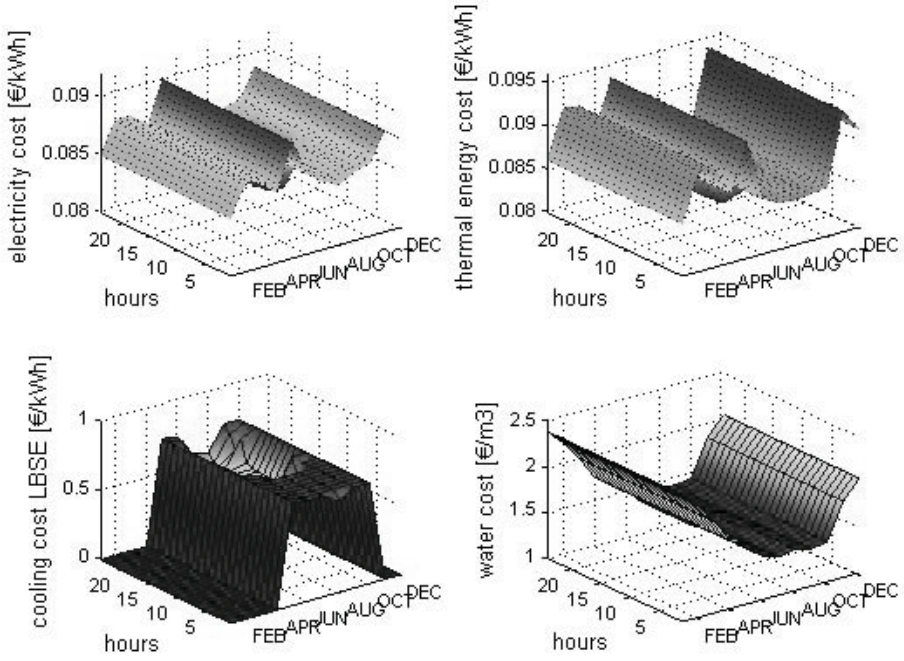

Fig. 4. Cost of products in polygeneration plant, alternative one.

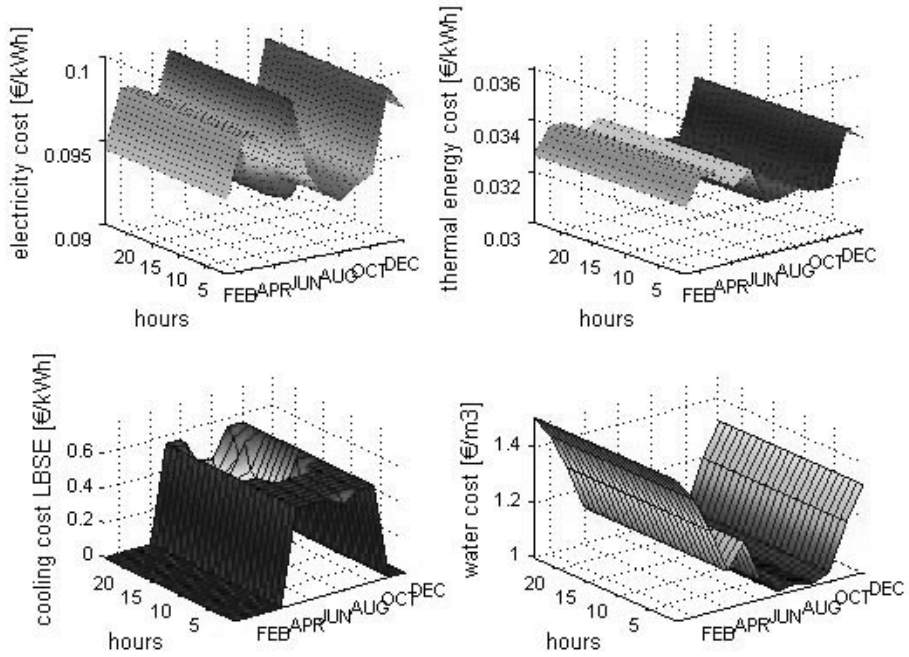

Fig. 5. Cost of products in polygeneration plant, alternative 2.

In Fig. 4 it can be seen that the thermoeconomic cost of electricity was in the range of 82-90€/MWh, thermal energy between 83 and 94€/MWh, cooling range from 400 to 700 €/MWh, and desalted water cost was in the range of 1.4-2.4 €/m^3, those figures belonged to alternative one. In Figure 5 presenting the second F-P alternative, thermoeconomic cost of electricity was in the range of 92-99 €/MWh (slightly higher than the alternative one), thermal energy was reduced up to the range of 32-34€/MWh, cooling cost was moved on the range of 280-500€/MWh, and finally the cost of desalted water varies from 1 to 1.5 €/m^3. These numbers give the marked effect of selecting the F-P definition on the polygeneration plant for the prime mover. Anyway, it seems that alternative two is more realistic than alternative one, since obtained costs could be better compared with the market prices, which are usually based on obtaining an additional bonus on the power generation under a cogeneration scheme.

Another fact that can be seen also in Fig. 4 and Fig. 5 is the similarity in shape in each plot, with the lowest cost presented in the summer season and the highest one in the winter season. This is due to the fact that whole plant is working at summer season, but the absorption chiller comes out of operation in winter and some useful heat is then dissipated into the atmosphere. Therefore, it is evident that the simultaneous production of the four products is advantageous from the economic point of view in these combined schemes.

5. Conclusions

Considering the results obtained it can be stated that TEC is a rational and powerful tool to allocate the cost of products in polygeneration systems to meet highly variable demands. Regarding the F-P definition, it is clear the advantage on the cost allocation to the different products of the polygeneration plant, specially for the prime mover that provides power and heat to the remaining three energy-type demands: in this particular case, alternative two (all the exergy resources charged to power generation) seems to be the better choice when compared with market costs, which are based on a bonus for an efficient power co-generation. Results also provided important differences between the costs of the products in the winter and summer periods, so

encouraging the fact that the adequate sizing of the plant is essential to find out the best yearly figures, even including auxiliary equipment to fulfill the seasonal peaks of power, heat for cooling purposes, and of course water. However, further detailed analyses are desirable to get an overall conclusion for the tourist sector in energy and water scarce areas.

Nomenclature

b	specific exergy, kJ/kg
B	total exergy, kW
C	economic cost, €
cp	specific heat, kJ/(kg·K)
F	fuel exergy, kW
k^*	unit exergy cost
P	pressure, product exergy, kPa, kW
Q	heat transfer rate, kW
r	interest rate, %
n	lifetime period, years
N_{op}	operating time, hours/year
T	temperature, K
Z	Capital cost rate, €/h

Subscripts and superscripts

0	reference environment
f	fuel
k	equipment or device
p	product

References

[1] Chicco, G. and Mancarella, P, 2009, Distributed multi-generation: A comprehensive view, Renewable and Sustainable Energy Reviews, 13(3), pp. 535-551.

[2] Serra, L. M., et al., 2009, Polygeneration and efficient use of natural resources, Energy, 34 (5), pp. 575-586.

[3] Valero, A., et al., 1994, CGAM problem: Definition and conventional solution, Energy, 19(3), pp. 279-286.

[4] da Gama Cerqueira, S.A.A., and Nebra, S.A. 1999, Cost attribution methodologies in cogeneration systems, Energy Conversion and Management, 40(15-16), pp. 1587-1597.

[5] Wang, Y. and Lior, N. 2007, Fuel allocation in a combined steam-injected gas turbine and thermal seawater desalination system, Desalination, 214(1-3), pp. 306-326.

[6] Kim, S.M. et al., 1998, Exergoeconomic analysis of thermal systems, Energy, 23(5), pp. 393-406.

[7] Rubio, C. and Uche, J., 2008, Feasibility analysis of a combined cooling-heating-power and desalted water plant in a non-residential building, Proceedings of ECOS 2008, Vol.3, Cracow, Poland.

[8] Rubio, C., et al, 2009, Selection and sizing procedure of polygeneration plants using mathematical programming, Proceedings of ECOS 2009, Foz do Iguaçu, Brazil.

[9] Rubio-Maya, C., 2009, Combined production of electricity, heat, cold and fresh water, in a sustainable mode for the tourist sector, PhD Thesis, Department of Mechanical Engineering, University of Zaragoza, [In Spanish].

[10] Ziegler, F., 1998, Relationships between temperature differences in heat exchangers of heat transformation devices, Revue Générale de Thermique, 37(7), pp. 549-555.

[11] Uche, J. 2000, Thermoeconomic analysis and simulation of a combined power and desalination plant, PhD Dissertation, Department of Mechanical Engineering, University of Zaragoza.

[12] Temir, G., and Bilge, D, 2004, Thermoeconomic analysis of a trigeneration system, Applied Thermal Engineering, 24(17-18), pp. 2689-2699

[13] Deng, J., et al., 2008, Exergy cost analysis of a micro-trigeneration system based on the structural theory of thermoeconomics, Energy. 33(9), pp. 1417-1426.

[14] Lozano, M.A. and Valero, A., 1993. Theory of the exergetic cost. Energy. 18(9), pp. 939-960.

Acknowledgments: The authors gratefully acknowledge the financial support of the Ministry of Spanish Government.

Investigation of the Introduction of Heat Pumps in the Residential Sector in Greece

Sotirios Karellas[a], Dionysios Giannakopoulos[a], Emmanuel Kakaras[a], Aggelos Doukelis[a], Konstantina Pappa[a], Nikolaos Barmparitsas[b], Eirinaios Eleftheriadis[b] and Peter Grunewald[b]*

[a] *Laboratory of Steam Boilers and Thermal Plants, National Technical University of Athens, Athens, Greece*
[b] *Daikin Hellas S.A., Athens, Greece*

Abstract: Heating of buildings represents a significant proportion of Europe's energy consumption while it also contributes a major source of greenhouse gas emissions, mainly through the combustion of heating oil and natural gas. On the other hand, accelerating climate warming and the potential depletion of natural resources have highlighted the need for rational energy use and energy efficient buildings. Towards this purpose, it is essential to evaluate the performance of all the alternative heating systems, one of them being the air-to-water heat pump. Heat pumps have been used successfully in countries in which electricity is produced with CO_2-free primary sources (e.g. France or Belgium). However, Greece is a country in which more than 50% of the electricity produced comes from the combustion of lignite in the main land, thus the potential of reducing CO_2 emissions by installing such units is subject to investigation. The purpose of this paper is to study the performance of heat pumps in comparison with oil-fired and gas-fired boilers, while taking into account not only the financial part but also the environmental impacts of each of the alternative heating systems.

Keywords: CO_2 emissions, Heat pump, Residential sector.

1. Introduction

The most widespread heating system in Greek residential buildings is the oil-fired boiler, which is often installed in combination with high temperature radiators. Natural gas-fired boilers are constantly gaining a market share, since natural gas was introduced to retail customers in 2001 [1]. Heat pumps, on the other hand, have been restricted to refrigeration and cooling purposes only. Split-type air conditioning units have become increasingly popular since the 1990's when their purchase cost dropped significantly [1].

Heat pumps are an extremely attractive technology as they can meet the energy requirements of buildings by using electrical energy which is only a fraction of the space heating and cooling energy produced. For this reason, they provide the opportunity to achieve significant savings in primary resources and the potential to reduce greenhouse gas emissions. Nevertheless, heat pumps cannot be considered as a guaranteed carbon-saving technology as their environmental performance is dependent on the sources used to produce the electrical energy that drives them. Furthermore, heat pumps' effect on energy bills in comparison with fuel-fired boilers, clearly relates to the electricity tariffs and prices of fossil fuels that apply for each country. In the above context, the present paper will discuss the introduction of air-to-water heat pumps to meet the heating, cooling and domestic hot water demand of Greek households. In order to make that comparison possible, it has been assumed that the typical household currently relies on a fuel-fired boiler, an air-to-air heat pump and an electrical water heater to meet those energy needs. Current data will be used regarding energy consumption in typical households, pricing of energy goods and finally the present and future synthesis of the Greek power generation network will be taken into account.

* Corresponding author: Sotirios Karellas, email: sotokar@mail.ntua.gr

2. Characteristics of air-to-water heat pumps

There are many different types of heat pumps available. This paper will focus on air-to-water heat pumps, which may present lower efficiency rates than ground source heat pumps, however the latter are characterized by substantial installation costs. Ease of installation and low capital cost as well as recent advancements in their operational features [2] have made air-to-water heat pumps even more appealing for utilization in residential buildings, especially for renovation applications.

The air-to-water heat pump that will be examined is a reversible type of heat pump that can be used for both heating and cooling and provides low temperature water (30-55°C). This unit can also be combined with a boiler tank and undertake domestic water heating load when it is not occupied with the space heating/cooling load. It should also be noted that the unit can operate at ambient temperatures of down to -20°C with the possibility of operating of a back up heater, depending on the dimensioning of the system.

The main factor which determines the heat pump's performance is ambient temperature and the set point of leaving water temperature. Other factors are the operating characteristics of the heat pump, the location of the outdoor and indoor unit, the defrost cycle, pipe run lengths and outdoor humidity. Data regarding the heat pump's average seasonal coefficient of performance is going to be provided by the manufacturer's data books.

3. Energy load of the typical Greek household

The cooling and heating energy demand depends on each dwelling's architectural features and insulation, on the climatologic conditions but it also reflects Greek people's lifestyle and their subjective sense of comfort. Although weather conditions in Greece during winter are mild, Greek buildings' insulation may vary significantly and depends strongly on the quality and type of construction. For this reason, the overall UA-value of the buildings' envelope will be considered a variable so as to account for well-insulated and poorly-insulated houses. For the purposes of this study the typical household is assumed to be situated in Athens, which lies in climatic zone B. Based on available statistical data from [3], the surface of the household will be considered to be 85 m^2 and the number of inhabitants 3.

3.1. Space heating demand

The heating period in Greece starts in the 1st of October and ends in the 30th of April. The indoor temperature is designed to be 20°C for all the spaces in the house. The heating load was calculated by utilizing degree-hour data available for Athens for a balance-point temperature of 18°C, as it is presented in [4]. The following table demonstrates the annual heating load for houses with different thermal loss rates, situated in Athens.

Table 1. Annual heating load for households with different total heat loss coefficients.

Thermal loss rate (W/K)	Required capacity (W)	Annual heating demand (KWh)
300	5640	8834
400	7520	11779
500	9400	14724
600	11280	17669
700	13160	20614
800	15040	23558
900	16920	26503
1000	18800	29448
1100	22560	35338
1200	28200	44172

Data presented in previous work [5] indicates that the specific annual heating demand (KWh/m^2) of dwellings in Athens ranges between 37,6 KWh/m^2 and 163,9 KWh/m^2 for insulated and non-insulated houses respectively. Another study [6] indicates 134 KWh/m^2 as the highest specific thermal energy consumption for climatic zone B. Combining this information with data from Table 1, it can be concluded that the average thermal loss rate of the typical household situated in Athens does not exceed 500 W/K.

3.2. Space cooling demand

The cooling period starts in the 1st of June and ends in the 30th of September. The cooling demand of the typical household was calculated by means of the degree-hour method, as it is presented in [4]. The balance-point temperature is assumed to be 24°C and the indoor design temperature is 26°C. The air-to-water heat pump's seasonal average

coefficient of performance for cooling is assumed to be 3. The air-to-air heat pump's seasonal coefficient of performance for cooling is assumed to be 3,3.

Table 2. Annual cooling load for houses with different total heat loss coefficients.

Thermal loss rate (W/K)	Required capacity (W)	Annual Cooling demand (KWh)
300	3150	2203
400	4200	2938
500	5250	3672
600	6300	4406
700	7350	5141
800	8400	5875
900	9450	6610
1000	10500	7344
1100	12600	8813
1200	15750	11016

3.3. Domestic hot water demand

One of the great advantages of heat pumps is that they can combine space heating with the provision of domestic hot water, by alternating between the two functions when they reach the required temperature set points. Despite the abundance of solar energy in Greece, many households still rely solely on fuel-fired boilers or electrical water heaters for the production of domestic hot water. According to [7] the average daily water consumption per person is 35 liters. For a family with 3 members this translates to Q = 960 KWh annually for domestic hot water, assuming an occupancy of 44 weeks a year. Grid water temperature is assumed to be 13°C in winter and 26°C in summer. Heat pump COP when producing warm water at 45°C is assumed to be 3, which results in an annual electrical energy consumption of 320 KWh. For the same amount of domestic hot water to be provided by a storage-type electrical water heater this would result in an electrical consumption of 1129 KWh assuming an efficiency ratio of 0,85.

4. Installation costs and energy bill calculations

Electricity tariffs for domestic consumers are determined by the Public Power Corporation. Electricity bills are calculated on a 4-month basis and the cost is divided into a fixed charge and a variable charge per electric KWh, both of them following an escalating pattern according to the total electrical energy consumption for the respective 4-month period. This fact has raised concern as to whether the extra electricity cost owning to a heat pump's energy consumption can increase electricity bills excessively and result in increasing the household's expenditure on heating, compared to oil-fired boilers. Based on [3], an average 4-month electrical energy consumption of 1800 KWh will be assumed. A seasonal COP of 3,6 will be assumed for the climatic conditions in Athens, in accordance with the manufacturer's data. Boilers' efficiencies have been considered to be 0,9 for the oil-fired boiler and 0,93 for the gas-fired boiler. The following table demonstrates the effect of the heat pump on energy bills, depending on the heat losses of the household. The use of a heat pump instead of a fuel-fired boiler and an air-to-air heat pump results in an increase in the electrical energy consumption whereas the avoidance of using an electrical water heater causes a reduction in the total amount of electrical energy consumed. The energy costs in Table 3 were calculated by determining the total variation in the electrical energy consumption of the household and also by assuming that 33% of total consumption falls within the low-tariff period which for winter applies between 15.30 – 17.30 and 02.00 – 08.00. For the purposes of this study current prices of heating oil were used, according to [8]. The price of natural gas in Greece is 20% lower than the price of heating oil. The results indicate that the replacement of oil-fired boilers by electrically driven heat pumps can yield considerable savings in a household's annual energy bills.

Table 3. Operating Cost comparison between different heating systems.

Annual heating demand (KWh)	Heat pump cost (€)	Oil-fired boiler cost (€)	Gas-fired boiler cost (€)
8834	251	583	452
11779	370	778	602
14724	492	972	753
17669	642	1167	903
20614	764	1361	1054
23558	886	1556	1204
26503	1008	1750	1355
29448	1130	1945	1506
35338	1377	2334	1807
44172	1744	2917	2258

Figure 1 demonstrates the capital cost of the different installation solutions for heating and cooling applications. These installation costs apply for a typical Greek household with a required capacity of 9,4 KW and represent the overall cost of the equipment which is required for every type of installation (radiators, chimney, pipeline, oil tank e.tc.)

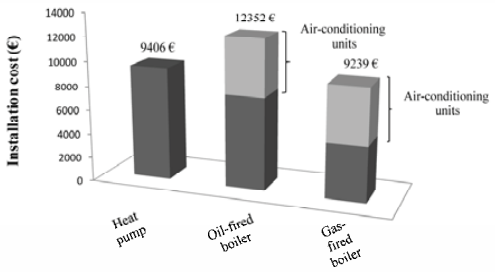

Fig. 1. Installation cost of alternative heating systems for both heating and cooling.

One main factor which is currently obstructing the penetration of heat pumps in the Greek market with regard to heating only applications is their high installation cost compared to conventional fuel-fired boiler systems. However, the savings that occur due to the operational cost of the heat pump compared to that of boilers can counterbalance the extra installation cost with a payback period of 3 years for the oil-fired boiler and 18 years for the gas-fired boiler.

In applications where both heating and cooling is needed the heat pump has the advantage that it combines two functions in one device and it rules out the need for installing separate air-to-air heat pumps. Therefore, it is more competitive in terms of space consumption and installation cost. As it can observed from Fig.1 the heat pump's cost is comparable to that of a gas-fired boiler combined with an air-to-air heat pump. The installation of an oil-fired boiler combined with air-conditioning units is the least cost efficient solution in those cases.

5. Environmental impact of alternative heating systems

In this section, the alternative heating systems mentioned are going to be evaluated in terms of their environmental performance, with the aim of establishing whether heat pumps can be considered as an environmentally friendly technology. The emissions owning to the heat pump's operation depend on the existing electricity grid and the seasonal performance of the heat pump.

The following table demonstrates the contribution of different fuels to the total electrical energy produced for 2009 as well as the imports and exports balance.

Table 4. Energy mix for 2009

	Percentage
Lignite	57,8 %
Oil	3,2 %
Natural Gas	17,8 %
Hydroelectric Power	9,4 %
RES and Other	3,6 %
Imports and Export Balance	8,3 %

According to the Public Power Corporation, the CO_2 emission factor of the country's electricity grid was 1 kg/KWh in 2008 and is planned to reach 0,9 kg/KWh in 2015 [9]. The following table demonstrates SO_2, NOx, and PM emission factors as well as PPC's strategic plans on reducing these emissions, in accordance with [10].

Table 5. Greek electricity grid emission factors in 2006 and estimated values for 2015.

Emission factor (gr/KWh)	2006	2015
SO_2	8,3	0,7
NO_x	1,7	1,1
PM	0,7	0,3

The following table demonstrates oil-fired and gas-fired emission factors according to [11] and [12].

Table 6. Emission factors of oil-fired and gas-fired boilers.

Emission factor (gr/KWh)	Heating oil	Natural gas
CO_2	260	200
SO_2	0,35	0,02
NO_x	0,35	0,15
PM	0,02	0

The following diagrams demonstrate the impact that the heat pump brings in the annual emissions profile of the typical household. It should be noted that the emissions depicted in the diagrams entail not only heating load coverage but also cooling load, domestic hot water load and electricity

demand, to serve the purpose of making an overall comparison of the alternative heating systems. Figures 2,4,6,8 present the calculated emissions based on present data for the electricity grid emission factors whereas figures 3,5,7,9 demonstrate the same data but based on future estimated values for the electricity grid emission factors.

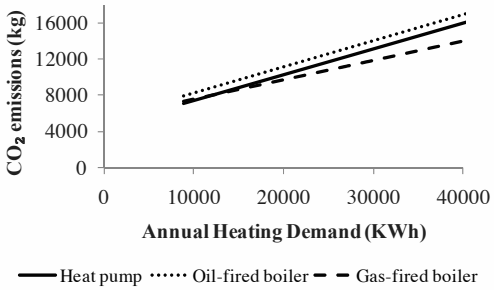

Fig. 2. CO_2 emissions for the present electricity grid CO_2 emission factor.

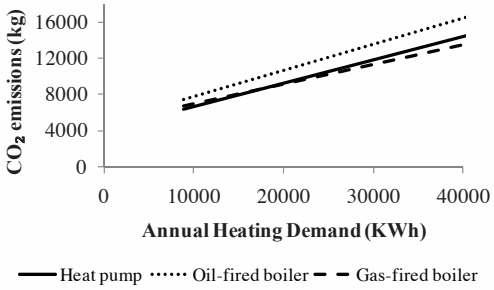

Fig. 3. CO_2 emissions for the future electricity grid CO_2 emission factor.

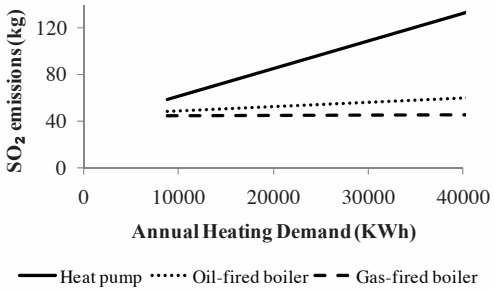

Fig. 4. SO_2 emissions for the present electricity grid SO_2 emission factor.

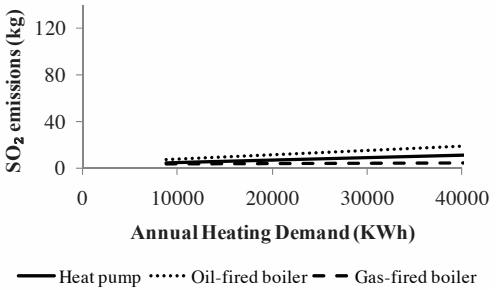

Fig. 5. SO_2 emissions for the future electricity grid SO_2 emission factor.

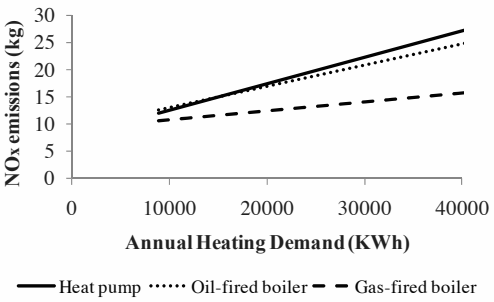

Fig. 6. NO_x emissions for the present electricity grid NO_x emission factor.

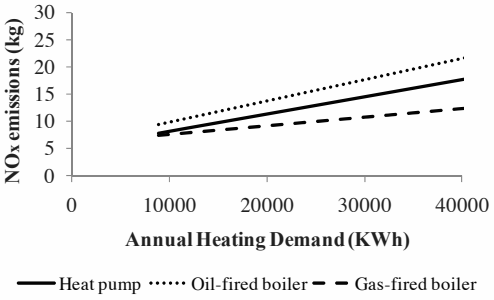

Fig.7. NO_x emissions for the future electricity grid NO_x emission factor.

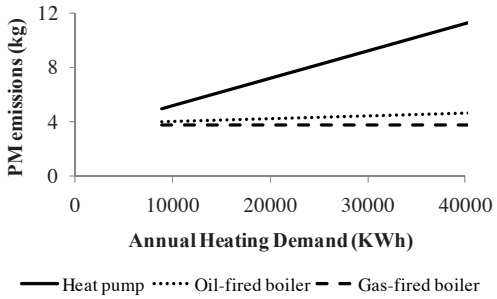

Fig. 8. PM emissions for the present electricity grid PM emission factor.

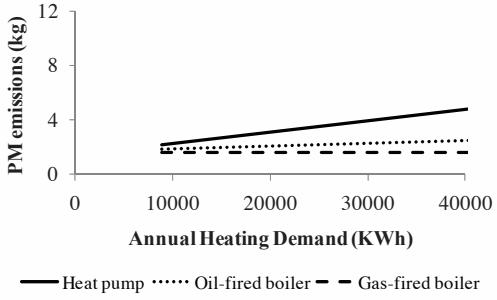

Fig. 9. PM emissions for the future electricity grid PM emission factor.

Figure 10 demonstrates the CO_2 emissions resulting from the application of heat pumps compared to fuel-fired boilers in order to meet an annual heating demand of 10000 KWh.

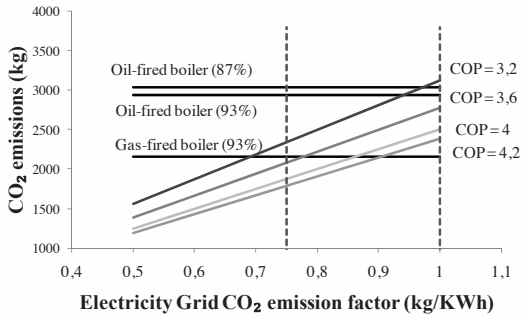

Fig. 10. Comparison of CO_2 emissions for alternative heating systems in relation to the electricity grid's CO_2 emission factor.

6. Discussion and Conclusions

Replacing an oil-fired boiler with a heat pump can lead to a CO_2 emissions reduction ranging between 4-10%. Even more significant reduction can be achieved if the energy system's environmental performance further improves.

There is a certain crossover point in terms of the heat pump's COP where the heat pump will produce more CO_2 emissions than the oil-fired boiler. This applies for the electricity grid's current CO_2 emission factor and occurs for COP values below 3,2 as it can be observed in Fig. 10.

Taking into account present data regarding SO_2 and NO_x emission factors, the oil-fired boiler seems more appealing than the heat pump, but future plans to reduce those emission factors can alternate the results in favor of the heat pump.

Heat pump's PM emission level is higher than that of fuel-fired boilers, even if future plans for the country's energy mix are taken into account.

The gas-fired boiler produces the lowest level of emissions of all three technologies. Only in cases of low annual heating demand, a high performance heat pump (with a COP larger than 3,2) produces less CO_2 emissions than the gas-fired boiler. This is due to the fact that domestic hot water preparation has been taken into account.

The replacement of old oil-fired boilers with air-to-water heat pumps in Greek households could contribute to alleviating the problem of pollution which is intense in densely-populated cities, such as Athens. However, such an electrification of heating energy production would result in extra emissions produced in power plants, nonetheless pollution that could be more easily abated [13].

A further investigation for future work could be the environmental comparison of the alternative heating systems while taking into account all the upstream processes regarding emissions.

References

[1] Papadopoulos, A. M., Oxizidis, S., Papandritsas, G., 2008, Energy, Economic and Environmental Performance of Heating Systems in Greek Buildings, Energy and Buildings, 40, pp. 224-230.

[2] Jenkins, D., et al., 2008, The Performance of Air-Source Heat Pumps in Current and Future Offices, Energy and Buildings 40, pp. 1901-1910.

[3] National Statistical Service of Greece URL:http://www.statistics.gr/portal/page/portal/ESYE

[4] Papakostas, K., and Kyriakis, N., 2005, Heating and Cooling Degree-Hours for Athens and Thessaloniki, Renewable Energy 30, pp. 1873-1880.

[5] Papakostas, K., Kyriakis, N., Oikonomou, D., 2006, Estimation of Energy Consumption for Heating in Residential Buildings of 36 Greek Cities, *Institute of Solar Technology Eighth National Conference on Renewable Energy Sources*, Aristotle University of Thessaloniki, Greece.

[6] Balaras, C., et al., European residential buildings and empirical assessment of the Hellenic building Stock, energy consumption, emissions, and potential energy savings, 2007, Building and Environment, 42, 1298-1314.

[7] Papakostas, K., Papageorgiou N. E., Sotiropoulos B. A., 1995, Residential Hot Water Use Patterns in Greece, Solar Energy, Vol. 54, No 6, pp. 369-374.

[8] Hellenic Republic Ministry of Development, URL:http://www.ypan.gr/flash_fuel/kafsima/MESES_TIMES.htm

[9] Public Power Corporation, URL: http://www.dei.gr/Documents/PERIV.gr.oct_09.pdf

[10] Public Power Corporation, URL:http://www.dei.gr/Documents/xatziargyriou26.11.08.pdf

[11] Center for Renewable Energy Resources, URL:http://www.cres.gr/kape/pdf/download/ependytes.pdf

[12] Technical Chamber of Greece, URL:http://library.tee.gr/digital/m2045/m2045_kouloubis.pdf

[13] Zogou, O., and Stamatelos, A., 1998, Effect of Climatic Conditions on The Design Optimization of Heat Pump Systems for Space and Heating and Cooling, Energy Convers. Mgmt Vol. 39, No7, pp. 609-622.

LOAD MANAGEMENT OF AIR-TO-WATER HEAT PUMPS FOR EXISTING HOUSES IN FRANCE

Sami Barbouchi[a], David Olmos-Mata, Anne-Sophie Coince[a]

[a]EDF R&D, "Energy in Buildings and Territories" Department, 77818 Moret-sur-Loing, France

ABSTRACT: On the total end-use energy consumed in France, space heating in buildings represents 20%. Furthermore, the use of old fuel boilers in existing houses contributes significantly to CO_2 emissions. Nowadays, electrical heat pumps represent an efficient alternative to these heating systems. Nevertheless, if an important part of fuel boilers are replaced by heat pumps, it could result in both an increase of the electricity consumption and an emphasis of peak electrical demand during the coldest days.

The objective of this study is to improve the load management of air to water heat pumps by taking advantage of the thermal capacitance of the building. During peak electrical demand, the idea is to turn off the heat pump in order to minimize its electric consumption, while satisfying required comfort conditions for the building. The influence of adding a storage tank and an overheating control system will also be analyzed. The obtained results will allow us defining the best solution according to different criteria.

Keywords: **air to water heat pump, building's thermal behavior, design of experiments, load management, peak electrical demand, 3R2C model.**

1 Introduction

In France, the buildings sector is the biggest energy consumer with 43% of the total end-use energy, among which 68% are due to the households [1]. This sector contributes to 21% of the Green House Effect (GHE) gases. Heating systems themselves represent 2/3 of the French energy consumption in the residential sector and are responsible for most of the CO_2 emissions because of fossil fuel heating systems.

Nowadays, air-to-water heat pumps represent an efficient alternative to old fuel boilers [2]. Nevertheless, these thermodynamic systems consume electricity and the replacement of a significant share of the current boilers could increase the peak demand during the coldest days and therefore lead to:

- blackouts,
- the use of the most expensive power plants,
- the use of CO_2 emitting power plants [3].

One solution consist in demand response [4] which is a tariff or program established to motivate changes in electric use by the end-use customers in response to changes in the electricity price. The study [5] shows how it is possible to reach load reduction by applying a specific pricing during the critical peak periods.

For heating, it is possible to use systems which don't consume electricity during peak period, but it is also possible to take advantage of the building thermal capacitance [6] or to add storage devices and to increase the set-temperature by overheating.

Some simulations applying the design of experiment (DOE) method [7,8] have been performed to define the best storage tank capacity and control strategy, depending on the required load shift. A similar method has been carried out by Fadi [9] to determine the influence of different parameters on the consumption of a low energy building.

The aim of this study is to find accurate solutions to ensure a safe deployment of these technologies, whatever the characteristics of

Corresponding Author: Barbouchi Sami, Email: sami.barbouchi@edf.fr

the environment (type of building, localization).

2 Numerical simulation

The simulations have been carried out under SIMULINK® [10] with the SIMBAD [11] building and HVAC toolbox, which is a library of models suitable for the development of HVAC control systems in buildings.
The solver is based on extrapolation and Newton method. The step time is fixed at 60 seconds.

2.1 Studied System

Next, the sub-systems that make up the global system will be presented:

2.1.1 Individual houses

For the house, a simple 3R2C mono-zone energy model has been chosen. In [12], it is possible to find the presentation of more detailed RC building models.
The 3R2C model consists of three resistances and two capacities, respectively standing for the thermal resistance and the wall's thermal capacitances (Fig. 1).

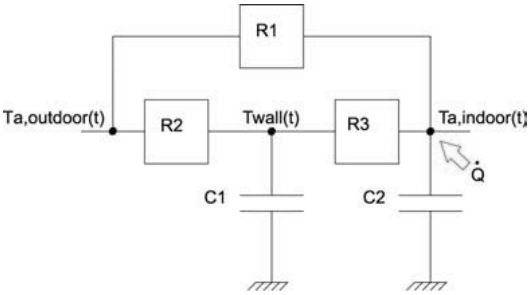

Fig. 1. 3R2C model's scheme.

The conductive heat transfer coefficient K_{cond} of the house can be directly calculated with the thermal resistances (1). The air flux renewal associated with K_a (2) is taken constant and equal to 72 W/K. The thermal heat loss coefficient is obtained with (3), and allows the calculation of the heat losses of the house (4). C_{total} corresponds to the total thermal capacitance of the house, which is the sum of the capacitance of the 3R2C model (5).

$$K_{cond} = \frac{1}{R_1} + \frac{1}{R_2 + R_3}, \quad (1)$$

$$K_a = \dot{m}_a c_{p,a}, \quad (2)$$

$$K_{total} = K_{cond} + K_a, \quad (3)$$

$$\dot{Q} = K_{total}\left(T_{a,int} - T_{a,out}\right), \quad (4)$$

$$C_{total} = C_1 + C_2. \quad (5).$$

The available individual houses in the SIMBAD library correspond to standard French houses with an area of 100 m^2 and different level of insulation. The conductive heat transfer coefficient K_{cond} and the total thermal capacitance C_{total} of the studied houses are indicated in the Table 1.

Table 1. Individual houses characteristics.

House	K_{cond} (W/K)	C_{total} (MJ/K)
House1	133	37
House2	103	37
House3	133	78
House4	103	78
House5	118	57

2.1.2 Climatic conditions

Simulations have been carried out for the two coldest weeks of the decennial weather conditions in Nancy (Fig. 2), which is located in the coldest area of France. In order to avoid the influence of the initial conditions, the first week has been repeated. Solar flux and occupation gain haven't been considered in order to place the problem in the worst conditions. Their contribution to the heating production has been estimated by simulation respectively around 11% and 3%.

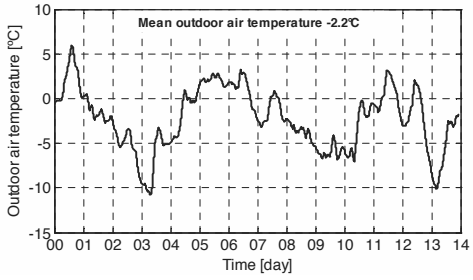

Fig. 2. Outdoor air temperature on 2 weeks for the simulation.

2.1.3 Hydronic system

A scheme of the hydronic system is represented on the Fig. 3. Karlsson and Fahlén, 2008 [13] have also worked on the modeling of systems composed of a hydronic heating system, a heat pump, radiators and a building.

In our configuration, to be able to control directly the indoor air temperature, a three-way valve has been added for varying flow rate in the radiators. Moreover, in order to avoid a nil flow rate, a bypassed small radiator has been added.

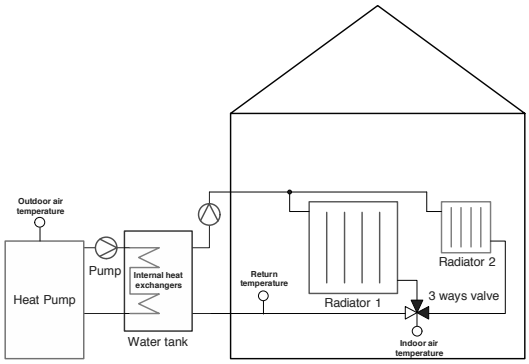

Fig. 3. Scheme with parallel tank.

The influence on the load management of a parallel storage tank has been studied by using a stratified water tank with an oversized internal heat exchanger.

2.1.4 Air-to-water heat pump

In order to couple a heat pump to the existing hydronic system, a high temperature heat pump with a supply temperature of 65ºC at –15°C has been chosen. To study the heat pump load-shedding during the coldest days, the heat pump has been sized so that its heating capacity is at least superior by 20% to the heat losses of the house the coldest day. However, in practice, the heat pump is sized in order its heating capacity is equal to heat losses at the balance point. Thus for outdoor air temperature under the balance point, the difference between the heat required and that supplied by the heat pump is normally obtained from auxiliary electrical resistance heaters.

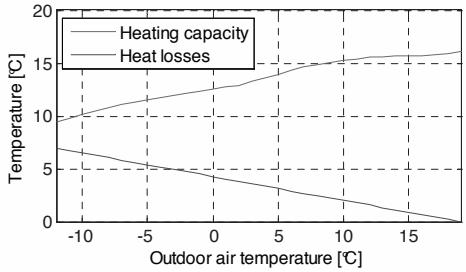

Fig. 4. Heating capacity of the heat pump and heat losses of the house.

The control of the heat pump is made according to the heat curve [14] on the water return temperature. The heat curve (6) expresses the set-temperature needed to ensure the comfort in the house as a function of the outdoor air temperature, the other parameters being fixed. It can be obtained by solving the system composed of the equations (4), (7) and (8). The equation (7) expresses the heat flow of a radiation [15]. For cast-iron radiators, the exponent *n* is taken equal to 1.31.

$$T_{w,return} = f(T_{a,out}) = T_{air,int} + \left[\left(\frac{K_{total}}{\tilde{c}}\right)\left(T_{a,int} - T_{a,out}\right)\right]^{\frac{1}{n}} + \frac{K_{total}}{2\dot{m}_w c_{p,w}}\left(T_{a,int} - T_{a,out}\right) \quad (6)$$

,

$$\dot{Q}_{radiator} = \tilde{c}\left(\frac{T_{radiator,w,in} + T_{radiator,w,out}}{2} - T_{a,int}\right)^n \quad (7)$$

,

$$\dot{Q}_{radiator} = \dot{m}_w c_{p,w}\left(T_{radiator,w,in} - T_{radiator,w,out}\right), \quad (8).$$

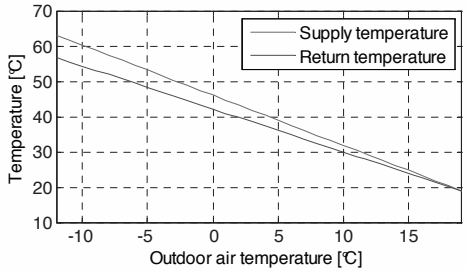

Fig. 5. Heat curve.

As the heating capacity of the heat pump is superior to the heat losses of the houses, the heat pump will start and stop in order that the supply energy is equal to the heat required. So, when the return temperature measured is above the set-temperature given by the heat

curve plus 1.5ºC, the heat pump will turn off and when it is below the set-temperature given by the heat curve minus 1.5ºC, it will turn on.

2.2 Control strategies

The load-shedding consists in preventing the heat pump from starting. It takes place the working days from 18:00 (Fig. 7). It finishes when the indoor air temperature is lower than the set-point temperature minus 0.5ºC (Fig. 7).

The objective of overheating is to have the storage tank overheated just before the load-shedding (Fig. 6). Overheating starting time is calculated by using the rising speed of the water return temperature. Thus, it is possible to reach the targeted temperature given by the heat curve calculated for the outdoor air temperature at 18:00 plus an overheating of 0ºC, +2ºC or 4ºC (Fig. 6).

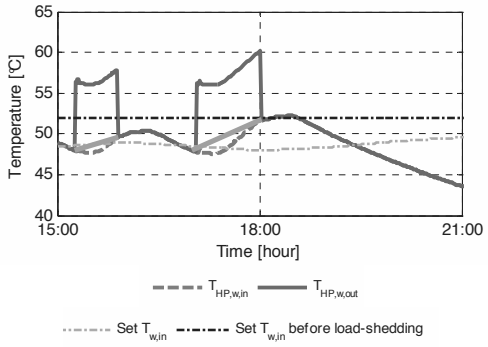

Fig. 6. Control of the heat pump according to the rising slope of the water return temperature.

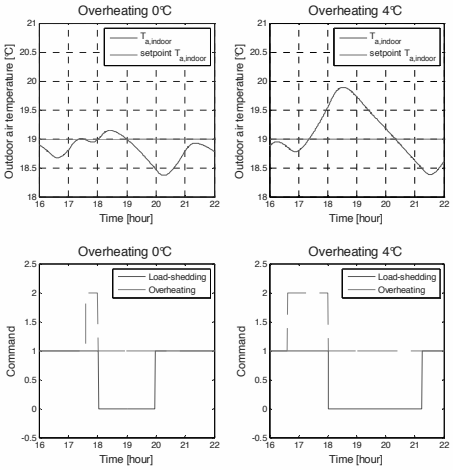

Fig. 7: Indoor temperature and heat pump commands for the building model with buffer tank connected in parallel during a classic winter day.

3 Results

3.1 Design of experiment

3.1.1 Chosen factors and responses

The design of experiments (DEO) is used to analyze the results of the simulations. So the influence of the factors on the chosen response is being studied. A multilevel factorial analysis is performed; in this case considering the number of factors, 36 simulations were needed. For this analysis, the chosen factors and responses are shown in Table 2 and Table 3. Other responses could have been chosen, as the global cost, which included the investment cost of the water tank and the operating cost linked to the price of the energy.

Table 2. DEO factors.

Factors	Unit	Levels		
		Low	Intermediate	High
K_{cond} (or X1)	W/K	103	-	133
C_{total} (or X2)	MJ/K	37	-	78
Overheating (or X3)	°C	0	2	4
V_{tank} (or X4)	L	94	252.5	411

Table 3. DEO responses.

Responses	Unit
Mean load-shedding period on 2 weeks (or Y1)	Min
Consumption on 2 weeks (or Y2)	KWh

With the results of simulation and with STATGRAPHICS [8], it is possible to make an analysis of the result and to determine the influence of each factor. Actually, the evaluation of the influence of each factor is determined with the polynomial regressions; one for mean load-shedding period (9) and an other one for the electric consumption (10). These regressions are obtained with of coefficient superior to 99%.

$$Y_1 = 35.73 + 2.647\,X_3 + 0.1442\,X_1 + 2.069\,X_2 + 0.1451\,X_4 + 0.7031\,X_3^2 + 0.0625\,X_3\,X_2 + 0.0197\,X_3\,X_4 - 0.0098\,X_1\,X_2 - 0.0009\,X_1\,X_4 \quad (9)$$

$$Y_2 = 100\,(2.775 + 0.0031\,X_3 + 0.0296\,X_1 - 0.0011\,X_2 - 0.0001\,X_4) \quad (10).$$

The influence of the overheating and the tank volume on the average load-shedding time and consumption will be studied for the house 5 (Table 1), which is the average one. This house represents 40% in terms of number and 30% of the national consumption of houses in France. For the rest of the study, this house will be the reference.

3.1.2 Mean load-shedding period on 2 weeks

The effects of the chosen factors are shown in Fig. 8. It can be observed that when the thermal capacitance, the overheating or the tank volume increase, load-shedding time ensuring comfort also increases. On the other hand, the load-shedding time falls when the heat losses coefficient increases. Fig. 9 shows the variation of average load-shedding time in function of the overheating temperature and the tank volume. The most influencing factor is the overheating. Fig. 9 allows also to select the appropriate tank volume and overheating in order to reach a specified load-shedding period.

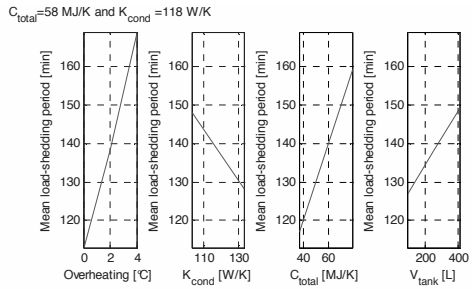

Fig. 8. Effects of the principal factors on mean load-shedding period.

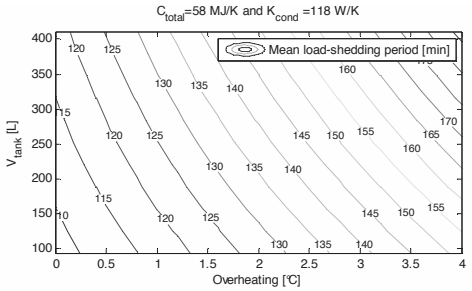

Fig. 9. Mean load-shedding period (minutes) in function of the overheating temperature and the tank volume.

3.1.3 Electric consumption on 2 weeks

For the electric consumption, as shown in Fig. 10, K_{cond} is the most important factor. The influences of the other factors on the consumption are almost negligible. Nevertheless, the higher overheating temperature is, the higher electric consumption is (Fig. 11). The thermal capacitance and the tank volume contribute to store thermal heat, and thus to increase mean load-shedding period. Since the outdoor air temperature is generally higher before 18:00, thermal storage losses are compensate by an improvement of the COP: the electricity can be saved by reducing the operating time of the heat pump after 18:00. However, the effect of the thermal capacitance and the tank volume is rather negligible compare to the conductive heat transfer coefficient of the house.

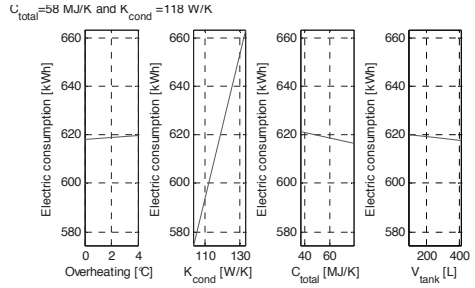

Fig. 10. Effects of the principal factors on electric consumption.

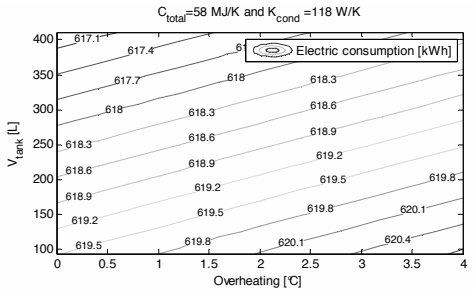

Fig. 11. Electric consumption (kWh) as a function of the overheating temperature and the tank volume.

3.1.4 Multiple response optimization

This optimization was performed to find two optima for the House5 (Table 1). The optimization consists in:

- minimizing the electric consumption and hit a target of 120 min for the load-shedding period,
- minimizing the electric consumption and maximizing the load-shedding period.

With STAGRAPHICS, it is possible to realize a multiple response optimization by using desirability functions [8] in our case each response has the same weight.

The results of minimizing the electricity consumption and hit a target of 120 minutes for the load-shedding period are displayed in Table 4.

Table 4. Results for the first optimization

Factors	Optimum
Overheating [°C]	0.2
V_{tank} [L]	411
K_{cond} [W/K]	118
C_{total} [MJ/K]	58
Response	Optimum
Electricity consumption [kWh]	617
Load shedding period [min]	120

The results of the multiple response optimization aiming at minimizing the electricity consumption and maximizing the load-shedding period are displayed Table 5.

Table 5. Results for the second optimization

Factors	Optimum
Overheating [°C]	4
V_{tank} [L]	411
K_{cond} [W/K]	118
C_{total} [MJ/K]	58
Response	Optimum
Electricity consumption [kWh]	618
Load shedding period [min]	187

The difference between the two optima is important in term of load-shedding period (almost 1.5 times longer), but not in term of electricity consumption.

3.1.5 Impact on the load curve

The heat pump load curve (mean input power on 2 hours) with a 411 L tank parallel system is shown, with no load management, in Fig. 12 and, with load management, in Fig. 13. At about 15 hours, there is a peak on the load curve due to overheating; next, there is a hole owing to load management and, finally, another peak caused by the heat pump restart.

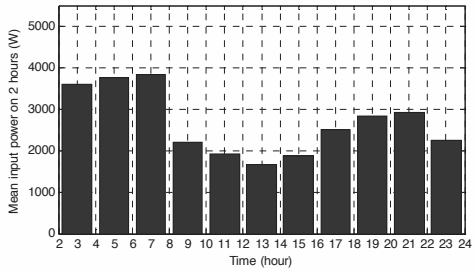

Fig. 12. Load curve without load-shedding and with a tank volume of 411 L.

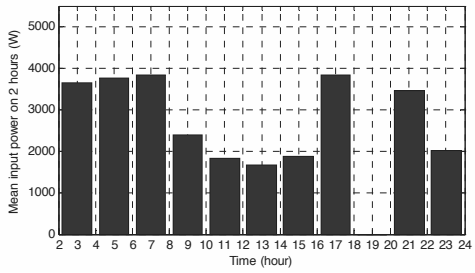

Fig. 13. Load curve with load-shedding, an overheating of 4°C and a tank volume of 411 L.

4 Conclusions

In this study a system composed of a house, a heat pump, a hydronic system was modeled. Thus several simulations have been carried out in order to analyze the influence of different parameters on the heat pump electric consumption and on the mean load-shedding period. It follows that it is possible with tank volumes, control strategies, and with the thermal capacitance of the house to stop the heat pump during more that 2 hours without altering the comfort. Overheating is an interesting solution to increase the load-shedding period because its effect on the electric consumption is very low, but leads to an increase of the load both before and after the load-shedding. This point could be counterbalanced with an appropriate control strategy on a wide set of heat pumps.

Nomenclature

c	specific heat, J/(kg K)
C	capacitance, MJ/K
$\widetilde{c}$	radiator transfer coefficient
K	conductance, W/K
$\dot{m}$	mass flow rate, kg/s
$\dot{Q}$	heat flow, W
R	thermal resistance, K/W
T	temperature, °C
V	volume, L

Subscripts and superscripts

a	air
HP	heat pump
int	interior
out	outdoor
w	water

References

[1] ADEME, 2002, Les chiffres clés du bâtiment, édition 2002.

[2] Barbouchi, S. and Ritz, J-B., 2006, High temperature heat pump for the retrofit market in France, IEA heat pump centre newsletter, retrofit heat pumps for buildings, volume 24, n°4.

[3] Almeida, M. A., et al., 2001, The potential for electricity conservation and peak load reduction in the household sector of Brazil. Energy-The International Journal, 413–429.

[4] US Department of Energy, 2006, Benefits of Demand Response in Electricity Markets and Recommendations for Achieving them, Report to the United States Congress.

[5] Herter, K., et al., A., 2006, An exploratory analysis of California residential customer response to critical peak pricing of electricity. Energy.

[6] Braun, J. E., 1990, Reducing energy costs and peak electrical demand though optimal control of building thermal storage. ASHRAE Transactions 96 2, pp. 876–888.

[7] Yang, K. and El-Hail, B., 2003, Design For Six Sigma – A Roadmap For Product Development. McGraw-Hill.
[8] Polhemus, N. W., 1999, Quality Control and Experimental Design – Statistical Analysis Using Statgraphics Plus. Statistical Graphics Corporation.
[9] Fadi, C., 2009, A new methodology for the design of low energy buildings, Energy and buildings 41, pp. 982-990.
[10] SIMBAD, 2005, Building and HVAC toolbox. Version 4.0. CSTB, France.
[11] SIMULINK, 2007, Dynamic System Simulation for MATLAB, Version 7.0, MathWorks Inc., USA.
[12] Wang, S. and Xu, X., 2006, Simplified building model for transient thermal performance estimation using GA-based parameter identification, Int. J. Thermal Sci. 45 (4), pp. 419–432.
[13] Karlsson, F., and Fahlén, P., 2008, Impact of design and thermal inertia on the energy saving potential of capacity controlled heat pump heating systems, International Journal of Refrigeration 31, pp. 1094–1103.
[14] NF EN 12098-1, 1996, Controls for heating systems - Part 1: Outside temperature compensated control equipment for hot water heating systems.
[15] ASHRAE, 2000, ASHRAE Handbook, Systems and Equipment, Atlanta, US, Chapter 32, Hydronic heat-distribution units and radiators.

Radiative cooling in northern Europe for the production of freezer temperatures

Martin Fält, Ron Zevenhoven

Department of Chemical Engineering, Thermal and Exchange Engineering, Turku, Finland

Abstract: The sky should not only be seen as a potential source of energy in the form of the sunlight but also as a source of energy in the form of cooling. This cooling is obtained through radiative heat exchange between a radiator, located on the surface of the earth, and cold air masses situated above this radiator. The possibility of using radiative cooling for areas located in northern Europe is investigated in this paper. Since the amount of cooling needed for refrigeration and air conditioning is expected to increase in the near future, so will also the amount of energy needed to produce it; as this is usually done through vapor compression. However, by the use of radiative cooling, energy need not be used in this same manner. Here, the potential of radiative cooling is investigated and compared for two different locations in Finland.

Keywords: Radiative cooling, Northern regions.

1. Introduction

The potential of using radiative cooling in northern Europe is investigated in this paper. A vast amount of cooling, and therefore energy, is needed for refrigeration and air conditioning. This paper will assess the possibility of using the sky instead of a vapor compression refrigeration processes as a passage to low temperatures. Radiative cooling has been studied for air conditioning by the use of flat plate solar collectors [1] and by the use of roof based components [2], even its' use during the day has been studied [3]. But its´ potential availability has been poorly studied for northern Europe although some studies have been made for southern Europe [4].

In northern Europe, low temperatures are available during winter, which is also a time when the air is dry and the skies are clear, even the days are short, all conditions that are the most favorable for radiative cooling. Therefore, since optimum conditions exist for low temperature skies, what would the performance of radiative cooling be?

In this study, a mathematical model was set up for a refrigeration system where weather data from two Finnish locations were used to assess its performance. These two different locations were selected as to give a representation of the different weather conditions that prevail in a northern country.

The apparatus that would perform the cooling would be a flat plate metal cooler containing a refrigerant. This refrigerant would be transported from the radiative cooler to the refrigerator where the heat exchange would take place through convection and conduction as it is done today. The surface of the metal plate would be coated with a suitable paint to give the surface good emitting properties in the infrared spectrum. The most important wavelength for radiative cooling is the interval 8-14 μm, referred to as the atmospheric window, which is the main interval where earth emits the heat it receives from the sun at shorter wavelengths. During the summer when sky temperatures are too high for deep cooling, the same refrigerant would be utilized to run in combination with a vapor compression refrigeration process cycle, thus giving the same cooling effect as in a conventional system. Alternatively, the flat plate collector could be used during the summer for air conditioning or as flat plate heat collectors for water.

2. System description

The system modeled in this paper consists of a radiator at a constant surface temperature T_{rad}. This radiator is subjected to different heat exchange processes, which are presented in Fig. 1.The different heat exchange processes involve both long and short wave radiative heat and forced convection heat. The results of the different heat exchanges are combined to get the total heat exchange of the system.

Corresponding Author: Martin Fält, Email: martin.falt@abo.fi

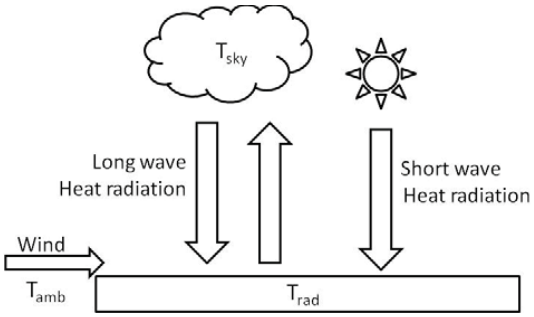

Fig. 1. Schematic view of the radiator and the heat streams.

2.1. Weather Data

As this paper studies the availability of passive cooling through heat radiation and convection in northern Europe, weather data was needed. The data was acquired from the Finnish Meteorological Institute for weather stations located in Sodankylä, Finland (67°22'N, 26°37'E) and in Helsinki, Finland (60°10'N, 24°56'E) [5]. These locations are presented in Fig. 2.

Fig. 2. Location of the weather stations used, 1: Sodankylä and 2: Helsinki. [6]

The data contains hourly average data for the years 2008 and 2009, of the ambient temperature, wind speed, long and short wave heat radiation data. The long-wave heat radiation data was measured by a CG4 pyrgeometer, which measures the incoming heat radiation in the range of *4.5μm – 40μm* [7]. With this data, the temperature T_{sky} can be calculated with (1). Here the emissivity ε_{sky} is chosen to be *=1* since the emissivity is already included in the $Q_{long\ wave}$ measured data. Here, σ is the Stefan-Boltzmann constant, with a value of $5.67\times10^{-8}\ W/m^2K^4$.

$$T_{sky} = \sqrt[4]{\frac{Q_{long\ wave}\cdot\sigma}{\varepsilon_{sky}}}\,. \qquad (1)$$

Wind that blows parallel to the roof window causes heat exchange by forced convection. To calculate this forced convective heat (2) and (3) are used. These equations give the convective heat exchange for turbulent exchanges over smooth surfaces at low wind speeds *(<3 m/s*). Here, v_{rad} is a reduced wind speed, at the radiator, that originates from the fact that the wind speeds are measured at a higher altitude than where the radiator is situated.

$$h_c = 1.8 + 3.8\cdot v_{rad}\,. \qquad (2)$$

For this case the wind data that was acquired was measured at a height of 10m and the assumed location of the radiator is set at a height of 5m. From this, a correction of the wind speed is made using (3). Here, γ and α are terrain parameters that describe the location of the radiator and the location for the wind measurement. The heights of the locations are the given by H_w and H_s, where the lower casings stand for the weather station and the site of the radiator. [8]

$$v_{rad} = \frac{\alpha_w\left(H_w/10\right)^{\gamma,w}}{\alpha_s\left(H_s/10\right)^{\gamma,s}}\cdot v\,. \qquad (3)$$

2.2. Heat exchanges

When T_{sky} is known the heat exchange from the radiator to the sky can be calculated for fixed radiator temperatures according to (4).

$$\dot{Q}_{rad\leftrightarrow sky} = \left(\varepsilon_{rad}T_{rad}^{\ 4} - \varepsilon_{sky}T_{sky}^{\ 4}\right)\cdot\sigma - \varepsilon_{rad}\dot{Q}_{short\,wave} \qquad (4)$$

Here $Q_{short\ wave}$ is the total heat radiation in the shortwave spectrum that originates from the sun. This shortwave heat radiation can cancel out the radiative cooling effect and therefore has to be taken into account. The emissivity of the radiator has been assumed to be $\varepsilon_{rad}=1$; this assumption is made since the potential of passive cooling is investigated and thus the maximal cooling effect is given when $\varepsilon_{rad}=1$. However, this article assumption of $\varepsilon_{rad}=1$ has also a disadvantage as it is assumed to be the same over the whole

wavelength spectrum. By the use of selective coatings that have high reflecting properties in the shortwave spectrum and high emitting properties in the long wave spectrum, it could be possible to avoid or diminish the heating effect caused by the sun.

The convective heat exchange was implemented into our model also according to (5) so that its' effect could also be evaluated.

$$\dot{Q}_{rad\leftrightarrow sky} = h_c \cdot \left(T_{rad} - T_{amb}\right). \quad (5)$$

The different heat exchange processes calculated by (4) and (5) are then combined together according to (6).

$$\dot{Q}_{tot} = \dot{Q}_{rad\leftrightarrow sky} + \dot{Q}_{rad\leftrightarrow amb}. \quad (6)$$

This way of combining convective and radiative heat exchange is called the additive method. Since this method has no physical basis an error is introduced, but as the temperature differences are small and air is not greatly affected by heat radiation the error should be negligible. [9]

3. Results and discussion

In this section various measurements and calculations based on these measurements are presented. First the temperature of the sky and ambient is calculated for the two locations. After this, the average radiative heat exchange per day is presented for a radiator temperature of 10°C; this is then further expanded to 3D-graphs which illustrate the same heat exchange for different radiator temperatures. The reason for choosing the average heat exchange per day originates from the fact that the cooling effect can be canceled out during the day by the sun. Finally, the radiator's cumulative frequency distribution of heat exchange at varying radiator temperatures is presented; where the heat for the radiative, convective and total heat transfer are all presented separately.

3.1. Temperature data

The temperature of the sky and the ambient for Sodankylä and for Helsinki are presented in Fig. 3 and Fig. 4.

This data was smoothed out with the Savitzky-Golay filtering method because the noise in the measurement was disturbing. A third order polynomial filter with a frame size of eighty-nine days was applied on the data to obtain a satisfactory result. When comparing these figures it is observable that the temperatures for both the ambient and the sky are lower in Sodankylä than in Helsinki. However, the temperature difference between the ambient and the sky is larger in Helsinki than in Sodankylä. It is also observable that the temperature difference is largest during autumn for both locations and for both year 2008 and 2009.

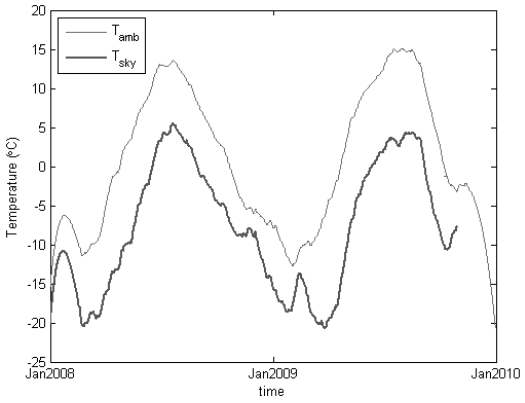

Fig. 3. Ambient temperatures T_{amb} and calculated sky temperature T_{sky} for the location in Sodankylä.

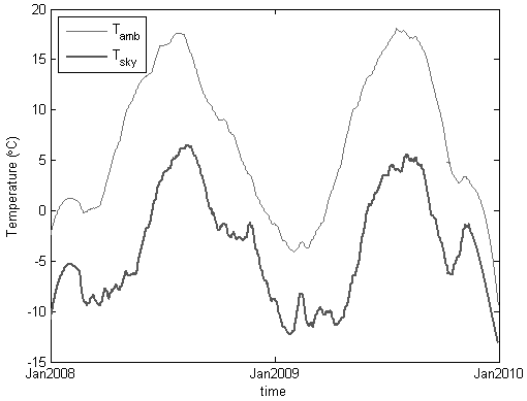

Fig. 4. Ambient temperatures T_{amb} and calculated sky temperature T_{sky} for the location in Helsinki.

Due to the lack of measurement data for the end of the year 2009 in the long wave heat radiation data, T_{sky} could not be calculated for the whole time period of 2008 to 2010 for Sodankylä. Smaller gaps in the order of some hours were also found elsewhere in the data, but these gaps could be filled with interpolated data.

3.2. Radiative heat exchange

The radiative heat radiation for a radiator at *10 °C* is presented in Fig. 5 for Sodankylä and for

Helsinki. Since sky temperatures were lower in Sodankylä than in Helsinki the heat exchange between the radiator and the sky was therefore larger in Sodankylä. The largest difference occurred during the winter when the difference between the two locations was 35 W/m^2. However, since Sodankylä is situated more to the north than Helsinki the amount of sunlight that strikes the radiator during the summer is larger than that in Helsinki; this reduces the amount of cooling attainable in Sodankylä to become smaller than that in Helsinki. This conclusion is further supported by comparing Fig. 3 and Fig. 4 where T_{sky} is higher in Helsinki than in Sodankylä during the summer. The difference is, however, not larger than 5 W/m^2.

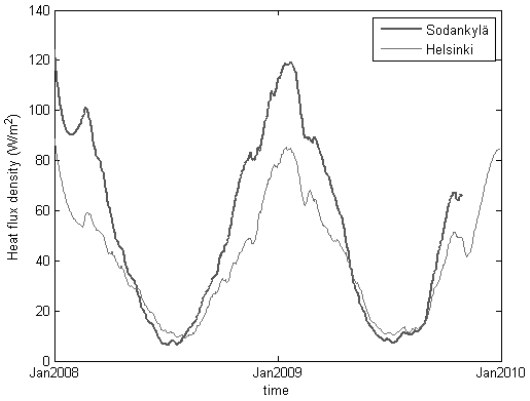

Fig. 5. Calculated radiative heat exchange between a radiator at 10 °C and the sky in Sodankylä and in Helsinki.

The radiative heat exchange for various radiator temperatures is presented in Fig. 6 for Sodankylä and in Fig. 7 for Helsinki. When, radiator temperatures decrease so does the rate of heat exchange, which is according to (4). The decreased heat exchange is shown in Fig. 6 and Fig. 7. The form of the cooling distribution is also seen in these figures as it was already in Fig. 5. This shows that the main cooling potential is attainable during the winter months, but that cooling to temperatures below room temperature, is also possible during the summer.

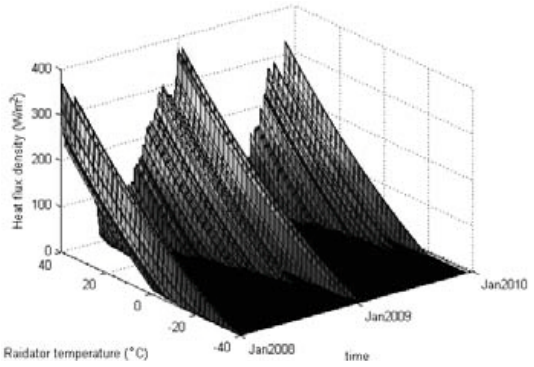

Fig. 6. Calculated radiative heat exchange between a radiator at various temperatures and the sky in Sodankylä.

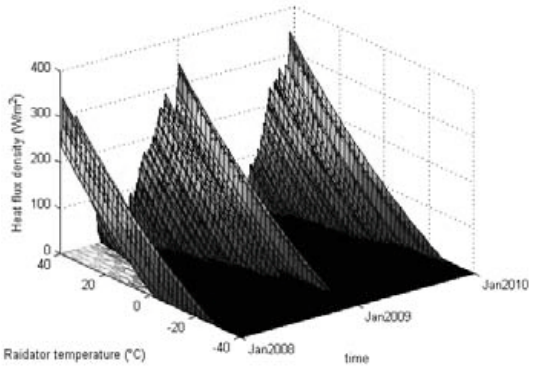

Fig. 7. Calculated radiative heat exchange between a radiator at various temperatures and the sky in Helsinki.

3.3. Probabilities, frequency distributions

The distribution of the cooling potential is further assessed in Fig. 8 to Fig. 14 where the cumulative frequency distribution of the heat exchange for various radiator temperatures is assessed. [10] Here the heat exchange is presented as isolines in W/m^2. These cumulative frequency distribution isolines describe for what length of time, a certain heat exchange could have been achieved, for a defined radiator temperature during the two-year measurement period. So for example Fig. 9 describes that a heat exchange of 50 W/m^2 could have been attained at a radiator temperature of -20°C for 10% of the time during the two-year period.

First the cumulative frequency distribution of heat radiation is assessed separately in Fig. 8 for Sodankylä and in Fig. 9 for Helsinki. When comparing, these two figures it is observable that

lower radiator temperatures are reachable for the same heat exchange in Sodankylä than in Helsinki. The radiator temperature difference between the two locations for equal heat exchanges is around 5°C.

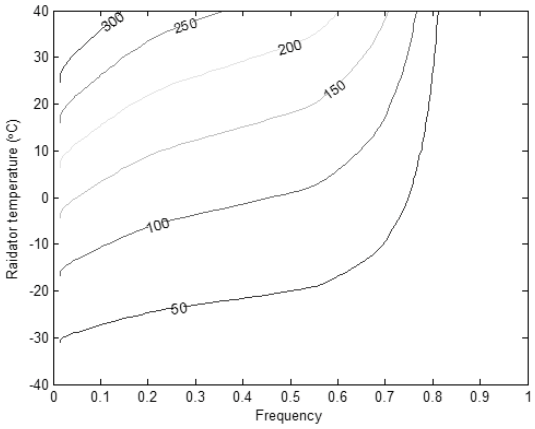

Fig. 8. Cumulative frequency distribution of radiative heat exchange in W/m^2 at different radiator temperatures in Sodankylä.

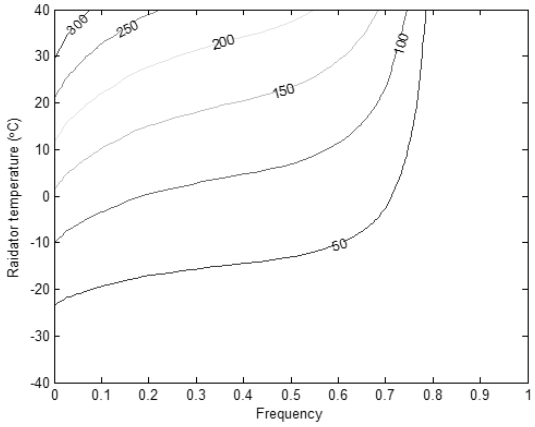

Fig. 9. Cumulative frequency distribution of radiative heat exchange in W/m^2 at different radiator temperatures in Helsinki.

The influence of convective heat transfer must also be assessed. This is done in Fig. 10 and in Fig.11 which present the cumulative frequency distribution of the convective heat exchange at various radiator temperatures for both Sodankylä and Helsinki. The amount of convective cooling is larger in Helsinki for higher radiator temperatures, but for lower radiator temperatures the amount of cooling is larger in Sodankylä.

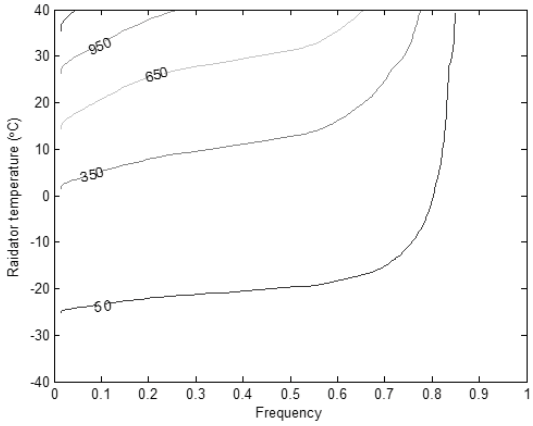

Fig. 10. Cumulative frequency distribution of convective heat exchange in W/m^2 for different radiator temperatures in Sodankylä.

The larger cooling potential in Helsinki at higher ambient temperatures originates from higher wind speeds in Helsinki than in Sodankylä; these wind speeds are presented in Fig. 12. The larger cooling at lower temperatures originates from lower ambient temperatures in Sodankylä than in Helsinki; the ambient temperatures were presented in Fig. 3. and in Fig. 4.

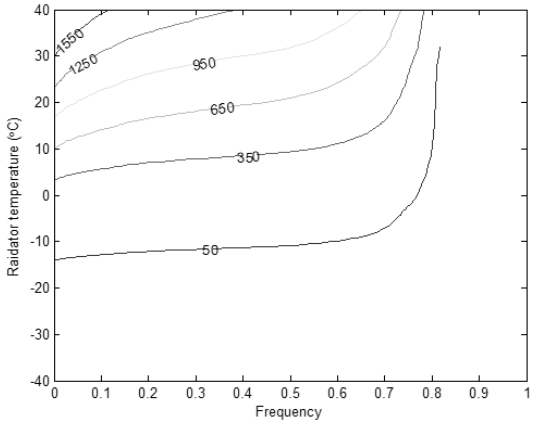

Fig. 11. Cumulative frequency distribution of convective heat exchange in W/m^2 for different radiator temperatures in Helsinki.

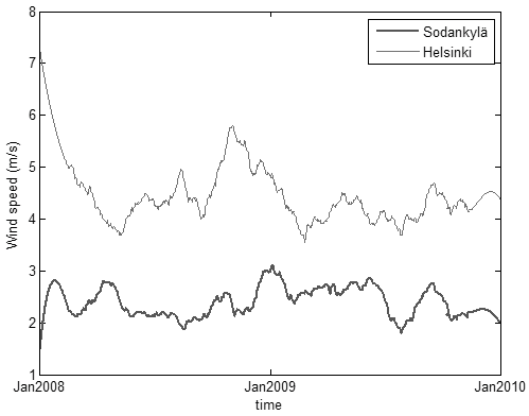

Fig. 12. Wind speeds in Sodankylä and in Helsinki.

When comparing the radiative transfer with the convective heat transfer it is obvious that convection has to be taken into account. The biggest difference that convection makes is that the order of magnitude of the heat transfer changes quite significantly. However, convective heat transfer can occasionally diminish the effect of radiative cooling and even sometimes cancel the cooling effect. The risk of cancelling effects is especially large during the summer when the ambient temperature is higher than that of the radiator.

The cumulative frequency distribution of the total heat transfer of a radiator is presented in Fig. 13 for Sodankylä and in Fig. 14 for Helsinki. When, comparing the total heat transfer of these two locations it is obvious that for higher radiator temperatures a larger amount of heat can be dissipated from the radiator to the ambient and to the sky in Helsinki. However, when radiator temperatures drop, the amount of dissipated heat will be larger in Sodankylä than that in Helsinki as was the case also for the pure convective heat transfer.

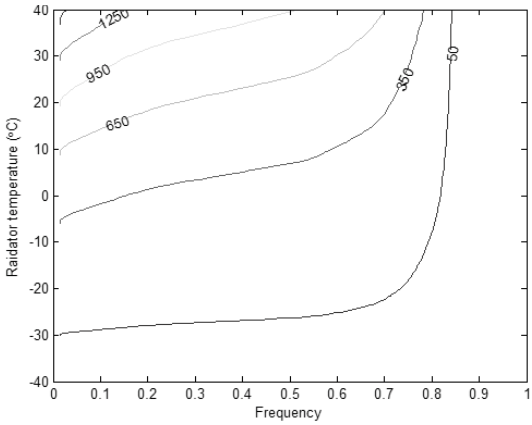

Fig. 13. Cumulative frequency distribution of the total heat exchange in W/m^2 for different radiator temperatures in Sodankylä.

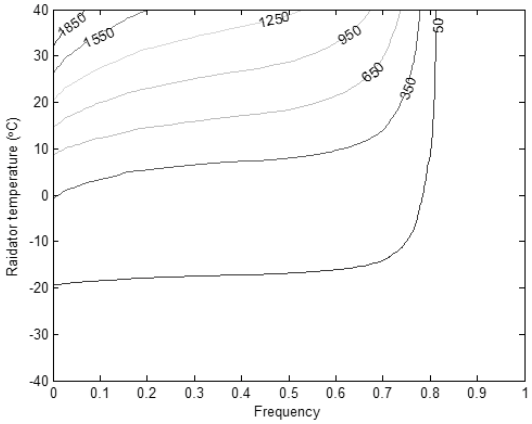

Fig.14. Cumulative frequency distribution of the total heat exchange in W/m^2 for different radiator temperatures in Helsinki.

4. Conclusions

The needed electricity for air conditioning is expected to increase by a tenfold during the next 40 years in Finland. [11] Therefore new cooling methods are needed also for the northern European conditions.

This article has presented the potential of utilization of radiative cooling in northern Europe. Radiative cooling has yet to be utilized for cooling in northern Europe but this paper showed that it can be used for air conditioning and even for cooling to lower temperatures. By the use of meteorological data obtained from the Finnish Meteorological Institute the heat exchange from a flat plate radiator has been modeled. This paper shows that a significant amount of cooling can be

obtained from a source that does not include the power intensive compression work as the traditional cooling does. By the utilization of radiative coolers, savings could be achieved for air-conditioning but also for the refrigeration of food products. The radiative coolers could also be used as solar collectors during times when sufficient cooling is not needed or attainable.

Nomenclature

c specific heat, J/(kg K)

h heat exchange coefficient, W/(m^2 K)

H height m

t temperature, °C

$\dot{Q}$ Heat flux density, W/m^2

v wind speed at measured site, m/s

Greek symbols

α Alpha terrain parameter

γ Gamma terrain parameter

ε Emissivity of a material

σ Stefan Boltzmann constant, W/(K^4 m^2)

τ Transmissivity of a material

Subscripts and superscripts

amb	ambient
c	convection
long wave	long wave radiation (>4.5μm)
rad	radiator
s	site
short wave	short wave radiation (< ~3μm)
sky	sky
w	wind tower

References

[1] Erell, E., and Etzion, Y., 2000, Radiative cooling of buildings with flat-plate solar collectors, Building and Enviroment, 35, pp. 297-305.

[2] Dimoudi, A., and Androutsopoulos. A., The cooling performance of a radiator based roof component, Solar Energy, 80, pp. 1039-1047.

[3] Nilsson, T., and Niklasson, G., 1995, Radiative cooling during the day: simulations and experiments on pigmented polyethylen cover foils. Solar Energy Materials and Solar Cells, 37, pp. 93-118.

[4] Oliveti, G, Arcuri, N and Ruffolo, S. Experimental investigation on thermal radiation exchange of horizontal outdoor surfaces. Building and Enviroment. 2003, 38, pp. 83-89.

[5] Finnish Meteorological Institute. Finnish Meteorological Institute. [Online] http://www.fmi.fi/en/.

[6] Bing Maps. *Bing*. [Online] Microsoft. [Cited: February 11, 2010.] http://www.bing.com/maps/.

[7] Kipp & Zonen. Instruction manual CG4 Pyrgeometer. [Online] July 13, 2004. [Cited: February 11, 2010.] http://www.kippzonen.com/?download/3391/CG+4+-+Manual.aspx.

[8] Parker, Danny S. Theoretical Evaluation of the NightCool Nocturnal radiation cooling concept. Florida : Florida Solar Energy Center, 2005. p. 40. FSEC-CR-1502-05.

[9] Modest, Michael F. Radiation combined with conduction and convection. Radiative Heat Transfer. San Diego : Elsevier Science, 2003.

[10] Adams, Robert A. Applications of integrations. Calculus: a complete course. 4th Edition. Ontario : Ron Doleman, 1999, 7, pp. 462-463.

[11] 1. Finnish Energy Industries. Turning challenges into opportunities — a carbon neutral vision for electricity and district heat for 2050. Helsinki : Finnish Energy Industries, 2009. p. 44.

Acknowledgments: This work is funded by Maj and Tor Nessling Foundation projects 2009301 and 2010362 “Solar heat engineering and carbon dioxide: energy recovery using a greenhouse gas”, and the Foundation for Åbo Akademi University.

Simulation and Experimental Results of a Small-size Solar-assisted Absorption Cooling System

Gianpiero Evola[a], Nolwenn Le Pierrès[a], François Boudehenn[b], Philippe Papillon[b]

[a] *LOCIE, CNRS FRE3220 - Université de Savoie, Polytech'Savoie, Le Bourget-Du-Lac Cedex, France*
[b] *INES, CEA-LITEN, Le Bourget-Du-Lac Cedex, France*

Abstract: In the context of the French research project ORASOL (Optimization of processes for solar cooling), a small-size solar-powered cooling system based on a water-cooled LiBr/H_20 absorption machine is being studied at INES (Institut National de l'Energie Solaire). The absorption machine is the one distributed by Rotartica, with a nominal cooling power as high as 4.5 kW, powered by 30 m^2 of flat-plate solar collectors. The heat rejection is carried out through horizontal ground pipes.
The results of the experimental campaign carried out during summer 2009 are discussed. The system has shown a good performance if looking at the absorption machine, but high overall electricity consumption due to the auxiliary devices.
Furthermore, a general mathematical model for the dynamic simulation of a LiBr/H_20 absorption machine has been developed and implemented on the simulation tool simSPARK. The model is based on simple mass and energy balances written on the single components of the machine, and it accounts for its transient behaviour and the thermal inertia of its components. The above-mentioned mathematical model is presented, as well as its adaptation to the real machine being tested, performed by using the appropriate values for the main physical parameters. Finally the comparison with the experimental results will be discussed, looking both at the steady state behaviour and at the capacity of simulating the transient effects.

Keywords: Solar-powered absorption chiller, experimental results, dynamic model.

1. Introduction

In recent years, the electric energy consumption due to air-conditioning systems has undergone a relevant increase. As an alternative to conventional air-conditioning systems, a growing interest is being focused on solar cooling processes, which can satisfactorily meet the cooling load and the comfort demand at a very low energy cost.

Currently, research activity is mostly devoted at improving the performances of this kind of systems, and at defining the optimal dimensioning criteria and the most appropriate control logic. In this context, the research project ORASOL started in France in 2007, with the aim of doing an experimental survey on the performance of five different solar cooling systems, and developing design tools based on the mathematical modelling of the cooling system components and their coupling with the building. Further information on the ORASOL research program can be found in [1]. In this framework, a test facility installed at INES is being studied, made up of a small-size solar-powered LiBr/H_20 absorption machine used for the air-conditioning of an office area.

An experimental campaign was carried out during summer 2009, from the 27/05 to the 10/09.

2. The experimental set-up

A simplified sketch of the experimental facility installed at INES is reported in Fig. 1. The absorption chiller is distributed by Rotartica, with a nominal cooling capacity as high as 4.5 kW, measured at the following conditions:

- Water inlet temperature at generator: 90°C.
- Water outlet temperature at evaporator: 12°C.
- Cooling water inlet temperature: 30°C.

The chiller is powered by hot water produced through a solar section composed of 25 flat-plate solar collectors (30 m^2 overall net absorbing surface); the collectors are installed on the roof of the building with a 30° tilt angle and facing south, and they are arranged in two batteries put in series. Actually, the collector field is slightly oversized with respect to the thermal power required by the absorption machine for summer operation, as it also accounts for winter operation. A compact heat exchanger separates the solar section from a four hundred-litre hot water storage tank.

Corresponding Author: Nolwenn Le Pierrès, Email: nolwenn.le-pierres@univ-savoie.fr

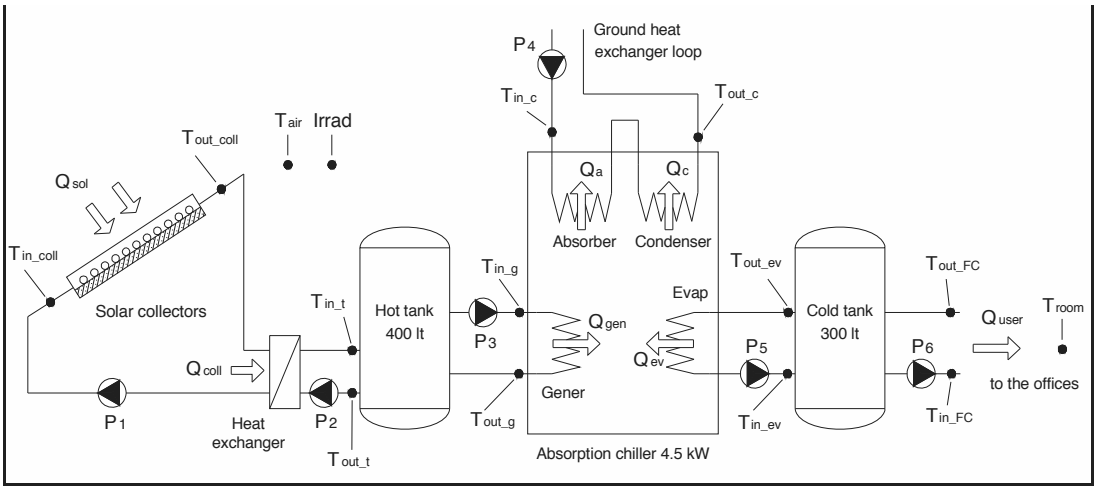

Fig. 1. Main components of the experimental rig and main measurement points

The latter is placed in a room inside the building, and the pipes between the collectors and the tank are very well insulated. An electric resistance is also available as a back-up system on the storage, but it was not connected as the main aim was to investigate the performance of the system when powered only by solar energy.

The chiller is water-cooled, and heat rejection is assisted by a ground heat exchanger made up with twenty-two horizontal polyethylene pipes divided into two layers, buried at a depth of 0.75 m and 1.1 m, respectively; the length of every pipe is around 100 m. On the user side, the cold water produced by the absorption machine is stored in a three hundred-litre water tank, and hence distributed to three fan-coils for the air-conditioning of the office area.

Fig. 1 also reports the position of the main measurement devices. All the temperatures of the water at the inlet and the outlet of each component are registered, as well as those outdoors and inside the office area, together with the solar irradiation available on the collector surface. A value is provided for each parameter every 120 seconds, as an average of the measurements within the last acquisition period. No measurements are available for the internal parameters of the absorption machine (pressures, temperatures, salt concentrations).

2.1. Daily performance

In the following, the performance of the system during the 14th of August is described; this day has been regarded as representative as it was a sunny day with a continuous cold demand from the users.

The evolution of the solar section is presented in Fig. 2. At around 9:00, when the solar irradiation available on the collectors, measured by the pyranometer, gets as high as 300 W/m^2, the circulator P1 on the primary loop switches on (see Fig.1). Then, the temperature of the hot water produced by the solar collectors rapidly increases, and it reaches its highest value of around 94°C at 15:00. The temperature increase inside the collectors varies between 6.5°C and 7.5°C, thanks to their arrangement in series and to the low flow rate (0.11 kg/s per m^2 of collecting surface).

When the solar irradiation comes to be lower than 200 W/m^2, the circulator P1 switches off (around 18:00). The efficiency of the solar field, defined as the ratio of the thermal power delivered to the water to the overall solar irradiation available on the net collecting surface, never exceeds 50%, and for around five hours (from 11:00 to 16:00) it keeps within 40% and 48%.

Fig. 3 shows the daily temperature profiles for the water flows through the absorption chiller. Around 11:00, as the water inside the hot storage reaches 80°C, the circulator P3 on the generator loop turns on (see Fig. 1); in a few minutes the same temperature is felt at the inlet of the generator, and the absorption chiller starts.

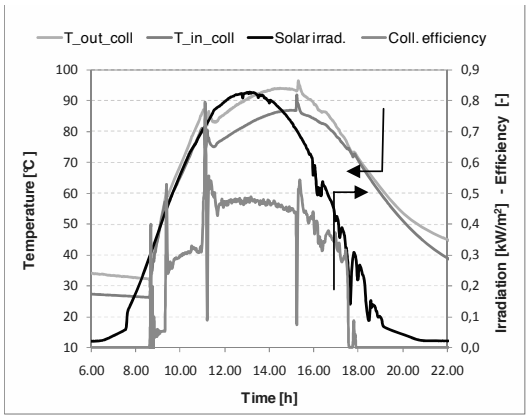

Fig. 2. Evolution of the main parameters in the solar collecting field (14/08/2009).

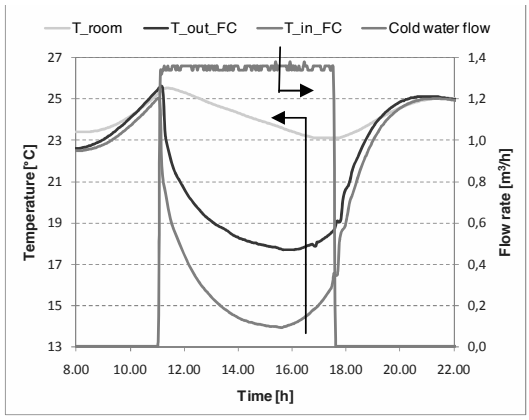

Fig. 4. Evolution of the main parameters from the user side (14/08/2009).

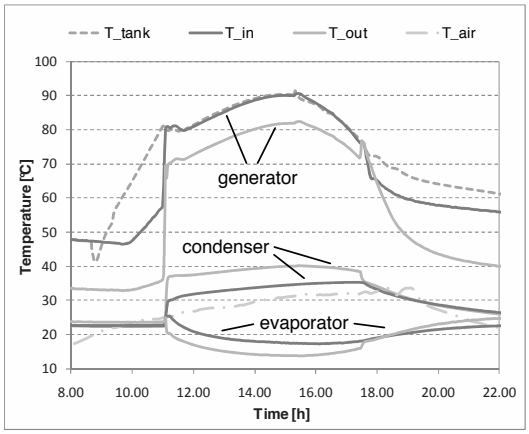

Fig. 3. Inlet and outlet temperature profiles for the absorption chiller (14/08/2009).

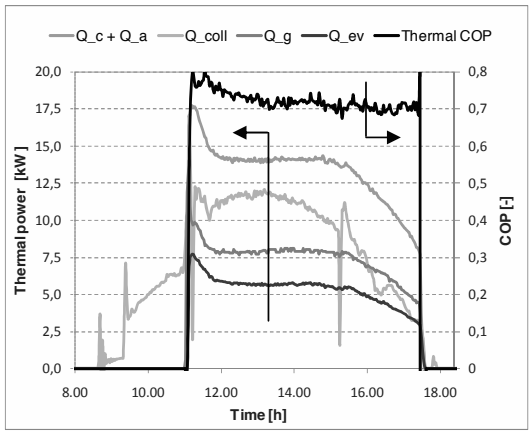

Fig. 5. Main thermal and cooling power profiles (14/08/2009).

The cold production is almost immediate, as can be noticed from the profile of inlet and outlet temperatures at the evaporator. The chiller produces cold water at mild temperatures, with a minimum value of 13.7°C obtained with the highest generator inlet temperature (90°C). On the heat rejection loop, the water inlet temperature is always in the range 30°C - 35°C, which means around two degrees higher than the outdoor dry bulb temperature. Such values let us presuppose that a more efficient heat rejection could be carried out by means of a wet cooling tower. The machine eventually stops when the inlet temperature at the generator gets lower than 76°C, which occurs at 17:40. The average operating parameters of the chiller are reported in Table 1. From the user side (see Fig. 4), as soon as the machine starts producing cold water the temperature available at the outlet of the cold storage for being distributed to the fan-coils rapidly lowers down to 14°C. Such a temperature is sufficient to keep the air in the conditioned offices between 23°C and 25°C throughout the whole working day. Finally, from Fig. 5 it is interesting to underline that the absorption chiller works with an almost constant and pretty high thermal COP (0.7 - 0.75); the cooling power keeps around 6 kW between 11:30 and 17:30, which means 30% more than the nominal capacity, thanks to the favourable operating conditions.

Table 1. Average operating parameters for the chiller

	Generator	*Evapor.*	*Condenser*
Water flow [m^3/h]	0.82	1.36	2.20
Temp. variation [°C]	8.4	5.3	3.4

The comparison between the profiles of the cooling power and of the overall solar energy collected provides information about the degree of deployment of the solar resource. We can state that during this day around 50% of the collected solar energy is turned into cold available for the air-conditioning of the offices.

2.2. Seasonal performance

Furthermore, the seasonal performance of the whole system was investigated, in order to identify the weak points and understand the way to improve the behaviour of small-size solar cooling systems based on absorption technology. To this aim, all the energy flows across each component of the system were assessed, starting from the measurement of the flow rates and their inlet and outlet temperatures, and integrating over time.

During the period going from the 17th of August to the end of the experimental campaign, a series of trials were also conducted in order to test the performance of the ground heat exchanger. A variable number of pipes, from four to eight, was closed; in these conditions, the operation of the absorption machine was obviously penalized, due to the poorer efficiency of the ground heat exchanger and the higher return temperature of the cooling water to the condenser. For this reason, all the performance parameters have been assessed twice: once for the entire season and once for the only period when the ground heat exchanger works correctly (27/05 to 16/08).

The two main parameters which have been assessed to evaluate the seasonal performance of the system are:

- COP_{sol}: it is the ratio of the overall cold delivered to the offices to the overall solar radiation available on the collecting surface. It is a measure of the degree of deployment of the solar resource.
- COP_{el}: it is the ratio of the overall cold delivered to the offices to the overall electric energy consumed by the system.

As a matter of fact, the electricity consumption is a very delicate matter in our installation, as it is the only energy input which is not free (the thermal energy comes entirely from the sun); it is associated with the pumps (solar circuit, distribution system), the fan-coils and the absorption machine itself. Actually, the Rotartica machine is different from conventional absorption chillers, as the absorption cycle is carried out into a rotating container, in order to improve the internal heat exchange and reduce the size of the machine. To maintain the rotation of the vessel, around 650 W of electric power are consumed during operation.

As far as COP_{sol} is concerned, in order to make a more in-depth analysis it can be written as follows (see Fig. 1 for details):

$$COP_{sol} = \frac{Q_{user}}{Q_{sol}} = \frac{Q_{coll}}{Q_{sol}} \cdot \frac{Q_{gen}}{Q_{coll}} \cdot \frac{Q_{ev}}{Q_{gen}} \cdot \frac{Q_{user}}{Q_{ev}} = \eta_{coll} \cdot \eta_{stor} \cdot COP_{th} \cdot \eta_{dist} \quad (1)$$

Where:

- η_{coll} is the efficiency of the solar section, which accounts for the thermal losses in the solar collectors and the primary loop.
- η_{stor} is the efficiency of the hot storage section, which accounts for the thermal losses in the heat exchanger, the secondary loop and the hot storage.
- COP_{th} is the thermal COP of the absorption machine.
- η_{dist} is the efficiency of the distribution subsystem, which accounts for the thermal losses in the cold storage, the distribution net and the fan-coils.

In Table 2 the values of the performance parameters described so far are reported. The system performs far better when the ground heat exchanger is completely activated (27/05 to 16/08), and one must refer to this period to carry out a correct analysis of the installation.

The average seasonal value of the electric COP (COP_{el} = 2.24) is not promising, if compared with the seasonal Energy Efficiency Ratio (EER) of a conventional air-cooled electrical chiller. The latter usually works with EER > 3, especially at high cold water outlet temperatures (12°C - 14°C); this value does not account for auxiliary devices, which only reduce to a pump for the distribution of cold water from the storage to the user. The low COP_{el} is unfortunately a limit of the Rotartica machine, but a correct management of the parasitic devices (pumps, fans) may help. As an example, the fan-coils in the offices often remained switched on during the night, determining an increase of the electricity consumption of about 15%, which could be easily avoided with more care from the users.

Table 2. Average performance parameters for the experimental installation

	Seasonal	*from 27/05 to 16/08*
COP_{el}	2.21	2.24
η_{coll}	0.322	0.322
η_{stor}	0.654	0.662
COP_{th}	0.696	0.700
η_{dist}	0.947	0.952
COP_{sol}	0.139	0.140

On the contrary, the average thermal COP of the absorption chiller (COP_{sol} = 0.7) can be regarded as a very positive result. Nevertheless, the average solar COP (COP_{sol} = 0.14) does not seem very good, even if higher than other similar solar cooling systems described in the literature [2]. Such a poor value may be attributed to the performance of the solar section. The average efficiency of the solar collectors is quite low (η_{coll} = 0.322), as can be also seen from Fig. 6, where the instantaneous efficiencies recorded during a representative week are reported, plotted against the ratio $(T_{capt} - T_{air})/I$. Due to the high temperatures needed by the absorption machine, evacuated tube solar collectors would have been preferable.

Furthermore, a very low efficiency is shown by the hot storage section (η_{stor} = 0.662), due to the thermal losses in the heat exchanger (around 8%) and in the water tank (around 26%). When the absorption machine turns off in the afternoon, the water inside the storage is normally at 76°C, but it decreases to less than 50°C until, in the following morning, the solar section is able to deliver new thermal energy (Fig. 3). This corresponds to about 13 kWh of thermal losses per night, and shows that the tank, even if insulated with 60 mm of polyurethane foam, is suitable for domestic hot water but not to manage such high temperatures.

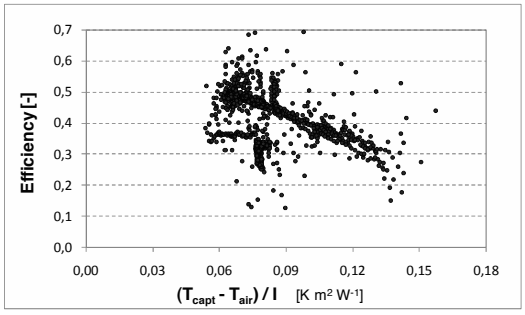

Fig. 6. Measured efficiency for the solar collectors (from 10/08 to 16/08)

3. The mathematical model

3.1. The general model

In the following, a description is provided for the general mathematical model developed in simSPARK environment to simulate the transient behaviour of a LiBr/water absorption chiller. The reference scheme of the machine is reported in Fig. 7, where the separation between high pressure and low pressure components is highlighted by the dashed line.

In order to simplify the formulation of the model, we assume that the mass flow of diluted solution conveyed by the solution pump from the absorber to the generator is constant. Other simplifying assumptions have been made for the model:

1. temperature, pressure and LiBr concentration are homogenous inside each component;
2. the generator pressure equals that in the condenser; the same relation holds for absorber and evaporator.
3. the LiBr/water solution inside the generator and the absorber is saturated;
4. the convective and radiative heat transfer between vapour and solution is neglected;
5. the absorber cooling water outlet temperature equals the condenser cooling water inlet temperature;
6. the vapour produced in the evaporator is saturated – no superheating is accounted for;
7. the fluid transport delay between two components is neglected;
8. all the heat exchangers have constant heat transfer coefficients;
9. the valves are adiabatic;

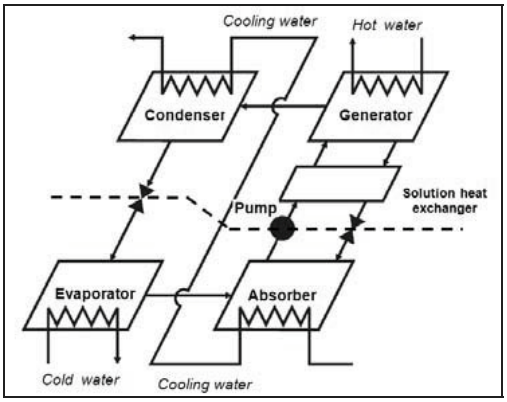

Fig. 7. Reference scheme for LiBr/H_2O absorption cycle

3.1.1 Generator / absorber

The equations used for the description of the generator refer to the scheme described in Fig. 8, and can be extended to the absorber, just accounting for the different directions of the mass flows.

Equations (2) and (3) represent the mass balance for solution and vapour in the generator, respectively. The ideal gas law (4) holds for the vapour; here the volume occupied by the vapour can be assessed by subtracting the volume of the solution from that of the entire vessel, see (5).

$$\dot{m}_{s,in} - \dot{m}_{s,out} - \dot{m}_{v,des} = \frac{dM_s}{d\tau} \quad (2)$$

$$\dot{m}_{v,des} - \dot{m}_{v,out} = \frac{dM_v}{d\tau} \quad (3)$$

$$M_v \cdot R_v \cdot T_v = p_v \cdot V_v \quad (4)$$

$$V_v = V_g - M_s / \rho_s \quad (5)$$

Furthermore, the LiBr mass balance (6) as well as the energy balance on the solution (7) hold. Here, the solution is assumed to be fully mixed at each time interval, then enthalpy and salt concentration for the solution leaving the vessel are assumed to be the same as those inside the vessel; their value can be defined as a function of pressure and temperature by using appropriate models for the thermodynamic properties of LiBr/water solution [3].

$$\dot{m}_{s,in} \cdot x_{s,in} - \dot{m}_{s,out} \cdot x_{s,out} = \frac{d}{d\tau}\left(M_s \cdot x_s\right) \quad (6)$$

$$\dot{Q}_{hx} - \dot{Q}_d = \dot{m}_{v,des} \cdot h_{v,des} + \dot{m}_{s,out} \cdot h_{s,out} + - \dot{m}_{s,in} \cdot h_{s,in} + \frac{d}{d\tau}\left(Mc_p \cdot T_s\right) \quad (7)$$

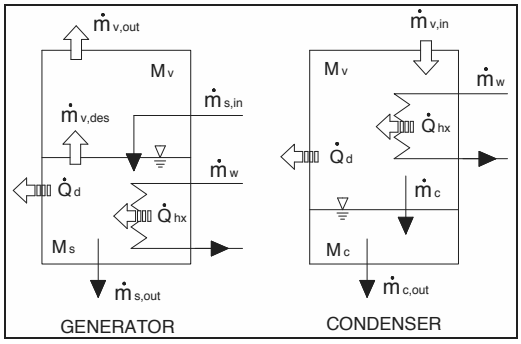

Fig. 8. Mass and energy flows for generator and condenser

The vapour desorbed at the generator can be assumed to be at thermal equilibrium with the diluted solution entering the component [4]; its enthalpy is assessed as a function of temperature and pressure [3].

The model also accounts for the thermal inertia of the shell. The shell is assumed at thermal equilibrium with the solution ($T_{sh} = T_s$), then its thermal capacity can be composed with that of the solution itself in (7), where $M = M_{sh} + M_s$ and c_p is the average heat capacity [5]. The heat dissipated through the walls of the vessel, Q_d, is neglected.

3.1.2 Heat exchangers

In order to evaluate the thermal flow Q_{hx} delivered to the solution, a model of the heat exchanger was also developed. According to this model, an intermediate temperature T_{hx} can be assigned to the surface of the heat exchanger, whose thermal capacity Mc_{hx} is a also accounted for. A distinction can then be made between the thermal flux $Q_{hx,w}$ moving from the water to the surface of the exchanger, see (8), and the flux Q_{hx} released by the exchanger to the solution, see (9), which depends on the internal heat transfer coefficient UA_{int}. The difference between these fluxes is stored on the body of the heat exchanger, see (10).

In order to solve the problem, one more equation is needed (11), which accounts for the external heat transfer coefficient of the heat exchanger, UA_{ext}, and the mean logarithmic temperature.

$$Q_{hx,w} = \dot{m}_w \cdot c_{p,w} \cdot \left(T_{w,in} - T_{w,out}\right) \quad (8)$$

$$Q_{hx} = UA_{int} \cdot \left(T_{hx} - T_s\right) \quad (9)$$

$$Q_{hx,w} - Q_{hx} = Mc_{hx} \cdot \frac{dT_{hx}}{d\tau} \quad (10)$$

$$Q_{hx,w} = UA_{ext} \cdot \frac{\left(T_{w,in} - T_{hx}\right) - \left(T_{w,out} - T_{hx}\right)}{\ln \frac{\left(T_{w,in} - T_{hx}\right)}{\left(T_{w,out} - T_{hx}\right)}} \quad (11)$$

The external (water - exchanger) and internal (exchanger - solution) heat transfer coefficients are assigned, as they depend on the conductivity of the metal and the water (solution) flow regime. By providing the water mass flow and its inlet temperature, the outlet temperature and the thermal flux released to the solution are obtained.

3.1.3 Condenser / evaporator

Fig. 8 also shows the scheme used to model the condenser. Equations (2) to (5) can be repeated, but we have to consider that:

- the liquid phase is represented by condensed vapour instead of LiBr/water solution;
- no vapour desorption has to be counted in (2);

Equation (7) can be applied to the vapour phase and written as:

$$\dot{Q}_{hx} - \dot{Q}_d = \dot{m}_c \cdot h_c - \dot{m}_{v,in} \cdot h_{v,in} + \frac{d}{d\tau}\left(Mc_p \cdot T_v\right) \quad (12)$$

The vapour and the condensate are saturated; the enthalpy of the inlet vapour equals that of the vapour flowing out of the generator. The equations can be extended to the evaporator, just accounting for the different directions of the mass flows.

3.1.4 Other devices

As stated before, the diluted solution flow rate in the solution pump is assumed constant and imposed as an input value. The strong solution flows from the generator to the absorber, driven by gravity and by the pressure difference, see Fig. 7; the pressure losses in the solution heat exchanger and the pipes may be described through a resistance coefficient ζ. Hence [6], the strong solution mass flow can be assessed as:

$$\dot{m}_s = C_d A \cdot \sqrt{\frac{2 \cdot \rho_s \cdot \left[\left(p_g - p_a\right) + \rho_s \cdot g \cdot \left(h + z\right)\right]}{\zeta}} \quad (13)$$

The level z of the solution inside the generator is continuously updated, as a function of the mass of solution actually contained inside the vessel; the distance h between the solution outlet at the generator and the solution inlet at the absorber is also accounted for. The same expression can be used to calculate the condensate mass flow from the condenser to the evaporator.

In both cases, the resistance coefficients are not set constant. In this model, we assume that they vary as a function of the fluid height inside the upper vessel, according to the equation: $\zeta = \zeta_0 \cdot (z_0/z)^2$, where ζ_0 and z_0 are nominal values. This corresponds to the control logic which is often adopted in absorption chillers, where an increase of the resistance is generated when the level of the liquid gets too low. Such a condition has consistently improved the stability of the model. Finally, no thermal inertia has been considered for the solution heat exchanger between generator and absorber (see Fig. 7). Its heat transfer coefficient UA_{hxs} is assumed constant and assigned as an input; its efficiency can be easily assessed as a function of UA_{hxs} and the solution mass flow, through well known relationships valid for counter-current heat exchangers.

3.2. Model adaptation to Rotartica chiller

The mathematical model described so far is a general model, aimed at being used for every kind of absorption chiller. Actually, the Rotartica machine is a very particular one, as:

- the absorption cycle is carried out into a rotating container;
- the solution pump is not electrically driven, as the pumping power is derived from rotation, by converting the kinetic energy at the outer radius into pressure [7].

Nonetheless, the model was applied to simulate the performance of the Rotartica machine used in the experimental system, with a special effort to the choice of the input parameters.

Table 3 reports the values of the main parameters adopted to describe the real absorption chiller; they were firstly defined through an in-depth study of the size and the materials of each component, and then optimized in order to improve the precision of the results. The water mass flow rates and their inlet temperature in every component of the absorption machine are known from the experimental data. As an output, the model provides the outlet temperatures and the thermal power exchanged inside each component, which can be compared to experimental results. The equations system is solved on SPARK using a Newton-Raphson procedure with forward finite difference approximation. The simulation is performed with a time step as long as 5 seconds.

A first comparison between experimental and simulated results from the same day previously described (14/08/2009) is given in Fig. 9.

Table 3. Main input parameters for the simulation of the Rotartica machine

$\dot{m}_{pump}$ =	0.031 kg/s	$UA_{int,c}$ =	6200 W/(m^{2}K)
UA_{hxs} =	42 W/(m^{2}K)	$UA_{ext,c}$ =	5080 W/(m^{2}K)
$\zeta_{o,g}$ =	1400	$UA_{int,ev}$ =	4640 W/(m^{2}K)
$\zeta_{o,c}$ =	1400	$UA_{ext,ev}$ =	3800 W/(m^{2}K)
$UA_{int,g}$ =	4730 W/(m^{2}K)	$UA_{int,a}$ =	7950 W/(m^{2}K)
$UA_{ext,g}$ =	8740 W/(m^{2}K)	$UA_{ext,a}$ =	5850 W/(m^{2}K)

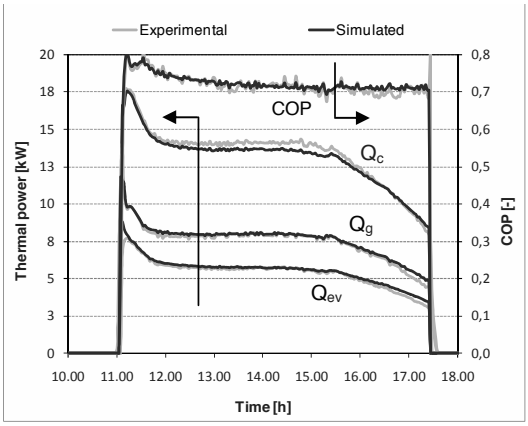

Fig. 9. Comparison of daily experimental and simulated thermal power profiles (14/08/2009)

There is a very good agreement in terms of thermal power and thermal COP. The error is always lower than 5%, that is to say lower than the estimated measurement uncertainty. The experimental and simulated temperature profiles are also very close to each other and not easily distinguished. As a second step, the simulation was extended to the entire test campaign (27/05 – 10/09). Table 4 reports the experimental and simulated overall thermal energies, as well as the seasonal average thermal COP. Even on a seasonal basis the reliability of the model is very high.

Table 4. Comparison between experimental and simulated seasonal performance of the chiller

	Experimental	*Simulated*	*Error*
Q_g [kWh]	3309	3313	+ 0.1 %
Q_{ev} [kWh]	2302	2358	- 2.2 %
$Q_c + Q_a$ [kWh]	5725	5598	+ 2.4 %
COP_{th} [-]	0.696	0.712	+ 2.3 %

Nomenclature

A	pipe section, m^2
c	specific heat, J/(kg K)
C_d	discharge coefficient, ad.
h	enthalpy, J/kg
m	mass flow rate, kg/s
M	mass, kg
p	pressure, Pa
Q	thermal flow, W
T	temperature, K
V	volume, m^3
x	LiBr concentration, ad.

Greek symbols

ρ	density, kg/m^3
τ	time, s

Subscripts and superscripts

a	absorber
c	condensate
ev	evaporator
g	generator
hx	heat exchanger
in	inlet
out	outlet
s	solution
v	vapour
w	water

References

[1] Lucas F. et al., 2008, ORASOL: A French Research Program for Solar Cooling Process Optimization, *Proceedings of 1st EUROSUN International Conference*, ISES, Lisbon.

[2] Syed A. et al., 2005, A novel experimental investigation of a solar cooling system in Madrid, Int. J. of Refriger, 28, pp. 859–871.

[3] Florides G. A. et al., 2006, Design and construction of a LiBr-water absorption machine, Energy Conversion and Management, 44, pp. 2483-2508.

[4] Alefeld G. and Radermacher R., 1993, *Heat Conversion Systems*, CRC, USA, Chapter 4.

[5] Shin Y. et al., 2009, Simulation of dynamics and control of a double-effect LiBr–H_2O absorption chiller, Applied Thermal Engineering, 29, pp. 2718-2725.

[6] Köhlenbach P. and Ziegler F., 2008, A dynamic simulation model for transient absorption chiller performance. Part I: the model, Int. J. of Refriger, 31 (2), pp. 217–225.

[7] Gilchrist K. et al., 2002, Process intensification applied to an aqueous LiBr rotating absorption chiller with dry heat rejection, Applied Thermal Engineering, 22, pp. 847-854.

Acknowledgments: The experimental installation has been financed in the framework of the European project SOLERA (FP6), coordinated by Fraunhofer ISE. The study of its performance has been conducted in the framework of the research project ORASOL ANR 06-PBAT-009-01.

Second Law Comparison of GAX Absorption-Compression Refrigeration (Hybrid GAX) and Absorption Refrigeration with GAX (Conventional GAX)

Mortaza Yari[a], Arash Zarin[b] and Sanubar Ghorbani[c]

[a] *Department of Mechanical Engineering, Faculty of Engineering, University of Mohaghegh Ardabili, Ardabil 179, Iran*
E-mail: myari@uma.ac.ir, myaari@yahoo.com
[b] *Department of Mechanical Engineering, Faculty of Engineering, University of Mohaghegh Ardabili, Ardabil 179, Iran*
E-mail: zarin_arash_60@yahoo.com
[c] *Department of Mechanical Engineering, Faculty of Engineering, University of Mohaghegh Ardabili, Ardabil 179, Iran*
E-mail: Sanubar.Ghorbani.faal@gmail.com

ABSTRACT: The GAX (generator absorber exchange) absorption cycle is an elegant way of achieving higher coefficient of performance (COP) with a cycle configuration that essentially appears to be a single stage absorption system. In the absorber and generator, the pressures and concentrations are maintained in such a way as to cause a temperature overlap between the absorber and generator. This provides the possibility that some of the heat of absorption may be rejected to the generator. In this paper a comparative study between GAX absorption-compression refrigeration (hybrid GAX) cycle and absorption refrigeration with GAX (conventional GAX) cycle using ammonia-water as working fluid with identical cold output is carried out. Simulation results are used to study the influence of the various operating parameters on the thermal loads of the components, exergy efficiency and total exergy destruction of both systems. It is found that for each condenser and evaporator temperature, there is an optimum generator temperature where the total exergy destruction of the hybrid GAX and conventional GAX absorption refrigeration systems is minimum. At this point the exergy efficiency of the systems becomes maximum. The effect of absorber pressure on the heat duties of the hybrid GAX cycle has also been studied.

Keywords: GAX, Absorption, Hybrid, Exergey Efficiency, Exery Destruction.

1. Introduction

In view of energy conservation becoming increasingly important, there is a need to optimize thermodynamic processes for minimum consumption of energy. Many constrains affect the performance of GAX absorption systems leading to the actual performance being much lower than the ideal reversible case. The first law method thermodynamic analysis is most commonly used to evaluate the cooling performance and optimize the operating parameters. This is however, concerned with conservation of energy and cannot show where irreversibility in the system occurs to cause COP degradation.

The exergy method, known as the second law analysis, is an important thermodynamic property that measures the useful work that can be product by a substance or the amount of work needed to complete a process. The concept exergy is extensively discussed in literature [1,2].

In this paper the thermodynamic comparison based on the first and second law of thermodynamics of GAX absorption cycle (Conventional GAX) and GAX absorption compression cycle (Hybrid GAX) has been carried out.

2. Description of GAX absorption compression cycle

Fig. 1 illustrates the main component of the GAX compression–absorption refrigeration cycle. the saturated solution is assumed to leave the absorber (1) and the generator (3), and saturated ammonia liquid is assumed to leave the condenser (8). Saturated vapour is assumed to leave the evaporator (11). The condensate pre-cooler sub-cools the refrigerant that leaves the condenser (8) by pre-heating the vapour entering the compressor (12). The high pressure cooled liquid refrigerant

(8) from the condensate pre-cooler inters the evaporator (10) through an expansion valve that reduces the pressure of the refrigerant to the evaporator pressure. The liquid refrigerant (10) vaporizes in the evaporator by absorbing heat from the room being conditioned, and the resulting low pressure saturated vapour (11) passes to the compressor (12) through the condensate pre-cooler. The compressor is placed between the evaporator and the absorber. The compressor increase the absorber pressure (15) higher than evaporator pressure. In the absorber, the refrigerant vapour is absorbed by the weak solution coming from generator (3) through an expansion valve (4) and forms the strong solution (1).

The term "strong solution" represents a solution that is strong with refrigerant (NH_3), while "weak solution" represents a solution that is weak with refrigerant. The strong solution (1) pumped to the generator pressure (2) is introduced into the high temperature part of the absorber, where it receives heat from absorber, and the refrigerant in it is boiled off in the generator. The remaining solution (3) flows back to the absorber and, thus, completes the cycle. The generator and absorber temperature ranges partially overlap. This overlapped heat is internally transferred from the absorber to the generator. The dotted line (Q_{gax} in Fig. 1) represents the heat exchange between the absorber and generator.

Main component of the conventional GAX cycle is the same as hybrid GAX cycle, only difference is that, there is not compressor in conventional GAX.

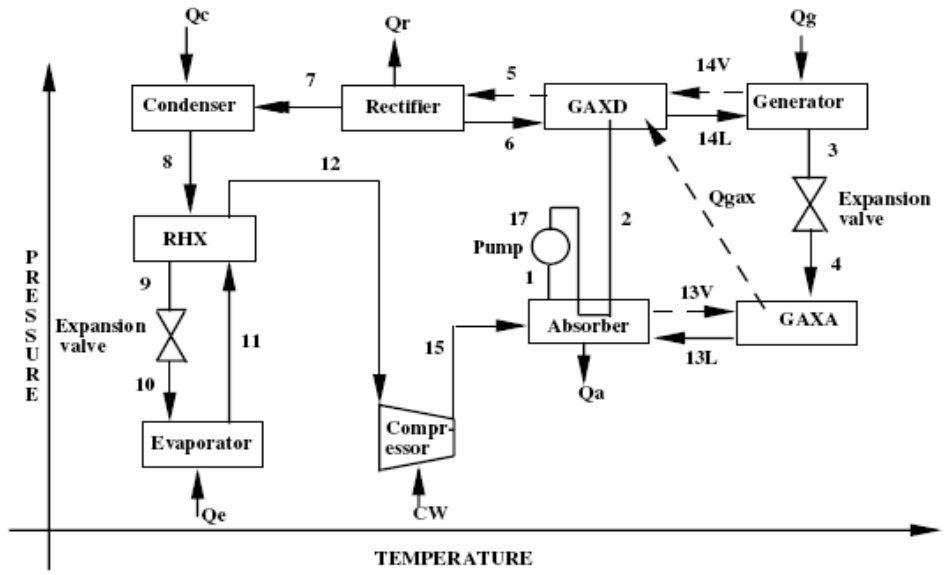

Fig.1. Schematic diagram of GAXAC cycle [3].

3. Thermodynamic analysis

For the thermodynamic analysis of the GAX absorption systems the principle of mass conservation, first and second law of thermodynamics are applied to each component of the system.

3.1. Mass conservation

Mass conservation includes the mass balance of total mass and each material of the solution. The governing equations of mass and type of material conversation for a steady state and steady flow system are:

$$\sum m_{in} - \sum m_{out} = 0 \quad (1)$$

$$\sum m_{in} x_{in} - \sum m_{out} x_{out} = 0 \quad (2)$$

Where m is the mass flow rate and x is the mass fraction of ammonia in the solution. The mass fraction of the system (Fig. 1) is calculated using the corresponding temperature and pressure data.

3.2. Energy method (the first law analysis)

The first law of thermodynamics yields the energy balance of each component of the GAX absorption systems as follows:

$$(\sum m_{in} h_{in} - \sum m_{out} h_{out}) + (\sum Q_{in} - \sum Q_{out}) + W = 0 \quad (3)$$

The energy balance equations for some of the components of the GAX absorption compression system are expressed as follows:

- Desorber:

$$m_2 h_2 + m_6 h_6 + Q_{gt} = m_5 h_5 + m_3 h_3 \quad (4)$$

- GAX desorber:

$$m_2 h_2 + m_6 h_6 + m_{14v} h_{14v} + Q_{rg} = m_5 h_5 + m_{14l} h_{14l} \quad (5)$$

- Absorber:

$$m_1 h_1 + m_2 h_2 + Q_{at} = m_{15} h_{15} + m_4 h_4 + m_{17} h_{17} \quad (6)$$

- GAX absorber:

$$m_{13l} h_{13l} + Q_{av} = m_{13v} h_{13v} + m_4 h_4 \quad (7)$$

The evaporator heat load is calculated as:

$$Q_{ev} = m_r \times (h_{11} - h_{10}) \quad (8)$$

Effectiveness of heat exchenger is defined as the ratio of actual heat transfer to the maximum possible heat transfer. Accordingly the effectiveness of heat exchenger is given as bellow:

$$\eta_{HX} = \frac{(h_8 - h_9)}{(h_8 - h^*_9)} \quad (9)$$

Where h_9^* represents the enthalpy of minimum heat capacity streams at the exit of the heat exchanger when it is cooled to the temperature of entry cold stream.

The pump power is calculated as:

$$W_p = (P_c - P_a) \times (v_c \times m_r)/\eta_p \quad (10)$$

$$h_{17} = h_1 + (W_p/m_r) \quad (11)$$

- Condenser:

$$Q_{cd} = m_7 \times (h_7 - h_8) \quad (12)$$

3.3. Exergy method (the second law analysis)

Exergy analysis is the combination of the first and second law of thermodynamics and is defined as the maximum amount of work, which can be produced by a stream or system as it is brought into equilibrium with a reference environment [1]. The total actual exergy change that occurs between the entrance and exits of the control volume, namely the sum of the reversible and the irreversible contributions to the total actual exergy change can be calculated by:

$$\Delta E = (\sum_i m_i . ex_i)_{in} - (\sum_i m_i . ex_i)_{out} \quad (13)$$

The first term on the right hand side of Eq. (13) is the actual total exergy of all streams flowing into the control volume and the second term is the actual total exergy of all streams flowing out of the control volume.

In Eq. (13), the exergies of heat and work transfer are already contained in the subtraction of the second term from the first term on the right hand side.

When neglecting changes in kinetic energy and potential energy and because there is no departure of chemical substances from the cycle to the environment, the chemical exergy is zero [4] the specific exergy ‘ex’ is calculated by:

$$ex = (h - h_0) - T_0 \times (s - s_0) \quad (14)$$

The exergy efficiency (rational efficiency) can be calculated as ratio between the net exergy produced by the evaporator (exergy desired output) and the input exergy to the generator plus mechanical work of the solution pump:

$$\eta_{exergy} = \frac{Q_{ev} \times \left(1 - \frac{T_0}{T_b}\right)}{\left[Q_g \times \left(1 - \frac{T_0}{T_h}\right) + W_p\right]} \quad (15)$$

In the hybrid GAX cycle the mechanical work of the compressor also added to the input exergy to the generator and mechanical work of the solution pump:

$$\eta_{exergy} = \frac{Q_{ev} \times \left(1 - \frac{T_0}{T_b}\right)}{\left[Q_g \times \left(1 - \frac{T_0}{T_h}\right) + W_p + W_c\right]} \quad (16)$$

T_b and T_h are the mean temperature of the cold source (in the evaporator) and hot source (in the generator), respectively.

Simulation was performed to evaluate the hybrid and conventional GAX cooling cycles with the assumption enumerated below:

1. Condenser pressure is the equilibrium pressure corresponding to the refrigerant concentration and the condenser temperature.
2. The condition of the refrigerant at the exit of the evaporator is saturated vapour, and the evaporator pressure is the saturated pressure at evaporator temperature.
3. The refrigerant pressure at the outlet of the compressor is the absorber pressure.
4. The approach temperature at either end of the GAX heat exchanger is assumed 0 K.
5. The efficiency of the solution pump is 0.5.
6. The efficiency of the heat exchanger (RHX) is 0.8.
7. Evaporation temperature is varied in the following range: T_{ev}=5-9 ^{0}C
8. Condensation temperature is varied in the following range: T_{cd}=37-40 ^{0}C
9. Generation temperature "T_g" is varied from 110^0 C to 180^0C.
10. Pressure losses in the pipelines are negligible except through the expansion valve.
11. The flow through all components of the cycle is under steady state.
12. The references environmental state is water at an environmental temperature T_0 of 25 ^{0}C and one atmospheric pressure (P_0).
13. The system produced chilled water, and generator is driven by pressurized hot water.
14. The system rejects heat to cooling water at the condenser and absorber.
15. Mass flow rate of refrigerant is constant.

4. Validation

To validate the simulation model, the result and the parameter profiles are compared with the simulation work presented in the literature [3,5]. From Fig. [2], it can be seen that at constant desorber and evaporator pressure (1548 and 478.4kPa, respectively), the generator heat supply shows a fast decreasing trend, and the compressor work shows a gradually increasing trend with absorber pressure and because of that the value of COP increases with increasing absorber pressure. Kang et al. [5] and Ramesh Kumar et al. [3] showed that at constant desorber and evaporator pressure, the cooling COP of the hybrid GAX system increases with increasing absorber pressure. The previous works claim that the COP increase that could be achieved is 24% and 30% (Kang et al. and A. Ramesh Kumar et al. respectively) higher than the standard GAX cycle and the present study predicts it as about 26.4% higher than the standard GAX cycle. Further, the simulation model for the conventional GAX cycle also is compared with the simulation works presented in literature [3,6]. For a given set of input parameters (T_g=163.3 ^{0}C, T_{cd}=40 ^{0}C, T_{ab}=40 ^{0}C, T_{ev}=5 ^{0}C, P_{ab}=1548.0 kPa, P_{ev}=478.4 kPa and ξ=0.35), the simulation of Ref. [6] predicts the COP value of 1.10, and the simulation of Ref. [3] predicts the COP value of 1.08, and the present simulation model for the conventional GAX cycle predicts the COP value as 1.103. These differences are mainly due to the number of idealized assumptions made in the models.

5. Result and discussion

A computer program to determine the thermodynamic properties of the saturated ammonia-water solution has been developed based on the correlations of Patek and Klomfar [7]. The relation between the saturation pressure, solution temperature and ammonia concentration of the ammonia-water mixture can also be obtained [8]. The input parameters to the simulation program are the concentration of the refrigerant leaving the rectifier, degassing ratio, temperature of condenser, evaporator and generator, efficiency of the pump and the effectiveness of the heat exchanger and compressor is assumed to be isentropic.

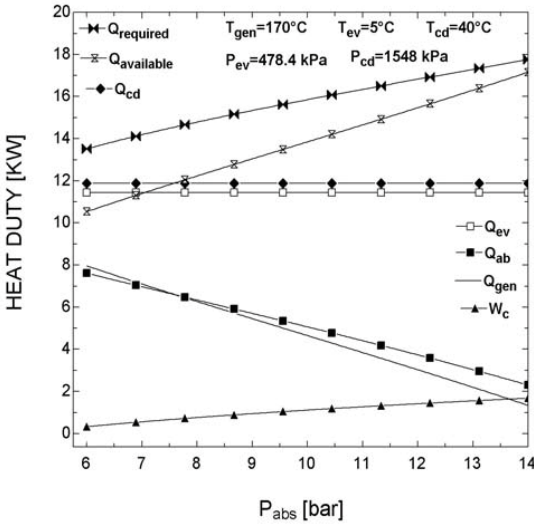

Fig.2. Variation of heat duty with various absorber pressure.

Increasing the absorber pressure at constant degassing range and generator temperature increases the absorber temperature. This increases the temperature glide in the absorber and desorber heat exchangers, resulting in the rise of heat availability in the absorber and the heat required in the desorber as shown in Fig. 2.

The heat availability is the rate of heat supplied to generate the refrigerant vapour in the GAX desorber from the GAX absorber. The mathematical expression is given in Eq. (7). The heat required is the rate of heat needed to generate the refrigerant vapour in the GAX desorber. The mathematical expression is given Eq. (5). The increases of mass flow rate at state point 13*v* results in the increases of heat availability in the absorber, and the decreases of mass flow rate at state point 14*v* results in the increases of heat required in the desorber. The rate of increment of heat availability is higher than the rate of the increment of heat requirement, causing the COP of the hybrid cycle to be high. Although the compression work required to run the compressor increases with absorber pressure, the internal heat recovered by the GAX cycle subdues the compressor effect, and the COP increases.

The dependence of Q_{av} and Q_{rq} on the generator temperature for the conventional and hybrid GAX cycles is shown in Fig. 5. It can be seen that at constant refrigerant flow rate, the Q_{av} value in the hybrid GAX when P_a is 916.87 kPa, is 5 kW higher than that in the conventional GAX and when P_{ab} is 716.87 kPa is 3kW higher than that in the conventional GAX.

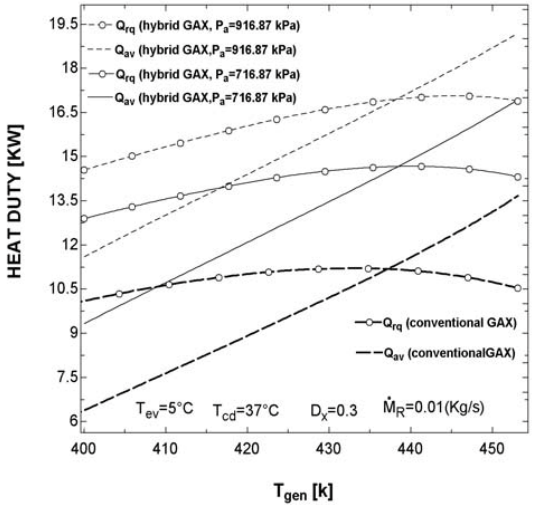

Fig.3. Variation of heat duty with various generator temperature.

The effects of generator, evaporator and condenser temperature on the thermal loads of the components are shown in Figs. 4-7. In all cases when generator temperature increases, the evaporator and condenser thermal loads (Q_{ev} and Q_{cd}) does not change and remain constant.

As it can be seen from these figures, when the generator temperature increases, the generator and absorber thermal loads (Q_{gen} and Q_{ab}) decrease. There is an optimum generator temperature which corresponds to a minimum Q_{gen} and Q_{ab}. If the generator temperature increases, Q_{gen} and Q_{ab} increase.

As it can be seen from Figs. 4-7, the rate of heat rejection in the absorber and the rate of heat supplied to the generator in the conventional GAX cycle is high when compared with the hybrid GAX cycle at all generator temperatures, and in hybrid GAX cycle when absorber pressure increases, the rate of heat rejection in absorber and the rate of heat supplied to the generator decrease. When absorber pressure increases, heat availability in GAX absorber increases and because of this by increasing absorber pressure, the rate of heat supplied to the generator decreases which affects directly the COP of the systems. Also we can see in Fig. 5 that after a specific generator temperature the rate of heat required to the desorber GAX (Q_{rq}) decreases. This decrement causes increment of rate of heat supplied to the generator (as it can be seen

from Figs. 4-7) after this temperature and leads to exergey efficiency decrement after this temperature (Figs. 8 and 9).

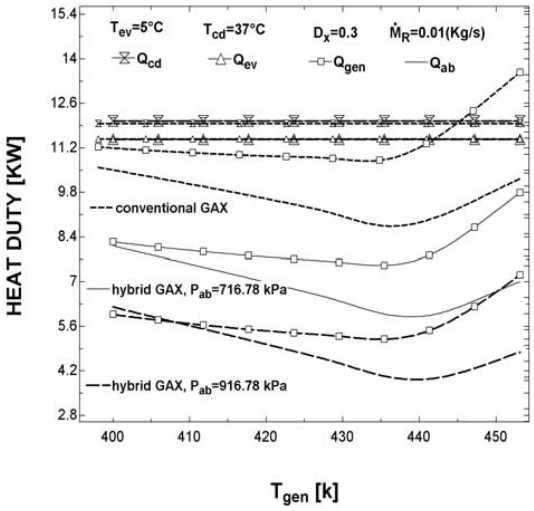

Fig.4. Variation of heat duty in the each component of conventional and hybrid GAX absorption cooling cycles (T_{cd}=37 ^{0}C , T_{ev}=5 ^{0}C)

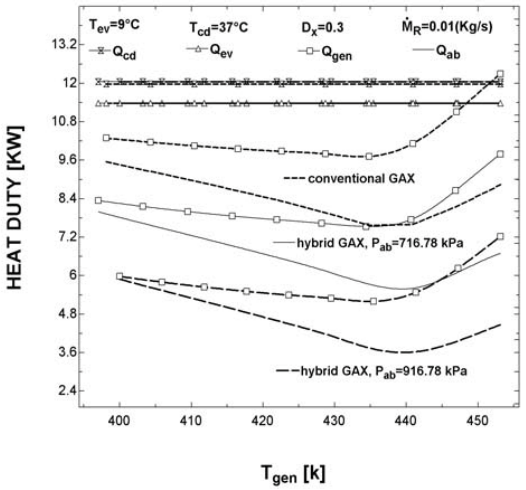

Fig.5. Variation of heat duty in the each component of conventional and hybrid GAX absorption cooling cycles (T_{cd}=37 ^{0}C, T_{ev}=9 ^{0}C)

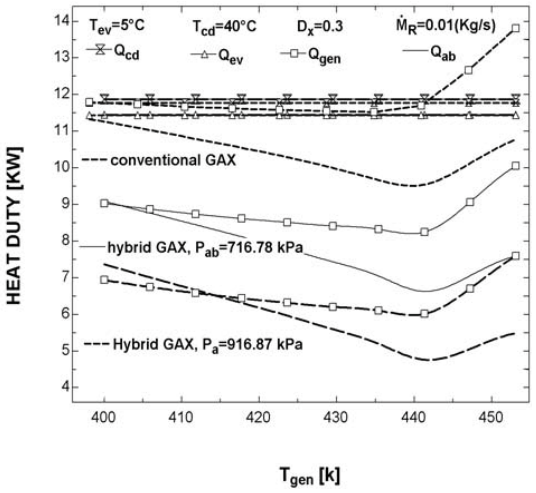

Fig.6. Variation of heat duty in the each component of conventional and hybrid GAX absorption cooling cycles (T_{cd}=40 ^{0}C, T_{ev}=5 ^{0}C)

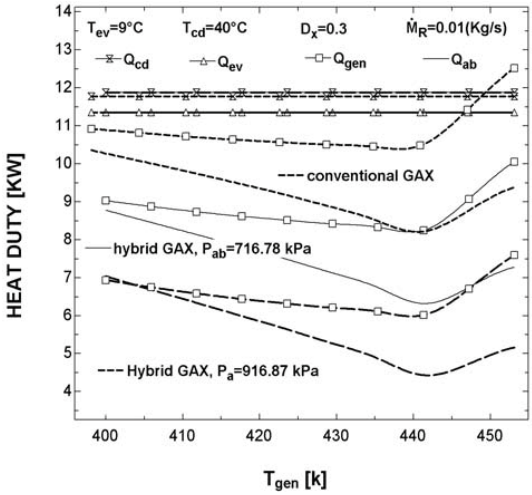

Fig.7. Variation of heat duty in the each component of conventional and hybrid GAX absorption cooling cycles (T_{cd}=40 ^{0}C, T_{ev}=9 ^{0}C)

The variation of exergy efficiency with generator temperature for conventional and hybrid GAX cycles at different condenser and evaporator temperatures is shown in Figs. 10 and 11. Exergy efficiency increase with a rise in the generator temperature for both cases (conventional and hybrid GAX cycle) up to a certain generator temperature (for a given evaporator and condenser temperature, there is an optimum generator temperature which corresponds to a maximum exergy efficiency) and then decrease.

When the evaporator temperature is varied from 5 ^{0}C to 9 ^{0}C and condenser temperature is varied

from 37 ^{0}C to 40 ^{0}C the maximum exergy efficiency value of the conventional GAX systems are in the range of 20.584-24.52% and for hybrid GAX cycles, when P_{ab}=716.87 kPa, are in the range of 22.36-27.63% and when P_{ab}=916.87 kPa are in the range of 24.77-31.06%.

As the efficiency of the second law is examined here, it is seen that exergy efficiency increases up to a certain generator temperature (variable with evaporation and condensation temperature). At higher generator temperature, exergy efficiency decline significantly. The reason for this is that the increase in the generator temperature negatively influences the exergy efficiency value as seen from Eqs. (15 and 16), and another reason is that after this temperature heat requirement decreases and causes to increment of heat supplied to the generator. It can be seen that the system experiences better exergy efficiency at low condenser temperature and low evaporator temperature. For every system, the exergy efficiency initially rises and declines continuously as the generator temperature increases.

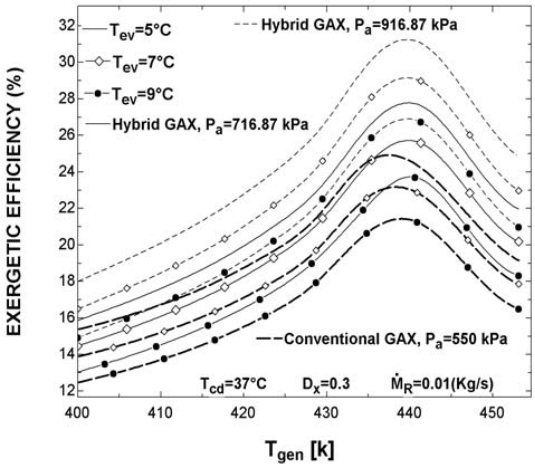

Fig. 8. Variation of exergy efficiency of conventional and hybrid GAX absorption cooling systems (T_{cd}=37 ^{0}C)

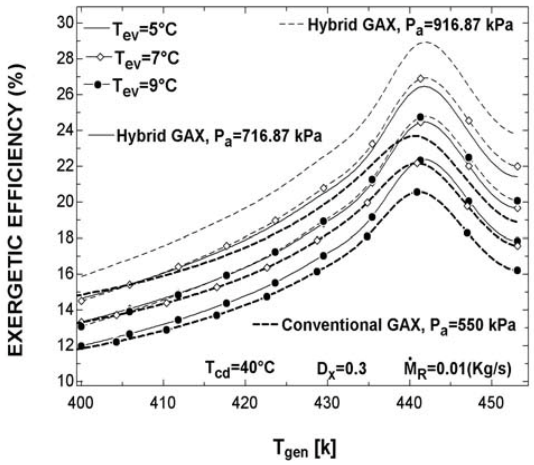

Fig. 9. Variation of exergy efficiency of conventional and hybrid GAX absorption cooling systems (T_{cd}=40 ^{0}C)

The variation of exergy change versus generator temperature for cooling at different condenser and evaporator temperatures is shown in Figs. 12 and 13. The exergy change of the two types of GAX absorption cooling systems declines gradually to a minimum value with an increase of generator temperature and then rises sharply. For each condenser and evaporator temperature there is a generator temperature at which the exergy change of the GAX absorption cooling systems is minimum.

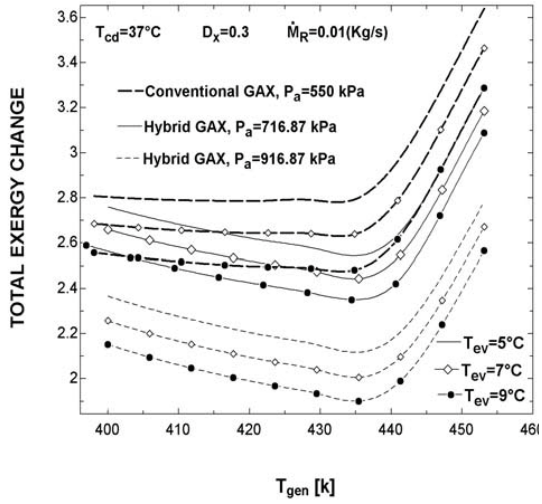

Fig.10. Variation of total exergy change in conventional and hybrid GAX absorption cooling systems (T_{cd}=37 ^{0}C).

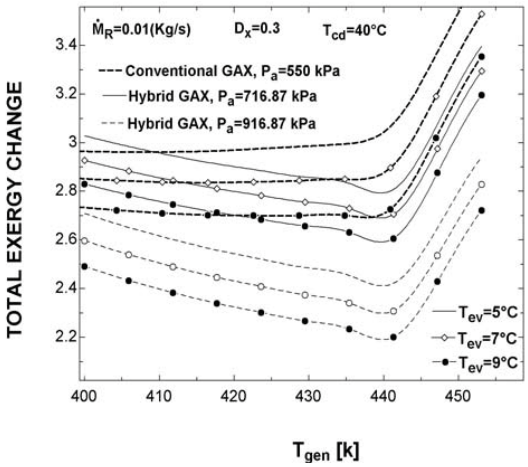

Fig.11. Variation of total exergy change in conventional and hybrid GAX absorption cooling systems (T_{cd}=40 ^{0}C).

6. Conclusion

In this study, the second law of thermodynamics is applied to conventional and hybrid GAX absorption cooling cycles. COP, thermal loads of all components, exergy efficiency and the change in exergy that occurs between the entrances of each component, total change in exergy of all components of the two systems are calculated from the thermodynamic properties of the working fluids at various operating conditions. The results show that COP of the cycle rises with increasing generator and evaporator temperatures, but decreases with increasing condenser temperature.

1. For each condenser and evaporator temperature, there is an optimum generator temperature where change in exergy of the conventional and hybrid GAX absorption cooling systems is minimum. At this point the exergy efficiency of the systems becomes maximum.
2. Exergy efficiency of the conventional and hybrid GAX absorption cooling systems initially rises with increasing generator temperature and then declines. By increasing evaporator temperature, exergey efficiency decreases and by increasing condenser temperature, exergy efficiency declines. Total exergy change of the conventional and hybrid GAX absorption cooling systems initially declines gradually with increasing generator temperature and then rises sharply. By increasing evaporator temperature, total exergy change declines and by rising condenser temperature, total exergy change increases.
3. The exergy efficiency rises with increasing absorber pressure and total exergy change decreases with increasing absorber pressure in hybrid GAX absorption cooling cycle.
4. This study shows that the exergy efficiency of hybrid GAX cycle increases compared to the exergy efficiency of conventional GAX cycle and it is 26.7% higher than the exergy efficiency of conventional GAX cycle.

Nomenclature

Q heat flow (KW)

T temperature (°C or K)

P pressure (kPa)

W power (kW)

v specific volume (m^3/kg)

h specific enthalpy (kj/kg)

s specific entropy (kj/kg K)

m mass flow rate (kg/s)

x mass fraction of ammonia (%)

ex specific exergy (kj/kg)

ΔE total change in exergy (KW)

RHX condenser pre-cooler

GAX generator absorber heat exchange

$GAX\ A$ GAX absorber

$GAX\ D$ GAX desorber

COP coefficient of performance

Greek symbols

η efficiency

ξ degassing range

Subscripts

0 refrence value

ab absorber

gen generator

ev evaporator

p pump

r refrigerant

cd condenser

gt total generator

rq required

at total absorber

av available

l liquid

v vapour

c compressor

References

[1] Kotsa JT. The exergy method of thermal plant analysis. Paris: Lavoisier; 1987.

[2]Bejan A. advanced engineering thermodynamics. New York: Wiley; 1988.

[3] A.Ramesh Kumar, M.Udayakumar. Simulation study on GAX absorption compression cooler. Energy conversion and management 2007; 48:2604-2610.

[4] Vidal A, Best R, Rivero R, Cervantes J. Analysis of a combined power and refrigeration cycle by the exergy method. Energy 2006;31: 3401-3414.

[5] Kang YT, Hong H, Park KS. Performance analysis of advanced hybrid GAX cycles: HGAX. Int J Refrig 1995; 18(4) :228-234.

[6] Herold KE, Radermacher R, Kelin SA. Absorption chillers and heat pumps. New York: CRC Press;1995. Pp 212-232.

[7] Patek J, Klofar J. Simple function for fast calculations of selected thermodynamic properties of the ammonia-water system. Int J Refrig 1995; 18(4):228-234.

[8] DA-Wen Sun. comparison of the performances of NH_3-H_2O, NH_3-$LiNO_3$ and NH_3-NaSCN absorption refrigeration systems. Energy conversion and management 1998;39:357-68

A Solar Space Heating plant for Greek Buildings with underfloor heating system

A. Stegou-Sagia, I.P. Koronaki, Z. Sagia

School of Mechanical Engineering,
Thermal Engineering Department,
National Technical University of Athens,
15780, Zografou, Athens, Greece,
tel 0030 2107721255,
fax 0030 2107723670,
email asagia@central.ntua.gr

Abstract: The objective of this paper is to present the sensitivity analysis of various components of a solar heating system combined with underfloor tubes focused on the type, slope and area of solar collector and storage tank size as well as on the underfloor system components. The collector types considered are the flat plate and evacuated tube collectors. The sensitivity analysis is based on an energy benefit analysis, i.e., the amount of useful energy collected. The system is modeled with TRNSYS computer program using data for a typical meteorological year (TMY) for two climatic zones in Greece and a six storey terraced building with total heated area 1955 m^2. The results indicate that for the present application evacuated tube collectors are the most energy-efficient system for solar heating applications whereas the optimum collector area for climatic zone B is 110 m^2, the optimum slope of the collector is 30° and the storage tank size is 70 m^3 while for climatic zone C the optimum collector area is 130 m^2, the optimum slope of the collector is 29.5° and the storage tank size is 90 m^3.

Keywords: Solar heating, underfloor systems, solar collectors, storage tank, sensitivity analysis

1. Introduction

There are a number of renewable energy sources which are available to provide space heating as well as heating of domestic water reducing the level of greenhouse gas emissions in comparison to fossil fuel based systems [1].

Solar energy is a renewable energy source that has found worldwide application in space heating, cooling and heating of domestic water. The sizing of a solar space heating system (SSH) in combination with a solar domestic hot water system (SDHW) [2] for a building is a complex problem involving a number of interrelated factors and parameters which include, among others, the building thermal characteristics, the collector size and slope, the storage tank size, the heat exchangers size, the solar radiation, and a number of economic parameters. The components of SSH and SDHW systems must be well selected, properly sized, and carefully assembled in order to ensure that the systems will function properly [2,3]. Oversizing of the systems is not advisable because of high initial cost, while undersizing may not provide significant savings of conventional fuels. The sensitivity analysis of the above systems factors can be achieved mainly by modeling and simulations [3,4] providing almost the same thermal performance information as experiments especially when water based thermo active building components as underfloor heating tubes are included.

Underfloor heating is one of the most efficient methods of heating dwellings as it runs at about 2ºC lower than central heating systems and delivers energy savings of between 15% and 50% depending on ceiling height [5]. Single thermostats in each room control the flow of the solar heated water through a valve and manifold into each room of the apartment building.

Underfloor heating tubes, are typically used in buildings in Central Europe. Usual internal diameter of the pipes varies between 17 and 25 mm. The distance between pipes is within the range 150 - 200 mm. Technologically, the design of underfloor heating tubes is based on the characteristics of other radiant systems: distance, diameter of pipes, supply water temperature and water mass flow rate [6]. Besides the direct

Corresponding Author: Athina Stegou-Sagia, Email: asagia@central.ntua.gr

heating capacity, the underfloor heating g tubes have also the thermal storage effect - the peak load during the day will be stored and removed during the night [7].

Influence of both convection and radiation can be expressed by means of combined heat transfer coefficient. The response time of the system is rather long due to its high thermal mass [8]. In order to avoid condensation, the water temperature or the surface temperature and the absolute humidity are controlled (surface temperature should be maintained above the dew-point of the ambient air for all operational conditions).

2. Description of the System

In the present study, solar space heating systems (SSH) in combination with solar domestic hot water systems (SDHW) will be analyzed for Greek climatic conditions (two representative towns of two climatic zones, Athens and Thessaloniki) [9] in combination with hydronic radiant flooring systems (underfloor heating) for an old terraced building which has recently been renovated in order to be used for students residence. On the basement, there are also three shops on the front, southeast side of the building. The building is consisted of 6 floors, apart the basement and an extended ground floor, big enough for heating tanks to be established. The heated spaces are counted approximately 1955 m^2, while the percentage of windows on southeast side is up to 48% including shops glazing. The building is divided in 19 thermal zones. Figure 1 depicts a typical floor.

All the information required to describe building's geometry and materials envelope is entered in Bui.file. The building bears insulated walls, with 0.060 m external insulation which thermal conductivity is k=0.1368 kJ/hmK, and non-insulated walls, consisted only of plaster and bricks, attached the buildings next to which is examined. Building's roof is also insulated with 0.060 m external insulation and covered with roof slates with k=7.92 kJ/hmK. The main building shell components properties are presented in Table 1. Greek brick has thermal conductivity k=2.592 kJ/hmK, specific heat capacity c_p=0.840 kJ/kgK and density ρ=1920 kg/m^3 [10]. All external walls have solar absorptance 0.6 and all internal 0.0. The convective heat transfer coefficient of walls with air is 25.2 kJ/hm^2K in the front face of thermal zone and 72 kJ/hm^2K in the back.

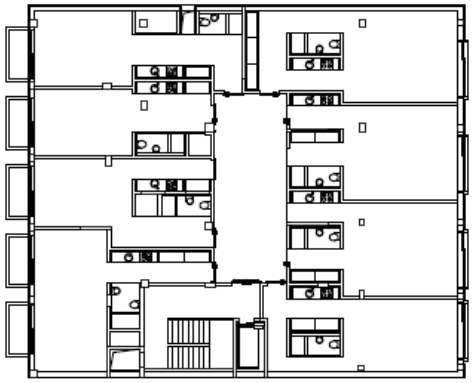

Fig. 1. Typical floor layout.

Table 1. Main building shell components properties.

Type of wall	Thickness (m)	Thermal Transmittance (W/m^2K)
External insulated wall	0.310	0.482
External non-insulated wall	0.250	1.939
Internal wall	0.150	2.765
Heating floor	0.440	0.273
Roof	0.370	0.365

The layers which are used to model the heating floor, started from the front face of thermal zone, are presented in Table 2. Parameter d is the thickness of each layer.

The active layer 'heating' is used to model the loops of pipes which are encased in the flooring. The pipe spacing, center to center, is 0.25 m. The pipe outside diameter is 0.028 m and its wall thickness is 0.003 m. The thermal conductivity of pipe material is 1.44 kJ/hmK. Every student studio has its own loop of pipes and that stands for one loop every 30 m^2. The specific heat capacity of water is 4.18 kJ/kgK.

Building's glazing is double with thermal transmittance U=2.83 W/m^2K and solar heat gain coefficient g=0.755. The frame of windows is 15% of the whole window area, with U=8.17 W/m^2K.
The heating schedule for residencies is 12 hours at 18◦C and 12 hours at 20◦C while, shops are heated at 21◦C only when they are open, that is 12 hours

every day, except Sunday. According to heating schedule, ventilation schedule is set to be 2 airchange/hour for 12 hours for studios and shops and 0 airchange/hour for the rest of the day. Infiltration is set to be 0.6 airchange/hour for studios and 1 airchange/hour for shops for the whole day.

Table 2. Heating floor layers [10],[12].

Layers	d (m)	k (kJ/hmK)	c_p (kJ/kgK)	ρ (kg/m^3)
Wooden floor	0.030	0.720	2.000	800
Air	0.075	0.828	1.007	1.1614
Heating		Active layer		
Air	0.025	0.828	1.007	1.1614
Thermal resistance I		0.23 hm^{2}K/kJ		
Polystyrene	0.040	0.130	1.250	25
Concrete	0.130	7.920	0.880	2300
Thermal resistance II		0.047 hm^{2}K/kJ		
Plasterboard	0.125	0.612	1.215	800
Plaster	0.015	4.320	0.835	1860

The number of occupants of each thermal zone is assumed as one person living in each studio and shops are occupied with no more than four people simultaneously. The degree of people's activity is seated, light work, typing for residencies and standing, light work or working slowly for shops according to ISO 7730 [12]. Taking into consideration all the internal gains, it is assumed that every person has one personal computer and every shop has two of them. Students residencies are illuminated by incandescent lamps with total heat gain 10 W/m^2 and shops with fluorescent ones with total heat gain 55 W/m^2 .

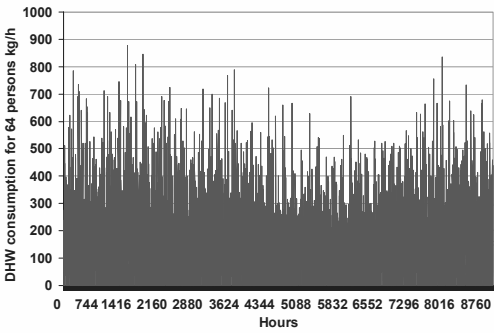

Fig. 2. Hourly profile of DHW consumption for 64 people.

An hourly profile for the whole year for 64 people, Fig.2, is used to simulate domestic hot water DHW consumption. The average consumption is estimated to be 50 lit/day/person [20].

Concerning the overall system hydronic circuit, a large, atmospheric pressure storage tank is used, from which water is pumped to the collectors by pump P1 in response to the differential thermostat T1. Domestic hot water is obtained by placing a second smaller tank and an auxiliary water heater which boosts the temperature of the sunheated water when required. If the water in the storage tank becomes too cool to provide enough heat, the second contact on the thermostat calls for heat from the auxiliary heater.

Standby heat in the tank becomes increasingly important as heating requirements increase. The heating load, winter availability of solar radiation, and availability of the auxiliary energy must be determined [11].

The sensitivity analysis of the examined system took place by computer modeling which presents many advantages as elimination of the expense of building prototypes, sensitivity analysis of the system components, estimation of the amount of energy delivered from the system, prediction of temperature variations of the system and many other less important ones. The complete solar system that is simulated, consists of a number of solar collectors, two thermally insulated vertical storage tanks, one for SSH system and one for SDHW system, two conventional auxiliary heaters and interconnecting piping. A schematic of the system showing also the simulation program information flow is shown in Fig. 3.

Commercially available building simulation programs can be used to determine behaviour of the system when installed in a particular building. Available capacity of the system, distributions of indoor temperatures and thermal comfort indices can be also evaluated. For the dynamic simulation of the entire system with embedded pipes acting together with the building construction, a validated model for the floor heating is used in TRNSYS 16. This software allows simultaneous performance assessments of all building components such as construction materials, glazing, HVAC systems, controls, indoor air quality, human thermal comfort and energy consumption.

The system is modeled by TRNSYS [12]. The flowchart consists of many subroutines that model subsystem components. The type number of every TRNSYS subroutine used to model each component is shown in Fig. 3.

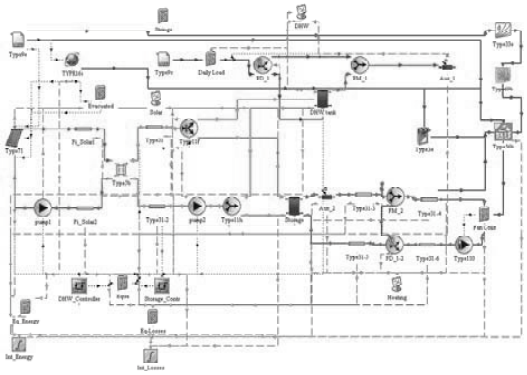

Fig. 3. TRNSYS model for the solar space heating application.

The mathematical models for the subsystem components are given in terms of their ordinary differential or algebraic equations.

In the current simulation temperature level control is used to control fluid flow through the solar collector loop, the domestic hot water loop and the space heating loop. Two TRNSYS differential controllers Type 2b [12] are used with the same upper input temperature which is the outlet collector temperature and default dead bands that stands for 7 ◦C for the upper dead band and 3 ◦C for the lower one. The first one referring to domestic hot water loop sets the lower input temperature equal to temperature to heat source of the domestic hot water tank and the monitoring temperature equal to temperature to load of the same tank. The other controller has relevant settings, referring to space heating storage tank. The controllers outputs are inputs at calculator's equations which are used to send the suitable signal to the pumps of each loop. In addition an extra equation is given to control the flow of underfloor heating system. The equations are presented in Table 3.

The construction and type of the solar collectors are important and relevant to the operation and efficiency of the whole system. Two types of solar collectors, modeled by TRNSYS, are evaluated in this study as follows [13,14]:

(a) Flat plate collectors.
The examined flat plate collectors are double glazed with tempered glass covers, copper absorber plates and black chrome selective surfaces with intercept 0.67 and efficiency slope 3.6 W/m^{2}K. When the collector circulation pump is not operating, the collectors drain back into the main storage tank. The storage tank is fitted with stratification manifolds on the inlet pipes from collector and load.

The characteristics of this type of collector are shown in Table 4.

(b) Evacuated tube collectors. These collectors are highly efficient, made of an absorber pipe enclosed within a larger glass tube. The absorber pipe may also be attached to a black copper fin that fills the tube (absorber plate). The space between the glass and the absorber is evacuated. The characteristics of the evacuated tube collector considered are shown in Table 5.

Table 3. Equations of Control signals.

Control signals	Equations
Solar collector loop	Maximum(Control signal of DHW, Control signal of Storage tank)
Domestic hot water loop	Minimum(Control signal of DHW, Control signal of Storage tank)
Space heating loop	Maximum(Control signal of DHW, Control signal of Storage tank)
Underfloor heating system	Hourly water mass flow/ Maximum value of water mass flow during the year

Table 4. Flat plate collector characteristics used in the TRNSYS simulations.

Parameters	Value
Specific heat of collector fluid (kJ/kgK)	4.05
Flow rate per unit area at test conditions (kg/hm^2)	63.36
Intercept efficiency	0.67
Efficiency slope (W/m^{2}K)	3.6

Table 5. Evacuated tube solar collector characteristics used in the TRNSYS simulations.

Parameters	Value
Specific heat of collector fluid (kJ/kgK)	4.05
Optical Efficiency	0.774
Overall heat loss coefficient (W/m^2K)	1.860

The different performances of the system employing these two types of collectors are investigated in order to select the most suitable for the present application.

Hot water is stored in a TRNSYS Type 4 [12] stratified storage tank. The vertical cylinder construction is made of copper and is thermally insulated polyurethane. The tank is protected by a galvanized outer shell 0.0006 m thick.

The system auxiliary heater (TRNSYS Type 6) [12] for space heating is assumed to have a maximum heating rate of 400000 kJ/h for Athens and 500000 kJ/h for Thessaloniki and a set upper temperature of 30 ◦C suitable for the underfloor heating system.

When domestic hot water is needed, solar heat is called first. If that will not hold the temperature, the solar heating system is turned off and the auxiliary is turned on [15].

3. Overall system

A number of runs are carried out in order to estimate the various factors affecting the performance of the system. All runs consider the presented building situated in two different climatic zones of Greece (representative weather data for Athens in climatic zone B and weather data for Thessaloniki in climatic zone C) [9]. The parameters considered are the following:

3.1. Sensitivity analysis of the collector slope angle

The solar heat gain from the system for various collector slope angles is shown in Fig. 4, Fig. 5. The optimum angles for Athens are: (i) 27.5◦ for the flat plate collector, (ii) 30◦ for the evacuated tube solar collector while for Thessaloniki are 27.5◦ for the flat plate collector, 29◦ for the evacuated tube solar collector.

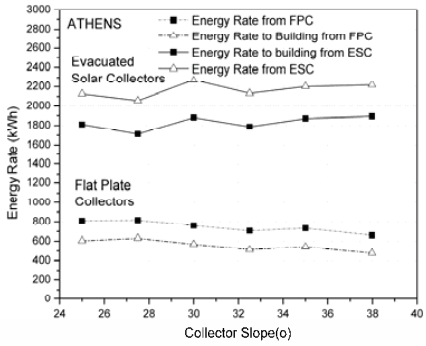

Fig. 4. Energy Rates for Flat Plate and Evacuated tube solar Collectors as a function of collector slope in Athens.

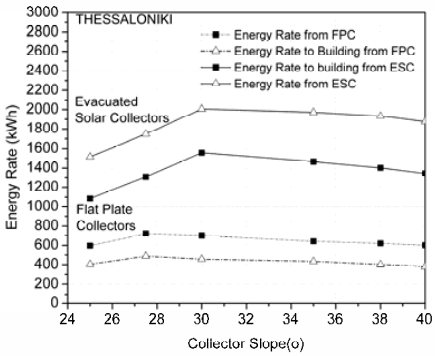

Fig. 5. Energy Rates for Flat Plate and Evacuated tube solar Collectors as a function of collector slope in Thessaloniki

The above two figures present the solar heat gained from two different solar collector types, flat plate collectors and evacuated solar collectors of mean yearly operating temperature of 48.8°C and 79.6°C respectively in Athens area (Climatic Zone B) and 44.3 °C and 73.2 °C in Thessaloniki area (Climatic Zone C).

3.2. Sensitivity analysis of the auxiliary heater thermostat setting

The auxiliary heater thermostat is used [16] in order to control the operation of the auxiliary heater, allowing it to operate only when the temperature of the fluid delivered to load is below an optimum value, which minimizes the required auxiliary heater input. The energy rate to and from the collectors versus the auxiliary heater thermostat setting is shown in Fig. 6.

It should be noted though that the collector heat gain diminishes with an increase in the thermostat setting, since fluid heated below this temperature is not utilized by the system.

The collector heat gain indicated in Fig. 6, shows that the heat obtained from the flat plate collectors is diminishing with a greater slope since this type of collector cannot operate with high efficiency at high temperatures.

The optimum range, taking into account yearly solar heat gains, of thermostat setting values is:

(i) 30÷33 ◦C for the flat plate
(ii) 33÷35 ◦C for the evacuated solar collector

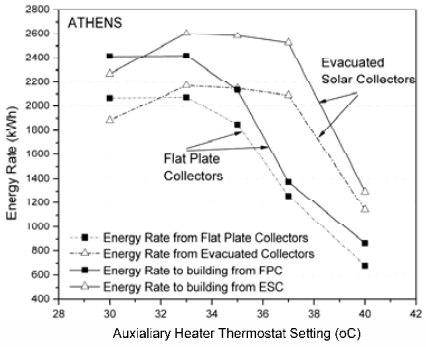

Fig. 6. Energy Rates for Flat Plate and Evacuated tube solar Collectors as a function of auxiliary heater thermostat setting (^{0}C).

3.3. Sensitivity analysis of the storage tank size

This parameter plays significant role in the sensitivity analysis of the system [17]. The auxiliary energy rate required by the system for different storage volumes is shown in Fig. 6. As it could be noticed, a smaller size tank results in less energy consumption by the auxiliary heater. The optimum size of the storage tank in Athens is: (i) 70 m^3 for the flat plate collector, (ii) 50 m^3 for the evacuated solar collectors.

Figure 7 also shows the effect of the storage tank size on the collector heat gain as well as on solar fraction for space heating.

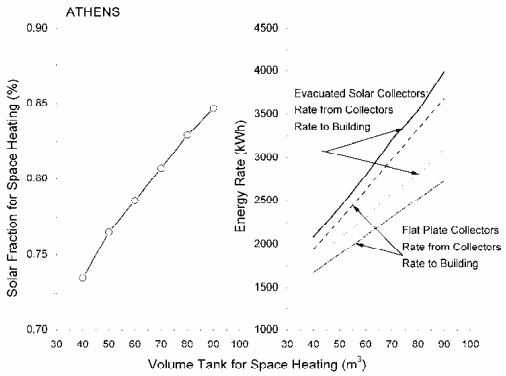

Fig. 7. Energy Rates for Flat Plate and Evacuated tube solar Collectors as a function of storage tank size – Solar fraction for evacuated tube solar collectors as a function of volume tank for space heating

3.4. Sensitivity analysis of the collector area

It is observed that when the collector area is increasing above a certain value, the collectors provide extra heat for the production of hot water [18,19].

Figure 8 gives the optimum collector area values for Athens which are 250 m^2 for flat plate collectors and 110 m^2 for evacuated tube solar collectors.

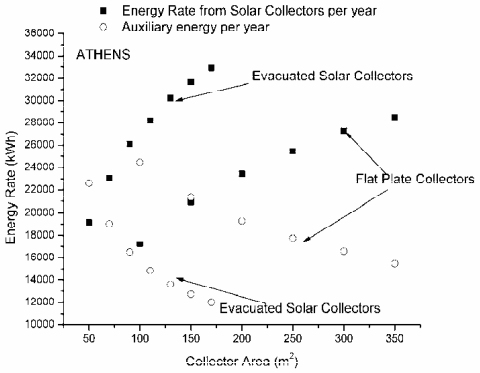

Fig. 8. Energy Rates for Flat Plate and Evacuated tube solar Collectors as a function of collector area.

4. System optimum performance

The solar fraction for space heating of the final system obtained from the sensitivity analysis study are presented in Fig.9.

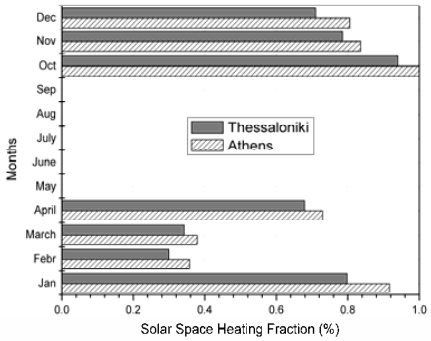

Fig. 9. Solar Fraction for space heating in Athens and Thessaloniki.

The heating load of the building reaches a maximum monthly value of 21405 kWh (in January) for Athens and 28906 kWh for Thessaloniki.

The maximum monthly load supplied by the solar system is 3287 kWh (in April). It should be pointed out that the solar system covers first the domestic hot water needs of the building.

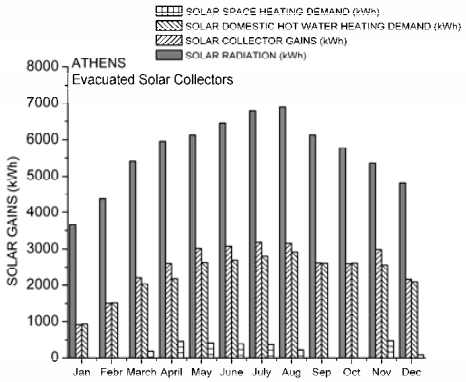

Fig. 10. Annual Solar Collector Gains as well as Space Heating Demand and Domestic Hot Water Heating Demand covered by ESC in Athens.

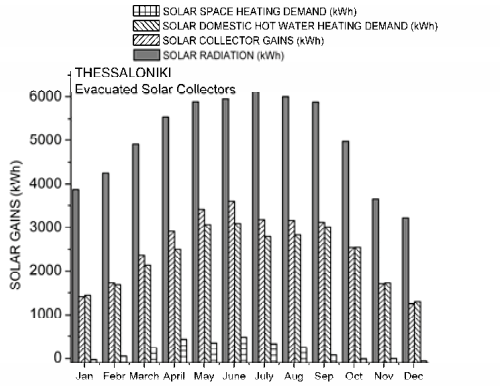

Fig. 11. Annual Solar Collector Gains as well as Space Heating Demand and Domestic Hot Water Heating Demand covered by ESC in Thessaloniki .

5. Conclusions

The aim of the current work was to present a method of utilizing solar energy for space heating in combination with underfloor heating of a six storey terraced building in Greece. The system is modeled with the TRNSYS program and the results show that solar collectors could be combined with underfloor heating systems giving remarkable solar fraction.

The final optimum system as obtained from the complete system simulations, consists of 110 m^2 evacuated tube collector tilted at 30° from horizontal and a 70 m^3 hot water storage tank for Athens (Climatic Zone B) and 130 m^2 evacuated tube collector tilted at 29.5° from horizontal and a 90 m^3 hot water storage tank for Thessaloniki (Climatic Zone C).

Runs of the TRNSYS program for the optimum system have shown that the annual space heating load of 46267 kWh in Athens is covered with a total supply of 45392 kWh of boiler heat (94%) and 2874.27 kWh of solar heat (6%) while the annual domestic hot water heating demand of 40783 kWh is covered with a total supply of 28131 kWh of solar heat (68.97%) and 12651.2 kWh (31.03%) of boiler heat.

The optimum system in Thessaloniki have shown that the annual space heating load of 106497 kWh is covered with a total supply of 102631 kWh of boiler heat (96%) and 3866.93 kWh of solar heat (4%) while the annual domestic hot water heating

demand of 40783 kWh is covered with a total supply of 27612.92 kWh of solar heat (67.7%) and 13169.76 kWh (32.3%) of boiler heat.

Judging from the findings above, it is assumed that similar results could be obtained from countries with high solar availability. However, before any decision is taken, on which type of solar system should be installed, the system needs to be analyzed with the suggested procedure.

Nomenclature

SSH Solar space heating system

SDHW Solar domestic hot water system

References

[1] Harvey D. L.D., 2006, *A handbook on Low-Energy Buildings and District Energy Systems – Fundamentals Techniques and Examples*, Earthscan.

[2] Kaldellis J.K., El-Samani K., Koronakis P., 2005, Feasibility analysis of domestic solar water heating systems in Greece, Renewable Energy, Vol.30, Issue 5, pp. 659-682.

[3] Henning H.M., Wiemken E., 2005, Decision scheme for the selection of the type of solar assisted air-conditioning system for a given load, *Proc. of International Conference Solar Air Conditioning*, pp. 231-235.

[4] Mahler B., 2005, Sensitivity analysis of Central Solar Heating Systems with Long Term Storage, *Proc. of Second European Solar Energy Conference - ESTEC*, pp.217-222.

[5] Athienitis A.K., Chen Y., 2000, The effect of solar radiation on dynamic thermal performance of floor heating systems., Solar Energy, 69(3), pp.229-237.

[6] Alkhalaileh M.T., Atieh K.A., Nasser N.G., Jubran BA., 1999, Modeling and simulation of solar pond floor heating system. Renewable Energy, 18(1, 2), pp.1-4.

[7] Zhai X.Q., Yang J.R., Wang R.Z., 2009, Design and performance of the solar-powered floor heating system in a green building, Renewable Energy, 34, pp.1700-1708

[8] Ho S.Y., Hayes R.E., Wood R.K., 1995, Simulation of the dynamic behaviour of a hydronic floor heating system. Heat Recovery Systems, 15(6), pp.505-519.

[9] Moustris K., Paliatsos A.G., Bloutsos A., Nikolaidis K., Koronaki I., Kavadias K., 2008, Use of neural networks for the creation of hourly global and diffuse solar irradiance data at representative locations in Greece, Renewable Energy, Vol.33, Issue 5, pp.928-932.

[10] Greek Presidential Degree: On the approval of thermal insulation for buildings. The Government Gazette, Issue 4, No. 362, 4/7/1979.

[11] Argiriou A.A., Balaras C.A., Kontoyiannidis S., Michel E., 2005, Numerical simulation and performance assessment of a low capacity solar assisted absorption heat pump coupled with a sub-floor system, Solar Energy, 79, pp. 290–301.

[12] Klein S.A. et al., TRNSYS Version. 16, Solar Energy Laboratory, University of Wisconsin-Madison (2004).

[13] ASHRAE (2005), *ASHRAE Handbook, Fundamentals*, Atlanta, GA.

[14] Duffie JA, Beckman WA., 2004, *Solar engineering of thermal processes*, John Wiley & Sons.

[15] Rekstad J., Meir M., Kristoffersen A.R., 2003, Control and energy metering in low temperature heating systems, Energy and Buildings, 35, pp.281–291.

[16] Alhamis A.I. and Sherif S. A., 1997, Feasibility study of a solar – assisted heating/cooling system for an aquatic centre in hot and humid climates, International Journal of Energy Research, Vol. 21, pp. 823-839.

[17] Wang L., Gwilliam J., Jones P., 2009, Case study of zero energy house design in UK, Energy and Buildings, 41, pp. 1215–1222.

[18] Tsilingiris P.T. and Machias A. V., 1990, Computer Simulation Calculations for estimation of the energy conservation in solar heated buildings, International Journal of Energy Research, Vol.14, pp.141-151.

[19] Ward, D. S. and Lof, G. O., 1975, Design and construction of a residential solar heating and cooling system, Solar Energy, 17(2), pp. 13-20.

[20] http://sel.me.wisc.edu/trnsys

Experimentals and Numerical Results of a Solar Sorption Refrigerator with Indirect Heating

Maria Eugênia Vieira da Silva[a], Maria Elieneide Araújo[a], Kaio Hemerson Dutra[a], and Erilson de Sousa Barbosa[a]

[a]*Laboratório de Energia Solar e Gás Natural - Bloco 718 Campus do Pici DEMP/CT/ UFC 60.455-760 Fortaleza-CE Tel.(85)33669641 Fax.(85)33669640 eugenia@sol.les.ufc.br*

Abstract: The development of new equipments that operate in sorption cycles is an alternative to conventional refrigeration systems because of the substitution of electrical energy by thermal energy. This paper presents the experimental and numerical results of a new sorption refrigerator operating with a solar flat plate collector. The pair silica RD-water was used as the sorption materials and the sorption bed was indirectly heated. The refrigerator has three components: an adsorber, a condenser, and an evaporator, which are connected by flexible, vacuum resistant piping. The adsorber was designed to allow both cooling and heating, without the need of an additional heat exchanger. In the heating phase, a flow of thermal oil is heated in the collector and moves to the adsorber to heat the silica bed. In the cooling phase, the adsorber is cooled in direct contact with ambient air. The experimental results validate the operation of the refrigerator: temperatures in the adsorber bed around 80ºC during the heating phase; and temperatures of 4.4ºC in the evaporator during the cooling phase. The COP value, defined as the ratio between the cooling effect and the amount of energy transferred to the absorber, was 0.12.

Keywords: Adsorption, Refrigerator, Solar Energy.

1. Introduction

Refrigeration and air conditioning are important areas in engineering and play an important role in energy consumption. According to the IRR [1], these systems are responsible for 15% of the world energy demand. The development of new alternatives to power refrigeration systems can contribute to decrease the impact cause by vapor compression systems. These impacts are the level of harmful gases (CFC, CHFC and HFC) and the consumption of treated water.

The use of sorption processes in refrigeration is a somewhat new concept and the technology is a scientific area to be explored. Its development can create a sustainable refrigeration industry.

To power vapor compression refrigeration systems, other forms of energy, including thermal energy, are transformed into electrical energy. In sorption cycles, the direct use of thermal energy can make them more energy efficient. Other advantages are the use of stationary parts and the lower operation and maintenance costs.

Areas with high intensity of solar radiation can use this energy in refrigeration without auxiliary heat storage systems, because the peak of the demand for refrigeration occurs at the same daytime as the peak of solar radiation.

The improvement of the sorption refrigeration cycle is associated with the enhancement of the refrigeration cycle and with the development of new materials. These two factors influence the technical and economical viability of new systems and can make them more competitive with vapor compression systems.

In the 1970s and 1980s, solar systems for air conditioning were studied and the results were presented in the literature. Among the interesting studies published are those presented in [2-4] and in [5-7]. This last author used flat plate solar collector to heat up zeolites. More recently, adsorption solar refrigeration has received more attention and some research results are presented in [8-11].

To study the experimental performance of the new sorption refrigeration with indirect solar heating, a prototype was built [12] and the results are presented in this paper. The important characteristic of this prototype was the indirect heating of the sorption material bed. Except for the solar collector, all components can be installed indoors.

Corresponding Author: Maria Eugênia Vieira da Silva, Email: eugenia@ufc.br

Because of its operation in the cooling and in the heating cycles, the adsorber was designed to have good heat dissipation in the cooling phase and good heat storage in the heating phase. It consisted of a two layer heat exchange. The lower layer was filled with the adsorbent material, forming the adsorption bed. In this bed, there was a coil connected to the solar collector that allowed the flow of the thermal oil. The bed was indirectly heated up during the hours of solar radiation. The adsorber was cooled in contact with the environment by transfering heat from the adsorbent bed to the ambient air through the walls. In the upper layer, the water vapor could freely flow, after being released from the bed.

The sorption pair used was silica gel RD (adsorbent) and water (adsorbat). The adsorbent characteristics were: higher selective capacity for water than other types of silica, low isosteric enthalpy, environmental friendliness, and lower desorption temperature that allowed the use of solar flat plat collector as the heat source.

To properly run the sorption refrigerator, resistant connections and accessories were necessary to guarantee the vacuum in the system, to avoid leakage and undesired gas that could reduce its performance or even stop its operation completely.

To determine the performance of the refrigerator using the experimental data, it was necessary to develop a correlation for the masses adsorbed and desorbed as a function of the pressure and temperature in the adsorber. This correlation was developed using the sorption data presented by [13] Chua *et al*. and a statistical analysis package called SAS (Statistical Analyses Software). For the non-linear regression, the Levenberg-Marquadrat algorithm [14,15] was used.

The refrigerator components were manufactured and tested at the solar laboratory, located in Fortaleza, Brazil (3º35´S and 38º45´W).

2. Theoretical Refrigeration Sorption Cycle

The theoretical refrigeration sorption cycle runs in an intermittent regime in two phases: the heating phase with heating, desorption and condensation processes; and the cooling phase with cooling, adsorption and evaporation processes. These processes are presented in a Clapeyron diagram, as in Fig. 1, where the tilted lines indicate the isosteric heating and cooling.

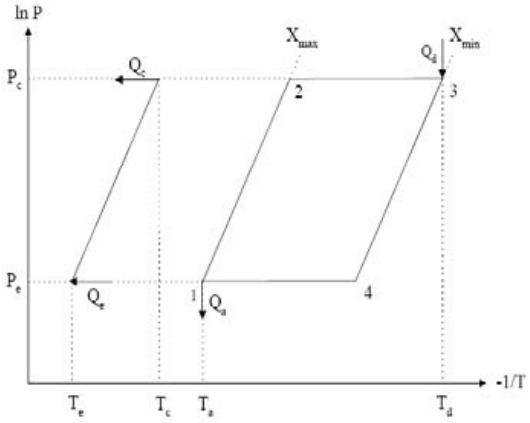

Fig. 1. Refrigeration sorption cycle in a Clapeyron Diagram

2.1. Isosteric heating

The cycle starts when the adsorbent is at low temperature T_a , and low pressure P_a , point (1). The amount of adsorbed mass depends on the values of these properties. The adsorbent is heated (from 1 to 2), isosterically, up to the desorption pressure, P_d .

2.2. Heating at Constant pressure - desorption

The continuous heating of the sorption material in the adsorber (from 2 to 3) at constant pressure causes the desorption of the adsorbat in the form of vapor, which flows to the condenser. When the adsorbat reaches the maximum temperature, the desorption process ceases.

2.3. Isosteric cooling

The liquid adsorbat in the condenser flows to the evaporator and, as the adsorber is cooled by an external medium reducing its temperature (from 3 to 4), a decrease in pressure in the circuit also occurs.

2.4. Constant pressure cooling - adsorption

In the next phase of the cycle, cooling takes place at constant pressure and the adsorption and evaporation processes occur as the adsorbent is cooled (from 4 to 1). Because the removal of heat in the evaporator occurs only during this period and not throughout the complete cycle, the mode of operation of the refrigeration cycle is intermittent.

2.5 Start of operation – heating phase

Solar radiation incident on the solar collector absorber plate heats up the thermal oil flux that flows through the absorber plate of the collector. This heated oil flux circulates by natural convection through the components, flowing from the collector to the adsorber to heat the sorption material bed. The energy not used in this heating process is either lost to the ambient or stored in the components and piping masses.

3. The Experimental Prototype

The components of the sorption refrigerator are: an adsorber, an evaporator, a condenser, and a high temperature solar collector. There are also control valves and connecting pipes.

The adsorber was installed at the highest position of the system. In the schematic in Fig. 2, all components and sensors are shown. The thermocouples were glued to the outside walls of the components and piping, except for the adsorber. A thermocouple was inserted inside the silica RD and an electric passing element was used. The pressure sensor was installed between the evaporator and the condenser.

3.1 Operation

Before the refrigerator was started, the system was evacuated by a vacuum pump connected in valve V1. This operation was necessary to remove undesired gases (air) from the system. When a value of about 3.10^{-2}mBar was reached, V1 was closed and the pump was disconnected from the system.

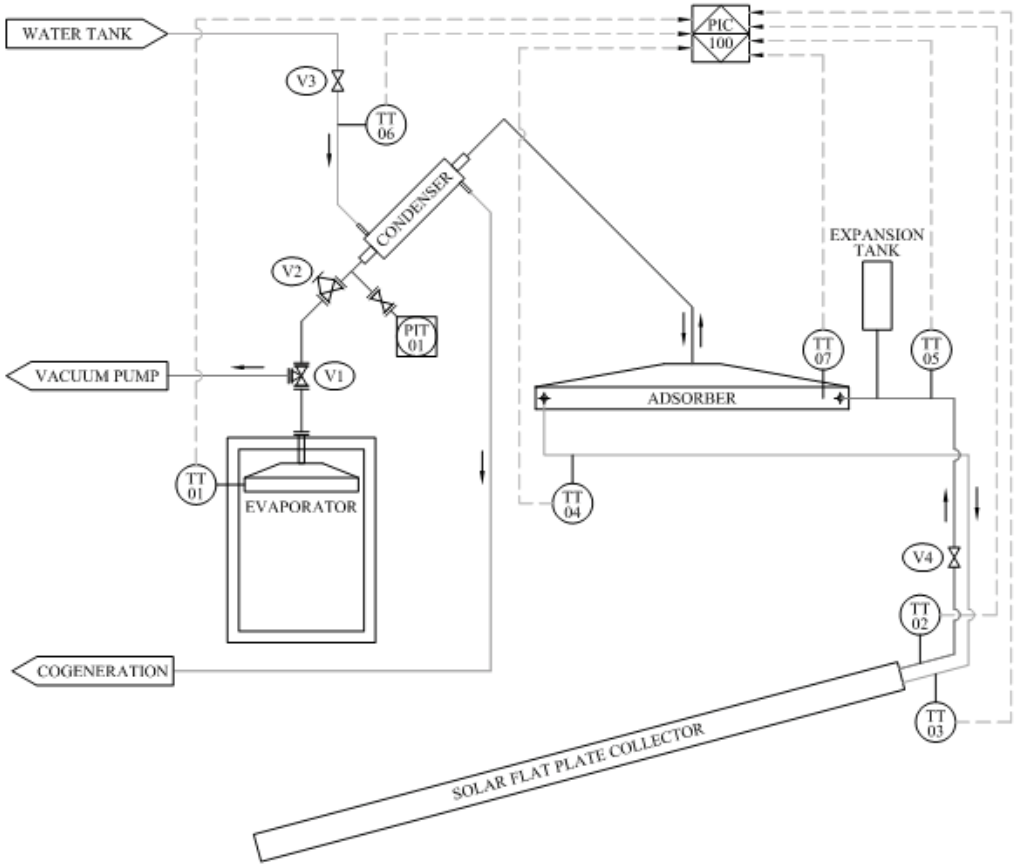

TT – temperature transmitter, PIT – pressure indicator and transmitter, PIC – data logger, V – valve

Fig. 2. Schematic drawing of the adsorption refrigerator with indirect heating by solar flat plate collector

The next step was to fill the evaporator with water, also using valve V1 and a calibrated container. Then, valve V2 was opened and the first adsorption process occurred, as part of the water vaporized and was adsorbed by the silica RD bed. At the end of this process, valve V2 was closed and part of the water that did not become vapor (remained in the evaporator) was cooled down. This cold water could be used in refrigeration and air conditioning applications.

The second phase of the refrigeration cycle started with the indirect heat transfer from the solar collector to the adsorbent bed. The thermal oil flux from the collector transferred heat to the adsorber, supplying the necessary energy for the water molecules, adsorbed in the previous phase, to be released. Valve V2 was kept closed until the released water vapor condensed in contact with a counter flow water flux in the condenser. After this process, valve V2 was opened to allow the return of the water to the evaporator, completing the refrigeration cycle.

During the heating phase, the adsorber was wrapped in an isolating cover to reduce heat losses to the ambient. This cover was removed during the cooling phase to allow the direct heat transfer from the adsorber to the ambient air.

Figure 3 shows a photograph of the sorption refrigerator prototype.

Fig. 3. Photograph of the refrigerator prototype

3.2. Adsorber

The adsorber is the most important component of the sorption refrigerator, and it is responsible for the adsorption and desorption processes, that is, to imprison and to set free the refrigerant fluid molecules in the cavitities of the sorption material.

The adsorber has parallel plane geometry at the bottom and a trapezoidal shape on the upper part to facilitate the flow of the fluid refrigerant from and to the evaporator. The bottom plane sheets were horizontally displayed, forming two spaces separated by a screen. The lower chamber was filled with the sorption material, silica gel type RD. In this material, there was a coil connected to the solar collector, through which a flow of thermal siphon oil was used to heat up the sorption material (indirect heating). As the sorption bet was heated to the desorption temperature for the associated pressure, the refrigerant fluid (adsorbate) was released from the solid material and flew, in the gaseous phase, through the screen to the upper chamber and to the evaporator.

3.3. Evaporator

The evaporator is the component responsible for the useful energy, that is, the cooling effect to be used in refrigeration and in air conditioning.

The evaporator has the geometry of a pyramid, with a square base, to obtain a larger superficial contact area, to increase the transfer rates and the flash effect.

3.4. Condenser

The condenser is a double stainless steel pipe heat exchanger to promote de phase change from gaseous to liquid (condensation) of the refrigerant fluid. The cooling medium was water, which flew in counter-current with the refrigerant fluid.

4. Measurements and data acquisition system

A data acquisition system with its sensors was installed to measure solar radiation intensity over the solar collector, pressure, and temperature in various points of the refrigerator, as shown in Fig. 2.

- Type K thermocouples (nickel-chromium) with an operating rage between -270°C and 1.372°C, and an analogical output between 6.458mV and 54.886mV were used to measure temperature.

- The pressure sensor had an operating range between 10^{-4}mBar and 10^{3}mBar, an analogical output between 0 and 10 V, with precision on 1 (one) decimal point.
- The data logger had 16 freely configurable and analogic channels.

4.1 Measured variables

The measured variables were:

- Temperature - thermocouples were installed in the adsorber (sorption material bed), on the evaporator walls, on the inlet and outlet pipe walls of the components: adsorber, condenser and solar collector.
- Pressure - a pressure sensor was installed in the piping connecting the adsorber to the evaporator, with a shut off valve installed between these components.
- Radiation - a precision pyranometer for global radiation was installed on the tilled collector plane.

All sensors were directly connected to the data logger and scanned in 2 second intervals. Mean values were stores at each minute.

5. Analytical Analysis

5.1. Energy and Mass Balance Equations

The heat and mass balance equations that characterize the performance of the components and which were used to determine the refrigerator coefficient of performance are presents in this section.

Solar energy incident on the collector was used to heat the thermal oil flow that circulated in natural convection between the collector and the adsorber. The thermal efficient curve of the solar collector was experimental determined in a test bench design according the European norm (ISO 9806), installed at the laboratory. Using the collector curve and the necessary weather data, the average efficiency value at temperatures around 140°C was 0.40.

The refrigeration effect was determined by the cooling produced in the evaporator. This cooling was sensed in the water mass in the evaporator, as well as in the metallic mass (evaporator stainless steel walls). The net cooling, in the water mass, was calculated by,

$$Q_{ev} = m_{w,ev} c_p \Delta T \qquad (1)$$

where $m_{w,ev}$ is the mass in the evaporator, c_p is the specific heat at constant pressure, and ΔT is the temperature difference in the water between the start and the end of the cooling process. With a similar equation, the cooling in the evaporator metallic walls, Q_{mw} , could be calculated substituting the mass of water and its specific heat at constant pressure by the metallic wall mass and stainless steel specific heat.

5.2. Coefficient of Performance

The coefficient of performance, COP, was determined as the ratio between the desired cooling effect and the total amount of energy given to the refrigerator.

The energy transferred to the refrigerator was the incident solar radiation on the tilted collector, Q_s which can be estimated as the total radiation incident on the absorber plate,

$$Q_s = A_c \eta \int_{t_1}^{t_2} S dt \qquad (2)$$

where t_1 and t_2 represent the time of sunrise and sunset on the tilted collector.

The coefficient of performance calculated using only the net cooling effect was determined as,

$$COP = \frac{Q_{ev}}{Q_s} \qquad (3)$$

and the actual cooling effect of the refrigerator, COP' , which represents all cooling of the refrigerator, could be calculated as,

$$COP' = \frac{Q_{ev} + \int \dot{Q}_{mw} dt + \int \dot{Q}_{ea} dt}{Q_s} \qquad (4)$$

where $\dot{Q}_{ea}$ represent the cooling losses from the evaporator walls to the ambient.

The mass adsorbed/desorbed in the cycle was indirectly determined from measurements of pressure and temperature in the adsorber. A correlation for the fractional filling of the adsorbent porous was developed. This correlation is presented in the Appendix. With this correlation and a numerical FORTRAN program, the amount of water in the silica RD bed was calculated at each datum point.

6. Results

When the refrigerator was in operation, the data acquisition system was scanning the sensors and storing the average values. Measurements for two consecutive cycles are presented in figures 4 and 5.

6.1. Heating Phase

The measure data in Fig.4 show the thermal oil temperature at the inlet and outlet of the solar collector, the temperature inside the adsorber (adsorbent bed), and the global solar radiation.

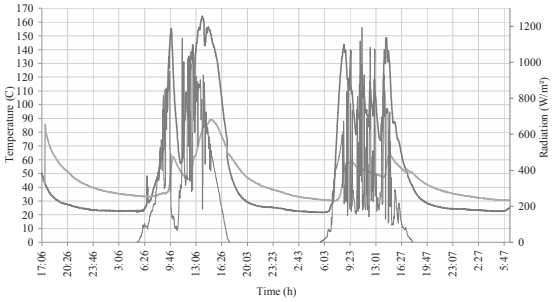

Fig. 4. Temperature and global radiation measurements during two consecutive heating phases.

These measurements show temperatures above 140°C in the collector outlet and above 80°C in the adsorber bed. These values were sufficient for the dessorption process at the adsorber pressure. During the two cycles, the average global radiation was 393 W/m², a low value, but the heat transfer processes proved to be good enough to guarantee the operation of the refrigerator.

6.2. Cooling Phase

The values measured during the cooling phases are presented in Fig.5. In the first cycle, the temperature in the evaporator was 4.4 °C and in the second cycle, this value was 9.4°C. It was concluded that, because of the low radiation level and consequently, a partial desorption process, the adsorption process could not be completed.

The real temperatures in the adsorption process were lower than the measured values, because the thermocouples were glued at the outside wall of the evaporator. Both the adsorbat mass and the metallic walls were cooled together. There were some conduction losses through the walls.

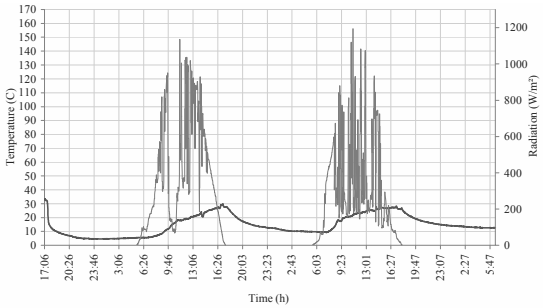

Fig. 5. Temperature measurements during two consecutive cooling phases.

6.3. Coefficients of Performance

The coefficient of performance in the heating phase was calculated as the ratio between the energy used in the desorption process in the period of 7:20h to 14:40h and the solar energy transferred to the adsorber in the same period. The desorption energy was estimated as the product of the mass desorbed, calculated using (A.1), and the desorption heat. The solar energy transferred to the adsorber was estimated using (2). The value for the COP in this phase was 0.20.

The coefficient of performance in the cooling phase was calculated using (4). The adsorption energy was estimated as the energy used to adsorb the mass of adsorbat in the period of 19:25h to 7:30h, divided by the incident solar radiation. This COP value was 0.12 and it represents the performance of the refrigerator.

7. Conclusions

Two complete cycles of the new solar sorption refrigerator with indirect cooling were presented in this paper. These results validate the operation of the refrigerator and the measurements allowed the calculation of its coefficient of performance.

In the heating phase, a COP value of 0.20 was found, even though the average intensity of the solar radiation was only 393 W/m². The overall COP was 0.12. Higher values can be reached with higher solar radiation intensities. When this value is low, the desorption process occurs, but incompletely. Energy is used the heat up the adsorbent bed, but the desorption temperature is not uniformly reached, decreasing the amount of the adsorbat released.

Nomenclature

A	area
c	specific heat, J/(kg ºC)
COP	coefficient of performance
H	adsorption isosteric enthalpy, J/kg
h	heat transfer coefficient, W/(m^2 K)
m	mass flow rate, kg/s
q	adsorbed quantity of adsorbate by the adsorbent under equilibrium conditions, kg/kg
P	pressure, Pa
Q	heat, J
R	gas universal constant, J/(kg K)
S	solar radiation flux, W/m²
T	temperature, °C
t	time, s

Greek symbols

η	efficiency
θ	porous fractional filling

Subscripts and superscripts

a	adsorption / ambient
c	condensation / collector
d	desorption
e	evaporation
ev	evaporator
m	monolayer capacity
mw	metal wall
s	surface
w	water

References

[1] IRR Guides (IIF-IIR, France), 2003, Saving Energy in Refrigeration, Air Conditioning and Heat Pump Technology. SAV-2-IIF-IIR.

[2] Löf, G.O. G., Lenz, T. G., Rao, S. 1982, Solar Refrigeration of Lithium Chloride Solutions in Open Cycle Absorption Cooling, ASME, 82-WA/Sol-6.

[3] Löf, G.O. G., Westhoff, M. A., Karaki, S, 1984, Performance Evaluation of an Active Solar Cooling System Utilizing low Cost Plastic Collectors and an Evaporatively-Cooled Absorption Chiller, SAN-30569-30.

[4] Löf, G.O. G., Cler, G. and Brisbane, T., 1988, Performance of a Solar Cooling J Solar Energy Engng 111, pp. 165-171.

[5] Tchernev, D. I., 1978, Solar Energy Applications of Natural Zeolites, zeolites 76, Arizona, pp.479-488.

[6] Tchernev, D. I., 1979, Solar Refrigeration Utilizing Zeolites. In Proceedings of the 14th International Energy Conversion Engineering Conference, Vol. 2, pp. 2070-2073.

[7] Tchernev. D. I., 1988, Closed cycle zeolite regenerative heat pump. Heat Transfer Enhancement and Energy Conservation. Hemisphere Publ. Co., pp.747-755.

[8] Pons, M., 1997, Analysis of the Adsorption Cycles with Thermal Regeneration Based on the Entropic Mean Temperatures, Elsevier Science Ltd, Applied Thermal Engineering Vol. 17, No. 7, pp. 615-627, France.

[9] Vasiliev, L. L.; et al., 2001, Solar-Gas Solid Sorption Refrigerator, Kluwer Academic Publishers, Adsorption 7, pp. 149 – 161, Netherlands.

[10] Restuccia, G.; et al, 199, Performance of Sorption Systems using New Selective Water Sorbents, ISHPC ’99, pp. 219-223.

[11] Wang, R. Z., 2000, An Energy Efficient Hybrid System of Solar Powered Water Heater and Adsorption Ice Maker, Solar Energy Science Ltd, vol. 68, pp. 189-195.

[12] Araújo, M. E, 2009, Validação Experimental de um Resfriador de Água operando em Ciclo de Adsorção com Aquecimento Solar Indireto, MsC. Dissertação, Universidade Federal do Ceará, Brasil.

[13] Chua, H. T; NG, K. C; Charkraborty, A; OO, N. M; Othman, M. A, 2002; Adsorption Characteristics of Silica Gel + Water Systems. J. Chem Eng. Data, 47, pp. 1177-1181.

[14] Levenberg, K., 1944, A Method for the Solution of Certain Non-linear Problems in Least Squares. Quarterly of Applied Mathematics, 2(2):164-168.

[15] Marquardt, D. W., 1963, *An Algorithm for the Least-Squares Estimation of Nonlinear Parameters*, SIAM Journal of Applied Mathematics, 11(2):431-441.

Acknowledgments: The authors would like to thank the Conselho Nacional de Desenvolvimento

Científico e Tecnológico [CNPq] for the financial support of the Project and the institutions Coordenação de Aperfeiçoamento de Pessoal de Nível Superior [CAPES] and Fundação Cearense de Apoio ao Desenvolvimento Científico e Tecnológico [FUNCAP] for a master´s degree fellowship.

Appendix

This section presents the correlation developed for the fractional filling of the adsorbent porous as a function of pressure and temperature. Using the isotherm sorption data from Chua *et al.* [3] and a nonlinear regression algorithm, the expression for the fractional filling of the adsorbent porous, θ, was developed as,

$$\theta = q \,/ q_m \Rightarrow q \,/ q_m = Ae^{(\Delta H / RT)} P^B \qquad \text{(A.1)}$$

where A and B were the constants determined. This equation was used to calculate the adsorbed and desorbed masses during the cooling and heating phases.

A Mesoscale Power Cycle Based on Classical Thermosize Effects

Gulru Babac and Altug Sisman

Energy Institute, Istanbul Technical University, Istanbul, Turkey

Abstract: Due to different transport regimes of gases confined in macro and nano domains, a chemical potential difference is induced between macro and nano structures under the same temperature gradient. This chemical potential difference can drive a gas flow and produce work. Isothermal gas flow under a chemical potential difference causes heat exchange between working gas and its environment. These effects are similar to thermoelectric effects and called here classical thermosize effects. In this paper, classical thermosize effects are discussed and mesoscale thermodynamic power cycles based on thermosize effects can be constructed. Heat, work and efficiency expressions are derived for thermodynamic analysis of this novel cycle. Variations of specific net work output and efficiency versus temperature ratio for different compression ratio are examined. Results constitute an elementary base for a possible construction of micro/nano heat engines based on thermosize effects.

Keywords: Classical Thermosize Power Cycles, Micro/Nano Heat Engines, Thermosize Effects.

1. Introduction

The flow characteristics in a system strongly depend on the domain sizes and therefore they are different at the macro and nano scales. In order to determine the flow characteristics, Knudsen number (l/L) which is the ratio of mean free path of particles (l) to the characteristic length (L) of the domain is commonly used. According to magnitude of the Knudsen number, flow regime is generally classified as continuum (or hydrodynamic) $\left(Kn < 10^{-3}\right)$, slip flow $\left(10^{-3} < Kn < 10^{-1}\right)$, transition $\left(10^{-1} < Kn < 10\right)$ and free molecular flow $\left(Kn > 10\right)$ [1].

In this study, ideal Maxwellian gas confined in a rectangular box is considered. The box is divided as macro and nano parts and temperature gradient is applied. Applied temperature gradient causes diffusion of gas particles from hot side to cold side and different transport regimes are induced in each part because of the size difference. Flow regime is dominated by particle-wall collisions $\left(Kn > 10\right)$ in the nano part while it is dominated by particle-particle collisions $\left(Kn < 10^{-3}\right)$ in the macro part and they are called as free molecular and continuum (or hydrodynamic) flow, respectively. These differences in flow regimes causes different chemical potential gradient in the macro and nano parts although they are under the same temperature gradient. Therefore, chemical potential difference is induced by a temperature gradient because of the size difference. This effect is very similar to the Seebeck effect in thermoelectric phenomena which is the electrical potential gradient induced by temperature gradient in a conductor. If it is allowed to gas flow between the regions having the same temperature but different chemical potentials, heat exchange between gas and environment is observed during the gas flow. This is also similar to the Peltier effect of thermoelectricity. Consequently, there is a strong analogy between these effects and the effects of thermoelectricity. The thermoelectric effects arise when the materials having different electrical properties are used together under the same temperature gradient. On the other hand, thermosize effects arise when the materials having different size are used together under the same temperature gradient. Therefore, these effects are called here classical thermosize effects (CTSE) to distinguished them from the thermosize effects (TSE) which have been firstly introduced by considering the wave character of particles (or quantum size effects) in literature [2]. To refer the quantum originated TSE, they are called here quantum thermosize effects (QTSE). CTSE are the dominant effects while QTSE are the tiny corrections on CTSE due to the wave character of particles.

Some thermodynamic cycles based on QTSE have been analyzed in literature [3, 4]. A basic power cycle based on CTSE has also been introduced recently [5]. The main purpose of this study is to consider some different modifications on the cycle to improve the efficiency and the net work output of the basic thermosize power cycle defined in [5].

Corresponding Author: Altug Sisman, Email: sismanal@itu.edu.tr

Advances in micro/nano fabrication technology may be allowed us to design and manufacture the nano scaled heat engines in the near future [6-8].

2. Classical thermosize effects

Monatomic ideal gases confined in a rectangular box are considered. The box is separated in macro and nano parts and thermally in contact with high (T_H) and low (T_L) temperature reservoirs, Fig. 1. At low temperature side, there is no separator and gas can flow between point 2 and point 3 whereas it is not allowed at high temperature side. Therefore, net particle flux is equal to zero in steady state. In the macro part, characteristic flow length is much bigger than the mean free path of particles and hydrodynamic regime determines the gas properties under temperature gradient. Process from 1 to 2 can be analyzed by using Navier-Stokes equation and for zero net particle flux condition it can be defined as a constant pressure process $\left(\nabla p = 0\right)$. On the other hand, characteristic flow length is much smaller than the mean free path of particles in the nano part. The continuum approach is break down and gas properties in this domain are determined by the free molecular flow regime. For zero net particle flux, the constant quantity is defined by Knudsen law [8]

$$\frac{P_{hot}}{\sqrt{T_{hot}}} = \frac{P_{cold}}{\sqrt{T_{cold}}} . \tag{1}$$

Therefore, 3-4 process is determined as $\nabla\left(p/\sqrt{T}\right) = 0$. This process may be called Knudsen process since (1) is called Knudsen law.

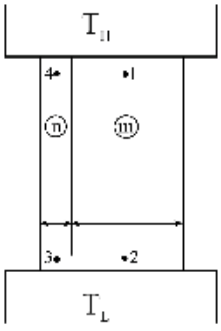

Fig. 1. Schematic view of a possible device based on classical thermosize effects. n and m indicate nano and macro parts respectively. T_L and T_H represent low and high temperature reservoirs.

Consequently the different transport regimes between the macro and nano parts, $\nabla p = 0$ and $\nabla\left(p/\sqrt{T}\right) = 0$ respectively, cause different chemical potential gradients under the same temperature gradient. This difference can be calculated from the chemical potential of a monatomic ideal gas given by [9]

$$\mu = -kT \ln\left(\frac{CT^{3/2}}{n}\right), \tag{2}$$

where T is temperature, k is the Boltzmann's constant, n is particle density, C is a constant given by $C = \left(2\pi mk\right)^{3/2}/h^3$, m is the atomic mass and h is the Planck's constant.

By using of the ideal gas equation of state, $p = nkT$, in the conditions of $\nabla p = 0$ and $\nabla\left(p/\sqrt{T}\right) = 0$, density variations in the macro and nano parts can be obtained in terms of n_2 and T_L as follows respectively,

$$n_m(T) = n_2 T_L/T , \tag{3}$$

$$n_n(T) = n_2\left(T_L/T\right)^{1/2} . \tag{4}$$

It should be noted that $n_2 = n_3$ due to the equality of temperatures $\left(T_2 = T_3 = T_L\right)$ and chemical potentials $\left(\mu_2 = \mu_3\right)$ at low temperature side. Therefore, net chemical potential difference, $\Delta\mu = \mu_4 - \mu_1$, is determined by using (2)-(4) as

$$\Delta\mu = \mu_4 - \mu_1 = -\frac{k}{2} T_H \ln(\tau), \tag{5}$$

where τ is the temperature ratio defined by $\tau = T_L/T_H$. This chemical potential difference can drive a gas flow if the disconnected parts at high temperature side are connected to each other. Consequently, temperature gradient and size difference by acting together create a driving force causing gas flow from region 1 to region 4. Therefore, a gas circulation which is able to produce work begins between the domains. It constitutes a thermodynamic gas power cycle which is based on the classical thermosize effects. A basic classical thermosize power cycle has been examined in [5]. It provides a reference cycle for a comparison of the improved version of the classical thermosize power cycle considered here.

3. The Basic classical thermosize power cycle

The basic thermodynamic power cycle given in Fig. 2, consists of two isothermal, one isobaric and one Knudsen processes.

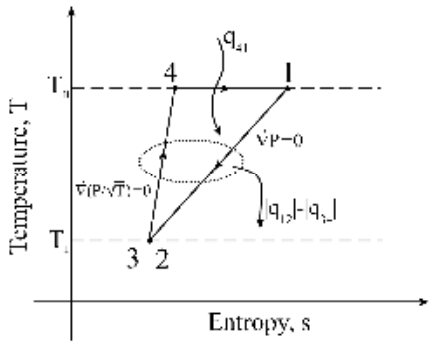

Fig. 2. T-s diagram of a basic classical thermo-size power cycle.

In order to examine the cycle, expressions of heat and work exchange should be derived for each process.

Isothermal heat exchange per transferred particle can be calculated as

$$q_{41} = \int_4^1 Tds = T_H\left(s_1 - s_4\right). \tag{6}$$

For an ideal Maxwell gas, the relation between entropy per particle and chemical potential is given by

$$s = \frac{5}{2}k - \frac{\mu}{T}. \tag{7}$$

By using (2), (6) and (7), q_{41} is obtained as,

$$q_{41} = \int_4^1 Tds = T_H\left(s_1 - s_4\right) = \left(\mu_4 - \mu_1\right) = -\frac{k}{2}T_H \ln(\tau). \tag{8}$$

In the cold side, points 2 and 3 have the same thermodynamic properties due to the equilibrium condition. Therefore,

$$q_{23} = 0. \tag{9}$$

Heat exchange for the processes (1-2) and (3-4) can be calculated from the following integrals by using (2)-(4) and (7),

$$q_{12} = \int_1^2 Tds = -\int_{T_H}^{T_L} Td\left(\frac{\mu}{T}\right)_p = -\frac{5}{2}kT_H\left(1-\tau\right), \tag{10}$$

$$q_{34} = \int_3^4 Tds = -\int_{T_L}^{T_H} Td\left(\frac{\mu}{T}\right)_{p/\sqrt{T}} = 2kT_H\left(1-\tau\right). \tag{11}$$

The net specific work output of the cycle is

$$\begin{aligned} w &= -\left(q_{12} + q_{23} + q_{34} + q_{41}\right) \\ &= \frac{k}{2}T_H\left[\ln(\tau) + \left(1-\tau\right)\right] \end{aligned} \tag{12}$$

and the net specific heat input q_{in} is equal to q_{41} given by (8). Therefore efficiency of this cycle can be obtained as

$$\eta = \frac{|w|}{q_{in}} = \frac{-w}{q_{41}} = 1 + \frac{1-\tau}{\ln\tau}. \tag{13}$$

Variation of the dimensionless specific work and efficiency with the temperature ratio are given in Figs 3a and 3b.

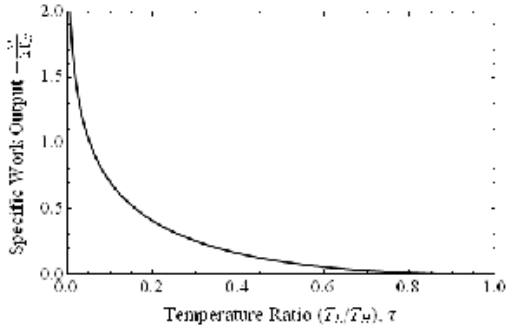

(a)

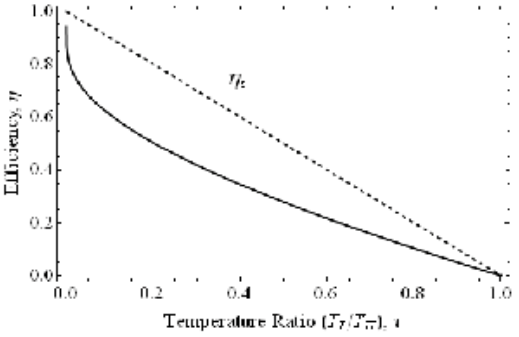

(b)

Fig. 3. a) Dimensionless net specific work output vs τ, b) Variation of the efficiency with temperature ratio, τ.

Efficiency and the Carnot efficiency versus to temperature ratio are shown in Fig. 3b. It is seen from the figure that specific work is less than kT_H for the wide range of τ and the difference between the efficiency of the cycle and that of Carnot reaches to its maximum value of 0.3 when τ =0.2.

A basic classical thermosize power cycle can be improved by introducing a compression process in between point 2 and point 3. An improved thermosize power cycle are analyzed in detail in the following sections.

4. An improved thermosize power cycle

In order to increase the efficiency of the basic thermosize power cycle, a compression process can be added in the cold temperature side. Compression ratio is defined as the pressure ratio of point 3 to point 2, $r_P = P_3/P_2$. *T–s* diagram of this improved power cycle is given in Fig. 4.

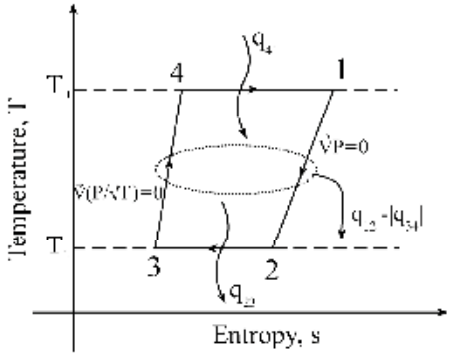

Fig. 4. An improved classical thermosize power cycle.

To analyse the improved power cycle, all the calculations given in the previous section, where $r_P = 1$, should be modified by considering $r_P \neq 1$.

The density relation between macro and nano parts on the cold side can be rewritten as, $n_3 = r_p n_2$, by using the ideal gas equation of state, $p = nkT$, and the equality of the temperatures on cold side $(T_2 = T_3 = T_L)$. Therefore, (3) and (4) are modified as follows

$$n_m(T) = n_2 T_L / T \,, \tag{14}$$

$$n_n(T) = n_2 r_p (T_L/T)^{1/2} \,. \tag{15}$$

Chemical potential differences at hot and cold sides can be calculated as

$$\mu_4 - \mu_1 = kT_H \ln\left(\frac{r_p}{\sqrt{\tau}}\right), \tag{16}$$

$$\mu_3 - \mu_2 = kT_H\tau \ln(r_p). \tag{17}$$

Exchanged heats during the processes (1-2), (2-3), (3-4) and (4-1) are calculated by using (8), (10), (11), (16) and (17)

$$q_{12} = -\frac{5}{2}kT_H(1-\tau), \tag{18}$$

$$q_{23} = -kT_H\tau \ln r_p \,, \tag{19}$$

$$q_{34} = 2kT_H(1-\tau), \tag{20}$$

$$q_{41} = kT_H \ln\left(\frac{r_p}{\sqrt{\tau}}\right). \tag{21}$$

The net specific work output and the efficiency of the cycle are obtained as

$$\begin{aligned} w &= -(q_{12} + q_{23} + q_{34} + q_{41}) \\ &= kT_H\left(\tau \ln r_p - \ln\left(\frac{r_p}{\sqrt{\tau}}\right) + \frac{1-\tau}{2}\right) \end{aligned} \tag{22}$$

$$\eta = \frac{|w|}{q_{in}} = \frac{-w}{q_{41}} = 1 - \frac{\left(\frac{1-\tau}{2} + \tau \ln r_p\right)}{\ln\left(\frac{r_p}{\sqrt{\tau}}\right)}. \tag{23}$$

It is clearly seen that the same equations given in the previous section are recovered when r_p goes to unity.

The dimensionless specific net work output and efficiency versus to temperature ratio are shown in Figs 5a and 5b respectively for different r_p values. It is shown that both efficiency and work output increases with increasing pressure ratio.

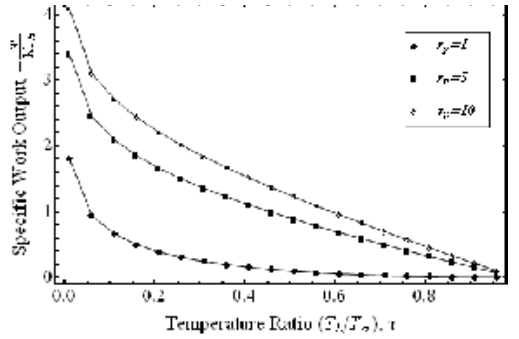

(a)

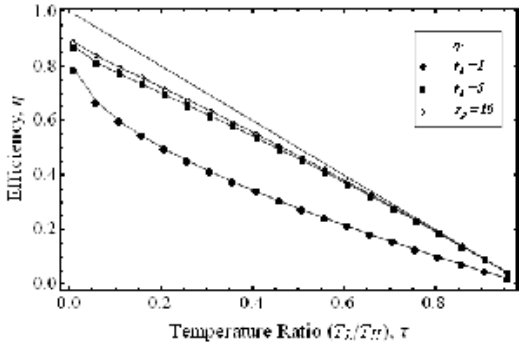

(b)

Fig. 5. a) Dimensionless specific net work output vs τ *for different* r_p *values, b) Variation of efficiency with temperature ratio* τ *for different* r_p *values.*

Even for the values of r_p smaller than unity, the cycle can still produce work up to a certain value of r_p. In this case, pressure of state 2 is bigger than that of state 3 and heat is absorbed from the cold reservoir during process 2-3. On the other hand, q_{12} is still bigger than q_{34} and heat energy difference between q_{12} and q_{34} should be rejected into the cold reservoir. Net heat exchange between gas and cold reservoir is negative. Therefore, there is a net heat rejection into the cold reservoir. Since the heat absorption from the hot reservoir is still bigger than the heat and net work output of the cycle is still negative, which means the cycle still produce work. On *T-s* diagram, the curve of process 1-2 crosses the curve of process 3-4, Fig. 6. Of course, the net work output decreases with smaller values of r_p.

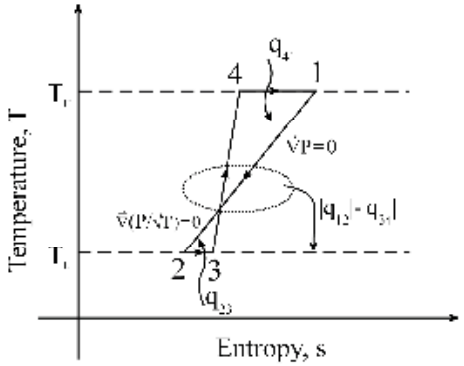

Fig. 6. Crossing effect on T-s diagram.

The cycle continues to produce work until a critical value $\left(r_p^*\right)$ of r_p which is obtained from (22). The condition for r_p to produce work $\left(w<0\right)$ is

$$r_p > \exp\left(\frac{1}{2}+\frac{\ln\sqrt{\tau}}{1-\tau}\right)=r_p^*. \qquad (24)$$

Under this critical value, the cycle needs net work input instead of output to operate.

5. Conclusion

The basic classical thermosize power cycle is improved by applying a compression process on the cold temperature region. The variation of efficiency and net work output with temperature ratio are analyzed for different r_p values. Additionally, even in the case of r_p is smaller than unity; the system can still produce work up to a critical value, r_p^*. Under this critical value, the cycle becomes a refrigeration/heat pump cycle. The results can be helpful to design micro/nano heat engines as well as for further works on refrigeration cycles. Classical thermosize refrigeration cycles is an undergoing work.

References

[1] Karniadakis, G.E., et al., 2005, *Micro and Nano flows: Fundamentals and Simulation*, second ed., Springer US.

[2] Sisman, A., and Muller, I., 2004, The Casimir-like size effects in ideal gases, Phys. Lett. A 320(5-6) , pp. 360-366.

[3] Nie, W., and He, J., 2008, Performance analysis of a thermosize micro/nano heat

engine, Physics Letters A 372(8), pp. 1168-1173.

[4] Nie, W., et al., 2009, Performance characteristic of a Stirling refrigeration cycle in micro/nano scale, Physica A 388(4), pp. 318-324.

[5] Babac, G., and Sisman, A., 2009, Thermosize effects and thermodynamic analysis of a thermosize power cycle, JETC10 Joint European Thermodynamics Conference [online journal], URL: http://www.jetc10.fys.ku.dk/fileadmin/user_upload/jetc10/materials/Aall_abstracts_combined.pdf

[6] Kang, J.W., and Hwang, H.J., 2004, Nanoscale carbon nanotube motor schematics and simulations for micro-electro-mechanical machines, Nanotechnology 15(11), pp. 1633-1638.

[7] Kang, J.W., 2005, Carbon nanotube oscillator operated by thermal expansion of encapsulated gases, Nanotechnology 16(11), pp. 2670-2676.

[8] Goddard, W.A., et al., 2007, *Handbook of Nanoscience*, Engineering, and Technology, second ed., CRC Press Taylor&Francis Group US.

[9] Reif, F., 1965, Fundemantals of Statistical and Thermal Physics, McGraw-Hill.

[10] Pathria, R.K., 1998, An ideal quantum gas in a finite-sized container, Am.J. Phys. 66(12), pp. 1080-85.

[11] Knudsen, M., 1910, Eine Revision der Gleichgewichtsbedingung der Gase. Thermische Molekularstromung, 336(1), pp. 205-229

Thermoeconomical Optimization of a Complex Heating System

Vladimir Nikulshin

Odessa National Polytechnic Univ., Ukraine

Abstract: In the design and operation of energy intensive systems, the possibility of improving the system's efficiency is very important to explore. The main way of improving efficiency is through optimization. This paper describes a general approach for thermoeconomical optimization of heat supply system (HSS) for cottage complex. The suggested method is based on the construction and analysis of a thermoeconomical expenditure graph. The method is illustrated with on example of optimization of real heating system for cottage complex with four buildings.

Keywords: Thermoeconomics, optimization, heating system.

1.Introduction

In the design and operation of energy intensive systems, the possibility of improving the system's efficiency is very important to explore. The main way of improving efficiency is through thermodynamic analysis and optimization.

The processes taking place in the complex energy intensive systems are characterized by mutual transformation of quantitatively different power resources.

For this reason the thermodynamic analysis of these systems requires the combined application of both laws of thermodynamics and demands the exergy approach [1,2].

These methods are universal and make it possible to estimate the fluxes and balances of all energy flows for every element of the system using a common criterion of efficiency.

Despite its usefulness, the benefits of the exergetic approach were not fully realized until recent years. One reason for this situation is the underestimation of exergetic functions for mathematical modeling, synthesis, and optimization of flow sheets. Another reason is the mathematical difficulty of the exergetic approach in thermodynamic analysis. Meanwhile, the increasing complexity of optimization problems requires more effective and powerful mathematical methods. Hence, during the last few years, many papers with different applications of exergetic methods have been published (see for example [3-8]).

The above referenced papers, as well as the author's earlier investigations [8-13] show that one of the most effective mathematical methods used for exergetic analysis and optimization is the method of graph theory [14,15]. The benefit of graph models can also be demonstrated by its flexibility and wide varieties of possible applications. Possible exergy topological methods include the sole use or combination of exergy flow graphs, exergy loss graphs, and thermoeconomical graphs [8-13].

The thermoeconomical approach allows to retain all advantages of exergy method and simultaneously estimate the investment and other monetary costs of a system.

In this Paper is developed the method of thermoeconomical optimization of a heat supply system for cottage complex .

2.Graph of thermoeconomical expendeture for heat supply system

Past optimization research of actual energy intensive systems was successfully conducted using exergy flow graphs [8,10,12] However, for considering the rather broad class of systems with pair interplay of flow , was suggested a graph of thermoeconomical expenditure [9,11].

This type of graph represents one kind of possible exergy-topological models.

In application to a heat supply system (HSS) it is a bipartite graph $Z = (C \cup H, \Gamma_n) = (C \cup H, D)$. The graph consists of the set of nodes $C \cup H$ corresponding to the multitude of heat sources $H = \{h_1, h_2, ..., h_j, ..., h_m\}$ and multitude of heat consumers $C = \{c_1, c_2, ..., c_i, ..., c_n\}$, as well as the set of arcs $D = \{h_i, c_j\}$, $i=1,2..., m$; $j=1,2..., n$; which represent the possible distribution of thermoeconomical expenditure in the HSS. The

graph of thermoeconomical expenditure is the simple graph of a view:

$$H \cap C = \varnothing \quad (1)$$

$$(\forall h_i \in H)\, \Gamma_n h_i \in C \quad (2)$$

$$(\forall c_i \in C)\, \Gamma_n c_j = \varnothing \quad (3)$$

Than every *i, j*- pair (h_i, c_j) from sets $H = \{h_1, h_2..., h_i,..., h_m\}$ and $C = \{c_1, c_2..., c_j..., c_n\}$ will be uniquely characterized with appropriate thermoeconomical expenditure Z_{ij}.
The problem of optimal, thermoeconomical synthesizing can be solved by minimizing the sum shown in Eq. (4)

$$Z_{\Sigma}^{\min} = \min \sum_i \sum_j Z_{ij} \quad (4)$$

Lets assume that the procedure of its optimization has s-steps. Also, lets take intermediate p-step $(1 \le p \le s)$ and assume that on the *p*-step the optimal pairs of $(m-m_p)$ heat sources h_i, $(m > m_p > 0)$ and $(n-n_p)$ of heat consumers c_j, $(n > n_p > 0)$, are found. Then in the result of minimizing the sum given in Eq. (4) on every *p*-step, the optimal system will be obtained [12].

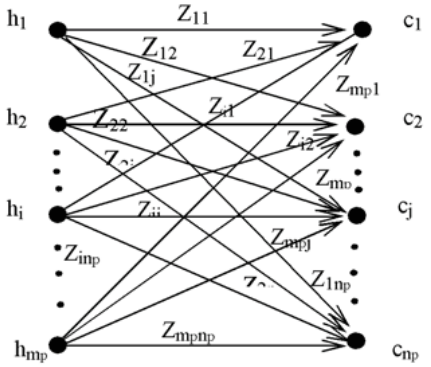

Fig. 1. Bipartite graph of thermoeconomical expenditure for a p-step.

Z_{11}	Z_{12}	…	Z_{1j}	…	Z_{1np}
Z_{21}	Z_{22}	…	Z_{2j}	…	Z_{2np}
…	…		…		…
Z_{i1}	Z_{i2}	…	Z_{ij}	…	Z_{inp}
…	…		…		…
Z_{mp1}	Z_{mp2}	…	Z_{mpj}	…	Z_{mpnp}

Fig. 2. Matrix of graph in Fig.1.

In order to optimize a p-step, the graph of thermoeconomical expenditure for a *p*-step $\bar{Z} = (\bar{H} \cup \bar{C}, \bar{\Gamma}_n) = (\bar{H} \cup \bar{C}, \bar{D})$ shown in Fig.1 will be considered.
Here

$$\begin{aligned} &H \cap \bar{C} = \varnothing \\ &(\forall h_i \in \bar{H})\ \bar{\Gamma}_n h \in \bar{C} \\ &(\forall c_i \in \bar{C})\ \bar{\Gamma}_n c_j = \varnothing \\ &H = \{h_1, h_2..., h_i,..., h_{mp}\} \\ &C = \{c_1, c_2..., c_j,..., c_{np}\} \end{aligned} \quad (5)$$

The set of arcs of the graph $\bar{Z} = (\bar{H} \cup \bar{C}, \bar{D})$
$\bar{D} = \{h_i, c_j\},\ i=1,2, \ldots, m_p;\ j=1,2, \ldots, n_p$
is defined as:

$$(h_i, c_j) \in \bar{D} \Rightarrow (h_i, c_j) = Z_{ij} \quad (6)$$

Set $\bar{D}$ can be divided into two subsets, $\bar{D}_1 \cup \bar{D}_2 = \bar{D}$ and $\bar{D}_1 \cap \bar{D}_2 = \varnothing$
for which conditions given in Eqs. (7) and (8) are satisfied.

$$\forall (h_i, c_j) \in \bar{D}_1 \Rightarrow Z_{ij} \neq \infty \quad (7)$$

$$\forall (h_i, c_j) \in \bar{D}_2 \Rightarrow Z_{ij} = \infty \quad (8)$$

The version with $D_2 = \varnothing$ is also possible but generally $D_2 \neq \varnothing$.
For finding the coupling that will minimize Eq. (4), a minimum bearing [8] of simple graph $\bar{Z} = (\bar{H} \cup \bar{C}, \bar{D})$ is found which corresponds to a unique matrix of thermoeconomical expenditure, MZ_{ij} of the size $m_p \times n_p$ (shown in Fig.2).
The minimization problem is reduced to finding row vectors $Z_i = \{Z_{i1}, Z_{i2}, \ldots, Z_{inp}\}$ and vectors of columns $Z_j = \{Z_{j1}, Z_{j2}, \ldots, Z_{jmp}\}$, that meet the condition given in Eq. (4).
By transforming the matrix MZ_{ij}, the elements under conditions Eq. (7) are eliminated from consideration.
The outcomes are elements Z_{ij}, which are optimal for the given p-step
The algorithm of the solution does not vary as the step is transitioned to $p+1$ and to $p = s$.
After each step, the sizes of a matrix MZ_{ij} will be diminished and at p = s the matrix becomes equal to zero point.
Step by step algorithm of this procedure is given in [12].

3.Optimal synthesis of a real heat supply system for cottage complex

It is necessary to design the optimal heat supply system for cottage complex with four buildings. The main characteristics of these buildings are given in table I.

Table I. Main characteristics of buildings

Number of building	Number of stores	Total square m^2	Number of residents
1	2	256	9
2	3	642	22
3	3	642	22
4	3	742	25

Building 1 was built and occupied 5 years ago. Buildings 2-4 are in different stages of construction (finishing of building and occupation is planed in the next year).
All four buildings are located in a corners of a square with a side 50 meters.
Heat supply of a building 1 is organized by a boiler non-condense type KV (see Table II).
For developed heating systems were considered two main options:

1. Using the cheaper boilers KV non-condense type (see Table II), but with low energy efficiency (85%).
2. Using more expensive modern boilers KC - condense type (see Table III), but with a rather high energy efficiency (95%).

Besides that for both options were considered the possibility not only to create individual heating system (one boiler -one building) but also to create a district heating y system (one boiler-few buildings).
In accordance with a rules given in [10-12] can be built the graph of thermoeconomical expenditure in designed HSS (see Fig.3.).
Here the nodes a_1 - a_4 of graph of thermoeconomical expenditure corresponds to the buildings 1-4 and arcs (a_i, a_j), $i=1,2,3,4$; $j=1,2,3,4$ corresponds to appropriate parts of heating grid.
For simplification of optimization procedure it will be helpful to include in the possible thermoeconomical expenditure Z_{ij}, $i=1,2,3,4$; $j=1,2,3,4$ not only thermoeconomical expenditure of a heating grid but also a part of thermoeconomical expenditure (proportionally to heat capacity) of a boiler.
It is clear that for the variant of individual heating system the heating network between the building will be absent.
In general case $Z_{ij} \neq Z_{ji}$, as a result the different heating demands in different buildings (in analyzed case only $Z_{23} = Z_{32}$).
Now it is possible to build the graph of thermoeconomical expenditure (see Fig. 4) in accordance with Eqs. (1)-(3) given above.
The multitude of heat sources $H = \{h_1, h_2, ..., h_j, ..., h_m\}$, $m=10$ corresponds to the possible variants of used boilers (with appropriate part of heating network for district heating variant) and multitude $C = \{c_1, c_2, ..., c_i, ..., c_n\}$, $n=4$ corresponds to of heat consumers (buildings 1-4).

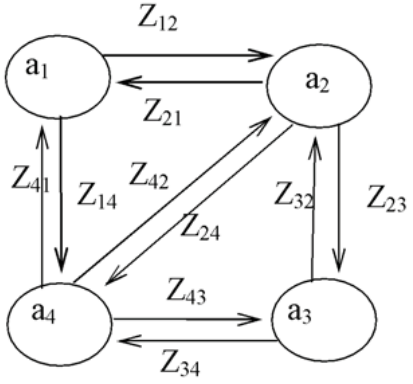

Fig. 3. Graph of possible thermoeconomical expenditure in designed HSS.

Table II. Main characteristics of non-condense boilers (type KV)

Heat capacity, kW	345	735	850	1520	2530
Price, USD	17,25	34,0	35,84	62,66	96,5
Corresponding node of graph	h_{11}	h_{21}	h_{31}	h_{41}	h_{51}

A fuel for boilers is natural gas (Price 0.0593 USD/m^3, Q=35 MJ/ m^3).
For calculations of heat demands were taken the follow integrated characteristics:

Table III. Main characteristics of condense boilers (type KC)

Heat capacity, kW	360	725	875	1640	2620
Price, USD	36,0	41,16	1,53	51,0	128,66
Corresponding node of graph	h_{12}	h_{22}	h_{32}	h_{42}	h_{52}

- demand for heating 1.2 kW/ m^2 for building 1(old design) and 1.1 kW/ m^2 for buildings 2-4 (modern design). The heating period October, 15 - April, 15.
- demand for heat water supply (all over the year) is120 liters per person per day (0.4 kW per person)
- speed of water in a pipes between buildings 1.5m/s

Investment cost in heating network (in pipelines) were calculated by Eq. (9)

$$K_c=(20+ 210d)L, \ USD \quad (9)$$

here d-diameter and L- length of pipeline.
Refund period (under request of a customer) is 5 years.
Thermoeconomical expenditures were calculated by the method given in [12].
Let's describe the first step (the other steps are analogously) of suggested approach on example of calculation of thermoeconomical expenditure for building 2.
In accordance with a heat demand (see Table IV) of a building 2 (node c_2 of graph in fig.4) it is possible to create a heating system from all heat sources (except h_{11}, h_{12}, which have the less of requested heat capacity). For this reason there are eight arcs, connected with a node c_2 and it is necessary to calculate the thermoeconomical expenditures on these arcs

Table IV. Heat demand of consumers

Consumer	Building 1	Building 2	Building 3	Building 4
Heat demand , kW	310	715	715	826
Corresponding node of graph in Fig.4	c_1	c_2	c_3	c_4

Arc $(h_{21}- c_2)$. Here a boiler is located in a building 2 so expenditures for heating network (pipe lines) between building will absent and the thermoeconomical expenditures will contain two parts "year price" of natural gas Z_{21}^{gas} and "year investment and operation cost" of boiler Z_{21}^{b} .

$$Z_{21}^{\Sigma} = Z_{21}^{gas} + Z_{21}^{b} = 28970 \ USD/year$$

Arc $(h_{22}- c_2)$- analogously to arc $(h_{21}- c_2)$.

$$Z_{22}^{\Sigma} = Z_{22}^{gas} + Z_{22}^{b} = 29070 \ USD/year$$

Arcs $(h_{31}- c_2)$ and $(h_{32}- c_2)$. Here a heat capacity of each of both boilers are bigger then requested 715 kW but they are not enough to cover some additional demand, so expenditures Z_{31}^{Σ} and Z_{32}^{Σ} will be for sure bigger then the same characteristics for previous variants so it is possible to exclude this option from further consideration.
Arc $(h_{41}- c_2)$. As a boiler can be also placed in the building 3 it is necessary to take into account expenditures of a pipe line network between buildings Z_{41}^{p}.
So now the total thermoeconomical expenditure will contain three parts:

$$Z_{41}^{\Sigma} = Z_{41}^{gas} + Z_{41}^{b} + Z_{41}^{p} = 28680 \ USD/year$$

Arc $(h_{42}- c_2)$-analogously to arc $(h_{41}- c_2)$.

$$Z_{42}^{\Sigma} = Z_{42}^{gas} + Z_{42}^{b} + Z_{42}^{p} = 27600 \ USD/year$$

Arcs (h_{51}- c_2) and (h_{52}- c_2) analogously to arcs (h_{41}- c_2) и (h_{42}- c_2), but a boiler can be placed in a building 4, were is located the maximum heat demand in all cottage complex.

$$Z_{51}^{\Sigma}=Z_{51}^{gas}+Z_{51}^{b}+Z_{51}^{p}=28450\ USD/year$$

$$Z_{52}^{\Sigma}=Z_{52}^{gas}+Z_{52}^{b}+Z_{52}^{p}=27700\ USD/year$$

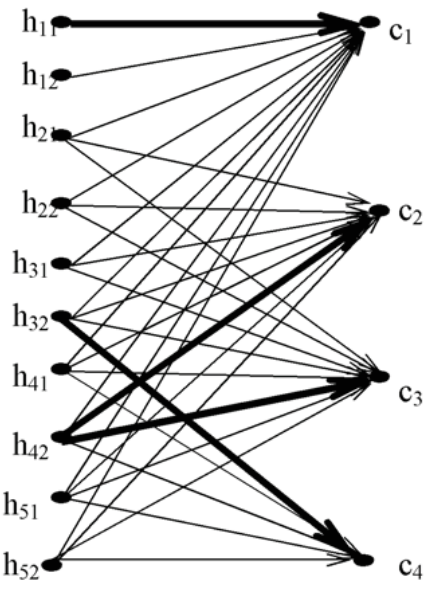

Fig. 4. A bipartite graph of possible thermoeconomical expenditure in HSS

It is easy to see that the minimum meaning of Z_{ij}^{Σ} is Z_{42}^{Σ}, which (it showed the optimization procedure) was also taken in the final variant of total optimal system.
The nodes of graph corresponding to optimal variant of heating supply system are marked by a bold lines in Fig.4.

Optimal variant provides:

Building 1 - retain the existing heating system from a boiler h_{11} -see table II (because the new boiler will not be refunded during 5 years).

$Z_{11}^{\Sigma}(1)=9600\ USD/year$ - in practices only cost of natural gas.

Building 2 and building 3 have a common heat supply system from one boiler h_{42} -see table III This boiler locates in the building 3 .

For building 2

$Z_{42}^{\Sigma}(2) = 27600$ USD/year

Building 3
$Z_{42}^{\Sigma}(3) = 27000\ USD/year$

It is clear that the different between $Z_{42}^{\Sigma}(2)$ and $Z_{42}^{\Sigma}(3)$ is a year expenditure of a pipe line between buildings 2 and 3.

Building 4 has an individual heat supply system from a boiler h_{32} (see table III).

$Z_{32}^{\Sigma}(4) = 33100\ USD/year$

Optimal (minimal) meaning of thermoeconomical expenditures for all cottage complex is

$$Z_{min}=Z_{11}^{\Sigma}(1)+Z_{42}^{\Sigma}(2)+Z_{42}^{\Sigma}(3)+Z_{32}^{\Sigma}(4)+ = 97320\ USD/year$$

Conclusion

The problem of optimisation of heating systems has to be solved separately from the problem of optimisation of other energy intensive systems. On the basis of the unique features of such a system it is possible to build an effective procedure for optimisation. The suggested method based on development and analysis of thermoeconomical expenditure graph. It allows one to find the optimal variant for this kind of systems with different types and numbers of heat consumers.
An example of optimal synthesis of a real heating system is given.

References

[1] Moran, M., Shapiro H.,2004,*Fundamentals of Engineering thermodynamics* , John Wiley & Sons Inc., New York.
[2] Tutns S., 2006, *Thermodynamics Concepts and Applications,* Cambrigr University Press.
[3] Rosen , M., Etele, J.,2004, Aerospace System and Exergy Analysis, Int. J. Exergy, Vol 1, N 4, pp. 411-425.
[4] Koroneos, C., Rivas, D.,2006, Exergetic analysis of Integrated Power Production Solar system. *Proc. of International Conference*

ECOS-06, Heraclion, Greece, pp.126-134.
[5] Branko, F., et al., 2006,Thermodynamic and Thermoeconomic analysis of a Brazilian Natural gas Thermal Power Plant, *Proc. of International Conference ECOS-06,* Heraclion, Greece, pp.203-209.
[6] Ertesvag, J., Kvamsdal, H., Bolland., 2005, Exergy analysis of a gas-turbine combined cycle power plant with precombustion CO2, Energy, N1, pp 25-39.
[7] Ozturk, H.,2005, Experimental evaluation of energy and exergy efficiency of a seasonal latent heat storage system fro green house heating, Energy Conversion & Management, 46, pp 1523-1542.
[8] Nikulshin, V., Wu, C., 2001,Thermodynamic analysis of energy intensive systems based on exergy-topological models, Exergy-an International Journal, Vol.1, pp. 173- 180.
[9] Nukulshin V., von Zedtwitz ., 2005, Optimization of heating systems with renewable energy sources, *Proc. of the 18-th International Conference ECOS-05,* Trondheim, Norway, pp.439-446.
[10] Nikulshin, V., Wu, C., 1999, Method of thermodynamic analysis and optimization of energy intensive systems on exergy flow graphs, Proc. of International Conference on Power and Energy Systems, Las Vegas, Nevada, USA, pp.489-491.
[11] Wu, C., Nikulshin, V., 2000, Method of thermoeconomical optimization of energy intensive systems with linear structure on graphs, International Journal of Energy Research, 24, pp.615-623.
[12] Nikulshin V., Bailey M., 2006, Nikulshina V., Thermodynamic analysis of air refrigerator on exergy graph, Thermal Science, Vol.10,No1, pp.99-110.
[13] Nikulshin V., von Zedtwitz V., 2007, The "entropy-cycle" method for thermodynamic analysis of energy intensive system, International Journal of Exergy, Vol. 4, No. 1, pp.74-86.
[14] Harary F., 1995,F., *Graph Theory*. Narosa Publishing House, New Deli.
[15] Balakrishnan V.K., 1997, *Graph Theory*, Shaumm's Outline Service, New York.

Thermodynamic Analysis of Air- Conditioning Systems with Steep Condition Lines

Nóbrega,C.E.L.[a], Brum, N.C.L.[b]

[a] *Centro Federal de Educação Tecnológica CEFET-Rio , Rio de Janeiro, Brazil*
[b] *Universidade Federal do Rio de Janeiro, Rio de Janeiro, Brazil.*

Abstract: In psychrometry, the process suffered by the air as it crosses the room (heating and humidification) is usually referred to as condition line.Whenever the condition line is significantly steep, it becomes difficult – or even impossible- to design a cooling coil whose characteristic process line is able to intersect the condition line at any point, making it impossible to reach the desired thermal comfort condition. Accordingly, the usual practice is to overcool the air stream below the desired dry-bulb temperature, so as to accomplish the desired level of humidity. The overcooled air stream is then re-heated up to the desired comfort temperature level, usually by means of an electricity-driven heating coil. An alternative would be to use a desiccant wheel to purge out the excess moisture within the fresh air stream. The fresh air stream is then succesively driven through a heat wheel, a cooling coil and a evaporative cooler, so as to intersect the room condition line. The energy requirements for both alternatives is compared, showing that that the efficiency of the desiccant cooling scheme increases with the steepness of the condition line.

Keywords: Enthalpy Recovery, Desiccant, Dehumidification.

1. Introduction

The proper design of an air conditioning systems is extremely depended on the characteristics of the thermal load to be attained, as well as on the outside atmospheric air condition. In particular, the inclination of the condition line, i.e., the room sensible heat factor (RSHF), has a prime impact on design parameters such as the fan-coil area and operating evaporator temperature. Some applications exhibit a characteristic steepness on the condition line, implying a greater contribution of the humidity to the total cooling load. That would be the case of applications with intense human activities, such as in dance halls or sports arenas. Even condition lines characteristic of more conventional applications such as office buildings can become steeper under partial load conditions or high levels of outside air humidity. Figure (1) shows a schematic representation of a typical single zone air-conditioning system. The fan coil is designed to handle both latent and sensible loads, and runs until the required humidity level is achieved [1]. At this point the air has been overcooled beyond the comfort condition (M), and has to be forced through a reheat coil to bring the temperature back to the room supply value (i).

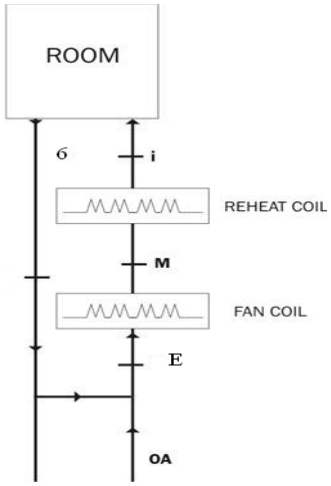

Fig. 1. Schematic representation of a Cooling-Reheat system.

2. Systems Description

Several systems combining desiccant and vapor-compression cooling have been proposed [2-5], with the common feature of handling the sensible and latent loads separately, rather than traditional cooling-reheat systems, which accomplish the cooling and the dehumidification in a single process.

Corresponding Author: Carlos Eduardo Nóbrega, Email: nobrega@pobox.com

Figure (2) shows a schematic representation of the proposed hybrid cycle. The outside air stream (OA) is collected and is forced through a desiccant wheel, where is heated and dehumidified. The air is then cooled by forcing it through a heat wheel. Then it is sub sequentially cooled at constant humidity and at constant enthalpy, forcing it through a cooling coil and a evaporative cooler, respectively. In the conditioned room the air state then evolves from the supply condition (5) to the room condition (6), which is also taken to be the return air condition. The evolution from (5) to (6) occurs through the condition line, and corresponds to the absorption of the room sensible and latent heat loads. The return air is then discarded at the same flow rate as the fresh air required by design conditions, which is usually around $27m^3/h$ per occupant. The remaining flow rate is recirculated through the cooling components.

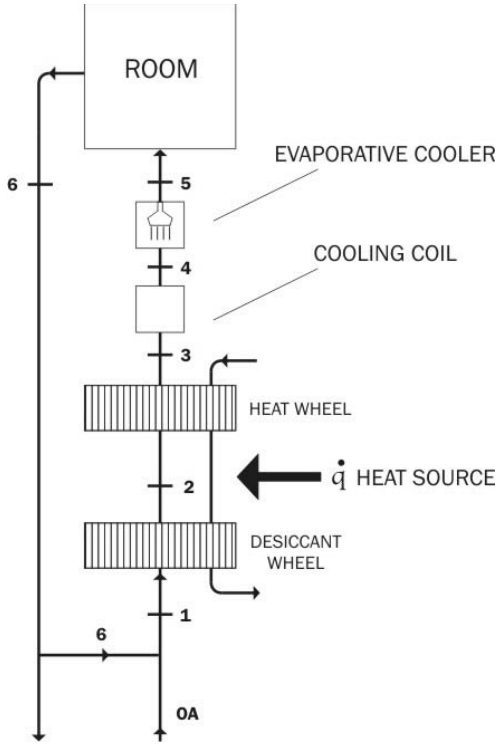

Fig. 2. Schematic representation of a single-zone hybrid system.

Figure (3) shows a psychrometric representation of the traditional reheat vapor-compression and the proposed hybrid cycle.

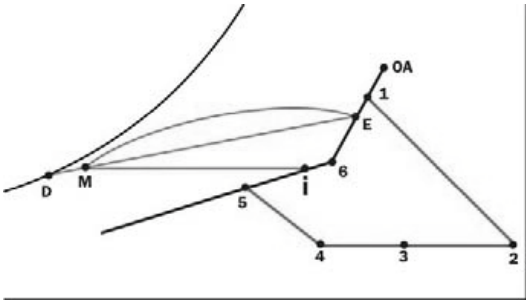

Fig. 3. Psychrometric representation of reheat and hybrid systems.

It can be seen that both outside air (OA) and the comfort condition (6) are the same for both cycles. Also, the condition line (RSHF) is represented by the dashed line through point (6), and is the same for both cycles. The condition line represents the ratio between the sensible and latent thermal loads offered by the room. Accordingly, the greater the latent load, the steeper will be the condition line. For the reheat cycle, the mixture between recirculated room air (6) and outside air (OA) results in state E, in the admission of the cooling coil. The simultaneous cooling and dehumidification, represented by the curve line, results in point (M), which represents the air state leaving the cooling coil. From this perspective, the state m is obtained by a mixture of two distinct streams. One stream gets in close contact with the finned metallic surface and reaches the saturation state (D), corresponding to the apparatus dew-point. Another stream flows through the coil by-passing the heat transfer surface and leaves the apparatus at the same state it was admitted (E). The by pass factor (BF), which represents the fraction of the total flow rate that by-passes the transfer surface is an important heat exchanger design parameter. Steep condition lines usually require a low BF value, in order to allow a thorough dehumidification. That usually implies high heat transfer areas and low values of the apparatus dew point (D). The air is then reheated at constant humidity, until it crosses the condition line at point (i). The sensible and latent loads then

bring the air from sate (i) to state (6). As for the hybrid cycle, the mixture between recirculated room air (6) and outside air (OA) results in state (1), in the admission of the desiccant wheel. The air is then heated and dried to state (2). The temperature rise results from the heat generated by the adsorption process, as well as from the heat transferred to the desiccant material, as the moisture is desorbed and dumped back to the atmosphere. The air is the cooled by a heat wheel to state (3), and sub sequentially by a cooling coil to state (4). An important feature of this cooling process is that, since it occurs at constant humidity, it will happen at a much higher temperature than the cooling process of the reheat cycle (E)-(M), which has to operate at point (D). This is possible because the hybrid cycle decouples the dehumidification and the cooling processes. The last step of the cooling process is the evaporative cooling, which occurs at constant enthalpy, up to it crosses the condition line at state (5). It will be shown that for the hybrid cycle, state (5) can be very close to state (i), allowing it to be a perfect replacement for the Reheat cycle, delivering air at he same comfort condition and volumetric flow rate. All the processes have been plotted using an electronic psychrometric chart [6].

3. Design Procedures

The required parameters for designing the cooling-reheat air-conditioning systems are the outside air state (OA), the room comfort condition (6), BF, the room sensible heat load (RSH), the room latent heat load (RLH) and the required flow rate of outside air (V_{OA}). The design procedure for this kind of system consists of the following steps [7].

1. Calculate the inclination of the condition line, RSHF (A.1). Calculate the outside air sensible and latent heat loads, OASH (A.3) and OALH (A.4) respectively. They represented the by-passed air contribution to the room thermal load.
2. With the given data and the calculated values of OASH and OALH, it is possible to calculate the effective sensible heat factor, ESHF (A.6). At this time, assume no need for reheat.
3. Plot the calculated value of ESHF on the psychrometric chart through point (6). The apparatus dew point (D) is given by the intersection of ESHF and the saturation curve.
4. If the value for T_D obtained in the previous step is too low, it has to be rejected. The lower the temperature T_D, the lower will be the coefficient of performance of the cooling cycle. In addition, temperatures below 0ºC will imply in frost formation. Accordingly, the usual practice is to choose a greater value for ESHF, anytime the value for T_D calculated in the previous step is lower than 7ºC. The corresponding new value for T_D has to be checked to satisfy the same criterion.
5. Calculate the reheat required to achieve the chosen value for ESHF (A.6).
6. Calculate the value of the effective ratio of sensible heat ERSH (A.7), which corresponds to the sum of the room, bypassed air and reheat sensible loads.
7. With the calculated value of ESHF and the apparatus dew point T_D, the total flow rate supplied to the room V_T can be calculated (A.8).
8. Since the outside air flow rate V_{OA} is given and the total flow rate V_T has just been calculated, the recirculated flow rate V_{rec} is obtained (A.9). Accordingly, the temperature (A.10) and humidity (A.11) of point (E) are obtained. Point (E) represents the air state in the admission of the cooling coil.
9. Once T_E is known, it's possible to calculate the air temperature at the outlet of the fan-coil, which corresponds to point (M) (A.12).
10. Once T_M is known (and the amount of reheat has already been calculated), the supply air state, represented by point (i) can be obtained (A.13).
11. The cooling capacity is given by the grand total heat, GTH (A.14). It is comprised of the room thermal load, outside air and reheat thermal load.

The required parameters for designing the hybrid system are the same as the vapor-compression. In addition, the simulation of the adsorption process requires the knowledge of the regeneration temperature, as well as the non-dimensional period

of revolution and length of the desiccant wheel. The design procedures for this kind of system consist of the following steps.

1. Determine the air supply state (5) by choosing a suitable supply temperature over the condition line (RSHF). For comfort conditions, it is advisable to choose (5) so that T_6-T_5 is at least 10ºC, as otherwise the conditioned space (room) might end too "windy".
2. With the supply air temperature T_5 the total flow rate supplied to the room V_T can be calculated (A.15).
3. Since the fresh air flow rate V_{oa} is a pre-set requirement and the total flow rate V_T has been calculated, the recirculated flow rate V_{rec} is obtained (A.9). Accordingly, the temperature and humidity of point 1 are obtained. Point (1) represents the air state in the admission of the desiccant wheel.
4. The mathematical modelling of the air temperature and humidity fields through the desiccant wheel is given by (A.16) to (A.19), using a finite volume technique [8-10]. The equations are solved using state (1) and choosing a regeneration temperature as input parameters. The non-dimensional period of revolution and length of the desiccant wheel are also required parameters. The simulation output parameters are the temperature T_2 and absolute humidity Y_2. Interesting to note that process (1)-(2) occurs at constant enthalpy, which means that air is heat is transferred to air in the same proportion humidity is transferred form air to the desiccant wheel.
5. Knowing state (2) and the effectiveness of the heat wheel, state (3) is determined, since $Y_3 = Y_2$.
6. State (4) is readily determined by the intersection of $Y_4 = Y_3 = Y_2$ with the line $h_4 = h_5$, since the evaporative cooling process occurs at constant enthalpy.
7. Since all the states comprising the cycle have been determined, the cooling capacity and the regeneration heat can be calculated by the product of the flow rates and enthalpy differences.

4. Results

The aforementioned design procedures will be performed step-by-step for a particular set of input parameters required to design both systems. This set will be referred to as the typical condition, which represents the summer design conditions for Rio de Janeiro, Brazil.

Outside Air (OA)-Typical Condition

$T = 34.1$ºC $RH_{OA} = 48.6\%$

Room Air (6)-Comfort Conditions:

$T_6 = 24$ºC $RH_6 = 50\%$

The procedure will be repeated for two different requirements of outside air flow rate (V_{OA}), room sensible and latent heat loads, so as to evaluate the influence of these parameters over each cycle performances, as illustrated by Table 1. Conditions (a) to (C) and (d) to (f) refer to decreasingly values of RSHF. The lower the value of RSHF, the more predominant will be the room latent heat load (RLH).

Table 1. Thermal Load Characteristics

	RSH (kW)	RLH (kW)	RSHF	V_{OA} (m^3/s)
condition a	35.0	15.00	0.70	1.0
condition b	33.5	18.10	0.65	1.0
condition c	32.0	20.64	0.61	1.0
condition d	35.0	15.00	0.70	2.0
condition e	33.5	18.10	0.65	2.0
condition f	32.0	20.64	0.61	2.0

The first two columns in Table (2) refer to the total cooling load and the reheat requirement of the Cooling-Reheat system. The third column refers to the total required volumetric flow rate, whereas the fourth column refers to the room supply air temperature, state (i). Comparing conditions (a), (b) and (c), it can be seen that continuous a decrease in the RSHF (i.e., an increase in the latent load RLH) increases the need for reheat, as it would be expected. It also increases the total required air flow rate. Since the outside air flow rate V_{OA} is constant for these conditions, the recirculated air flow rate is increased from conditions (a) to (c). This effect tends to offset the increase in the total cooling load due to the increased reheat. Accordingly, the total cooling

load increase from condition (a) to (b), but slightly decreases from condition (b) to condition (c).

Table 2. Design Characteristics of the Reheat Cycle.

Reheat Cycle				
	Chiller Cooling Capacity	Required Reheat	Total Air Flow Rate V_T	Supply Air Temp. T_i
	Kw	Kw	m^3/s	ºC
Cond. a	92.50	10.13	2.75	13.5
Cond. b	115.00	20.50	3.28	15.7
Cond. c	112.00	29.18	3.71	17.0
Cond. d	126.40	11.80	2.87	14.0
Cond. e	141.60	22.13	3.40	15.9
Cond. f	149.40	30.60	3.82	17.1

Another important design parameter is the supply air temperature, T_i, which shows to increase with the increase in RSHF value. This is a consequence of the increased need for reheat, from conditions (a) to (c) and from conditions (d) to (f). The closer T_i gets to the comfort room temperature T_6, the higher will be required total volumetric air flow rate, for a given thermal load. As a consequence, this might result in a windy, uncomfortable environment. Accordingly, since the comfort room temperature T_6 is always kept constant at 24ºC, the supply temperature T_i should be around 17ºC, at highest. It can also be noted that, when the air flow rate is doubled (conditions (d) to (f)), the system is able to deliver air at the same conditions as in conditions (a) to (c).

Table 3. Design Characteristics of the Hybrid Cycle T_{reg} = 120ºC.

Hybrid Cycle				
	Chiller Cooling Capacity	Required Heat	Total Air Flow Rate V_T	Supply Air Temp. T_5
	Kw	Kw	m^3/s	ºC
Cond. a	33.3	286.3	2.76	13.5
Cond. b	28.3	346.1	3.34	15.7
Cond. c	22.8	393.0	3.71	17.0
Cond. d	29.8	301.1	2.90	14.0
Cond. e	30.1	354.7	3.40	15.9
Cond. f	31.5	398.1	3.82	17.1

The first two columns in Table (3) refer to the total cooling load and the heat requirement of the Hybrid system. The third column refers to the total required volumetric flow rate, whereas the fourth column refers to the room supply air temperature, state (5). Comparing Tables (2) and (3), it can be seen that points (i) and (5) can be perfectly coincidental, that is, the Hybrid cycle is capable of supplying air at the same condition as the Reheat cycle. As for the chiller cooling capacity, it can be seen that it is reduced to approximately one third, for the Hybrid cycle. Accordingly, it would require less energy then the Reheat cycle, even less if one considers that cooling without dehumidification can occur at a higher temperature (and thus at a higher COP) than cooling with simultaneous dehumidification, which necessarily requires a lower temperature than the air dew point. However, the calculation of the work required to drive the cycle would require specific knowledge of the kind of chiller and refrigerant properties, which are beyond the scope of the present study. Conversely, comparing the heat requirements of both cycles, it is observed that the Hybrid cycle requires as much as ten times more than the Reheat cycle.

Table 4. Design Characteristics of the Evaporative Cooler T_{reg} = 120ºC.

	Evaporative Cooler Effectiveness ε_{EC}	T_4-T_5
		(ºC)
Cond. a	0.85	13.0
Cond. b	0.81	14.1
Cond. c	0.78	14.5
Cond. d	0.86	14.6
Cond. e	0.80	13.8
Cond. f	0.75	13.2

The first two columns in Table (4) refer to the effectiveness (A.20) and the temperature drop across the evaporative cooler, respectively. An effectiveness of 100% would correspond to air being supplied to the room (state (5)) at the saturation state. However, this would correspond to a very unrealistic situation; since point (5) has to lie over the condition line (RSHF), as otherwise

the comfort condition (state (6)) will not be attained. Accordingly, it can be seen that the evaporative cooler effectiveness ε_{EC} has to be significantly less than 100%, which contradicts some desiccant cooling design procedures [11]. It is also noticeable that the temperature drop across the evaporative cooler is of the order of 15ºC. This is considerably higher than the usual figure (4ºC) for the evaporative cooling unassisted by desiccants, in the ambient conditions studied.

5. Conclusion

A Hybrid cooling cycle is proposed, and its energy requirements were compared to those of a traditional Reheat Cycle. The supply air condition (point (5)) is a key design parameter, and for desiccant cooling systems is usually excessively close to the room comfort condition (point (6)). As a consequence it usually requires a high air flow rate, so as too meet the room thermal load. Accordingly, the application of desiccant open cycles is commonly restricted to all outdoor applications, without air recirculation. It was shown that the introduction of a sensible cooling coil in the desiccant cycle allows it to meet the same supply air condition and flow rate as traditional Cooling-Reheat Cycles. Referring to Figure (3), this means that point (i) can exactly match point (5), which makes the Hybrid Cycle an alternative to the traditional Reheat Cycle, as far as the comfort condition and air renovation are of concern. Nevertheless, the great requirement for regeneration heat exhibited by the Hybrid cycle may inhibit its application unless an inexpensive thermal source is available, such as a solar collector or an engine waste heat recovery system. It was also shown that, if the comfort conditions are to be attained, the evaporative cooler efficiency has to be less as low as 75% in some cases.

Nomenclature

BF	by-pass factor
C_p	specific heat, J/(kg K)
ESHF	effective sensible heat factor
ERSH	effective room sensible heat
GTH	grand total heat
h	enthalpy, kJ/(Kg K)
h_g	latent heat, kJ/(Kg)
$\dot{m}$	mass flow rate, kg/s
OALH	outside air Latent Heat
OASH	outside air sensible seat
OASH	outside air total seat
RH	relative humidity
RLHF	room latent heat
RSH	room sensible heat
RSHF	room sensible heat factor
RTH	room total heat
T	temperature, °C
V	flow rate, m^3/s
Y	absolute humidity

Greek symbols

ρ	air density
λ	dimensionless parameter

Subscripts and superscripts

a	outside air
rec	recirculated air
reg	regeneration air
T	Total air
w	desiccant material
*	non-dimensional

References

[1] Kuehn, T.H, Ramsey, J.W., Threlkeld, J.L., 1998, *Thermal Environmental Engineering*, Prentice-Hall, New Jersey, USA.

[2] Mazei, P., Minichiello, F., Palma, D., Desiccant HVAC Systems for Commercial Buildings, 2002, Applied thermal Engineering, (22), pp: 545-560.

[3] Mandegari, M., Pahlavanzadeh, H., F., 2009, Introduction of a New Definition for effectiveness of desiccant Wheels, Energy, (34), pp: 797-803.

[4] Niu, J.L., Zhang, L.Z, Zuo, H.G., 2002, Energy Saving Potential of Chilled-Ceiling

combined with desiccant Cooling in Hot and Humid Climates, Energy and Buildings, (62), pp:487-495

[5] La, D. et al., 2010, Technical Development of Rotary Desiccant Dehumidification and Air-Conditioning: A Review, Renewable and Sustainable Energy Reviews, (14), pp: 130-147.

[6] PSYCHROMETRIC ANALYSIS, 2007, Software Package, Ver.6, ASHRAE, Atlanta, USA..

[7] Wang, S.K., 2002, Handbook of Air-Conditioning and Refrigeration, Mc-Graw Hill, New York, USA.

[8] Nobrega, C.E., Brum, N.C.L.; 2009, Modelling and Simulation of Heat and Enthalpy Recovery Wheels", Energy (34), pp: 2063-2068.

[9] Nobrega, C.E., Brum, N.C.L.; 2009, Influence of Isotherm Shape over Desiccant Cooling Cycles Performance, Heat Transfer Engineering 30(4), pp: 302-308.

[10] Nobrega, C.E., Brum, N.C.L.; 2007, A Comparative Study of Heat and Enthalpy Rotary Exchangers, *Proc. 20th International Conference on Efficiency, Cost, Optimization, Simulation and Environmental Impact of Energy Systems, ECOS 2007,* ed. SG Editoriali, pp.1233-1239.

[11] Kanoglu, M., Bolatturk, A., Altuntop, N., 2007, Effect of Ambient Conditions on the First and Second Law Performance of an Open Desiccant Cooling Process, Renewable Energy (32), pp: 931-946.

Appendix

$$RSHF = \frac{RSH}{RSH + RLH} \quad (A.1)$$

$$RTH = RSH + RLH \quad (A.2)$$

$$OASH = \rho C_P V_T (T_{OA} - T_i) \quad (A.3)$$

$$OALH = \rho h_g V_T (Y_{OA} - Y_i) \quad (A.4)$$

$$OATH = OASH + OALH \quad (A.5)$$

$$ESHF = \frac{RSH + BF\left(OASH\right) + REHEAT}{RTH + BF(OATH)} \quad (A.6)$$

$$ERSH = RSH + BF(OASH) + REHEAT \quad (A.7)$$

$$V_T = \frac{ERSH}{\rho C_P (T_6 - T_D)(1 - BF)} \quad (A.8)$$

$$V_T = V_{OA} + V_{rec} \quad (A.9)$$

$$T_E = \frac{V_{OA} T_{OA} + V_{rec} T_6}{V_T} \quad (A.10)$$

$$Y_E = \frac{V_{OA} Y_{OA} + V_{rec} Y_6}{V_T} \quad (A.11)$$

$$T_M = T_D + BF\left(T_E - T_D\right) \quad (A.12)$$

$$T_i = T_M + \frac{REHEAT}{\rho C_P V_T} \quad (A.13)$$

$$GTH = RTH + OATH + REHEAT \quad (A.14)$$

$$V_T = \frac{RSH}{\rho C_P (T_6 - T_5)} \quad (A.15)$$

$$\frac{\partial Y}{\partial x^*} = Y_w - Y \quad (A.16)$$

$$\frac{\partial W}{\partial t^*} = \lambda_2 \left(Y - Y_w\right) \quad (A.17)$$

$$\frac{\partial T}{\partial x^*} = T_w - T \quad (A.18)$$

$$\frac{\partial T_w}{\partial t^*} = \left(T - T_w\right) + \lambda_1 \left(Y - Y_w\right) \quad (A.19)$$

$$\varepsilon_{EC} = \frac{T_4 - T_5}{T_4 - T_{SAT}} \quad (A.20)$$

Active and Passive Desiccant Wheels for Air-Conditioning in Mediterranean Areas

Koronaki I[a]. , Rogdakis E.[b], Kakatsiou K[c].

[a] *Mechanical Engineering Department, National Technical University of Athens, Greece*
[b] *Mechanical Engineering Department, National Technical University of Athens, Greece*
[c] *Mechanical Engineering Department, National Technical University of Athens, Greece*

Abstract: This paper examines five different desiccant-based dehumidification systems using alternative arrangements of an enthalpy wheel and/or desiccant wheel and/or sensible heat wheel will be applied and compared according to their coefficient of performance. The essence of a desiccant dehumidifier is a wheel rotating at 10-60 rpm and packed with porous solid desiccant. The air to be dehumidified flows through a portion of the wheel and moisture is adsorbed. The wheel then rotates into an air stream that has been heated in order to regenerate the desiccant by driving moisture from the desiccant.
Three kinds of rotating wheels, a sensible heat wheel, which lacks a desiccant and so transfers only sensible heat; a passive desiccant wheel which transfers both sensible and latent heat and will henceforth be referred to as an enthalpy wheel; and an active desiccant wheel, which removes moisture while adding heat to the incoming air stream and will henceforth be referred to simply as a desiccant wheel, will be examined and compared in combination in various ways.

Keywords: Desiccant cooling, desiccant wheels, air-conditioning, coefficient of performance, evaporative coolers.

1. Introduction

Evaporative and desiccant cooling technology for air conditioning has been increased during the last decade, as an alternative to the conventional vapor compression systems which are responsible for large amounts of CO_2 release to the environment as well as for the use of harmful refrigerants regarding greenhouse effect and ozone depletion potential.
Unlike conventional evaporative cooling systems, desiccant cooling systems are open heat driven cycles that provide indoor comfort even in hot and humid weather. All studies have shown that, since the air does not have to be cooled below its dew point, utilization of waste heat or solar energy can be realized and that reduction in humidity, corrosion and microbiologic activity is achieved. The entire operation takes place at atmospheric pressure, eliminating the need for capital-intensive, pressure-sealed units. This makes them very environmentally friendly technology choice if properly designed, sized and managed in use.

1.1 Passive desiccant wheels

Passive desiccants wheels do not remove much moisture, and the moisture content of the supply air leaving the wheel depends on the dryness of exhaust air leaving the building. However, passive wheels reactivate the desiccant adiabatically. They require no energy apart from what is contained in the exhaust airstream. So hourly operating costs are considerably lower than for active desiccant wheels. They are used in commercial buildings to dehumidify ventilation air. Passive desiccants usually dry cheaply, helping the cooling system to moderate the humidity.

1.2 Active desiccant wheels

An advantage of active desiccant wheels is that they dry the supply air continuously, in all weather conditions, regardless of the moisture content of the exhaust air. Also, they can be reactivated with outside air instead of exhaust air, so they offer installation flexibility because the exhaust air does not have to be brought back to the unit. On the other

Corresponding Author: Koronaki I, koronaki@central.ntua.gr

hand, active wheels require heat input to dry the air, which adds operating cost.

The amount of moisture removed by an active desiccant wheel depends on a number of variables including the entering air temperature and moisture, the type and quantity of desiccant, the depth of the wheel, the surface area of the honeycomb, the velocity of air moving through the wheel and the wheel rotation speed.

2. System configurations

In this study, the ventilation cycle (Pennington cycle) shown in Figure 1, and recirculation cycle shown in Figure 2 were investigated in which a rotary heat exchanger was saturated with a solid desiccant, converting the heat exchanger into an adiabatic regenerative dehumidifier, which takes in ambient air and adsorbs the moisture in it. This air is then sensibly and again evaporatively cooled before being introduced into the conditioned space. The return air is first evaporatively cooled and allowed to pass through a sensible heat exchanger to recover the heat of adsorption from the supply air. It is then heated with a low grade thermal energy source and used to regenerate the desiccant.

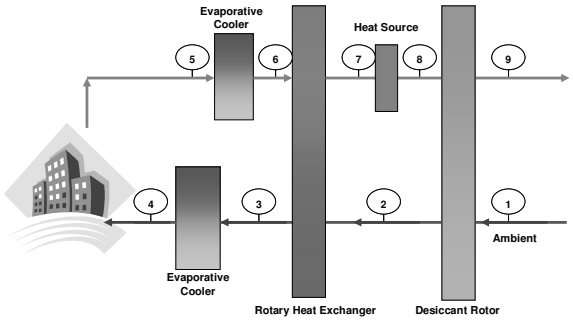

Fig. 1. Schematic of open desiccant cooling system operating in ventilation mode.

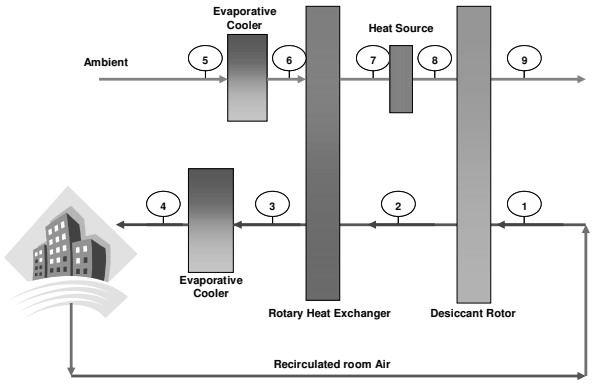

Fig. 2. Schematic of open desiccant cooling system operating in recirculation mode.

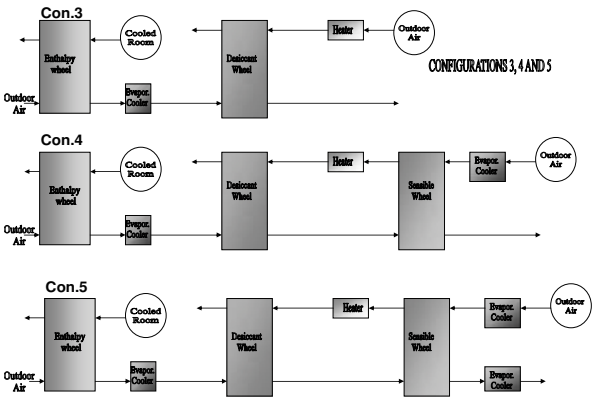

Fig. 3. Desiccant-based dehumidification systems using alternative arrangements of an enthalpy wheel, a desiccant wheel and a sensible heat wheel

Figure 3 shows three more systems which are examined using an enthalpy, a desiccant and a sensible heat wheel in various combinations.

Configuration 3 involves an enthalpy wheel, a cooling coil and a desiccant wheel. The incoming air is first cooled and then dehumidified by the enthalpy wheel, and then it is cooled further if needed with a cooling coil before passing through the desiccant wheel. The air entering the desiccant wheel is near saturation, so the performance of the desiccant

Corresponding Author: Koronaki I, koronaki@central.ntua.gr

wheel is enhanced while permitting moderate regeneration temperatures.

Configuration 4 involves an enthalpy, a desiccant and a sensible heat wheel, as well as an option to bypass the desiccant and sensible heat wheels when the enthalpy wheel alone provides sufficient dehumidification.

Configuration 5 is similar to 4, except that waste or solar heat outside air is used to regenerate the desiccant wheel.

A computer program has been developed to simulate the performance of the above desiccant cooling configurations.

For the simulation of the dehumidifier the analogy method of Banks [5] was used. The dehumidifier wheel has been taken to be of rotating configuration. The wheel is simultaneously regenerated by passing hot air through the half sector.

Design conditions

The parameters that affect systems design are: ambient conditions, inside (room) conditions, regeneration air temperature before the dehumidifier, supply and return air flow rates, and design sensible and latent cooling loads. For the present analysis the following were taken into account:

Ambient conditions. Ambient conditions are based on ARI Standard 1060 (2005). These values are T_1 (DB)=35°C, T_1 (WB)=24°C

Inside (room) conditions. Recommended standard design conditions for a residential air conditioner are based on ARI Standard 1060 (2005) and the values are T_5 (DB)=26.7°C, RH_5 = 50%

Regeneration air temperature. The air coming out of the conditioned space undergoes different processes of cooling and then heating depending upon the cooling and heating requirements of the process air. This air is evaporatively cooled before being introduced into the rotary heat exchanger. It is then heated with a low grade thermal energy source and used to regenerate the desiccant. Hence, fixing the final state of air for the regeneration process would give a better picture of the influence of this constraint on the cycle. In this study, this was fixed at various temperatures 75, 90, 100°C. These temperatures are also proven acceptable according to the studies performed on a rotary dehumidifier.

Sensible Heat Factor expresses the ratio between sensible heat load and total heat load in the room. This coefficient was varied during the analysis from 0.35 to 0.90.

Two performance indices, COP and dehumidification capacity were predicted from the computer simulation results.

The COP value was calculated as follows:

$$COP = \frac{Enthalpy\ \ difference\ \ room\ \ and\ \ \sup ply\ \ air}{\text{Regenerati on heat per unit process air mass flowrate}} * \frac{1}{ratio} \quad (1)$$

where ratio is the ratio of mass flow rate at the regeneration to the process air stream, thus ratio=m_{reg}/m_{proc}

3. Results and discussions

The results are given in Fig. 4 to 8 for various values of SHF, ratio and regeneration temperature.

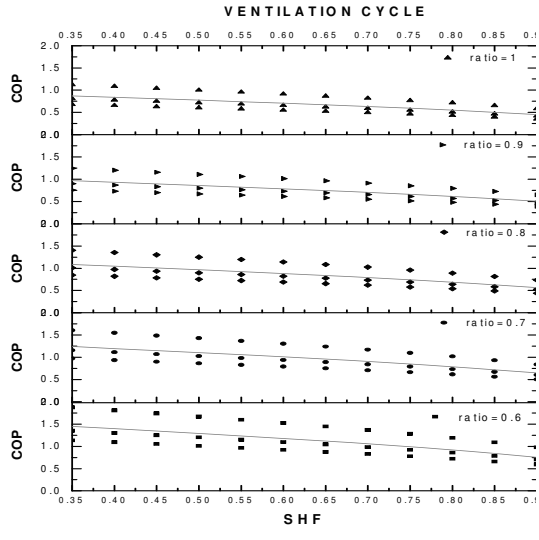

Fig. 4. Coefficient of Performance in Ventilation cycle with different ratios, SHF and regeneration temperatures (75 °C the lowest curves, 90 °C the middle ones and 100 °C the upper).

Corresponding Author: Koronaki I, koronaki@central.ntua.gr

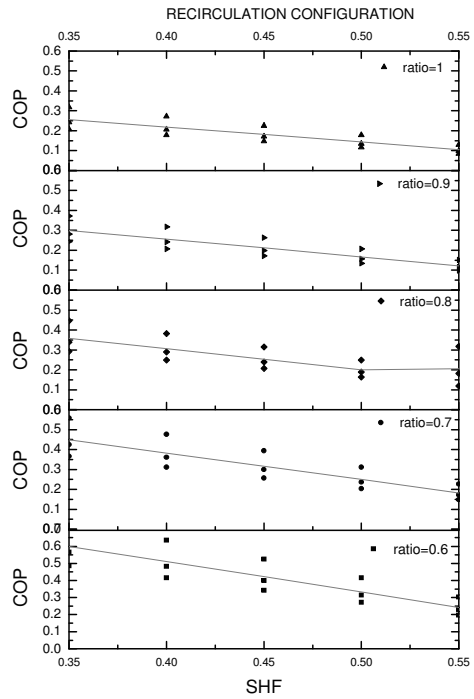

Fig. 5. Coefficient of Performance in Recirculation cycle with different ratios, SHF and regeneration temperatures.

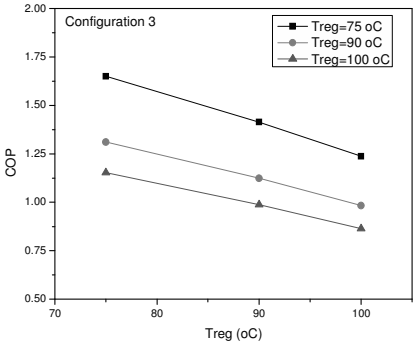

Fig. 6. Coefficient of Performance in Configuration 3 with different regeneration temperatures.

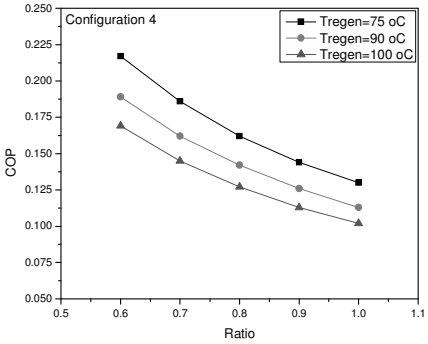

Fig. 7. Coefficient of Performance in Configuration 4 with different regeneration temperatures.

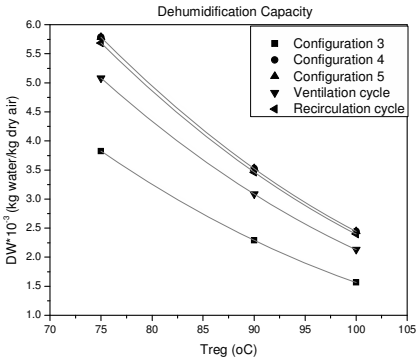

Fig. 8. Dehumidification ability in all five cycles.

In this paper, the performance of several cycles for solid desiccant air-conditioning systems has been predicted.

The main results emerging from these results are as follows.

1. The COP values drop as the ratio increases for all cycles. Ratio is an important factor in deciding the actual COP, as it determines the mass flow rate that can be dehumidified.
2. Between the above five cycles, Configuration 3 gives better performance for all regeneration temperatures. Of course, it has no additional heat exchanger reducing the amount of heat given for the cycle. Although its performance is better than the other cycles, it cannot perform effectively as a device that dehumidifies the indoor air stream.
3. Cycles using evaporative coolers give even better performance due to the high effectiveness values of

Corresponding Author: Koronaki I, koronaki@central.ntua.gr

the Evaporative Coolers. The capital costs involved are also expected to be much higher.

4. Conclusions

Taking into account the above analysis for all the models it could be derived that the performance of a desiccant system for space air-conditioning depends on a group of parameters and conditions, implicating the system's operation parameters such as the Sensible Heat Factor, the achieved Regeneration Temperature and environmental conditions such as ambient temperature and humidity ratio.

1. Simple desiccant cooling cycles as the Ventilation cycle, with evaporative coolers, show small fluctuations in the COP values with changing SHF values.

2. The novel conceptual cycle (Configuration 5) gives a reasonably high and consistent dehumidification capacity for the outdoor conditions studied in this paper.

3. Cycles using wet-surface heat exchangers (evaporative coolers) give higher performance (COP) than other cycles.

4. Cycles with sensible heat exchangers (SHE) have a greater effect on dehumidification capacity than cycles without them. This is because SHE also affect the air temperature at the inlet to the dehumidifier.

5. Amongst the analyzed cycles, Ventilation Cycle has been found to have better Coefficient of Performance than the other cycles, whilst Configuration 5 has been found to dehumidify better the incoming to the room air.

The above results are useful for the development of desiccant cooling systems that are free from CFCs, and which require much less electric power consumption. Further work in this direction is in progress.

Corresponding Author: Koronaki I, koronaki@central.ntua.gr

References

[1] P. Mavroudaki, C.B. Beggs, P.A. Sleigh, S.P. Halliday, 2002, The potential for solar powered single-stage desiccant cooling in southern Europe. **Applied Thermal Engineering**; 22; 1129-1140.

[2] S.P. Halliday, C.B. Beggs, P.A. Sleigh, 2002, The use of solar desiccant cooling in the UK: a feasibility study. **Applied Thermal Engineering**; 22; 1327-1338.

[3] The American Society of Heating, Refrigerating and Air-Conditioning Engineers, 2004, **ASHRAE Handbook: HVAC Systems and Equipment.** SI Edition; Supported by ASHRAE Research.

[4] R.K. Collier, 1996, **Desiccant dehumidification and cooling systems: Assessment and analysis**, Battelle Pacific Northwest Laboratories, Collier Engineering, p. 20-24, 27, 29, 32, 43, 46, 52-57.

[5] I.L. Maclaine-Cross, (1988). Proposal for a desiccant air conditioning system, **ASHRAE Trans.** 94(2), 1997-2009.

[6] J.J. Jurinak, J.W. Mitchell, 1984, Effect of matrix properties on the performance of a counterflow rotary dehumidifier. **ASME J Heat Transfer;**106(3):638–45.

[7] P.J. Banks, 1985, Prediction of heat and mass regenerator performance using nonlinear analogy method:Part2-Comparision of Methods. **J Heat Transfer**;107(1):230–7.

[8] A. Kodama, T. Hirayama, M. Goto, T. Hirose, R.E. Critoph, 2001, The use of psychometric charts for the optimization of a thermal swing desiccant wheel, **Applied Thermal Engineering** 21, 1657–1674.

Thermoeconomic Diagnosis to Micro – Polygeneration System.

García-Castillo L. M, Gutiérrez-González A. P, Rangel-Hernández V. H,

Zaleta-Aguilar A.

Department of Mechanical Engineering, University of Guanajuato

Salamanca – Valle de Sgo. Km. 3.5 + 1.8, Salamanca, Guanajuato. C.P. 36885. Mexico.

Abstract:

In this paper thermoeconomic analysis is performance from to thermodynamics laws and economic principles, applied to micro – polygeneration systems that use an organic waste, in order to assess their potential use in micro- company in the industrial and agricultural sector of Mexico. The analysis is carried out by the laws of thermodynamics and the theory of energy cost this is a main methodological approach in the field of thermoeconomic. This study focuses in polygeneration system on the range to 10 – 100 kW, which consists of a system of biogas digesters, stationary generator methane gas engine y heat recovery systems, which are proposed as an alternative to micro – polygeneration systems.

Key words: Micro – polygeneration, thermoeconomic, exergy.

1. Introduction

A thermoeconomic analysis is a very powerful tool for the diagnosis of thermal systems because it identifies the type, place and magnitude of the thermal losses in them. To identify and to assess the losses permits to improve the design of those systems. This means that by the application of the thermoeconomic concepts, it is possible to calculate the impact of an anomaly upon the system, for instance, in terms of additional fuel consumption. The system under study is a micro - polygeneration system because is has the simultaneous production of bio gas, electric and thermal energy. It is composed of a bio digester with an 600 m^3/day capacity, a gas engine with an 60 kW capacity and a heat recovery installed which uses the exhaust gases of combustion for hot water generation. The thermoeconomic analysis demonstrates that with this configuration, the micro polygeneration system needs to be improved.

A thermoeconomic analysis combines exergy analysis and economic principles in order to provide information that is not available, but crucial in the design and operation of energy systems.

The application of the thermoecomonic analysis has been developed since 1990 by Valero and co-workers [1], whom have shown the principle characteristics of this approach.

The present paper gives the results on the exergy analysis of a gas cycle – based polygeneration power plant. The thermoeconomic analysis is applied to the engine and equipments involved in the micro polygeneration system. The power plant is composed of four systems. They are the bio digester, gas engine, generator and heat recovery.

2. Assumptions used in the analysis.

Fig. 1 shows the schematic diagram of a micro – polygeneration system, which uses bio gas as fuel and water as refrigerant.

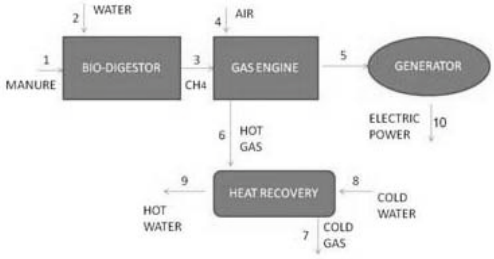

Figure 1: Micro – polygeneration system sketch.

For the purpose of analysis the following assumptions are made:

- The reference environment state for the system is defined by the environmental conditions; P=1.01 bar y T=25 °C.
- Pressure losses in the heat recovery from combustion gases are less than 10 %.
- The water in the heat recovery was added to liquid state
- The system is in steady state.

3. Thermodynamic analysis

The second law analysis, i.e the exergy analysis, calculates the system performance based on exergy, which is defined as the maximum possible reversible work obtainable in bringing the state of the system to equilibrium with that of environment. The total exergy of a system can be divided into two components: physical exergy and chemical exergy;

$$\dot{E} = \dot{E}^{Ph} + \dot{E}^{Ch} \qquad (1)$$

For each stream the specific exergy is calculated as the amount of physical and chemical inputs, neglecting kinetic and potential energy, as show in the equation

$$e_i = e_i^{F} + e_i^{Q} = \left(h_i - h_{i,0}\right) - T_0\left(s_i - s_{i,0}\right) + e_i^{Q} \qquad (2)$$

where h_0, T_0, s_0 are evaluated at the dead state. The physical exergy component is associated whit the work obtainable in bringing a stream of matter from its initial state to a state that is in thermal and mechanical equilibrium with the environment.

The chemical exergy component is associated whit the work obtainable in bringing a stream of matter from the state that is in thermal and mechanical equilibrium with the environment to a state of that stream of matter that is in the most stable configuration in equilibrium whit the environment.

The composition of biogas used is determined in Table 1.

Table 1: The composition of biogas

Gas	%
Methane CH_4	55 – 70
Carbon Dioxide CO_2	35 – 40
Hydrogen H_2	1 – 3
Nitrogen N_2	0.5 – 3

The chemical of bio gas is obtained from Kotas [4] and using the composition of the table is determined that the estimated value is 51 875 kJ/kg.

A detailed exergy analysis includes calculating exergy destruction, exergy loss, exergy efficiency, and exergy destruction ratio in each component of the system along whit the overall system. In a control volume the steady – state exergy balance can be expressed as:

$$\sum \dot{E}_{in} - \sum \dot{E}_{out} - \dot{Q}\left(1 - \frac{T_0}{T}\right) - \dot{W} - \dot{E}_D = 0 \qquad (3)$$

The exergy destruction in a component is calculated from the exergy balance as:

$$\dot{E}_{D,k} = \dot{E}_{F,k} - \dot{E}_{P,k} - \dot{E}_{L,k} \qquad (4)$$

The exergy efficiency of the components and the overall system shows what percentage of the fuel exergy can be found in the product exergy.

$$\varepsilon_k = \dot{E}_{P,k} / \dot{E}_{L,k} \qquad (5)$$

4. Thermoeconomic analysis

The thermoeconomic analysis requires a proper Fuel – Product – Loss definition of the system to show the real production purpose of its subsystems by attributing a well defined role.

The exergy cost (B*),defines the amount of total exergy resources needed in the upstream processes that came into existence in the thermodynamic conditions specific to a point in a process exergy. The unit exergy cost is the relation between exergy and the exergy cost of an item or thermodynamic condition for a process exergy.

The exergoeconomics cost of all the flows that appear in the system´s F-P-L definition are obtained through exergy costing principles, discussed by Bejan et al. [3]. Exergy costing involves formulation of cost balances for each component. A cost balance applied to the *kth* component shows that the sum of the cost rates associated with all exiting streams equals the sum of cost rates of all entering streams plus the appropriate charge due to the capital investment (Z_k^{Cl}) and operating and maintenance expenses (Z_k^{OM}). Thus, the total cost of the exiting exergy streams equals the total expenditure to obtain them. Accordingly, for a component receiving a heat transfer and generating power, the cost balance equation would be,

Exergetic cost theory is a fundamental concept for Thermoeconomic analysis, which proposes an allocation of costs based on resources, products and losses suggests a breakdown of the production system under the concept that a process or production system may be regarded as a set of subsystems linked by flows of matter and energy.

$$\sum_e \dot{C}_{e,k} + \dot{C}_{w,k} = \dot{C}_{q,k} + \sum_i \dot{C}_{i,k} + \dot{Z}_k \tag{6}$$

Where

$$\dot{Z}_k = \dot{Z}_k^{CI} + \dot{Z}_k^{OM}$$

$$\sum_e \left(c_e \dot{E}_e\right)_k + c_{w,k}\dot{W}_k = c_{q,k}\dot{E}_{q,k} + \sum_i \left(c_i \dot{E}_i\right)_k + \dot{Z}_k \tag{7}$$

The variables in Eq. (7) are determined by solving a system of equations, i.e. the cost balance equations along with required auxiliary equations.

5. Results

With the implementation of previous theories and the use of thermodynamic laws determines the energy and the exergy balances for each stream which accompany the process.

Table 2 shows the characteristics of the stream involved in the process and the exergy generated in each.

Table 2: Streams specifications.

Stream	Description	Mass flow (kg/s)	Pressure (bar)	Temperature (°C)	Exergy (kJ/kg)	(kW)
1	Manure	-	1.013	25	0	0
2	Water	-	1.013	25	0	0
3	Methane	0.003994	1.10	25	65.06	0.283
4	Air	0.07065	1.013	25	0.04425	0,00313
5	Engine power	-	-	-	-	50.97
6	Hot Gas	0.08118	1.148	426.7	164.4	13.34
7	Cold Gas	0.08118	1.02	384	128.6	10.44
8	Cold Water	0.04	1.20	25	0.0191	0.0007
9	Hot water	0.04	1.154	54	5.614	0.2245
10	Electric power	-	-	-	-	48.43

Table 3 shows the relationship obtained bye applying the F-P-R, which allows for the values of B* for each stream.

Table 3: Fuel – products – loss definitions of the micro - polygeneration system.

Subsystems	Fuels	Products	Losses
Bio digestor	$B^*_1 + B^*_2$	B^*_3	-
Gas Engine	$B^*_3 + B^*_4$	B^*_5	B^*_6
Generator	B^*_5	B^*_{10}	-
Heat Recovery	B^*_6-B^*_7	B^*_9-B^*_8	-

Table 4 shows the results when applying the Exergy Cost Theory; we see the value for each process stream.

Table 4: Thermodynamics Property and Exergy Cost.

		Thermodynamics Properties				Exergy Cost	
Stream	m (kg/seg)	P	T	E (kW)	B (kW)	B* (kW)	k*
1	-	1.013	25	0	0	0	-
2	-	1.013	25	0	0.00313	0.00313	1
3	0.003994	1.10	25	65.06	0.283	0.00313	0.11
4	0.07065	1.013	25	0.04425	0.00313	0.00313	1
5	-	-	-	-	50.97	0.00626	0.00013
6	0.08118	1.148	426.7	164.4	13.34	0	0
7	0.08118	1.02	384	128.6	10.44	0	0
8	0.04	1.20	25	0.0191	0.0007	0.0007	1
9	0.04	1.154	54	5.614	0.2245	0.0007	00.003
10	-	-	-	-	48.43	0.00626	00.00013

Table 5 shows the cost per unit time and the generated power bye the system for each stream.

Tabla 5: Thermodynamic cost for the system.

Stream	Cost rates ($/h)	Cost per exergy unit ($/kW)
1	0	0
2	0	0
3	0.0003782	0.001336
4	0	0
5	0.0001415	0.0003809
6	0	0
7	0	0
8	0	0.00002
9	7.3 e-6	0.000032
10	6 e-5	0.01942

4. Conclusions

The stream 5 has a higher exergy which represents the power generated by the combustion engine to bio gas.

The stream 5 has a higher exergy cost, because it is associated with the fuel source for bio gas generation. These not surprising given that these streams represent the driving force for the micro polygeneration system.

Heat recovery is not an exergetic cost because it uses the removal of heat from the waste stream (combustion gases) engine and also water eating uses a gravity pumping system eliminates the use of a pumping system.

However for industrial use is not recommended because the amount of water used for heat recovery is small for this power range, so it does not meet the demands required by the industry.

We recommend using a heat recovery system positioned in the engine cooling system.

Nomenclature.

Nomenclature	
B^*	Exergetic Cost
C_e	Cost of exergy associated with material stream
c_e	Cost per unit of exergy associated with material stream
C_q	Cost of exergy associated with transfer heat
c_q	Cost per unit of exergy associated with transfer heat
C_w	Cost of exergy associated with transfer power
c_w	Cost per unit of exergy associated with transfer power
E	Total Exergy
E^{Ch}	Chemical Exergy
E_D	Exergy destruction
$E_{F,k}$	Fuel Exergy
e_i	Exergy for each stream
e_i^F	Physical Exergy
E_{in}	Energy In
e_i^Q	Chemical Exergy
$E_{L,k}$	Loss Exergy
E_{out}	Energy Out
$E_{P,k}$	Product Exergy
E^{Ph}	Physical Exergy
F	Fuel
F^*	Raw Material Cost
h_i	Enthalpy
$h_{i,0}$	Enthalpy at dead state
k^*	Total Unit Cost
P	Product
P^*	Products
Q	Heat
R	Loss
S_i	Entropy
$S_{i,0}$	Entropy at dead state
T_0	Temperature
W	Power
Z_k	Total Cost
Z_k^{CI}	Capital Investment
Z_k^{OM}	Operating and Maintenance Expenses
ε_k	Exergy efficiency

References

[1]. M.A Lozano, A. Valero. Teoría del coste exegético. Abril de 1898.

[2]. Tsatsaronis, G. Pisa,J. 1994. Exergoeconomic evaluation and optimization of energy systems application to the CGAM problem, Energy, v.19,287-321 p.

[3]. Bejan, A. Tsatsaronis, G. Moran, M. 1996. Thermal design and optimization. John Wiley and sons, 542 p.

[4]. Kotas, T.J. The exergy method of thermas plant analysis, Krieger Publishing Company, Florida 1995.

[5]. Y.Mustafá "Análisis termo económico de los parámetros de la combustión en ciclos combinados con gasificación integrada" Tesis de maestria Universidad de Guanajuato. (2000).

[6]. Misra,P.K. sahoo, S. Sahoo, A. Gupta. Thermoeconomic optimization of a single effect water/LiBr vapour absorption refrigeration system. International journal of refrigeration 26 (2003); 158 – 169.

Exergy Saving Potencial and Real Cost for Centralized Chilled-Water Climatization Systems

Yarelis Valdivia [a], Juan Carlos Armas[a], Carlos Pérez[b] and Margarita Lapido[a]

[a] *Universidad de Cienfuegos, Cienfuegos, Cuba*
[b] *Universidad Autónoma de Baja California, Mexicali, México*

Abstract: The exergy method was applied to determine the exergy and monetary costs of chilled-water climatization systems. This procedure allowed to identify avoidable irreversibilities by means of operational or technical improvements assuming that a limit exists for these irreversibilities that cannot be recovered because they are implicit to design and operation conditions of equipments. The analysis showed that when varying compressor efficiency from 0.7 to 0.88, 33% of the total cost is due to investment costs. Also 3% of recoverable total costs for modified exergoeconomic factor were investment costs. This analysis was carried out for the rest of the components in the system analized and exergy saving potentials were obtained. This evaluation allows the designer to improve planning for real achievable energy saving.

Keywords: Exergy, Exergy cost, Monetary cost.

1. Introduction

Synthesis and energy systems optimization, including production costs, price of final products and many other practical problems where thermodynamics and economy are tightly related have been subjects of interest for the past two decades. The design of efficient and effective cost of systems is one of the major engineering challenges. Combining exergy and economics provides a powerful tool for a systematic study and systems optimization.

Several authors have been working on thermoeconomics applied to energy systems, for instance [1] pointed out that exergy concept is not only crucial for studies of efficiency but for economic analysis too. These criteria derived from second law of thermodynamics are a quantitative analysis tool from which it is possible to obtain the efffect of each component on the energy consumption of the system making possible to identify lost work leaks in order to prevent them and ultimately optimize the system. There are a relatively few works published on determining avoidable and unavoidable destruction of exergy and monetary flows over individual components of a system and in general on chilled-water climatization systems [2-7]. More published work has been found referred to gas turbine cogeneration [8]. Other authors have developed a new method to calculate avoidable and unavoidable exergy as well as monetary flows for individual components taking into account simple vapor-compression refrigeration systems. They quantified specific savings on the avoidable part of both exergy and monetary flows. Similary in this work, an exergy-based method to determine real exergetic and monetary cost for centralized chilled-water climatization systems is applied for avoidable and unavoidable cost determination.

2. Methodology

The exergetic analysis calculates the maximum possible energy saving under real conditions for every single equipment. On the other hand irreversibilities account for thermodynamic waste of energy and represent all of the energy that could be saved. However in practice it is not possible avoiding all irreversibilities because the effect impossed by the physical design making

Corresponding Author: Yarelis Valdivia, Email: yvaldivia@ucf.edu.cu

these irreversibilities could not be considered as a matter of energy saving.

The exergy analysis on a system can be performed by considering each component separately. Identifying the equipment where the largest exergy destruction occurs shows up the direction for potencial improvements. With exergetic analysis by components and adding cost flow determination it is possible to calculate avoidable cost of exergy losses. Based on these criteria, a realistic comparison between operation conditions and design conditions can be established and the actual energy saving computed.

2.1. Optimization procedure

Optimization procedure was developed by authors in previous study using a hybrid model [9] incorporating thermoeconomic criteria and artificial intelligence tools.

A real installation is a case base (Fig.1) with the objective to compare finals products cost between base system and optimized system obtained for same refrigeration load and reference cost of each component.

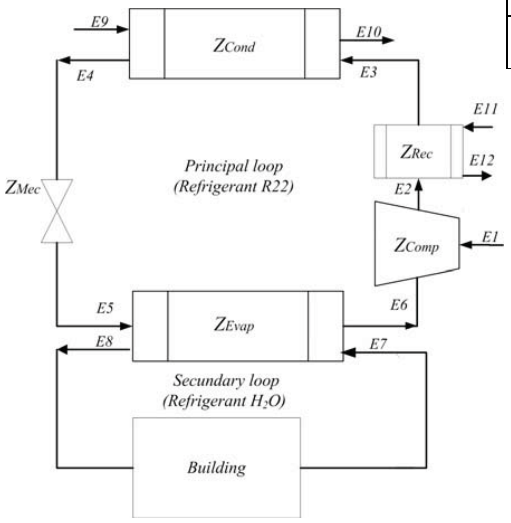

Fig. 1. Physical scheme of centralized chilled-water climatization installation.

In order to establish a thermoeconomic comparison between base case and optimized case, operational and design parameters of the system are varied: chilled water temperature (T_8), hot water temperature in recovery outlet (T_{12}), air temperature in condenser outlet (T_{10}) and compressor performance (η).

For this, GA performs a scan within a range of possible values and the results are the optimal values for design and operating conditions that the system must operate in order to obtain an optimum efficiency value that allows exergy technical savings, shown in Table 1.

Table 1. Parameter variation in determining avoidable exergy cost

Operational and design parameters	Actual case	Optimized case
Chilled water temperature	8ºC	7 ºC
Hot water temperature at recovery outlet	44.7ºC	46ºC
Air temperature at condenser outlet	35ºC	37ºC
Compressor performance, (η)	0.7	0.88

Actual and optimized cases are compared from thermoeconomic point of view intending to improve equipment efficiency and determining the percentage of avoidable irreversibilities, the reference [7] shows a function for these calculations.

Thus outflow exergies (E^*_P) are calculated for each component (1) and their irreversibilities E^*_{DZi} (2). Also zonal costs Z^*_i for each component are recalculated (3 to 5) and unitary cost of external flows entering the system are defined (fuel costs, c_F).

$$E_{P_{Zi}} = m_{out}\left[\left(h_{out} - h_0\right) - T_0\left(s_{out} - s_0\right)\right] \quad (1)$$

$$E_{D_{Zi}} = \sum E_{in} - \sum E_{out} \quad (2)$$

2.2. Equations for calculating zonal component costs

Compressor

$$Z_{cm} = Z_{R_{cm}} \left[\frac{N_{cm}}{N_{R_{cm}}} \right]^{m_{cm}} \left[\frac{\eta}{(0.9 - \eta)} \right]^{n_{cm}} \quad (3)$$

Heat exchangers

$$Z_{HE} = Z_{R_{HE}} \left[\frac{\Delta T_{\max_{IC}} - \Delta T_{\min_{HE}} \cdot (-\ln(1 - \varepsilon_{HE}))}{\ln \left[\frac{\Delta T_{\max_{HE}}}{\Delta T_{\min_{HE}}} \right]} \right] \cdot \left[\frac{E_{HE_{out}}}{T_0} \right] \quad (4)$$

Expansion device

$$Z_{Exp} = Z_{R_{Exp}} \cdot E_{Exp_{out}} \quad (5)$$

2.3. Avoidable and unavoidable costs

To determinate the cost of final products of centralized chilled-water climatization system, part form design and operation conditions given, where the operational parameters were measured in the real installation taken as a base case.
Are given the equations for determining the avoidable and unavoidable cost for the component (Z_i) of the centralized chilled-water climatization system.
To calculate avoidable and unavoidable cost are given follow equations:

Avoidable exergetic destruction unit

$$E_{DZi_{unit}}^{UN} = \left[\frac{E_{DZ_i^*}}{E_P^*} \right]^{UN} \quad (6)$$

Unavoidable exergetic destruction

$$E_{DZi}^{UN} = E_P \left[\frac{E_{DZi^*}^*}{E_P^*} \right]^{UN} \quad (7)$$

Avoidable exergetic destruction

$$E_{DZ_i^*}^{AV} = E_{DZi} - E_{DZ_i^*}^{UN} \quad (8)$$

Avoidable exergetic cost flow

$$C_{Z_i^*}^{AV} = c_F \cdot E_{DZ_i^*}^{AV} \quad (9)$$

Unavoidable exergetic cost flow

$$C_{Z^*_{\mathrm{i}}}^{\mathrm{UN}} = c_F \cdot E_{\mathrm{DZ}^*_{\mathrm{i}}}^{\mathrm{UN}} \quad (10)$$

Unavoidable cost destrucction unit

$$Z_{i\ unit}^{*UN} = \left[\frac{Z_i^*}{E_P^*} \right] \quad (11)$$

Unavoidable cost destruction

$$Z_i^{*UN} = E_{P_{Z_i^*}} \left[\frac{Z_i^*}{E_P^*} \right]^{UN} \quad (12)$$

Avoidable cost destrucction

$$Z_i^{*AV} = Z_i^* - CD_{Z_i^*}^{UN} \quad (13)$$

Exergoeconomic factor of the installation

$$f_K = \frac{Z_i^*}{Z_i^* + C_{Z_i^*}^{UN} + C_{Z_i^*}^{AV}} \times 100 \quad (14)$$

Corresponding Author: Yarelis Valdivia, Email: yvaldivia@ucf.edu.cu

In the procedure, avoidable cost flows of each component of the system are calculated, which results are shown in Table 2 to 4.

Table 2: Calculation of cost flows at new conditions

Components	E_P^* $[kW]$	E_{DZ_i} $[kW]$	$E_{DZ_i^*}$ $[kW]$	δE_{DZ_i} [%]	Z_i^* $[\$/h]$	$E_{DZ_i}^{*UN}$ $[kW]$	$E_{DZ_i}^{*UN}$ $[kW]$
Compressor	103.800	9.217	1.190	67%	0.171	1.130	8.087
Recovery	104.790	4.950	3.918	26%	0.012	3.879	1.074
Condenser	77.935	27.331	24.242	13%	0.009	23.283	4.051
Evaporator	91.180	21.660	14.840	46%	0.026	13.733	7.930

Table 3. Calculation of avoidable cost flows

Components	$C_{Z_i^*}^{AV}$ $[\$/h]$	Z_{iUnit}^{*UN} $[\$/kWh]$	Z_i^{*UN} $[\$/h]$	Z_i^{*AV} $[\$/h]$	$C_{Z_i^*}^{UN}$ $[\$/h]$
Compressor	0.291	1.600 e-03	0.162	8.700 e-03	0.047
Recovery	0.039	0.115 e-03	0.012	0.119 e-03	0.140
Condenser	0.146	0.115 e-03	0.008	0.344 e-03	0.838
Evaporator	0.2855	0.290 e-03	0.024	2.00 e-03	0.494

*Table 4. Comparison between avoidable cost flows and exergoeconomic factor fK y f*K.*

Components	$Z_i^* + C_{Z_i^*}^{UN+AV}$ $[\$/h]$	$Z_i^{*AV} + C_{Z_i^*}^{AV}$ $[\$/h]$	$\frac{Z_i^{*AV} + C_{Z_i^*}^{AV}}{Z_i^* + C_{Z_i^*}^{UN+AV}}$	f_K	f_K^*
Compressor	0.508	0.2998	59%	33%	3%
Recovery	0.190	0.039	19%	6%	0.3%
Condenser	0.993	0.146	15 %	0.8 %	0.2 %
Evaporator	0.806	0.287	36%	3%	0.6%

Table 4 shows the relation between exergoeconomic factor of the installation f_K and the modified exergoeconomic factor f^*_K. Factor f_K indicates the contribution of investment cost on total costs associated to each component:

$$Z^*_i + C_{Zi^*}^{UN+AV} \quad (15)$$

While factor f^*_K shows the contribution of investment cost recoverable on total cost recoverable associated to each component of the system:

$$Z^{*AV}_i + C_{Zi^*}^{AV} \quad (16)$$

In the specific case of the compressor, factor f_K shows that 33% of the total cost associated to this component is for investment cost, while factor f^*_K shows that 3% of the total

cost recoverable of the compressor is investment costs.

As an important aspect to note is from consideration in this component, the percentage of total costs could be theoretically prevented with current technology and economic environment by approximately 60%.

Conclusions

1. With the study of technical savings potential of exergy in each component, can be obtained their optimum ranges of work, allowing the designer to have a quantitative and qualitative criteria of possible variants to execute the selection of the equipment or modify the operational strategies.

2. The study of savings potential of exergy allows stratification of avoidable and unavoidable potential of irreversibilities of the components of the system, making concrete plans about true potential of savings. This evaluation differs from what exist in practice, in which it work on an impressive way with a potential savings covering the total destruction (avoidable and unavoidable).
3. From detailed study of exergetic and monetary flows, exergoeconomic factor of the installation was able to identify that their small values correspond to the behavior of avoidable cost flows, then making changes to the system it was found that there is a considerable avoidable potential (20.04 kW).

Nomenclature

A	area, m^2
C	exergy cost flow, $/hr
c_F	fuel costs
E	output exergetic current flows, kW
ED	irreversibilities of output exergetic flows
EP	output exergy flows
fK	exergoeconomic factor of the installation, %
fK*	modify exergoeconomic factor, %
h	enthalpy, kJ/kg
I	irreversibility, kW
m	mass flow rate, kg/s
N	power, kW
Ncm	exergetic product of compressor, kW
N_{Rcm}	reference power, kW
Q	heat flow, kW
s	entropy, kJ/kgK
T	temperature, °C
TML	logarithmic mean temperature
ΔT	temperature difference
U	overall heat transfer coefficient, kW/m^2K
Z	zonal cost, $
ZR	reference cost, $/kW
Zi*	zonal cost for components, $/hr

Greek Symbols

ε	effectiveness
η	compressor performance

Subscripts and superscripts

UN	unavoidable
AV	avoidable
air	air
Cond	condenser
D	destruction
in	inlet
Evap	evaporator
H2O	water
i	component
HE	heat exchanger
out	outlet
max	maximum
min	minimum
Exp	expansion device
mcm	exponent power ratio
ncm	exponent efficiency ratio
R	reference
Rec	recovery
unit	unit
0	environmental conditions

Corresponding Author: Yarelis Valdivia, Email: yvaldivia@ucf.edu.cu

References

[1] Wall, G., 1993, Exergy, ecology and democracy-concepts of a vital society, ENSEC' 93, Int. Conferens on Energy Systems and Ecology, Cracow, Poland, July 5-9.

[2] Cruz Fonticiella, O.M.; González Petit Jean, M.L., 2006a, Hacia un costo real del flujo exergético y monetario de un sistema de refrigeración por compresión de vapor, Ponencia COMEC. 27 al 30 de Noviembre 2006a. UCLV. Santa Clara. Cuba.

[3] Cruz Fonticiella, O.M.; González Petit Jean, M.L., 2006b, Cálculo del costo real de la climatización de salas de control de la Industria Azucarera, Centro Azúcar No. 4. Noviembre-Diciembre.

[4] Dentice d´Accadia, M.; De Rossi, F., 1998, Thermoeconomic optimization of a refrigeration plant, International Journal of Refrigeration, Elsevier Science Ltd. and IIR, Vol 21. No.1, pp. 42-54.

[5] Dentice d´Accadia, M.; Vanoli. L., 2004, Thermoeconomic optimization of the condenser in a vapour compression heat pump, International Journal of Refrigeration 27, Elsevier Ltd, pp. 433-441.

[6] De Rossi F., et.al., 1999, EASY, Exergetic Analysis of Vapour Compression Systems, Napoli. Italia, Liguore Editore.

[7] Armas Valdes, Juan C., 2008a, Procedimiento para la optimización de sistemas de climatización centralizados por agua helada desde la etapa de diseño conceptual, Ph.D thesis, CEEMA, UCF, Cuba.

[8] El-Sayed, Yehia M., 2003, The Thermoeconomics of Energy Conversions Advanced Energy Systems Analysis, California USA, Elsevier.

[9] Armas Valdes, Juan C., 2008b, Procedimiento para la optimización del diseño conceptual de sistemas de climatización centralizada por agua helada, Revista Energética No. 39, pp. 5-18.

[10] González, Petit Jean M. L.; Cruz Fonticiella, O.M., 2006, Método para la determinación de las destrucciones evitables e inevitables del flujo exergético y monetario de un sistema de refrigeración por compresión de vapor. Investigación, Conjunta UV- UCLV, Xalapa. Ver. México.

[11] Tsatsaroni, G.; Park, Moung-Ho., 2002, On avoidable and unavoidable exergy destructions and investment costs in thermal systems, Energy Conversion & Management 43, Pergamon, Elsevier Science Ltd. pp. 1259-1270.

Preliminary Study of a 400Hz Travelling Wave Thermoacoustic Refrigerator

Bo Yu[a,b], Wei Dai[a], Ercang Luo[a]

[a] *Key Laboratory of Cryogenics, Technical Institute of Physics and Chemistry, Chinese Academy of Sciences, Beijing, China, 100190*
[b] *Graduate University of the Chinese Academy of Sciences, Beijing 100049, China*

Abstract: High frequency operation of thermoacoustic systems brings the advantages of higher power density and more compact size. This paper introduces our recent work on a 400Hz traveling wave thermoacoustic refrigerator driven by a standing wave engine. With high pressure helium gas as the working fluid, preliminary experiments give a cooling power of 48.9 W at the temperature of 0 ℃ with the heating power of the engine being 1000W. Compared with our work formerly done on a similar system with frequency below 100 Hz, the efficiency is rather low. Numeric model is used here to help analyzing the possible reason for this low efficiency.

Keywords: Thermoacoustic, Traveling wave, Refrigerator

1. Introduction

Refrigerators based on Stirling cycle have long been pursued as the possible substitutes for those conventional refrigerators based on vapour compression cycle. These refrigerators show merits of high intrinsic efficiency, environment-friendliness and multi-functional capability such as combined heat and electricity generation. The invention of travelling wave thermoacoustic refrigerator (TWTR) further boosts the technology development by using loop configuration to eliminate the displacer normally found in Stirling refrigerator without sacrificing the efficiency [1], at least, theoretically. Over the past ten years, much research work has been done [2-5].

When the TWTR is integrated with a thermoacoustic engine, the whole system could be heat-driven and of no moving components, which are very attractive for some applications. We have theoretically and experimentally investigated such a system with normal frequency around 50-80Hz [4-5]. As the system axial dimension is directly related to the acoustic wavelength which is inverse to the working frequency, higher frequency operation will lead to a much reduced system size with higher power density.

This paper introduces our recent preliminary work on a 400Hz system consisting of a thermoacoustic standing wave engine and a travelling wave refrigerator. The following section describes the details of the experiment system. The third section gives some preliminary experimental results. The fourth section gives the simulation and some discussions. Finally, some conclusions are made.

2. Experimental setup

Fig 1 shows the schematic of the traveling wave thermoacoustic refrigerator driven by a standing wave thermoacoustic engine. The TWTR mainly includes a regenerator, ambient and cold heat exchangers, a thermal buffer tube, a compliant cavity and the inertial mass. The unique characteristic of this refrigerator is that the thermal buffer tube is actually composed of five parallel

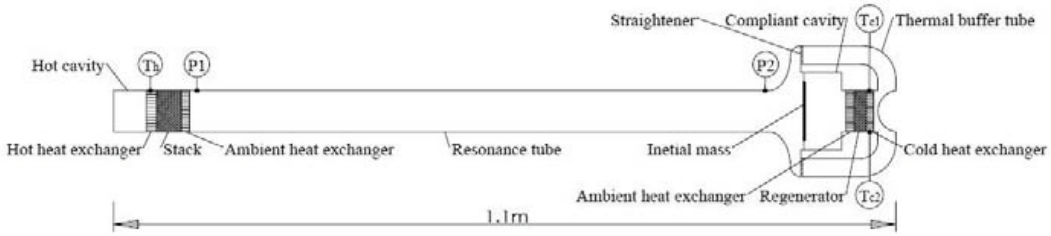

Fig.1. Schematic of the travelling wave thermoacoustic refrigerator driven by a standing wave thermoacoustic engine.

Corresponding Author: Ercang Luo, Email: ecluo@mail.ipc.ac.cn

tubes symmetrically arranged around the system axis. The inertial mass, which consists of two thin metal pieces sandwiching a piece of flexible membrane by bolts, is used to provide the inertance for the TWTR [7]. It not only makes the inertial element compact but also can suppress the DC flow in loop.

The standing wave thermoacoustic engine mainly includes a hot cavity, a stack, hot and ambient heat exchangers, resonance tube. Finely-manufactured stacks are used in the standing wave engine for a relatively high efficiency operation.

A brief on the components of the refrigerator and the engine are listed in Table 1and 2, respectively.

Table1. Details of the travelling wave thermoacoustic refrigerator

Inertial mass	14.5g-20.7g
Compliant cavity	95 mm i.d. length 45 mm
Ambient heat exchanger	50 mm i.d. 10 mm long,0.045 m^2 heat exchange area.
Regenerator	50 mm i.d. 15 mm long, 150-300 mesh stainless steel screens.
Cold heat exchanger	50 mm i.d. 10 mm long, 0.043 m^2 heat exchange area.
Thermal buffer tube	five 22-mm-diameter tubes in parallel, length 170 mm.
Flow straightener	Two pieces of 150-mesh screen.

Table2. Details of the standing wave thermoacoustic engine

Hot cavity	50mm i.d. length 40 mm
Hot heat exchanger	50 mm i.d. 20 mm long with about 0.1 m^2 heat exchange area.
Stack	50 mm i.d. 45 mm long
Ambient heat exchanger	50 mm i.d. 15 mm long, 0.078 m^2 heat exchange area.
Resonance tube	50mm i.d. length 790 mm

In the experiments, in order to increase the power density, an average pressure of 5.0MPa helium gas is used. The dynamic pressure is measured by two pressure sensors P1 and P2 which are placed near the ambient heat exchanger of engine and the inlet of the refrigerator, respectively, as shown in Fig 1. The heater block temperature of the engine is monitored by a K-type thermocouple. Electrical heaters are placed at the cold heat exchanger to simulate cooling power. Two calibrated Pt sensors are symmetrically mounted on the cold heat exchanger to measure the cold end temperature. Cooling water temperature is kept at around 20℃.

3. Experimental results

In the experiment, we mainly optimized the regenerator and the inertial mass for a good operation.

3.1 Optimization of the mesh number of the regenerator screen

An optimum regenerator not only has good heat transfer between gas and solid but also has less viscous loss. Generally, high-mesh-number-screen would be a good choice for a high operating frequency. This is because the thermal penetration depth is inversely proportional to the square root of the frequency. In fact, the thermal penetration depth is usually 4-5 times more than hydraulic radius of the regenerator according to Ref. [2-5].

In the experiment, taking the mesh number of 300 as example, the spontaneous gas oscillation started with the frequency of 398 Hz when the temperature of the heater blocker exceeded about 300℃. Then, keeping the heating power at 1000 W, we measured the cooling powers at different cooling temperatures.

Fig 2 gives the cooling power curves of the TWTR with different mesh number of regenerator screen. Obviously, mesh number of 200 gives the best performance, whose hydraulic radius is about 0.027mm. In addition, the corresponding thermal

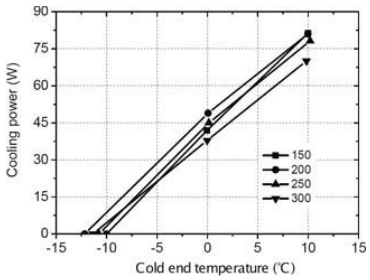

Fig.2. Cooling power curves of the TWTR with different mesh number of regenerator screen. The heating power of the engine is kept at 1 kW. The inertial mass is 16.5g.

penetration depth is about 0.05mm which is only about twice of the hydraulic radius. It may imply that the viscous loss could be more serious for a high operating frequency.

3.2 Influence of the inertial mass

The inertial mass provides the inertance for the TWTR. So, it is also important to choose an appropriate inertial mass for a good operation. Fig 3 shows the cooling power curves of the TWTR with different inertial mass. For the inertial mass of 16.5 g, a lowest cold end temperature of -12.2 ℃ was obtained and the cooling power at 0 ℃ and 10 ℃ are 48.9 W and 81 W, respectively. Thus, the corresponding total COP (i.e. cooling power divided by heating power) of the system is respectively 0.049 and 0.081, which are much lower than our previous work on the similar system with frequency below 100 Hz [4,5].

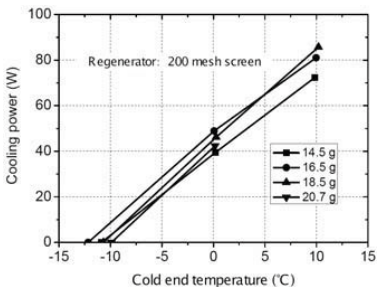

Fig.3. Cooling power curves of the TWTR with different inertial mass. The heating power of the engine is kept at 1 kW.

Fig 4 gives the onset temperature of the system, equilibrium temperature of the heater block and dynamic pressure amplitudes when the cooling temperature is 0℃. Obviously, when the inertial mass increases, the onset temperature and equilibrium temperature get higher, and dynamic pressure amplitudes become smaller. The dynamic pressure amplitude near the ambient heat exchanger of engine is about twice of the pressure at the entrance of the TWTR.

To help understanding of the reason for the low thermal efficiency, numeric simulation of the TWTR has been done as introduced in the following section.

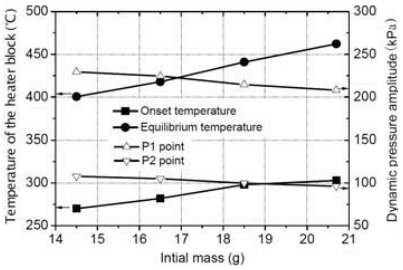

Fig.4. The onset temperature of the system, the equilibrium temperature of heater block and dynamic pressure amplitudes when the cooling temperature is 0 ℃.

4. Simulation and discussions

The numerical simulation model was based on linear thermoacoustic theory [8, 9]. Ignoring the minor losses and turbulence influence, the main control equations are

$$\frac{d\widetilde{U}}{dx} + R_1\widetilde{p} - R_3\widetilde{U} = 0 \qquad (1)$$

$$\frac{d\widetilde{p}}{dx} + R_2\widetilde{U} = 0 \qquad (2)$$

$$\frac{dH}{dx} = Q \ , H = c_1 + c_2\frac{dT_x}{dx} \qquad (3)$$

where $\widetilde{p}$, $\widetilde{U}$ are complex dynamic pressure and volume flow rate, T_x is the mean temperature of the gas, H is the total energy. Q is the heat input to the gas from the outside of the system. R_1 , R_2 , R_3 , c_1 , c_2 are functions of the fluid passage geometry, average pressure, volume flow rate, frequency, temperature distribution etc. Details of the numeric schemes has been introduced in [5,6]

Besides the control equations above, dynamic equation for the inertial mass is also required. Ignoring the damping loss, the equation is:

$$\tilde{P}(n+1) = \tilde{P}(n) - i\omega(\frac{m}{A^2} - \frac{K}{\omega^2 A^2})\tilde{U}(n) \qquad (4)$$

A is the cross sectional area, m is moving mass and K is spring constant. The volume flow rates of the both sides of the membrane are equal:

$$\tilde{U}(n+1) = \tilde{U}(n) \qquad (5)$$

Thus, with the measured frequency and the dynamic pressure at point P1, the simulation for the resonance tube and the TWTR-loop can be done.

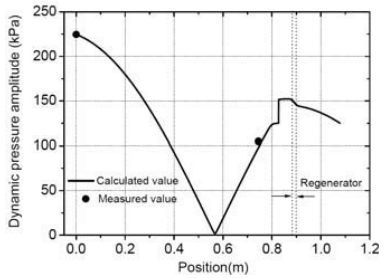

Fig.5. Distribution of dynamic pressure amplitude in resonance tube and the TWTR when the cold end temperature is 0 ℃. The inertial mass is 16.5 g. The mesh number of the regenerator is 200#.

Fig 5 gives the calculated distribution of dynamic pressure amplitude. It can be seen that the calculated and measured dynamic pressure at point P2 shows a rather good agreement.

Fig 6 gives the calculated distribution of acoustic power. From the figure, there are 62 W acoustical power emitted from the engine, which is delivered to the resonance tube. It decreases to 42 W at the entrance of the TWTR-loop. So, the COP of the TWTR at 0 ℃ is about 1 and the efficiency relative to Carnot is about 8%. The output efficiency relative to Carnot of the engine is about 7.5%. With these numbers, it implies that efficiencies of both the engine and the cooler are still rather low and needs much improvement.

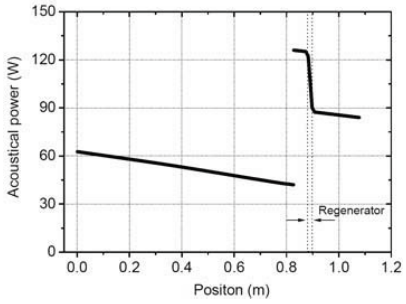

Fig.6. Distribution of acoustic power in resonance tube and the TWTR when the cold end temperature is kept at 0 ℃. The inertial mass is 16.5 g. The mesh number of the regenerator is 200#.

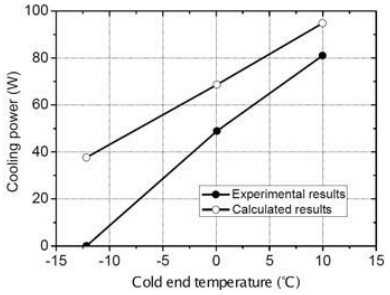

Fig.7. Comparison between the calculated and experimental results on cooling power. The inertial mass is 16.5g. The mesh number of the regenerator is 200#.

In addition, the comparison between the calculated and experimental results on cooling power is shown in Fig 7. The difference is rather large and increases as the cold end temperature decreases.

5.Conclusion

This paper introduces our recent preliminary work on a high frequency 400 Hz thermoacoustic refrigerator. Experimental results show that the thermal efficiency needs to be much improved. Working at this high frequency, the refrigerator could be very sensitive to component dimensions and minor losses, especially associated with the special loop configuration. Besides, the match between the engine and the refrigeration could also be very important for both efficiencies. Further investigation, both experimentally and numerically, are being carried out in our lab.

References

[1] Swift, G. W., Gardner, D. L., and Backhaus, S., 1999, Acoustic recovery of lost power in pulse tube refrigerators. J. Acoust. Soc. Am, 105 (2), pp. 711-724.

[2] Poese, M., 2004, An Evolution of Compact Thermoacoustic Refrigerator Design [Ph.D. Thesis], The Pennsylvania State University.

[3] Tijiani, M.E.H. and Spoelstra, S., 2008, Study of a coaxial thermoacoustic-stirling cooler. Cryogenics 48, pp. 77-82.

[4] Luo, E., et al., 2006, Thermoacoustically driven refrigerator with double thermoacoustic Stirling cycles. Applied Physics Letters, 88, 074102.

[5] Dai W., et al., 2006, Detailed study of a traveling wave thermoacoustic refrigerator driven

by a traveling wave thermoacoustic engine. J. Acoust. Soc. Am, 119 (5), pp. 2686-2692.

[6] Dai W., Luo E., Yu G., 2006, A simple method to determine the frequency of engine-included thermoacoustic systems, Cryogenics, 46(11), pp. 804-808

[7] Li S., 2009, Study on Traveling-wave Thermoacoustic Engine, Refrigerator and the Coupling Law in between [Ph.D. Thesis], Beijing: Technical Institute of Physics and Chemistry of Chinese Academy of Sciences

[8] Swift G. W., 2002, Thermoacoustics: A Unifying Perspective for Some Engines and Refrigerator. Acoustical Society of America, Sewickley, PA.

[9] Xiao, J.H., Thermoacoustic effects and thermoacoustic theory for regenerative cryocoolers (heat engines), Ph.D Dissertation, Institute of Physics, Chinese Academy of Sciences (1990) (in Chinese).

Acknowledgments: This work is supported by the National Natural Science Foundation of China (No.50625620 and No.50890181) and the National Basic Research Program of China (No.2010CB227 303).

Efficiency of an arrangement in series of irreversible thermal engines working at maximum power

Ricardo Páez-Hernández and Delfino Ladino-Luna

Área de Física de Procesos Irreversibles, Departamento de Ciencias Básicas, Universidad Autónoma Metropolitana -Azcapotzalco, Av. San Pablo No. 180 Col. Reynosa Tamaulipas CP 02200 México DF. MÉXICO

Abstract: In this work is developed a model of an arrangement in series of irreversible thermal engines like Carnot, working at maximum power, which consist of k reservoirs connected in series. At first we used three reservoirs, and we calculated its efficiency, later four and calculated its efficiency and so on until generalizing to k reservoirs, and we get an efficiency expression similar to the one of Curzon-Ahlborn, the irreversibilities are taken into account by irreversibility parameter R. Finally we present some comments.

Keywords: Irreversibility, Efficiency, Non-endoreversible, Maximum Power.

1. Introduction

Thermodynamic efficiency is known as one of the most popular criteria after Carnot [1] to analyze the performance of thermal engines. Carnot found that any engine extracting heat from a reservoir at temperature T_1 has to deliver some heat to a reservoir at lower temperature T_2 while work is at progress. Moreover, Carnot showed that maximum efficiency in the cyclic process is

$$\eta_C = 1 - T_2/T_1 \,, \tag{1}$$

which is known as Carnot efficiency. However this has little practical relevance, since it refers to processes cycling along reversible paths which deliver work infinitely slowly. The limitations of Classical Equilibrium Thermodynamics (CET) to formulate useful criteria describing the performance of real engines motivated the development of a new field, known as *Finite Time Thermodynamics* (FTT) [2,3], which keeps the formalism as close as possible to equilibrium thermodynamics while introducing simple modifications to take into account the main sources of irreversibility observed in real engines.

A paradigmatic model in FTT is owed to Curzon-Ahlborn (CA) [4], who considered a Carnot cycle at finite time and as an endoreversible approximation; i.e., the only sources of irreversibility are associated with the heat transfers between the reservoirs and the working system. Assuming that the heat transfers obey a Newton law, they found that the engine working at maximum power has the efficiency given by,

$$\eta_{CAN} = 1 - \sqrt{T_2/T_1} \,. \tag{2}$$

The previous expression was obtained firstly by Chambadal [5] and Novikov [6] using a simple model, which is named *endoreversible Curzon-Ahlborn-Novikov engine* (CAN). Equation (2) has been derived recently from theory of linear irreversible thermodynamics systems of coupled heat engines, under the assumption that all of those engines are working at maximum power output.

The endoreversible engine is mainly based in the idea that, for many processes, it is possible to conceive the internal relaxation time as being negligibly short compared with the duration of the full process. Previous research [8] has recently proposed a manner to include the internal contributions to the global entropy production by means of the Clausius inequality. If any internal irreversibility is considered, then the Clausius inequality gives,

$$\Delta S_{1w} + \Delta S_{2w} < 0, \tag{3}$$

where ΔS_{1w} is the entropy along the hot isothermal branch and ΔS_{2w} is the entropy change corresponding to the cold isothermal compression.

Expression (3) becomes an equality by means of

$$\Delta S_{1w} + R\Delta S_{2w} = 0. \tag{4}$$

Where R is called the non-endoreversibility parameter, given by

Corresponding autor: Ricardo Páez-Hernández Email: phrt@correo.azc.uam.mx

$$R = \Delta S_{1w}/|\Delta S_{2w}|. \quad (5)$$

2. Non-endoreversible engine working at maximum power

For the case of a non-endoreversible CAN engine, as the one shown in figure 1, using the second law of thermodynamics we can write,

$$\frac{Q_1}{T_{1w}} = R\frac{Q_2}{T_{2w}} \quad \text{or} \quad \frac{Q_2}{Q_1} = \frac{1}{R}\frac{T_{2w}}{T_{1w}} \quad (6)$$

where Q_1 and Q_2 are the heat exchanges between the heat engine, linked by using the linear Newton heat transfer law given by

$$Q_1 = \alpha(T_1 - T_{1w}) \quad \text{and } Q_2 = \beta(T_{2w} - T_2). \quad (7)$$

T_{1w} and T_{2w} are absolute temperatures of working substance, α and β are the thermal conductances and T_1 and T_2 are the reservoir temperatures shown in figure 1, the efficiency inside of the CAN engine is

$$\eta_{ne} = 1 - \frac{1}{R}\frac{T_{2w}}{T_{1w}}. \quad (8)$$

Following the procedure step-by-step to calculate the work per unit time, the power output, presented in [8,9], but now using (8) instead of $\eta = 1 - (T_{2w}/T_{1w})$, we have (see Appendix A)

$$W(\eta_{ne}, R) = \alpha\beta\eta_{ne}\left[\frac{RT_1(1-\eta_{ne})-T_2}{(\alpha+\beta R)(1-\eta_{ne})}\right], \quad (9)$$

The point η^*_{MP} where the function of (9) reaches its maximum value is obtained by means of $(\partial W/\partial\eta_{ne})|_{\eta^*_{MP}} = 0$, and this condition gives

$$\eta_{ne}^2 - 2\eta_{ne} + \left(1 - \frac{1}{R}\frac{T_2}{T_1}\right) = 0, \quad (10)$$

that is,

$$\eta^*_{MP} = 1 - \sqrt{\frac{T_2}{RT_1}}, \quad (11)$$

which is a kind of non-endoreversible CAN efficiency. The power output for endoreversible CAN engines is zero at $\eta_{ne} = 0$ and when $\eta = \eta_C$ [8,11], and for the non-endoreversible case $W(\eta_{ne}, R)$ has zeros at $\eta_{ne} = 0$ and we have

$$\eta_{ne} = \eta'_C = 1 - \frac{1}{R}\frac{T_2}{T_1} \quad (12)$$

that is, at some kind of non-endoreversible Carnot efficiency.

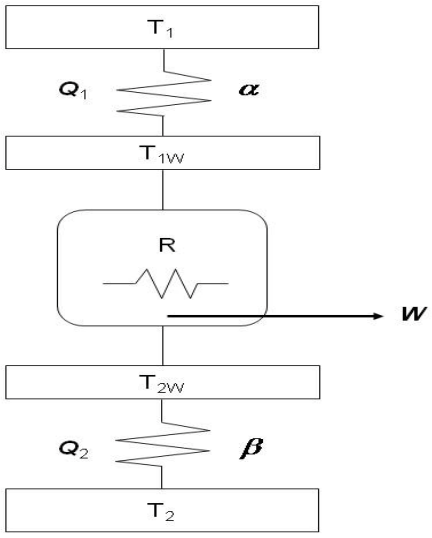

Fig. 1. Schematic for Curzon-Ahlborn-Novikov non-endoreversible engine.

3. Series of irreversible thermal engines at maximum power

Heat engines with several heat sources are common for many real-world applications such as industrial heat-recovery systems and solar energy installations, which provide heat at different rates, and even more importantly at different temperatures. For instance, on solar energy installations these differences can come about because the angle towards the sun may differ or because some solar collectors might be at a larger distance from the central plant and thus the losses along the transport pipes cause a change in the effective temperature of the engine.

A schematic diagram of a thermal engine system is shown in figure 2. Four irreversible Carnot heat engine cycles in series form a single cycle operating between reservoirs at temperatures T_H and T_C ($T_H > T_C$). Waste heat from the first cycle is used totally as the heat source for the second, third cycle. The working fluids in each cycle system flow continuously so that combined cycle operate in steady state. T_i is the sink temperature of the first cycle or the source temperature for the second.

According to figure 2, for *k=4* we obtain the thermal efficiency η as

$$\eta = \left(\dot{W}_1 + \dot{W}_2 + \dot{W}_3 + \dot{W}_4\right)/\dot{Q}_1 = \left(\dot{W}_1/\dot{Q}_1\right) + \left(\dot{W}_2/\dot{Q}_3\right)\left(\dot{Q}_3/\dot{Q}_1\right) + \left(\dot{W}_3/\dot{Q}_5\right)\left(\dot{Q}_5/\dot{Q}_1\right) + \left(\dot{W}_4/\dot{Q}_7\right)\left(\dot{Q}_7/\dot{Q}_1\right) \quad (13)$$

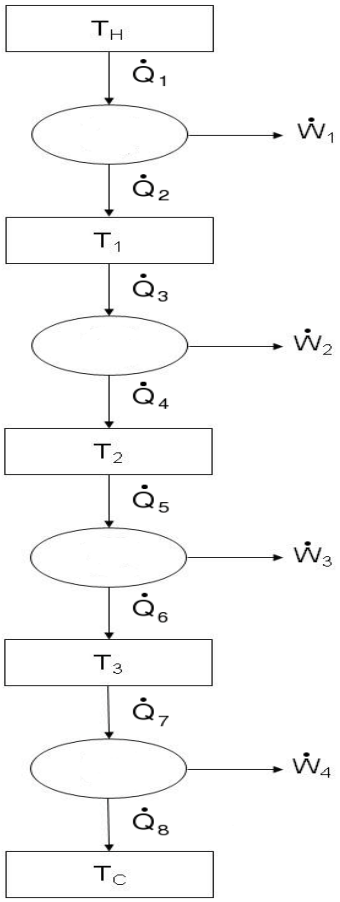

Fig. 2. Schematic diagram of an irreversible Carnot combined heat engine.

$$\eta = \eta_1 + \eta_2(1-\eta_1) + \eta_3(1-\eta_1)(1-\eta_2) + \eta_4(1-\eta_1)(1-\eta_2)(1-\eta_3) \quad (14)$$

where η_1, η_2, η_3 and η_4 are the efficiencies of the first, second, third and fourth cycles respectively. $\dot{W}_1$, $\dot{W}_2$, $\dot{W}_3$, and $\dot{W}_4$ are the powers produced by the combined cycle respectively. $\dot{Q}_1$ is the heat flow absorbed at temperature T_H and $\dot{Q}_3$ is the heat flow input to the second cycle, and so the other heat fluxes.

The first law of thermodynamics is used to analyse this system, and we obtain [12]

$$\dot{W}_1 = \dot{Q}_1 - \dot{Q}_2 \quad (15)$$
$$\dot{W}_2 = \dot{Q}_3 - \dot{Q}_4 \quad (16)$$
$$\dot{W}_3 = \dot{Q}_5 - \dot{Q}_6 \quad (17)$$
$$\dot{W}_4 = \dot{Q}_7 - \dot{Q}_8 \quad (18)$$
$$\dot{Q}_2 = \dot{Q}_3 \quad (19)$$
$$\dot{Q}_4 = \dot{Q}_5 \quad (20)$$
$$\dot{Q}_6 = \dot{Q}_7 \quad (21)$$
$$\dot{W} = \dot{W}_1 + \dot{W}_2 + \dot{W}_3 + \dot{W}_4. \quad (22)$$

Now, as we mentioned in section 1, for non-endoreversible engine, the second law of thermodynamics gives

$$\dot{Q}_1/T_H = R\,\dot{Q}_2/T_1 \quad (23)$$
$$\dot{Q}_3/T_1 = R\,\dot{Q}_4/T_2 \quad (24)$$
$$\dot{Q}_5/T_2 = R\,\dot{Q}_6/T_3 \quad (25)$$
$$\dot{Q}_7/T_3 = R\,\dot{Q}_8/T_C \quad (26)$$

where $\dot{Q}_2$ is the heat released from the first cycle to the reservoir at temperature T_1 and $\dot{Q}_4$ is the heat rejected from the second cycle to temperature T_2. $\dot{W}$ is the total power produced by the engine. Using (13)-(26), and after a little algebra (shows in Appendix B) the thermal efficiency of the combined engine, becomes

$$\eta = 1 - [T_C/(R^4 T_H)]. \quad (27)$$

Equation (23) is reduced to Carnot´s efficiency when R=1, i.e. reversible case. Now if the number of cycles is k (14) and (23) can be generalized as

$$\eta = \eta_1 + \eta_2(1-\eta_1) + \eta_3(1-\eta_1)(1-\eta_2) + \eta_4(1-\eta_1)(1-\eta_2)(1-\eta_3) + \cdots + \eta_k[(1-\eta_1)(1-\eta_2)(1-\eta_{k-1})] \quad (28)$$

and

$$\eta_k = 1 - \left[T_C/\left(R^k T_H\right)\right], \quad (29)$$

where k is cycles number.

In figure 3 we show the irreversibility effect in the efficiency for some values of R and T_C.

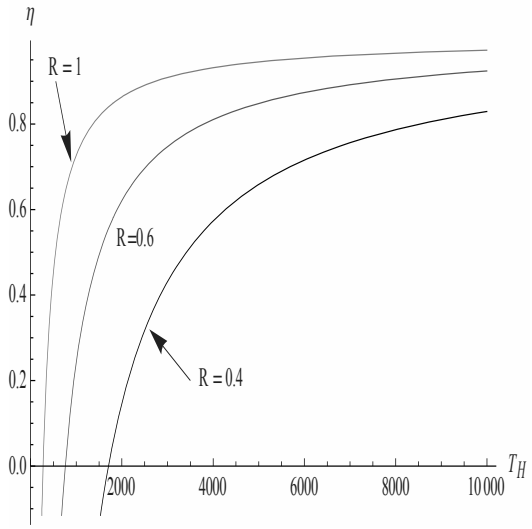

Fig.3. Plots of the three values of irreversibility parameter R and T_C=273C, using (27), these shows the irreversibility effect.

4. Comment

The interest of this work is regarding teaching and as an immediate application of FTT. Some results are taken from literature. Nevertheless, others are new obtained from the model. Here it is shown that real models can be approximate as a series of cycles working at maximum power output. The results could be considered for an irreversible engine. It is also important to remark that (27) is reduced to (12) when there is only one cycle.

References

[1] Carnot S, 1824, Reflexions sur la Puissance Motrice du Feu, et sur les Machines Propres Developer cette Puissance (Bachelier, Paris).

[2] De Vos, 1992, Endoreversible Thermodynamics of Solar Energy Conversion (Oxford University, Oxford).

[3] Wu, L. Chen, 1992 (Nova Science, New York), Recent Advances in Finite-time Thermodynamics.

[4] Curzon F. and Ahlborn B. 1975, Efficiency of a Carnot Engine at Maximum Power Output. Am. J. Phys. **43**, 22.

[5] Novikov I. I. 1958, J. Nuclear energy II 7, 125.

[6] Chambadal P. (Armand Colin, Paris, 1957), Les Centrales Nucleaires.

[7] Van der BroeckC. 2005, Thermodynamic Efficiency at Maximum Power Phys. Rev. Lett. **95** 6557.

[8] L A Arias-Hernández and F Angulo-Brown, 1994, A general property of endoreversibles thermal engines, Rev. Mex. Fis. **40**.

[9] F Angulo-Brown, L A Arias-Hernández and R Páez-Hernández, 1999, A general property of non-endoreversibles thermal engines, J. of Phys D: Appl. Phys. **32** 1415.

[10] Angulo-Brown F 1991, An Ecological Optimization Criterion for Finite time heat Engines J. Appl. Phys. **69** 7465.

[11] De Vos, A 1992, Endoreversible Thermodynamics of Solar Energy Conversion (Oxford:Oxford University Press).

[12] Göktun S and Yavuz H 1997, The optimum performance of an irreversible solar-driven Carnot refrigerator and combined heat engine J. Phys. D: Appl. Phys. **30** 3317.

Energetic Performance of an Irreversible Power Cycle in the Efficient–Power Working Regime

L. A. Arias–Hernandez [a], *M. A. Barranco–Jimenez* [b] *and F. Angulo–Brown* [a]

[a] *Escuela Superior de Física y Matemáticas del IPN, Ciudad de México, MÉXICO*
[b] *Escuela Superior de Cómputo del IPN, Ciudad de México, MÉXICO*

Abstract: In this work we show the results obtained from optimizing a completely irreversible power cycle model in the "Efficient Power Output" working regime. Starting from a model of an irreversible energy converter that operates in cycles, we build different characteristic functions. One of them is the "Efficient Power Output" used by Stucki (and later by Yilmaz). We compare the performance of the converter in this working regime with those of maximum power output, maximum efficiency and maximum ecological function, and we find that its power output is similar to that of maximum power output working regime, its efficiency is comparable to the maximum efficiency working regime, but its dissipation is bigger than the dissipation of the maximum ecological function working regime.

Keywords: Non-equilibrium and irreversible thermodynamics, Performance characteristics of energy conversion systems, figure of merit

1. Introduction

The experimental curves of power output versus efficiency of real energy converters are loop shaped curves [1]. These loop shaped curves contain all the physical operational points of these thermal engines, in agreement with the restrictions of their design (size and materials). However, most of these points lack of practical economic interest, because they correspond to working regimes of high power output but low efficiency, or high efficiency at low power output or low efficiency and low power output, including the operation point limit that corresponds to the state of thermodynamic equilibrium where the efficiency and power output are null. In all these points of operation the recovery of the investment or the maintenance costs of the energy converter elevate the price of the kilowatt-hour [2, 3]. From the above, it is deduced that the region of practical interest lies between the point of maximum power output and the point of irreversible maximum efficiency, because the points of operation inside this region can be points of operation of high efficiency and acceptable power output. On the other hand, the objective functions whose optimization corresponds to the realization of diverse objectives in the operation of the energy converters, supplement the information necessary that allows us to analytically find the characteristic functions for several operation modes. For this reason, in the technical literature have been proposed a wide variety of objective functions, for example, the power output and the efficiency [2, 3], but only the so–called Compromise Functions, like Ecological Function [4, 5, 6], Omega Function [7] and Efficient Power Output [8, 9], represent operation modes located in the region of practical interest [10]. In this work we study a completely irreversible power cycle under the Efficient Power Output working regime (defined as the power output times the efficiency). By means of our energy converter model we can reproduce the characteristic loop shaped curves observed by Gordon and Huleihil [1]. The motivation of this study resides in the fact that in the models in which this objective function has been used these loop shaped curves were not obtained [8, 9], and just indirect evidence is provided that this operation mode is within the practical region. With the purpose of accurately locating the Efficient Power Output operation point (MP_η) between those of Maximum Power Output (MP) and Maximum Efficiency ($M\eta$), several characteristic functions are calculated such as, absorbed heat, power output, efficiency and the so–called Compromise Function. Then we use them to describe the performance of the irreversible energy converter, and to determine if the model predictions under the MP_η–regime are reasonably close

Corresponding author: L. A. Arias–Hernandez, Email: larias@esfm.ipn.mx, larias0570@gmail.com

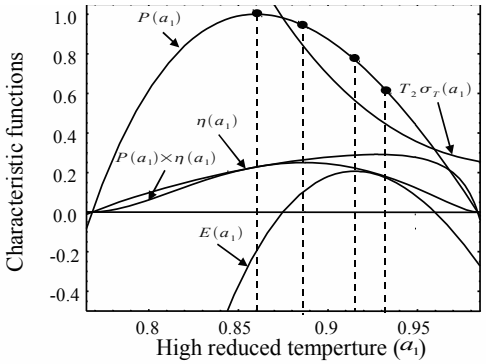

Figure 1: Characteristic functions of an irreversible power cycle. The points show the reduced temperatures that maximize each function.

to the experimental data of plants of electric generation.

2. Characteristic functions

To build the completely irreversible power cycle model we take a power cycle where the external irreversibilities are due to the transfer of heat among the work substance and the heat reservoirs at high temperature and low temperature respectively, while the working substance undergoes cycles that are irreversible due to viscosities, turbulences, Lenz's currents, etc. These phenomena contribute to the total entropy production with a term that is always positive. Then, the expression for this characteristic function is given by:

$$\sigma_t = \frac{Q_c}{T_2} - \frac{Q_a}{T_1} + \frac{Q_a}{T_{1t}} - \frac{Q_c}{T_{2t}} + \sigma_i > 0, \qquad (1)$$

with Q_a the flow of absorbed heat and Q_c the flow of heat rejected and where the following order relationship is satisfied among the temperatures of the reservoirs (T_i) and the temperatures of the working fluid (T_{it}): $T_1 > T_{1t} > T_{2t} > T_2 > 0$. Also, as the working fluid makes cycles, its entropy production should be null, this provides a connection among the external part and the internal part of the energy converter, given by the following equation:

$$\sigma_{st} = \frac{Q_a}{T_{1t}} - \frac{Q_c}{T_{2t}} + \sigma_i = 0, \qquad (2)$$

since the flows of heat are functions of the reservoirs' temperatures and the working fluid temperatures. Here it should be introduced the phenomenological law of heat transfer, the simplest election is the Newton's cooling law, so we obtain:

$$\frac{1-a_1}{a_1} - (1-a_2) + \frac{\sigma_i}{g} = 0. \qquad (3)$$

In this expression the definitions of the reduced temperatures have been introduced: $a_1 = T_{1t}/T_1$ is the "high reduced temperature" and $a_2 = T_2/T_{2t}$ the "low reduced temperature", we also have considered that the conductance g is the same one for the absorbed heat and the rejected heat.

From 3 it is possible to solve for the reduced temperature a_2 in terms of the reduced temperature a_1 and the irreversibility parameter defined as $f = \sigma_i/g$. With this equation we will be able to write the characteristic functions as functions of these variables. Then the flows of heat are written as:

$$Q_a = \alpha T_1 (1 - a_1) \qquad (4)$$

and

$$Q_c = \alpha T_1 \tau \left[\frac{a_1}{(2-f)a_1 - 1} - 1 \right], \qquad (5)$$

with $\tau = T_2/T_1$. Substituting the above equations into 1 and making the product with the lowest temperature in the system, we build the dissipation function of the power cycle:

$$\Phi = \alpha T_1 \tau \frac{(f-2)(a_1-2)a_1 - 2}{1 + (f-2)a_1}. \qquad (6)$$

Using the first law of the thermodynamics we find the power output of the irreversible cycle:

$$P = \alpha T_1 \left\{ 1 - a_1 - \tau \left[\frac{a_1}{(2-f)a_1 - 1} - 1 \right] \right\}. \qquad (7)$$

Also from the definition of thermal efficiency we get:

$$\eta = 1 - \tau \frac{1 + (f-2)a_1}{[1 + (f-2)a_1](a_1 - 1)}. \qquad (8)$$

If these characteristic functions present some point of interest can be themselves objective functions to optimize the operation of the cycle, or it is also possible to build linear combinations of them to obtain other objective functions to achieve some particular objective in the operation of the cycle. In Fig. 1 some of these objective functions are shown.

One of the first linear combination of characteristic functions that becomes an objective function, was the ecological function [4, 5],

$$E = P - \Phi. \qquad (9)$$

Several authors have shown that this function means a good compromise between the power output of the

cycle and their dissipation [4, 5, 6, 7]. This fact implies that a power cycle operated under the Maximum Ecological Function (ME) working regime has good economic properties compared with those of other regimes, for example, that of MP–regime or that of minimum dissipation function (*md*) regime [4, 5].

Finally, the objective function that we will analyze in this work is the Efficient Power Output, introduced by Stucki and later by Yilmaz [8, 9], given by:

$$P_\eta = P \times \eta. \tag{10}$$

From Fig. 1 we can observe, that this function is convex with only one maximum point, then a high reduced temperature exists that maximizes this function, it is in this reduced temperature where we will evaluate the characteristic functions (6, 7, 8) to study the energy performance of the power cycle under this operation regime. We follow the usual methodology in this type of studies [2, 3]. To find the optimal reduced temperatures, we will take the derivatives of each objective function respect to the high reduced temperature and solving for a_1 each equation,

$$\left.\frac{\partial P}{\partial a_1}\right|_{a_1^{MP}} = 0, \quad \left.\frac{\partial \eta}{\partial a_1}\right|_{a_1^{M\eta}} = 0, \quad \left.\frac{\partial E}{\partial a_1}\right|_{a_1^{ME}} = 0$$

and

$$\left.\frac{\partial P_\eta}{\partial a_1}\right|_{a_1^{MP_\eta}} = 0.$$

3. Energetic performance

In Fig. 1 we have marked on the corresponding curve to the power output ($P(a_1)$), the high reduced temperature a_1 corresponding to MP–regime, MP_η–regime, ME–regime and $M\eta$–regime respectively. We see that a hierarchy exists among the several power output points of each working regime of the irreversible power cycle model, i.e., if we evaluate the characteristic function "Power Output" (7) at the optimal reduced temperatures corresponding to each regime, we can draw these curves for the interval of reported values of τ ($\tau \in [0.3,\ 0.7]$) for actual generation plants and we observe that

$$P\left(a_1^{MP}\right) > P\left(a_1^{MP_\eta}\right) > P\left(a_1^{ME}\right) > P\left(a_1^{M\eta}\right). \tag{11}$$

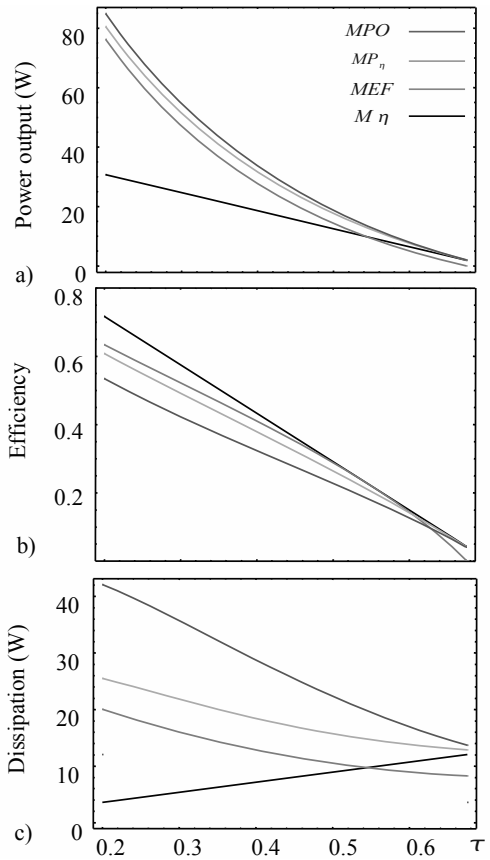

Figure 2: a) Power output for the $M\eta$–regime (black), ME–regime (red), MP_η–regime (green) and MP–regime (blue). b) Efficiency of the irreversible power cycle in each operation mode (in the same order that in the incise a). c) Dissipation of the irreversible irreversible power cycle (in the same order that in the incise a).

This is shown in the Fig. 2a, also in Fig. 2b the curves of the efficiencies and in Fig. 2c the curves of the dissipation of the irreversible power cycle corresponding to each regime are shown.

From the curves shown in Fig. 2 we can say that the power output corresponding to the MP_η–regime has a similar value to that corresponding to the MP–regime. On the other hand, and according to the above mentioned, the efficiency of the MP_η–regime is under both the efficincies corresponding to the $M\eta$–regime and ME–regime. Finally, as it was expected, the dissipation of the MP_η–regime is smaller than that of MP–regime, but bigger than the dissipation of the other two working regimes ($M\eta$ and ME). These results suggest that the MP_η–regime

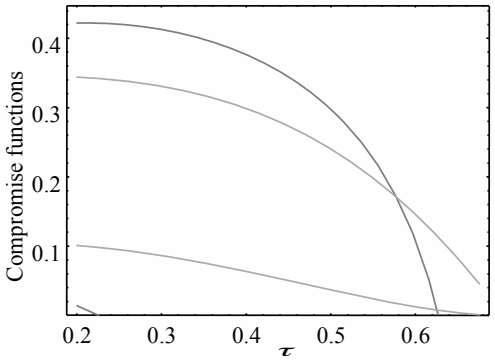

Figure 3: Compromise Functions. The superior curves corresponds to the relative distance between the power output and the dissipation, for the MP_η–regime (red) and ME–regime (green). The inferior ones corresponds to the relative distance among the power output and the efficiency in the corresponding operation modes (in the same order that in the case of the upper curves).

lies between the MP and $M\eta$–regimes. Thus, this working regime could mean a good compromise in the sense of the so–called compromise functions defined as [5, 6, 10],

$$C^i_{P-\Phi} = \frac{P\left(a_1^i\right)}{P\left(a_1^{MP}\right)} - \frac{\Phi\left(a_1^i\right)}{\Phi\left(a_1^{MP}\right)} \tag{12}$$

and

$$C^i_{P-\eta} = \frac{P\left(a_1^i\right)}{P\left(a_1^{MP}\right)} - \frac{\eta\left(a_1^i\right)}{\eta\left(a_1^{MP}\right)}, \tag{13}$$

with $i = MP_\eta,\ ME$. These curves are shown in Fig. 3. We observe that indeed the compromise that is achieved in the MP_η–regime is reasonably good, although the one achieved in the ME–regime is of better quality.

4. Conclusions

From the results obtained in this work, we can conclude that the MP_η working regime of a completely irreversible power cycle model has economic properties that locate it among the compromise operation modes, i.e., the power output in this regime is around 90% of the maximum that we can achieve in this model (MP–power output), while the decrease in its efficiency is not significant because it is around 80% of the maximum efficiency ($M\eta$–efficiency). The results obtained with this brief study shows that the information provided by the objective functions, allows us to analyze the energetic performance of these energy converters, yet under conditions of total irreversibility without knowing each detail of the cycle, and it is only necessary to take into account that the dissipation has only two contributions, the internal and external ones. We think that the results here reported can be used, for example, in studies as those made about the economical cost of the intermittence of the renewable energy sources [11].

References

[1] Gordon J.M. and Huleihil M. General Performance Characteristics of Real Heat Engines. *Journal of Applied Physics*, 72(3):829–837, 1992.

[2] Sieniutycs S. and Salamon P. *Finite Time Thermodynamics and Thermoeconomics*. Taylor and Francis, New York, USA, 1990.

[3] Chen L. Wu C. and Chen J. *Recent Advances in Finite-Time Thermodynamics*. Nova Science, New York, USA, 1999.

[4] Angulo-Brown F. An Ecological Optimization Criterion. *Journal of Applied Physics*, 69(11):7465–7469, 1991.

[5] Arias-Hernández L.A. and Angulo-Brown F. A General Property of Endoreversible Thermal Engines. *Journal of Applied Physics*, 81(7):2973–2979, 1997.

[6] Angulo-Brown F. and Arias-Hernández L.A. Reply to "Comment on 'A General Property of Endoreversible Thermal Engines' " [J. Appl. Phys. 89, 1518 (2001)]. *Journal of Applied Physics*, 89(2):1520–1521, 2001.

[7] Calvo-Hernández A. et al. Unified Optimization Criterion for Energy Converters. *Physical Review E*, 63(3):0371021–0371024, 2001.

[8] Stucki J.W. The Optimal Efficiency and the Economic Degrees of Coupling of Oxidative Phosphorylation. *European Journal of Biochemstry*, 109(1):269–283, 1980.

[9] Yilmaz T. A New Performance Criterion for Heat Engines: Efficient Power. *Journal of the Energy Institute*, 79(1):38–41, 2006.

[10] Arias-Hernandez L.A. et al. First–Order Irreversible Thermodynamic Approach to a Simple Energy Converter. *Physical Review E*, 77(01):0111231–0111238, 2008.

[11] Barranco-Jiménez M.A. et al. Study on the Intermittence of Certain Energy Sources Based on a Nonendorreversible Power Plant. S. A. Nebra, S. Oliveira, eds., *Proceedings of ECOS 2009*, pages 79–88, Foz do Iguaçu, 2009, ABMC.

Acknowledgments: SIP–COFAA–EDI–IPN–MÉXICO and CONACYT–SNI–MÉXICO.

AUTHOR'S INDEX

KEYWORD'S INDEX

ecos 2010

SPONSORS

ÉCOLE POLYTECHNIQUE FÉDÉRALE DE LAUSANNE

Schweizerische Eidgenossenschaft
Confédération suisse
Confederazione Svizzera
Confederaziun svizra

Office fédéral de l'énergie OFEN

INSTITUTIONAL PARTNERS

Lausanne

canton de vaud
LIBERTÉ ET PATRIE

TECHNICAL PARTNERS

ALPIQ

ecleer

HOLDI GAZ

BG
Ingénieurs Conseils
Ingenieure & Berater
Consulting Engineers

SUPPORTING ORGANIZATION

ASME
SETTING THE STANDARD

International centre for applied thermodynamics
ICAT
1997